WILEY-VCH

Edited by
Gernot Frenking and Sason Shaik

The Chemical Bond

Chemical Bonding Across the Periodic Table

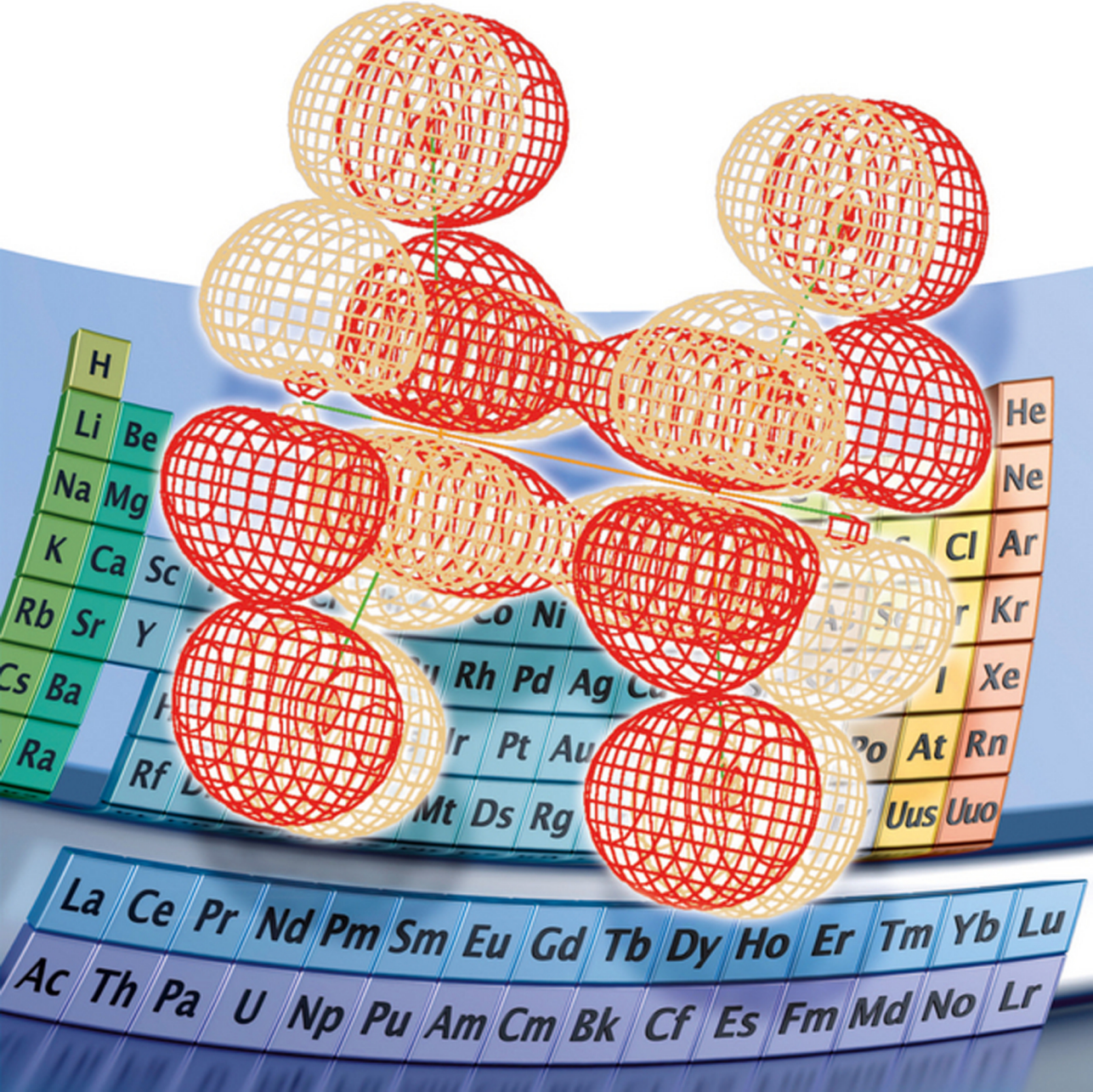

Edited by Gernot Frenking and Sason Shaik

The Chemical Bond

Related Titles

Frenking, G., Shaik, S. (eds.)

The Chemical Bond
Fundamental Aspects of Chemical Bonding

2014
ISBN: 978-3-527-33314-1;
also available in digital formats

Reiher, M., Wolf, A.

Relativistic Quantum Chemistry
The Fundamental Theory of Molecular Science
Second Edition

2014
Print ISBN: 978-3-527-33415-5;
also available in digital formats

Fleming, I.

Molecular Orbitals and Organic Chemical Reactions – Student Edition

2009
Print ISBN: 978-0-470-74659-2;
also available in digital formats

Matta, C.F., Boyd, R.J. (eds.)

The Quantum Theory of Atoms in Molecules
From Solid State to DNA and Drug Design

2007
Print ISBN: 978-3-527-30748-7;
also available in digital formats

Edited by Gernot Frenking and Sason Shaik

The Chemical Bond

Chemical Bonding Across the Periodic Table

WILEY-VCH
Verlag GmbH & Co. KGaA

Editors

Prof. Dr. Gernot Frenking
Philipps-Universität Marburg
FB Chemie
Hans-Meerwein-Strasse
35032 Marburg
Germany

Prof. Dr. Sason Shaik
Hebrew University
Institut of Chemistry
Givat Ram Campus
91904 Jerusalem
Israel

Library of Congress Card No.: applied for

British Library Cataloguing-in-Publication Data
A catalogue record for this book is available from the British Library.

Bibliographic information published by the Deutsche Nationalbibliothek
The Deutsche Nationalbibliothek lists this publication in the Deutsche Nationalbibliografie; detailed bibliographic data are available on the Internet at <http://dnb.d-nb.de>.

Print ISBN: 978-3-527-33315-8
ePDF ISBN: 978-3-527-66468-9
ePub ISBN: 978-3-527-66467-2
mobi ISBN: 978-3-527-66466-5
oBook ISBN: 978-3-527-66465-8

Cover-Design Adam-Design, Weinheim
Typesetting Laserwords Private Limited, Chennai, India
Printing and Binding betz-druck GmbH, Darmstadt

Printed on acid-free paper

Contents

Preface

The chemical bond is the backbone of chemistry. It defines chemistry as the science of understanding and transformation of the physical world in terms of interatomic interactions, which are considered as chemical bonds. Thus, chemistry appears right at the beginning as a fuzzy discipline because the distinction between chemical and nonchemical interatomic interactions is not exactly defined, which creates ongoing controversial debates. But the fuzziness of chemical bonding posed no obstacle for the advancement of chemical research from an esoteric playground to a highly sophisticated academic discipline, which became the basis for industrial growth and economic wealth. In the absence of a physical understanding of chemical bonding, chemists used their imagination and creativity for designing models that proved to be very useful for rationalizing experimental observations.

The development of chemical bonding models, which is an integral part of the progress in experimental chemistry, is a fascinating chapter in the history of mankind. It goes beyond the mere realm of natural science and is part of the evolution of human culture. Chemists analyzed and synthesized in the past centuries a steadily increasing number of new compounds, which required a systematic ordering system to become comprehensible. In order to understand the enormous diversity of molecules and solids, which constitute the chemical universe, chemists developed bonding models that served two purposes. One purpose was to provide an understanding for the observed species, which were classified according to well-defined rules. The second purpose was to establish a guideline for new experiments; a goal that needed a scientific hypothesis in order to distinguish research from random activity.

Originally, chemists suggested bonding models that appeared as simple sketches of connections between atoms that were finally recognized as the elementary building blocks of molecules and solids. The heuristically developed models were continuously refined like a neural network where experimental observations and hypotheses served as guidelines for improving the patterns and archetypes that were used to rationalize new findings. Already in the nineteenth century, chemists realized that atoms might possess different valencies for the formation of chemical bonds without knowing their physical meaning. It is amazing how much progress was made in experimental chemical research without actually knowing much about the constitution of atoms and the nature of the interatomic interactions. The

bonding models became the language by which chemists circulate information about molecular structures and reactivities using simple terms that were refined along with the progress in chemical research.

An important step for bridging the gap between chemistry and physics was made in 1916 when G.N. Lewis suggested that the bond line which so far was only used as pictorial representation for a chemical bond without physical meaning, should be identified with a pair of electrons. Lewis knew that his suggestion did not explain the nature of the chemical bond in terms of basic laws of physics, because the classical expression for electrostatic interactions did not agree at all with experimental data. Lewis proposed his model despite the defiance of the physical laws, because of his firm belief that the immense body of chemical facts supported his idea (e.g., the preponderance of molecules with an even number of electrons). Thus, to justify his belief, he postulated that in the atomic world *there might be different forces* than in the macroscopic world. This intuitively derived model of electron-pair bonding is still the most commonly used archetype for a chemical bond. He could not have foreseen the revolution, which followed from quantum theory that was introduced by Schrödinger and Heisenberg in 1926. One year later, Heitler and London published their landmark paper where they applied quantum theory to describe the interactions between two hydrogen atoms in the bonding and antibonding state of H_2. It was the birth of quantum chemistry, which provided the first physically sound description of the covalent chemical bond.

It is remarkable that the work by Heitler and London that outlined for the first time a physically correct description of the chemical bond did not replace the Lewis picture of electron-pair bonding that was based on intuition rather than on elementary physics. One reason is the dramatically different appeal of the two approaches for human imagination of the chemical bond. The Lewis picture is simple to use and it proved as extremely powerful ordering scheme for molecular structures and reactivities. Chemists are generally happy with such models. The quantum theoretical description of interatomic interactions introduced the wave function Ψ as the central term for chemical bonding, which is in contrast an elusive object for human imagination, as evidenced by the intensive discussions about the meaning and the interpretation of Ψ mainly in the physics community.

An important step for building a bridge between the Lewis picture of chemical bonding and quantum theory was made by Pauling in his seminal book *The Nature of the Chemical Bond*, which was published in 1939. Pauling's work showed that the heuristically derived electron-pair paradigm of Lewis could be dressed by quantum theory keeping the notion of localized bonds in terms of the valence bond (VB) approach. It is thus not surprising that the VB model was well accepted by the chemical community, which quickly adapted the VB notions such as resonance and hybridization for discussing molecular structures and reactivities. The alternative approach of molecular orbital (MO) theory that was developed by Mulliken and Hund was initially met with scepticism by most chemists, because the picture of a localized chemical bond did not seem to be contained in the delocalized MOs. The resistance against MO theory did not change by the fact that phenomena

such as the stability of aromatic compounds and spectroscopic data could easily be explained with MOs.

The situation gradually changed during the 1950s till the 1970s, when the advantages of implementing the MO theory became more and more apparent. The development of computer codes by Dewar and Pople, first for semiempirical approaches and then for *ab initio* methods, paved the way for the acceptance of MO methods. MO theory could much easier become coded into computer programs, which along with the dramatic development of computer hardware produced numerical results with increasing accuracy. Ruedenberg showed that the delocalized MOs could be converted into localized orbitals via unitary transformations, which recovered the Lewis picture even from MO calculations. The breakthrough came with the big success of MO theory of not only explaining but also predicting the reaction course and the stereochemistry of pericyclic reactions. The MO-based frontier orbital theory and Woodward–Hoffmann rules became a standard model for chemical bonding and reactivity, which culminated in awarding the 1981 Nobel Prize to Kenichi Fukui and Roald Hoffmann.

While VB theory nearly disappeared during that time from the horizon of quantum chemistry, it remained remarkably alive in the description of molecular structures and bonding by experimental chemists. In spite of the sweeping success of MO-based quantum chemical methods, which were increasingly used by the general chemical community, the qualitative models that chemists continued to use for sketching molecules and chemical reactions rested often on the picture of localized two-electron bonds. This is because of the unsurpassed simplicity and usefulness of the Lewis bonding model and the associated rules. What can be observed in 2014 is a complementary coexistence of VB and MO models, where the choice of a chemist for answering a question depends on the particular problem and his preference for a specific approach. Also, there has been a remarkable renaissance of VB methods in recent years, which provide an arsenal of bonding models that have been very helpful for explaining molecular structures and reactivities.

The development of quantum chemical methods focussed for a long time on more accurate techniques and efficient algorithms for obtaining numerical results for increasingly larger molecules and for the calculation of reaction pathways. The famous request by Charles Coulson *Give us insight, not numbers* seemed to have been buried under the quest for more reliable data and little attention was paid to the interpretation of the calculated numbers. The situation has clearly changed in the past two decades. Numerous methods were developed, which aimed at building a bridge between the wealth of numerical data and conceptual models that convert the calculated results into a qualitative understanding of molecular structures and reactivities. Quantum theoretical results can often be presented in terms of figures and schemes rather than merely by presenting tables with numbers, which appeals to the aptitude of most experimental chemists for sensory perception. This does not mean that traditional models such as the Lewis electron pair for chemical bonding have to be abandoned. On the contrary, well-defined partitioning schemes have been introduced, which make it possible to assign calculated numbers that come from accurate quantum chemical calculations to classical concepts replacing

handwaving arguments. Although such numbers are not measurable values, they can often be interpreted in terms of physically meaningful expressions, which provide a well-defined ordering scheme for molecular structures and reactivities.

Volume 1 of this book has 11 chapters that present and discuss the physical understanding of the chemical bond and introduce the most important methods that are presently available for the interpretation of molecular structures and reactivities. On the other hand, Volume 2 has 18 chapters, which describe the application of modern theoretical models to chemical bonding in molecules containing main elements, transition metals, and lanthanides and actinides, including clusters, solids, and surfaces across the periodic table. An important section of Volume 2 is dedicated to the weak interactions, such as dispersion, halogen bonding, and hydrogen bonding.

There is some overlap between some chapters, which is intended. Chemical bonding can be described with several models and it is sometimes useful to consider it from different perspectives. In judging the performance of different methods one should consider the device that bonding models are not right or wrong, they are more or less useful. It was the goal of the editors to give a comprehensive account of the present knowledge about the chemical bond and about the most important quantum chemical methods, which are available for describing chemical bonding. The two volumes of *The Chemical Bond* are intended to be an authoritative overview of the state-of-the-art of chemical bonding.

Marburg, Germany — *Gernot Frenking*
Jerusalem, Israel — *Sason Shaik*

List of Contributors

Pere Alemany
Universitat de Barcelona
Institut de Química Teòrica i Computacional (IQTCUB) and Departament de Química Física
Diagonal 647
08028 Barcelona
Spain

Katharina Boguslawski
ETH Zurich
Laboratorium für Physikalische Chemie
Vladimir-Prelog-Weg 2
8093 Zurich
Switzerland

and

McMaster University
Department of Chemistry and Chemical Biology
1280 Main Street West
Hamilton
Ontario L8S 4M1
Canada

Alexander I. Boldyrev
Utah State University
Department of Chemistry and Biochemistry
0300 Old Main Hill
Logan, UT 84322-0300
USA

Enric Canadell
Institut de Ciència de Materials de Barcelona (ICMAB-CSIC)
Campus de la UAB
08193 Bellaterra
Spain

Timothy Clark
Computer-Chemie-Centrum der Friedrich-Alexander-Universitaet Erlangen-Nürnberg
Nägelsbachstrasse 25
91052 Erlangen
Germany

and

University of Portsmouth
Centre for Molecular Design
King Henry Building
King Henry I Street
Portsmouth PO1 2DY
United Kingdom

David Danovich
The Hebrew University
Institute of Chemistry and the
Lise-Meitner Minerva Center for
Computational Quantum
Chemistry
Edmond J. Safra Campus
91904 Jerusalem
Israel

Thom H. Dunning Jr.
University of Illinois
Department of Chemistry
600 S. Mathews Avenue
Urbana, IL 61801
USA

Israel Fernández
Universidad Complutense de
Madrid
Departamento de Química
Orgánica
Facultad de Ciencias Químicas
Avda. Complutense s/n
28040 Madrid
Spain

Ivo A. W. Filot
Eindhoven University of
Technology
Institute for Complex Molecular
Systems and Laboratory for
Inorganic Materials Chemistry
5600 MB Eindhoven
The Netherlands

Gernot Frenking
Philipps-Universität Marburg
Fachbereich Chemie
Hans-Meerwein-Strasse
35032 Marburg
Germany

Laura Gagliardi
University of Minnesota
Department of Chemistry
Supercomputing Institute
and Chemical Theory Center
Minneapolis MI 55455
USA

Stefan Grimme
Mulliken Center for Theoretical
Chemistry
Institut für Physikalische und
Theoretische Chemie
der Universität Bonn
Beringstr.4
53115 Bonn
Germany

Rainer Herges
University of Kiel
Otto Diels-Institute for
Organic Chemistry
24118 Kiel
Germany

Hajime Hirao
Nanyang Technological
University
Division of Chemistry and
Biological Chemistry
School of Physical and
Mathematical Sciences
21 Nanyang Link 637371
Singapore

Eluvathingal D. Jemmis
Indian Institute of Science
Department of Inorganic and
Physical Chemistry
Bangalore 560012
India

Nikolas Kaltsoyannis
University College London
Christopher Ingold Laboratories
Department of Chemistry
20 Gordon Street
London WC1H 0AJ
UK

Martin Kaupp
Technische Universität Berlin
Institut für Chemie
Theoretische
Chemie/Quantenchemie
Sekr. C7
Strasse des 17. Juni 115
10623 Berlin
Germany

Andrew Kerridge
University College London
Christopher Ingold Laboratories
Department of Chemistry
20 Gordon Street
London WC1H 0AJ
UK

Ivan A. Popov
Utah State University
Department of Chemistry and
Biochemistry
0300 Old Main Hill
Logan, UT 84322-0300
USA

Chakkingal P. Priyakumari
Indian Institute of Science
Education and Research
Thiruvananthapuram
School of Chemistry
CET Campus
Thiruvananthapuram
Kerala 695 016
India

Markus Reiher
McMaster University
Department of Chemistry and
Chemical Biology
1280 Main Street West
Hamilton
Ontario L8S 4M1
Canada

Rutger A. van Santen
Eindhoven University of
Technology
Institute for complex molecular
sciences and Laboratory for
Inorganic Materials Chemistry
5600 MB Eindhoven
The Netherlands

Sason Shaik
The Hebrew University
Institute of Chemistry and the
Lise-Meitner Minerva Center for
Computational Quantum
Chemistry
Edmond J. Safra Campus
91904 Jerusalem
Israel

Ralf Tonner
Philipps-Universität Marburg
Fachbereich Chemie
Hans-Meerwein-Strasse
35032 Marburg
Germany

Xiaoqing Wang
Nanyang Technological University
Division of Chemistry and Biological Chemistry
School of Physical and Mathematical Sciences
21 Nanyang Link
Singapore 637371

David E. Woon
University of Illinois
Department of Chemistry
600 S. Mathews Avenue
Urbana, IL 61801
USA

1
Chemical Bonding of Main-Group Elements

Martin Kaupp

1.1
Introduction and Definitions

Prior to any meaningful discussion of bonding in main-group chemistry, we have to provide a reasonably accurate definition of what a main-group element is. In general, we assume that main-group elements are those that essentially use only their valence s- and p-orbitals for chemical bonding. This leads to a number of borderline cases that require closer inspection. Assuming that the *outer* d-orbitals, that is, those with principal quantum number n equal to the period in question, are not true valence orbitals (see discussion of *outer* d-orbital participation in bonding later in the text), we may safely define groups 13–18 as main-group elements. Group 1 is also reasonably assigned to the main groups, albeit under extreme hydrostatic pressures it appears that the elements K, Rb, and Cs turn from ns^1 metals into transition metals and use predominantly their *inner* $(n-1)$ d-orbitals for bonding [1]. However, sufficiently high pressures may change fundamental bonding in many elements and compounds [2]. We disregard here such extreme pressure conditions and count group 1 in the main groups.

Matters are less straightforward for group 2: whereas Be and Mg utilize only their s- and p-orbitals, Ca, Sr, Ba, and Ra use their *inner* $(n-1)$ d-orbitals predominantly in covalent bonding contributions when sufficiently positively charged, as we discuss in the following text [3]. This leads to a number of peculiar structural features that bring these elements into the realm of ''non-VSEPR d^0 systems'' that encompass early transition elements and even lanthanides, and they have also been termed ''honorary d-elements'' [4]. The heavy group 2 elements are nevertheless usually placed with the main groups, and it seems appropriate to include the discussion of these interesting features in the last section of this chapter.

It thus remains to discuss the inclusion of groups 11 and 12. The group 11 elements Cu, Ag, Au, and Rg clearly have a too pronounced involvement of their $(n-1)$ d-orbitals in bonding, even in their lower oxidation states, to be safely considered main-group elements. The group 12 elements Zn, Cd, Hg, and Cn are usually considered to be main-group or ''post-transition'' elements. Yet recently quantum-chemical predictions [5] of oxidation-state Hg(+IV) in the form of the

The Chemical Bond: Chemical Bonding Across the Periodic Table, First Edition.
Edited by Gernot Frenking, Sason Shaik.

molecular tetra-fluoride have been confirmed by low-temperature matrix-isolation IR spectroscopy [6]. This molecule is clearly a low-spin square-planar d^8 complex and thus a transition-metal species. Other, less stable Hg(+IV) compounds have been examined computationally [7], and calculations predict that the tetra-fluoride should be yet more stable for Cn (eka-Hg, element 112) [8]. However, in the largest part of the chemistry of these two elements, and in all of the accessible chemistry of Zn [9] and Cd, d-orbital participation in bonding is minor. We note in passing that Jensen [10] has vehemently opposed assignment of mercury to the transition metals based on the ''extreme conditions'' of the low-temperature matrix study of HgF_4. The present author disagrees with this argument, as the role of the matrix is only to separate the HgF_4 molecules from each other and to thus prevent aggregation and stabilization of HgF_2. The low temperature is admittedly needed for entropic reasons. It is large relativistic effects that render the borderlines between the later d-elements and the main groups fuzzy in the sixth and seventh period. We nevertheless agree that the oxidation state +IV of Hg or Cn is an exception rather than the rule in group 12 chemistry, and thus discussion of the more ''regular'' bonding in group 12 belongs to this chapter.

If d-orbital participation in bonding is absent or at least an exception, main-group bonding may be considered simpler than that for transition-metal and f-element species. Although this is true from a general viewpoint, the variety of unusual bonding situations in main-group chemistry is nevertheless fascinating, ranging from the more common localized situations encountered in organic chemistry to delocalized bonding in, for example, electron-poor borane clusters or electron-rich noble-gas compounds to situations with even more complicated bonding-electron counts, for example, for radical-ion species or the bonding situations that may be envisioned for amorphous carbon [11]. We observe that the relative sizes of the valence s- and p-orbitals crucially influence periodic trends, and that hybridization is a more complicated matter than usually considered. In this chapter we focus mostly on general aspects and periodic anomalies, providing a basis for more specific discussions in some of the other chapters of this book.

1.2
The Lack of Radial Nodes of the 2p Shell Accounts for Most of the Peculiarities of the Chemistry of the 2p-Elements

The eigenfunctions of a Hermitean operator form a (complete) orthonormal set. This seemingly abstract mathematical condition is fundamental for the presence of nodes in wave functions. The nodes are needed to ensure orthogonality of the, exact or approximate, solutions of the Schrödinger equation. From the simplest examples like a particle in a box (closely related to the nodal characteristics of valence orbitals of extended π-systems), it is a short way to the radial and angular eigenfunctions of the hydrogen atom, which also define qualitatively the nodal structure of the atomic orbitals (AOs) of many-electron atoms. Orthogonality of AOs may be ensured either via the angular part (determined by the quantum numbers l and m_l) or via

the radial part (determined by quantum number n). AOs with different angular momentum are generally orthogonal via their angular part. But valence (and outer core) AOs with increasing principal quantum number n develop nodes in their radial part to stay orthogonal to inner orbitals (with lower n) of the same angular momentum. Although this is exactly true only for the isolated atom, where n, l, and m_l are good quantum numbers, it also carries over approximately to atoms in molecules, with strong consequences for chemistry. The introduction of radial nodes by this ''primogenic repulsion'' [12] (a term indicating the necessity of staying orthogonal to the inner shells) moves the outer maximum of a radial wave function successively outwards, which makes it more diffuse. At the same time, we have to recall that the radial solutions of the Schrödinger equation for the hydrogen atom may also be written as an effective differential equation of a particle in an l-dependent potential. This effective potential contains a repulsive term due to centrifugal forces for $l \geq 1$ but not for $l = 0$. As a consequence, s-orbitals have finite amplitude at the nucleus, whereas p-, d- or f-orbitals vanish at the nucleus (within a nonrelativistic framework). However, most importantly for the present discussion, the repulsive centrifugal term moves the outer maximum of the p-orbitals to larger radii. Therefore, np-orbitals tend to be larger and more diffuse than the corresponding ns-orbitals, with the major exception of $n = 2$ – because of the lack of a radial node, the 2p-orbital is actually similar in size to the 2s-orbital, which has one radial node to stay orthogonal to the 1s-shell [13]. The approximate relative sizes of the valence s- and p-orbitals in period 2 and 3 many-electron atoms from relativistic Hartree–Fock calculations are shown in Figure 1.1. On average, the 2p-orbitals are less than 10% larger than the 2s-orbitals, whereas the 3p-orbitals

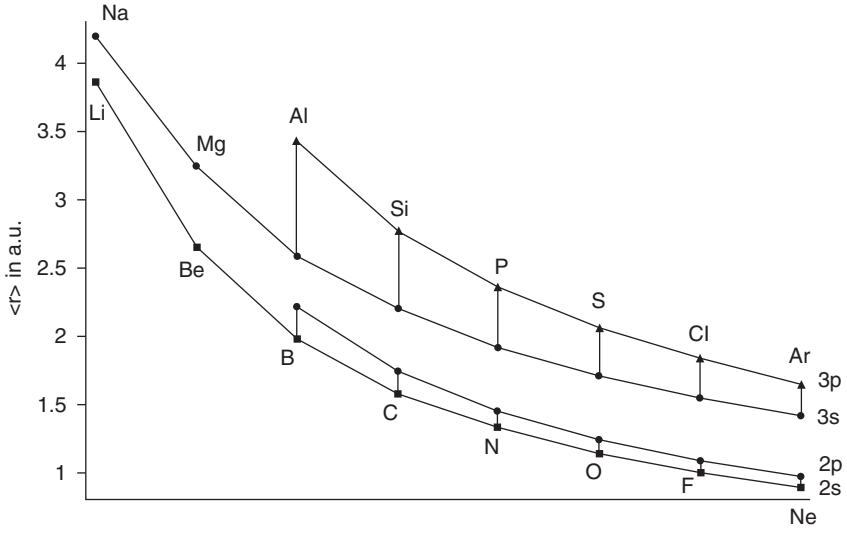

Figure 1.1 Radial expectation values for the valence s- and p-orbitals in periods 2 and 3 of the periodic table (approximate numerical Dirac-Hartree-Fock values from Ref. [14]). Figure adapted from Ref. [13].

exceed the 3s-orbitals by 20–33%. Differences increase further down a given group (modified by spin-orbit coupling for the heavier elements) [13].

The similarity of the radial extent of 2s- and 2p-shells is a decisive factor that determines the special role of the 2p-elements within the p-block, and the main consequences will be discussed further below. We note in passing that the lack of a radial node of the 3d-shell and the resulting small radial extent is crucial for many properties of the 3d-elements, and the nodelessness and small size of the 4f-shell is important for lanthanide chemistry [15]. Finally, the lack of a radial node of the 1s-AO distinguishes H and He from all other elements of the Periodic Table, with far-reaching consequences (different ones for H and He) for their chemistry. These aspects have been discussed elsewhere [16].

1.2.1 High Electronegativity and Small Size of the 2p-Elements

Because of the small r-expectation value of the nodeless 2p-shell, the valence electrons of the 2p-block elements tend to move on average particularly close to the positive nuclear charge. Shielding by the 1s- and 2s-shells is relatively poor, leading to high ionization potentials and electron affinities and, hence, high electronegativity. Indeed, the electronegativities (ENs) of the p-block elements are known to exhibit a particularly large decrease from the second period (first row) to the third period (second row). This holds for all EN scales, with vertical jumps increasing from left to right in the row (from a difference of about 0.4 between B and Al to one of about 0.9–1.0 between F and Cl), consistent with the higher percentage of p-character and the smaller size of the orbitals for the elements further to the right in a given row. The further drop from the third to the lower periods is much less pronounced and nonmonotonous, for reasons discussed later in the text. This makes it already obvious that the nodelessness and small size of the 2p-shell is decisive for rendering the 2p-block elements different from their heavier homologues. The overall small size of the 2p-elements can be appreciated from any tabulation of atomic, ionic, or covalent radii. Again, a jump from the 2p- to the 3p-elements is apparent, with much less pronounced increases (in some cases small decreases from 3p to 4p, see following text) towards the heavier p-block elements. This does of course in turn lead to overall lower coordination-number preferences of the 2p-element, as is well known. The smaller radii *and* the high electronegativities of the 2p-elements are behind their strict obediance of the octet rule, in contrast to the apparent behavior of their heavier homologues, as will be discussed in more detail later in the text.

1.2.1.1 Hybridization Defects

In addition to the *absolutely* small size of the 2p-shell, the *relative* similarity of its radial extent to that of the 2s-orbital (see earlier text) is crucial for understanding the differences between the 2p-elements and their heavier congeners. Covalent bonding is often discussed using the tools of valence-bond (VB) theory (see Chapter 5 in Volume 1), and hybridization is a main requirement of VB models. Kutzelnigg, in

his classical article on bonding in higher main-group elements in 1986 [13], has pointed out that the assumptions of isovalent hybridization are only fulfilled for mutually orthogonal hybrids at a given atom. This orthogonality in turn is only achievable to a good approximation when, for example, the valence s- and p-orbitals of a p-block main-group element exhibit comparable overlap with the orbitals of the bonding partner, that is, when they have comparable radial extent. And, as we have seen above, this is the case only in the 2p-series because of the nodelessness of the 2p-shell, whereas for the heavier p-block elements the centrifugal term in the effective potential makes the *n*p-orbitals significantly larger than the *n*s-orbitals (Figure 1.1). Then isovalent hybridization becomes much less favorable. To save the concept of hybridization, it then becomes unavoidable to drop the orthogonality requirement, and Kutzelnigg has introduced the term ''hybridization defects'' and a corresponding mathematical definition for the deviations from ideal, orthogonal, isovalent hybrids [13, 17]. However, the use of non-orthogonal hybrids for the heavier main-group elements in turn wipes out the well-known and still widely used relations between hybridization and bond angles and leads to very different p/s hybridization ratios than one might expect at first glance from structures. It appears that even more than 25 years after Kutzelnigg's milestone paper many chemists are not yet aware of these considerations, and inorganic-chemistry text books tend to ignore these aspects (but see Refs [16, 18]). We thus describe the obvious consequences of large hybridization defects for the heavier p-block elements and their relative smallness for the 2p-series in some detail here. Note that the question of orthogonality of hybrids and thus of hybridization defects arises also when considering bonding in transition-metal complexes from a VB point of view [3, 16]. Here it is mainly the ($n-1$) d- and *n*s-orbitals that are involved in bonding (see Chapter 7 in this book). It is obvious that their radial extent will not be comparable in all cases, and thus hybridization defects have to be taken into account.

Most practical quantum-chemical calculations use some flavor of molecular-orbital (MO) theory, in recent years in particular within the framework of Kohn–Sham density functional theory. Within MO theory, hybridization is not needed. But to connect to the widely used qualitative hybridization arguments, we can extract local hybridizations a posteriori by using some kind of population analysis. The prerequisite is that we can analyze well-localized MOs. In other words, small ''localization defects'' are required (i.e., Hund's localization condition should be fulfilled reasonably well) [13]. Then we can analyze the hybridization of some kind of localized MOs. The choice of localized MOs and of population analysis does of course to some extent determine the numerical values of the hybridization ratios we get from such analyses, but the qualitative conclusions obtained by different methods are similar. Kutzelnigg in 1986 [13] used Boys' localization [19] and Mulliken populations [20]. The latter have the disadvantage of exhibiting strong basis-set dependencies. A widely used, and nowadays readily available, approach is to consider the natural atomic orbital (NAO) hybridizations of natural localized Molecular Orbitals (NLMOs) within Weinhold's natural bond orbital (NBO) scheme [21]. We note in passing that, although the outcome of the

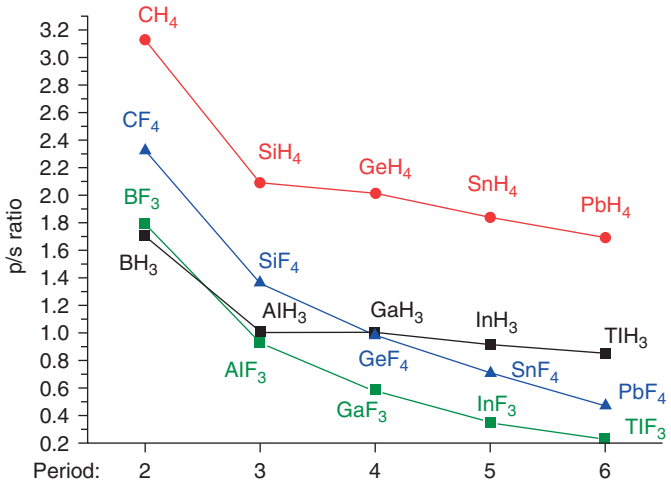

Figure 1.2 NAO/NLMO p/s hybridization ratios for hydrides and fluorides of second and third period elements in their maximum oxidation state (B3LYP/def2-TZVP results).

NBO scheme for d-orbital participation in main-group chemistry (see later text) might to some extent be biased by placing the outer d-orbitals into the "natural Rydberg set" of the NAO scheme [22], no such problem arises regarding the relative role of s- and p-orbitals. Figure 1.2 illustrates the NAO/NLMO p/s hybridization ratios of some simple compounds when moving down a given p-block main group. Starting with simple homoleptic hydrogen compounds in the maximum oxidation state of the central element (Figure 1.2; lone pairs are absent), we see clearly that the 2p-compounds exhibit hybridizations that correspond reasonably well to those expected from the bond angles and the usual formal considerations. This holds notably well for hydrocarbons, in line with the relative success and popularity of using bond angles to discuss hybridization (and vice versa) in organic chemistry. In contrast, the 3p- or 4p-compounds exhibit much larger *n*s- and lower *n*p-character in their bonding hybrids. It is clear, that here the usual simple relations between bond angles and central-atom hybridization cease to function.

Replacing hydrogen by fluorine as bonding partner (Figure 1.2) leads to a drastic reduction of the p/s ratios. Obviously, hybridization defects are enhanced significantly by the more electronegative fluorine substituents [23, 24] (for as yet unclear reasons, BF_3 is an exception to this rule). This goes parallel to strongly positive charges of the central atoms. As the central atom contracts, the sizes of its s- and p-orbitals become even more disparate: the contraction of the valence s-orbitals is more pronounced than that of the p-orbitals. This has further consequences for the bonding and chemistry of such compounds (see below). Note that even for a carbon compound like CF_4, hybridization defects are now already pronounced, and relations between bond angle and hybridization are not straightforward anymore. This also means that the assumptions of Bent's rule [25] on the

relations between bond angles and hybridization for heteroleptically substituted systems have to be modified to account for such hybridization defects.

1.2.2
The Inert-Pair Effect and its Dependence on Partial Charge of the Central Atom

Hybridization defects cause a general weakening of covalent bonds. This is related to the fact that hybridization is effective in stabilizing molecules by (i) improving bonding orbital overlaps and by (ii) minimizing destabilizing antibonding interactions [13]. Hybrids made from s- and p-orbitals with too dissimilar sizes are ineffective for both of these aspects and, thus, make poor covalent bonds (the overall benefits from hybridization may also decrease further down the group [13]). This affects, in particular, compounds of the heavier p-block elements in their maximum oxidation state. Here the valence s-orbital *has to be involved in bonding* and, thus, is required to hybridize to some extent with the p-orbitals. In contrast, in lower oxidation states, the valence s-character of the heavy p-block element tends to accumulate in a non-bonding lone-pair (lp) type orbital, and the bonds tend to be made largely by essentially unhybridized p-orbitals. This is more favorable for making stable bonds. The latter relationships can be extracted easily from the p/s hybridization ratios of ammonia and its heavier homologues in Figure 1.3: whereas isovalent hybridization is still effective for ammonia itself, the segregation into a lone-pair NLMO of predominant s-character and bonds with predominant p-character is apparent for the heavier homologues. Fluorine substitution does again enhance hybridization defects, and thus isovalent hybridization is largely absent now even for NF_3.

These observations provide a modern framework for rationalizing the inert-pair effect, that is, the fact that the highest oxidation state becomes increasingly

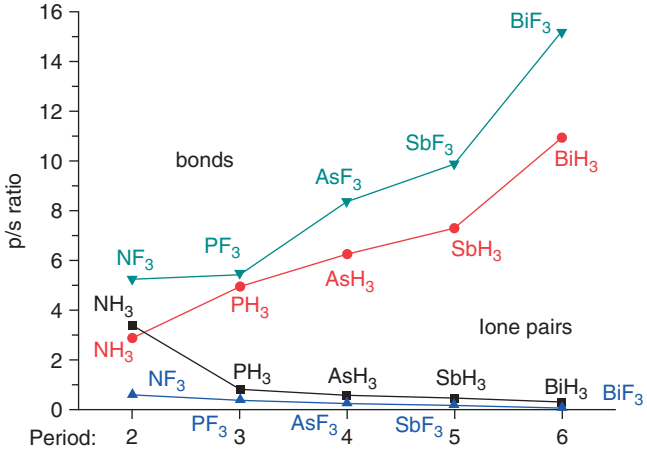

Figure 1.3 NAO/NLMO p/s hybridization ratios for bonds and lone pairs of second- and third-period hydrides and fluorides in lower oxidation state (B3LYP/def2-TZVP results).

unfavorable when moving down a given p-block main group. The first explanations based on an energetic unavailability of the *n*s-orbital were quickly found to be untenable and were replaced in the 1950s by Drago's [26] balance between the necessary energy for promotion to the higher valence state and the additional binding energy provided by the extra bonds in the high-valence compound. Due to a general weakening of bonds down a given group, the balance would then be shifted towards a destabilization of the higher oxidation state. The above considerations on hybridization defects tell us that, for example, an sp^3 valence state will never be reached in a compound like PbX_4 (cf. Figure 1.2) [24]. Instead, the lack of effective isovalent hybridization weakens the covalent bonds in the highest oxidation state. As hybridization is largely absent in the lower oxidation states (see earlier text), essentially pure p-orbitals are then used for bonding, making relatively strong bonds and thus stabilizing the two-electron-reduced oxidation state.

This also provides us with a ready explanation for why the inert-pair effect is much more pronounced for the truly inorganic compounds of a given heavy p-block element than for organoelement compounds or hydrides: [24] electronegative substituents like halogen, alkoxy or amido functionalities enhance hybridization defects dramatically in the highest oxidation state (cf. Figure 1.2), whereas the anyway marginal hybridization in the lower oxidation state is affected much less (cf. Figure 1.3). This explains why, for example, organolead compounds are actually much better known in their oxidation state +IV (e.g., tetraalkyl lead compounds, which for a long time, were used extensively as antiknock additives in gasoline), whereas inorganic lead(IV) compounds are either very unstable or, at least, strongly oxidizing, and lead(II) is the dominant oxidation state [24]. Similar comparisons may be made, for example, for Tl or Bi inorganic versus organoelement compounds. And successive substitution of alkyl groups by electronegative substituents is well known to destabilize the highest oxidation state. We mention here in passing, that for the 6p-elements, the 6p/6s size differences and thus the hybridization defects are aggravated (cf. Figures 1.2, 1.3) by the relativistic contraction of the 6s-orbital (see later text), leading to much more pronounced inert-pair effects compared to the 5p-homologues. The often found designation of the inert-pair effect as a relativistic effect is, however, partly misleading: relativistic effects are comparably unimportant for the hybridization defects of the 4p- and 5p-elements. Indeed, even the term ''inert-pair effect'' is somewhat unfortunate, given that in the highest oxidation state, the valence s-orbital participates *more* in bonding (relative to the p-orbitals) than assumed from the usual correlations with bond angles (Figure 1.2).

Related observations pertain to the stability of carbenes and their heavier homologues. It is well known that, for example, CH_2 has a triplet ground state, whereas its heavier homologues feature closed-shell singlet ground states with increasing singlet-triplet gaps down the group. This can be easily rationalized in comparison with the NLMO hybridizations for NH_3 and its heavier homologues (cf. Figure 1.3): isovalent hybridization is still favorable in the second period. Thus, the gain in exchange energy for a triplet state formed by the single occupation of one pure carbon 2p-orbital with π-symmetry and of one carbon-centered approximate $2s2p^2$ hybrid with σ-symmetry is sufficient to render it energetically competitive with the

double occupation of the sp^2 hybrid for the closed-shell singlet. In contrast, in SiH_2 hybridization, defects give the σ-type Si-centered orbital largely 3s-character and the Si-H bonds mostly 3p-character. It is clear that double occupation of the σ-type lp is now favored in spite of the loss of exchange energy, giving a singlet ground state. Consequently, we expect that electronegative substituents (i) favor singlet over triplet ground states even for carbenes (and stabilize the singlet further for the heavier homologues) and (ii) stabilize the carbene overall compared to a corresponding tetravalent carbon compound. It is, thus, natural that in N-heterocyclic or ''Arduengo-type'' carbenes (NHCs), [27] the first stable carbenes found, the carbon atom is bound to two electronegative nitrogen atoms. Although cyclic delocalization and a +M-effect of the nitrogen free electron pairs on the carbene center are often invoked to rationalize the stability of NHCs, it is clear that the electronegativity of the substituents is also important as it favors hybridization defects of the carbon 2s- and 2p-orbitals and thus stabilizes both the lower oxidation state and the singlet ground state.

Mercury is the only metal that is liquid at room temperature; and it is well known that this is caused by the relativistic contraction of the 6s-shell [28, 29], which makes hybridization between 6s- and 6p- orbitals more difficult and thus diminishes the binding strength. That is, relativistically enhanced hybridization defects are responsible for the low cohesion energy and low melting and boiling points of mercury (e.g., compared to cadmium). The nevertheless reasonably inert character of elemental mercury is the consequence of an inert-pair effect also in the possible reaction products: relatively weak bonds in Hg(II) compounds, specifically when bound to very electronegative substituents, are due to strong hybridization defects. NAO/NLMO hybridization ratios for linear HgX_2 molecules (e.g., $6s6p^{0.20}5d^{0.14}$ for HgH_2, $6s6p^{0.06}5d^{0.21}$ for HgF_2) suggest that 6s6p- (or 6s5d-) hybrids may be less suitable qualitative bonding descriptions in such compounds than three-center four-electron bonding involving only the 6s-orbital (cf. discussions about Natural Population Analysis, NPA [22]). Interestingly, relatively weak intra molecular and intermolecular interactions in Hg(II) compounds are also responsible for the widespread occurrence of Hg(I)-species with Hg–Hg bonding [30] and for the existence of $Hg(IV)F_4$ under low-temperature matrix isolation conditions (see earlier text) [5, 6].

As already discussed, electronegative substituents destabilize the heavy p-block elements in their maximum oxidation state. Computationally, this may be seen clearly for calculated energies for 1,1-elimination reactions. For example, along the series PbR_4, PbR_3F, PbR_2F_2, $PbRF_3$, PbF_4 (R = H, CH_3), elimination of R_2, RF or F_2 becomes less endothermic or more exothermic [24]. However, at the same time, it is found, that the Pb-R and Pb-F bonds become shorter along the same series. That is, increasing hybridization defects due to electronegative substituents destabilize the Pb(IV) compounds thermochemically; yet they contract the bonds, essentially due to the smaller size of the more positively charged central atom [24]. Indeed, as the 6s-character of the bonds increases on average with increasing fluorine substitution, they become shorter, consistent with the smaller size of 6s- compared to 6p-orbitals. Yet the large difference in the sizes of 6s- and

6p-orbitals is at the same time responsible for the bond weakening. This leads to a breakdown of the frequently and implicitly assumed correlation between bond length and bond strength (in this case binding energy). This has been tested in more detail computationally by constructing the heavy ethane homologue Sn_2H_6 (with staggered structure and direct Sn–Sn bonding) and its successively fluorine-substituted analogues $Sn_2H_xF_{6-x}$ ($x = 0$-5) [31]. It turns out that, indeed, shorter Sn–Sn bond lengths in the fluorine-substituted derivatives do not correspond to larger but, in most cases, to lower Sn–Sn binding energies. That is, contraction of the Sn–Sn bonds due to the increasingly positive central-atom charges goes parallel to weaker bonds due to hybridization defects. Correlations with Sn-Sn stretching frequencies are also in disagreement with, for example, Badger's rule [31]. Further computations on the analogous series with E = C, Si, Ge indicates similar behavior for Ge as found for Sn, a more complicated, different behavior for carbon because of negative hyperconjugation effects, and the most "normal" behavior with reasonable correlation between shorter bonds and larger dissociation energies for E = Si [32]. We note that a similar breakdown of the correlation between bond lengths and binding energies has been found experimentally [33] (and was in part analyzed computationally [34]) for transition-metal phosphine complexes, where the more electronegative substituents give shorter but weaker $TM-PX_3$ bonds (see also Chapter 7 in this book). Again, hybridization defects are responsible for this breakdown of the usual bond-length/bond-strength correlations.

1.2.3
Stereo-Chemically Active versus Inactive Lone Pairs

A related but separate question concerns the "stereo-chemical activity" of the free electron pair in the oxidation state, two units below the maximum one. As we have seen earlier, simple relations between hybridization (and thus of s- or p-character of the lp) and bond angles fail for the heavier p-block compounds, because of hybridization defects. The VSEPR model assumes intrinsically that a lp will exhibit a space requirement in the coordination space of the central atom, in fact, more than a covalent single bond. Something like a "stereo-chemically inactive lp" is thus clearly outside the assumptions of the VSEPR model. Indeed, for coordination numbers below 6, the presence of lp is always found to exert a stereo-chemical influence, both in molecules or in extended solid-state structures. For larger coordination numbers than 6, the structural preferences are anyway not very clear-cut and dominated by fluxional situations. It is thus coordination number 6 that gives rise to notable exceptions to the VSEPR model and to a very subtle balance between different influences. Among molecular systems, XeF_6 is the most widely considered case [35–37]. While xenon hexafluoride exhibits partly ionized bonding and a clear stereo-chemical activity of the lone pair in the solid state, gas-phase spectroscopic studies suggest that gas-phase XeF_6 is a fluxional system, consistent with a nonnegligible but weak stereo-chemical activity [35]. Computational studies show that the energy difference between C_{3v} and C_{2v} distorted octahedral and regular O_h structures are (i) very small and (ii) very difficult

to calculate [36, 37]. Whereas early non-relativistic Hartree-Fock calculations give strongly distorted C_{3v} minima and very high-lying O_h structures, both relativistic effects (because of the contraction of the Xe 5s-orbital) and electron correlation stabilize the O_h structure [36]. The most recent and accurate calculations [37] used explicitly correlated CCSD(T)-F12b methods and showed the C_{3v} minima to be about 4 kJ mol^{-1} below the C_{2v}–symmetrical pseudo-rotation transition states and about 7–8 kJ mol^{-1} below the O_h-symmetrical stationary point on the potential energy surface (without vibrational corrections), consistent with a fluxional situation in the gas phase. XeF_6 is, thus, a remarkable border-line case, just barely on the side of a stereo-chemically active lp. The isoelectronic 5p-anions IF_6^- and TeF_6^{2-} appear to behave very similarly, according to computations [36]. Notably, however, the calculations suggest that, in contrast to these 5p-species, valence-isoelectronic compounds of both lighter and heavier central atoms exhibit regular octahedral structures [36]! For the 3p- or 4p-species (e.g., ClF_6^-, BrF_6^-), this may be attributed to the smaller size of the central atom and thus to steric crowding. In contrast, calculations for 6p-species like PoF_6^{2-}, AtF_6^- or RnF_6 indicate that the large relativistic contraction of the 6s-orbital renders the lp stereo-chemically inactive and thus favors the O_h structures [36].

Another important aspect related to the presence of stereochemically active lp are trends in inversion barriers and thus the question of the configurational stability of, for example, amines versus phosphines, carbanions versus silyl anions, and so on. The inversion barriers tend to increase sharply from the 2p- to the homologous 3p-systems. For example, ammonia is fluxional with an inversion barrier of ca. 25 kJ mol^{-1}, in the range of zero-point vibrations [38]. In contrast, PH_3 exhibits a barrier of ca. 130 kJ mol^{-1} and, thus, is a much more rigid molecule [39]. Computations suggest that the barriers further increase moderately to AsH_3 and SbH_3 and, then again, more sharply to BiH_3 (due to the relativistic contraction of the 6s-orbital) [40]. Analogous considerations hold for substituted amines and phosphines. Similarly, carbanions tend to have much smaller inversion barriers than the corresponding silyl anions, which is of fundamental importance for the configurational stability of enantiomers in the case of chiral substitution patterns [41]. These differences between the 2p-species and their heavier homologues (and the relativistically enhanced barriers for the 6p-species) may be rationalized straightforwardly from the above considerations on hybridization defects: pyramidal minimum structures of amines or carbanions are expected to still exhibit to a reasonable approximation isovalent hybridization of both bonding and free electron pairs. In contrast, for phosphines or silyl anions, the lp have largely s-character and the bonds largely p-character (cf. Figure 1.3). At the trigonal transition state for inversion, the lp is required by symmetry to be a pure p-orbital, whereas the bonding orbitals have to hybridize the s- and p-orbitals. Whereas this leads to reasonably sp^2-hybridized bonding at the transition state for the 2p-elements, appreciable hybridization defects apply for the heavier congeners (with large s-character involved in the E–H bonds). As a consequence of the arising poor bonding overlap, the transition state is destabilized in the latter case, leading to substantially increased inversion barriers.

Table 1.1 Central-atom NPA charges Q(E) and NAO/NLMO hybridization ratios of bonds (BD) and lone pairs for minima and inversion transition states of ammonia homologues[a].

		Q (E)	BD	Lone pair
NH_3	min	−1.04	$sp^{2.87}$	$sp^{3.39}$
	TS	−1.11	$sp^{1.99}$	p
NH_2F	min	−0.38	N-H: $sp^{2.93}$ N-F: $sp^{5.22}$	$sp^{1.58}$
	TS	−0.51	N-H: $sp^{1.38}$ N-F: $sp^{2.80}$	p
NHF_2	min	0.14	N-H: $sp^{3.06}$ N-F: $sp^{5.18}$	$sp^{0.93}$
	TS	0.00	N-H: $sp^{0.92}$ N-F: $sp^{1.98}$	p
NF_3	min	0.58	$sp^{5.24}$	$sp^{0.62}$
	TS	0.44	$sp^{1.30}$	p
PH_3	min	0.02	$sp^{4.95}$	$sp^{0.81}$
	TS	−0.21	$sp^{1.52}$	p

[a] B3LYP/def2-TZVP results.

These considerations are supported by the NAO/NLMO hybridization ratios of NH_3 versus PH_3 at both minimum and transition-state structures (Table 1.1).

Most notably, we may use this framework also to understand the effect of electronegative substituents on inversion barriers. For example, the barrier increases substantially from NH_3 to NH_2F to NHF_2 to NF_3 (cf. also Ref. [42]), consistent with an increase in hybridization defects along this series at the planar transition-state structure (Table 1.1): differences between N–H and N–F bond hybridizations reflect the different H and F electronegativities, consistent with an appropriately modified version (accounting for hybridization defects, see earlier text) of Bent's rule [25]. Interestingly, the N–H bonds at the minimum structure are still close to idealized sp^3 hybridization even in NH_2F and NHF_2, whereas the nitrogen lone pair and the N–F bond(s) feature increasing separation of the nitrogen s-character into the former. At the inversion transition state, the N–H bonds in NH_3 still exhibit the nominal sp^2 hybridization for a trigonal coordination. The substantial and worsening hybridization defects are particularly notable for the N–H bonds in NH_2F and NHF_2; and then they are also significant for the N–F bonds in NHF_2 and especially in NF_3. One might therefore expect to have very large barriers for species like PF_3, AsF_3, SbF_3, or BiF_3. However, in these cases it has been found unexpectedly by computations that inversion proceeds not via a D_{3h}-symmetrical trigonal but via a C_{2v}-symmetrical Y-shaped transition state, leading to lower barriers and, indeed, an inverted trend with the barriers decreasing down the group [43].

1.2.4
The Multiple-Bond Paradigm and the Question of Bond Strengths

Similar arguments may be applied to the relative instabilities and the often ''trans-bent'' structures of multiple bonds between the heavier p-block elements. Very often, these well-studied phenomena are rationalized from the singlet–triplet energy gaps of the carbene-like constituents that make up a given XX'E=E'YY' olefin analogue (or from the doublet–quartet gaps of carbyne analogues for alkyne analogues), using the framework of the Carter–Goddard–Trinquier–Malrieu (CGTM) model [44, 45]. That is, when for example the S-T gap of the carbene, silylene, and so on is large, the bonding is described as a donor–acceptor interaction of singlet closed-shell fragments, thus explaining both the relatively weak bond and the structural distortions from a planar olefin-like arrangement. For small S-T gaps, one combines conceptually triplet open-shell fragments, leading to the standard description of olefin-type double bonding with planar structure. However, just as we have argued above for the stabilities of NHCs and related species, it may actually be more worthwhile to put the relative sizes of s- and p-orbitals, rather than energies, into focus. We then argue via isovalent hybridization to explain the olefin-like case and via increasing hybridization defects for heavier p-block central atoms and for electronegative substituents.

This then also explains the influence of electronegative substituents. For example, enhanced hybridization defects for the positively charged carbon centers explain straightforwardly why the C=C double bond in C_2F_4 is much weaker than that in ethylene: on one hand, the C–C sigma bonding is weakened by the incresased hybridization defects in the fluorine-substituted olefin; on the other hand, the singlet CF_2 fragment is not affected adversely as carbon s- and p-orbitals segregate into lp and C–F bonds, respectively (see above). Similarly, the trans-bent structures of silenes, germenes, or stannenes reflect the lack of efficient isovalent hybridization. In fact, the double bonds are sufficiently weak that the isolated singlet ER_2 fragments become more stable down the group, which is just another manifestation of the inert-pair effect. As we have seen earlier, the latter can be conveniently discussed via hybridization defects for the high-valent compound (in the present case the olefin-homologue) and via segregation of s- and p-orbitals in the low-valent situation (i.e., for the fragments). This closes the circle of arguments and shows that the consideration of the relative sizes of valence s- and p-orbitals does indeed provide a broad framework for discussing periodic trends of main-group structure, stability, and bonding. Similar considerations may be applied to the energetics and bending of formal triple bonds [46].

Evaluation of σ- and π-bond increments reveals that for the 2p-elements of groups 15, 16, and 17, weakening of the corresponding single bonds by the so-called ''lone-pair bond weakening effect'' (LPBW) [47] works in favor of multiple bonding, whereas this aspect does not apply to the heavier homologues. Examples are the weak E-E single bonds of hydrazine, hydrogen peroxide, or difluorine compared to diphosphine, hydrogen disulfide, or dichlorine, respectively. Notably, the LPBW effect is yet another result of the particularly compact, nodeless

2p-shell: the π-type lp exhibit substantial Pauli repulsion with the σ-bonding orbitals [48]. Interestingly, from a VB point of view, such compounds frequently may be classified as charge-shift-bonding cases (See Chapter 5 in Volume 1).

1.2.5 Influence of Hybridization Defects on Magnetic-Resonance Parameters

For the heavier p-block elements, hybridization defects lead to enhanced *n*s-character in bonds, more than one might expect from structural considerations (see earlier). This holds for the highest oxidation state of the central atom, whereas the s-character concentrates into lps for the lower oxidation states, leaving predominantly p-character for the bonding orbitals. One quantity that is known to be particularly strongly connected to the s-character in bonds is indirect NMR spin–spin coupling constants [49]. The Fermi-contact part of such coupling constants depends crucially on the s-character of the valence orbitals involved in bonding as the communication between the nuclear spin moments happens exclusively via the spherically symmetrical part of the spin density around a given nucleus. Larger s-character enhances the communication, leading to larger coupling constants in absolute terms (the sign of the coupling depends also on the relative signs of the two nuclear g-values) for compounds, where the two atoms involved are in their maximum oxidation state. Matters become more complicated when lone pairs are present; then, the bonds have largely p-character. The coupling constants tend to be smaller and are also potentially influenced by involvement of the lp and by other coupling terms.

It has furthermore been demonstrated [50], that a related Fermi-contact mechanism dominates spin-orbit effects on the NMR chemical shifts of nuclei connected to heavy-atom centers (the so-called ''heavy-atom effect on the light-atom shielding,'' HALA [51], even though the NMR nucleus may also, in fact, be a heavy atom). Here s-character in bonding has also been found to be extremely important in defining the magnitude of such ''spin-orbit shifts'' (SO shifts). Therefore, the SO shifts are large for p-block elements in their maximum oxidation state (even larger for hydrogen [52, 53]), whereas the SO effects are typically small in lower oxidation states because of the predominant p-character in the bonds [54, 55].

As we have learned earlier, electronegative substituents enhance hybridization defects and, thus, increase the s-character in the bonds. This explains why, for example, substitution of the hydrogen atoms in CH_3I by fluorine atoms in CF_3I does essentially double the spin-orbit effects on the ^{13}C shifts because of the heavy iodine substituent, from about −30 ppm to about −60 ppm, reducing the high-frequency shift in the ^{13}C spectrum from about 145 ppm at the nonrelativistic level to about 115 ppm upon inclusion of spin-orbit coupling [49]. The NPA charge on carbon increases from −0.70 in CH_3I to +0.85 in CF_3I, and consequently, the p/s hybridization ratio of the C-I bond (NAO/NLMO value) decreases from $sp^{4.14}$ to $sp^{1.96}$ (B3LYP/def2-TZVP results). This explains the more efficient Fermi-contact mechanism (direct contributions from fluorine SO coupling are small). Along the same line of argument, the more-than-linear increase of ^{13}C spin-orbit shifts with

n along the series $CH_{4-n}I_n$, compared to the only linear increase along the series $CBr_{4-n}I_n$, has been rationalized; whereas the positive charge on carbon and, thus, the carbon s-character of the C–I bonds increases with n in the former series, it stays relatively constant in the latter series (because of the similar electronegativities of Br and I) [54].

Other properties in magnetic resonance may be mentioned here, for example, hyperfine couplings. As the isotropic hyperfine coupling also depends crucially on the spherical spin-density distribution around the nucleus in question, s-character in bonding and, thus, hybridization defects will be important. Obviously, for open-shell radicals the s-character of the singly occupied MO(s) is the most crucial aspect, but spin polarization of doubly occupied MOs with core or valence s-character may also be relevant (e.g., when the singly occupied molecular orbital is of pure p-character at the given atom).

1.3
The Role of the *Outer* d-Orbitals in Bonding

Whether or not the outer d-orbitals are true valence orbitals for the heavier p-block elements and, thus, allow the octet rule to be violated in ''hypervalent compounds'' has been one of the most controversial questions in main-group bonding for decades. Whereas, during the past 15 years, the balance has dipped clearly to the side of the d-orbitals acting only as polarization functions rather than having a true valence-orbital character, it is worthwhile to consider here briefly why the controversy has lasted so long. We will then put the hypervalency issue particularly into the context of radial nodes. Other aspects of the topic are discussed in Chapter 3 in this book.

In the early days of discussions of main-group bonding, it was probably Pauling's electroneutrality principle [56] that favored a picture of the outer d-orbitals as influential valence orbitals: resonance structures with appreciably positive formal charges on the central p-block main-group atom were considered to be unlikely and disfavored. Therefore, for example, a semipolar resonance structure for the sulfate ion with only single S–O bonds, a dipositive formal charge on sulfur, and a negative formal charge on each of the oxygen atoms, consistent with the original suggestion by Lewis [57], was disregarded in the 1960s or 1970s. Hypervalent resonance structures with four S=O double bonds have dominated the inorganic-chemistry textbooks (in fact, they still do so today!). On the other hand, the discovery of noble-gas compounds in the early 1960s gave a boost to three-center four-electron bonding models [58] and MO-based scenarios that avoided ''true'' hypervalency. In the 1970s, when the first realistic *ab initio* wave functions could be obtained, bonding analyses were inevitably done using Mulliken's population analysis [20]. As we now know, the Mulliken populations are not only very basis-set dependent (earlier text), but they also tend to provide a much too covalent picture when the electronegativities of the bonding partners differ significantly. This ''cemented'' the electroneutrality-principle point of view for many more years. More up-to-date

methods, either of population-analysis type (e.g., natural population analysis [21]) or of real-space type (e.g., Bader's quantum theory of atoms in molecules, QTAIMs [59]), give a more ionic picture in general and for hypervalent p-block compounds, in particular. This supports multicenter bonding and negative hyperconjugation in MO language or, equivalently, partially ionic resonance structures and no-bond double-bond resonance in VB language. d-Orbital participation, thus, is inevitably computed to be much less pronounced than suggested by Mulliken populations. As partial atomic charges are no true observables (no, not even the QTAIM ones!), none of these schemes alone can provide a definite answer to the true covalency and, thus, to the quantitative involvement of the d-orbitals in bonding. In fact, one can find weaknesses in essentially any of the analysis methods, for example, a bias *against* d-orbital participation in the NBO scheme (because of the classification of the d-functions with the ''natural Rydberg set'' [22]) or a possibly too ionic description by QTAIM charges [60]. Yet the accumulated information provided by a wide range of the most refined models available does, indeed, provide a much less covalent, less electro-neutral picture and, thus, a smaller involvement of the outer d-orbitals in bonding than assumed before.

We may place the issue of hypervalent bonding into the more general context of the discussion throughout this chapter: hypervalent p-block compounds are stabilized by semipolar or partially ionic resonance structures in VB language or by multicenter bonding in MO language. Either way, a partial positive charge on the central atom is desirable. This is favored by (i) a high electronegativity of the substituents and by (ii) a low electronegativity of the central atom. This is why fluorine substitution is most favorable in stabilizing hypervalent compounds, followed by oxygen substitution. At the same time, it is clear that the high electronegativity and small size of the 2p-elements makes them rather unfavorable as central atoms, consistent with observation. The nodelessness of the 2p-shell renders the 2p-elements electronegative and small and, thereby, helps to fulfill the octet rule in the 2p-series. In contrast, the heavier p-block elements are larger and less electronegative and, thus, favored as central atoms. In other words, the nodal structure of the valence *n*p-orbitals, rather than the availability of the outer *n*d-orbitals, is decisive for the apparent violation of the octet rule for the heavier elements.

Of course, the octet is usually not actually violated. Multicenter bonding models require some MOs that are essentially nonbonding and concentrated only on the substituents, and thus, the number of electrons in the valence shell of the central atom rarely exceeds the octet. However, here we should distinguish, between what Musher [61] more than 40 years ago termed hypervalent compounds of first and second kind, respectively. In the first class, the central atom is not in its maximum oxidation state, and thus, the central-atom *n*s-character concentrates in a lp. Then, as we have discussed in detail above, the bonds are made mainly from *n*p-orbitals of the central atom, and thus, the assumptions of the usual three-center-four-electron bonding models are nicely fulfilled. In contrast, hypervalent compounds of the second kind exhibit the maximum oxidation state and, thus, necessarily involve the *n*s-orbitals fully in bonding. One thus sees (i) extensive hybridization defects

(see earlier text), (ii) a more complicated bonding pattern in which the *n*s-orbitals are also involved in multicenter delocalization [62], and c) often a subtle ''true'' hypervalency. The latter point has been demonstrated most convincingly by Häser [63] in his unique analysis scheme: Häser's method is based on projecting the one-particle density matrix onto spheres around the atom. Expansion of the radius of the sphere around the central atom in, for example, PF_5 or SF_6 followed by integration of the AO contributions to the sphere populations up to a certain radius around the central atom indicated that the octet was violated, albeit very slightly, in contrast to hypervalent compounds of the first kind (e.g. XeF_2), where no octet violation could be registered by this approach. Closer analysis indicated populations with d-symmetry around the central atom in hypervalent compounds of the second kind [61]. However, these populations did not possess true valence-orbital character but essentially described the outermost rim of the attractive potential trough of the atom, already close to the substituents. Interesting further insights were obtained regarding the multicenter delocalization in, for example, PF_5 [61]. Indeed, analyses of such species by natural resonance theory (NRT [64], based on a superposition of Lewis structures from strictly localized NBOs) also indicate slight violations of the octet in contrast to compounds of the first kind. An aspect that deserves further scrutiny is to what extent the octet may also be violated when multicenter delocalization involves predominantly π-type orbitals on the substituents (in the sulfate ion or iso-electronic ions little octet violation mentioned earlier seems to be apparent from NRT, but more systems need to be analyzed). Unfortunately Häser's approach has not been pursued further, because of his early demise. The method appears to be very powerful in the context of hypervalency discussions or for monitoring hybridization.

1.4
Secondary Periodicities: Incomplete-Screening and Relativistic Effects

So far the nodal structure of the valence s- and p-orbitals themselves has been in our focus, allowing us to explain the special role of the 2p-elements compared to their heavier homologues. The further modulations of chemical and physical properties as we descend to a given group from period 3 on are often summarized under the term ''secondary periodicity'' [65, 66]. The main influences here are incomplete screening of nuclear charge by filled core or semi-core shells and the effects of special relativity. The former reflect shell structure of the atom as a whole and are already important for differences and similarities of the homologous third and fourth period elements, whereas the latter become crucial mainly for the chemistry of the sixth period elements. These aspects have been discussed in detail in various review articles (see, e.g., Refs [16, 28, 67]), and we, thus, touch them only briefly.

The most well-known incomplete-screening effect in the periodic table, the lanthanide contraction, is due to the successive filling of the 4f-shell by 14 electrons, leading to a contraction of the size of the later lanthanides and of the elements

following them in the sixth period. This lanthanide contraction is most notable for the early 5d transition metals (e.g., regarding the similarity of the properties of Zr and Hf). It is still effective for the late 5d- and early 6p-elements, but in this case it is overshadowed by the relativistic contraction of the 6s-shell (see below) [65]. The combined action of lanthanide contraction and relativity is responsible for a somewhat higher electronegativity of, for example, Pb versus Sn. As discussed above, the relativistic contraction of the 6s-shell is responsible for an enhancement of the inert-pair effect for the 6p-elements.

Somewhat less well known but nevertheless important is the incomplete screening of nuclear charge by filling of the 3d-shell (sometimes called the ''scandide contraction'' [28, 65]). It is responsible for a contraction of the valence orbitals of the 4p-elements, in particular of those following directly on the 3d-series. This leads to a pronounced similarity of the electronegativities (in fact a slightly larger one for the 4p-element in the modern scales) and covalent radii of Al versus Ga, Si versus Ge, P versus As, and so on. For example, in covalent bonds to carbon or hydrogen, Ga is slightly smaller than Al (even more so for element-element bonds). In contrast, the slightly higher electronegativity of Ga reduces electrostatic interactions in more ionic compounds, and thus, a more ''normal'' behavior with larger bond lengths for Ga is found, for example, for halides. Whereas this has not been studied in detail so far, the scandide contraction probably enhances hybridization defects for the early 4p-elements as it likely affects the 4s-orbitals more than the 4p-orbitals and, thus, may overall increase the relevant differences in their radial extent. This may explain certain irregularities in the chemical properties for 3p- versus 4p- homologues, even further to the right in the p-block, that is, for S versus Se or Cl versus Br.

It is interesting that incomplete screening of nuclear charge appears to be most pronouncedly caused by those shells that have no radial node such as the 3d- and 4f-shells. It is so far unclear why, for example, the 4d-contraction should be less effective than the 3d-contraction (the actinide contraction would be smaller than the lanthanide contraction without relativistic effects but is significantly enhanced by the latter, thus becoming overall larger [68]). We may even consider a ''2p-contraction'' in the comparison of ionization energies and electronegativities for Li versus Na or Be versus Mg. It has been shown computationally [69, 70], that the question whether Li or Na is more electronegative depends on the bonding situation: while σ-bonded ligands with some covalency (e.g., hydride or alkyl) give rise to a somewhat higher electronegativity of Na compared to Li, more electronegative ligands with some π-donor character (e.g., NH_2, OH, halogen, Cp) give more positive Na than Li charges. Closer analysis indicates that the Li 2s-orbital is very well shielded by the 1s core shell, whereas the 3s-orbital of Na experiences more incomplete shielding by the 2p-shell [65]. Together with the opposing effect of the larger radius of Na compared to Li, this leads to these somewhat unusual and subtle trends. Pyykkö has analyzed them further using ''pseudo atoms'' in which core shells have been deleted and the nuclear charge has been reduced, in analogy to earlier related studies for the lanthanide and scandide contractions

[65, 69, 71]. Notably, the observation of ''inverted lithium-sodium electronegativities'' by computations had been motivated by peculiar anomalies in the gas-phase thermochemistry of the group 1 elements [65].

1.5 ''Honorary d-Elements'': the Peculiarities of Structure and Bonding of the Heavy Group 2 Elements

We have already concluded that the *outer* d-orbitals of the p-block elements are polarization functions but no true valence orbitals. This is well-known to be different for the *inner* d-orbitals of the transition metals, which dominate covalent bonding in the transition series. The heavier group 2 elements (Ca, Sr, Ba, Ra) also exhibit such *inner* (*n*-1)d-orbitals. Whereas these play essentially no role in bonding for the bulk metals or for neutral metal clusters, which are clearly dominated by the valence s-orbitals of the elements, matters become different with increasing positive charge on a given heavy group 2 element. Indeed, as we proceed to the most electronegative bonding partners (e.g., fluorine or oxygen), the *absolute* role of covalent bonding decreases, but the *relative* role of the (*n*-1)d-orbitals in the diminishing covalent bonding contributions increases to the extent that, for a molecule like BaF_2, covalent bonding is almost entirely due to the Ba 5d-orbitals. This places these elements at the border line with the early transition metals and the lanthanides, and Pyykkö has coined the term ''honorary d-elements'' to indicate this [4]. The importance of d-orbital involvement in bonding for the heavy alkaline earth elements is not a purely theoretical matter but manifests itself in structural peculiarities. The oldest example are observations in the 1960s that the molecular dihalides of the heavier group 2 elements in the gas phase may actually exhibit bent rather than linear structures whereas the Be or Mg dihalides are all clearly linear (see Ref. [3] for further literature). Different spectroscopic or electron diffraction techniques gave partly conflicting results, and the bent nature of molecules like BaF_2 was later established beyond doubt by up-to-date computational methods [72]. Such calculations provided evidence that even smaller bending angles and larger linearization energies could be obtained when replacing halogen or other π-donor ligands by pure σ-donors like hydride [73] or alkyl [74] ligands. Indeed, experimental evidence for bent group 2 or lanthanide(II) dialkyl complexes is now available [75]. Bending of the group 2 metallocenes had been discussed even earlier. However, from today's perspective, these metallocenes are at best quasi-linear with very shallow bending potential curves, as π-bonding actually favors linear arrangements [76].

Detailed bonding analyses gave a rather interesting picture of those factors that favor the bent or linear structures: [3] linearity is obviously enhanced by Pauli or electrostatic repulsion between the M–X bonds or between X^- anions, respectively, in agreement with the assumptions of the VSEPR model. Two apparently very different factors favoring bending had been discussed controversially for decades, (i) involvement of (*n*-1)d-orbitals in *σ*-bonds to the ligands (see earlier text) and

(ii) ''inverse'' polarization of the M^{2+} cations, leading to an electrostatic stabilization of the bent structure. Computations [67, 68] indicated that (i) both factors contribute to the bending and (ii) they are not strictly separable. The latter point may be appreciated from the fact that the polarizability of the cation is dominated by its outermost $(n-1)$p-shell. The $(n-1)$d-orbitals, thus, act as the primary polarization functions of the semi-core orbitals. At the same time, bending due to involvement of the valence $(n-1)$d-orbitals in covalent bonding will clearly lead to Pauli repulsion with the core and thus deformation of the penultimate p-shell. Therefore the covalent and core-polarization aspects of bending are closely interrelated as could be shown by a number of analysis procedures [67, 68]. The complications are due to the fact that outermost core $(n-1)$p- and valence $(n-1)$d-orbitals share the same principal quantum number.

The role of π-bonding is also subtle: for the given group 2 examples with ''weak π-donor'' halide or related ligands, π-bonding clearly favors the linear structures [77]. For more covalent transition-metal examples with strong donor ligands like ZrO_2, overlap of the π-type oxygen lp with an in-plane Zr d-orbital actually favors even more pronounced bending [72]. These aspects show up also for more complex heteroleptic complexes. Indeed, the ''non-VSEPR'' structures are not restricted to exotic dicoordinate species but extend also to higher coordination numbers. For example, both computations and experiments indicate that rather peculiar structures may be favored for dimeric M_2X_4 systems [78, 79] for exactly the same reasons that also account for the bending of the monomers. This author has argued that many peculiar bulk solid-state structures of heavy alkaline-earth dihalides or dihydrides (and of many early transition-metal compounds) also reflect the involvement of the $(n-1)$d-orbitals in σ-bonding [3].

To complete the link to the transition metals, we note in passing that the peculiar distorted trigonal prismatic structures of species like WH_6 or $W(CH_3)_6$ or the preferences for square pyramidal rather than trigonal bipyramidal structures of TaH_5 or $Ta(CH_3)_5$ may be rationalized along similar lines (again π-bonding for analogous halide complexes gives the ''classical'' VSEPR structures in those cases). Importantly, however, covalency is much more important for such d^0 species further to the right in the periodic table, and at the same time, core polarizability is expected to be much less pronounced than for group 2 species. Therefore, a covalent interpretation of such structures by d-orbital participation in σ- (and partly π-) bonding is much more reasonable than arguing via core polarization as has been done within the framework of a proposed ''extended VSEPR model'' [80] based on the Laplacian of the charge density. More detailed arguments may be found in Ref. [3]. We note that a decomposition of the Laplacian into strictly localized NBOs for complexes like Me_3NbCl_2 and Me_2NbCl_3 confirms the ''covalent'' rationalization; [81] it turns out that maxima in the negative Laplacian, previously tagged ''core shell charge concentrations'' within extended VSEPR studies, in fact, reflect the backside lobes of the $(n-1)$d-orbitals involved in covalent σ-bonding. This is consistent with the fact that the ''charge concentrations'' are even present when a frozen core is used [82].

1.6 Concluding Remarks

In this chapter, we have tried to emphasize general aspects of main-group chemical bonding, with particular emphasis on periodic trends. The periodic table remains the most important classification tool in chemistry, and it is crucial to understand even subtle secondary periodicities if one is to make efficient use of the various elements for different chemical applications. The radial nodal structure of the valence orbitals has been pointed out to account for more of the known trends than most practitioners of chemistry are aware of. For example, the inversion barriers of phosphines or silyl anions, the dependence of the inert-pair effect on the electronegativity of the substituents, the stability of carbene- or carbyne-type species or of multiple bonds between heavy main-group elements are all intricately linked to hybridization defects of s- and p-valence orbitals of disparate sizes. Even the question of hypervalency is closely connected to the effects of ''primogenic repulsion''.

Further important influences on the periodic trends arise from partial screening of nuclear charge (including lanthanide/actinide contraction, scandide contraction, and even a 2p-contraction) and from the effects of special relativity. Various aspects of main-group bonding are covered in more detail elsewhere in this book.

References

1. See, e.g.: (a) Mahan, A.K. (1984) *Phys. Rev. B*, **29**, 5982–5985; (b) Ahuja, R., Eriksson, O., and Johansson, B. (2000) *Phys. Rev. B*, **63**, 014102/1–014102/3.
2. See, e.g.: Grochala, W., Hoffmann, R., Feng, J., and Ashcroft, N.W. (2007) *Angew. Chem. Int. Ed.*, **46**, 3620–3642.
3. Kaupp, M. (2001) *Angew. Chem. Int. Ed.*, **40**, 3534–3565.
4. (a) Pyykkö, P. (1978) *J. Chem. Soc., Faraday Trans.*, 1256–1276; (b) Gagliardi, L. and Pyykkö, P. (2003) *Theor. Chem. Acc.*, **110**, 205–210.
5. (a) Kaupp, M. and Schnering, H.G.v. (1993) *Angew. Chem., Int. Ed. Engl.*, **32**, 861–863; (b) Kaupp, M., Dolg, M., Stoll, H., and Schnering, H.G.v. (1994) *Inorg. Chem.*, **33**, 2122–2131.
6. Wang, X., Andrews, L., Riedel, S., and Kaupp, M. (2007) *Angew. Chem. Int. Ed.*, **46**, 8371–8375.
7. (a) Riedel, S., Straka, M., and Kaupp, M. (2005) *Chem. Eur. J.*, **11**, 2743–2755; (b) Riedel, S., Straka, M., and Kaupp, M. (2004) *Phys. Chem. Chem. Phys.*, **6**, 1122–1127.
8. Seth, M., Schwerdtfeger, P., and Dolg, M. (1997) *J. Chem. Phys.*, **106**, 3623–3632.
9. (a) Schlöder, T., Kaupp, M., and Riedel, S. (2012) *J. Am. Chem. Soc.*, **134**, 11977–11979; (b) Riedel, S., Kaupp, M., and Pyykkö, P. (2008) *Inorg. Chem.*, **47**, 3379–3383.
10. Jensen, W.B. (2008) *J. Chem. Educ.*, **85**, 1182–1183.
11. (a) See, e.g.: Jungnickel, G., Köhler, Th., Haase, M., Deutschmann, S., Stephan, U., Blaudeck, P., and Frauenheim, Th. (1995) *J. Noncryst. Sol.*, **183**, 161–174; (b) Kohler, Th., Frauenheim, Th., and Jungnickel, G. (1995) *Phys. Rev. B*, **52**, 11837–11844, and references therein.
12. Pyykkö, P. (1979) *Phys. Scr.*, **20**, 647–651.
13. Kutzelnigg, W. (1984) *Angew. Chem., Int. Ed. Engl.*, **23**, 272–295.
14. Desclaux, J.P. (1973) *At. Data Nucl. Data Tables*, **12**, 311–406.
15. Kaupp, M. (2007) *J. Comput. Chem.*, **28**, 320–325.

16. Kaupp, M. (2012) in *Huheey-Keiter-Keiter Anorganische Chemie – Prinzipien von Struktur und Reaktivität* (ed. R. Steudel), 4th German Ed, Chapter 18, de Gruyter, Berlin, pp. 1043–1097.
17. Kutzelnigg, W. (1988) *Theochem*, **169**, 403–419.
18. See, e.g.: Klapötke, T.M. and Tornieporth-Oetting, I.C. (1994) *Nichtmetallchemie*, Verlag Chemie, Weinheim.
19. Foster, S. and Boys, S.F. (1960) *Rev. Mod. Phys.*, **32**, 296–302.
20. Mulliken, R.S. (1950) *J. Phys. Chem.*, **72**, 4493–4503.
21. Reed, A.E., Curtiss, L.A., and Weinhold, F. (1988) *Chem. Rev.*, **88**, 899–926.
22. (a) Maseras, F. and Morokuma, K. (1992) *Chem. Phys. Lett.*, **195**, 500–504; (b) But see: Landis, C.R. and Weinhold, F. (2007) *J. Comput. Chem.*, **28**, 198–203.
23. Kaupp, M. and Schleyer, P.v.R. (1992) *Angew. Chem., Int. Ed. Engl.*, **31**, 1224–1226.
24. Kaupp, M. and Schleyer, P.v.R. (1993) *J. Am. Chem. Soc.*, **115**, 1061–1073.
25. Bent, H.A. (1961) *Chem. Rev.*, **61**, 275–311.
26. Drago, R.S. (1958) *J. Phys. Chem.*, **62**, 353–357.
27. See, e.g. Rojisha, V.C., De, S., and Parameswaran, P. (2012) *Inorg. Chem.*, **51**, 8265–8274.
28. Pyykkö, P. (1988) *Chem. Rev.*, **88**, 563–594.
29. Gaston, N. and Schwerdtfeger, P. (2006) *Phys. Rev. B*, **74**, 024105/1–024105/12.
30. Kaupp, M. and Schnering, H.G.v. (1994) *Inorg. Chem.*, **33**, 4179–4185.
31. Kaupp, M., Metz, B., and Stoll, H. (2000) *Angew. Chem. Int. Ed.*, **39**, 4607–4609.
32. Kaupp, M. and Riedel, S. (2004) *Inorg. Chim. Acta*, **357**, 1865–1872.
33. Ernst, R.D., Freeman, J.W., Stahl, L., Wilson, D.R., Arif, A.M., Nuber, B., and Ziegler, M.L. (1995) *J. Am. Chem. Soc.*, **117**, 5075–5081.
34. Frenking, G., Wichmann, K., Fröhlich, N., Grobe, J., Golla, W., Le Van, D., Krebs, B., and Läge, M. (2002) *Organometallics*, **21**, 2921.
35. (a) See, e.g.: Pitzer, K.S. and Bernstein, L.S. (1975) *J. Chem. Phys.*, **63**, 3849–3856; (b) Cutler, J.N., Bancroft, G.M., Bozek, J.D., Tan, K.H., and Schrobilgen, G.J. (1991) *J. Am. Chem. Soc.*, **113**, 9125–9131; (c) For solid-state structural data, see: Hoyer, S., Emmler, T., and Seppelt, K. (2006) *J. Fluorine Chem.*, **127**, 1415–1422, and references therein.
36. Kaupp, M., van Wüllen, C., Franke, R., Schmitz, F., and Kutzelnigg, W. (1996) *J. Am. Chem. Soc.*, **118**, 11939–11950.
37. Peterson, K.A., Dixon, D.A., and Stoll, H. (2012) *J. Phys. Chem. A*, **116**, 9777–9782.
38. See, e.g.: Swalen, J.D. and Ibers, J.A. (1962) *J. Chern. Phys.*, **36**, 1914–1918.
39. Weston, R.E. (1954) *J. Am. Chern. Soc.*, **76**, 2645–2650.
40. See, e.g.: Schwerdtfeger, P., Laakkonen, L.J., and Pyykkö, P. (1992) *J. Chem. Phys.*, **96**, 6807–6819, and references therein.
41. (a)For computational studies on silyl anions, see, e.g.: Flock, M. and Marschner, C. (2002) *Chem. Eur. J.*, **8**, 1024–1030; (b) Flock, M. and Marschner, C. (2005) *Chem. Eur. J.*, **11**, 4635–4642; (c) Däschlein, C., Bauer, S.O., and Strohmann, C. (2011) *Eur. J. Inorg. Chem.*, 1454–1465, and references therein.
42. See, e.g.: Schmiedekamp, A., Skaarup, S., Pulay, P., and Boggs, J.E. (1977) *J. Chem. Phys.*, **66**, 5769–5776.
43. (a) See, e.g.: Arduengo, A.J. III,, Dixon, D.A., and Roe, D.C. (1986) *J. Am. Chem. Soc.*, **108**, 6821–6823; (b) Dixon, D.A. and Arduengo, A.J. III, (1987) *J. Am. Chem. Soc.*, **109**, 338–341; (c) Schwerdtfeger, P., Boyd, P.D.W., Fischer, T., Hunt, P., and Liddell, M. (1994) *J. Am. Chem. Soc.*, **116**, 9620–9633.
44. See, e.g.: Power, P.P. (1999) *Chem. Rev.*, **99**, 3463–3503.
45. (a) Carter, E.A. and Goddard, W.A. III, (1986) *J. Phys. Chem.*, **90**, 998–1001; (b) Trinquier, G. and Malrieu, J.-P. (1987) *J. Am. Chem. Soc.*, **109**, 5303–5315.
46. See, e.g.: Lein, M., Krapp, A., and Frenking, G. (2005) *J. Am. Chem. Soc.*, **127**, 6290–6299.
47. Sanderson, R.T. (1983) *Polar Covalence*, Academic Press, New York.

48. Shaik, S., Danovich, D., Wu, W., and Hiberty, P.C. (2009) *Nat. Chem.*, **1**, 443–449.
49. See, e.g.: Mason, J. (1987) *Multinuclear NMR*, Plenum Press, New York, and references cited therein.
50. Kaupp, M., Malkina, O.L., Malkin, V.G., and Pyykkö, P. (1998) *Chem. Eur. J.*, **4**, 118–126.
51. Pyykkö, P., Görling, A., and Rösch, N. (1987) *Mol. Phys.*, **61**, 195–205.
52. Hrobárik, P., Hrobáriková, V., Meier, F., Repiský, M., Komorovský, S., and Kaupp, M. (2011) *J. Phys. Chem. A*, **115**, 5654–5659.
53. Hrobárik, P., Hrobáriková, V., Greif, A.H., and Kaupp, M. (2012) *Angew. Chem. Int. Ed.*, **51**, 10884–10888.
54. Bühl, M., Kaupp, M., Malkin, V.G., and Malkina, O.L. (1999) *J. Comput. Chem.*, **20**, 91–105.
55. Relativistic Effects on NMR Chemical Shifts Kaupp, M. (2004) in *Relativistic Electronic Structure Theory II: Applications*, Theoretical and Computational Chemistry, Chapter 9 (ed. P. Schwerdtfeger), Elsevier, Amsterdam, pp. 552–597.
56. See, e.g.: Pauling, L. (1952) *J. Phys. Chem.*, **56**, 361–365.
57. Lewis, G.N. (1916) *J. Am. Chem. Soc.*, **38**, 762–785.
58. (a) See, e.g.: Rundle, R.E. (1947) *J. Am. Chem. Soc.*, **69**, 1327–1331; (b) Rundle, R.E. (1964) *J. Am. Chem. Soc.*, **85**, 112–113; (c) Pimentel, G.C. (1951) *J. Chem. Phys.*, **19**, 446–448.
59. Bader, R.W.F. (1990) *Atoms in Molecules: A Quantum Theory*, Oxford University Press, Oxford.
60. Reed, A.E. and Weinhold, F. (1985) *J. Chem. Phys.*, **83**, 735–746.
61. Musher, J.I. (1969) *Angew. Chem., Int. Ed. Engl.*, **8**, 54–68.
62. For a nice illustration, see: Steudel, R. (2008) *Chemie der Nichtmetalle*, 3rd edn, de Gruyter, Berlin.
63. Häser, M. (1996) *J. Am. Chem. Soc.*, **118**, 7311–7325.
64. See, e.g.: Suidan, L., Badenhoop, J.K., Glendening, E.D., and Weinhold, F. (1995) *J. Chem. Educ.*, **72**, 583–586, and references therein.
65. Biron, E.V. (1915) *Zh. Russk. Fiz. Khim. Obsch.*, **47**, 964–988.
66. Pyykkö, P. (1979) *J. Chem. Res. (S)*, 380–381.
67. See, e.g.: Pyykkö, P. (2011) *Phys. Chem. Chem. Phys.*, **13**, 161–168, and references therein.
68. (a) See, e.g.: Küchle, W., Dolg, M., and Stoll, H. (1997) *J. Phys. Chem. A*, **101**, 7128–7133; (b) Laerdahl, J.K., Fægri, K. Jr.,, Visscher, L., and Saue, T. (1998) *J. Chem. Phys.*, **109**, 10806–10817; (c) Seth, M., Dolg, M., Fulde, P., and Schwerdtfeger, P. (1995) *J. Am. Chem. Soc.*, **117**, 6597–6598.
69. Lambert, C., Kaupp, M., and Schleyer, P.v.R. (1993) *Organometallics*, **12**, 853–859.
70. Pyykkö, P. (2001) *Int. J. Quantum Chem.*, **85**, 18–21.
71. Bagus, P.S., Lee, Y.S., and Pitzer, K.S. (1975) *Chem. Phys. Lett.*, **33**, 408–411.
72. Kaupp, M., Schleyer, P.v.R., Stoll, H., and Preuss, H. (1991) *J. Am. Chem. Soc.*, **113**, 6012–6020.
73. Kaupp, M., Schleyer, P.v.R., Stoll, H., and Preuss, H. (1991) *J. Chem. Phys.*, **94**, 1360–1366.
74. Kaupp, M. and Schleyer, P.v.R. (1992) *J. Am. Chem. Soc.*, **114**, 491–497.
75. (a) Eaborn, C., Hitchcock, P.B., Izod, K., and Smith, J.D. (1994) *J. Am. Chem. Soc.*, **116**, 12071; (b) Eaborn, C., Hitchcock, P.B., Izod, K., Lu, Z.-R., and Smith, J.D. (1996) *Organometallics*, **15**, 4783; (c) Eaborn, C., Hawkes, S.A., Hitchcock, P.B., and Smith, J.D. (1997) *Chem. Commun.*, 1961.
76. Kaupp, M., Schleyer, P.v.R., Stoll, H., and Dolg, M. (1992) *J. Am. Chem. Soc.*, **114**, 8202–8208.
77. Kaupp, M. (1999) *Chem. Eur. J.*, **5**, 3632–3643.
78. Kaupp, M. and Schleyer, P.v.R. (1993) *J. Am. Chem. Soc.*, **115**, 11202–11208.
79. (a) Westerhausen, M., Löw, R., and Schwarz, W. (1996) *J. Organomet. Chem.*, **513**, 213–229; (b) Westerhausen, M. (1994) *J. Organomet. Chem.*, **479**, 141–151; (c) Westerhausen, M., Hartmann, M., and Schwarz, W. (1996) *Inorg. Chem.*, **35**, 2421–2426; (d) Caulton, K.G., Chisholm, M.H., Drake, S.R., and Streib, W.E. (1990)

Angew. Chem. Int. Ed., **29**, 1483–1485; (e) Caulton, K.G., Chisholm, M.H., Drake, S.R., Folting, K., and Huffman, J.C. (1993) *Inorg. Chem.*, **32**, 816–820; (f) Darr, J.A., Drake, S.R., Hursthouse, M.B., and Malik, K.M.A. (1993) *Inorg. Chem.*, **32**, 5704–5708.

80. (a) Bytheway, I., Gillespie, R.J., Tang, T.-H., and Bader, R.W.F. (1995) *Inorg. Chem.*, **34**, 2407–2414; (b) Bytheway, I., Popelier, P.L.A., and Gillespie, R.J. (1996) *Can. J. Chem.*, **74**, 1059–1071.

81. McGrady, G.S., Haaland, A., Verne, H.P., Volden, H.V., Downs, A.J., Shorokhov, D., Eickerling, G., and Scherer, W. (2005) *Chem. Eur. J.*, **11**, 4921–4934.

82. Bader, R.W.F., Gillespie, R.J., and Martin, F. (1998) *Chem. Phys. Lett.*, **290**, 488–494.

2
Multiple Bonding of Heavy Main-Group Atoms

Gernot Frenking

2.1
Introduction

Chemical experience has shown that compounds with multiple bonds between heavier main-group atoms are much more difficult to synthesize, and that they often exhibit greatly different geometries than their counterparts of the first octal row [1]. The most prominent examples are the group-14 homologues of ethylene and acetylene. The chemical bonds in $H_2C{=}CH_2$ and $HC{\equiv}CH$ are archetypical examples for σ- and π-bonding in planar alkenes and linear alkynes. By contrast, quantum chemical calculations show that the equilibrium structures of E_2H_4 feature a trans-bent (E = Si, Ge) or a doubly hydrogen-bridged geometry (E = Sn, Pb) [2], and the ground state potential energy surfaces (PESs) of E_2H_2 possess energy minima structures with highly unusual geometries, none of them being linear HEEH (Scheme 2.1) [3]. Experimental evidence is in agreement with the theoretical predictions. Ditetrylenes E_2R_4, which could be isolated with bulky substituents R possess pyramidally coordinated ER_2 groups [1, 2a, 4]. The recent isolation of ditetrylynes E_2R_2 showed that the molecules have a trans-bent geometry where the bending angle is between 95 and140° [5]. Experimental studies of the parent systems E_2H_2 using low-temperature matrix techniques revealed that the energetically lowest lying isomers exhibit singly and doubly hydrogen-bridged geometries, [6] which are difficult to explain in terms of Lewis structures.

The striking differences in the equilibrium geometries of E_2R_4 and E_2R_2 suggest that chemical bonding of elements of the first octal row is significantly different from the heavier congeners. A seminal paper about the topic by Kutzelnigg was published thirty years ago where the author discusses quantum theoretical findings about chemical bonding in heavier main-group compounds [7]. A crucial difference between atoms of the first and higher octal rows, lies in the spatial distribution of the s and p valence orbitals that are engaged in covalent bonding. The cores of the lighter atoms contain only s atomic orbitals (AOs), whereas the cores of the heavier homologues include also occupied p AOs that enlarge the radius of the valence p' orbitals due to p-p' repulsion between electrons in the p(core) and p'(valence) orbitals. As a consequence, the s and p valence AOs of first row atoms are localized

The Chemical Bond: Chemical Bonding Across the Periodic Table, First Edition.
Edited by Gernot Frenking, Sason Shaik.

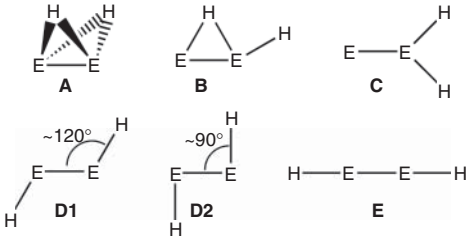

Scheme 2.1 Overview of the structures of E_2H_2 isomers **A–E** which are relevant for the discussion of the bonding situation.

in roughly the same region of space, whereas the p valence AOs of higher row atoms are much more extended in space than the respective s valence AOs. This may cause substantial differences in the σ- and π-bonds between atoms of the first octal row and the heavier main-group elements. Kutzelnigg came to the conclusion that the difference between the spatial distribution of the s and p valence orbitals implies that single bonds between the first row elements are weak and multiple bonds are strong, whereas for the second or higher row elements, single bonds are strong and multiple bonds weak [7]. Note that this does not mean that the π bonding in the latter bonds is weak. The key principles of the main-group chemical bonding and of important trends in the Periodic Table are discussed by Kaupp in Chapter 4 of Vol. 2.

In this chapter, we discuss the differences between multiple bonded main-group atoms of the first and higher octal rows in the light of modern quantum chemical methods. Rather than analyzing numerous species that possess multiple bonds between heavy main-group elements, we present a very detailed investigation of multiple bonded systems that exhibit archetypical bonding properties in representative molecules that may be used as models for other species. Firstly, we examine the intrinsic features of σ- and π-bonds in compounds that are not influenced by substituents and where the interacting fragments of the first and heavier octal rows that lead to a multiple bond have the same electronic ground state. To this end, we analyze chemical bonding in the diatomic group-15 molecules E_2 (E = N – Bi) with an energy decomposition analysis (EDA), which gives a quantitative account of the strength of σ- and π-bonding, without using a reference compound. Readers who are not familiar with the EDA may want to read the chapter ''The EDA View of Chemical Bonding'' which is presented by Frenking and Bickelhaupt in Volume 1 of this book. The substantial difference between chemical bonding of light and heavy main-group atoms and the relevance of σ and π interactions on the chemical reactivity of the associated molecules comes clearly to the fore by comparing the systems N_2/P_2 with N_4/P_4.

Secondly, we analyze a class of compounds which possess multiple bonded heavy main-group atoms that carry ligand atoms. We will show that the unusual equilibrium geometries of ditetrylynes E_2R_2 may be straightforwardly explained when the electron configuration of the bonded fragments ER and the nature of the E–E interatomic interactions is analyzed in terms of molecular orbital (MO)

interactions. The Lewis model of electron-pair bonding can be recovered when it is extended beyond electron-sharing σ- and π-bonds.

Finally, we want to point out that most of the calculated data in this article come from DFT calculations using different functional and basis sets. For technical aspects we refer to the original papers that are cited in the text.

2.2 Bonding Analysis of Diatomic Molecules E_2 ($E = N - Bi$)

The diatomic molecules of the group-15 elements E_2 ($E = N - Bi$) are ideally suited to study the essentials of σ- and π-bonding, which are not distorted by substituents or by geometrical constraints. The EDA results in Table 2.1 provide deep insights into the nature of the E–E bonds [8].

A comparison of the bond lengths, and bond dissociation energies of E_2, which were calculated at the BP86/TZ2P+ level with the experimental values [9], shows good agreement. The E–E bonds become longer and weaker when E becomes heavier, that is, the trend for the bond strength is $N_2 \gg P_2 > As_2 > Sb_2 > Bi_2$. The weakening of the bonds for heavier elements is because of the energy of the valence electrons, which are further away from the nucleus, and thus, are less strongly

Table 2.1 Energy partitioning analysis of the E–E bond in E_2 for $E = N$ - Bi (BP86/TZ2P+).

	N_2	P_2	As_2	Sb_2	Bi_2
ΔE_{int}	−240.2	−118.5	−97.3	−74.2	−64.6
ΔE_{Pauli}	802.2	317.6	276.8	219.3	201.9
ΔE_{Elstat} [a]	−312.8 (30.0%)	−186.3 (42.7%)	−181.5 (48.5%)	−159.0 (54.2%)	−150.8 (56.6%)
ΔE_{Orb} [a]	−729.6 (70.0%)	−249.8 (57.3%)	−192.7 (51.5%)	−134.5 (45.8%)	−115.7 (43.4%)
ΔE_{σ} [b]	−478.7 (65.6%)	−148.7 (59.5%)	−116.2 (60.3%)	−81.0 (60.3%)	−72.4 (62.6%)
ΔE_{π} [b]	−250.9 (34.4%)	−101.1 (40.5%)	−76.4 (39.7%)	−53.4 (39.7%)	−43.2 (37.4%)
Overlap σ [f]	1.59 (68.2%)	1.49 (70.3%)	1.40 (70.7%)	1.36 (72.3%)	1.21 (70.8%)
Overlap π [f]	0.74 (31.8%)	0.63 (29.7%)	0.58 (29.3%)	0.52 (27.7%)	0.50 (29.2%)
Hybridization	s: 37.5%	s: 20.8%	s: 15.4%	s: 11.6%	s: 8.0%
of the σ bond	p: 61.9%	p: 77.8%	p: 83.9%	p: 87.9%	p: 91.9%
R(E–E) [c]	1.102 (1.098) [d]	1.911 (1.893) [d]	2.113 (2.103) [d]	2.504 (2.48) [e]	2.660 (2.660) [d]
D_e	240.2	118.5	97.3	74.2	64.6
D_o [c]	236.9 (225.0) [d]	117.4 (116.1) [d]	96.7 (91.3) [d]	73.8 (71.3) [d]	64.3 (47.0) [d]

The interacting fragments are two atoms E in the ^4S ground state ($s^2p_x^1p_y^1p_z^1$). Energy values are given in kcal mol^{-1}. Bond lengths are given in Å.

[a] The values in parentheses give the percentage contribution to the total attractive interactions $\Delta E_{elstat} + \Delta E_{orb}$.

[b] The values in parentheses give the percentage contribution to the total orbital interactions ΔE_{orb}.

[c] Experimental results are given in parenthesis.

[d] Reference [9a].

[e] Reference [9b].

[f] The values in parentheses give the percentage contribution to the total orbital overlap.

attracted by the nucleus. Therefore, their covalent (orbital) interactions with the valence electrons of other atoms are usually[1] weaker than for valence electrons of lighter isoelectronic atoms. We want to point out that the weakening and the lengthening of the E–E bond is particularly large from nitrogen to phosphorous.

Inspection of the EDA results suggests that the attractive N–N interactions come mainly (70%) from orbital (covalent) interactions ΔE_{orb}, whereas 30% are contributed by electrostatic (coulombic) attraction ΔE_{elstat}. The percentage contribution of ΔE_{orb} in the heavier systems becomes gradually less and reaches 43.4% in Bi_2, whereas the electrostatic term becomes more important. The most interesting information comes from the breakdown of the orbital interactions into the contribution of the σ- and π-orbitals. Table 2.1 shows that ΔE_{σ} contributes about two-thirds (65.6%) to ΔE_{orb} in N_2, whereas ΔE_{π} contributes about one-third (34.4%) to covalent bonding.[2] The hybridization of the N–N σ-bond has a higher s contribution (37.5%) than the P–P bond (20.8%), which concurs with the finding that atoms of the first octal row exhibit larger s/p hybridization than the heavier homologues [7]. However, *the strength of the σ-bonds does not appear to be related to the hybridization, but rather to the atom type, and to the interatomic distance*. Table 2.1 shows that the percentage contribution of the valence s orbital to the E–E bonding becomes continuously smaller for the heavier atoms; it reaches only 8.0% in Bi_2. However, the contribution of ΔE_{σ} to the total orbital interactions rises from P_2 (59.5%) to Bi_2 (62.6%), where it has nearly the same value as in N_2 (65.6%). Although the s contribution to the σ-bonding continuously decreases, the relative contribution of the E–E σ-bond to ΔE_{orb} increases from E = P to E = Bi.

The ratio of the energy contributions of the σ- and π-orbitals correlates quite well with the overlap of the orbitals, which provide between 68.2 and 72.3% (σ), and between 27.7 and 31.8% (π) of the total overlap, respectively. *The data in Table* 2.1 *show that the ratio of the strength of σ- and π-bonding does not change significantly for the heavier E_2 molecules*. The relative energy contribution of ΔE_{π} even increases from N_2 (34.4%) to P_2 (40.5%) before it slightly decreases to Bi_2 (37.4%), where the percentage contribution is still larger than in N_2. The overlap integrals for the σ- and π-orbitals suggest slightly smaller contributions of the π-orbitals of the

1) There are some exceptions to the trend of weaker bonds of heavier atoms which may, for example, be caused by strong Pauli repulsion which becomes relevant when an atom has a doubly filled valence orbital. A prominent example is F_2 which has a weaker bond than Cl_2 (For a discussion, see G. Frenking, F. M. Bickelhaupt, Vol. 1, Chapter 4). Another factor which may lead to stronger bonds for heavier atoms are relativistic effects which become important for very heavy elements. Thus, donor–acceptor bonds of complexes of the third transition metal row are often stronger than chemical bonds of the second transition metal row. See the chapters about relativistic effects on chemical bonding (Vol. 1, Chapter 11) and about chemical bonding of transition metals (Vol. 2, Chapter 7) in this book.

2) This appears to be in agreement with the general understanding that σ-bonds are stronger than π-bonds. However, the conclusion ignores the contribution of the Pauli repulsion to the interatomic interactions, which plays an important role for the strength and for the equilibrium distance of covalent bonds. There is only Pauli repulsion between the electrons in σ orbitals of N_2 which makes the total σ interactions to become repulsive which is in agreement with earlier work by Kutzelnigg.[7] For a thorough discussion of the bond in N_2 we refer to Vol. 1, Chapter 4 of this book.

heavier molecules E_2 to the total overlap (27.7% – 29.7%) than in N_2 (31.8%), but the differences are not very large.[3] *The conclusion is that the experimentally observed lower stability of heavier main-group compounds with multiple bonds compared with compounds of the first octal row elements does not come from intrinsically weaker π-bonds between atoms of the higher octal rows.* But why is triply bonded N_2 a stable molecule, whereas the heavier group-15 elements under normal conditions are only stable as singly bonded oligomeric or polymeric species E_n? This question will be addressed in the next section.

2.3 Comparative Bonding Analysis of N_2 and P_2 with N_4 and P_4

The intrinsic difference between σ- and π-bonding of nitrogen and the heavier group-15 atoms can be analyzed by comparing the molecules E_2 and E_4 (T_d) for E = N, P [10]. The calculated (BP86/TZ2P+) reaction energies for formation of the tetraatomic species provide striking evidence for the vast variation in chemical bonding:

$$2N_2 \rightarrow N_4(T_d) + 158.9\,\text{kcal mol}^{-1} \tag{2.1}$$

$$2P_2 \rightarrow P_4(T_d) - 59.7\,\text{kcal mol}^{-1} \tag{2.2}$$

The theoretical reaction energy for the dimerization of P_2 (reaction (2.2)) which considers the correction for zero-point vibrational energies is $\Delta E_R{}^o = -58.0\,\text{kcal mol}^{-1}$. This is in good agreement with the experimental value of $\Delta E_R{}^o = -53.6\,\text{kcal mol}^{-1}$ [11]. The calculated reaction energies make it understandable why N_2 does not dimerize, whereas P_2 does. But what is the driving force for the different behavior? More precisely: Is there a particular term of the interatomic interactions which can be identified as the dominant factor that yields the drastically different energies for reactions (2.1) and (2.2)?

Table 2.2 shows the EDA results for the tetraatomic species N_4 and P_4 and a comparison of the calculated data per atom with the values for N_2 and P_2. The intrinsic interaction energy ΔE_{int} for N_4 ($-322.6\,\text{kcal mol}^{-1}$) is only slightly larger than for P_4 ($-293.1\,\text{kcal mol}^{-1}$). This may be compared with the results for the diatomic species given in Table 2.1, which show that the ΔE_{int} value for N_2 ($-240.2\,\text{kcal mol}^{-1}$) is much higher than for P_2 ($-118.5\,\text{kcal mol}^{-1}$). A comparison of the ΔE_{int} values per atom for the two systems reveals a qualitative difference between the nitrogen and phosphorous systems. The interaction energy for a single nitrogen atom in N_4 ($-80.7\,\text{kcal mol}^{-1}$) is clearly smaller than in N_2 ($-120.1\,\text{kcal mol}^{-1}$), whereas the ΔE_{int} value for a phosphorous atom in P_4 ($-73.3\,\text{kcal mol}^{-1}$) is larger than in P_2 ($-59.3\,\text{kcal mol}^{-1}$). However, this is a trivial

3) There is no direct relationship between the energy contributions ΔE_{orb} of the σ- and π-orbitals and the overlap, because the energy of the electrons depends on the interactions with all other electrons and nuclei.

Table 2.2 EDA results in kcal mol^{-1} for E_4 (E = N, P) (BP86/TZ2P+) and comparison with E_2.

	E_4	1/4 E_4	1/2 E_2
		E = N	
ΔE_{int}	−322.6	−80.7	−120.1
ΔE_{Pauli}	1636.6	409.2	401.1
ΔE_{elstat}[a]	−705.4 (36.0%)	−176.4 (36.0%)	−156.4 (30.0%)
ΔE_{orb}[a]	−1253.7 (64.0%)	−313.4 (64.0%)	−364.8 (70.0%)
ΔE_{σ}[b]	−1253.7 (100.0%)	−313.4 (100.0%)	−239.4 (65.6%)
ΔE_{π}[b]	–	–	−125.5 (34.4%)
Hybridization[d]	s: 7.0%	s: 7.0%	s: 37.5%
of the σ bond	p: 92.5%	p: 92.5%	p: 61.9%
R(N−N)	1.464	1.464	1.102
		E = P	
ΔE_{int}	−293.1	−73.3	−59.3
ΔE_{Pauli}	972.3	243.1	158.8
ΔE_{elstat}[a]	−545.7 (43.1%)	−136.4 (43.1%)	−93.2 (42.7%)
ΔE_{orb}[a]	−719.8 (56.9%)	−180.0 (56.9%)	−124.9 (57.3%)
ΔE_{σ}[b]	−719.8 (100.0%)	−180.0 (100.0%)	−74.4 (59.5%)
ΔE_{π}[b]	—	—	−50.6 (40.5%)
Hybridization[d]	s: 5.2 %	s: 5.2 %	s: 20.8%
of the σ bond	p: 93.2%	p: 93.2%	p: 77.8%
R(P−P)	2.221 (2.223)[c]	2.221	1.911

The interacting fragments are four atoms E in the ^{4}S ground state ($s^2p_x^1p_y^1p_z^1$). Bond lengths are given in Å.

[a] The values in parentheses give the percentage contribution to the total attractive interactions $\Delta E_{elstat} + \Delta E_{orb}$.

[b] The values in parentheses give the percentage contribution to the total orbital interactions ΔE_{orb}.

[c] Experimental value, Ref. [12].

[d] There is a small contribution from the d polarization functions.

result, because the interacting atoms are in the electronic ground state, and therefore, the differences between the ΔE_{int} values for 4N and 4P are identical to the dimerization energies, which are given in Eqs. (2.1) and (2.2). The crucial question concerns the EDA terms which are responsible for the opposite trends in the stabilization energies of N_2/N_4 and P_2/P_4.

The data in Table 2.2 show that the ΔE_{Pauli} values per atom slightly increase from N_2 (401.1 kcal mol^{-1}) to N_4 (409.2 kcal mol^{-1}), but they increase even more from P_2 (158.8 kcal mol^{-1}) to P_4 (243.1 kcal mol^{-1}). Thus, the differences between the Pauli repulsion do not explain the P−P bond strengthening from dimer to tetramer. The electrostatic attraction per atom calculated in P_4 (−136.4 kcal mol^{-1}) is stronger than in P_2 (−93.2 kcal mol^{-1}), but it also increases from N_2 (−156.4 kcal mol^{-1}) to N_4 (−176.4 kcal mol^{-1}). Although the increase of ΔE_{elstat} in the phosphorous species is stronger than in the nitrogen molecules, the unidirectional trend of the

Coulomb attraction does not agree with the opposite trend of the total interaction energy. A reverse trend is found, however, for the calculated values of the orbital interactions. The calculated ΔE_{orb} values per atom clearly decrease from N_2 ($-364.8\,kcal\,mol^{-1}$) to N_4 ($-313.4\,kcal\,mol^{-1}$), but they significantly increase from P_2 ($-124.9\,kcal\,mol^{-1}$) to P_4 ($-180.0\,kcal\,mol^{-1}$). *It follows that the opposite trend in the bond strength between the nitrogen, and phosphorous systems N_2/N_4 and P_2/P_4 comes mainly from the change in the covalent (orbital) bonding in the molecules.*

The finding that the orbital interactions are the crucial term for the opposite change of the bond strengths in N_2/N_4 versus P_2/P_4 can be made more specific through further analysis of the σ-bonds. The calculated value of $\Delta E_\sigma = -180.0\,kcal\,mol^{-1}$ for one phosphorous atom in P_4 which has three σ-bonds suggests that the ΔE_σ value for one P–P bond in the tetramer is $-120.0\,kcal\,mol^{-1}$. This is less than the ΔE_σ value in P_2 ($-148.7\,kcal\,mol^{-1}$), but the strength of the three P–P σ-bonds (−360.0 kcal/mol) overcompensates for the triple bond (σ- and two π-bonds) in P_2 (−249.8 kcal/mol). In N_4, the value of $\Delta E_\sigma = -313.4\,kcal\,mol^{-1}$ for one nitrogen atom suggests that the N–N σ-bond strength is $-208.9\,kcal\,mol^{-1}$, which is much weaker than the σ-bond in N_2 ($-478.8\,kcal\,mol^{-1}$). In contrast to P_4, the strength of the three N–N σ-bonds in N_4 ($3 \times -208.9 = -626.7\,kcal\,mol^{-1}$) does not compensate for the σ- and two π-bonds in N_2 ($-729.6\,kcal\,mol^{-1}$). *Thus, the crucial difference between the nitrogen and phosphorous systems lies in the strength of the E–E σ-bonds in N_4 and P_4, but not in the π-bonds of E_2. More specifically, it is the substantial weakening of the N–N σ-bond in N_4 which makes N_2 more stable than the tetraatomic species.*

Note that the strength of the E–E σ-bonds in E_4 is *not* related to the hybridization, but rather to the E–E bond lengths in the tetraatomic systems. The calculated P–P bond length in P_4 (2.221 Å) is in excellent agreement with the experimental value (2.223 Å) [12]. Table 2.2 shows that the % s contributions to the σ-bond in N_4 (7.0%), and P_4 (5.2%) have similarly low values. However, the bond lengthening from N_2 to N_4 ($\Delta R = 0.362$ Å) is larger than from P_2 to P_4 ($\Delta R = 0.310$ Å). The N–N bond of N_2 becomes 32.8% longer in the tetraatomic molecule, whereas the P–P bond of P_2 is stretched by only 16.2%. This explains why the N–N σ-bonds in N_4 become much weaker than in N_2 compared to the P–P σ-bond weakening in P_4 relative to P_2. Because the equilibrium distances of covalent bonds E–E are determined by Pauli repulsion, which has a very steep gradient in the region of orbital overlap rather than by the overlap of the bonding orbitals [13], it may be concluded that *the origin of the different change in the σ-bond strength of the systems N_2/N_4, and P_2/P_4 comes from Pauli repulsion.* This is a somewhat paradoxical result, because the calculated values for ΔE_{Pauli} do not correlate with the opposite trend of the bond strengths in the two systems. The important role of the Pauli repulsion for the relative stability of the E_4 isomers comes to the fore when the ΔE_{Pauli} values per atom are compared with the data for E_2. Although the E–E bonds in the tetramers are significantly longer than in the dimers, the Pauli repulsion per atom in N_4 and P_4 is larger than in N_2 and P_2, respectively. This is because each atom in E_4 encounters Pauli repulsion by three other atoms whereas in E_2 there is Pauli repulsion with only one atom. Because further shortening of covalent σ-bonds is in most cases not because

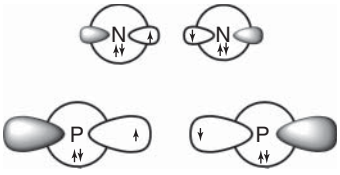

Figure 2.1 Schematic representation of the s and p valence orbitals of nitrogen and phosphorous in the diatomic molecules which show the different s/p ratio of the radii.

of weaker attraction but to the increase in ΔE_{Pauli}, the effect of Pauli repulsion is the prevention of stronger σ-bonding. A related case is discussed by Frenking, and Bickelhaupt in Chapter 4 in Vol. 1, where the reason for the weaker bond in F_2 compared to Cl_2 is examined.

The reasoning in the earlier paragraph suggests that the driving force for the lengthening of the E–E bonds in E_4 is the Pauli repulsion, which is stronger than in E_2. But why is the Pauli repulsion between the nitrogen atoms in (T_d) N_4 so much stronger than between the phosphorus atoms in (T_d) P_4? The answer to this question paves the way for the ultimate explanation of the very low stability of (T_d) N_4. Table 2.1 shows that the σ bond in N_2 has a much higher contribution from the valence s AO (37.5%) than the σ bond in P_2 (20.8%). As pointed out by Kutzelnigg [7], the 2s and 2p valence AOs of first octal-row atoms have a similar radius whereas the *n*p ($n \geq 3$) valence AOs of the heavier main-group atoms posses a larger radius than the *n*s AOs. In the bonding region where the valence orbitals overlap, the nitrogen atoms encounter 2s–2s Pauli repulsion between the doubly occupied 2s AOs in a higher degree than phosphorus atoms experience Pauli repulsion between the 3s–3s AOs. This is schematically shown in Figure 2.1. Thus, the higher stability of P_4 compared with P_2, and the lower stability of N_4 over N_2 can be traced down to the different ratio of the radii for the *n*s/*n*p valence orbitals for $n = 2$ and $n = 3$.

The conclusion of the bonding analysis is as follows. The different stabilities of N_4 and P_4 with regard to N_2 and P_2 arise from the change in the strength of the σ-bonds, but not from the strength of the π-bonds in the diatomic molecules. The N–N bonds in N_4 are 32.8% longer than in N_2, which means that the σ-bonds in N_4 are rather weak. The covalent interactions of three N–N σ-bonds are weaker than the σ- and π-bonds in N_2. By contrast, the P–P bonds in P_4 are only 16.2% longer than in P_2, and therefore, the covalent interactions of three P–P σ-bonds are stronger than the σ- and π-bonds in P_2. The equilibrium bond lengths of the N–N and P–P bonds are determined by Pauli repulsion, which may, therefore, be considered as the origin of the opposite stability order of the nitrogen and phosphorous systems E_2 and E_4. The unlike effect of the Pauli repulsion on the stability of (T_d) E_4 versus E_2 for the nitrogen and phosphorous systems comes from the different radii of the *n*s/*n*p valence orbitals for $n = 2$ and $n = 3$.

2.4
Bonding Analysis of the Tetrylynes HEEH (E = C – Pb)

Quantum chemical calculations show that there are four energetically low-lying energy minima **A**, **B**, **C**, **D1** (Figure 2.2) on the singlet PES of E_2H_2 (E = Si – Pb) [3]

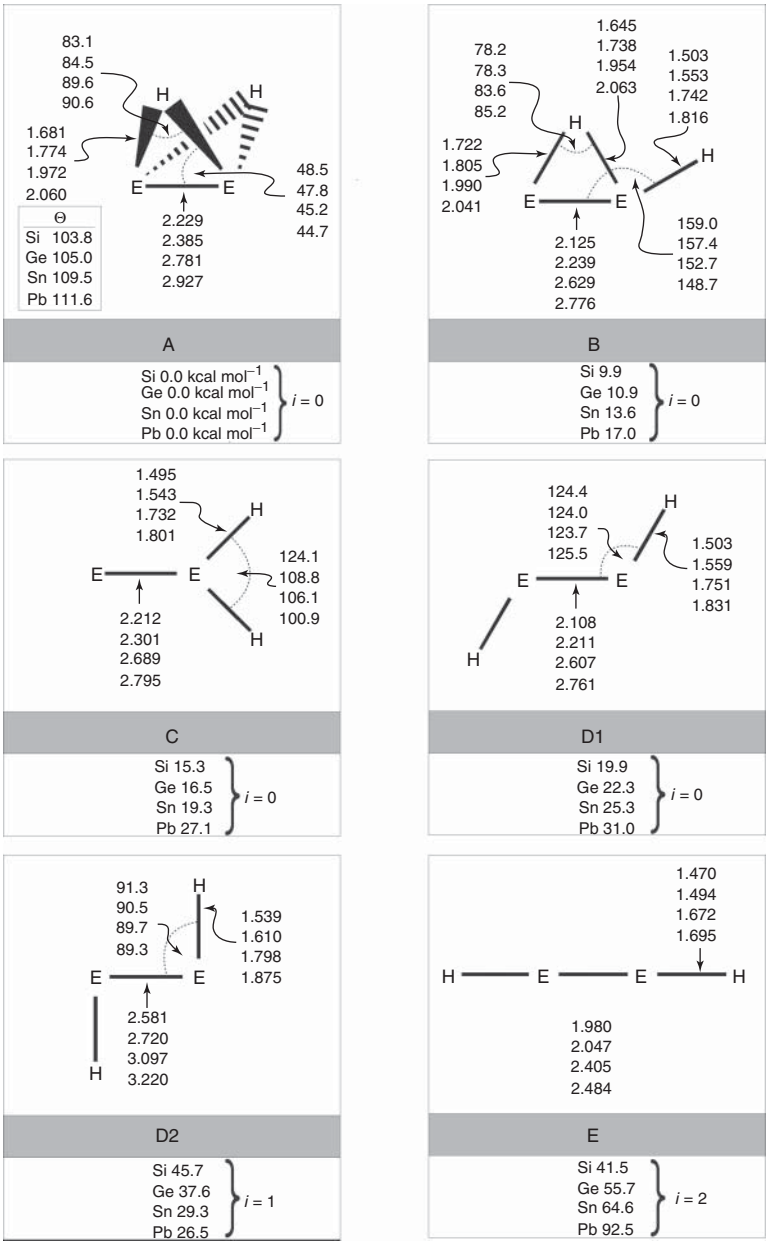

Figure 2.2 Optimized structures of E_2H_2 isomers **A**–**E** at BP86/QZ4P. Bond lengths are given in Å, angles in degree. The values for Θ give for structure **A** the dihedral angle between the E_2H and E_2H' planes. The relative energies with respect to **A** are given at the bottom of each entry in kcal mol^{-1} together with the number of imaginary frequencies *i*.

The linear, triply bonded structure HE≡EH (**E**), which is the global energy minimum for E = C, is an energetically high-lying second order saddle point (number of imaginary frequencies i = 2). The trans-bent structure **D2**, which has a more acute bonding angle H–E–E of ~90° , and a significantly longer E–E distance than **D1**, is a transition state ($i = 1$). The energy ordering of the six structures is **A** < **B** < **C** < **D1** < **D2** < **E** for nearly all heavy atoms. The only exceptions occur for the transition state **D2**, where **D2(Si)** > **E(Si)** and **D2(Pb)** < **D1(Pb)**. For all heavier elements, E holds that the doubly bridged butterfly structure **A** is the global energy minimum, and the singly bridged isomer **B** is the next low-lying isomer. The vinylidene form **C** is the only isomer that is an energy minimum structure for all group-14 atoms.

The theoretically predicted unusual structures **A** and **B** were confirmed by spectroscopic studies on Si_2H_2 in low-temperature matrices [14]. The doubly, hydrogen-bridged equilibrium structures of the heavier homologues Ge_2H_2, Sn_2H_2, and Pb_2H_2 could also become identified in low-temperature matrices [15]. Derivatives E_2R_2, which carry bulky aryl substituents R, have, in the meantime, been synthesized, and structurally characterized by X-ray analysis for all group-14 atoms E [5]. The experimentally derived geometries of E_2R_2 exhibit a trans-planar arrangement of R, which resembles structure **D1** for E = Si, Ge, Sn,[5a–c] whereas the lead homologue Pb_2R_2, which features a much more acute bending angle [5d] R–Pb–Pb of 94°, may better be considered as a derivative of **D2** [16].

The results of the quantum chemical calculations and the experimental observations are a challenge to chemical bonding theory to explain the unusual findings in terms of bonding models. Four questions are addressed in this section, which will be dealt with in a didactical way. We refer to the original literature, which is cited below for technical details. The questions are:

1) Why is the triply bonded, linear structure of acetylene HC≡CH not an energy minimum for HE≡EH (E = Si – Pb) but an energetically, high-lying saddle point on the PES?
2) Why do the heavier group-14 homologies of C_2H_2 possess significantly different geometries in a variety of energetically, low-lying equilibrium structures?
3) What is the bonding situation in the isomers **A – D** of E_2H_2?
4) Why do the substituted homologues E_2R_2 have trans-bent equilibrium geometries? Do they possess E-E triple bonds?

2.5 Explaining the Different Structures of the Tetrylynes HEEH (E = C – Pb)

The key to answering the questions above lies in the electronic state of the fragments EH, which are engaged in E–E bonding in E_2H_2. Because the vinylidene isomer **C** has a different atomic connectivity where the hydrogen atoms are bonded to only one atom E, we do not include it in our discussion which is, thus, restricted to isomers **A**, **B**, **D1**, **D2**, and **E**.

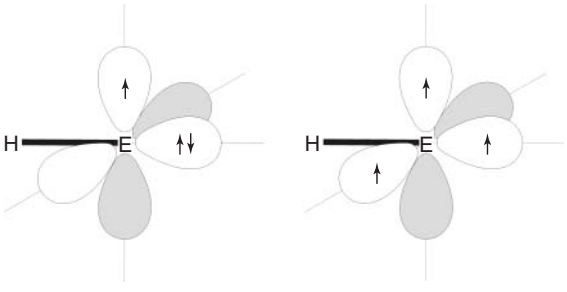

$^2\Pi$ $^4\Sigma^-$

exp.	calc.	
0.0		
16.7	15.4	(E = C)
36.4	38.6	(E = Si)
47.8	47.1	(E = Ge)
44.5	45.9	(E = Sn)
50.3	52.0	(E = Pb)

Figure 2.3 Schematic representation of the electron configuration of the $^2\Pi$ electronic ground state, and the $a^4\Sigma^-$ excited state of EH (E = C–Pb). The experimental [9a], and calculated (BP86/QZ4P) excitation energies are given in kcal mol^{-1}.

Figure 2.3 shows schematically the electronic ground state (X $^2\Pi$) and the first excited state (a $^4\Sigma^-$) of EH, as well as the calculated and experimental excitation energies X $^2\Pi \rightarrow a^4\Sigma$. It is obvious that the triply bonded species HE≡EH requires the excited quartet state a $^4\Sigma^-$ of EH for the formation of a σ-bond and a degenerate π-bond. The excitation energy increases from carbon to lead, which means that it is energetically much easier to excite CH than for the heavier EH species from the X $^2\Pi$ ground state to the a $^4\Sigma^-$ excited state in order to form a triple bond. One could now pose the question like a salesman: Is the stabilization that is associated with the formation of a HE≡EH triple bond large enough to compensate for the X $^2\Pi \rightarrow$ a $^4\Sigma^-$ excitation energy ΔE_{exc} of two EH species? The energy gain of the triple bond must also be larger than the bond energy that comes from the interactions of two EH molecules in the X $^2\Pi$ ground state. The question may be addressed with quantum chemical methods, because the linear species HE≡EH, and the associated bond dissociation energy D_e for the reaction HE≡EH → 2 EH (a $^4\Sigma^-$) can be calculated. Table 2.3 gives the numerical results of the calculations.

The calculated data show a net energy gain of $D_e - 2 \times \Delta E_{exc} = 240.0$ kcal for the formation of a C≡C triple bond. This value is much higher than the bond energy of a C–C single bond, which would come from the coupling of the unpaired electrons in the (X $^2\Pi$) ground state of CH (Figure 2.3). It is, therefore, energetically profitable for CH to excite to the $^4\Sigma^-$ quartet state, because the stabilization which is gained from the formation of the triple bond is larger than the sum of the excitation energy and the energy of a C–C single bond.

The situation looks very different for the heavier homologues EH. Table 2.3 shows that the net energy gain of $D_e - 2 \times \Delta E_{exc}$ in the case of silicon is only 44.5 kcal, which is much less than the typical value for a Si–Si single bond (75 kcal mol^{-1}) [17].

Table 2.3 Calculated bond dissociation energies D_e (kcal mol^{-1}) of linear HE≡EH → 2 EH ($a^4\Sigma^-$), and $X^2\Pi \rightarrow a^4\Sigma^-$ excitation energies ΔE_{exc} (kcal mol^{-1}) of EH at BP86/QZ4P.

E	D_e	ΔE_{exc}	$D_e - 2 \times \Delta E_{exc}$
C	270.9	15.44	240.0
Si	121.6	38.56	44.5
Ge	113.3	47.09	19.0
Sn	89.4	45.87	−2.3
Pb	69.0	52.01	−35.0

The energy balance becomes even more unfavorable for germanium, where the energy gain $D_e - 2 \times \Delta E_{exc}$ is only 19.0 kcal mol^{-1}, whereas the average bond energy of a Ge–Ge single bond is around 67 kcal mol^{-1} [18]. The calculated values of $D_e - 2 \times \Delta E_{exc}$ for tin and lead are even negative, which indicates that there is no driving force for the formation of isomer **E** for these elements at all.

The calculated values for the difference between the X $^2\Pi \rightarrow$ a $^4\Sigma^-$ excitation energy of EH and the HE≡EH bond strength suggest that the heavier homologues of EH dimerize through the X $^2\Pi$ ground state which has one unpaired electron (Figure 2.3). This answers the first of the questions above: *The linear structures HE≡EH are not minima on the PES, because the a $^4\Sigma^-$ excited state of EH, which is required for the formation of the triple bond, is too high in energy*. We want to point out that this reasoning is analogous to the explanation for the nonplanar equilibrium structures of the heavy group-14 homologues of ethylene H_2EEH_2, which was suggested by Trinquier and Malrieu [19] and by Carter and Goddard [20]. These authors pointed out that the carbon–carbon double bond in ethylene $H_2C{=}CH_2$ comes from the electron-sharing interactions of the CH_2 fragments in the $^3B_1$ triplet state, whereas the E–E bonds in the heavier homologues $H_2E{\leftrightarrow}EH_2$ are due to donor–acceptor bonding between the EH_2 fragments in the $^1A_2$ ground state (Figure 2.4) [18]. The same reasoning will be used to explain the formation of the unusual isomers of E_2H_2.

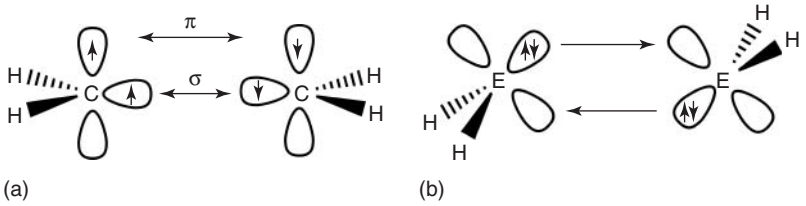

Figure 2.4 Bonding model of Trinquier/Malrieu/Carter/Goddard for (a) orbital interaction between two CH_2 fragments in the $^3B_1$ state which leads to σ and π bonding in $H_2C{=}CH_2$, and (b) orbital interactions between two EH_2 fragments (E = Si – Pb) in the $^1A_2$ state which leads to donor–acceptor double bonding in $H_2E \rightleftarrows EH_2$.

Coupling of the unpaired electrons of two EH moieties in the X $^2\Pi$ ground state gives rise to different structural isomers. It is obvious that none of them can have a linear arrangement HEEH. Figure 2.5 shows three different arrangements of (X $^2\Pi$) EH where the coupling of the unpaired electrons leads to an E-E σ-bond. Geometry optimization of the planar *syn* arrangement, which is shown in Figure 2.5a, yields an energetically high-lying transition state which has an unfavorable bonding situation. The lone-pair (lp) electrons are coplanar to each other, although the vacant p(π) AOs remain empty, which leads to an electron sextet at E. The situation becomes much more favorable in the arrangement, which is shown in Figure 2.5b, where one EH bond is rotated by 90° about the E–E axis. The E–H bonds are now mutually facing the vacant p(π) AOs, which enables the donation of E–H electronic charge into the formally empty orbitals. The E–H bonds are tilting in order to maximize the E–H donation which straightforwardly leads to the doubly bridged butterfly structure **A**. Here, the atoms E attain an electron octet through the three-centre, two-electron bonds, as is found in B_2H_6. Unlike in diborane, the bridging hydrogen atoms are not in a *trans* position because the vacant p(π) acceptor orbitals are not available when the E–H moieties are in an *anti* arrangement (Figure 2.5c). The latter form, which is a transition state, is unfavorable, because the atoms E retain an electron sextet where the p(π) orbitals remain vacant. It leads to structure **D2**, which does play a role for E = Pb with large substituents R instead of hydrogen. This will be discussed further in the following paragraphs.

Figure 2.5b shows that the E–E bonding in the doubly bridged butterfly structure **A**, which is the global energy minimum for E_2H_2 (E = Si – Pb), comprises three components: One is an electron-sharing σ-bond, whereas the other two components are two equivalent EH donor–acceptor bonds. Thus, E_2H_2 (**A**) possesses an E-E triple bond, but the components of the electron-pair bonding differ from a classical triple bond, which has a σ-bond, and a degenerate π-bond. One may argue that the arrangement of the EH fragments, which is shown in Figure 2.5b should give rise to electron donation from the lone pair (lp) electrons rather than from the E–H bonds, because donation from lp orbitals is usually considered to be stronger than charge donation from bonding orbitals. This holds for elements of the first octal row, but not necessarily for the heavier main-group atoms. The lp orbitals of heavy main-group atoms are nearly pure s orbitals, which may become energetically lower lying than sp hybridized bonding orbitals. Also, the E–H bonds of heavier atoms E are more polarised toward hydrogen, because of the decreasing electronegativity of E. This makes the E–H bonding orbital a better charge donor than lp orbitals.

Figure 2.5 shows schematically how structures **A** and **D2** are developed through orbital interactions yielding an electron-sharing σ-bond between two (X $^2\Pi$) EH moieties, but structures **B** and **D1** are still missing. Figure 2.6 displays three different arrangements of (X $^2\Pi$) EH where the coupling of the unpaired electrons leads to an E–E π-bond, which is weaker than a E–E σ-bond. However, additional donor–acceptor interactions could stabilize the π-bonded species, which might lead to energetically low-lying structures. Figure 2.6a displays such an arrangement where the E–E π-bond is further supported by one EH donor–acceptor, and one lp donor–acceptor bond. The E–H charge donation of one EH into the vacant

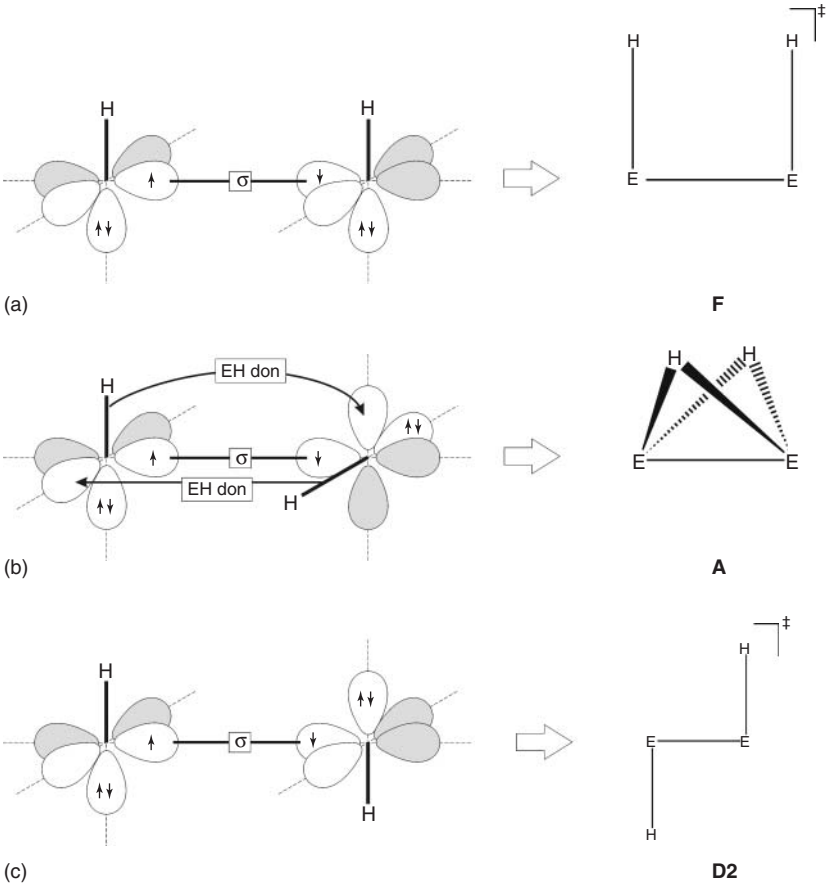

Figure 2.5 Qualitative model for the orbital interactions between two EH molecules in different orientations where the unpaired electrons yield a σ bond.

p(π) orbital of the other EH fragment induces a bending of the latter E–H bond toward the bridging hydrogen. This explains nicely the unusual geometry of the planar isomer **B**, where the terminal hydrogen atom is tilted toward the bridging hydrogen atom. A qualitative comparison of the orbital interactions in structure **B** (one electron-sharing π-bond, one EH donor–acceptor bond, and one lp donor–acceptor bond), and structure **A** (one electron-sharing σ-bond, and two EH donor–acceptor bonds) suggests that the former isomer should be an energetically higher lying form that agrees with the calculated energies, which are given in Figure 2.2.

The qualitative bonding model for structure **B** is supported by a topographical analysis of the calculated electronic structure which rests on the QTAIM (Quantum Theory of Atoms in Molecules) method.[4] Figure 2.7 shows the Laplacian of

4) The QTAUM method is described in Vol. 1, Chapter 8.

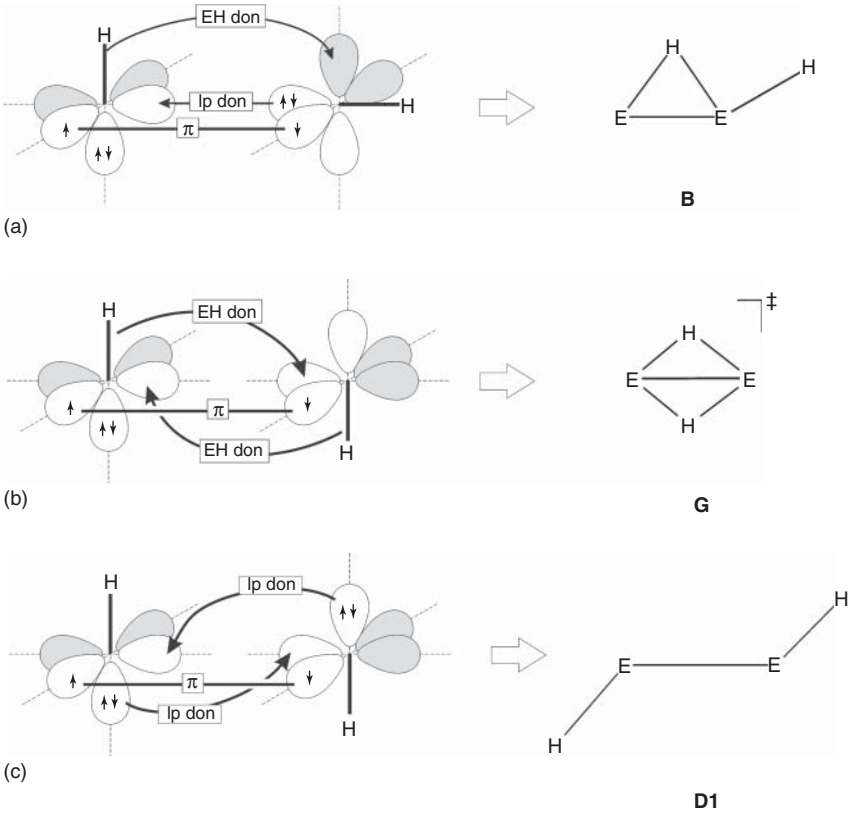

Figure 2.6 Qualitative model for the orbital interactions between two EH molecules in different orientations where the unpaired electrons yield a π bond.

the electronic charge distribution $\nabla^2\rho(r)$ in the molecular plane, which is more instructive than the charge distribution $\rho(r)$ itself, because it visually displays a relative accumulation of electronic charge. Solid lines indicate areas of charge concentration ($\nabla^2\rho(r) < 0$), whereas dashed lines show areas of charge depletion ($\nabla^2\rho(r) > 0$). There are four areas of charge concentration, which can be identified with the help of the bonding model of Figure 2.6a. One area is found along the Si–H terminal bond, where it is polarized toward hydrogen, which agrees with its higher electronegativity. Another area is found at the bridging hydrogen atom which extends towards both silicon atoms. A third area of charge concentration is visible between the silicon atoms. Note that the latter area has its maximum closer to the Si($-H_{terminal}$) atom, and that it is a bit below the Si–Si bond path which is slightly bent. This is in agreement with the notation that the Si–Si σ-bond comes from the charge donation of the lp electrons of Si($-H_{terminal}$). Finally, there is an area of charge concentration at the left silicon atom of Figure 2.7, which comes from the lp electrons that are shifted outwards, because the Si-H bond of the latter

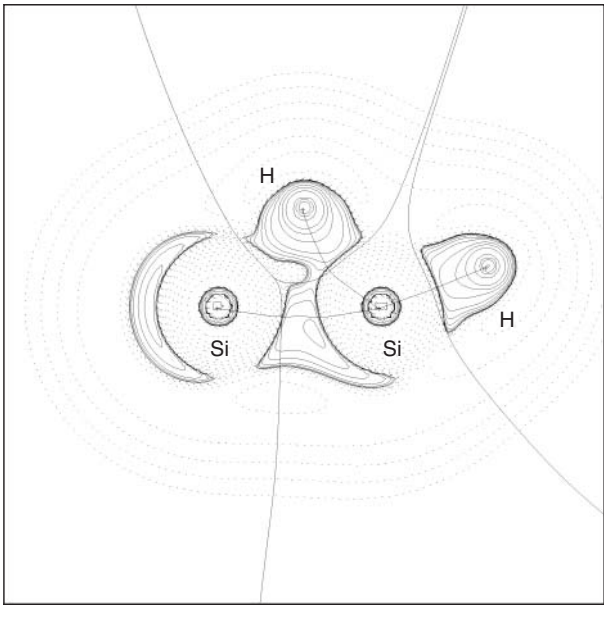

Figure 2.7 Contour line diagram $\nabla^2\rho(r)$ of isomer **B** of Si_2H_2. Solid lines indicate areas of charge concentration ($\nabla^2\rho(r) < 0$) whereas dashed lines show areas of charge depletion ($\nabla^2\rho(r) > 0$). Solid lines which connect the atomic nuclei are the bond paths, whereas solid lines which separate the atomic basins give the zero-flux surfaces in the molecular plane.

silicon atom bends toward the vacant p(π) orbital of the right SiH fragment. The charge concentration of the Si–Si π bond is not visible in Figure 2.7 because it is orthogonal to the molecular plane.

Figure 2.6b exhibits another orientation of two EH molecules where the unpaired electrons yield a π-bond whereas the EH bonds are in a *trans* position. The π-bonding between the EH fragments is now enhanced by two degenerate donor–acceptor interactions between the EH bonding orbitals, and the empty p(π) orbitals of the interacting fragments. The latter orbital interactions are maximized when the hydrogen atoms adopt a doubly bridged planar (D_{2h}) structure **G**, which has not yet been considered. There are three bonding components in **G**, one E–E π-bond, and a degenerated pair of E–H donor–acceptor bonds. The qualitative arguments that have been advanced earlier predict that **G** should be more strongly bonded than **B**, because the E-H donation is stronger than lp donation. Quantum chemical calculations show that structure **G** is indeed lower in energy than **B** [3]. However, calculations of the Hessian matrices reveal that structure **G** is a transition state whereas the energetically higher lying form **B** is an energy minimum for all elements E = Si – Pb. This is because **G** is located on the PES in the vicinity of the global energy minimum structure **A**. Structure **G** is the transition state for the degenerate flapping rearrangement $\mathbf{A} \rightarrow [\mathbf{G}]^{\ddagger} \rightarrow \mathbf{A}$.

Figure 2.6c shows the same starting arrangement of the EH fragments as in 5b, where the donor–acceptor interactions now come from lp donation instead of E-H donation. This yields structure **D1**, which should be higher in energy than **B**, and still higher than **G**. Quantum chemical calculations show that the stability order is indeed **G** > **B** > **D1**, which is in agreement with the stronger E-H donation than lp donation. Whereas structure **D1** is the energetically highest lying energy minimum of the E_2H_2 isomers **A – D1**, which has not yet been experimentally observed, it becomes important when hydrogen is replaced by a bulky substituent. Visual inspection of the isomers that are shown in Figure 2.2 makes it obvious that the trans-bent form **D1** becomes energetically favored when steric repulsion between the substituents R in E_2R_2 are strong enough to overcompensate the energy differences which are calculated between the E_2H_2 isomers. The steric repulsion between the bulky substituents in Pb_2R_2, where R is a large aryl group, also turns structure **D2** into an energy minimum [16], which in the case of lead is lower in energy than the **D1** isomer (Figure 2.2).

2.6 Energy Decomposition Analysis of the Tetrylynes HEEH (E = C – Pb)

The discussion of the E–E bonding in tetrylynes HEEH in terms of interactions between the fragments EH leads to a straightforward explanation for the unusual geometries for the isomers, which are found as equilibrium structures on the E_2H_2 PES. The calculated energy ordering of the isomers **A – D** was rationalized with the strength of the different orbital interactions for electron-sharing, and donor–acceptor bonds. A quantitative estimate of the different types of orbital interactions can be made with the help of EDA calculations, which have proven to be very useful for the comparison of N_2 and P_2 with N_4 and P_4. The bonding analysis of the tetrylynes HEEH emphasized the relevance of orbital interactions for explaining the different isomers. Therefore, we focus on the strength of the orbital term ΔE_{orb} for the various orbital interactions that have been calculated for the isomers **A – D**, and for the linear form **E**. The results are shown in Table 2.4. For a complete presentation of the EDA results, which are not relevant for the present discussion, we refer to the literature [3].

The ΔE_{orb} results for acetylene give the strength of the σ-bond to be $-215.5\,kcal\,mol^{-1}$,[5] and the degenerate π-bond as $2 \times -86.2\,kcal\,mol^{-1}$. The contribution of π-bonding to the total orbital interactions in HC≡CH [**E(C)**] is thus 44.4%, which is somewhat higher than in N≡N, where it is 34.4% (Table 2.1). The π contribution to ΔE_{orb} changes very little when one goes from HC≡CH to HSi≡SiH [**E(Si)**] (44.1%), HGe≡GeH [**E(Ge)**] (43.0%), HSn≡SnH [**E(Sn)**] (41.6%), and HPb≡PbH [**E(Pb)**] (42.6%). As noted above for the systems E_2, the contribution

5) The calculated orbital interactions of the EDA have negative values, because the system becomes lower in energy due to the mixing of the orbitals. Therefore, we use negative values for the strength of the orbital interactions in the text.

Table 2.4 Number and strength (given in parentheses in kcal mol^{-1}) of the stabilizing orbital interactions ΔE_{orb} in E_2H_2 structures **A**, **B**, **D1**, **D2**, and **E** calculated by the EDA method, and strength of the electrostatic attraction, pauli repulsion, and total interaction.

Bonding Type	A	B	D1	D2	E
			C_2H_2		
σ-bond					1 (−215.5)
π-bond					2 (2 x −86.2)[a]
EH-donation					—
lp-donation					—
$\Sigma \Delta E_{orb}$					3 (−387.9)
ΔE_{elstat}					−147.5
ΔE_{Pauli}					255.4
ΔE_{int}					−280.0
			Si_2H_2		
σ-bond	1 (−116.8)	—	—	1 (−74.9)	1 (−96.9)
π-bond	—	1 (−43.7)	1 (−41.7)	—	2 (2 × −38.25)[a]
EH-donation	2 (2 × −66.7)	1 (−77.5)	—	—	—
lp-donation	—	1 (−71.7)	2 (2 × −52.65)	—	—
$\Sigma \Delta E_{orb}$	3 (−250.2)	3 (−192.9)	3 (−147.0)	1 (−74.9)	3 (−173.4)
ΔE_{elstat}	−128.9	−118.2	−82.3	−68.6	−61.5
ΔE_{Pauli}	286.9	229.6	162.1	101.4	109.9
ΔE_{int}	−92.5	−81.4	−67.2	−42.1	−125.0
			Ge_2H_2		
σ-bond	1 (−94.5)	—	—	1 (−62.9)	1 (−96.4)
π-bond	—	1 (−37.8)	1 (−36.7)	—	2 (2 × −36.3)[a]
EH-donation	2 (2 × −59.4)	1 (−70.2)	—	—	—

lp-donation	—	1 (−51.8)	2 (2 × −40.85)	—	—
$\Sigma\ \Delta E_{orb}$	3 (−213.3)	3 (−159.8)	3 (−118.4)	1 (−62.9)	3 (−169.0)
ΔE_{elstat}	−137.5	−127.8	−82.5	−67.8	−85.5
ΔE_{Pauli}	268.9	217.9	146.3	92.2	135.9
ΔE_{int}	−82.0	−69.7	−54.6	−38.6	−118.6
		Sn_2H_2			
σ-bond	1 (−71.1)	—	—	1 (−51.5)	1 (−76.6)
π-bond	—	1 (−28.6)	1 (−27.6)	—	2 (2 × −27.25)
EH-donation	2 (2 × −47.7)	1 (−54.8)	—	—	—
Lp-donation	—	1 (−34.1)	2 (2 × −28.75)	—	—
$\Sigma\ \Delta E_{orb}$	3 (−166.5)	3 (−117.5)	3 (−85.0)	1 (−51.5)	3 (−131.0)
ΔE_{elstat}	−127.1	−111.9	−68.7	−63.8	−79.5
ΔE_{Pauli}	224.2	174.9	113.6	81.1	115.0
ΔE_{int}	−69.4	−54.5	−40.1	−34.4	−95.5
		Pb_2H_2			
σ-bond	1 (−59.9)	—	—	1 (−44.8)	1 (−71.9)
π-bond	—	1 (−24.3)	1 (−23.2)	—	2 (2 x −26.65)[a]
EH-donation	2 (2 × −42.3)	1 (−43.6)	—	—	—
lp-donation	—	1 (−20.2)	2 (2 × −18.15)	—	—
$\Sigma\ \Delta E_{orb}$	3 (−144.5)	3 (−88.1)	3 (−59.5)	1 (−44.8)	3 (−125.2)
ΔE_{elstat}	−129.0	−94.1	−45.7	−61.8	−73.6
ΔE_{Pauli}	209.1	138.1	77.4	74.8	117.7
ΔE_{int}	−64.3	−44.2	−27.8	−32.0	−81.1

[a]The interacting fragments are EH in the a $^2\Pi$ excited state for isomers **A–D2** and EH in the $^4\Sigma^-$ ground state for isomer **E**.

of π-bonding to multiple bonds does not change very much for heavier main-group elements.

The EDA results for the silicon isomers will be discussed in more detail in order to demonstrate the wealth of information which is gained by the bonding analysis. Please note that the interacting fragments in the case of the linear systems HE≡EH are two EH species in the X $^4\Sigma^-$ ground state, whereas it is the a $^2\Pi$ excited state in the other cases. Table 2.4 shows that the Si–Si σ-bond of **A(Si)** is stronger (−116.8 kcal mol^{-1}) than in **E(Si)** (−96.9 kcal mol^{-1}), although the Si–Si distance in the former molecule is longer (2.229 Å) than in the latter (1.980 Å). This can be explained by the hybridization of the interacting orbitals of the SiH fragments which are sp hybridized in the linear species **E(Si)**, whereas the side-on approach of the SiH fragments that leads to **A(Si)** (Figure 2.5b) uses a silicon p AO for the formation of the electron-sharing σ-bond. The overlap, and thus, the strength of the orbital interactions between p(σ) AOs is larger at longer distances than between sp hybrids. Another interesting result is the strength of the SiH donation in the doubly bridged species **A(Si)**. Table 2.4 shows that the SiH donor–acceptor bond (−66.7 kcal mol^{-1}) is much stronger than the Si-Si electron-sharing π-bond in **E(Si)** (−38.25 kcal mol^{-1}). The EDA calculations show that the strength of ΔE_{orb} of the triple bond in **A(Si)**, which has a σ bond and two SiH donor–acceptor bonds is larger (−250.2 kcal/mol) than the conventional triple bond in **E(Si)**, where $\Delta E_{orb} = -173.4$ kcal mol^{-1}. The electrostatic attraction ΔE_{elstat} between the SiH moieties in **A(Si)** is also much stronger (−128.9 kcal mol^{-1}) than in **E(Si)** (−61.5 kcal mol^{-1}), which comes from the better overlap of the p(σ) electron of SiH with the Si nucleus of the other SiH fragment in the former isomer than the sp electron of SiH in **E(Si)**. Although both attractive terms ΔE_{orb} and ΔE_{elstat} suggest stronger attraction in **A(Si)** than in **E(Si)**, the total interaction energy ΔE_{int} of the latter is larger (−125.0 kcal mol^{-1}) than in the former (−92.5 kcal mol^{-1}). This is because the doubly bridged global energy minimum form **A(Si)** encounters significantly stronger Pauli repulsion ΔE_{Pauli} (286.9 kcal mol^{-1}) than the linear form **E(Si)** (109.9 kcal mol^{-1}).[6)]

Table 2.4 also gives the three orbital components of the singly bridged isomer **B(Si)**. The data calculated suggest that the strongest bonding comes from the SiH donor–acceptor bond (−77.5 kcal mol^{-1}), followed by the lp donor–acceptor bond (−71.7 kcal mol^{-1}), and the significantly weaker π-bond (−43.7 kcal mol^{-1}). The numerical results agree with the qualitative reasoning in the previous section that EH donation of heavier main-group elements is stronger than lp donation. The SiH donor–acceptor bond in **B(Si)** is stronger than in **A(Si)** because the Si-Si distance in the former isomer is shorter than in the latter (Figure 2.2). The total orbital interactions in **B(Si)** ($\Delta E_{orb} = -192.9$ kcal mol^{-}), and the electrostatic attraction ($\Delta E_{elstat} = -118.2$ kcal mol^{-1}) are weaker than in **A(Si)** ($\Delta E_{orb} = -250.2$ kcal mol^{-1}; $\Delta E_{elstat} = -128.9$ kcal mol^{-1}), but the weaker Pauli

6) A related case where the hybridization of the interacting orbitals plays a crucial role for the strength of the energy terms of the EDA has been found for the phosphane complexes $(CO)_5$TM-PMe_3 and $(CO)_5$TM-PCl_3 (TM = Cr, Mo, W), which are discussed in Vol. 2, Chapter 7.

repulsion in the singly bridged isomer **B(Si)** partly compensates for the weaker attraction. The total interaction energy of **B(Si)** ($\Delta E_{int} = -81.4$ kcal mol^{-1}) compared with **A(Si)** ($\Delta E_{int} = -92.4$ kcal mol^{-1}) largely accounts for the energy difference of 9.9 kcal mol^{-1} between the two isomers (Figure 2.2).

The trans-bent isomer **D1(Si)** possesses, according to the bonding model in Figure 2.6c, two lp donor–acceptor bonds, and a π-bond. The π-bonding in **D1(Si)** has about the same strength (–41.7 kcal/mol) as in **B(Si)**, but the lp donor–acceptor bonds of the former isomer are significantly weaker (2 x -52.65 kcal/mol) than in the latter isomer (-71.7 kcal/mol). This is because the lp donor–acceptor bond in **B(Si)** is arranged in a linear way, which leads to maximum overlap, whereas the lp donor–acceptor bonds in **D1(Si)** are bent (Figure 2.6a and c). The total orbital interactions in **D1(Si)** are clearly weaker ($\Delta E_{orb} = -147.0$ kcal mol^{-1}) than in the other triply bonded isomers. Finally, the trans-bent form **D2(Si)**, which has only a single bond, exhibits a σ-orbital interaction of –74.9 kcal mol^{-1}. The σ-orbital interaction in **D2(Si)** is much weaker than in **E(Si)** (–96.9 kcal mol^{-1}), and in **A(Si)** (–116.8 kcal mol^{-1}) because the Si–Si distance increases in the same order (Figure 2.2).

The EDA results for the other tetrylenes E_2H_2 (E = Ge, Sn, Pb) show the same order for the energy terms of the respective isomeric forms **A – E**, except for **D1(Pb)** < **D2(Pb)**. Therefore, they will not be discussed here. Examination of the EDA results for **D1(Pb)** and **D2(Pb)** shows that the attractive contribution of the three orbital interactions in the triple bonded isomer **D1(Pb)** is stronger (–59.5 kcal mol^{-1}) than the σ-orbital interaction in **D2(Pb)** (–44.8 kcal mol^{-1}). The latter isomer encounters slightly weaker Pauli repulsion $\Delta E_{Pauli} = 74.8$ kcal mol^{-1} than the former species (77.4 kcal mol^{-1}). However, the dominant term which tips the energy scale in favor of **D2(Pb)** is the electrostatic attraction ΔE_{elstat}, which is clearly stronger (–61.8 kcal mol^{-1}) than in **D1(Pb)** (–45.7 kcal mol^{-1}). It holds that ΔE_{elstat} [**D1(E)**] > [**D2(E)**] (Table 2.4) for the other elements. The change in the strength of the electrostatic attraction is probably caused by relativistic effects. The ΔE_{elstat} term in **D1(E)** comes mainly from the overlap of the lone-pair electrons in the sp hybridized orbitals of EH with the nucleus of the other EH moiety (Figure 2.6c). The lone-pair MO in PbH is nearly a pure s AO of lead, which becomes relativistically contracted. The electrostatic attraction in **D2(E)** comes mainly from the overlap of the singly occupied p-orbital of EH with the nucleus of the other EH moiety (Figure 2.5c). There is no change in the hybridization for the heavier elements, and thus the overlap of the electron in the p-orbital is less affected by relativity.

In summary, the EDA results provide quantitative support for the bonding model of interacting EH moieties for the explanation of the structures, and relative energies of the E_2H_2 isomers. In this way, it is possible to replace assumptions and guesswork with calculated data which come from an unambiguously defined EDA of the system. The data calculated are not observable quantities, but they can be interpreted in a physically meaningful way. Moreover, they do not require an external reference system for calibrating the data.

2.7 Conclusion

The most important conclusions about the differences between multiple bonds of heavy main-group atoms, and atoms of the first octal row, which arise from the bonding analyses of the two systems, are as follows.

There is no particular weakening of π-bonding in multiple bonds of the heavy main-group atoms. On the contrary, the relative contribution of π-bonding to the total bond strength is slightly higher in the heavier systems P_2 – Bi_2 than in N_2. The drastic differences between the chemical bonding of atoms of the first and higher octal rows comes to the fore by comparing the dimerization energies of N_2 and P_2 yielding the tetrahedral species N_4 and P_4. The higher stability of P_4 (T_d) and the much lower stability of N_4 (T_d) with regard to the diatomic species, comes from the substantially larger weakening of the N–N σ-bonds compared with the P–P σ-bonds in the tetrahedral species. The sum of the three P–P σ-bond energies in P_4 is higher than the sum of one σ- and one degenerate π-bond in P_2, but the three N–N σ-bonds in N_4 are weaker than σ- and π-bonding in N_2. The crucial factor which leads to the weak N–N bonds in N_4 is the rather long N–N bonds which are 32.8% longer than in N_2. In contrast, the P–P bonds in P_4 are only 16.2% longer than in P_2. Because the equilibrium distances in N_4 and P_4 are determined by Pauli repulsion, which prevents shorter bonds, it can be concluded that the origin for the different stabilities of N_4 and P_4 relative to the diatomic molecules is the exchange repulsion.

The unusual equilibrium structures of the tetrylynes HEEH (E = Si, Ge, Sn, Pb) can be explained in terms of interactions between the EH moieties in the ($X^2\Pi$) electronic ground state, which differ from HC≡CH which is bound through interactions between CH in the $a^4\Sigma^-$ excited state. Bonding between two ($X^2\Pi$) fragments of the heavier EH hydrides is favored over the bonding in the $a^4\Sigma^-$ excited state because the $X^2\Pi \rightarrow a^4\Sigma^-$ excitation energy of EH (E = Si, Ge, Sn, Pb) is significantly higher than for CH, whereas the stabilizing contribution of the π-bonds become weaker.

The energy minimum structures **A**, **B**, and **D1** possess E–E triple bonds, but the bonding components of the triple bonds are different from the σ- and degenerate π-bonding of linear HE≡EH. The doubly bridged global energy minimum **A** of E_2H_2 has three bonding orbital contributions, one electron-sharing σ-bond, and two donor–acceptor bonds of the E–H bonding orbitals. The singly bridged isomer **B** also has three bonding orbital contributions: one electron-sharing π-bond, one E–H donor–acceptor bond, and one lone-pair donor–acceptor bond. The trans-bent form **D1** has one π-bond, and two lone-pair donor–acceptor bonds, whereas **D2** has only one σ-bond as a stabilizing orbital contribution. The strength of the stabilizing orbital contributions in the different isomers of E_2H_2 can be estimated with EDA calculations.

The pivotal difference between the C_2H_2 system, where HC≡CH is the only energy minimum structure with the given atomic connectivity, and E_2H_2, which has several nonlinear energy minima is traced back to the $X^2\Pi \rightarrow a^4\Sigma^-$ excitation

energies of EH, which are much higher than for CH. The concept of taking the electronic states of the fragments A and B for explaining the geometries and bonding situation of molecules AB, which possess a multiple bond, which was introduced many years ago [19, 20] is not restricted to double and triple bonds between group-14 atoms. It is a very powerful model for understanding the complexity of multiple bonds of heavy main-group elements in terms of electron-sharing, and donor–acceptor bonds. Another example has recently been presented in a theoretical study of the heavier group-14, and group-15 homologues of HCN and HNC which exhibit linear, bent, or even cyclic equilibrium geometries [21].

Acknowledgment

This work was supported by the Deutsche Forschungsgemeinschaft.

References

1. (a) Weidenbruch, M. (1999) *Eur. J. Inorg. Chem.*, 373; (b) Power, P.P. (1998) *J. Chem. Soc., Dalton Trans.*, 2939.
2. (a) Grützmacher, H. and Fässler, T.F. (2000) *Chem. Eur. J.*, **6**, 2317; (b) Jacobsen, H. and Ziegler, T. (1994) *J. Am. Chem. Soc.*, **116**, 3667; (c) Trinquier, G. (1991) *J. Am. Chem. Soc.*, **113**, 144.
3. Lein, M., Krapp, A., and Frenking, G. (2005) *J. Am. Chem. Soc.*, **127**, 6290.
4. (a) Power, P.P. (1999) *Chem. Rev.*, **99**, 3463; (b) Weidenbruch, M. (2002) *J. Organomet. Chem.*, **646**, 39.
5. (a) E = Si: Sekiguchi, A., Kinjo, R., and Ichinohe, M. (2004) *Science*, **305**, 1755; (b) E = Ge: Stender, M., Phillips, A.D., Wright, R.J., and Power, P.P. (2002) *Angew. Chem. Int. Ed.*, **41**, 1785; (c) E = Sn: Phillips, A.D., Wright, R.J., Olmstead, M.M., and Power, P.P. (2002) *J. Am. Chem. Soc.*, **124**, 5930; (d) E = Pb: Pu, L., Twamley, B., and Power, P.P. (2000) *J. Am. Chem. Soc.*, **122**, 3524.
6. (a) Bogey, M., Bolvin, H., Demuyneck, C., and Destombes, J.-L. (1991) *Phys. Rev. Lett.*, **66**, 413; (b) Cordonnier, M., Bogey, M., Demuynck, C., and Destombes, J.-L. (1992) *J. Chem. Phys.*, **97**, 7984; (c) Wang, X., Andrews, L., and Kushto, G. (2002) *J. Phys. Chem. A*, **106**, 5809; (d) Wang, X., Andrews, L., Chertihin, G.V., and Souer, P.F. (2002) *J. Phys. Chem. A*, **106**, 6302; (e) Andrews, L. and Wang, X. (2002) *J. Phys. Chem. A*, **106**, 7697; (f) Wang, X. and Andrews, L. (2003) *J. Am. Chem. Soc.*, **125**, 6581.
7. Kutzelnigg, W. (1984) *Angew. Chem.*, **96**, 262; *Angew. Chem., Int. Ed. Engl.* 1984, **23**, 272.
8. EDA results of the diatomic molecules N2 – Bi2 which were obtained with a different functional (PBE) that yields slightly different numerical values have been discussed in: Esterhuysen, C. and Frenking, G. (2004) *Theor. Chem. Acc.*, **111**, 381; Erratum: *Theoret. Chem. Acc.*, 2005, **113**, 294.
9. (a) Huber, K.P. and Herzberg, G. (1979) *Constants of Diatomic Molecules*, New York, Van Nostrand-Reinhold; (b) Sontag, H. and Weber, R. (1982) *J. Mol. Spectrosc.*, **91**, 72.
10. Jerabek, P., Frenking, G. (2014) *Theor. Chem. Acc.*, **133**, 1447.
11. Calculated from the differences between the heats of formation which are reported in: Lias, S.G., Bartmess, J.E., Liebman, J.F., Holmes, J.L., Levin, R.D., and Mallard, W.G. (1988) *J. Phys. Chem. Ref. Data*, **17** (Suppl. 1), 872p.
12. Brassington, N.J., Edwards, H.G.M., and Long, D.A. (1981) *J. Raman Spectrosc.*, **11**, 346.

13. (a) Krapp, A., Bickelhaupt, F.M., and Frenking, G. (2014) *Chem. Eur. J.*, **12**, 9196; (b) Frenking, G. and Bickelhaupt, F.M. (2014) The EDA perspective of chemical bonding, *The Chemical Bond*, Vol. 1, Chapter 4, Wiley-VCH Verlag GmbH, Weinheim.
14. (a) Bogey, M., Bolvin, H., Demuyneck, C., and Destombes, J.-L. (1991) *Phys. Rev. Lett.*, **66**, 413; (b) Cordonnier, M., Bogey, M., Demuynck, C., and Destombes, J.-L. (1992) *J. Chem. Phys.*, **97**, 7984; (c) For a review, see: Karni, M., Apeloig, Y., Kapp, J., and Schleyer, P.v.R. (2001) in *The Chemistry of Organic Silicon Compounds*, vol. 3 (ed. Y. Apeloig), John Wiley & Sons, Ltd, Chichester, p. 1.
15. (a) Wang, X., Andrews, L., and Kushto, G. (2002) *J. Phys. Chem. A*, **106**, 5809; (b) Wang, X., Andrews, L., Chertihin, G.V., and Souer, P.F. (2002) *J. Phys. Chem. A*, **106**, 6302; (c) Andrews, L. and Wang, X. (2002) *J. Phys. Chem. A*, **106**, 7696; (d) Wang, X. and Andrews, L. (2003) *J. Am. Chem. Soc.*, **125**, 6581.
16. Chen, Y., Hartmann, M., Diedenhofen, M., and Frenking, G. (2001) *Angew. Chem. Int. Ed.*, **40**, 2052.
17. Luo, Y.-R. (2007) *Comprehensive Handbook of Chemical Bond Energies*, CRC Press, Boca Raton, FL.
18. For a discussion of the bonding model, see: Driess, M. and Grützmacher, H.J. (1996) *Angew. Chem. Int. Ed.*, **35**, 828.
19. (a) Trinquier, G. and Malrieu, J.-P. (1987) *J. Am. Chem. Soc.*, **109**, 5303; (b) Trinquier, G. and Malrieu, J.-P. (1989) *J. Am. Chem. Soc.*, **111**, 5916.
20. Carter, E.A. and Goddard, W.A. (1986) *J. Phys. Chem.*, **90**, 998.
21. Devarajan, D. and Frenking, G. (2012) *Chem. Asian J.*, **7**, 1296.

3
The Role of Recoupled Pair Bonding in Hypervalent Molecules

David E. Woon and Thom H. Dunning Jr.

3.1
Introduction

Many elements possess the ability to form more bonds than expected based upon the number of unpaired electrons that are present in their atomic ground states. The elements P, S, Cl, Kr in the p-block and the elements below them in the periodic table behave in this manner. Compounds involving these elements that exceed the nominal valence for a given column are said to be *hypervalent* or *hypercoordinated*, terms coined by Musher [1] and Schleyer [2], respectively.

Typical examples of hypervalent compounds include SF_4 and SF_6, where sulfur forms four and six bonds, respectively, in spite of the fact that the ^3P ground state of S has only two unpaired electrons. By contrast, oxygen is almost exclusively mono- or divalent; OH and H_2O are stable but OF_4 and OF_6 are not. Other examples of small stable (or metastable) hypervalent fluoride compounds include PF_5, ClF_3, ClF_5, and XeF_n, ($n = 2, 4, 6$). Radicals such as SF_3, SF_5, and PF_4 have also been observed but are difficult to study in the laboratory because of their high reactivity. Nonetheless, they represent hypervalent or hypercoordinated species.

Explanations for the existence of hypervalent species started with Pauling's proposal of d orbital hybridization [3] where, for example, a set of sp^3d^2 hybrid orbitals on sulfur was put forward to account for the hexavalence of SF_6. Chemical computations [4] ruled out the participation of d atomic orbitals. A later model, the Rundle–Pimentel three-center, four-electron (3c-4e) bonding model [5], does not require d orbital participation and, so, is consistent with chemical computations. Other hypervalency models include the diabatic state model of Dixon and coworkers [6] and the democracy principle of Cooper and coworkers [7]. These various models provide useful insights into some aspects of the electronic structure of hypervalent molecules, but they don't provide an overarching description of these molecules that enables connections to be drawn between hypervalency and related molecular phenomena.

In 2009, based on an extensive set of high-level calculations on SF_n ($n = 1–6$), we introduced the concept of recoupled pair bonding [8], which meshes well with most of the extant models but offers additional insight regarding the electronic states,

The Chemical Bond: Chemical Bonding Across the Periodic Table, First Edition.
Edited by Gernot Frenking, Sason Shaik.

structures, energetics, properties, and reactivity of hypervalent elements and their compounds. The recoupled pair bond model accounts for a variety of ''anomalous'' behaviors of compounds of the elements of the late p-block below the first row, including: (i) the stability of hypervalent compounds; (ii) the oscillation of the bond dissociation energies of hypervalent compounds between very low and high values; (iii) the stability of excited states that are unbound or only weakly bound for first row compounds; (iv) the preference for edge (T-shaped) rather than vertex (D_{3h}-like) transition states for inversion of polyfluorinated phosphorus species and similar compounds; and (*v*) the unusual reactivity of various late p-block compounds such as the barrierless reaction between the closed shell species dimethyl sulfide and F_2. These examples are described in various publications [8–16] and summarized in a review article [17]. In this chapter, we describe the foundations of the concept of recoupled pair bonding using SF, SF_2, and other sulfur fluoride compounds as archetypes and contrast their behavior against OF and OF_2. We also compare and contrast the recoupled pair bond model with the other models of hypervalency described earlier [5–7].

3.2 Multireference Wavefunction Treatment of Bonding

Analyzing how orbitals and orbital couplings change as bonds form or break is an effective approach for gaining insight into the nature of bonding behavior. To do this consistently for any chemical bond type calls for the use of multireference wavefunction methods. We examine both natural orbitals (NOs) from multi-configurational self-consistent field (MCSCF) wavefunctions [18] and approximate generalized valence bond (GVB) orbitals derived from these NOs. An MCSCF calculation is a limited configuration interaction (CI) calculation, where excitations are only allowed into a small set of orbitals and the orbitals and configuration coefficients are variationally optimized. The CI vector coefficients thus generated can be used to transform NOs from the MCSCF calculation into approximate GVB orbitals by means of the following expressions:

$$\sigma_R = \sqrt{\frac{c_1'}{c_1' - c_2'}}\ \sigma_b + \sqrt{\frac{-c_2'}{c_1' - c_2'}}\ \sigma_a$$
$$\sigma_L = \sqrt{\frac{c_1'}{c_1' - c_2'}}\ \sigma_b - \sqrt{\frac{-c_2'}{c_1' - c_2'}}\ \sigma_a \qquad (3.1)$$

where σ_b and σ_a are the bonding and antibonding NOs, respectively, c_1' and c_2' are renormalized CI vector coefficients for the two configurations involving these orbitals ($\sigma_b^2\sigma_a^0$ and $\sigma_b^0\sigma_a^2$), and σ_R and σ_L are the resulting approximate GVB orbitals. The overlap S_{RL} between the two approximate GVB orbitals is given by:

$$S_{RL} = \frac{c_1' + c_2'}{c_1' - c_2'} \qquad (3.2)$$

The orbital transformation defined by Eq. (3.1) enforces both strong orthogonality and perfect pairing. These constraints are not required of a general GVB wavefunction [19], and much of our current work dispenses with these constraints. However, approximate GVB orbitals describe the essence of both covalent and recoupled pair bonds.

The calculations discussed in this section and in later sections were all performed with the MOLPRO suite of programs [20]. Orbital images were generated with gOpenMol (*www.csc.fi/english/pages/gOpenMol*); contours of amplitude ± 0.10, ± 0.15, and ± 0.20 are shown.

As an introductory example of the approach taken later in this chapter, Figure 3.1a depicts the NOs and GVB orbitals for a typical covalent bond, the σ bond of ground state OH ($X^2\Pi$). The 3σ bonding and 4σ antibonding orbitals were transformed into the $3\sigma_L$ and $3\sigma_R$ GVB orbitals with CI vector coefficients 0.9937 and −0.1048 for the $3\sigma^2\,4\sigma^0$ and $3\sigma^0\,4\sigma^2$ configurations, respectively. The overlap for this bond pair is 0.809 (valence lone-pair or bond pair overlaps usually fall in the range of 0.7–0.9). With the GVB orbitals, it is straightforward to see the degree to which the O and H orbitals are polarized toward the other atom, which is substantial for both atoms but more pronounced for H than for O. This is consistent with expectations drawn from the respective electronegativities of the two atoms.

A second example, H_2O, is depicted in Figure 3.1b–e. But, before we can proceed with the discussion, we describe another useful orbital transformation: localization of symmetry orbitals. Figure 3.1b shows the two C_{2v} bonding molecular orbitals (MOs) of H_2O taken from a Hartree–Fock (HF) calculation. The $3a_1$ orbital has even symmetry (++), while the $1b_2$ orbital has odd symmetry (+−). If we take the two linear combinations $\sqrt{1/2}(3a_1) \pm \sqrt{1/2}(1b_2)$ of these orbitals, we see that two equivalent orbitals are produced (shown on the right side of the row). These are designated as $\sigma_{b,L}$ and $\sigma_{b,R}$. because they are bond orbitals localized between O and the left and right H atoms, respectively. It is evident by inspection that each of these localized MOs closely resembles the σ bond MO of OH shown in Figure 3.1a. The general concept of localized (equivalent) molecular orbitals is well described in a series of papers by Lennard-Jones and coworkers [21].

Proceeding, Figure 3.1c depicts the bonding ($3a_1$,$1b_2$) and antibonding NOs ($4a_1$,$2b_2$) for H_2O from an MCSCF calculation using an active space of four electrons in these four orbitals. The CI vector coefficients for the configurations $(3a_1)^2(4a_1)^0(1b_2)^2(2b_2)^0$, $(3a_1)^0(4a_1)^2(1b_2)^2(2b_2)^0$, and $(3a_1)^2(4a_1)^0(1b_2)^0(2b_2)^2$ are 0.9891, −0.0735, and −0.0742, respectively. The NOs were transformed with these values into the GVB orbitals shown in Figure 3.1d. The overlaps in each pair are about 0.86. We note that the first and third GVB orbitals (H_{++},H_{+-}) have more amplitude on H than the other two GVB orbitals (O_{++},O_{+-}). When each of these pairs is localized, the final set of GVB orbitals is produced, as shown in Figure 3.1e. There are left and right pairs of orbitals that originated on each H and O. The localized GVB orbitals very much resemble the corresponding GVB orbitals of OH shown in Figure 3.1a. We use both of these transformations in the following text to analyze bonding of compounds formed from F and either S or O. It should be

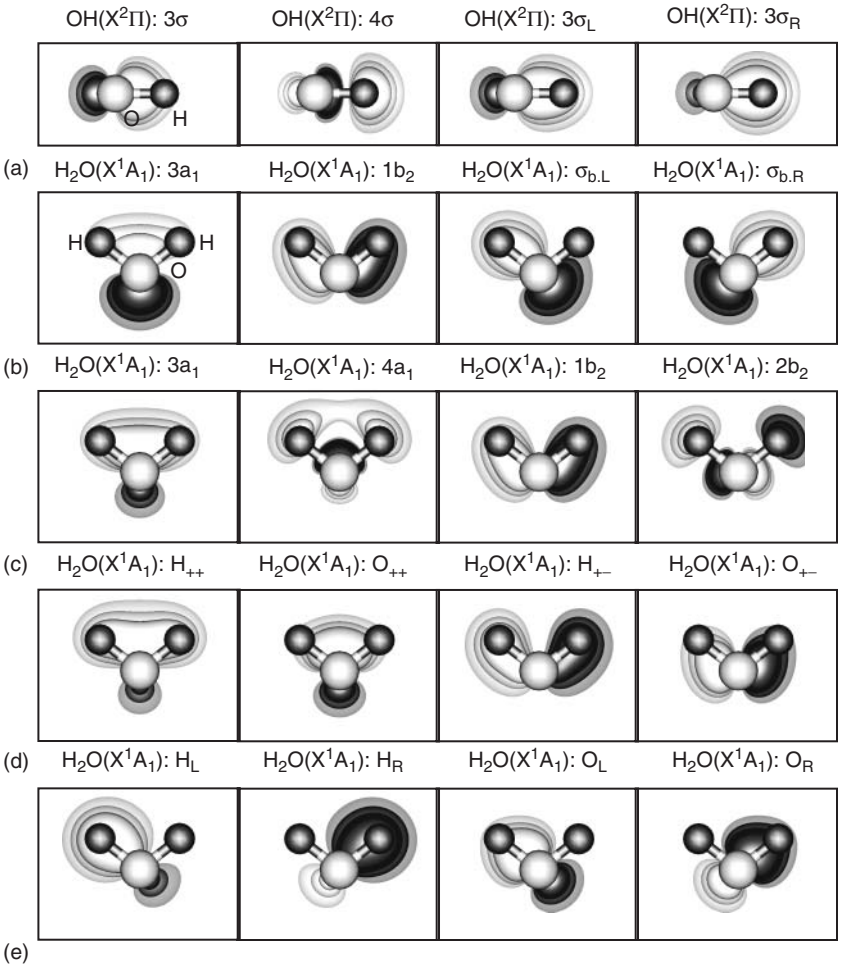

Figure 3.1 (a) Natural (3σ,4σ) and GVB ($3\sigma_L$,$3\sigma_R$) orbitals for OH; (b) C_{2v} symmetry ($3a_1$,$1b_2$) and localized ($\sigma_{b,L}$, $\sigma_{b,R}$) MO orbitals for H_2O; (c) natural orbitals ($3a_1$,$4a_1$,$1b_2$,$2b_2$) for H_2O; (d) C_{2v} symmetry (H_{++},O_{++}, H_{+-},O_{+-}) GVB orbitals for H_2O; (e) localized (H_L,H_R,O_L,O_R) GVB orbitals for H_2O.

noted that in true GVB calculations, unlike MCSCF calculations, the orbitals are naturally localized.

Structures and energies for SF–SF_6, OF, and OF_2 were obtained using restricted singles and doubles coupled cluster theory with a perturbative triples correction, [RCCSD(T)] [22] using large correlation consistent basis sets [23]. The notation ''AVXZ'' indicates the assignment of the aug-cc-pVXZ set to F and O and the aug-cc-pV(X+d)Z set to S (X = {T,Q}). Some of the results are from Davidson-corrected multireference configuration interaction (MRCI+Q) calculations [24]. Our studies have found that results from the MRCI+Q or RCCSD(T) methods compare well

with the available experimental data. Our work also found that harmonic zero point energies (ZPEs) computed with density functional theory at the B3LYP/AVTZ level are often sufficient for correcting equilibrium bond dissociation energies (D_e) to 0 K (D_0) [8].

3.3 Low-Lying States of SF and OF

Figure 3.2 depicts the potential energy curves for the bound states of OF and SF that dissociate to ground state atoms. We will focus on identifying the origin of bond stability for the ground and first excited states of each compound, starting with the ground states.

The $^2\Pi$ ground state of SF was initially characterized by Carrington *et al.* [25]; it has a bond length (R_0) of 1.55946 Å [26]. OF was first formed in matrix studies performed by Arkell *et al.* [27] and has a bond length (R_e) of 1.35398192 Å [28]. Ground state OF and SF are both bound by typical two-electron polar covalent bonds that arise by singlet coupling the electrons in the singly occupied valence p orbitals of S/O and F. The Π_x component in SF arises from:

$$\mathrm{SF}(\mathrm{X}^2\Pi_x) : \mathrm{S}\left[(\mathrm{core})\,3s^2 3p_x 3p_y^{\,2} 3p_z\right] \otimes \mathrm{F}\left[(\mathrm{core})\,2s^2 2p_x^{\,2} 2p_y^{\,2} 2p_z\right] \qquad (3.3)$$

The Π_y component is obtained by rotating the above configuration by 90°; the configurations for OF($X^2\Pi$) are analogous, with the O 2s and 2p orbitals replacing

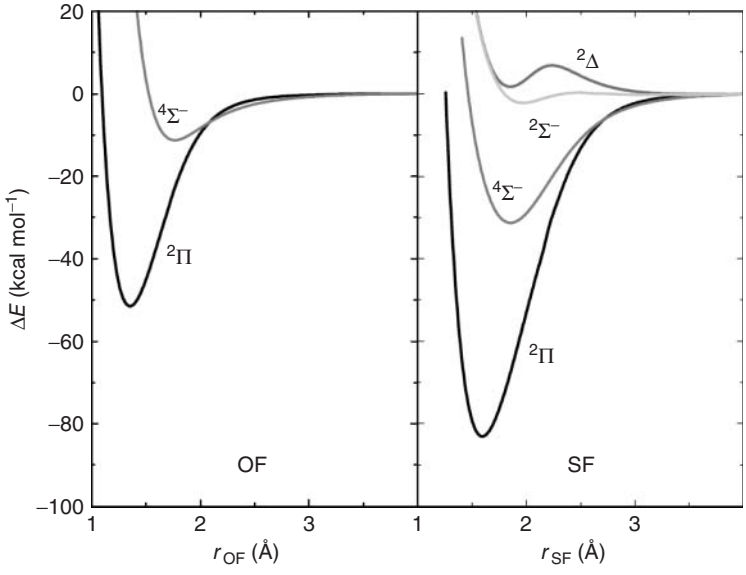

Figure 3.2 Potential energy curves of the bound states of OF and SF from ground state atoms, $O(^3P)/S(^3P) + F(^2P)$, at the MRCI+Q/AV5Z level.

the S 3s and 3p orbitals in Eq. (3.3). In the simplest MCSCF wavefunction that can properly describe bond dissociation of SF($X^2\Pi$), the non-bonding electrons are carried over as singly or doubly occupied σ and π_x/π_y orbitals, whereas the $S[3p_z] \otimes F[2p_z]$ interaction results in σ bonding and antibonding orbitals. In SF($X^2\Pi$), the bonding and antibonding orbitals in the three configuration MCSCF wavefunction are 7σ and 8σ. Thus the wavefunction is:

$$\mathrm{SF}\left(X^2\Pi_x\right) : Y_{\mathrm{MCSCF}} = A(\mathrm{core})\, 5\sigma^2 6\sigma^2 2\pi_x{}^2 3\pi_x 2\pi_y{}^2 3\pi_y{}^2 \times \left[c_{20}7\sigma^2 + c_{11}7\sigma 8\sigma + c_{02}8\sigma^2\right]\Theta \tag{3.4}$$

where Θ is a spin function appropriate for the $^2\Pi$ state. We can represent the algebraic statement of the wavefunction in Eq. (3.4) graphically with the following orbital coupling diagram (which also represents the ground state of OF):

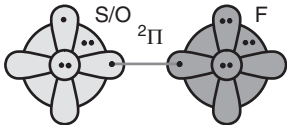

The singlet coupling between the electrons in the singly occupied valence p orbitals of S/O and F is indicated with the gray tie-bar, which denotes the inclusion of the (2,0), (1,1), and (0,2) occupations of the bonding and antibonding orbitals formed from the contributing orbitals, as given in Eq. (3.4). When the covalent bond forms in SF/OF($X^2\Pi$), the c_{20} and c_{02} MCSCF CI vector coefficients change in a well-behaved manner. As $R_{\mathrm{SF}} \to \infty$, c_{20} and c_{02} approach $\pm\sqrt{1/2}[1-(1/2)^2]$ and c_{11} approaches 1/2, thus describing the $S/O(^3P) + F(^2P)$ separated atom limit. As $R_{\mathrm{SF}} \to R_e$, c_{20} approaches 1 while c_{02} and c_{11} approach 0. The wavefunction thus increasingly resembles the HF wavefunction as the bond forms.

Approximate GVB orbitals $7\sigma_R$ and $7\sigma_L$ (with strong orthogonality and perfect pairing constraints imposed) were obtained from the 7σ and 8σ NOs using c_{20} and c_{02} (after renormalization), as noted above. The NOs and approximate GVB orbitals for SF($X^2\Pi$) are depicted in Figure 3.3 at several interatomic separations, along with the orbitals for OF($X^2\Pi$) at R_e for comparison. The bonding orbital (7σ) for SF($X^2\Pi$) is clearly shifted toward F at R_e, as one expects of a polar covalent bond, whereas the antibonding orbital is distributed over both atoms (more on S than F) with a nodal plane in between the two atoms. The GVB orbitals show the nature of the polarization in even greater detail than the NOs: the F $2p_z$ orbital barely shifts toward S, whereas the S $3p_z$ orbital delocalizes significantly onto F. This delocalization builds $S^{\delta+}F^{\delta-}$ character into the bond. The overlap between the two GVB orbitals increases from zero at $R = \infty$ to 0.788 at R_e. Less polarization is evident in OF($X^2\Pi$), consistent with the smaller difference between the electronegativities of O and F as compared to S and F.

The bond dissociation energies (D_e) of ground state SF and OF are 83.3 and 50.9 kcal mol^{-1}, respectively, at the RCCSD(T)/AVQZ level. The bond lengths (R_e) at the same level of theory are 1.601 and 1.353 Å, respectively.

In 2005, Yang and Boggs [29] predicted the existence of a low-lying $^4\Sigma^-$ excited state of SF. Other prior calculations found that the state is also present in OF [30],

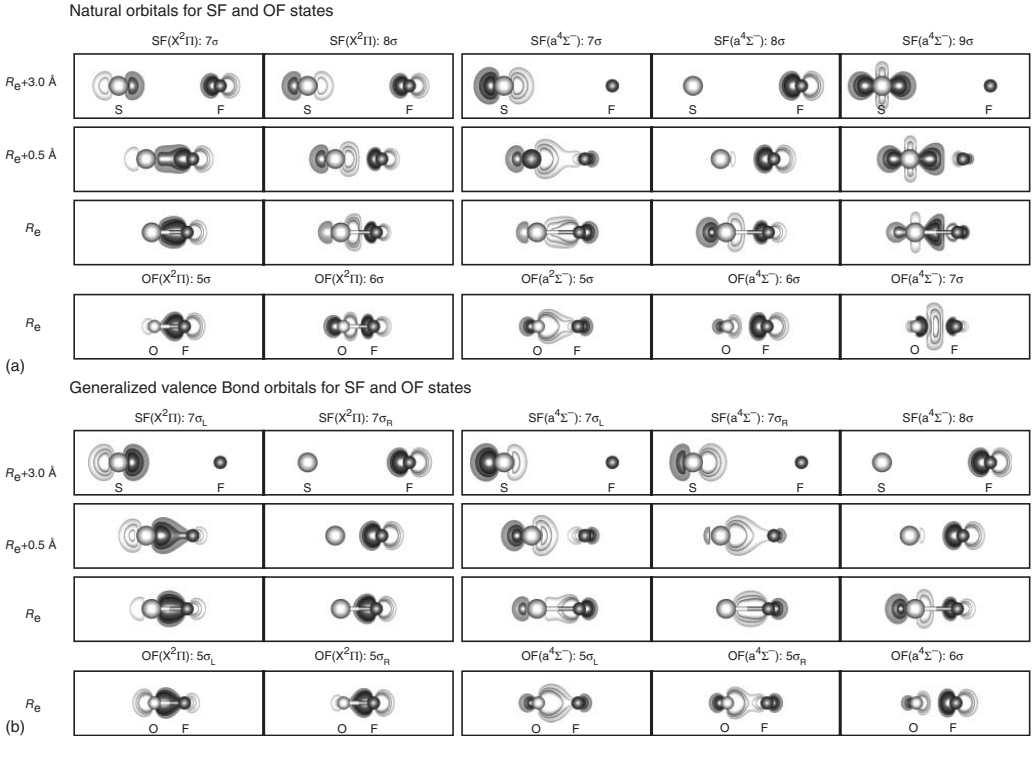

Figure 3.3 Natural and generalized valence bond orbitals of SF/OF($X^2\Pi$, $a^4\Sigma^-$) at the AVTZ level. (a) Natural orbitals for SF and OF states; (b) Generalized Valence Bond orbitals for SF and OF states.

although it is bound very weakly (<10 kcal mol^{-1}). Although the bond in SF($a^4\Sigma^-$) is much weaker than that in SF($X^2\Pi$), it is still bound by 36.2 kcal mol^{-1} (D_e) at the RCCSD(T)/AVQZ level. The bond length of SF($a^4\Sigma^-$), 1.882 Å, is substantially longer than that of the ground state. This unusual state arises if the S 3p orbital that interacts with the F 2p orbital is *doubly occupied* rather than *singly occupied* as it is in the ground state. The atomic configurations are:

$$\mathrm{SF}(a^4\Sigma^-) : \mathrm{S}\left[(\mathrm{core})\, 3s^2 3p_x 3p_y 3p_z{}^2\right] \otimes \mathrm{F}\left[(\mathrm{core})\, 2s^2 2p_x{}^2 2p_y{}^2 2p_z\right] \tag{3.5}$$

Remarkably, the three-electron interaction S [$3p_z{}^2$] ⊗ F [$2p_z$] yields a bond of moderate strength with no barrier to its formation when dynamic correlation is included (a barrier is found at the RHF and MCSCF levels [8]).

Although the MCSCF wavefunction for SF($a^4\Sigma^-$) is dominated by the HF configuration for all interatomic separations from the well outward, it is instructive to consider the NOs and GVB orbitals for a simple multireference wavefunction, one that is restricted to double excitations into the first σ virtual (9σ). Again keeping nonbonding electrons in singly or doubly occupied orbitals as they are in S and F, the spatial wavefunction for the $^4\Sigma^-$ state is

$$\begin{aligned}\mathrm{SF}(a^4\Sigma^-) : \mathrm{Y}_{\mathrm{MCSCF}} = {} & A(\mathrm{core})\, 5\sigma^2 6\sigma^2 2\pi_x{}^2 3\pi_x 2\pi_y{}^2 3\pi_y 8\sigma \\ & \times \left[c_{20} 7\sigma^2 + c_{11} 7\sigma 9\sigma + c_{02} 9\sigma^2\right] \Theta'\end{aligned} \tag{3.6}$$

where Θ′ is the spin function appropriate for the $^4\Sigma^-$ state. The manner in which the orbitals change during bond formation in SF($a^4\Sigma^-$) is quite different from what was observed above in SF($X^2\Pi$) (see Figure 3.3). The 7σ orbital remains essentially doubly occupied from large separations down to R_e, but its character changes dramatically. It begins as the S $3p_z{}^2$ orbital at dissociation and becomes a bond orbital that is heavily delocalized onto F as R_e is approached. Concomitantly, the singly occupied 8σ orbital changes from the F $2p_z$ orbital to a S-dominated antibonding orbital as the bond forms.

Once again, the GVB orbitals provide additional insight beyond what the NOs offer. In the atom, excitation from the $3p_z$ orbital to the $3d_{z^2}$ orbital [9σ in Figure 3.3a] results in a pair of highly overlapping (S = 0.862) 3p lobe orbitals ($3p_{z+}$, $3p_{z-}$); one orbital that has its amplitude directed toward F ($3p_{z+}$), whereas the other orbital is directed away from F ($3p_{z-}$). As the bond forms, both orbitals delocalize onto F. At R_e, the inner S lobe orbital, $7\sigma_L$, resembles the S GVB orbital in SF($X^2\Pi$), while the other GVB orbital, $7\sigma_R$, has become a $2p_z$-like orbital on F that is slightly polarized toward S. Note that the S atomic electron pair has become a shared (molecular) electron pair in both the MCSCF and GVB interpretations, but the GVB interpretation shows that this bond formation can be viewed as a *recoupling of the orbitals*. At $R = \infty$, the coupling is between the left and right S lobe orbitals, whereas at R_e, the right S lobe orbital is coupled to the F $2p_z$ orbital (the changes in the orbitals are even clearer in the full GVB wavefunction). Unlike the covalent bond in the ground state, where the overlap between the bonding orbitals increases from zero at $R = \infty$ to a value of about 0.8 at R_e, in the $a^4\Sigma^-$ state the two orbitals remain strongly coupled with an overlap of 0.8–0.9 during the entire

process of bond formation. In addition, a third electron is present in an orbital (8σ) that hinders the bond formation. In the MCSCF and strong orthogonality GVB wavefunctions, the electron in this *antibonding orbital* causes the bond length of SF($a^4\Sigma^-$) to be about 0.3 Å longer than the bond length of SF($X^2\Pi$) and the bond strength to be nearly 50 kcal mol^{-1} weaker. We call the process where an atomic pair of electrons interacts with a third electron to yield a bond pair and an inhibiting leftover electron *recoupled pair bonding*.

The orbital coupling diagram for SF($a^4\Sigma^-$) is shown below. Note the new orbital symbols used to describe the S lobe orbitals ($3p_{z+}$, $3p_{z-}$).

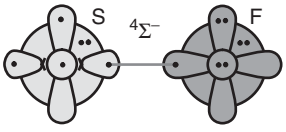

The three singly occupied orbitals are coupled as a quartet in SF($a^4\Sigma^-$), but they can also be coupled as a doublet to yield the bound $^2\Sigma^-$ and $^2\Delta$ states shown in Figure 3.2. One of our publications discusses the low-spin excited states of SF, SF_2, and other sulfur halides [15].

The contrast between the orbitals of OF($a^4\Sigma^-$) and SF($a^4\Sigma^-$) in Figure 3.3 is quite pronounced and accounts for the weakness of the bond in the OF case. In both the natural and GVB orbitals in OF, the pair (the doubly occupied 5σ NO or the $5\sigma_L-5\sigma_R$ coupled GVB pair) remains localized on O, with only a small amount of delocalization onto F. The antibonding orbital (6σ) is dominated by F character. We describe OF($a^4\Sigma^-$) as a *frustrated recoupled pair bond*. Consequently, the bond energy (D_e) of OF($a^4\Sigma^-$) is very weak, just 8.5 kcal mol^{-1} at the RCCSD(T)/AVQZ level. The bond length (R_e) is 1.742 Å, nearly 0.4 Å longer than in ground state OF($X^2\Pi$).

In contrast to covalent bonding, these results indicate that recoupled pair bonding is a *conditional* form of bonding. It is evident from our studies [8–17] that the ability to form a recoupled pair bond depends upon two factors: how tightly the lone-pair electrons are bound to the central atom and the electronegativity of the incoming ligand. For example, F, Cl, Br, and other strongly electronegative ligands such as OH are able to recouple the $3p^2$ pair of ground state S atom, but weakly electronegative ligands such as H cannot. Likewise, the electrons of Cl are more tightly bound than the electrons of S to their respective nuclei, and as a consequence recoupling is more difficult in Cl [12].

Prior to our series of publication, it was not recognized that the bonding in the simple diatomic species SF had any bearing on understanding hypercoordination in sulfur compounds. In fact, it provides a great deal of insight into sulfur's bonding motifs. Examining the ground and excited states of triatomic SF_2 expands our understanding of the role of recoupled pair bonding in sulfur even further.

3.4 Low-Lying States of SF_2 and OF_2 (and Beyond)

SF_2 is an archetype for the ways in which covalent and recoupled pair bonding can be combined to yield different stable states. Three low-lying states of SF_2 (X^1A_1, a^3B_1, b^3A_2) can be formed by adding a second F atom to $SF(X^2\Pi)$ and $SF(a^4\Sigma^-)$. The orbital coupling diagrams for the three states are:

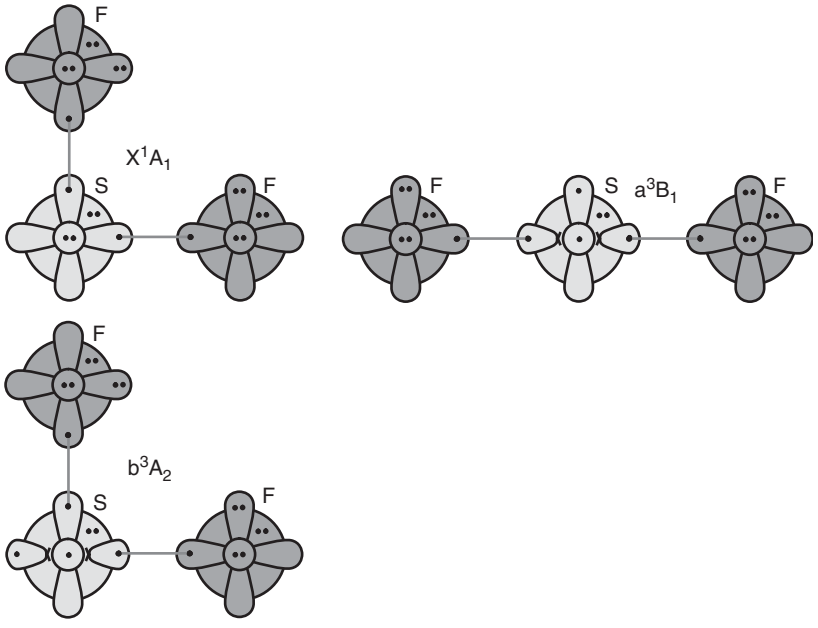

As for the diatomics, each orbital pair indicates the inclusion of three configurations in the MCSCF wavefunction. With the two orbital couplings present in all three states of SF_2, there are thus nine configurations in the minimal multireference wavefunction. We now discuss the nature of the bonding in each of the three states of SF_2 in turn. We then discuss these states in OF_2. Unless otherwise noted, all results in this section are at the RCCSD(T)/AVQZ level.

3.4.1 $SF_2(X^1A_1)$

The $^1A_1$ ground state of SF_2 is formed by singlet coupling the electrons in the singly occupied orbitals of $SF(X^2\Pi)$ and $F(^2P)$ to form a second covalent bond. The energy of the second bond is 91.0 kcal mol^{-1}, which is comparable to, but slightly larger than, the covalent bond energy of 83.3 kcal mol^{-1} for ground state SF. The bond angle of $SF_2(X^1A_1)$ is 97.9°, and the S–F bond length is 1.592 Å. The bond length is only slightly smaller than that in ground state SF, 1.601 Å and the bond

angle is consistent with forming a bond with the singly occupied $3\pi_x$ orbital of $SF(X^2\Pi)$.

The NOs and approximate GVB orbitals of $SF_2(X^1A_1)$ are shown in Figure 3.4a in both delocalized (C_{2v} symmetry) form and localized on each S–F bond using the procedure described in Section 3.2. The localized left and right bond pair orbitals (BP_L, BP_R) are equivalent, well-localized on one of the bonds, and very much resemble the polarized NO bond pair for $SF(X^2\Pi)$ shown in Figure 3.2a. The four C_{2v} symmetry GVB orbitals (F_{++}, F_{+-}, S_{++}, S_{+-}) were transformed in the same manner into localized orbitals (F_L, S_L, F_R, S_R), which are also very similar to the GVB orbitals for $SF(X^2\Pi)$ depicted in Figure 3.3b.

3.4.2 $SF_2(a^3B_1)$

The a^3B_1 state of SF_2 can be formed by singlet coupling the electron in the orbital left over from recoupling the S $3p^2$ pair of $SF(a^4\Sigma^-)$, the 8σ orbital, to the electron in the singly occupied orbital of $F(^2P)$, yielding a quasi-linear structure with a bond angle of 162.7° and a bond length of 1.666 Å. The bond length is much smaller than that for $SF(a^4\Sigma^-)$, 1.882 Å. The energy (D_e) of the second bond is 106.3 kcal mol^{-1}, about 15 kcal mol^{-1} greater than the larger of the two covalent bond energies of $SF_2(X^1A_1)$. Because of the strength of the second SF bond, $SF_2(a^3B_1)$ lies only 31.8 kcal mol^{-1} above $SF_2(X^1A_1)$ (ΔE_e).

The natural and GVB bond orbitals for $SF_2(a^3B_1)$ are shown in Figure 3.4b in both C_{2v} symmetry and localized on each S–F bond as described earlier. Given how greatly the X^1A_1 and a^3B_1 states of SF_2 differ in energy and geometry, the differences between the bonding orbitals are subtle rather than distinctive: All of the bonds are highly polarized toward F. Although the orbitals of $SF_2(a^3B_1)$ appear to be more polarized that those of ground state SF_2, the differences are small.

To understand the structure and stability of $SF_2(a^3B_1)$, it is necessary to look at all of the valence orbitals of the molecule. Figure 3.5 depicts the changes in the GVB orbitals that are singlet coupled when the new bond forms from $F(^2P) + SF(a^4\Sigma^-)$ as a function of R (constrained to be linear as the $^3\Sigma^-$ state). The F 2p orbital changes very little, but the strong antibonding character of the $10\sigma_R$ orbital [derived from the 8σ orbital of $SF(a^4\Sigma^-)$] is dramatically reduced as the second bond forms. This accounts for the much shorter bond length of $SF_2(a^3B_1)$ compared to $SF(a^4\Sigma^-)$ as well as the much larger energy of the second bond. We identify the bonding arrangement of $SF_2(a^3B_1)$ as a *recoupled pair bond dyad*. Recoupled pair bond dyads are largely responsible for the stability of the hypercoordinated compounds of P, S, Cl, Kr, and related elements.

The presence of one or more recoupled pair bond dyads in a compound has implications beyond the geometry and energetics of the equilibrium structure. For example, asymmetric vibrational stretching of the atoms in the F–S–F dyad reintroduces antibonding character as each of the S–F bonds lengthens in turn, and this results in an infrared vibrational feature that is very intense. The predicted

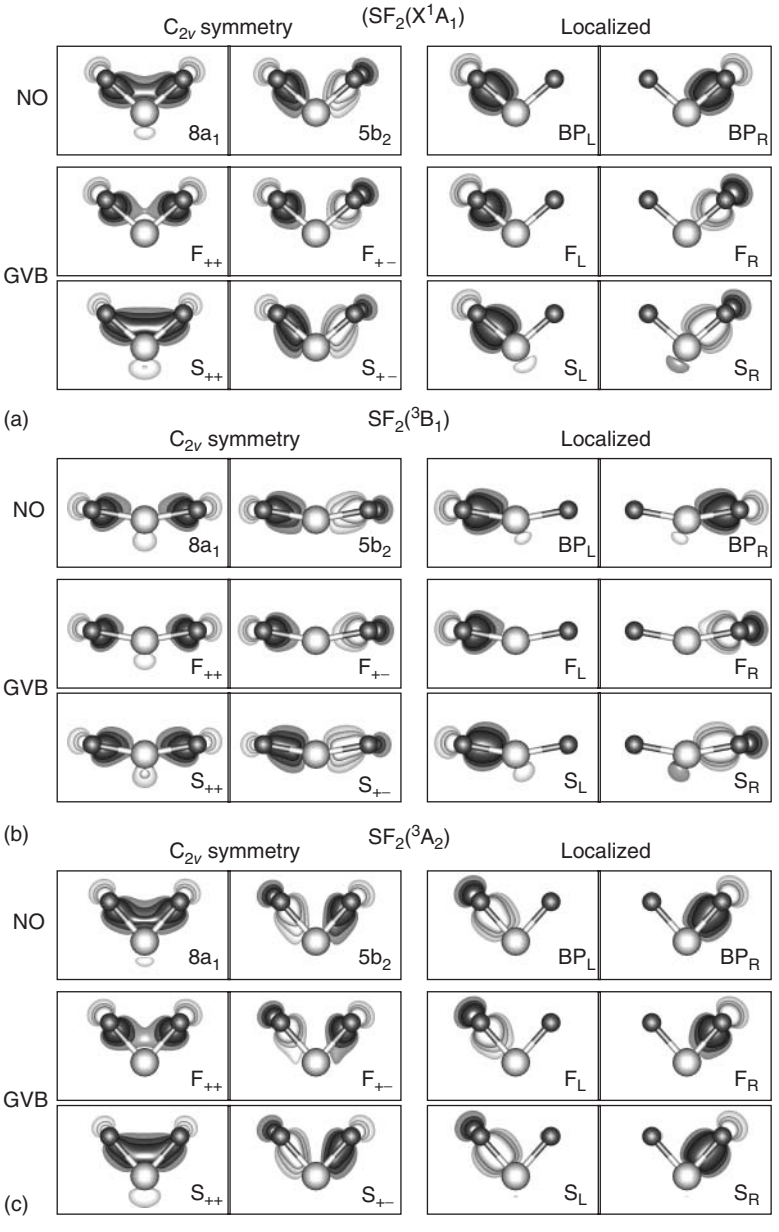

Figure 3.4 Natural and generalized valence bond orbitals of $SF_2(X^2A_1, a^3B_1, b^3A_2)$ at the AVTZ level; the orbital localization procedure is described in the text.

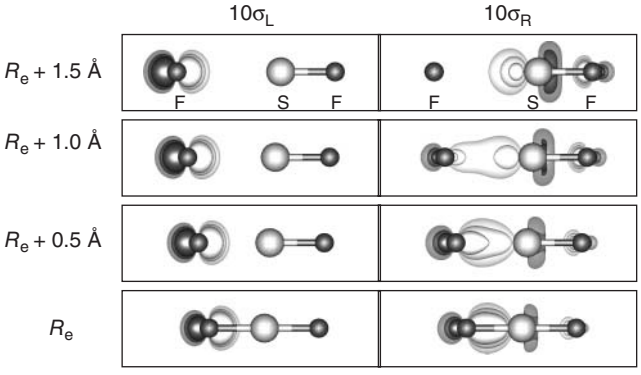

Figure 3.5 Generalized valence bond orbitals for $SF(a^4\Sigma^-) + F(^3P) \rightarrow SF_2(^3\Sigma^-)$ at various separations at the AVTZ level.

intensity of the asymmetric stretching mode in $SF_2(a^3B_1)$ is about three times larger than that of $SF_2(X^1A_1)$.

The deviation of $SF_2(a^3B_1)$ from linearity can be understood by examining the in-plane doubly and singly occupied orbitals ($7a_1$ and $9a_1$) shown in Figure 3.6. The singly occupied $9a_1$ orbital projects more on the interior side of the F–S–F bond to avoid the electrons in the orbital derived from the S $3s^2$ pair ($7a_1$). The doubly occupied $7a_1$ orbital is competing for the same region of space as the $9a_1$ orbital and causes the displacement of the higher energy, singly occupied $9a_1$ orbital. This, in turn, leads to the bent structure for the $SF_2(a^3B_1)$ state.

3.4.3 $SF_2(b^3A_2)$

The b^3A_2 state of SF_2 forms when the singly occupied orbital of $F(^2P)$ is coupled to either of the two singly occupied 3p-like π orbitals of $SF(a^4\Sigma^-)$ as shown earlier. The bond energy (D_e) for forming $SF_2(b^3A_2)$ from $SF(a^4\Sigma^-)$ and $F(^2P)$ is 88.1 kcal mol^{-1}, comparable to the covalent bonds in $SF_2(X^1A_1)$. $SF_2(b^3A_2)$, is 18.2 kcal mol^{-1} less stable (ΔE_e) than $SF_2(a^3B_1)$ and has an acute bond angle of 83.1°. The bond length, 1.656 Å, is comparable to that of $SF_2(a^3B_1)$. Once again the localized natural and GVB bonding orbitals for $SF_2(b^3A_2)$ are similar to those of the other two states as depicted in Figure 3.4c.

$SF_2(b^3A_2)$ is less stable than $SF_2(a^3B_1)$ because in this case the antibonding character of the orbital leftover from the recoupling remains in the SF bonding region. The singly occupied orbital of $SF_2(b^3A_2)$ is plotted in Figure 3.6; the antibonding character of the $3b_2$ orbital can be easily recognized despite the fact that it is now distributed over two SF bonds. The bonding in $SF_2(b^3A_2)$ is a resonance between the two ways that one covalent and one recoupled pair bond can be localized in each of the S–F bonds. The $3b_2$ orbital reflects the averaging of the antibonding character associated with a recoupled pair bond. The increased

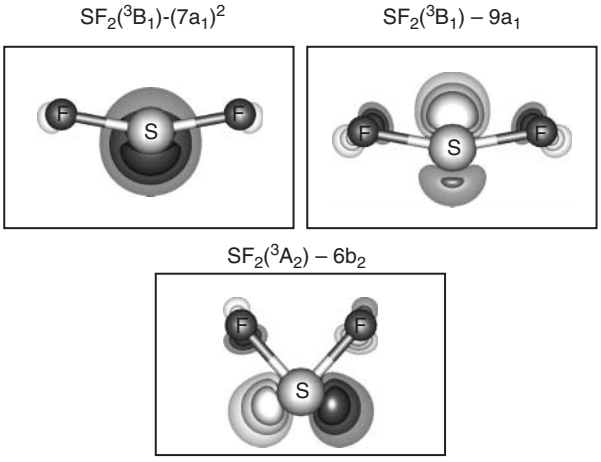

Figure 3.6 Selected in-plane orbitals for $SF_2(a^3B_1, b^3A_2)$ at the AVTZ level.

bond length and acute bond angle of $SF_2(b^3A_2)$ reflects the effort to minimize the interaction of the antibonding character distributed between the two bonds.

Note that the $SF_2(b^3A_2)$ state can also be formed by recoupling the doubly occupied π orbital in the $SF(X^2\Pi)$ state. The energy for this process is 41.0 kcal mol^{-1}, only slightly larger than the energy of the recoupled pair bond in the $SF(a^4\Sigma^-)$ state.

Finally, if C_{2v} symmetry is broken, which happens if one of the F atoms in $SF_2(b^3A_2)$ is replaced with Cl to yield $SFCl(^3A'')$, two distinct minima are possible, one where the recoupled pair bond is between S and F and one where it is between S and Cl. We showed that $SFCl(^3A'')$ does indeed have two *bond stretch isomers*, although the barrier between the isomers is very small [13].

3.4.4
$OF_2(X^1A_1)$

The bonding in $OF_2(X^1A_1)$ is analogous to $SF_2(X^1A_1)$, although the second bond energy, 40.6 kcal mol^{-1}, is weaker rather than stronger than the first bond energy of 50.9 kcal mol^{-1}. The bonds are weaker in OF and OF_2 versus SF and SF_2 because the shorter bond lengths bring the F lone-pairs closer to the bond pairs of OF and OF_2 and to the lone-pairs of O.

3.4.5
Triplet states of OF_2

Attempts to locate the $^3B_1$ state of OF_2 revealed stability issues that are not found in calculations for the $SF_2(a^3B_1)$ state. A metastable minimum is found at the RCCSD(T)/AVTZ level, but no $^3B_1$ minimum is obtained at the MRCI+Q/AVTZ level. At both levels of theory, a weakly bound complex with $^3A''$ symmetry exists between $OF(X^2\Pi)$ and $F(^2P)$. At the RCCSD(T)/AVTZ level, the O–F distances are

1.352 and 2.132 Å and the bond angle is 104.7°, but the complex is only bound by 1.75 kcal mol^{-1}. There is no minimum for a $^3A_2$ state for OF_2 with either RCCSD(T) or MRCI+Q.

3.4.6
SF_3 and SF_4

The ground state of SF_3, $SF_3(X^2A')$, is a quasi-planar T-shaped molecule (see Figure 3.7) that consists of a F-S-F dyad and S–F covalent bond; the remaining electron occupies a S 3p-like orbital. $SF_3(X^2A')$ can be formed from each of the three states of SF_2, and the energetics are consistent with those of the states of SF and SF_2 already discussed. For example, if SF_3 is formed from $SF_2(a^3B_1) + F$, a covalent bond is added to the existing dyad. The calculated energy for this addition is 87.8 kcal mol^{-1}, much like the other covalent bond energies. Likewise, if SF_3 is formed from $SF_2(b^3A_2) + F$, the third F completes the F–S–F dyad and removes the antibonding character of the $3b_2$ orbital. The bond energy for this process is 106.6 kcal mol^{-1}, which is very similar to energy found for adding F to $SF(a^4\Sigma^-)$ to complete the dyad in $SF_2(a^3B_1)$. Finally, SF_3 can be formed from $SF_2(X^1A_1) + F$. The bond energy for this addition is 56.0 kcal mol^{-1}. This energy reflects the cost of recoupling the $3p^2$ pair, but it is larger because one of the two covalent bonds in $SF_2(X^1A_1)$ rearranges to form the F–S–F dyad.

The geometry of the $SF_3(X^2A')$ state is closely related to that of the $SF_2(a^3B_1)$ state: the bond lengths of the dyad bonds are 1.657 Å (SF_3) versus 1.666 Å (SF_2) and the dyad bond angle is 163.4° (SF_3) versus 162.7° (SF_2). Further, the length of the SF covalent bond in SF_3 is 1.566 Å, which is only slightly shorter that in $SF_2(X^1A_1)$, 1.592 Å.

An isomer of SF_3 consisting of two covalent bonds and a recoupled pair bond plus an electron in the left over (antibonding) orbital was sought, but no stationary point was found. However, if one of the F atoms is replaced with Cl, three minima are obtained in SF_2Cl [13], one of which has two covalent bonds. The global minimum consists of a F–S–Cl dyad and a covalent S–F bond, but the structure with a F–S–F dyad and covalent S–Cl bond is only 0.6 kcal mol^{-1} less stable. The least stable, third minimum consists of two S–F covalent bonds and an S–Cl recoupled pair bond. It lays just 8.2 kcal mol^{-1} above the second isomer. Our studies have shown that recoupled pair bonding leads to much more complex potential energy surfaces with a much richer array of stable structures (and transition states) than previously recognized.

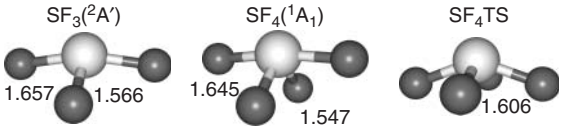

Figure 3.7 Structures of SF_3 and SF_4 species. Bond lengths in Å at the RCCSD(T)/AVQZ level.

$SF_4(X^1A_1)$ is formed straightforwardly from $SF_3(X^2A') + F$. The structures of SF_3 and SF_4 are very similar and the new covalent bond has an energy of 98.8 kcal mol^{-1} (see Figure 3.6). The structure of $SF_4(X^1A_1)$ can already be anticipated from the existing bond and singly occupied orbitals of $SF(a^4\Sigma^-)$: a near linear arrangement of two F atoms with S that constitute a recoupled pair bond dyad and two additional covalent S-F bonds roughly perpendicular to the F-S-F dyad axis and about 90° from each other. The transition state for interchanging the F-S-F dyad and the two covalent bonds involves two F-S-F dyads. It lays just 11.0 kcal mol^{-1} above the ground state and anticipates the structure of SF_5.

3.4.7
SF_5 and SF_6

As SF_4 has no unpaired electrons, further bond formation requires recoupling the remaining lone-pair of S, which is derived from the $3s^2$ orbital (though this orbital has acquired considerable 3p character as interactions with the bond pairs displace it away from the S nucleus). $SF_5(X^2A_1)$ has two F–S–F dyads and an S–F recoupled pair bond. $SF_6(X^1A_1)$ is formed by completing the third F–S–F dyad. The bond energies (D_e) for forming SF_5 and SF_6 via addition to their respective SF_{n-1} species are 41.1 (recoupled pair bond) and 109.2 kcal mol^{-1} (recoupled pair bond dyad).

In this section, we explored the manner in which hypercoordination emerges in the ground states of SF_n as the ability to recouple the $3p^2$ and $3s^2$ atomic pairs of ground state S. We saw that the evidence for this emergence is already exhibited in the excited states of SF and SF_2. We also learned that O holds onto its lone-pair electrons too tightly for them to be recoupled very extensively, even by the most electronegative neutral atom, F.

3.5
Comparison to Other Models

In the following text we compare and contrast the recoupled pair bond model with three models that have also been proposed to rationalize the existence and stability of hypervalent molecules.

3.5.1
Rundle–Pimentel 3c-4e Model

The model most widely used to explain hypervalence is the three-center, four-electron (3c-4e) model of Rundle and Pimentel [5]. Coulson [31] analyzed the 3c-4e model and suggested a valence bond resonance model that shares some similarities with the MO model. Under this model, the bond is posited to arise primarily from resonance between $F–X^+F^-$ and $F^-X^+–F$ charge structures (with contributions from other charge configurations). Weinhold and Landis [32] incorporated natural bond orbital analysis and natural resonance theory in what is perhaps the most

sophisticated treatment of the 3c-4e model to date. The various concepts derived from the 3c-4e model aim to explain why hypervalent bonds exist but are weaker than covalent bonds and why highly electronegative ligands such as F are required to form hypervalent compounds. As we have shown earlier, and discuss further in the following text, the notion of recoupled pair bonds and recoupled pair bond dyads provide very rich insights into the nature of hypervalency and a number of related chemical phenomena.

The 3c-4e model draws upon basic molecular orbital theory, in which valence p orbitals on a central atom and two ligand atoms in a linear arrangement give rise to a bonding orbital (of odd symmetry), a so-called nonbonding orbital (of even symmetry), and an antibonding orbital (of odd symmetry). If the central atom provides a pair of electrons and each ligand provides one electron, then the resulting four electrons fill the bonding and nonbonding orbitals, leaving the destabilizing antibonding orbital unoccupied (see Figure 1 in Cheung *et al*. [33]). Although $SF_2(a^3B_1)$ is not quite linear, its orbitals are representative of the 3c-4e model: the $5b_2$ and $8a_1$ orbitals depicted in Figure 3.3b are consistent, respectively, with the bonding and nonbonding orbitals of the 3c-4e model. Proponents of the model argue that the bonding is weaker in a 3c-4e system than in two 2c-2e covalent bonds because only the bonding orbital is strongly stabilizing, whereas the non-bonding orbital provides little or no stabilization. In this model, it is asserted that strongly electronegative ligands are needed to prevent the electrons of the nonbonding orbital from being too close to the central atom [33].

The exercise of localizing the C_{2v} symmetry orbitals onto each S–F bond for all three low-lying states of SF_2 demonstrates that the $8a_1$ orbital is not truly a nonbonding orbital in the $SF_2(a^3B_1)$ state. Like the other two states, it is simply an antisymmetric combination of two ionic S–F bonds. Other workers, such as Ponec *et al*. [34], have shown that a 3c-4e bond is essentially two highly ionic bonds, in agreement with this conclusion. In fact, localization of the orbitals indicates that the ionic character of the ($8a_1$, $5b_2$) orbitals in $SF_2(a^3B_1)$ is only marginally larger than that for the ($8a_1$, $5b_2$) orbitals in $SF_2(X^1A_1)$.

By only considering minimum structures where the HF configuration dominates, the 3c-4e model has missed the important insights that the process of bond formation provides. A deeper understanding is further hindered by focusing on the $(\text{bonding})^2(\text{nonbonding})^2$ configuration rather than the two-step process where two new bonds form with the electrons in the lone-pair orbital. Kiang and Zare [35] did note that 2c-3e bonding in odd-*n* SF_n species such as SF_3 and SF_5 should be particularly weak according to molecular orbital theory, but even this awareness was not exploited by subsequent workers to refine the 3c-4e model.

Our studies have shown that covalent and recoupled pair bonding are competitive alternatives. The results for SF_2 show that it is possible to find states of the same compound that involve pure covalent bonding, a recoupled pair bond dyad, or a mixture of covalent and recoupled pair bonding. There is no suggestion in the 3c-4e model that such variety is possible. The 3c-4e model offers only limited insight into the excited states of a compound where the bonding may be very different from that in the ground state.

3.5.2 Diabatic States Model

Grant and coworkers [6] argue that understanding the bonding in families such as PF_n, SF_n, PF_nO_m, SF_nO_m, and so on is confused by computing bond energies adiabatically rather than diabatically. If a ligand is interacting with a closed shell species, they advocate using an asymptote that is consistent with the bonding in the minimum energy structure rather than the ground state asymptote. This yields more consistent bond energies for a related family of molecules like SF_n. In the case of the SF_n family, they reported bond energies of 104.6 kcal mol^{-1} for SF_3 dissociating to $SF_2(b^3A_2) + F(^2P)$ and 104.7 kcal mol^{-1} for SF_5 dissociating to $SF_4(a^3A_1) + F(^2P)$ instead of to ground state products. These values are similar to the energies of 104.8 and 95.5 they reported for SF_6 and SF_4 dissociating to ground state SF_5 and SF_3 (plus F), respectively. The authors then state, ''These results are consistent with the inherent instability of the sulfur radicals as compared to the closed-shell species and show the reorganization of electron density that occurs on spin pairing to form the lone-pairs in SF_4 and SF_2'' (p. 3153).

If we start with the S atom, however, and follow the suggestion of Grant *et al.* [6], problems are encountered. Ground state $S(^3P)$ can only form two bonds without some form of reorganization. The ^5S state of S results if a 3p electron is excited into the 4s orbital. In principle, this quintet state could provide all of the singly occupied orbitals needed to form SF_4, although having one of the orbitals (4s) to be a Rydberg orbital presents some conceptual difficulties. As we noted earlier, $SF(a^4\Sigma^-)$ clearly possesses the scaffolding of singly occupied orbitals needed to form SF_4. The second $^4\Sigma^-$ state of SF does, in fact, arise from the $S(^5S) + F(^2P)$ asymptote as shown in Figure 3.8, so it is the natural asymptote to use as a diabatic reference. It could be argued that the potential energy curves in Figure 3.8 reflect a strongly avoided crossing (and with a minimum spacing of 45 kcal mol^{-1}, it is certainly that!). In this view, the diabatic states would be $SF(a^4\Sigma^-)$ correlated with $S(^5S) + F(^2P)$ and a second, repulsive state that dissociates to ground state atoms. However, since the experimental $S(^3P) - S(^5S)$ state separation is 52 624 cm^{-1} (150.5 kcal mol^{-1}) [31], the diabatic bond energy would be over 185 kcal mol^{-1} (the sum of the S atom triplet-quintet state separation and 36.2 kcal mol^{-1}). Also, the successive bond energies for adding F atoms to $SF(a^4\Sigma^-)$, $SF(a^3B_1)$, and $SF_3(X^2A')$ to build up to SF_4 do not reflect the consistency exhibited by the approach taken by Grant *et al.* [6]; the values are 106.3, 87.8, and 98.8 kcal mol^{-1} for the three additions, respectively.

Although using diabatic rather than adiabatic energies for computing bond strengths does provide more consistent bond energies, it does not appear to be overly advantageous to use this model – the variations in bond energies, although reduced, are still rather large. Instead, our studies indicate that the variations in energies are meaningful indicators of whether electron pair coupling or recoupling and/or bond reorganization has occurred.

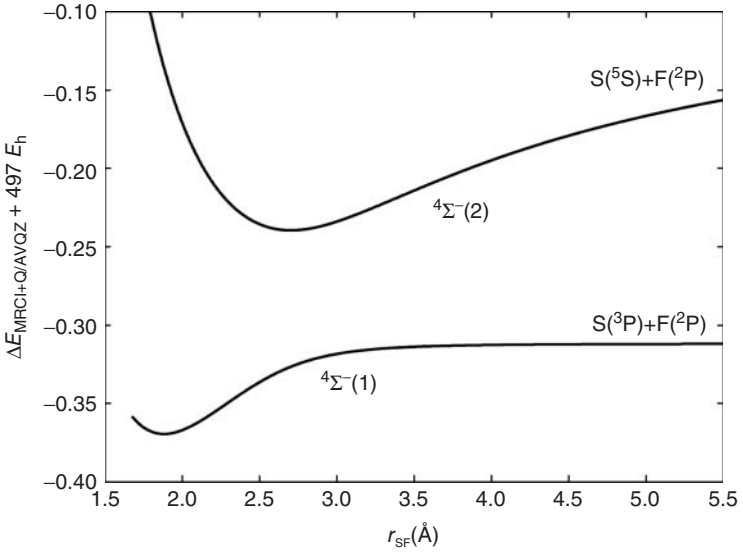

Figure 3.8 Potential energy curves of the first two $^4\Sigma^-$ states of SF at the MRCI+Q/AVQZ level. Asymptotes are noted.

3.5.3
Democracy Principle

The democracy principle of Cooper and coworkers [7] states that any valence electron can participate in bonding if it is energetically favorable to do so. This implies a similar conditionality as found with the recoupled pair bonding model. The recoupled pair bonding model provides insights into the conditions under which it is energetically favorable to form the type of bonds – recoupled pair bonds – that lead to hypervalence.

3.6
Concluding Remarks

This chapter describes a new model for understanding the origin of hypervalent behavior that is supported by detailed computational studies of the second row, late p-block halides – the *recoupled pair bonding* model. Recoupling a pair of electrons in a lone-pair orbital frees up two electrons for bond formation. It directly accounts for hypervalence by making more electrons available for bond formation than indicated by the number of unpaired electrons possessed by an atom in its ground state. However, recoupling only occurs if a ligand is able to recouple an existing electron pair. Unlike covalent bonding, *recoupled pair bonding is conditional*. The model recognizes cases where the ligand is unable to recouple a pair (e.g., SH does not have a bound $^4\Sigma^-$ state) and where recoupling is minimal, such as in the

frustrated recoupled pair bond in OF($a^4\Sigma^-$) as well as in a fully recoupled pair bond such in SF($a^4\Sigma^-$). The pair of bonds formed from recoupling the electrons in a lone-pair orbital is termed a *recoupled pair bond dyad*. The recoupled pair bond dyad is very stable and accounts for the stability of hypervalent compounds. The bonds in a dyad are coupled in a manner that is not present in a pair of covalent bonds, as breaking one of the bonds introduces antibonding character in the surviving bond, substantially weakening it.

Although the discussion in this chapter has focused on recoupling of p^2 and s^2 pairs in S, we have also explored the bonding in the fluorides of Cl and P [11, 12] and found that recoupled pair bonding accounts for hypercoordinated ClF_n and PF_n compounds as well as excited states of their non-hypercoordinated compounds. Moreover, we have also found in published [14] and ongoing studies that recoupled pair bonding is also present in the oxides and hydroxides of these molecules, in the halides of the third row, p-block elements (As, Se, Br, Kr), and is even responsible for the formation of various compounds of Be and the early p-block elements B and C when their $2s^2$ pairs become active by participating in recoupled pair bonding. Furthermore, recoupled pair bonds not only occur in hypervalent molecules; they are also found in the excited states of covalently bound late p-block compounds, such as the excited states of SF_2. An understanding of recoupled pair bonding is critical to understanding the structures, energies, and reactivities of the compounds of many elements.

References

1. Musher, J.I. (1969) The chemistry of hypervalent compounds. *Angew. Chem., Int. Ed. Engl.*, **8**, 54–68.
2. Schleyer, P.v.R. (1984) Hypervalent compounds. *Chem. Eng. News*, **62** (22), 4.
3. Pauling, L. (1931) The nature of the chemical bond. Application of results obtained from the quantum mechanics and from a theory of paramagnetic susceptibility to the structure of molecules. *J. Am. Chem. Soc.*, **53**, 1367–1400.
4. Kutzelnigg, W. (1984) Chemical bonding in higher main group elements. *Angew. Chem., Int. Ed. Engl.*, **23**, 272–295.
5. (a) Rundle, R.E. (1947) Electron deficient compounds. *J. Am. Chem. Soc.*, **69**, 1327–1331; (b) Rundle, R.E. (1964) On the probable structure of XeF_4 and XeF_2. *J. Am. Chem. Soc.*, **85**, 112–113; (c) Pimentel, G.C. (1951) The bonding of trihalide and bifluoride ions by molecular orbital theory. *J. Chem. Phys.*, **19**, 446–448.
6. Grant, D.J., Matus, M.H., Switzer, J.R., Dixon, D.A., Francisco, J.S., and Christe, K.O. (2008) Bond dissociation energies in second-row compounds. *J. Phys. Chem. A*, **112**, 3145–3156.
7. Cooper, D.L., Cunningham, T.P., Gerratt, J., Karadakov, P.B., and Raimondi, M. (1994) Chemical bonding to hypercoordinate second-row atoms: d orbital participation vs. democracy. *J. Am. Chem. Soc.*, **116**, 4414–4426.
8. Woon, D.E. and Dunning, T.H. Jr., (2009) Theory of hypervalency: recoupled pair bonding in SF_n ($n = 1–6$). *J. Phys. Chem. A*, **113**, 7915–7926.
9. Woon, D.E. and Dunning, T.H. Jr., (2009) A comparison between polar covalent bonding and hypervalent recoupled pair bonding in diatomic chalcogen halide species $\{O,S,Se\} \times \{F,Cl,Br\}$. *Mol. Phys.*, **107**, 991–998.
10. Chen, L., Woon, D.E., and Dunning, T.H. Jr., (2009) Bonding in ClF_n ($n = 1–7$) molecules: further insight into

the electronic structure of hypervalent molecules and recoupled pair bonds. *J. Phys. Chem. A*, **113**, 12645–12654.

11. Woon, D.E. and Dunning, T.H. Jr., (2010) Recoupled pair bonding in PF_n ($n=1$–5). *J. Phys. Chem. A*, **114**, 8845–8851.
12. Woon, D.E. and Dunning, T.H. Jr., (2011) Hypervalency and recoupled pair bonding in the *p*-block elements. *Comput. Theor. Chem.*, **963**, 7–12.
13. Leiding, J., Woon, D.E., and Dunning, T.H. Jr., (2011) Bonding and isomerism in $SF_{n-1}Cl$ ($n=1$–6). *J. Phys. Chem. A*, **115**, 329–341.
14. Leiding, J., Woon, D.E., and Dunning, T.H. Jr., (2011) Bonding in SCl_n ($n=1$–6): a quantum chemical study. *J. Phys. Chem. A*, **115**, 4757–4764.
15. Leiding, J., Woon, D.E., and Dunning, T.H. Jr., (2012) Theoretical studies of the excited doublet states of SF and SCl and singlet states of SF_2, SFCl, and SCl_2. *J. Phys. Chem. A*, **116**, 1655–1662.
16. Leiding, J., Woon, D.E., and Dunning, T.H. Jr., (2012) Insights into the unusual barrierless reaction between two closed shell molecules, $(CH_3)_2S + F_2$, and it $H_2S + F_2$ analogue: role of recoupled pair bonding. *J. Phys. Chem. A*, **116**, 5247–5255.
17. Dunning, T.H. Jr., Woon, D.E., Leiding, J., and Chen, L. (2013) The first row anomaly and recoupled pair bonding in the halides of the late p-block elements. *Acc. Chem. Res.*, **46**, 359–368.
18. (a) Werner, J.-J. and Knowles, P.J. (1985) A second order multiconfiguration SCF procedure with optimum convergence. *J. Chem. Phys.*, **82**, 5053–5063; (b) Knowles, P.J. and Werner, H.-J. (1985) An efficient second-order MC SCF method for long configuration expansions. *Chem. Phys. Lett.*, **115**, 259–267.
19. Goddard, W.A. III (1967) Improved quantum theory of many-electron systems. II. The basic method. *Phys. Rev.*, **157**, 81–93.
20. Werner, H.-J., Knowles, P.J., Lindh, R., Manby, F.R., Schütz, M., Celani, P., Korona, T., Mitrushenkov, A., Rauhut, G., Adler, T. B., Amos, R.D., Bernhardsson, A., Berning, A., Cooper, D. L., Deegan, M.J.O., Dobbyn, A.J., Eckert, F., Goll, E., Hampel, C., Hetzer, G., Hrenar, T., Knizia, G., Köppl, C., Liu, Y., Lloyd, A. W., Mata, R. A., May, A. J., McNicholas, S.J., Meyer, W., Mura, M.E., Nicklass, E., Palmieri, P., Pflüger, K., Pitzer, R., Reiher, M., Schumann, U., Stoll, H., Stone, A.J., Tarroni, R., Thorsteinsson, T., Wang, M., and Wolf, A.M. Version 2009.1, www.molpro.net (accessed 27 November 2013).
21. (a) Lennard-Jones, J. (1949) The molecular orbital theory of chemical valency. I. The determination of molecular orbitals. *Proc. R. Soc. London*, **198A**, 1–13; (b) Lennard-Jones, J. (1949) The molecular orbital theory of chemical valency. II. Equivalent orbitals in molecules of known symmetry. *Proc. R. Soc. London*, **198A**, 14–26; (c) Hall, G.G. and Lennard-Jones, J. (1950) The molecular orbital theory of chemical valency. III. Properties of molecular orbitals. *Proc. R. Soc. London*, **202A**, 155–165; (d) Lennard-Jones, J. and Pople, J.A. (1950) The molecular orbital theory of chemical valency. IV. The significance of equivalent orbitals. *Proc. Roy. Soc. London*, **202A**, 166–180; (e) Pople, J.A. (1950) The molecular orbital theory of chemical valency. V. The structure of water and similar molecules. *Proc. R. Soc. London*, **202A**, 323–336; see also subsequent papers in this series.
22. (a) Purvis, G.D.III and Bartlett, R.J. (1982) A full coupled-cluster singles and doubles model: the inclusion of disconnected triples. *J. Chem. Phys.*, **76**, 1910–1918; (b) Raghavachari, K., Trucks, G.W., Pople, J.A., and Head-Gordon, M. (1989) A fifth-order perturbation comparison of electron correlation theories. *Chem. Phys. Lett.*, **157**, 479–483; (c) Knowles, P.J., Hampel, C., and Werner, H.-J. (1993) Coupled cluster theory for high spin, open shell reference wave functions. *J. Chem. Phys.*, **99**, 5219–5227; (d) Watts, J.D., Gauss, J., and Bartlett, R.J. (1993) Coupled-cluster methods with noniterative triple excitations for restricted open-shell Hartree-Fock and other general single

determinant reference functions. Energies and analytical gradients. *J. Chem. Phys.*, **98**, 8718–8733.

23. (a) Dunning, T.H. Jr., (1989) Gaussian basis sets for use in correlated molecular calculations. I. The atoms boron through neon and hydrogen. *J. Chem. Phys.*, **90**, 1007–1023; (b) Kendall, R.A., Dunning, T.H. Jr., and Harrison, R.J. (1992) Electron affinities of the first-row atoms revisited. Systematic basis sets and wave functions. *J. Chem. Phys.*, **96**, 6796–6806; (c) Woon, D.E. and Dunning, T.H. Jr., (1993) Gaussian basis sets for use in correlated molecular calculations. III. The atoms aluminum through argon. *J. Chem. Phys.*, **98**, 1358–1371; (d) Dunning, T.H. Jr., Peterson, K.A., and Wilson, A.K. (2001) Gaussian basis sets for use in correlated molecular calculations. X. The atoms aluminum through argon revisited. *J. Chem. Phys.*, **114**, 9244–9253.

24. (a) Werner, J.-J. and Knowles, P.J. (1988) An efficient internally contract multiconfiguration-reference configuration interaction method. *J. Chem. Phys.*, **89**, 5803–5814; (b) Knowles, P.J. and Werner, H.-J. (1988) An efficient method for the evaluation of coupling coefficients in configuration interaction calculations. *Chem. Phys. Lett.*, **145**, 514–522; (c) Langhoff, S.R. and Davidson, E.R. (1974) Configuration interaction calculations on the nitrogen molecule. *Int. J. Quantum Chem.*, **8**, 61–72.

25. Carrington, A., Currie, G.N., Miller, T.A., and Levy, D.H. (1969) Gas-phase electron resonance spectra of SF and SeF. *J. Chem. Phys.*, **50**, 2726–2732.

26. Endo, Y., Saito, S., and Hirota, E. (1982) The microwave spectrum of the SF radical. *J. Mol. Spectrosc.*, **92**, 443–450.

27. Arkell, A., Reinhard, R.R., and Larson, L.P. (1965) Matrix infrared studies of OF compounds. I. The OF radical. *J. Am. Chem. Soc.*, **87**, 1016–1020.

28. Miller, C.E. and Drouin, B.J. (2001) The $X_1\,^2\Pi_{3/2}$ and $X_2\,^2\Pi_{1/2}$ potential energy surfaces of FO. *J. Mol. Spectrosc.*, **205**, 312–318.

29. Yang, X. and Boggs, J.E. (2005) Ground and valence-excited states of SF: a multireference configuration interaction with single and double excitations+Q study. *J. Chem. Phys.*, **122**, 194307.

30. (a) Xie, F.-Q., Xia, Y.-X., and Huang, M.-B. (1993) Electronic states of the FO radical. An MRSDCI study. *Chem. Phys. Lett.*, **203**, 598–602; (b) Lane, I.C. and Orr-Ewing, A.J. (2000) Valence and rydberg states of FO: an ab initio search for electronic transitions. *J. Phys. Chem.*, **104**, 8759–8764.

31. Coulson, C.A. (1964) The nature of bonding in xenon fluorides and related molecules. *J. Chem. Soc.*, **1964**, 1442–1454.

32. Weinhold, F. and Landis, C.R. (2005) Valency and Bonding, A Natural Bond Orbital Donor-Acceptor Perspective, Cambridge University Press, Cambridge, pp. 275–306.

33. Cheung, Y.-S., Ng, C.-Y., Chiu, S.-W., and Li, W.-K. (2003) Application of three-center-four-electron bonding for structural and stability predictions of main group hypervalent molecules: the fulfillment of the octet shell rule. *J. Mol. Struct. (THEOCHEM)*, **623**, 1–10.

34. Ponec, R., Yuzhakov, G., and Cooper, D.L. (2004) Multicenter bonding and the structure of electron rich molecules. Model of the three-center four-electron bonding reconsidered. *Theor. Chem. Acc.*, **112**, 419–430.

35. Kiang, T. and Zare, R.N. (1980) Stepwise bond dissociation energies in sulfur hexafluoride. *J. Am. Chem. Soc.*, **102**, 4024–4029.

4
Donor–Acceptor Complexes of Main-Group Elements

Gernot Frenking and Ralf Tonner

4.1
Introduction

There are two ways of forming a covalent two-electron bond between fragments A and B. A chemical bond A–B may either come from the electron-sharing interactions between the open-shell fragments $A^{\bullet}$ and $B^{\bullet}$, where each fragment contributes one electron to covalent bonding, or, in the second approach, the donor fragment A| provides both electrons to the bond, while fragment B serves as the electron acceptor (Figure 4.1a,b). The latter type of covalent interaction is called a donor–acceptor bond. Historically outdated names, which are still sometimes used, are ''dative bond'' and ''semi-polar'' bond. Following the electron-pair paradigm of Gilbert Lewis [1], the donor and acceptor moieties are termed Lewis base and acid, respectively. An electron-sharing bond and a donor–acceptor bond are easily distinguished by breaking the bond A–B. The former bond breaks homolytically, whereas the latter bond breaks heterolytically. In this chapter, we will use the notation A→B for a donor–acceptor bond and A–B for an electron-sharing bond.

We want to point out that electron-sharing bonds A–B and donor–acceptor bonds A→B are *both* covalent bonds where the main-group atoms use their (*n*)s and (*n*)p valence orbitals for chemical bonding. The A→B bond arises from the mixing of the doubly occupied valence orbitals of A and the vacant valence orbitals of B, while the electron-sharing bond A–B comes from the mixing of the singly occupied valence orbitals of A and B. The covalent interactions of both types of bonds may be enhanced by electrostatic attraction, which is a major component not only in polar bonds, but also in most nonpolar electron-sharing bonds A–A when orbital overlap is considered [2]. For a detailed discussion of this point, see the chapter ''The EDA Perspective of Chemical Bonding'' in volume 1 of this book.

Covalent bonding in main group chemistry is usually discussed in terms of electron-sharing bonding A–B. Donor–acceptor bonds A→B play only a minor role. They are frequently introduced for discussing the chemistry of group 13/15 complexes. By contrast, chemical bonding in transition metal (TM) compounds, where the metal atoms use their (*n*)s and ($n-1$)d valence orbitals for chemical bonding [3], is usually introduced using the donor–acceptor model suggested

The Chemical Bond: Chemical Bonding Across the Periodic Table, First Edition.
Edited by Gernot Frenking, Sason Shaik.

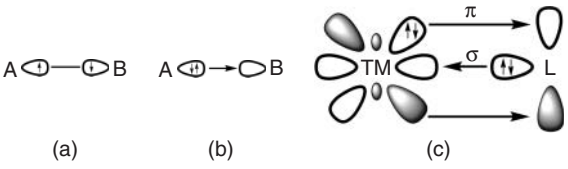

Figure 4.1 Schematic representation of various types of covalent bonding. (a) Electron-sharing bonding. (b) Donor–acceptor bonding. (c) Dewar–Chatt–Duncanson bonding model for transition metal complexes.

by Dewar [4] and further developed in TM chemistry by Chatt and Duncanson [5] (Dewar–Chatt–Duncanson, DCD). The DCD bonding model considers the σ donation from a ligand L to a transition metal TM←L and the concomitant π backdonation TM→L as the main components of chemical bonding in TM complexes (Figure 4.1c) [6]. The bonding in most TM molecules comes from TM←L σ donation and TM→L π backdonation. It was recently shown that there are compounds where the metal–ligand interactions come from TM←L π donation and TM→L σ backdonation, which may be identified with a reversed DCD model [7]. Chemical bonding in TM compounds has been extensively discussed in the chapter "Chemical Bonding in Transition Metal Compounds" in volume 2 of this book. The reason that TM bonding is usually discussed in terms of donor–acceptor interactions, whereas covalent bonding in main group chemistry is generally introduced through electron-sharing interactions between hybrid orbitals, comes from the finding that the latter type of bonding is prevalent for main group compounds, whereas TM compounds are typically bonded through donor–acceptor bonds.

Nevertheless, donor–acceptor complexes are also known for main group compounds. Typical examples are adducts between group 13 Lewis acids of boron BX_3 or aluminum AlX_3, where X is a hydrogen or halogen atom, and group 15 Lewis bases, such as amines NR_3 or phosphines PR_3. The chemical bond in group 13/15 complexes has been analyzed in detail and is well understood [8]. Haaland [9] has shown that it is very useful to distinguish between electron-sharing bonds A–B and donor–acceptor bonds A→B of main group compounds. Donor–acceptor bonds are usually much weaker and longer than electron-sharing bonds of the same elements. This must be kept in mind when chemical bonds between the same types of atoms are compared.

This chapter deals with (i) novel main-group molecules EL_2, which possess unusual chemical bonds best-described in terms of donor–acceptor interactions L→E←L, where E is, in most cases, a single atom, and (ii) a related class of compounds E_2L_2 that possess donor–acceptor bonds to a diatomic fragment L→EE←L. Some compounds discussed here have earlier been termed *ylides*. An ylide is a neutral molecule containing a formally negatively charged atom (usually carbon) directly attached to a heteroatom with a formal positive charge (usually nitrogen, phosphorus or sulfur), and in which both atoms have full octets of electrons [10]. Phosphorus ylides $R_3P^{(+)}\text{-}C^{(-)}R'_2$ are a typical example. It is important to realize that the bond between $R_3P^{(+)}$ and $C^{(-)}R'_2$ is understood

as an electron-sharing bond between the formally charged fragments in this bonding picture. An alternative view, which is less common, considers ylides as donor–acceptor complexes $R_3P{\rightarrow}CR'_2$. It is shown in this chapter that there are compounds in main-group chemistry where the donor–acceptor bonding model is more useful for describing the bonding situation than electron-sharing bonding between charged fragments. Bonding models are neither wrong nor right, they are rather more or less useful. The usefulness of the donor–acceptor model becomes evident by its ability to explain molecular structures of known compounds and to predict new molecules with unusual bonds.

4.2 Single-Center Complexes EL_2

Chemical bonds to a neutral main group atom E are usually considered covalent bonds that come from the electron-sharing interactions of unpaired electrons of atom E. In the following section, we discuss compounds EL_2, which are better described in terms of donor–acceptor interactions L→E←L.

4.2.1 Carbones CL_2

Carbones CL_2 are a class of dicoordinated carbon compounds, where a σ-donor ligand L binds to a bare carbon atom in the ^1D excited state through donor–acceptor interactions L→C←L. The term *carbone* was coined for the first time in 2009 by Frenking and Tonner, who summarized recent theoretical work about divalent carbon(0) compounds [11]. The carbon atom in carbones has the formal oxidation state zero and it retains its valence electrons as two electron lone-pairs, one with σ symmetry and one with π symmetry. Thus, carbones CL_2 are clearly distinguished from carbenes CR_2, which are dicoordinated C(II) compounds with two electron-sharing bonds R–C–R, where the carbon atom has only one electron pair that exhibits σ symmetry (Figure 4.2) [12].

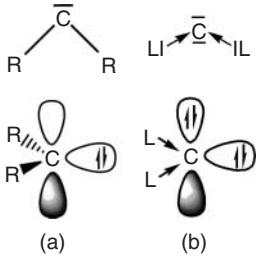

Figure 4.2 Schematic representation of chemical bonding in (singlet) carbenes CR_2 (a) and carbones CL_2 (b) with the associated lone-pair orbitals.

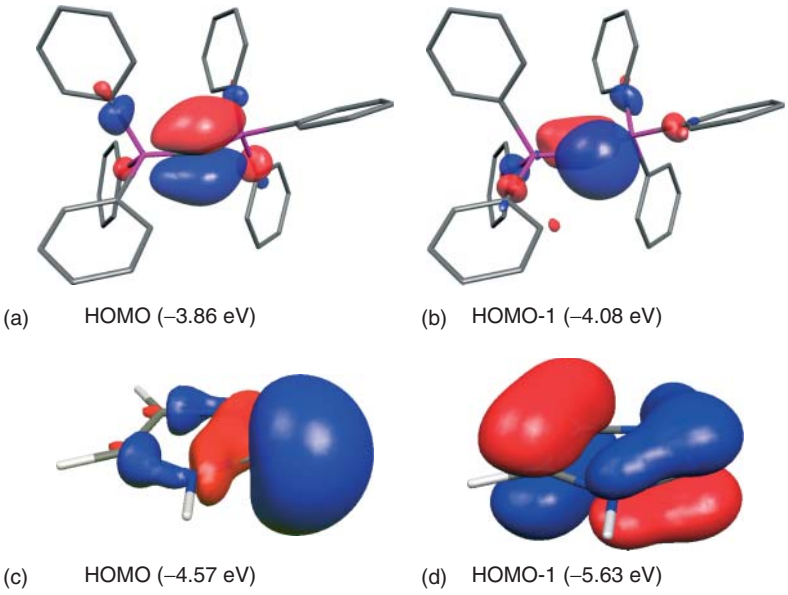

Figure 4.3 Shape of (a) the HOMO and (b) the HOMO-1 of the carbone $C(PPh_3)_2$ and (c) HOMO and (d) HOMO-1 of the N-heterocyclic carbene (NHC).

Persistent carbenes were introduced into synthetic chemistry by Bertrand, who isolated the first carbene $R_2P–C–SiR'_3$ in 1988 [13], and by Arduengo [14], who synthesized the *N*-heterocyclic carbenes (NHCs) in 1991. Stable carbones were actually isolated much earlier than carbenes. In 1961, Ramirez *et al.* [15] reported on the synthesis of the compound hexaphenyl-carbodiphosphorane $C(PPh_3)_2$. The authors assumed that the molecule has a linear structure $Ph_3P=C=PPh_3$, which they described with resonance structures in terms of double bonds between phosphorous and carbon and as a double ylide $Ph_3P=C=PPh_3 \leftrightarrow Ph_3P(+)–C(2–)–(+)PPh_3$. An X-ray structure analysis by Kaska [16] in 1978 revealed that $C(PPh_3)_2$ has a strongly bent geometry with a P–C–P bending angle of 131.7°. However, this did not change the perception of the bonding situation in carbodiphosphorane in terms of carbon–phosphorous electron-sharing bonds for a long time.

Figure 4.3 shows the two highest lying occupied orbitals HOMO and HOMO-1 of $C(PPh_3)_2$ and the parent NHC. It becomes obvious that $C(PPh_3)_2$ has two electron lone-pairs at the central carbon atom, that is, one π lone-pair, which is the HOMO, and one σ lone-pair, which is the HOMO-1 (Figure 4.3a,b). This is in striking contrast to the HOMO and HOMO-1 of the NHC (Figure 4.3c,d). The latter HOMO is a σ lone-pair MO that has a similar shape to the HOMO-1 of $C(PPh_3)_2$. The HOMO-1 of NHC is a delocalized π orbital that extends over all ring atoms. The carbon–phosphorous bonding in $C(PPh_3)_2$ comes solely from the donation of the phosphorous lone-pair electrons into the vacant AOs of carbon in the ^1D singlet state, while the carbon–nitrogen bonding in NHC comes from electron-sharing interactions. Thus, there is a significant difference between the bonding situation

Table 4.1 First and second proton affinities (MP2/def2-TZVPP//BP86/SVP in kcal mol^{-1}) and NBO partial charges (BP86/def2-TZVPP//BP86/SVP) at the central carbon q(C) for dicoordinated carbon compounds [18].

R	First PA	Second PA	q(C)
N-heterocyclic carbenes NHC^R			
Me	262.3	71.8	0.04
Ph	264.7	100.1	0.08
NH_2	253.9	76.7	−0.01
NMe_2	259.8	106.5	0.02
Mesityl	270.4	105.3	0.08
Adamantyl	274.9	105.7	0.05
Carbodiphosphoranes $C(PR_3)_2$			
Me	278.4	156.2	−1.47
Ph	280.0	185.6	−1.43
NH_2	280.0	153.5	−1.51
NMe_2	279.9	174.9	−1.64
Mesityl	280.7	201.1	−1.47
Cyclohexyl	280.5	184.0	−1.56
Carbodicarbenes $C(NHC^R)_2$			
H	292.3	155.3	−0.51
Me	294.3	168.4	−0.50
Tetraaminoallenes $(R_2N)_2C{=}C{=}C(NR_2)_2$			
Me	282.5	151.6	−0.21
Et	268.2	175.8	−0.22

of the dicoordinated carbon atoms in carbodiphosphorane and NHC, which also comes to the fore by means of the atomic partial charge at the central carbon atom. The partial charge in $C(PPh_3)_2$ is $q(C) = -1.43$ e, whereas in NHC^{Me}, which has methyl groups at nitrogen, it is $q(C) = 0.04$ e [17].

Table 4.1 gives the calculated partial charges q(C) at the dicoordinated carbon atom of NHCs and $C(PR_3)_2$ carrying various substituents. The partial charges for the carbodiphosphoranes are between −1.43 e and −1.64 e, whereas the values for the NHCs suggest an essentially neutral carbon atom. Another striking difference is indicated by the calculated proton affinities (PAs) of the compounds [18]. The first PAs of the NHCs (253.9–274.9 kcal mol^{-1}) are not very different from the rather uniform values for $C(PR_3)_2$ (278.4–280.7 kcal mol^{-1}), but the second PAs of the carbodiphosphoranes are much larger (153.5–201.1 kcal mol^{-1}) than the second PAs of the NHCs (71.8–106.5 kcal mol^{-1}). This can be explained by the occurrence of only one electron lone-pair in NHCs, while there are two electron lone-pairs in $C(PR_3)_2$ having the ability to bind to a proton.

Hexaphenylcarbodiphosphorane $C(PPh_3)_2$ may be considered a prototype carbone CL_2. It is, thus, useful to analyze the bonding situation of $C(PPh_3)_2$ in more detail. The orbital interactions in CL_2, which are associated with charge

Table 4.2 Energy decomposition analysis at BP86/TZ2P with the EDA-NOCV method of the carbon–ligand interactions in carbodiphosphorane $C(PPh_3)_2$ and carbodicarbene $C(NHC^{Me})_2$. All values in kcal mol^{-1}.

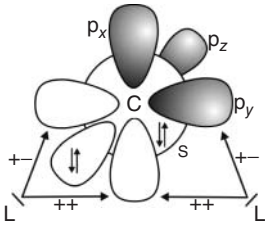

C: $X^3P \rightarrow {}^1D$ 43.5 kcal mol^{-1} (BP86/TZ2P)

Compound	**$C(PPh_3)_2$**	**$C(NHC^{Me})_2$**
Interacting fragments	**C (^{1}D) $(PPh_3)_2$**	**C (^{1}D) $(NHC^{Me})_2$**
ΔE_{int}	−192.3	−267.3
ΔE_{Pauli}	738.4	917.6
ΔE_{elstat} [a]	−284.0 (30.5%)	−354.6 (29.9%)
ΔE_{orb} [a]	−646.7 (69.5%)	−830.4 (70.1%)
ΔE_{σ} (L→C←L (+,+) donation) [b]	−384.2 (59.4%)	−517.7 (62.3%)
$\Delta E_{\pi\parallel}$ (L→C←L (+,-) donation) [b]	−190.5 (29.5%)	−196.0 (23.6%)
$\Delta E_{\pi^{\perp}}$ (L←C→L π backdonation) [b]	−65.0 (10.1%)	−98.8 (11.9%)
ΔE_{rest} [b]	−6.9 (1.1%)	−17.8 (2.1%)
ΔE_{prep}	63.6	87.3
D_e	128.6	180.0

[a] The values in parentheses give the percentage contribution to the total attractive interactions $\Delta E_{elstat} + \Delta E_{orb}$.
[b] The values in parentheses give the percentage contribution to the orbital interactions ΔE_{orb}.

donation L→C←L of the ligands L to the carbon atom in the ^{1}D reference state with the valence electron configuration $2s^2 2p_x{}^0 2p_y{}^0 2p_z{}^2$, are shown schematically at the top of Table 4.2. The $2p_x$ AO is the acceptor orbital for the in-phase (+/+) combination of the σ-donor orbitals of L, while the $2p_y$ AO is the acceptor orbital for the in-plane $\pi_{\parallel}$ donation of the out-of-phase (+/−) lone-pair combination. The occupied $2p_z$ AO of carbon is available for out-of-plane $\pi_{\perp}$ backdonation L←C→L into vacant orbitals of the ligand L. The strength of the donor–acceptor interactions $Ph_3P{\rightarrow}C{\leftarrow}PPh_3$ has been assessed in quantitative terms with the help of the EDA [19] (Energy decomposition analysis) calculations. Table 4.2 gives the results of EDA-NOCV calculations, where the natural orbital for chemical valence (NOCV) method [20] makes it possible to partition the total orbital interactions between C(^{1}D) and 2 PPh_3 into pairwise contributions of occupied and vacant orbitals of the

fragments. Details of the EDA-NOCV method are described in the chapter ''The EDA Perspective of Chemical Bonding'' in volume 1 of this book and, therefore, are not given here.

The EDA-NOCV results give a total interaction energy between C (^{1}D) and 2 PPh_3 of $\Delta E_{int} = -192.3$ kcal mol^{-1} [21]. Thus, the average value for the intrinsic $Ph_3P\rightarrow C$ donor–acceptor bond is 96.15 kcal mol^{-1}, which is rather high. The attractive carbon–ligand bonding contributions come mainly from the orbital (covalent) interactions, which provide 69.5%, whereas the Coulombic attraction contributes 30.5% to the overall binding interactions. The qualitative orbital interactions, which are shown at the top of Table 4.2, are quantified by the breakdown of ΔE_{orb} into the pairwise orbital contributions derived from the EDA-NOCV calculations. The largest value comes from the $Ph_3P\rightarrow C\leftarrow PPh_3$ σ donation of the (+,+) combination of the phosphine lone-pair orbitals, which provides 59.4% of ΔE_{orb}. The in-plane $\pi_{\parallel}$ donation of the (+,−) combination of the ligand lone-pair orbitals supplies another 29.5%. Thus, the total $Ph_3P\rightarrow C\leftarrow PPh_3$ donation amounts to 88.9% of the orbital interactions, whereas the $Ph_3P\leftarrow C\rightarrow PPh_3$ $\pi_{\perp}$ backdonation provides only 10.1% of ΔE_{orb}. The rest term ΔE_{rest} comes from the remaining orbital interactions, which are less important.

The bond dissociation energy (BDE) for breaking the carbon–phosphorous bonds is much smaller ($D_e = 128.6$ kcal mol^{-1}) than the interaction energy ΔE_{int}. The energy difference $\Delta E_{prep} = 63.6$ kcal mol^{-1} comes mainly from the excitation energy of the carbon atom from the X^3P ground state to the ^{1}D excited state, which is calculated as 43.5 kcal mol^{-1}. The remaining difference of 20.1 kcal mol^{-1} is a result of the geometry relaxation of the PPh_3 fragments.

There are further carbones where the phosphine groups of carbodiphosphorane are replaced by CO: $(Ph_3P)C(CO)$ and $C(CO)_2$, which have been synthesized and structurally characterized. The former compound has a bending angle of 145.6° at carbon, which is somewhat wider than in $C(PPh_3)_2$. Carbon suboxide, which is usually described in textbooks with double bonds O=C=C=C=O, has a linear geometry in the solid state [22] but exhibits a bending angle (OC)–C–(CO) of 156.0° in the gas phase, which is difficult to understand with the bonding model of cumulenic double bonds [23]. The donor–acceptor model of carbones easily explains the trend of the bending angle in $C(PPh_3)_2$ (131.7°), $C(CO)(PPh_3)$ (145.6°), and $C(CO)_2$ (156.0°) with the π-acceptor strength of CO, which leads to an increase of the π backdonation L←C→L and, thus, to a widening of the bending angle.

The introduction of the donor–acceptor bonding model for carbones CL_2 gave rise to theoretical studies of new species where some of them could become synthesized. Figure 4.4a shows the calculated geometry of the carbodicarbene $C(NHC^{Me})_2$, where the phosphine groups of carbodiphosphorane are replaced by NHC^{Me} with a saturated carbon–carbon bond in the ring. Investigations of TM complexes with PR_3 and NHC as ligands suggest that they have similar properties as donor species. The theoretically predicted bending angle (NHC^{Me})–C–(NHC^{Me}) of 131.8° is indeed very similar to the calculated value of 136.3° for the angle (Ph_3P)–C–(PPh_3). Figure 4.4b shows the geometry of the benzoannelated carbodicarbene $C(Bz\text{-}NHC^{Me})_2$, which could, in the meantime, be prepared and structurally

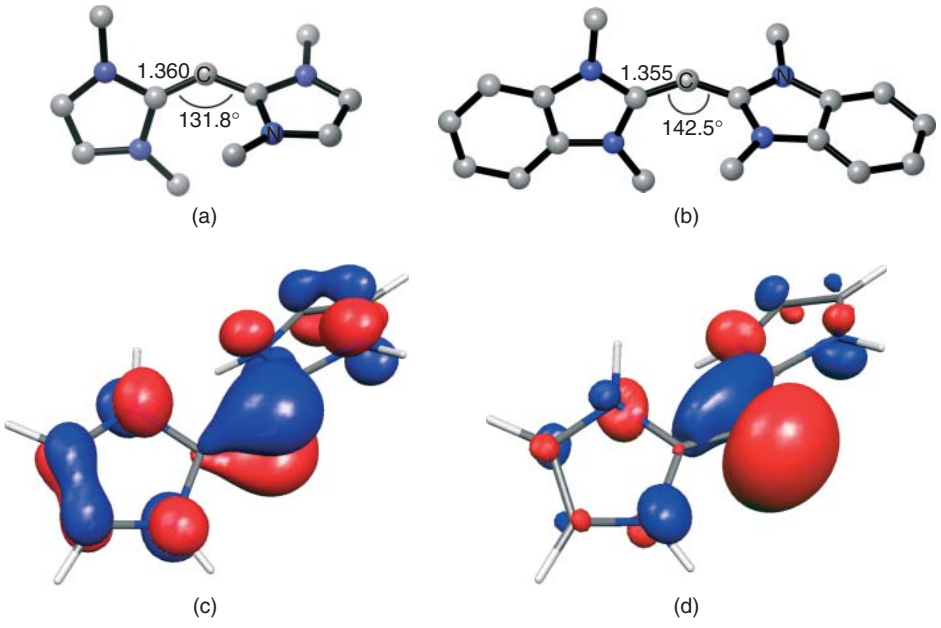

Figure 4.4 (a) Calculated geometry and most important bond length and angles of the carbodicarbene $C(NHC^{Me})_2$. (b) Calculated bond lengths and angles of the carbodicarbene $C(NHC^{Bz})_2$. Shape of (c) HOMO (−2.94 eV) and (d) HOMO-1 (−3.24 eV) of $C(NHC)_2$.

characterized [24]. The calculated (142.5°) and experimental (134.8°) values for the bending angle at the dicoordinated carbon are very similar to the theoretical data of $C(NHC^{Me})_2$. Figure 4.4c and d show the HOMO and HOMO-1 of the carbodicarbene $C(NHC)_2$. The HOMO-1 is a σ-type lone-pair orbital. The HOMO is a π-type MO that has the largest coefficient at the dicoordinated carbon atom, but it is somewhat delocalized over the NHC rings. The calculated first and second PAs of the carbodicarbenes shown in Table 4.1 clearly suggest that they should be considered to be carbones, because the values of the second PA are similar to the data for the carbodiphosphoranes. Note that the negative partial charges at the divalent C(0) atom of $C(NHC^R)_2$ are much smaller (−0.50 e and −0.51 e) than in $C(PR_3)_2$.

Table 4.2 gives also the EDA-NOCV data for $C(NHC^{Me})_2$, which may be compared with the data for carbodiphosphoranes. The carbon–ligand bonding in the carbodicarbene is significantly stronger relative to $C(PPh_3)_2$, but the breakdown of the total interaction energy ΔE_{int} into the different terms indicates that the nature of the bonding in the two compounds is very similar. The attractive interactions stem for both molecules mainly from orbital (covalent) bonding, which contributes approximately 70% of the attraction whereas the electrostatic bonding contributes approximately 30%. The strongest orbital interactions come in both molecules from the σ and $\pi_{\parallel}$ components of the L→C←L donation, whereas the L←C→L $\pi_{\perp}$ backdonation contributes only 10–12% to ΔE_{orb}.

There is another group of carbones showing the value of the donor–acceptor bonding model for dicoordinated carbon compounds. Calculations of the carbodiylides $C(ECp)_2$, where Cp = cyclopentadienyl and E = Al – Tl, give strongly bent molecules with bending angles CpE-C-ECp between 102 and 104°, two electron lone-pairs at carbon and large values for the first and second PAs, which show that the compounds should be considered as carbones CpE→C←ECp [25]. By contrast, the boron homologue $C(BCp)_2$ possesses a linear geometry, which suggests that it should be described as a substituted derivative of the parent system HB=C=BH, which has been synthesized in a low-temperature matrix [26]. The comparison of the calculated vibrational frequencies with the experimental data was evidence for a linear equilibrium geometry.

The recalculation of $C(BH)_2$ in light of the bonding situation of carbones led to a surprising finding. The potential energy surface of the molecule has *two* energy minima, one being linear and one being significantly bent with a bending angle of 90.4°, both of which are energetically nearly degenerate [27]. Figure 4.5 shows the equilibrium geometries of the two species and the energy profile for the isomerization pathway, which has an activation barrier of only 2.33 kcal mol^{-1} at the highly accurate coupled cluster level.

The occurrence of two energy minima for $C(BH)_2$ shows that isomers which have electron-sharing bonds HB=C=BH and donor–acceptor bonds HB→C←BH may lead to coexisting species that can be experimentally identified through their different vibrational spectra [27]. The different bonding situations come to the fore when the occupied valence orbitals of the two isomers, which are shown in

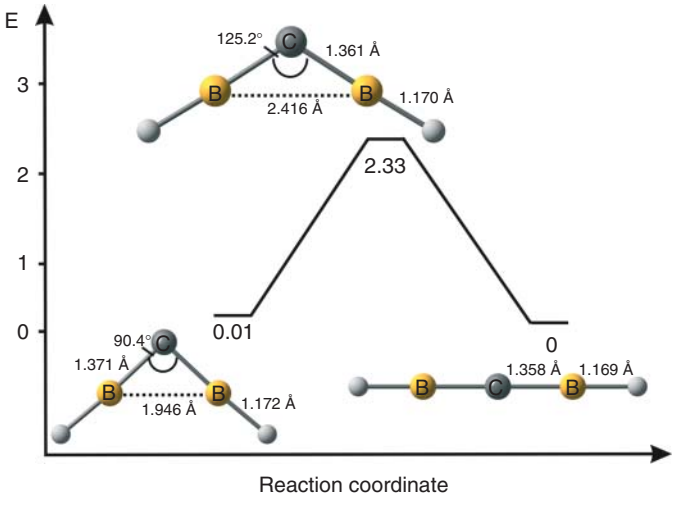

Figure 4.5 Calculated energy curve (AE-CCSD(T)/cc-pCVQZ, energies in kcal/mol) for the interconversion of the bent and linear forms of $C(BH)_2$. Optimised geometries of the two structural isomers of $C(BH)_2$ and the transition state for interconversion. (Data are taken from Ref. [27].)

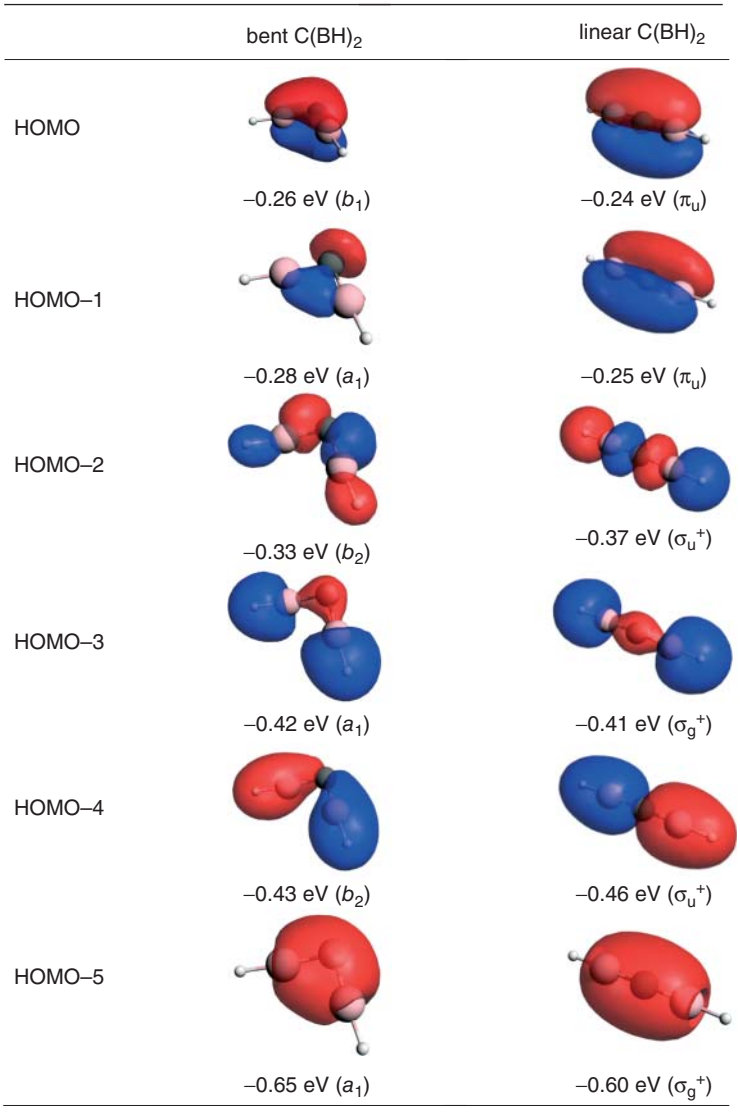

Figure 4.6 Shape and eigenvalues of the occupied valence orbitals of bent and linear $C(BH)_2$. (Data are taken from Ref. [27].)

Figure 4.6, are compared with each other. The linear structure exhibits the classical MOs, which can be expected for the delocalized BCB three-center π bonds (HOMO and HOMO-1), and the σ bonds, which possess an increasing number of nodes from HOMO-5 to HOMO-2. The HOMO and HOMO-1 of the bent form resemble the HOMO and HOMO-1 of the carbodicarbene $C(NHC)_2$ (see Figure 4.4c,d), where the HOMO is a π-type orbital, which has the largest coefficient at the

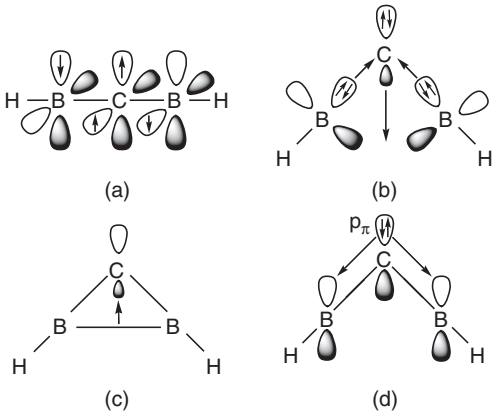

Figure 4.7 Schematic representation of relevant orbital interactions in (a) linear $C(BH)_2$ and in (b–d) bent $C(BH)_2$. The boron–carbon σ bonding in b and c depicts the same situation, but it uses different starting points.

dicoordinated carbon atom, whereas the HOMO-1 is a σ-type lone-pair MO at carbon. The HOMO of bent $C(BH)_2$ is clearly delocalized over the boron atoms, which can be assigned to HB←C→BH π backdonation. Note that the backside lobe of the HOMO-1 σ lone-pair MO also exhibits some HB←C→BH σ backdonation into the formally vacant p AOs of boron which are orthogonal to the C-B-H axis, which nicely explains the rather acute B–C–B bending angle. The plus and minus combination of the HB→C←BH donation is evident from the shape of the HOMO-5/HOMO-3 (+) and HOMO-4/HOMO-2 (–) orbitals that mix with the B–H bonding contributions.

Figure 4.7 shows the bonding situation in the linear and bent isomers of $C(BH)_2$ schematically. The linear cumulene, which may be written with the Lewis structure HB=C=BH, has classical two-center two-electron C–B σ bonds and two three-center two-electron π bonds. Each C–B π bond extends over the entire B–C–B framework, which means that all valence AOs of boron are partially occupied, although the Lewis structure HB=C=BH suggests that there is only an electron sextet at boron. The delocalized π bonding yields partial triple-bond character, which explains why the C–B bond distances in the linear form are clearly shorter than that of a standard double bond (1.45 Å), and only slightly longer than that of a standard triple-bond (1.33 Å) [28]. The acute B–C–B angle in the bent isomer can be explained with the backside donation of the σ lone-pair MO into the vacant p AOs of boron (Figure 4.7b). An alternative view uses the cyclic structure, which is shown in Figure 4.7c, as a starting point where the B–B bond donates electrons into the formally empty σ AO of carbon yielding the HOMO-1. Since the largest coefficient of the latter orbital (Figure 4.6) is at carbon, the orbital interactions, which are shown in Figure 4.7b, appear more useful. The HB←C→BH π backdonation, which leads to the HOMO, is shown in Figure 4.7d.

4.2.2
Isoelectronic Group 15 and Group 13 Homologues $(N^+)L_2$ and $(BH)L_2$

Is the donor–acceptor model also valid for other complexes, EL_2, where E is a first octal-row atom?. The answer is yes [21]. Isoelectronic nitrogen cation complexes $(N^+)L_2$ with the ligands L = CO and N_2 have been synthesized and were structurally characterized by X-ray analysis in 1999 [29]. The carbonyl complex $(N^+)(CO)_2$, which is isoelectronic to carbon suboxide, has a more acute bending angle OC–(N^+)–CO of 130.7° than OC–C–CO (156.0°). The pentanitrogen complex $(N^+)(N_2)_2$ exhibits an even smaller bending angle NN–(N^+)–NN of 116.5°. The homologous carbon complex $C(N_2)_2$ is not known experimentally. A mixed carbone $C(PClR_2)(N_2)$ was synthesized in 1987 [30], but the structure could not be determined. The phosphine complex $(N^+)(PPh_3)_2$ was isolated by Appel and Hauss [31] in 1961 and was structurally characterized shortly afterwards [32] .

Figure 4.8c shows the optimized geometry of $(N^+)(PPh_3)_2$, which may be compared with the isoelectronic parent carbone $C(PPh_3)_2$ that is also displayed (Figure 4.8a). The calculated bending angle P–N–P of 138.6° for the former compound (exp.: 142°) is very similar to the theoretical P–C–P angle of 136.3° for carbodiphosphorane (exp.: 131.7°). Figure 4.8e also shows the optimized geometry of $(BH)(PPh_3)_2$, which is another molecule that is isoelectronic to $C(PPh_3)_2$. The calculated bending angle P–B–P is slightly more acute (131.1°) than in the carbon and nitrogen homologues. The boron complex $(BH)(PPh_3)_2$ has not yet become known experimentally.

Table 4.3 shows the donor–acceptor orbital interactions schematically at the top between the phosphine ligands and the N^+ and BH acceptor species. The calculated excitation energy of the triplet electronic ground state to the singlet reference state $X^3P \rightarrow {}^1D$ of N^+ is higher (63.9 kcal mol^{-1}) than for C (43.5 kcal mol^{-1}; Table 4.2). However, the nitrogen cation is a much stronger electron acceptor than the carbon atom, which should easily compensate for the higher excitation energy that is required to access the ^1D state. The L→(N^+)←L donor–acceptor interactions of the N^+ cation should be significantly stronger than the L→C←L attraction. The assumption is supported by the results of the EDA-NOCV calculations, which are given in Table 4.3. The interaction energy in $(N^+)(PPh_3)_2$ is much stronger ($\Delta E_{int} = -447.1$ kcal mol^{-1}) than in $C(PPh_3)_2$ ($\Delta E_{int} = -192.3$ kcal mol^{-1}; Table 4.2). The EDA-NOCV data in Tables 4.2 and 4.3 show that the stronger bonding in $(N^+)(PPh_3)_2$ comes mainly from the significantly larger donation in Ph_3P→(N^+)←PPh_3 compared with Ph_3P→C←PPh_3, which overcompensates for the weaker electrostatic attraction and Ph_3P←(N^+)→PPh_3 π backdonation, as well as the higher preparation energy for $C(PPh_3)_2$. The theoretically predicted BDE of $D_e = 363.5$ kcal mol^{-1} suggests that the nitrogen–phosphorus bonds are very strong, in line with the experimental abundance of this compound.

Table 4.3 gives also the EDA-NOCV data for $(BH)(PPh_3)_2$ [21]. The B–H bond in the borylene complex takes the position of the carbon σ lone-pair of $C(PPh_3)_2$, whereas the π lone-pair of the BH moiety must be excited from the σ position in the $X^1\Sigma^+$ ground state of BH. The excitation energy $X^1\Sigma^+ \rightarrow {}^1\Delta$ is

Table 4.3 Energy decomposition analysis at BP86/TZ2P+//BP86/SVP of the donor-acceptor interactions in $(N^+)(PPh_3)_2$ and $(BH)(NHC^{Me})_2$. All values in kcal mol^{-1}.

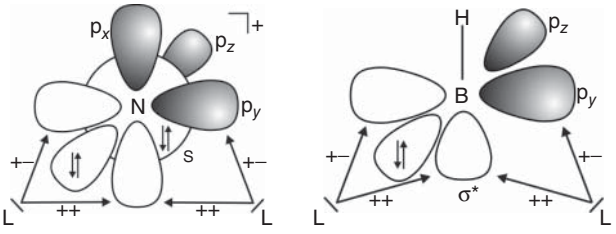

N^+: $X^3P \rightarrow {}^1D$ 63.9 kcal mol^{-1} (BP86/TZ2P+)
BH: $X^1\Sigma^+ \rightarrow {}^1\Delta$ 128.4 kcal mol^{-1} (BP86/TZ2P+)

Compound	**$[N(PPh_3)_2]^+$**	**$(BH)(PPh_3)_2$**
Interacting fragments	**N^+ (^1D) $(PPh_3)_2$**	**(BH) ($^1\Delta$) $(PPh_3)_2$**
ΔE_{int}	−447.1	−223.6
ΔE_{Pauli}	724.8	229.7
ΔE_{elstat} [a]	−219.3 (18.7%)	−154.8 (34.1%)
ΔE_{orb} [a]	−952.6 (81.3%)	−298.6 (65.9%)
ΔE_{σ} L→E←L (+,+) donation [b]	−503.6 (52.9%)	−123.9 (41.5%)
$\Delta E_{\pi\parallel}$ L→E←L (+,−) donation [b]	−392.6 (41.2%)	−90.4 (30.3%)
$\Delta E_{\pi^\perp}$ L←E→L π backdonation [b]	−23.9 (2.5%)	−78.0 (26.1%)
ΔE_{rest} [b]	−32.5 (3.4%)	−6.3 (2.1%)
ΔE_{prep}	83.6	139.0
D_e	363.5	84.6

[a] The values in parentheses give the percentage contribution to the total attractive interactions $\Delta E_{elstat} + \Delta E_{orb}$.
[b] The values in parentheses give the percentage contribution to the orbital interactions ΔE_{orb}.

very high (128.4 kcal mol^{-1}), which makes the formation of borylene complexes $(BH)L_2$ thermodynamically difficult. Table 4.3 shows that the interaction energy in $(BH)(PPh_3)_2$ ($\Delta E_{int} = -223.6$ kcal mol^{-1}) is actually higher than in $C(PPh_3)_2$ (see Table 4.2), but the preparation energy of the borylene complex is quite large ($\Delta E_{prep} = 142.0$ kcal mol^{-1}), which comes mainly from the electronic excitation energy of BH. The BDE of $(BH)(PPh_3)_2$ ($D_e = 84.6$ kcal mol^{-1}) is, therefore, much smaller than for carbodiphosphorane. Note that the $Ph_3P\leftarrow(BH)\rightarrow PPh_3$ π back-donation is significantly stronger ($\Delta E_{\pi^\perp} = -78.0$ kcal mol^{-1}) than in $C(PPh_3)_2$ and $(N^+)(PPh_3)_2$, because the π lone-pair orbital of boron is a better donor than those of carbon and N^+.

Table 4.4 gives the EDA-NOCV results of further nitrogen cation complexes $(N^+)L_2$ with $L = N_2$, CO, NHC^{Me} and the cyclic alkyl amino carbene (CAAC) which

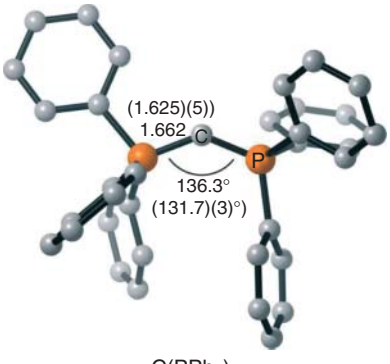

(a) $C(PPh_3)_2$

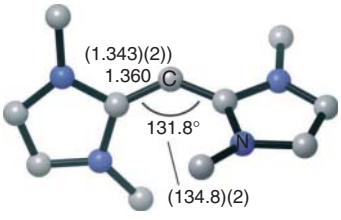

(b) $C(NHC^{Me})_2$

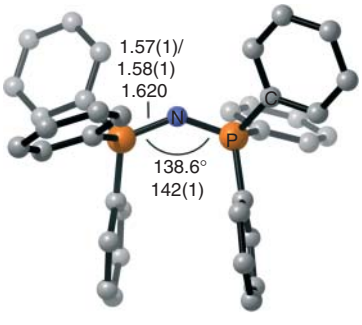

(c) $(N^+)(PPh_3)_2$

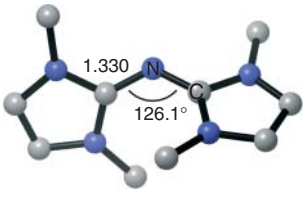

(d) $(N^+)(NHC^{Me})_2$

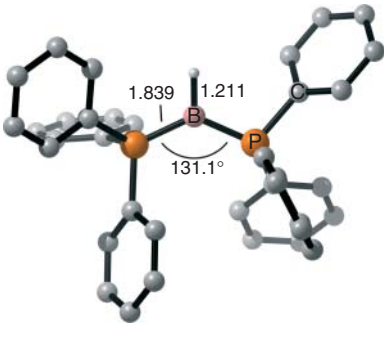

(e) $(BH)(PPh_3)_2$

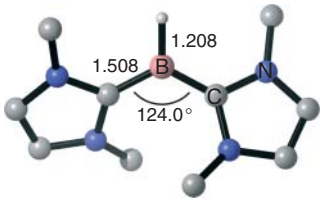

(f) $(BH)(NHC^{Me})_2$

Figure 4.8 Calculated geometries (BP86/def2-TZVPP) of the carbones CL_2 and isoelectronic nitrogen cation complexes $(N^+)L_2$ and borylene complexes $(BH)L_2$ with L = PPh_3, NHC^{Me}, N_2, CO, CAAC. Bond lengths in Å, angles in degree. Experimental values are given in parentheses. The experimental values for $C(NHC^{Me})_2$ refer to the benzoannelated homologue. (a) $C(PPh_3)_2$, (b) $C(NHC^{Me})_2$, (c) $(N^+)(PPh_3)_2$, (d) $(N^+)(NHC^{Me})_2$, (e) $(BH)(PPh_3)_2$, (f) $(BH)(NHC^{Me})_2$, (f) $(N^+)(N_2)_2$, (h) $(BH)(N_2)_2$, (i) $(N^+)(CO)_2$, (j) $(BH)(CO)_2$, (k) $(N^+)(CAAC)_2$, (l) $(BH)(CAAC)_2$. (All data are taken from Ref. [21].)

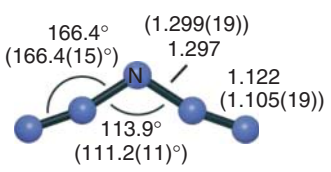

(g) $(N^+)(N_2)_2$

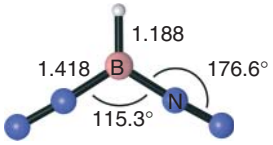

(h) $(BH)(N_2)_2$

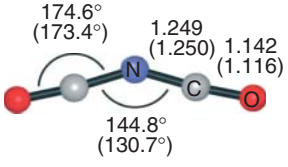

(i) $(N^+)(CO)_2$

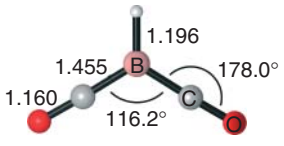

(j) $(BH)(CO)_2$

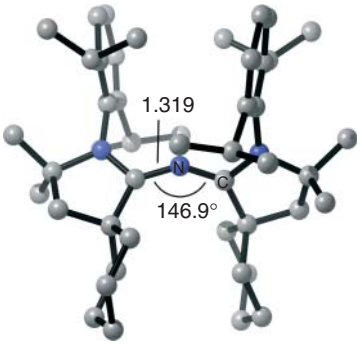

(k) $(N^+)(CAAC)_2$

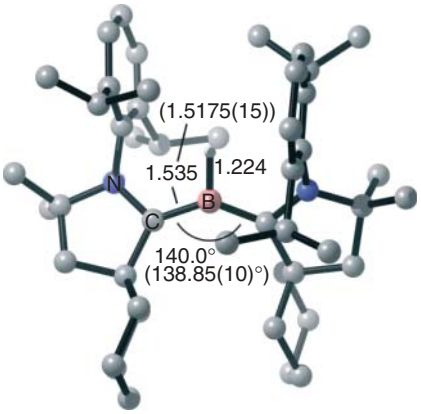

(l) $(BH)(CAAC)_2$

Figure 4.8 (*Continued*)

was synthesized by Bertrand [33]. The CAAC ligand is derived from NHC but has only one nitrogen atom in the five-membered ring, and a spiro carbon atom replaces the second nitrogen atom. Figure 4.8 shows the optimized geometries of the complexes $(N^+)L_2$.

The EDA-NOCV results suggest that the strength of the bonding interactions $L{\rightarrow}(N^+){\leftarrow}L$, which is given by ΔE_{int}, increases for L with the order $N_2 < CO < PPh_3 < NHC^{Me} < CAAC$. Note that the trend of the ΔE_{int} values does not fully agree with the trend of the orbital interactions. The orbital term for L = CO, for example, is larger ($\Delta E_{orb} = -1129.7\,kcal\,mol^{-1}$) than for $L = PPh_3$ ($\Delta E_{orb} = -952.6\,kcal\,mol^{-1}$) and for $L = NHC^{Me}$ ($\Delta E_{orb} = -1039.9\,kcal\,mol^{-1}$), although the overall attraction in the carbonyl complex is weaker. It shows that orbital interactions are not

Table 4.4 Energy decomposition analysis at BP86/TZ2P+//BP86/SVP with the EDA-NOCV method of the donor-acceptor interactions in $(N^+)L_2$ with L = PPh_3, CO, NHC^{Me} and CAAC [21]. All values in kcal mol^{-1}.

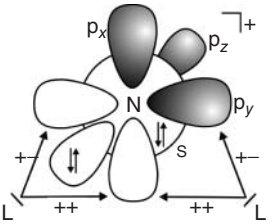

$X^3P \rightarrow {}^1D$ 43.5 kcal mol^{-1} (exper.: 29.1 kcal mol^{-1})

Ligand L	**N_2**	**CO**	**NHC^{Me}**	**CAAC**
Interacting fragments	**N^+ (^1D) $(N_2)_2$**	**N^+ (^1D) $(CO)_2$**	**N^+ (^1D) $(NHC^{Me})_2$**	**N^+ (^1D) $(CAAC)_2$**
ΔE_{int}	−226.5	−353.3	−509.6	−538.3
ΔE_{Pauli}	709.3	1007.6	881.1	965.5
ΔE_{elstat} [a]	−171.0 (18.3%)	−231.1 (17.0%)	−350.8 (25.2%)	−370.1 (24.6%)
ΔE_{orb} [a]	−764.9 (81.7%)	−1129.7 (83.0%)	−1039.9 (74.8%)	−1133.7 (75.4%)
ΔE_σ L→(N^+)←L (+,+) donation [b]	−412.0 (53.9%)	−655.4 (58.0%)	−598.4 (57.5%)	−653.9 (57.7%)
$\Delta E_{\pi\parallel}$ L→(N^+)←L (+,−) donation [b]	−282.4 (36.9%)	−397.9 (35.2%)	−361.2 (34.7%)	−335.5 (29.6%)
$\Delta E_{\pi^\perp}$ L←(N^+)→L π backdonation [b]	−46.7 (6.1%)	−58.7 (5.2%)	−39.1 (3.8%)	−109.0 (9.6%)
ΔE_{rest} [b]	−23.8 (3.1%)	−17.7 (1.6%)	−41.2 (4.0%)	−35.3 (3.1%)
ΔE_{prep}	85.9	83.7	116.5	133.9
D_e	140.6	269.6	393.1	404.4

[a] The values in parentheses give the percentage contribution to the total attractive interactions $\Delta E_{elstat} + \Delta E_{orb}$.
[b] The values in parentheses give the percentage contribution to the orbital interactions ΔE_{orb}.

always a faithful probe for the trend of bonding interactions! Other factors, such as the electrostatic attraction and Pauli repulsion, may change the order of the total interactions of a chemical bond. This is an important result, because changes in covalent bonding are often explained only in terms of orbital interactions. Note that the CAAC←(N^+)→CAAC π backdonation is significantly stronger ($\Delta E_{\pi^\perp} = -109.0$ kcal mol^{-1}) than for the other ligands L. This means that the CAAC ligand may serve as a much more powerful π acceptor than NHC^{Me}, CO and N_2. The BDEs D_e exhibit the same order (N_2 < CO < PPh_3 < NHC^{Me} < CAAC) for L as for the interaction energies ΔE_{int}. Since the weakest bonded complexes $(N^+)L_2$ with L = N_2, CO, PPh_3 could become isolated, it should be possible to synthesize the analogous adducts with L = NHC^{Me} and CAAC as well [34].

Table 4.5 Energy decomposition analysis at BP86/TZ2P+//BP86/SVP with the EDA-NOCV method of the donor-acceptor interactions in $(BH)L_2$ with $L = PPh_3$, CO, NHC^{Me} and CAAC [21]. All values in kcal mol^{-1}

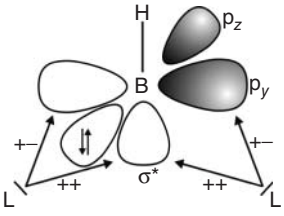

$X^1\Sigma^+ \rightarrow {}^1\Delta$ 128.4 kcal mol^{-1} (exper.: 131.5 kcal mol^{-1})

Ligand L	**N_2**	**CO**	**NHC^{Me}**	**CAAC**
Interacting fragments	**(BH) ($^1\Delta$) $(N_2)_2$**	**(BH) ($^1\Delta$) $(CO)_2$**	**(BH) ($^1\Delta$) $(NHC^{Me})_2$**	**(BH) ($^1\Delta$) $(CAAC)_2$**
ΔE_{int}	−209.4	−262.8	−314.4	−333.9
ΔE_{Pauli}	239.7	219.3	279.0	303.8
ΔE_{elstat} [a]	−103.9 (23.2%)	−121.5 (25.2%)	−224.0 (37.8%)	−231.3 (36.3%)
ΔE_{orb} [a]	−345.1 (76.8%)	−360.5 (74.8%)	−369.3 (62.2%)	−406.4 (63.7%)
ΔE_σ L→(BH)←L (+,+) donation [b]	−118.2 (34.2%)	−130.9 (36.3%)	−140.5 (38.0%)	−136.8 (33.7%)
$\Delta E_{\pi\parallel}$ L→(BH)←L (+,−) donation [b]	−90.8 (26.3%)	−104.0 (28.9%)	−102.4 (27.7%)	−110.1 (27.1%)
$\Delta E_{\pi^\perp}$ L←(BH)→L π backdonation [b]	−127.7 (37.0%)	−122.1 (33.8%)	−108.2 (29.3%)	−149.5 (36.8%)
ΔE_{rest} [b]	−8.4 (2.5%)	−3.5 (1.0%)	−18.2 (5.0%)	−10.0 (2.5%)
ΔE_{prep}	141.6	140.8	166.6	176.0
D_e	67.8	122.0	147.8	157.9

[a] The values in parentheses give the percentage contribution to the total attractive interactions $\Delta E_{elstat} + \Delta E_{orb}$.
[b] The values in parentheses give the percentage contribution to the orbital interactions ΔE_{orb}.

Table 4.5 shows the analogous borylene complexes $(BH)L_2$ with $L = N_2$, CO, NHC^{Me} and CAAC. The calculated geometries are displayed in Figure 4.8. The EDA-NOCV data contain a wealth of information that will only be discussed in the light of the donor–acceptor bonding model. The trend for the strength of the binding interactions ΔE_{int} exhibits the order $N_2 < PPh_3 < CO < NHC^{Me} < CAAC$, which is slightly different from that of $(N^+)L_2$. The carbonyl complex $(BH)(CO)_2$ is more strongly bonded than $(BH)(PPh_3)_2$, whereas the reversed order is calculated for the $(N^+)L_2$ compounds. Inspection of the EDA-NOCV data in Tables 4.3 and 4.5 reveals that the orbital interactions are mainly responsible for the stronger bonding in $(BH)(CO)_2$ than in $(BH)(PPh_3)_2$, which, in turn, comes from the significantly stronger L←(BH)→L π backdonation for L = CO than for $L = PPh_3$. Table 4.5 shows that L←(BH)→L π backdonation is very strong in the complexes investigated, which

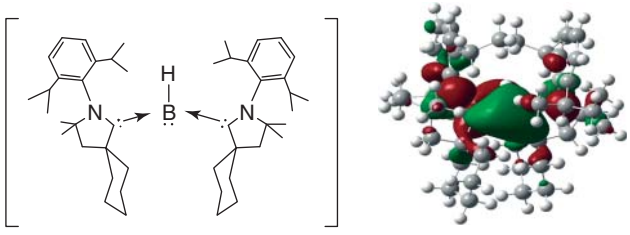

(a) (b)

Figure 4.9 (a) Schematic representation of the donor-acceptor bonds in $(BH)(CAAC)_2$. (b) Plot of the HOMO of $(BH)(CAAC)_2$. (Reproduced from Ref. [35].)

agrees with chemical intuition. It is the most important contribution to the total interactions for the borylene complexes with $L = N_2$ and CAAC. In general, the three types of orbital interactions, that is, (+,+) σ donation, (+,−) σ donation, and π backdonation, have a similar magnitude and are all important for the donor–acceptor interactions in $(BH)L_2$.

The EDA-NOCV results for $(BH)(PPh_3)_2$ and $(BH)(NHC^{Me})_2$ suggest that BH ($^1\Delta$) is an intrinsically stronger Lewis acid than C (^{1}D), because the ΔE_{int} values in the borylene complexes are larger than in the carbones (Tables 4.2 and 4.5). Nonetheless, the $(BH)L_2$ species require a much higher excitation energy for the BH fragment than carbon and, thus, the BDE of the borylene complexes are smaller than those of CL_2. However, the strongest bonded borylene complexes, $(BH)(NHC^{Me})_2$ and $(BH)(CAAC)_2$, possess theoretically predicted BDEs of $D_e = 147.8$ kcal mol^{-1} and $D_e = 157.9$ kcal mol^{-1}, which are even higher than for the parent carbone $C(PPh_3)_2$ ($D_e = 128.6$). The calculated data suggest that $(BH)L_2$ complexes with N-heterocyclic ligands might be stable under normal laboratory conditions. This finding was confirmed by the synthesis and X-ray structure analysis of the complex $(BH)(CAAC)_2$, which is shown in Figure 4.8l [35]. It is the first compound in which a tricoordinated boron atom carries a π electron pair, which makes it isostructural to an amine. The bonding analysis supports the classification of $(BH)(CAAC)_2$ as a borylene ligand that is isoelectronic to the yet unknown carbone $C(CAAC)_2$. Figure 4.9a sketches the donor–acceptor interactions in $(BH)(CAAC)_2$ and Figure 4.9b shows the HOMO of the molecule. It is easily identified as a boron lone-pair MO which donates some electronic charge of the formally vacant carbon p(π) acceptor orbitals. The strength of the latter interactions can be estimated from the EDA-NOCV results that are given in Table 4.5.

4.2.3
Donor–Acceptor Bonding in Heavier Tetrylenes ER_2 and Tetrylones EL_2 (E = Si – Pb)

The relevance of the donor–acceptor bonding model as a distinctively different binding mode from electron-sharing bonding (Figure 4.1a,b) for heavier group 14 compounds becomes evident by comparing the compounds in which $SiCl_2$ is bonded to the carbenes NHC and CAAC. Figure 4.10a shows the optimized

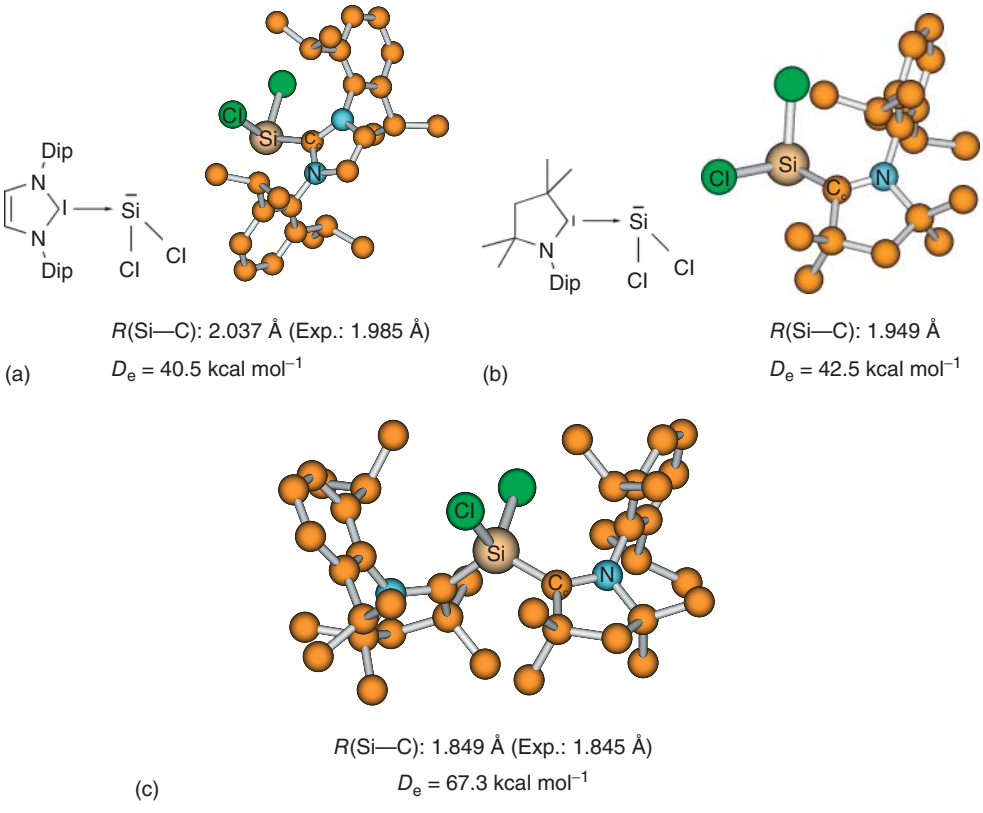

Figure 4.10 (a) Calculated structures (M05-2X/SVP) of (a) $CAAC^{Dip}\rightarrow SiCl_2$; (b) $NHC^{Dip}\rightarrow SiCl_2$; (c) $Cl_2Si(CAAC^{Dip})_2$. The bond dissociation energies D_e of the Cl_2Si-L_n bonds were calculated at M05-2X/def2-TZVPP//M05-2X/SVP. (The data are taken from Refs [36, 38].)

geometry of the complex $NHC^{Dip}\rightarrow SiCl_2$ (Dip = 2,6-iPr$_2$C$_6$H$_3$), which carries bulky aryl groups at nitrogen. The molecule has been synthesized and structurally characterized. The x-ray analysis gave a Si–C bond length of 1.985 Å, which is slightly shorter than the calculated value of 2.037 Å [36, 37].

The complex $NHC^{Dip}\rightarrow SiCl_2$ was reacted with the $CAAC^{Dip}$ ligand with the goal of synthesizing the related complex $CAAC^{Dip}\rightarrow SiCl_2$. Calculations predict that the latter adduct (Figure 4.10b) should have a slightly shorter (1.949 Å) and stronger (D_e = 42.5 kcal/mol) Si–C bond than $NHC^{Dip}\rightarrow SiCl_2$, which has a BDE of D_e = 40.5 kcal mol^{-1}. The CAAC ligand has only one nitrogen atom in the ring and, thus, the carbene carbon atom of the CAAC ligand is a better π-acceptor, which, consequently, binds stronger than the NHC ligand. This explains the shorter and stronger bond in $CAAC^{Dip}\rightarrow SiCl_2$ than in $NHC^{Dip}\rightarrow SiCl_2$. However, the reaction gives a totally different product. Instead of binding *one* $CAAC^{Dip}$ ligand, the $SiCl_2$

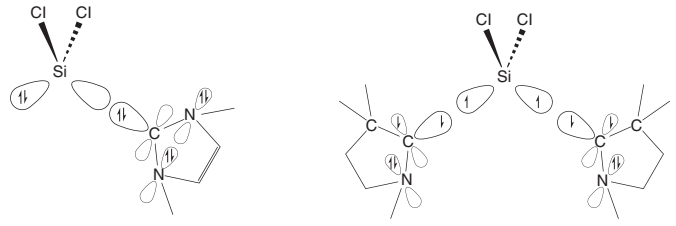

(a) (b)

D_e = 40.5 kcal mol^{-1}

NHC^{Dip} = 88.9 kcal mol^{-1}

D_e = 67.3 kcal mol^{-1}

ΔE(S/T):

$SiCl_2$ = 60.1 kcal mol^{-1}

$CAAC^{Dip}$ = 49.9 kcal mol^{-1}

D_e(T) = 227.2 kcal mol^{-1}

ΔE = 227.5 kcal mol^{-1} - 60.1 kcal mol^{-1} $-2 \times$ 49.9 kcal mol^{-1} = 67.3 kcal mol^{-1}

Figure 4.11 Schematic representation of (a) the donor-acceptor bonding in $NHC^{Dip} \rightarrow SiCl_2$ and (b) electron-sharing bonding in $Cl_2Si(CAAC^{Dip})_2$. The energies were calculated at the M05-2X/def2-TZVPP//M05-2X/SVP level of theory. (The data are taken from Ref. [38].)

species binds *two* ligands in the compound $Cl_2Si(CAAC^{Dip})_2$ [38]. However, there is only one vacant valence orbital in $SiCl_2$!

This surprising experimental finding can be explained by a change in the nature of the silicon–carbon bonding in $Cl_2Si(CAAC^{Dip})_2$. Figure 4.10c shows that the Si–C bonds in the latter compound are much shorter than in the complex $CAAC^{Dip} \rightarrow SiCl_2$, which suggests that the silicon–carbon bonding in $Cl_2Si(CAAC^{Dip})_2$ comes from electron-sharing interactions rather than donor–acceptor interactions. This is schematically shown in Figure 4.11. The formation of two electron-sharing Si–C bonds is possible when the fragments $SiCl_2$ and $CAAC^{Dip}$ formally bind through their excited triplet states rather than the singlet ground states. Figure 4.11b shows that the qualitative bonding model leads to two unpaired electrons at the $CAAC^{Dip}$ ligands that, according to Hund's rule, should yield a triplet state for $Cl_2Si(CAAC^{Dip})_2$. This is indeed the case. Electron paramagnetic resonance (EPR) measurements of the latter compound reveal that it has a triplet ground state [38].

The binding of two $CAAC^{Dip}$ ligands in $Cl_2Si(CAAC^{Dip})_2$ while only one NHC^{Dip} ligand is bonded in $Cl_2Si(NHC^{Dip})$ can be explained when the calculated bond strengths and the singlet-triplet (S/T) gaps are considered. Figure 4.11 shows that the calculated BDE for two ligands of $Cl_2Si(CAAC^{Dip})_2$ is $D_e = 67.3$ kcal mol^{-1}, which is higher than the BDE of $CAAC^{Dip} \rightarrow SiCl_2$ ($D_e = 42.5$ kcal mol^{-1}). The formation of two C–Si electron-sharing bonds is energetically favorable compared with the creation of one C→Si donor–acceptor bond although the former interaction

Table 4.6 Proposed nomenclature for divalent E(0) compounds.

E	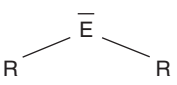 **Divalent E(II): ylidene**	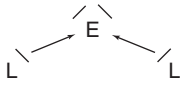 **Divalent E(0): ylidone**
C	Carbene	Carbone
Si	Silylene	Silylone
Ge	Germylene	Germylone
Sn	Stannylene	Stannylone
Pb	Plumbylene	Plumbylone

requires electronic excitation of the fragments. The interaction energy between the triplet fragments ($\Delta E = 227.5\,\text{kcal mol}^{-1}$) compensates for the S/T gap of $SiCl_2$ ($60.1\,\text{kcal mol}^{-1}$) and the $CAAC^{Dip}$ ligands ($2 \times 49.9\,\text{kcal mol}^{-1}$). This is not the case for the hypothetical molecule $Cl_2Si(NHC^{Dip})_2$. The S/T gap of the NHC^{Dip} ligand is much higher ($88.9\,\text{kcal mol}^{-1}$) than for $CAAC^{Dip}$, which makes the compound $Cl_2Si(NHC^{Dip})_2$ thermodynamically unstable.

Investigations on donor–acceptor complexes of heavier group 14 homologues of carbones are at an early stage, but there is experimental evidence that compounds EL_2 (E = Si – Pb), which exhibit a similar bonding situation L→E←L to carbones, are not only energy minima, but may also exist as stable compounds. The generic name ''tetrylone'' has been suggested for compounds EL_2, which carry two lone-pair orbitals at atom E (Table 4.6) [39]. Figure 4.12 shows the shape and eigenvalues of the two energetically highest lying occupied orbitals of the carbodiphosphorane analogues $E(PPh_3)_2$. It becomes obvious that the HOMO of all compounds is a π-type lone-pair orbital with some backbonding to the phosphorous orbitals. The HOMO-1 is a σ-type lone-pair MO where the backside lobe at atom E extends in a bonding fashion with the phosphorous atoms. Note that the HOMO of the compounds becomes energetically higher lying for heavier atoms E, while the HOMO-1 exhibits a reverse trend. The σ-type lone-pair MO is lower in energy for the heavier group 14 atoms, which comes from the increasing participation of the ligand orbitals. The double lone-pair character of $E(PPh_3)_2$ is supported by the calculated first and second PAs, which are given in Table 4.7 [40]. The first PAs but particularly the second PAs of $E(PPh_3)_2$ are significantly larger than those of the NHC homologues NHE (E=Si–Pb) which are also shown. Note that the values in Table 4.7 were calculated at a different theoretical level than the PAs of the compounds that are shown in Table 4.1. This is the reason that the data for the carbon compounds in the two tables differ slightly.

Table 4.7 gives also the first and second PAs of the NHC complexes $E(NHC)_2$ [40]. The second PAs of the latter tetrylones are somewhat smaller than those of $E(PPh_3)_2$ but they are clearly larger than the values for the tetrylenes NHE.

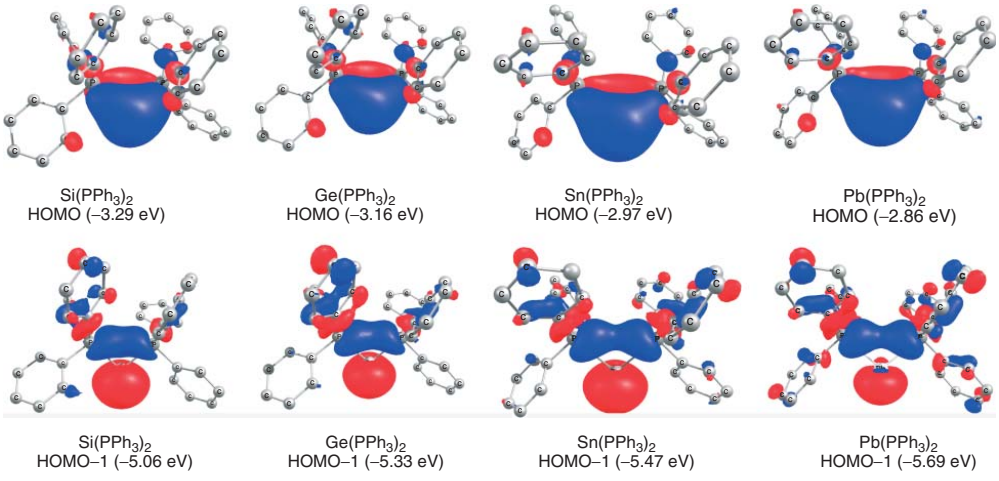

Figure 4.12 Plot of the HOMO and HOMO-1 of $E(PPh_3)_2$ (E = Si – Pb). Eigenvalues of the orbitals at BP86/def2-TZVPP. (Data are taken from Ref. [40].)

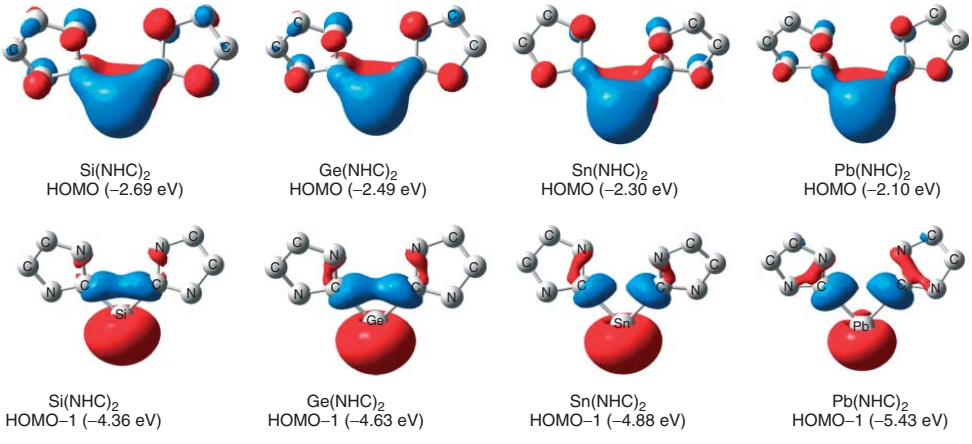

Figure 4.13 Plot of the HOMO and HOMO-1 of $E(NHC)_2$ (E = Si–Pb). Eigenvalues of the orbitals at BP86/def2-TZVPP. (Data are taken from Ref. [41a,b].)

Table 4.7 Calculated first and second proton affinities at BP86/def2-TZVPP for $E(PPh_3)_2$, $E(NHC)_2$ and NHE in kcal mol^{-1} [40].

	$E(PPh_3)_2$		$E(NHC)_2$		NHE	
E	**1. PA**	**2. PA**	**1. PA**	**2. PA**	**1. PA**	**2. PA**
C	280.1	188.3	289.2	148.4	253.0	51.7
Si	279.4	186.0	275.9	166.7	208.0	82.2
Ge	276.0	174.8	275.7	154.0	199.6	82.3
Sn	272.2	164.0	277.9	141.5	201.8	80.6
Pb	270.7	147.1	273.8	114.9	205.7	66.8

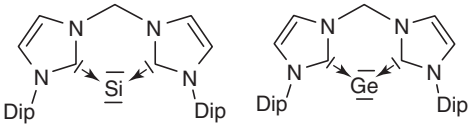

Figure 4.14 Schematic representation of the isolated silylone and germylone $E(NHC^{Dip}\text{-}NHC^{Dip})$.

Figure 4.13 shows the two energetically highest lying occupied MOs of the tetrylones $E(NHC)_2$ [39, 41]. The shape of the orbitals clearly identifies them as π-type (HOMO) and σ-type (HOMO-1) lone-pair orbitals. Divalent E(0) complexes with carbene ligands were the first examples of stable tetrylones that were isolated and structurally characterized by x-ray analysis. The first silylone SiL_2 that could be synthesized was the siladicarbene $Si(CAAC^{Dip})_2$, which was prepared by reduction of the compound $Cl_2Si(CAAC^{Dip})_2$ mentioned above [42]. Another siladicarbene $Si(NHC^{Dip}\text{-}NHC^{Dip})$, where the two NHC^{Dip} ligands are bridged via a methylene group (Figure 4.14), was recently synthesized [43], which was quickly followed by the isolation of the analogous germadicarbene $Ge(NHC^{Dip}\text{-}NHC^{Dip})$ [43b]. The donor–acceptor bonding model is not only helpful for the interpretation of the structure of known molecules, but also serves as a useful guideline for finding new compounds with unusual bonds.

4.3 Two-Center Complexes E_2L_2

In 2008, Robinson and coworkers reported on the serendipitous synthesis of the disilicon compound $Si_2(NHC^{Dipp})_2$ (Dipp = diisopropylphenyl), which was obtained when $SiCl_4$ was reacted with NHC^{Dipp} [44]. The authors also presented the results of quantum chemical calculations which suggested that the bonding situation in the molecule can be understood in terms of $(NHC^{Dipp})\rightarrow SiSi\leftarrow(NHC^{Dipp})$ donor–acceptor interactions. In the following years, numerous analogues of the

Robinson compound with the general formula L→EE←L (with E being atoms of groups 13 – 15 and L being a σ donor ligand) were isolated [45]. It opened an exciting area of low-valent main group chemistry, which continues to thrive [46]. In the following pages, we will show that the two-center complexes L→EE←L are related to the one-center complexes L→E←L, which exhibit particular bonding situations that can be understood in the light of modern methods of bonding analysis. Similar to the cases of one-center complexes EL_2, new two-center complexes E_2L_2 could become isolated after calculations showed that they are viable targets for synthetic efforts. We will only discuss the group 14 complexes Si_2L_2 – Pb_2L_2 and the first octal-row group 13, and group 15 species B_2L_2 and N_2L_2 with the ligand NHC^{Me}, as well as the phosphine complex $N_2(PPh_3)_2$, because these examples are sufficient to demonstrate the usefulness of the bonding model and the theoretical methods which are employed to analyze the electronic structure.

4.3.1
Two-Center Group 14 Complexes Si_2L_2 – Pb_2L_2 (L = NHC)

Figure 4.15 shows the calculated equilibrium geometries of the group 14 complexes $Si_2(NHC^{Me})_2$–$Pb_2(NHC^{Me})_2$ [47]. The theoretical bond lengths and angles of the molecules agree quite well with the experimental values of the complexes $Si_2(NHC^{Dipp})_2$–$Sn_2(NHC^{Dipp})_2$. The lead complex $Pb_2(NHC^{R})_2$ has not yet been synthesized.

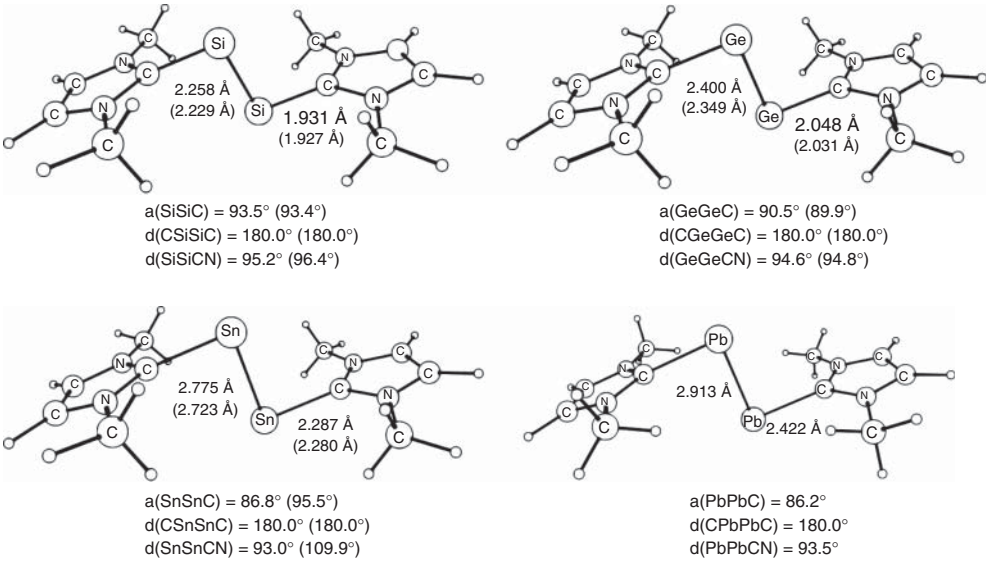

Figure 4.15 Calculated structures (BP86/def2-TZVPP) of complexes $E_2(NHC^{Me})_2$ (E = Si–Pb). Experimental values of N-substituted homologues are shown in parentheses. (The calculated data are taken from Ref. [47], and the experimental values from Refs. [44, 45a,b].)

The geometries of group 14 complexes $E_2(NHC^{Me})_2$ possess a trans arrangement of the NHC^{Me} ligands at the E_2 moieties with rather acute bending angles N–E–E between 86 and 93°. As a starting point for a discussion of the E_2–L_2 bonding, we present in Figure 4.16 a qualitative view of the electron configurations of E_2 in the $X^3\Sigma_g^-$ triplet ground state and in the $^1\Delta_g$ excited singlet state, which is the electronic reference state for the complexes $E_2(NHC^{Me})_2$. Note that the electronic ground state of the first member in the series, C_2, is the $X^1\Sigma_g$ singlet state that has the valence electron configuration $1\sigma_g^2,1\sigma_u^2,1\pi_u^2,1\pi_u'^2$, where the $2\sigma_g$ orbital is vacant. The electron configuration and the associated bonding situation in the first octal-row diatomic molecules E_2 (E = Li – F) is discussed in the chapter "The EDA Perspective of Chemical Bonding" in volume 1 of this book. Compounds C_2L_2 are currently being investigated with theoretical and experimental methods [48]. It appears that they are borderline cases between donor–acceptor complexes and electron-sharing bonded species.

Figure 4.16 shows that the vacant $1\pi_u'$ and $1\pi_g'$ orbitals of the $^1\Delta_g$ excited state of E_2 may serve as acceptor orbitals for the lone-pair donor orbitals of the ligands lying in the same plane. The orbitals explain why the equilibrium geometries of the molecules have a trans-configuration. The $(NHC^{Dipp})\rightarrow EE\leftarrow(NHC^{Dipp})$ donation of the (+/–) combination of the donor orbitals involves the bonding $1\pi_{u'}$ MO, whereas the (+/+) combination donates electronic charge into the vacant $1\pi_g'$ orbital. Figure 4.16 shows that $X^3\Sigma_g^- \rightarrow {}^1\Delta_g$ excitation energy of E_2 is compensated by the donor–acceptor interactions, which make the complexes $E_2(NHC^{Me})_2$ thermodynamically stable with regard to dissociation. The calculated BDEs for the E_2-$(NHC^{Me})_2$ bonds show the order Si > Ge > Sn > Pb.

The donor–acceptor interaction in the complexes $E_2(NHC^{Me})_2$ can be quantitatively analyzed with the EDA-NOCV method. The numerical results are given in Table 4.8. The intrinsic interaction energies ΔE_{int} between $E_2(^1\Delta_g)$ and 2 NHC^{Me} show the same order as the BDEs Si > Ge > Sn > Pb. The EDA-NOCV calculations suggest that the E_2-$(NHC^{Me})_2$ bonds have a higher electrostatic than covalent character. This is given by the percentage values of ΔE_{elstat} and ΔE_{orb}. The largest contribution to the orbital interactions come from the $(NHC^{Me})\rightarrow EE\leftarrow(NHC^{Me})$ donation, which arises from the in-phase (+,+) and out-of-phase (+,–) combination of the donor orbitals of the ligands. The $(NHC^{Me})\leftarrow EE\rightarrow(NHC^{Me})$ backdonation of the (+/+) and (+/–) combinations of the in-plane orbitals (see Figure 4.17c, d for the notation) is much weaker. This is in agreement with the calculated charge distribution, which indicates that the fragments E_2 carry a negative partial charge (Table 4.8). Note that the assignment of σ and π symmetry is made with respect to the C–E–E–C plane. The change in the electronic structure which is associated with the orbital interactions in $E_2(NHC^{Me})_2$ is shown in Figure 4.17.

The first column in Figure 4.17 shows the deformation densities $\Delta\rho$, which are coupled to the donor–acceptor interactions between the most important pairs of occupied and vacant fragment orbitals that are given in the last two columns. The color coding for the charge flow of $\Delta\rho$ is red→blue. The plots of the density deformations and the orbitals come from the calculations of $Si_2(NHC^{Me})_2$. The

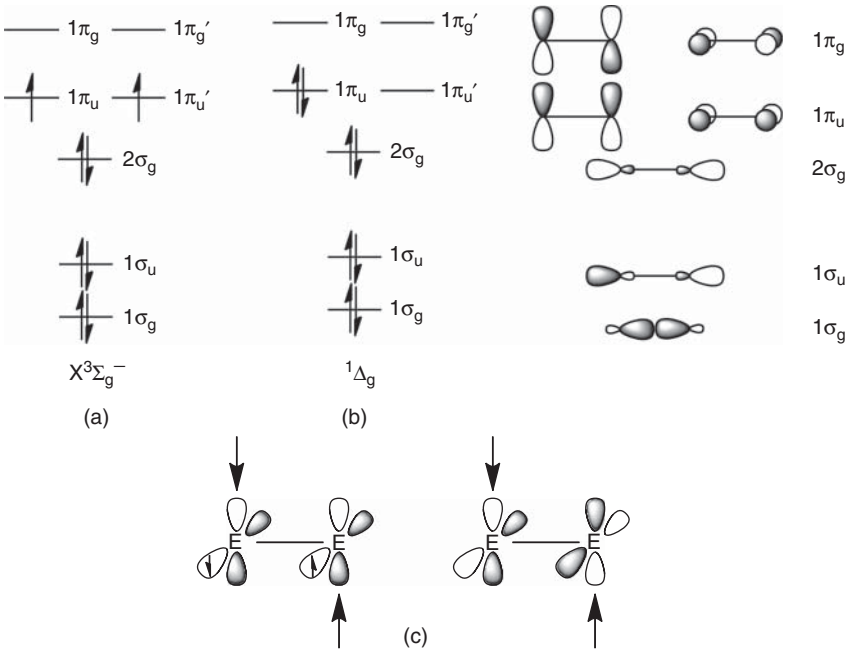

$Si_2[X^3\Sigma_g^-] \rightarrow Si_2[^1\Delta_g]$	= 19.7 kcal mol^{-1}
$Si_2(NHC^{Me})_2 \rightarrow Si_2[X^3\Sigma_g^-] + 2\ NHC^{Me}$	= 94.8 kcal mol^{-1}
$Ge_2[X^3\Sigma_g^-] \rightarrow Ge_2[^1\Delta_g]$	= 18.2 kcal mol^{-1}
$Ge_2(NHC^{Me})_2 \rightarrow Ge_2[X^3\Sigma_g^-] + 2\ NHC^{Me}$	= 78.4 kcal mol^{-1}
$Sn_2[X^3\Sigma_g^-] \rightarrow Sn_2[^1\Delta_g]$	= 15.5 kcal mol^{-1}
$Sn_2(NHC^{Me})_2 \rightarrow Sn_2[X^3\Sigma_g^-] + 2\ NHC^{Me}$	= 61.5 kcal mol^{-1}
$Pb_2[X^3\Sigma_g^-] \rightarrow Pb_2[^1\Delta_g]$	= 14.5 kcal mol^{-1}
$Pb_2(NHC^{Me})_2 \rightarrow Pb_2[X^3\Sigma_g^-] + 2\ NHC^{Me}$	= 51.6 kcal mol^{-1}

(d)

Figure 4.16 Qualitative sketch of the valence MOs of diatomic main-group molecules E_2 (E = Si – Pb). Orbital occupation in the (a) $X^3\Sigma_g^-$ ground state and (b) excited $^1\Delta_g$ state. (c) Schematic representation of the L→EE←L donation from the (+,–) combination of the donor orbitals into the bonding $1\pi_u$' MO and from the (+,+) combination of the donor orbitals into the antibonding $1\pi_g$' MO. (d) Calculated energies of the $X^3\Sigma_g^- \rightarrow {}^1\Delta_g$ excitation energies and bond dissociation energies of $E_2(NHC^{Me})_2$ at BP86/def2-TZVPP.

Table 4.8 Energy decomposition analysis with the EDA-NOCV method at BP86/TZ2P+ of the donor-acceptor interactions in the group 14 complexes $E_2(NHC^{Me})_2$ (E = Si – Pb). NBO partial charges at the E_2 moiety $q(E_2)$. Energy values in kcal mol^{-1} and charges in e.

	$E_2(NHC^{Me})_2$			
Interacting fragments	**E = Si** $Si_2[^1\Delta_g](NHC^{Me})_2$	**E = Ge** $Ge_2[^1\Delta_g](NHC^{Me})_2$	**E = Sn** $Sn_2[^1\Delta_g](NHC^{Me})_2$	**E = Pb** $Pb_2[^1\Delta_g](NHC^{Me})_2$
ΔE_{int}	−120.0	−101.1	−84.1	−70.1
ΔE_{Pauli}	364.7	317.3	251.3	206.1
ΔE_{elstat} [a]	−267.1 (55.1%)	−247.9 (59.2%)	−213.6 (63.7%)	−178.8 (64.8%)
ΔE_{orb} [a]	−217.6 (44.9%)	−170.6 (40.8%)	−121.9 (36.3%)	−97.3 (35.2%)
$\Delta E_{\sigma 1}$ L→(E_2)←L (+,+) donation [b]	−66.6 (30.6%)	−49.1 (28.8%)	−26.4 (21.7%)	−23.2 (23.8%)
$\Delta E_{\sigma 2}$ L→(E_2)←L (+,−) donation [b]	−85.5 (39.3%)	−69.2 (40.6%)	−48.3 (39.6%)	−38.6 (39.7%)
$\Delta E_{\sigma 3}$ L←(E_2)→L (+,+) backdonation [b]	−29.7 (13.7%)	−26.8 (15.7%)	−26.8 (22.0%)	−19.1 (19.6%)
$\Delta E_{\sigma 4}$ L←(E_2)→L (+,-) backdonation [b]	−10.7 (4.9%)	−9.3 (5.5%)	−7.0 (5.7%)	−7.8 (8.0%)
ΔE_{π} [b]	−12.0 (5.5%)	−6.1 (3.6%)	−4.2 (3.4%)	−1.9 (2.0%)
ΔE_{rest} [b]	−13.1 (6.0%)	−10.1 (5.9%)	−9.2 (7.5%)	−6.7 (6.9%)
$q(E_2)$	−0.28	−0.37	−0.35	−0.34

[a] The values in parentheses give the percentage contribution to the total attractive interactions $\Delta E_{elstat} + \Delta E_{orb}$.
[b] The values in parentheses give the percentage contribution to the orbital interactions ΔE_{orb}.

heavier systems exhibit similar shapes; therefore, we only give the numerical results here.

The strongest orbital interactions (Figure 4.17b) arise from the donation of the HOMO of the ligands $(NHC^{Me})_2$, which is the (+,−) combination of the lone-pair donor orbitals, into the bonding LUMO ($1\pi_u$') of E_2. The second strongest orbital interaction comes from the (+,+) combination of the donor orbital of $(NHC^{Me})_2$, which is the HOMO-1, into the antibonding LUMO+1 ($1\pi_g$') of E_2 (Figure 4.17a). The former interaction is stronger than the latter, because the acceptor orbitals of E_2 for the (+,−) σ donation are much lower in energy than those of the (+,+) σ donation. The quantitative EDA-NOCV results, which are given in Table 4.8 and Figure 4.17, are in agreement with the qualitative sketch of the orbital interactions shown in Figure 4.16. Note that the occupied orbitals of the complexes $E_2(NHC^{Me})_2$, which come mainly[1)] from the HOMO-LUMO interactions of the fragments, and which are shown in the second column of Figure 4.17b, are very low in energy. The classification of the resulting MOs of the complexes is between HOMO-8 (E = Sn) and HOMO-12 (E = Pb). The deformation densities $\Delta\rho_1$ and $\Delta\rho_2$ visualize the charge flow, which is associated with the orbital interactions HOMO→LUMO and HOMO-1→LUMO-1, respectively. It becomes obvious that $\Delta\rho_2$ leads to a

1) The orbitals of the complex are a mixture of several fragment MOs. Columns 3 and 4 show the most important pairs of orbitals which lead to the associated MO of the complex.

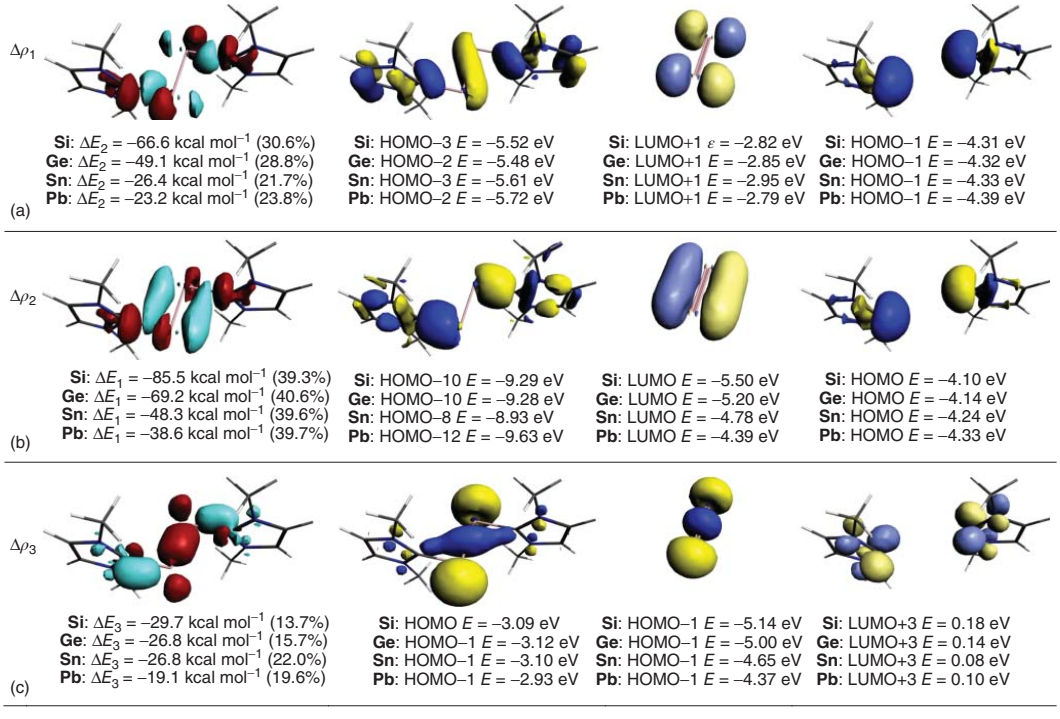

Figure 4.17 (a–e) Plot of the deformation densities $\Delta\rho$ of the pairwise orbital interactions between E_2 and $(NHC^{Me})_2$ in the complexes $E_2(NHC^{Me})_2$ (E = Si–Pb) and associated interaction energies ΔE. Shape of the most important interacting occupied and vacant orbitals of E_2 and $(NHC^{Me})_2$ which yield relevant occupied orbitals of $E_2(NHC^{Me})_2$.

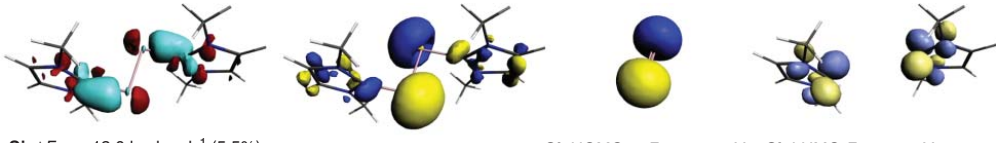

$\Delta\rho_4$

(d)

Si: ΔE_4 = –12.0 kcal mol^{-1} (5.5%)
Ge: ΔE_4 = –6.1 kcal mol^{-1} (3.6%)
Sn: ΔE_4 = –4.2 kcal mol^{-1} (3.4%)
Pb: ΔE_4 = –1.9 kcal mol^{-1} (2.0%)

Si: HOMO–2 E = –5.10 eV
Ge: HOMO–3 E = –5.53 eV
Sn: HOMO–2 E = –5.58 eV
Pb: HOMO–5 E = –6.23 eV

Si: HOMO–2 E = –9.17 eV
Ge: HOMO–2 E = –10.2 eV
Sn: HOMO–2 E = –9.35 eV
Pb: HOMO–2 E = –10.9 eV

Si: LUMO E = 0.05 eV
Ge: LUMO E = 0.07 eV
Sn: LUMO E = 0.06 eV
Pb: LUMO E = 0.14 eV

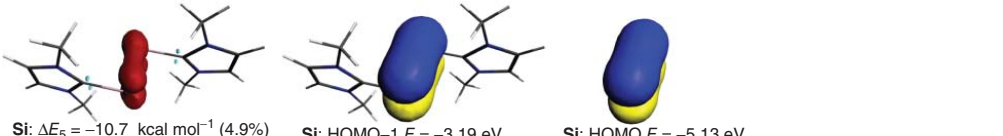

$\Delta\rho_5$

(e)

Si: ΔE_5 = –10.7 kcal mol^{-1} (4.9%)
Ge: ΔE_5 = –9.3 kcal mol^{-1} (5.5%)
Sn: ΔE_5 = –7.0 kcal mol^{-1} (5.7%)
Pb: ΔE_5 = –7.8 kcal mol^{-1} (8.0%)

Si: HOMO–1 E = –3.19 eV
Ge: HOMO E = –3.00 eV
Sn: HOMO E = –2.91 eV
Pb: HOMO E = –2.71 eV

Si: HOMO E = –5.13 eV
Ge: HOMO E = –4.82 eV
Sn: HOMO E = –4.41 eV
Pb: HOMO E = –4.05 eV

Figure 4.17 (*Continued*)

strengthening of the E–E π bond, while $\Delta\rho_1$ indicates a strengthening of the NHC–E bonds. Note, however, that there is no direct connection between the charge flow and the MOs that are shown in Figure 4.17. This is because the MOs come from the SCF calculations, whereas $\Delta\rho$ is given by the NOCV calculations.

Figure 4.17c and d also show the deformation densities $\Delta\rho_3$ and $\Delta\rho_4$, which are associated with the $(NHC^{Me})\leftarrow EE\rightarrow(NHC^{Me})$ σ backdonation. There are two in-plane orbital interactions that come from backdonation of the bonding HOMO-1 of E_2 into the (+,+) combination of the vacant ligand orbitals that possess local π symmetry ($\Delta\rho_3$). The second one arises from the backdonation of the antibonding HOMO-2 of E_2 into the (+,−) combination of the ligand orbitals ($\Delta\rho_4$). The charge flow $\Delta\rho_3$ signals a weakening of the E–E and strengthening of the NHC-E bonds, whereas $\Delta\rho_4$ indicates stronger NHC–E bonds.

The plot of the deformation density $\Delta\rho_5$ and the associated orbitals that refer to the out-of-plane π interactions are interesting. Figure 4.17e displays the π HOMO of $E_2(NHC^{Me})_2$ (HOMO-1 in case of $Si_2(NHC^{Me})_2$). It has essentially the same shape as the HOMO of the free ligand E_2, but the energy levels of the π orbitals in the complex are significantly raised. The small stabilization of 7.0 – 10.7 kcal mol^{-1} comes from the weak $L\leftarrow(E_2)\rightarrow L$ π backdonation, as indicated by the vanishingly small blue area of charge concentration at the ligand orbitals. Note that the NHC rings are perpendicular to the CEEC plane, which means that the $(NHC^{Me})\leftarrow EE\rightarrow(NHC^{Me})$ out-of-plane π backdonation is prevented by the structure of the molecule. The driving force for the rotation of the NHC rings from the CEEC plane can be identified with the charge flow that is associated with the density deformation $\Delta\rho_3$ (Figure 4.17c), which comes from a strong orbital interaction ($\Delta E_3 = -19.1$ to -29.7 kcal mol^{-1}) in the molecules. The shape of $\Delta\rho_3$ makes it obvious that the vacant π orbital of the NHC rings is involved in the interactions, which also explains why the EEC bond angle in the group 14 complexes $E_2(NHC^{Me})_2$ is very acute (Figure 4.15).

In the above section, we analyzed the bonding situation in the group 14 complexes $E_2(NHC^{Me})_2$, which serve as a model for the system E_2L_2. The extension to other ligands L is straightforward. The phosphine complexes $E_2(PMe_3)_2$ have also been studied and the results were compared with the data for $E_2(NHC^{Me})_2$, but they are not discussed here [47]. This work focuses on the general understanding of the nature of the bonding in E_2L_2 but it does not strive to discuss variations of the same theme.

4.3.2
Two-Center Group 13 and Group 15 Complexes B_2L_2 and N_2L_2

The structures and bonding situation of the group 13 homologues $B_2(NHC^{Me})_2$ - $Tl_2(NHC^{Me})_2$ and the group 15 complexes $N_2(NHC^{Me})_2$–$Bi_2(NHC^{Me})_2$ can be discussed in a similar way as the related group 14 complexes [49, 50]. The difference between the latter species and the former complexes is that the E_2 fragments have one occupied orbital less (group 13) or more (group 15) than the group 14 moieties. The extension of the donor–acceptor model from the group 14 complexes to the

homologues of groups 13 and 15 is mostly straightforward and shall therefore not be discussed in detail. However, the first octal-row adducts, $B_2(NHC^{Me})_2$ and $N_2(NHC^{Me})_2$, exhibit special features which deserve to be presented here. We also discuss the phosphine complex $N_2(PPh_3)_2$, which was already synthesized in 1964 by Appel and Schöllhorn [51], but the structure and bonding situation was not recognized at the time.

Figure 4.18 shows the calculated equilibrium geometry of the boron complex $B_2(NHC^{Me})_2$, which is in very good agreement with the experimental geometry of $B_2(NHC^{R})_2$, which carries bulky substituents R [45c]. Unlike the heavier complexes $E_2(NHC^{Me})_2$ (E = Al – In) that possess a similar trans-arrangement of the NHC^{Me} ligands as the group 14 adducts $Si_2(NHC^{Me})_2$–$Pb_2(NHC^{Me})_2$, the boron adduct has a linear coordination mode $(NHC^{Me})\rightarrow BB\leftarrow(NHC^{Me})$ with a very short boron–boron bond length of 1.470 Å. The linear arrangement of the boron species and the anti-periplanar coordination of the heavier group-13

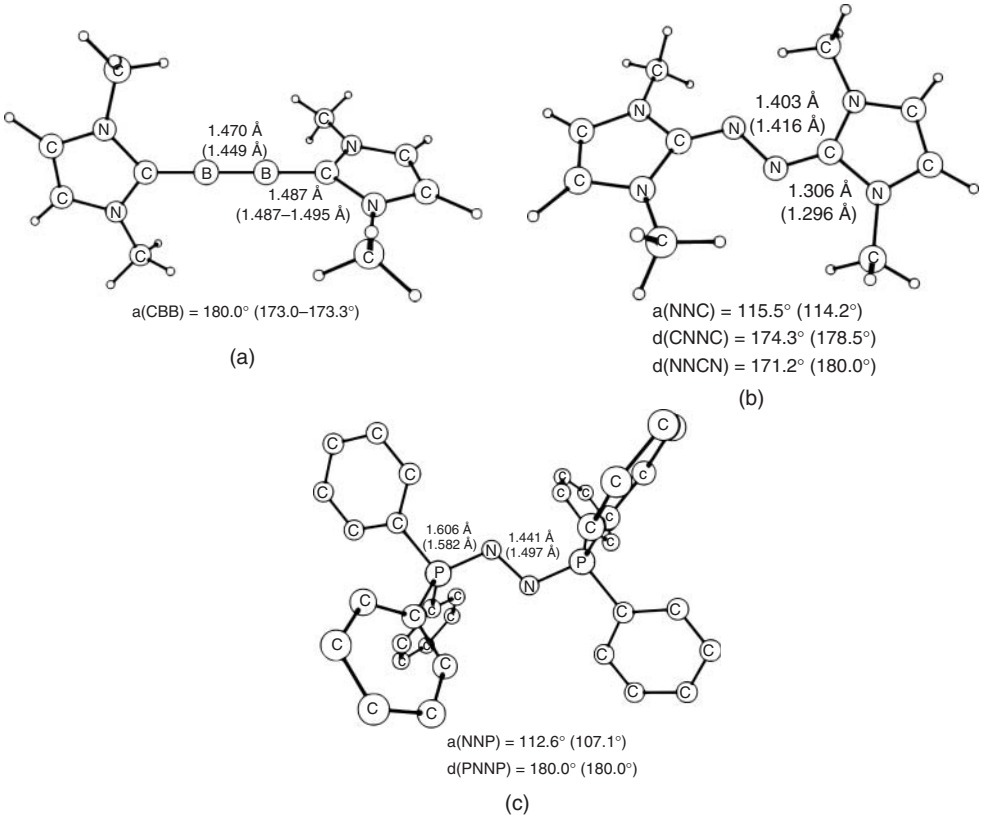

Figure 4.18 Calculated structures (BP86/def2-TZVPP) of complexes $B_2(NHC^{Me})_2$, $N_2(NHC^{Me})_2$ and $N_2(PPh_3)_2$. Experimental values of the N-substituted homologues of $B_2(NHC^{Me})_2$ and $N_2(NHC^{Me})_2$ are shown in parentheses. (The calculated data are taken from Ref. [50], and the experimental values from Refs [45c, 49, 52].)

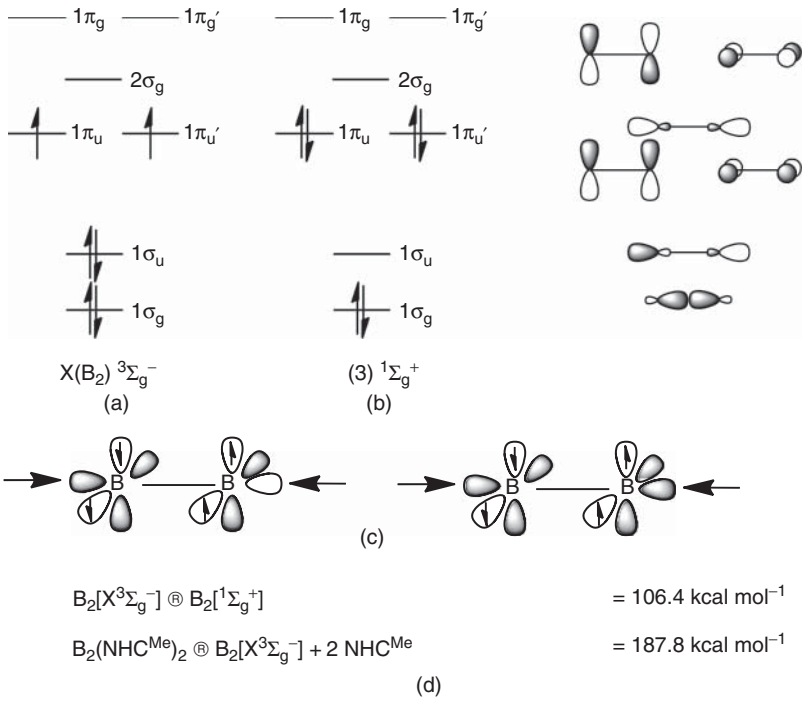

Figure 4.19 Qualitative sketch of the valence MOs of B_2 in the (a) $X^3\Sigma_g^-$ ground state and (b) excited (3) $^1\Sigma_g^+$ state. (c) Schematic representation of the L→BB←L donation from the (+,−) combination of the donor orbitals into the antibonding $1\sigma_u$ MO of B_2; and from the (+,+) combination of the donor orbitals into the bonding $2\sigma_g$ MO of B_2; (d) Calculated energies of the excitation energy of B_2 from the ground state to the reference state and bond dissociation energy D_e of $B_2(NHC^{Me})_2$ at BP86/def2-TZVPP. (Data reproduced from Ref. [47].

homologues can be explained with the help of the qualitative MO diagrams, which are shown in Figure 4.19. B_2 has a $X^3\Sigma_g^-$ ground state (Figure 4.19a). A linear coordination mode L→BB←L requires two vacant σ orbitals for donation to B_2. The appropriate excited state is the (3) $^1\Sigma_g^+$ state, which is 106.4 kcal/mol higher in energy than the $X^3\Sigma_g^-$ ground state (Figure 4.19b). The large excitation energy is overcompensated for by the very strong (NHC^{Me})→BB←(NHC^{Me}) bonds, which have a BDE $D_e = 187.8\,\text{kcal mol}^{-1}$.

Detailed insight into the nature of the (NHC^{Me})-BB-(NHC^{Me}) interactions is provided by the results of EDA-NOCV calculations. The numerical data are given in Table 4.9. The intrinsic interaction energy of the linear coordinated boron complex is, as expected, very large ($\Delta E_{int} = -307.5\,\text{kcal mol}^{-1}$). The contribution of the orbital interactions in $B_2(NHC^{Me})_2$ provides 55.5% to the total attraction, which means that the bond is slightly more covalent than electrostatic. There are four major

Table 4.9 Energy decomposition analysis with the EDA-NOCV method at BP86/TZ2P+ of the donor–acceptor interactions in the complexes $B_2(NHC^{Me})_2$, $N_2(NHC^{Me})_2$ and $N_2(PPh_3)_2$. NBO partial charges at the E_2 moiety $q(E_2)$. Energy values in kcal mol^{-1} and charges in e.

	$B_2(NHC^{Me})_2$	$N_2(NHC^{Me})_2$	$N_2(PPh_3)_2$
Interacting fragments	$B_2[(3)^1\Sigma_g^+]$ $(NHC^{Me})_2$	$N_2[^1\Gamma_g]$ $(NHC^{Me})_2$	$N_2[^1\Gamma_g]$ $(PPh_3)_2$
ΔE_{int}	−307.5	−374.3	−300.1
ΔE_{Pauli}	259.0	1237.7	853.4
ΔE_{elstat}[a]	−252.3 (44.5%)	−530.5 (32.9%)	−377.4 (32.7%)
ΔE_{orb}[a]	−314.2 (55.5%)	−1081.6 (67.1%)	−776.1 (67.3%)
$\Delta E_{\sigma 1}$ L→(E_2)←L (+,+) donation[b]	−112.7 (35.9%)	−424.4 (39.2%)	−357.9 (46.1%)
$\Delta E_{\sigma 2}$ L→(E_2)←L (+,−) donation[b]	−86.9 (27.7%)	−450.0 (41.6%)	−289.8 (37.3%)
$\Delta E_{\pi 1}$ L←(E_2)→L π backdonation[b]	−48.0 (15.3%)	−92.0 (8.5%)	−46.9 (6.0%)
$\Delta E_{\pi 2}$ L←(E_2)→L π' backdonation[b]	−42.4 (13.5%)	−34.4 (3.2%)	−23.6 (3.0%)
ΔE_{rest}[b]	−24.2 (7.7%)	−80.8 (7.5%)	−57.9 (7.6%)
$q(E_2)$	−0.36	−0.89	−1.73

[a]The values in parentheses give the percentage contribution to the total attractive interactions $\Delta E_{elstat} + \Delta E_{orb}$.
[b]The values in parentheses give the percentage contribution to the orbital interactions ΔE_{orb}.

components of ΔE_{orb}, which can be identified with the Dewar–Chatt–Duncanson model of σ donation and π backdonation.

Figure 4.20 shows the deformation densities and the associated orbital pairs which dominate the orbital interaction in $B_2(NHC^{Me})_2$. The largest contribution comes from the (NHC^{Me})→BB←(NHC^{Me}) (+,+) donation (35.9%), which is followed by the (NHC^{Me})→BB←(NHC^{Me}) (+,−) donation (27.7%). The strength of the two components of the (NHC^{Me})←BB→(NHC^{Me}) π backdonation amounts to 28.8% altogether. Note that the (+,+) σ donation is stronger than the (+,−) donation, although the acceptor orbital in the latter interaction is much lower in energy than in the former interaction (Figure 4.20a,b). This can be explained by the antibonding nature of the lower lying LUMO of B_2, whereas the higher lying LUMO+1 is a σ bonding MO. The two components of the π backdonation are not degenerate, because the NHC rings are not exactly perpendicular. We want to draw attention to the shape of the occupied molecular orbitals of $B_2(NHC^{Me})_2$, which are also shown in Figure 4.20. The σ bonding HOMO-6 (Figure 4.20a) and the π bonding HOMO and HOMO-1 (Figure 4.20c,d) suggest that the diboron compound has a B≡B triple bond. The antibonding effect of the HOMO-13 (Figure 4.20b) is compensated by the bonding contribution of the low-lying bonding B–B orbital, which comes from the 2s orbitals. It is not shown in Figure 4.20, because it does not involve (NHC^{Me})-BB-(NHC^{Me}) interactions. This orbital is mainly the $1\sigma_g$ MO of B_2 (Figure 4.19). The synthesis of the complex $B_2(NHC^{Dipp})_2$ containing a B≡B

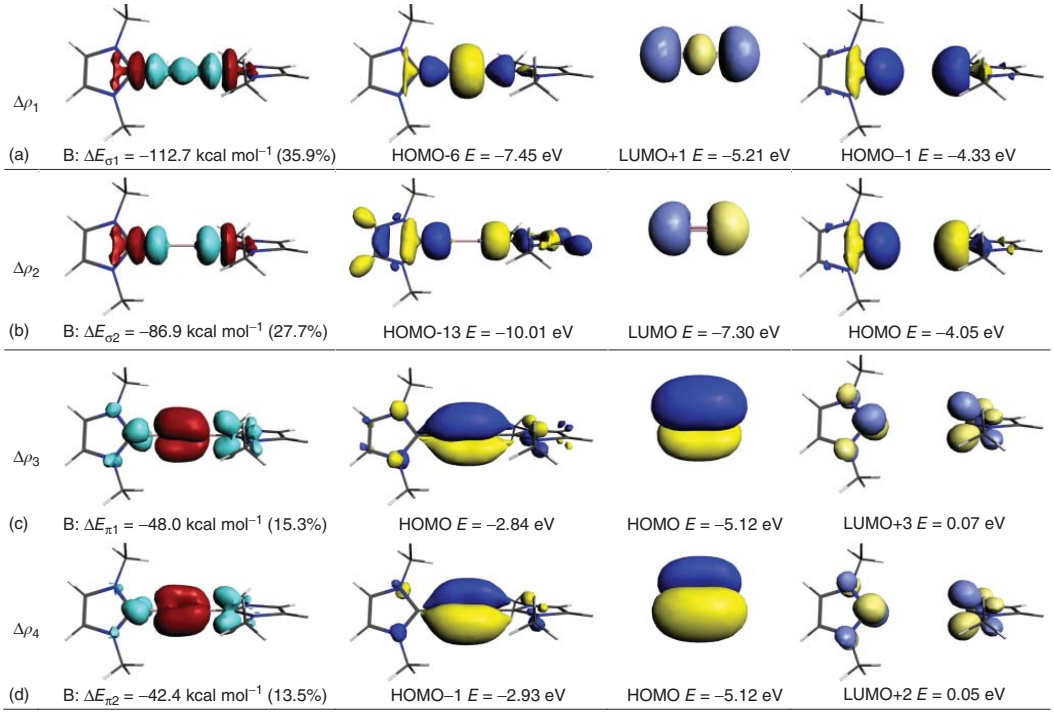

Figure 4.20 Plot of the deformation densities $\Delta\rho$ of the pairwise orbital interactions between B_2 and $(NHC^{Me})_2$ in the complex $B_2(NHC^{Me})_2$ and associated interaction energies ΔE. Shape of the most important interacting occupied and vacant orbitals of B_2 and $(NHC^{Me})_2$ which yield relevant occupied orbitals of $B_2(NHC^{Me})_2$.

triple bond [45c], which came after a theoretical study suggested that it might become isolated [50a], is a triumph of the donor–acceptor bonding model.

Figure 4.18 shows also the calculated geometries of the dinitrogen complexes $N_2(NHC^{Me})_2$ and $N_2(PPh_3)_2$, which agree quite well with the experimental structures [49, 52]. Both molecules have an anti-periplanar arrangement like the group 14 complexes $Si_2(NHC^{Me})_2$–$Pb_2(NHC^{Me})_2$ (Figure 4.15), but the bond angle EEC in the latter molecules is much more acute than in $N_2(NHC^{Me})_2$, and the NHC rings in $N_2(NHC^{Me})_2$ are not orthogonal to the CEEC plane as it is the case in the group-14 complexes.

Figure 4.21 shows the MO diagram and the orbital occupation of N_2 in the $X^1\Sigma_g^+$ ground state and the $^1\Gamma_g$ excited state. The latter state is the energetically lowest lying singlet state where two vacant π orbitals ($1\pi_u$' and $1\pi_g$') allow a trans arrangement of the donor ligands, as shown in Figure 4.21c. The (+,−) donation of the donor lone-pairs takes place in the bonding $1\pi_u$' MO whereas the (+,+) donation occurs in the antibonding $1\pi_g$' orbital. These interactions should provide the dominant contribution to the donor–acceptor bonding in N_2L_2. The numerical results of the EDA-NOCV calculations for $N_2(NHC^{Me})_2$ and $N_2(PPh_3)_2$, which are given in Table 4.9, support the qualitative model. The strongest orbital interactions come from the (+,+) and the (+,−) combination of the σ lone-pairs L→NN←L. The latter term is slightly stronger than the former when $L = NHC^{Me}$ while the reverse order if found when $L = PPh_3$. The L←NN→L π backdonation from the occupied antibonding $1\pi_g$ MO and from the bonding $1\pi_u$ MO are significantly smaller than the σ donation. Note that the partial charge at the N_2 fragment in $N_2(PPh_3)_2$ is much larger (−1.73 e) than in $N_2(NHC^{Me})_2$ (−0.89 e) which suggests that the phosphine ligand is a much stronger charge donor than NHC^{Me}. The calculated energies for the associated orbital interactions do not agree with the large difference between the partial charges $q(N_2)$. This is an indication that the amount of charge flow does not always correlate with the associated stabilization energy.

The calculated total interaction energies between N_2 ($^1\Gamma_g$) and L_2 suggest (Table 4.9) that the NHC^{Me} ligands are more strongly bonded to N_2 ($\Delta E_{int} = -374.3$ kcal mol^{-1}) than the phosphine ligands ($\Delta E_{int} = -300.1$ kcal mol^{-1}). Although the donor–acceptor interactions in $N_2(NHC^{Me})_2$ and $N_2(PPh_3)_2$ are very large, they are not sufficiently strong to compensate for the excitation energy $N_2[X^1\Sigma_g^+] \rightarrow N_2[^1\Gamma_g]$ (328.6 kcal mol^{-1}) and for the relaxation of the fragments. Figure 4.21 shows that the dissociation of $N_2(NHC^{Me})_2$ into the relaxed fragments in the electronic ground state is only slightly endoenergetic, by 10.1 kcal mol^{-1}. The dissociation becomes exergonic ($\Delta G^{298} = -14.2$ kcal mol^{-1}) when entropic and temperature effects are considered [47]. The dissociation of $N_2(PPh_3)_2$ is also an exoenergetic process ($D_e = -47.5$ kcal mol^{-1}), and becomes strongly exergonic at room temperature ($\Delta G^{298} = -74.5$ kcal mol^{-1}) [49]. This means that the dinitrogen complexes are thermodynamically unstable species that are only kinetically stable molecules. The very large donor–acceptor interaction between N_2 in the $^1\Gamma_g$ references state and the phosphine ligands provide a rationale for the findings.

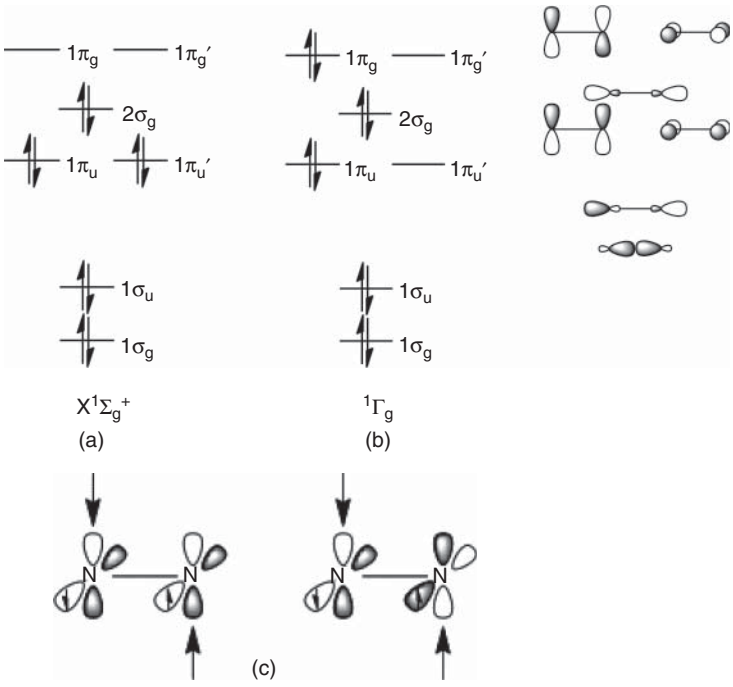

$N_2[X^1\Sigma_g^+] \rightarrow N_2[^1\Gamma_g]$ = 328.6 kcal mol^{-1}

$N_2(NHC^{Me})_2 \rightarrow N_2[X^1\Sigma_g^+] + 2\ NHC^{Me}$ = 10.1 kcal mol^{-1}

$N_2(PPh_3)_2 \rightarrow N_2[X^1\Sigma_g^+] + 2\ PPh_3$ = –47.5 kcal mol^{-1}

(d)

Figure 4.21 Qualitative sketch of the valence MOs of N_2 and orbital occupation in the (a) $X^1\Sigma_g^+$ ground state and (b) excited $^1\Gamma_g$ state; (c) schematic representation of the L→EE←L donation from the (+,–) combination of the donor orbitals into the bonding $1\pi_u$' MO of N_2; and from the (+,+) combination of the donor orbitals into the antbonding $1\pi_g$' MO of N_2; (d) Calculated energy of the excitation energies of N_2 from the $X^1\Sigma_g^+$ ground state to the excited $^1\Gamma_g$ reference state and bond dissociation energies D_e of N_2L_2 (L = NHC^{Me} and PPh_3) at BP86/def2-TZVPP [49].

The EDA-NOCV results of $N_2(NHC^{Me})_2$ and $N_2(PPh_3)_2$ in Table 4.9 and the associated deformation densities which are shown in Figures 4.22 and 4.23 provide a comprehensive picture of the bonding situation in the dinitrogen complexes. Figure 4.22a,b and 4.23a,b illustrate the σ charge flow red→blue for L→NN←L between the occupied and vacant orbitals of N_2 and 2L while Figure 4.22c,d and 4.23c,d exhibit the L←NN→L π backdonation. Due to the large occupation of the antibonding π* orbitals in N_2, the N–N distance in N_2L_2 is very long. The Lewis structure, which depicts the bonding situation in the dinitrogen complexes is shown in Figure 4.24.

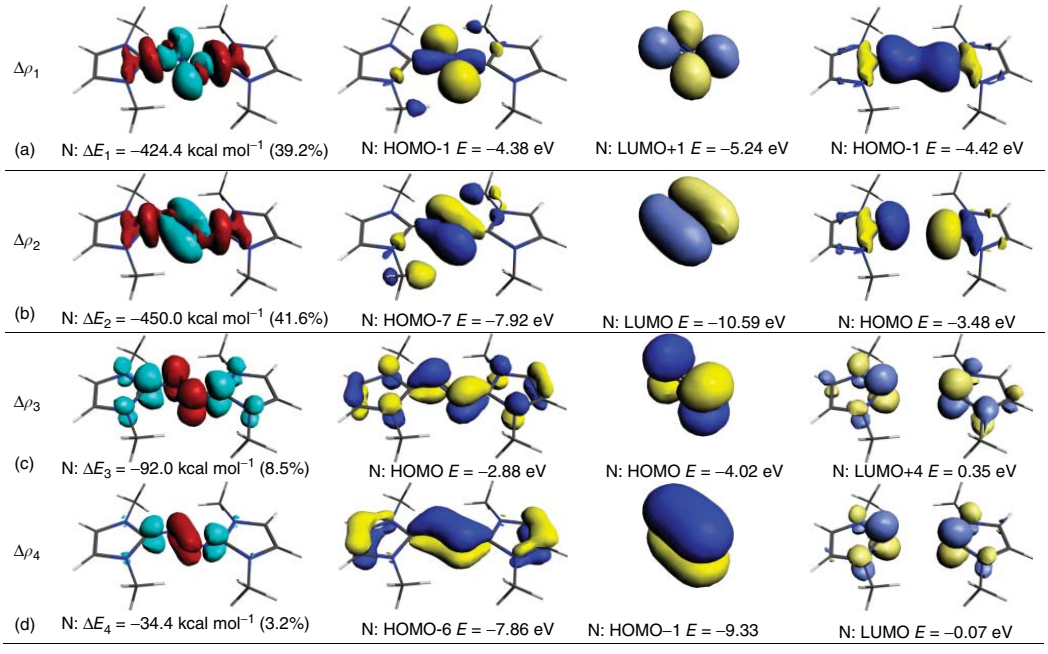

Figure 4.22 Plot of the deformation densities $\Delta\rho$ of the pairwise orbital interactions between N_2 and $(NHC^{Me})_2$ in the complex $N_2(NHC^{Me})_2$ and associated interaction energies ΔE. Shape of the most important interacting occupied and vacant orbitals of N_2 and $(NHC^{Me})_2$ which yield relevant occupied orbitals of $N_2(NHC^{Me})_2$.

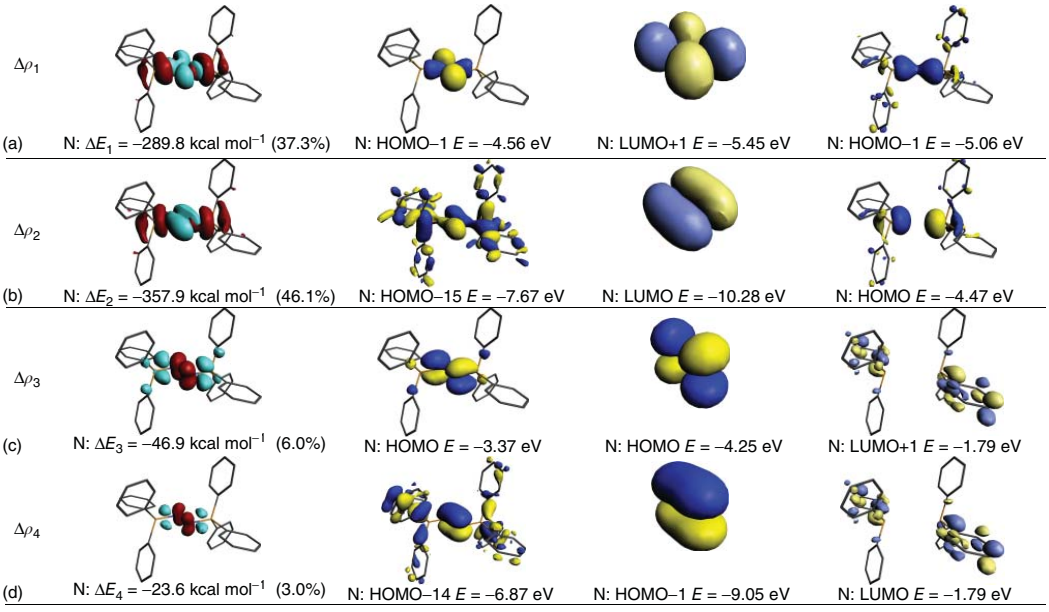

Figure 4.23 Plot of the deformation densities $\Delta\rho$ of the pairwise orbital interactions between N_2 and $(PPh_3)_2$ in the complex $N_2(PPh_3)_2$ and associated interaction energies ΔE. Shape of the most important interacting occupied and vacant orbitals of N_2 and $(PPh_3)_2$ which yield relevant occupied orbitals of $N_2(PPh_3)_2$.

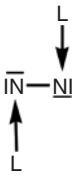

Figure 4.24 Schematic representation of the bonding situation in terms of a Lewis structure for N_2L_2.

4.4 Summary and Conclusion

There are two major conclusions that can be drawn from this chapter. One conclusion is the relevance of the donor–acceptor bonding model for main-group compounds. The analysis of the bonding situation in the tetrylones EL_2 (E = C – Pb) shows that it is useful to discuss the chemical bonds in terms of donor–acceptor interactions L→E←L that explain the equilibrium structures and chemical reactivities of the molecules. The donor–acceptor bonding model is also valid for explaining the bonds in the related molecules $(N^+)L_2$ and $(BH)L_2$. New compounds such as carbodicarbenes $C(NHC)_2$, silylones SiL_2, germylones GeL_2 and borylene complexes $(BH)L_2$, which were predicted using the donor–acceptor bonding model, may be synthesized. The donor–acceptor bonding model is also very useful for understanding the structures of the two-center complexes E_2L_2 where E is an atom from groups 13–15. The molecules can be understood in terms of donor–acceptor interactions L→EE←L between E_2 in an electronically excited singlet reference state and the donor ligands L. The different conformations of the complexes $E_2(NHC^{Me})_2$ can be explained with the electronic reference states of E_2 and the symmetry of the vacant acceptor orbitals. A striking proof for the validity of the model is the theoretically predicted diboron adduct NHC→BB←NHC, which has a linear arrangement of the ligands at the B≡B moiety that possesses a boron–boron triple bond. The donor–acceptor bonding model also explains the finding that $N_2(NHC^{Me})_2$ and $N_2(PPh_3)_2$ are stable molecules which have high melting points, although the dissociation of N_2 is a strongly exergonic process. The second conclusion concerns the detailed insight into the nature of the donor–acceptor bonds which can be gained with modern methods of bonding analysis.

References

1. (a) Lewis, G.N. (1916) *J. Am. Chem. Soc.*, **38**, 762; (b) Lewis, G.N. (1923) *Valence and the Structure of Atoms and Molecules*, American Chemical Society Monograph Series, John Wiley & Sons, Inc., New York.
2. (a) Krapp, A., Bickelhaupt, F.M., and Frenking, G. (2006) *Chem. Eur. J.*, **12**, 9196; (b) Spackman, M.A. and Maslen, E.N. (1986) *J. Phys. Chem.*, **90**, 2020; (c) Hirshfeld, F.L. and Rzotkiewicz, S. (1974) *Mol. Phys.*, **27**, 1319.
3. Frenking, G. and Fröhlich, N. (2000) *Chem. Rev.*, **100**, 717.
4. Dewar, M.J.S. (1951) *Bull. Soc. Chim. Fr.*, **18**, C79.
5. (a) Chatt, J. and Duncanson, L.A. (1953) *J. Chem. Soc.*, 2929; (b) Leigh, G.J. and Winterton, N. (eds) (2002) *The Legacy of Joseph Chatt*, The Royal Society, London.

6. For a discussion of the DCD bonding model in the light of quantum chemical calculations see:Frenking, G. (2002) in *The Legacy of Joseph Chatt* (eds G.J. Leigh and N. Winterton), The Royal Society, London, p. 111.
7. Goedecke, C., Hillebrecht, P., Uhlemann, T., Haunschild, R., and Frenking, G. (2009) *Can. J. Chem.*, **87**, 1470.
8. (a) Bessac, F. and Frenking, G. (2006) *Inorg. Chem.*, **45**, 6956; (b) Loschen, C., Voigt, K., Frunzke, J., Diefenbach, A., Diedenhofen, M., and Frenking, G. (2002) *Z. Allg. Anorg. Chem.*, **628**, 1294.
9. Haaland, A. (1989) *Angew. Chem.*, **101**, 1017; *Angew. Chem., Int. Ed. Engl.*, **28**, 992.
10. Johnson, A.W. (1993) *Ylides and Imines of Phosphorus*, Wiley-Interscience Publication, New York, Chichester, Brisbane, Toronto, Singapore.
11. Tonner, R. and Frenking, G. (2009) *Pure Appl. Chem.*, **81**, 597.
12. Frenking, G. and Tonner, R. (2011) *WIREs Comput. Mol. Sci.*, **1**, 869.
13. (a) Igau, A., Grützmacher, H., Baceiredo, A., and Bertrand, G. (1988) *J. Am. Chem. Soc.*, **110**, 6463; (b) Igau, A., Baceiredo, A., Trinquier, G., and Bertrand, G. (1989) *Angew. Chem.*, **101**, 617; *Angew. Chem., Int. Ed. Engl.*, **28**, 621.
14. Arduengo, A.J. III, Harlow, R.L., and Kline, M. (1991) *J. Am. Chem. Soc.*, **113**, 2801.
15. Ramirez, F., Desai, N.B., Hansen, B., and McKelvie, N. (1961) *J. Am. Chem. Soc.*, **83**, 3539.
16. Hardy, G.E., Zink, J.I., Kaska, W.C., and Baldwin, J.C. (1978) *J. Am. Chem. Soc.*, **100**, 8002.
17. Tonner, R. and Frenking, G. (2008) *Chem. Eur. J.*, **14**, 3260.
18. Tonner, R., Heydenrych, G., and Frenking, G. (2008) *Chem. Phys. Chem.*, **9**, 1474.
19. (a) Morokuma, K. (1971) *J. Chem. Phys.*, **55**, 1236; (b) Ziegler, T. and Rauk, A. (1979) *Inorg. Chem.*, **18**, 1755.
20. (a) Mitoraj, M. and Michalak, A. (2007) *Organometallics*, **26**, 6576; (b) Mitoraj, M.P., Michalak, A., and Ziegler, T. (2009) *J. Chem. Theory Comput.*, **5**, 962; (c) Mitoraj, M.P., Michalak, A., and Ziegler, T. (2009) *Organometallics*, **28**, 3727.
21. Celik, M.A., Sure, R., Klein, S., Kinjo, R., Bertrand, G., and Frenking, G. (2012) *Chem. Eur. J.*, **18**, 5676.
22. Ellern, A., Drews, T., and Seppelt, K. (2001) *Z. Anorg. Allg. Chem.*, **627**, 73.
23. (a) Jensen, P. and Johns, J.W.C. (1986) *J. Mol. Spectrosc.*, **118**, 248; (b) Tanimoto, M., Kuchitsu, K., and Morino, Y. (1970) *Bull. Chem. Soc. Jpn.*, **43**, 2776; (c)For a high-level ab initio calculation of C_3O_2 see: Koput, J. (2000) *Chem. Phys. Lett.*, **320**, 237.
24. (a) Dyker, C.A., Lavallo, V., Donnadieu, B., and Bertrand, G. (2008) *Angew. Chem.*, **120**, 3250; *Angew. Chem. Int. Ed.*, 2008, **47**, 3206; (b) Fürstner, A., Alcarazo, M., Goddard, R., and Lehmann, C.W. (2008) *Angew. Chem.*, **129**, 3254; *Angew. Chem. Int. Ed.*, 2008, **47**, 3210.
25. Klein, S. and Frenking, G. (2010) *Angew. Chem.*, **122**, 7260; *Angew. Chem. Int. Ed.*, **49**, 7106.
26. (a) Hassanzadeh, P. and Andrews, L. (1992) *J. Am. Chem. Soc.*, **114**, 9239; (b) Hassanzadeh, P., Hannachi, Y., and Andrews, L. (1993) *J. Phys. Chem.*, **97**, 6418.
27. Barua, S.R., Allen, W.D., Kraka, E., Jerabek, P., Sure, R., and Frenking, G. (2013) *Chem. Eur. J.*, **19**, 15941.
28. (a) Pyykkö, P. and Atsumi, M. (2009) *Chem. Eur. J.*, **15**, 12770; (b) Pyykkö, P., Riedel, S., and Patzschke, M. (2005) *Chem. Eur. J.*, **11**, 3511.
29. (a) Christe, K.O., Wilson, W.W., Sheehy, J.A., and Boatz, J.A. (1999) *Angew. Chem.*, **111**, 2112; *Angew. Chem. Int. Ed.*, 1999, **38**, 2004; (b) Bernhardi, I., Drews, T., and Seppelt, K. (1999) *Angew. Chem.*, **111**, 2370; *Angew. Chem. Int. Ed.*, **38**, 2232.
30. Sotiropoulos, J.-M., Baceiredo, A., and Bertrand, G. (1987) *J. Am. Chem. Soc.*, **109**, 4711.
31. Appel, R. and Hauss, A. (1961) *Z. Anorg. Allg. Chem.*, **311**, 290.
32. Dahl, L.F., Handy, L.B., and Ruff, J.K. (1970) *J. Am. Chem. Soc.*, **92**, 7327.
33. Lavallo, V., Canac, Y., Prasang, C., Donnadieu, B., and Bertrand, G. (2005)

Angew. Chem., **117**, 5851; *Angew. Chem. Int. Ed.*, 2005, **44**, 5705.

34. The related dicarbene complex $(N^+)(NHC^*)_2$ where NHC* is a saturated N-heterocyclic carbene has been synthesized by: Ma, T., Fu, X., Kee, C.W., Zong, L., Pan, Y., Huang, K.-W., and Tan, C.-H. (2011) *J. Am. Chem. Soc.*, **133**, 2828.
35. Kinjo, R., Donnadieu, B., Celik, M.A., Frenking, G., and Bertrand, G. (2011) *Science*, **333**, 610.
36. Ghadwal, R.S., Roesky, H.W., Merkel, S., Henn, J., and Stalke, D. (2009) *Angew. Chem.*, **121**, 5793; *Angew. Chem. Int. Ed.*, 2009, **48**, 5683.
37. Donor-acceptor bonds tend to become shorter in the solid state than in the free molecule due to intermolecular interactions. The bond shortening is particularly large (up to 1 Å) when the bonds are weak. For a discussion see: Jonas, V., Frenking, G., and Reetz, M.T. (1994) *J. Am. Chem. Soc.*, **116**, 8741.
38. Mondal, K.C., Roesky, H.W., Schwarzer, M.C., Frenking, G., Neudeck, S., Tkach, I., Wolf, H., Kratzert, D., Herbst-Irmer, R., Niepötter, B., and Stalke, D. (2013) *Angew. Chem.*, **125**, 1845; *Angew. Chem. Int. Ed.*, 2013, **52**, 1801.
39. Takagi, N., Shimizu, T., and Frenking, G. (2009) *Chem. Eur. J.*, **15**, 8593.
40. Takagi, N., Tonner, R., and Frenking, G. (2012) *Chem. Eur. J.*, **18**, 1772.
41. (a) Takagi, N., Shimizu, T., and Frenking, G. (2009) *Chem. Eur. J.*, **15**, 3448; (b) Takagi, N. and Frenking, G. (2011) *Theor. Chem. Acc.*, **129**, 615.
42. Mondal, K.C., Roesky, H.W., Klinke, F., Schwarzer, M.C., Frenking, G., Niepötter, B., Wolf, H., Herbst-Irmer, R., and Stalke, D. (2013) *Angew. Chem.*, **125**, 3036; *Angew. Chem. Int. Ed.*, **52**, 2963.
43. (a) Xiong, Y., Yao, S., Inoue, S., Epping, J.D., and Driess, M. (2013) *Angew. Chem.*, **125**, 7287; *Angew. Chem. Int. Ed.*, **52**, 7147; (b) Xiong, Y., Yao, S., Tan, G., Inoue, S., and Driess, M. (2013) *J. Am. Chem. Soc.*, **135**, 5004.
44. Wang, Y., Xie, Y., Wei, P., King, R.B., Schaefer, H.F. III, Schleyer, P.v.R., and Robinson, G.H. (2008) *Science*, **321**, 1069.
45. (a) E = Ge: Sidiropoulos, A., Jones, C., Stasch, A., Klein, S., and Frenking, G. (2009) *Angew. Chem.*, **121**, 9881; *Angew. Chem. Int. Ed.*, **48**, 9701; (b) E = Sn: Jones, C., Sidiropoulos, A., Holzmann, N., Frenking, G., and Stasch, A. (2012) *Chem. Commun.*, **48**, 9855; (c) E = B: Braunschweig, H., Dewhurst, R.D., Hammond, K., Mies, J., Radacki, K., and Vargas, A. (2012) *Science*, **336**, 1420; (d) E = P: Wang, Y., Xie, Y., Wie, P., King, R.B., Schaefer, H.F. III, Schleyer, P.v.R., and Robinson, G. (2008) *J. Am. Chem. Soc.*, **130**, 14970; (e) E = As: Abraham, M.Y., Wang, Y., Xie, Y., Wei, P., Schaefer, H.F. III, Schleyer, P.v.R., and Robinson, G.H. (2010) *Chem. Eur. J.*, **16**, 432.
46. Yang, Y. and Robinson, G.H. (2012) *Dalton Trans.*, **41**, 337.
47. (a) Holzmann, N. (2013) *Bonding Situation in NHC and Phosphine Complexes $[(L)_m(E_mH_n)]$ (m = 1, 2; n = 0–4) of Group 13–15 and their Applicability as Soluble Hydrogen Storage Systems*, PhD thesis, Philipps-Universität Marburg, Marburg, Germany. (b) Holzmann, N., Jones, C., and Frenking, G., to be published.
48. Dutton, J.L. and Wilson, D.J.D. (2012) *Angew. Chem.*, **124**, 1506; *Angew. Chem. Int. Ed.*, **51**, 1477.
49. Holzmann, N., Dange, D., Jones, C., and Frenking, G. (2013) *Angew. Chem.*, **125**, 3078; *Angew. Chem. Int. Ed.*, **52**, 3004.
50. (a) Holzmann, N., Stasch, A., Jones, C., and Frenking, G. (2011) *Chem. Eur. J.*, **17**, 13517; (b) Holzmann, N., Stasch, A., Jones, C., and Frenking, G. (2013) *Chem. Eur. J.*, **19**, 6467.
51. Appel, R. and Schöllhorn, R. (1964) *Angew. Chem.*, **76**, 991; *Angew. Chem., Int. Ed. Engl.*, **3**, 805.
52. Reinmuth, M., Neuhäuser, C., Walter, P., Enders, M., Kaifer, E., and Himmel, H.-J. (2011) *Eur. J. Inorg. Chem.*, **2011**, 83.

5
Electron-Counting Rules in Cluster Bonding – Polyhedral Boranes, Elemental Boron, and Boron-Rich Solids

Chakkingal P. Priyakumari and Eluvathingal D. Jemmis

5.1
Introduction

> *"If we lived on a planet where nothing ever changed, there would be nothing to figure out. If we lived in an unpredictable world where things changed in random and very complex ways we wouldn't be able to figure things out. But we live in an in-between universe where things change, but according to patterns, rules, or, as we call them, laws of nature. And so it becomes possible to figure things out."*
>
> Carl Sagan

Throughout the history of chemistry, man has been curious about the nature of the chemical bond. The idea of electron pairing as the basic mechanism of chemical bond as proposed by G. N Lewis in the 1920s was followed by its quantum mechanical interpretation by Heitler and London, which led to the celebrated valence bond theory. Lewis' idea of the eight-electron requirement for the stability of an atom was named as Octet rule by Irwin Langmuir, and has become a rule of thumb for chemists thereafter. This was followed by the 18-electron rule for transition metal complexes. The formulation of the Hückel $4n+2$ rule of aromaticity in the 1930s as part of the LCAO-MO theory was another breakthrough. By this time, the chemist's notion of 2c-2e bond had already been questioned by the boranes, of Alfred Stock and others, described as electron-deficient compounds. However, these were still exceptions in an electron-sufficient world of chemistry, dominated by the chemistry of carbon. Comparisons were inevitable between the chemistry of carbon and boron. Boranes were notorious for their instability and high reactivity. This is attributed to electron deficiency. Later on, the synthesis of stable polyhedral boranes aroused much curiosity and challenged the bonding concepts and electron-counting rules of the time. By carefully observing the relationship between the structure and the number of electrons of polyhedral boranes described by many, Wade proposed a set of empirical rules, named after him. These rules were given a theoretical interpretation by molecular orbital theory. The research in borane chemistry was accelerated by Wade's rules. Soon boranes developed

The Chemical Bond: Chemical Bonding Across the Periodic Table, First Edition.
Edited by Gernot Frenking, Sason Shaik.

into a separate area on its own. New terms such as *three-dimensional aromaticity* emerged along with it, analogous to Hückel aromaticity. Although the Wade's rules were developed for borane clusters, it went beyond and proved to be widely applicable to other main group clusters as well, including zintl phases and ions. Admittedly, these are the ways of chemists to get a transferable model from the electronic structure description available from quantum mechanics. This chapter is an attempt to extend this so that a relationship, similar to that exists between benzenoid aromatics and graphite through the Hückel $4n+2$ π electron rule as well as between methane and diamond through tetracoordinate tetrahedral carbon that we take for granted, evolves in the chemistry of boron. Extension of Wade's rules to condensed polyhedral systems led to the mno rule, which simplified the structural chemistry of molecular clusters. This also provided the links that are required between boranes and allotropes of elemental boron. The aim here is to give details of these developments so that these are easily accessible to any chemist.

5.2 Wade's Rule

Any discussion on cluster chemistry of boron must start with Wade's rule, which helped to understand and to predict the stability of monopolyhedral boranes. The concept of the chemical bond has an electron-sufficient origin, where 2c-2e bond was all that was known. The discovery of the bridged structure for diborane showed the limitation of the 2c-2e bond [1–3]. Diborane (B_2H_6) has 14 valence orbitals and 12 valence electrons (VEs) and hence was considered as an electron-deficient molecule. The bridged structure of diborane necessitated the concept of 3c-2e bond. The structure could be considered analogous to that of a diprotonated ethylene (Figure 5.1). If B_2H_6 had the classical 2c-2e bonding structure as in the case of C_2H_6, the seven two-center links will require seven pairs of VEs; whereas only six are available. In the nonclassical multicenter bonded structure the number of bonding molecular orbitals (BMOs) is six; the four BH BMOs and the two multicenter orbitals as shown in Figure 5.1. The rest of the orbitals are antibonding. As six electron pairs are available, diborane is electron sufficient. Multicenter bonding is nature's way of attaining electron sufficiency. The contributions of Wade, Williams, Rudolf, Lipscomb, Grimes, Hawthorn, and many others brought boron chemistry and its systematization to the forefront of chemical research [4].

A series of boranes, B_4H_{10}, B_5H_9, B_5H_{11}, B_6H_{10}, and $B_{10}H_{14}$ among them, synthesized by Alfred Stock (Figure 5.2) led the demand for better understanding of boranes [5]. Structural studies on these showed deltahedral frameworks [5]. X-ray diffraction studies on metal borides of the type MB_6 revealed the first closed deltahedral framework of boron, the B_6 octahedron [6, 7]. This was followed by the synthesis of closed deltahedral borane dianions of the general formula $B_nH_n^{2-}$ ($n=5-12$) (Figure 5.3) with $2(n-2)$ faces and $3(n-2)$ edges [5]. The trigonal bipyramidal $B_5H_5^{2-}$, among these, escaped synthesis so far; however, the isoelectronic $C_2B_3H_5$ is known. These close-to-spherical polyhedra that can be

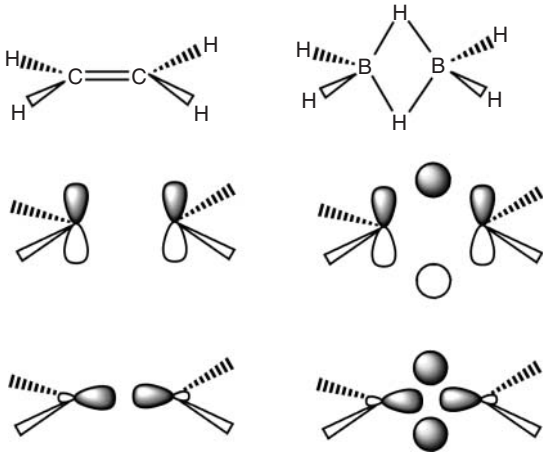

Figure 5.1 Frontier MOs of ethylene and diborane.

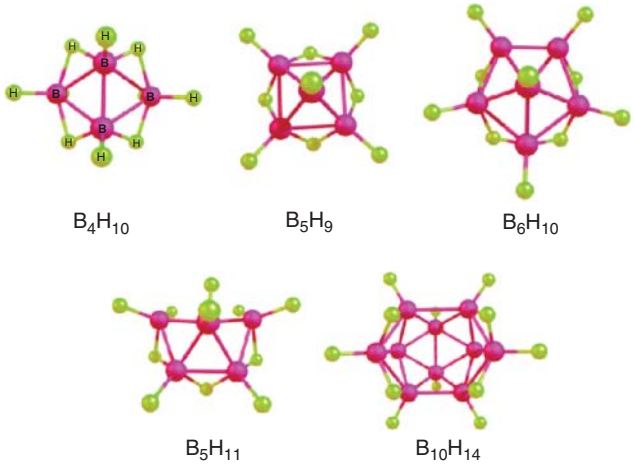

Figure 5.2 Structures of representative open polyhedral boranes.

obtained from n number of vertices are known as *closo* (cage-like) as they have closed structures with only triangular faces. The dianionic nature of closo-B_nH_n is indicative of the presence of $n+1$skeletal BMOs. The open, neutral boranes initially synthesized by Alfred Stock are related to the closo polyhedral dianions, $B_nH_n^{2-}$, in that they can be obtained from closo structures by the removal of one or two vertices (BH units) followed by hydrogenation to keep the required number of electrons (Figure 5.4). The polyhedral fragment derived from the closo cage by the removal of one vertex is called *nido* (meaning nest); similarly, the removal of two vertices leads to arachno (spider-web) structure. Deltahedral boranes, which are related to each other by the addition or removal of vertices (Figure 5.4), have the same

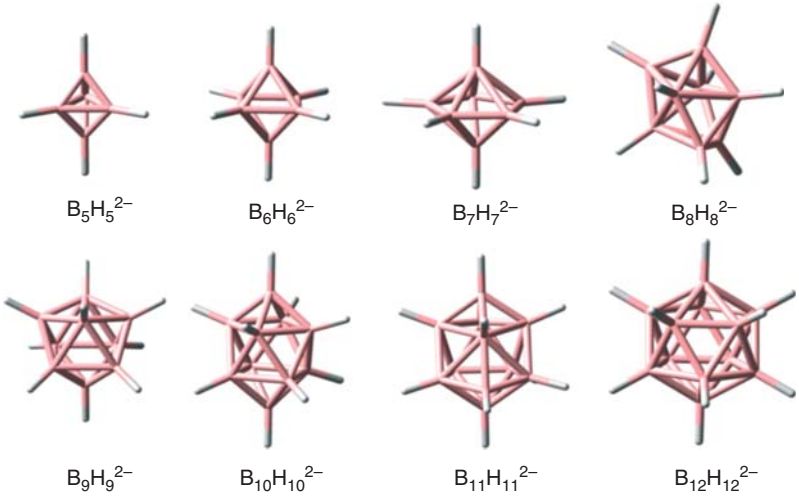

Figure 5.3 Closo borane anions, $B_nH_n^{2-}$, $n = 5–12$.

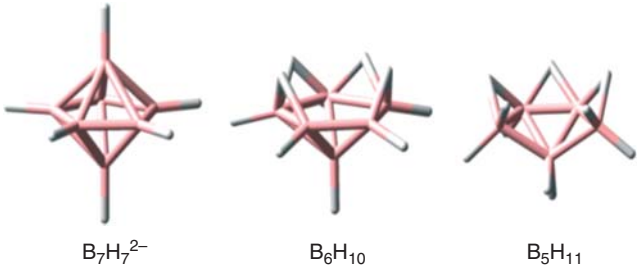

Figure 5.4 Closo–nido–arachno connection.

number of skeletal electrons. Before trying to understand the closo–nido–arachno relationship and electron count, the following points must be noted: (i) each BH unit contributes two electrons for skeletal bonding; (ii) each bridging hydrogen atom contributes one electron for skeletal bonding; (iii) the BH_2 unit present in nido and arachno clusters, although appears similar to a two-orbital one-electron donor, could be better viewed as BH^- and H^+ so that one of the hydrogens (endo-hydrogen) can be viewed as the cluster component. Endo-hydrogen is the one that lies on the inner, near-spherical surface formed by the boron vertices, whereas exo-hydrogen is the one that is on the outer sphere (Figure 5.5).

Consider $(BH)_n^{2-}$; the only nido and arachno neutral boranes related to this and experimentally available are $(BH)_{n-1}H_4$ and $(BH)_{n-2}H_6$ (Figure 5.4). The skeletal electron counting of $(BH)_n^{2-}$, $(BH)_{n-1}H_4$, and $(BH)_{n-2}H_6$ are shown here:

$(BH)_n^{2-}$: n BH units provide n pairs; two negative charges provide one pair; total $n + 1$ pairs.

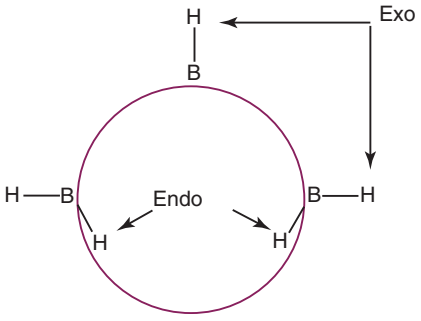

Figure 5.5 Two types of hydrogen atoms in polyhedral borane structures.

- $(BH)_{n-1}H_4$: $n-1$ BH units provide $n-1$ pairs; four bridging hydrogen atoms provide two pairs; total $n+1$ pairs.
- $(BH)_{n-2}H_6$: $n-2$ BH units provide $n-2$ pairs; six bridging hydrogen atoms provide three pairs; total $n+1$ pairs.

For example, $B_7H_7^{2-}$, B_6H_{10} and B_5H_{11} have eight pairs of skeletal electrons. Thus, the skeletal electronic requirement (SEP) of n-vertex closo, $n-1$ vertex nido and $n-2$ vertex arachno is $n+1$. *In other words, SEP requirement of n-vertex closo, nido, and arachno structures are n+1, n+2, and n+3, respectively*. This is known as *Wade's rule* [8, 9].

An explanation for Wade's rule is available through MO theory (Figure 5.6) [10, 11]. BH units in closo-$B_nH_n^{2-}$ are assumed to be *sp* hybridized; the n outward pointing sp hybrid orbitals form exohedral BH bonds. The $2n$ unhybridized p orbitals, which are tangential to the surface, form linear combinations to give n bonding and n antibonding surface molecular orbitals. The n inward-pointing sp hybrid orbitals form linear combinations to give *one* core BMO and $n-1$ higher

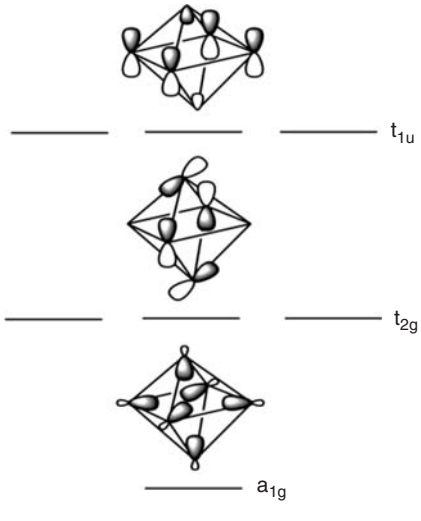

Figure 5.6 Skeletal bonding MOs of closo-$B_6H_6^{2-}$.

energy antibonding molecular orbitals (ABMOs). Thus, there will be *one* core BMO and n surface BMOs to be filled to obtain a stable structure, leading to a total of $n+1$ skeletal BMOs. Thus, the skeletal electronic requirement of closo-B_nH_n is $n+1$ pairs, whereas B_nH_n has only n pairs. This explains why closo-boranes exist as dianions, $B_nH_n^{2-}$. SEP requirement remains the same even after the removal of one or two vertices (to give nido- and arachno clusters, respectively), as the bonding character of the $n+1$ BMOs is not changed significantly by the removal of one or two vertices. Thus, the electronic requirement of an n vertex nido cluster will be the same as that of an $n+1$ vertex closo cage (i.e., $n+1+1$ SEP). Similarly, the electronic requirement of an n vertex arachno cluster will be the same as that of an $n+2$ vertex closo-cage (i.e., $n+2+1$). *In summary, the SEP requirement of a polyhedral borane cluster is n+1+p, where p is the number of missing vertices (p=0, 1,2 for closo, nido, and arachno respectively). Thus closo, nido, and arachno clusters can be represented by* $B_nH_n^{2-}$, $B_nH_n^{4-}$, $B_nH_n^{6-}$, *respectively. The neutral polyhedral boranes synthesized by Stock are protonated forms of* $B_nH_n^{4-}$ *and* $B_nH_n^{6-}$ (B_nH_{n+4}, B_nH_{n+6}).

Nido clusters are formed by the removal of the highest degree vertex from the closo cluster (Figure 5.7). Boranes prefer the deltahedral structure as this ensures the largest number of bonding contacts. Keeping this in mind, one might wonder why the removal of highest degree vertex is preferred as it removes maximum number of bonding links. Removal of a vertex leads to a nido tetranion, where the HOMO and hence the negative charge is concentrated mostly on the open face. The negative charge could be better stabilized when it is delocalized over a larger area. Similarly, when the tetranion is protonated (B_nH_{n+4}), the bridging protons can be part of the skeletal bonding without steric destabilization only when the open face is large enough to accommodate them. The removal of a second vertex to give arachno structures can happen in two ways; either adjacent or nonadjacent to the first vertex that is removed. It is clear from Figure 5.7 that removal of a nonadjacent vertex leads to the borane equivalent of the stable aromatic hydrocarbon, $C_5H_5^{1-}$. Obviously, this indicates that removal of nonadjacent vertices is the one that is favorable. On the other hand, all the neutral arachno boranes have the vertices removed from the adjacent sides. It has been shown that the six endo-hydrogen

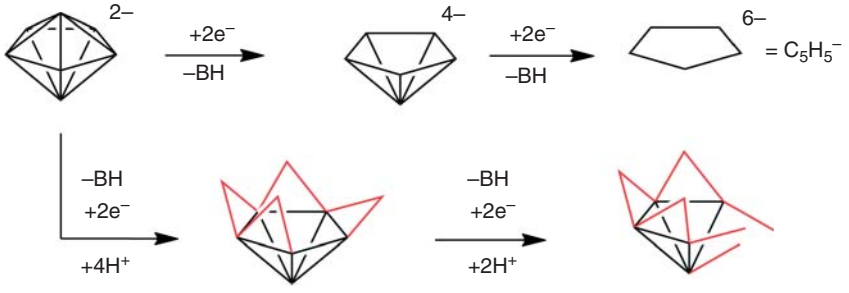

Figure 5.7 Formation of nido and arachno structures from closo (red bridging lines indicate bridging hydrogen atoms).

atoms are better accommodated in the open face formed by the adjacent vertex removal [12].

The closo-nido-arachno pattern of borane clusters has changed the status of boranes from rule breakers to pattern makers [12]. Although the term *electron-deficient compounds* is attributed to borane clusters, they are actually electron sufficient for the structures they adopt. Deviation from the Wade count is observed in the case of some closo- 8, 9, and 11 vertex systems. For example, the closo-metallaborane, $(\eta^5\text{-}C_5H_5)_4Ni_4B_4H_4$ has 10 SEPs, which is more than that required by Wade's rule [13]. Closo-B_8Cl_8 and B_9Cl_9 have 2 electrons less compared to the Wade count. This unusual feature of tolerating n or $n+2$ SEPs rather than the usual $n+1$ SEPs in the case of closo-B_nH_n clusters with $n = 8$, 9 and 11 is attributed to the nondegenerate nature of the frontier orbitals. Addition of two electrons to a nondegenerate LUMO or removal of two electrons from a nondegenerate HOMO leads to closed shell species, and the subsequent changes in bond lengths and angles help preserve sufficient HOMO-LUMO gap required for attaining the stability. This is only a partial story as we need to worry about the electrons added by the substituents. Addition of two electrons to a closo cluster having degenerate LUMO or removal of two electrons from a closo cluster having degenerate HOMO will lead to Jahn–Teller distortion. Yet another rule breaker is tetrahedron, which is the smallest deltahedron. Although it is a closo structure with only triangular faces, it cannot exist with the Wade count of $n+1$ SEPs. Rather, it requires $n+2$ or n SEPs. This is attributed to the *a*, *t*, and *e* symmetries of the skeletal orbitals. The HOMO of neutral B_4H_4 is triply degenerate and the LUMO is doubly degenerate. Thus, B_4Cl_4 with four SEPs and C_4H_4 with six SEPs exist, but not $B_4H_4^{2-}$ [14–16].

5.3
Localized Bonding Schemes for Bonding in Polyhedral Boranes

The *topological approach* based on localized bonding schemes was the initial attempt to explain the chemical bonding in deltahedral boranes. This was soon replaced by the above-mentioned *MO approach*. Nevertheless, being of historical importance, a brief description is given here [17]. This is based on the following assumptions: (i) each boron will form one exohedral 2c-2e BH bond and hence will contribute three sp^3 hybrid orbitals for skeletal bonding; (ii) in order to eliminate the electron deficiency, one 3c-2e bond must be formed per boron atom; (iii) each edge of the polyhedral skeleton must be accounted either by a 2c-2e bond or by a 3c-2e bond (Figure 5.8a); (iv) two boron atoms cannot be simultaneously bonded by both a 2c-2e and 3c-2e bond as this will require too close an arrangement of orbitals (Figure 5.8b). These rules are collectively called *topological rules*.

Consider a polyhedral borane of the general formula $(BH)_pH_q$. Let *s, t, y, and x* denote 3c-2e B-H-B, 3c-2e B-B-B, 2c-2e B-B, and extra BH bonds (Figure 5.9). The equations of balance are

$s+t = p$; (three-center orbital balance: total number of 3c-2e bonds will be equal to the number of boron atoms)

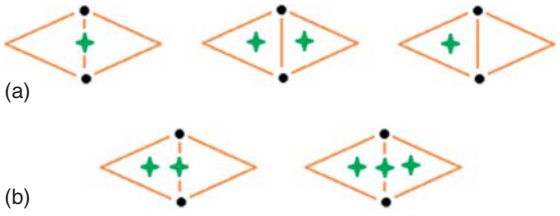

Figure 5.8 (a) Topologically allowed and (b) forbidden bonding schemes (star along the bond indicates 2c-2e bond; star on the triangular face indicates 3c-2e bond), according to styx rules of Lipscomb.

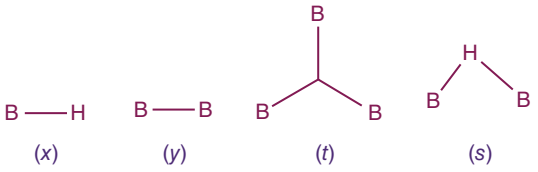

Figure 5.9 Types of skeletal bonds in polyhedral borane skeleton.

$s+x = q$; (H balance: the hydrogens other than those involved in exohedral BH bond formation will be used for 3c-2e B–H–B bond and for the endo B–H bond)

$p + (q/2) = s + t + y + x$, which implies $y = (s-x)/2$; (electron balance: p BH units provide p pairs and q extra hydrogen atoms provide $q/2$ pairs for skeletal bonding; their sum should be equal to the total number of skeletal bond pairs).

From the equations of balance it could be derived that $s = (q/2) + y$, which indicates that $s \geq (q/2)$, as $y \geq 0$. The maximum value of s is q, which is the case when all the extra hydrogen atoms are used for 3c-2e B–H–B bond. Thus, the values of s can range from $q/2$ to q. In case of more than one *styx* codes for the same borane, that which is most symmetric and sticks to the topological rules mentioned previously is selected.

Consider, for example, B_5H_{11}: $p = 5$; $q = 6$; $3 \leq s \leq 6$. Applying the equations of balance one can generate the *styx* table (Figure 5.10). The fourth row is readily eliminated as it contains negative values. The valence structures corresponding to 3203, 4112, and 5021 are shown in Figure 5.10. 5021 can be neglected as it violates the rule that two vertices should not simultaneously be connected both by a 2c-2e bond and a 3c-2e bond. Taking 3203 and 4112, the former is the most symmetric one and hence is chosen as the dominant valence structure of B_5H_{11}.

Styx formalism can be applied to charged structures as well, by hydrogenating them to get the neutral borane and then treating each B–H–B (s) as protonated B–B(y). For example, $B_5H_5^{2-}$ could be treated as B_5H_7. The *styx* code could be derived as 2310. Considering s as protonated y, the code becomes 0330. This implies that the bonding in $B_5H_5^{2-}$ could be explained by three 3c-2e B–B–B bonds and

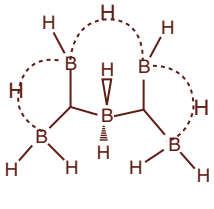

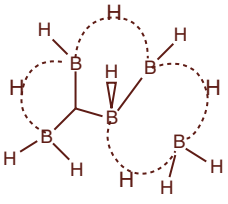

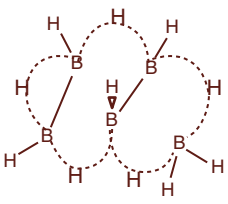

s	t	y	x
3	2	0	3
4	1	1	2
5	0	2	1
6	–1	3	0

Figure 5.10 Possible bonding schemes of B_5H_{11} based on *styx* formalism.

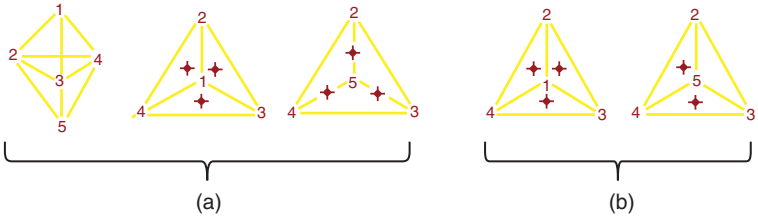

Figure 5.11 Localized bonding schemes of (a) $B_5H_5^{2-}$ and (b) B_5H_5.

three 2c-2e B–B bonds (Figure 5.11a). Applying *styx* formalism on neutral B_5H_5 results in the code 0500 and hence requires five 3c-2e B–B–B bonds, which will violate the topological rule, as the skeletal connectivity of the fourth boron atom exceeds three (Figure 5.11b). Similarly, one cannot draw a satisfactory topological structure for $B_5H_5^{4-}$ (*styx* code 0160). Thus, topology explains why B_5H_5 prefers to be a dianion. A similar experiment on B_4H_4 will explain why it prefers to be neutral or tetranion rather than a dianion. The neutral B_4H_4 requires four 3c-2e B–B–B bonds (Figure 5.12b); $B_4H_4^{4-}$ requires six 2c-2e B–B bonds (Figure 5.12a); both are topologically allowed. $B_4H_4^{2-}$ with the *styx* code 0230 will result in the unfavorable topology in which an edge can be accounted both by a 2c-2e bond and a 3c-2e bond. Thus, the localized bonding approach is in agreement with the predictions of MO theory. In the case of octahedron and icosahedron, however, a discrepancy arises. For both of these deltahedra, the localized bonding approach based on *styx* predicts the existence of neutral, dinegative, and tetranegative species; whereas according to MO theory, neutral and tetranegative species will be radicals. This disagreement

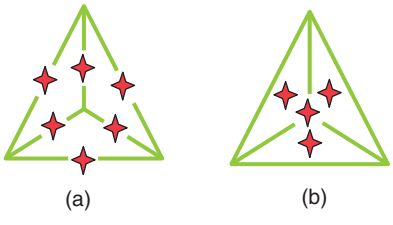

Figure 5.12 Localized bonding schemes of (a) $B_4H_4^{4-}$ and (b) B_4H_4.

between the two approaches is due to the high symmetry of these two deltahedra. In order to get the actual skeletal symmetry, bond order and atomic charges using this localized bonding scheme, a large number of resonance structures have to be considered, which makes this approach more complicated compared to the MO approach [18, 19].

5.4
4*n*+2 Interstitial Electron Rule and Ring-Cap Orbital Overlap Compatibility

The *styx formalism* and the more successful *Wade's rules* for the electronic requirement helped provide a yes/no answer for the existence of polyhedral borane clusters. But one should not overemphasize the importance of electron-counting rules. Molecules satisfying the same rule need not have the same thermodynamic stability. Electron-counting rules can be used as a tool for predicting the existence of molecules, but not for assessing their relative stability. Criteria based on electronic structure theory are required for evaluating the stability of molecules. Qualitative ideas can help in this process as well. The ''ring-cap orbital overlap compatibility'' is one such idea that connects the deltahedral boranes to aromatic hydrocarbons.

Several of the closo polyhedral boranes, $B_mH_m^{2-}$ with $m = 5–7$ can be conceptually fragmented into rings and caps (Figure 5.13). It is assumed that only the π-MOs

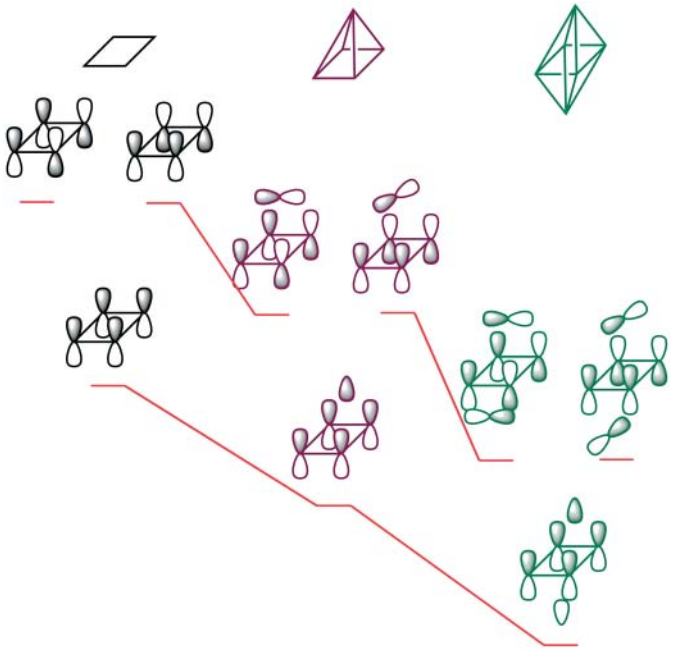

Figure 5.13 Construction of the skeletal MOs of pyramidal borane by the ring–cap interaction.

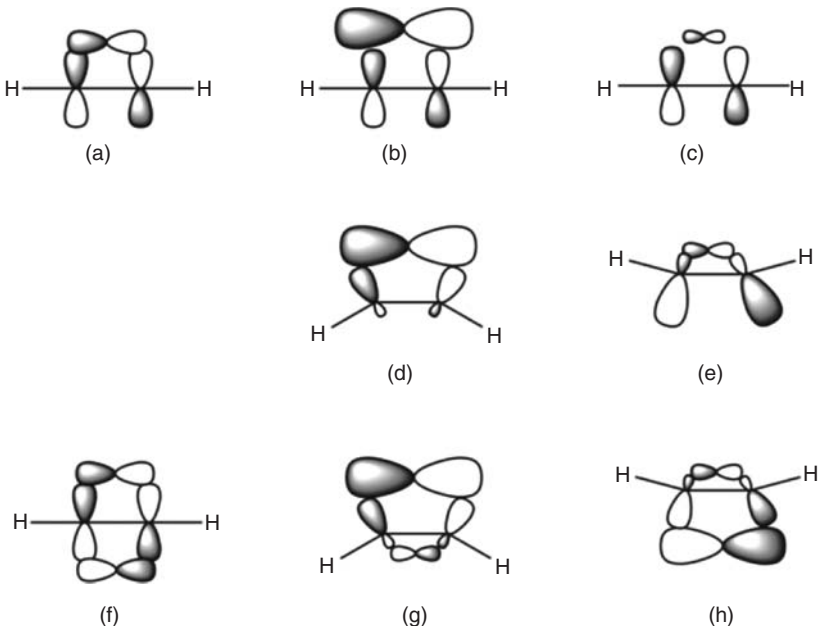

Figure 5.14 (a–h) Ring–cap orbital overlap compatibility and distortion of B–H bonds.

of the ring are involved in the ring-cap bond formation. As the *a* and *e* symmetry of the ring π-MOs are retained even after capping, the electronic requirement will be six; these electrons, which are involved in the ring-cap bond formation, are called *interstitial electrons*. In general, $4n + 2$ (n is an integer) interstitial electrons are necessary for the ring-cap bonding in pyramidal boranes. The fragmentation into rings and caps directly leads to a qualitative criterion to assess the stability of pyramidal boranes, carboranes, heteroboranes, and so on. Polyhedral molecules, where the orbitals of the cap have optimum overlap with the orbitals of the ring (Figure 5.14a), will be more stable. Situations *b* and *c* are unfavorable. The ring orbitals undergo rehybridization, resulting in the bending of ring hydrogen atoms toward or away from the cap to achieve a better overlap (Figure 5.14d, e). For bicapped systems, if one cap is small, the other should be large (Figure 5.14g, h); if one cap is a perfect match, the other also should be for maximum stability (Figure 5.14f) [20, 21].

The relative isomer stabilities of polyhedral carboranes and heteroboranes can be qualitatively explained by the orbital compatibility rule. The relative preferences of BH caps to borocycles of various sizes follow the order $5 > 4 \gg 3 \sim 6$. As the CH cap has a less diffused set of orbitals, the order becomes $4 > 3 > 5 \gg 6$ [22]. The various positional isomers of trigonal bipyramidal $C_2B_3H_5$, octahedral $C_2B_4H_6$ and pentagonal bipyramidal $C_2B_5H_7$ are shown in Figure 5.15. The only known positional isomer of $C_2B_3H_5$ is 1, 5-$C_2B_3H_5$. Both the isomers of $C_2B_4H_6$ are known, while only 2, 3- and 2, 4- isomers are known for $C_2B_5H_7$, carbon cap being incompatible for a five-membered ring. The 1,7-$C_2B_5H_7$ would be very high

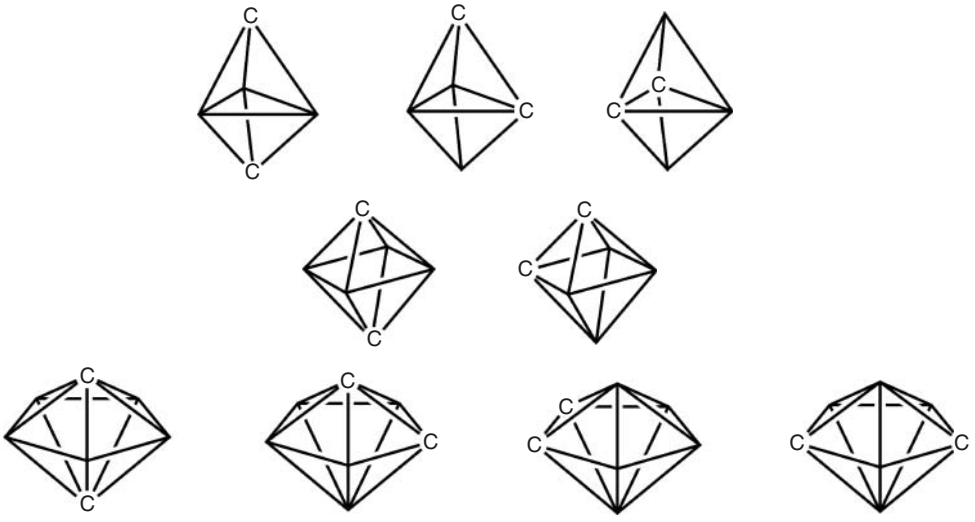

Figure 5.15 Positional isomers of $C_2B_3H_5$, $C_2B_4H_6$, and $C_2B_5H_7$.

in energy. As BH has the least preference to cap a three- or six-membered ring, trigonal bipyramidal $B_5H_5^{2-}$ and hexagonal bipyramidal $B_8H_8^{2-}$ may not exist; $B_8H_8^{2-}$ is known with a bisdisphenoid structure (Figure 5.3). The bipyramidal nature of polyhedral boranes, $B_nH_n^{2-}$, cannot be retained with $n > 7$, as per the rule of orbital compatibility. Although hexagonal bipyramidal borane structure is unknown, it might be possible to stabilize it by replacing the BH caps with relatively larger ones such as BeH, Li, or transition metal fragments [20].

Larger polyhedra can be thought of as being constructed from smaller nido-fragments. For example, icosahedral $B_{12}H_{12}^{2-}$ can be obtained from two pentagonal bipyramids. If the overlap requirements of the individual fragments coincide with that of the polyhedron, the latter must be highly stable. The exohedral BH bonds of the B_5 ring in B_6H_{10} are tilted toward the cap by $\sim 25^0$, in order to achieve better ring-cap overlap (Figure 5.16). The ring hydrogen atoms in icosahedral $B_{12}H_{12}^{2-}$

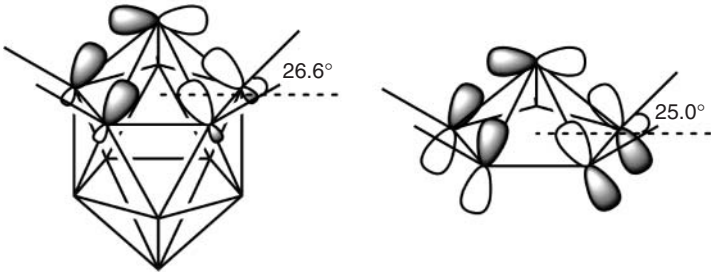

Figure 5.16 $B_{12}H_{12}^{2-}$ and B_6H_{10} (bridging hydrogen atoms of B_6H_{10} are not shown), showing the matching of B–H bond directions.

are bent toward the cap by 26.6° by the symmetry of icosahedron, which is very close to that in pentagonal pyramidal B_6H_{10}. This coincidence of the symmetry-dictated bent angle of icosahedron and that required by a pentagonal pyramidal borane renders $B_{12}H_{12}^{2-}$ exceptionally stable [23].

5.5 Capping Principle

Capping of a triangular face of a polyhedron does not alter the SEP requirement. For example, SEP requirement of nido-square pyramid will be the same as that of the octahedron (Wade's rules) and of the capped square pyramid (capping principle) (Figure 5.17). The retention of the bonding orbitals on capping the open face (square) is already described in the previous section. On the other hand, the situation is different while capping a triangular face. The orbitals of the polyhedron are involved in the intra-polyhedral bonding so that their interaction with the cap orbitals will be very weak. Thus capping cannot generate any new BMO. Capping offers alternate geometries for the same number of SEPs and vertices; with 7 SEPs and 6 vertices both an octahedron and capped square pyramid are possible; yet alternate geometries are known only with transition metal clusters. For example, the $Os_6(CO)_{18}^{2-}$ octahedral structure, which is isolobally similar to $B_6H_6^{2-}$, on protonation give $Os_6(CO)_{18}H^{1-}$ and $Os_6(CO)_{18}H_2$. The former has the H capping a face of the octahedron, whereas the latter assumes a capped square pyramidal geometry, where the two H atoms bridge the open face of the nido structure. Protonation of $B_6H_6^{2-}$ gives $B_6H_7^{1-}$, where H caps an octahedral face, whereas diprotonation to give B_6H_8 ruptures the structure; thus, $B_6H_6^{2-}$ is unstable in strongly acidic solutions. But the rearrangement to capped nido structures should not be generalized to all metal clusters; for example, $Ru_6(CO)_{18}^{2-}$ does not rearrange on protonation. While $Co_3Cp_3B_3H_5$ (CoCp is isolobal to BH) exhibits an octahedral structure, $Ru_3Cp_3B_3H_8$ (RuCp is isolobal to BH^+) exhibits a capped square pyramidal structure, where one BH unit caps a trigonal face formed by the RuCp fragments [24]. This can be attributed to the fact that the open face of a nido structure can accommodate four H atoms compared to a closo structure. In general, it is difficult to say beforehand which geometry will be preferred on protonation as the energy differences are not very large; what can be said is that it

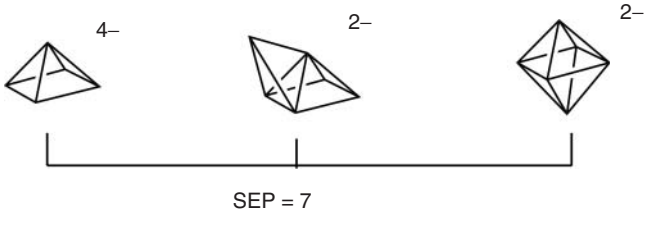

Figure 5.17 Nido, capped-nido, and closo structures with the same SEP.

will be either closo or capped nido. With more number of endo H atoms (>2) , the preference goes to capped nido.

5.6
Electronic Requirement of Condensed Polyhedral Boranes – mno Rule

The first condensed polyhedral borane, $B_{20}H_{16}$ (Figure 5.18) was synthesized in 1963 [25]. It has two icosahedral units condensed via the sharing of four vertices and is a neutral molecule. This contradicted the then prevalent observation that all closo-polyhedral boranes are dianions. A direct application of Wade's rule to $B_{20}H_{16}$ demands a charge of +2 (Wade's rule demands $n+1 = 20+1 = 21$ pairs; 16 BH units provide 16 pairs; 4 shared boron atoms provide 6 pairs; altogether, 22 electron pairs are available). Thus, it became obvious that Wade's rule, which was formulated for monopolyhedral boranes, needs modification to be applicable to condensed polyhedral boranes. Although the synthesis of $B_{20}H_{16}$ was followed by the synthesis of a large number of condensed polyhedral boranes, metallaboranes, carboranes, heteroboranes, and so on, the inability to organize them using an easily applicable electron-counting rule kept them in the background of polyhedral borane chemistry. Figure 5.18 shows some of the well-characterized condensed polyhedral boranes. We have been concerned about the structural chemistry of boron for a long time. A major effort was to find a relationship between the compounds of boron and the allotropes of the element, similar to that exists between benzene and graphite via the Hückel $4n+2$ π electron rule, and CH_4 and diamond via tetracoordinate tetrahedral carbon. The obvious candidate as a building block for boron is $B_{12}H_{12}^{2-}$. The necessity to understand the electronic requirements for condensation of polyhedral boranes became imperative in this context.

Let us begin by discussing the different kinds of exo-polyhedral interactions observed in borane clusters (Figure 5.19). All the structures shown are experimentally known, except D, which is known only with bridging CO or CH_3 instead of

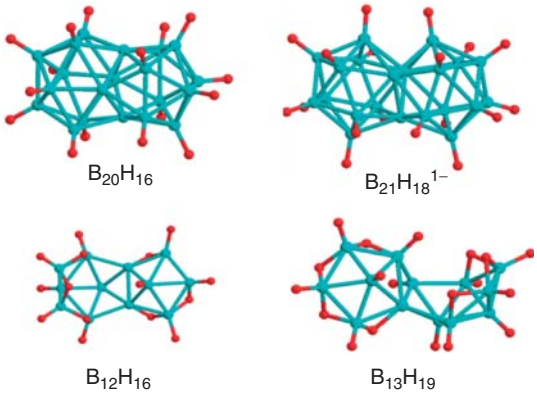

Figure 5.18 Examples of condensed polyhedral boranes.

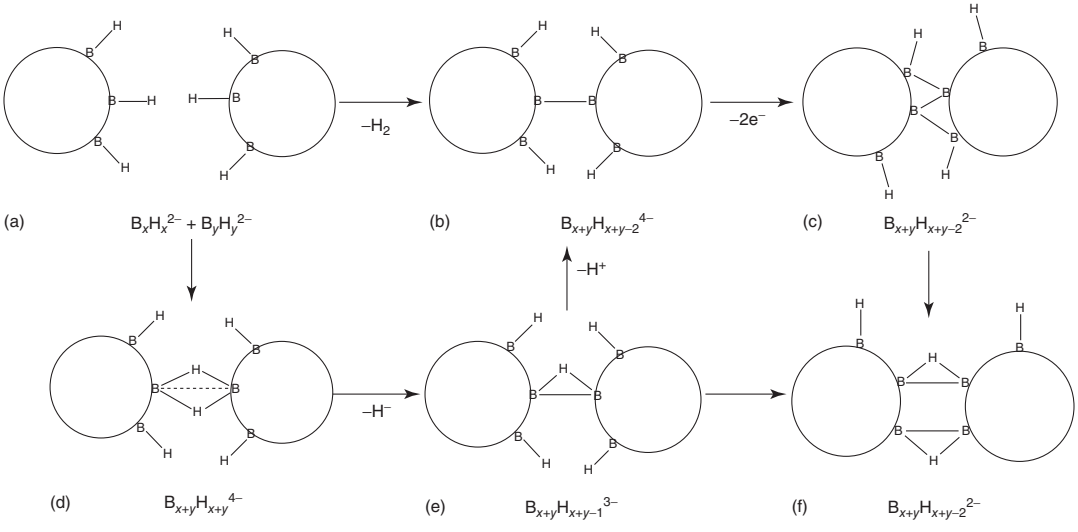

Figure 5.19 (a–f) Exo-polyhedral interactions in polyhedral borane clusters.

bridging H. Although the exo-bonding in D resembles the bonding in diborane, it actually differs in that each boron atom contributes only one *sp* hybrid orbital for the bonding, the rest being used for the intra-polyhedral bond formation. As a result, two of the four electrons, donated by two boron atoms and two bridging hydrogen atoms, occupy any of the unstable levels shown in Figure 5.20a. Replacing the interacting boron atoms with transition metals or replacing the bridging H atoms with CO or CH_3 can stabilize structure D, as the *d* orbitals of transition metals, π* of CO and pseudo-π* of CH_3 can bring down one of the unstable levels to the bonding region (Figure 5.20b) [26].

Exo-polyhedral interactions (Figure 5.19) do not affect the skeletal bonding in individual monomeric units and hence Wade's rules can still be applied. These macro-polyhedral boranes where Wade's rule is applicable can be called *connected polyhedral boranes*, in contrast to *condensed polyhedral boranes* in which the monomeric units share one or more boron vertices and do not obey Wade's rule. In order to be applicable to condensed polyhedral boranes as well, Wade's rule can be extended by incorporating a new variable, *m*, corresponding to the number of polyhedra. In Wade's *n*+1+*p* rule, 1 is added to include the core BMO. If *m* closo clusters condense to form a condensed polyhedral borane, there will be *m* core BMOs. Thus, the *n*+1+*p* rule can be modified to $m+n+p$, where *m* is the number of polyhedra [27–29]. Let us apply the rule to $B_{20}H_{16}$, which is formed by the condensation of two icosahedral units by sharing four vertices (Figure 5.18). Thus, *m*=2; *n*=20; *p*=0; as per $m+n+p$ rule, $B_{20}H_{16}$ requires 22 SEPs. The 16 BH units in $B_{20}H_{16}$ provide 16 pairs; 4 shared boron atoms provide 6 pairs; altogether, 22 pairs are available, which is exactly what the $m+n+p$ rule demands. This explains why $B_{20}H_{16}$ exists as a neutral species. The bis-nido-$B_{12}H_{16}$ (Figure 5.18) is formed by the edge-sharing condensation of nido-B_8 unit and nido-B_6 unit. Here, *m*=2; *n*=12; *p*=2; thus, 16 SEPs are required for stability. Ten BH units provide 10 pairs. Two shared boron atoms provide three pairs. Six bridging H atoms provide three pairs. Altogether, there are 16 pairs so that $B_{12}H_{16}$ is electron sufficient as per the $m+n+p$ rule. Another bis-nido-polyhedron, $B_{13}H_{19}$ is formed by the condensation of nido-B_9 unit and nido-B_6 unit. Here, *m*=2; *n*=13; *p*=2. Thus, the $m+n+p$ rule demands 17 SEPs. Twelve BH units provide 12 pairs; the shared boron atom without exohedral bond provides 1.5 pairs; 7 bridging hydrogen atoms provide 3.5 pairs; altogether, there are 17 pairs that make it electron sufficient. Closo $B_{21}H_{18}^{1-}$ (Figure 5.18) is formed by the face-sharing condensation of two icosahedral units. As per the $m+n+p$ rule, $B_{21}H_{18}$ needs 23 SEPs, whereas only 22.5 are available. This indicates that it should exist with a negative charge. This prediction, first made in 2000, was proved by its synthesis in 2007 [27, 30]. Bis-arachno-edge-sharing systems reveal the equivalence of the $m+n+p$ rule to Hückel 4*n*+2 rule. This is illustrated in Figure 5.21 with the hypothetical hexagonal bipyramid, $B_8H_8^{2-}$ as the monopolyhedral unit. The condensation followed by the removal of four caps results in the boron equivalent of naphthalene, $B_{10}H_8^{-10}$ [31].

Yet another condensation mode, namely, single-vertex-sharing condensation, which leads to sandwich-type structures, is unknown with boron-only skeleton, whereas structures where the shared atom is a larger main group atom or transition

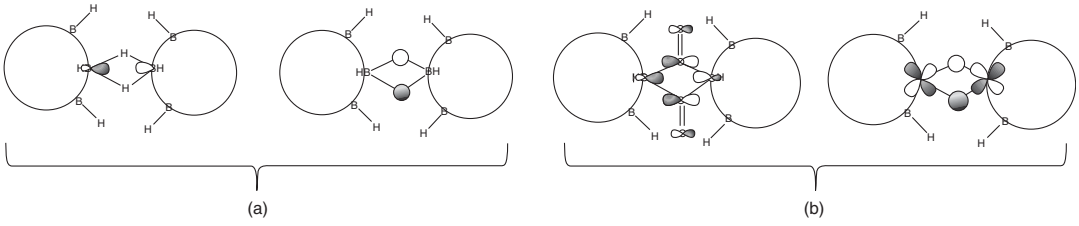

Figure 5.20 (a) Unfavorable exo-polyhedral interactions and (b) ways to make them favorable.

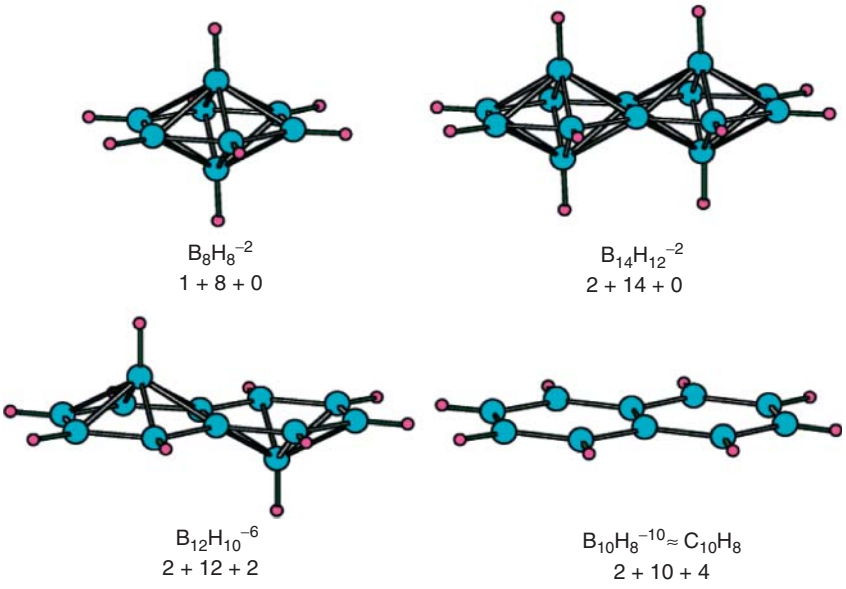

Figure 5.21 Equivalence of Huckel $4n+2$ pi electron rule and the mno rule; Hückel $4n+2$ rule can be viewed as a special case of the mno rule.

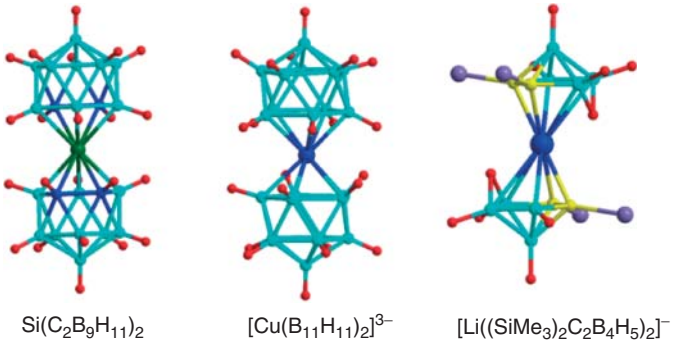

Figure 5.22 Single-vertex-shared polyhedral clusters.

metal atom are known largely in metallaborane-chemistry (Figure 5.22). This mode of condensation is a special case, where the two subclusters need to satisfy Wade's rule separately. Consider a closo single-vertex-shared condensed polyhedral borane. Let a and b be the number of vertices of each subcluster including the shared atom; the first cage requires $a+1$ and the second cage requires $b+1$ SEPs. Summing up, $a+b+m$ SEPs are required; but $a+b=n+1$ (as the common vertex has been counted twice), where n is the total number of vertices; one can be replaced by zero, the number of single-vertex-sharing condensations. Thus, the

rule can be modified to $m+n+o$ to include single-vertex-shared condensations as well. This rule is commonly known as the mno rule. The mno rule can be extended to incorporate the nido- and arachno- clusters and also to include the consequence of capping. *Thus, the skeletal electronic requirement of condensed polyhedral clusters is m+n+o+p−q, where m = number of polyhedra; n = number of vertices; o= number of single-vertex condensations; p = number of missing vertices; q = number of caps* [28].

Consider $Si(C_2B_9H_{11})_2$ (Figure 5.22); here, $m = 2$; $n = 23$; o=1; thus, according to the mno rule, it requires 26 SEPs. Eighteen BH units provide 18 pairs; 4 CH units provide 6 pairs; Si provide 2 pairs; thus, a total of 26 pairs that satisfies the mno requirement are available. In $Cu(B_{11}H_{11})_2^{3-}$, the mno requirement of 26 SEPs is satisfied by 22 pairs provided by 22 BH units, 2.5 pairs provided by Cu, and 1.5 pairs provided by three negative charges. In $[Li((SiMe_3)_2C_2B_4H_5)_2]^{1-}$, the mno rule requires 16 SEPs (2 + 13 + 1). Four $C(SiMe_3)$ units provide six pairs; eight BH units provide eight pairs; Li and the one negative charge provide one pair; two bridging H atoms provide one pair. Altogether, there are 16 pairs available, which satisfies the mno rule. The generalized $m+n+o+p-q$ rule can be applied to metallocenes as well, by considering them as bis-nido-single-vertex-shared condensations. For example, consider ferrocene; the SEP requirement as per $m+n+o+p-q$ rule is $2+11+1+2-0 = 16$ pairs. This is satisfied by the 15 pairs provided by 10 CH units and one pair provided by Fe. Subtracting the 10 C–C σ-bonding MOs from this (in metallocenes, it is assumed that only the π-MOs of the ligand are involved in M–L bonding) and then including the three pairs of electrons of Fe (occupying metal-like a_{1g} and e_{2g} orbitals) will lead to 18 electrons – this shows the equivalence of $m+n+o+p-q$ rule to 18-electron rule. Thus, a molecular orbital explanation for mno rule for single-vertex-shared condensations can be obtained analogous to metallocenes (Figure 5.23). While using mno rule, for single-vertex-shared condensations, one should know how many electrons the central atom will contribute toward skeletal bonding. This can be understood from the MO diagram shown (Figure 5.23). The metal-like orbitals, a_{1g} and e_{2g} (circled levels, Figure 5.23) need 6 electrons altogether, and does not contribute much to the skeletal bonding; the remaining electrons of the metal, which occupy the ligand-like orbitals can be considered as the contribution of the metal for skeletal bonding. In the case of ferrocene, the six electrons of Fe fill the three metal orbitals; the remaining two electrons of Fe and 10π electrons from two C_5H_5 fragments occupy the six ligand-like orbitals (levels shown inside the box). Thus, Fe is a two-electron donor in sandwich complexes. *In general, a transition metal with n VEs will donate n−6 electrons for skeletal bonding*. A main group central atom donates all its electrons. Figure 5.23 is valid with a main group central atom as well, as the major skeletal bonding MOs (shown in the box) remains the same, although the stabilization of the e_{1g} level due to *d* orbital overlap is lost.

The MO scheme shown in Figure 5.23 also explains the existence of the so-called slipped sandwich complexes. Occupancy in the e_{1g}* MO results in the build-up of antibonding interaction between the ring and the metal atom, which could be alleviated by the slipping of the ligands (Figure 5.24). For example, consider

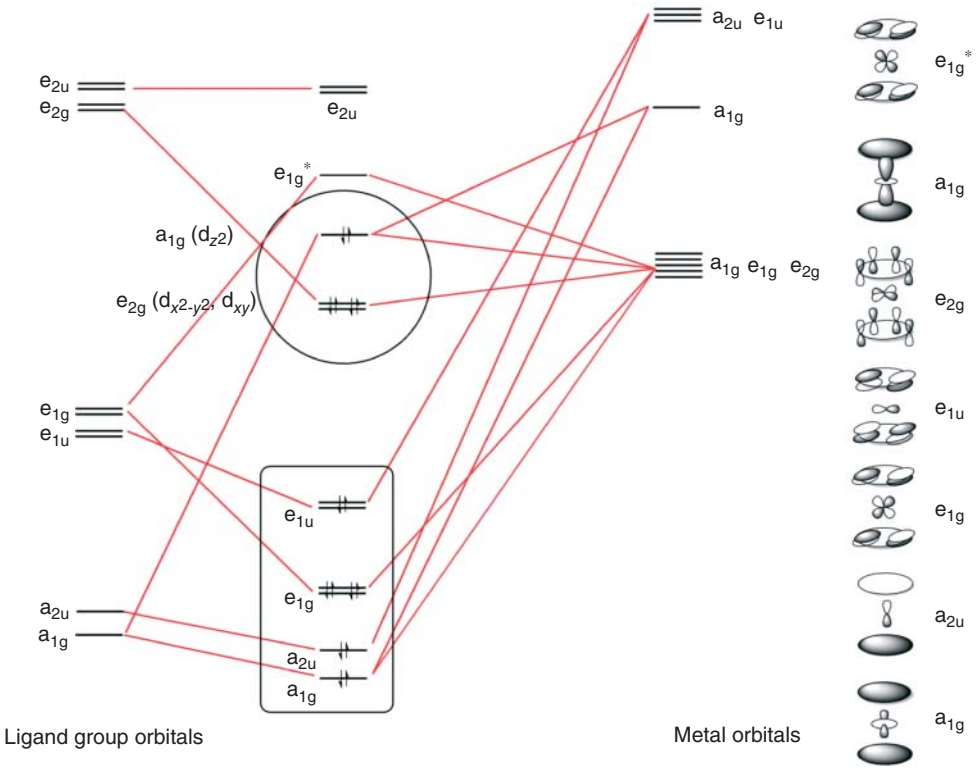

Figure 5.23 MO diagram for sandwich complexes.

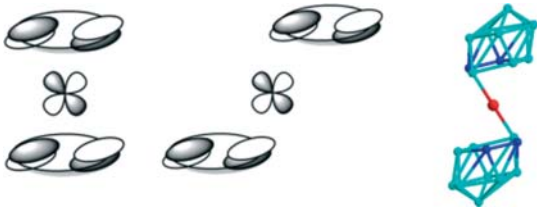

Figure 5.24 Slipped sandwich complex; slipping reduces the antibonding interactions when more electrons than needed are present.

$Cu(C_2B_9H_{11})_2^{1-}$; here, the mno rule demands $2+23+1=26$ pairs, whereas 27 are available. The extra two electrons will occupy the e_{1g}* MO and, as expected, Jahn–Tellar distortion takes place, reducing the antibonding interactions [32].

The generating formula, including charges for condensed polyhedral boranes, depends on the type of condensation involved. Figure 5.25 shows the variation of charge requirements as a function of increasing condensation. Each shared boron

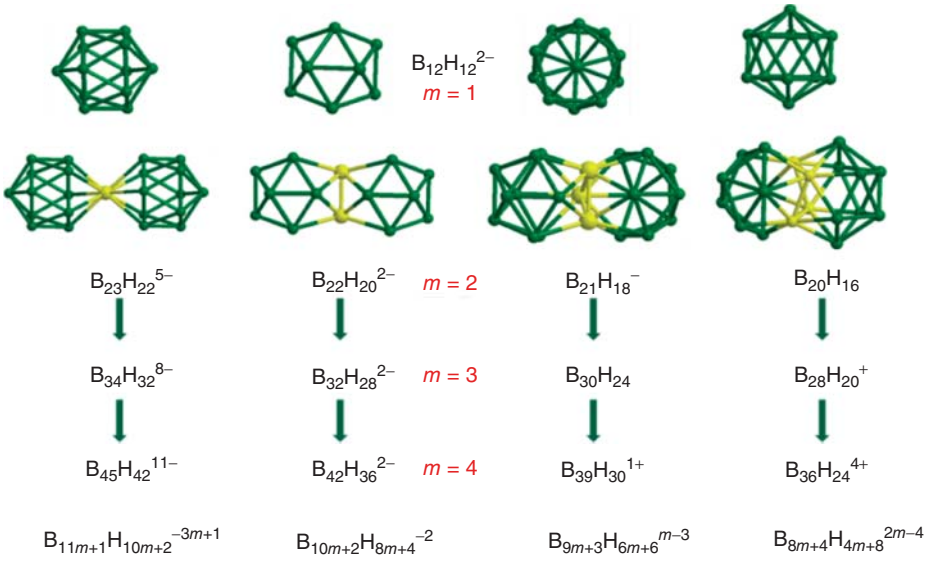

Figure 5.25 Generic formulae for variation of charge with increasing condensation for icosahedra.

atom contributes one electron extra to the skeletal bonding compared to BH units. In the edge-shared condensation, the 2e requirement of each cage (to fill the core MO of each cage) is satisfied by the two extra electrons provided by the shared atoms and by the two negative charges. Thus, charge requirement of edge-shared systems remains constant with the increase in condensation. *Thus, dianionic closo boranes condense to form dianionic condensed polyhedral borane; this is analogous to the condensation of neutral benzene units to form neutral graphene.* Extended boron-rich solids formed via edge-sharing condensation are known. MgB_4 is an example of nido-edge-sharing condensation (Figure 5.26). The electronic requirement of the

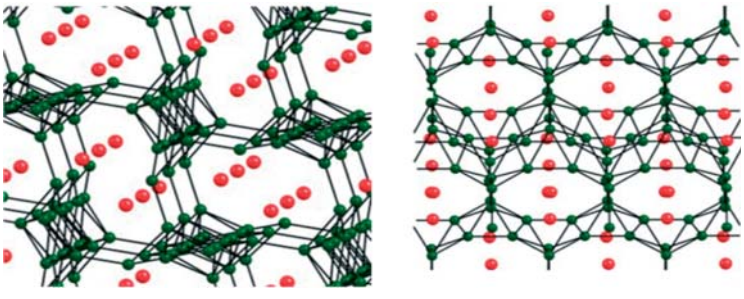

Figure 5.26 Extended structure based on edge-shared condensation.

boron network is satisfied by the Mg atoms present. In face-sharing condensation, 2e requirement of each cage is satisfied by the three extra electrons provided by the shared boron atoms and by the one negative charge. Each further face-sharing adds one positive charge. In four-vertex sharing, the 2e requirement of each cage is satisfied by the four extra electrons provided by the sharing atoms. Thus, this mode of condensation results in a neutral structure and each further condensation adds two positive charges. In single-vertex-sharing condensation, $n+1$ surface BMOs are formed. Two electrons from each of the n vertices will contribute to the n surface BMOs. The extra one electron from the shared atom will half-fill the (n+1)th surface BMO. Thus, to completely fill the (n+1)th surface BMO and the two core BMOs, five extra electrons are required. Each successive condensation will add three negative charges. Thus, all condensations except edge sharing results in charge accumulation [31].

5.7
Factors Affecting the Stability of Condensed Polyhedral Clusters

5.7.1
Exo-polyhedral Interactions

Single-vertex-sharing condensation constitutes an example where the exohedral interactions destabilize the system to such an extent that it violates the mno rule. When the shared atom is a small main group atom such as boron, the antibonding interactions between the ring-fragment orbitals in the e_{1g} MO raises its energy from the bonding region to the antibonding region. As a result, four electrons have to be removed from the system, resulting in a charge of −1 instead of −5. The antibonding interactions can be alleviated by replacing the shared boron with larger atoms such as Al, Ga, and so on, as this increases the distance between the two rings. It is clear from Figure 5.27 that the exohedral hydrogen atoms on both sides of the shared atom are so close to each other that steric destabilization might arise. Replacing the shared atom by larger atoms can minimize the steric interaction as this will also result in the bending of the ring-hydrogen atoms away from the shared atom as per the rule of orbital compatibility. The only known boron-only single-vertex-shared system is formed from two trigonal bipyramids; this is present as part of β-rhombohedral boron. In other single-vertex-shared systems known, the shared atom is either a larger main group atom or a transition metal. It could be seen that the exohydrogens across the shared atom are so close in the closo edge-shared icosahedral system as well. This can be reduced by the removal of vertices to give bis-nido or arachno or nido-arachno systems; all known edge-shared systems belong to this category (Figure 5.18). The closo-icosahedral face-shared system, $B_{21}H_{18}^{1-}$ is known experimentally. The crystal structure shows an elongation of B−B bonds across the shared face, so that the destabilizing steric interactions are minimized. These interactions are negligible in the case of 4-vertex-shared condensation, closo $B_{20}H_{16}$ being the well-known example. The

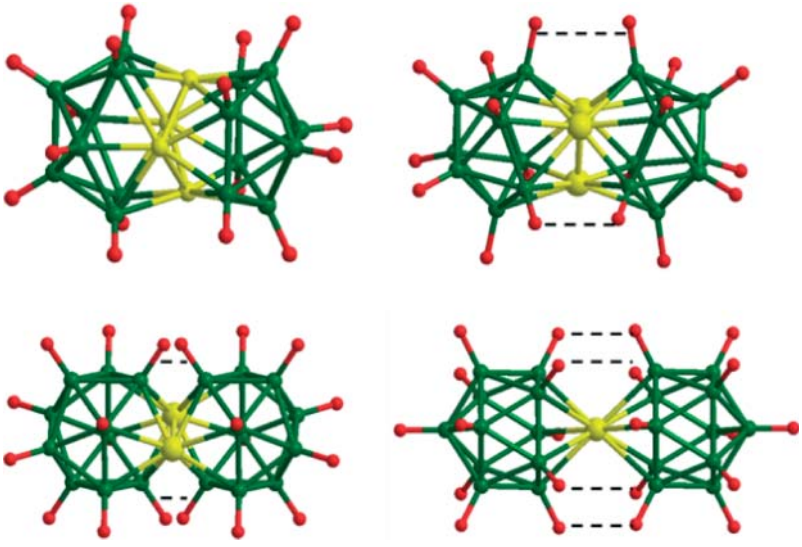

Figure 5.27 Exo-polyhedral destabilizing interactions (indicated by dotted lines) in condensed icosahedral structures.

extent of these interactions depend on the the nature of the polyhedra as well as on the nature of the shared atoms. The interaction can even be stabilizing in some cases. Thus, it is difficult to generalize the effect of exohedral interactions on the stability of condensed polyhedral clusters [33].

5.7.2 Orbital Compatibility

Orbital compatibility plays a major role in deciding the stability of condensed polyhedral boranes, especially in the case of face-shared and four-vertex-shared systems. A larger cluster will have frontier orbitals that are less diffused so that they prefer to form part of a smaller cluster. Similarly, a smaller cluster has frontier orbitals with large spread and hence can be a constituent of a larger cluster efficiently (Figure 5.28). Macropolyhedral clusters can adopt different structures; orbital compatibilty is one of the several factors that determine the relative stability. The stability for the face-shared condensed polyhedral systems follows the order closo(12)-closo(7) > closo(11)-closo(8) > closo(10)-closo(9) and is an example of the effect of orbital compatibility in deciding the relative stability [34, 35]. Steric factors and inherent stability of the subunits are also other factors that affect the relative stability. Energetics of the following isodesmic equation (Eq. (5.1)) involving triangular face-shared condensation can be a good indication of the preference of the larger cluster to condence with smaller (Table 5.1).

$$\text{closo}(n_1) - \text{closo}(n_1) + \text{closo}(n_2) - \text{closo}(n_2) \rightarrow 2\,\text{closo}(n_1) - \text{closo}(n_2) \qquad (5.1)$$

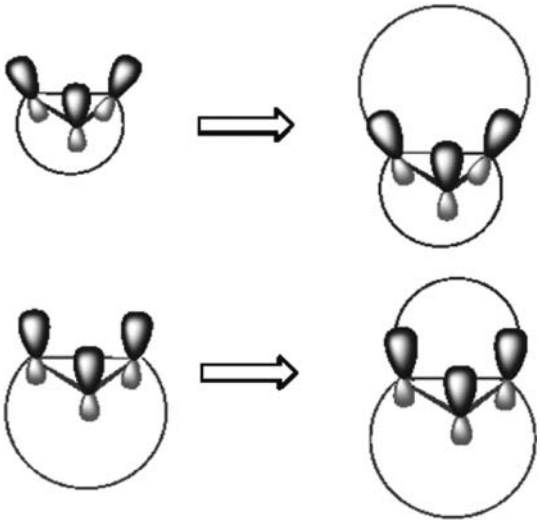

Figure 5.28 Orbital compatibility: indicates preference of the larger cluster to condense with the smaller ones.

Table 5.1 Reaction energies (ΔH in kcal/mol) of Eq. (5.1) at the B3LYP/6-31g* level of theory.

n_1	n_2 5	6	7	8	9	10	11	12
5	0	—	—	—	—	—	—	—
6	−8.6	0	—	—	—	—	—	—
7	1.2	−7.1	0	—	—	—	—	—
8	−17.8	−1.8	7.7	0	—	—	—	—
9	−18.7	−23.8	6.9	7.9	0	—	—	—
10	−31.6	−55.3	−17.6	−5.9	0.9	0	—	—
11	−26.7	−33.6	−10.5	−2.9	8.3	−2.5	0	v
12	−50.5	−68.8	−36.3	−13.1	−21.2	−17.7	3.1	0

5.8 Hypoelectronic Metallaboranes

The adherence of the large number of polyhedral boranes, metallaboranes, and heteroboranes to the set of electron-counting rules was a triumph. Later, chemistry witnessed the advent of a series of electron-deficient metallaboranes, in relation to the electron-sufficient ones that follow the mno rule, with geometries that differ

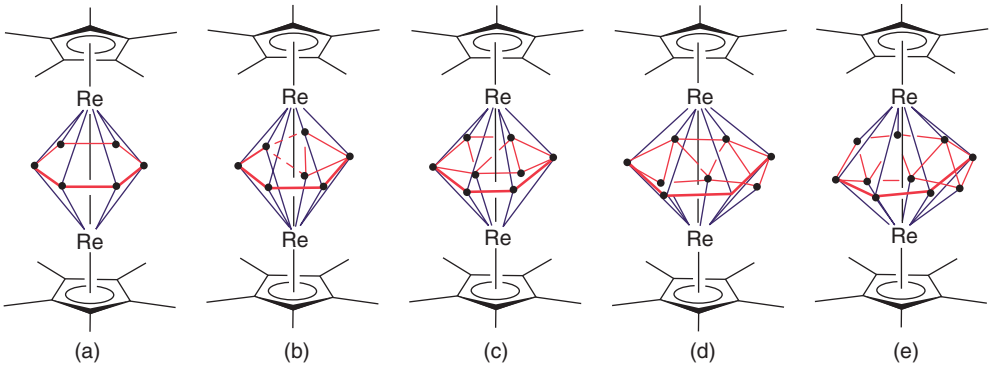

Figure 5.29 (a–e) Homologous series of hypoelectronic rhenaboranes.

from the canonical most spherical polyhedra of borane cages. These so-called hypoelectronic species are characterized by high coordination of the metal and cross-cage metal–metal bonding. A homologous series of such clusters of Rhenium are shown in Figure 5.29. According to the mno rule, $m + n + o + p$ (3+18+2+2=25) electron pairs are required for $(C_5Me_5Re)_2B_6H_6$. The actual electron count available is only 22 electron pairs, where Re donates 1 electron each to the polyhedral skeletal bonding. Thus, $(C_5Me_5Re)_2B_6H_6$ is deficient by three pairs of electrons as per the mno rule. The cross cage bonding can compensate one pair; still there is a deficiency of two pairs. How can clusters with such high electron deficiency exist? This question is answered by a comparison of the MOs with those of the triple-decker sandwich complexes (Figure 5.30). Triple-decker complexes with only five-membered-ring decks require 24 electron pairs $(3 + 17 + 2 + 2)$ as per the mno rule. When we subtract the σ-bonding MOs of the ligand, it comes to nine pairs. Triple-decker complexes are known to obey a 30 VE rule. If we subtract the six pairs of nonbonding electrons from two metal atoms it becomes nine. Thus, the mno rule coincides with the 30 VE rule. (VE count includes the electrons donated by the decks (π-electrons) and the electrons in the metal. For example, in $(C_5Me_5)_3Ru_2^+$, the three $C_5Me_5^-$ ligands will donate a total of 18 electrons; two Ru^{2+} possess total 12 electrons; thus, VE = 18 + 12 = 30). When the middle deck has a large diameter, the two metal atoms come close to each other and hence e_2' gets destabilized by interaction with the σ-orbitals of the middle deck. The decreased M–M distance destabilizes a_2', which is antibonding between the two metal atoms. The pushing up of e_2' and a_2' into the antibonding regions decreases the electron requirement by three pairs. This is why $(C_5Me_5Re)_2B_6H_6$ with SEP count (22 SEP), which is less than the mno count (25 SEP), is stable. By choosing different metal-ligand combinations, one can have different VE counts possible for triple decker complexes, electronic requirement being a function of several variables [36–40].

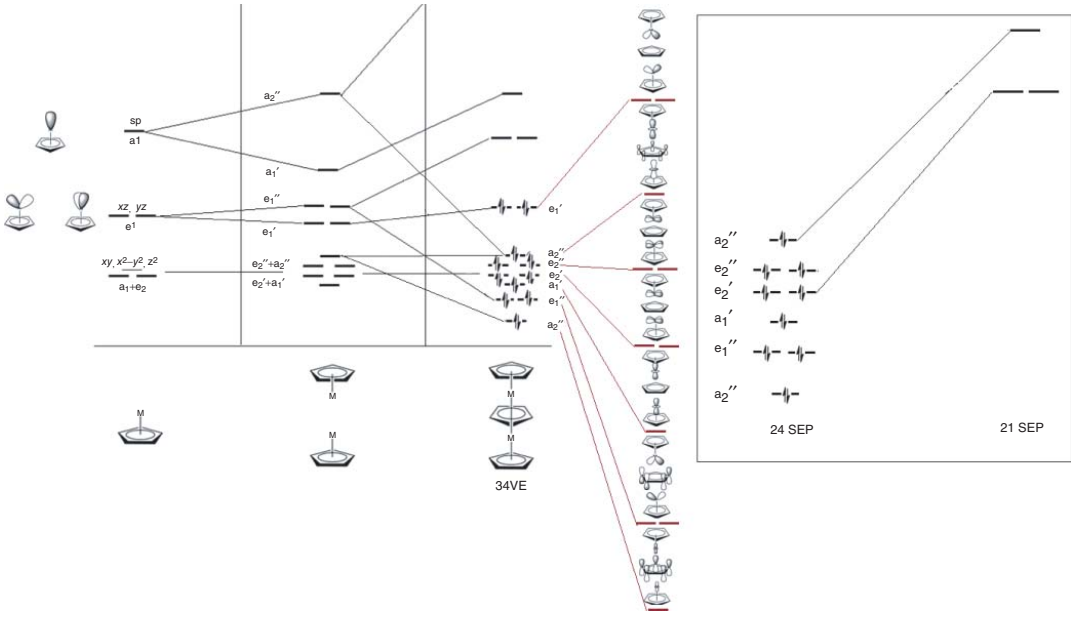

Figure 5.30 MO diagram of triple-decker sandwich complexes. Orbitals that get destabilized with large-ring-middle-deck are shown in the box.

5.9
Electronic Structure of Elemental Boron and Boron-Rich Metal Borides – Application of Electron-Counting Rules

The propensity of boron to form polyhedral structures is reflected also in the structures of elemental boron and boron-rich metal borides. In hydrocarbon chemistry, benzene is characterized by its extra stability; the thermodynamically most stable allotrope of carbon, namely, graphite is formed by the condensation of benzene units. This beautiful relationship between compounds and allotropes exists in boron chemistry as well, where the stable allotropes of elemental boron and many of the boron-rich metal borides are made up of icosahedral subunits. The understanding of the electronic structure and hence the properties of these complex structures is largely simplified by the electron-counting rules. In fact, it is this long-standing quest for understanding that brought us to study the electron-counting rules. This is explained in detail with some examples in the following section.

5.9.1
α-Rhombohedral Boron

Although the number of allotropes known for elemental boron is 16, the structure of most of them remains ambiguous. α- rhombohedral boron and β-rhombohedral boron are the two allotropic forms with unambiguous crystal structure and electronic structure [41]. The unit cell of α-boron is a B_{12} unit (Figure 5.31). Each boron atom can provide one electron for exohedral bonding. The red-labeled boron atoms

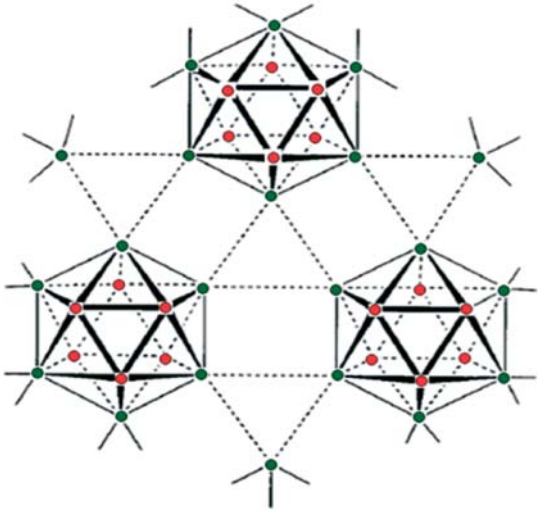

Figure 5.31 Bonding in α-rhombohedral boron. Triangles formed by dotted lines connecting the green spheres indicate 3c-2e bonds.

form exohedral 2c-2e bonds with neighboring B_{12} units. The green-labeled boron atoms form 3c-2e bonds with neighboring B_{12} units. Each green-labeled boron atom uses one-third of an electron pair to form the three-center bond. Altogether, the six green-labeled boron atoms of each B_{12} unit use $6*(2/3) = 4$ electrons for the exohedral 3c-2e bonding, leaving two electrons available for the skeletal bonding, thereby making each B_{12} unit electron sufficient.

5.9.2 β-Rhombohedral Boron

The exploration of the structure of β-rhombohedral boron began in the 1950s; the crystal structure is complicated by disorders in the form of interstitial atoms and partial occupancies [42–44]. Theoretical studies on the idealized unit cell containing 105 boron atoms have revealed electron deficiency, pointing to a metallic character, which is contradictory to the experimental observation that it is a semiconductor [45]. Let us develop the structure in a systematic way. The overriding structural element here is also the icosahedral B_{12} unit.

The large structural fragment (B_{84}) of the unit cell in the β-rhombohedral boron begins with an inner B_{12} (Figure 5.32a). Each boron atom of the inner B_{12} unit is attached exohedrally to 12 other boron atoms (marked red), which constitutes the second B_{12} unit. Each boron atom of the outer B_{12} unit is connected to a pentagon, thereby constituting an outer shell of $12*5 = 60$ boron atoms (Figure 5.32c). The 12 pentagonal pyramids on the surface of B_{84} can be classified into two sets, the first set consisting of the blue pyramids and the second set consisting of the yellow pyramids (Figure 5.33a). The first set of B_6 pyramids are juxtaposed with six B_{84} units in the rhombohedral directions to complete six B_{12} units. The yellow pyramids are linked to a B_{10} unit (dark red spheres). Two more yellow pyramids from two other B_{84} units are also linked to the same B_{10} unit, thereby constituting a B_{28} unit (Figure 5.33b). The B_{28} unit is connected to a boron atom, which is

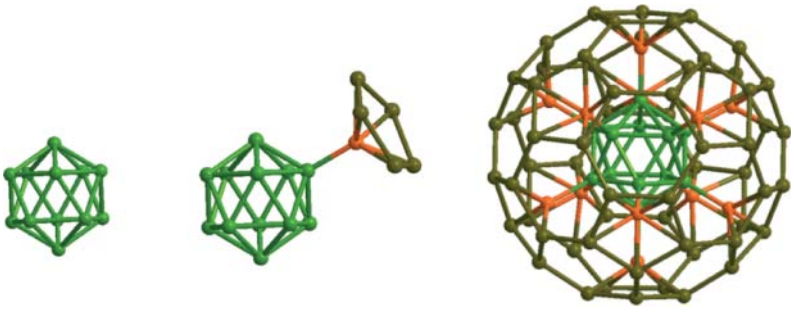

Figure 5.32 (a) Icosahedron; (b) icosahedron with one vertex connected to pentagonal pyramid; (c) icosahedron with all vertices connected to pentagonal pyramid to form the B_{84} unit.

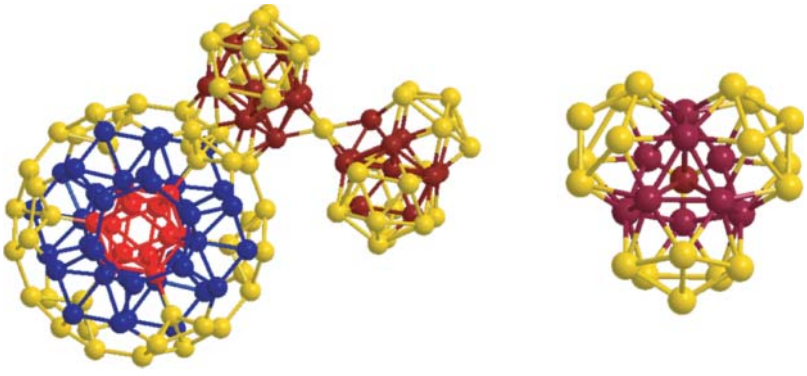

Figure 5.33 (a) B_{84} unit attached with B_{10} unit (dark red spheres), which is part of B_{57}; (b) B_{28} unit.

connected to another B_{28} unit to form $B_{28}-B-B_{28} = B_{57}$ unit(Figure 5.33a). For the sake of an easy electron counting, the B_{105} unit cell can be fragmented into a B_{57} and B_{48}, the latter being composed of the inner B_{12} unit (red spheres) and the six blue B_6 pyramids of B_{84} ($6*B_6 + B_{12}$) (Figure 5.33a).

As the pyramids in the B_{48} fragment complete icosahedron in the extended structure, the electronic requirement of each pyramid is one electron. The central B_{12} unit requires two electrons. Thus, the total electronic requirement of the B_{48} fragment is $6*1+2 = 8$ electrons. The B_{57} fragment is formed by the condensation of six icosahedra (each B_{28} unit consists of three icosahedra (Figure 5.33b) and two trigonal bipyramids. The latter is shown by blue spheres in Figure 5.34. According to the mno rule, 66 electron pairs are required; 67.5 electrons are available. Thus, B_{57} has three electrons excess. In fact our attention to the requirement of an electron-counting rule for boranes was initially drawn by the necessity of finding

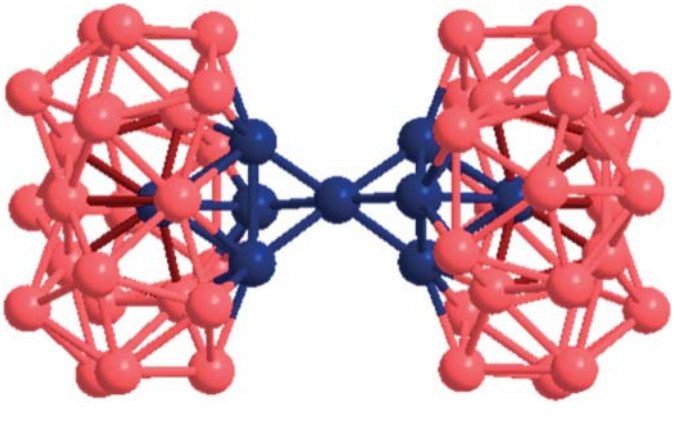

Figure 5.34 B_{57} unit; blue spheres indicates single-vertex-shared trigonal bipyramids.

out the electron requirement of the B_{57} unit. Summarizing, the B_{48} fragment requires eight electrons and B_{57} fragment has three electrons excess. Thus, the idealized unit cell B_{105} is deficient by five electrons. This is the reason for the calculated band structure. Obviously, there is more to the problem.

Careful analysis of the X-Ray diffraction data indicates that the refinement is better with a unit cell of 106.66 boron atoms. The extra 1.66 boron atoms provide the five electrons (1.66×3) requirement of the allotrop. This would still involve the charge separation in the solid, a B57 unit with three positive charges and a segment of the B_{48} part with three negative charges. Nature does not prefer a charge separation. Further analysis of the diffraction data showed that the refinement is better when the B_{57} part has one atom less. This is logical as the B_{56} unit (as opposed to the B_{57} unit) does not need the +3 charge any more. The boron atom missing is from the trigonal B_3 ring of the trigonal bipyramid (Figure 5.34). The eight electron requirement of the B_{48} fragment is satisfied by the presence of four interstitial boron sites per unit cell, having total percentage occupancy equal to 38.8, 44.0, 47.8 in three different samples. Each site being sixfold, these percentages translate into 7, 8, and 8.5 electrons((38.8/100)*6*3), not far from the necessary 8 electrons, which is almost equal to 2.66 boron atoms. *The real unit cell should then contain* $105-1+2.66=106.66$ *boron atoms (* $4B_{12}+B_{28}-B-B_{27}+2.66B$*), which is close to the experimental result* [46]. As the β-boron crystal structure consists of voids too large to accommodate foreign atoms, the requirement of eight electrons in B_{104} ($B_{56}+B_{48}$) can be met by doping. For example, eight Li atoms can satisfy this requirement, thereby leading to the structure Li_8B_{104} or LiB_{13}, which is an already known example in literature with a β-rhombohedral structure [47]. Similarly, various compositions of Fe-doped β-boron are known, but the maximum solubility corresponds to the composition $FeB_{26.6}$ correspoding to approximately Fe_4B_{104}. This is in agreement with the electronic requirement described so far, as four Fe atoms donate 8 electrons (at this composition of large Fe concentration, Fe exists as Fe^{2+}) [48–52]. By using different foreign atoms in different combinations to satisfy the electronic requirement of B_{104}, it is possible to have a large variety of borides. Several of them are synthesized; the structures awaiting are infinite.

5.9.3
Alkali Metal-Indium Clusters

The mno rule can be applied to other clusters as well. Only a few examples are given here. Three alkali–metal–indium clusters, namely, (1) $K_{34}In_{92.30}Li_{12.70}$, (2) $K_{14}Na_{20}In_{91.82}Li_{13.18}$, and (iii) $K_{14}Na_{20}In_{96.30}$ were synthesized and characterized by Corbett *et al* in 2004 [53]. These are the first examples containing triply fused indium icosahedra, In_{28}. Electronic requirement of the In–Li framework is satisfied by the alkali metal atoms that surround the framework clusters. The structure of (1) and (2) contains $In_{28}-In-In_{28}$ units as in the case of β-rhombohedral boron (Figure 5.35a); (3) has $In_{28}-In-In-In_{28}$ unit instead (Figure 5.35b). In the refined structures of (1) and (2), the unit cell has nine 12-bonded icosahedral $In_{10.9}Li_{1.1}$, which requires $9\ (12+26)=342$ electrons, where 12 electrons are required for exohedral bonding

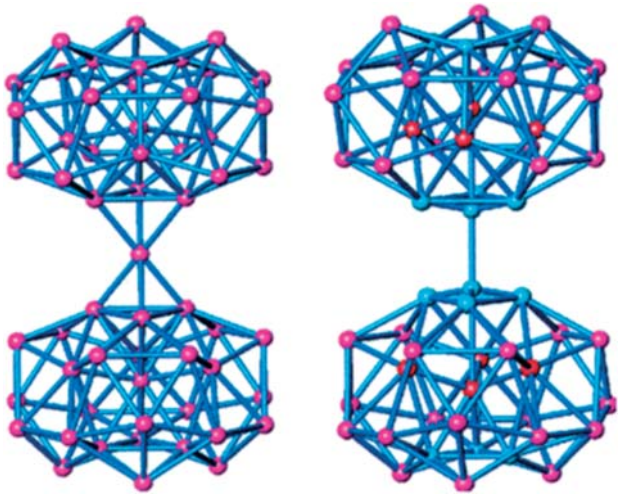

Figure 5.35 (a) $In_{28}-In-In_{28}$, (b) $In_{28}-In-In-In_{28}$.

and 26 electrons (13 pairs) for the skeletal bonding; three 12-bonded icosahedral In_{12}, which requires 3 (12 + 26) = 114 electrons; three 36-bonded $In_{47.6}Li_{9.4}$ (similar to B_{57} in β-rhombohedral boron), which requires 3 (132 + 36) = 504 electrons *as per the mno rule*. Thus, (1) and (2) require 960 electrons. The experimental average of the electrons available for (1) and (2) is 969.4, implying a metallic character; in fact, these clusters are metallic. The electron count for the ideal defect-free $A_{34}In_{105}$ is 1047 electrons (A = Na, K). But this would place electrons in strongly antibonding states. This problem is solved either by doping with electron poorer atoms such as Li as in the case of (1) and (2) or by the fractional occupancies as in the case of (3). The refined structure of (3) has 968.7 electrons. This is quite close to that of (1) and (2). *There is a distinct minimum in the DOS (density of states) of the ideal* In_{105}^{34-} *at ~7.4 eV corresponding to 960 electrons, which is in agreement with the predictions based on electron-counting rules.*

5.9.4
Electronic Structure of $Mg_{\sim 5}B_{44}$

A new type of magnesium boride, $Mg_{\sim 5}B_{44}$, was synthesized and characterized by Hillebrecht *et al* in 2010 [54]. The unit cell contains four B_{19+1} and eight B_{12} units. The eight B_{12} units require 8 pairs of electrons. The B_{19} fragment is a bis-nido-face-shared polyhedral structure and is connected to a unique boron atom via two 2c-2e bonds (Figure 5.36). According to the mno rule, B_{19} fragment requires 23 electron pairs (19 + 2 + 2); the unique boron atom needs 4 electrons to have four 2c-2e bonds with four icosahedra. Thus, B_{19+1} fragment needs 25 pairs of electrons; as 22 pairs are available, each B_{19+1} unit requires 3 more pairs of electrons. Thus, the

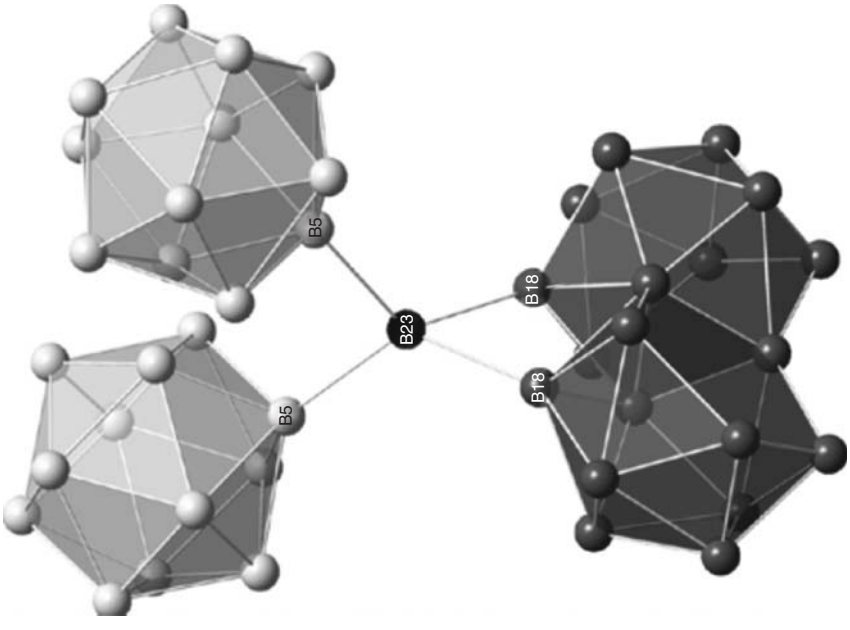

Figure 5.36 B_{19+1} unit attached to two icosahedral units.

total electronic requirement per unit cell is $4*3+8=20$ pairs, which are satisfied by 20 Mg atoms.

5.10 Conclusion

Structure-electron count relationship is a powerful tool to understand and predict the structure and electronic properties of molecules and solids. An electron-counting rule, similar to the Hückel $4n+2$ rule, which connects benenoid aromatics to graphene, is developed for taking icosahedral $B_{12}H_{12}^{-2}$ through polycondensation to beta-rhombohedral boron. This mno rule brings macropolyhedral boranes and metallaboranes, boron-rich metal borides, polyhedral metal clusters, and polymetallocenes under the same umbrella. A large number of metal borides and other intermetallics have been synthesized so far; the structure and composition of many of them are quite ambiguous. Their chemistry is complicated by partial occupancies and vacancies. The mno rule proved to be very useful to understand these complex structures. It turns out that the partial occupancies and vacancies envisaged as structural defects in solids requires major concern, because these defects may be necessary for electron sufficiency and hence stability. Many compositions of boron carbides or metal borides or intermetallics can be predicted on the basis of elecron-counting rules, but the experimental realization of these is an emerging challenge. Blind application of electron-counting rules should be

avoided, as the rules are the results of a generalization based on existing facts. Diborane apparently violated the 2c-2e bonding concept. But this led to expansion of bonding: the concept of 3c-2e bond evolved. The condensed molecule $B_{20}H_{16}$ did not obey Wade's rule; then came the mno rule. The hypoelectronic metallaboranes seemed to violate all bonding concepts; but then it turned out that it is possible to explain their bonding in relation with triple-decker sandwich complexes. While following the electron-counting rules, one should keep in mind that the rules are not rigid, as they may change depending on several variables, known and unknown. A proper understanding of these variables is necessary for the efficient application of the existing rules and also for the development of an improved set of rules. The story is far from complete. The two recent experimental studies of the relative stability of alpha- versus beta-rhombohedral boron gave conflicting results [55, 56] The inherent complexity resulting from the infinite possibilities keep the structural chemistry of boron ever exciting and evolving.

References

1. Mulliken, R.S. (1947) The structure of diborane and related molecules. *Chem. Rev.*, **41** (2), 207–217.
2. Walsh, A.D. (1947) 21. Co-ordinate links formed by bonding electrons: a suggestion regarding the structure of diborane. *J. Chem. Soc.*(Resumed), 89–92.
3. Hedberg, K. and Christensen, B. (1951) Additions and corrections-a reinvestigation of the structures of diborane and ethane by electron diffraction. *J. Am. Chem. Soc.*, **73** (12), 5929–5929.
4. Grimes, R.N. (2011) *Carboranes*, Academic Press, New York.
5. King, R.B. (2001) Three-dimensional aromaticity in polyhedral boranes and related molecules. *Chem. Rev.*, **101** (5), 1119–1152.
6. Allard, G. (1932) X-ray study of some borides. *Bull. Soc. Chim. Fr.*, **51**, 1213.
7. Pauling, L. and Weinbaum, S. (1943) *Z. Kristallogr.*, **87**, 181.
8. Wade, K. (1971) The structural significance of the number of skeletal bonding electron-pairs in carboranes, the higher boranes and borane anions, and various transition-metal carbonyl cluster compounds. *J. Chem. Soc., D: Chem. Commun.*, (15), 792–793.
9. Wade, K. (1972) Skeletal electron counting in cluster species. Some generalisations and predictions. *Inorg. Nucl. Chem. Lett.*, **8** (6), 559–562.
10. Rudolph, R.W. and Pretzer, W.R. (1972) Hueckel-type rules and the systematization of borane and heteroborane chemistry. *Inorg. Chem.*, **11** (8), 1974–1978.
11. Rudolph, R.W. (1976) Boranes and heteroboranes: a paradigm for the electron requirements of clusters? *Acc. Chem. Res.*, **9** (12), 446–452.
12. Wade, K. (2003) Evolving patterns in boron cluster chemistry. *Pure Appl. Chem.*, **75**, 1315–1323.
13. Bowser, J.R. *et al.* (1979) Nickel-boron ''hybrid'' clusters. Synthesis of polyhedral nickelaboranes and nickelacarboranes from small borane and carborane anions. Crystal structure of (.eta.5-C5H5)4Ni4B4H4. *J. Am. Chem. Soc.*, **101** (21), 6229–6236.
14. O'Neill, M.E. and Wade, K. (1983) Relationships between interatomic distances and electron numbers for D3h tricapped trigonal prismatic 9-atom cluster systems. *Polyhedron*, **2** (9), 963–966.
15. O'Neill, M.E. and Wade, K. (1983) Closo clusters with unusual electron numbers: the significance of frontier orbital degeneracies and bonding characteristics. *J. Mol. Struct. (THEOCHEM)*, **103**, 259–268.
16. O'Neill, M.E. and Wade, K. (1984) Closo clusters with unusual electron numbers: localized bond schemes for

n-atom clusters with n, (n + 1) or (n + 2) skeletal electron pairs. *Polyhedron*, **3** (2), 199–212.
17. Eberhardt, W.H., Crawford, B., and Lipscomb, W.N. (1954) The valence structure of the boron hydrides. *J. Chem. Phys.*, **22** (6), 989–1001.
18. Grenda, S.C. (1989) An alternate method of determining styx values and their utility. *J. Chem. Educ.*, **66** (8), 639.
19. Dikshit, S.K. and Singh, R. (1992) Semitopological representation of electronic structure of complex boron hydrides and ions using styx numbers. *J. Chem. Educ.*, **69** (4), 274.
20. Jemmis, E.D. (1982) Overlap control and stability of polyhedral molecules. Closo-Carboranes. *J. Am. Chem. Soc.*, **104** (25), 7017–7020.
21. Jemmis, E.D. and Schleyer, P.v.R. (1982) Aromaticity in three dimensions. 4. Influence of orbital compatibility on the geometry and stability of capped annulene rings with six interstitial electrons. *J. Am. Chem. Soc.*, **104** (18), 4781–4788.
22. Jemmis, E.D., Jayasree, E.G., and Parameswaran, P. (2006) Hypercarbons in polyhedral structures. *Chem. Soc. Rev.*, **35** (2), 157–168.
23. Pathak, B. *et al.* (2006) Reversal of stability on metalation of pentagonal-bipyramidal (1-MB6H72-, 1-M-2-CB5H71-, and 1-M-2,4-C2B4H7) and Icosahedral (1-MB11H122-, 1-M-2-CB10H121-, and 1-M-2,4-C2B9H12) Boranes (M = Al, Ga, In, and Tl): energetics of condensation and relationship to binuclear metallocenes. *J. Am. Chem. Soc.*, **128** (33), 10915–10922.
24. Fehlner, T.P. (2002) A systematic approach to the varied roles of transition metals in metallaborane chemistry. *Proc. Indian Natl. Sci. Acad.*, **68**, 579–596.
25. Dobrott, R.D., Friedman, L.B., and Lipscomb, W.N. (1964) Molecular and crystal structure of B[sub 20]H[sub 16]. *J. Chem. Phys.*, **40** (3), 866–872.
26. Gaines, D.F. *et al.* (1978) The chemistry of beryllaboranes. Characterization and reactions of beryllium bis(tetrahydroborate), Be(BH4)2, and beryllium bis(octahydrotriborate), Be(B3H8)2. *Inorg. Chem.*, **17** (6), 1516–1522.
27. Balakrishnarajan, M.M. and Jemmis, E.D. (2000) Electronic requirements of polycondensed polyhedral boranes. *J. Am. Chem. Soc.*, **122** (18), 4516–4517.
28. Jemmis, E.D., Balakrishnarajan, M.M., and Pancharatna, P.D. (2001) A unifying electron-counting rule for macropolyhedral boranes, metallaboranes, and metallocenes. *J. Am. Chem. Soc.*, **123** (18), 4313–4323.
29. Jemmis, E.D., Balakrishnarajan, M.M., and Pancharatna, P.D. (2001) Electronic requirements for macropolyhedral boranes. *Chem. Rev.*, **102** (1), 93–144.
30. Bernhardt, E. *et al.* (2007) Closo-[B21H18]−: a face-fused diicosahedral borate ion. *Angew. Chem. Int. Ed.*, **46** (16), 2927–2930.
31. Jemmis, E.D. and Jayasree, E.G. (2003) Analogies between boron and carbon. *Acc. Chem. Res.*, **36** (11), 816–824.
32. Mingos, D.M.P. and Forsyth, M.I. (1978) Molecular orbital analysis of the "slip" distortion in electron rich sandwich complexes derived from the 1,2-C2B9H112- ligand. *J. Organomet. Chem.*, **146** (3), C37–C42.
33. Jemmis, E.D. and Pancharatna, P.D. (2003) Condensed polyhedral boranes and analogous organometallic clusters: a molecular orbital and density functional theory study on the cap–cap interactions. *Appl. Organomet. Chem.*, **17** (6-7), 480–492.
34. Shameema, O. and Jemmis, E.D. (2008) Orbital compatibility in the condensation of polyhedral boranes. *Angew. Chem. Int. Ed.*, **47** (30), 5561–5564.
35. Shameema, O. and Jemmis, E.D. (2009) Relative stability of closo-closo, closo-nido, and nido-nido macropolyhedral boranes: the role of orbital compatibility. *Chem. Asian J.*, **4** (8), 1346–1353.
36. Lauher, J.W. *et al.* (1976) Triple-decker sandwiches. *J. Am. Chem. Soc.*, **98** (11), 3219–3224.
37. Jemmis, E.D. and Reddy, A.C. (1988) Electronic structure of triple-decker sandwich compounds with P5, P6, As5, and CnHn as middle rings. *Organometallics*, **7** (7), 1561–1564.
38. Ghosh, S., Beatty, A.M., and Fehlner, T.P. (2001) Synthesis and characterization of bicapped hexagonal

bipyramidal 2,3-Cl2-1,8-{Cp*Re}2B6H4 [{Cp*Re}2{μ-η6:η6-1,2-B6H4Cl2}, Cp* = η5-C5Me5]: the missing link connecting (p − 2) skeletal electron pair hypoelectronic rhenaboranes and 24-valence electron triple-decker complexes. *J. Am. Chem. Soc.*, **123** (37), 9188–9189.

39. Ghosh, S. *et al.* (2001) Synthesis of [(Cp*Re)2BnHn] n=8–10: metal boride particles that stretch the cluster structure paradigms. *Angew. Chem. Int. Ed.*, **40** (6), 1125–1128.
40. Wadepohl, H. (2002) Hypoelectronic dimetallaboranes. *Angew. Chem. Int. Ed.*, **41** (22), 4220–4223.
41. Albert, B. and Hillebrecht, H. (2009) Boron: elementary challenge for experimenters and theoreticians. *Angew. Chem. Int. Ed.*, **48** (46), 8640–8668.
42. Hughes, R.E. *et al.* (1963) The structure of β-rhombohedral boron. *J. Am. Chem. Soc.*, **85** (3), 361–362.
43. Hoard, J.L. *et al.* (1970) The structure analysis of β-rhombohedral boron. *J. Solid State Chem.*, **1** (2), 268–277.
44. Slack, G.A. *et al.* (1988) The crystal structure and density of β-rhombohedral boron. *J. Solid State Chem.*, **76** (1), 52–63.
45. Prasad, D.L.V.K., Balakrishnarajan, M.M., and Jemmis, E.D. (2005) Electronic structure and bonding of β-rhombohedral boron using cluster fragment approach. *Phys. Rev. B*, **72** (19), 195102.
46. Jemmis, E.D. and Balakrishnarajan, M.M. (2001) Polyhedral boranes and elemental boron: direct structural relations and diverse electronic requirements. *J. Am. Chem. Soc.*, **123** (18), 4324–4330.
47. Kobayashi, M. *et al.* (1995) Rietveld analysis of LiB13 with β-rhombohedral boron structure. *J. Alloys Compd.*, **221** (1–2), 120–124.
48. Callmer, B. and Lundström, T. (1976) A single-crystal diffractometry investigation of iron in β-rhombohedral boron. *J. Solid State Chem.*, **17** (1–2), 165–170.
49. Slack, G.A. *et al.* (1988) X-ray study of transition-metal dopants in β-boron. *J. Solid State Chem.*, **76** (1), 64–86.
50. Kazanin, M.M. and Kutasov, V.V. (1989) Fe impurity in α-,β-boron and in some boron compounds. *Phys. Status Solidi (A)*, **113** (1), 143–149.
51. Kuhlmann, U. *et al.* (1992) Influence of interstitially soluted iron on structural, optical and electrical properties of β-rhombohedral boron. *J. Alloys Compd.*, **186** (2), 187–200.
52. Nakayama, T. *et al.* (1997) Mössbauer spectroscopy and electrical conductivity of fe-dopedβ-rhombohedral boron. *J. Solid State Chem.*, **133** (1), 342–346.
53. Li, B. and Corbett, J.D. (2004) Phase stabilization through electronic tuning: electron-poorer alkali-metal–indium compounds with unprecedented In/Li clusters. *J. Am. Chem. Soc.*, **127** (3), 926–932.
54. Pediaditakis, A. *et al.* (2010) Binary boron-rich borides of magnesium: single-crystal investigations and properties of MgB7 and the new boride Mg∼5B44. *Inorg. Chem.*, **49** (23), 10882–10893.
55. Parakhonskiy, G. *et al.* (2011) Experimental pressure-temperature phase diagram of boron: resolving the long-standing enigma. *Sci. Rep.*, **1**, 1–7, article 96.
56. Solozhenko, V.L. and Kurakevych, O.O. (2013) Equilibrium p-T phase diagram of boron: experimental study and thermodynamic analysis. *Sci. Rep.*, **3**, 1–8, article 2351.

6
Bound Triplet Pairs in the Highest Spin States of Monovalent Metal Clusters

David Danovich and Sason Shaik

6.1
Introduction

It has become customary to consider that, with the exception of odd-electron bonding, the chemical bond usually requires electron pairing. However, the emergence of dispersion as an important sticky glue of molecular shape and stability [1] teaches us that weak interactions can bring about substantial bonding energy when the interactions accumulate and involve many atoms (see also Chapter 1 in Vol. 1). This chapter discusses one of these bonding motifs that originates from weak interactions, but is distinct from dispersion and *it involves charge-shift resonance energy that binds triplet pairs*, which in turn resonate throughout the cluster and bring about substantial bonding, reaching 19 kcal mol^{-1} per single atom. This bonding mechanism was referred to as *no-pair ferromagnetic* (NPFM) bonding [2, 3], and was shown to bind high-spin clusters of univalent atoms (Li, Na, Cu, Ag, Au) without even a single electron pair in the valence shell. Two of these beautiful clusters of gold, $^{9}Au_8$ and lithium, $^{11}Li_{10}$, are displayed in Figure 6.1. This bonding type and its underlying factors is the topic of this chapter.

Except for the intellectual interest in the nature of the bonding that generates such beautiful clusters, some no-pair clusters have actually been probed by experimental techniques. Thus, laser-induced photoassociation spectroscopy of the triplet lithium, sodium, potassium, rubidium, and cesium dimers showed a weakly bound $^{3}\Sigma_u^+$ state [4]. In fact, there exists spectroscopic evidence also for the no-pair alkali trimer species ($^{4}A'$), $^{4}Li_3$, $^{4}Na_3$, and $^{4}K_3$ [5, 6]. But not only alkali clusters, copper seems also capable of this form of bonding, as may be deduced from the characterization of the $^{3}\Sigma_u^+$ state of $^{3}Cu_2$ [7]. As such, some no-pair clusters exist and are real entities. This enriches the scope of chemical bonding and forms a strong incentive to investigate the origins of the bonding interactions, which reach 19 kcal mol^{-1} per atom without any electron pairing.

Before venturing into this topic, it is important to stress that these high-spin species are excited states, with ground states having the normal electron pair bonding. But, as will be argued later, the maximum spin states can be stabilized by

The Chemical Bond: Chemical Bonding Across the Periodic Table, First Edition.
Edited by Gernot Frenking, Sason Shaik.

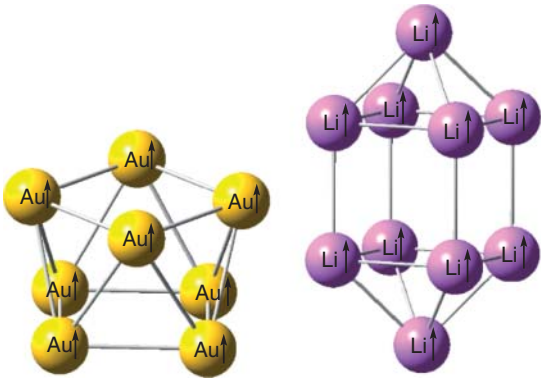

Figure 6.1 Two no-pair ferromagnetic clusters, $^{9}Au_{8}$ and $^{11}Li_{10}$. The superscripts correspond to the 2S+1 spin multiplicity value. The spins illustrate the nature of the ferromagnetic electronic structure.

strong magnetic and electric fields[1)] and become ground states for these clusters. These prospects make the no-pair clusters all the more attractive.

6.2 Can Triplet Pairs Be Bonded?

Consider the ferromagnetic pair in H↑↑H, namely, the $\sigma^1\sigma^{*1}$ state of H_2 (referred to also as $^3\Sigma_u^+$). Figure 6.2 shows the energy curves for the ground state and the no-pair $^3\Sigma_u^+$ state. It is seen that while the ground state, where an electron pair exists, is strongly bound, the ferromagnetic state is repulsive and the ratio $\Delta E_{ST}/D_e = 2.44$ tells us that the triplet repulsion is much larger than the bonding interaction ($D_e = 104\,\text{kcal mol}^{-1}$).

Near these energy curves, we show the structure of the $\pi^1\pi^{*1}$ ferromagnetic state of ethylene ($^3B_{1u}$). It is seen that the triplet state assumes a perpendicular structure that relieves the triplet repulsion in the ferromagnetic state. So, it seems that ferromagnetic pairs are normally not bonded. Still, one might wonder whether the ferromagnetic repulsion can ever become ferromagnetic bonding without any external influence.

6.2.1 A Prototypical Bound Triplet Pair in $^3Li_2$

The initial clue, for us, that the answer may indeed be positive concerns the ferromagnetic state Li↑↑Li ($^3\Sigma_u^+$) of Li_2, as shown in Figure 6.3. Thus, early

1) Unpublished results for the electric field effect on the stability of the no-pair copper and gold dimers. For example, in a field of 0.015 a.u., $^3Cu_2$ is stabilized compared to $^1Cu_2$ by ~7 kcal mol^{-1}.

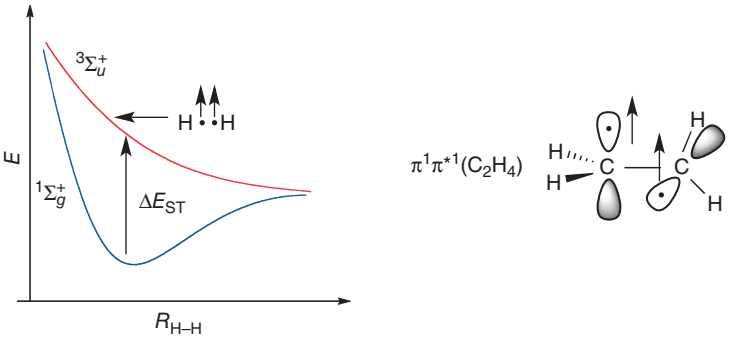

Figure 6.2 Singlet and triplet energy curves (b3p86/aug-cc-pVTZ) for the ground state and the ferromagnetic state H↑↑H ($^3\Sigma_u^+$) of H_2. Also shown is a cartoon of structure of the ππ* state of ethylene (this structure, according to b3lyp/cc-pVTZ, is a local minimum on the potential energy surface).

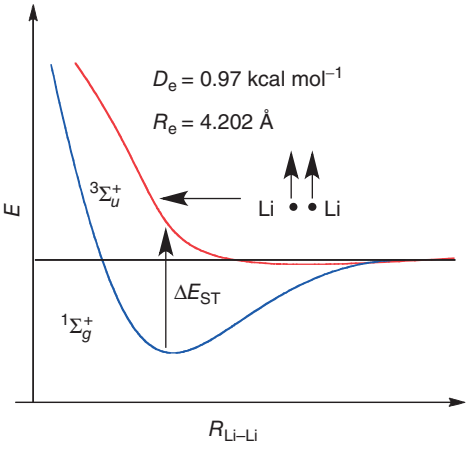

Figure 6.3 Singlet and triplet energy curves for the ground and the ferromagnetic Li↑↑Li ($^3\Sigma_u^+$) states of Li_2, using CCSD/aug-cc-pCVQZ calculations.

calculations (1972 on) [8] showed that the $^3\Sigma_u^+$ state of Li_2 has a very small ratio, $\Delta E_{ST}/D_e \sim 1.24$, and a shallow minimum with a weakly bonded triplet pair, $D_e < 1$ kcal mol^{-1}. Figure 6.3 displays our own calculations. Thus, it seems that ferromagnetic pairs can experience some bonding, albeit weak. Is this a weak van der Waals interaction? As the introduction already reveals, the answer is 'no'! These are not merely weak interactions, but rather results of a new bonding motif that merits articulation and experimental investigation.

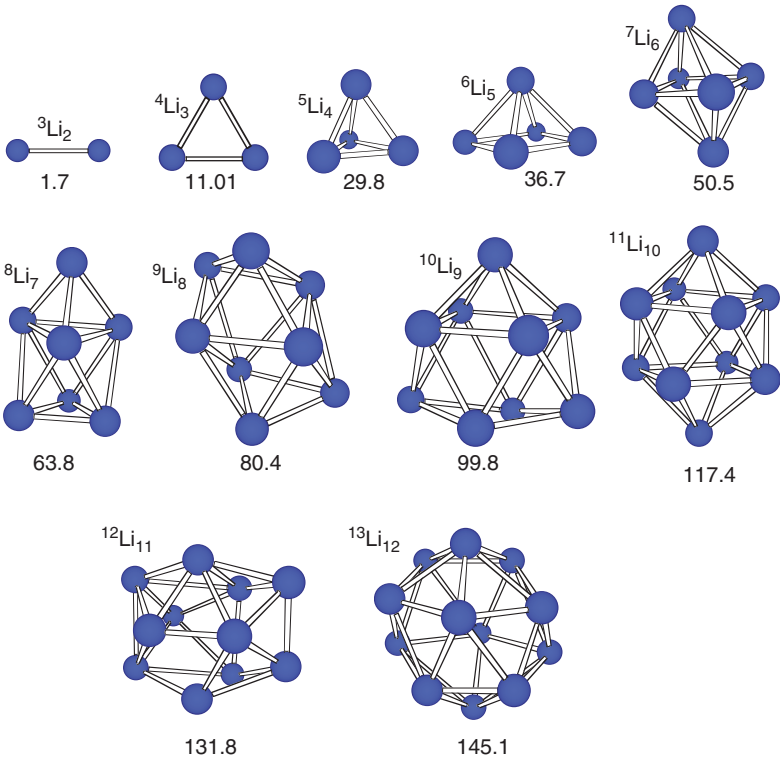

Figure 6.4 NPFM $^{n+1}Li_n$ clusters and their bonding energies (kcal mol^{-1}) calculated with b3p86/cc-pVDZ. (Reproduced with permission from Figure 5 of Ref. [2c].)

6.2.2
The NPFM Bonded Series of $^{n+1}Li_n$ ($n = 2–10$)

Figure 6.4 which shows $^{n+1}Li_n$ clusters calculated by means of density functional theory (DFT) [2a,c] answers these questions unequivocally. Yes, there are many ferromagnetic clusters, with bonding energy that climbs steeply and reaches about 12 kcal mol^{-1} for a single Li atom. Furthermore, these bonding energies were calculated with *standard DFT* (see Appendix 6.A for methods). As such, these are not dispersion interactions because standard DFT methods lack dispersion interactions. It is important therefore to understand the origins of these intriguing interactions.

6.3
Origins of NPFM Bonding in $^{n+1}Li_n$ Clusters

A clear way of deciphering the NPFM bond is by usage of valence bond (VB) theory (see Chapter 5, Vol. 1, for VB methods). This has been done starting 1999 and

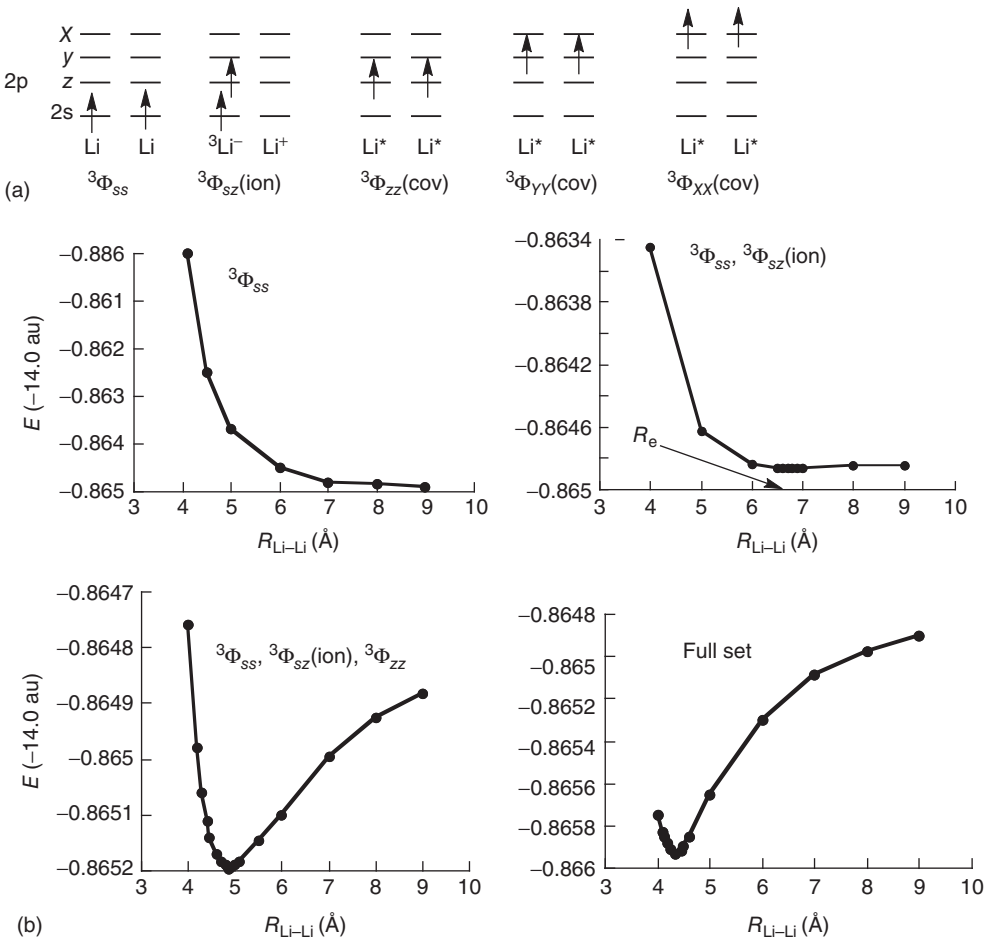

Figure 6.5 NPFM bonding in $^3Li_2$. (a) Fundamental ($^3\Phi_{ss}$) and excited VB structures ($^3\Phi_{sz}$(ion), $^3\Phi_{zz}$(cov) and $^3\Phi_{xx(yy)}$(cov)). z is the Li–Li axis. (b) Breathing orbital valence bond (BOVB) computed (BOVB/cc-pVDZ) energy variation along the Li–Li distance for various VB wave functions. (Reproduced with permission from Figure 3 in Ref. [2a].)

onwards [2a,b,c,d,e,f,g], and the results are in described in Figure 6.5. Figure 6.5a shows all the VB structures that can be generated by distributing the two valence electrons in the valence orbitals. The fundamental configuration is $^3\Phi_{ss}$, which accommodates the two valence electrons in the 2s orbitals of the lithium atoms. The structure labeled as $^3\Phi_{sz}$(ion) is a triplet charge-transfer (CT) structure, wherein one electron is transferred from the 2s orbital of one Li to the $2p_z$ orbital of the second atom; there are two such structures. Finally, $^3\Phi_{zz}$(cov) and $^3\Phi_{xx(yy)}$(cov) are covalent structures, which distribute the valence electrons in the 2p orbitals; the most important being $^3\Phi_{zz}$(cov).

Figure 6.5b shows the breathing orbital valence bond (BOVB) computed energy curves of various state wave functions. The first one on the left-hand side shows the energy of the fundamental structure $^3\Phi_{ss}$ plotted along the Li···Li distance. It is seen that this structure is repulsive, much like the corresponding structure for the FM state of H_2 (Figure 6.2). The second plot shows a linear combination of the fundamental structure with the two triplet ionic structures. It is seen that the addition of $^3\Phi_{sz}$(ion) results in an incipient FMNP bond. Adding the other structures in the third and fourth plots deepens the energy well to its final BOVB value, which is $D_e = 0.639$ with a cc-pVDZ basis set and 0.888 kcal mol^{-1} for cc-pCVTZ; [2a] the CCSD values for the two basis sets are $D_e = 0.738$ and 0.902 kcal mol^{-1}. The agreement of VB with the standard coupled cluster method is satisfactory. The final VB wave function is shown in Eq. (6.1):

$$^3\Psi_{\mathrm{NPFM}}(^3\Sigma_u^+) = 0.909\,^3\Phi_{ss} + 0.029\,^3\Phi_{sz}(\mathrm{ion}) + 0.027\,^3\Phi_{zz} + 0.003\,^3\Phi_{xx(yy)} \qquad (6.1)$$

It is seen that the NPFM bonding of the $^3\Sigma_u^+$ state of Li_2 is dominated by the fundamental structure but exhibits significant mixing of the ionic CT structure and the covalent *zz*-structure (recall, *z* is the Li–Li axis).

6.3.1 Orbital Cartoons for the NPFM Bonding of the $^3\Sigma_u^+$ State of Li_2

To endow the notion of *NPFM bonding* with a qualitative aspect, one may need an orbital picture that is in harmony with the VB model. This can be done by combining the VB structures and rewriting the wave function, in Eq. (6.1), using transformed orbitals that involve hybridization and mixing of the 2s and 2p orbitals (Textbox 6.1) [2a,c]. Figure 6.6 shows the resulting orbital cartoons for various stages of the NPFM-bond wave function (Eq. (6.1)) for the $^3\Sigma_u^+$ state.

Figure 6.6a depicts the orbital cartoon for the fundamental VB structure $^3\Phi_{ss}$, which is repulsive; these are simply the 2s orbitals of the two Li atoms having parallel-spin electrons. By adding the $^3\Phi_{zz}$(cov) structure with an appropriate coefficient, we can rewrite the two-structure wave function in terms of two new VB structures, wherein each Li possess hybridized 2s–2p_z orbitals (Textbox 6.1) [2a,c]. Figure 6.6b shows a cartoon of this wave function, which is seen to involve a resonating mixture of two structures with orbitals that are hybrids of the 2s, and 2p_z atomic orbitals (AOs) on the same center. It is seen that in each one of the structures in Figure 6.6b, the triplet pair of electrons occupy an *in–out* or an *out–in* pair of hybrids, such that the average distance of the electron pair increases. Thus, in addition to the resonance energy that $^3\Phi_{zz}$(cov) brings by combining with the fundamental structure, it mitigates also the triplet repulsion of the electron pair in the 2s orbitals of the $^3\Phi_{ss}$ structure. Note that the wave function in Figure 6.6b is antisymmetric with respect to inversion about the center of symmetry in the mid Li···Li distance, it has *u* symmetry, and the overall state assignment is $^3\Sigma_u^+$ (see Appendix 6.B). Finally, we can add the ionic CT structures, $^3\Phi_{sz}$(ion), to the *in–out* ⇔ *out–in* resonating wave function. Now, each hybrid will develop a small delocalization tail on the other atom, as shown in Figure 6.6c, which depicts one

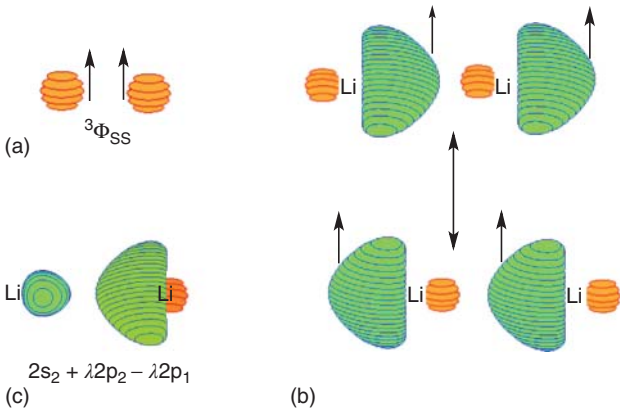

Figure 6.6 Orbital cartoons for the $^3\Sigma_u^+$ state using the VB wave function in Eq. (6.1): (a) the 2s orbitals in the fundamental structure $^3\Phi_{ss}$. (b) The hybrids for the wave function made from a linear combination of $^3\Phi_{ss}$ and $^3\Phi_{zz}$ resulting in an *in–out* ⇔ *out–in* resonating wave function. (c) A cartoon of a single orbital on the right hand Li atom, after adding also the $^3\Phi_{sz}$(ion) structures. (Reproduced with permission from Scheme 3 in Ref. [2c].)

of the hybrid orbitals, and its corresponding tail on the other atom. Much like in generalized valence bond (GVB) theory [9], the delocalization tail provides the bonding to the wave function. Thus, each VB structure plays a clear physical role in shaping the NPFM bonding of Li_2 in the $^3\Sigma_u^+$ state: the $^3\Phi_{zz}$(cov) structure lowers the Pauli repulsion of the fundamental structure and adds some resonance energy, while $^3\Phi_{sz}$(ion) further adds some charge-shift (CS) covalent-ionic resonance energy that binds the triplet pair.

Textbox 6.1

An orbital picture can be constructed by grouping the linear combination of the VB structures in Eq. (6.1) into a more compact wave function that contains hybridized and semi-localized AOs [2a,c]. The wave function is dominated by the fundamental structure, $^3\Phi_{ss}$, and has smaller but significant contributions of the excited covalent structure $^3\Phi_{zz}$(cov), and the ionic structures, $^3\Phi_{sz}$(ion). The $\Phi_{xx(yy)}$ structures are neglected. To have a better appreciation of the individual effects of $^3\Phi_{zz}$(cov) and $^3\Phi_{sz}$(ion), on the fundamental structure, $^3\Phi_{ss}$, we shall carry out the procedure in two steps:

1) Starting with the combination of $^3\Phi_{ss}$ and $^3\Phi_{zz}$(cov), a wave function, with the proper $^3\Sigma_u^+$ symmetry, can be rewritten as follows (dropping normalization constants in the Slater determinants here and elsewhere):

$$^3\Phi_{ss} + c\,^3\Phi_{zz} = |(2s_1 + \lambda 2p_1)(2s_2 + \lambda 2p_2)| + |(2s_1 - \lambda 2p_1)(2s_2 - \lambda 2p_2)|; \quad c = \lambda^2 \tag{6.T1}$$

The wave function, in Eq. (6.T1) is seen to involve a resonating mixture of two structures with orbitals, which are hybrids of the 2s, and $2p_z$ AOs on the same center. However, these are *in–out* and *out–in* pair of hybrids. This wave function and the hybrid orbitals are depicted (using $c = 0.090$ to accentuate the hybridization in Figure 6.6b).

2) Adding the ionic structures and transforming the orbitals, one obtains the same *in–out* and *out–in* hybrids but each has now a small delocalization tail on the other atom (as shown in Figure 6.6c):

$$^3\Psi_{\mathrm{NPFM}} = |(2s_1 + \lambda 2p_1)(2s_2 + \lambda 2p_2 - \lambda 2p_1)| + |(2s_1 - \lambda 2p_1 + \lambda 2p_2)(2s_2 - \lambda 2p_2)| \quad (6.T2)$$

An alternative representation of *NPFM* bonding was described by McAdon and Goddard [3a], using interstitial orbitals. The two representations are ultimately equivalent [2a,c].

6.4 Generalization of NPFM Bonding in $^{n+1}Li_n$ Clusters

Let us try now to comprehend the intriguing rise in the bonding energy of the NPFM clusters $^{n+1}Li_n$ in Figure 6.4. An additional feature of the clusters in Figure 6.4 is their global geometries, which are different from those of the ground-state Li_n clusters, which are all low-spin species. Thus, starting from the trimer onward, the NPFM clusters form symmetric clusters, having roughly uniform Li···Li distances with high coordination numbers for each Li atom, whereas the ground-state clusters are less symmetric and become three-dimensional at larger clusters. Figure 6.7 displays side-by-side examples of the $^5Li_4$ and $^7Li_6$ NPFM clusters vis-à-vis the singlet ground-state clusters, $^1Li_4$ and $^1Li_6$. It is seen that while $^5Li_4$ is a good symmetric tetrahedron, the ground-state $^1Li_4$ is a flat rhombic structure. Similarly, $^7Li_6$ is a distorted octahedron with bond distances that differ by 0.9 Å, while $^1Li_6$ has two closely lying structures; [10] the less stable one ($\Delta E = 4.6$ kcal mol^{-1} according to B3LYP/aug-cc-pVTZ [10]) is a planar triangular structure, while the most stable one is an anti-prism with bond distances that differ by 1 Å. Our modeling addresses these features of the NPFM clusters.

6.4.1 VB Mixing Diagram Representation of the Bonding in $^3Li_2$

Figure 6.8 shows a VB mixing diagram that describes the bonding in $^3Li_2$. It is seen that $^3\Phi_{ss}$ suffers from Pauli repulsion relative to the two separate Li atoms, indicated in Figure 6.8 as $\delta\varepsilon_{\mathrm{rep}}$. At the same time, the fundamental structure mixes with the excited structures and is stabilized by a mixing energy, ΔE_{mix}, which is a sum of the mixing contributions due to all the excited VB structures.

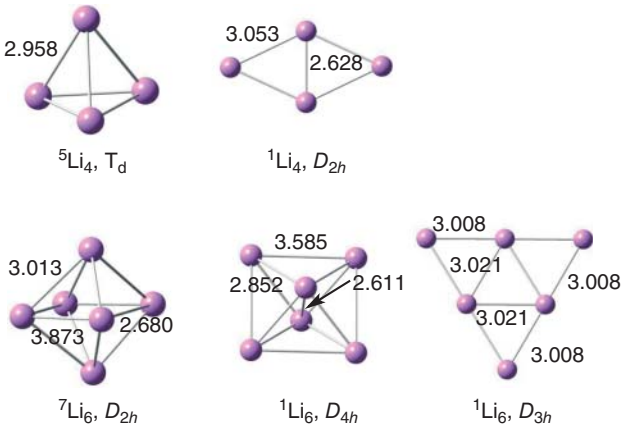

Figure 6.7 Structures and key bond lengths (Å) for the NPFM clusters [2b], $^5Li_4$ and $^7Li_6$ vis-à-vis their ground-state clusters, $^1Li_4$ and $^1Li_6$ [10], calculated with b3p86/cc-pVDZ. (Reproduced with permission from Figure 4 in Ref. [2g].)

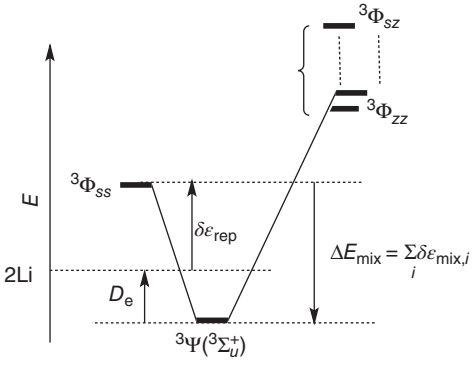

Figure 6.8 A VB-mixing diagram that describes the bonding in $^3Li_2$ as a result of mixing of the excited VB structures into the fundamental structure. $\delta\varepsilon_{rep}$ is the Pauli repulsion energy of $^3\Phi_{ss}$ relative to 2Li at infinity. ΔE_{mix} is the total mixing energy given as a sum of the individual mixing terms, $\Delta E_{mix} = \sum_i \delta\varepsilon_{mix,i}$, due to the various excited configurations. (Reproduced with permission from Figure 7 in Ref. [2g].)

The beauty of VB theory is that all the terms in Figure 6.8 can be quantified. Thus, using the recently produced BOVB/cc-pVDZ results [2a], we get the following quantities, $\delta\varepsilon_{rep} = 1.504\,\text{kcal mol}^{-1}$ and $\Delta E_{mix} = -2.145\,\text{kcal mol}^{-1}$. As the major contributions to the mixing energy (>80%) come from inclusion of the $^3\Phi_{zz}$(cov) configuration and the two ionic ones, $^3\Phi_{sz}$(ion), the average contribution of each to the mixing energy is $\delta\varepsilon_{mix} = -0.714\,\text{kcal mol}^{-1}$. These are all small quantities that can be treated by usage of perturbation theory applied to the fundamental structure.

6.4.2
VB Modeling of $^{n+1}Li_n$ Patterns

Extending the VB mixing paradigm to a general NPFM cluster, $^{n+1}Li_n$, can model the trends that shape the structure and bonding in these clusters. As the mixing terms are all small quantities, the problem can be treated by usage of perturbation theory applied to the fundamental structure. As such, using these quantities, we may extend the VB analysis to model the bonding energy of any cluster size, if we know how to express the balance of Pauli repulsion and mixing for any cluster of any shape.

Thus, as shown in Scheme 6.1, a given $^{n+1}Li_n$ possesses three types of structures. Scheme 6.1a shows the fundamental VB structure, $^{n+1}\Phi_{s(1)s(2)s(3)\ldots s(n)}$, wherein all the electrons reside in the 2s orbitals of the Li atoms in the clusters, having spin up, and hence leading to Pauli repulsion. The other configurations are the triplet 2s–2p ionic types and the 2p–2p covalent types, shown in Schemes 6.1b and 6.1c, respectively. For example, $^{n+1}\Phi_{s(1)p(1)s(3)\ldots s(n)}$ is an ionic structure in which an electron from the 2s orbital of the second Li atom was transferred to the 2p orbital of the first atom. Similarly, $^{n+1}\Phi_{p(1)p(2)s(3)\ldots s(n)}$ is a covalent structure wherein the 2s electrons in the first and second Li atoms were excited into the 2p orbitals.

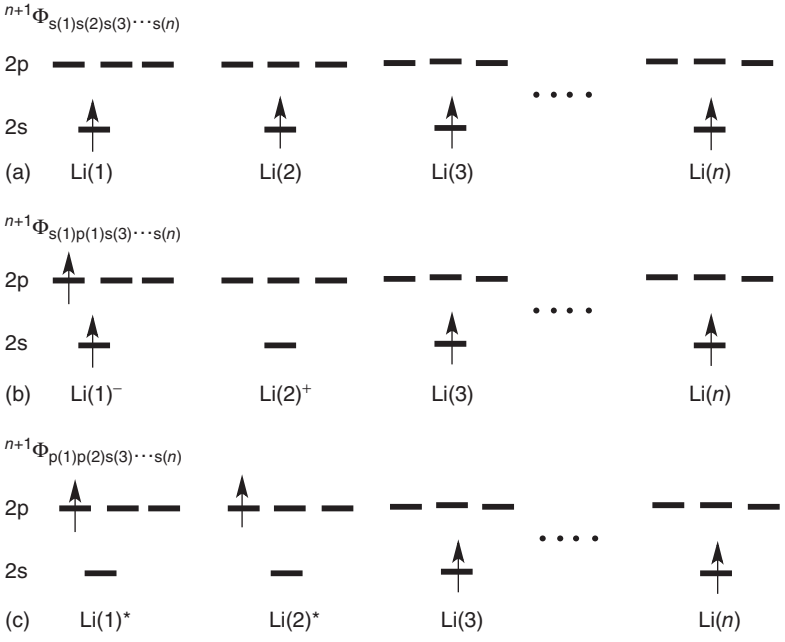

Scheme 6.1 VB configuration types for a general $^{n+1}Li_n$ cluster: (a) the fundamental structure. (b) The ionic structures. (c) The covalent 2p–2p structures.

There are, of course, also poly-ionic and poly-excited covalent structures, which one could have considered for the modeling. However, to this end, we need some simplifying assumptions to avoid the explosion of terms. Therefore, to assess the Pauli repulsion in the fundamental VB structure, we count only the close-neighbor repulsions, such that the total repulsion is a sum of the close-pair repulsion terms. It is easy to show that the sum of such terms is minimized when all the terms are identical. This necessarily means that the NPFM clusters will strive to assume structures with uniform Li···Li distances to minimize the Pauli repulsion. The total repulsive energy can then be expressed as follows:

$$\Delta E_{\text{rep}} = 0.5\delta\varepsilon_{\text{rep}} \sum_j C_j = 0.5\delta\varepsilon_{\text{rep}} C_{\text{tot}} \tag{6.2}$$

The factor 0.5 in Eq. (6.2) avoids the double counting of the pairwise repulsion terms. Thus, the repulsive energy of the fundamental atom is given as one-half of the product of fundamental close-neighbor repulsion ($\delta\varepsilon_{\text{rep}}$) times the sum of the coordination numbers C_j of all the atoms in the cluster, where j is the atom number in the cluster. When the cluster is symmetric, these coordination numbers are identical for all atoms, and the expression is simplified to include the total coordination number of the cluster, C_{tot}.

Turning now to the VB mixing term, ΔE_{mix}, we assume that the main contributions come from the mono-ionic and mono-excited covalent structures in Scheme 6.1. We further assume that each such excited VB structure contributes the same individual mixing term, $\delta\varepsilon_{\text{mix}}$, which can be taken from the above-given $^3Li_2$ calculations. Therefore, the total mixing term is simply $\delta\varepsilon_{\text{mix}}$ multiplied by the number of excited VB structures.

In order to determine the numbers of the excited VB structures, we need the number of valence orbitals in which we can populate the Li electron. This leads to Eq. (6.3), where N_{ao} is the number of the valence orbitals each atom uses to distribute its valence electron. The rest of the terms were already clarified:

$$\Delta E_{\text{mix}} = [0.5(N_{\text{ao}}^2 - 1)C_{\text{tot}} + N_{\text{ao}}]\delta\varepsilon_{\text{mix}} \tag{6.3}$$

The total bond energy is the negatively signed balance between the mixing and repulsive terms, and it becomes:

$$D_{\text{e}}(^{n+1}\text{Li}_n) = -[0.5(N_{\text{ao}}^2 - 1)C_{\text{tot}} + N_{\text{ao}}]\delta\varepsilon_{\text{mix}} - 0.5\delta\varepsilon_{\text{rep}} C_{\text{tot}} \tag{6.4}$$

In using Eq. (6.4), we neglect π-interactions, which are not too important for the dimer, such that each atom in the cluster has $N_{\text{ao}} = 3$, that is, the 2s orbital and two tangential 2p orbitals, which contribute to σ bonding in the NPFM cluster; $N_{\text{ao}} = 2$ for the dimer.

Furthermore, for an infinite cluster size, one can express the bond energy per atom, D_{e}/n, quite simply as:

$$\frac{D_{\text{e}}(^{n+1}\text{Li}_n)}{n} = -4C\delta\varepsilon_{\text{mix}} - 0.5\delta\varepsilon_{\text{rep}} C \quad (n \to \text{infinity}) \tag{6.5}$$

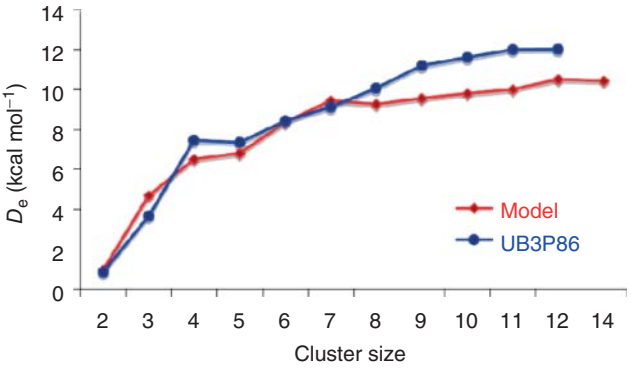

Figure 6.9 Plots of D_e/n values (kcal mol^{-1}) versus the cluster size n in $^{n+1}Li_n$; the blue curve is calculated by b3p86/cc-pVDZ, and the red curve by the VB model Eq. (6.4). (Reproduced with permission from Figure 8 in Ref. [2g].)

Here, C is the coordination number (or the average one) of an atom in the clusters. The rest of the terms are as in Eq. (6.4). This expression shows how the bond energy per atom depends crucially on its coordination number C in the cluster. Equations (6.4) and (6.5) together predict in principle that NPFM clusters will tend to assume structures having maximum coordination numbers that maximize the mixing term. Considering only the repulsive term, one predicts symmetric clusters with uniform bond lengths, which minimizes the repulsion. Deviations from symmetry may well be induced by the mixing terms, which prefer shorter distances. The interplay of repulsion and mixing will strike a balance that may produce nonuniform distances.

Figure 6.9 shows a plot of the bonding energy per atom, D_e/n, against the cluster size n. The blue curve corresponds to the DFT results, while the red one traces the VB modeling based on Eq. (6.4). The VB modeling does quite well. Thus, the VB curve shows the initial jump in the bond energy per atom on going from $n=2$ to $n=4$ (due to the increase in the coordination number for an atom), and then the convergence of the bond energy per atom for a cluster size around $n=10$. The converged VB value is 10.5 versus ~12 kcal mol^{-1} for the DFT calculations [2c].

It is apparent that the simple model captures the computational results: it predicts the propensity for symmetric uniform shapes of the NPFM cluster, based on the minimum Pauli repulsion argument (see preceding text), and the trends in the bonding energy per atom. The bonding energy per atom is cumulative and rising steeply with the coordination number. The same treatment can be applied to all NPFM clusters of the other alkali metals, Na, K, Cs, and Rb. The $^{n+1}Na_n$ clusters have already been investigated [2d], and it was demonstrated that the bonding energies were by far lower than in the corresponding $^{n+1}Li_n$ clusters. It was shown that the reason was the higher 4s–4p gap in Na and the longer Na···Na distances. These two factors raise the energy of the excited VB structures, which involve s → p excitations, and thereby reduce the VB mixing drastically. On the basis of the D_e

value of the $^3K_2$ dimer, which is larger than for $^3Na_2$, the $^{n+1}K_n$ clusters will be more strongly bonded than the corresponding $^{n+1}Na_n$ clusters.

6.5 NPFM Bonding in Coinage Metal Clusters

As we have already mentioned, copper uses NPFM bonding, as may be deduced from the characterization of the $^3\Sigma_u^+$ state of $^3Cu_2$ [7]. We therefore extend herein the VB modeling of NPFM bonding to coinage metals [2e,f]. Coinage metals [11–13] possess valence configurations $nd^{10}(n+1)s^1$ that are analogous in a way to the monovalent alkali metals. As was shown in the original treatment of the $^{n+1}Cu_n$ ($n = 2$–14) clusters [2e], the bond energy per Cu atom reaches 18–19 kcal mol^{-1}. Therefore, the no-pair clusters of the coinage metals may be significantly stickier than the corresponding alkali cluster. In the gold cluster, relativistic effects may contribute to this stickiness [14]. In view of the great surge of interest in gold clusters [15], such an application may be of broad interest. Interestingly, gold surfaces are known to induce sudden magnetization upon adsorption of layers of organic thiols, owing to formation of "bonded triplet pairs" as proposed by the Naaman *et al*. [16].

6.5.1 Structures and Bonding of Coinage Metal NPFM Clusters

Much like in the Li clusters, here too the most stable NPFM structures have three-dimensional geometries starting already with $^5M_4$, which is tetrahedral [17]. These clusters are depicted in Figure 6.10, where the bond lengths are indicated only for $^{n+1}Au_n$, and bonding energies are indicated in the order Cu/Ag/Au.

These most stable geometries of the NPFM clusters in Figure 6.10 are very similar for all coinage metals, with two exceptions for the clusters with $n = 5$ and 6, where the most stable isomer depends on the metal [2f]. However, the differences between the total energies of the different isomers in these cases are small, and one can consider the Au clusters as representative of all the coinage metals without making much of an error [2f]. Thus, as in the case of the NPFM clusters of Li, here too the structures are close to being symmetrical with point-group symmetry being generally higher than the symmetry of the corresponding clusters in their ground state [2f,2g].

Figure 6.11 displays the structures of the $^5Au_4$ and $^7Au_6$ side by side with the corresponding ground states, $^1Au_4$ and $^1Au_6$. Again, as pointed out for the Li clusters, here too the NPFM clusters are three-dimensional cages, whereas the ground states are flat clusters. Note that the bond lengths in the NPFM clusters are not much longer than those of the corresponding ground state despite the fact that the NPFM clusters are bonded without a single electron pair. Considering all the monovalent atoms we showed so far, it is clear that we are seeing a

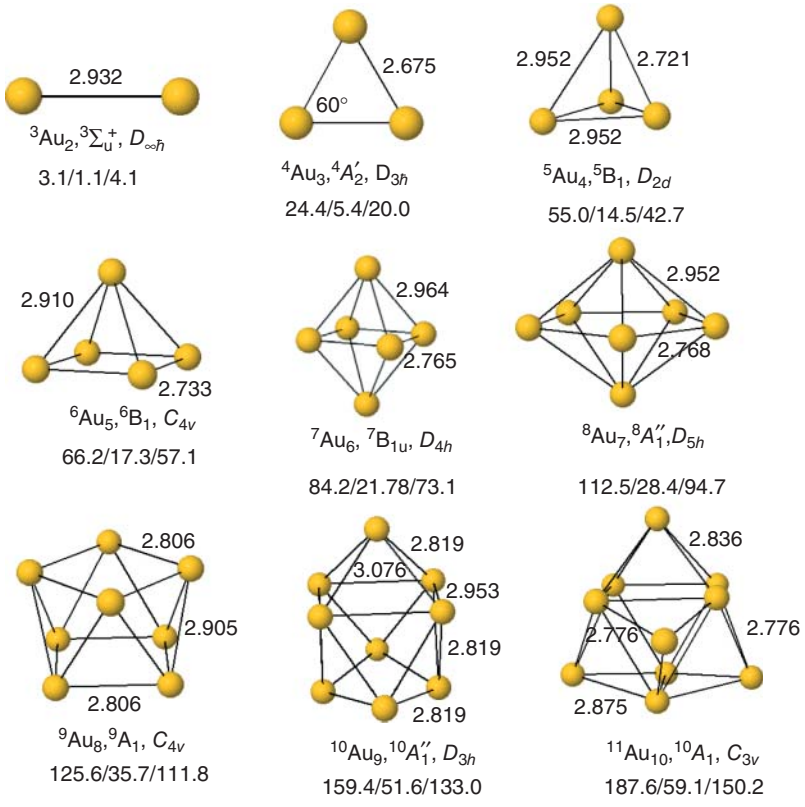

Figure 6.10 b3p86/St-RECP optimized structures, their point groups, and state assignments for the most stable coinage metal clusters in the NPFM states, $^{n+1}M_n$. The bond length values (Å) are shown only for $^{n+1}Au_n$. Bond dissociation energies (D_e, in kcal mol^{-1}) are shown below the structures in the order Cu/Ag/Au. (Reproduced with permission from Figure 4 in Ref. [2f].)

topological behavior of NPFM bonding, which seems to transcend the identity of the metal.

The total D_e values, which are noted in Figure 6.10, underneath the structures, exhibit a familiar trend to the Li clusters, showing that NPFM bonding, which starts weak in the dimer, can reach as much as 187.6 kcal mol^{-1} for the $^{11}Cu_{10}$ cluster. The D_e/n quantity gauges the cluster stability and its growing capacity is plotted in Figure 6.12. It is seen that D_e/n increases dramatically by about 10–15 times as the cluster grows. Thus, D_e/n starts as ~1–2 kcal mol^{-1} or so for the dimers and reaches 19 kcal mol^{-1} for Cu and 15 kcal mol^{-1} for gold atoms, which are remarkably high binding energies for clusters with no electron pairing. The no-pair silver clusters are rather weakly bonded and the D_e/n value converges to less than 6 kcal mol^{-1}, for $^{11}Ag_{10}$. In the entire coinage series, the steepest increase of D_e/n occurs in the transition from the dimer to the trimer. Another significant increase of D_e/n occurs also between the trimer and the tetramer.

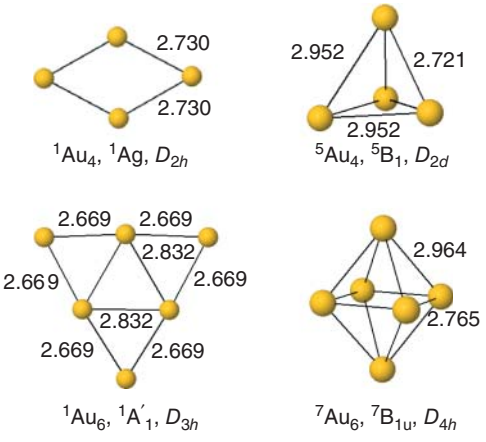

Figure 6.11 The b3p86/St-RECP optimized structures and key bond lengths (Å) of the NPFM clusters, $^5Au_4$ and $^7Au_6$, vis-à-vis their ground-state clusters, $^1Au_4$ and $^1Au_6$ [2f].

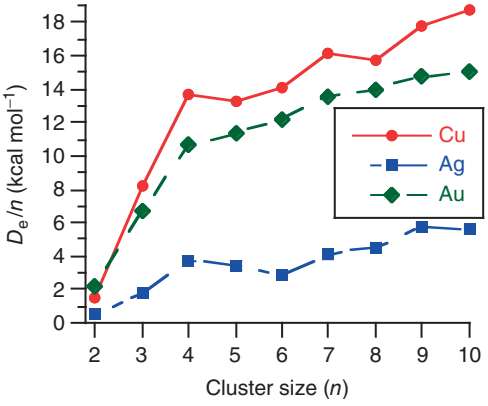

Figure 6.12 Dependence of the bond dissociation energies per atom, D_e/n (kcal mol^{-1}), on cluster size for the no-pair states of the coinage metal clusters. (Reproduced with permission from Figure 6 in Ref. [2f].)

6.6 Valence Bond Modeling of the Bonding in NPFM Clusters of the Coinage Metals

As demonstrated for the lithium clusters [2a,c], NPFM bonding can be understood by means of VB mixing theory. The VB picture of the coinage metal is similar in this sense, but it is different in the nature and multitude of the excited VB structures that can mix into the fundamental VB structure. Figure 6.13 shows some of the VB structures and the corresponding VB mixing diagram for the $^3M_2$ coinage metal dimers.

Thus, as shown in Figure 6.13a, the fundamental structure is the covalent $^3\Phi_{ss}$ with the two valence electrons in the $(n+1)$s AOs of the two coinage metal atoms.

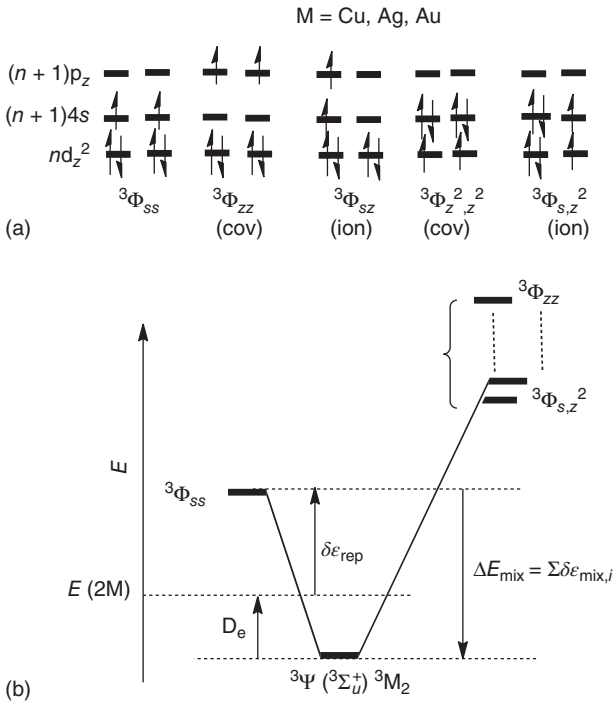

Figure 6.13 (a) Some VB configurations that contribute to NPFM bonding in the no-pair dimers, $^3M_2(^3\Sigma_u^+)$, for M = Cu, Ag, and Au. (b) The corresponding VB-mixing diagram. (Reproduced with permission from Scheme 2 in Ref. [2f].)

There are higher lying VB structures, which involve singly occupied nd_{z^2}, and $(n+1)p_z$ AOs. Some of these are ionic triplet configurations, such as $^3\Phi_{sz}{}^2$, which involves electron transfer from the nd_{z^2} AO of one metal to the $(n+1)$s AO of the second, or $^3\Phi_{sz}$, which involves an electron transfer from the $(n+1)$s AO of one atom to the $(n+1)p_z$ AO of the second. In addition, there are excited covalent configurations, where the two valence electrons occupy the $(n+1)p_z$ AOs of the two atoms, as in $^3\Phi_{zz}$, or the nd_{z^2} AOs of the two atoms, as in $^3\Phi_{z^2z^2}$. Thus, the coinage metals have many more excited VB structures, which can sustain the NPFM bonding compared with the alkali metals.

As we argued for lithium, the fundamental $^3\Phi_{ss}$ configuration is purely repulsive, and the repulsive term $\delta\varepsilon_{rep}$, in Figure 6.13b arises from the two triplet electrons as well as from the d^{10}–d^{10} closed-shell Pauli repulsions. The NPFM bonding will arise only from the mixing of the excited ionic and covalent configurations, each of which contributes a $\delta\varepsilon_{mix,i}$ element as shown in Figure 6.13b. Thus, at a given M–M distance, the net NPFM bonding will be a balance between the repulsive interactions in the fundamental structure ($\delta\varepsilon_{rep}$) and the sum of the mixing interaction terms due to all the excited configurations ($\Delta E_{mix} = \Sigma_i \delta\varepsilon_{mix,i}$). As we move to larger and

larger clusters, there will always be one fundamental configuration, ${}^{n+1}\Phi_{s(1)s(2)\ldots s(n)}$, with repulsive interactions between the singly occupied *n*s orbitals on neighboring atoms. However, now the number of excited ionic and covalent configurations increases in a nonlinear manner as each atom can have many ionic and covalent triplet configurations with each neighboring atom, thus dramatically augmenting the stabilization energy.

As we showed for ${}^{n+1}Li_n$ [2a,c], the bond dissociation energy (D_e) due to NPFM-bonding can be expressed in a simple analytical form. Thus, assuming that the elementary repulsion term ($\delta\varepsilon_{rep}$) is the same for all pairs of bonded atoms and that it involves only the close-neighbor atoms, allows us to use the repulsion term extracted from a VB calculation of the respective dimer molecule and evaluate the total repulsion by multiplying this pair repulsion by the number of close-neighbor M···M pairs in the cluster. In addition, assuming that the various excited configurations each contribute an identical close-neighbor mixing term, $\delta\varepsilon_{mix}$, which is the same as in the corresponding dimer, ${}^3M_2$, allows us to evaluate the total mixing term for any cluster size. Simply counting the number of ionic and covalent excited configurations that a given atom has with its close neighbors, and multiplying the resulting number of configurations by the elementary mixing term, achieves this. We further truncate the number of excited configurations to the lowest excitations involving electron shifts from the *n*d AOs to singly occupied $(n+1)$s AOs and from $(n+1)$s to $(n+1)$p.

These simplifications allow us to model the NPFM binding energy based on Eq. (6.6):

$$D_e = -\left[\frac{\left(N_{ao}+9\right)C_{tot}}{2} + N_{ao}\right]\delta\varepsilon_{mix} - \frac{C_{tot}\delta\varepsilon_{rep}}{2} \tag{6.6}$$

Only s- and p-AOs are counted for N_{ao} [2e]. Details of the deriving Eq. (6.6) can be found in the VB model equations section of Appendix 6.C. The equation is analogous to Eq. (6.4) for the Li clusters. However, here the multiplier of the total coordination number, C_{tot}, is significantly higher because now there are ionic and covalent structures that result from the *n*d orbitals to the $(n+1)$s orbitals.

Owing to limitations of the VB software, we were able to calculate only the energy of the fundamental configuration, ${}^3\Phi_{ss}$, and evaluate thereby the pair-repulsion term in the ${}^3M_2$ species. The mixing terms was then obtained by least-square fitting of Eq. (6.6) to the computed D_e/n quantities. To test the fit quality, we used a second method, whereby we fit Eq. (6.6) by least-square fitting of both the repulsion and mixing terms. Both approaches led to similar results, which can be found in the supporting information document of the original paper [2f].

Using UB3P86/St-RECP D_e/n data, the best-fitted pair-repulsion terms are 16.4 kcal mol^{-1} for Cu, 6.0 kcal mol^{-1} for Au, and 0.8 kcal mol^{-1} for Ag atoms. The values for ${}^{n+1}Cu_n$ and ${}^{n+1}Au_n$ are much larger than those obtained for ${}^{n+1}Li_n$, which make physical sense as the coinage metals have, in addition, d^{10}–d^{10} repulsive terms, which the Li cluster do not have. Indeed, the VB-calculated repulsion terms are 14.3 for Cu (at $R_e = 2.60$ Å) and 11.8 kcal mol^{-1} for Au (at $R_e = 2.93$ Å), which are large, in the right order, and much larger than the corresponding elementary

repulsion calculated by VB for Li (1.504 kcal mol^{-1}). The smaller repulsion of Au versus Cu may reflect the relativistic shrinkage of the 6s orbitals of Au, which lowers the $6s^1$–$6s^1$ repulsion. The fitted $5s^1$–$5s^1$ repulsive term of Ag is much too small, and this may reflect the poor quality of the fit. Indeed, the VB calculation for the $5s^1$–$5s^1$ fundamental VB structure of $^3Ag_2$ gives significant values, which depend on the equilibrium distance taken for the dimer; 8.6 kcal mol^{-1} (at $R_e = 3.12$ Å).

The best-fitted elementary mixing terms are $\delta\varepsilon_{mix} = -1.3245$, -0.6902, and -0.1653 kcal mol^{-1} for Cu, Au, and Ag. The relative ordering of these values can be rationalized by the calculated d–s orbital energy gaps for the atoms. According to the VB mixing model (Figure 6.13b), larger gaps will result in small mixing terms and vice versa for smaller gaps. The gaps can in turn be understood on the basis of various effects that have been discussed by Pyykkö and Desclaux [18]. Thus, Cu is affected by the "$3d^{10}$-contraction" and hence is 3d-4s gap should be smaller than the 4d-5s gap in Ag, while in Au, the 5d-6s gap shrinks relative to Ag by the relativistic shrinkage [18]. Further support of these considerations is provided by inspecting the σ and σ* orbitals of the M_2 dimers, which show that Cu has the largest d-contribution, while Ag the smallest. All the dimers have $(n+1)$p contributions to the σ and σ* orbitals as well, but these contributions are quite similar to the three atoms. Thus, the order of the mixing terms ($\delta\varepsilon_{mix}$) obtained from the two-parameter fit is physically reasonable. Again, the $\delta\varepsilon_{mix}$ obtained for Ag from the two-parameter fit procedure may seem very small. Using the VB-computed $\delta\varepsilon_{rep}$ gave a value of $\delta\varepsilon_{mix} = -0.5931$ kcal mol^{-1}, which is still smaller than the corresponding values for Cu and Au.

Inserting these fitted values into the Eq. (6.6) enables us to calculate D_e/n values for the larger clusters. Figure 6.14 shows plots of the VB modeled and DFT-computed D_e/n values for the $^{n+1}Cu_n$, $^{n+1}Au_n$ and $^{n+1}Ag_n$ clusters veruss the cluster size n. It is apparent from either that quality of the fit is very good for Cu and Au, having R^2 values of 0.97 for Cu, 0.98 for Au, and of a lesser quality for Ag atoms with $R^2 = 0.89$. However, taking the series together, it is clear that the VB model

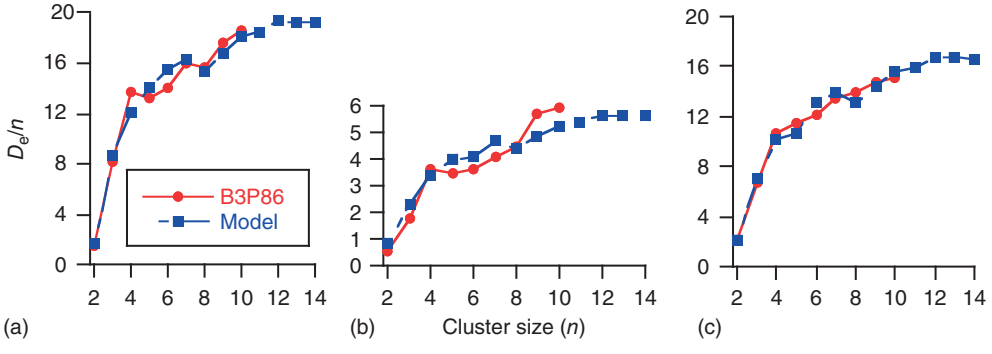

Figure 6.14 Fits between b3p86/St-RECP calculated (red), for (a) copper, (b) silver, and (c) gold clusters, and VB model estimated (blue) D_e/n values (kcal mol^{-1}) as a function of cluster size. (Reproduced with permission from Figure 9 in Ref. [2f].)

describes well the entire pattern of NPFM bonding in these three coinage metals. Furthermore, inspection of Figure 6.14 shows that the VB-modeled D_e/n curve fits nicely the DFT-calculated one; the VB-modeled curve reproduces the steep rise of the D_e/n observed when moving from $^3M_2$ to $^{n+1}M_n$ clusters, and it converges at approximately 19.5 kcal mol^{-1} for the copper (Figure 6.14a), 16.5 kcal mol^{-1} for the gold (Figure 6.14c), and 5 kcal mol^{-1} for silver (Figure 6.14b).

The VB model can be used also to account for the puzzling behavior of the Cu versus Au clusters. Thus, as can be seen from Figure 6.10, $^3Au_2$ is more strongly bound than $^3Cu_2$. By contrast, as the cluster grows, the trend is reversed, and the Cu clusters get more strongly bonded with a converged D_e/n value of ~19.5 kcal mol^{-1} relative to ~16.5 kcal mol^{-1} for the Au clusters. The VB model in Figure 6.13b and Eq. (6.6) explains this reversal well. Thus, Eq. (6.6) shows that the total D_e is a balance between the mixing and repulsion terms; with a larger multiplier for the $\delta\varepsilon_{mix}$ term (in Eq. (6.6)) compared with the $\delta\varepsilon_{rep}$ term. This larger multiplier signifies the fact that the number of excited VB configurations, which can mix into the fundamental VB structure, increases much faster than the number of pair repulsions as the cluster grows. Thus, the $^3Cu_2$ dimer, with the larger repulsive term, is weakly bound compared with $^3Au_2$. However, as the cluster grows, the number of contributing VB configurations increases, the total mixing term starts to dominate the bonding, and because the elementary mixing term for Cu is significantly larger than the corresponding one for Au, the D_e and D_e/n values for the $^{n+1}Cu_n$ clusters become larger than for those the $^{n+1}Au_n$ clusters.

6.7
NPFM Bonding: Resonating Bound Triplet Pairs

The earlier discussion shows that the VB modeling inherent in Eqs. (6.4) and (6.6) captures qualitatively and semiquantitatively the essence of the NPFM bonding in the no-pair clusters of the lithium and coinage metals. NPFM bonding arises primarily from bound triplet electron pairs that spread over all the close neighbors of a given atom in the clusters.

The bound triplet pair owes its stabilization to the resonance energy provided by the mixing of the local ionic configurations, $[^3M(\uparrow\uparrow)^-]$ M^+ and M^+ $[^3M(\uparrow\uparrow)^-]$, and the various excited covalent configurations (e.g., involving p_z and d_{z^2} AOs) into the fundamental covalent structure $^3(M\uparrow\uparrow M)$ with the s^1s^1 electronic configuration. As we demonstrated for $^{n+1}Li_n$ clusters [2a,c], in Figure 6.6, the mixing of the excited covalent structures into $^3(M\uparrow\uparrow M)$ generates a covalent structure with hybrid orbitals that assume an *in–out* ⇔ *out–in* orientations and thereby keep the triplet electrons further apart compared with the fundamental s^1s^1 structure. This lowers the triplet repulsion and introduces some resonance energy. The stabilization is further augmented by mixing of the ionic structures, which buttress the bonding by covalent-ionic resonance energy [2a]. Thus, if we consider each diatomic triplet pair and its ionic plus covalent fluctuations as a local NPFM bond, we can regard the electronic structure of a given $^{n+1}M_n$ cluster as *a resonance hybrid of all the local*

NPFM bonds that each atom forms with all of it close neighbors. It is clear therefore that these clusters strive to maintain maximum coordination, with optimal number of short distances for every atom in the cluster, in order to both minimize the triplet repulsion as well as maximize the total resonance energy of the triplet pairs.

In the case of alkali metals, the local FM bond involves only two electrons in *n*s and *n*p orbitals, while in the coinage-metal clusters, there are $(n+1)$s and $(n+1)$p orbitals, as well as filled *n*d-orbitals that contribute components of 3-electron bonding because of the participation of these orbitals in the ionic fluctuations (Figure 6.13). Thus, the no-pair coinage metal clusters, and especially $^{n+1}Cu_n$ and $^{n+1}Au_n$, are more strongly bonded than the corresponding alkali metal clusters [2b,c,d]. It is important to emphasize that the mixing of the excited VB structures is not equivalent to a simple hybridization effect, for example, 2s-2p_z in $^{n+1}Li_n$. This is evidenced by the fact that Hartree–Fock (HF) wave function for $^3Li_2$ ($^3\Sigma_u^+$) is unbound and repulsive throughout the internuclear distance , despite the significant hybridization of the 2s and 2p_z orbitals, more so than in the post-HF wave functions, which are bound. What is needed for bonding is static and dynamic correlations, which are provided by CASSCF and CCSD(T) methods, as well as in the VB method used to investigate the NPFM clusters [2a].

6.8 Concluding Remarks: Bound Triplet Pairs

The chapter discusses NPFM bonding in the maximum-spin states of alkali and coinage metal clusters as a result of *bonded triplet pairs*. It is important to recognize that these are not van der Waals clusters, as the bonding energies arise from DFT method that do not include dispersion corrections and as the bonding energies per atom are large. It is shown that the bonding energy per atom, D_e/n, grows rapidly with the cluster size and exhibits a strongly nonadditive behavior, converging to values as large as 16–19 kcal mol^{-1} for gold and copper; values that are of the order of normal spin-paired bonds in metals.

The VB analysis of the problem shows that a weak stabilization of the triplet pair in the dimer can become a remarkably strong force that binds together monovalent atoms without even a single electron pair. This is achieved because the steeply growing number of excited VB structures endows the triplet pair with a cumulative effect of stabilization that is maximized when the cluster is compact with an optimal coordination number of the atoms. Thus, *the nonadditive behavior of the binding energy is gauged by the number of VB structures available for mixing with the fundamental repulsive structure*, $^{n+1}\Phi_{s(1)\ldots s(i)\ldots s(n)}$.

As we noted in the introduction, spectroscopic evidence is available for small no-pair dimers and trimers [4a,b,c, 5a,b,c,d, 6a,b, 7] and therefore the elucidation of NPFM bonding is not a mere academic exercise. An additional potential interest in this kind of clusters is their relationship to Bose–Einstein condensates, in which the quantum states of all atoms are identical, and to Fermi ''gases'' of fermionic isotopes of alkali metals, (e.g., K with atomic mass 40) in magnetic fields [6, 19].

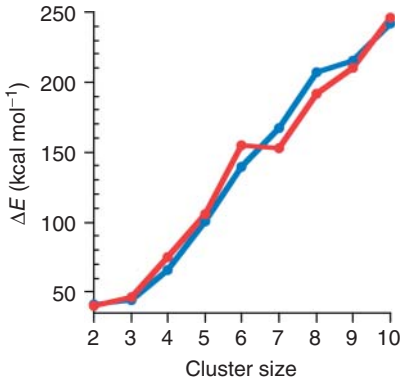

Figure 6.15 b3p86/St-RECP excitation energies (ΔE, kcal mol^{-1}) from the ground states to the no-pair states plotted against the cluster size, n, for $^{n+1}Cu_n$ (blue) and $^{n+1}Au_n$ (red) clusters. (Reproduced with permission from Figure 16 in Ref. [2g].)

Finally, having maximum magneticity, no-pair clusters are also interesting for their potential applications in nanochemistry.

However, despite the fact that the no-pair states are rather low lying, they are still not accessible for ground-state manipulations under ambient conditions. Figure 6.15 shows the relative energy of the no-pair states relative to the ground states for Cu and Au clusters. At the highest cluster size, the energy gap reaches ~245 kcal mol^{-1}.

As these excited states have large magnetic moments relative to their ground state, these no-pair clusters can be stabilized within powerful magnetic fields relative to the ground states and become the ground states. The recent report of Helgaker *et al* [20] shows that in sufficiently strong magnetic fields as those existing in the atmospheres of white dwarfs, even $^3H_2$, which lies some ~250 kcal mol^{-1} (at the same computational level as used for the metal clusters) above the ground state, becomes bound and accessible. It is clear that the NPFM bonded clusters described here will require weaker magnetic fields to become ground states. Furthermore, as shown in our original studies,[1)] usage of external electric fields will reduce the energy gap further, such that the application of magnetic and electric fields may eventually attain the goal of creating ground-state magnetic clusters of coinage metals. Once this is achieved, the usage of magnetic clusters offers new horizons of possibilities.

A more complete mini-periodic table of NPFM bonding will have to include the heavy alkali metals (K, Cs, Rb, Fr), and the group III metalloids, such as B, Al, and so on. In view of the importance of the ionic structures, the heteroatomic clusters may be even more strongly bonded. Thus, even though the principles of NPFM bonding are clear, still some future work thus lies ahead.

For all these reasons, and for the mere fact *that NPFM is a novel bonding form*, it is essential to draw the attention of the community to these clusters.

Appendix

6.A
Methods and Some Details of Calculations

All density functional and CCSD(T) calculations for the alkali metal clusters were performed with Gaussian94 and Gaussian98 program packages [21, 22]. *Ab initio* VB calculations for the Li dimer were done with the *ab initio* VB program TURTLE [23]. All density functional calculations for the coinage metal clusters presented here were performed with the Gaussian03 program package [24]. CCSD(T) calculations of coinage metal clusters were carried out with Gaussian03 and MOLPRO 2006.1 program packages [25]. VB calculations for coinage metal dimers were performed with the *ab initio* VB program Xiamen-01 [26]. For Li clusters, we used BOVB calculations (see Chapter 5, Vol. 1) for the dimer. For the coinage metals, we used VBSCF (see Chapter 5) to obtain the repulsive interactions in the purely covalent structure of the dimer with ns^1ns^1 electronic configuration. The VB calculations of the dimer used the cc-pVDZ basis set for Li, and the 1997 Stuttgart relativistic small effective core potential (St-RECP) [27] with an extended valence basis set (with (8s7p6d)/[6s5p3d] contractions) for coinage metals [2a,c,f].

The DFT calculations presented here were obtained with B3P86, in combination with cc-pVDZ for Li clusters, and St-RECP for coinage metals, hence, UB3P86/St-RECP. Specifically, UB3P86/St-RECP was shown [2e,f] to have a very small basis set superposition error (BSSE), and was compatible with the results of the extended augmented double zeta atomic natural orbital (ANO) basis set of Roos *et al.* [28] Other DFT methods were tried, and the results were similar to UB3P86 [2f].

Benchmark calculations, as well as all other computational tests and details are described in detail in the original literature [2a,c,f].

6.B
Symmetry Assignment of the VB Wave Function

Dropping normalization constants, the wave function in Figure 6.6b can be written as follows:

$$^3\Psi_{ss+zz}=^3\Phi_{ss} + c^3\Phi_{zz} = |(2s_1 + \lambda 2p_1)(2s_2 + \lambda 2p_2)|+|(2s_1-\lambda 2p_1)(2s_2-\lambda 2p_2)|;$$

$$c = \lambda^2 \tag{6.B1}$$

In this form, the hybrid orbitals orient themselves as *in–out* ⇔ *out–in* in the two VB structures. Using its form without the hybridization, we have

$$^3\Psi_{ss+zz}=^3\Phi_{ss} + c^3\Phi_{zz} = |(2s_1)(2s_2)| + c|(2p_1)(2p_2)| \tag{6.B2}$$

Application of the $D_{\infty h}$ point-group operations on this wave function will show that E, C_∞, and σ_v leave the wave function invariant, while operation by C_2, i, and S_∞ invert its sign. With these characters, it transforms as the irreducible

representation Σ_u^+. Becaise it has a triplet spin, it is assigned as ${}^3\Sigma_u^+$. Further, adding the CT configurations (Φ_{sz}) does not change this assignment.

6.C
The VB Configuration Count and the Expressions for *D*e for NPFM Clusters

Coinage Metal Clusters: The VB model equation for D_e is composed of two terms. One is the repulsive interaction between triplet pairs, while the other is the mixing term due to the excited structures.

The repulsion interaction term involves only the close-neighbor atoms. The number of the close-neighbor pairs, N_{rep}, is

$$N_{rep} = \frac{1}{2}\sum_{i=1}^{n} C_i = \frac{1}{2}C_{tot} \tag{6.C1}$$

where C_i is the coordination number of atom *i*. Assuming that all the pairs share the same value of repulsion energy, $\delta\varepsilon_{rep}$, then, the repulsions of triple pairs becomes simply:

$$\Delta E_{rep} = \frac{1}{2}C_{tot}\delta\varepsilon_{rep} \tag{6.C2}$$

Using the simple assumptions that the various excited structures contribute identical mixing terms, the mixing energy can be evaluated by counting the number of excited structures. The number of excited structures is truncated such that only those structures that involve double excitations from the ensemble of singly occupied orbitals $(n+1)$s or single excitations from the doubly occupied orbitals *n*d are counted. Furthermore, we examine the excitation model where the electrons in the *n*d orbitals can be transferred only to the $(n+1)$s orbitals. In this case, the *n*d orbitals serve a role of polarization functions for the 4s orbitals.

The excited structures with electron exchanges between close neighbors are composed of ionic and covalent types. In VB theory, the mixing between an excited structure (ionic) and the fundamental structure is proportional to the resonance (transfer) integral between the centers that participate in the electron transfer. As this integral diminishes rapidly with distance between the centers, the important ionic structures are mono-ionic structures with close-neighbor electron transfer. The number of neighbor atom pairs is one-half of the total coordinate number, $0.5C_{tot}$. For each pair of atoms, A–B, there are two ionic structures, A^-B^+, and A^+B^-. For double excitations from the singly occupied orbitals, two electrons occupy two of the N_{ao} orbitals of the anion, where N_{ao} is the number of singly occupied $(n+1)$s and virtual $(n+1)$p orbitals. The number of ways for generating these electron-transferred structures is $0.5N_{ao}(N_{ao}-1)$. In addition, we have to consider transfer from the doubly occupied *n*d-orbitals to the singly occupied $(n+1)$s orbitals. Only β-electron of five *n*d(B) orbitals can be transferred to the $(n+1)$s orbital of atom A. This would yield the following number of ionic structures:

$$N_{ion} = \left[\frac{1}{2}N_{ao}\left(N_{ao}-1\right)+5\right]C_{tot} \tag{6.C3}$$

Two types of covalent structures are involved: in the first type, all the singly occupied orbitals are the same. For instance, for Cu_4, the configurations are |ssss>, $|pppp>_z$, $|pppp>_x$ (two tangential p orbitals are used, e.g., p_z, p_x). The total number of these structures is N_{ao}. The other types of covalent structures are generated by replacing a neighbor … ss … in the fundamental structure … ssss … by a pair of the other $N_{ao}-1$ orbitals. For instance, for Cu_4, there are sspp, ppss, … The number of these covalent structures is $0.5\ N_{ao}(N_{ao}-1)C_{tot}$. Hence, the number of covalent structure would be

$$N_{cov} = \frac{1}{2}(N_{ao} - 1)C_{tot} + N_{ao} \tag{6.C4}$$

Thus, the total number of structures for $^{n+1}M_n$ is

$$N = N_{ion} + N_{cov} = \frac{1}{2}(N_{ao}^2 + 9)C_{tot} + N_{ao} \tag{6.C5}$$

Based on this counting, the equation of D_e is written as

$$D_e = -0.5C_{tot}\delta\varepsilon_{rep} - [0.5(N_{ao}^2 + 9)C_{tot} + N_{ao}]\delta\varepsilon_{mix} \tag{6.C6}$$

Alkali Metal Clusters: The Pauli repulsion energy in the fundamental structure follows Eq. (6.C2). The number of excited ionic and covalent structures can be calculated as follows:

The number of covalent structures is identical to Eq. (6.C4), while the number of ionic structures is based on the discussion in the paragraph before Eq. (6.C3). Without the part of the d-orbitals, which are absent here, this number is

$$N_{ion} = [0.5N_{ao}(N_{ao} - 1)]C_{tot} \tag{6.C7}$$

Thus, the total number of structures for $^{n+1}Li_n$ and other NPFM alkali clusters, is

$$N = N_{ion} + N_{cov} = 0.5(N_{ao}^2 - 1)C_{tot} + N_{ao} \tag{6.C8}$$

The mixing energy is given by the product of the number of excited covalent and ionic VB structures by the close-neighbor term $\delta\varepsilon_{mix}$. Thus, the D_e becomes:

$$D_e(^{n+1}Li_n) = -[0.5(N_{ao}^2 - 1)C_{tot} + N_{ao}]\delta\varepsilon_{mix} - 0.5\delta\varepsilon_{rep}C_{tot} \tag{6.C9}$$

References

1. (a) Grimme, S. and Schreiner, P.R. (2011) *Angew. Chem. Int. Ed.*, **50**, 12639–12642; (b) Fokin, A.A., Chernish, L.V., Gunchenko, P.A., Tikhonchuk, E.Y., Hausmann, H., Serafin, M., Dahl, J.E.P., Carlson, R.M.K., and Schreiner, P.R. (2012) *J. Am. Chem. Soc.*, **134**, 13641–13650.
2. (a) Danovich, D., Wu, W., and Shaik, S. (1999) *J. Am. Chem. Soc.*, **121**, 3165–3174; (b) de Visser, S.P., Alpert, Y., Danovich, D., and Shaik, S. (2000) *J. Phys. Chem. A*, **104**, 11223–11231; (c) de Visser, S.P., Danovich, D., Wu, W., and Shaik, S. (2002) *J. Phys. Chem. A*, **106**, 4961–4969; (d) de Visser, S.P., Danovich, D., and Shaik, S. (2003) *Phys. Chem. Chem. Phys.*, **5**, 158–164; (e) de Visser, S.P., Kumar, D., Danovich, M., Nevo, N., Danovich, D., Sharma, P.K., Wu, W., and Shaik, S. (2006) *J. Phys. Chem. A*, **110**, 8510–8518;

(f) Danovich, D. and Shaik, S. (2010) *J. Comput. Theor. Chem.*, **6**, 1479–1489; (g) Danovich, D. and Shaik, S. (2014) *Acc. Chem. Res.*, **47**, 417–426.

3. (a) For an early treatment of some high-spin rings, see: McAdon, M.H. and Goddard, W.A. III, (1988) *J. Phys. Chem.*, **92**, 1352–1365; (b) The name ''no-pair clusters'' was coined in Glukhovtsev, M.N. and Schleyer, P.v.R. (1993) *Isr. J. Chem.*, **33**, 455–466.
4. (a) Higgins, J., Hollebeck, T., Reho, J., Ho, T.-S., Lehmann, K.K., Rabitz, H., Scoles, G., and Gutowski, M. (2000) *J. Chem. Phys.*, **112**, 5751–5761; (b) Brühl, F.R., Miron, R.A., and Ernst, W.E. (2001) *J. Chem. Phys.*, **115**, 10275–10281; (c) Fioretti, A., Comparat, D., Crubellier, A., Dulieu, O., Masnou-Seeuws, F., and Pillet, P. (1998) *Phys. Rev. Lett.*, **80**, 4402–4405.
5. (a) Higgins, J., Callegari, C., Reho, J., Stienkemeier, F., Ernst, W.E., Lehmann, K.K., Gutowski, M., and Scoles, G. (1996) *Science*, **273**, 629–631; (b) Higgins, J., Ernst, W.E., Callegari, C., Reho, J., Lehmann, K.K., and Scoles, G. (1996) *Phys. Rev. Lett.*, **77**, 4532–4535; (c) Higgins, J., Callegari, C., Reho, J., Stienkemeier, F., Ernst, W.E., Gutowski, M., and Scoles, G. (1998) *J. Phys. Chem. A*, **102**, 4952–4965; (d) Reho, J., Higgins, J., Nooijen, M., Lehmann, K.K., Scoles, G., and Gutowski, M. (2001) *J. Chem. Phys.*, **115**, 10265–10274.
6. (a) Cvitas, M.T., Soldan, P., and Houston, J.M. (2005) *Phys. Rev. Lett.*, **94**, 033201-1–033201-4; (b) Quemener, G., Honvault, P., Launay, J.-M., Soldan, P., Potter, D.E., and Houston, J.M. (2005) *Phys. Rev. A*, **71**, 032722-1–032722-10.
7. (a) Bondybey, V.E. (1982) *J. Chem. Phys.*, **77**, 3771–3772; (b) Huber, K.P. and Herzberg, G. (1979) *Constants of Diatomic Molecules*, Van Nostrand Reinhold, New York; (c) Rohlfing, E.A. and Valentini, J.J. (1986) *J. Chem. Phys.*, **84**, 6560–6566.
8. For a few of the earlier calculations of these bound dimers, see: (a) Kutzelnigg, W., Staemler, V., and Gélus, M. (1972) *Chem. Phys. Lett.*, **13**, 496–500; (b) Olson, M.L. and Konowalow, D.D. (1977) *Chem. Phys.*, **21**, 393–399; (c) Konowalow, D.D. and Fish, J.L. (1984) *Chem. Phys.*, **84**, 463–475; (d) Kaldor, U. (1990) *Chem. Phys.*, **140**, 1–6.
9. (a) Goddard, W.A. III,, Dunning, T.H., Hunt, W.J., and Hay, P.J. (1973) *Acc. Chem. Res.*, **6**, 368–376; (b) Goodgame, M.M. and Goddard, W.A. III, (1985) *Phys. Rev. Lett.*, **54**, 661–664.
10. Tai, T.B., Nhat, P.V., Nguyen, M.T., Li, S., and Dixon, D.A. (2011) *J. Phys. Chem. A*, **115**, 7673–7686.
11. McAdon, M.H. and Goddard, W.A. III, (1988) *J. Chem. Phys.*, **88**, 277–302.
12. Morse, M.D. (1986) *Chem. Rev.*, **86**, 1049–1109.
13. Lombardi, J.R. and David, B. (2002) *Chem. Rev.*, **102**, 2431–2460.
14. See for example, (a) Pyykkö, P. (2002) *Angew. Chem. Int. Ed.*, **41**, 3573–3578; (b) Pyykkö, P. (1997) *Chem. Rev.*, **97**, 597–636.
15. See for example, (a) Schwerdtfeger, P. (2003) *Angew. Chem. Int. Ed.*, **42**, 1892–1895; (b) Hakkinen, H. (2008) *Chem. Soc. Rev.*, **37**, 1847–1859; (c) Bao, K., Goedecker, S., Koga, K., Lancon, F., and Neelov, A. (2009) *Phys. Rev. B*, **79**, 041405-1–041405-4(R).
16. (a) Carmeli, I., Leitus, G., Naaman, R., Reich, S., and Vager, Z. (2003) *J. Chem. Phys.*, **118**, 10372–10375; (b) L'vov, V.S., Naaman, R., Tiberkevich, V., and Vager, Z. (2003) *J. Chem. Phys. Lett.*, **381**, 650–653; (c) Naaman, R. and Vager, Z. (2006) *Phys. Chem. Chem. Phys.*, **8**, 2217–2224.
17. (a) A full configuration-interaction study of the tetrahedral $^5Li_4$ cluster confirmed the nature of the no-pair bond:Monari, A., Pitarch-Ruiz, J., Bendazzoli, G.L., Evangelisti, S., and Sanches-Martin, J. (2008) *J. Chem. Theory Comput.*, **4**, 404–413; (b) Coupled-Cluster study of 'no-pair' bonding in the tetrahedral $^5Cu_4$ cluster:Verdicchio, M., Evangelisti, S., Leininger, T., Sánchez-Marín, J., and Monari, A. (2011) *Chem. Phys. Lett.*, **503**, 215–219.
18. Pyykkö, P. and Desclaux, J.-P. (1979) *Acc. Chem. Res.*, **12**, 276–281.
19. Cvitas, M.T., Soldan, P., Houston, J.M., Honvault, P., and Launay, J.-M. (2005) *Phys. Rev. Lett.*, **94**, 200402-1–200402-4.

20. Lange, K.K., Tellgren, E.I., Hoffmann, M.R., and Helgaker, T. (2012) *Science*, **337**, 327–331.
21. Frisch, M.J., Trucks, G.W., Schlegel, H.B., Gill, P.M.W., Johnson, B., Robb, M.A., Cheeseman, J.R., Keith, T., Peterson, G.A., Montgomery, J.A., Jr., Raghavachari, K., Al-Laham, M.A., Zakrzewski, V.G., Ortiz, J.V., Foresman, J.B., Cioslowski, J., Stefanov, B.B., Nanayakkara, A., Challacombe, M., Peng, C.Y., Ayala, P.Y., Chen, W., Wong, M.W., Andres, J.L., Replogle, E.S., Gomperts, R., Martin, R.L., Fox, D.J., Binkley, J.S., Defrees, D.J., Baker, J., Stewart, J.J.P., Head-Gordon, M., Gonzalez, C., and Pople, J.A. (1995) Gaussian 94, Revision D.4, Gaussian, Inc., Pittsburgh, PA.
22. Frisch, M.J., Trucks, G.W., Schlegel, H.B., Scuseria, G.E., Robb, M.A., Cheeseman, J.R., Zakrzewski, V.G., Montgomery, J.A., Jr., Stratmann, R.E., Burant, J.C., Dapprich, S., Millam, J.M., Daniels, A.D., Kudin, K.N., Strain, M.C., Farkas, O., Tomasi, J., Barone, V., Cossi, M., Cammi, R., Mennucci, B., Pomelli, C., Adamo, C., Clifford, S., Ochterski, J., Peterson, G.A., Ayala, P.Y., Cui, Q., Morokuma, K., Malick, D.K., Rabuck, A.D., Raghavachari, K., Foresman, J.B., Cioslowski, J., Ortiz, J.V., Stefanov, B.B., Lui, G., Liashenko, A., Piskorz, P., Komaromi, I., Gomperts, R., Martin, R.L., Fox, D.J., Keith, T., Al-Laham, M.A., Peng, C.Y., Nanayakkara, A., Gonzalez, C., Challacombe, M., Gill, P.M.W., Johnson, B.G., Chen, W., Wong, M.W., Andres, J.L., Head-Gordon, M., Replogle, E.S., and Pople, J.A. (1998) Gaussian 98, Revision A.9, Gaussian, Inc, Pittsburgh, PA.
23. Verbek, J., Langenberg, J.H., Byrman, C.P., Dijkstra, F., van Lenthe, J.H. (1997) TURTLE – An ab initio VB/VBSCF Program, University of Utrecht, Utrecht.
24. Frisch, M.J., Trucks, G.W., Schlegel, H.B., Scuseria, G.E., Robb, M.A., Cheeseman, J.R., Montgomery, J.A., Jr., Vreven, T., Kudin, K.N., Burant, J.C., Millam, J.M., Iyengar, S.S., Tomasi, J., Barone, V., Mennucci, B., Cossi, M., Scalmani, G., Rega, N., Petersson, G.A., Nakatsuji, H., Hada, M., Ehara, M., Toyota, K., Fukuda, R., Hasegawa, J., Ishida, M., Nakajima, T., Honda, Y., Kitao, O., Nakai, H., Klene, M., Li, X., Knox, J.E., Hratchian, H.P., Cross, J.B., Bakken, V., Adamo, C., Jaramillo, J., Gomperts, R., Stratmann, R.E., Yazyev, O., Austin, A.J., Cammi, R., Pomelli, C., Ochterski, J.W., Ayala, P.Y., Morokuma, K., Voth, G.A., Salvador, P., Dannenberg, J.J., Zakrzewski, V.G., Dapprich, S., Daniels, A.D., Strain, M.C., Farkas, O., Malick, D.K., Rabuck, A.D., Raghavachari, K., Foresman, J.B., Ortiz, J.V., Cui, Q., Baboul, A.G., Clifford, S., Cioslowski, J., Stefanov, B.B., Liu, G., Liashenko, A., Piskorz, P., Komaromi, I., Martin, R.L., Fox, D.J., Keith, T., Al-Laham, M.A., Peng, C.Y., Nanayakkara, A., Challacombe, M., Gill, P.M.W., Johnson, B., Chen, W., Wong, M.W., Gonzalez, C., and Pople, J.A. (2004) Gaussian 03, Revision C.02, Gaussian, Inc., Wallingford, CT.
25. Werner, H.-J., Knowles, P.J., Lindh, R., Manby, F.R., Schutz, M., Celani, P., Korona, T., Rauhut, G., Amos, R.D., Bernhardsson, A., Berning, A., Cooper, D.L., Deegan, M.J.O., Dobbyn, A.J., Eckert, F., Hampel, C., Hetzer, G., Lloyd, A.W., McNicholas, S.J., Meyer, W., Mura, M.E., Nicklass, A., Palmieri, P., Pitzer, R., Schumann, U., Stoll, H., Stone, A.J., Tarroni, R., and Thorsteinsson, T. MOLPRO, version 2006.1, a package of ab initio programs, see *www.molpro.net* (accessed 4 November 2013).
26. (a) Song, L., Mo, Y., Zhang, Q., and Wu, W. (2003) XMVB: An ab initio Non-orthogonal Valence Bond Program, Xiamen University, Xiamen; (b) Song, L., Mo, Y., Zhang, Q., and Wu, W. (2005) *J. Comput. Chem.*, **26**, 514–521.
27. Dolg, M., Stoll, H., Preuss, H., and Pitzer, R.M. (1993) *J. Phys. Chem.*, **97**, 5852–5859.
28. Pou-Amerigo, R., Merchan, M., Nebot-Gil, I., Widmark, P.O., and Roos, B. (1995) *Theor. Chim. Acta*, **92**, 149–181.

7
Chemical Bonding in Transition Metal Compounds

Gernot Frenking

7.1
Introduction

There are two major differences between the chemical bonding of transition metals (TMs) and main-group elements. One difference concerns the atomic orbitals that are involved in the chemical bonds. Covalent bonding of main-group elements is best described in terms of s/p hybridization of the (*n*)s and (*n*)p valence orbitals obeying the octet rule. In contrast, the valence orbitals of the TMs are the $(n-1)$s and $(n-1)$d AOs which are supplemented by the (*n*)p orbitals [1]. This leads to the 18-electron rule, which is, however, less strict than the octet rule. It has, therefore, been suggested that the bonds in TM compounds could be described using only the $(n-1)$s and $(n-1)$d AOs, while the (*n*)p AOs should be considered as polarization functions, like the d AOs of main-group elements, rather than as valence orbitals [2]. This view has been challenged in quantum chemical studies, which indicate that the (*n*)p AOs of the TMs are genuine valence orbitals [3]. However, all studies agree that the (*n*)p orbitals are much less important than the $(n-1)$s and $(n-1)$d AOs for the chemical bonding of TMs.

The second major difference concerns the bonding models that have proven to be useful for discussing chemical bonding in TM compounds and main-group molecules. Covalent bonds E_1-E_2 of main-group elements E are usually described in terms of electron-sharing interactions, where each atom E contributes one electron in an sp^x hybridized orbital yielding a σ-bond or one electron in a p(π) AO which gives a π-bond (Figure 7.1a). In contrast, chemical bonds of TM compounds are generally introduced in chemistry textbooks in terms of donor–acceptor interactions between the metal TM and a ligand L.[1)] The TM-L are then described using a synergistic bonding model of TM←L σ-donation and TM→L π-backdonation, where a doubly occupied AO of one bonding partner

1) Donor–acceptor bonding in main-group compounds has been recognized in recent years as an important bonding motif not only for classical group-13/15 Lewis acid-base pairs. This is discussed in chapter 4 in Volume 2.

The Chemical Bond: Chemical Bonding Across the Periodic Table, First Edition.
Edited by Gernot Frenking, Sason Shaik.

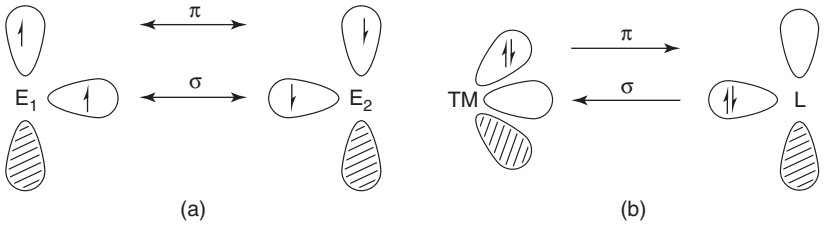

Figure 7.1 Schematic representation of: (a) Electron-sharing σ- and π-bonding between two main-group atoms E^1 and E^2 and: (b) Donor–acceptor bonding between a transition metal TM and ligand L according to the DCD model, which exhibits TM←L σ-donation and TM→L π-backdonation.

donates electronic charge into the vacant AO of the other species (Figure 7.1b). This model was originally introduced by Dewar to describe TM-olefin interactions in ethene complexes [4]. It was systematically extended by Chatt and Duncanson [5] to other classes of TM compounds and, therefore, it is nowadays referred to as the Dewar–Chatt–Duncanson (DCD) model [6]. The DCD model is the most widely used bonding scheme for TM compounds. A large part of this chapter describes the scope and the limitations of the DCD model in the light of modern quantum chemical methods, which are available for a charge, and energy partitioning analysis of the chemical bond [7]. A variety of quantum chemical methods has been developed that makes it possible to span a bridge between qualitative bonding concepts and accurate theoretical calculations. In this way it is possible to assign numerical values to conceptual terms that places the discussion on the strength and relevance of concepts like σ donation or π backdonation on firmer grounds. However, it is important to realize that such numbers are not observable quantities and that they depend on the definition within a particular method. A good method for analyzing a chemical bond should fulfill the following conditions: (i) It should be based on an accurate quantum chemical calculation, which gives correct bond energies and geometries. (ii) The mathematical terms should be unambiguously defined. (iii) The numerical values should not change very much at different levels of theory. (iv) There should be a connection between the calculated terms and observable quantities such as the bond energy.

We do not strive in this article to present as many classes of compounds as possible; rather, a discussion of the chemical bonding in representative classes of TM compounds, which exemplifies characteristic types of metal-ligand interactions, is given. Unlike a textbook, we do not present a systematic discussion of the differences between the first, second and third TM compounds nor do we compare molecules of the early TM atoms with the late TMs. But we think that the chosen examples cover most aspects of chemical bonding of the TMs. Prior to this, a discussion of the essential features of the TM valence orbitals is presented.

7.2
Valence Orbitals and Hybridization in Electron-Sharing Bonds of Transition Metals

The shape of the sp^n valence orbitals of main-group atoms and their correlation with molecular structures and bond angles (sp hybrids → linear, sp^2 hybrids → trigonal planar, sp^3 hybrids → tetrahedral) are well-known. They are taught nowadays in introductory courses of chemistry and they are a standard part of chemistry textbooks. Much less is known about sd^n hybrids. Figure 7.2 shows the shape of sd^n hybrid orbitals and their corresponding polyhedral coordination geometries, which have been given by Landis [2c].

It becomes obvious that the molecular shapes that are associated with sd^n hybridized orbitals differ strongly from sp^n hybrids. This is because d orbitals have more lobes than p orbitals, which makes the correlation between sd^n hybridization and bond angles less obvious. The theoretical bond angles, for example, between

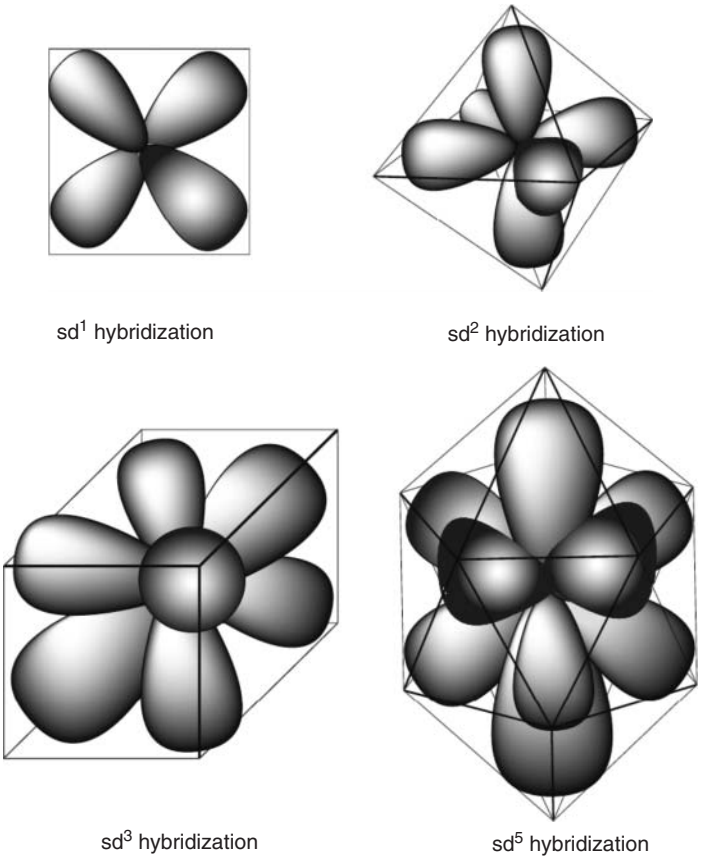

Figure 7.2 Graphical representation of sd^n hybrid orbitals and their corresponding polyhedral coordination geometries.

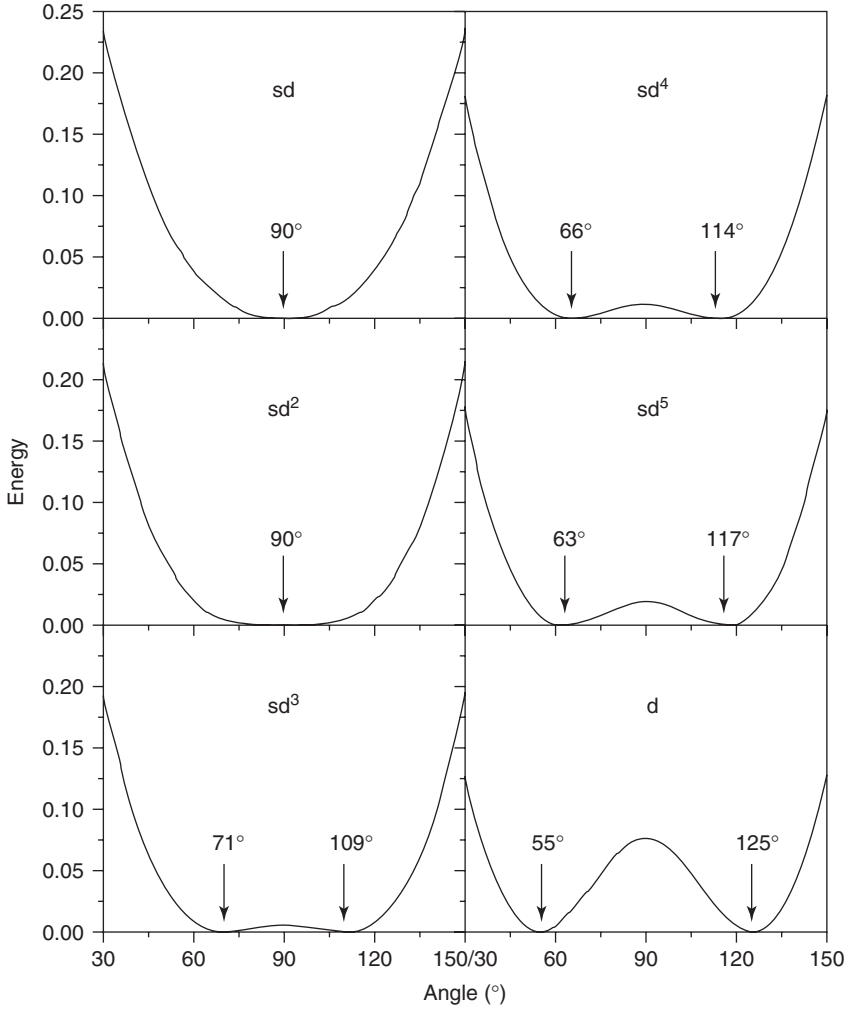

Figure 7.3 Energies of pairs of sd^n hybrid orbitals and pure d orbitals as a function of the bond angle.

two substituents R in compounds TMR_2 (sd hybridized) and TMR_3 (sd^2 hybridized) which have TM-R σ-bonds are 90°, where the latter species are predicted to have a pyramidal (C_{3v}) geometry. This is in agreement with the experimental geometries of $TM(Mes)_3$ (TM = Rh, Ir; Mes = 2,4,6-Trimethylphenyl) [8]. The higher substituted systems TMR_x ($x = 4–6$) have sd^n ($n = 3–5$) hybrid orbitals at TMs, which give energy minima at two different bond angles (Figure 7.3) [9]. It becomes clear that the equilibrium geometries of the latter molecules do not agree with the VSEPR (Valence Shell Electron Pair Repulsion) model [10].

Figure 7.2 shows that the polyhedron that is associated with sd^5 hybridization of a molecule TMR_6 is an icosahedron but not an octahedron that might intuitively be expected for a sextuply coordinated TM compound. This concurs with *ab initio* calculations of CrH_6 and WH_6, which show that the O_h forms are energetically very high lying (>100 kcal mol^{-1} above the global minima) saddle points on the potential energy surface [11]. Figure 7.3 suggests that the ideal bonding angle between the two substituents R in TMR_6 is 63° or 117°. This can be achieved in molecular structures which have C_{3v} or C_{5v} symmetry [2a]. Experimental support for the bonding model of sd^n hybridization in TMR_n compounds with TM-R σ-bonds comes from the x-ray structure of $W(CH_3)_6$. A careful analysis of the equilibrium geometry reveals that the molecule has C_3 symmetry [12], which deviates strongly from the maximum symmetry form that is predicted by the VSEPR model [10].

The correlation between sd^n hybridization and molecular structure for TMR_x compounds is only valid when the TM-R bonds have no or very few π-orbital interactions. This holds, for example, when R is hydrogen or an alkyl group. Most substituents R have occupied π-orbitals that yield some degree of π-bonding, which has a very strong influence on the molecular geometry [13]. This holds in particular when R has lone-pair orbitals like halogens, OR and NR_2. Compounds such as $TMCl_4$ (TM = Ti, Zr, Hf) have T_d structures, which still agree with the sd^n hybridization model (Figure 7.3), but the quintuply substituted molecules VF_5, $NbCl_5$, and $TaCl_5$ have D_{3h} symmetry and the sextuply coordinated systems WX_6 (X = F, Cl, Br) possess Oh symmetry, which deviates from the prediction of the σ-bond model.

It is illuminating to compare the sd^n hybridization in TM compounds, which carry substituents with and without lone-pair orbitals, with sp^n hybridization in relation to main-group molecules. Table 7.1 shows the results for Me_2TMCl_2 (TM = Ti, Zr, Hf) and Me_2ECl_2 (E = C, Si, Ge, Sn, Pb) [14]. All main-group compounds have

Table 7.1 NBO Analysis of Me_2MCl_2 (M = C, Si, Ge, Sn, Pb, Ti, Zr, Hf) at MP2/VDZ+P[a].

	Calc. (exp.) Bond angle		M–C[b]				M–Cl[b]			
	C–M–C	Cl–M–Cl	% M	% s(M)	% p(M)	% d(M)	% M	% s(M)	% p(M)	% d(M)
Me_2CCl_2	113.1 (113.0)	108.7 (108.3)	52.5	31.4	68.5	0.1	46.1	18.6	81.1	0.2
Me_2SiCl_2	114.2 (114.7)	108.2 (107.2)	26.4	29.3	69.2	1.5	22.8	20.7	76.8	2.6
Me_2GeCl_2	118.3 (121.7)	106.6 (106.1)	29.1	30.7	68.8	0.5	22.3	19.3	79.4	1.3
Me_2SnCl_2	122.0 (110.1)	105.9 (107.5)	26.9	30.6	69.3	0.2	18.4	19.4	79.8	0.8
Me_2PbCl_2	128.9	105.1	31.2	31.8	68.2	0.0	18.6	18.2	81.6	0.2
Me_2TiCl_2	102.7 (106.2)	120.1 (116.7)	29.5	22.7	0.1	77.2	16.6	27.1	0.3	72.6
Me_2ZrCl_2	105.0	117.6	21.4	24.2	0.2	75.7	12.5	25.7	0.5	73.8
Me_2HfCl_2	104.9	116.5	15.6	25.5	5.4	69.1	9.8	24.4	11.0	64.6

[a] Taken from Ref. [14].
[b] % M gives the polarization of the M–C and M–Cl bonds; % s(M), % p(M) and % d(M) give the hybridization of the M–C and M–Cl bonds at the central atom M.

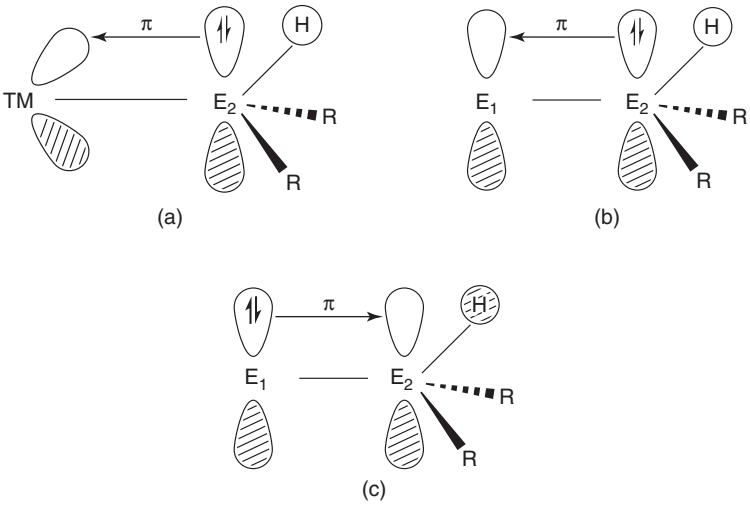

Figure 7.4 Schematic representation of: (a) Agostic interactions. (b) Negative hyperconjugation. (c) Hyperconjugation.

tetrahedral structures where the C–E–C angle is always larger and the Cl–E–Cl angle is smaller than 109.5°. The NBO analysis of the valence orbitals at atom E indicates that the % s character in the sp^n hybridized E–C orbitals is higher than in the E–Cl orbitals. This is in agreement with Bent's rule, which states that the % s character is larger in orbitals that are directed toward electropositive elements [15]. Inspection of the data calculated for Me_2TMCl_2 shows the opposite trend. The C–TM–C angle is always smaller and the Cl–E–Cl angle is larger than 109.5°. Additionally, the % s character in the sd^n hybridized TM–C orbitals is smaller than in the TM–Cl orbitals. It has been shown in a very detailed study that the more obtuse Cl–TM–Cl angle is enforced by TM ← Cl π-backdonation of the chlorine lone-pair electrons rather than the sd^n hybridization, which is actually not very different between the TM–C and TM–Cl bonds (Table 7.1) [13a].

TM-R π-bonding may play an important role even when the substituent R does not possess a lone-pair orbital. There are compounds $L_nTM\text{-}CHR_2$ which have C–H bonds that are rather long, while the acute bond angle TM–C–H is much smaller than 109°. The hydrogen atom is bridging the TM–C bond, which suggests π-bonding between the C–H bond and the d(π) AO of TM (Figure 7.4a). These have been termed ''agostic interactions'' [16], which occur in early TMs that possess vacant d(π) AOs. Such a type of interaction is not restricted to C–H bonds. It is a frequent phenomenon, for example, in TM compounds that carry silyl $SiHR_2$ or boryl BHR substituents. Agostic interactions may be considered as a special case of negative hyperconjugation that is found in main-group compounds where an occupied E^2-X π-orbital interacts with a vacant p(π) of an atom E^1 in the fragment E^1-E^2X (Figure 7.4b). The reverse donation from an occupied p(π) of an atom E^1 into a vacant E^2-X π^*-orbital is termed hyperconjugation (Figure 7.4c). The latter interaction may be found in late TM compounds where the metal possesses d(π)

lone-pair orbitals but it has not (yet) been given a new notation. Hyperconjugation, as shown in Figure 7.4c, is sometimes denoted as $\pi \rightarrow \sigma^*$ interaction, which is a misnomer. The terms σ and π are symmetry assignments for orbitals which are symmetric or antisymmetric with respect to a mirror plane. Thus, there cannot be any interaction between two orbitals which have σ- and π-symmetry because they are orthogonal to each other.

7.3 Carbonyl Complexes $TM(CO)_6^q$ ($TM^q = Hf^{2-}$, Ta^-, W, Re^+, Os^{2+}, Ir^{3+})

Carbonyl complexes $TM(CO)_n$ are a good starting point for a bonding analysis of TM compounds because they can be considered as a parent system for TM complexes in the same way as hydrocarbons are used as parent compounds for organic molecules. Figure 7.5 shows a qualitative description of bonding between a TM and a CO in terms of the DCD model as it is found in many chemistry textbooks. The main bonding contributions come from the electron donation of the CO σ HOMO into an empty d(σ) orbital of the metal and the backdonation from occupied d(π) orbitals of the metal into the unoccupied π*-orbital of CO.

The qualitative model, which is shown in Figure 7.5, can quantitatively be examined with the energy decomposition analysis (EDA) [17], which provides not only an estimate for the strength of the σ- and π-orbital bonding, but also for other components of the TM–CO bonding. The EDA has been described in detail in Vol. 1, Chapter 4, of the present book series and elsewhere [18] and, therefore, it is not discussed here. Table 7.2 gives the EDA results for TM–CO bonding in the series of isoelectronic complexes $TM(CO)_6^q$ ($TM^q = Hf^{2-}$, Ta^-, W, Re^+, Os^{2+}, Ir^{3+}), where the interactions between a CO ligand and the metal fragment $TM(CO)_5^q$ are investigated [3b]. The experimentally known compounds [19] are well-suited for a bonding analysis of carbonyl complexes, because the influence of the charge q on the different energy terms can be evaluated.

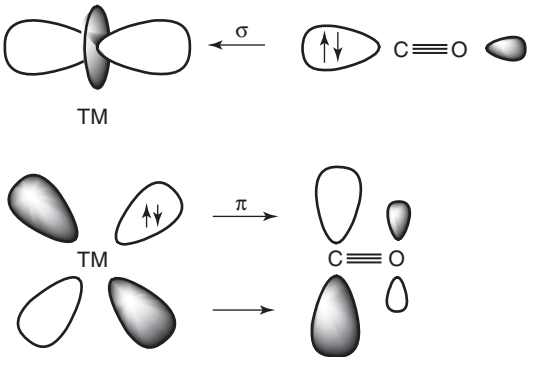

Figure 7.5 Schematic representation of synergistic TM←CO σ-donation and TM→CO π-backdonation.

Table 7.2 Energy decomposition analysis at BP86/TZP of $TM(CO)_6^q$ using the fragments $TM(CO)_5^q + CO$.[a]

	$Hf(CO)_6^{2-}$	$Ta(CO)_6^-$	$W(CO)_6$	$Re(CO)_6^+$	$Os(CO)_6^{2+}$	$Ir(CO)_6^{3+}$
ΔE_{int}	−56.6	−51.3	−49.6	−52.7	−61.9	−78.9
ΔE_{Pauli}	76.6	100.7	118.3	126.9	125.4	115.9
ΔE_{elstat}[b]	−59.4 (44.6%)	−76.6 (50.4%)	−90.1 (53.6%)	−97.7 (54.4%)	−98.5 (52.6%)	−93.1 (47.8%)
ΔE_{orb}[b]	−73.8 (55.4%)	−75.5 (49.6%)	−77.9 (46.4%)	−81.9 (45.6%)	−88.9 (47.4%)	−101.8 (52.2%)
$\Delta E_\sigma(a_1)$[c]	−17.2 (23.3%)	−25.8 (34.3%)	−35.9 (46.1%)	−47.3 (57.8%)	−60.1 (67.6%)	−75.4 (74.2%)
$\Delta E(a_2)$	0.00	0.00	0.00	0.00	0.00	0.00
$\Delta E(b_1)$	0.05	0.02	−0.03	−0.07	−0.09	−0.10
$\Delta E(b_2)$	−0.05	−0.07	−0.07	−0.07	−0.06	−0.05
$\Delta E_\pi(e)$[c]	−56.6 (76.7%)	−49.6 (65.8%)	−41.9 (53.8%)	−34.4 (42.1%)	−28.6 (32.2%)	−26.2 (25.8%)
ΔE_{prep}	5.8	3.1	3.7	4.4	5.0	5.2
$\Delta E (= -D_e)$	−50.8	−48.3	−46.0	−48.4	−56.9	−73.7
R(TM–C)	2.195	2.112	2.061	2.036	2.034	2.055

Energy values in kcal mol^{-1}. Bond lengths R in Å.
[a] Values are taken from Ref. [3b].
[b] The value in parentheses gives the percentage contribution to the total attractive interactions $\Delta E_{elstat} + \Delta E_{orb}$.
[c] The value in parentheses gives the percentage contribution to the total orbital interactions $\Delta E_{orb.}$

The interaction energies ΔE_{int} calculated for the $(CO)_5TM^q$–CO bonds show that the neutral complex $W(CO)_6$ has the weakest bond ($\Delta E_{int} = -49.6$ kcal mol^{-1}) of the hexacarbonyls. The bond strength increases for both the positively and the negatively charged carbonyls where the largest value is found for the trication $Ir(CO)_6^{3+}$ ($\Delta E_{int} = -78.9$ kcal mol^{-1}). An intuitive guess suggests that ionic (Coulombic) attraction enhances the bonding interactions in the charged systems. The data calculated for ΔE_{int} do not support the suggestion. The electrostatic attraction $(CO)_5TM^q$-CO strongly decreases from $W(CO)_6$ ($\Delta E_{elstat} = -90.1$ kcal mol^{-1}) to $Hf(CO)_6^{2-}$ ($\Delta E_{elstat} = -78.9$ kcal mol^{-1}), which does not agree with the overall increase of the bond strength. Table 7.2 shows that the electrostatic attraction increases further for the positively charged complexes $Re(CO)_6^+$ ($\Delta E_{elstat} = -97.7$ kcal mol^{-1}) and $Os(CO)_6^{2+}$ ($\Delta E_{elstat} = -98.5$ kcal mol^{-1}), but then it slightly decreases for $Ir(CO)_6^{3+}$ ($\Delta E_{elstat} = -93.1$ kcal mol^{-1}). The electrostatic interactions in $(CO)_5TM^q$-CO come mainly from the attraction between the σ lone-pair electrons of CO and the nucleus of TM. The trend of the calculated values for ΔE_{elstat} can thus be explained with the TM–CO bond length that decreases stepwise from $Hf(CO)_6^{2-}$ (2.195 Å) to $Os(CO)_6^{2+}$ (2.034 Å) and then increases for $Ir(CO)_6^{3+}$ (2.055 Å).

The values calculated for the $(CO)_5TM^q \leftarrow CO$ σ-donation consecutively increase from $Hf(CO)_6^{2-}$ to $Ir(CO)_6^{3+}$, whereas the $(CO)_5TM^q \rightarrow CO$ π-backdonation decreases in the same order. This is reasonable, because the vacant d(π) acceptor orbital of $(CO)_5TM^q$ becomes lower in energy when q becomes less negative or

more positive, whereas the opposite trend holds for the occupied d(σ) orbital of $(CO)_5TM^q$. Table 7.2 shows that the $(CO)_5W \rightarrow CO$ π-backdonation in $W(CO)_6$ is a bit stronger than the $(CO)_5W \leftarrow CO$ σ-donation. The latter interaction dominates the orbital interactions in the cations, whereas the former term becomes stronger in the negatively charged systems. It could be argued that the opposite trends of ΔE_σ and ΔE_π are responsible for the U-shaped trend of the total interaction ΔE_{int}. Inspection of the calculated values in Table 7.2 show that this assumption is only partly in agreement with the data. The total orbital interaction ΔE_{orb} increases from $W(CO)_6$ to $Ir(CO)_6^{3+}$ with roughly the same stepsize as the interaction ΔE_{int}, but the correlation does not hold from $W(CO)_6$ to $(Hf(CO)_6^{2-}$. Here, the orbital interaction ΔE_{orb} decreases, whereas the interaction ΔE_{int} increases (Table 7.2). The EDA results suggest that both attractive terms, ΔE_{orb} and ΔE_{elstat}, become smaller in the anions, but the $(CO)_5TM^q$–CO bonds become stronger. This is because the Pauli repulsion ΔE_{Pauli} strongly decreases, which overcompensates the weakening of the attractive terms.

The compounds $TM(CO)_6^q$ can be used to investigate the metal-CO interactions in even greater detail by analysing the interactions between the bare metal center TM^q and the ligand cage $(CO)_6$. Figure 7.6 shows the qualitative orbital correlation diagram of the valence orbitals of TM^q-$(CO)_6$ in an octahedral field, as it is found in chemistry textbooks [20]. The σ donor orbitals of the six CO ligands split in an octahedral field into three sets of orbitals which have e_g, t_{1u}, and a_{1g} symmetry. Figure 7.6 shows that the metal acceptor orbitals are the s AO (a_{1g}), p AOs (t_{1u}), and the e_g set of d AOs. The remaining set of (t_{2g}) d AOs of a d^6 TM is occupied and serves as a donor orbital for the $TM^q \rightarrow (CO)_6$ π-backdonation. Because of the high symmetry of the octahedral ligand field, the contributions of the e_g, t_{1u}, and a_{1g} orbitals to the $TM^q \leftarrow (CO)_6$ σ-donation give the relative importance of the d, p, and s metal valence orbitals directly to the metal-ligand bonding. The strength of the associated orbital interactions can be estimated with EDA calculations for the system TM^q-$(CO)_6$, where the six valence electrons of the metal center TM^q occupy the (t_{2g}) d AOs of the metal.

Table 7.3 gives the results of the EDA of TM^q-$(CO)_6$. The focus of the following discussion lies on the breakdown of the orbital term ΔE_{orb} into the contributions of the orbitals, which have different symmetry. The contribution of the t_{2g} orbitals which gives the $TM^q \rightarrow (CO)_6$ π-backdonation is rather small in the trication $Ir(CO)_6^{3+}$, but it becomes stronger when the metal is less positively charged and it is the dominant orbital term in the neutral and negatively charged hexacarbonyls. The opposite trend is found for the e_g orbitals, which clearly make the largest contribution to the $TM^q \leftarrow (CO)_6$ σ-donation. The e_g term is always much larger than the t_{1u} and a_{1g} terms. The data calculated suggest that the $TM^q \rightarrow (CO)_6$ π-backdonation is stronger than the $TM^q \leftarrow (CO)_6$ σ-donation when $TM^q = W$, Ta^-, Hf^{2-}, whereas the order is reversed when $TM^q = Re^+$, Os^{2+}, Ir^{3+}.

Table 7.3 also gives the energy contributions by the t_{1g} and t_{2u} orbitals, which are not shown in Figure 7.6. The complete set of orbitals that contribute to ΔE_{orb} is shown in Figure 7.7. It becomes obvious that the t_{1g} and t_{2u} MOs are occupied ligand orbitals. The energy contributions of the latter are a result of the relaxation

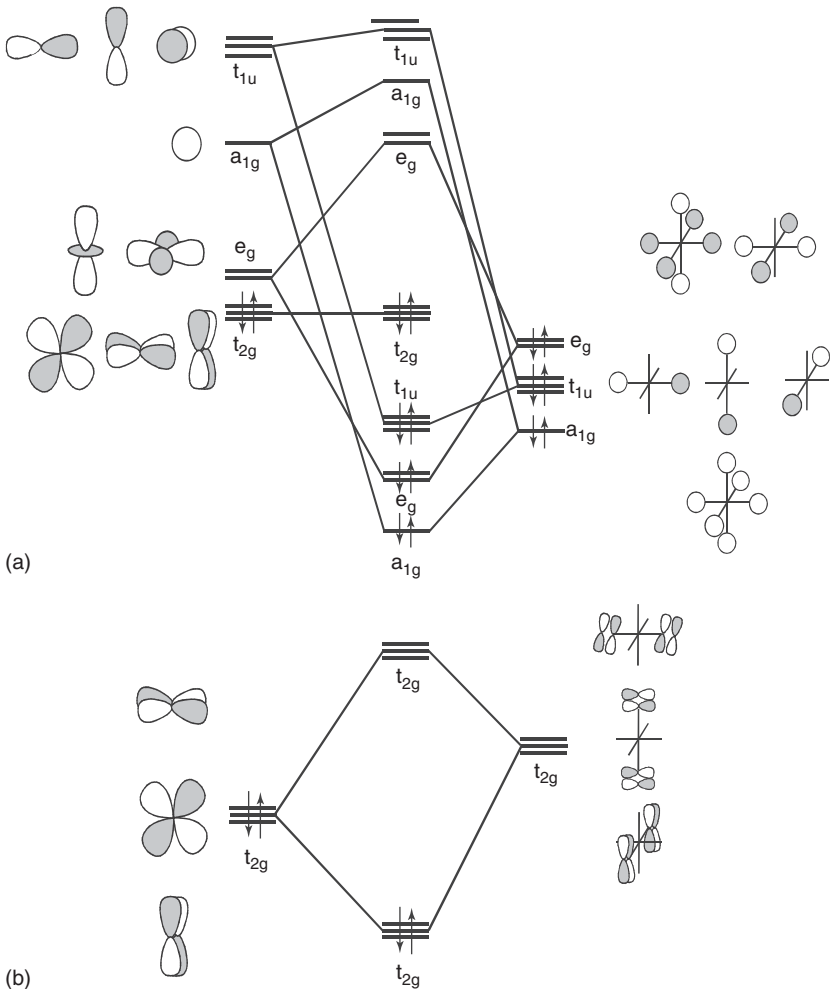

Figure 7.6 Splitting of the orbital energy levels of an octahedral d^6 transition metal complex TML_6, where the ligand L has (a) occupied donor orbitals with σ-symmetry and (b) empty acceptor orbitals with π-symmetry.

of the ligand orbitals in the final step of the energy partitioning analysis. Thus, part of the stabilization energy, which comes from the orbital term, is not related to the metal-ligand bonding. Figure 7.7 also shows that the t_{1u} term gives the TM ← $(CO)_6$ σ-donation into the metal p(σ) AO. Part of the t_{1u} stabilization energy comes from the TM ← $(CO)_6$ π-donation of the occupied π-orbitals of CO into the empty p(π) AO of the metal. In order to estimate the σ and π contributions to the t_{1u} term, the size of the overlaps of the metal p orbitals with the σ- and π-orbitals of $(CO)_6$ may be employed. Table 7.3 shows that the π contribution to the t_{1u} term that is estimated in this way is always much smaller than the σ contribution.

Table 7.3 Energy decomposition analysis at BP86/TZP of $TM(CO)_6^q$ using the fragments $TM^q + (CO)_6$.[a]

	$Hf(CO)_6^{2-}$	$Ta(CO)_6^-$	$W(CO)_6$	$Re(CO)_6^+$	$Os(CO)_6^{2+}$	$Ir(CO)_6^{3+}$
ΔE_{int}	−543.9	−525.6	−473.9	−456.6	−544.4	−801.6
ΔE_{Pauli}	367.4	413.4	438.8	454.5	451.3	420.9
ΔE_{elstat}[b]	−358.6 (39.4%)	−397.6 (42.3%)	−396.2 (43.4%)	−375.1 (41.2%)	−353.4 (35.5%)	−337.8 (27.6%)
ΔE_{orb}[b]	−552.7 (60.6%)	−541.3 (57.7%)	−516.4 (56.6%)	−536.0 (58.8%)	−642.3 (64.5%)	−884.7 (72.4%)
$\Delta E_\sigma(a_{1g})$[c]	−9.5 (1.7%)	−10.5 (1.8%)	−15.4 (2.8%)	−27.4 (4.6%)	−47.6 (6.4%)	−78.8 (7.5%)
$\Delta E(a_{2g})$	0.0	0.0	0.0	0.0	0.0	0.0
$\Delta E_\sigma(e_g)$[c]	−83.4 (14.6%)	−113.1 (20.3%)	−159.1 (29.3%)	−233.7 (39.6%)	−348.8 (46.9%)	−520.7 (49.5%)
$\Delta E(t_{1g})$[c] π(CO)	−1.3 (0.3%)	−1.0 (0.2%)	−2.9 (0.5%)	−8.9 (1.5%)	−19.4 (2.6%)	−33.9 (3.2%)
$\Delta E_\pi(t_{2g})$[c]	−437.4 (76.6%)	−397.6 (71.2%)	−308.2 (56.8%)	−200.3 (34.0%)	−101.1 (13.6%)	−43.8 (4.2%)
$\Delta E(a_{1u})$	−0.03	−0.04	−0.03	0.0	−0.02	−0.02
$\Delta E(e_u)$	0.0	−0.00	0.00	0.0	0.00	0.00
$\Delta E(t_{2u})$[c] π(CO)	−2.7 (4.8%)	−2.0 (0.4%)	−4.4 (0.8%)	−11.6 (2.0%)	−23.9 (3.2%)	−40.2 (3.8%)
$\Delta E_{\sigma,\pi}(t_{1u})$[c]	−18.4 (3.2%)	−17.2 (3.1%)	−26.5 (4.9%)	−54.0 (9.2%)	−101.4 (13.6%)	−167.3 (15.9%)
$\Delta E_\sigma(t_{1u})$[d]	−13.0	−12.1	−18.7	−38.5	−74.0	−125.7
$\Delta E_\pi(t_{1u})$[d]	−5.4	−5.2	−7.9	−15.5	−27.4	−41.7

Energy values in kcal mol^{-1}.
[a] Values are taken from Ref. [3b].
[b] The value in parentheses gives the percentage contribution to the total attractive interactions $\Delta E_{elstat} + \Delta E_{orb}$.
[c] The value in parentheses gives the percentage contribution to the total orbital interactions $\Delta E_{orb.}$
[d] The σ and π contributions of the T_{1u} orbitals have been estimated from the size of the overlaps.

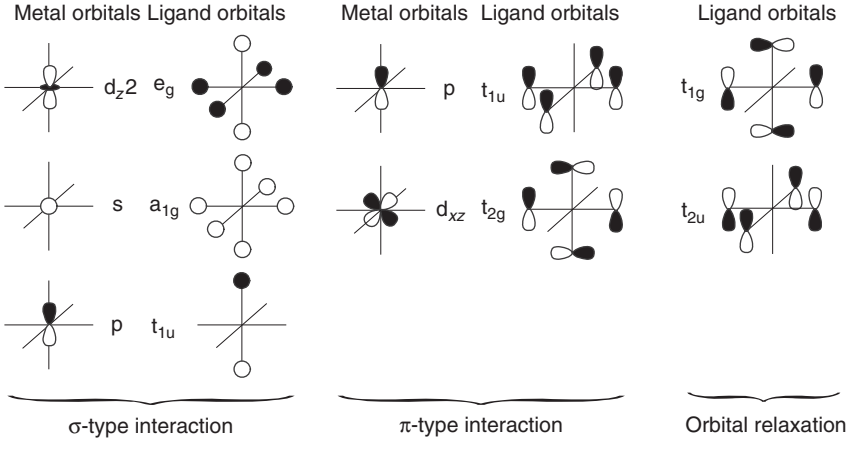

Figure 7.7 Graphical representation of the orbitals that give rise to the energy terms in the EDA decomposition of TM^q-$(CO)_6$ given in Table 7.3.

The discussion above shows that the combination of (i) the heuristic DCD model, shown in Figure 7.5, with (ii) the qualitative correlation diagram, shown in Figure 7.6, and (iii) the EDA results, given in Table 7.3, complement each other nicely. At the same time, they demonstrate the progress which has been made in the past 60 years in modelling the chemical bond in TM complexes. Methods such as the EDA do not replace previous qualitative models. Rather, they serve as a bridge between heuristic bonding models, which have proven to be useful for the interpretation of molecular structures and reactivities, and the physical mechanism of bond formation. The EDA provides a quantitative estimate of the energy terms which are used in chemical bonding theory. This shows major progress in chemical bonding theory.

Before leaving the topic of carbonyl complexes, we will briefly discuss the bonding interactions in a particular class of metal carbonyls, which have been termed ''nonclassical carbonyls'' [21]. Most carbonyl complexes $TM(CO)_n$ have C–O stretching frequencies which are smaller than for free CO (2143 cm^{-1}). Non-classical carbonyls possess C–O stretching modes where the wavenumbers are > 2143 cm^{-1}. The lower wavenumbers of classical carbonyls can be explained in terms of TM → CO π-backdonation into the CO π*-orbital (Figure 7.5), which weakens the C–O bond. Table 7.3 also gives the C–O stretching frequencies calculated for $TM(CO)_6^q$. There is a continuous trend of decreasing wavenumbers from $Ir(CO)_6^{3+}$ to $(Hf(CO)_6^{2-}$ with rather large intervals of ~100 cm^{-1}. The trend correlates nicely with the increase of the $TM^q \rightarrow (CO)_6$ π-backdonation in the same order. While these results can be taken as evidence that the lowering of the CO stretching frequency below 2143 cm^{-1} is indeed caused by increasing TM → CO π-backdonation, it is not clear why $Os(CO)_6^{2+}$ and $Ir(CO)_6^{3+}$ exhibit vibrational frequencies ν(C–O) > 2143 cm^{-1}.

The dominant orbital interactions in $Os(CO)_6^{2+}$ and $Ir(CO)_6^{3+}$ come from $TM^q \leftarrow (CO)_6$ σ-donation. It has been suggested that the 5σ donor orbital of CO is antibonding and, therefore, donation from the HOMO would strengthen the C–O bonding [22]. Inspection of the shape of the 5σ HOMO of CO shows, however, that there is no node between the atoms. Calculations of HCO^+ and COH^+ show, furthermore, that the C–O bond length becomes shorter in the former cation but it becomes clearly longer in the latter species. Since the charge donation from CO to H^+ occurs in both cases through the 5σ HOMO of CO, the opposite change in the C–O distance cannot be explained with the antibonding nature of the orbital. A plausible explanation is found when the effect of a proton or a positive charge Q on the polarization of the valence orbitals of CO is considered [23]. This is schematically shown in Figure 7.8. Analysis of the σ- and π-orbitals revealed that the MOs in the CO moiety become less polarized in HCO^+ and QCO^+, which therefore become stronger, while they become more polarized in COH^+ and COQ^+ and thus weaker than in free CO. The electrostatic effect on the polarization of the valence orbitals of CO provides a straightforward explanation for the change of the C-O stretching frequency in the absence of strong π-backdonation.

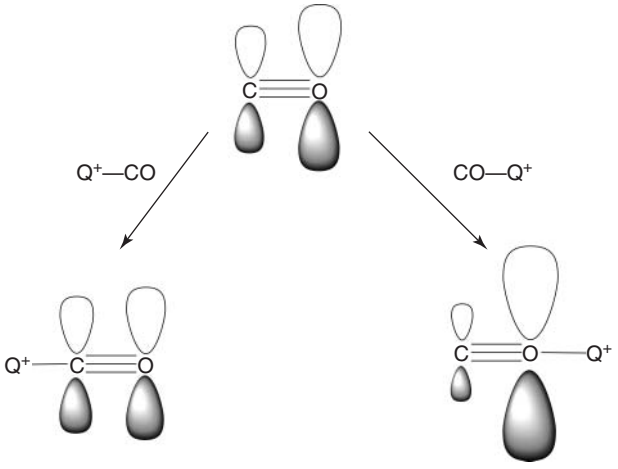

Figure 7.8 Schematic representation of the change in the polarization of the π-orbital of CO when a positive charge becomes attached to the carbon or the oxygen atom. The same effect is found for the σ-orbitals.

7.4 Phosphane Complexes $(CO)_5$TM-PR_3 and N-Heterocyclic Carbene Complexes $(CO)_5$TM-NHC (TM = Cr, Mo, W)

TM phosphane complexes L_nTM-PR_3 are ubiquitious species in TM chemistry, which are experimentally known for virtually all metals. Phosphane ligands are considered strong σ-donors and weak π-acceptors, because they have an energetically rather high-lying σ lone-pair donor orbital in phosphorous, which is the HOMO of PR_3, whereas the antibonding π*-orbital is not a strong acceptor, unless R is a halogen or OPR_3, which significantly lower the energy of the π*-orbital (Figure 7.9a and b). The ligand property of phosphanes are often compared with N-heterocyclic carbenes (NHCs), which have become very important ligands in TM chemistry in the last two decades because complexes with NHC ligands are very efficient catalysts for a variety of chemical reactions [24]. NHC ligands are also considered mainly as σ-donors and weak π-acceptors. The σ-donation takes place via the carbon σ lone-pair orbital, whereas the formally vacant p(π) AO of carbon serves as the acceptor orbital (Figure 7.9c and d). The latter orbital receives significant charge from the π lone-pair orbitals of the neighboring nitrogen atoms, which strongly reduces the acceptor strength of the p(π) AO of carbon. Theoretical studies suggest that NHCs may become weak π-donors in TM complexes via the partially filled p(π) AO of carbon [25].

A comparative analysis of phosphane complexes $(CO)_5$TM-PR_3 (TM = Cr, Mo, W), which possess different substituents R, with NHC complexes $(CO)_5$TM-NHC with the help of EDA calculations provides deep insights into the nature of the metal-ligand interactions. Since the metal fragment $W(CO)_5$ has also been used in the earlier chapter about carbonyl complexes, it is possible to compare the

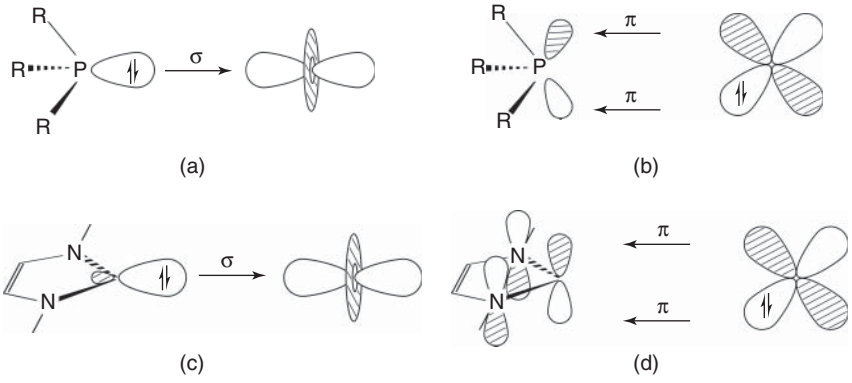

Figure 7.9 Schematic representation of synergistic donor–acceptor interaction in transition metal complexes with phosphane and NHC ligands. (a) TM ← PR_3 σ-donation; (b) TM → PR_3 π-backdonation; (c) TM ← NHC σ-donation; (d) TM → NHC π-backdonation.

Table 7.4 Energy decomposition analysis at BP86/TZP of $TM(CO)_5PR_3$ using the fragments $TM(CO)_5$ + PR_3.[a]

	$Cr(CO)_5PMe_3$	$Mo(CO)_5PMe_3$	$W(CO)_5PMe_3$	$Cr(CO)_5PCl_3$	$Mo(CO)_5PCl_3$	$W(CO)_5PCl_3$
ΔE_{int}	−43.7	−40.9	−46.4	−27.8	−26.1	−31.1
ΔE_{pauli}	96.5	85.6	99.3	78.4	70.1	83.3
ΔE_{elstat}[b]	−85.1 (60.7%)	−80.7 (63.8%)	−94.9 (65.1%)	−49.6 (46.7%)	−45.3 (47.3%)	−55.8 (48.8%)
ΔE_{orb}[b]	−55.1 (39.3%)	−45.8 (36.2%)	−50.8 (34.9%)	−56.6 (53.3%)	−51.0 (52.9%)	−58.5 (51.2%)
ΔE_{σ}[c]	−41.0 (74.3%)	−33.1 (72.3%)	−37.3 (73.4%)	−30.4 (53.7%)	−26.3 (51.5%)	−31.2 (53.3%)
ΔE_{π}[c]	−14.2 (25.7%)	−12.7 (27.7%)	−13.5 (26.6%)	−26.2 (46.3%)	−24.7 (48.5%)	−27.3 (46.7%)
ΔE_{prep}	2.5	3.0	2.6	1.0	2.5	2.5
ΔE (= $-D_e$)	−41.2	−37.9	−43.8	−26.8	−23.7	−28.6
R(TM–P)	2.390	2.553	2.552	2.300	2.467	2.459

Energy values in kcal mol^{-1}. Bond lengths R in Å.
[a]Values are taken from Ref. [26].
[b]The value in parentheses gives the percentage contribution to the total attractive interactions $\Delta E_{elstat} + \Delta E_{orb}$.
[c]The value in parentheses gives the percentage contribution to the total orbital interactions ΔE_{orb}.

phosphane and NHC ligands with CO. At the same time a comparison can be made between complexes of the first, second, and third TM row.

Table 7.4 shows the EDA results for the phosphane complexes $(CO)_5$TM-PMe_3 and $(CO)_5$TM-PCl_3 (TM = Cr, Mo, W) where the bond lengths and BDEs pose a challenge for chemical bonding models. The calculated TM–P distances in $(CO)_5TM-PMe_3$ are clearly longer than in $(CO)_5TM-PCl_3$, but the former complexes have significantly larger bond dissociation energies D_e than the latter species [26]. The EDA data, which provide a detailed insight into the nature of the $TM-PR_3$ bonds, give a straightforward answer to the question about the origin of the puzzling bond length/bond energy relationship [27]. The preparation energies

ΔE_{prep} are in all cases very small. The differences between the BDEs are thus directly related to the strength of the TM–PR_3 interactions, which are stronger in $(CO)_5TM\text{-}PMe_3$ than in $(CO)_5TM\text{-}PCl_3$ (Table 7.4). Which of the energy terms that contribute to the interaction energy ΔE_{int} is responsible for the bond length/bond energy relationship?

Inspection of the orbital interactions shows that the π-backdonation ΔE_π for $(CO)_5TM \rightarrow PCl_3$ is, as expected, significantly stronger than for $(CO)_5TM \rightarrow PMe_3$. In contrast, the σ-donation ΔE_σ $(CO)_5TM \leftarrow PCl_3$ is weaker than for $(CO)_5TM \leftarrow PMe_3$. The σ lone-pair orbital of PCl_3 is a much weaker donor than the HOMO of PMe_3 because it has a much higher % s character of 80% than the latter which has 51% of s [26]. However, the strength of the total orbital interactions ΔE_{orb} in $(CO)_5TM\text{-}PCl_3$ is a little higher than in $(CO)_5TM\text{-}PMe_3$, which does not agree with the trend of ΔE_{int}. *The relative bond strengths of the latter two systems are examples where the trend cannot be explained in terms of orbital interactions!*

Table 7.4 shows that the Pauli repulsion ΔE_{Pauli} in the series $(CO)_5TM\text{-}PCl_3$ is always weaker than in the compounds $(CO)_5TM\text{-}PMe_3$. The reason for this is similar to the weak $(CO)_5TM \leftarrow PCl_3$ σ-donation: The more compact σ lone-pair orbital of PCl_3, which has a much higher % s character than in PMe_3, encounters less overlap with the occupied orbitals of TM, although the TM–PCl_3 distance is smaller than R(TM-PMe_3). Thus, neither ΔE_{orb} nor ΔE_{Pauli} explain the order for the TM–PR_3 bond strength. The explanation is rather given by the values calculated for the electrostatic term ΔE_{elstat} which show that the Coulombic attraction in $(CO)_5TM\text{-}PMe_3$ is much stronger (between −80.7 and −94.9 kcal mol^{-1}) than in $(CO)_5TM\text{-}PCl_3$ (between −45.3 and −55.8 kcal mol^{-1}). The electrostatic attraction in $(CO)_5TM\text{-}PR_3$ comes mainly from the overlap of the phosphorous lone-pair electrons with the nucleus of TM. The larger % s character of the σ-HOMO of PMe_3 compared with PCl_3 yields stronger attraction even at longer TM–P distances.

The EDA data show that the nature of the $(CO)_5TM\text{–}PR_3$ bonding changes little between the metals of the first, second, and third TM row atoms Cr, Mo, W. The TM–PR_3 bond strength given by ΔE_{int} for the second-row element Mo is weaker than for Cr, which agrees with the general trend that chemical bonds of atoms within a group of the periodic system tend to become weaker when the atom is in a higher row. This is because the valence electrons of heavier atoms are farther away from the nucleus and their interactions with other atoms are, therefore, weaker [28]. However, first TM row atoms may sometimes have weaker bonds than second TM elements in cases where π-backdonation is absent or negligible. The 3d valence orbitals of the first TM row atoms are nodeless and, therefore, they can penetrate into the core of the atoms, which leads to rather small radii for the 3d AOs. Thus, σ-bonded ligands, which are bonded to first TM row atoms, may encounter Pauli repulsion with the outer core 3p electrons, which can lead to weaker bonds than isoelectronic second TM row atoms. The stronger bonds of the third TM row element tungsten are because of relativistic effects, which are well-understood [29].

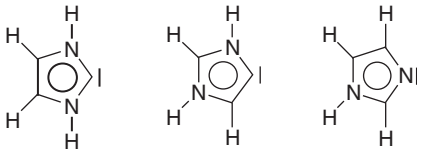

Figure 7.10 Schematic representation of the tautomers of N-heterocyclic carbenes. (a) ''normal'' NHC (imidazol-2-ylidene) **NHC(*n*)**. (b) ''abnormal'' NHC (imidazol-4-ylidene) **NHC(a)**. (c) Imidazol **NHC(I)**.

A detailed account of relativistic effects on chemical bonding is given in Volume 1, Chapter 11, of the present book.

Table 7.5 gives the EDA results for the NHC complexes $(CO)_5$TM-NHC(*n*) and for the tautomers $(CO)_5$TM-NHC(a) and $(CO)_5$TM-NHC(I) (Figure 7.10) [30]. Complexes with all three tautomeric forms of the NHC ligands are experimentally known. The NHC(a) ligands which bind through the C4/C5 position are termed ''abnormal'' because NHC ligands commonly coordinate through the C2 position leading to the ''normal'' complexes $(CO)_5$TM-NHC(*n*). The imidazole tautomer NHC(I) that binds through nitrogen is the most stable isomer of the free ligands.

The EDA results for the complexes $(CO)_5$TM-NHC(n) show (Table 7.5) that the NHC(*n*) ligand binds more strongly to the metal than PMe_3 and particularly PCl_3 (Table 7.4). The breakdown of the orbital term into σ- and π-contributions reveal that NHC(*n*) is a stronger σ-donor and a weaker π-acceptor than the phosphane ligands. The ''abnormal'' ligand NHC(a) binds still a little stronger to TM$(CO)_5$ than the ''normal'' tautomer NHC(*n*), which comes from slightly stronger σ-donation in $(CO)_5$TM ← NHC(a) and, thus, also yields stronger electrostatic attraction. The nature of the metal-ligand bonding in the imidazole complexes $(CO)_5$TM-NHC(I) is very similar to the bonding in $(CO)_5$TM-NHC(*n*) and $(CO)_5$TM-NHC(a) (Table 7.5). The weaker bonding in the former isomers comes from the energetically lower-lying nitrogen lone-pair orbital compared with the carbene σ-donor orbital.

7.5
Ethylene and Acetylene Complexes $(CO)_5$TM-C_2H_n and Cl_4TM-C_2H_n (TM = Cr, Mo, W)

The nature of the chemical bonding between a TM and alkene or alkyne ligands can be discussed with two different models, which are depicted in Figure 7.11. The bonding can be considered to arise either from donor–acceptor interactions between the alkene or alkyne ligand and the TM fragment (Figure 7.11a and c) or as electron-sharing interactions between triplet fragments, which lead to a metallacyclic compound (Figure 7.11b and d). The TM ← ligand σ-donation arises from the occupied in-plane $\pi_{\|}$-MOs of the alkene or alkyne ligands (which has σ-symmetry in the complex) whereas the TM → ligand π-backdonation occurs

Table 7.5 Energy decomposition analysis at BP86/TZP of $TM(CO)_5NHC$ using the fragments $TM(CO)_5$ + NHC.[a]

Metal fragment Ligand	$Cr(CO)_5$ $Cr(CO)_6$	$Mo(CO)_5$ NHC(n)	$W(CO)_5$ $W(CO)_6$	$Cr(CO)_5$ $Cr(CO)_6$	$Mo(CO)_5$ NHC(a)	$W(CO)_5$ $W(CO)_6$	$Cr(CO)_5$ $Cr(CO)_6$	$Mo(CO)_5$ NHC(l)	$W(CO)_5$ $W(CO)_6$
ΔE_{int}	−53.9	−51.5	−58.3	−57.5	−55.4	−62.1	−31.9	−31.8	−36.6
ΔE_{Pauli}	112.3	103.7	124.3	112.5	106.7	126.0	58.4	56.5	69.2
ΔE_{elstat}[b]	−110.6 (66.5%)	−107.8 (69.5%)	−129.1 (70.7%)	−113.1 (66.5%)	−112.9 (69.6%)	−133.5 (70.9%)	−59.6 (66.0%)	−59.8 (67.7%)	−72.1 (68.1%)
ΔE_{orb}[b]	−55.7 (33.5%)	−47.4 (30.5%)	−53.5 (29.3%)	−57.0 (33.5%)	−49.2 (30.4%)	−54.7 (29.1%)	−30.7 (34.0%)	−28.5 (32.3%)	−33.7 (31.9%)
ΔE_{σ}[c]	−46.0 (82.6%)	−38.6 (81.5%)	−43.5 (81.3%)	−48.2 (84.6%)	−41.1 (83.5%)	−45.6 (83.4%)	−25.5 (82.9%)	−23.4 (82.1%)	−27.7 (82.0%)
ΔE_{π}[c]	−9.7 (17.4%)	−8.8 (18.5%)	−10.0 (18.7%)	−8.8 (15.4%)	−8.1 (16.5%)	−9.1 (16.6%)	−5.3 (17.1%)	−5.1 (17.9%)	−6.1 (18.0%)
ΔE_{prep}	2.2	2.2	2.6	1.7	2.3	2.5	1.0	1.2	1.5
$\Delta E\ (= -D_e)$	−51.7	−49.3	−55.7	−55.9	−53.1	−59.6	−31.0	−30.6	−35.1
R(TM–L)	2.090	2.238	2.228	2.108	2.252	2.245	2.161	2.299	2.282

Energy values in kcal mol^{-1}. Bond lengths R in Å.

[a] Values are taken from Ref. [30].

[b] The value in parentheses gives the percentage contribution to the total attractive interactions $\Delta E_{elstat} + \Delta E_{orb}$.

[c] The value in parentheses gives the percentage contribution to the total orbital interactions ΔE_{orb}.

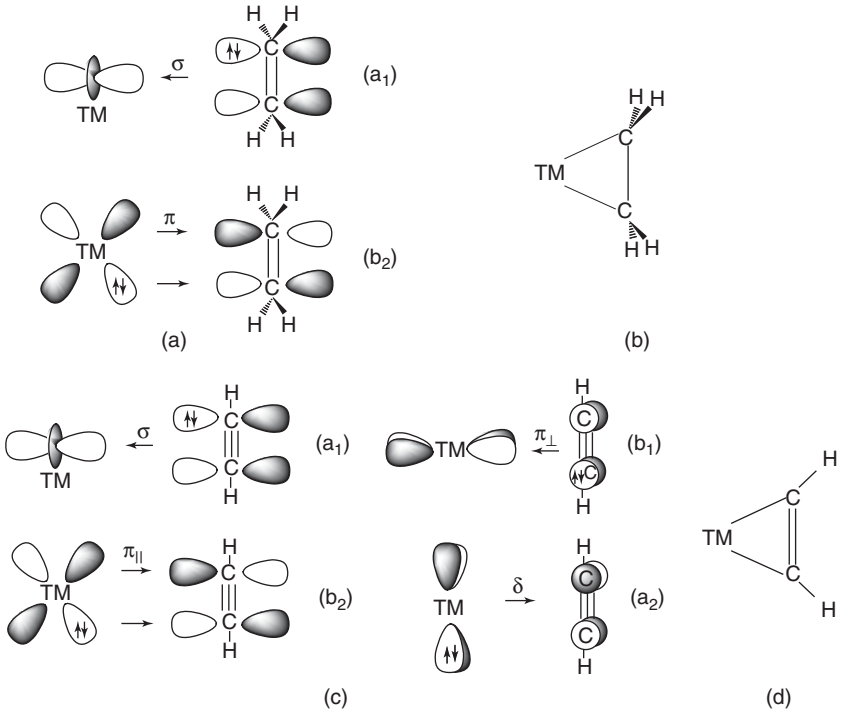

Figure 7.11 Schematic representation of synergistic donor–acceptor interactions in transition metal complexes with ethylene and acetylene ligands and associated symmetry assignment (C_{2v}) and bonding in metallacylic molecules. (a) TM ← C_2H_4 σ-donation (a_1) and TM → C_2H_4 π-backdonation (b_2). (b) Metallacyclopropane. (c) TM ← C_2H_2 in-plane σ-donation (a_1), TM → C_2H_2 in-plane $\pi_{||}$-backdonation (b_2), TM ← C_2H_4 out-of-plane $\pi_{\perp}$-donation (b_1) and TM → C_2H_2 δ-backdonation. (d) Metallacyclopropene.

through charge donation from the occupied d_{xz} MO of the metal to the vacant $\pi_{||}$*-orbital of the ligand. Alkyne ligands have additional occupied and vacant out-of-plane $\pi_{\perp}$-orbitals, which lead to TM←ligand $\pi_{\perp}$-donation and TM → ligand δ-backdonation (Figure 7.11c).

A similar dichotomy of bonding models exists for other classes of TM compounds where the chemical bond can be discussed either in terms of electron-sharing interactions TM-R or as donor–acceptor bond TM-L. Examples are TM compounds with carbenes CR_2 or carbynes CR as ligands, which can be considered as either Fischer-type complexes or as Schrock-type alkylidenes and alkylidynes [31, 32]. We want to emphasize that the two bonding models should be considered as sketches of two extreme situations, whereas the electronic situation of real molecules has components of both forms. The value of such dichotomic models lies in the fact that they establish an ordering scheme, which is very useful for describing the physical and chemical properties of molecules.

The choice of the interacting fragments for the EDA calculations is crucial for the numerical results and for the interpretation of the bonding situation. We discuss two sets of compounds $(CO)_5TM\text{-}C_2H_n$ and $Cl_4TM\text{-}C_2H_n$ (TM = Cr, Mo, W; $n = 2, 4$) where chemical intuition suggests that the former compounds are donor–acceptor complexes where one CO ligand of $TM(CO)_6$ is replaced by C_2H_n, while the second molecules are derived from $TMCl_6$ and, therefore, chemical bonding in $Cl_4TM\text{-}C_2H_n$ should be discussed in terms of electron-sharing interactions. The choice of closed-shell fragments for $(CO)_5TM\text{-}C_2H_n$ and open-shell fragments for $Cl_4TM\text{-}C_2H_n$ is supported by earlier theoretical studies of the system with the help of a charge-decomposition analysis [33]. There may be compounds where the choice of the interacting fragments for the EDA calculation is not as straightforward as in the present case. In such situations, all suitable pairs of interacting fragments may be employed for the EDA calculation. That pair of fragments, which gives the smallest absolute value for ΔE_{orb}, should then be used for the interpretation of the bonding situation, because it indicates that that pair of fragments is the most suitable for the bond formation.

Table 7.6 shows the EDA results for $(CO)_5TM\text{-}C_2H_n$ (TM = Cr, Mo, W) [34]. The BDEs and the intrinsic interaction energies ΔE_{orb} exhibit the same trend Mo < Cr < W as the phosphane and NHC complexes that were discussed earlier. The metal-ligand bonds have a slightly more electrostatic than covalent character. The molecules have C_{2v} symmetry and, thus, the contributions, which come from orbitals that possess different symmetry can be directly assigned to the orbital interactions, which are shown in Figure 7.11. The EDA data suggest that the

Table 7.6 Energy decomposition analysis at BP86/TZP of $(CO)_5TM\text{-}C_2H_x$ using the fragments $TM(CO)_5$ and C_2H_x.[a]

Metal fragment	$Cr(CO)_5$		$Mo(CO)_5$		$W(CO)_5$	
Ligand	C_2H_4	C_2H_2	C_2H_4	C_2H_2	C_2H_4	C_2H_2
ΔE_{int}	−29.9	−29.6	−25.6	−26.5	−35.4	−38.1
ΔE_{Pauli}	83.9	86.2	69.1	74.9	93.0	103.5
ΔE_{elstat}[b]	−59.5 (52.3%)	−59.8 (51.7%)	−52.0 (55.0%)	−54.5 (53.8%)	−70.0 (54.5%)	−75.0 (52.9%)
ΔE_{orb}[b]	−54.3 (47.7%)	−56.0 (48.3%)	−42.6 (45.0%)	−46.9 (46.3%)	−58.4 (45.5%)	−66.6 (47.1%)
$\Delta E(a_1)\sigma$[c]	−29.0 (53.5%)	−27.1 (48.4%)	−20.4 (47.9%)	−19.8 (42.3%)	−28.8 (49.3%)	−28.4 (42.6%)
$\Delta E(a_2)\delta$[c]	−0.6 (1.2%)	−1.3 (2.3%)	−0.6 (1.5%)	−1.1 (2.2%)	−0.7 (1.3%)	−1.4 (2.1%)
$\Delta E(b_1)\pi_\perp$[c]	−2.2 (4.0%)	−2.5 (4.5%)	−2.1 (5.0%)	−3.0 (6.4%)	−2.7 (4.6%)	−4.1 (6.1%)
$\Delta E(b_2)\pi_\parallel$[c]	−22.5 (41.4%)	−25.1 (44.9%)	−19.4 (45.6%)	−23.0 (49.0%)	−26.2 (44.9%)	−32.8 (49.2%)
ΔE_{prep}	6.3	8.4	4.9	7.5	7.5	11.6
$\Delta E(= -D_e)$	−23.6	−21.2	−20.6	−19.0	−27.9	−26.6
R(C–C)	1.383	1.237	1.375	1.235	1.388	1.245

Energy values in kcal mol^{-1}. Bond lengths R in Å.

[a] Values are taken from Ref. [34].

[b] The value in parentheses gives the percentage contribution to the total attractive interactions $\Delta E_{elstat} + \Delta E_{orb}$.

[c] The value in parentheses gives the percentage contribution to the total orbital interactions ΔE_{orb}.

Table 7.7 Energy decomposition analysis of $Cl_4TM\text{-}C_2H_x$ at BP86/TZP using triplet fragments $TMCl_4$ and C_2H_x.[a]

Metal fragment	$MoCl_4$		WCl_4	
Ligand	C_2H_4	C_2H_2	C_2H_4	C_2H_2
ΔE_{int}	−126.1	−153.1	−139.7	−169.4
ΔE_{pauli}	209.1	268.7	257.9	313.9
ΔE_{elstat}[b]	−132.6 (39.6%)	−165.9 (39.3%)	−172.8 (43.5%)	−206.8 (42.8%)
ΔE_{orb}[b]	−202.6 (60.4%)	−256.0 (60.7%)	−224.7 (56.5%)	−276.5 (57.2%)
$\Delta E(a_1)\sigma$[c]	−101.9 (50.3%)	−121.4 (47.4%)	−116.0 (51.6%)	−135.0 (48.8%)
$\Delta E(a_2)\delta$[c]	−2.5 (1.2%)	−2.8 (1.1%)	−2.8 (1.2%)	−2.4 (0.9%)
$\Delta E(b_1)\pi_\perp$[c]	−6.9 (3.4%)	−27.4 (10.7%)	−8.4 (3.7%)	−30.0 (10.9%)
$\Delta E(b_2)\pi_\parallel$[c]	−91.3 (45.1%)	−104.4 (40.8%)	−97.5 (43.4%)	−109.1 (39.4%)
ΔE_{prep}	133.9	141.2	126.8	131.5
$\Delta E(= -D_e)$	7.8	−11.9	−12.9	−37.9
R(C–C)	1.429	1.307	1.451	1.317

Energy values in kcal/mol. Bond lengths R in Å.
[a]Values are taken from Ref. [34].
[b]The value in parentheses gives the percentage contribution to the total attractive interactions $\Delta E_{elstat} + \Delta E_{orb}$.
[c]The value in parentheses gives the percentage contribution to the total orbital interactions ΔE_{orb}.

$(CO)_5TM\text{-}C_2H_n$ bonding can be discussed in terms of the DCD bonding model, where the $(CO)_5TM \leftarrow C_2H_n$ σ-donation (a_1 symmetry) and the $(CO)_5TM \rightarrow C_2H_n$ π-backdonation (b_2 symmetry) have similar strengths. The $\Delta E(a_1)$ σ contribution of the ethylene complexes is always slightly stronger than that of the acetylene complexes, whereas the $\Delta E(b_2)\pi_\parallel$ term of the latter species is a bit larger than that of the former compounds. The contributions $\Delta E(a_2)\delta$ which indicate δ-bonding and $\Delta E(b_1)\pi_\perp$ which come from the out-of-plane $\pi_\perp$-orbital (Figure 7.11c) are negligible even for the acetylene complexes. Note that the interaction energies of the ethylene and acetylene ligands in $(CO)_5Cr\text{-}C_2H_n$ and $(CO)_5Mo\text{-}C_2H_n$ are nearly identical, whereas ΔE_{int} for $(CO)_5W\text{-}C_2H_4$ is a bit smaller than for $(CO)_5Mo\text{-}C_2H_2$ (Table 7.6). The BDEs of $(CO)_5TM\text{-}C_2H_4$ are always slightly larger than for $(CO)_5TM\text{-}C_2H_2$ because the preparation energies of the latter are bigger. This shows that the BDE is not a reliable probe for the strength of the chemical bond.[2)]

The EDA results for the metal-ligand interactions in the metallacyclic compounds $Cl_4TM\text{-}C_2H_n$ (TM = Mo, W), which are shown in Table 7.7, are very different from the data for the ethylene and acetylene complexes. There are no results for the chromium compounds because of SCF problems [34]. The electron-sharing

2) The bond dissociation energy includes the geometrical and electronic relaxation of the fragments of the fragments A and B after breaking the bond A–B which can be very large. There are many thermodynamically unstable compounds where the fragments A and B are energetically even lower lying than the molecule A–B which leads to negative values for the BDE which obviously makes them unsuitable as measure for the bond strength.

interactions ΔE_{int} of the metal-carbon bonds in $Cl_4TM\text{-}C_2H_n$ are much stronger than the donor–acceptor interactions in $(CO)_5TM\text{-}C_2H_n$ (Table 7.6). However, the bond dissociation energies are rather small. The theoretically predicted BDE of $Cl_4Mo\text{-}C_2H_4$ is even positive. Thus, this molecule is only kinetically stable. The small values for the BDEs are caused by the large preparation energies which come mainly from the large singlet to triplet excitation of the C_2H_x ligands.

The largest contributions to the orbital term ΔE_{orb} in $Cl_4TM\text{-}C_2H_n$ come from $\Delta E(a_1)\sigma$ and $\Delta E(b_2)\pi_{\|}$, which are associated with the formation of the TM–C bonds. The $\Delta E(b_1)\pi_{\perp}$- and $\Delta E(a_2)\delta$-contributions arise from the out-of-plane $(CO)_5TM \leftarrow C_2H_n$ $\pi_{\perp}$-donation and the $(CO)_5TM \rightarrow C_2H_n$ δ-backdonation (Figure 7.11c). Table 7.7 shows that the former interaction makes a noticeable contribution to ΔE_{orb}, which might be taken as an explanation as to why the intrinsic interaction energies of the metallacyclopropenes $Cl_4TM\text{-}C_2H_2$ are about 30 kcal mol^{-1} stronger than in the metallacyclopropanes $Cl_4TM\text{-}C_2H_4$. However, such reasoning is arbitrary. The EDA data indicate that the contributions from $\Delta E(a_1)\sigma$ and $\Delta E(b_2)\pi_{\|}$ are also much stronger in the former compounds than in the latter. The total strength of the orbital interactions ΔE_{orb} in $Cl_4TM\text{-}C_2H_2$ is approximately 50 kcal mol^{-1} bigger than in $Cl_4TM\text{-}C_2H_4$ (Table 7.7). The stronger covalent interactions in the former systems are compensated by the Pauli repulsion ΔE_{orb}, which comes from the interactions between the occupied orbitals of the fragments. Thus, it may be argued that the stronger binding interactions in the metallacyclopropenes $Cl_4TM\text{-}C_2H_2$ actually comes from the larger Coulombic term ΔE_{elstat} which is approximately 30 kcal mol^{-1} bigger than in $Cl_4TM\text{-}C_2H_4$.

7.6
Group-13 Diyl Complexes $(CO)_4Fe$-ER (E = B – Tl; R = Ph, Cp)

Metal complexes with group-13 diyl ligands ER, where the atom E = B–Tl is in the oxidation state I, are ideally suited to compare the chemical bonding of TMs with ligands that come from a whole group of the periodic system. At the same time the influence of the substituent R on the nature and the strength of metal-ligand interactions can be studied. Figure 7.12 shows the relevant orbital interactions schematically and also the most important contribution to the electrostatic attraction in TM–ER interactions.

The TM–ER orbital interactions can be straightforwardly explained with the DCD bonding model. There is TM ← ER σ-donation from the lone-pair electrons of the ligand into the d(σ) AO of the metal and TM → ER π-backdonation from the d(π) AOs of TM into the p(π) AOs of atom E. The strength of the latter interaction will be influenced by π-donation E ← R when the substituent R has π lone-pair electrons. The Cp (Cp = cyclopentadienyl) ligand which has a facial orientation toward atom E is a very strong π-donor, whereas the phenyl group Ph which has a horizontal orientation is a poor π-donor. It may, therefore, be expected that the TM → ER π-backdonation in $(CO)_4Fe$-ECp should be much weaker than in $(CO)_4Fe$-EPh.

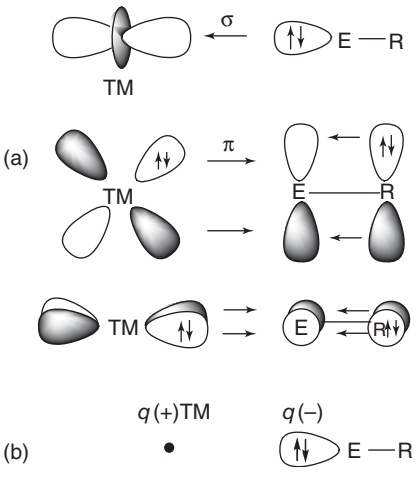

Figure 7.12 Schematic representation of synergistic donor–acceptor interactions in transition metal complexes with group-13 diyl ligands ER (E = B – Tl). (a) TM ← ER σ-donation and TM → ER π-backdonation. (b) Coulombic attraction between the lone-pair electrons of the ER ligand and the nucleus of TM.

The qualitative suggestion of the DCD bonding model may be quantitatively tested by the EDA.

The EDA results for the complexes $(CO)_4$Fe-ECp are given in Table 7.8 [35]. The data come from the axial isomers which are more stable than the equatorial form. There is a continuous decrease of the BDE and the interaction energy from the lightest atom boron to the heaviest atom thallium, except for the increasing ΔE_{int} values from In to Tl. The latter can be explained with relativistic effects, which are particularly strong for the elements of the sixth row. Note that the increase of the $(CO)_4$Fe–ER bonds interaction is not obvious from the BDEs, which are lower than for $(CO)_4$Fe-InCp. This is because the preparation energy of the thallium complex is significantly larger (19.5 kcal mol^{-1}) than for the indium complex (7.3 kcal mol^{-1}).

The breakdown of ΔE_{int} into the energy contributions reveals a decrease of the strength for all three terms when the atoms become heavier, except for thallium, which exhibits a small increase for the attractive and the repulsive interactions. The covalent character of the $(CO)_4$Fe–TlCp bonds, which is given by the percentage contributions of ΔE_{orb} to the attractive interactions, continuously decreases. The orbital term is clearly dominated by the TM ← ECp σ-donation, which contributes between 81% and 89% to ΔE_{orb}. The contribution of TM → ECp π-backdonation is very small in all complexes.

Table 7.9 shows the EDA results for the complexes $(CO)_4$Fe-EPh. The BDE and the metal-ligand interaction energies are larger than for $(CO)_4$Fe-ECp. The EDA data suggest that all three terms possess bigger values in the latter complexes than in the former species. It is, therefore, not possible to identify a particular interaction that is responsible for the stronger bonds in the phenyl substituted compounds.

Table 7.8 Energy decomposition analysis at BP86/TZP of $(CO)_4$Fe–ECp(ax) using the fragments Fe$(CO)_4$ and Cp.[a]

	BCp	AlCp	GaCp	InCp	TlCp
ΔE_{int}	−90.3	−65.2	−31.7	−27.1	−33.1
ΔE_{Pauli}	211.6	154.3	69.8	63.6	64.1
ΔE_{elstat} [b]	−186.0 (61.6%)	−112.1 (51.1%)	−47.1 (46.6%)	−40.0 (44.1%)	−42.7 (44.0%)
ΔE_{orb} [b]	−115.9 (38.4%)	−107.4 (48.9%)	−54.4 (53.4%)	−50.7 (55.9%)	−54.2 (56.0%)
ΔE_{σ} [c]	−93.8 (80.9%)	−92.3 (85.9%)	−47.2 (86.8%)	−45.3 (89.3%)	−48.9 (89.4%)
ΔE_{π} [c]	−22.1 (19.1%)	−15.1 (14.1%)	−7.2 (13.2%)	−5.4 (10.7%)	−5.8 (10.6%)
ΔE_{prep}	15.0	12.5	8.7	7.3	19.5
ΔE (= $-D_e$)	−75.3	−52.7	−23.0	−19.8	−13.6
q(Fe)	−0.56	−0.58	−0.51	−0.49	−0.45
q(E)	0.32	1.18	0.96	1.06	0.89
R(Fe–E)	1.968	2.253	2.395	2.548	2.578

Calculated NBO charges q in e. Energy values in kcal/mol. Bond lengths R in Å.
[a]Values are taken from Ref. [35].
[b]The value in parentheses gives the percentage contribution to the total attractive interactions $\Delta E_{elstat} + \Delta E_{orb}$.
[c]The value in parentheses gives the percentage contribution to the total orbital interactions ΔE_{orb}.

Table 7.9 Energy decomposition analysis at BP86/TZP of $(CO)_4$Fe–EPh(ax) and $(CO)_4$Fe-CO(ax) using the fragments Fe$(CO)_4$ and Ph or CO, respectively.[a]

	BPh	AlPh	GaPh	InPh	TlPh	CO
ΔE_{int}	−110.3	−73.2	−61.0	−48.8	−49.4	−54.6
ΔE_{Pauli}	276.6	173.8	129.5	112.3	98.7	134.8
ΔE_{elstat} [b]	−230.4 (59.6%)	−127.3 (51.5%)	−102.3 (53.7%)	−87.0 (54.0%)	−79.3 (53.5%)	−98.0 (51.7%)
ΔE_{orb} [b]	−156.5 (40.4%)	−119.7 (48.5%)	−88.2 (46.3%)	−74.1 (46.0%)	−68.8 (46.5%)	−91.4 (48.3%)
ΔE_{σ} [c]	−104.3 (66.6%)	−98.2 (82.0%)	−73.0 (82.8%)	−63.4 (85.6%)	−59.8 (86.9%)	−47.6 (52.1%)
ΔE_{π} [c]	−52.2 (33.4%)	−21.5 (18.0%)	−15.2 (17.2%)	−10.7 (14.4%)	−9.0 (13.1%)	−43.8 (47.9%)
ΔE_{prep}	10.1	9.4	8.7	8.1	8.6	8.1
ΔE (= $-D_e$)	−100.2	−63.8	−52.3	−40.7	−40.8	−46.5
R (Fe–E)	1.803	2.217	2.296	2.478	2.478	—

Energy values in kcal mol^{-1}. Bond lengths R in Å.
[a]Values are taken from Ref. [35].
[b]The value in parentheses gives the percentage contribution to the total attractive interactions $\Delta E_{elstat} + \Delta E_{orb}$.
[c]The value in parentheses gives the percentage contribution to the total orbital interactions ΔE_{orb}.

The contribution of the TM → EPh π-backdonation to ΔE_{orb} is somewhat stronger than the TM → ECp π-backdonation, which agrees with the notion that Cp is a strong π-donor E ← Cp, whereas Ph is a very weak π-donor E ← Ph. However, the increase in TM → ER π-backdonation from R = Cp to R = Ph clearly shows that the overall strength of the contribution from π-backdonation in $(CO)_4$Fe-EPh remains

much smaller than the $(CO)_4Fe \leftarrow EPh$ σ-donation. This becomes obvious by comparing the contribution of σ-donation and π-backdonation in $(CO)_4$Fe-ECp and $(CO)_4$Fe-EPh with the values for $(CO)_4$Fe-CO, which are also shown in Table 7.9. The carbonyl ligand is a much stronger π-acceptor than ECp and EPh. A significant contribution from π-orbital interactions is only found in $(CO)_4$Fe-BPh where the π-backdonation to the borylene ligand contributes 33.4% to ΔE_{orb} (Table 7.9).

It is instructive to analyse the nature of the $(CO)_4$Fe-ER bonds in more detail. Table 7.8 also gives the atomic partial charge of the atoms Fe and E in the complexes $(CO)_4$Fe-ECp that are bonded to each other. The iron atom always carries a negative charge q(Fe) where the values are between −0.58 and −0.45 e. The group-13 atom E is positively charged. Boron has a positive charge of +0.32 e whereas the heavier atoms carry positive charges between +1.18 and +0.89 e (Table 7.8). Atomic partial charges are frequently used to estimate the strength of the electrostatic interaction between bonded atoms. This is a very error-prone approach, because atomic partial charges are scalar properties, which do not reveal any information about the topography of the charge distribution in a molecule. The results calculated for $(CO)_4$Fe-ECp are a striking example of the failure in using partial charges for estimating electrostatic interactions. The opposite charges for q(Fe) and q(E) would suggest strong electrostatic attraction, which at first sight agrees with the large values for ΔE_{elstat} (Table 7.8). However, according to the atomic partial charges, the electrostatic attraction in the Fe–B bond should be weaker than in the Fe–Al bond, because the boron atom carries a much smaller positive charge (+0.32 e) than aluminum (+1.18 e), which should overcompensate for the shorter Fe-B distance. On the contrary, the ΔE_{elstat} data suggest that the electrostatic attraction in the Fe–B bond is much stronger ($-186.0\,kcal\,mol^{-1}$) than in the Fe–Al bond ($112.1\,kcal\,mol^{-1}$).

The reason for the opposite trend is easily understood when the nature of the electrostatic interaction in $(CO)_4$Fe-ECp is considered. The main component for the electrostatic interactions in the Fe–E bond comes from the overlap of the σ lone-pair electrons of ECp with the nucleus of the iron atom of $(CO)_4$Fe that is deshielded in the region toward the ECp ligand [36]. This means that the electrostatic attraction between Fe and E in $(CO)_4$Fe-ECp stems from *the interaction between the local concentration of negative charge of the overall positively charged atom E and the local depletion of negative charge of the overall negatively charged atom Fe*. The value of the atomic partial charge can be misleading when it comes to estimating the electrostatic interaction in a particular direction towards another atom. Thus, *partial charges should not be used as indicators for the strength of electrostatic interactions* [37].

The virtue of evaluating the energy terms of the EDA separately becomes obvious when the trend of the different contributions to the metal-ligand interactions in $(CO)_4$Fe-ECp and $(CO)_4$Fe-EPh for different atoms is considered. Figure 7.13 shows the curves for the Pauli repulsion ΔE_{Pauli}, the electrostatic attraction ΔE_{elstat}, and the orbital (covalent) interactions ΔE_{orb} from boron to thallium. It also shows the trend of the π-orbital contribution to the total orbital interactions ΔE_{orb}. It becomes obvious that the increase of all terms in both systems is rather moderate from Tl to Ga, but then it becomes steeper for Al and particularly for B. The only

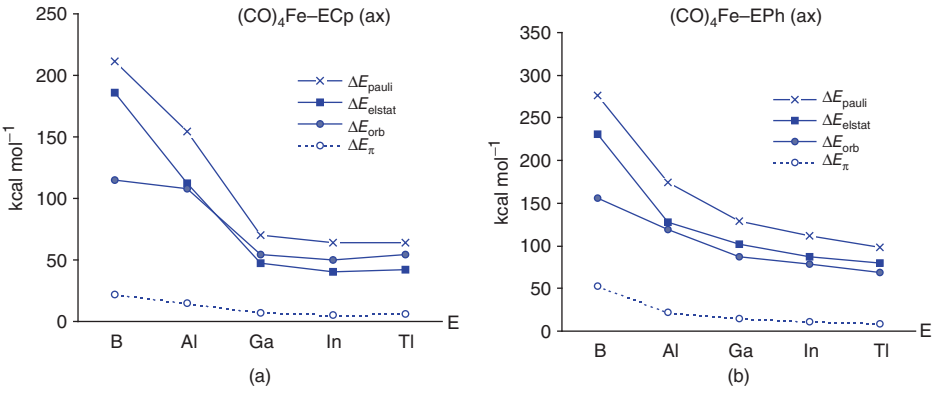

Figure 7.13 Trends of the absolute values of the Pauli repulsion ΔE_{Pauli}, electrostatic interactions ΔE_{elstat}, total orbital interactions ΔE_{orb} and π-orbital interactions ΔE_{π} to the Fe–E bonding interactions in the axial isomers of (a) $(CO)_4Fe–EC_p$ and (b) $(CO)_4Fe–EPh$.

term which does not follow the general trend is the orbital term ΔE_{orb}, whose increase from Al to B is much shallower than for the other terms. This can be explained by the nature of the $(CO)_4Fe$-ER orbital interactions, which is dominated by $(CO)_4Fe \leftarrow EPh$ σ-donation for both systems. Figure 7.12 shows that the overlap of the σ-donor orbital of ligand ER with the tubular-shaped lope of the d_z2 orbital of TM attains an opposite sign at short distances, thus leading to antibonding orbital interactions. This roughly cancels the increase of the bonding orbital interactions which, therefore, remains nearly constant. The electrostatic interactions that come from the attraction between the σ lone-pair electrons of ER and the nucleus of TM do not depend on the sign of the orbitals. Therefore, the electrostatic term exhibits a steep increase at shorter distances.

7.7
Ferrocene Fe(η5-Cp)2 and Bis(benzene)chromium Cr(η6-Bz)2

The accidental synthesis of ferrocene $Fe(\eta^5\text{-}Cp)_2$ (Cp = Cyclopentadiene C_5H_5) in 1951 [38] introduced a new class of compounds in TM chemistry, which posed a challenge to chemical bonding theory. The initial suggestion of a structure with two Fe-C_5H_5 σ-bonds was soon corrected in favor of a π-bonded sandwich structure [39]. A qualitative orbital correlation model for ferrocene, which is also valid for other metallocenes, was introduced by Shustorovic and Dyatkina [40]. It may straightforwardly applied for the metal-ligand interactions in bis(benzene)chromium $Cr(\eta^6\text{-}Bz)_2$, which was synthesized in 1955 [41]. Ferrocene and bis(benzene)chromium can be considered as parent compounds for the large class of metallocene and arene complexes, which are generally known as sandwich compounds $TM(\eta\text{-}L_{cyc})_2$. The ring size of L_{cyc} may vary from 3 to 8 and the ring

atoms in the ligand can be others than carbon, but essentially all stable sandwich compounds obey the 18-electron rule [42].

Figure 7.14 shows a correlation diagram, which gives the relevant orbitals of a d^6 TM with the reference electron configuration $(a_{1g})^2(e_{2g})^4(e_{1g})^0$ and a cyclic 12 π-aromatic sandwich ligand that can be used for ferrocene and bis(benzene)chromium. The symmetry assignments of the orbitals are related to the D_{6h} conformation of $Cr(Bz)_2$ and to the D_{5d} form of $Fe(Cp)_2$. The equilibrium geometry of ferrocene has an eclipsed conformation of the Cp rings that yields D_{5h} symmetry, whereas $Cr(Bz)_2$ has staggered benzene rings in the D_{6h} energy minimum structure [43]. However, the energy difference between the D_{5h} and D_{5d} forms of ferrocene is very small ($< 0.1\,\text{kcal mol}^{-1}$) and the nature of the metal-ligand interactions is essentially the same in the two conformations. Because the molecular orbitals in the D_{5d} form of $Fe(Cp)_2$ have the same symmetry as in the D_{6h} conformation of $Cr(Bz)_2$, we use the former conformation for the bonding analysis in ferrocene.

In order to recognize the overall symmetry of the orbitals, which are shown in Figure 7.14, one must consider one horizontal and one vertical mirror plane of the complex. Thus, the a_{1g} and a_{2u} orbitals of the complexes have σ-symmetry, the e_{1u} and e_{1g} orbitals have π-symmetry, and the e_{2g} and e_{2u} orbitals have δ-symmetry. According to the qualitative bonding model shown in Figure 7.14, the σ- and π-orbitals describe TM ← L donation, whereas the δ-orbitals describe TM → L backdonation. The strength of the different orbital interactions and the contributions that come from electrostatic attraction and Pauli repulsion may be quantitatively estimated with EDA calculations. The numerical results are shown in Table 7.10.

The first column in Table 7.10 gives the results for $Cr(Bz)_2$, which were calculated using a Cr atom with the valence electron configuration $(a_{1g})^2(e_{2g})^4(e_{1g})^0$ as a reference state and $(Bz)_2$ as fragments [44]. The occupied valence orbitals of Cr are d_z2, d_{xy} and $d_x2\text{-}_y2$. The calculations predict that the interaction energy between the excited chromium atom and the $(Bz)_2$ ligand is $\Delta E_{int} = -268.5\,\text{kcal mol}^{-1}$. The largest component of the interaction energy comes from the attractive orbital term ΔE_{orb} ($-377.2\,\text{kcal mol}^{-1}$), whereas the electrostatic attraction ΔE_{elstat} ($-230.5\,\text{kcal mol}^{-1}$) is clearly weaker than the covalent attraction. The EDA calculations thus suggest that the metal-ligand bonding in bis(benzene)chromium is 62.1% covalent and 37.9% electrostatic. The largest contribution to the covalent interactions comes from the e_{2g} (δ) orbitals, which give 73.4%. Thus, the energy partitioning analysis indicates that bis(benzene)chromium is a δ-bonded molecule.

The choice of the interacting fragments for ferrocene is not as simple as for bis(benzene)chromium. Table 7.10 shows the results where two different fragmentation patterns were employed. The first set of data come from EDA calculations where the interacting moieties are isoelectronic with the fragments of $Cr(Bz)_2$, that is, Fe^{2+} has the valence electron configuration $(a_{1g})^2(e_{2g})^4(e_{1g})^0$ that interacts with $(Cp^-)_2$. Table 7.10 shows that the interaction energy between the charged fragments is much larger ($\Delta E_{int} = -893.9\,\text{kcal mol}^{-1}$) than for bis(benzene)chromium. The largest contribution comes from the electrostatic term ($\Delta E_{elstat} = -599.9\,\text{kcal mol}^{-1}$)

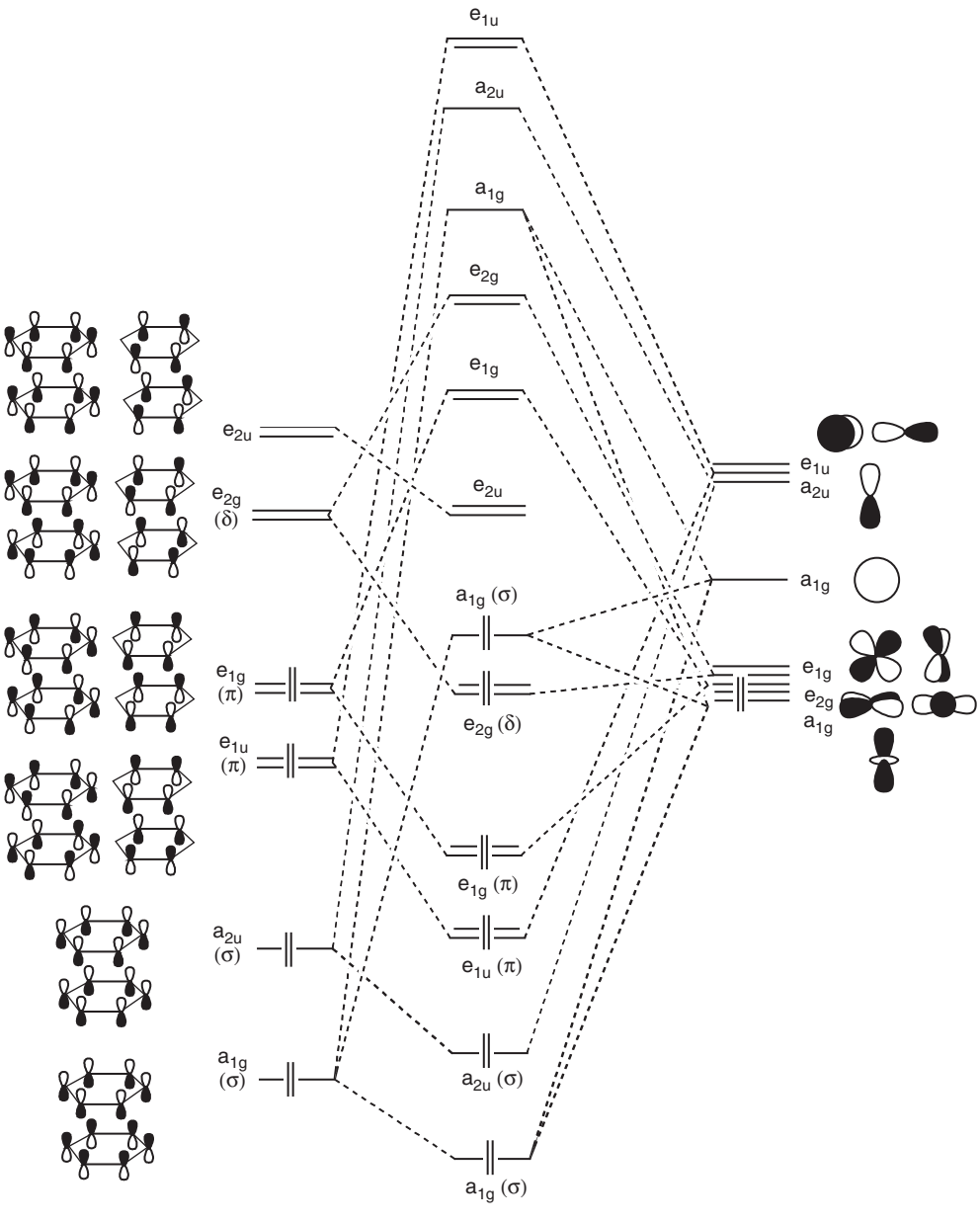

Figure 7.14 MO correlation diagram between a d^6 transition metal with the electron configuration $(a_{1g})^2(e_{2g})^4(e_{1g})^0$ and a cyclic 12 π-aromatic sandwich ligand for ferrocene Fe(η^5-Cp)$_2$ and bis(benzene)chromium Cr(η^6-Bz)$_2$. The shapes of the ligand orbitals have been taken from the Bz$_2$ ligand. The orbitals of the Cp$_2$ ligands look very similar.

Table 7.10 Energy decomposition analysis of $Cr(Bz)_2$ (D_{6h}) and $Fe(Cp)_2$ (D_{5d}) at BP86/TZP.[a]

(D_{6h}, D_{5d})	(a) $Cr(Bz)_2$ $Cr[d_{z^2}, d_{xy}, d_{x^2-y^2}]^6$	(b) $Fe(Cp)_2$ $Fe^{2+}[d_{z^2}, d_{xy}, d_{x^2-y^2}]^6$	(c) $Fe(Cp)_2$ $Fe^{2+}[d_{z^2}, d_{xy}, d_{x^2-y^2}]^6[d_{xz}, d_{yz}]^{\alpha\alpha}$
ΔE_{int}	−268.5	−893.9	−274.2
ΔE_{Pauli}	339.2	279.9	409.6
ΔE_{elstat}[b]	−230.5 (37.9%)	−599.9 (51.1%)	−307.5 (45.0%)
ΔE_{orb}[b]	−377.2 (62.1%)	−573.9 (48.9%)	−376.3 (55.0%)
$\Delta E_{\sigma}(a_{1g})$[c]	−35.4 (9.4%)	−48.6 (8.5%)	−24.6 (6.4%)
$\Delta E(a_{2g})$	0.0	0.0	0.0
$\Delta E(b_{1g})$[c]	−0.1 (<1%)	[d]	[d]
$\Delta E(b_{2g})$[c]	−0.2 (<1%)	[d]	[d]
$\Delta E_{\pi}(e_{1g})$[c]	−55.6 (14.7%)	−371.2 (64.7%)	−231.2 (61.4%)
$\Delta E_{\delta}(e_{2g})$[c]	−277.0 (73.4%)	−47.8 (8.3%)	−111.9 (29.7%)
$\Delta E(a_{1u})$	0.0	0.0	0.0
$\Delta E_{\sigma}(a_{2u})$[c]	−2.9 (<1%)	−28.3 (4.9%)	−2.9 (<1%)
$\Delta E(b_{1u})$[c]	−0.2 (<1%)	[d]	[d]
$\Delta E(b_{2u})$[c]	−0.1 (<1%)	[d]	[d]
$\Delta E_{\pi}(e_{1u})$[c]	−3.8 (1.0%)	−61.5 (10.7%)	−4.8 (1.3%)
$\Delta E_{\delta}(e_{2u})$[c]	−1.8 (<1%)	−16.6 (2.9%)	−1.0 (<1%)

The electron configurations of the metal fragments are given above. The electron configurations of the ligands are (a) neutral benzene dimer $(Bz)_2$, (b) Cp_2^{2-} and (c) triplet $Cp_2^{\beta\beta}$. Energy values in kcal mol^{-1}.

[a] Values are taken from Ref. [44].

[b] The value in parentheses gives the percentage contribution to the total attractive interactions $\Delta E_{elstat} + \Delta E_{orb}$.

[c] The value in parentheses gives the percentage contribution to the total orbital interactions $\Delta E_{orb.}$

[d] There is no representation of this symmetry in the point group D_{5d}.

but the covalent attraction is only slightly weaker ($\Delta E_{orb} = -573.9$ kcal mol^{-1}). Thus, the calculations indicate that the strength of the covalent bonding in ferrocene (48.9%) is nearly as high as the electrostatic bonding (51.1%). The large value for ΔE_{orb} can be explained with the energetically low-lying acceptor orbitals of Fe^{2+}, which strengthen the TM ← L donation. The calculated values for orbitals with different symmetry show that the contributions of the TM ← L donor interactions (σ- and π-orbitals) in $Fe(Cp)_2$ are clearly stronger than in $Cr(Bz)_2$, whereas the TM → L backdonation (δ-orbitals) is weaker. The largest contribution to the covalent bonding in ferrocene comes from the e_{1g} (π) orbitals, which give 64.7% of ΔE_{orb} (Table 7.10).

The analysis of the bonding situation in ferrocene may be biased in favor of TM ← L donation because of the choice of charged fragments Fe^{2+} and $(Cp^-)_2$. Table 7.10 shows the results of a second energy partitioning analysis of $Fe(Cp)_2$, where the neutral fragments Fe and Cp_2 are employed as interacting species. The problem of occupying the degenerate e_{1g} orbitals with only two electrons was solved by choosing the triplet state of Fe, with a valence electron

configuration $(a_{1g})^2(e_{2g})^4(e_{1g})^{\alpha\alpha}$ and a triplet state of Cp_2 with the valence occupation $(a_{1g})^2(a_{2u})^2(e_{1u})^4(e_{1g})^{\beta\beta}$. Table 7.10 shows that the interaction energy for the neutral fragments ($\Delta E_{int} = -274.2$ kcal mol^{-1}) is much less than for the charged fragments. However, the *relative* contributions of ΔE_{elstat} and ΔE_{orb} are very similar in both analyses. The calculations show that the Fe–$(Cp)_2$ bonding between neutral Fe and Cp_2 is 45.0% electrostatic and 55.0% covalent. The breakdown of the latter term into orbitals having different symmetry indicates that the e_{1g} (π) orbitals contribute 61.4% of ΔE_{orb}, which is not much less than the value of 64.7% that was calculated when charged fragments were used (Table 7.10). The contribution of the δ-bonding orbitals are larger when neutral fragments are used (29.7%) than in the case of charged fragments (8.3%) but the main conclusion remains that the covalent bonding in ferrocene comes mainly from π-orbitals.

The nature of the chemical bonding in sandwich compounds has also been analyzed with the EDA for the group-15 homologues of ferrocene $Fe(\eta^5\text{-}E_5)_2$ and for isoelectronic titanocenes $Ti(\eta^5\text{-}E_5)_2^{2-}$ (E = CH, N, P, As, Sb) [45]. The results show interesting variations in that they give a detailed insight into the nature of the metal-ligand bonding in metallocenes. However, there are principally no new findings that need to be discussed here. The interested reader may consult the original papers for the results.

7.8 Cluster, Complex, or Electron-Sharing Compound? Chemical Bonding in $Mo(EH)_{12}$ and $Pd(EH)_8$ (E = Zn, Cd, Hg)

The chemical bonding in TM compounds, which was presented in the previous chapters, was discussed either in terms of electron-sharing interactions or, more often, in terms of donor–acceptor bonding using the DCD model. There are compounds where the two types of bonding cannot be easily distinguished and where both bonding models may be valid. The reader should realize that nature does not know bonding models but only interactions between electrons and nuclei, which are conveniently sketched in models in order to become comprehensible by the limited understanding of the human mind. Thus, bonding models are not right or wrong, but they are more or less useful. The chemical bonding in the class of ''molecular alloys'', which is introduced and discussed in this chapter, is an illustrative example of this.

Fischer and coworkers isolated a series of compounds between 2008 and 2010 with the general formula $TM(ZnR)_n$ with TM = Mo, Ru, Rh, Ni, Pd, Pt and R = Me, Cp^*, where the atom TM is in the center of the ligand cage $(ZnR)_n$ which exhibits a rather regular polyhedron around TM (Figure 7.15, top row) [46]. The coordination number $n = 8, 9, 10, 12$ extends beyond the highest coordination number for TM complexes of monodentate ligands, which is nine. Theoretical studies suggested that the compounds $TM(ZnR)_n$, where the substituents R are methyl and Cp^*, may be considered as substituted variants of the parent systems $TM(ZnH)_n$ (Figure 7.15, bottom row) [46a,d]. The latter compounds have molecular geometries with high

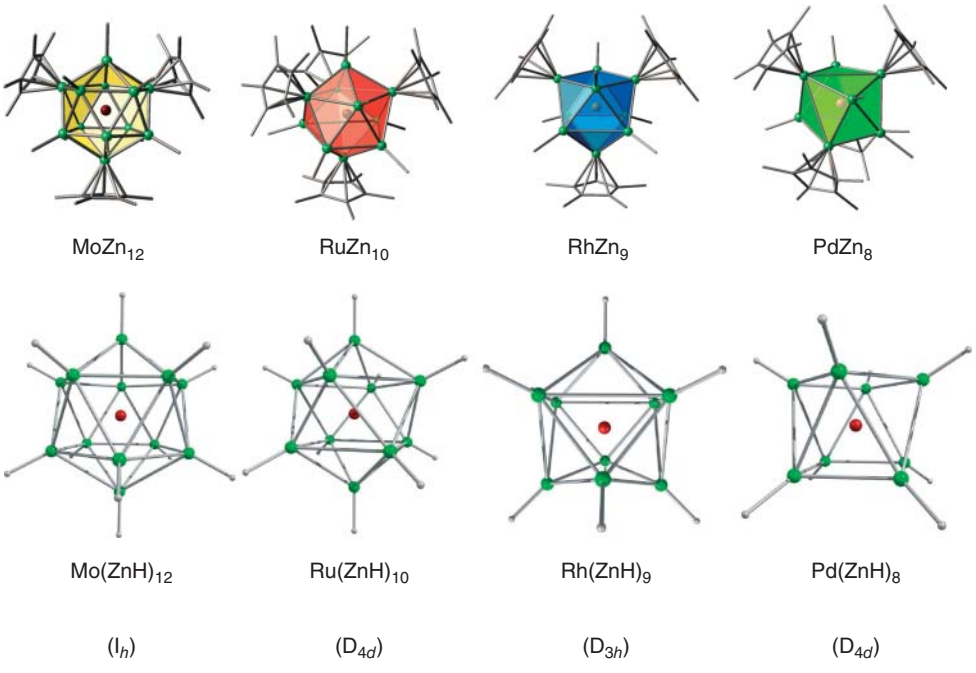

Figure 7.15 Molecular structures of the central moieties $MoZn_{12}$, $RuZn_{10}$, $RhZn_9$, and $PdZn_8$ showing the coordination polyhedron around the central metal TM and the corresponding parent molecules $Mo(ZnH)_{12}$, $Ru(ZnH)_{10}$, $Rh(ZnH)_9$, and $Pd(ZnH)_8$.

symmetry, where $Mo(ZnH)_{12}$ is an icosahedron (I_h), whereas $Pd(ZnH)_8$ is a dodecahedron (D_{4d}) that is derived from a cubic form, which is twisted by 90°. The systems $Ru(ZnH)_{10}$ (D_{4d}) and $Rh(ZnH)_8$ (D_{3h}) are bicapped and monocapped homologues of the dodecahedron, respectively. A common feature of all systems is the fulfilment of the 18-electron rule where the groups ZnR are considered as one-electron ligands. On the other hand, the cage structure of $TM(ZnR)_n$ allows it to seem possible that the molecules might be considered as endohedral cluster compounds where the TM is encapsulated in a barred $(ZnR)_n$ enclosure. The lines, which are drawn in Figure 7.15, denote the atomic connectivity but they do not indicate chemical bonding nor can they be identified with electron pairs. Where are the electrons in $TM(ZnR)_n$ and what is the bonding situation in the unusual TM compounds?

In a situation like this, it is helpful to carry out an AIM analysis of the electron density. Figure 7.16a shows the molecular graphs and the contour line diagram of the Laplacian distribution $\nabla^2\rho(r)$ of $Mo(ZnH)_{12}$ in a plane, which contains a $Mo(ZnH)_4$ moiety. The most important finding concerns the bond paths, which are shown as solid lines that connect the atomic nuclei. There are bond paths for the Mo–Zn and Zn–H interactions, but there is no Zn–Zn' bond path! This is a strong indication that the Mo-Zn interactions in $Mo(ZnH)_{12}$ are much stronger than the Zn-Zn' interactions. The chemical bonds in $Mo(ZnH)_{12}$ which are suggested by

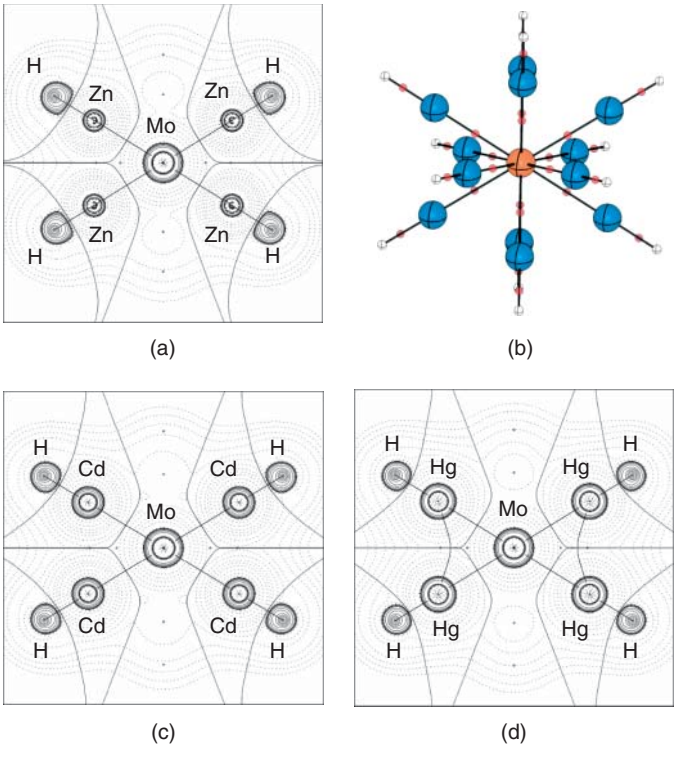

Figure 7.16 Contour line plots of the Laplacian $\nabla^2\rho(r)$ of the electron density of (a) $Mo(ZnH)_{12}$, (b) Plot of the molecular graph of $Mo(ZnH)_{12}$ which shows the bond paths and the bond critical points (red dots), (c) $Mo(CdH)_{12}$, and (d) $Mo(HgH)_{12}$ in a plane which contains a $Mo(EH)_4$ moiety. Solid lines connecting the atoms represent the bond paths. Solid lines which separate the atomic basins indicate the zero-flux surfaces crossing the molecular plane.

the AIM are displayed in Figure 7.16b. The twelve Mo-Zn bond paths point into the corners of a dodecahedron that shows the overall symmetry of the molecule. The individual bond paths cannot be associated with electron pairs, because the number of valence electrons of Mo (6) and the ligand cage ZnH_{12} (12) does not give 24 valence electrons.

Inspection of the valence MOs of $Mo(ZnH)_{12}$ together with the AIM results provide a comprehensive picture of the bonding situation. Figure 7.17 shows an orbital correlation diagram for the three highest lying occupied MOs of the molecule, which are occupied by 18 valence electrons. The HOMO is a triply degenerate (t_{1u}) orbital where each component has two HZn–ZnH bonding contributions. The contribution of the valence p AOs of Mo to the HOMO is negligible. In contrast, the quintuply degenerated HOMO-1 (h_g) and the nondegenerated HOMO-2 (a_g) possess large contributions from the valence d and s AOs of Mo, respectively, which mix in a bonding fashion with valence p functions of Zn and 1s functions of H. It follows that the latter orbitals describe mainly Mo–Zn bonding whereas the HOMO

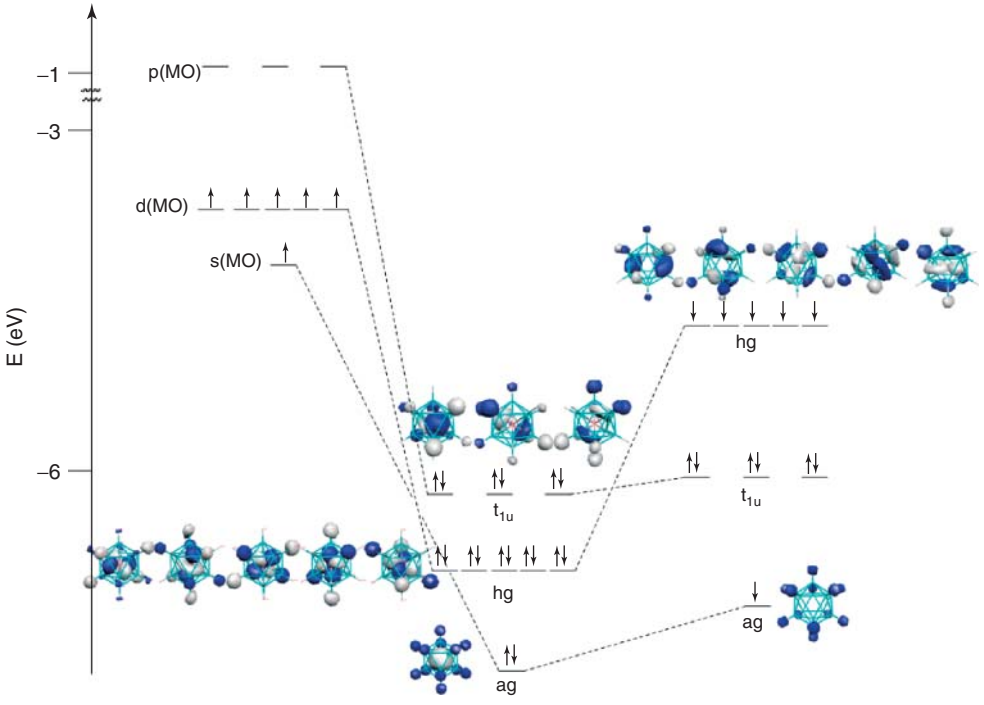

Figure 7.17 MO correlation diagram for the three highest lying MOs of $Mo(ZnH)_{12}$.

can be associated with Zn–Zn bonding. Chemical bonding in $Mo(ZnH)_{12}$ may thus be described in terms of six sd^5 hybridized orbitals of Mo which have octahedral symmetry (Figure 7.2) and twelve ZnH valence orbitals yielding six MOs, that is, the HOMO-1 and HOMO-2 which are occupied by 12 electrons. Alternatively, the Mo–ZnH bonding may be described in terms of six three-center two-electron bonds. The remaining six electrons which occupy the Zn–Zn bonding (t_{1u}) HOMO are delocalized over the $(ZnH)_{12}$ cage. This means that there is only 1/4 electron pair for each Zn–Zn bonding, which is not enough to yield a Zn–Zn bond path. Figures 7.16c and d also show the molecular graphs and the contour line diagrams of the Laplacian distribution $\nabla^2\rho(r)$ of the heavier ligand homologues $Mo(CdH)_{12}$ and $Mo(HgH)_{12}$. The former species shows similar features as for $Mo(ZnH)_{12}$, but the mercury homologue exhibits bond paths for Hg–Hg' interactions that are inwardly curved. This does not indicate a qualitatively different bonding situation as in the lighter homologues. Rather, it means that the deformation of the "softer" valence electrons of Hg, which is induced by the Hg–Hg' interactions, is sufficient to exhibit a bond path.

The results of the orbital correlation diagram are quantitatively supported by EDA calculations whose results are given in Table 7.11. The total attraction between Mo with the electron configuration $5s^14d^5$ and $(ZnH)_{12}$ with the electron configuration ag^1hg^5 has a slightly higher electrostatic character (57.2%) than orbital (covalent)

Table 7.11 Energy decomposition analysis of $Mo(ZnH)_{12}$ (I_h) at BP86/TZP.[a]

ΔE_{int}	−348.8
ΔE_{Pauli}	594.5
ΔE_{elstat}[b]	−540.1 (57.2%)
ΔE_{orb}[b]	−403.2 (42.8%)
$\Delta E_{orb}(a_g)$ (s)[c]	−96.4 (23.9%)
$\Delta E_{orb}(h_g)$ (d)[c]	−288.0 (71.5%)
$\Delta E_{orb}(t_{1u})$ (p)[c]	−18.3 (4.5%)
ΔE_{orb}(rest) (pol)[c]	−0.5 (0.1%)

The interacting fragments are $Mo(5s^1 4d^5)$ and $(ZnH)_{12}$ with an electron configuration ag^1hg^5. Energy values in kcal mol^{-1}.
[a]Values are taken from Ref. [46a].
[b]The percentage values in parentheses give the contribution to the total attractive interactions $\Delta E_{elstat} + \Delta E_{orb}$.
[c]The percentage values in parentheses give the contribution to the total orbital interactions ΔE_{orb}.

character (42.8%). The breakdown of the covalent term ΔE_{orb} into the individual Mo-ZnH orbital contributions shows that 23.9% comes from the bonding of the valence s orbital of Mo, whereas 71.5% comes from the valence d orbitals. The contribution of the valence p orbitals of Mo is very small. Thus, $Mo(ZnH)_{12}$ can be considered as a TM compound that has twelve Mo–ZnH electron-sharing bonds between an sd^5 hybridized Mo atom, which provides six electrons, and twelve ZnH ligands, which supply another six electrons. There are twelve electrons available for Mo–ZnH bonding overall, which means that the metal-ligand interactions can be described in terms of a three-center two-electron bonds. The remaining six valence electrons occupy Zn–Zn bonding orbitals, which yield weak intra-ligand bonding. This is responsible for the rather high coordination number of the compounds.

The chemical bonding in $TM(ZnH)_n$ where $n = 10, 9, 8$ is very similar to the bonding situation in $(ZnH)_{12}$ [46]. Figure 7.18a–c show the molecular graphs and the contour line diagrams of the Laplacian distribution $\nabla^2\rho(r)$ of $Ru(ZnH)_{10}$, $Rh(ZnH)_9$, and $Pd(ZnH)_8$. There are bond paths for the TM-ZnH interactions in all cases but there are no Zn–Zn bond paths. This also holds for the Laplacian distribution of the heavier homologue $Pd(CdH)_8$, which is shown in Figure 7.18d. The nature of the bonding in $Pd(ZnH)_8$ and $Pd(CdH)_8$ will be discussed in more detail, because it shows that it is sometimes more convenient to modify the bonding model for the interpretation of the electronic structure along a series of related molecules.

Palladium has 10 valence electrons, which is more than the number of ligands EH in $Pd(EH)_8$ (E = Zn, Cd). A discussion in terms of Pd-EH electron-sharing bonds is more complicated than changing the interpretation of the chemical bonding in favor of the DCD donor–acceptor model. A natural choice for the interacting fragments in the two molecules is Pd (d^{10}) and the ligand cage $(EH)_8$ in the $^1A_1$ electronic

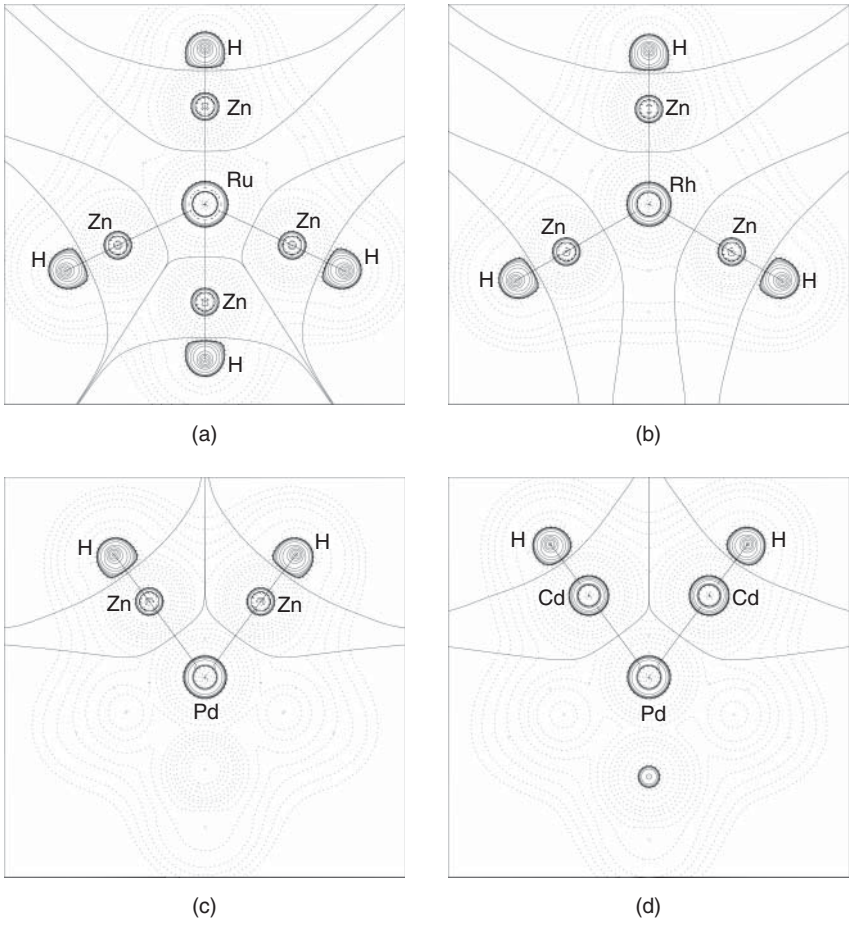

Figure 7.18 Contour line plots of the Laplacian $\nabla^2\rho(r)$ of the electron density of (a) $Ru(ZnH)_{10}$, (b) $Rh(ZnH)_9$, (c) $Pd(ZnH)_8$, and (d) $Pd(CdH)_8$. Solid lines connecting the atoms represent the bond paths. Solid lines that separate the atomic basins indicate the zero-flux surfaces crossing the molecular plane.

state. The vacant s valence AO of Pd is then available for $Pd \leftarrow (ZnH)_8$ donation, while the filled valence d AOs of Pd may engage in $Pd \rightarrow (CdH)_8$ backdonation. Table 7.12 shows the EDA results for $Pd(ZnH)_8$ and $Pd(CdH)_8$, where Pd (d^{10}) and the ligand cage $(EH)_8$ in the $^1A_1$ electronic state are used as interacting fragments.

The EDA data suggest that the strongest attraction between Pd (d^{10}) and $(EH)_8$ comes from the Coulomb interactions (77%), whereas the orbital interactions contribute only 23% to the total attraction. A comparison of the data with the results for $Mo(ZnH)_{12}$ is not valid because of the choice of different electron configurations of the fragments. The breakdown of ΔE_{orb} into the different terms shows that the strongest contributions come from the $Pd(d) \rightarrow (EH)_8$ backdonation,

Table 7.12 EDA results of $Pd(ZnH)_8$ and $Pd(CdH)_8$ at BP86/TZ2P+.[a]

	$Pd(ZnH)_8$ (D_{4d})	$Pd(CdH)_8$ (D_{4d})
ΔE_{int}	−201.2	−179.7
ΔE_{Pauli}	402.4	344.1
ΔE_{elstat}[b]	−467.7 (77.5%)	−404.7 (77.3%)
ΔE_{orb}[b]	−135.8 (22.5%)	−119.2 (22.8%)
$\Delta E(a_1)$ (s, d_z2) [c]	−21.7 (16.0%)	−20.5 (17.2%)
$\Delta E(b_2)$ (p_z)[c]	−5.4 (4.0%)	−5.6 (4.7%)
$\Delta E(e_1)$ (p_x, p_y)[c]	−11.0 (8.1%)	−11.2 (9.4%)
$\Delta E(e_2)$ (d_{xy}, $d_{x^2-y^2}$)[c]	−43.6 (32.1%)	−35.8 (30.1%)
$\Delta E(e_3)$ (d_{xz}, d_{yz})[c]	−54.1 (39.8%)	−46.0 (38.6%)

Fragments are Pd in the $ns^0(n\text{-}1)d^{10}$ and $(EH)_8$ in the corresponding $^1A_1$ singlet state. Energies in kcal mol^{-1}.
[a]Values are taken from Ref. [46d].
[b]The percentage values in parentheses give the contribution to the total attractive interactions $\Delta E_{elstat} + \Delta E_{orb}$.
[c]The percentage values in parentheses give the contribution to the total orbital interactions ΔE_{orb}.

Table 7.13 EDA-NOCV results of $Pd(ZnH)_8$ and $Pd(CdH)_8$ at BP86/TZ2P+.[a]

	$Pd(ZnH)_8$ (D_{4d})	$Pd(CdH)_8$ (D_{4d})
ΔE_{int}	−201.2	−179.7
ΔE_{Pauli}	402.4	344.1
ΔE_{elstat}[b]	−467.7 (77.5%)	−404.7 (77.3%)
ΔE_{orb}[b]	−135.8 (22.5%)	−119.2 (22.8%)
Pair 1	−27.2 (*d*)	−22.7 (*d*)
Pair 2	−27.2 (*d*)	−22.7 (*d*)
Pair 3	−11.5 (*s*)	−12.7 (*s*)
Pair 4	−21.8 (*d*)	−17.5 (*d*)
Pair 5	−21.8 (*d*)	−17.5 (*d*)
Pair 6	−5.4 (*p*)	−5.5 (*p*)
Pair 7	−5.4 (*p*)	−5.3 (*p*)
Pair 8	−5.4 (*p*)	−5.3 (*p*)
Pair 9	−10.5 (*d*)	−7.7 (*d*)

Fragments are Pd in the $ns^0(n-1)d^{10}$ and $(EH)_8$ in the corresponding $^1A_1$ singlet state.Energies in kcal mol^{-1}. See Figure 7.19 for graphical representations of NOCV pairs 1–9 and deformation densities.
[a]Values are taken from Ref. [46d].
[b]The percentage values in parentheses give the contribution to the total attractive interactions $\Delta E_{elstat} + \Delta E_{orb}$.

which has e_2 and e_3 symmetry. The strength of the Pd(p) ← $(EH)_8$ donation is much weaker than the backdonation. With the EDA data, however, it is not possible to distinguish between the contributions of the electron donation of $(EH)_8$ to the empty s orbital of Pd and the back-donation of the Pd(d_z2) AO to $(EH)_8$ as they belong to the same irreducible representation a_1 of the D_{4d} point group. A differentiation is possible with the help of EDA-NOCV calculations that provide a fragmentation of ΔE_{orb} into individual pair contributions between orbitals of the two fragments whose identity can be clarified by the shape of the associated deformation densities. Table 7.13 gives the results of the EDA-NOCV calculations of $Pd(ZnH)_8$ and $Pd(CdH)_8$, while Figure 7.19 shows the deformation densities of the nine orbital pairs for the latter molecule.

The EDA-NOCV results in Table 7.13 show the strength of the individual orbital-pair interactions. The assignment of the orbital contributions to the Pd valence

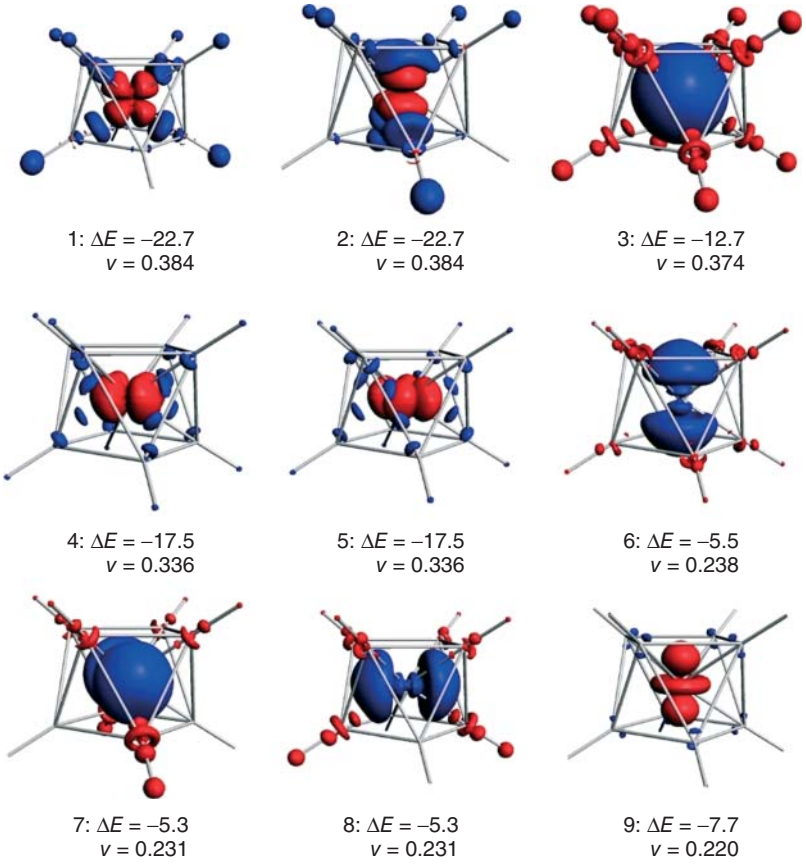

Figure 7.19 Plot of the NOCV deformation densities of $Pd(CdH)_8$. Blue surfaces indicate regions of charge accumulation; red surfaces indicate regions of charge depletion. Energy values ΔE of the corresponding orbital interactions in kcal/mol and NOCV eigenvalues ν.

orbitals are easily made when the shapes of the AOs of the central atoms are considered in the deformation densities that are shown in Figure 7.19. Thus, the NOCV pairs 1, 2, 4, 5, and 9 represent interactions of the five d AOs of the Pd atom with the CdH ligands, the NOCV pair 3 represents the interaction with the s AO and the pairs 6, 7, and 8 represent interactions with the p AOs. The deformation of the densities, which takes place in the direction red → blue, shows the electron flow of donation and backdonation as can be expected from the choice of the interacting fragments. The ligands donate electron density to the empty p and s AOs of the Pd atom, while the occupied d orbitals provide backdonation to the ligands.

In summary, the analysis of the metal–ligand interactions in the ''molecular alloys'' $Mo(EH)_{12}$ and $Pd(EH)_8$ suggest that the compounds should be classified as genuine TM compounds and not as endohedral clusters. The metal–ligand bonding is much stronger than the interligand bonding which serves to keep the ligand cage together. The metal–ligand interactions can be discussed in terms of electron-sharing bonding as well as donor–acceptor bonding, depending on the number of valence electrons of the metal and the number of ligands.

7.9
Metal–Metal Multiple Bonding

The synthesis of the dirhenium compound $K_2[Re_2Cl_8]$ by Cotton *et al*. in 1965 [47] introduced a type of bonding into synthetic chemistry that had not been known before. It was suggested that the dianion $[Re_2Cl_8]^{2-}$ possesses a rhenium–rhenium quadruple bond which has one σ, one degenerate π, and one δ component. The work was the starting point for very active experimental research that led to the synthesis of a large number of homo- and heterodinuclear compounds with metal–metal quadruple bonds [48]. Numerous theoretical studies were devoted to the question about the strength of the σ, π, and δ components of the quadruple bond. Multireference calculations using CASPT2 by Gagliardi and Roos reported the effective Re–Re bond orders for $[Re_2Cl_8]^{2-}$, which were calculated with the CASPT2 method [49]. This is discussed in Vol. 2, Chapter 9 of this book. The calculated values of 0.92 for the σ-bond, 1.74 for the π-bond, and 0.54 for the δ-bond suggest that the strength of the bonding contributions has the order $\pi > \sigma > \delta$. Sakaki and coworkers calculated the energy difference between the $^1A_{1g}$ ground state and the $^3A_{2u}$ excited state of $[Re_2Cl_8]^{2-}$ [50]. The theoretical value of 12.1 kcal mol^{-1} was related to the $\delta \rightarrow \delta^*$ excitation and it was suggested that the adiabatic excitation energy of 12.1 kcal mol^{-1} indicates the strength of the δ-bond in $Re_2Cl_8^{2-}$.

Figure 7.20 shows a plot of the three highest lying occupied orbitals taken from DFT calculations at BP86/TZ2P, which are related to Re–Re bonding, and the lowest lying vacant orbital of $Re_2Cl_8^{2-}$. It becomes obvious that the (a_{1g}) HOMO-10 features the σ-bond, the degenerate (e_{1u}) HOMO-1 displays the two components of the π-bond, the (b_{2g}) HOMO is the δ-bond, whereas the (b_{1u}) LUMO is the corresponding δ*-orbital. The strength of the three orbital components of the Re–Re bonding may be estimated with the help of EDA calculations [51].

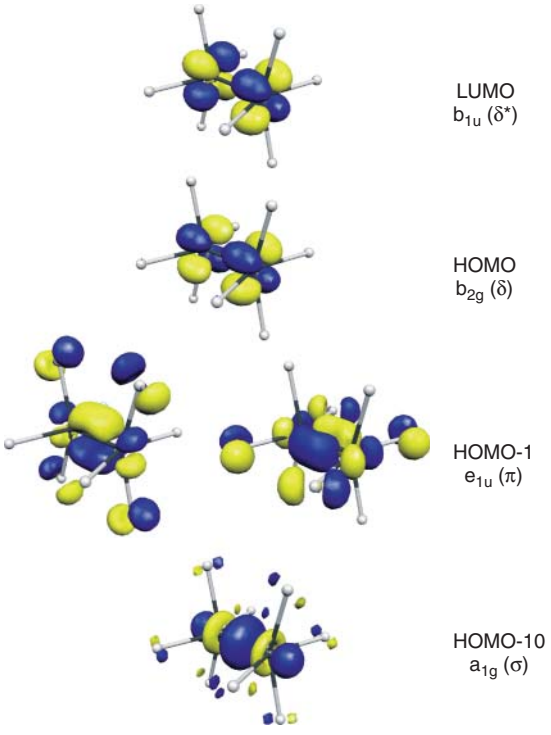

Figure 7.20 Plot of the antibonding δ^* LUMO and the occupied valence orbitals HOMO, HOMO-1, and HOMO-10 of $Re_2Cl_8^{2-}$ showing the Re–Re bonding orbitals possessing σ-, π-, and δ-symmetry.

The EDA calculations of $Re_2Cl_8^{2-}$ were carried out using the fragments $ReCl_4^-$ in the ($^5B_2$) quintet state, which have four unpaired electrons. The data calculated give an intrinsic Re–Re interaction energy of $\Delta E_{int} = -54.2$ kcal mol^{-1}. The breakdown of the energy terms of the EDA indicates that the orbital (covalent) contribution to ΔE_{int} amounts to 46.8% of the attractive Re-Re interactions, whereas the electrostatic attraction ΔE_{elstat} contributes 53.2%. Note that the electrostatic interactions between the negatively charged $ReCl_4^-$ fragments are strongly attractive. The explanation for the attraction can be given if one realizes that the charge distribution in $ReCl_4^-$ and in $Re_2Cl_8^{2-}$ is highly anisotropic. The negative charge is located at the chlorine atoms, which carry a partial charge in $Re_2Cl_8^{2-}$ of −0.29 e, whereas the Re atoms have a positive charge of +0.16 e. The electrostatic stabilization comes mainly from the attraction between the electron density in the occupied d_z2 orbital of Re with the nucleus of the other Re atom.

The strongest contributions to the orbital interactions in $Re_2Cl_8^{2-}$ come from the π-orbitals. The calculated (Table 7.14) give that the e(π) orbitals provide 59.8% of the ΔE_{orb} term, whereas 39.3% come from σ-interactions. This is in contrast to multiple bonding between main-group atoms where σ-bonding is usually stronger

Table 7.14 EDA results of $Re_2Cl_8^{2-}$ and Os_2Cl_8 at BP86/TZ2P+.[a]

	$Re_2Cl_8^{2-}$ (D_{4h})	Os_2Cl_8 (D_{4h})
ΔE_{int}	−54.2	−92.7
ΔE_{pauli}	405.4	256.8
ΔE_{elstat} [b]	−244.5 (53.2%)	−151.7 (43.4%)
ΔE_{orb} [b]	−215.2 (46.8%)	−197.9 (56.6%)
ΔE (a_1) σ[c]	−84.5 (39.3%)	−97.6 (49.3%)
ΔE (a_2)[c]	−0.1 (0.1%)	−0.1 (<0.1%)
ΔE (b_1) ($\delta_{x^2-y^2}$)[c]	−1.5 (0.7%)	−2.9 (1.5%)
ΔE (b_2) (δ_{xy})[c]	−0.5 (0.2%)	0.9 (−0.5%)
ΔE (e) π[c]	−128.6 (59.8%)	−98.2 (49.6%)

The interacting fragments are $ReCl_4^-$ and $OsCl_4$ in the ($^5B_2$) quintet state. Energies in kcal mol^{-1}.
[a] Values are taken from Ref. [51].
[b] The percentage values in parentheses give the contribution to the total attractive interactions $\Delta E_{elstat} + \Delta E_{orb}$.
[c] The percentage values in parentheses give the contribution to the total orbital interactions ΔE_{orb}.

than π-bonding [7b, 36]. A surprising EDA result is the negligible contribution of the $b_2(\delta_{xy})$ orbitals to the ΔE_{orb} term. The data calculated suggest that the Re-Re δ-orbital shown in Figure 7.20 (HOMO) provides only −0.5 kcal mol^{-1}, which is just 0.2% of the attractive orbital interactions. The contribution of the $b_1(\delta_x 2_y 2)$ orbitals, which comes from the metal $d_x 2_y 2$ AOs that are engaged in Re–Cl bonding, is slightly higher (−1.5 kcal mol^{-1}, 0.7%). The EDA results suggest that there is practically nil stabilization of the electrons in the $5d_{xy}$ AO of Re through Re–Re interactions.

It may be argued that the weak δ-bond in $Re_2Cl_8^{2-}$ is the result of the overall negative charge of the molecule. Table 7.14 shows that the EDA results for Os_2Cl_8, which is isoelectronic with $Re_2Cl_8^{2-}$. The intrinsic metal–metal bond strength in Os_2Cl_8 is higher ($\Delta E_{int} = -92.7$ kcal mol^{-1}) than in $Re_2Cl_8^{2-}$ ($\Delta E_{int} = -54.2$ kcal mol^{-1}), which is due to the significantly weaker Pauli repulsion in the former molecule. The attractive terms ΔE_{elstat} and ΔE_{orb} are weaker in the neutral compound than in the dianions. We want to point out that the electrostatic attraction between the neutral fragments $OsCl_4$ is weaker ($\Delta E_{elstat} = -151.7$ kcal mol^{-1}) than between the charged species $ReCl_4^-$ ($\Delta E_{elstat} = -244.7$ kcal mol^{-1}). This is a striking proof of the failure of using partial charges as a measure for Coulombic interactions.

Table 7.14 shows that the strength of the σ-bonding in Os_2Cl_8 (−97.6 kcal mol^{-1}) is now nearly the same as the π-bonding (−98.2 kcal mol^{-1}). The contribution of the δ-bonding to the orbital interaction remains negligible. The value calculated, which comes from the $b_2(\delta_{xy})$ orbitals, is slightly positive (0.9 kcal mol^{-1}), which means that the effect of the electrostatic interactions on the energy level of the latter orbital compensates the small energy lowering that arises from the mixing of the orbitals.

7.10 Summary

Chemical bonding in TM compounds was considered in the past as an insurmountable obstacle for *ab initio* quantum chemistry [52]. The research that is discussed in this chapter is striking evidence that this statement is no longer valid. There has been remarkable progress in the last few decades concerning analyses of the numerical results of accurate quantum chemical calculations that provide deep insight into the nature of the chemical bonding of TMs. Several charge and energy decomposition schemes have been developed and were successfully applied for the examination of the bonding situation in TM compounds after they were first calculated with *ab initio* or DFT methods. Unlike earlier work, which was based on approximate methods and *ad hoc* assumptions of the binding interactions in molecules, these methods can be used to provide qualitative bonding models that are in agreement with the actual electronic structure and with the physical mechanism that leads to a chemical bond. The models are not only useful for an understanding of the chemical bonds, but also as ordering schemes for the different classes of molecules. The discussion of the various topics, which are presented here and elsewhere [1, 7], indicate that the DCD bonding model which was suggested in the early-1950s [4–6] remains valid. The DCD model becomes particularly helpful in combination with accurate quantum chemical calculations that provide a quantitative estimate of the energy terms associated with the bonding scheme. The charge and energy partitioning methods may serve as a bridge between the numerical results of quantum chemical calculations and qualitative descriptions of TM compounds.

Acknowledgment

This work was financially supported by the Deutsche Forschungsgemeinschaft.

References

1. Frenking, G. and Fröhlich, N. (2000) *Chem. Rev.*, **100**, 717.
2. (a) Landis, C.R., Firman, T.K., Root, D.M., and Cleveland, T. (1998) *J. Am. Chem. Soc.*, **120**, 1842; (b) Landis, C.R., Cleveland, T., and Firman, T.K. (1998) *J. Am. Chem. Soc.*, **120**, 2641; (c) Firman, T.K. and Landis, C.R. (1998) *J. Am. Chem. Soc.*, **120**, 12650.
3. (a) Bayse, C.A. and Hall, M.B. (1999) *J. Am. Chem. Soc.*, **121**, 1348; (b) Diefenbach, A., Bickelhaupt, F.M., and Frenking, G. (2000) *J. Am. Chem. Soc.*, **122**, 6449.
4. Dewar, M.J.S. (1951) *Bull. Soc. Chim. Fr.*, **18**, C79.
5. Chatt, J. and Duncanson, L.A. (1953) *J. Chem. Soc.*, 2929.
6. For a discussion of the history and the application of the DCD bonding model in transition metal chemistry see: Leigh, G.J. and Winterton, N. (eds) (2002) *Modern Coordination Chemistry: The Legacy of Joseph Chatt*, The Royal Society, London.
7. (a) Frenking, G., Wichmann, K., Fröhlich, N., Loschen, C., Lein, M., Frunzke, J., and Rayón, V.M. (2003) *Coord. Chem.*

Rev., **238–239**, 55; (b) Lein, M. and Frenking, G. (2005) in *Theory and Applications of Computational Chemistry: The First 40 Years* (eds C.E. Dykstra, G. Frenking, K.S. Kim, and G.E. Scuseria), Elsevier, Amsterdam, p. 367.

8. (a) Hay-Motherwell, R.S., Wilkinson, G., Hussain-Bates, B., and Hursthouse, M.B. (1992) *J. Chem. Soc., Dalton Trans.*, 3477; (b) Hay-Motherwell, R.S., Hussain-Bates, B., Hursthouse, M.B., and Wilkinson, G. (1990) *J. Chem. Soc., Chem. Commun.*, 1242.
9. Root, D.M., Landis, C.R., and Cleveland, T. (1993) *J. Am. Chem. Soc.*, **115**, 4201.
10. Gillespie, R.J. and Hargittai, I. (1991) *The VSEPR Model of Molecular Geometry*, Prentice-Hall, Englewood Cliffs, NJ.
11. (a) Shen, M., Schaefer, H.F., and Partridge, H. (1992) *J. Chem. Phys.*, **98**, 508; (b) Kang, S.K., Tang, H., and Albright, T.A. (1993) *J. Am. Chem. Soc.*, **115**, 1971; (c) Tanpipat, N. and Baker, I. (1996) *J. Phys. Chem.*, **100**, 19818.
12. (a) Pfennig, V. and Seppelt, K. (1996) *Science*, **271**, 626; (b) Kaupp, M. (1996) *J. Am. Chem. Soc.*, **118**, 3018; (c) Kaupp, M. (1998) *Chem. Eur. J.*, **4**, 1678; (d) Kaupp, M. (1998) *Chem. Eur. J.*, **4**, 2059; (e) Kaupp, M. (1999) *Angew. Chem.*, **111**, 3219; *Angew. Chem. Int. Ed.* 1999, **38**, 3034.
13. (a) Kaupp, M. (1999) *Chem. Eur. J.*, **5**, 3631; (b) Pyykkö, P. (1997) *J. Phys. Chem. A*, **101**, 8017.
14. Jonas, V., Boehme, C., and Frenking, G. (1996) *Inorg. Chem.*, 2097.
15. Bent, H.A. (1961) *Chem. Rev.*, **61**, 275.
16. (a) Brookhart, M. and Green, M.L.H. (1983) *J. Organomet. Chem.*, **250**, 395; (b) Brookhart, M., Green, M.L.H., and Parkin, G. (2007) *Proc. Natl. Acad. Sci. U.S.A.*, **104**, 6908.
17. (a) Morokuma, K. (1971) *J. Chem. Phys.*, **55**, 1236; (b) Ziegler, T. and Rauk, A. (1977) *Theor. Chim. Acta*, **46**, 1.
18. (a) Bickelhaupt, F.M. and Baerends, E.J. (2000) in *Reviews in Computational Chemistry*, Vol. 15 (eds K.B. Lipkowitz and D.B. Boyd), Wiley-VCH Verlag GmbH, New York, p. 1; (b) Frenking, G., Wichmann, K., Fröhlich, N., Loschen, C., Lein, M., Frunzke, J., and Rayón, V.M. (2003) *Coord. Chem. Rev.*, **238–239**, 55; (c) Lein, M. and Frenking, G. (2005) in *Theory and Applications of Computational Chemistry: The First 40 Years* (eds C.E. Dykstra, G. Frenking, K.S. Kim, and G.E. Scuseria), Elsevier, Amsterdam, p. 367.
19. (a) Ellis, J.E. and Chi, K.-M. (1990) *J. Am. Chem. Soc.*, **112**, 6022; (b) Calderazzo, F., Englert, U., Pampaloni, G., Pelizzi, G., and Zamboni, R. (1983) *Inorg. Chem.*, **22**, 1865; (c) Heinemann, F., Schmidt, H., Peters, K., and Thiery, D. (1992) *Z. Kristallogr.*, **198**, 123; (d) Bruce, D.M., Holloway, J.H., and Russel, D.R. (1978) *J. Chem. Soc., Dalton Trans.*, 1627; (e) Holloway, J.H., Senior, J.B., and Szary, A.C. (1987) *J. Chem. Soc., Dalton Trans.*, 741; (f) Bach, C., Willner, H., Wang, C., Rettig, S.J., Trotter, J., and Aubke, F. (1996) *Angew. Chem.*, **108**, 2104; *Angew. Chem., Int. Ed. Engl.* 1996, **35**, 1974; (g) Arnesen, S.V. and Seip, H.M. (1966) *Acta Chem. Scand.*, **20**, 2711.
20. Albright, T.A., Burdett, J.K., and Whangbo, M.H. (2013) *Orbital Interactions in Chemistry*, 2nd edn, John Wiley & Sons, Inc., New York.
21. (a) Lupinetti, A.J., Frenking, G., and Strauss, S.H. (1998) *Angew. Chem., Int. Ed. Engl.*, **37**, 2113; (b) Lupinetti, A.J., Strauss, S.H., and Frenking, G. (2001) in *Progress in Inorganic Chemistry*, Vol. 49 (ed. K.D. Karlin), John Wiley & Sons, Inc., New York, p. 1.
22. (a) Bickelhaupt, F.M., Radius, U., Ehlers, A.W., Hoffmann, R., and Baerends, E.J. (1998) *New J. Chem.*, **22**, 1; (b) Radius, U., Bickelhaupt, F.M., Ehlers, A.W., Goldberg, N., and Hoffmann, R. (1998) *Inorg. Chem.*, **37**, 1080; (c) Ehlers, A.W., Baerends, E.J., Bickelhaupt, F.M., and Radius, U. (1998) *Chem. Eur. J.*, **4**, 210.
23. (a) Goldman, A.S. and Krogh-Jespersen, K. (1996) *J. Am. Chem. Soc.*, **118**, 12159; (b) Lupinetti, A.J., Fau, S., Frenking, G., and Strauss, S.H. (1997) *J. Phys. Chem. A*, **101**, 9551.
24. Recent reviews: (a) de Frémont, P., Marion, N., and Nolan, S.P. (2009) *Coord. Chem. Rev.*, **253**, 862; (b) Kühl, O. (2009) *Coord. Chem. Rev.*, **253**, 2481; (c) Tapu, D., Dixon, D.A., and Roe, C. (2009) *Chem. Rev.*, **109**, 3385; (d)

Lin, J.C.Y., Huang, R.T.W., Lee, C.S., Bhattacharyya, A., Hwang, W.S., and Lin, I.J.B. (2009) *Chem. Rev.*, **109**, 3561; (e) Arnold, P.L. and Casely, I.J. (2009) *Chem. Rev.*, **109**, 3599; (f) Díez-González, S., Marion, N., and Nolan, S.P. (2009) *Chem. Rev.*, **109**, 3612; (g) Poyatos, M., Mata, J.A., and Peris, E. (2009) *Chem. Rev.*, **109**, 3677; (h) Samojłowicz, C., Bieniek, M., and Grela, K. (2009) *Chem. Rev.*, **109**, 3708; (i) van Otterlo, W.A.L. and de Koning, C.B. (2009) *Chem. Rev.*, **109**, 3743; (j) Monfette, S. and Fogg, D.E. (2009) *Chem. Rev.*, **109**, 3783; (k) Alcaide, B., Almendros, P., and Luna, A. (2009) *Chem. Rev.*, **109**, 3817; (l) Hindi, K.M., Panzner, M.J., Tessier, C.A., Cannon, C.L., and Youngs, W.J. (2009) *Chem. Rev.*, **109**, 3859; (m) Corbern, R., Mas-Marz, E., and Peris, E. (2009) *Eur. J. Inorg. Chem.*, **2009**, 1700; (n) de Fremont, P., Marion, N., and Nolan, S.P. (2009) *Coord. Chem. Rev.*, **253**, 862; (o) Herndon, J.W. (2009) *Coord. Chem. Rev.*, **253**, 1517; (p) Jacobsen, H., Correa, A., Poater, A., Costabile, C., and Cavallo, L. (2009) *Coord. Chem. Rev.*, **253**, 687; (q) Radius, U. and Bickelhaupt, F.M. (2009) *Coord. Chem. Rev.*, **253**, 678; (r) Delaude, L. (2009) *Eur. J. Inorg. Chem.*, 1681; (s) Arduengo, A.J. III, and Iconaru, L.I. (2009) *Dalton Trans.*, 6903; (t) McGuinness, D. (2009) *Dalton Trans.*, 6915; (u) Teyssot, M.-L., Jarrousse, A.-S., Manin, M., Chevry, A., Roche, S., Norre, F., Beaudoin, C., Morel, L., Boyer, D., Mahiou, R., and Gautier, A. (2009) *Dalton Trans.*, 6894; (v) Cazin, C.S.J. (2009) *C. R. Chim.*, **12**, 1173; (w) Hahn, F.E. and Jahnke, M.C. (2008) *Angew. Chem.*, **120**, 3166; *Angew. Chem. Int. Ed.* 2008, **47**, 3122.

25. (a) Jacobsen, H. (2005) *J. Organomet. Chem.*, **690**, 6068; (b) Jacobsen, H., Correa, A., Costabile, C., and Cavallo, L. (2006) *J. Organomet. Chem.*, **691**, 4350.
26. Frenking, G., Wichmann, K., Fröhlich, N., Grobe, J., Golla, W., Le Van, D., Krebs, B., and Läge, M. (2002) *Organometallics*, **21**, 2921.
27. The failure of a correlation between bond length and bond strength has been noted in the literature: (a) Cremer, D., Wu, A.N., Larsson, A., and Kraka, E. (2000) *J. Mol. Model.*, **6**, 396; (b) Kaupp, M., Metz, B., and Stoll, H. (2000) *Angew. Chem. Int. Ed.*, **39**, 4607.
28. Kutzelnigg, W. (1984) *Angew. Chem. Int. Ed.*, **23**, 272.
29. Pyykkö, P. (1988) *Chem. Rev.*, **88**, 563.
30. Tonner, R., Heydenrych, G., and Frenking, G. (2007) *Chem. Asian J.*, **2**, 1555.
31. (a) Dötz, K.H., Fischer, H., Hofmann, P., Kreissl, F.R., Schubert, U., and Weiss, K. (1983) *Transition Metal Carbene Complexes*, Verlag Chemie, Weinheim; (b) Schrock, R. (1979) *Acc. Chem. Res.*, **12**, 98; (c) Nugent, W.A. and Mayer, J.M. (1988) *Metal-Ligand Multiple Bonds*, John Wiley & Sons, Inc., New York; (d) Fischer, H., Hofmann, P., Kreissl, F.R., Schrock, R.R., Schubert, U., and Weiss, K. (1988) *Carbyne Complexes*, John Wiley & Sons, Inc., New York; (e)Kreissl, F.R. (ed.) (1993) *Transition Metal Carbyne Complexes*, Kluwer Academic Publishers, Dordrecht.
32. A detailed bonding analysis of Fischer- and Schrock-type carbene and carbyne complexes using the EDA approach has been given in: Lein, M., Szabó, A., Kovács, A., and Frenking, G. (2003) *Faraday Discuss.*, **124**, 365.
33. (a) Pidun, U. and Frenking, G. (1995) *Organometallics*, **14**, 5325; (b) Pidun, U. and Frenking, G. (1996) *J. Organomet. Chem.*, **525**, 269; (c) Pidun, U. and Frenking, G. (1997) *J. Chem. Soc., Dalton Trans.*, 1653.
34. Nechaev, M.S., Rayón, V.M., and Frenking, G. (2004) *J. Phys. Chem. A*, **108**, 3134.
35. Uddin, J. and Frenking, G. (2001) *J. Am. Chem. Soc.*, **123**, 1683.
36. Krapp, A., Bickelhaupt, F.M., and Frenking, G. (2006) *Chem. Eur. J.*, **12**, 9196.
37. The failure of atomic partial charges to estimate the strength or even the direction of Coulomb interactions is not restricted to metal-ligand interactions. A detailed analysis of the covalent and electrostatic bonding between CO and a proton shows that H^+ encounters in HCO^+ stronger attraction of the formally positive carbon atom than in COH^+ by the negatively charged oxygen

atom: Lupinetti, A., Fau, S., Frenking, G., and Strauss, S.H. (1997) *J. Phys. Chem. A*, **101**, 9551.

38. (a) Kealy, T.J. and Pauson, P.L. (1951) *Nature*, **168**, 1039; (b)Another paper which reported about the synthesis of ferrocene was submitted earlier, but it was published later: Miller, S.A., Tebboth, J.A., and Tremaine, J.F. (1952) *J. Chem. Soc.*, 633.

39. (a) Fischer, E.O. and Pfab, W. (1952) *Z. Naturforsch.*, **76**, 377; (b) Wilkinson, G., Rosenblum, M., Whiting, M.C., and Woodward, R.B. (1952) *J. Am. Chem. Soc.*, **74**, 2125.

40. Shustorovich, E.M. and Dyatkina, E.M. (1959) *Dok. Akad. Nauk. SSSR*, **128**, 1234.

41. Fischer, E.O. and Hafner, W. (1955) *Z. Naturforsch.*, **10b**, 665.

42. Elschenbroich, C. (2006) *Organometallics*, 3rd edn, Wiley-VCH Verlag GmbH, Weinheim.

43. (a) Haaland *Acta*, A. (1965) *Chem. Scand.*, **19**, 41; (b) Haaland, A. and Nilsson, J.E. (1968) *Acta Chem. Scand.*, **22**, 2653; (c) Haaland, A. (1979) *Acc. Chem. Res.*, **12**, 415.

44. Rayón, V.M. and Frenking, G. (2003) *Organometallics*, **22**, 3304.

45. (a) Frunzke, J., Lein, M., and Frenking, G. (2002) *Organometallics*, **21**, 3351; (b) Lein, M., Frunzke, J., and Frenking, G. (2003) *Inorg. Chem.*, **42**, 2504.

46. (a) Cadenbach, T., Bollermann, T., Gemel, C., Fernández, I., von Hopffgarten, M., Frenking, G., and Fischer, R.A. (2008) *Angew. Chem.*, **120**, 9290; *Angew. Chem. Int. Ed.* 2008, **47**, 9150; (b) Cadenbach, T., Bollermann, T., Gemel, C., Tombul, M., Fernández, I., von Hopffgarten, M., Frenking, G., and Fischer, R.A. (2009) *J. Am. Chem. Soc.*, **131**, 16063; (c) Gonzalez-Gallardo, S., Prabusankar, G., Cadenbach, T., Gemel, C., von Hopffgarten, M., Frenking, G., and Fischer, R.A. (2010) *Structure and Bonding*, **136**, 147; (d) Bollermann, T., Cadenbach, T., Gemel, C., von Hopffgarten, M., Frenking, G., and Fischer, R.A. (2010) *Chem. Eur. J.*, **16**, 13372.

47. Cotton, F.A. and Harris, C.B. (1965) *Inorg. Chem.*, **4**, 330.

48. Cotton, F.A., Murillo, C.A., and Walton, R.A. (2005) *Multiple Bonds Between Metal Atoms*, 3 edn, Springer Science and Business Media, Inc., New York.

49. Gagliardi, L. and Roos, B. (2003) *Inorg. Chem.*, **42**, 1599.

50. Saito, K., Nakao, Y., Sato, H., and Sakaki, S. (2006) *J. Phys. Chem. A*, **110**, 9710.

51. Krapp, A., Lein, M., and Frenking, G. (2008) *Theor. Chem. Acc.*, **120**, 313.

52. Hofmann, P. (1983) in *Transition Metal Carbene Complexes* (eds K.H. Dötz, H. Fischer, P. Hofmann, F.R. Kreissl, U. Schubert, and K. Weiss), Verlag Chemie, Weinheim, p. 113.

8
Chemical Bonding in Open-Shell Transition-Metal Complexes

Katharina Boguslawski and Markus Reiher

8.1
Introduction

Modern quantum chemistry has achieved a remarkable quantitative description of atomic interactions and molecular stability. These benefits come, however, at the expense of a fading qualitative understanding [1]. In this chapter, we review the state of the art of quantitative numerical quantum chemistry and show how conceptual qualitative understanding can be recovered using the example of open-shell transition-metal complexes and clusters. Although transition-metal complexes are of central importance in bioinorganic chemistry and metal-mediated catalysis [2, 3] and thus play a crucial role in the process of bond breaking and bond making in chemical reactions, their theoretical description remains a challenging task for quantum chemistry because of the near degeneracies of their electronic states [4].

The chemical bond is a basic concept in chemistry and its understanding is thus of fundamental interest for both experimental and theoretical chemists. As bonds are broken and formed during reactions, understanding of the bonding phenomenon can serve as a guide to synthesis. In cases where an experimental analysis of chemical structures or properties is indecisive and ambiguous, quantum chemical calculations are a complement and provide deeper insights into chemical reactivity and the nature of the bond. In particular, quantum chemistry provides quantitative information on electronic structures and a variety of analysis tools for our qualitative understanding.

Lewis introduced the idea of the chemical bond as a pairing and sharing phenomenon of electrons between neighboring atoms [5]. Despite its striking simplicity, Lewis' model of covalent bonding remained the basis of how to describe chemical bonds and, in particular, of how to draw structures of chemical compounds. While the largest number of bonds between main group elements was found to be three (for instance, in dinitrogen or acetylene), higher bond orders, that is, a higher total number of covalent bonds between two neighboring atoms, have been formed for molecules containing transition metals because of the additional shell of *d*-orbitals, which can then participate in the bond-forming process in addition to the *s*- and *p*-orbitals. Detailed theoretical and experimental work on

The Chemical Bond: Chemical Bonding Across the Periodic Table, First Edition.
Edited by Gernot Frenking, Sason Shaik.

stable multibonded transition metals followed [6] and led to the first experimental evidence of quintuple bonding in 2005 [7].

Quantum chemistry provides two different languages for a modular design principle of molecules, built from atoms representing the elementary building blocks to be treated as open quantum systems [8]. In the basis-set expansion approach, many-particle states are expressed by an expansion into a basis set. The second approach relies on the electron density that is decomposed to assign atomic basins to particular regions in three-dimensional space. These conceptually different descriptions of atoms in molecules yield different notions of chemical bonding with advantages and shortcomings.

If a vector space representation of electronic states is chosen, that is, a basis-set expansion, two types of basis sets are needed. One for the many-electron states and one for the one-particle states. For the latter, two choices became popular, the molecular orbital (MO) [9] and valence bond (VB) [10] expansions. Both influenced the understanding and interpretation of the chemical bond. A bonding analysis can then be performed in terms of their basic quantities. Although both representations of the wave function can be transformed (at least partially) into each other [11, 12], most commonly an MO analysis is employed in electronic structure calculations for practical reasons. Besides, a VB description is often limited to small atomic basis sets as (semi-)localized orbitals are required to generate the VB structures [13]. If, however, diffuse functions with large angular momenta are included in the atomic orbital basis, a VB analysis suffers from their delocalization tails. As a consequence, the application of VB methods can often be limited to organic molecules.

In this chapter, we review quantum chemical theories developed to describe chemical bonding in open-shell (transition metal) compounds. We review some important electronic structure methods that provide us with the central ingredient for an analysis of the chemical bond, the electronic wave function. We then discuss how information from the electronic wave function is extracted for a qualitative interpretation of the electronic structure. For this purpose, different approaches are described to extract local quantities from quantum states. An example is the local spin concept, which can be employed to study spin–spin interactions in terms of a Heisenberg coupling model. Finally, the difficulty of describing electronic structures of open-shell molecules accurately is highlighted as an example.

8.2 Theoretical Foundations

The total wave function Ψ of a molecule comprising N electrons and M nuclei depends on all electronic $\{\mathbf{r}_i\}$ and nuclear $\{\mathbf{R}_I\}$ coordinates. It can be obtained by solving the time-independent Schrödinger equation [14–16],

$$\hat{\mathscr{H}}\Psi(\{\mathbf{r}_i\},\{\mathbf{R}_I\}) = E\Psi(\{\mathbf{r}_i\},\{\mathbf{R}_I\}) \tag{8.1}$$

where the Hamiltonian in its first quantized form (in Hartree atomic units, $\hbar = m_e = 4\pi\varepsilon_0 = 1$) can be given exactly in the nonrelativistic limit of quantum

mechanics [17],

$$\hat{\mathscr{H}} = -\frac{1}{2}\sum_{i}^{N}\nabla_i^2 - \frac{1}{2}\sum_{I}^{M}\frac{1}{m_I}\nabla_I^2 + \sum_{i<j}^{N}\frac{1}{|\mathbf{r}_i - \mathbf{r}_j|} + \sum_{I<J}^{M}\frac{Z_I Z_J}{|\mathbf{R}_I - \mathbf{R}_J|} - \sum_{I}^{M}\sum_{i}^{N}\frac{Z_I}{|\mathbf{r}_i - \mathbf{R}_I|} \tag{8.2}$$

with nuclear masses m_I and nuclear charges Z_I. Lowercase letters are used to index electrons, while uppercase letters indicate nuclei. To arrive at a simpler starting equation, we can employ the Born–Oppenheimer approximation [18, 19] in which the total wave function can be written as a simple product of a nuclear $\chi(\{\mathbf{R}_I\})$ and an electronic part $\Psi_{\text{el}}(\{\mathbf{r}_i\})$. The electronic wave function $\Psi_{\text{el}}(\{\mathbf{r}_i\})$ depends on all electronic coordinates, while the nuclear coordinates enter as fixed parameters. Within the Born–Oppenheimer approximation, the electronic states are solutions of the electronic Schrödinger equation,

$$\hat{\mathscr{H}}_{\text{el}}\Psi_{\text{el}} = E_{\text{el}}\Psi_{\text{el}} \tag{8.3}$$

with the electronic energy E_{el} and the electronic Hamiltonian (in Hartree atomic units)

$$\hat{\mathscr{H}}_{\text{el}} = \hat{\mathscr{H}} + \frac{1}{2}\sum_{I}^{M}\frac{1}{m_I}\nabla_I^2 \tag{8.4}$$

It is important to note that we are mainly interested in the electronic part of the total wave function because we wish to study electronic structures at a particular molecular structure (usually an equilibrium or transition-state structure). The parameterization of the electronic wave function ansatz and its (variational) optimization are keystones of electronic structure theory.

8.2.1 Definition of Open-Shell Electronic Structures

A general and, at the same time, intuitive definition of open-shell molecules is not that straightforward to give, but it can be provided in the context of MO theory, where a molecule is considered to be *open shell* if its valence shell contains orbitals that are partially occupied. Open-shell systems can be encountered when the number of α-electrons differs from the number of β-electrons, and, as a consequence, nonzero eigenvalues of the total squared spin operator $\hat{\mathbf{S}}^2$ are obtained (in atomic units),

$$\hat{\mathbf{S}}^2\Psi_{\text{el}} = S(S+1)\Psi_{\text{el}} \tag{8.5}$$

where S can adopt the values $S = \frac{1}{2}, 1, \ldots$. However, open-shell systems are not constrained to possess nonzero $\hat{\mathbf{S}}^2$ eigenvalues, but they can be encountered if the molecules are composed of two or more centers that are antiferromagnetically coupled to form an overall singlet state with an equal number of α and β electrons. In a one-determinant picture, such systems can be understood to contain one (or several) fragment(s), for example, a metal center, with a certain amount of spin

excess and a second (or several) fragment(s) with a certain amount of opposite spin excess. However, the total spin polarization would still be zero as the picture of excess spin is an artifact of a one-determinant description [20].

8.2.2 The Configuration Interaction Ansatz

In order to solve Eq. (8.3), we can expand the electronic wave function Ψ_{el} in a complete set of many-electron functions, Φ_I, also called electronic configurations or Slater determinants,

$$\Psi_{\mathrm{el}} = \sum_{I=0}^{k} C_I \Phi_I \tag{8.6}$$

with expansion coefficients C_I and a (in actual calculations, finite) set of one-particle functions (orbitals) $\{\phi_{I_i}\}$.

In the limit $k \to \infty$, which implies that the number of one-particle functions also goes to ∞, we obtain the exact solution of the electronic Schrödinger equation, which is the full configuration interaction (FCI) ansatz. A (still finite) expansion of the FCI wave function is only accomplishable for the smallest systems [21, 22] and further approximations to Eq. (8.6) are mandatory.

8.2.2.1 The Truncation Procedure

In the simplest case for $k = 1$, we obtain the one-determinant wave function of the Hartree–Fock theory. The energy difference with respect to the FCI reference,

$$E_{\mathrm{el}}^{\mathrm{corr}} = E_{\mathrm{el}}^{\mathrm{FCI}} - E_{\mathrm{el}}^{\mathrm{SD}} \tag{8.7}$$

is defined as the correlation energy [23], where $E_{\mathrm{el}}^{\mathrm{SD}}$ is the ground-state energy corresponding to a one-determinant wave function. In order to account for correlation effects, k must be chosen larger than 1. However, the number of independent expansion coefficients C_I should be reduced as much as possible owing to the computational cost. This can be achieved either by restricting the sum of Eq. (8.6) to contain only a set of preselected electronic configurations [9] or by reparameterizing the expansion coefficients C_I, which leads to a smaller number of degrees of freedom without explicitly truncating the set of electronic configurations [24].

8.2.2.2 Density Matrices

Density matrices, in particular, the so-called first- and second-order reduced density matrices, are important quantities in the theoretical description of electronic structures because they contain all the essential information of the system under study. Given a set of orthonormal MOs, we define the first-order reduced density matrix $\mathbf{D}$ with matrix elements D_{pq} as the expectation value of the excitation operator $\hat{E}_{pq} = a_{p\alpha}^{\dagger} a_{q\alpha} + a_{p\beta}^{\dagger} a_{q\beta}$ with respect to some electronic wave function Ψ_{el},

$$D_{pq} = \langle \Psi_{\mathrm{el}} | a_{p\alpha}^{\dagger} a_{q\alpha} + a_{p\beta}^{\dagger} a_{q\beta} | \Psi_{\mathrm{el}} \rangle \tag{8.8}$$

where p, q indicate the (spatial) MOs involved in the excitation process, ϕ_p and ϕ_q, respectively, and $a^\dagger$ and a are the fermionic creation and annihilation operators [9]. The diagonal elements D_{pp} are the orbital occupation numbers and are restricted to the interval $0 \leq D_{pp} \leq 2$. A particularly useful set of occupation numbers are the *natural-orbital occupation numbers* η_p, which are the eigenvalues of the first-order reduced density matrix. The natural-orbital occupation numbers are of special importance in the analysis of effective bond orders for multireference wave functions that are discussed subsequently.

Similarly, we can define the second-order reduced density matrix **d** whose matrix elements are determined from the expectation value of $\hat{E}_{pq}\hat{E}_{rs}$,

$$d_{pqrs} = \langle \Psi_{\mathrm{el}} | \sum_{\sigma\tau \in \{\alpha,\beta\}} a^\dagger_{p\sigma} a^\dagger_{r\tau} a_{s\tau} a_{q\sigma} | \Psi_{\mathrm{el}} \rangle \tag{8.9}$$

We can write the first- and second-order reduced density matrix spatially resolved in terms of MOs $\{\phi_i\}$

$$\rho(\mathbf{r};\mathbf{r}') = \sum_{pq} D_{pq} \phi_p(\mathbf{r}') \phi^*_q(\mathbf{r})$$

and

$$\rho(\mathbf{r}_1, \mathbf{r}_2; \mathbf{r}'_1, \mathbf{r}'_2) = \sum_{pqrs} d_{pqrs} \phi_p(\mathbf{r}'_1) \phi_r(\mathbf{r}'_2) \phi^*_q(\mathbf{r}_1) \phi^*_s(\mathbf{r}_2)$$

respectively. Both formulations are equivalent. The diagonal part of **D** (or similarly, $\rho(\mathbf{r};\mathbf{r}) = \rho(\mathbf{r})$) represents the electron density.

8.2.3 *Ab Initio* Single-Reference Approaches

The simplest way of truncating the complete set of electronic configurations is to include those Slater determinants in the CI expansion that differ by one, two, three, and so on spin orbitals compared to some reference configuration Φ_0. *Truncated* CI expansions then are linear combinations of the reference determinant and all singly, doubly, triply, and so on ''excited'' configurations. For instance, the CI singles doubles (CISD) wave functions can be written as

$$\Psi^{\mathrm{CISD}}_{\mathrm{el}} = \Phi_0 + \sum_{i}^{\mathrm{occ}} \sum_{a}^{\mathrm{unocc}} C^a_i a^\dagger_a a_i \Phi_0 + \sum_{j<i}^{\mathrm{occ}} \sum_{b<a}^{\mathrm{unocc}} C^{ab}_{ij} a^\dagger_a a^\dagger_b a_j a_i \Phi_0 \tag{8.10}$$

where $a^\dagger$ and a are again the fermionic creation and annihilation operators that allow us to substitute spin orbitals in the electronic (reference) configuration Φ_0. The CI coefficients $C^{a\cdots}_{i\cdots}$ are the expansion coefficients and the sums run over two sets of spin orbitals, which are either occupied (indicated by $i, j, \ldots$) or unoccupied (indicated by $a, b, \ldots$) in the reference configuration.

A different representation of the FCI wave function is obtained from the coupled cluster (CC) theory [25–27], where the CC wave function $\Psi^{\mathrm{CC}}_{\mathrm{el}}$ is expressed by means of an exponential function of the *cluster operator* $\hat{T}$,

$$\Psi^{\mathrm{CC}}_{\mathrm{el}} = \exp\,(\hat{T})\Phi_0 \tag{8.11}$$

where $\hat{T} = \hat{T}_1 + \hat{T}_2 + \hat{T}_3 + \ldots$ contains spin-orbital substitution operators given by

$$\hat{T}_1 = \sum_i \sum_a t_i^a a_a^\dagger a_i, \quad \hat{T}_2 = \sum_{ij} \sum_{ab} t_{ij}^{ab} a_a^\dagger a_b^\dagger a_j a_i,$$
$$\hat{T}_3 = \sum_{ijk} \sum_{abc} t_{ijk}^{abc} a_a^\dagger a_b^\dagger a_c^\dagger a_k a_j a_i \tag{8.12}$$

and so on. t_i^a, t_{ij}^{ab}, … are the CC amplitudes that can be related to the CI coefficients $C_{i\ldots}^{a\cdots}$. An approximate representation of the FCI wave function can be obtained if the cluster operator is truncated at a given excitation level so that the $C_{i\ldots}^{a\cdots}$ coefficients can be reconstructed from a subset of amplitudes (singles, doubles, etc.) and their wedge products [27].

If the single-determinant model is a good approximation of the exact solution, the single-reference CC expansion, for which Φ_0 is the Hartree–Fock determinant, is a convenient parameterization of the FCI coefficients. For open-shell molecules that exhibit a non-negligible multireference character, the standard single-reference CC approach should not yield reliable electronic energies and its multireference extensions should be employed instead [26–29]. Nevertheless, the unrestricted CC variant was shown to capture some of the multireference character [30].

As single-reference models break down when occupied and virtual orbitals become near-degenerate, which can be found, for instance, at the dissociation limit and in di- or triradicals, Krylov [31, 32] introduced a spin-flipping approach where a high-spin triplet state (or quartet state in the case of triradicals) is chosen as the reference wave function [32]. As dynamic and nondynamic correlation effects are considerably smaller for a triplet state than for the corresponding singlet state, a triplet-reference wave function can be accurately described within a single-reference model. The target state can then be an open-shell singlet wave function treated as an excited state with respect to the triplet-reference configuration, that is, a set of target configurations of proper spin symmetry is obtained through spin-flipping excitations from the triplet state, for example, $\alpha \rightarrow \beta$.

8.2.4 *Ab Initio* Multireference Approaches

A single-reference description often breaks down if several electronic configurations have similar energies and static correlation becomes important [33]. In order to account for static electron correlation effects, we must adopt a multideterminant description of the electronic state without any reference to a particular determinant. An extension of truncated CI-based approaches are thus methods that simultaneously optimize both the C_I coefficients and the orbital basis used to construct the electronic configurations [34]. Hence, such multiconfigurational self-consistent field (MCSCF) methods [35] can be considered as a combination of CI and SCF techniques to be employed to generate an appropriate zero-order reference for a subsequent CI or perturbation theory treatment. Similar to single-reference approaches, the configurations that are to be included in the wave function expansion need to be selected before an MCSCF calculation. A common procedure in

choosing the configuration subspace is to divide the orbital space, that is, the set of spatial orbitals, into different subspaces and then to distribute the electrons among these subspaces according to a specific occupation pattern.

The most popular MCSCF method is the complete-active-space self-consistent-field (CASSCF) approach [36], where the orbital space is divided into three disjoint subspaces; an *inactive*, an *active*, and an *external* one [36, 37]. The configurations contained in the CASSCF wave function expansion are then completely defined. While the inactive orbitals are doubly occupied in all configurations, the external orbitals are unoccupied. All remaining *active* electrons, which are not contained in the inactive subspace, are distributed over the active orbitals in such a way that an FCI subspace is generated within the active space. In the standard CASSCF approach, *all* orbitals are optimized, which, however, might not be always necessary. In cases where the starting orbitals are already well described as, for example, the core orbitals, they can be excluded from the orbital optimization procedure and can be kept frozen during all MCSCF optimization steps. The crucial step in a CASSCF calculation is the construction of the active orbital space. Its application to larger molecular systems requires a profound knowledge of the electronic structure and a careful selection of the active orbitals so that the static electron correlation energy can be efficiently described within the FCI subspace.

In order to reduce the computational cost and to increase the number of correlated electrons and orbitals, additional constraints can be enforced on the configuration space so that ineffective configurations are removed [38–41]. Furthermore, the active space itself can be partitioned into several subspaces for which different occupational restrictions are imposed. Examples of such MCSCF approaches are the restricted active space SCF (RASSCF) method [42, 43] and the generalized active space (GAS) ansatz [42, 44] (further variants can be found in Refs. [45–52]). Although they allow for treatment of much larger active spaces in terms of electrons and orbitals, a balanced active space is more difficult to obtain than in the traditional CASSCF method owing to the larger number of possibilities of how to partition the complete orbital space into inactive and active subspaces and the variable choices of occupational restrictions in each of these active subspaces. MCSCF approaches are thus not black-box methods; they allow for the description of complicated electronic systems if the active subspaces and occupational restrictions have been *carefully* defined.

Because the contribution of the external orbitals to the correlation energy is neglected, this missing dynamic correlation can be essentially recovered in two ways: multireference configuration interaction (MRCI) or multireference perturbation theory (MRPT) approaches [53].

The most popular way of including dynamic correlation upon a CASSCF reference wave function [54–57] is the second-order perturbation theory (CASPT2) developed by Roos and coworkers [58]. However, in contrast to the single-configurational case, where the definition of the zeroth-order Hamiltonian is universal and taken as the sum of the one-electron Fock operators, the generalization of the zeroth-order Hamiltonian to the multiconfigurational case is not straightforward [59, 60]. A different, theoretically more justified approach is to

include the two-electron terms into the zeroth-order Hamiltonian [59], which was successfully applied by Malrieu and coworkers and is known under the acronym NEVPT2 [61]. The original CASPT2 method has been extended in several ways (see, for instance, the restricted active space second-order perturbation theory treatment (RASPT2) [56, 62]) in order to overcome computational difficulties and the limitations in the dimension of the active orbital space present in standard CASSCF calculations.

In MRCI, the wave function is constructed according to Eq. (8.6), allowing all excitations up to a predefined order except that a multideterminant expansion is taken as reference which, for instance, can be obtained from a preceding CASSCF calculation [63]. As the number of determinants can grow considerably for larger molecules, MRCI might become computationally unfeasible. Although the number of variational parameters can be reduced by different means, for example, internally contracted theory [64], an MBPT treatment of dynamic correlation in multireference electronic systems is preferred over MRCI [65].

The generalized valence bond (GVB) approach was one of the first methods where semilocalized orbitals, as developed by Coulson and Fischer, have been employed to polyatomic molecules [66–72]. GVB is typically applied within a restricted formulation introducing two simplifications for the construction of the VB structures (for a simple diatomic molecule AB, there are two VB structures; the so-called ionic structures, A^+B^- and A^-B^+, and a covalent structure, $A\cdot\!-\!\cdot B$). In the first simplification, the perfect pairing (PP) approximation, which generates only one VB structure for the entire calculation, is employed. The GVB wave functions exhibit then a particular simple form and can be expressed as a product of the so-called *geminal* two-electron functions and the nonactive core and open, that is, singly occupied α orbitals. Each geminal function is constructed from a singlet-coupled GVB pair $(\varphi_{A_i}, \varphi_{B_i})$, which is associated with one particular bond (between the centers A_i and B_i) or lone pair of the molecule. Within the PP approximation, the active part of the GVB-PP electronic wave function $\Psi_{\mathrm{el}}^{\mathrm{GVB-PP}}$ reads [13]

$$\begin{aligned}\Psi_{\mathrm{el}}^{\mathrm{GVB-PP}} = |(|\varphi_{A_1}\overline{\varphi}_{B_1} - \overline{\varphi}_{A_1}\varphi_{B_1}|)(|\varphi_{A_2}\overline{\varphi}_{B_2} - \overline{\varphi}_{A_2}\varphi_{B_2}|)\ \cdots \\ (|\varphi_{A_n}\overline{\varphi}_{B_n} - \overline{\varphi}_{A_n}\varphi_{B_n}|)|\end{aligned} \tag{8.13}$$

with n geminal functions, $|\varphi_{A_i}\overline{\varphi}_{B_i} - \overline{\varphi}_{A_i}\varphi_{B_i}|$, encoding a total number of n bonds between the centers A_i and B_i. Here, the overbar denotes that an orbital is occupied by a β electron, while simple Latin letters are employed for orbitals occupied by α electrons. Each pair of active electrons is thus described by two (variationally optimized) nonorthogonal, that is, overlapping orbitals. Because GVB-PP considers only *one* valence bond coupling of the electrons (perfect pairing), it represents a special case of the GVB approach where all possible spin couplings of active orbitals are included in the VB structure.

Typically, GVB-PP calculations are carried out within an orthogonal orbital basis, which is called the strong orthogonality constraint. This second simplification ensures that all orbitals are orthogonal to each other unless they are singlet paired. However, the strong orthogonality constraint was simply introduced for

computational convenience and does not imply a serious restriction, because the orbitals are nevertheless assumed to hardly overlap.

Any converged CI-type wave function can be interpreted in a VB picture employing an orbital transformation. The electronic structure can then be resolved in terms of two-center bonds. Radon *et al.* [73] presented a VB-type analysis of a CASSCF wave function, where the contributions of different VB structures (covalent and ionic) to the CASSCF wave function can be identified. In order to classify each configuration incorporated in the complete-active-space configuration-interaction (CASCI) expansion in terms of its resonance structure, an orbital localization needs to be performed so that the delocalized natural orbitals can be clearly identified as, for instance, metal or ligand type. The total weight of one particular resonance structure can then be determined from the weights of all configurations contributing to this particular resonance structure. Note that such a transformation into a set of localized orbitals does not change the CASSCF wave function, but facilitates an analysis of electronic structures in terms of a VB-like picture.

So far, we focused on conventional quantum chemical approaches that approximate the FCI wave function by truncating the complete N-particle Hilbert space based on predefined configuration selection procedures. In a different approach, the number of independent CI coefficients can be reduced without pruning the FCI space. This is equivalent to seeking a more efficient parameterization of the wave function expansion, where the CI coefficients are approximated by a smaller set of variational parameters that allow for an optimal representation of the quantum state of interest. Different approaches, which we will call *modern* solely to distinguish them from the standard quantum chemical methods, have emerged from solid-state physics.

A modern multireference electron correlation method, which was introduced into quantum chemistry more than 15 years ago, is the density-matrix renormalization-group (DMRG) algorithm [74–78] developed by White [79, 80]. DMRG allows the treatment of much larger active spaces than those that are computationally feasible with standard approaches *without* explicitly truncating the FCI wave function expansion. We demonstrated that DMRG yields qualitatively accurate electronic wave functions even for compact, strongly correlated electronic structures such as transition-metal complexes [81–86] and that DMRG can be employed to study molecular systems that are rather challenging for standard approaches [85, 87].

The DMRG algorithm optimizes a special class of quantum states called matrix product states (MPS) [88–90]. Usually, an MPS wave function is expressed in the canonical way, employing left- or right-normalized matrices [90]. In the case of DMRG, a mixed-canonical MPS is obtained, which incorporates both left- and right-normalized matrices $\mathbf{A}$,

$$\Psi_{\mathrm{el}}^{\mathrm{MPS}} = \sum_{\{\mathbf{n}\}} \mathbf{A}^{n_1} \ \ldots \ \mathbf{A}^{n_{i-1}} \mathbf{\Psi}^{n_i n_{i+1}} \mathbf{A}^{n_{i+2}} \ \ldots \ \mathbf{A}^{n_L} | n_1 \ \ldots \ n_L \rangle \tag{8.14}$$

where the Slater determinants Φ_I are given in their occupation number representation [9] and each occupation number vector $\mathbf{n} = |n_1 \ \ldots \ n_L\rangle$ is constructed from L one-particle functions, that is, from the active orbitals, usually referred to as

sites, with occupation numbers η_{n_i}. In this equation, the left- and right-normalized matrices $\mathbf{A}^{n_i}$ depend on the local sites n_i, where the left-normalized matrices are defined on sites $n_1, \ldots, n_{l-1}$, while right-normalized matrices are obtained on sites $n_{l+2}, \ldots, n_L$. The $\mathbf{\Psi}$ matrix contains the elements from the CI vector obtained from diagonalizing the electronic Hamiltonian matrix.

Thus, the high-dimensional coefficient tensor has been replaced by a product of matrices with at most $4Lm^2$ variational parameters, where m^2 is the dimension of $\mathbf{A}$. In order to ensure that the number of degrees of freedom is smaller than the dimension of the complete N-particle Hilbert space, the exact $\tilde{\mathbf{A}}$ matrices of dimension $\tilde{m}^2$ need to be approximated by some lower dimensional matrices $\mathbf{A}$ with $m < \tilde{m}$, where m is the so-called number of renormalized active-system states. The calculation of the $\mathbf{A}$ matrices is performed iteratively by the DMRG algorithm under the constraint that the approximate MPS wave function is as close as possible to the complete MPS representation [90, 91].

From Eq. (8.14), we can immediately read off the CI coefficients of the wave function expansion. If we write the summation over the elements of the eigenvector of $\hat{H}_{\mathrm{el}}$ explicitly, we obtain for the CI coefficient of one Slater determinant $\mathbf{n}$

$$C_{\mathbf{n}} = \sum_{m^S}^{m} \sum_{m^E}^{m} \Psi_{m^S n_l n_{l+1} m^E} \left(\mathbf{A}^{n_2} \ \ldots \ \mathbf{A}^{n_{l-1}}\right)_{n_1;m^S} \left(\mathbf{A}^{n_{l+2}} \ \ldots \ \mathbf{A}^{n_L}\right)_{m^E;n_L} \tag{8.15}$$

In order to reconstruct a CASCI-type wave function expansion, which contains the most important configurations, a Monte Carlo sampling routine can then be employed to sample the complete N-particle Hilbert space [92].

In practical calculations, the active orbitals need to be aligned along a one-dimensional lattice in order to optimize the $\mathbf{A}$ matrices iteratively. However, this orbital ordering crucially determines the convergence behavior of DMRG [82, 93, 94] and hence an improved orbital ordering needs to be found for optimal performance. This can be achieved, for instance, by means of quantum information theory concepts [82] employing entanglement measures such as mutual information [95] or single-orbital entropies [96, 97]. Furthermore, different acceleration techniques have been developed to prevent the convergence into local minima for small matrix dimensions [98–100].

Nevertheless, the optimization of an MPS might be difficult for general molecules that do not inherit a linear structure for which a mapping upon a one-dimensional lattice would be evident. Furthermore, the MO basis preferentially consists of delocalized orbitals with no spatial information, which prohibits a unique orbital ordering, while localization procedures that keep the orthogonality property among the orbitals cannot be efficiently performed for complex molecules. A nonlinear tensor network ansatz for the electronic wave function can overcome these difficulties and incorporate nonlocal correlations. In contrast to an MPS ansatz, where only two orbitals are directly connected, the complete-graph tensor-network (CGTN) approach [24] replaces the CI coefficient tensor by a network of tensors that connects all orbitals with each other. Originally, such tensor network ansätze had been proposed for simple spin Hamiltonians [101–103], while the first implementation of tensor network states (TNSs) for the full quantum chemical Hamiltonian was

the CGTN ansatz [24] followed by TNS studies for transition-metal complexes and clusters [104, 105]. The CGTN wave function reads

$$\Psi_{\text{el}}^{\text{CGTN}} = \sum_{n_1 \ldots n_L}^{q} \prod_{\alpha}^{L} \prod_{\beta \leq \alpha} f_{\alpha\beta}^{n_\alpha n_\beta} |n_1 \ \ldots \ n_L\rangle \tag{8.16}$$

where $f_{\alpha\beta}^{n_\alpha n_\beta}$ depends on pairs of orbitals α and β. The CGTN state is optimized by a variational Monte Carlo approach. The accuracy of the CGTN approach may be increased by including higher order correlators in the wave function ansatz [103], that is, tensors that depend on three or four orbitals, or more.

8.2.5 Density Functional Theory for Open-Shell Molecules

A different – and the most popular – approach to describe open-shell electronic structures is the density functional theory (DFT) [106, 107], where the system and its properties are completely determined by the electron density $\rho(\mathbf{r})$. The most widespread implementation of DFT is the Kohn–Sham formalism [108] in which an artificial reference system of noninteracting electrons is introduced to yield exactly the same electron density as the fully interacting system. In Kohn–Sham DFT, the electronic energy is a functional of $\rho(\mathbf{r})$ and can be partitioned into several contributions,

$$E_{\text{el}}[\rho] = T_s[\rho] + V_{\text{ext}}[\rho] + J[\rho] + E_{\text{xc}}[\rho] \tag{8.17}$$

In this equation, $T_s[\rho]$ is the kinetic energy of the noninteracting reference system, $V_{\text{ext}}[\rho]$ the interaction energy with some external potential, $J[\rho]$ the Coulomb interaction of the electrons, and $E_{\text{xc}}[\rho]$ represents the exchange–correlation functional that accounts for all exchange and correlation effects of the system and contains the nonclassical contribution to the electron–electron interaction as well as the difference in the kinetic energy of the fully interacting system from the noninteracting surrogate system. The exchange–correlation energy $E_{\text{xc}}[\rho]$ is the only unknown term in Eq. (8.17) and its functional form needs to be approximated.

We can incorporate more physics into the approximate exchange–correlation potentials by introducing additional variables such as the individual spin components of $\rho(\mathbf{r})$, $\rho^\alpha(\mathbf{r})$ and $\rho^\beta(\mathbf{r})$, which sum up to the total electron density [109],

$$\rho(\mathbf{r}) = \rho^\alpha(\mathbf{r}) + \rho^\beta(\mathbf{r}) \tag{8.18}$$

and yield the spin density,

$$\rho^s(\mathbf{r}) = \rho^\alpha(\mathbf{r}) - \rho^\beta(\mathbf{r}) \tag{8.19}$$

In particular, for any nonsinglet state with total spin S (and in the absence of a magnetic field), the eigenstates of $\hat{\mathbf{S}}^2$ are $2(S+1)$-fold degenerate and the total electron density and spin density for each spin projection are connected through a

simple scaling relation [110],

$$\rho^{S_z}(\mathbf{r}) = \rho^{S_z=S}(\mathbf{r}), \quad \rho^{s,S_z}(\mathbf{r}) = \left(\frac{S_z}{S}\right)\rho^{s,S_z=S}(\mathbf{r}) \tag{8.20}$$

The additional information of the spin density $\rho^s(\mathbf{r})$ can then be directly exploited in the exchange–correlation functionals. For open-shell systems, two different restrictions are possible when introducing the noninteracting reference system [109, 111]. We can require (i) that only the total electron density of the fully interacting and of the reference system agree or (ii) that, in addition, the spin densities of the two systems are exactly the same. The first condition leads to a spin-restricted Kohn–Sham DFT formulation, while for the latter a spin-unrestricted Kohn–Sham DFT framework is required [109].

8.3 Qualitative Interpretation

8.3.1 Local Spin

The concept of local properties, that is, properties of atoms or groups of atoms within one molecule, is a useful tool for the interpretation of abstract wave functions in terms of intuitive building blocks. In principle, any molecular property can be partitioned and distributed over a set of subsystems of a molecule, which then provides information for a qualitative analysis and understanding of bonding. However, such a partitioning is not unique and requires additional (*ad hoc*) assumptions. Still, within the realm of these assumptions, useful qualitative reasoning is possible. One important local concept for open-shell molecules is the decomposition of the total molecular electron spin $\hat{\mathbf{S}}^2$,

$$\langle\hat{\mathbf{S}}^2\rangle = \sum_A \langle\hat{\mathbf{S}}^2\rangle_A + \sum_{\substack{A,B \\ A\neq B}} \langle\hat{\mathbf{S}}^2\rangle_{AB} \tag{8.21}$$

Although the spin state of atom (or a group of atoms) A within a molecule is not observable, local spins are employed for the description of spin–spin interactions between magnetic centers, similar to the metal centers of transition-metal clusters, in terms of a Heisenberg spin-coupling model and led to considerable interest in the development of partitioning schemes of the total spin expectation value during the past decade [20, 112–128].

If we want to assign local-spin values to (atomic) subsystems, a definition of an atomic basin is required. Clark and Davidson proposed a framework where local molecular spin operators $\hat{\mathbf{S}}_A$ are obtained from projections of the total molecular spin operator [112, 118] upon atomic basins A. The one- and two-center contributions to the total $\langle\hat{\mathbf{S}}^2\rangle$ are then obtained from the expectation value of the local spin operator $\langle\hat{\mathbf{S}}_A^2\rangle$ and of diatomic products of local spin operators $\langle\hat{\mathbf{S}}_A\hat{\mathbf{S}}_B\rangle$, respectively. However, Clark and Davidson's decomposition leads to nonvanishing

local-spin contributions in closed-shell molecules [115]. This insufficiency could be cured by an alternative partitioning scheme proposed by Mayer [117, 119], where the expectation value of the $\hat{\mathbf{S}}^2$ operator, in the case of a single-determinant wave function, has been written in terms of the spin-density matrix $\rho^s(\mathbf{r};\mathbf{r}')$. As $\rho^s(\mathbf{r};\mathbf{r}')$ is zero for closed-shell restricted wave functions, Mayer's decomposition scheme yields by construction zero local spin values for any closed-shell singlet state.

As many open-shell molecules can only be described accurately within a multideterminant picture, partitioning schemes that can be applied to multideterminant wave functions as well are required. In contrast to the single-determinant case, an $\langle\hat{\mathbf{S}}^2\rangle$ decomposition is not straightforward for multireference wave functions and different partitioning schemes have been developed [120, 121, 124, 125, 127]. Mayer [121] suggested that three physical requirements need to be fulfilled by an appropriate decomposition scheme. He proposed that (i) zero local spin values should be obtained for closed-shell restricted wave functions, (ii) in the dissociation limit, the local $\langle\hat{\mathbf{S}}^2\rangle$ values on the atoms or fragments should be equal to the local spin values of the free atoms or fragments, that is, proper asymptotics are required, and (iii) the multireference expression should reduce to the single-determinant formulation if the general wave function is replaced by a single determinant. However, the decomposition scheme developed by Mayer based on these conditions was dependent on the S_z value for nonsinglet states. In order to cure this insufficiency, Alcoba *et al.* [120] introduced a fourth requirement, where (iv) (in the absence of magnetic fields) the one- and two-center terms should be independent of S_z and derived a *spin-free* decomposition of $\langle\hat{\mathbf{S}}^2\rangle$.

It was, however, demonstrated by Ramos-Cordoba *et al.* [127] that there actually exists a continuum of different partitioning schemes of $\langle\hat{\mathbf{S}}^2\rangle$ for both single- and multideterminant wave functions that fulfill all physical requirements mentioned and from which the individual decomposition formulas naturally emerge. Their analysis is carried out in three-dimensional space in contrast to the preceding approaches performed in a Hilbert-space formulation. A generalization of the latter to the physical space can be easily accomplished [117, 125] and we will employ the physical-space notation as presented in Ref. [127].

Given an N-electron wave function, the $\langle\hat{\mathbf{S}}^2\rangle$ expectation value reads in terms of the (spinless) first- and second-order reduced density matrices, $\rho(\mathbf{r}_1;\mathbf{r}_1')$ and $\rho_2(\mathbf{r}_1,\mathbf{r}_2;\mathbf{r}_1',\mathbf{r}_2')$, respectively,

$$\langle\hat{\mathbf{S}}^2\rangle = \frac{3}{4}\int \rho(\mathbf{r}_1;\mathbf{r}_1)\mathrm{d}\mathbf{r}_1 - \frac{1}{4}\int\int \rho_2(\mathbf{r}_1,\mathbf{r}_2;\mathbf{r}_1,\mathbf{r}_2)\mathrm{d}\mathbf{r}_1\mathrm{d}\mathbf{r}_2 - \frac{1}{2}\int\int \rho_2(\mathbf{r}_1,\mathbf{r}_2;\mathbf{r}_2,\mathbf{r}_1)\mathrm{d}\mathbf{r}_1\mathrm{d}\mathbf{r}_2 \tag{8.22}$$

where the normalization of the second-order reduced density matrix was modified to $N(N-1)$ (instead of the usual normalization condition of $N(N-1)/2$). $\rho_2(\mathbf{r}_1,\mathbf{r}_2;\mathbf{r}_1',\mathbf{r}_2')$ can be further expressed by the first-order density matrix elements and the cumulant of the second-order density matrix, $\Gamma(\mathbf{r}_1,\mathbf{r}_2;\mathbf{r}_1',\mathbf{r}_2')$, which contains the deviation from the exact expression of $\rho_2(\mathbf{r}_1,\mathbf{r}_2;\mathbf{r}_1',\mathbf{r}_2')$ if it is written in

terms of $\rho(\mathbf{r}_1;\mathbf{r}'_1)$ only,

$$\rho_2(\mathbf{r}_1,\mathbf{r}_2;\mathbf{r}'_1,\mathbf{r}'_2) = \rho(\mathbf{r}_1;\mathbf{r}'_1) - \frac{1}{2}\rho(\mathbf{r}_1;\mathbf{r}'_2)\rho(\mathbf{r}_2;\mathbf{r}'_1) - \frac{1}{2}\rho^{\mathrm{s}}(\mathbf{r}_1;\mathbf{r}'_2)\rho^{\mathrm{s}}(\mathbf{r}_2;\mathbf{r}'_1) + \Gamma(\mathbf{r}_1,\mathbf{r}_2;\mathbf{r}'_1,\mathbf{r}'_2) \tag{8.23}$$

Combining Eqs. (8.23) and (8.22) and using the effectively unpaired electron density introduced by Takatsuka [129],

$$u(\mathbf{r}) = 2\rho(\mathbf{r}) - \int \rho(\mathbf{r};\mathbf{r}')\rho(\mathbf{r}';\mathbf{r})\mathrm{d}\mathbf{r}' \tag{8.24}$$

one obtains a working equation to derive decompositions of $\langle\hat{\mathbf{S}}^2\rangle$ that fulfill all physical requirements mentioned earlier. It is important to note that although all possible expressions for the partitioning of $\langle\hat{\mathbf{S}}^2\rangle$ are equivalent upon integration, that is, they yield the same total spin expectation value $\langle\hat{\mathbf{S}}^2\rangle$, the one- and two-center integrals defined over the one- and two-center domains result in different contributions to the local expectation values. Ramos-Cordoba *et al.* generalized the different partition formulas by introducing a freely varying weighting factor a to modulate the one- and two-center contributions. Their formula for the $\langle\hat{\mathbf{S}}^2\rangle$ expectation value reads [127]

$$\langle\hat{\mathbf{S}}^2\rangle = a\int u(\mathbf{r}_1)\mathrm{d}\mathbf{r}_1 - (1-2a)\int\int\left[\Gamma(\mathbf{r}_1,\mathbf{r}_2) - \frac{1}{2}\rho^{\mathrm{s}}(\mathbf{r}_1;\mathbf{r}_2)\rho^{\mathrm{s}}(\mathbf{r}_2;\mathbf{r}_1)\right]\mathrm{d}\mathbf{r}_1\mathrm{d}\mathbf{r}_2 - \frac{1}{2}\int\int\left[\Gamma(\mathbf{r}_1,\mathbf{r}_2;\mathbf{r}_2,\mathbf{r}_1) - \frac{1}{2}\rho^{\mathrm{s}}(\mathbf{r}_1)\rho^{\mathrm{s}}(\mathbf{r}_2)\right]\mathrm{d}\mathbf{r}_1\mathrm{d}\mathbf{r}_2 \tag{8.25}$$

where $\Gamma(\mathbf{r}_1,\mathbf{r}_2) = \Gamma(\mathbf{r}_1,\mathbf{r}_2;\mathbf{r}_1,\mathbf{r}_2)$ and $\rho^{\mathrm{s}}(\mathbf{r}_1) = \rho^{\mathrm{s}}(\mathbf{r}_1;\mathbf{r}_1)$ are the diagonal elements of the second-order cumulant matrix and spin density matrix, respectively. The choice of the parameter a uniquely determines the $\langle\hat{\mathbf{S}}^2\rangle$ decomposition scheme. In particular, if $a = 3/8$, Mayer's general decomposition formula for singlet states [121] emerges, while for $a = 1/2$, Alcoba's partitioning scheme [125] is obtained. Furthermore, the physical requirements (i) to (iii) are fulfilled for any value of a and hence there exists a continuum of possible partitionings of $\langle\hat{\mathbf{S}}^2\rangle$.

Eq. (8.25) represents a general starting point to decompose $\langle\hat{\mathbf{S}}^2\rangle$ into its one- and two-atomic contributions. For this purpose, a proper identification of atomic domains in a molecule is mandatory. In the physical-space analysis employed here, an atom in a molecule is confined to some region in space around its nucleus and hence the atomic and diatomic contributions can be easily obtained if the integration is restricted over the atomic domains only (see also subsequently). For the decomposition of any physical quantity $f(\mathbf{r})$, we thus introduce nonnegative weighting functions $w_A(\mathbf{r})$ for each atomic domain A so that the total quantity can be written as a sum over its atomic contributions,

$$\int f(\mathbf{r})\mathrm{d}\mathbf{r} = \int \sum_A w_A(\mathbf{r})f(\mathbf{r})\mathrm{d}\mathbf{r} \tag{8.26}$$

In particular, the weighting functions satisfy the following completeness relation (employing Dirac's bra-ket notation)

$$\int |\mathbf{r}\rangle \sum_A w_A(\mathbf{r}) \langle \mathbf{r}| = 1, \quad \text{with} \quad w_A(\mathbf{r}) \geq 0 \quad \forall A \tag{8.27}$$

where we assume that the weighting functions are strictly positive, including zero. In short-hand notation, the identity of Eq. (8.27) is often written as $\sum_A w_A(\mathbf{r}) = 1$. Similarly, we can decompose any two-center integral into its diatomic domains,

$$\int\int f(\mathbf{r}_1, \mathbf{r}_2) \mathrm{d}\mathbf{r}_1 \mathrm{d}\mathbf{r}_2 = \int\int \sum_A w_A(\mathbf{r}_1) \sum_B w_B(\mathbf{r}_2) f(\mathbf{r}_1, \mathbf{r}_2) \mathrm{d}\mathbf{r}_1 \mathrm{d}\mathbf{r}_2 \tag{8.28}$$

Now, the decomposition of the integrals of Eq. (8.25) into its atomic and diatomic contributions can be performed straightforwardly and one obtains [127]

$$\begin{aligned} \langle \hat{\mathbf{S}}^2 \rangle_A = a \int & w_A(\mathbf{r}_1) u(\mathbf{r}_1) \mathrm{d}\mathbf{r}_1 \\ & -(1-2a) \int\int w_A(\mathbf{r}_1) w_A(\mathbf{r}_2) \left[\Gamma(\mathbf{r}_1, \mathbf{r}_2) - \frac{1}{2} \rho^{\mathrm{s}}(\mathbf{r}_1; \mathbf{r}_2) \rho^{\mathrm{s}}(\mathbf{r}_2; \mathbf{r}_1) \right] \mathrm{d}\mathbf{r}_1 \mathrm{d}\mathbf{r}_2 \\ & -\frac{1}{2} \int\int w_A(\mathbf{r}_1) w_A(\mathbf{r}_2) \left[\Gamma(\mathbf{r}_1, \mathbf{r}_2; \mathbf{r}_2, \mathbf{r}_1) - \frac{1}{2} \rho^{\mathrm{s}}(\mathbf{r}_1; \mathbf{r}_1) \rho^{\mathrm{s}}(\mathbf{r}_2; \mathbf{r}_2) \right] \mathrm{d}\mathbf{r}_1 \mathrm{d}\mathbf{r}_2 \end{aligned} \tag{8.29}$$

and [127]

$$\begin{aligned} \langle \hat{\mathbf{S}}^2 \rangle_{AB} = & -(1-2a) \int\int w_A(\mathbf{r}_1) w_B(\mathbf{r}_2) \left[\Gamma(\mathbf{r}_1, \mathbf{r}_2) - \frac{1}{2} \rho^{\mathrm{s}}(\mathbf{r}_1; \mathbf{r}_2) \rho^{\mathrm{s}}(\mathbf{r}_2; \mathbf{r}_1) \right] \mathrm{d}\mathbf{r}_1 \mathrm{d}\mathbf{r}_2 \\ & -\frac{1}{2} \int\int w_A(\mathbf{r}_1) w_B(\mathbf{r}_2) \left[\Gamma(\mathbf{r}_1, \mathbf{r}_2; \mathbf{r}_2, \mathbf{r}_1) - \frac{1}{2} \rho^{\mathrm{s}}(\mathbf{r}_1; \mathbf{r}_1) \rho^{\mathrm{s}}(\mathbf{r}_2; \mathbf{r}_2) \right] \mathrm{d}\mathbf{r}_1 \mathrm{d}\mathbf{r}_2 \end{aligned} \tag{8.30}$$

So far, we have reviewed how to derive an atomic decomposition of $\langle \hat{\mathbf{S}}^2 \rangle$ for a general a. However, the conditions (i) to (iv) are not sufficient to obtain a unique partitioning as they are all satisfied for arbitrary values of a, and hence additional conditions need to be defined in order to fix the parameter a. Ramos-Cordoba *et al.* investigated the behavior of the general formula of Eq. (8.25) with respect to a for a one-electron and a simple two-electron model system and concluded that the best choice of a should be 3/4. Furthermore, they demonstrated that the local spin values for diamagnetic molecules are very small indeed and similar if $a = 3/4$, independent of the basis set or atomic definitions, that is, the choice of the weighting functions $\{w_A(\mathbf{r})\}$ in the physical-space analysis. Yet, a large basis-set dependence was still observed in the Hilbert-space formulation, although the effects were smallest if a was set to 3/4.

8.3.2
Broken Spin Symmetry

The concept of local spins facilitates the analysis of complex wave functions and the description of magnetically coupled centers in terms of spin–spin interactions

localized on different parts of the molecule. In principle, two different coupling schemes can be distinguished: (i) a ferromagnetic case where the interacting atoms or fragments bear some amount of the same spin excess or (ii) an antiferromagnetic coupling scheme where the interacting atoms or fragments have opposite spin excess. In both cases, a multideterminant description of the electronic structure is required. However, we can also enforce a one-determinant picture for cases that actually represent multideterminant problems. The goal to approximate the wave function by a single-Slater determinant can only be accomplished if the symmetry of the system is broken [130], which leads to broken spin symmetries in the case of spin–spin interactions within a spin-unrestricted Kohn–Sham framework [131].

In the single-determinant approach, Noodleman's broken-symmetry solution [132–134] must be converged within an SCF procedure. In general, this can be accomplished in two ways. First, we can choose a proper starting guess, which is then manipulated to result in the desired local spin distributions [135]. For instance, the MOs from a previous high-spin calculation of the same molecule are employed as initial guess orbitals where the spins localized at one of the coupled centers are inverted. This procedure, however, might converge to a Slater determinant that does not describe the targeted local spin distribution.

A formally better approach is to employ a constrained optimization protocol as proposed by Van Voorhis and coworkers [136, 137], where the desired state is obtained directly by minimizing the energy subjected to constrain the local spin values on the spin-coupled fragments *A*. The advantage of such a scheme is the capability to optimize any local spin distribution and to study different possible magnetic coupling schemes. This constrained optimization is achieved by introducing additional Lagrange multipliers λ_A, which enforce the local spin values. As the broken-symmetry formulation mainly focuses on the description of local high-spin centers, the projected local spins $\langle \hat{S}_{zA} \rangle$ are chosen as the constraint quantities so that on each fragment a predefined difference M_{sA} between α and β electrons is enforced. Including these additional spin constraints, we obtain a new Lagrange functional [137, 138] for unrestricted approaches, which reads

$$\mathscr{L} = E_{\mathrm{el}} - \sum_{i}^{N} \varepsilon_i (\langle \phi_i | \phi_i \rangle - 1) - \sum_{A} \lambda_A (\langle \hat{S}_{zA} \rangle - M_{sA}) \tag{8.31}$$

where the first sum ensures orthogonality of the one-particle functions. The variation of the Lagrange functional, $\delta\mathscr{L} = 0$, yields the desired orbitals for which the constraints are satisfied and hence the actual local spin values are similar to the ideal M_{sA}. It is important to note that owing to the Lagrange multipliers $\{\lambda_A\}$, an additional potential that explicitly depends on $\{\lambda_A\}$ is introduced, which breaks the symmetry between the α and β electrons [137]. In the constrained optimization approach of Van Voorhis and coworkers, the Lagrange multipliers are updated after each SCF iteration step so that the local spin constraints are fulfilled exactly and hence the effective potential is simultaneously optimized in each SCF step.

Since the Slater determinant is obtained within a constrained optimization procedure, it may not represent a local minimum of the unconstrained potential energy surface, that is, if the effective potential is removed. To avoid this problem,

a simple extension to Van Voorhis' protocol has been added in our group [138]. Instead of considering a set of fixed local spin values $\{M_{sA}\}$, the optimization is performed for a predefined acceptance range of possibly allowed constrained values and for a fixed set of Lagrange multipliers. If the actual local spin values are sufficiently close to the ideal $\{M_{sA}\}$, $\{\lambda_A\}$ are subsequently optimized in each SCF iteration step until convergence to a local minimum is achieved.

8.3.3 Analysis of Bond Orders

The bond order represents an important concept in understanding chemical bonding. However, as with many other qualitative quantities that describe molecular electronic distributions, for example, local spins, the bond order does not correspond to any physical observable and thus cannot be determined as an expectation value from a quantum chemical operator. As a consequence, there does not exist a unique definition for the bond order. Since the very first days of MO theory, chemical intuition has been employed to define such a concept for both closed- and open-shell molecules [139–147] and the first definition of the number of bonds between the two centers of symmetric diatomic molecules was formulated by Herzberg [148]. It was based on a simple electron counting scheme, where the bond order was equal to half the difference between the number of bonding electrons and the number of *loosening* electrons. However, the Herzberg approach was restricted to either diatomic molecules or to polyatomic molecules with strongly localized MOs.

In MO theory, the Mulliken population analysis [149], where the population of the MOs is decomposed into atomic populations and diatomic overlap populations, considerably influenced the formulation of bonding concepts, although it does not describe a bond order *per se*. On the basis of the Mulliken population analysis, Mayer introduced a popular definition of the number of bonds BO^{M}_{AB} between two centers A and B originally formulated for one-determinant wave functions [142–144, 150],

$$BO^{\mathrm{M}}_{AB} = \sum_{\nu\in A}\sum_{\mu\in B}\left[(\mathbf{PS})_{\mu\nu}(\mathbf{PS})_{\nu\mu} + (\mathbf{P}^s(S,S_z)\mathbf{S})_{\mu\nu}(\mathbf{P}^s(S,S_z)\mathbf{S})_{\nu\mu}\right] \tag{8.32}$$

where $\mathbf{P}$ is the first-order reduced density matrix represented in the atomic orbital basis set, $\mathbf{S}$ is the overlap matrix of the atomic orbital basis, while $\mathbf{P}^s(S,S_z)$ is the spin density matrix for the spin projection S_z as defined in Eq. (8.19), but written here in explicit matrix representation in the atomic orbital basis. In particular, for closed-shell systems, $\mathbf{P}^s(S,S_z) = \mathbf{0}$ and BO^{M}_{AB} contains only the first term on the right-hand-side of Eq. (8.32). However, Mayer's formula yields different bond multiplicities BO^{M}_{AB} for different spin projections S_z as it explicitly depends on the spin density for one of the $2S+1$ possible S_z values of the total molecular spin S. Furthermore, Eq. (8.32) has been determined solely for Hartree–Fock-like electronic structures, while its validity for multireference wave functions has been postulated [143] without a sound theoretical basis [151, 152].

In order to obtain a bond order formula for open-shell systems that can be applied for both the independent-particle model and correlated wave functions and which simultaneously yields unique bond orders for all spin multiplet components (in the absence of a magnetic field), Alcoba *et al.* [151, 152] derived a general expression (in the Hilbert space partitioning scheme) from a second-order reduced density matrix. Furthermore, as the first- and second-order reduced density matrices are invariant with respect to the spin projection, they are only a function of the total spin or similarly of the maximum projection $S = S_z$ and the bond order can be evaluated for the highest spin-projected state $S_z = S$. They arrived at the following expression for the bond order

$$BO_{AB} = \sum_{\nu \in A} \sum_{\mu \in B} [(\mathbf{PS})_{\mu\nu}(\mathbf{PS})_{\nu\mu} + (\mathbf{P}^s(S,S)\mathbf{S})_{\mu\nu}(\mathbf{P}^s(S,S)\mathbf{S})_{\nu\mu}] \tag{8.33}$$

which is similar to Mayer's expression given in Eq. (8.32) if we substitute $S_z = S$, but differs in the rigorous arguments and fundamental concepts employed in the derivation (invariant with respect to S_z and valid for both single- and multi-determinant wave functions).

Nevertheless, a very convenient picture of the bond-order concept, which is frequently applied in inorganic chemistry, is based on electron-counting schemes. Such an approach, however, represents an oversimplified analysis of the chemical bond, in particular, if single-reference wave functions are employed. In order to allow for a more quantitative description, the concept of bond order can be straightforwardly extended to multireference problems [153–155] without giving up the *recipe* of counting electrons in bonding and antibonding orbitals. For any multireference wave function, Roos *et al.* [155] have defined an effective bond order EBO_{AB} between two centers, A and B, in a molecule, which reads

$$EBO_{AB} = \frac{1}{2}(\eta_b^{AB} - \eta_a^{AB}) \tag{8.34}$$

where η_b and η_a are the natural occupation numbers for the bonding and antibonding pair of natural orbitals, which have noninteger values in the intervals $1 \leq \eta_b \leq 2$ and $0 \leq \eta_a \leq 1$, while $\eta_b + \eta_a = 2$. To obtain the total EBO_{AB} for a particular bond, A–B, all EBO_{AB} contributions are to be added up. As the natural occupation numbers can have noninteger values, this will lead in general to fractional bond orders compared to the integer valued formal bond index. By definition, the *true* bond order is then determined as the lowest integer larger than the total EBO_{AB} value. The advantage of the EBO analysis compared to partitioning schemes based on density matrices is its method- and basis-set independence, which is not the case for density-matrix-based formulations in the Hilbert-space analysis (owing to the Mulliken type of partitioning).

For a reliable estimate of the bond multiplicity, the active space should contain (at least partially) the bonding and antibonding MOs that describe, for example, the metal–metal bond of interest. In the case of strong bonds, for which $\eta_b \approx 2$, while $\eta_a \approx 0$, the corresponding EBO contribution is equal to 1. For weak bonds, η_b strongly deviates from 2 and *vice versa* η_a from 0 which reduces the overall EBO, while in the limit $\{\eta_a, \eta_b\} \rightarrow 1$, the contribution to the total EBO vanishes and the

bond is replaced by antiferromagnetic coupling between the centers *A* and *B*. In particular, the weak interactions of metal *d*-orbitals, which leads to the formation of δ-orbitals, can be described as an intermediate between antiferromagnetic coupling and true bond formation and hence significantly reduces the total EBO with respect to the maximum possible multiplicity (which is equal to the number of unpaired electrons in the valence shell).

In a pioneering study, the EBO analysis indicated a quintuple bond in the bare U_2 molecule [156, 157] and was further applied to larger diuranium compounds and other actinide-containing clusters [158, 159], where the possibility of a bond order higher than five was then discarded. Different studies on the bonding in transition metal dimers followed [160–168] where special interest was devoted to dichromium complexes [160–165]. In particular, the bare Cr_2 species represents the shortest metal–metal bond distance observed to date (1.64 Å), with a formal quintuple bond but a rather weak Cr–Cr bonding energy [163]. A larger bond order was only found for the higher group homologs of Cr_2, Mo_2 and W_2, respectively, which give rise to much stronger bonds [155]. According to EBO studies with a CASPT2 reference wave function, the maximum bond order observed for any two atoms in the periodic table is present in the Mo_2 and W_2 diatomics and comprises a hextuple bond. However, an EBO analysis of general dinuclear clusters containing ligands is not straightforward to apply because of the additional mixing of metal *d*-orbitals and ligand orbitals and the strong delocalization of natural orbitals. A clear identification of the bonding and antibonding contributions to the metal–metal bond is mandatory for a reliable EBO value, which will be difficult if the natural orbitals are strongly delocalized over the whole molecule.

8.3.4
Atoms in Molecules

The main requirement in the determination of bond orders is to derive rules on how to measure "the number of electrons shared between two atoms." For this purpose, a definition of an atom in a molecule is required, which, however, cannot be formulated in a unique and unambiguous way [169]. Quantum chemical calculations are typically performed in the Hilbert-space analysis, where atoms are defined by their basis orbitals. Such an analysis, however, strongly depends on both the atomic basis set chosen and the type of wave function used. The position-space representation, on the other hand, where atoms are defined as basins in three-dimensional physical space does not suffer from these insufficiencies. In this chapter, we present one option for a three-dimensional atomic decomposition scheme and the reader is referred to Refs. [170–173] for further examples.

In a physical-space analysis, a weight function $w_A(\mathbf{r})$ is introduced for every atom *A* in the molecule in order to decompose the complete space into its atomic domains Ω_A. The weight functions satisfy the conditions given in Eq. (8.27) and thus project a physical quantity upon its atomic contributions. In principle, two conceptually different types of weight functions can be defined; (i) the physical space can be partitioned into disjoint atomic domains or (ii) the individual regions

in space assigned to each atom do not exhibit sharp boundaries but rather a continuous transition from one atom to the other and are thus called *fuzzy* atoms (e.g., Ref. [170]).

In the first case, $w_A(\mathbf{r})$ is equal to one in the domain Ω_A, while all other weight functions vanish

$$w_A(\mathbf{r}) = \begin{cases} 1 & \text{if } \mathbf{r} \in \Omega_A \\ 0 & \text{otherwise} \end{cases} \tag{8.35}$$

If such a partition scheme is to be employed, the atomic domains Ω_A need to be defined explicitly. The most frequently applied decomposition is Bader's Atoms in Molecules (AIM) approach [174, 175] where the atomic domains Ω_A are divided by surfaces that are determined on the basis of the topology of the electron density. As the atomic volumes (or domains) are determined from the properties of the electron density, the AIM scheme can be applied to any electron density calculated from a general wave function. In AIM theory, the boundary condition for an atom in a molecule requires the gradient vector field of the electron density $\nabla\rho(\mathbf{r})$ to have zero flux [174, 176],

$$\nabla\rho(\mathbf{r})\cdot\mathbf{n}(\mathbf{r}) = 0 \quad \forall\mathbf{r} \in \delta\Omega_A \tag{8.36}$$

where $\mathbf{n}(\mathbf{r})$ is the unit vector normal to the surface $\delta\Omega_A$ at $\mathbf{r}$ and $\mathbf{r}$ is constrained to lie on the volume boundary $\delta\Omega_A$. A surface that obeys the above-given equation is called a *zero-flux* surface. We may refer the reader to Ref. [177], where a systematic AIM analysis of transition-metal complexes was carried out. As the atomic volumes are disjoint, the atomic overlap integrals $S^A_{\mu\nu}$ simplify to

$$S^A_{\mu\nu} = \int w_A(\mathbf{r})\chi^*_\mu(\mathbf{r})\chi_\nu(\mathbf{r})\mathrm{d}\mathbf{r} = \int_{\Omega_A} \chi^*_\mu(\mathbf{r})\chi_\nu(\mathbf{r})\mathrm{d}\mathbf{r} \tag{8.37}$$

where the integration is restricted to the atomic domain Ω_A with atomic orbitals $\{\chi_\nu(\mathbf{r})\}$. This expression for the atomic overlap matrix can be directly inserted into Eq. (8.33) so that the bond order within the AIM partitioning reduces to [147]

$$BO_{AB} = \sum_{\nu,\mu} [(\mathbf{PS}^A)_{\mu\nu}(\mathbf{PS}^B)_{\nu\mu} + (\mathbf{P}^s\mathbf{S}^A)_{\mu\nu}(\mathbf{P}^s\mathbf{S}^B)_{\nu\mu}] \tag{8.38}$$

where $\mathbf{P}^s$ is assumed to be the spin density matrix for the highest spin projection $S_z = S$ and the summation runs over all atomic orbital basis functions (note that contributions from bases functions that are not contained in Ω_A are automatically neglected as encoded in the overlap matrix elements of Eq. (8.37)). The bond-order concept was introduced into the theory of AIM first by Ángyán *et al.* [178] followed by the definition of a delocalization index proposed by Fradera *et al.* [179, 180], which reduces for the single-determinant wave function to the ordinary bond-order formula of Ángyán, but differs for correlated wave functions. However, the definition of the bond order proposed in Ref. [179] yields chemically too high bond orders for N_2 and F_2 and the formula as given in Eq. (8.38) (which is equivalent to the definition of Ref. [178]) is recommended [147].

8.3.5 Entanglement Measures for Single- and Multireference Correlation Effects

From the perspective of the independent particle model, electron correlation effects are caused by electronic interactions beyond the mean-field Hartree–Fock-type Description [23]. As electrons occupy spatial orbitals differently (as can be measured, e.g., in terms of their natural occupation numbers being the eigenvalues of the *one-electron* reduced density matrix), electron correlation may also be quantified by measuring the interaction strength of any pair of these orbitals. This is no physical interaction such as the Coulomb interaction of a pair of electrons. Instead, a quantum entanglement measure is required, which describes the entanglement of an open quantum system (in this case, one or two selected orbitals) with an environment (that is the complement of all other orbitals in the active space under consideration). Such measures can be defined within the framework of quantum information theory. Examples are the von Neumann entropy and the mutual information [181]. Different entanglement measures based on the von Neumann entropy, which exploit the knowledge about the one- or two-particle reduced density matrix to characterize electron correlation effects, have been proposed [182–197]. However, one may also exploit the eigenvalues of the *one-* and *two-orbital* density matrix, in which many-electron states (rather than electronic degrees of freedom) that are not defined on the orbital (or pair of orbitals) under consideration are traced out. In contrast to the one- and two-particle reduced density matrices that are defined for a fixed number of particles (one or two electrons), the one- and two-orbital density matrices are obtained from a many-particle density matrix by tracing out all environment states not belonging to orbital i or to the orbital pair i, j; these matrices are thus defined for a one- or two-orbital Fock space of dimension 4 or 16, respectively. In the simpler case of only one orbital, the four states refer to an unoccupied, spin-up, spin-down and doubly occupied spatial orbital (embedded in the environment of all other orbitals of the active space).

The eigenvalues of the one- and two-orbital density matrices, $w_{\alpha;i}$ and $w_{\alpha;i,j}$, respectively, can then be employed to determine the von Neumann entropy of each spatial orbital. This yields the so-called single-orbital entropy [96],

$$s(1)_i = -\sum_{\alpha=1}^{4} w_{\alpha;i} \ln \; w_{\alpha;i} \tag{8.39}$$

which encodes how much orbital i "knows" about any other orbital j [181], and the two-orbital entropy between a pair i, j of orbitals [95],

$$s(2)_{i,j} = -\sum_{\alpha=1}^{16} w_{\alpha;i,j} \ln \; w_{\alpha;i,j} \tag{8.40}$$

Qualitatively speaking, $s(1)_i$ measures the quantum correlation of orbital i with all remaining orbitals contained in the active space, while $s(2)_{i,j}$ measures this correlation of the pair of orbitals i and j embedded in the complement of orbitals in the active space. The quantum entanglement among two orbitals embedded in

an active space can be quantified by the mutual information [95],

$$I_{i,j} = \frac{1}{2}(s(2)_{i,j} - s(1)_i - s(1)_j)(1 - \delta_{ij}) \tag{8.41}$$

where the two-orbital entropy $s(2)_{i,j}$ is reduced by the quantum correlations of all states defined on each of the orbitals i and j individually, that is, by subtraction of $s(1)_i$ and $s(1)_j$. These entropy and information measures have been shown to be very valuable in classifying electron correlation effects [86].

Owing to their general definition applicable to any kind of many-electron wave function used for the construction of the reduced density matrices, the single-orbital entropy and the mutual information represent convenient measures of entanglement, which can be employed to quantify different types of correlation present in arbitrary (open-shell) electronic structures. In particular, they allow us to identify strongly correlated orbitals (large single-orbital entropies), which can usually be identified with singly occupied orbitals in the Hartree–Fock reference configuration, as well as bonding and antibonding orbital pairs, which are involved in bond-breaking processes.

As a first example, we review how the mutual information and single-orbital entropy can be employed to track bond-formation/-breaking processes and how they can be utilized to discriminate between different types of chemical bonds at the example of N_2 [198]. Figure 8.1 shows the dissociation curve of N_2 and mutual information diagrams calculated for different distances along the dissociation path. In this particular case, the entanglement measures should resolve the breaking of two π-bonds and one σ-bond. Each mutual-information 'suns' in Figure 8.1 shows the color-coded value of the mutual information of every pair of orbitals as determined from DMRG wave functions correlating 10 electrons in 46 MOs at different interatomic distances [198]. To remind the reader of the textbook knowledge about the molecular frontier orbitals in this prototypical diatomic, they are depicted for the equilibrium (top left in Figure 8.1) distance and for an elongated bond lengths (top right in Figure 8.1). These six orbitals are the bonding σ- and π-orbitals and their corresponding antibonding counterparts. The mutual information is largest for a corresponding pair of bonding and antibonding orbitals as indicated by the blue lines in Figure 8.1. An order of magnitude smaller is the quantum entanglement of noncorresponding orbitals within this set of six frontier orbitals (red lines in Figure 8.1). All other orbital correlations are another order of magnitude weaker (green lines in Figure 8.1). It is very satisfying for conceptual chemistry that an elaborate quantum description (here, in terms of the DMRG algorithm) recovers the essential features of the bond formation in N_2. Moreover, it is interesting to see that along the dissociation path of N_2 into two nitrogen atoms, different bonds are broken at different internuclear distances, which can be seen in the evolution of the mutual information and also from an analysis of the single-orbital entropies (not shown; see the original paper for a detailed discussion [198]). If the N atoms are pulled apart, the single-orbital entropies corresponding to the π–π^*-orbital pairs increase considerably faster than those corresponding to the σ–σ^*-orbital pair. At an intermediate bond length of approximately 1.7 Å onwards, the $s(1)$ values of the bonding and antibonding σ-orbital pair increase

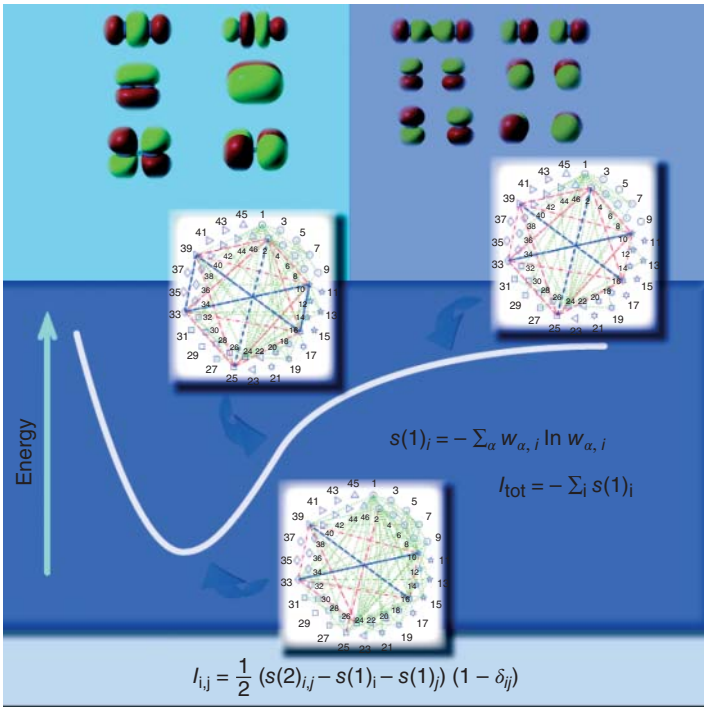

Figure 8.1 Dissociation curve of dinitrogen, N_2, calculated with the DMRG approach [198]. Mutual information diagrams ('suns') show the color-coded value of the entanglement among any pair of orbitals. Strong entanglement results in a blue, medium entanglement in a red, and weak entanglement in a green connection line. All blue lines connect the bonding π- and σ-orbitals with their antibonding counterparts. These three orbital pairs are shown for the equilibrium distance in the upper left corner and for an elongated bond length in the upper right corner. For illustration purposes, the equations defining the relevant entanglement measures (discussed in the text) are also depicted.

most substantially, while the growth of single-orbital entropies associated with the π–π^*-orbital pairs decreases. Thus, the entanglement analysis corroborates the typical triple-bond picture of the N_2 molecule and even shows that the weak π-bonds break first.

As a second example, we review the case of an open-shell iron nitrosyl molecule ($S = \frac{1}{2}$) embedded in a field of four point charges of −0.5e each located in the xy-plane perpendicular to the F–N bond axis as depicted in Figure 8.2(b) (see also further down). The point charge environment models a square-planar ligand field and emulates the one-particle states (orbitals) of larger iron nitrosyl compounds, for example, salen- and porphyrin-containing iron nitrosyl complexes [87]. The entanglement diagrams of the mutual information and single-orbital entropy determined from a DMRG calculation correlating 13 electrons in 29 orbitals [85, 86] are displayed in Figure 8.2a.

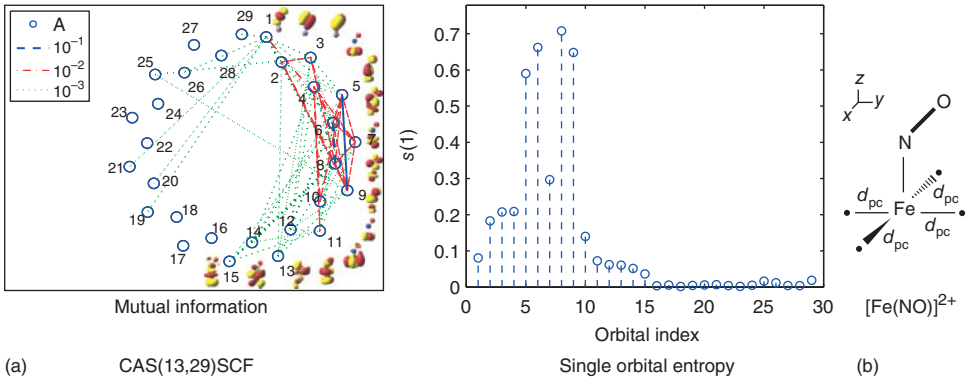

Figure 8.2 (a) Mutual information and single-orbital entropies $s(1)$ for a DMRG[13,29] calculation for the $[Fe(NO)]^{2+}$ molecule surrounded by four point charges at a distance of $d_{pc} = 1.131$ Å from the iron center as depicted in (b). The orbitals are numbered and sorted according to their CASSCF natural occupation numbers. Each orbital index indicates one MO. The orbital index for $s(1)$ and the orbital number in the mutual information diagram correspond to the same natural orbital. ((Panel a has been reprinted (adapted) with permission from Boguslawski, K.; Tecmer, P.; Legeza, O.; Reiher, M. *J. Phys. Chem. Lett.* **2012**, 3, 3129–3135. Copyright (2012) American Chemical Society.)

We can identify three different interaction strengths of the mutual information and single-orbital entropy: (i) orbitals that are strongly entangled correspond to large mutual information (orbitals connected by blue lines) and large single-orbital entropies ($s(1)_i > 0.5$); (ii) entanglement of intermediate strength (connected by red lines) and medium-sized single-orbital entropies ($0.1 < s(1)_i < 0.5$) and (iii) weakly entangled orbitals (connected by green lines) that feature small single-orbital entropies ($s(1)_i < 0.1$). The blue lines link a bonding combination of the Fe 3*d*- and NO π^*-orbitals with its corresponding antibonding combination (there are two of them, #5–#9 and #6–#8), which are required for an accurate treatment of nondynamic correlation effects (and thus bond breaking), while orbitals that are usually included in standard electron correlation calculations to capture static correlation effects are connected by red lines. The dynamic correlation energy can eventually be accounted for by exciting electrons into orbitals that are linked by green lines.

Entanglement diagrams based on mutual information and single-orbital entropy represent thus a valuable tool to detect the single- or multireference nature of electronic structures. Furthermore, the evolution of correlation effects can be easily measured along a reaction path. Orbitals that are important for bond breaking or bond making become strongly entangled ($I_{ij} > 0.1$, $s(1)_i > 0.5$) when atoms are pulled apart or pushed together, which thereby allows us to identify orbitals that are involved in bond-altering processes.

8.4
Spin Density Distributions—A Case Study

So far, we have encountered the spin density as a variable both in the description of electronic structures of open-shell character and in the analysis of local quantities such as local spins or bond orders. For an accurate treatment of open-shell molecules, spin–spin interactions and chemical bonding, reliable spin densities are thus mandatory. However, the determination of reliable spin density distributions can be a difficult task in quantum chemistry [199, 200]. Examples of such difficult cases are iron nitrosyl complexes containing salen or porphyrin ligands for which DFT spin densities considerably depend on the approximate exchange–correlation functional [87, 199].

As the spin density in iron nitrosyl complexes was shown to be dominated by the iron nitrosyl moiety [87], we studied the performance of different quantum chemical methods for determining accurate spin densities for this particular fragment [85, 87] whose structure has been extended by four point charges (see Figure 8.2b) in order to ensure that the $[Fe(NO)]^{2+}$ molecule is a representative model system for the full-fledged complexes.

8.4.1
A One-Determinant Picture

In Ref. [87], eight different approximate exchange–correlation density functionals have been investigated; BP86, BLYP, OLYP, OPBE, TPSS, TPSSh, M06-L and B3LYP. For the doublet configuration shown in Figure 8.3, the DFT spin density distributions strongly depend on the density functional, while for the quartet state, qualitatively similar spin densities are obtained (and are thus not shown here). In particular, the exchange–correlation functionals can be arranged in three different groups according to the degree of spin polarization observed in the spin density. While OLYP, OPBE and M06-L yield completely spin-polarized systems with a pure excess of β-electron density (yellow surface) around the NO fragment and an excess of α-electron density (blue surface) around the metal center (see Figure 8.3), for BP86, BLYP and TPSS, additionally a small amount of α-electron density was found around the NO ligand. By contrast, the hybrid exchange–correlation functionals TPSSh and B3LYP result in broken-symmetry-like solutions with strongest spin polarization. Figure 8.3 displays the spin density difference plots obtained from one selected density functional of each group with respect to OLYP. The qualitative differences and variable degrees of spin polarization are encoded in the blue (less α electron density than OLYP) and yellow (more α electron density than OLYP) isosurface of the difference distributions.

The differences in the spin density can be traced back to different occupational patterns of the Kohn–Sham MOs. Figure 8.3b displays the seven highest molecular spin orbitals that differ for all investigated exchange–correlation density functionals. They represent combinations of the Fe 3*d*- and NO π^*-orbitals. The corresponding α- and β-components are grouped together and sorted according to the

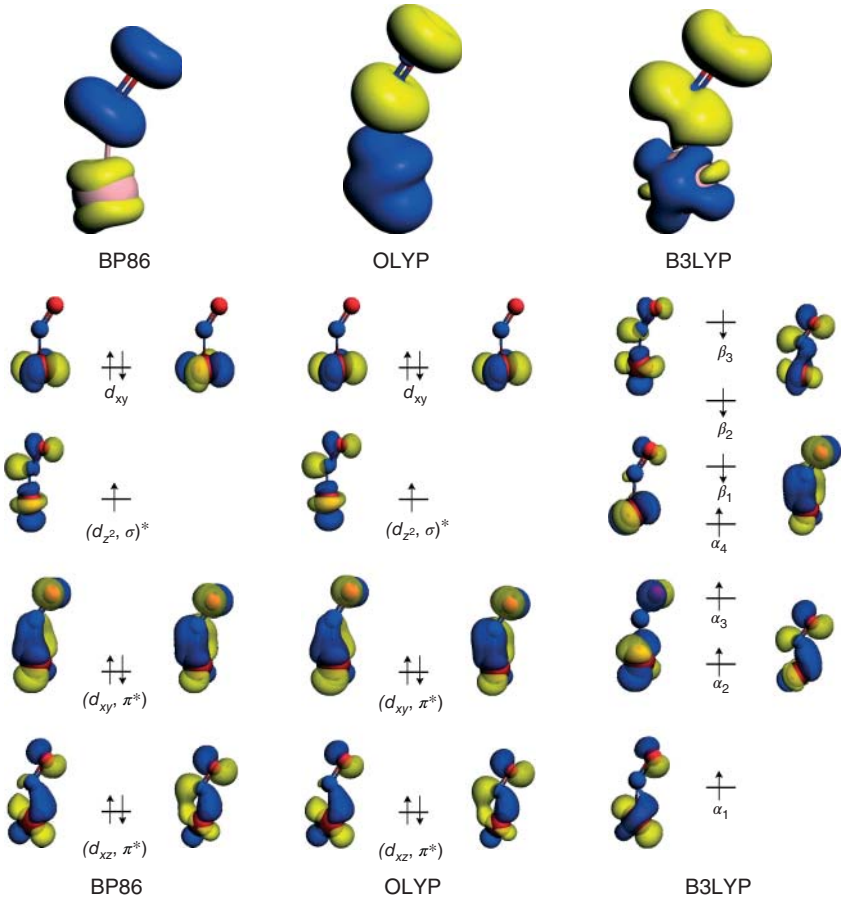

Figure 8.3 Spin density distribution for OLYP, spin density difference distributions with respect to OLYP and the seven highest occupied MOs that determine the spin densities. An isovalue of 0.003 was chosen. A blue surface indicates an excess of α-electron density, while a yellow surface encodes an excess of β-electron density and *vice versa* for the spin density difference distribution. (Reprinted (adapted) with permission from Boguslawski, K.; Jacob, C.R.; Reiher, M. *J. Chem. Theory Comput.* **2011**, 7, 2740–2752. Copyright (2011) American Chemical Society.)

α-spin orbitals. For BP86 and OLYP, the different distributions of α- and β-electron densities originate from the varying degree of delocalization of the spin orbitals. In the case of BP86, α-electrons are stronger delocalized over the NO π^*-orbitals compared to OLYP and thus result in a small excess of α-electron density located around the nitrogen atom. The broken-symmetry-like solution obtained for the hybrid density functionals can also be understood when analyzing the molecular spin orbitals. In general, different orbitals are obtained for α and β electrons. While α-electrons preferentially occupy metal orbitals, β-electrons are strongly delocalized over the NO π^*-orbitals, which leads to purely spin-polarized systems.

Hence, in order to decide which approximate exchange–correlation functionals yield sufficiently accurate spin density distributions, electron correlation methods needed to be applied [85, 87].

8.4.2 A Multiconfigurational Study

As the accuracy of electron correlation methods is limited by the choice of the dimension of the active orbital space, the convergence behavior of the spin density with respect to the size of the active space must be studied to ensure that accurate *ab initio* spin densities are obtained. Although the CASSCF spin densities were quantitatively converged for medium-sized active orbital spaces, larger active spaces (more than 13 electrons correlated in 13 orbitals) were found to be unstable, that is, active space orbitals have been rotated out of the active space during the MCSCF procedure, while the spin densities started to diverge compared to the smaller sized CASSCF results.

In order to obtain a spin density that is quantitatively converged with respect to the dimension of the active space, additional empty ligand orbitals have to be included in the MCSCF calculation. Such large active spaces (without truncating the complete N-particle Hilbert space) can only be handled by modern electron correlation methods such as the DMRG algorithm. A converged spin density distribution (both with respect to the active space and the DMRG parameter set) could be obtained for a DMRG(13,29) calculation employing 2048 renormalized active-system states and is shown in Figure 8.4. In particular, the DMRG(13,29)[2048] reference spin density does not possess purely separated α- and β-electron densities, but a small amount of α-electron density is located around the nitrosyl ligand. Taking the DMRG(13,29)[2048] spin density as reference, we can now assess the quality of the different CASSCF spin densities. Figure 8.4 shows some selected CASSCF–DMRG spin density difference distributions (a complete list can be found in Ref. [85]). If the number of active orbitals is gradually increased, the spin densities clearly oscillate around the DMRG(13,29)[2048] reference distribution. The situation becomes even worse if the number of active electrons is enlarged to 13, which leads to CASSCF spin densities that deviate even more strongly from the DMRG reference (owing to the instability of the active space). In particular, all CASSCF spin densities *qualitatively* differ from the DMRG reference and yield either purely spin polarized system (of CAS(11,11)-type) or too much α-electron density around the nitrogen atom (of CAS(11,12)-type).

Similarly, we can investigate DFT–DMRG spin density difference distributions displayed in Figure 8.4. In general, the deviations from the DMRG(13,29)[2048] reference are larger than for the CASSCF spin densities and more severe for the group of functionals containing OLYP as well as all hybrid density functionals, while the smallest differences were obtained for BP86 (similarly, small differences are also observed for BLYP and TPSS). However, despite the large quantitative differences, a qualitatively correct spin density distribution could be determined

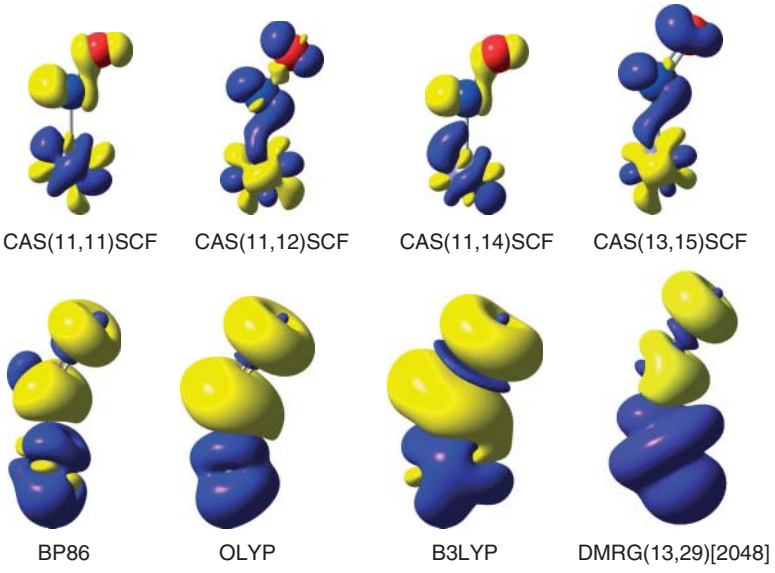

Figure 8.4 CAS(*x*,*y*) SCF and DFT spin density difference distributions with respect to the DMRG(13,29)[2048] reference spin density determined for 2048 renormalized active-system states. *x* indicates the number of electrons correlated in *y* orbitals. An isovalue of 0.001 was chosen for isosurface plots. A blue surface indicates an excess of α-electron density, while a yellow surface encodes an excess of β-electron density for the spin densities and vice versa for the spin density difference distribution. The CAS(*x*,*y*) SCF calculations were performed with the MOLPRO [201] program package employing Dunning's cc-pVTZ atomic basis set [202, 203], while in the DMRG calculations the natural orbitals from the preceding CAS(11,14) SCF calculation are taken as orbital basis. (Reprinted (adapted) with permission from Boguslawski, K.; Marti, K. H.; Legeza, O; Reiher, M. *J. Chem. Theory Comput.* **2012**, 8, 1970–1982. Copyright (2012) American Chemical Society.)

with the BP86 exchange–correlation density functional (and similarly, with BLYP and TPSS), which was not possible in the CASSCF calculations.

8.5 Summary

In this chapter, we reviewed different quantum chemical approaches to determine local quantities from (multireference) wave functions in order to provide a qualitative interpretation of the chemical bond in open-shell molecules. Chemical bonding in open-shell systems can be described by covalent interactions and electron-spin coupling schemes. For different definitions of the (effective) bond order as well as various decomposition schemes of the total molecular spin expectation value into local contributions, advantages and shortcomings have been pointed out. For open-shell systems, the spin density distribution is an essential ingredient in the

evaluation of the local quantities presented and for the qualitative understanding of chemical bonding.

As an example of an open-shell transition-metal complex we discussed some of the pitfalls of present-day DFT and CASSCF calculations in determining accurate spin density distributions in open-shell transition-metal complexes. An accurate description of the spin density and of the electronic structure is mandatory for a subsequent qualitative analysis of the chemical bonding. This could only be accomplished by employing the DMRG algorithm to produce an accurate CASCI-type electronic wave function.

Although such multireference procedures have computational limitations, they are currently the only approaches to correctly describe all spin states of an open-shell system. It is, however, a formidable task to correctly describe all possible states in spin-coupled systems as is well illustrated in Ref. [204] for the nucleation of antiferromagnetically coupled chromium dihalides. Noodleman's approach, although computationally very efficient, is of limited accuracy, a deficiency that is further enhanced by the limited accuracy of Kohn–Sham models for open-shell transition-metal complexes and clusters in general. Only the high-spin state can be described by a single-determinant wave function. The anti-ferromagnetically coupled low-spin state usually comes out reasonably well in the broken-symmetry approach, but for intermediate spin states one usually assumes a Heisenberg spin-ladder diagram for computational reasons. However, as molecules may undergo a significant distortion upon changing their spin states (Jahn–Teller distortions are a prominent example), such simple approximations become less and less valid.

It can thus be anticipated that theoretical research into the description of open-shell molecules, and especially into open-shell Transition-metal complexes and clusters, will continue to be important and successful in the future.

Acknowledgments

We gratefully acknowledge financial support by a grant from the Swiss National Science Foundation (project 200020_144458/1). K.B. thanks the Fonds der Chemischen Industrie for a Chemiefonds scholarship.

References

1. Podewitz, M., Stiebritz, M.T. and Reiher, M. (2011) *Faraday Discuss.*, **148**, 119–135.
2. Gray, H.B., Stiefel, E.I., Valentine, J.S. and Bertini, I. (2006) *Biological Inorganic Chemistry: Structure and Reactivity*, University Science Book.
3. Carreira, E.M. and Kvaerno, L. (2009) *Classics in Stereoselective Synthesis*, Wiley-VCH Verlag GmbH, Weinheim.
4. Reiher, M. (2009) *Chimia*, **63**, 140–145.
5. Lewis, G.N. (1916) *J. Am. Chem. Soc.*, **38**, 762–785.
6. Cotton, F.A., Murillo, C.A. and Walton, R.A. (2005) *Multiple Bonds Between Metal Atoms*, Springer, New York.
7. Nguyen, T., Sutton, A.D., Brynda, M., Fettinger, J.C., Long, G.J. and Power, P.P. (2005) *Science*, **310**, 844–847.
8. Amann, A. and Müller-Herold, U. (2011) *Offene Quantensysteme. Die Primas Lectures*, 1st edn, Springer, Heidelberg.

9. Helgaker, T., Jørgensen, P. and Olsen, J. (2000) *Molecular Electronic-Structure Theory*, John Wiley & Sons, Ltd, Chichester.
10. Shaik, S.S. and Hiberty, P.C. (2004) *A Chemist's Guide to Valence Bond Theory*, Wiley-Interscience.
11. Trinquier, G., Malrieu, J.P. and Garcia-Cuesta, I. (1991) *J. Am. Chem. Soc.*, **113**, 6465–6473.
12. Bachler, V. (2004) *J. Comput. Chem.*, **25**, 343–367.
13. Hiberty, P.C. and Shaik, S. (2007) *J. Comput. Chem.*, **28**, 137–151.
14. Löwdin, P.-O. Correlation problem in many-electron qunatum mechanics, in *Advances in Chemical Physics*, vol. **I**, John Wiley & Sons, Inc., New York, 1958.
15. Szabo, A. and Ostlund, N.S. (1989) *Modern Quantum Chemistry: Introduction to Advanced Electronic Structure Theory*, McGraw-Hill.
16. Piela, L. (2007) *The Ideas of Qunatum Chemistry*, Elsevier.
17. Reiher, M. and Wolf, A. (2009) *Relativistic Quantum Chemistry: The Fundamental Theory of Molecular Science*, John Wiley & Sons, Inc., Weinheim.
18. Born, M. and Oppenheimer, J.R. (1927) *Ann. Phys.*, **84**, 0457–0484.
19. Born, M. and Huang, K. (1954) *Dynamical Theory of Crystal Lattices*, Oxford University Press, Oxford.
20. Reiher, M. (2007) *Faraday Discuss.*, **135**, 97–124.
21. Olsen, J., Jørgensen, P. and Simons, J. (1990) *Chem. Phys. Lett.*, **169**, 463–472.
22. Mitrushenkov, A.O. (1994) *Chem. Phys. Lett.*, **217**, 559–565.
23. Löwdin, P.-O. (1955) *Phys. Rev.*, **97**, 1509–1520.
24. Marti, K.H., Bauer, B., Reiher, M., Troyer, M. and Verstraete, F. (2010) *New J. Phys.*, **12**, 103008.
25. Crawford, T.D. and Schaefer, H.F. (2007) An introduction to coupled cluster theory for computational chemists, in *Reviews in Computational Chemistry*, John Wiley & Sons, Inc., Hoboken, NJ.
26. Shavitt, I. and Bartlett, R.J. (2009) *Many-Body Methods in Chemistry and Physics*, Cambridge University Press, Camebridge.
27. Lyakh, D.I., Musiał, M., Lotrich, V.F. and Bartlett, R.J. (2012) *Chem. Rev.*, **112**, 182–243.
28. Ivanov, V.V., Lyakh, D.I. and Adamowicz, L. (2009) *Phys. Chem. Chem. Phys.*, **11**, 2355–2370.
29. Jeziorski, B. (2010) *Mol. Phys.*, **108**, 3043–3054.
30. Kowalski, K., Krishnamoorthy, S., Villa, O., Hammond, J.R. and Govind, N. (2010) *J. Chem. Phys.*, **132**, 154103.
31. Krylov, A.I., (2001) *Chem. Phys. Lett.*, **338**, 375–384.
32. Krylov, A.I. (2006) *Acc. Chem. Res.*, **39**, 83–91.
33. Roos, B.O. and Ryde, U. (2003) Molecular orbital theory (SCF Methods and Active Space SCF), *Comprehensive Coordination Chemistry II*, Elsevier Ltd.
34. Szalay, P.G., Müller, T., Gidofalvi, G., Lischka, H. and Shepard, R. (2012) *Chem. Rev.*, **112**, 108–181.
35. Hinze, J. and Roothaan, C.C.J. (1967) *Prog. Theor. Phys. Suppl.*, **40**, 37–51.
36. Roos, B.O. (1987.) The complete active space self-consistent field method and its applications in electronic structure calculations, in *Ab initio Methods in Quantum Chemistry—II* (ed. K. Lawley), John Wiley & Sons, Ltd., Chichester.
37. Shepard, R. (1987) The multiconfiguration self-consistent field method, in *Advances in Chemical Physics*, John Wiley & Sons, Inc., New York.
38. Ivanic, J. and Ruedenberg, K. (2001) *Theor. Chem. Acc.*, **106**, 339–351.
39. Ivanic, J. and Ruedenberg, K. (2002) *Theor. Chem. Acc.*, **107**, 220–228.
40. Bytautas, L., Ivanic, J. and Ruedenberg, K. (2003) *J. Chem. Phys.*, **119**, 8217–8224.
41. Bytautas, L. and Ruedenberg, K. (2009) *Chem. Phys.*, **356**, 64–75.
42. Olsen, J., Roos, B.O., Jørgensen, P. and Jensen, H.J.A. (1988) *J. Chem. Phys.*, **89**, 2185–2192.
43. Malmqvist, P.-A., Rendell, A. and Roos, B.O. (1990) *J. Phys. Chem.*, **94**, 5477–5482.
44. Fleig, T., Olsen, J. and Marian, C.M. (2001) *J. Chem. Phys.*, **114**, 4775–4790.
45. Yaffet, L.G. and Goddard, W.A. III (1976) *Phys. Rev. A*, **13**, 1682–1691.

46. Panin, A.I. and Simon, K.V. (1996) *Int. J. Quantum Chem.*, **59**, 471–475.
47. Panin, A.I. and Sizova, V. (1996) *J. Comput. Chem.*, **17**, 178–184.
48. Nakano, H. and Hirao, K. (2000) *Chem. Phys. Lett.*, **317**, 90–96.
49. Potts, D.M., Taylor, C.M., Chaudhuri, R.K. and Freed, K.F. (2001) *J. Chem. Phys.*, **114**, 2592–2600.
50. Ivanic, J. (2003) *J. Chem. Phys.*, **119**, 9364–9376.
51. Ma, D., Li Manni, G. and Gagliardi, L. (2011) *J. Chem. Phys.*, **135**, 044128.
52. Bytautas, L., Henderson, T.M., Jiménez-Hoyos, C.A., Ellis, J.K. and Scuseria, G.E. (2011) *J. Chem. Phys.*, **135**, 044119.
53. Celani, P. and Werner, H.-J. (2000) *J. Chem. Phys.*, **112**, 5546–5557.
54. Andersson, K., Malmqvist, P.-A., Roos, B.O., Sadlej, A.J. and Wolinski, K. (1990) *J. Phys. Chem.*, **94**, 5483–5488.
55. Pierloot, K. (2003) *Mol. Phys.*, **101**, 2083–2094.
56. Roos, B.O. (2008) Multiconfigurational quantum chemistry for ground and excited states, in *Radiation Induced Molecular Phenomena in Nucleic Acids* (eds M.K. Shukla and J. Leszczynski), Springer.
57. Pierloot, K. (2011) *Int. J. Quantum Chem.*, **111**, 3291–3301.
58. Andersson, K., Malmqvist, P.-A. and Roos, B.O. (1992) *J. Chem. Phys.*, **96**, 1218–1226.
59. Dyall, K.G. (1995) *J. Chem. Phys.*, **102**, 4909–4918.
60. Pulay, P. (2011) *Int. J. Quantum Chem.*, **111**, 3273–3279.
61. Angeli, C., Cimiraglia, R., Evangelisti, S., Leininger, T. and Malrieu, J.-P. (2001) *J. Chem. Phys.*, **114**, 10252–10264.
62. Malmqvist, P.-A., Pierloot, K., Shahi, A.R.M., Cramer, C.J. and Gagliardi, L. (2008) *J. Chem. Phys.*, **128**, 204109.
63. Buenker, R.J., Peyerimhoff, S.D. and Butscher, W. (1978) *Mol. Phys.*, **35**, 771–791.
64. Werner, H.-J. and Knowles, P.J. (1988) *J. Chem. Phys.*, **89**, 5803–5814.
65. Helgaker, T., Jørgensen, P., Olsen, J. and Klopper, W. (2004) *ChemInform*, **35**, 57–88.
66. Goddard, III, W.A. (1967) *Phys. Rev.*, **157**, 81–93.
67. Ladner, R.C. and Goddard, III, W.A. (1969) *J. Chem. Phys.*, **51**, 1073–1087.
68. Goddard, III, W.A. and Ladner, R.C. (1971) *J. Am. Chem. Soc.*, **93**, 6750–6756.
69. Hunt, W.J., Hay, P.J. and Goddard, III, W.A. (1972) *J. Chem. Phys.*, **57**, 738–748.
70. Goddard, III, W.A., Dunning, T.H. Jr., Hunt, W.J. and Hay, P.J. (1973) *Acc. Chem. Res.*, **6**, 368–376.
71. Goddard, III, W.A. and Harding, L.B. (1978) *Ann. Rev. Phys. Chem.*, **29**, 363–396.
72. Faglioni, F. and Goddard, III, W.A. (1999) *Int. J. Quantum Chem.*, **73**, 1–22.
73. Radon, M., Broclawik, E. and Pierloot, K. (2010) *J. Phys. Chem. B*, **114**, 1518–1528.
74. Yaron, D., Moore, E.E., Shuai, Z. and Bredas, J.L. (1998) *J. Chem. Phys.*, **108**, 7451–7458.
75. White, S.R. and Martin, R.L. (1999) *J. Chem. Phys.*, **110**, 4127–4130.
76. Legeza, O., Noack, R., Sólyom, J. and Tincani, L. (2008) Applications of quantum information in the density-matrix renormalization group, in *Computational Many-Particle Physics*, vol. **739** (eds H. Fehske, R. Schneider and A. Weisse), Springer, Berlin/Heidelberg.
77. Marti, K.H. and Reiher, M. (2010) *Z. Phys. Chem.*, **224**, 583–599.
78. Chan, G.K.-L. and Sharma, S. (2011) *Annu. Rev. Phys. Chem.*, **62**, 465–481.
79. White, S.R. (1992) *Phys. Rev. Lett.*, **69**, 2863–2866.
80. White, S.R. and Noack, R.M. (1992) *Phys. Rev. Lett.*, **68**, 3487–3490.
81. Marti, K.H., Ondik, I.M., Moritz, G. and Reiher, M. (2008) *J. Chem. Phys.*, **128**, 014104.
82. Barcza, G., Legeza, O., Marti, K.H. and Reiher, M. (2011) *Phys. Rev. A*, **83**, 012508.
83. Kurashige, Y. and Yanai, T. (2009) *J. Chem. Phys.*, **130**, 234114.
84. Sharma, S. and Chan, G.K.-L. (2012) *J. Chem. Phys.*, **136**, 124121.

85. Boguslawski, K., Marti, K.H., Legeza, O. and Reiher, M. (2012) *J. Chem. Theory Comput.*, **8**, 1970–1982.
86. Boguslawski, K., Tecmer, P., Legeza, O. and Reiher, M. (2012) *J. Phys. Chem. Lett.*, **3**, 3129–3135.
87. Boguslawski, K., Jacob, C.R. and Reiher, M. (2011) *J. Chem. Theory Comput.*, **7**, 2740–2752.
88. Perez-Garcia, D., Verstraete, F., Wolf, M. and Cirac, J. (2007) *Quantum Inf. Comput.*, **7**, 401–430.
89. Verstraete, F., Murg, V. and Cirac, J. (2008) *Adv. Phys.*, **57**, 143–224.
90. Schollwöck, U. (2011) *Ann. Phys.*, **326**, 96–192.
91. Schollwöck, U. (2005) *Rev. Mod. Phys.*, **77**, 259–315.
92. Boguslawski, K., Marti, K.H. and Reiher, M. (2011) *J. Chem. Phys.*, **134**, 224101.
93. Mitrushenkov, A.O., Linguerri, R., Palmieri, P. and Fano, G. (2003) *J. Chem. Phys.*, **119**, 4148–4158.
94. Moritz, G., Hess, B. and Reiher, M. (2005) *J. Chem. Phys.*, **122**, 024107.
95. Rissler, J., Noack, R.M. and White, S.R. (2006) *Chem. Phys.*, **323**, 519–531.
96. Legeza, O. and Sólyom, J. (2003) *Phys. Rev. B*, **68**, 195116.
97. Legeza, O. and Sólyom, J. (2004) *Phys. Rev. B*, **70**, 205118.
98. Legeza, O., Röder, J. and Hess, B.A. (2003) *Phys. Rev. B*, **67**, 125114.
99. White, S. (2005) *Phys. Rev. B*, **72**, 180403.
100. Chan, G.K.-L. and Head-Gordon, M. (2002) *J. Chem. Phys.*, **116**, 4462–4476.
101. Schuch, N., Wolf, M.M., Verstraete, F. and Cirac, J.I. (2008) *Phys. Rev. Lett.*, **100**, 040501.
102. Mezzacapo, F., Schuch, N., Boninsegni, M. and Cirac, J.I. (2009) *New J. Phys.*, **11**, 083026.
103. Changlani, H.J., Kinder, J.M., Umrigar, C.J. and Chan, G.K.-L. (2009) *Phys. Rev. B*, **80**, 245116.
104. Marti, K.H. and Reiher, M. (2011) *Phys. Chem. Chem. Phys.*, **13**, 6750–6759.
105. Neuscamman, E. and Chan, G.K.-L. (2012) *Phys. Rev. B*, **86**, 064402.
106. Parr, R.G. and Yang, W. (1989) *Density-Functional Theory of Atoms and Molecules*, Oxford University Press, New York.
107. Orio, M., Pantazis, D.A. and Neese, F. (2009) *Photosynth. Res.*, **102**, 443–453.
108. Kohn, W. and Sham, L.J. (1965) *Phys. Rev.*, **140**, A1133–A1138.
109. Jacob, C.R. and Reiher, M. (2012) *Int. J. Quantum Chem.*, **112**, 3661–3684.
110. McWeeny, R. (2004) *Spin in Chemistry*, Dover Publications, New York.
111. von Barth, U. and Hedin, L. (1972) *J. Phys. C*, **5**, 1629–1642.
112. Clark, A.E. and Davidson, E.R. (2001) *J. Chem. Phys.*, **115**, 7382–7392.
113. Davidson, E.R. and Clark, A.E. (2001) *Mol. Phys.*, **100**, 373–383.
114. Clark, A.E. and Davidson, E.R. (2002) *J. Phys. Chem. A*, **106**, 6890–6896.
115. Herrmann, C., Reiher, M. and Hess, B.A. (2005) *J. Chem. Phys.*, **122**, 34102.
116. Herrmann, C., Yu, L. and Reiher, M. (2006) *J. Comput. Chem.*, **27**, 1223–1239.
117. Mayer, I. (2007) *Chem. Phys. Lett.*, **440**, 357–359.
118. Davidson, E.R. and Clark, A.E. (2007) *Phys. Chem. Chem. Phys.*, **9**, 1881–1894.
119. Podewitz, M., Herrmann, C., Malassa, A., Westerhausen, M. and Reiher, M. (2008) *Chem. Phys. Lett.*, **451**, 301–308.
120. Alcoba, D.R., Lain, L., Torre, A. and Bochicchio, R.C. (2009) *Chem. Phys. Lett.*, **470**, 136–139.
121. Mayer, I. (2009) *Chem. Phys. Lett.*, **478**, 323–326.
122. Podewitz, M. and Reiher, M. (2010) *Adv. Inorg. Chem.*, **62**, 177–230.
123. Torre, A., Alcoba, D.R., Lain, L. and Bochicchio, R.C. (2010) *J. Phys. Chem. A*, **114**, 2344–2349.
124. Mayer, I. and Matito, E. (2010) *Phys. Chem. Chem. Phys.*, **12**, 11308–11314.
125. Alcoba, D.R., Torre, A., Lain, L. and Bochicchio, R.C. (2011) *J. Chem. Theory Comput.*, **7**, 3560–3566.
126. Alcoba, D.R., Torre, A., Lain, L. and Bochicchio, R.C. (2011) *Chem. Phys. Lett.*, **504**, 236–240.
127. Ramos-Cordoba, E., Matito, E., Mayer, I. and Salvador, P. (2012) *J. Chem. Theory Comput.*, **8**, 1270–1279.
128. Ramos-Cordoba, E., Salvador, P. and Reiher, M. (2013) *Chem. Eur. J.*, **19**, 15267–15275.

129. Takatsuka, K., Fueno, T. and Yamaguchi, K. (1978) *Theor. Chem. Acc.*, **48**, 175–183.

130. Scuseria, G.E., Jiménez-Hoyos, C.A., Henderson, T.M., Samanta, K. and Ellis, J.K. (2011) *J. Chem. Phys.*, **135**, 124108.

131. Neese, F. (2004) *J. Phys. Chem. Solids*, **65**, 781–785.

132. Noodleman, L. (1981) *J. Chem. Phys.*, **74**, 5737–5743.

133. Noodleman, L. and Davidson, E.R. (1986) *Chem. Phys.*, **109**, 131–143.

134. Noodleman, L. and Case, D.A. (1992) *Adv. Inorg. Chem.*, **38**, 423–470.

135. Greco, C., Fantucci, P., Ryde, U. and Gioia, Ld. (2011) *Int. J. Quantum Chem.*, **111**, 3949–3960.

136. Wu, Q. and Van Voorhis, T. (2005) *Phys. Rev. A*, **72**, 024502.

137. Rudra, I., Wu, Q. and Van Voorhis, T. (2006) *J. Chem. Phys.*, **124**, 024103.

138. Herrmann, C., Podewitz, M. and Reiher, M. (2009) *Int. J. Quantum Chem.*, **109**, 2430–2446.

139. Wiberg, K.B. (1968) *Tetrahedron*, **24**, 1083–1096.

140. Armstrong, D.R., Perkins, P.G. and Stewart, J.J.P. (1973) *J. Chem. Soc., Dalton Trans.*, 838–840.

141. Natiello, M.A. and Medrano, J.A. (1984) *Chem. Phys. Lett.*, **105**, 180–182.

142. Mayer, I. (1985) *Theor. Chim. Acta*, **67**, 315–322.

143. Mayer, I. (1986) *Int. J. Quantum Chem.*, **29**, 73–84.

144. Mayer, I. (1986) *Int. J. Quantum Chem.*, **XXIX**, 477–483.

145. Bochicchio, R.C. (1991) *J. Mol. Struct.*, **228**, 209–225.

146. Alcoba, D.R., Bochicchio, R.C., Lain, L. and Torre, A. (2007) *Chem. Phys. Lett.*, **442**, 157–163.

147. Mayer, I. (2007) *J. Comput. Chem.*, **28**, 204–221.

148. Herzberg, G. (1929) *Z. Phys.*, **57**, 601–630.

149. Mulliken, R.S. (1955) *J. Chem. Phys.*, **23**, 1833–1840.

150. Mayer, I. (1983) *Chem. Phys. Lett.*, **97**, 270–274.

151. Alcoba, D.R., Bochicchio, R.C., Lain, L. and Torre, A. (2008) *Phys. Chem. Chem. Phys.*, **10**, 5144–5146.

152. Lobayan, R.M., Alcoba, D.R., Bochicchio, R.C., Torre, A. and Lain, L. (2010) *J. Phys. Chem. A*, **114**, 1200–1206.

153. Hall, M.B. (1987) *Polyhedron*, **6**, 679–684.

154. Brynda, M., Gagliardi, L., Widmark, P.-O., Power, P.P. and Roos, B.O. (2006) *Angew. Chem. Int. Ed.*, **45**, 3804–3807.

155. Roos, B.O., Borin, A.C. and Gagliardi, L. (2007) *Angew. Chem. Int. Ed.*, **46**, 1469–1472.

156. Gagliardi, L. and Roos, B.O. (2005) *Nature*, **433**, 848–851.

157. Gagliardi, L., Pyykkö, P. and Roos, B.O. (2005) *Phys. Chem. Chem. Phys.*, **7**, 2415–2417.

158. Roos, B.O., Malmqvist, P.-A. and Gagliardi, L. (2006) *J. Am. Chem. Soc.*, **128**, 17000–17006.

159. Roos, B.O. and Gagliardi, L. (2006) *Inorg. Chem.*, **45**, 803–807.

160. Ferrante, F., Gagliardi, L., Bursten, B.E. and Sattelberger, A.P. (2005) *Inorg. Chem.*, **44**, 8476–8480.

161. La Macchia, G., Gagliardi, L., Power, P.P. and Brynda, M. (2008) *J. Am. Chem. Soc.*, **130**, 5104–5114.

162. La Macchia, G., Aquilante, F., Veryazov, V., Roos, B.O. and Gagliardi, L. (2008) *Inorg. Chem.*, **47**, 11455–11457.

163. Brynda, M., Gagliardi, L. and Roos, B.O. (2009) *Chem. Phys. Lett.*, **471**, 1–10.

164. La Macchia, G., Li Manni, G., Todorova, T.K., Brynda, M., Aquilante, F., Roos, B.O. and Gagliardi, L. (2010) *Inorg. Chem.*, **49**, 5216–5222.

165. Li Manni, G., Dzubak, A.L., Mulla, A., Brogden, D.W., Berry, J.F. and Gagliardi, L. (2012) *Chem. Eur. J.*, **18**, 1737–1749.

166. Infante, I., Gagliardi, L. and Scuseria, G.E. (2008) *J. Am. Chem. Soc.*, **130**, 7459–7465.

167. Poineau, F., Forster, P.M., Todorova, T.K., Gagliardi, L., Sattelberger, A.P. and Czerwinski, K.R. (2010) *Inorg. Chem.*, **49**, 6646–6654.

168. Zall, C.M., Zherebetskyy, D., Dzubak, A.L., Bill, E., Gagliardi, L. and Lu, C.C. (2012) *Inorg. Chem.*, **51**, 728–736.

169. Parr, R.G., Ayers, P.W. and Nalewajski, R.F. (2005) *J. Phys. Chem. A*, **109**, 3957–3959.

170. Hirshfeld, F.L. (1977) *Theor. Chim. Acta*, **44**, 129–138.

171. Becke, A.D. (1988) *J. Chem. Phys.*, **88**, 2547–2553.

172. Matito, E., Solà, M., Salvador, P. and Duran, M. (2007) *Faraday Discuss.*, **135**, 325–345.

173. Bultinck, P., Van Alsenoy, C., Ayers, P.W. and Carbó-Dorca, R. (2007) *J. Chem. Phys.*, **126**, 144111.

174. Bader, R.F.W. (1990) *Atoms in Molecules: A Quantum Theory*, Oxford University Press, Oxford.

175. Matta, C.F. and Boyd, R.J. (2007) *The Quantum Theory of Atoms in Molecules: From Solid State to DNA and Drug Design*, 1st edn, Wiley-VCH Verlag GmbH.

176. Bader, R.F.W. (2010) *J. Phys. Chem. A*, **114**, 7431–7444.

177. Eickerling, G., Mastalerz, R., Herz, V., Scherer, W., Himmel, H.-J. and Reiher, M. (2007) *J. Chem. Theory Comput.*, **3**, 2182–2197.

178. Angyán, J.G., Loos, M. and Mayer, I. (1994) *J. Phys. Chem.*, **98**, 5244–5248.

179. Fradera, X., Austen, M.A. and Bader, R.F.W. (1999) *J. Chem. Phys.*, **103**, 304–314.

180. Fradera, X. and Solà, M. (2002) *J. Comput. Chem.*, **23**, 1347–1356.

181. Vedral, V. (2002) *Rev. Mod. Phys.*, **74**, 197–233.

182. Ziesche, P. (1995) *Int. J. Quantum Chem.*, **56**, 363–369.

183. Nalewajski, R.F. (2000) *J. Phys. Chem. A*, **104**, 11940.

184. Nalewajski, R.F. (2004) *Chem. Phys. Lett.*, **386**, 265.

185. Nalewajski, R.F. (2005) *J. Math. Chem.*, **38**, 43.

186. Luzanov, A.V. and Prezhdo, O.V. (2005) *Int. J. Quantum Chem.*, **102**, 582–601.

187. Huang, Z. and Kais, S. (2005) *Chem. Phys. Lett.*, **413**, 1–5.

188. Huang, Z., Wang, H. and Kais, S. (2006) *J. Mod. Opt.*, **53**, 2543–2558.

189. Nalewajski, R.F. (2006) *Information Theory of Molecular Systems*, Elsevier, Amsterdam.

190. Juhász, T. and Mazziotti, D.A. (2006) *J. Chem. Phys.*, **125**, 174105.

191. Luzanov, A.V. and Prezhdo, O. (2007) *Mol. Phys.*, **105**, 2879–2891.

192. Nalewajski, R.F. (2008) *J. Math. Chem.*, **43**, 265.

193. Nalewajski, R.F. (2010) *Information Origins of the Chemical Bond*, Nova Science Publishers, Hauppauge, NY.

194. Greenman, L. and Mazziotti, D.A. (2010) *J. Chem. Phys.*, **133**, 164110.

195. Alcoba, D.R., Bochicchio, R.C., Lain, L. and Torre, A. (2010) *J. Chem. Phys.*, **133**, 144104.

196. Pelzer, K., Greenman, L., Gidofalvi, G. and Mazziotti, D.A. (2011) *J. Phys. Chem. A*, **115**, 5632–40.

197. Nalewajski, R.F. (2011) *J. Math. Chem.*, **49**, 806.

198. Boguslawski, K., Tecmer, P., Barcza, G., Legeza, O. and Reiher, M. (2013) *J. Chem. Theory Comput.*, **9**, 2959–2973.

199. Conradie, J. and Ghosh, A. (2007) *J. Phys. Chem. B*, **111**, 12621–12624.

200. Kossmann, S. and Neese, F. (2010) *J. Phys. Chem. A*, **114**, 11768–11781.

201. Werner, H.-J., Knowles, P.J., Lindh, R., Manby, F.R., Schütz, M., Celani, P., Korona, T., Mitrushenkov, A., Rauhut, G., Adler, T.B., Amos, R.D., Bernhardsson, A., Berning, A., Cooper, D.L., Deegan, M.J.O., Dobbyn, A.J., Eckert, F., Goll, E., Hampel, C., Hetzer, G., Hrenar, T., Knizia, G., Köppl, C., Liu, Y., Lloyd, A.W., Mata, R.A., May, A.J., McNicholas, S.J., Meyer, W., Mura, M.E., Nicklass, A., Palmieri, P., Pflüger, K., Pitzer, R., Reiher, M., Schumann, U., Stoll, H., Stone, A.J., Tarroni, R., Thorsteinsson, T., Wang, M. and Wolf, A. (2009) *MOLPRO, Version 2009.1, a Package of ab Initio Programs*, Cardiff University, University of Stuttgart, Cardiff, Stuttgart.

202. Dunning, T.H. Jr. (1989) *J. Chem. Phys.*, **90**, 1007–1023.

203. Balabanov, N.B. and Peterson, K.A. (2005) *J. Chem. Phys.*, **123**, 064107.

204. Vest, B., Hermann, A., Boyd, P.D.W. and Schwerdtfeger, P. (2010) *Inorg. Chem.*, **49**, 3169–3182.

9
Modeling Metal–Metal Multiple Bonds with Multireference Quantum Chemical Methods

Laura Gagliardi

9.1
Introduction

In 1965 F. A. Cotton and C. B. Harris [1] synthesized $K_2[Re_2Cl_8]\cdot 2H_2O$, which presents a surprisingly short Re–Re distance of 2.24 Å. On the basis of this discovery, they introduced the concept of a multiple bond between two metal atoms. Cotton analyzed the bonding using simple molecular orbital (MO) theory and stated that the two Re atoms are bonded through a quadruple bond [1, 2].

Ever since this discovery, the research on metal–metal multiple bonding has flourished [3–7]. Electron rich metal–metal moieties raise substantial interest because of their unique electronic and optical properties. Several new examples of metal–metal multiply bonded compounds have appeared in the recent literature.

In this chapter some systems containing a homo-bimetallic multiple bond, which have been recently synthesized and studied with quantum chemical methods, are analyzed. The chapter is organized as follows. In Section 9.2 a brief description of the computational tools employed in this analysis is presented. In Section 9.3 the classical case of $Re_2Cl_8^{2-}$ is reviewed. In Section 9.4 group VI homo-nuclear diatomic molecules, namely Cr_2, Mo_2, and W_2 are discussed. In Section 9.5 homo-bimetallic compounds containing the Cr_2, Mo_2 and W_2 moieties are described. In Section 9.6 some recently synthesized Fe_2 compounds are reported. Finally in Section 9.7 some perspective and some conclusions are offered.

9.2
Multireference Methods and Effective Bond Orders

Most of the description of metal–metal multiple bonds presented in this paper are based on calculations performed with the complete active space self-consistent-field (CASSCF) method [8] followed by second order perturbation theory, CASPT2 [9]. The CASSCF method guarantees a qualitatively correct representation of the electronic structure, and the metal–metal multiple bonds. The subsequent

The Chemical Bond: Chemical Bonding Across the Periodic Table, First Edition.
Edited by Gernot Frenking, Sason Shaik.

CASPT2 treatment ensures quantitatively correct energy differences among different electronic states.

The choice of the active space is the challenging aspect of these calculations. An appropriate active space should include the metal–metal bonding and antibonding orbitals and also the necessary ligand orbitals that interact with the metal d- and s-type orbitals. This active space comprises at least all the *n*d (n = 3, 4 or 5) and (*n* + 1)s orbitals forming the M–M multiple bond, namely, 12 orbitals. From a CASSCF wavefunction it is possible to compute the effective bond order (EBO) [10, 11] which quantifies the formation of a chemical bond. For a single bond the EBO is defined as:

$$\mathrm{EBO} = (\eta_b - \eta_{ab})/2 \tag{9.1}$$

where η_b and η_{ab} are the occupation numbers of the bonding and antibonding MO pair derived from the CASSCF wavefunction. In multiply bonded systems the individual values generated from the various pairs of bonding and antibonding orbitals (e.g., σ, π, and δ) are added up to obtain the total EBO. Notice that η_b and η_{ab} can assume any value between zero and two and are not necessarily integral numbers. Equation (9.1) thus implies that the EBO value will always be lower or at most equal to the bond order that one obtains from conventional MO theory, where the orbitals have an occupation number always equal to either 2, 1, or 0.

The EBO concept relies on a multi-configurational wavefunction and takes into account the effect of electron correlation involving the antibonding orbitals. There are various ways of quantifying bond orders [12–14]. The Natural Bond Orbital (NBO) valence and bonding concepts are also extensively used in the analysis of multiple bonds. NBO, like EBO, is based on a quantum mechanical wavefunction. The NBO description of a bond can be derived by variational, perturbative, or density functional theory (DFT) approximations of arbitrary form and accuracy [15].

9.3 The Multiple Bond in $Re_2Cl_8^{2-}$

As already mentioned in the Introduction, Cotton [1, 2] stated that the two Re atoms are bonded through a quadruple bond in $Re_2Cl_8^{2-}$. The short rhenium–rhenium bond between two $ReCl_4^-$ moieties was described as one σ, one degenerate π, and one δ bond. This work inspired experimental research that brought about the discovery of homo- and hetero-dinuclear compounds with metal–metal quadruple bonds [16].

CASPT2 calculations [17] on this species showed that the σ bond has an EBO of 0.92, the π bond has the value of 1.74, whereas the bond order of the δ-bond is only 0.54. This means that the δ bond is rather weak. The total EBO was reported to be 3.2, to be compared with a formal total bond order of 4. The strength of the δ bond in $Re_2Cl_8^{2-}$ was also investigated by Ohnishi *et al.* [18]. They calculated the energy difference between the $^1A_{1g}$ ground state and the $^3A_{2u}$ excited state, which is 12 kcal mol^{-1}. The populations of the δ and δ* orbitals in the $^1A_{1g}$ state were

reported to be 1.52 and 0.48, respectively, while the $^3A_{2u}$ state has nearly identical δ and δ^* orbital populations of 1.01 and 0.99. Ponec *et al*. [7]. analyzed the Re–Re bond using the formalism of the analysis of domain averaged Fermi holes. Their results confirmed the substantial reduction in the bond order of the Re–Re bond. Krapp *et al*. [3]. employed the energy decomposition analysis (EDA), to investigate the Re–Re multiple bond. Their study shows that the $b_2(\delta_{xy})$ orbitals contribute to the Re–Re bond in the $^1A_{1g}(\delta^2\delta^{*0})$ ground state in a negligible quantity. The vertical excitation of one and two electrons from the bonding δ orbital into the antibonding δ^* orbitals yielding the singly and doubly excited states $^1A_{1g}(\delta^1\delta^{*1})$ and $^1A_{1g}(\delta^0\delta^{*2})$ gives a destabilization of 17.5 and 36.1 kcal mol^{-1}, respectively, which is nearly the same as the total excitation energies. More recently, Ponec *et al*. [6] compared the performance of different methods of including relativistic effects, namely, all-electron relativistic and pseudopotential methods, in the description of the Re–Re bonding in the $Re_2Cl_8^{2-}$.

9.4 Homonuclear Diatomic Molecules: Cr_2, Mo_2, and W_2

In this Section the metal–metal multiple bond in the Cr_2, Mo_2, and W_2 diatomic molecules will be compared.

Bondybey *et al*. found the bond length of Cr_2 to be 1.679 Å [19], and according to some laser-induced fluorescence spectroscopic experiment, they calculated its dissociation energy to be 1.53 ± 0.06 eV. Even though this bond is considered quite short and has a formal bond order (FBO) of six, its relevance was largely questioned [20] because of its significantly lower dissociation energy. This is in comparison to the analogous species involving atoms from the second or third row. Dependent upon the reported theoretical studies, the description of the bonding in Cr_2 has ranged from a hextuple bond [20–23], through a single bond [24], to a complete absence of bonding between the two chromium centers [20].

The six unpaired electrons on each Cr atom with a ground state $(3d)^5(4s)^1$, ^7S, form the Cr–Cr bond. A hextuple bond can in theory be made between the two chromium atoms. CASPT2 calculations [25] have been employed to predict spectroscopic constants and a potential curve, which resulted in good agreement with experiment [26]. The electronic structure of Cr_2 at equilibrium is described by including in the active space six bonding orbitals ($4s\sigma_g$, $3d\sigma_g$, $3d\pi_u$, and $3d\delta_g$) and six corresponding antibonding orbitals ($4s\sigma_u$, $3d\sigma_u$, $3d\pi_g$, $3d\delta_u$). Bonding and antibonding orbitals are paired together. In each pair the two occupation numbers add up to 2.00, which makes it possible to attach an EBO to each pair. The 4s atomic orbitals form a σ bond with an EBO of 0.90. It has been suggested that this orbital should be considered as a Rydberg orbital [27] rather than as a truly bonding orbital. Although it is true that at the equilibrium bond distance (1.68 Å) the 4s–4s interaction is repulsive because of the much larger size of the 4s orbitals compared to the 3d's, the $4s\sigma_g$ orbital is, doubly occupied with only a small occupation of the corresponding antibonding orbital $4s\sigma_u$.

The other five pairs form the 3d bonds in the Cr–Cr complexes and they present quite a different binding power. The 3dσ-orbital pair creates a bond with an EBO of 0.77, whereas the 3dπ bonds exhibit an EBO of 0.81 each, and the 3dδ bonds an EBO of 0.58 each. The total EBO then adds up to 4.45. Therefore, the Cr–Cr bond is closer to a quadruple bond, rather than a hextuple or quintuple bond, because the δ bonds are very weak and could also be considered as two pairs of antiferromagnetically coupled 3dδ atomic orbitals. The CASSCF/CASPT2 conclusions presented by Roos [25] yield a bond distance of 1.66 (1.68) Å and a bond energy (D_0) of 1.65 (1.53) eV (experimental values are given within parentheses).

The discrepancy in size between the 3d and 4s orbitals makes the Cr–Cr bond weak. The 4s orbitals are significantly larger than the 3d ones and generate a 4s–4s bond at a considerably longer bond distance than the 3d–3d bonds. This difference in size weakens the 3d bonds and makes the 4s bonds repulsive at equilibrium geometry. The bond energy for Cr_2, which is only 1.66 eV (compared with 3.17 eV for PhCrCrPh; see Section 9.5), is a manifestation of this situation and confirms that there is no direct relation between bond order and bond energy. An additional contributing factor is the repulsive interaction between the closed 3p shells, which have about the same radial extension as the 3d orbitals. Table 9.1 summarizes the bond orders (FBO and EBOs) for Cr_2, Mo_2, and W_2 together with their dissociation energy and equilibrium bond distance.

The Cr_2 system has been and will continue being a benchmark test for quantum chemical methods because its ground state presents one of the most complicated electronic structures that can be found among metal dimers, as discussed earlier. DFT, with various exchange-correlation (xc) functionals, is not able to reproduce the correct shape of the potential energy curve (PEC) and the spectroscopic constants of the ground state. Only the BLYP functional is capable of reproducing the first minimum and the shelf-like potential along the potential energy surface (PES), whereas traditional hybrid functionals like B3LYP fail to show the region at 2.5 Å [28]. Furthermore, spin contamination affects all DFT results, pinpointing the fact that a single closed-shell configuration represents a too simplistic description of the bonding pattern in the Cr dimer [11]. Density matrix renormalization group (DMRG) algorithms [29–32] have also been employed to generate CASSCF-quality reference functions for the study of electronic structure of the chromium dimer [33].

Let us now move to the second- and third-row analogues of Cr_2. For the second-row transition metals, and even more so for the third-row, the imbalance between the s and d orbitals diminishes. Relativistic effects also play an important role

Table 9.1 Formal and effective bond orders for Cr_2, Mo_2 and W_2, together with their calculated dissociation energy (eV) and equilibrium bond distance (Å).

System	FBO	EBO	*De* (eV)	R_{eq} (Å)
Cr_2	6	4.5	1.6	1.66
Mo_2	6	5.2	4.4	1.95
W_2	6	5.2	5.4	2.01

in making the two sets of orbitals more equal in size. Relativity has the effect of contracting orbitals of σ- and π-type, whereas those with higher angular momentum are expanded. As such the s and d orbitals in the second, and especially third row, transition metals will be more equal in size. Remarkably this will enhance the bond strength of the corresponding diatoms. A theoretical study [10], using relativistic multi-configurational quantum chemical methods, predicted a bond energy of 4.41 eV (4.48) for Mo_2 and 5.37 (5 ± 1) eV for W_2. The bond distances were 1.95 (1.94) and 2.01 Å, respectively, (experimental values are given within parentheses). The slight difference in distance is a manifestation of the relativistic contraction in the W_2 molecule. The computed EBO is 5.17 for Mo_2 and 5.19 for W_2, and much closer to six than for Cr_2. Figure 9.1 illustrates the difference in the potential curves (See also Table 9.1). The increased bond energy in Mo_2 and W_2 compared to Cr_2 can partly be explained by the decreased electron repulsion in the more diffuse 4d and 5d shells compared to the compact 3d shell. For heavier elements, spin-orbit coupling, which is often quenched in the molecule but large in the atoms, will decrease the bond energy. For example, it reduces D_0 in W_2 by more than 1 eV.

These results have inspired subsequent studies on other transition metal dimers, both homo-nuclear and hetero-nuclear. Ruiperez *et al.* [34] investigated the MU heterobimetallic dimers (M = Cr, Mo, W) using the CASPT2 method. Their results showed that the EBO of MoU (5.5) is higher than that for W_2 (5.2). These heterodimers present short bond distances and large dissociation energies, which make these molecules interesting in synthetic bimetallic organometallic chemistry. In a heterodimer, the bond is not purely covalent. The difference in electronegativity between the two metals is a source of some ionicity. Electrostatic effects are important for the strength of the bond. Uranium (1.38, in the Pauling electronegativity scale) is less electronegative than chromium (1.66), molybdenum (2.16), and

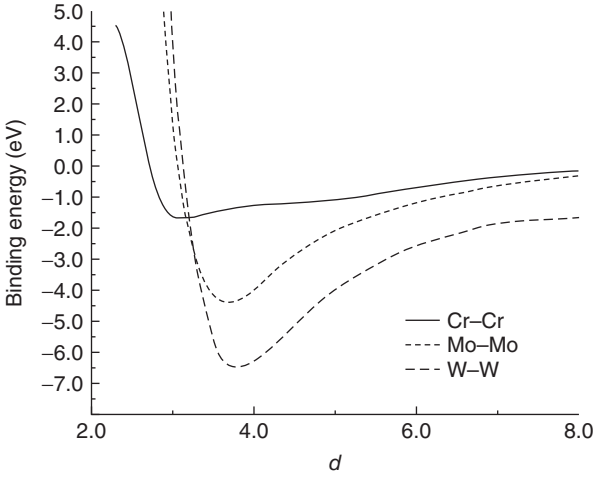

Figure 9.1 Potential curves for Cr_2, Mo_2, and W_2; d = metal–metal distance in atomic units.

tungsten (2.36), so one would expect CrU to be more ionic than WU. The charge transfer (CT) from uranium to M increases along the series. However, this increase does not automatically turn into a stronger bond: the force constants follow an irregular trend where CrU has the largest value. In CrU, the size differences between the 4s and 3d orbitals on chromium and between the 5f orbitals and 6d and 7s orbitals on uranium are responsible for the formation of a minimum at short distances and a shelf-like potential at longer distances. In this latter region, the bond is dominated mostly by the 4s–7s interaction. In molybdenum and tungsten, the size difference between the $(n+1)$s and nd orbitals is mitigated by relativistic effects but does not disappear completely. As a consequence, MoU and WU, each present a single broad minimum. With the force constant being roughly inversely proportional to the width of the potential well, MoU and WU present computed force constants smaller than that of CrU, which has a sharper minimum at short distances. On the other hand, the spin-orbit coupling is usually much larger in the isolated atoms than in the molecule. Thus, the actual dissociation energies of the MU heterodimers are smaller upon inclusion of this term, with the largest effect seen for WU (see Table 9.1). The latter presents a spin-orbit De of 4.14 eV, 1.23 eV smaller than the spin-free value. In CrU, the spin-orbit coupling reduces the *De* value of only 0.59 eV, from 3.88 to 3.29 eV.

Dong *et al*. [35] analyzed the multiple bimetallic bond of Cr–Cr, V–Mn, V–Tc, Nb–Mn, Cr–Mo, Mo–Mo, and Nb–Tc using CASPT2. They determined the bimetallic bond length, NBO, EBO, formal shortness ratio (FSR) values, and Mulliken charge populations for these systems. The V–Mn molecule presents the shortest bond length value and the largest FSR value in the series.

A couple of recent papers on different transition metal dimers are discussed here. Buchachenko *et al*. [36] studied a different dimer, Mn_2, and showed that this is also a typical challenging case for quantum chemical methods. They performed calculations by employing a set of methods including coupled cluster, multireference configuration interaction (CI) methods, and CASPT2. They showed that different methods predict different electronic structures for this system and tried to rationalize the differences among different methods.

Angeli and Cimiraglia [37] studied the $^9\Sigma_g$ and $^7\Delta_u$ states of the iron dimer, which according to a long-standing debate are the most probable candidates for the assignment of the ground state, with multireference perturbation theory up to the third order in the energy. At short internuclear distances the $^7\Delta_u$ state originates from the interaction of a ground-state ^{5}D Fe atom with an excited-state ^{5}F, whereas at large distances it results from the van der Waals interaction of two ^{5}D atoms. At all levels of calculation the $^9\Sigma_g$ term is lower in energy than the short-range $^7\Delta_u$ state and was assigned as the ground state of Fe_2. The authors showed that the calculation of the PECs for these two states represents a challenge even for the most advanced quantum chemical methods.

Metal–metal multiple bonds in diatomics still attract the attention of the community because they are per-se fascinating and they represent a challenge for novel quantum chemical methods. We now move to the description of systems containing core metal–metal multiple bonds.

9.5
Cr_2, Mo_2, and W_2 Containing Complexes

The discussion will start with some compounds containing the Cr_2 central unit. The main difference between Cr_2 and the analogous RCrCrR species (R = generic ligand) lies in the fact that in the latter, a pair of 4s electrons is used to form the Cr–R bonds with the ligands and, therefore, only the remaining 3d electrons can be involved in the Cr–Cr bonding. Then, the ten 3d electrons could result in a fivefold interaction.

A breakthrough discovery in the area of multiple bonding in transition metal chemistry, took place in 2005, with the report of the first Cr–Cr complex Ar′CrCrAr′ with a fivefold Cr–Cr interaction by Power's group [38, 39]. The Ar′CrCrAr′ (Ar′ = C_6H_3-2,6(C_6H_3-2,6-Pr^i_2)$_2$) complex exhibits a planar trans-bent structure with a very short Cr–Cr bond (1.8351(4) Å) and a Cr–Cr–C angle of 102.78(3)°. As in other species containing terphenyl ligands as kinetically stabilizing agents, the secondary Cr–C interaction involving an *ipso*-carbon of one of the flanking aryl rings is also relatively short (2.294(3) Å). Other low-valent chromium–chromium species were then synthesized by either employing modified terphenyl ligands (including electron donating/withdrawing substituents), or new ligands containing nitrogen. By replacing the central phenyl ring of the terphenyl ligand with OMe, $SiMe_3$ or F, Wolf *et al*. obtained three new variants of the Ar′CrCrAr′ [40]. Nonetheless, the synthesized structures were quite alike to the prototypical Ar′CrCrAr′ and the Cr–Cr bond remained the same in all these species. The most substantial features of these analogs of Ar′CrCrAr′ are once again the trans-bent solid-state structures with very short Cr–Cr distances that lie in the narrow range of 1.8077(7)–1.8351(4) Å. The small changes in the Cr–Cr distances could not be attributed to the electron-withdrawing or -donating power of the para substituents, but are attributed instead to crystal-packing effects. The Cr–Cr bond is thus insensitive to the electronic nature of the substituent at the para position of the central aryl ring.

Subsequent studies showed that the chemistry of the Cr–Cr complexes is not limited to the use of the bulky terphenyl moieties, but occurs also in the presence of other types of supporting ligands. Most notably, nitrogen-containing ligands can stabilize multiply bonded metal–metal species. Two derivatives of diimines ligands where each chromium atom interacts with two nearby nitrogens were reported. Kreisel *et al*. [41]. synthesized a dichromium compound (μ-η^2-$^{H}L^{iPr}$)$_2$$Cr_2$, $^{H}L^{iPr}$ = *N,N*′-bis(2,6-diisopropylphenyl)-1,4-diazadiene, where the Cr–Cr core is coordinated by two diazadienes. In this compound, the geometry around each Cr atom is trigonal planar, with each metal coordinated to two N atoms from two bridging diazadiene ligands as well as by the neighboring Cr atom. Of particular interest is the very short Cr–Cr distance of 1.8028(9) Å (shorter by ~0.03 Å than the previously reported Ar′CrCrAr′). Moreover, because of the nature of the N_2CrCrN_2 core (close to planar arrangement around Cr_2) in this complex, no secondary interactions of Cr with other parts of the ligands are involved. A similar compound, L_2Cr_2, L = [6-(2,4,6-triisopropylphenyl)pyridin-2-yl](2,4,6-trimethylphenyl)amide, with a

slightly different ligand containing two unequivalent nitrogens (one pyridino and one imino) was recently reported by Noor *et al*. [42]. This compound is characterized by an exceptionally short Cr–Cr distance of 1.749(2) Å and a rather short Cr–N_{amido} bond length (1.998(4) Å).

Furthermore, additional studies illustrate that the five-fold Cr–Cr bond does not necessarily imply planar (or close to planar) structures as in the case of the RCrCrR or RN_2CrCrN_2R species, but can also be stabilized by a somewhat unexpected arrangement of the ligands. Tsai *et al*. [43]. have synthesized a paramagnetic molecule containing three diimine ligands forming a cage (lantern) that hosts a Cr–Cr core with a Cr–Cr interaction of 1.8169(7) Å. Reduction of this molecule afforded its diamagnetic congener; this is a stable entity and exhibits the shortest Cr–Cr bond known to date of (1.7397(9) Å) for anything else than the Cr diatom itself. Some recent synthetic work on the cleavage of the Cr–Cr bond by the disproportionation induced by intramolecular axial coordination has been reported by Tsai's group [44].

Carrasco *et al*. [45] prepared and characterized new quadruply bonded dimolybdenum complexes of the terphenyl ligand $Ar^{Xyl}{}_2$ $[Mo_2(Ar^{Xyl}{}_2)(O_2CMe)_3]$ $[Mo_2(Ar^{Xyl}{}_2)(O_2CH)_2] = C_6H_3\text{-}2,6\text{-}(C_6H_3\text{-}2,6\text{-}Me_2)_2)$. Bulky terphenyl ligands are used to suppress possible side reactions in low-coordinated complexes, and to increase the stability in a metal–metal bonded compounds [46, 47]. By choosing $[Mo_2(O_2CR)_4]$ (R = Me, H) as metal precursors, the mono- and bis-terphenyl derivatives $[Mo_2(Ar^{Xyl}{}_2)(O_2CMe)_3]$, and $[Mo_2(Ar^{Xyl}{}_2)(O_2CMe)_3]$, respectively, were isolated and characterized. Because of the steric pressure exerted by the bulky $Ar^{Xyl}{}_2$ group, these compounds present very unusual four-coordinate, 14-electron structures derived from a square pyramidal geometry that has an empty basal site. These compounds have a potential as precursors for so far unknown low-coordinate second row diorganometal(II) species.

Among the low valent chromium–chromium complexes, four new molecules with Cr–Cr cores using modified bis(amidinate) ligands with short N–N distances were reported, by Hsu *et al*. [48]. These species present an extremely short metal–metal bond of 1.74 Å, which was considered independent of the steric hindrance of the ligands [28].

These experimental achievements have inspired the computational chemistry community and have been followed by several computational studies trying to assess the nature of these multiple bonds [12, 14, 39, 41, 48–61]. CASPT2 calculations were performed on several of these systems. A simplified model of Ar′CrCrAr′ where the Ar′ ligands were replaced by two phenyl rings, the PhCrCrPh was considered [62]. The interaction of the two chromium atoms leads in this case to five, rather than six, metal–metal bonding MOs, along with their antibonding counterparts. The CASPT2 optimization results in two structures, (the first one is trans-bent) with the computed Cr–Cr and Cr–C distances of Cr–Cr = 1.75 Å and Cr–C = 2.02 Å, respectively. These distances are slightly shorter than the experimentally determined values in the case of the corresponding Ar′CrCrAr′ (Cr–Cr = 1.83 Å, Cr–C = 2.15 Å) and this discrepancy arises from additional weak interactions with the ligands. The extra aryl substituents in Ar′CrCrAr′, because

of steric and electronic factors as well as the presence of an additional Cr–Phenyl ring interaction, weaken both the Cr–Cr and Cr–C bonds. The second low-lying PhCrCrPh structure is linear, with a short Cr–Cr bond of 1.678 Å and Cr–C bond of 2.040 Å. It is only 1 kcal mol^{-1} lower in energy than the trans-bent structure. The Cr–Cr bond energy, obtained by comparing the energy of the PhCrCrPh complex with that of two CrPh units, yields a value of 76 kcal mol^{-1}. This is nearly twice the bond energy found for Cr_2 (36 kcal mol^{-1}). The interaction of the 4s electrons is repulsive at equilibrium geometry, causing an important weakening of the Cr–Cr bond, as explained in the case of Cr_2. Such weakening does not occur in the PhCrCrPh structure because of the direct involvement of the 4s electrons in the Cr–C bond with the ligand (see, however, the discussion in the following text on the possible remaining effect of the 4s orbital on the Cr–Cr bond distance).

The PhCrCrPh CASSCF wavefunction presents a major configuration with a total weight of 45% and all the bonding orbitals occupied $(\sigma_g)^2(\pi_u)^4(\delta_g)^4$. The second dominating configuration has a weight of 9% and corresponds to a double excitation $(\delta_g)^2 \rightarrow (\delta_u)^2$ showing the weakness of the 3dδ bond. The analysis of the occupation numbers in a manner analogous to the Cr_2 case, yields a total EBO of 3.52. The difference between the total EBO's calculated for PhCrCrPh and Cr_2, (3.52 vs 4.45) is only because of the remaining single bond formed by the 4s electrons in the additional Cr–C bond with the ligand.

Finally, the entire Ar′CrCrAr′ species where the ligands were kept to include the secondary interaction of the chromium atoms with the π system of the ligand presents a total EBO of 3.43 [61], almost identical to the one obtained for PhCrCrPh [62].

Kreisel *et al.* [41] reported on a dinuclear compound that exhibits a very short chromium–chromium distance. The geometry around each chromium atom is trigonal planar with each metal being coordinated by two N atoms from two different diazadiene ligands as well as by the neighboring Cr atom (Figure 9.2). The extremely short Cr–Cr distance of 1.8028(9) Å, made it the shortest metal–metal distance reported when the paper was published.

A model compound of the Kreisel species has been investigated computationally [60] in which the terphenyl moieties were replaced with the ligands containing nitrogen, such as the diimines. Although the total EBO was found to be similar in the case of the RCrCrR and RN_2CrCrN_2R species, the bonding situation and the interactions involved are slightly different.

The dominating configuration in the CASSCF wavefunction is the closed shell configuration $(Cr–Cr)\sigma^2(Cr–Cr)\pi^4(Cr–Cr)\delta^2$-$(Cr–N)\pi^4$, with a weight of 60%. All the other configurations contribute to the wavefunction with weights lower than 5%. A localization of the MOs along the Cr–Cr bond yielded a total EBO of 3.43. The occupation numbers for the Cr–Cr bonding orbitals and their antibonding counterparts are $\sigma_g(1.81)$, $\sigma_u(0.17)$, $\pi_u(1.81)$, $\pi_g(0.18)$, $\pi_u(1.80)$, $\pi_g(0.19)$, $\delta_g(1.70)$, $\delta_u(0.29)$, $\delta_g(0.75)$, $\delta_u(0.19)$. Table 9.2 summarizes FBOs and EBOs for several of the species discussed so far.

The Cr–Cr quintuple bond in Ar′CrCrAr′ has been recently investigated with a newly developed energy and density decomposition scheme by Ndambuki and

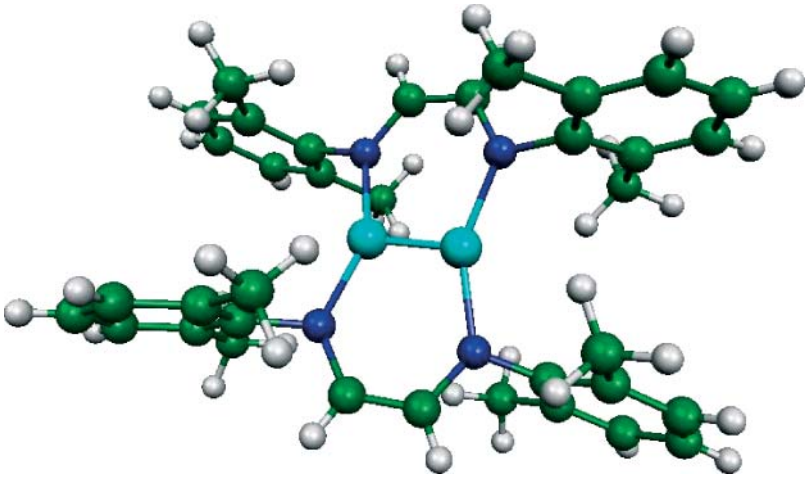

Figure 9.2 Molecular structure of the Cr_2 diazene species synthesized by Kreisel *et al*. [41].

Table 9.2 Formal and effective bond orders for several species containing the Cr_2 moiety, together with their calculated dissociation energy (eV) and Cr–Cr equilibrium bond distance (Å), when available. $Re_2Cl_8^{2-}$ is also reported for comparison (see Section 9.3).

System	FBO	EBO	*De* (eV)	R_{M-M} (Å)
MeCrCrMe	5	3.0	2.1	1.85
PhCrCrPh	5	3.5	3.3	1.75
Ar′CrCrAr′	5	3.4	—	1.83
RN_2CrCrN_2R	4	3.4	—	1.80
$Re_2Cl_8^{2-}$	4	3.2	0.7	2.26

Ziegler [56]. The new approach combines the extended transition state (ETS energy decomposition method) [63] with the natural orbitals for chemical valence (NOCV) density decomposition scheme [64–66] within the same theoretical framework. The results show that in addition to the five bonding components of the Cr–Cr bond, the quintuple bond is augmented by secondary Cr–C interactions involving the Cr-ipso-carbon of the flanking aryl rings. The presence of isopropyl groups is further shown to stabilize Ar′CrCrAr′ through stabilizing van der Waals dispersion interactions. The ETS and NOCV have also been combined in a study on the shortest, fully supported metal–metal bond (Cr–Cr = 1.73 Å) in $Cr_2[Ar'NC(NMe_2)NAr']_2$ [57]. This is the first time that the strength of the metal–metal bonding components has been determined in a supported metal–metal bond by an energy decomposition scheme.

Other members of the Ar-MM-Ar series (Ar = 2,6-$(C_6H_5)_2$-C_6H_3, M = Cr, Mo, W) and the set of $M_2(dpa)_4$ (dpa = 2,2'-dipyridylamide, M = Cr, Mo, W, U) and trans-$Mo_2(TiPB)_2BTh_2$ compounds ((TiPB = 2,4,6-triisopropyl benzoate; Th = thiophene)) have also been investigated computationally [67]. The EBO values

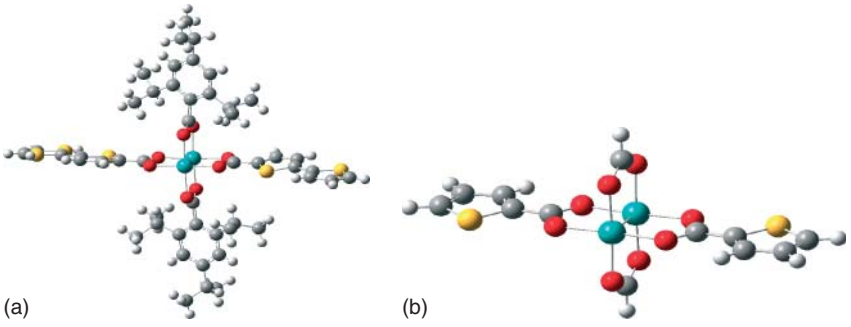

Figure 9.3 Experimentally determined structure (a) of trans-$Mo_2(TiPB)_2BTh_2$ and simplified structure (b) used in the calculation. Mo atoms are light blue, O atoms are red, C atoms are gray, S atoms are yellow, H atoms are white.

and weights of the dominating electronic configurations show that the magnitude of the M–M bond order goes as: Cr < Mo ≃ W, in agreement with the trend found for the simpler Ph-MM-Ph models and for the diatomic molecules [10, 62]. The relative bond order is maintained along the series as Ph is replaced by Ar: the Mo–Mo and W–W bond orders are about one unit larger than the Cr–Cr bond order. At the CASPT2 level the Cr–Cr bond is 0.08 Å longer in Ar–CrCr–Ar than in Ph–CrCr–Ph, whereas the EBO remains the same. Steric encumbrance might be the reason for this bond lengthening (Figure 9.3).

The ground state of the trans-$Mo_2(TiPB)_2BTh_2$ system is a singlet 1Ag state. The wavefunction is dominated, about 75% by the Hartree–Fock $\sigma^2\,\pi^4\,\delta^4$ configuration; the second most important configuration, about 7%, corresponds to a double excitation. Natural orbitals and their occupation number are reported in Figure 9.4. The EBO is equal to 3.4.

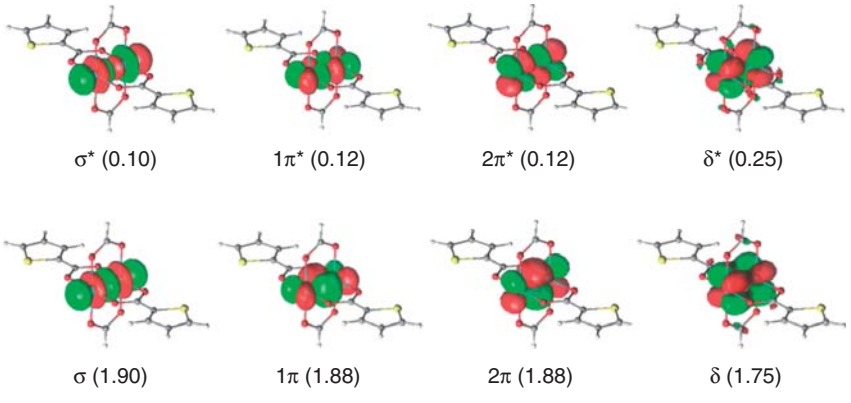

Figure 9.4 Natural orbitals and occupation numbers for the 1Ag ground state of the simplified structure of trans-$Mo_2(TiPB)_2BTh_2$.

9.6 Fe_2 Complexes

Beyond the Group VI dimers, M–M complexes featuring other first-row transition metals are also interesting. For iron, complexes with Fe–Fe bonds are largely known, in particular for iron carbonyl clusters and their derivatives. If one does not consider Fe–Fe compounds with carbonyl ligands, then the number of known species with Fe–Fe interactions significantly decreases [68–70]. Nguyen *et al.* [69] proposed that the diiron complex $[Fe_2(C_6H_3\text{-}2,6\text{-}(C_6H_3\text{-}2,6\text{-}^iPr_2)_2)_2]$ is diamagnetic, though this assignment does not match the $S = 3$ prediction from multi-configurational quantum chemical calculations [61]. Moreover, $Fe_2(DPhF)_3$ and $Fe_2(DPhF)_4$ (DPhF = diphenylforamidinate) both possess high-spin electronic configurations ($S = 7/2$ and 4, respectively), which is uncommon in other Fe–Fe complexes [71, 72]. A hexairon complex was recently reported with a high magnetic moment, $S = 6$; but, for six ferrous centers, the analogous "high-spin" configuration would be $S = 12$ [73]. The only other high-spin Fe–Fe species are gas-phase $[Fe_2]^0$ and $[Fe_2]^-$ with $S = 4$ and $S = 7/2$ ground spin-states, respectively [74, 75]. It is also important to notice that $Fe_2(DPhF)_3$ is one of a few examples of a formally mixed-valent Fe(II)Fe(I), although these other complexes are low-spin in contrast to $Fe_2(DPhF)_3$ [76].

The iron–iron bond $Fe_2(DPhF)_3$ has been recently reexamined [77], extending the previous studies by Cotton, Murillo *et al.* [71, 72]. The electronic structure of $Fe_2(DPhF)_3$ was calculated by employing both DFT and multi-configurational quantum chemical methods. The natural orbitals arising from the CASSCF employed to describe this system are 13 in total. Ten of the 13 orbitals are completely localized on the Fe–Fe bond. They are the σ, π, and δ bonding and antibonding orbitals, resulting from symmetry-adapted linear combinations of the Fe 3d atomic orbitals. The three remaining orbitals are primarily composed of the Fe 4s, 4p, and 4d atomic orbitals interacting to form σ and π bonding and antibonding orbitals with some minor contribution from the ligand N-atoms. The near degeneracy of each π- and δ-orbital pair is consistent with an approximate 3-fold symmetry about the Fe–Fe vector.

At the CASPT2 level of theory the ^8A ground state has a single dominating configuration $(\sigma)^2(\pi)^4(\pi^*)^2(\sigma^*)^1(\delta)^2(\delta^*)^2$, with a weight of 73%. The natural orbital occupation numbers of $(\sigma)^{1.85}(\pi)^{3.64}(\pi^*)^{2.30}(\sigma^*)^{1.06}(\delta)^{2.00}(\delta^*)^{2.00}(4\sigma)^{0.10}(4\pi)^{0.06}$ add up to an EBO of 1.15. Using an SCF-Xα-SW calculation on the truncated molecule $Fe_2(HNCHNH)_3$, Cotton *et al.* [71] previously computed a similar configuration $(\sigma)^2(\pi)^4(\pi^*)^2(\sigma^*)^1(\delta)^2(\delta^*)^2$, with a bond order of 1.5. It is of no surprise that the EBO value is lower than the value reported by Cotton because in CASSCF one accounts for the partial occupation of the antibonding orbitals not represented in the dominant configuration. The overall effect is to decrease the Fe–Fe bonding so that it is only slightly larger than a single bond. Finally, the charge and spin densities of the two iron atoms are identical with values of +1.17 and +3.49, respectively. These values reinforce the highly delocalized, high-spin $Fe^{1.5}Fe^{1.5}$ assignment for the diiron unit.

Bulky guanidinate ligands have been used to stabilize metal(I) dimers [78]. Fohlmeister *et al*. [79] have investigated iron(I) and manganese(I) dimers, [M2{m-N,N'-(DipN)2CR}2] (M = Fe or Mn; R = tBu, N(C6H11)2, or NiPr2). These compounds are unknown and have the potential to exhibit rare examples of multiple bonding between the metals. The iron(I) dimers are especially interesting, as the current shortest known Fe–Fe bond (2.198 Å) exists in a related mixed valence amidinate bridged complex, $[Fe^{I/II}{}_2\{m\text{-}N,N'\text{-}(PhN)_2CPh\}_3]$ [71], which has a FBO of 1.5. The Fe–Fe interaction in this high-spin complex ($S = 7/2$) is ferromagnetic. In the following text, the $[Fe^{I}{}_2(\mu\text{-}N,N'\text{-Pipiso})_2]$ species (Pipiso = $[(DipN)_2C(cis\text{-}2,6\text{-}Me_2NC_5H_8)]$) is discussed [80].

In the compound, the central $[Fe_2]^{2+}$ unit is bridged by two delocalized guanidinate ligands. Both Fe centers have T-shaped coordination geometries and the inner $Fe_2N_4C_2$ entity is essentially planar. The Fe–Fe distance of 2.1270(7) Å in this compound is shorter than all of the more than 7000 Fe–Fe interactions listed in the Cambridge Crystallographic Database, and it is shorter than the sum of two covalent radii for both low-spin iron (2.64 Å) and high-spin iron (3.04 Å) [81].

DFT and multi-configurational CASSCF and CASPT2 calculations were performed on a simplified model of $[Fe^{I}{}_2(\mu\text{-}N,N'\text{-Pipiso})_2]$, $[Fe_2\{\mu\text{-}N,N'\text{-}[(2,6\text{-}Me_2C_6H_3)N]_2CNMe_2\}_2]$, to gain further insight into its electronic structure and the nature of the very short Fe–Fe bond in the compound. The septet state ($S = 3$) was found to be the ground state at DFT level. The dominant electronic configuration for the septet state (62.3 %) yields a formal Fe–Fe bond order of two. In the CASSCF calculation the active space is composed of 14 metal-based valence electrons. Eight of these occupy four bonding MOs (σ-and π-type), four singly occupy antibonding MOs (σ* and π*-type), and two singly occupy essentially non-bonding orbitals (of δ and δ* character). This gives rise to a bond order of two, and yields six unpaired electrons for the $S = 3$ spin state dimer. However, when partial occupancies of the CASSCF total ground state natural orbitals are taken into account, an EBO of 1.19 is obtained (compared with an EBO of 1.29 for the $S = 2$ state). As a result, it is reasonable to conclude that this exceptionally short Fe–Fe interaction is because it possesses significant multiple bonding character between the two high spin iron(I) centers. Investigations into the utility of these highly reactive compounds as reagents for small molecule activations are under-way.

9.7 Concluding Remarks

Examples of metal–metal multiple bonding have been presented. The analysis is based on results from quantum chemical calculations performed with multireference methods. This approach allows us to quantify the degree of multiple bonding by using the concept of EBO. The Re–Re bond in $Re_2Cl_8{}^{2-}$ has first been discussed. This system marked the beginning of the era of multiple bonds. Group VI diatomic molecules have then been reported, namely Cr_2, Mo_2, and W_2, together with the metal–metal bond differences along the series. Metal–metal bonds in complexes

containing these bimetallic units, recently synthesized by various groups, have then been described. Finally some systems presenting a Fe–Fe multiple bonding have been reviewed. Ligand effects have been discussed extensively because they definitely affect the metal–metal multiple bonds. Synthetically, compounds with the metals in low formal oxidation states can be obtained only because of the ligand choice. The chemistry of systems containing metal–metal multiple bonds is flourishing. Efforts in various laboratories are aimed at also synthesizing systems containing hetero-bimetallic multiple bonds among first-row transition metals. The potential of these species in the activation of small species like CO_2, CO, O_2, and CH-bond is worth exploring. Metal–metal multiple bonds are challenging for quantum chemical methods because in order to be properly described, a method has to include strong electron–electron correlation and relativistic effects. They can thus represent test benchmarks for newly developed quantum chemical methods. Nevertheless, quantum chemistry plays and will continue to play a major role in this field, thanks to its predictive power.

Acknowledgment

This material is based upon work supported by the National Science Foundation under grant number CHE–1212575.

References

1. Cotton, F.A. and Harris, C.B. (1965) *Inorg. Chem.*, **4**, 330.
2. Cotton, F.A. (1965) *Inorg. Chem.*, **4**, 334.
3. Krapp, A., Lein, M., and Frenking, G. (2008) *Theor. Chem. Acc.*, **120**, 313.
4. Saito, K., Nakao, Y., Sato, H., and Sakaki, S. (2006) *J. Phys. Chem. A*, **110**, 9710.
5. Takagi, N., Krapp, A., and Frenking, G. (2010) *Can. J. Chem.-Rev. Canadienne Chim.*, **88**, 1079.
6. Ponec, R., Bucinsky, L., and Gatti, C. (2010) *J. Chem. Theory Comput.*, **6**, 3113.
7. Ponec, R. and Yuzhakov, G. (2007) *Theor. Chem. Acc.*, **118**, 791.
8. Roos, B.O., Taylor, P.R., and Siegbahn, P.E.M. (1980) *Chem. Phys.*, **48**, 157.
9. Andersson, K., Malmqvist, P.-Å., and Roos, B.O. (1992) *J. Chem. Phys.*, **96**, 1218.
10. Roos, B.O., Borin, A.C., and Gagliardi, L. (2007) *Angew. Chem. Int. Ed.*, **46**, 1469.
11. Brynda, M., Gagliardi, L., and Roos, B.O. (2009) *Chem. Phys. Lett.*, **471**, 1.
12. Weinhold, F. and Landis, C.R. (2007) *Science*, **316**, 61.
13. Reed, A.E., Curtiss, L.A., and Weinhold, F. (1988) *Chem. Rev.*, **88**, 899.
14. Wagner, F.R., Noor, A., and Kempe, R. (2009) *Nat. Chem.*, **1**, 529.
15. Weinhold, F. (2012) *J. Comput. Chem.*, 33.
16. Cotton, F.A., Murillo, C.A., and Walton, R.A. (2005) Multiple Bonds Between Metal Atoms, 3rd edn, Springer, Berlin.
17. Gagliardi, L. and Roos, B.O. (2003) *Inorg. Chem.*, **42**, 1599.
18. Ohnishi, Y.Y., Matsunaga, T., Nakao, Y., Sato, H., and Sakaki, S. (2005) *J. Am. Chem. Soc.*, **127**, 4021.
19. Bondybey, V.E. and English, J.H. (1983) *Chem. Phys. Lett.*, **94**, 443.
20. Goodgame, M.M. and Goddard, W.A. (1981) *J. Phys. Chem.*, **85**, 215.

21. Boudreaux, E.A. and Baxter, E. (2001) *Int. J. Quantum Chem.*, **85**, 509.
22. Boudreaux, E.A. and Baxter, E. (2004) *Int. J. Quantum Chem.*, **100**, 1170.
23. Boudreaux, E.A. and Baxter, E. (2005) *Int. J. Quantum Chem.*, **102**, 866.
24. Thomas, E.J., Murray, J.S., O'Connor, C.J., and Politzer, P. (1999) *J. Mol. Struct.* (THEOCHEM), **487**, 177.
25. Roos, B.O. (2003) *Collect. Czech. Chem. Commun.*, **68**, 265.
26. Frenking, G. and Tonner, R. (2007) *Nature*, **446**, 276.
27. Casey, S.M. and Leopold, D.G. (1993) *J. Phys. Chem.*, **97**, 816.
28. Bauschlicher, C.W. and Partridge, H. (1994) *Chem. Phys. Lett.*, **231**, 277.
29. Marti, K.H., Ondik, I.M., Moritz, G., and Reiher, M. (2008) *J. Chem. Phys.*, **128**, 014104.
30. Neuscamman, E., Yanai, T., and Chan, G.K.L. (2009) *J. Chem. Phys.*, **130**, 124102.
31. Yanai, T., Kurashige, Y., Ghosh, D., and Chan, G.K.L. (2009) *Int. J. Quantum Chem.*, **109**, 2178.
32. Ghosh, D., Hachmann, J., Yanai, T., and Chan, G.K.L. (2008) *J. Chem. Phys.*, 128.
33. Kurashige, Y. and Yanai, T. (2011) *J. Chem. Phys.*, 135.
34. Ruiperez, F., Merino, G., Ugalde, J.M., and Infante, I. (2013) *Inorg. Chem.*, **52**, 2838.
35. Dong, H., Meng, Q.Y., Chen, B.Z., and Wu, Y.B. (2012) *J. Organomet. Chem.*, **717**, 108.
36. Buchachenko, A.A., Chalasinski, G., and Szczesniak, M.M. (2010) *J. Chem. Phys.*, 132.
37. Angeli, C. and Cimiraglia, R. (2011) *Mol. Phys.*, **109**, 1503.
38. Nguyen, T., Sutton, A.D., Brynda, M., Fettinger, J.C., Long, G.J., and Power, P.P. (2005) *Science*, **310**, 844.
39. Frenking, G. (2005) *Science*, **310**, 796.
40. Wolf, R., Ni, C., Nguyen, T., Brynda, M., Long, G.J., Sutton, A.D., Fischer, R.C., Fettinger, J.C., Hellman, M., Pu, L.H., and Power, P.P. (2007) *Inorg. Chem.*, **46**, 11277.
41. Kreisel, K.A., Yap, G.P.A., Dmitrenko, O., Landis, C.R., and Theopold, K.H. (2007) *J. Am. Chem. Soc.*, **129**, 14162.
42. Noor, A., Wagner, F.R., and Kempe, R. (2008) *Angew. Chem. Int. Ed.*, **47**, 7246.
43. Tsai, Y.C., Hsu, C.W., Yu, J.S.K., Lee, G.H., Wang, Y., and Kuo, T.S. (2008) *Angew. Chem. Int. Ed.*, **47**, 7250.
44. Huang, Y.L., Lu, D.Y., Yu, H.C., Yu, J.S.K., Hsu, C.W., Kuo, T.S., Lee, G.H., Wang, Y., and Tsai, Y.C. (2012) *Angew. Chem. Int. Ed.*, **51**, 7781.
45. Carrasco, M., Faust, M., Peloso, R., Rodriguez, A., Lopez-Serrano, J., Alvarez, E., Maya, C., Power, P.P., and Carmona, E. (2012) *Chem. Commun.*, **48**, 3954.
46. Zhu, Z., Brynda, M., Wright, R.J., Fischer, R.C., Merrill, W.A., Rivard, E., Wolf, R.R., Fettinger, J.C., Olmstead, M.M., and Power, P.P. (2007) *J. Am. Chem. Soc.*, **129**, 10847.
47. Rivard, E. and Power, P.P. (2007) *Inorg. Chem.*, **46**, 10047.
48. Hsu, C.W., Yu, J.S.K., Yen, C.H., Lee, G.H., Wang, Y., and Tsai, Y.C. (2008) *Angew. Chem. Int. Ed.*, **47**, 9933.
49. Takagi, N., Krapp, A., and Frenking, G. (2011) *Inorg. Chem.*, **50**, 819.
50. Van der Maelen, J.F. and Cabeza, J.A. (2012) *Inorg. Chem.*, **51**, 7384.
51. Wu, L.C., Hsu, C.W., Chuang, Y.C., Lee, G.H., Tsai, Y.C., and Wang, Y. (2011) *J. Phys. Chem. A*, **115**, 12602.
52. Landis, C.R. and Weinhold, F. (2006) *J. Am. Chem. Soc.*, **128**, 7335.
53. Merino, G., Donald, K.J., D'Acchioli, J.S., and Hoffmann, R. (2007) *J. Am. Chem. Soc.*, **129**, 15295.
54. Ponec, R. and Feixas, F. (2009) *J. Phys. Chem. A*, **113**, 8394.
55. Ponec, R., Yuzhakov, G., and Sundberg, M.R. (2005) *J. Comput. Chem.*, **26**, 447.
56. Ndambuki, S. and Ziegler, T. (2012) *Inorg. Chem.*, **51**, 7794.
57. Ndambuki, S. and Ziegler, T. (2013) *Inorg. Chem.*, **52**, 3860.
58. Gorelsky, S.I. (2012) *J. Chem. Theory Comput.*, **8**, 908.
59. La Macchia, G., Li Manni, G., Todorova, T.K., Brynda, M., Aquilante, F., Roos, B.O., and Gagliardi, L. (2010) *Inorg. Chem.*, **49**, 5216.
60. La Macchia, G., Veryazov, V., Roos, B.O., and Gagliardi, L. (2008) *Inorg. Chem.*, **47**, 11455.

61. La Macchia, G., Gagliardi, L., Power, P.P., and Brynda, M. (2008) *J. Am. Chem. Soc.*, **130**, 5104.

62. Brynda, M., Gagliardi, L., Widmark, P.O., Power, P.P., and Roos, B.O. (2006) *Angew. Chem. Int. Ed.*, **45**, 3804.

63. Ziegler, T. and Rauk, A. (1977) *Theor. Chim. Acta*, **46**, 1.

64. Michalak, A., DeKock, R.L., and Ziegler, T. (2008) *J. Phys. Chem. A*, **112**, 7256.

65. Michalak, A., Mitoraj, M., and Ziegler, T. (2008) *J. Phys. Chem. A*, **112**, 1933.

66. Ziegler, T. and Rauk, A. (1979) *Inorg. Chem.*, **18**, 1755.

67. Li Manni, G., Dzubak, A.L., Mulla, A., Brogden, D.W., Berry, J.F., and Gagliardi, L. (2012) *Chem. Eur. J.*, **18**, 1737.

68. Yao, J.W., Cole, J.C., Pidcock, E., Allen, F.H., Howard, J.A.K., and Motherwell, W.D.S. (2002) *Acta Crystallogr., Sect. B: Struct. Sci.*, **58**, 640.

69. Nguyen, T., Merrill, W.A., Ni, C., Lei, H., Fettinger, J.C., Ellis, B.D., Long, G.L., Brynda, M., and Power, P.P. (2008) *Angew. Chem. Int. Ed.*, **47**, 9115.

70. Hess, C.R., Weyhermuller, T., Bill, E., and Wieghardt, K. (2009) *Angew. Chem. Int. Ed.*, **48**, 3703.

71. Cotton, F.A., Daniels, L.M., Falvello, L.R., Matonic, J.H., and Murillo, C.A. (1997) *Inorg. Chim. Acta*, **256**, 269.

72. Cotton, F.A., Daniels, L.M., Matonic, J.H., and Murillo, C.A. (1997) *Inorg. Chim. Acta*, **256**, 277.

73. Zhao, Q.L., Harris, T.D., and Betley, T.A. (2011) *J. Am. Chem. Soc.*, **133**, 8293.

74. Leopold, D.G., Almlof, J., Lineberger, W.C., and Taylor, P.R. (1988) *J. Chem. Phys.*, **88**, 3780.

75. Hubner, O. and Sauer, J. (2002) *J. Chem. Phys.*, **116**, 617.

76. Liu, T.B. and Darensbourg, M.Y. (2007) *J. Am. Chem. Soc.*, **129**, 7008.

77. Zall, C.M., Zherebetskyy, D., Dzubak, A.L., Bill, E., Gagliardi, L., and Lu, C.C. (2012) *Inorg. Chem.*, **51**, 728.

78. Jones, C. (2010) *Coord. Chem. Rev.*, **254**, 1273.

79. Fohlmeister, L., Liu, S.S., Schulten, C., Moubaraki, B., Stasch, A., Cashion, J.D., Murray, K.S., Gagliardi, L., and Jones, C. (2012) *Angew. Chem. Int. Ed.*, **51**, 8294.

80. Jin, G.X., Jones, C., Junk, P.C., Lippert, K.A., Rose, R.P., and Stasch, A. (2009) *New J. Chem.*, **33**, 64.

81. Cordero, B., Gomez, V., Platero-Prats, A.E., Reves, M., Echeverria, J., Cremades, E., Barragan, F., and Alvarez, S. (2008) *Dalton Trans.*, 2832.

10
The Quantum Chemistry of Transition Metal Surface Bonding and Reactivity

Rutger A. van Santen and Ivo A. W. Filot

10.1
Introduction

Increased capabilities of computational hardware have made possible impressive advances in the development and implementation of quantum-chemical computational tools. Current possibilities of studying computationally complex chemical systems with chemically relevant accuracy have made it an invaluable technique that complements experimental methods. In surface science and computational catalysis, this is in particular the case for calculations based on density functional theory (DFT) electronic structure calculations [1–5]. The large body of detailed experimental surface science results of adsorption and surface reactivity at molecular or atomic level [6, 7] has given a great impetus to the theoretical studies that we review.

On the basis of the results of computational quantum-chemical studies, this chapter presents an introductory review of our current understanding of the electronic basis of adsorbate chemisorption and activation on transition-metal surfaces.

In the first sections of this chapter, we discuss the nature of the surface chemical bond of adsorbed atoms and molecules. Computational access to the transition states of surface reactions has given reactivity rules of surface reactions, which we discuss in later sections dealing with adsorbate bond activation and formation.

The details of the DFT electronic structure calculations and their limitations are not explicitly referred to. These have been discussed extensively elsewhere [1–5, 7, 8]. Focus is on the evaluation of the results of such calculations to provide a framework for an understanding of chemical bonding features that underpin surface reactivity phenomena.

A quantum chemical conceptual description of the nature of the surface chemical bond has been developed in the past decades [1, 3, 4, 9]. We will use these surface chemical bonding concepts to understand adsorbate site preference as a function of transition-metal electronic structure. The relation between coordinative unsaturation of surface atoms and degree of localization of valence electrons is an important theme that will repeatedly return. It is important because it

The Chemical Bond: Chemical Bonding Across the Periodic Table, First Edition.
Edited by Gernot Frenking, Sason Shaik.

directly relates adsorption to differences in surface atom reactivity. It is basic to understand differences in reactivity of different surfaces as well as to understand particle-size-dependent effects.

The second part of this chapter is devoted to a discussion of surface elementary reactions. We limit ourselves mainly to an analysis of the rules that define the nature of the transition states of diatomic molecules such as CO or NO with a molecular π bond as well as of molecules such as CH_4 and NH_3 with σ chemical bonds. Our interest is to understand differences in elementary rate constants as a function of surface topology and again as a function of coordinative unsaturation of the surface atoms.

Since L. Pauling, chemical bonding in a transition metal is to be understood as resonance of paired electrons over interatomic bonds [10]. Because of the high coordination with surrounding metal atoms, more nearest neighbor–neighbor atom bonds are present in the metal than valence electrons that can be paired. Hence, single-bond-localized molecular orbital formation between two metal atoms cannot occur and electrons are delocalized.

The tight-binding quantum-chemical model with molecular orbitals that are a linear combination of atomic orbitals provides a reasonable description of the delocalization of the d valence electrons. The s,p valence electrons are well described as free electrons [11].

The metal–metal interatomic interaction is generally weaker than the strong interaction, with the adsorbates chemisorbed to the surface. Therefore, adatoms or admolecules tend to localize electrons into the surface complex fragment orbitals formed between the adsorbate and surface atoms.

The surface complex of adsorbate and metal surface has many features in common with molecular complexes, except that an energetic compromise between delocalized chemical bonds in the metal and the localized surface complex chemical bond has to be found. The localization of valence metal electrons by chemisorption will come at a cost. The bond strengths between the metal atoms that participate in bonding with the adsorbate and the neighboring metal atoms that do not directly participate in this bond will weaken. When the surface becomes covered with a high concentration of strongly interacting adsorbates, this weakening of metal atom–metal atom bonds may even lead to reconstruction of the surface, as we discuss in Section 10.5.

The planar structure of surface terraces puts a geometric constraint on the orientation of the molecular or atomic species that are part of the adsorption overlayer. For instance, two coadsorbed CO molecules on a metal surface will not be able to interact with the same surface metal atom. This remains the case even on more open and step-edge sites. The direct repulsive interaction between the adsorbates inhibits their close approach as the direction of the surface adsorbate chemical bond is constrained. Therefore, one will rarely observe the high coordination of several adsorbates to the same surface metal atom as observed in coordination complexes of small metallic clusters.

To a significant extent, the electron occupancy of the d-valence electron band of the transition-metal surface atoms determines trends in adsorbate adsorption

energies. For surface alloys, changes [12] in adsorption energy can be correlated with the total number of valence electrons involved in surface alloy complexes. Also, in this case when the valence electron shell becomes saturated, the adsorbate interaction energy is minimum.

A very elegant molecular orbital treatment of the quantum chemistry of the surface chemical bond has been provided for by Hoffmann [9]. The interaction energy of the adsorbate–surface complex is determined by the sum of the energies of electron-occupied bonding and antibonding surface orbital fragments. These surface fragment orbitals are not completely localized. They incorporate the changes that occur within the other bonds of the adsorbate as well as surrounding metallic environment. Concepts such as Pauli repulsion and rehybridization of chemical bonds remain useful. Compared to coordination complexes, the electron occupation of the highest surface fragment orbital is not determined by a fixed number of electrons within the surface complex, but by the condition that the chemical potential of the electrons that are part of the molecular complex is the same as that of the bulk metal. Hence, the energy of the highest occupied orbital in the adsorbate–surface complex has to be the same as the Fermi energy of the metal.

The physics community has developed a theoretical description of the surface chemical bond, which borrows from scattering theory [13, 14]. The Newns–Anderson description of the surface chemical bond is that of a scattering resonance of colliding conduction electrons [15, 16]. These theories have been essential for the development of a detailed understanding of the compromise between localization of electrons in a surface bond versus delocalization of the valence electrons in the metal.

To illustrate this and to introduce some basic surface chemical bonding concepts, we present in the next section a short exposition of the Newns–Anderson view of the surface chemical bond [17]. This is followed by Section 10.3 with the quantum-chemists approach. Chemical bonds of adsorbed atoms and molecules are discussed in terms of the electron occupation of bonding and antibonding molecular orbitals in the interacting system of adsorbate and surface. This can be done because of the many DFT calculations that are available on this topic.

In Section 10.4, this is applied to an analysis of chemisorption to alloys and nanoparticles. Section 10.5 has as focus high-coverage lateral effects. Reorganization of the metal surface by reconstruction is also discussed. The final sections deal with the analysis of transition states.

The chemical bonding features of the transition state of surface reactions in which adsorbate chemical bonds are formed or broken are close to those of the dissociated state. As we will see, this arises from the strong electronic interactions with the surface that are necessary to activate such chemical bonds.

An important geometric factor that affects differences in activation energies is the structure of the metal surface. This dependence on surface structure will be very different for adsorbates in which a chemical bond is activated over a single metal atom, as a CH bond in CH_4, than when a particular surface ensemble of metal atoms is required, as for the dissociation of CO or N_2. This topic is described in detail in the final sections of this chapter.

10.2
The Elementary Quantum-Chemical Model of the Surface Chemical Bond

We will formulate the Newns–Anderson model within the language of molecular orbital theory. When the adsorbate is represented with a single s-atomic orbital, the Newns–Anderson model can be understood as sketched in Figure 10.1a and b [17, 18]. We consider the case where the highest occupied metal valence orbital, the Fermi level, has the same energy as an electron in the isolated adsorbate orbital. Figure 10.1a illustrates the situation when the adsorbate only weakly interacts with the surface.

When chemisorption can be considered as a weak disturbance, the electron densities of adsorbate and surface orbitals will be hardly affected. Then, for an adsorbate with one atomic orbital, the interaction energy, ΔE_a, can be calculated using Fermi's golden rule expression [19]:

$$\Delta E_a = 2\int_{-\infty}^{E_F} \mathrm{d}E\, \rho_m(E)\, |<\varphi_a|H_{int}|\psi_E>|^2\, \delta(E-\alpha) \tag{10.1}$$

In Eq. (10.1), $\rho_m(E)$ is the surface electronic density of states. H_{int} the interaction Hamiltonian, φ_a the adsorbate atomic orbital, ψ_E a metal surface orbital, and α the energy of an adsorbate orbital. The tight-binding overlap energy between adsorbate and surface atomic orbital is described as β' and that between two metal atomic orbitals as β. As the adsorbate atomic orbital energy equals the Fermi level energy and metal orbitals are half-filled, a simple expression results for the interaction energy:

$$\Delta E_a \approx -2\beta'^2 \rho_m(E_F) \tag{10.2a}$$

Relation Eq. (10.2a) gives the adsorbate interaction energy as a function of the surface local density of states (LDOS) $\rho_m(E_F)$. For a cubic lattice with metals that contribute one s-atomic orbital per metal atom to a first approximation, the LDOS can be considered independent of electron energy and is given by van Santen [17]:

$$\rho_m(E_F) \approx \frac{1}{4\sqrt{N_s}|\beta|} \tag{10.2b}$$

Equation (10.2a) expresses the interaction energy in terms of the tight-binding overlap energy β' and the surface atom LDOS $\rho_m(E_F)$. This local electronic density of states is considered independent of the energy and is the inverse of the surface metal atom local electron density bandwidth W_{metal} of Figure 10.1. The dispersion of the surface electron energies is due to the delocalization of the metal electrons and proportional to the square root of the number of surface atom neighbors N_s and the metal atom–metal atom overlap energy β. The originally discrete atomic orbital energy of the adsorbate becomes Lorentzian broadened with width W_a:

$$W_a = \frac{2\beta'^2}{\sqrt{N_s}|\beta|} \tag{10.3}$$

This broadening is due to the slight delocalization of the adsorbate electrons by interaction with the surface metal atom. This interaction increases with the square

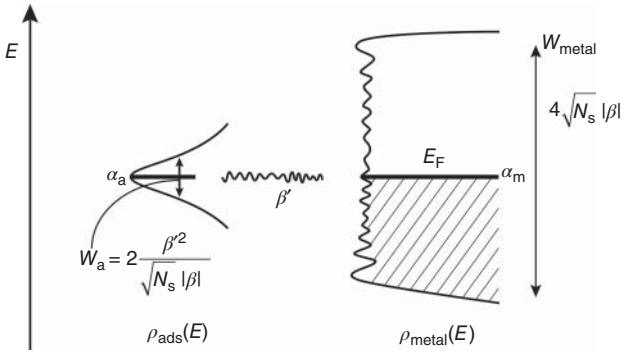

(a)

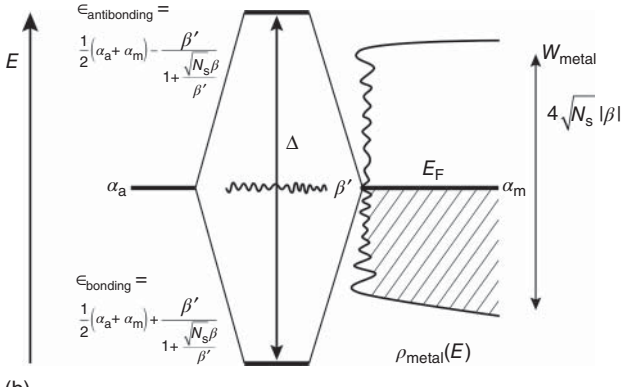

(b)

Figure 10.1 Elementary quantum-physical view of the surface chemical bond. Schematic illustration of the electronic structure of the adsorption complex that consists of an adatom atomic orbital of energy α_a that interacts with overlap energy β' with a surface atom that is part of a simple cubic lattice. The surface electron density of states is represented by $\rho_{metal}(E)$. It has a bandwidth W_{metal}. The surface metal band bandwidth is related to the number of surface metal atom neighbors N_s and metal atom–metal atom overlap energy β. The atomic orbital energy of metal atom α_m is assumed to be equal to that of the adsorbate. The metal valence band is half filled with electrons. E_F is the Fermi level, the energy of the highest occupied metal orbital. Symbols are explained in text. (a) Weak adsorption limit. $\rho_{ads}(E)$ is the adsorbate local density of states (LDOS) that results from the interaction with the surface. W_a is the bandwidth of adatom LDOS; (b) Surface molecule complex limit. Δ is the difference in energy of the bonding and antibonding surface fragment orbitals, $\epsilon_{bonding}$ and $\epsilon_{antibonding}$ are their respective energies.

of β' and is counteracted by the energy cost to localize surface electrons to pair with the adsorbate electron. The broadened adatom electron density can be considered to consist of a small band of occupied bonding orbitals with electron energies below the center of the of $\rho_{ads}(E)$ and unoccupied antibonding orbitals above this position.

When the overlap energy β' increases, the adatom local electron density of states bandwidth increases gradually until a limiting value of β' is crossed. This is called the *surface molecule limit* [18]:

$$|\beta'| > \sqrt{N_s}|\beta| \tag{10.4}$$

As indicated in Figure 10.1b, beyond this value two discrete new energy levels appear. The low orbital energy represents a bonding molecular orbital that develops between adatom and interacting surface atom, the higher orbital corresponding to the related antibonding orbital. The difference, Δ, between these orbitals is a measure of the effective interaction energy between adatom and metal surface:

$$\Delta = \frac{2|\beta'|}{1 + \frac{\sqrt{N_s}\beta}{\beta'}} \tag{10.5}$$

Equation (10.5) shows that Δ becomes larger when the interaction β' of adsorbate with the metal surface increases. In the extreme limit of very large β', one notes that the interaction energy is simply 2 β'. This is the well-known molecular orbital energy expression for the attractive interaction between two atomic orbitals of the same energy that each contributes one electron. The correction term to this value relates to the energy cost to localize an electron on the surface atom that interacts with the adsorbate. The larger the degree of electron delocalization of the surface electrons, the weaker the surface complex interaction energy becomes. The interaction energy increases with increasing degree of coordinative unsaturation of the surface metal atomic orbitals, because the electrons then become more localized.

We now discuss how the adsorption energy changes with increasing electron occupation of the surface valence electron band. According to the quantum chemists' view, this change relates to a change in distribution of electron occupation over bonding or antibonding surface–adsorbate fragment orbitals.

The bonding and antibonding nature of such molecular orbital fragments can be deduced from the overlap population density of states (OPDOS), which is defined as [9]:

$$\begin{aligned}\pi_{ij}(E) &= \sum_n < \varphi_i|\psi_n > | \ \delta(E - E_n) < \psi_n|\varphi_j > \\ &= \sum_n c_i^n c_j^n \ \delta(E - E_n)\end{aligned} \tag{10.6}$$

In Eq. (10.6), c_i^n is the coefficient of orbital φ_i in molecular orbital ψ_n. The molecular orbitals ψ_n are eigensolutions of the adsorbate–surface molecule secular equation with eigenvalue E_n, which are the molecular orbital energies. The OPDOS measures the phase relation of wavefunctions delocalized over different atoms as a function of molecular orbital energy. π_{ij} is positive when an orbital fragment between two atoms is bonding and negative when it is antibonding.

The bond order overlap population (BOOP) is defined as the sum of the occupied corresponding OPDOS matrix elements [9]:

$$P_{ij} = 2\int_{-\infty}^{E_F} \mathrm{d}E\, \pi_{ij}(E) = \sum_{k=1}^{\mathrm{occ}} n_k c_i^k c_j^k \tag{10.7}$$

n_k is the electron orbital occupation. The BOOP, as defined here within the framework of molecular orbital theory, can be considered the quantum-mechanical equivalent of bond order, in the way it was defined by Pauling [10]. In case the periodicity of the metal molecular orbitals is explicitly considered, the BOOP is equivalent to the crystal orbital overlap population defined by Hoffmann [9].

For the two limiting cases of Figure 10.1, the OPDOS function π_{01} between interacting adsorbate orbital and surface atomic orbital is sketched in Figure 10.2a and b.

One observes that at the lower valence electron energy, the nature of the fragment molecular orbitals is bonding. At higher energies, π_{01} indicates a change in the fragment molecular orbital from bonding to antibonding character. It implies that

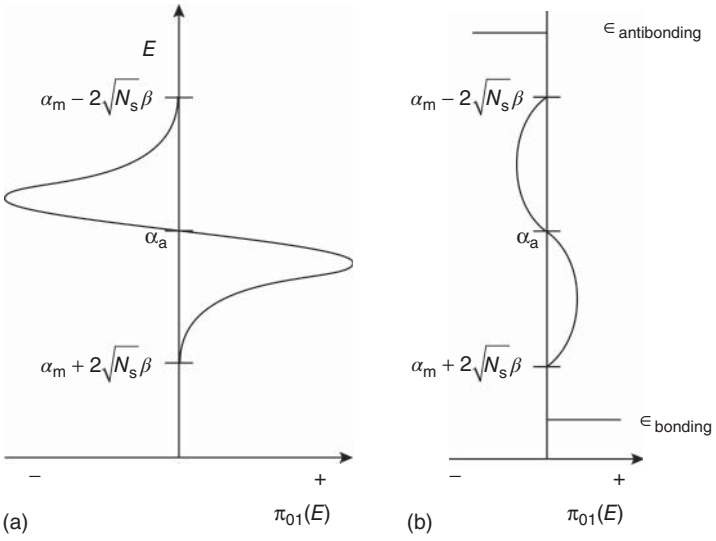

Figure 10.2 Schematic illustration of overlap population density of states (OPDOS) of the electronic structure of the same adsorption model as in Figure 10.1. In the tight-binding adsorption model, one s-type adsorbate atomic orbital interacts with surface atom of a cubic s-atomic orbital metal lattice. β is overlap energy of metal atomic orbitals; β' the overlap energy between adsorbate atomic orbital and surface atom atomic orbital, Ns is the coordination number of the metal surface atom. αa is the energy of adsorbate atomic orbital, αm is the energy of metal atomic orbital. (a) OPDOS π01(E) for the weak adsorption limit: $\frac{\beta'^2}{N_s\beta^2} \ll 1$. (b) OPDOS $\pi_{01}(E)$ for surface molecule limit: $\frac{\beta'^2}{N_s\beta^2} \gg 1$. $\in_{bonding}$ and $\in_{antibonding}$ are the discrete eigenenergies of the adsorption complex [18].

there is a maximum electron orbital occupancy beyond which further occupation of the fragment molecular orbitals weakens the chemical bond and hence the adsorption energy will decrease. The highest molecular orbital that is occupied in the surface complex has an energy that cannot exceed the Fermi level of the electrons in the bulk of the metal. Otherwise, there would be no equilibrium between bulk metal electrons and the electrons of surface complex.

In the particular example chosen, the maximum attractive energy is found when the metal atomic orbitals are half-filled. Upon a further increase of the electron density per metal atom, antibonding surface fragment orbitals become occupied and the interaction energy will decrease. Interestingly, in the case of the simple cubic lattice also, the cohesive energy of the metal has a maximum when the electron occupancy per metal atom exceeds half of its capacity, because in the metal antibonding metal orbitals become occupied as well.

The model illustrates the reason for the generally observed decrease in adsorption energy of an adsorbate to a transition-metal surface when, in a row of the group VIII metals of the periodic system, the d-valence electron count is increased beyond five electrons per atom. When the d-valence electron band is half-filled, the cohesive energies of the corresponding metals are also the maximum.

10.3
Quantum Chemistry of the Surface Chemical Bond

10.3.1
Adatom Adsorption Energy Dependence on Coordinative Unsaturation of Surface Atoms

Here, we analyze the electronic details of the surface chemical bond based on state-of-the-art DFT electronic structure calculations [5]. We address the relation between bond energy of the adatom as a function of its coordination number N_c with the surface atoms as well as coordinative unsaturation of the surface atom, defined by its coordination number with neighbor metal atom N_s. We illustrate this in a detailed discussion of the chemisorption of a C atom to different surfaces of Ru. In the DFT calculations, the surface is modeled as a metal slab chosen with enough metal layers that energies become independent of layer thickness. The surface atom positions and distances change slightly in contact with the adsorbate, because of the weakened metal atom–metal atom bond by interaction with the adsorbing atom.

It is important to distinguish first-shell coordination of the adsorbate and second-shell coordination number of surface atoms with surrounding metal atoms, as is shown in Table 10.1.

In Table 10.1 [3], a comparison is made of computed adsorption energies of C atoms attached at different sites on different surfaces of Ru. The energies have been ranked according to the coordination number N_c of the C atom, which is the first number in the fourth column of Table 10.1. The number within brackets in

Table 10.1 Adsorption energies (in kJ/mol) with respect to C gas phase and Ru(0001) bare surface.

Surface	Site	E_{ads} (kJ mol^{-1})	$N_{neighbors}$ of Ru for C (and for Ru)
Ru(0001)	Top	497	1 (9)
	Bridge	631	2 (9)
	Hollow hcp	688	3 (9)
	Hollow fcc	648	3 (9)
Ru(11$\bar{2}$0)	Top up	549	1 (7)
	Top down	675	3 (7) + 1 (11)
	Bridge short	666	2 (7)
	Bridge long	579	2 (7) + 2 (11)
Ru(1010)	Hollow	678	2 (11) + 1 (7)
Ru(1015)	hcp	714	2 (7) + 1 (9)

DFT/VASP calculations [5], with PW91 functional.
(Reproduced with permission from I. Ciobica and R. A. van Santen, 2005, unpublished.)

that column is the number of metal atom neighbors N_s of the metal atom(s) in contact with the adsorbed C atom.

A clear trend is observed: as long as the coordination number of the C atom does not change, its interaction energy will increase when the coordinative unsaturation of the metal surface atom increases. This trend predicted in the previous section is confirmed by the more rigorous quantum-chemical DFT results of Table 10.1. The adsorption energy of the C atom increases with increasing surface metal atom coordination number N_c. This relates to the C atom valency, as is discussed in detail in Section 10.3.5.

The calculations can also be used to analyze the electronic differences that cause the dependence law of the chemisorption energy of adatoms as a function of metal atom coordination N_s.

Figure 10.3 compares for the C atom adsorbed atop of a Ru atom of the Ru (0001) surface the changes in local and partial densities of states of the valence electrons with that for threefold adsorbed C.

Figure 10.3 compares the partial density of states (PDOS) of the $2p_x$, $2p_y$, and $2p_z$ atomic orbitals on the adsorbed C atom and that of the 4d-valence atomic orbitals on Ru for the one- and threefold adsorption sites of the Ru(0001) surface. The PDOS is defined as

$$\rho_i(E) = \sum_n < \varphi_i|\psi_n > \delta(E - E_n) < \psi_n|\varphi_i > \\ = \sum_n |c_i^n|^2 \, \delta(E - E_n) \qquad (10.8)$$

The LDOS is this function $\rho_i(E)$ summed over all atomic orbitals on a particular atom.

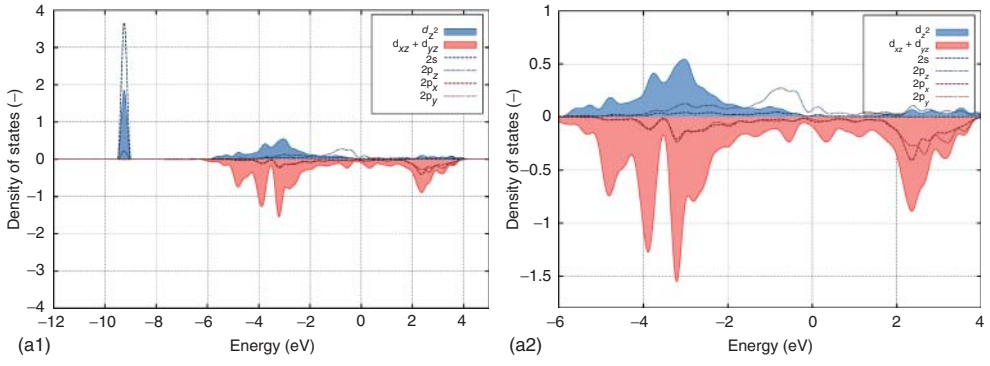

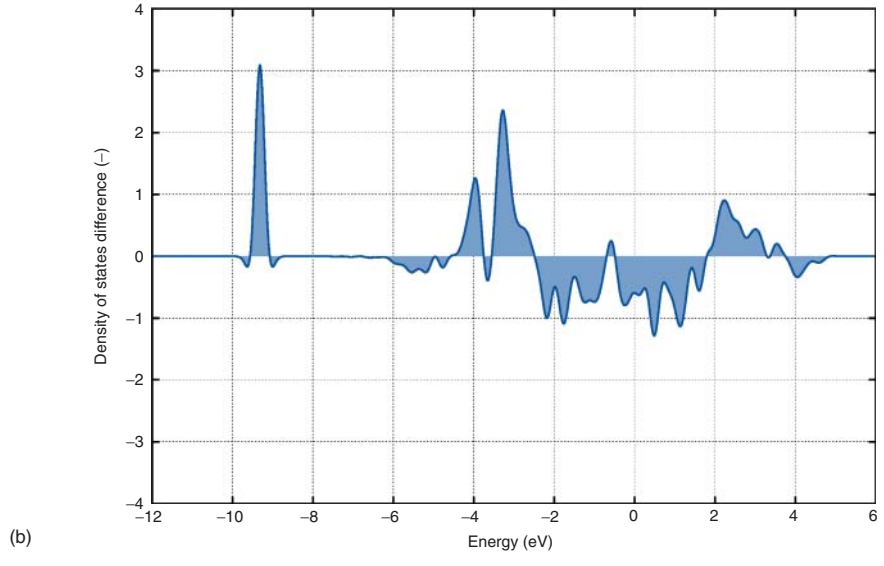

Figure 10.3 The changes in partial densities of states (PDOS) for a C atom adsorbed atop and threefold to the Ru(0001) surface according to DFT (VASP) computations with PBE functional. (a) PDOS of surface atom and adsorbate atomic orbitals of C atom adsorbed atop (a2) is partial blow up of data also presented in (a1). (b) D-valence electron difference plots of surface atom with and without atop adsorbed C atom. (c) PDOS of surface atom and adsorbate atomic orbitals of C atom adsorbed threefold (c2) is partial blow up of data also presented in (c1). (d) D-valence electron difference plots of surface atom with and without threefold adsorbed C atom. (e1) PDOS of the valence electrons of a bulk Ru atom; dark areas denote electron occupied density; (e2) PDOS of the valence electrons of the Ru (0001) surface atom (I.A.W. Filot and R.A.V. Santen, 2013, unpublished), dark areas denote electron occupied density.

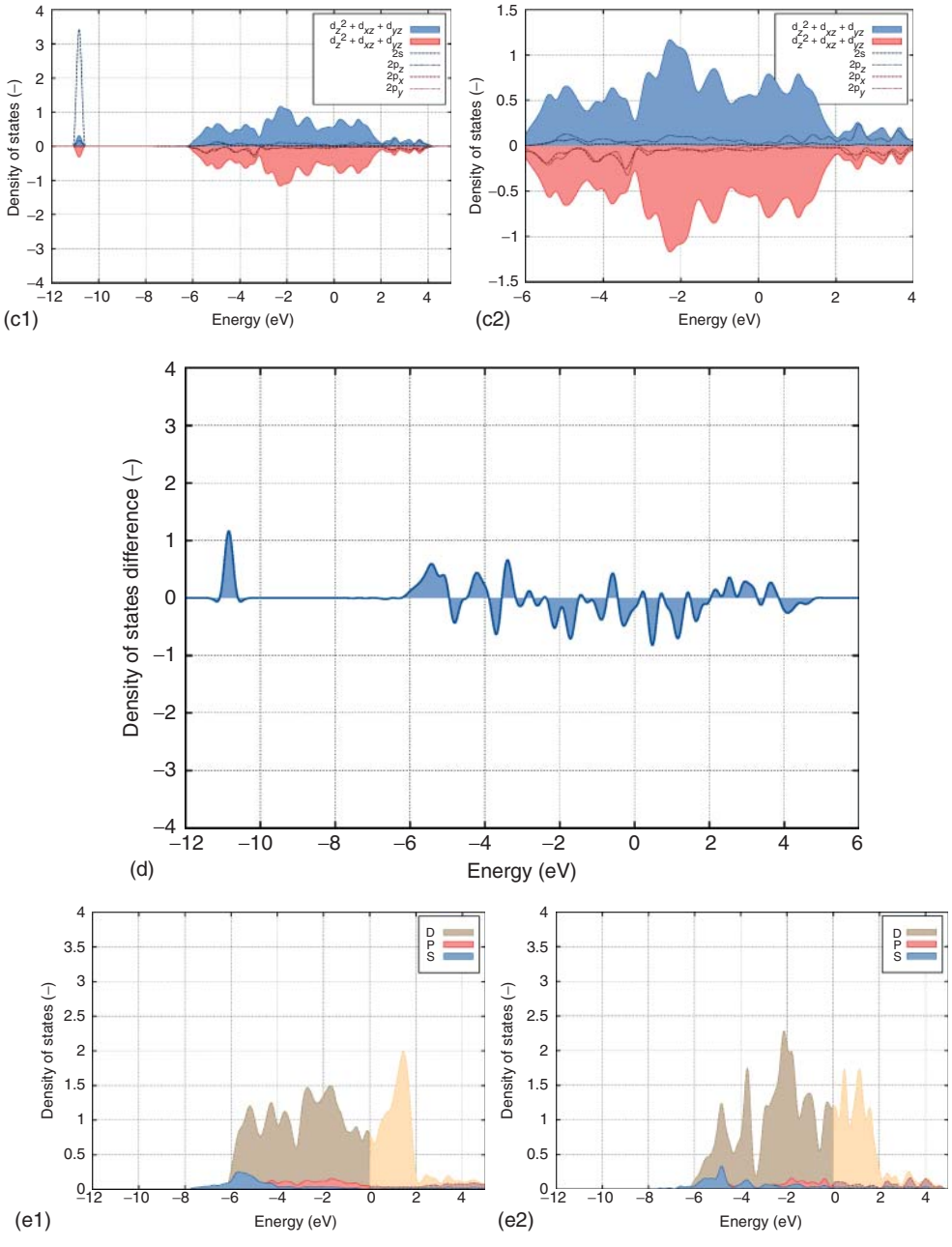

Figure 10.3 (*Continued*)

The partial local electron densities of the C atom adsorbed atop are shown in Figure 10.3a. In Figure 10.3b, the corresponding change in d-valence electron distribution between that before and after adsorption is shown. In Figure 10.3c and d, a similar comparison is made for the case of threefold adsorbed C. Figure 10.3e shows the PDOS of the valence electron densities on the bulk metal atom and that on the surface atom.

The difference between the PDOS of the free surface (Figure 10.3e2) and that of the surface atom in contact with the C atom is striking (Figure 10.3a and b). Most interesting are the changes around the Fermi level. When in Figure 10.3a and b one studies the density changes below the Fermi level, a large downward-shifted density increase in the PDOS of the d-valence electrons is observed. This is followed by a decrease in d-valence electron density over an energy regime of several electron volts around the Fermi level, and then at above 2 eV there again is an increase in PDOS. These are indications of the formation of bonding and antibonding surface fragment orbitals.

In Figure 10.3a, below the d-valence electron band, the sharp peak around −9.3 eV relates to the interaction of the σ symmetric $2p_z$ and s atomic hybridized C orbital. Its character is mainly 2s. As can be seen in Figure 10.3c, it is part of a bonding molecular surface fragment orbital, which is shifted lower when C adatom coordination increases. The corresponding antibonding surface density fragment appears as a highly broadened feature in the d-valence electron band regime.

A peak that corresponds to the nonbonding σ symmetric mainly $2p_z$ orbital is found around −1 eV. This orbital is available for reaction of an H atom, when CH_{ads} would be formed.

The bonding and antibonding surface PDOS contributions due to interaction with the C-$2p_x$ and C-$2p_y$ orbitals appear as density maxima at −3.5 and + 2.5 eV. This part of the density of states representation looks very similar to the sketched situation in Figures 10.1b and 10.2b, which represents the surface molecule limit within the Newn–Anderson model. In Figure 10.3a, the PDOS at −3.5 eV can be identified with the bonding surface fragment orbitals with a significant contribution of the $2p_x$ and $2p_y$ atomic orbitals of the adsorbed C atom. The corresponding antibonding PDOS is found around +2.5 eV. The d-valence electron density in between switches from bonding to antibonding character. The attractive contributions to the adsorbate bond are to a significant extent determined by the population of bonding π symmetric orbital interactions.

The PDOS distributions, as shown in Figure 10.3a, will be very similar when different metals are studied. When metals with different valence electron occupation are compared, the relative position of the Fermi level, defined in Figure 10.3a as the 0.0 eV position, will change. When the d-valence electron occupation increases, the Fermi level will shift to the right, and a larger fraction of antibonding surface fragment orbitals will become occupied. This explains, for instance, the decrease in C adsorption energy when adsorption to Ru, Rh, and Pd is sequentially compared (Section 10.3.3).

The PDOSs of the threefold adsorbed C atom in Figure 10.3c shows a bonding contribution of σ symmetric surface fragment orbitals at the lower value of −11 eV.

This increases the interaction energy. The nonbonding $2p_z$ contribution overlaps with the d-valence electron density and is spread over a large energy interval.

The PDOSs of the π-symmetric surface orbital fragments show also a stronger interaction in the threefold adsorption site. The bonding density of states is shifted to lower energies, which will give a larger contribution to the attractive interaction. A larger fraction of the antibonding orbital density of states now appears above the Fermi level. As one notes, especially for the d-valence electron density difference plot of Figure 10.3d, the energy gap between bonding and antibonding orbitals surface fragment electron density has increased. This energy gap is a measure of the strength of the covalent interaction. As we discuss in Section 10.3.4, this increase is approximately proportional to the square root of the adsorbate coordination number. The attractive interaction with the C atom $2p_x$ and $2p_y$ orbitals has thus become stronger.

The comparison in Figure 10.3e of the PDOS of bulk and surface Ru atoms shows expected changes in the d-bandwidth W as well as a change in the average energy of the d-valence electron band electrons $\overline{\epsilon}_d$. As can be seen from Table 10.2, there is a decrease in the bandwidth on the surface atom by 1.52 eV and a small shift $\Delta\overline{\epsilon}_d$ of 0.39 eV upward of the average density of states energy of the occupied d-valence electrons. The upward shift of the d-valence electrons is related to increased localization of the valence electrons, which is accompanied by a small change in the electron occupation of the d-valence electron band at the surface. Narrowing of the d-valence electron band decreases the unoccupied fraction of the valence electron density for metals with a valence electron band that is more than half-filled. The increased electron occupation of the d-valence electrons that results increases the average repulsive energy between the electrons in the atomic orbital concerned. Hence, the atomic orbital energy contribution to the molecular orbital energy shifts to higher energy. The resulting upward average energy shift reduces electron transfer between surface and bulk [18, 20], so that bulk and surface chemical potential remain in equilibrium.

Table 10.2 Comparison of average d-valence electron energies ($\overline{\epsilon}_d$), d-valence electron band width (W), and adsorption energies of C (E^C_{ads}).

N_s	$\overline{\epsilon}_d$ (eV)	W (eV)	E^C_{ads} (kJ mol^{-1})
12	−2.94 (−1.83)	4.58	–
9	−2.55 (−1.62)	4.06	−657
7	−2.19 (−1.39)	3.60	−705

$\overline{\epsilon}_d$ and W are compared for bulk Ru atom, Ru atom of (0001) surface, and (1120) surface, respectively. C is adsorbed atop to Ru(0001) and Ru(1120) surface, respectively. $\overline{\epsilon}_d$ with brackets is average energy for full valence bond, without brackets of occupied valence electrons. DFT/VASP calculations [5] with PBE functional
I.A.W. Filot and R.A.V. Santen, 2013, unpublished.

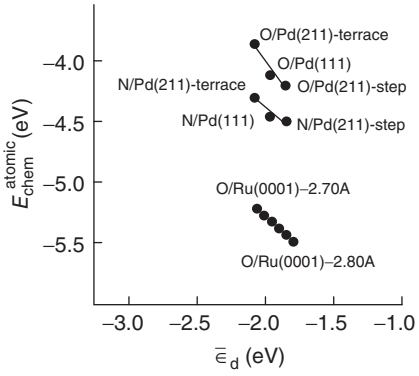

Figure 10.4 Atomic (E_{chem}^{atomic}) binding energy as a function of the d-band center $\bar{\epsilon}_d$, the average position of the d-valence band of the metal surface. For the Ru (0001), density of states has been changed by altered Ru–Ru distances. (Adapted from Ref. [21]).

In an early paper, Nørskov *et al.* [21] noted the relation between this upward d-valence electron band position and the increase in adsorption energy that is illustrated in Figure 10.4.

A comparison of the changes in PDOS for C adsorbed to the Ru(0001) surface and C adsorbed atop of the Ru (1120) surface will indicate the relative importance of average d-valence electron energy differences versus d-bandwidth changes. In Figure 10.5, changes in d-valence band PDOS are shown for the C atom adsorbed atop a Ru atom of the Ru(1120) surface.

Comparison of Figures 10.5c and 10.3e illustrates the contraction of the d-valence electron density width for the more coordinatively unsaturated metal surface atom. As Table 10.2 shows, the average d-valence electron band energy shifts further upward. Figure 10.5a and b again demonstrate the similarity of chemisorption with the surface molecule limit. Bonding and antibonding surface fragment orbitals are formed between carbon atom $2p_x$ and $2p_y$ atomic orbitals and surface d-valence electrons. In agreement with the predictions of the Newns–Anderson model, the difference in energy between the bonding and antibonding electron densities is now larger than that for adsorption to the less coordinatively unsaturated Ru(0001) surface. For the case $N_s = 7$, this difference $\Delta = 6.4$ eV can be compared with the $N_s = 9$ case with a Δ of 5.7 eV. In Figure 10.5a and b, the d-valence electron density near the Fermi level is shifted downward by −2.5 eV. This is more than the d-valence electron shift of −1.5 observed in Figure 10.3a and b when the C atom is adsorbed on the Ru(0001). The increased adsorption energy on the coordinatively unsaturated atom is reflected in this larger downward-shifted d-valence electron density near the Fermi level. It represents increased stability because of the lower energy of the bonding surface fragment orbital of the interacting C $2p_x$ and $2p_y$ atomic orbitals with transition-metal d-valence atomic orbitals. There is essentially no change in the interaction with the C-2s electrons, and interaction with the $2p_z$ orbital remains nonbonding.

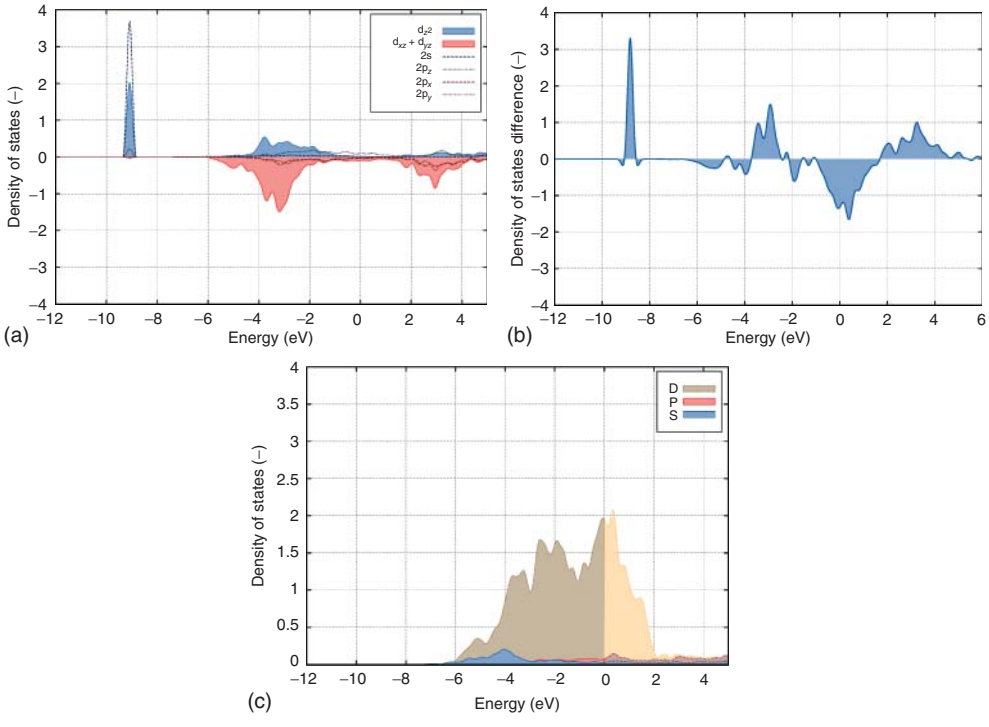

Figure 10.5 (a) PDOS of Ru(1120) surface atom with C atom adsorbed atop; (b) PDOS difference of C atom adsorbed atop on Ru(1120) surface and free Ru(1120) surface; (c) PDOS of Ru atom of Ru(1120) surface, dark areas indicate electron occupied valence bands, light areas indicate non electron occupied valence bands (I.A.W. Filot and R.A.V. Santen, 2013, unpublished).

One concludes that bonding is covalent. When surface atom coordination changes, the increased localization of the electrons is responsible for increased adsorption energies. The actual position of $\overline{\epsilon}_d$ is not of dominating importance, it merely reflects the decrease in d-valence band width W. The Newns–Anderson model applies and the chemical bond in the surface complex approximates the surface molecule limit.

Electronic interactions are very different when surface chemical bond formation is dominated by interaction with adsorbate orbitals that do not overlap with the d-valence electron band energy. This becomes relevant when molecular fragments dominated by bonding with strong σ bonds adsorb. We discuss this explicitly in Section 10.3.4 for adsorption of ammonia. In this case, the average d-valence electron band position $\overline{\epsilon}_d$ is found to be important.

In Section 10.3.2, we study the dependence of adatom adsorption energy on the position of the metal in the periodic system.

10.3.2
Adatom Adsorption Energy as a Function of Metal Position in the Periodic System

The elementary model of the surface chemical bond introduced in Section 10.2 indicates that changes in the electron occupation in the surface valence electron band will affect the strength of the surface chemical bond. It alters the distribution of electrons over the bonding and antibonding surface fragment orbitals formed upon chemisorption.

This is highlighted by Tables 10.2 and 10.3 that show DFT-computed adsorption energies of C and O atoms, respectively, on the dense surfaces of the group VIII and IB metals of the periodic system. The structures of the surfaces considered are the same as well as the coordination of the adsorbed atoms.

For both adatoms, when moving to the left along a row of the periodic system of the group VIII transition metals, there is a trend of increasing adsorption energy. This trend is in parallel with the decreasing d-valence electron occupation of the metals considered.

We have described in the previous paragraphs that the adatom chemical bond becomes more attractive when bonding surface fragment orbitals become occupied with electrons, but that the adsorption energy decreases when antibonding surface fragment orbitals become occupied. When the d-valence electron occupation changes, this will affect the relative distribution over the bonding as well antibonding surface fragment orbitals. For the group VIII metals of the periodic systems, the Fermi level is located within the antibonding part of the surface–adatom LDOS. Hence, a decrease in bulk d-valence electron density will increase the attractive part of the adsorption energy.

The change in adsorption energies is sensitive to valence band occupation rather than the change in surface metal atom LDOS $\rho_m(E_F)$ because chemisorption behaves according to the surface molecule limit. The interaction strength of adsorbate with surface is large compared to the fluctuations in surface metal electron density of states. Therefore, changes in the adsorbate bond energy relate rather to changed occupation of bonding and antibonding surface fragment molecular orbitals.

A comparison of the changes in adatom adsorption energies of C and O in a column of the periodic system shows different trends. C binds more strongly

Table 10.3 DFT/VASP-calculated adsorption energies of atomic C on surfaces of (111) structure as a function of metal position in the periodic system.

	Fe[a]-769 (−695)	**Co-668**	**Ni-629**	**Cu-476**
	Ru-688	Rh-690	Pd-645	Ag-338
Re-713	Os-696	Ir-675	Pt-657	Au-411

PW91 functional, energies in kilojoules per mole.
[a]hcp and fcc, not bcc.
Reproduced with permission from (I. Ciobica and R. A. van Santen, 2005, unpublished) [3].

to Pt than Ni, whereas this is reverse for the more electronegative oxygen. These differences will be used to illustrate that in addition to d-valence electron occupation, differences in electron affinity, with important consequences for interaction with the s,p valence electron band, as well as differences in the spatial extend of the d-valence electrons are also important [9].

From right to left in a row of the periodic systems, the ionization potential of the metal atom or workfunction of the corresponding metal decreases and the spatial extent of the d-valence electrons also increases. Moving down in a column of the periodic system, the metal workfunction tends to increase as well as the spatial extent of the d-valence electrons. The position of the d-valence band is also affected by the altered screening when f-electron atomic orbitals become occupied [9].

The adsorbed state can be considered as formed in a two-step process; an interaction with the free valence electrons of the metal surface, mainly described by the valence s and p atomic orbitals followed by the interaction with the d-valence electrons [22–24]. In the first step of this process, partially occupied adatom orbitals become occupied; in the second stage of this process, the interaction evolves with the metal d-valence band, that is, the main interaction responsible for differences between metal surfaces.

The occupancy of the free-electron valence band, built mainly from s- and p-valence atomic orbitals can be considered close to constant with one electron per metal atom. This is due to hybridization of the atomic orbitals by formation of the metal atom–metal atom bonds. Within free electron theory, its energy is mainly determined by the density of the metal atoms [25]. When an adatom adsorbs, the charge density on the adatom adjusts so that the chemical potential on the adatom becomes equal to that at the surface. When the adatom orbital is half occupied, this results in an attractive interaction because of electron transfer to the adsorbate. When the adatom orbital is doubly occupied, the interaction becomes repulsive, because of the increase in electron kinetic energy due to the Pauli electron exclusion rule [25]. The interaction with adatoms is rather independent of the coordination of the adatom with the surface.

The difference in adsorption energy trends of C and O in a column of the periodic system can be used to illustrate the contributions of the two different types of interactions. Interaction between free valence electrons and adatom gives initial electron transfer between adsorbate and surface electrons, which equalizes the electron chemical potential. O_{ads} will get a higher charge than C_{ads} and therefore will more strongly interact with the surface of lower workfunction (ionization potential). The atom in this state then is considered to interact with the metal d-valence band. The lower energy of the valence O_{ads} 2p atomic orbitals compared to that of the C_{ads} 2p atomic orbitals, with respect to Fermi level, implies a weaker covalent interaction. In the case of O_{ads}, a larger fraction of antibonding surface fragment orbitals will be occupied. As the spatial extent of the d-valence atomic orbitals of Pt is larger than that of Ni, the covalent contribution is more important for Pt than for Ni. This explains, for instance, the stronger interaction energy of O_{ads} to Ni compared to that of Pt, but the reverse order for C_{ads} (Tables 10.3 and 10.4). Interestingly, CO_{ads} follows the trend of C_{ads}.

Table 10.4 DFT/VASP-calculated adsorption energies of atomic O on surfaces of (111) structure as a function of metal position in the periodic system.

	Fe[a]-714 (−640)	Co-550	Ni-496	Cu-429
	Ru-557	Rh-469	Pd-382	Ag-321
Re-634	Os-533	Ir-428	Pt-354	Au-270

PW91, functional, energies in kilojoules per mole.
[a]hcp and fcc, not bcc.
Reproduced with permission from (I. Ciobica and R. A. van Santen, 2005, unpublished) [3].

10.3.3 Molecular Adsorption; Adsorption of CO

As an example of molecular adsorption, we provide in this section a detailed discussion of the chemisorption bond of CO adsorbed to a transition-metal surface.

There is an essential difference between adsorption of an atom and that of a molecule. The attractive part to the chemical surface bond with an adatom is mainly due to interaction of the partially occupied (2p) adatom atomic orbitals. In the case of molecular adsorption, the attractive part to the molecular surface chemical bond is due to the interaction with the doubly occupied highest occupied molecular orbital (HOMO) and the empty low-lying lowest unoccupied molecular orbitals (LUMOs).

For CO, its HOMO is the lone pair 5 σ orbital and its LUMOs are the unoccupied 2 π* orbitals. Elementary chemical bonding theory describes the interaction with a molecule as CO only through chemical bonding contributions through its HOMO and LUMOs. We will see that this is a rather approximate view of the surface chemical bond, because of the important hybridization that occurs in the adsorbing molecule.

The interaction with the 5 σ orbital is called *donative*, because this doubly occupied orbital can only donate electrons to the solid; the interaction with the empty 2 π* orbitals is backdonative. It can only accept electrons. This chemical bonding scheme is basic to the Chatt–Duncanson–Dewar chemical bonding view of bonding of CO with a metal atom in carbonyl complexes [26, 27] or the related Blyholder view when applied to surfaces [28].

A consequence of the Blyholder model for adsorption of CO to a surface is that the attractive interaction with surface valence orbitals will decrease for the donative interaction when the receiving metal valence electrons increase electron occupation, but for the backdonative interaction it will increase. Changes in d-valence electron occupation thus tend to have a counteracting effect on the overall interaction energy changes. This is well illustrated by Figure 10.6, which compares the changes in adsorption energies of CO with that of the sum of the corresponding adatom energies of C and O that are generated upon dissociation. A comparison is made for CO dissociation on different metal surfaces that have the same structure. The change in the sum of adatom energies is much larger than that in the molecular

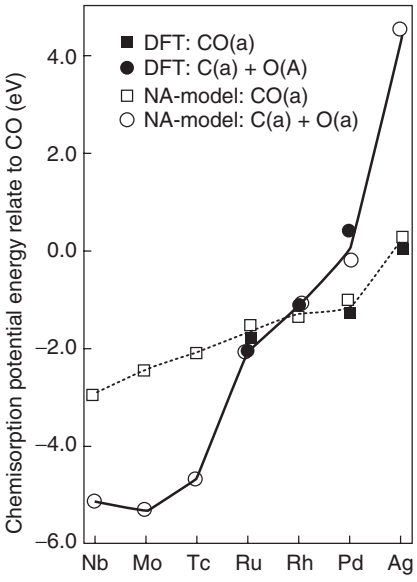

Figure 10.6 Calculated variation in the adsorption energy of molecular CO compared with atomically adsorbed C and O for close-packed surfaces of the 4d transition metals. Solid symbols are DFT calculations; open symbols are Newns–Anderson model effective medium calculations. (Adapted from Ref. [24]).

adsorption energies. So, the reactivity of the metal surface will correlate primarily with the sum of the adatom energies generated upon molecular bond cleavage!

In contrast to the preference for high coordination of adsorption of atoms as C, O, or N, the CO molecule generally prefers low-coordination sites. This is due to the different preferences of the HOMO and LUMO interactions for low and high coordination, respectively. The chemical bonding aspects that are basic to this phenomenon are discussed in detail in the next part of this subsection and also the following section on surface group orbitals.

It appears that the DFT method does not always predict the relatively small energy differences that determine coordination of CO to a transition-metal surface properly. There is often a bias for higher coordination than experimentally found. This is mainly because it does not calculate the balance of donating and backdonating interactions properly. In Table 10.5, the column labeled 'Site' indicates with an asterisk the experimentally observed site preferences for low surface coverage. The calculated energies of adsorption that are given in columns 2 and 3 of Table 10.5 are discussed in detail subsequently. One notes that in order to properly predict the preferred site, the accuracy of the calculation has to be at least 5 kJ mol^{-1}. The differences in adsorption energies on different metal surfaces are larger. As expected, again the adsorption bond energy increases with decreasing surface metal atom coordination or decreasing d-valence electron occupancy when transition metals are compared in the same row of the periodic system.

Table 10.5 Results of linear regression corrections of chemisorption energy versus singlet–triplet splitting energy.

Surface	Site	E_{chem}^{GGA}	E_{chem}^{corr}
Pt(111)	Top*	1.717	1.560
	Bridge	1.758	1.433
	Hcp	1.793	1.397
	E_{t-h}	−0.076	0.164
Rh(111)	Top*	1.866	1.673
	Bridge	1.920	1.581
	Hcp	2.059	1.644
	E_{t-h}	−0.193	0.030
Pd(111)	Top	1.385	1.247
	Bridge	1.784	1.487
	hcp*	1.962	1.602
	E_{t-h}	−0.577	−0.355
Cu(lll)	Top*	0.746	0.621
	Bridge	0.822	0.576
	Hcp	0.889	0.610
	E_{t-h}	−0.143	0.011
Pt(100)	Top*	1.954	1.796
	Bridge*	2.139	1.824
	Hollow	1.698	1.246
	E_{t-h}	0.256	0.551
Rh(100)	Top*	1.905	1.723
	Bridge*	2.092	1.774
	Hollow	2.087	1.603
	E_{t-h}	−0.182	0.120
Pd(100)	Top	1.494	1.348
	Bridge*	1.927	1.641
	Hollow	1.937	1.503
	E_{t-h}	−0.443	−0.155
Cu(100)	Top*	0.830	0.703
	Bridge	0.834	0.620
	Hollow	0.831	0.441
	E_{t-h}	−0.001	0.262

The DFT-GGA values for the chemisorption energies are given, along with the corrected energies obtained by extrapolation. Positive value of E_{t-h} indicates that top site is preferred. For each substrate, the site found to be preferred by experiment is marked with an asterisk.
Adapted from Ref. [29].

Table 10.5 column 2 compares DFT data from state-of-the-art calculations on the adsorption of CO to different sites and surfaces. One notes substantial differences between predicted and experimental preference of site. These deviations relate to the inaccurate prediction of the $5\sigma-2\pi^*$ molecular energy difference of DFT methods [30].

Mason *et al*. [29] correlated DFT-calculated adsorption energies of CO with different predictions of the $5\sigma-2\pi^*$ singulet–triplet transition energies in gas-phase CO using different pseudopotentials in the calculations. They then extrapolated trends in calculated CO adsorption energies as a function of the singlet–triplet energy to that of the exact singlet–triplet excitation energy of gas-phase CO. These results are presented in the third row of Table 10.5

This idea is based on the notion that chemisorption of a molecule can also be considered as stabilization of a singlet–triplet excited molecule by electron exchange with the metal surface [31]. An electron of an occupied molecular orbital can exchange with a surface metal electron of different spin, which then has to occupy an unoccupied molecular orbital. The total charge on the adsorbed molecule changes little. The intramolecular bond is weakened, because electrons shift from bonding to antibonding molecular orbitals.

Table 10.5 compares in columns 2 and 3 the calculated adsorption energies of CO with and without the extrapolated correction. The corrections are given in column 4 of Table 10.5. The preferred adsorption site is substantially altered, and upon correction the proper minimum adsorption site is predicted.

The preference of CO to adsorb with low coordination relates to the very different coordination preferences of the donating interactions versus backdonating interactions. When doubly occupied orbitals interact with the surface, the bonding and antibonding surface fragment orbitals that are formed can both become occupied and the resulting interaction energy becomes weak or repulsive. The Pauli repulsive interaction between doubly occupied orbitals is approximately proportional to N_c, the adsorbate coordination number:

$$E_{\text{rep}}^{\text{Pauli}} = -4N_c\beta' S' \tag{10.9}$$

In Eq. (10.9), β' is the overlap energy and S' the corresponding overlap between adsorbate and surface atomic orbitals. Approximate Eq. (10.9) applies when ad molecule orbitals are s-symmetric and the metal electrons are also described by s-atomic orbital. Equation (10.9) is a familiar expression within molecular orbital theory and is deduced from tight binding theory including overlap of the atomic orbitals as in extended Hückel theory (Hoffmann) is used [9].

According to Eq. (10.9), the repulsive interaction is minimized for low-coordination adsorption. Within the Blyholder adsorption model of CO adsorption, it implies that the donative 5σ interaction becomes increasingly less attractive and may even become repulsive when the molecule adsorbs in high coordination.

In contrast, the backdonative interaction between occupied surface valence orbitals and empty unoccupied adsorbate orbitals prefers high-coordination site adsorption. In this case, mainly bonding surface fragment orbitals become occupied with electrons. The interaction is attractive and approximately proportional to $\sqrt{N_c}$ [18]; N_c is the effective coordination number of the molecular orbitals concerned.

This attractive backdonative contribution to the adsorbate bond energy increases with increasing electron occupation of the bonding surface fragment orbitals of the surface complex. This happens when d-valence electron occupancy of the

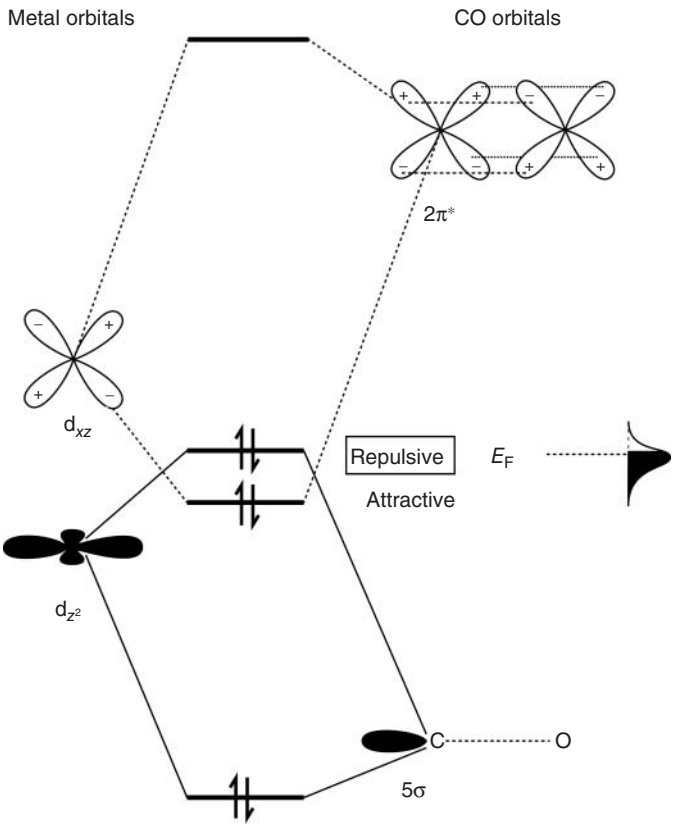

Figure 10.7 Schematic representation of the orbital interaction scheme of CO with a surface metal atom according to the Blyholder model. Only interaction is considered of the 5σ (donative) and 2π* orbitals (backdonative) of CO and d_{z^2} and d_{xz} atomic orbitals of the metal atom.

metal increases. The backdonating interaction with the 2π* orbitals belongs to this category.

The molecular orbital scheme that corresponds to the Blyholder adsorption model is schematically summarized in Figure 10.7.

In a very elementary way for atop adsorption, the interaction of CO valence orbitals with a single metal atom is indicated. The formation of bonding and antibonding surface fragment orbitals is sketched. For the σ-type surface fragment orbitals, the bonding orbitals become completely occupied. The main contribution to this fragment orbital is from the 5σ molecular orbital of CO. The corresponding antibonding orbital fragment consists mainly of the upward-shifted d-valence electrons localized on the surface metal atom. Its occupation will depend on the Fermi level of the system. When this antibonding orbital is completely occupied, the overall contribution of the σ symmetric orbital interaction will be repulsive. The electron occupancy of this σ-type antibonding orbital will decrease with a

decrease in metal d-valence orbital electron occupancy. Also, when coordinative unsaturation of the surface atom decreases, the upward shift of the average energy of the d-valence electron energy distribution would decrease electron occupancy of the σ symmetric antibonding surface orbital. It is more upward pushed and a larger fraction of its electron density becomes higher than the Fermi level. The decrease in antibonding surface fragment orbital electron occupancy will result in an increase of the overall attractive energy of the σ-type surface molecular orbitals.

For the π-type molecular surface orbitals, the bonding surface orbital fragment orbital becomes partially occupied. The corresponding antibonding π symmetric surface molecular orbital will remain unoccupied. Electron occupation of the bonding π symmetry surface fragment orbital will depend on the position of the Fermi level. For this case, when the d-valence electron occupation decreases, it will result in a decreased occupation of the bonding π symmetric surface fragment orbital, with a decrease in the attractive interaction as a result.

The changes in attractive interaction of the σ symmetric donative interaction and the π symmetric backdonating interacting are thus seen to counteract.

In contrast, they enforce each other when surface atom coordination decreases. The upward shift of the d-valence electron energy will result in a larger downward shift of the bonding surface fragment orbital with respect to the average d-valence electron band position than when the surface atom coordinative unsaturation is less. The upward d-valence electron average energy shift decreases the energy difference between molecular 2 π* orbital and surface d-valence electrons. There is an increase in the attractive interaction energy when surface atom coordinative unsaturation results.

The molecular orbital interaction scheme of Figure 10.7 is supported by the early extended Hückel calculation by Hoffmann on CO adsorption to the Ni surface [32].

We now provide a detailed orbital analysis of the interaction of CO with a Ru surface in low and high coordination based on more recent computational studies. As no periodical DFT code is available to calculate the OPDOS (Eq. (10.6)) between the surface and molecule, we compare in Figure 10.8 the OPDOSs of adsorbed CO, atop and threefold coordinated from DFT calculations on a cluster of Ru (A.L. Yakovlev and R.A. van Santen, 2005, unpublished), that gives comparable adsorption energies as CO adsorbed to the Ru(0001) surface. We compare computed orbital features on the clusters with electron density changes from periodic DFT calculations for CO adsorbed to the Ru surface in Figure 10.10. In Figure 10.8, not only the OPDOSs are shown as a function of orbital energy but also the orbitals with maximum density.

The strong CO–Ru interaction implies that bonding and antibonding orbital fragments are again separated by an energy gap and that the chemisorbed state can be described as a molecular surface complex. The orbital structures indicate substantial rehybridization of the molecular orbitals within the CO molecule. The lower bonding peaks are due to interaction of the 4σ and 5σ CO molecular orbitals with the surface, the corresponding antibonding orbitals are at −9.5,−6.5, −3, and 0 eV, respectively. As the Fermi level in these calculations is at −4.8 eV, not all of the antibonding σ symmetric orbital fragments are occupied. Comparison with

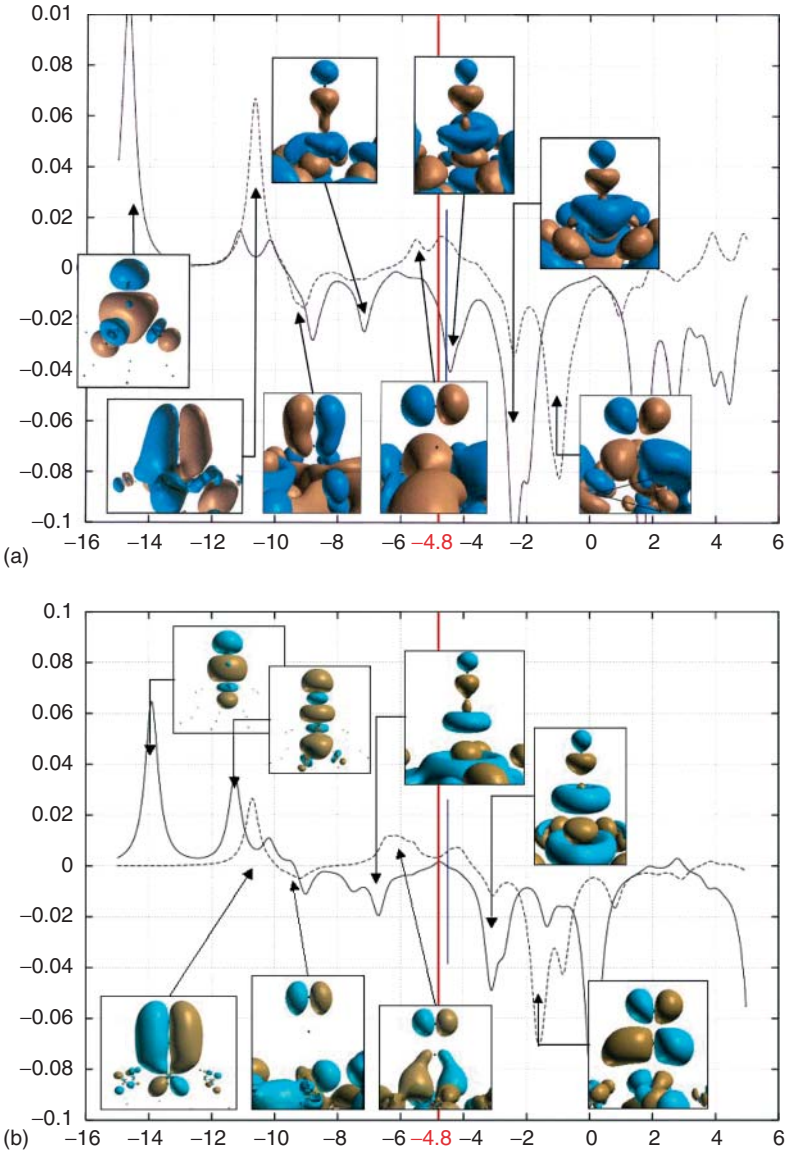

Figure 10.8 Electronic structures of CO interacting with a Ru19 cluster. Overlap population densities of states are represented of the carbon atomic orbitals of CO interacting with Ru d-valence electrons as a function of electron orbital energies. Orbital densities are shown for energies of maximum electron density. —, σ-Symmetric orbital interactions; ---, π-symmetric orbital interactions. The Fermi level is at –4.8 eV indicated in red (a) Ru19-CO, with CO adsorbed atop; (b) Ru19-CO with CO adsorbed threefold (A.L. Yakovlev and R.A. van Santen, 2005, unpublished). (Adapted from Ref. [3]).

the σ symmetric OPDOS of threefold coordinated CO indicates a decrease in the overall interaction with the σ-type orbital fragments. As for the atop adsorbed state, there is a bonding 4σ-type interaction at −14.5 eV, However, while there is a bonding 5σ-type orbital at −12 eV for atop adsorbed CO, two small bonding peaks appear around −11 eV for threefold adsorbed CO. Corresponding high-intensity antibonding σ-type fragments are observed at −8.5, −7, and −4.5 eV below the Fermi level, respectively. The corresponding antibonding σ orbital fragments above the Fermi level have also shifted to lower energies, indicative of an overall weaker interaction between the σ symmetric orbitals. It is due to the decreased overlap of the σ CO molecular orbitals and the surface in threefold coordination. The stronger interaction of the σ-type surface orbital fragments atop results in a decreased population of antibonding surface fragment orbitals and hence to a smaller repulsive or stronger attractive interaction atop. The lower energy of CO adsorbed in threefold interaction (−116 kJ mol^{-1}) versus that of CO adsorbed atop (−192 kJ mol^{-1}) is indicative of a reduced Pauli repulsive interaction between the σ-type surface fragment orbitals, as the interaction with the π symmetric orbitals is attractive. The interaction between π-type orbital fragments is much stronger in threefold coordination as observed from the higher energy of the unoccupied antibonding π fragment orbital with a significant 2π* contribution, whereas the bonding dominantly 1π contributions has a similar energy as in the atop position. One notes the low density on the C atom of CO in the energy regime −4 to −6 eV. This is the signature of strong rehybridization of the π-type molecular orbitals of CO. It results in a substantial weakening of the CO bond in threefold coordination than atop, owing to increasing occupation of the 2π* CO molecular orbital.

For the atop adsorbed state, the consequences of rehybridization are schematically illustrated by the orbital interaction schemes in Figure 10.9 [33]:

The three atomic orbitals that interact (one metal d, one carbon p, and one oxygen p) form, respectively, a bonding, nonbonding, and an antibonding surface

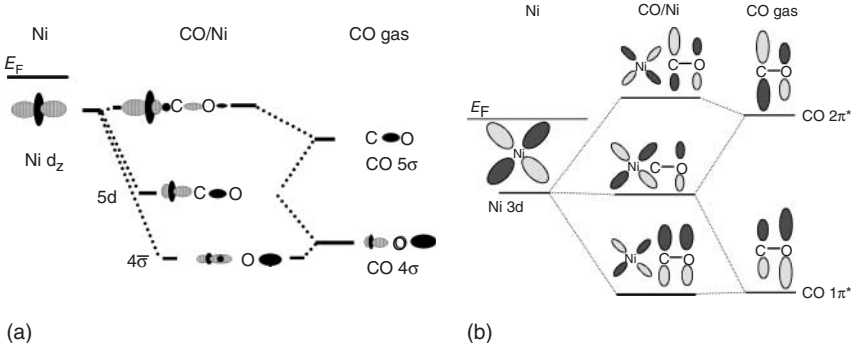

Figure 10.9 Schematic representation of the changes in hybridization of CO adsorbed to a surface Ni atom. An allylic electron structure is formed in this model of a single CO molecule interacting with a Ni atom. (a) Schematic orbital diagram of the σ interactions. (b) Schematic orbital diagram of the π-orbital structure. (Reproduced with permission from Ref. [33]).

fragment orbital. The π-type orbital fragments of Figure 10.8 between −4 and −6 eV correspond to the nonbonding orbital fragments with a low electron density on the C atom, but a high one on the oxygen atom. This can also be observed in the calculations of CO adsorbed to the Ru(0001) surface of Figure 10.10 at a similar energy position compared to the Fermi level, which in these figures is located at 0.0 eV.

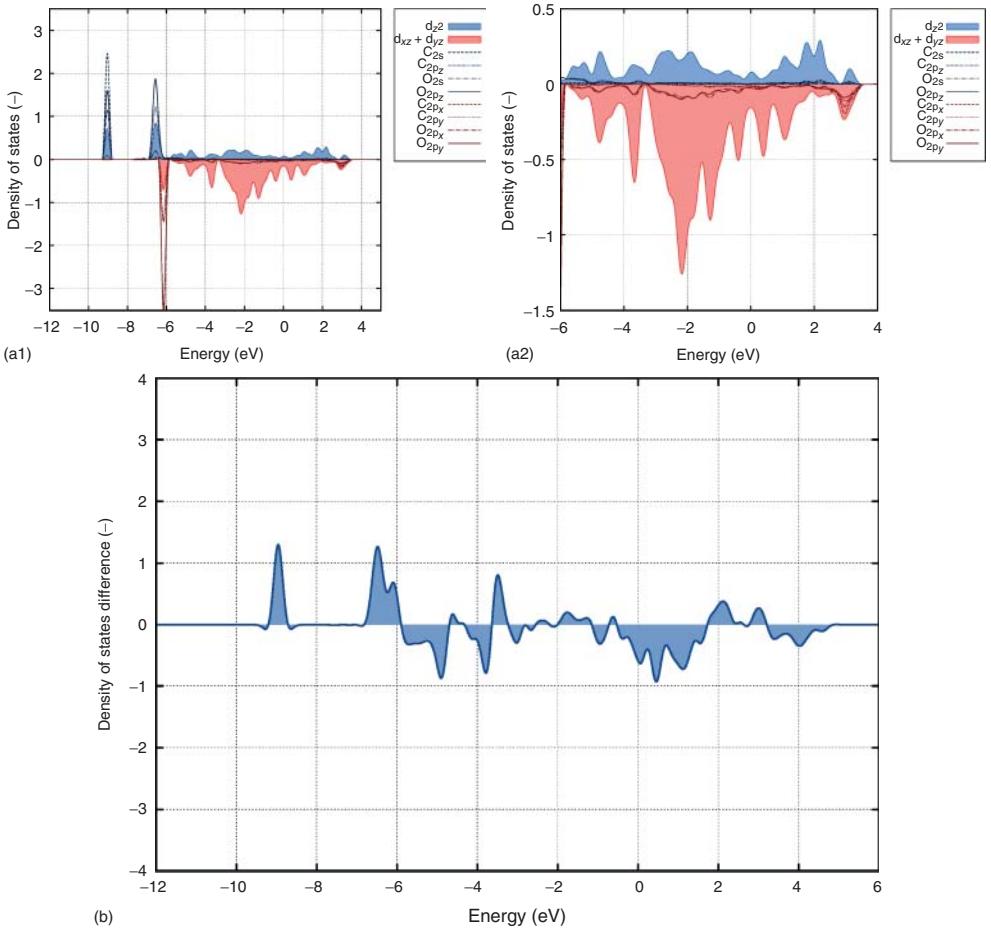

Figure 10.10 PDOS of surface atom in contact with atop and threefold adsorbed CO on the Ru(0001) surface. Similar VASP-DFT calculations as in Figures 10.3 and 10.5; (a) PDOS of CO adsorbed atop and of metal valence d-atomic orbitals (a2 is partial blow up of a1); (b) LDOS difference of the valence electron density localized on the surface metal atom with and without threefold adsorbed CO (I.A.W. Filot and R.A.V. Santen, 2013, unpublished).

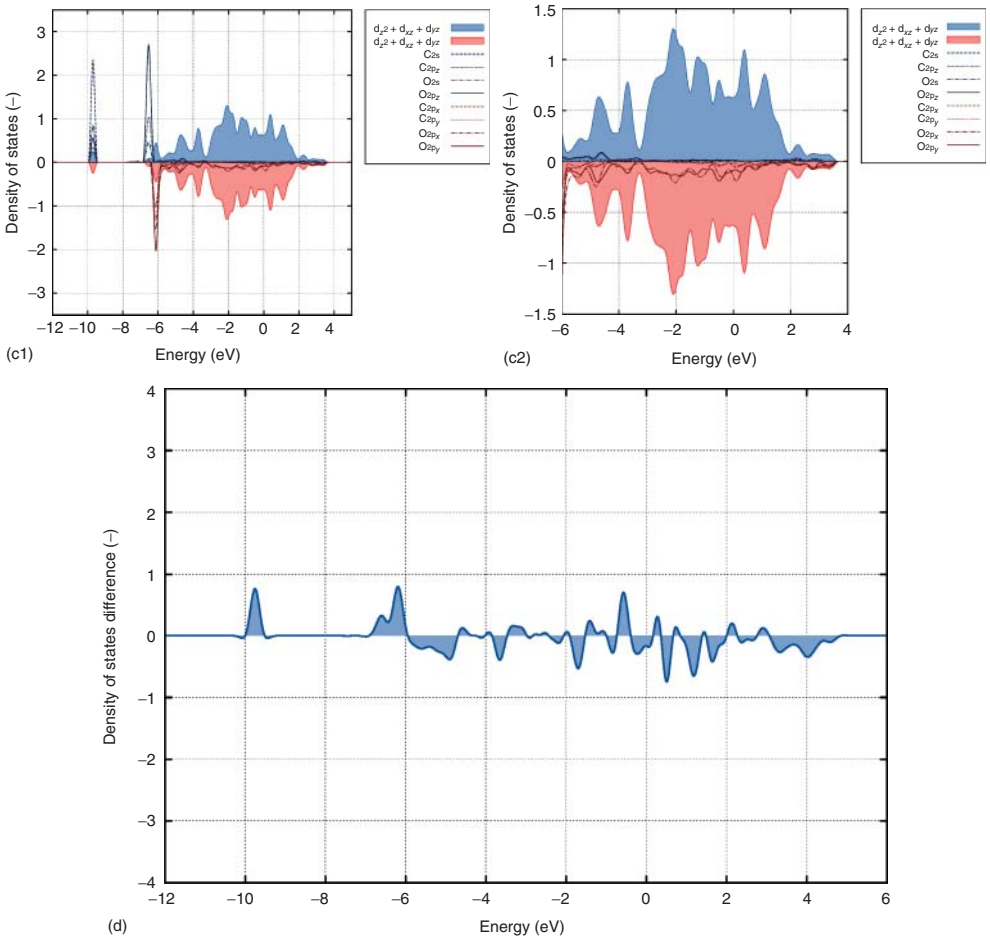

Figure 10.10 (*Continued*)

Figures 10.10 shows PDOS changes of the metal valence electron density and CO adsorbed atop and threefold calculated using periodical DFT/VASP [5] calculations. Calculated adsorption energies of CO are 190 and 180 kJ mol^{-1}, respectively. Not withstanding the difference with the ADF (A.L. Yakovlev and R.A. van Santen, 2005, unpublished), calculated adsorption energies calculated for the Ru cluster of Figure 10.8 electronic features of the admolecular bond are quite similar. It illustrates the complementarity of both approaches.

As we saw in Figure 10.3 when we analyzed the chemical bonding of a C atom adsorbed to the Ru surface, the d-valence electron density becomes depleted in particular energy regions. We also observe the increases in d-valence electron density where bonding and antibonding surface complex molecular orbitals are formed. Again, we see a split off of the density in the regime of the C-$2p_z$ energy, but a more complex pattern in the energy regime of high d-valence electron

density. It confirms the hybridizion that occurs within the CO molecule between the different σ symmetry and π symmetry orbitals of the CO molecule. The location of the corresponding increases and decreases in d-valence electron density correlates well with the OPDOS changes we presented in Figure 10.3a and b. Their interpretation is therefore similar. The analysis of chemical bonding of CO on carefully selected clusters to simulate chemisorption to a surface is seen to be quite successful, which illustrates the localized nature of the chemisorption bond.

In summary, we have discussed chemical bonding models of adsorbed CO of increasing sophistication.

Essential to all of them is the interplay of occupied HOMOs and unoccupied LUMOs. When surface or adsorption geometries change, these interactions may be affected differently. For metals of different d-valence electron occupation, donative and backdonating interactions counteract, whereas for metal surfaces of different coordinative unsaturation the increased interactions will enforce each other. On the other hand, when surface coordination of the molecule changes, the two type interactions again counteract. For adsorbed CO, the 5σ HOMO orbital has a weak attractive interaction in atop position that becomes weaker or even repulsive at high-coordination sites. The 2π* LUMO interaction is strongly attractive, and it becomes stronger when the CO molecule adsorbs at high-coordination sites.

The overall effect of the interaction of a molecule with the metal surface is that the intramolecular bond is weakened because of increased electron population of intramolecular antibonding orbitals and electron depletion of intramolecular bonding orbitals.

10.3.4
Surface Group Orbitals

Here, we analyze in more detail the electronic features that determine low or high coordination of an adsorbate in relation to the symmetry of interacting adsorbate orbitals. For this, it is important to introduce the concept of surface group orbitals.

We initially use the preference of the ammonia molecule to adsorb atop of a surface metal atom to introduce this concept.

The HOMO of ammonia is a σ-type lone-pair orbital, similar to the 5σ orbital of CO. The LUMOs of ammonia are of antibonding character and localized between the nitrogen atom and hydrogen atoms. Because of the strong interaction of H atom and nitrogen, the energy difference between HOMOs and LUMOs is so large that we can ignore the interaction with the NH_3 LUMO in the chemisorptive bond of ammonia with the metal surface.

The σ symmetric lone-pair orbital of ammonia is doubly occupied and hence as we discussed in Section 10.3.2 will experience a repulsive interaction with the metal free electrons. The attractive interaction to the chemisorption energy is mainly due to the interaction of the donative interaction of the ammonia σ symmetric lone-pair molecular orbital with metal d-valence electrons.

We illustrate the electronic changes of ammonia adsorbed to a surface atom of a Rh(100) and Rh(111) surface in Figure 10.11. The DFT-computed adsorption

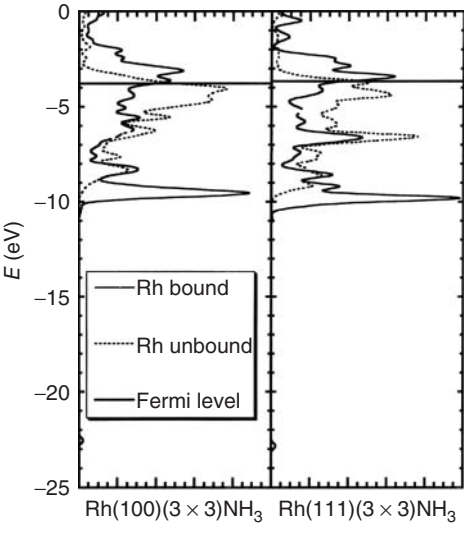

Figure 10.11 The PDOS of a free Rh atom and a Rh bound to NH_3 on Rh (100) and Rh (111), respectively. (Adapted from Ref. [34]).

energies are 82 and 91 kJ mol^{-1}, respectively. This is substantially lower than the adsorption energies of CO discussed in the previous section. It is due to the absence of the backdonative interaction. On the two surfaces, the interaction energies in twofold coordination decrease to 36 and 13 kJ mol^{-1}, respectively [34].

Figure 10.11 shows the PDOS of the d_{z^2} orbital on the interacting Rh atom without (unbound) and with interaction of ammonia (bound). The PDOSs of the valence d_{z^2} atomic orbital density on the unbound Rh atoms show the expected decreased bandwidth and upward shift for the 100 surface in which the surface atom has less neighbors than the atom that is part of the Rh(111) surface. When ammonia adsorbs, we note the appearance of two new large LDOS peaks. One below the d-valence electron band that corresponds to the bonding surface fragment orbital between the N_{atom} of NH_3 and the Rh surface atom, the other near the Fermi level that corresponds to the density of states of the antibonding surface fragment orbitals, which are mainly localized on the metal d_{z^2} atomic orbital. On the surface with the lower metal atom neighbor coordination, the unoccupied PDOS above the Fermi level is larger. It implies less occupation of antibonding orbitals and hence a slightly stronger attractive interaction. The initially more close location to the Fermi level of the $\overline{\in}_d$ of the d-valence electrons on Rh(100) compared to that of the Rh(111) d-valence electrons causes more of the antibonding surface orbital fragment density to be pushed above the Fermi level.

As no periodic codes are available to calculate OPDOS distributions, we compare site dependence of ammonia further for ammonia adsorbed to a Cu cluster. Figure 10.12 shows LDOS and OPDOS densities for ammonia adsorbed one- and twofold to a representative Cu cluster [35]:

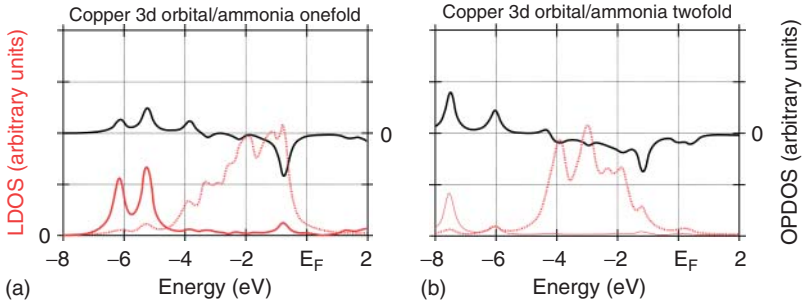

Figure 10.12 Local densities of states (LDOS) of NH_3 lone-pair σ orbital interacting with cluster copper orbitals and the corresponding overlap population densities of states (OPDOS) on Cu(9,4,5), and Cu(8,6,2) clusters, respectively. Both clusters model Cu atoms at the (100) surface. Each graph shows — LDOS of NH_3 σ orbital, --- LDOS of central copper orbitals, and — OPDOS; (a) onefold coordination of ammonia. Calculated adsorption energy of NH_2 equals – 110 kJ mol^{-1}; (**b**) twofold coordination of NH_3 adsorption. Calculated adsorption energy if ammonia is −70 kJ mol^{-1}. (Adapted from Ref. [35])

In Figure 10.12, the orbital interactions are shown between the lone-pair orbital of ammonia and the d-valence electrons of Cu of ammonia adsorbed one- or twofold to a Cu cluster simulating the Cu(100) surface. Bonding surface fragment orbitals have substantially lower energy positions for ammonia adsorbed in twofold compared to onefold coordination position. The weaker interaction of NH_3 in twofold coordination is due to the lower energy of the occupied antibonding orbital fragments formed between Cu valence electrons and ammonia. The attractive contribution to the chemical bond is due to the unoccupied antibonding orbital fraction. The higher location of the d-valence electron band of onefold coordinated ammonia increases this fraction.

It is a general feature of the LDOS of the d-valence electron band to get a very different energy distribution dependent on the coordination of the adsorbate. It is due to the different local symmetry combination of orbitals that interact with the adsorbate when coordination changes. This is schematically illustrated in Figure 10.13.

This schematic figure sketches differences in the metal valence band electron density structure based on a tight-binding description with one atomic orbital per metal atom [17]. For the generalization to d-atomic orbitals, we refer to [36].

When an s-type adsorbate orbitals interacts with a two- or threefold surface site, because of symmetry it will interact with orbital combinations (Eqs. (10.10a) and (10.10c)), respectively. Equations (10.10b) and (10.10d) give the corresponding group orbital energies. In Eqs. (10.10e) and (10.10f), the corresponding expressions for the asymmetric surface group orbital combinations are given:

$$\varphi_{2s} = \frac{1}{\sqrt{2}}(\varphi_1^0 + \varphi_2^0) \tag{10.10a}$$

$$\varepsilon_{2s} = \alpha_m + \beta \tag{10.10b}$$

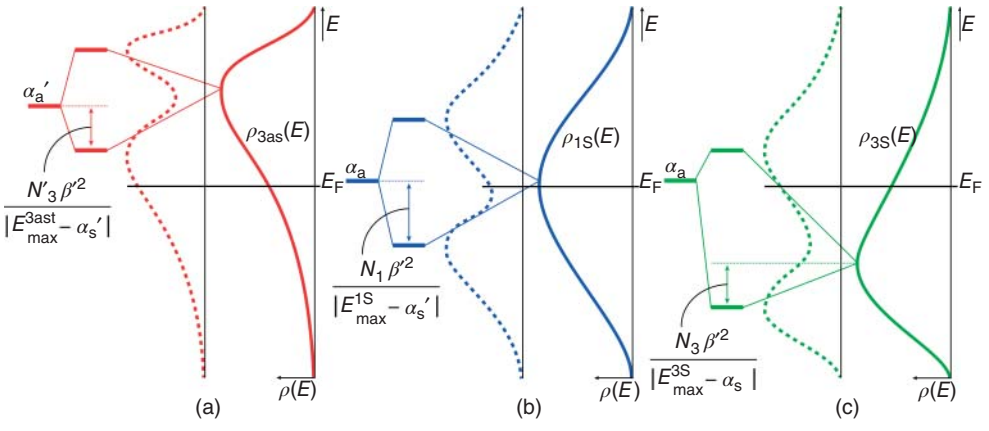

Figure 10.13 Schematic illustration of interaction of atomic orbital with metal surface group orbital local density of states. Metal orbitals are constructed from one s-atomic orbital per atom. α_e' is adsorbate orbital energy with asymmetric orbital symmetry with respect to surface normal. α_e is adsorbate orbitals with symmetric orbital symmetry. The drawn LDOS $\rho(E)$ lines correspond to metal surface group orbital densities before interaction. The broken lines belong to metal surface group orbitals LDOS interacting with adsorbate orbital. The downward-shifted bonding orbital energies of the adsorbate LDOS are indicated; (**a**) asymmetric adsorbate orbital interacting in twofold coordination; (**b**) symmetric adsorbate orbital interacting in atop coordination; and (**c**) symmetric orbital interacting in three fold coordination.

$$\varphi_{3s} = \frac{1}{\sqrt{3}}(\varphi_1^0 + \varphi_2^0 + \varphi_3^0) \tag{10.10c}$$

$$\varepsilon_{3s} = \alpha_m + 2\beta \tag{10.10d}$$

$$\varphi_{3as} = \frac{1}{\sqrt{6}}(\varphi_1^0 + \varphi_2^0 - 2\varphi_3^0) \tag{10.10e}$$

$$\varepsilon_{3as} = \alpha_m - \beta \tag{10.10f}$$

An asymmetric adsorbate orbital such as a p atomic orbital, when oriented parallel to the surface, will interact with asymmetry orbital combinations (Eq. (10.10e)).

α_m is the atomic orbital energy of the metal s-atomic orbital and β the corresponding overlap energy. Upon interaction of these surface cluster symmetry orbitals with the surrounding lattice, the corresponding group orbital density of states (GODOS) broadens. As illustrated in Figure 10.13, their respective maxima coincide with the respective energies of Eq. (10). The adsorbate orbital forms bonding and antibonding orbital combinations with the surface group metal orbitals of relevant symmetry. Because the LDOS of the s-symmetric combinations have lower energy in high coordination, surface fragment orbitals antibonding with respect to adsorbate bond formation will be occupied for lower valence band filling, than for two- or onefold coordination. As long as no antibonding orbital fragments are

occupied, interaction in high coordination will always be preferred. Once, by an increase in the valence band electron density, the antibonding orbital fragments become occupied, the interaction energy weakens. Because at the same Fermi level position, a higher fraction of antibonding orbitals is occupied by electrons in high-coordination sites, the Pauli repulsive interaction will start to dominate the chemical bond energy. Hence, adatom s-symmetric interactions will favor low-coordination sites at high valence band electron occupation. This tends to be the situation when doubly occupied s-type adatoms interact with group VIII metal d-valence electrons. At lower band filling, when only bonding surface fragment orbitals become occupied, high coordination becomes preferred because the bonding orbital contributions are pushed further down the higher surface coordination. Hence, they will give the larger attractive contribution to the chemical bond energy.

In Figure 10.14, for a slab calculation with the extended Hückel method of Ag, the group orbital projections onto the valence band 6s PDOS are shown for the interaction with an adsorbate with an s-atomic orbital in three-, two-, or onefold coordination. Note the enhancement of density at low energy for the threefold symmetric group orbital compared to that of the twofold symmetry group orbital or the PDOS of the s orbital of a single metal atom.

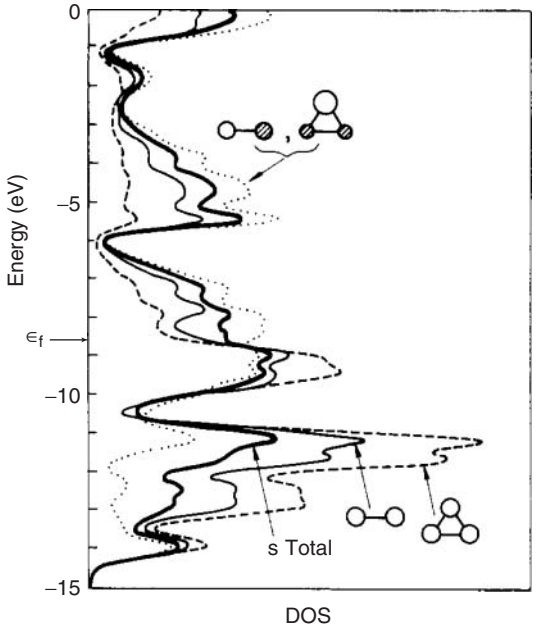

Figure 10.14 Partial density of states (PDOS) and group orbital densities of states (GODOS) for surface Ag 5s orbitals in bare Ag(111) slab according to the extended Hückel method. The dark solid line is the total Ag 5s PDOS. The Ag 5s GODOS are (s + s), dotted, and (s − s), thin solid line. The triangular Ag, group orbitals are (s + s+ s), dashed, and the degenerate set (2s − s − s) and (s − s), again the thin solid line. (Adapted from Ref. [37]).

π-type orbitals antisymmetric with respect to the surface normal will not interact with an s-type metal atomic orbital when adsorbed atop. They will interact with the d-valence atomic orbitals of the same symmetry. In higher coordination, they will interact with antisymmetric combinations of metal atom atomic orbitals. This leads to the surface group orbital combinations as in Eq. (10.10e). Now the upper part of the metal valence electron band that is dominated by antibonding valence orbitals is probed. As indicated in Figure 10.13, bonding and antibonding surface fragment orbitals are formed. As the upper part of the metal valence band is probed, usually a substantial part of the antibonding density of states will be higher than the Fermi level. Then, mainly bonding surface fragment orbitals are occupied, which will favor adsorption to high-coordination sites.

In summary, there are two essentially different chemical bonding interactions that cause an adsorbate to be adsorbed in low or high coordination. The interaction with doubly occupied HOMO molecular orbitals of σ type tends to direct the adsorbate to low-coordination sites. The interaction with π symmetric adsorbate orbitals tends to direct the adsorbate to high-coordination sites. The stronger the interaction with the d-valence electrons and the higher the electron occupation, the relatively stronger the atop driving interaction becomes.

10.3.5
Adsorbate Coordination in Relation to Adsorbate Valence

Classical chemical bonding theory relates trends in energies with the free valence of interacting fragments. In chemisorption, this gives a relation between free adsorbate valence and coordination to the metal surface.

In the previous sections, we have extensively discussed the chemical bonding features that drive an adsorbate toward low or high surface atom coordination. In Section 10.3.1, it has been discussed that an adatom such as C preferentially adsorbs at high coordination, whereas in Section 10.3.3, we saw that a coordinatively saturated molecule generally prefers adsorption at a low coordination site.

Here, we compare adsorption of adsorption intermediates with varying free valence, compare their adsorption energies and study their preference for particular adsorption sites.

Metals with d-valence atomic orbitals that extend in space can be expected to strongly interact with adsorbate orbitals. When they also have a high d-valence electron occupation, it will direct adsorption intermediates to specific surface coordination sites. For instance, on Pt [38] or Ru surfaces, the NH_3 [39] molecule will adsorb atop. The NH_2 fragment will adsorb in twofold coordination and NH in threefold coordination [40]. On these metals, atomic oxygen will adsorb twofold and OH onefold [38]. Similar coordination rules are found for CH_3, CH_2, and CH. The C atom prefers coordination in a fivefold coordination as available on the (100) surface of a face-centered cubic (fcc) metal, with four metal atom neighbors in the plane and one below.

This relation between surface coordination and adsorbate free valence is based on the atop driving interaction of HOMO orbitals of σ symmetry. This will be

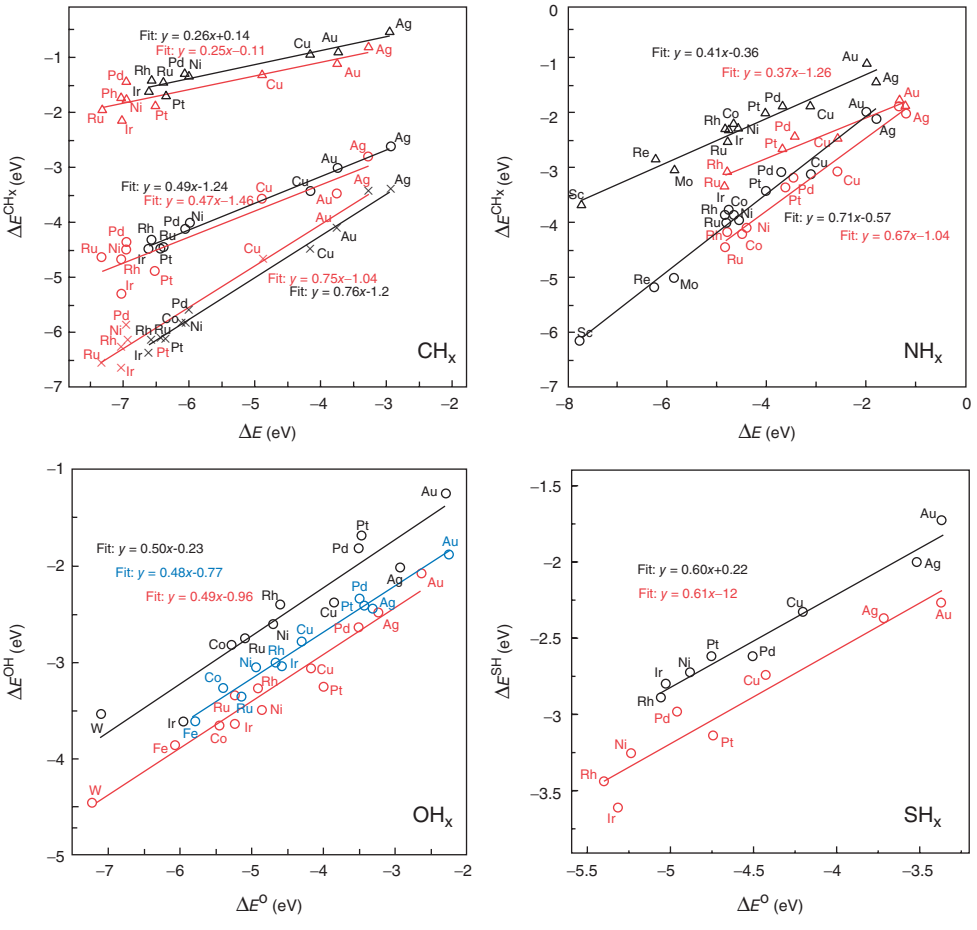

Figure 10.15 Adsorption energies of CH_x intermediates (crosses: $x = 1$; circles: $x = 2$; triangles: $x = 3$), NH_x intermediates (circles: $x = 1$; triangles: $x = 2$), OH, and SH intermediates plotted against adsorption energies of C, N, O, and S, respectively. The adsorption energy of molecule A is defined as the total energy of A adsorbed in the lowest energy position outside the surface minus the sum of the total energies of A in vacuum and the clean surface. The data points represent results for close-packed (black) and stepped (red) surfaces on various transition-metal surfaces. In addition, data points for metals in the fcc(100) structure (blue) have been included for OH_x. (Reproduced with permission from Ref. [42]).

significant only when the interaction with d-valence orbitals is strong and the d-valence electron band has a high degree of electron occupation [41]. Site preference will change toward higher coordination when we compare adsorption to transition metals moving from the right to the left in a row of the periodic system.

In Figure 10.15, for a particular surface topology, DFT-computed interaction energies of XH_x intermediates are compared with the adsorption energies of the X_{ads} atom as a function of metal substrate. The curves of Figure 10.15

show convincingly that there is a relation between adsorbate adsorption energy and adsorption energy. The adsorption energy increases with increasing loss of substituents attached to the atom of the adsorbate that binds to the surface. These scaling relations have been discovered by Nørskov *et al*. [42]. They validate the bond order conservation rules predicted earlier qualitatively by Shustorovich [43]. According to the bond order conservation rules, the strength of bonding to a XH_x molecule or fragment increases with a decrease of x. The total valence, which can be considered a total bond strength capacity, of an atom as X is considered constant and distributes when XH bonds are formed. For instance, when one XH bond is formed, the total valence of X is available and the XH bond is strong. When two bonds are formed, the total valence has to be distributed over two bonds, and hence the bondstrength of these bonds will weaken. When more XH bonds are formed with the X atom, the individual bondstrenghths weaken further. On the basis of Morse potentials, Shustorovich developed elegant analytical expressions that provide a way to calculate this successive weakening of the XH bonds [3, 43].

The slopes of the curves are interesting and can be understood on the basis of the general principle of bond order conservation. They relate to available free valence, which implies the possibility of stronger bonding of XH_x to the metal surface when x decreases. In Figure 10.15, the slopes of the different curves are directly related to the difference in free valence. So is the slope of the CH_3/C adsorption energies ratio 1 : 4, that of the CH_2/C adsorption energies ratio 1 : 2 and that of CH/C equal to 3 : 4. The slopes are proportional to available free valence. This is also found for the analog molecules NH_3 and OH_2. The ratios of OH adsorption energies versus that of adsorbed O have slope 1 : 2 and that of NH_2 versus that of the adsorbed N atom for the (111) surfaces 1 : 3 [44].

However, there is also a significant scatter in the data, and correlation may vary with surface structure. An example is the difference in adsorption energies of CH_{ads} and $CH_{2,ads}$ on different surfaces of Ru. The primary reason for such differences is that the geometrically optimum coordination is not always possible on each surface. For instance, on the fcc (111) surface, C_{ads} is destabilized compared to C adsorbed to the (100) surface, because hybridization leads to preference of C_{ads} for the four coordinated site. Also, on surfaces that are steplike, hydrogen-bonding-type agostic interactions with metal surface will increase the adsorption energies [44] compared to the ''ideal'' case.

10.4
Metal Particle Composition and Size Dependence

10.4.1
Alloying: Coordinative Unsaturation versus Increased Overlap Energies

The altered surface properties of metal alloys can also be interpreted in terms of valence electron delocalization changes. Delocalization changes because of altered metal atom–metal atom overlap energies and different positions of the

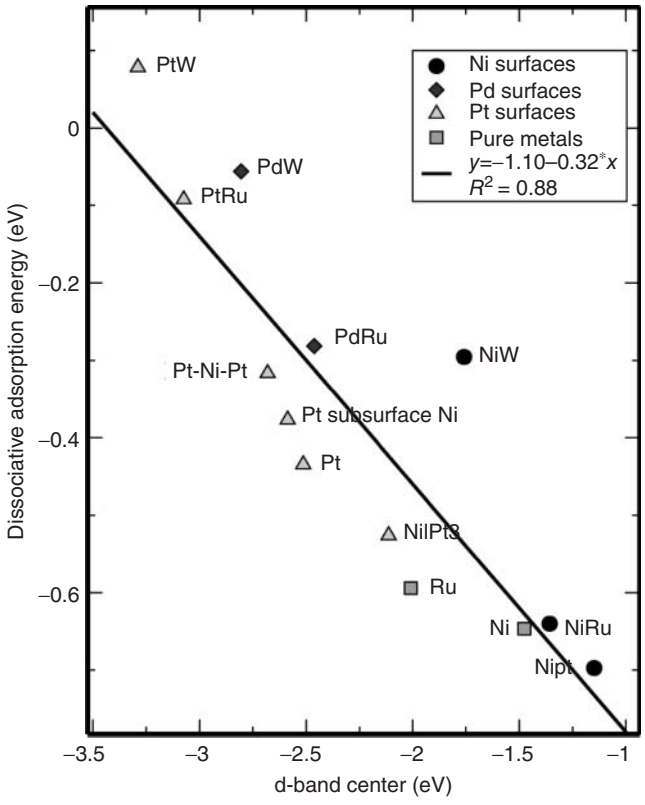

Figure 10.16 Correlation between the dissociative adsorption energy of H_2 on bimetallic surfaces and the d-band center of those surfaces. (Reproduced with permission from Ref. [45]).

d-valence electron band energies of the alloying components. In this subsection, we review chemisorption to metal overlayers of Ni alloys [45]. The particular case is interesting because the altered chemisorption properties have been found to be correlated with differences in shifts of the average position of the d-valence electrons of Ni (Figure 10.16). As we learned in Section 10.3.1, this is a measure of the delocalization of the d-valence electrons on the Ni atom. The more upward the average energy position of the d-valence electron band, the more localized are the valence electrons.

In Figure 10.16, the calculated dissociation energy of H_2 to different systems is compared with the corresponding average position of the energy of Ni d-valence electrons.

The calculated dissociation energy of H_2 increases linearly with decreasing energy $\overline{\epsilon}_d$. Because of the mismatch between metal atom radii and substrate metal atom distances, the overlayer metal–metal atom distances can be very different compared to the case where the metal overlayer and substrate are the same

atoms. When the overlayer of Ni atoms is on top of a Pt substrate, their distance increases compared to the nonalloyed Ni surface. Therefore, within the Ni layer, the interaction between the Ni atoms has decreased. Because of the larger Pt radius, the Pt atoms also interact more weakly with the Ni atoms than the Ni atoms in the Ni metal. The overall result is increased localization of the d-valence electrons on the Ni atoms in the Ni overlayer, which is measured by the increase of $\overline{\epsilon}_d$. Hence, the chemisorption energy of H atoms with the Ni overlayer increases compared to that of the Ni surface. When the Ni overlayer is positioned on a metal of larger radius, the Ni atoms in the overlayer become stressed. This happens when the Ni atoms are deposited on Ru or W. However, the covalent interaction of the Ni valence electrons with the d-valence electrons of W and Ru is quite different from the previously discussed Pt case. Because W and Ru have less d-valence electrons, they interact stronger with Ni than does Pt. W has a very strong interaction and the interaction of Ni with Ru is in between that of W and Pt.

The increased covalent interaction between Ni and Ru balances the loss in electron delocalization due to the stretched distance between the Ni atoms. Hence, the interaction energies with H are unaltered. However, because of the increasing covalent interaction with W, which has more extended d-atomic orbitals and a lower d-valence electron count compared to Ru, the Ni d-valence electron delocalization increases for the Ni/W system. Hence, the interaction energy with H is found to decrease.

The relation between adsorption energy of H_{ads} and $\overline{\epsilon}_d$ has the same electronic basis as that of ammonia adsorption discussed in Section 10.3.4. The LDOS on the H atom is located at an electron energy low compared to that of the d-valence electron band of Ni. The bonding surface fragment orbitals between H_{ads} and metal surface will also have a low-energy position below the d-valence band. The antibonding orbitals will have a high energy that overlaps with the density of the d-valence electrons. It will have a mainly d-valence electron character. The upward-shifted d-valence electron band has a position closer to the Fermi level. Upon interaction with the H atom atomic orbital, it will be pushed further upward. The d-valence band that is initially closer to the Fermi level will obtain the lower electron occupation.

The adsorption energy is determined by the distribution over bonding and antibonding surface fragment orbitals. There is no significant change in position of the bonding surface fragment orbital (effects of unfavorable upward shift of ED and increase in d-valence electron localization cancel), but there is a decrease in electron population of the bond-weakening antibonding surface fragment orbital. The overall effect is an increase of the adsorption energy of the H atom to the Ni overlayer.

10.4.2
Particle Size Dependence

As is illustrated in Figure 10.17, a decrease in particle size, even when shape is maintained, changes the ratios of corner, edge, and terrace atoms. Because of the

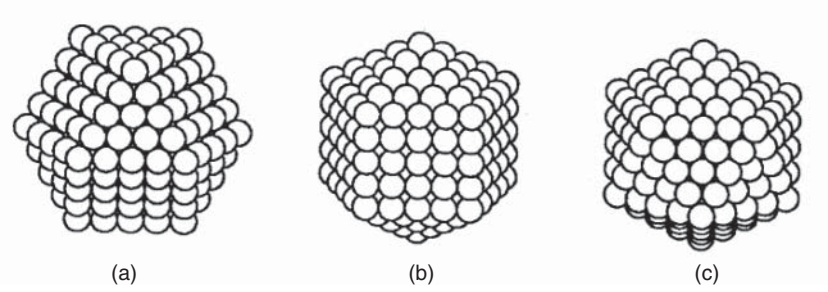

Figure 10.17 Some examples of small particles. (**a**) fcc cuboctahedron, (**b**) decahedron, and (**c**) icosahedron.

different degree of coordinative unsaturation of the surface atoms, a decrease in particle size will change the average reactivity of the particle.

As long as transition-metal particles are at least larger than a nanometer, they can be considered metallic. When the particle gets molecular dimensions of a few atoms, the molecular orbitals will have energy differences larger than kT, and quantum effects have to be considered. Here, we consider particles of sizes at which they still can be considered metallic. However as we will see, this does not mean that the valence electron LDOS or chemisorption energies on a particle do not vary with particle size even when its local coordination is unaltered. This is very well known from experience with DFT calculations on transition-metal slabs representing a surface. A thickness of the slab of typically 5–7 atomic layers is often required to obtain interaction energies independent of increasing slab thickness. Changes in metal–metal atom bond distances will alternatively increase or decrease as a function of layer thickness. Also, the adsorption energy does not change uniformly with increased metal slab thickness.

The effect of decreased coordination of surface metal atoms compared to the bulk leads to small decreases in the bond distances with atoms in the subsurface layer. Because of bond order conservation, discussed in Section 10.3.5, this increased bonding of metal atoms in the subsurface layer to those in the surface layer will weaken bonds with metal atoms in the next subsurface layers. The result is a decaying alternating strengthening and weakening of the interaction energies between atoms in layers perpendicular to the surface layer.

On metal particles, these decaying alternating increases and decreases in the interaction energies between the surface metal atoms generated by the corner and edge atoms lead to small particle-size-dependent changes in the reactivity of the atoms. At low coverage, this leads to small changes in the adsorption energies, which are discussed in this subsection.

In Section 10.5, we analyze the consequences of lateral effects between adsorbed molecular species in the chemisorbed overlayer. The presence of steps and kinks in nanoparticles alters the steric constraints of packing of molecules in high-coverage overlayers, which will be seen to result in large increases in adsorption energies at high coverage [46, 47].

In Section 10.6.1, we study the consequences of the presence of steps and kinks in the overall reactivity of nanoparticles by altered geometric options for transition state formation.

To illustrate the changes in adsorption energies on surface atoms that do not have altered surface topologies but become part of a different nanoparticle here, we use results of DFT calculations of low-coverage adsorption on Pd and Au particles.

The smaller terraces on nanoparticles, terminated by edge and kink atoms, also allow for relaxation of the metal atom–metal atom distances in the lateral direction. The increased coordinative unsaturation of the nanoparticle surface atoms lead to contraction of the average metal atom–metal atom distances. For cuboctahedral nanoparticles, this is illustrated in Figure 10.18.

Results of DFT calculations of the interaction energy of CO in threefold coordination as a function of the decreased Pd–Pd atom distances on the Pd nanoparticles are shown in Figure 10.19 [48]:

The increased delocalization of the Pd atom valence electrons with decreasing Pd–Pd atom bond distance causes the CO adsorption energy to decrease with decreasing particle size. The decreases in adsorption energies found are less than 10% compared to the adsorption energies on the same site for the fully extended surface.

It is interesting to compare the CO adsorption studies on Pd with related studies on Au clusters of varying shown in Figure 10.20. The concentration of coordinatively unsaturated sites increases when nanoparticle size decreases. Adsorption is compared on sites with different degrees of coordinative unsaturation. When particle size decreases, the change in coordinative unsaturation of the

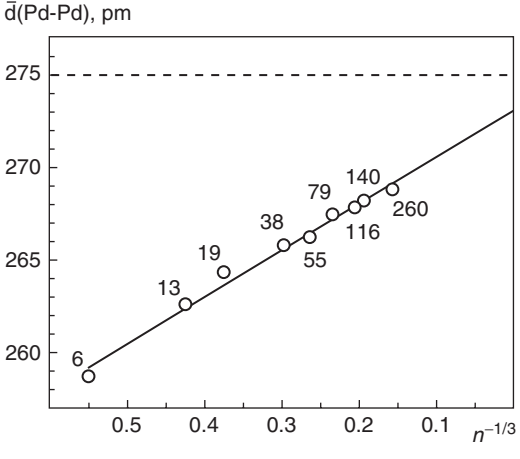

Figure 10.18 Average bond distances $\bar{d}$(Pd–Pd) of Pd_n clusters as a function of $n^{-1/3}$ calculated at LDA level. Extrapolation to infinite cluster size yields $\bar{d}$(Pd–Pd) = 273.1 pm. The experimental value of bulk Pd, 275 pm, is indicated by the dashed horizontal line. (Reproduced with permission from Ref. [48]).

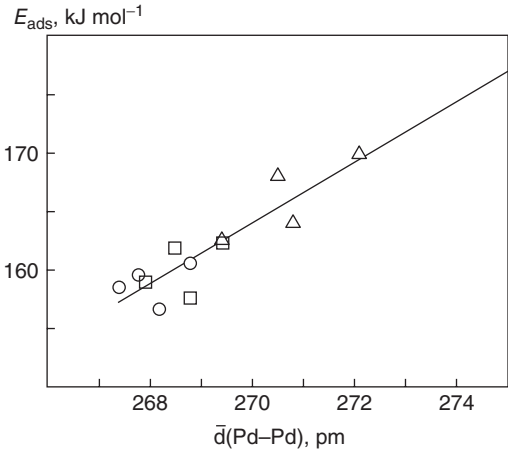

Figure 10.19 Adsorption energies E_{ads} of CO to the cuboctahedral Pd_n clusters with (n) 79, 116, 140, 260 of Figure 10.18 as a function of the average distance di(Pd–Pd) from three computational strategies: (i, circles) cluster geometry fully optimized with O_h symmetry constraints; geometry of the outer shell (surface) optimized with nearest-neighbor Pd–Pd distance of the cluster core fixed at (ii, squares) 270 pm and (iii, triangles) 275 pm. The solid line results from a least-squares fit of the entire data set. (Adapted from Ref. [48]).

surface metal atoms with decreasing particle size dominates the changes in adsorption energies of CO. However, for adsorbed oxygen, significant deviations occur compared to the prediction of the adsorption energy based only on change in surface atom coordination. Adatom adsorption energies are more sensitive to substrate changes than the CO molecule. In the atom compensation between donating and backdonating interactions, changes are absent, and this was discussed in Section 10.3.2. In Figure 10.20a and b. the red squares indicate interaction energies with the extended surfaces (except for those labeled with an *m*) and the open squares interaction with Au clusters (numbers indicate their size).

These deviations in adsorption energies from extrapolated surface atom values relate to changes in the electronic structure of these clusters. They are due to the high fraction of surface atoms over bulk atoms. We will illustrate this for the M_{13} and M_{55} cuboctahedral clusters.

The M_{13} atom cluster is a unique cluster. It is highly symmetric and has only one bulk atom. The highly symmetric environment of its central atom localizes its valence electrons. The central atom orbitals mainly interact with symmetrical combinations of the atomic orbitals of the atoms of the outer sphere. This limits their interaction to only a few molecular orbitals localized on the outer atoms.

This is illustrated in Figure 10.21 for Rh_{13} and Rh_{55} clusters of shape similar to that of the Au clusters. The localization of d-valence electrons on the inner atom (Figure 10.21a) is clearly seen from the substantial gaps between the LDOS peaks

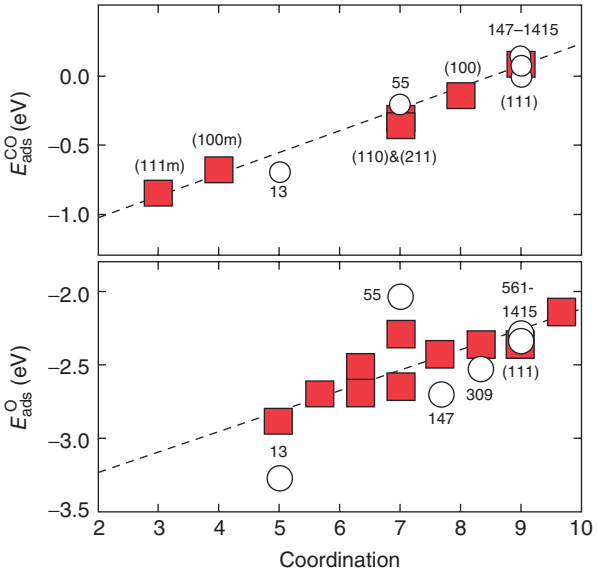

Figure 10.20 Facet adsorption energy of CO (top) and O (bottom) as a function of the average coordination number of the gold atoms in the nearest proximity. Cluster calculations are denoted by white circles. Bulklike calculations (marked with red squares) have been performed to separate size effects due to the electronic structure of clusters from effects that can be attributed to the local geometry. The dashed line fits the coordination trend for the bulklike systems. For CO, the surface type is indicated for each bulklike calculation. An appended m refers to adatom calculations that model local monomer systems. For O, the bulklike calculations correspond to threefold coordinated sites on (211) surfaces as well as steps and adatom plateaus on (111) surfaces. (Reproduced with permission from Ref. [49]).

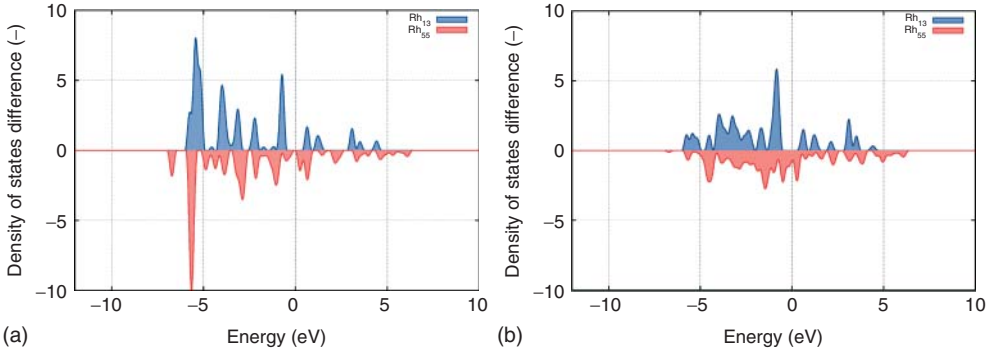

Figure 10.21 Valence d-electron local densities of states (LDOS) of internal center atom (a) and surface atom (b) of Rh_{13} and Rh_{55} cuboctahedral nanoclusters calculated using VASP-DFT with PBE functional, Fermi level at 0.0 eV. (I.A.W. Filot and R.A.v. Santen, 2013, unpublished).

on the inner atom compared to that of the LDOS on the outer atoms (Figure 10.21b). Delocalization of the LDOS of the surface atoms has now decreased more than expected from geometrical arguments (compare, for instance, with Figure 10.5c). This will enhance chemisorption slightly compared to adsorption on a particle that has a low fraction of surface atoms compared to the number of bulk atoms. Also, the Rh_{55} cluster still shows considerable electron localization on the central atom, but now the surface atom LDOS has become more delocalized because of the presence of a subsurface layer of atoms (I.A.W. Filot and R.A.v. Santen, 2013, unpublished).

The difference in the interaction energies O with the Au_{55} and Au_{147} clusters is remarkable. Possibly, the contraction of Au–Au distances on the smaller particle, as discussed for the Pd particle, explains the weakening of the interaction with O on the Au_{55} particle.

The important conclusion to be drawn is that differences in interaction energies of an adsorbate with a metal-surface owing to particle size change are dominated by the effect of altered surface coordination. Only when a particle becomes less than 1.5 nm, the LDOS at the surface atoms undergoes a change, which will affect adsorption energies. As we see in Section 10.5, the effect of particle size variation on adsorption may be much more significant at high surface coverage [46, 47] than the low-coverage cases we have discussed so far.

10.5
Lateral Interactions; Reconstruction

The adsorbate–adsorbate interactions that develop when surface adsorbate concentration increases can be distinguished into direct repulsive steric and through metal interactions. The latter tend to be attractive when adsorption occurs on neighboring metal atoms, but repulsive when the adsorbates share a bond with the same metal atom. Interestingly, these lateral effects also behave differently for small nanoparticles compared to extended surfaces.

We initiate the discussion of these lateral effects by studying molecular adsorption of CO in detail. This is followed by a description of lateral effects of high-concentration adsorption layers of adatoms. The dominant difference is the absence of direct-contact repulsive effects for the case of the adatoms.

For molecular as well atomic adsorption, we will see that at high coverage, surface reconstruction is general phenomena.

On dense surfaces, the steric interactions cause molecules such as CO or NO to have maximum overlayer concentrations of typically 0.3–0.5 adsorbate molecules per metal atom. This in contrast to the maximum coordination ratios of small metal clusters, which can be as high as three or four molecules of CO per metal atom [50, 51].

For nanometer particles, it has recently been discovered that maximum overlayer adsorbate-surface atom ratios can be very different from those typically measured at extended surfaces [46, 47].

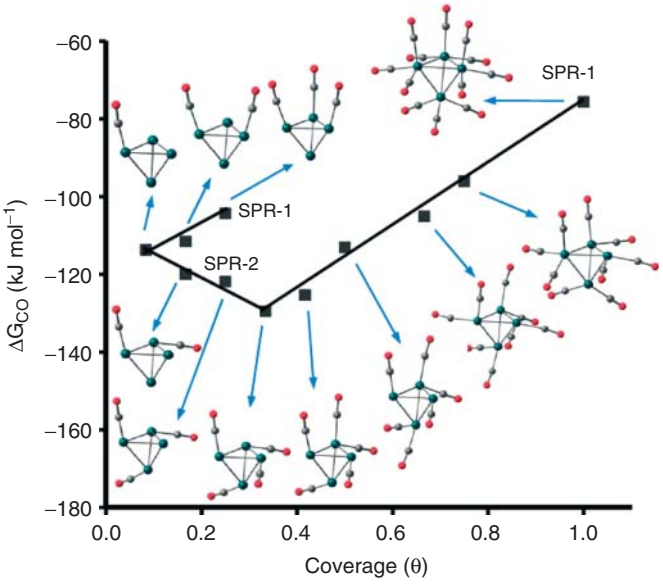

Figure 10.22 Gibbs free energy changes (ΔG^{o}_{CO}) per CO for the adsorption of carbon monoxide on $Rh_4(3,1)$ cluster as a function of CO coverage θ (SATP, $P = 1$bar, $T = 298.15$ K). (Reproduced with permission from Ref. [52]).

As a reference to this phenomenon, we discuss first the dependence of the CO interaction with a small Rh_4 cluster [52], as illustrated in Figure 10.22. This we use to illustrate the two basic interactions that control lateral effects.

For the Rh_4 cluster, the maximum ratio of adsorbed CO versus Rh atom is 3. This agrees with predictions according to the 18-electron rule [50, 51]. The 18-electron rule relates stability of clusters with metal atom valence electron count.

One interesting aspect of Figure 10.22 is that in contrast to expectation, it shows increasing stability of adsorbed CO with increasing CO cluster concentration until a ratio CO/Rh atom = 1 is reached. The release of direct repulsive interactions is possible by bending away of the CO molecules from configurations where they would otherwise have through space repulsive contact. Such direct repulsive interactions occur when the CO molecules adsorb in parallel to the Rh_4 cluster. This direct repulsive interaction is of the order of 20 kJ mol^{-1}. The through metal bond interaction is responsible for the increased stabilization of CO with increased coverage below the ration of CO/Rh =1 and is of the order of 10 kJ mol^{-1}. This attractive interaction is due to the weakened metal atom–metal atom interaction energies when metal atoms become involved with an additional bond to the interacting CO molecule. It is reflected in the longer metal atom distances. The bond order conservation principle of Section 10.3.5 again applies.

When the CO/Rh ratio increases beyond one, the CO interaction energy steadily decreases. The repulsive effect of shared coordination to a single metal atom

decreases the interaction energy per CO molecule. This repulsive interaction dominates and will be on the order of 15 kJ mol^{-1}.

On a metal terrace, the bending away of the CO molecule as observed for the cluster is geometrically not possible. Therefore, on the metal surface, the interaction between CO molecules will always be more repulsive, even when two CO molecules each adsorb on a separate neighboring metal atom. Because of these direct repulsive interactions with increasing coverage, one often observes a shift of the CO positions from their initially favored positions to less favored positions [6, 53]. On corrugated surfaces, some release of this repulsive interaction may be possible because of small changes in the bond angles with the metal surface normal.

Mason *et al*. [54] have studied computationally as a function of CO coverage siting of CO and the corresponding changes in CO adsorption energies. They used the same method to properly predict preferred adsorption sites of CO, as discussed in Section 10.3.3. Similarly, as for the cluster of Figure 10.22, they identify through space repulsion, bonding competition through shared metal atom bonding and through metal interaction as the three factors that determine lateral interaction of adsorbed CO. Table 10.6 summarizes their results for the (111) surface of three different metals. The siting notation used is elucidated by the accompanying figure.

Table 10.6 Calculated results for adsorption energy of CO (E_{chem}) at different surface coverage values Θ on the (111) surfaces of Pt, Rh, and Pd (in electron volts). Notation in Table refers to site location as in legend of Figure 10.23.

	Pt(111)		Rh(111)		Pd(111)	
	E_{chem}	E_{int}	E_{chem}	E_{int}	E_{chem}	E_{int}
			Θ = 0.25			
t	1.56		1.67		1.25	
b	1.43		1.58		1.49	
h	1.40		1.64		1.60	
f	1.43		1.64		1.63	
			Θ = 0.5			
tt	1.27	0.29	1.35	0.32	0.93	0.32
bb1*	1.12	0.31	1.25	0.33	1.15	0.34
bb2	1.07	0.36	1.40	0.18	1.09	0.40
bb3*	1.36	0.07	1.55	0.03	1.44	0.05
tb*	1.45	0.04	1.56	0.06	1.31	0.06
hh*	1.03	0.37	1.33	0.31	1.19	0.41
hf	1.21	0.20	1.53	0.11	1.40	0.21
			Θ = 0.75			
thf*	1.19	0.27	1.39	0.26	1 .15	0.34
			Θ = 1			
tttt	0.74	0.82	0.53	1.14	0.39	0.86
hhhh*	0.31	1.09	0.76	0.88	0.46	1.14

E_{int} is lateral interaction energy.
Reproduced with permission from Ref. [54].

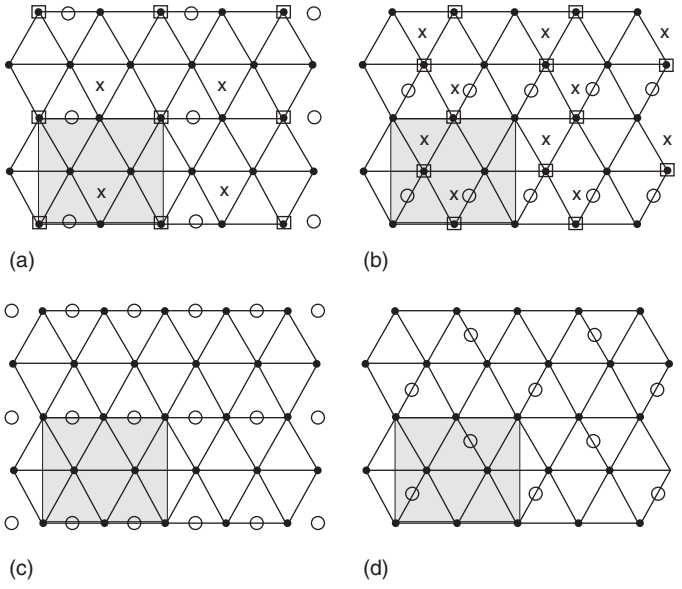

Figure 10.23 (a) Schematic of the (111) surface with CO at $\Theta = 0.25$. Overlayer t is indicated by squares, b by circles, and h by "X." The cell is indicated by the shaded region. (b) Schematic of the (111) surface with CO at $\Theta = 0.5$ in overlayer tt (squares), the bb1 overlayer pattern (circles), and the hh pattern ("X"). (c) Schematic of the (111) bb2 structure. (d) Schematic of the (111) bb3 structure. (Reproduced with permission from Ref. [54]).

In Table 10.6, adsorption energies for CO adsorption are presented as a function of four coverages. A detailed analysis is given of the adsorption energies as a function of CO siting. The nearest-neighbor CO environment can be deduced from Figure 10.23.

A substantial decrease in the adsorption energy of CO is generally observed with increasing coverage. Through space, nearest-neighbor interactions estimated are to be on the order of 20 kJ mol^{-1}.

Backdonation of metal electrons into the CO $2\pi^*$ orbital increases the charge on the parallel-oriented CO molecules and depletes the d-valence electron band of electrons. The former increases the direct repulsive interaction, the latter increases metal atom–metal atom interactions, but also decreases electron backdonation. It results in an overall increase of the repulsion of neighbor CO molecules with approximately 10 kJ mol^{-1}. Shared bonding of CO adsorbed in bridge coordination and atop leads to additional repulsive interactions on the order 10–20 kJ mol^{-1}. This interaction energy value is very similar to that found for the Rh_4 cluster of Figure 10.22.

It is a general observation that for CO interacting with Pt surfaces, when CO coverage becomes high release of repulsive CO interactions occurs by relocation of surface metal atom positions [6, 53].

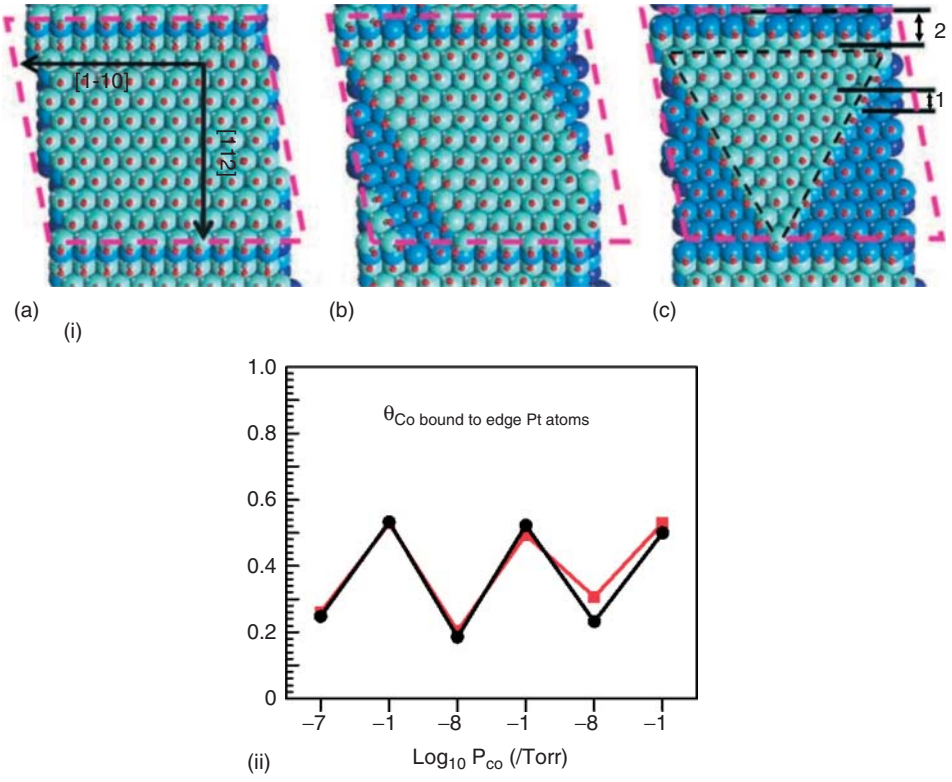

Figure 10.24 (I) Models of double-stepped Pt(557) surface covered by CO at high pressure used in the DFT calculations: (a) unrestructured terrace, (b) parallelogram-shaped nanoclusters, and (c) triangular-shaped nanoclusters. Dashed line frames in each image show the periodic supercell used in the DFT calculations. First- and second-layer Pt atoms are represented with olive green and blue balls, respectively. Red dots represent the oxygen atoms of CO molecules. In (c), 1 and 2 indicate step-edge heights (one or two Pt atoms); (II, d) coverage of CO molecules adsorbed on low-coordination sites as a function of pressure. The red curve is the coverage calculated with the O1s XPS peak at 533.1 eV. For the black curve, a Pt4f peak component has been used. (Reproduced with permission from Ref. [55]).

An excellent paper by Tao *et al.* [55] demonstrates that higher CO coverages than possible on a terrace can be found because of significant restructuring of the surface in small clusters, so that the number of kink and step-edge sites is substantially increased (Figure 10.24). Bending away of the CO molecules becomes possible at the step edges into nonparallel directions that relax direct repulsive interactions. The surface restructuring cost is overcome by increased coverage with CO molecules on the surface clusters, as the CO interaction energy is substantially higher than the Pt–Pt metal atom bond energies.

Lateral interactions affect chemisorption on small clusters differently compared to surfaces. For CO at low-coverage adsorption, energy differences are relatively

small, whereas this can be very different when one compares adsorption energies at high coverage. On the cluster, metal atom–metal atom bond distances, weakened by interaction with adsorbed molecules, are able to relax in contrast to metal atoms that are part of extended surfaces. The increased metal atom–metal atom distances reduce delocalization of surface valence electrons and hence reduce the repulsive interactions between coadsorbed CO molecules. At the same time, it will strengthen the covalent interaction with the CO molecules.

The comparison of computed CO adsorption energies of CO adsorbed to a Ru surface and nanoparticle of Figure 10.25 illustrates the importance of the different packing of the CO molecules for the two cases. Computed CO adsorption energies are shown as a function of CO coverage on a Ru(0001) surface and a 201-atom-containing cuboctahedral Ru cluster. On the Ru(0001) surface, the CO adsorption energies steeply decline beyond a fractional CO coverage of 0.3. On the 201-atom cluster at low CO coverage, one observes the expected small increase in CO adsorption energy with surface atom coordinative unsaturation on edge and corner atoms. At high CO coverage, the absolute values of the CO adsorption energies decrease, but the CO adsorption values remain high. At the metal cluster edges and corners, with their more open space, vicinal or even higher CO coordination with a surface metal atom becomes possible, similar to the very small molecular Rh cluster of Figure 10.22.

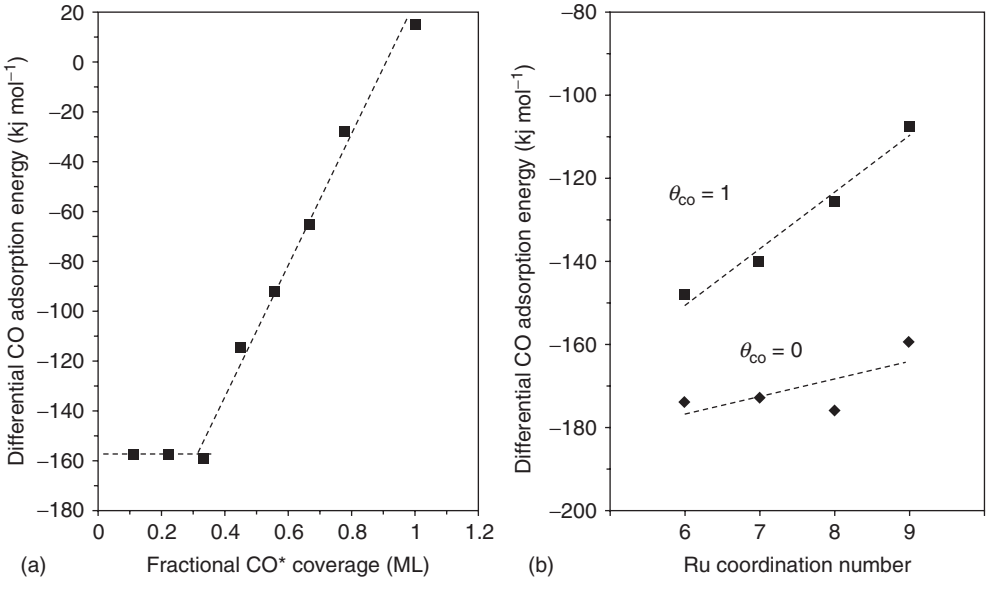

Figure 10.25 (a) Effect of fractional CO* coverage on calculated differential CO adsorption energies for the 3×3 Ru(0001) surface; (b) Site coordination number effects on calculated differentials adsorption energies for isolated CO* species (black squares, rotated) at one monolayer and CO* species at one monolayer (CO*/Ru_{surf} or $\theta_{CO} = 1$) coverage(straight square) on Ru_{201} clusters. (Reproduced with permission from Ref. [47]).

Repulsive through-space interaction energies also play an important role when the reactivity of larger molecular fragments is studied. For instance, the recombination of CH_3 fragments on a surface terrace to form ethane is inhibited, because the CH_3 fragments are adsorbed parallel to the surface normal [56]. No C–C bond formation occurs because the CH_3 umbrellas repulsively interact, so that the carbon atoms in the respective molecular adsorbed fragments cannot meet. A similar repulsive interaction prevents insertion of CO into a CH_3 intermediate adsorbed to a surface terrace [57].

On a metal surface, CO insertion occurs instead into an adsorbed CH_2 [58] or CH [59] fragment. The direct repulsive effect is absent.

Adatom lateral interactions are dominated by through metal interactions, as direct steric interaction is absent. When the adatom shares bonding to a surface metal atom with another adatom, their interaction will be repulsive. This is because a metal atom decreases coordinative unsaturation when other atoms attach. The resulting repulsive interaction will be a few times 10 kJ mol^{-1}. On the other hand, when two adatoms interact indirectly so that each adatom–metal atom bond is separated by one metal–metal atom distance the lateral interaction will be attractive. This is the consequence of bond weakening of bonds directed to a metal atom, when its coordinative unsaturation decreases.

A good illustration of the consequences of such bond weakening of metal atom–metal atom bonds upon adsorption is the row pairing phenomenon. This is illustrated in Figure 10.26 for O adatoms adsorbed at high coverage to the (520) or (730) surface of Pt [60]. The calculations refer to electrochemical experiments and hence indicate the electrode potential instead of the O_2 pressure that equilibrates O adsorption from the water phase.

Increased coverage with O adatoms leads to coadsorption of O adatoms that now share bonding with the same metal atom. This not only leads to repulsive interactions between the atoms that share bonding to the same metal atom but it also may weaken the neighboring metal atom–metal atom bonds considerably. As we found for reconstruction induced by CO adsorption, a driving force for surface reconstruction develops toward a surface state with lower density of surface metal atoms, which will release the tension within the surface due to the increasing weakening of the metal atom–metal atom bonds. An additional driving force is the result of the decrease in the number of metal atom–metal atom neighbors, which will increase the strength of the individual metal atom adsorbated bonds, as is illustrated in Figure 10.27 [60].

Figure 10.27 illustrates the energetics involved in the missing row reconstruction of the Cu(110) surface. Note the energy cost to remove the Cu atoms, but the gain in energy because of the increased Cu–O interactions.

It has also been shown on Co that increased adsorption of C atoms on the (111) surface of a small particle with fcc bulk structure leads to transformations of the Co(100) surface. This surface becomes stabilized because the C atom prefers the fivefold coordination possible on this surface. The reconstruction will generate step-edge sites on the surface because of the decreased Co metal density on the more open [87], which are potential sites for low-activation CO bond cleavage as

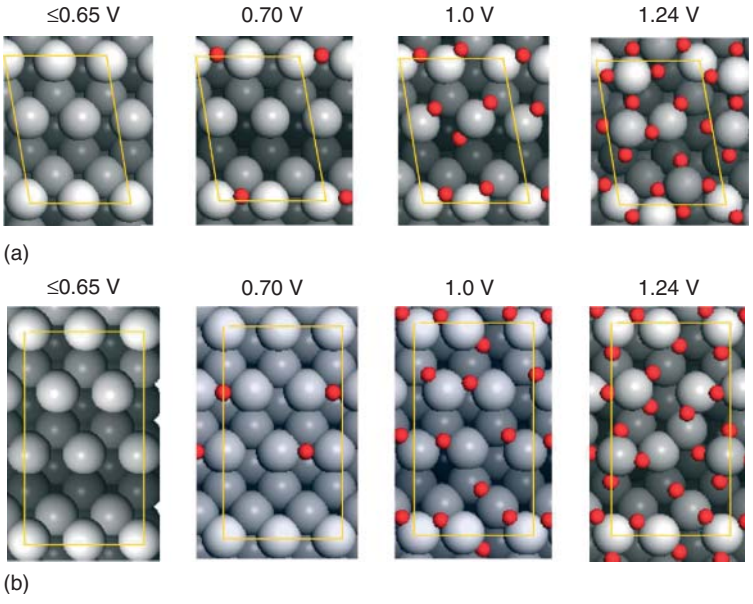

Figure 10.26 Surface reconstruction of Pt surfaces induced by O adsorption. Top views of the most stable structures of adsorbed O adsorbed to (a) Pt(520) and (b) (730) surfaces, respectively, at different electrode potentials, that generate O_{ads} electrocatalytically from water. The yellow lines indicate the surface unit cells that have been used in the calculations. (Reproduced with permission from Ref. [61]).

we discuss next. The larger ease of relaxation of bond distances at the smaller nanoparticles and access to sublattice sites at the edges will allow sublattice diffusion by hydrogen or carbon atoms, whereas for large particles this would not occur [62].

10.6
Adsorbate Bond Activation and Formation

10.6.1
The Reactivity of Different Metal Surfaces

We discuss in this section the relation between type of adsorbate bond activated and its dependence on surface structure. In heterogeneous catalysis, this has important consequences for the particle size and shape dependence of catalytic reactions, where the rate is controlled by a particular bond activation reaction.

This subsection begins with a short summary of particle-size-dependence observations of chemical bond activation. Next, the Bronsted–Evans–Polanyi relation that relates activation energies of elementary surface reaction steps with the corresponding reaction energies is introduced. In the subsections that follow, the

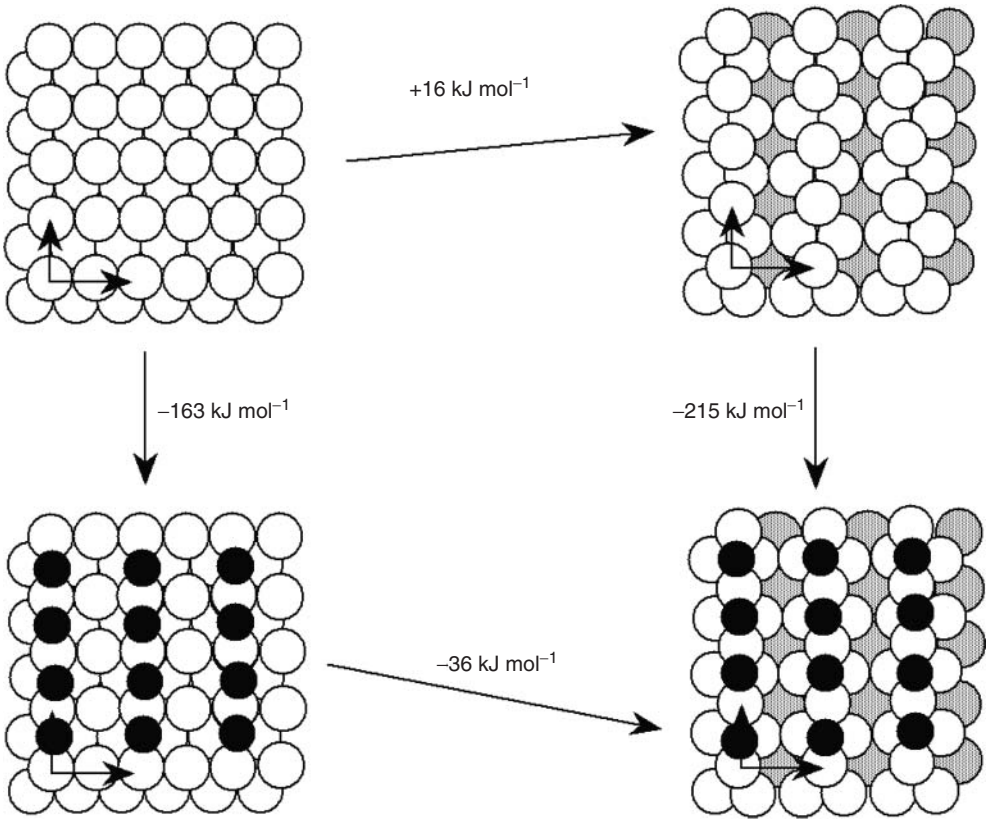

Figure 10.27 The missing row construction of the Cu(110) surface induced by adsorption with O adatoms. The energy changes of nonoxygen covered and oxygen covered surfaces are compared. (Reproduced with permission from Ref. [60]).

electronic and structural requirements for low activation energies of bond cleavage and bond formation reactions of small molecular adsorbates are introduced.

It will appear that the particle size dependence of chemical bond activation distinguishes two reaction categories: reactions in which the activation of σ bonds is rate controlling versus reactions in which activation of molecular π bonds is rate determining.

The chemistry of σ bond activation is quite different from that of the activation of π bonds. This is summarized in brief here. Then, we discuss its consequences for particle size dependence.

Activation of σ-type CH bonds as in an alkane is the prototype of a reaction where the reaction center is a single (surface) metal atom. This in contrast to the activation of a π bond as in CO or N_2, which requires an ensemble of surface atoms.

The driving force for bond dissociation is the stability of the adsorbed surface fragments that are generated upon dissociation. The interaction energies of an H

atom or alkyl fragment do not strongly vary when the number of surface atoms to which they coordinate changes. They tend to prefer atop adsorption slightly. For this reason and the better overlap of CH adsorbate orbitals with metal atom d-valence atom orbitals, dissociation of a σ CH bond as in methane will usually occur over a single metal atom.

This is very different for dissociation of a molecular π bond as in CO or NO. The atoms C, O, or N that are generated upon dissociation of CO or NO are only stable when highly coordinated to a surface atom. Then, the high-coordination requirement for stable adsorption of a C or O atom requires at least an ensemble of five or six metal atoms as reaction center for the dissociation of the diatomic molecule.

As illustrated in Figure 10.28 in heterogeneous catalysis for nanosized metal particles, one distinguishes three types of transition-metal particle-size-dependent behavior. When activation of σ-type CH bonds is rate controlling, the rate of reaction normalized per surface atom, TOF (turn over frequency) tends to increase with a decrease in particle size. This is the behavior according to curve II. It is due to the relative increase in the fraction of more reactive coordinatively unsaturated surface atoms.

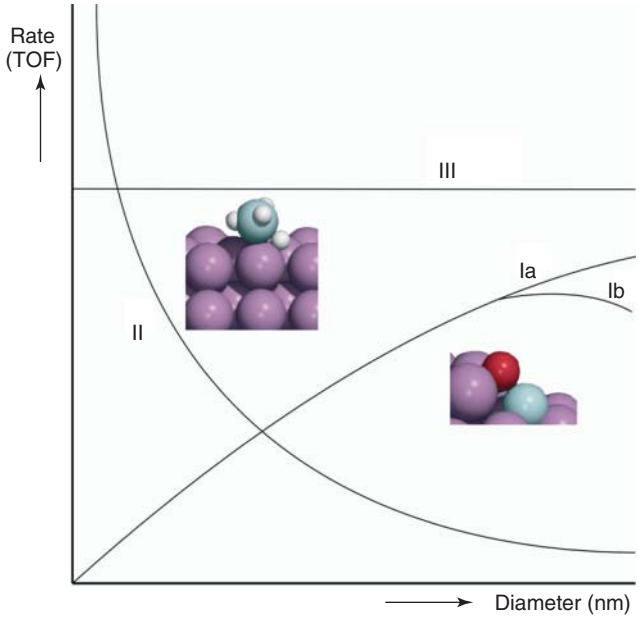

Figure 10.28 Schematic illustration of particle size dependence of the rate of a heterogeneous catalytic reaction. Curves Ia and Ib correspond to the activation or formation of a molecule with π type valence electrons. Curves II and III refer to activation of molecular σ bond and formation of molecular σ bond, respectively. (Adapted from Ref. [63]).

The changes in activation energies with increasing coordinative unsaturation of σ-type bonds are discussed in detail in Section 10.6.2.3. As we see in that section when coordinative unsaturation of the surface atom changes, the activation energy of the CH bond cleavage reaction change is close to that of the reaction energy of this reaction. This is an example of Brønsted–Evans–Polanyi-type behavior that is explained in the second part of this introductory section. Because of this relation, microscopic reversibility dictates that the activation energy of the reverse reaction in which a CH bond is formed will not change [42] with coordinative unsaturation of the surface atom. Therefore, a reaction rate limited in the rate of formation of a CH bond from adsorbed H atom and alkyl will behave according to curve III of Figure 10.28.

Low-activation energy dissociation of diatomic molecules with π bonds requires a specific topology of the adsorption site. Not only is a large ensemble of surface atoms necessary but an arrangement in a step-edge topology is also needed. This is discussed in Section 10.6.2.1.

When one compares the relative stability of such step-edge sites on a surface of a particle of decreasing size, it appears that on surfaces less then a particular size such step-edge sites cannot anymore be supported [64, 65]. Hence, the low-activation barriers for dissociation as well as recombination disappear on small particles. As a consequence, the rate of reaction controlled by activation of molecular π bonds decreases when the size of the nanoparticle is below this particle size [44]. The behavior of curves I of Figure 10.28 results.

In the final part of this subsection, we introduce the Brønsted–Evans–Polanyi relation (for early Refs. [66, 67], for later Refs. [44, 68–71] The change in activation energies with coordinative surface atom *unsaturation* that is nearly proportional with the change in reaction energy, as found for methane activation, is an example of this linear activation energy–reaction energy relation. It applies to surface elementary reactions that are compared on surfaces of different composition or structure as long as their reaction path is similar and reaction center has a similar topology, given by Eq. (10.11).

$$\Delta E_{act} = \alpha_{BEP} \Delta E_{react} \; (0 \leq \alpha_{BEP} \leq 1) \tag{10.11}$$

For a dissociation reaction on a surface, the proportionality parameter α_{BEP} is close to one, because bond activation requires a strong interaction with the metal surface. As it causes the structure of the activated molecule in the transition state to be close to that of the final dissociated state, its energetics will closely follow that of the final state energy [3, 24].

This is illustrated in Figure 10.29. The activation energies of the forward reaction closely follow the change in reaction energies and hence the reverse reaction of recombination of molecular fragments on the surface to form the molecular chemical bond has very similar activation energies. This is the principle of microscopic reversibility.

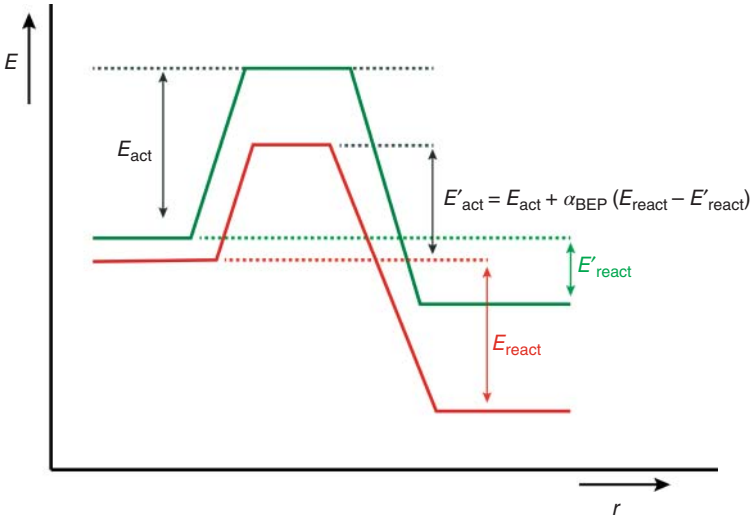

Figure 10.29 Schematic illustration of Brønsted–Evans–Polanyi relationship between activation energy (E_{act}) change and reaction energy (E_{react}) change. α_{BEP} proportionality constant defined in Eq. (10.11). Green nonreactive surface and red reactive surface.

10.6.2 The Quantum-Chemical View of Bond Activation

10.6.2.1 Activation of the Molecular π Bond (Particle Shape Dependence)

The activation of a π bond as in CO or N_2 requires an ensemble of five or six metal atoms in the configuration of a surface step. In Figure 10.30, a comparison of the activation energies on a step-site and surface of Ru is given [88].

The change of activation barrier of CO by altered surface topology is substantial. In the case of CO, activation by Ru is more than 100 kJ mol^{-1}. Similar large changes are found for other transition metals. The phenomenon is general. Similar large changes are found for activation of other diatomic molecules with π bonds as N_2, NO, or O_2.

In this particular case of change in the activation energy of molecular π bond cleavage by altered surface topology, the Brønsted–Evans–Polany relation Eq. (10.11) does not apply. There is no relation between change in activation energy and reaction energy because the change in activation energy corresponds to a change in reaction path of the dissociation reaction.

We discuss here the chemical bonding aspects that determine this surface topology dependence.

It is discussed in Section 10.3.2 that when a molecule as CO adsorbs to the surface the antibonding $2\pi^*$ orbitals becomes partially occupied by electrons because of backdonation from the metal surface. This weakens the internal C–O bond strength. The stronger the covalent interaction with the surface, the more weakened the C–O bond in the adsorbed CO molecule.

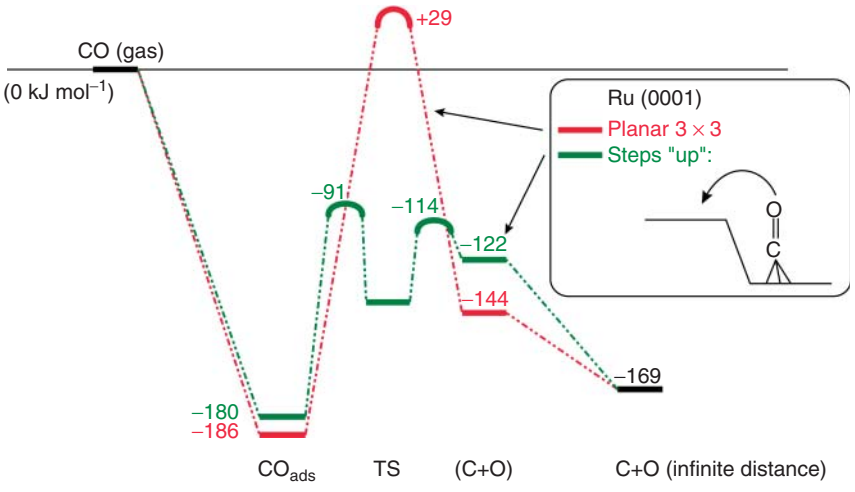

Figure 10.30 DFT-calculated CO adsorption energies and activation of CO dissociation on Ru(0001) terrace and step-edge site (kJ/mol). (Adapted from Ref. [88].)

On the nonstepped surface, the CO molecule will adsorb perpendicular to the surface. Orbital mixing between CO and surface orbitals is only possible through the M–C contact. Stretching of the C–O bond and bending toward the surface of adsorbed CO will cost energy until the transition state is reached. Then the molecule becomes adsorbed side-on instead of its original perpendicular orientation. When a CO molecule is in this side-on adsorbed state parallel to the surface, both the C and O atoms have contact with the surface. Compared to the perpendicular adsorbed state, molecular orbital overlap increases and the antibonding $2\pi^*$ orbital will get a further increased electron occupation. This will increasingly weaken the C–O bond. Beyond the transition state, the carbon metal atom and oxygen metal atom interactions increase and the molecule dissociates.

Figure 10.30 illustrates the likeness of the geometrical as well as electronic structure of the CO in its dissociated state compared to that in the transition state [44]. The changes in electron density are shown for a terrace and step-edge site. Especially in the transition state on the step-edge site, with the lower barrier, the electron density between the C and O atoms in the transition state has become very small.

There are three factors that contribute to the low-energy activation energy on a step-edge site. The contact of CO through its C as well as O atom with the metal surface provides increased backdonation of electrons into the unoccupied CO $2\pi^*$ orbital. This weakens already strongly the bond in its adsorbed initial state. Second, the geometry of the step-edge site requires little stretch of the CO bond to reach its transition state. Importantly, different from the situation in the transition state on the nonstepped surface the C and O atoms of the dissociating CO molecule do not share a chemical bond with the same surface metal atom. As we have seen in Section 10.5 dealing with lateral interactions, the difference between in energy

between a coadsorbed state in which the atoms share a chemical bond with the same metal atom or not may be of repulsive nature and can be on the order of 50 kJ mol^{-1}.

10.6.2.2 The Uniqueness of the (100) Surface

Similarly as on a step-edge site, dissociation of π-bonded molecules on the square (100) surface of an fcc crystal becomes substantially lower than on the (111) surface. For NO dissociation and recombination, the corresponding energetic and structural differences are shown in Figures 10.31 [44].

One should note the remarkable similarity in activation energy dependence on surface structure as we discussed in the previous section for activation of CO. Remarkable is the low activation energy of NO on the (100) surface compared to that on the (111) surface and the closeness in its value compared to that at the step-edge site. Figure 10.32b shows that the NO molecules dissociates on the (100)

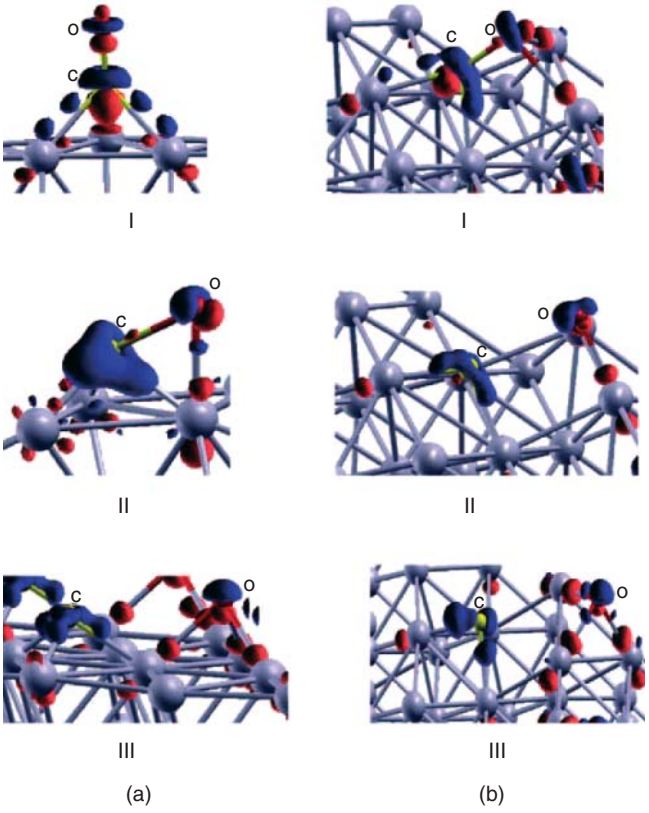

Figure 10.31 Charge density difference plots of CO on the Ru(0001) surface (a) and stepped Ru(1015) surface (b): I, initial state; II, transition state; and III, final state. The red and blue regions indicate the charge lost and gained, respectively. (Reproduced with permission from Ref. [44]).

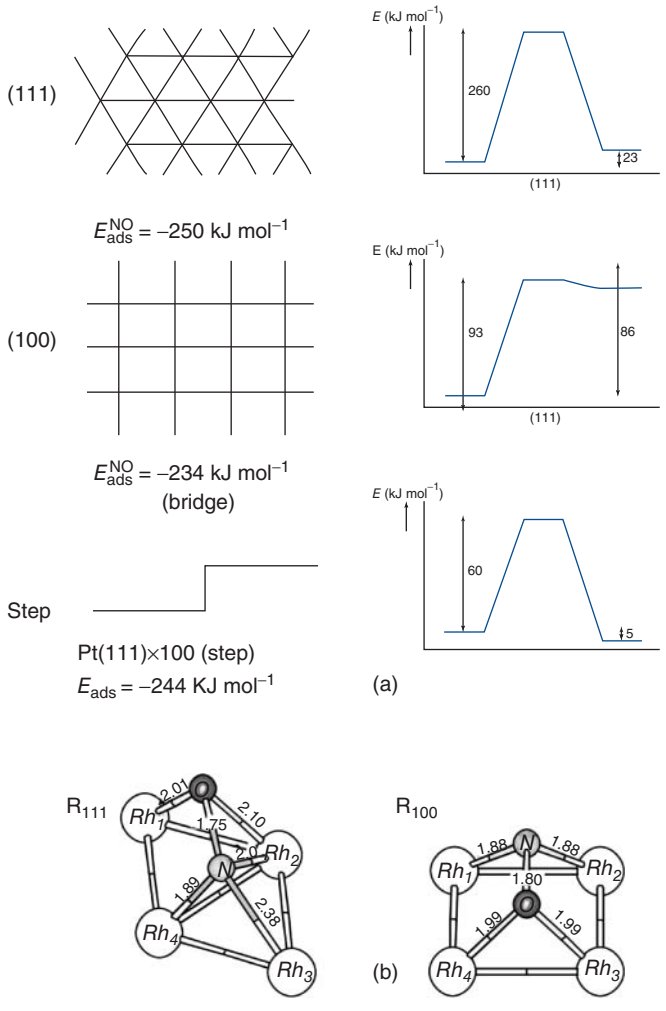

Figure 10.32 (a) Schematic representation of NO dissociation energies on (top) Pt(111), (middle) Pt(100), and (bottom) stepped Pt surfaces. (Reproduced with permission from Ref. [44]); (b) tansition states for NO dissociation computed for Rh(111) and Rh(100) surfaces. (Reproduced with permission from Ref. [73]).

surface through a transition state in which the atoms generated upon dissociation do not share a chemical bond with the same metal atom [72]. This is similar to that on the step-edge site. The recombination reaction of N and O on the (100) surface has a substantially lower barrier even compared to that on the step-edge, because of the unfavorable thermodynamics of the relative energies of N_{ads} and O_{ads} compared to that of adsorbed NO. It relates to the unstable coordination to the (100) surface of the adsorbed N_{ads} atom, that prefers threefold coordination instead

of the fourfold coordination offered by this surface. Similarly, recombination of N_{ads} to form N_2 has a low activation energy on this surface.

A cubic particle of fcc structure will have only (100) planes. Reactions that preferentially are catalyzed by a (100) surface will show increased catalyst performance when catalyzed by such a cubic particle. Apart from N_{ads} recombination to give N_2 or NO, the recombination of NH_2 fragments is also preferred on the (100) surface [74, 75].

10.6.2.3 Activation of the Molecular σ Bond; CH_4 and NH_3

One of the distinguishing features of the activation of a molecular CH, NH, or OH bond is that it usually occurs through a transition state in contact with a single metal atom. The energy differences of the three stages of the dissociation reaction are illustrated for CH_4 in Figure 10.33 [76, 77].

Differences in the activation energies are due to differences in the reactivity of the activating surface atom. This relates as we have seen to the degree of coordinative unsaturation of that atom. Changes in the activation energies are comparable to that of the reaction energies. The transition state structure again is close to that of the final state and the Brønsted–Evans–Polanyi parameter α_{BEP} close to 1.

Ammonia activation profiles for three different surface structures are shown in Figure 10.34. Activation of CH_4 is sensitive to coordinative unsaturation of the surface atoms, whereas this is not the case for activation of NH_3 [74].

Different from methane, it already will strongly interact in the predissociation adsorbed state. This is due to the availability for adsorption through the free valence of NH_3. For methane, the molecule has to distort substantially so that close contact between C and H atom becomes possible and CH bond activation can occur. This is different for NH_3. Through its lone-pair orbital, it is initially adsorbed atop of a metal atom. While NH_2 prefers adsorption in twofold coordination, upon dissociation

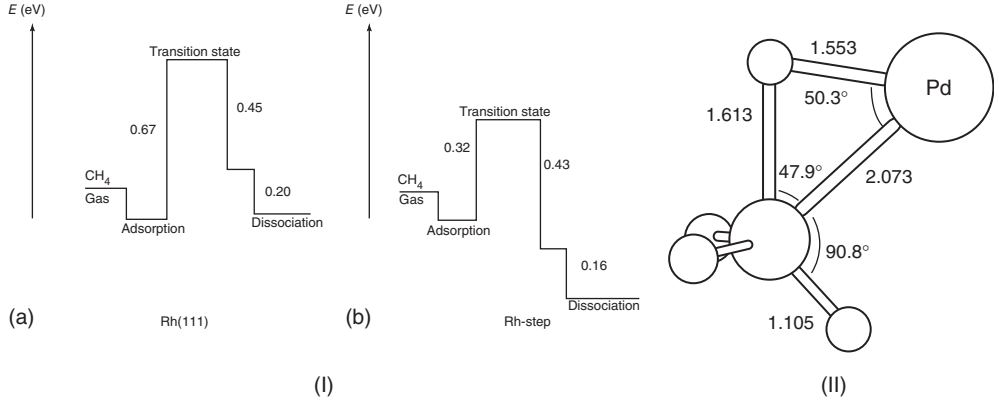

Figure 10.33 Activation of methane. (a,b) Changes in energy of a dissociating methane molecule activated by a surface atom on a Rh(111) surface and step-edge atom. (Reproduced with permission from Ref. [76]). (c) transition state structure of methane activated by Pd atom. (Reproduced with permission from Ref. [77]).

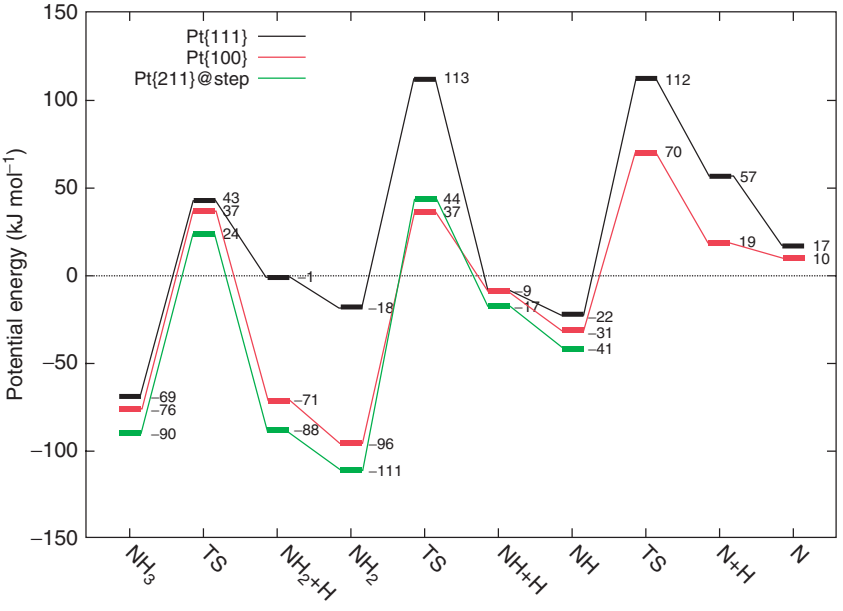

Figure 10.34 DFT-calculated reaction energy diagram for the dissociation of NH_x, 1, 2, 3 over Pt(100), Pt(111), and stepped Pt(211). (All calculations were carried out using a 2×2 unit cell with 25% coverage). The energies are with respect to NH_3 in the gas phase. (Reproduced with permission from Ref. [78]).

the shift to this position only occurs after activation of NH of the NH_3-adsorbed molecule in the atop coordination site. Once the NH bond in NH_3 is dissociated, the NH_2 fragment will move to the twofold coordination site. Changes in energy of NH_3 and NH_2 adsorbed to a single atom will be similar when coordination of that atom changes. Therefore, there is little change in activation energy.

The barriers of NH_3 activation on the Pt surface decrease substantially when the H atom becomes accepted by O_{ads} or OH_{ads}, as is illustrated in Figure 10.35 [38, 78]:

The essential reasons for this promotional effect of O_{ads} and OH_{ads} are the relatively weak interactions of H_{ads} as well as O_{ads} with the Pt metal surface. It results in the formation of a stronger OH bond from O_{ads} and H_{ads} than that of the H–Pt bond.

The reason for the decreased activation energy on the (100) surface compared to that on the (111) surface is that O-NH transition states on the latter occur without sharing of bonding of N and O to the same metal atom. The lowering of the reaction barriers for activation with OH_{ads} compared to activation with O_{ads} on the Pt(111) surface is related to this. OH prefers atop adsorption. Hence, in the transition state with ammonia, no sharing of bonds with the same metal atom has to occur. This in contrast to activation on the Pt(111) surface of $NH_{3,ads}$ by coadsorbed O_{ads}. Because of the preferred high coordination of adsorbed O on this surface, in the transition

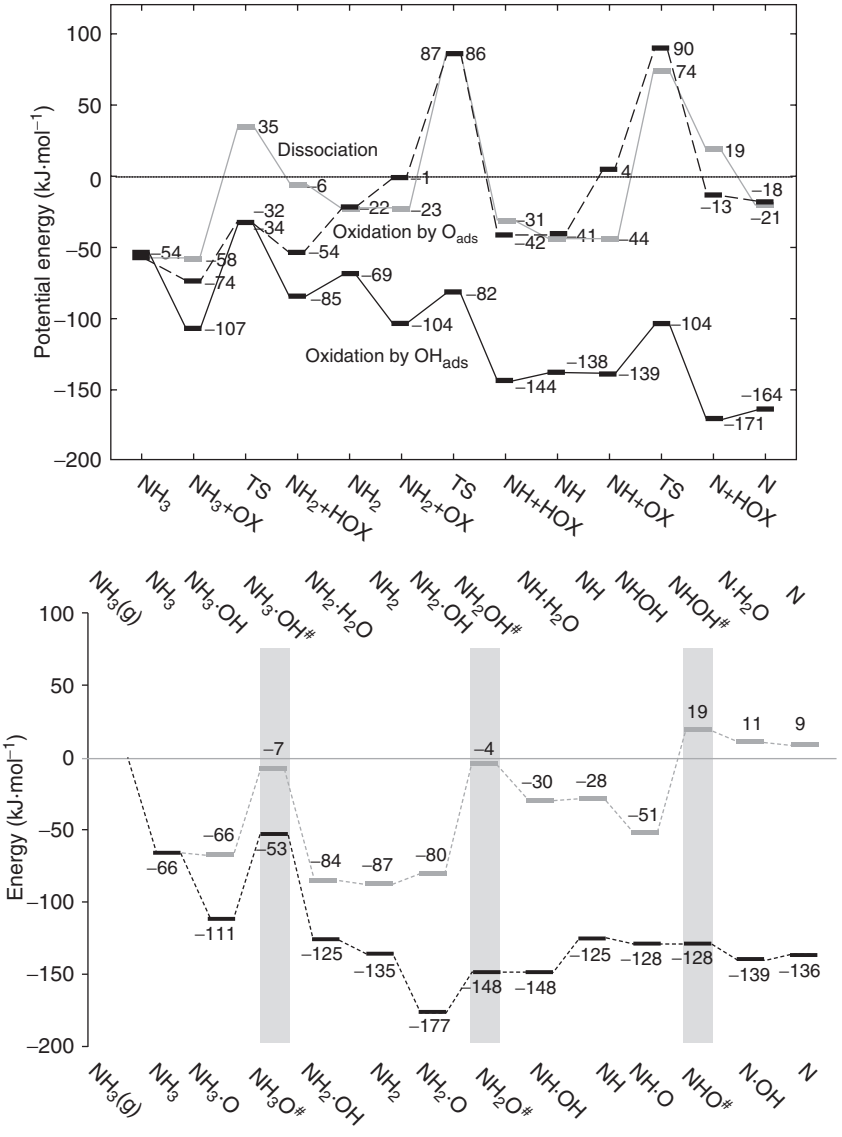

Figure 10.35 (a) Reaction energy diagram of the dehydrogenation reactions of NH_x on Pt(111). All total energies are with respect to NH_3(g), Pt(111)(s), $3O_{ads}$, and $3H_{ads}$ and are zero-point energy corrected. O_X or HO_X on the abscissa mean oxidant or hydrogenated oxidant and can be OH, O, or an empty site or their hydrogenated forms. All NH_x + (H)O_X coadsorbate states are with lateral interactions. In all "single" adsorbate states, we assume no lateral interactions. (Reproduced with permission from Ref. [38]). (b) Reaction pathway for the oxidative dehydrogenation of ammonia over Pt(100) assisted by O (black line, bottom legend) and OH (gray line, top legend). The energies are with respect to NH_3(g) + $3O_{ads}$ + $3OH_{ads}$, ZPE corrected. (Reproduced with permission from Ref. [79]).

state, it has to share a chemical bond with the nitrogen atom of adsorbed NH. This causes a high activation energy of the dissociation reaction of the NH bond, whereas the thermodynamically reaction of the H atom with O_{ads} is favored over Pt metal activation of the NH_3 bond.

10.7 Transition State Analysis: A Summary

An interesting way to analyze the bond energy changes of a dissociating molecule is provided by the activation strain bond model proposed by Bickelhaupt [80, 81]. For the activation of methane on the Rh(111) surface, this is illustrated in Figure 10.36:

Within the activation strain model, the energy cost to stretch the CH bond in methane in its transition state is deduced from the energy of the corresponding distorted state in the gas phase. The transition state energy is considered to result from the interaction energy of the distorted methane molecule with the metal surface. As one observes from Figure 10.36, straining the CH bond toward its transition state geometry weakens the bond energy by approximately 40%. The interaction with the metal surface assists dissociation because of stabilizing M–H and M–C interactions. This results in a lower overall activation energy.

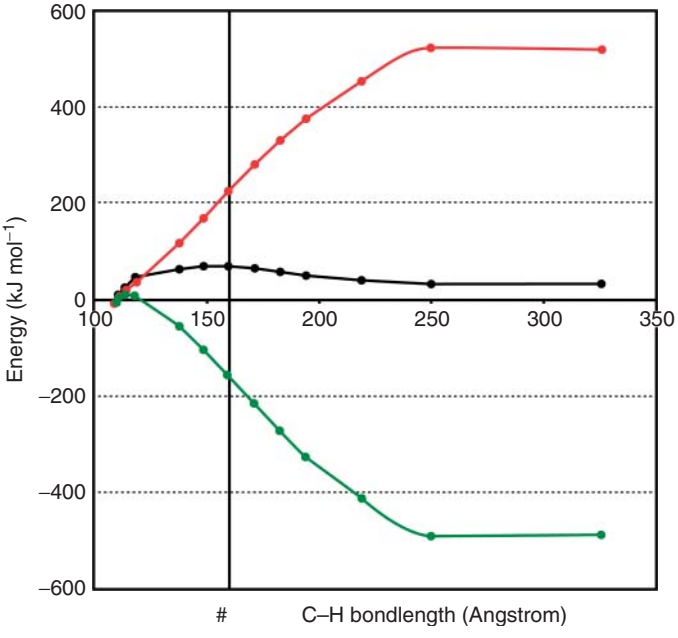

Figure 10.36 Activation strain model analysis of the CH_4 dissociation on the Rh(111) surface. Interaction energy as a function of reaction coordinate (black line). ΔE_{strain} of the CH_4 molecule as a function of reaction coordinate (red line). ΔE_{int}. # indicates the position of the transition state (green line). (Adapted from Ref. [82]).

On the other hand, in the transition state, the interaction with the metal will also weaken the interaction between C–H in the dissociating CH bond. This is not accounted for in the comparison made within the strain activation model. Hence, the gas-phase strain energy estimate of the bond energy of CH in the transition state provides an upper bound to it and the interaction with the surface metal atom will be overestimated.

This follows well from a bond order analysis (Eq. (10.7)) of the changing interactions when the molecule moves form its initial state through transition state to final state. This is illustrated in Table 10.7.

We observe the initial bond order of the CH bond that is cleaved to be close to one. It decreases to 0.29 in the transition state. This implies a more substantial weakening in contrast to the assumption of the activation strain model. The M–H and M–C bond orders are, respectively, 0.38 and 0.43, to be compared with the final state values 0.42 and 0.54, respectively. Compared to the initial CH bond interaction in the transition state, the CH bond interaction has been substantially weakened. One also finds that the M–C and M–H interactions are already close to those of the final state. The bonding interactions are distributed in a close to even distribution over the three bonds of H–C, C–Rh, and H–Rh. In the final state, the dissociating H atom moves to a twofold adsorption site. The closeness of the bondorders of the C–Rh bond and one of H–Rh bonds to those in the final state illustrates the late transition state nature of CH bond activation.

An alternative way to analyze the interaction changes in the transition is the barrier decomposition analysis by Crawford and Hu [83] (Figure 10.37).

Because transition states are late, they start the analysis by a comparison of the transition state interactions with those of the final state dissociated state values. Crawford and Hu [83] estimate the activation energy for recombination based on the assumption that the interaction energy between the dissociating fragments is negligible in the transition state. This is the other extreme choice compared to that of the activation strain model. The transition state energy for recombination then consists of the energy to bring the fragments together into the pretransition state from which recombination will start. This will usually be a repulsive energy, which can be significant when the recombining atoms share bonding with the same metal atom. In a second step, the energy cost is added when the adatom–metal atom

Table 10.7 Bond orders of the bonds involved in the methane activation C-Rh, C-H, and H-Rh at the reactant, transition, and product states.

Bond	Reactant state	Transition state	Product state
C-H	0.99	0.29	<0.2
C-Rh1	–	0.43	0.54
H-Rh1	–	0.38	0.42
H-Rh2	–	<0.2	0.49

Reproduced with permission from Ref. [44].

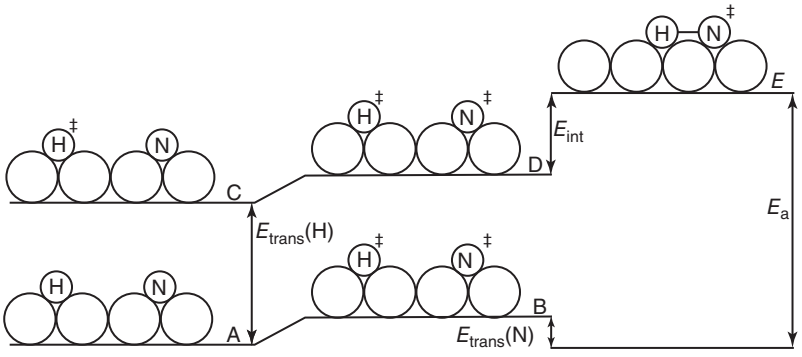

Figure 10.37 Schematic illustration of the barrier decomposition analysis. In state A, the reactants are far apart on the surface at their equilibrium geometries and not interacting with each other. In state B, the reactants are still far apart, although N has been activated to its transition-state geometry. State C is similar to state B only H is activated. In state D, both reactants are activated to their respective transition-state geometries but are not interacting. In state E, the reactants are at their transition-state locations and interacting. (Reproduced with permission from Ref. [83]).

distances are stretched until the transition state is reached. In this approach, the difference in activation energies, when reaction fragments share or do not share bonding with the same metal surface atom in their respective transition states, is immediately obvious.

As long as the structures of transition state and dissociated state are close, changes in metal–atom interactions will lead to the Brønsted–Evans–Polanyi relation between activation energy and reaction energy of a surface elementary reaction. Interestingly, microscopic reversibility implies that the Brønsted–Evans–Polanyi proportionality constant for recombination is typically 0.1. This implies that the ratio of the energy of the surface fragments in the transition state compared to the dissociated state is a constant and on the order of 90%.

We conclude this section by addressing the topic of symmetry relations of the electronic interactions between adsorbate and surface for low-activation energy reaction barriers. These can be considered as generalizations of symmetry rules deduced for metal–organic complexes [84, 85].

Orbital symmetry rules of chemical reactivity have been originally proposed and are known as the *Woodward–Hoffmann rules* useful to organic synthesis. The Woodward–Hoffman rules [86] apply to organic reactions without catalyst and explain why some reactions only proceed when photochemically activated. The rule derives from the necessity to circumvent the strong repulsive interaction, the Pauli repulsion, which arises when occupied orbitals of reacting molecular fragments of the same symmetry interact in their ground state. In the photochemical process, this Pauli repulsion is overcome by excitation of an electron to an unoccupied molecular orbital of different symmetry. This reduces the electron occupation of the repulsive antibonding orbitals and assists in the formation of the new chemical bonds. Hence, it now makes reaction possible.

In a nonphotochemical reaction, the repulsive Pauli interaction can only be relieved by coupling of the antibonding occupied molecular orbital with unoccupied orbitals that have the same symmetry. Then repulsive antibonding orbitals can release electrons into the unoccupied orbital. As Hoffmann explained in later papers dealing with organometallic reactions, the d-symmetry of unoccupied transition metal orbitals [84, 85] on the metal cation in these complexes reduces reaction barriers by providing an interaction with the occupied antibonding orbitals, which partially depletes them from an electron. For instance, when a C–C bond is formed, between two molecular fragments with atomic or molecular orbitals that are doubly occupied, Pauli repulsion occurs. The bonding and antibonding orbital fragments that evolve between the C–C bonds will both be doubly occupied. When the electron-occupied antibonding C–C orbital can interact with an empty metal cation d-atomic orbital, electron transfer will reduce electron occupation of the antibonding C–C orbital. As a consequence, Pauli repulsion between the reacting C–C atoms reduces and the transition state energy is lowered. This is the basic concept behind the low activation energy of reductive elimination in which a molecular bond is formed. The reverse process is oxidative addition by which a molecular bond dissociates and molecular fragments attach to the organometallic cation. In oxidative addition, an electron is accepted by a bond-weakening unoccupied adsorbate orbital from an occupied transition metal cation d-atomic orbital of proper symmetry.

On the surface, essentially the same electronic changes occur, but now on the metal atoms that are embedded in the surface. For instance, the strong interaction of H and alkyl generated upon RCH_2 bond dissociation of an alkane generates strong localized covalent bonds. Formally, each consumes one electron from the metal as in oxidative addition. Using a quantum-chemical description, the bonding surface fragment orbitals have low energies with large coefficients on adsorbed H or alkyl orbitals. On the other hand, the antibonding surface fragments are mainly localized on the metal atom with large contributions of the d-valence electrons, which are pushed upward. In this process, a fraction of the d-valence electron density will be pushed above the Fermi level. This reduces the electron occupation of the surface valence atoms. This is the analog of oxidative addition with reduction of electrons on the reacting metal atom.

In the transition state of the dissociating alkane molecule, an unoccupied orbital asymmetric with respect to the σ symmetric CH bond becomes partially populated during the dissociation process. When parallel to the surface, it interacts with a partially occupied asymmetric d-valence atomic orbital of the transition metal. The increased population of the asymmetric CH orbital will weaken the CH bond and hence lowers the activation energy for bond cleavage. The quantum-chemistry of the surface oxidative addition process is illustrated for dissociative adsorption in Figure 10.38.

A similar process occurs on the ensemble of surface atoms that activates dissociation of a molecular π bond. Then, the antibonding unoccupied orbital of the molecule has to interact with surface group orbitals of similar symmetry on the ensemble of surface atoms. When the unoccupied molecular orbital becomes

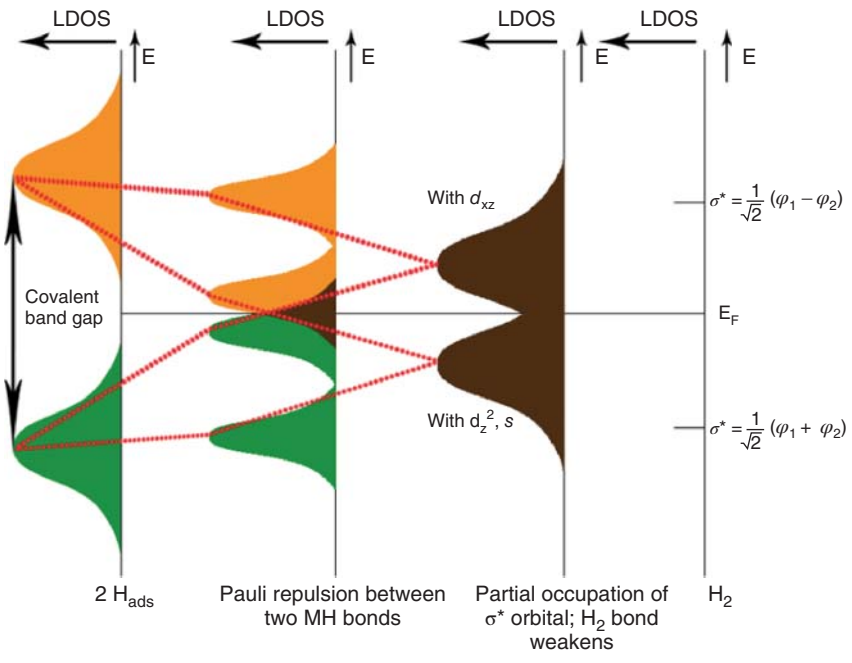

Figure 10.38 Schematic comparison of the transformation of the local density of states (LDOS) of gas-phase H_2 (right scheme) into that of two adsorbed H atoms (left scheme).

occupied, it will weaken the intramolecular bond. The surface group orbitals, which activate the antibonding unoccupied adsorbate orbital, will be an asymmetric combination of metal s-atomic orbitals and d-atomic orbitals of similar symmetry as the orbital to be activated of the adsorbate. A low barrier of dissociation requires interaction with asymmetric surface symmetry group orbitals that are occupied by electrons. A low barrier for recombination will be found when partially empty asymmetric surface symmetry group orbitals of low energy are available.

The activation energy of diatomic molecules with π bonds strongly depends on the topology of the reaction center, which determines the details of the dissociation reaction path. The thermodynamics of this dissociation reaction is mainly determined by the adsorption energies of the adatoms, as C, N, or O that are generated by the dissociation process. Differently from the adsorbates that we discussed earlier, which mainly interact through σ molecular fragments bonds, the dominant interaction of these atoms with the metal surface atoms is through the atomic 2p orbitals. Upon interaction with the metal surface atoms, these orbitals form bonding and antibonding surface fragment orbitals around the Fermi level. These chemical bonding features agree well with the Newns–Anderson description of the surface chemical bond, which considers the surface complex between adsorbate and surface atoms an embedded surface molecule. Coordinative unsaturation of the surface metal atoms, a major theme of this chapter, enhances

their covalent interaction with adsorbate orbitals and hence will not only tend to increase adsorption energies, but because of the Brønsted–Evans–Polanyi relation will also lower activation energies as long as there are no changes of the surface site.

References

1. Gross, A. (2009) *Theoretical Surface Science*, Springer-Verlag, Berlin, Heidelberg.
2. Sholl, D.S. and Steckel, J.A. (2009) *Density Functional Theory: A Practical Introduction*, John Wiley & Sons, Inc., Hoboken, NJ.
3. For a short introduction see: Appendix 6, van Santen, R.A. and Neurock, M. (2006) in *Molecular Heterogeneous Catalysis* (eds R.A. van Santen and M. Neurock), Wiley-VCH Verlag GmbH & Co. KGaA, 423–460.
4. Nilsson, A., Pettersson, L.G.M., and Nørskov, J.K. (eds) (2008) *Chemical Bonding at Surfaces and Interfaces*, Elsevier, Amsterdam.
5. Marsman, M., Kresse, G., and Furthmueller, J. (2011) VASP, the Guide, University of Vienna, Available from: http://cms.mpi.univie.ac.at/vasp/vasp.html.
6. Somorjai, G.A. (1994) *Introduction to Surface Chemistry and Catalysis*, John Wiley & Sons, Inc., New York.
7. Ertl, G. (2009) *Reactions at Solid Surfaces*, John Wiley & Sons, Inc., Hoboken, NJ.
8. Schleyer, P.v.R. (1998) *Encyclopedia of Computational Chemistry*, John Wiley & Sons, Inc., New York.
9. Hoffmann, R. (1988) *Solids and Surfaces*, Wiley-VCH Verlag GmbH, Weinheim.
10. Pauling, L. (1950) *The Nature of the Chemical Bond*, Oxford University Press.
11. Seitz, F. (1940) *The Modern Theory of Solids*, McGraw-Hill, New York.
12. Calle-Vallejo, F., Martínez, J.I., García-Lastra, J.M., Rossmeisl, J., and Koper, M.T.M. (2012) *Phys. Rev. Lett.*, **108**, 116103.
13. Koutecký, J. (1957) *Phys. Rev.*, **108**, 13–18.
14. Grimley, T.B. (1960) in *Advances in Catalysis*, vol. 12 (eds P.W.S.D.D. Eley and B.W. Paul), Academic Press, pp. 1–30.
15. Newns, D.M. (1969) *Phys. Rev.*, **178**, 1123–1135.
16. Anderson, P.W. (1961) *Phys. Rev.*, **124**, 41–53.
17. van Santen, R.A. (1991) *Theoretical Heterogeneous Catalysis*, World Scientific.
18. van Santen, R.A. and Neurock, M. (2007) *Russ. J. Phys. Chem. B*, **1**, 261–291.
19. Schiff, L.I. (1955) *Quantum Mechanics*, McGraw-Hill, New York.
20. Groß, A. (2006) *Top. Catal.*, **37**, 29–39.
21. Mavrikakis, M., Hammer, B., and Nørskov, J.K. (1998) *Phys. Rev. Lett.*, **81**, 2819–2822.
22. Bligaard, T. and Nørskov, J.K. (2008) in *Chemical Bonding at Surfaces and Interfaces* (eds A. Nilsson, L.G.M. Pettersson, and J.K. Nørskov), Elsevier, Amsterdam, pp. 255–316.
23. Nilsson, A., Pettersson, L.G.M., Hammer, B., Bligaard, T., Christensen, C.H., and Nørskov, J.K. (2005) *Catal. Lett.*, **100**, 111–114.
24. Hammer, B. and Nørskov, J.K. (2000) in *Advances in Catalysis*, vol. 45 (eds H.K. Bruce and C. Gates), Academic Press, pp. 71–129.
25. Puska, M.J., Nieminen, R.M., and Manninen, M. (1981) *Phys. Rev. B*, **24**, 3037–3047.
26. Chatt, J. and Duncanson, L.A. (1953) *J. Chem. Soc. (Resumed)*, **28**, 2939–2947.
27. Dewar, M.J.S. (1951) *Bull. Soc. Chim. Fr.*, **18**, C79.
28. Blyholder, G. (1964) *J. Phys. Chem.*, **68**, 2772–2777.
29. Mason, S.E., Grinberg, I., and Rappe, A.M. (2004) *Phys. Rev. B*, **69**, 161401.
30. Gil, A., Clotet, A., Ricart, J.M., Kresse, G., García-Hernández, M., Rösch, N., and Sautet, P. (2003) *Surf. Sci.*, **530**, 71–87.

31. Triguero, L., Pettersson, L.G.M., Minaev, B., and Ågren, H. (1998) *J. Chem. Phys.*, **108**, 1193–1205.
32. Sung, S.S. and Hoffmann, R. (1985) *J. Am. Chem. Soc.*, **107**, 578–584.
33. Föhlisch, A., Nyberg, M., Bennich, P., Triguero, L., Hasselström, J., Karis, O., Pettersson, L.G.M., and Nilsson, A. (2000) *J. Chem. Phys.*, **112**, 1946–1958.
34. Frechard, F., van Santen, R.A., Siokou, A., Niemantsverdriet, J.W., and Hafner, J. (1999) *J. Chem. Phys.*, **111**, 8124–8130.
35. Biemolt, W., van de Kerkhof, G.J.C.S., Davies, P.R., Jansen, A.P.J., and van Santen, R.A. (1992) *Chem. Phys. Lett.*, **188**, 477–486.
36. van Santen, R.A. (1987) *J. Chem. Soc., Faraday Trans. 1*, **83**, 1915–1934.
37. Zonnevylle, M.C., Hoffmann, R., van den Hoek, P.J., and van Santen, R.A. (1989) *Surf. Sci.*, **223**, 233–257.
38. Offermans, W.K., Jansen, A.P.J., and van Santen, R.A. (2006) *Surf. Sci.*, **600**, 1714–1734.
39. Popa, C., Offermans, W.K., van Santen, R.A., and Jansen, A.P.J. (2006) *Phys. Rev. B*, **74**, 155428.
40. Crawford, P. and Hu, P. (2006) *J. Phys. Chem. B*, **110**, 4157–4161.
41. van Santen, R.A. (1991) *Theoretical Heterogeneous Catalysis*, World Scientific, p. 239.
42. Abild-Pedersen, F., Greeley, J., Studt, F., Rossmeisl, J., Munter, T.R., Moses, P.G., Skúlason, E., Bligaard, T., and Nørskov, J.K. (2007) *Phys. Rev. Lett.*, **99**, 016105.
43. Shustorovich, E. (1986) *Surf. Sci. Rep.*, **6**, 1–63.
44. van Santen, R.A., Neurock, M., and Shetty, S.G. (2009) *Chem. Rev.*, **110**, 2005–2048.
45. Kitchin, J.R., Nørskov, J.K., Barteau, M.A., and Chen, J.G. (2004) *Phys. Rev. Lett.*, **93**, 156801.
46. Allian, A.D., Takanabe, K., Fujdala, K.L., Hao, X., Truex, T.J., Cai, J., Buda, C., Neurock, M., and Iglesia, E. (2011) *J. Am. Chem. Soc.*, **133**, 4498–4517.
47. Loveless, B.T., Buda, C., Neurock, M., and Iglesia, E. (2013) *J. Am. Chem. Soc.*, **135**, 6107.
48. Yudanov, I.V., Metzner, M., Genest, A., and Rösch, N. (2008) *J. Phys. Chem. C*, **112**, 20269–20275.
49. Kleis, J., Greeley, J., Romero, N.A., Morozov, V.A., Falsig, H., Larsen, A.H., Lu, J., Mortensen, J.J., Dułak, M., Thygesen, K.S., Nørskov, J.K., and Jacobsen, K.W. (2011) *Catal. Lett.*, **141**, 1067–1071.
50. Mingos, D.M.P. (1998) *Essential Trends in Inorganic Chemistry*, Oxford University Press, Inc., New York.
51. Albright, T.A., Burdett, J.K., and Whangbo, M.H. (1985) *Orbital Interactions in Chemistry*, John Wiley & Sons, Inc., New York.
52. Zeinalipour-Yazdi, C.D. and van Santen, R.A. (2012) *J. Phys. Chem. C*, **116**, 8721–8730.
53. Orita, H. and Inada, Y. (2005) *J. Phys. Chem. B*, **109**, 22469–22475.
54. Mason, S.E., Grinberg, I., and Rappe, A.M. (2006) *J. Phys. Chem. B*, **110**, 3816–3822.
55. Tao, F., Dag, S., Wang, L.W., Liu, Z., Butcher, D.R., Bluhm, H., Salmeron, M., and Somorjai, G.A. (2010) *Science*, **327**, 850–853.
56. Zheng, C., Apeloig, Y., and Hoffmann, R. (1988) *J. Am. Chem. Soc.*, **110**, 749–774.
57. Cheng, J., Hu, P., Ellis, P., French, S., Kelly, G., and Lok, C.M. (2008) *J. Phys. Chem. C*, **112**, 9464–9473.
58. Zhuo, M., Tan, K.F., Borgna, A., and Saeys, M. (2009) *J. Phys. Chem. C*, **113**, 8357–8365.
59. van Santen, R.A., Markvoort, A.J., Filot, I.A.W., Ghouri, M.M., and Hensen, E.J.M. (2013) *Phys. Chem. Chem. Phys.*, **15**, 17038–17063.
60. Frechard, F. and van Santen, R.A. (1998) *Surf. Sci.*, **407**, 200–211.
61. Zhu, T., Hensen, E.J.M., van Santen, R.A., Tian, N., Sun, S.-G., Jacob, T., and Kaghazchi, P. (2013) *Phys. Chem. Chem. Phys.*, **15**, 2268–2272.
62. Yudanov, I.V., Neyman, K.M., and Rösch, N. (2004) *Phys. Chem. Chem. Phys.*, **6**, 116–123.
63. Van Santen, R.A. (2009) *Acc. Chem. Res.*, **42**, 57–66.
64. van Hardeveld, R. and Hartog, F. (1969) *Surf. Sci.*, **15**, 189–230.
65. van Hardeveld, R. and van Montfoort, A. (1966) *Surf. Sci.*, **4**, 396–430.

66. Boudart, M. (1968) *Kinetics of Chemical Processes*, Prentice-Hall.
67. van Santen, R.A. and Niemantsverdriet, J.W. (1995) *Chemical Kinetics and Catalysis*, Plenum Press, London.
68. Bligaard, T., Nørskov, J.K., Dahl, S., Matthiesen, J., Christensen, C.H., and Sehested, J. (2004) *J. Catal.*, **224**, 206–217.
69. Loffreda, D., Delbecq, F., Vigné, F., and Sautet, P. (2009) *Angew. Chem. Int. Ed.*, **48**, 8978–8980.
70. Logadottir, A., Rod, T.H., Nørskov, J.K., Hammer, B., Dahl, S., and Jacobsen, C.J.H. (2001) *J. Catal.*, **197**, 229–231.
71. Pallassana, V. and Neurock, M. (2000) *J. Catal.*, **191**, 301–317.
72. Ge, Q. and Neurock, M. (2004) *J. Am. Chem. Soc.*, **126**, 1551–1559.
73. Loffreda, D., Simon, D., and Sautet, P. (2003) *J. Catal.*, **213**, 211–225.
74. Rosca, V. and Koper, M.T.M. (2006) *Phys. Chem. Chem. Phys.*, **8**, 2513–2524.
75. Koper, M.T.M. and van Santen, R.A. (1999) *J. Electroanal. Chem.*, **476**, 64–70.
76. Liu, Z.-P. and Hu, P. (2001) *J. Chem. Phys.*, **115**, 4977–4980.
77. Diefenbach, A., de Jong, G.T., and Bickelhaupt, F.M. (2005) *J. Chem. Theory Comput.*, **1**, 286–298.
78. Offermans, W.K., Jansen, A.P.J., van Santen, R.A., Novell-Leruth, G., Ricart, J.M., and Pérez-Ramírez, J. (2007) *J. Phys. Chem. C*, **111**, 17551–17557.
79. van Santen, R.A., Offermans, W.K., Ricart, J.M., Novell-Leruth, G., and Pérez-Ramírez, J. (2008) *J. Phys.: Conf. Ser.*, **117**, 012028.
80. Diefenbach, A. and Bickelhaupt, F.M. (2004) *J. Phys. Chem. A*, **108**, 8460–8466.
81. de Jong, G.T. and Bickelhaupt, F.M. (2007) *ChemPhysChem*, **8**, 1170–1181.
82. Bunnik, B.S., Kramer, G.-J., and van Santen, R. (2010) *Top. Catal.*, **53**, 403–416.
83. Crawford, P. and Hu, P. (2006) *J. Chem. Phys.*, **124**, 044705–044707.
84. Thorn, D.L. and Hoffmann, R. (1978) *J. Am. Chem. Soc.*, **100**, 2079–2090.
85. Berke, H. and Hoffmann, R. (1978) *J. Am. Chem. Soc.*, **100**, 7224–7236.
86. Woodward, R.B. and Hoffmann, R. (1969) *Angew. Chem., Int. Ed. Engl.*, **8**, 781–853.
87. Ciobîcă, I.M., van Santen, R.A., van Berge, P.J., and van de Loosdrecht, J. (2008) *Surf. Sci.*, **602**, 17–27.
88. Ciobîcă, I.M. and van Santen, R.A. (2003) *J. Phys. Chem. B*, **107**, 3808–3812.

11
Chemical Bonding of Lanthanides and Actinides

Nikolas Kaltsoyannis and Andrew Kerridge

11.1
Introduction

The fascinating electronic structure and bonding in compounds of the 4f (lanthanide, Ln) and 5f (actinide, An) elements present many significant challenges to computational chemistry. The combination of strong electron correlation within the valence orbital manifold, the weakness of the ligand field experienced by the metal centers, and relativistic effects are found nowhere else in the periodic table, and all must be properly accounted for in order to derive meaningful insight. For the actinide elements, in particular, it is vital that we rise to the theoretical challenge. The actinides lie at the heart of the nuclear fuel cycle (and, unfortunately, nuclear weapons), yet the intense radioactivity which makes these elements suitable for these uses also renders their experimental study highly problematic. There is arguably nowhere else in the periodic table where computational chemistry can play such an important role.

Chemically, the f elements are hard, and the bonding in their compounds has a large ionic component. The chemistry of the lanthanides is dominated by the trivalent oxidation state, as is that of the actinides after plutonium, whereas the earlier actinides display a much wider range of oxidation states owing to the larger radial extent of the 5f versus the 4f orbitals. The degree to which this greater diffuseness results in a covalent contribution to the bonding in compounds of the early actinides, particularly versus 4f analogues, is a recurring theme in f element chemistry.

In this chapter, we first present an overview of some of the technical difficulties that make f element computational chemistry so challenging, before going on to a number of examples of the uses of different theoretical approaches and the chemical insight they can provide. We shall focus on recent, topical examples that illustrate applications of some of the analytical techniques presented in Volume 1 of this book.

The Chemical Bond: Chemical Bonding Across the Periodic Table, First Edition.
Edited by Gernot Frenking, Sason Shaik.

11.2
Technical Issues

Different approaches are required in order to surmount the challenges presented to quantum chemistry by the f elements. For example, in high-valent complexes where f orbital occupation is low, Kohn–Sham density functional theory (KSDFT) [1], a single configurational method that treats electron correlation via an approximate fitted functional form, can be applied. The same approach can also be taken when ligand fields are sufficiently large such that the f orbital manifold exhibits significant splitting. This approach has the advantage that relativistic effects [2], which must be incorporated into quantum chemical calculations on molecules containing f elements, can be included in a number of ways. The best (but most expensive) of these involves the explicit four-component solution of the Dirac equation. A more approximate approach reduces the complexity of the problem by considering only the two electronic components of the solution to the Dirac equation. Further approximations are possible; the most popular of these involve the separation of scalar relativistic effects from those caused by spin-orbit coupling, via either the Douglas–Kroll-Hess (DKH) Hamiltonian or the zeroth order regular approximation (ZORA). It is even possible to remove the explicit consideration of relativistic effects entirely through the use of relativistic effective core potentials (RECPs) [3]. These replace the core electrons (which are most strongly affected by scalar relativistic effects) with an effective potential experienced by the valence electrons.

In situations where there is high f orbital occupation and/or ligand field splitting is small, the molecular wavefunction cannot be adequately described by a single Slater determinant. In such cases, multi-configurational methods are required. These methods incorporate static correlation via configuration interaction (CI) [4], that is, the interaction between energetically similar Slater determinants, and are capable of producing a highly accurate description of the electronic structure. Such approaches, however, limit the ways in which relativistic effects can be incorporated. Typically, the molecular wavefunction is allowed to relax with respect to a Hamiltonian incorporating only scalar relativistic effects, although RECPs can again be used. Spin-orbit coupling is then included in an *a posteriori* manner.

Whilst both mono- and multi-configurational approaches find a variety of applications in f block quantum chemistry (we shall encounter several such applications in this chapter) it is critical that the relative importance of the phenomena discussed here are properly considered and accounted for in order to produce quantitatively valid descriptions of bonding in these complicated and fascinating compounds.

11.3
The Energy Decomposition Approach to the Bonding in f Block Compounds

As described in Chapter 4 of Volume 1, analysis of chemical bonding can be performed by combining a fragment approach to the molecular structure of a chemical system with the decomposition of the total bonding energy (E_B) as

$$E_B = E_E + E_P + E_O$$

where E_E, E_P, and E_O are, respectively, the electrostatic interaction, Pauli repulsion and orbital mixing terms [5].

Recall that the electrostatic component is calculated from the superposition of the unperturbed fragment densities at the molecular geometry, and corresponds to the classical electrostatic effects associated with Coulombic attraction and repulsion. The electrostatic contribution is most commonly dominated by the nucleus–electron attractions and, therefore, has a stabilizing influence. The Pauli component is obtained by requiring that the electronic antisymmetry conditions be satisfied. It comprises the destabilizing interactions between occupied orbitals and is responsible for steric repulsion. The orbital mixing component represents a stabilizing factor originating from the relaxation of the molecular system because of the mixing of occupied and unoccupied orbitals on the different fragments, and can involve electron-pair bonding, charge-transfer or donor–acceptor interactions, and polarization. We will now examine the application of the EDA to two molecular f element systems.

11.3.1
A Comparison of U–N and U–O Bonding in Uranyl(VI) Complexes

The traditional view of the bonding in actinide compounds is that it is largely ionic with hard metal centers favoring hard ligands, and it is certainly the case that oxygen-donor ligands are commonplace in actinide chemistry, particularly so, for high oxidation states. The reactions summarized in Scheme 11.1 are, therefore, rather surprising, as solutions of $UO_2Cl_2(Cy_3PNH)_2$ **1** ($Cy = C_6H_{11}$) do not react with Cy_3PO even with an excess of the latter or at an elevated temperature (40 °C) [6]. By contrast, adding two equivalents of Cy_3PNH to $UO_2Cl_2(Cy_3PO)_2$ **2** results in

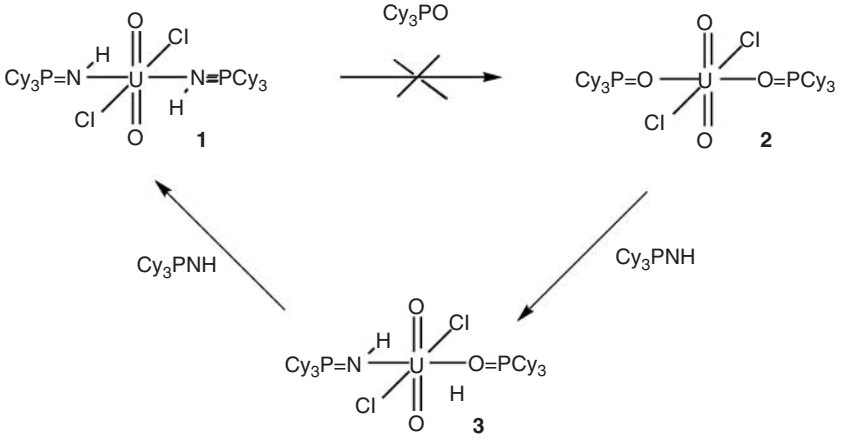

Scheme 11.1

Table 11.1 Energy decomposition of the U–N/O bonds (kJ mol^{-1}) in **1**, **2**, and **3**. For **1** and **2** the data are the average of the two bonds.

	1	2	U–N in 3	U–O in 3
Electrostatic interaction	−304.3	−217.3	−305.9	−222.4
Pauli repulsion	315.2	217.3	313.5	230.9
Prerelaxation energy	10.9	0.0	7.6	8.5
Orbital interaction	−174.1	−144.4	−178.0	−146.2
Total bonding energy	−163.2	−144.4	−170.5	−137.7

the immediate displacement of the Cy_3PO ligand and the quantitative formation of $UO_2Cl_2(Cy_3PNH)_2$.

KSDFT and EDA analysis was used to study the U–N/O bonds in these systems, and the data are collected in Table 11.1. The molecules were broken down into two closed-shell, neutral fragments, $UO_2Cl_2(Cy_3PNH)$ and Cy_3PNH for **1** and $UO_2Cl_2(Cy_3PO)$ and Cy_3PO for **2**. It is clear that the uranium-phosphinimine bonds are stronger than the uranium-phosphine oxide bonds, in agreement with the experimental conclusions summarized in Scheme 11.1. For **2**, the prerelaxation term (the sum of the electrostatic and Pauli contributions) is zero, whereas for **1** it is slightly positive, and the overall negative total bonding energy results from the favorable orbital term. It is noticeable that the orbital interaction is significantly more negative for **1** than for **2**, and we can attribute the greater U–N bond energy to this more favorable orbital interaction.

The strengths of the U–N and U–O bonds have been probed further by studying the intermediate **3** seen between **1** and **2** in Scheme 11.1. These data are given in the final two columns of Table 11.1, and it can be seen that the U–N bond is once again significantly more stable than the U–O bond. Furthermore, the prerelaxation term is almost exactly the same in the two bonds, and hence the greater stability of the U–N bond clearly arises from its larger orbital interaction.

11.3.2 Toward a 32-Electron Rule

The 18-electron rule, on which much of transition metal chemistry is based, formally corresponds to the full occupation of the *n*s, *n*p, and (*n*−1)d orbitals of the central atom in a complex. Pyykkö and coworkers wondered if the chemical availability of the valence 5f orbitals in the early actinides would permit the formation of a formally 32-electron compound, and argued that the 6p valence band of an icosahedral $[Pb_{12}]^{2-}$ cage would form a perfect partner for the 5f orbitals of an encapsulated actinide such as plutonium [7]. They, therefore, studied a series of ionic and neutral systems in which the $[Pb_{12}]^{2-}$ cage surrounds an f block metal center such that the 26 electrons of the $[Pb_{12}]^{2-}$ 6p band are supplemented by a further six electrons. The I_h symmetry of the lead cage was preserved in four cases: $Yb@Pb_{12}$, $Pu@Pb_{12}$, $[Am@Pb_{12}]^{+}$, and $[Cm@Pb_{12}]^{2+}$. Analysis of the valence

Table 11.2 Energy decomposition (eV) of M@Pb_{12}, starting from $[Pb_{12}]^{2-}$ and M^{2+} fragments.

	Yb@Pb_{12}	**Pu@Pb_{12}**
Electrostatic interaction	−18.12	−21.54
Pauli repulsion	9.22	16.39
Prerelaxation energy	−8.89	−5.15
Orbital interaction	−11.07	−17.02
Total bonding energy	−19.96	−22.17

molecular orbitals of these systems revealed that, for plutonium, the 7s, 7p, 6d, and 5f orbitals are all hybridized with the $[Pb_{12}]^{2-}$ cage orbitals, and that this compound is the first example of a centered 32-electron system. A similar conclusion was reached for the americium system, but the energetic stabilization of the 5f orbitals at curium is such that they hybridize little with the cage orbitals, and hence ''the Cm cluster does not fully correspond to a 32e system.'' An analogous conclusion was reached for Yb@Pb_{12}, in which the 4f orbitals do not strongly hybridize with the cage.

Table 11.2 shows the results of an EDA analysis on the neutral ytterbium and plutonium complexes. The total bonding energy is substantially more negative for the plutonium system, even though the sum of the prerelaxation electrostatic and Pauli components is much more favorable in the lanthanide compound. The much larger orbital term in the actinide compound reflects the appreciably larger hybridization of the 5f orbitals with the $[Pb_{12}]^{2-}$ cage.

11.4
f Block Applications of the Electron Localization Function

As described in Chapter 10 of Volume 1, the electron localization function (ELF) is a measure of the likelihood of finding an electron in the vicinity of a reference electron located at a given point and with the same spin; it measures the spatial localization of the reference electron. ELF values close to unity correspond to spatial regions of significant electron localization, as occurs in core orbitals, lone pairs, and strong bonds. In their study of Pu@Pb_{12}, Pyykkö and coworkers noted strong deformation of the electron density around each lead center in the direction of the central plutonium ion, as well as a local ELF maximum in the region between the plutonium ion and the lead atoms of the cage [7]. These characteristics are clearly indicative both of radial bonding between the cage and the encapsulated ion and significant hybridization between the plutonium 5f and lead 6p orbitals, all of which support the conclusion drawn from the energy decomposition study. The complementarity of the EDA and ELF analyses was further demonstrated by $[Am@Pb_{12}]^{+}$ and $[Cm@Pb_{12}]^{2+}$; the former exhibited a similar ELF to that of

the plutonium complex, whereas the latter showed only weak hybridization, and therefore a significantly reduced ELF maximum in the Cm–Pb bonding region.

In a later study [8], the same authors investigated another series of potential 32-electron systems, the organometallic $M@C_{28}$ ($M = Ce, Th, Pa^{+}, U^{2+}, Pu^{4+}$) cage complexes. Here, analysis of the ELF revealed that, whilst $Ce@C_{28}$ showed only a weak local maximum in the bonding region between the ion and the cage, all the actinide complexes showed strong maxima. This characteristic was most pronounced in the experimentally realizable Pu^{4+} complex, but was sufficiently strong in all complexes for the authors to characterize them as 32-electron systems.

Analysis of the ELF has also been used to understand the bonding in the uranium methylidyne complexes X_3UCH (X = F, Cl, Br) [9]. The ELF of each of these complexes was characterized by a ring-shaped disynaptic basin lying perpendicular to the U–C bond, a defining feature of the ELF in the prototypical C–C triple bond of ethyne, leading the authors to assert the existence of an unprecedented U–C triple bond.

As a final example of the utility of the ELF in understanding bonding in f element complexes, we consider its application in the characterization of bonding in the trivalent coordination complexes F_3MCO (M = Nd, U, Am) [10]. Here, the authors showed that, whereas standard orbital and population analysis methods appeared appropriate for the neodymium and uranium complexes, they became ambiguous when applied to the americium analogue. Whereas these standard analyses revealed significant back donation from U^{3+} to the π-accepting carbonyl ligand, a feature absent in the neodymium complex, the americium derivative was found to have a similar charge to that of neodymium and a spin density close to the free ion value of 6 a.u. Evidence of a small but nonnegligible back donation in the americium complex was found only by consideration of the delocalization indices of the topological basins of the ELF and the electron density. This was interpreted by the authors as evidence of a ''low magnitude covalent interaction,'' and may be a contributing factor in the observed selectivity of certain ligands for An^{3+} ions over their Ln^{3+} counterparts. This theme is developed more fully in the next section.

11.5
Does Covalency Increase or Decrease across the Actinide Series?

As previously noted, the 5f orbitals of the early actinide elements have a larger radial extension than their 4f counterparts, and 5f orbital involvement in the bonding in compounds of the first few actinides is not uncommon. Hence the bonding in compounds of, for example, uranium, is often found to be more covalent than in analogous compounds of the lanthanide series. The larger orbital interaction in $Pu@Pb_{12}$ versus $Yb@Pb_{12}$, discussed earlier, is typical. A recent KSDFT investigation of $[M(BH_4)_2(18\text{-crown-}6)]^{+}$ (M = Ce, U) revealed that the U–BH_4 interaction is more covalent than in the cerium analogue, as evidenced by Mulliken population and natural population analyses. M-BH_4 π bonding MOs were found to contain significantly more uranium character than

cerium, with almost no 4f involvement in the latter set of orbitals [11]. Meskaldji *et al.* probed the electronic structure and bonding in dithiolene complexes, $[M(dddt)_3]^{3-}$ (M = Nd, U; dddt = 5,6-dihydro-1,4-dithiin-2,3-dithiolate), and found that the 5f contribution to the frontier MOs in the uranium compound was much more significant than the 4f involvement in $[Nd(dddt)_3]^{3-}$, with noticeable metal → ligand backbonding in $[U(dddt)_3]^{3-}$ [12]. Szigethy *et al.* explored the comparison between Ce(IV) and Pu(IV), and found surprising coordination geometry differences in their 5-bromo-3-hydroxy-2-methylpyran-4-one complexes [13]. The authors speculated that ''the larger role of both f and d orbital bonding in Pu(IV) compared to Ce(IV) explains this difference.''

It is generally accepted that as the actinide series is crossed, the chemistry increasingly resembles that of the lanthanides; ionic bonding and a single (trivalent) oxidation state dominate. The extent to which the so-called minor actinides – americium and curium – retain a degree of covalency in their bonding has important ramifications in nuclear waste management, and has been the subject of many studies over the last decade or more [14]. One of the key investigations was that of Prodan *et al.*, who probed AnO_2 (An = Th–Es) using screened hybrid density functional theory [15]. Whereas the data for early actinides are close to the formal expectations, the spin densities on the formally An(IV) centers indicated that there are increasing deviations from the formal values toward the center of the 5f series. Americium and curium experience enhancements of their spin densities, attributed by Prodan *et al.* to the actinide borrowing oxygen spin density, the mechanism for this process being the increasing degeneracy between the actinide 5f orbitals and the oxygen 2p levels across the series. On the basis of these spin density data, the authors concluded that, contrary to the generally perceived view of actinide chemistry, covalency actually *increases* toward the center of the 5f series.

Figure 11.1 presents valence MO energy level diagrams for pseudo-tetrahedral $AnCp_4$ from Th–Cm ($Cp = \eta^5\text{-}C_5H_5$) [16]. The eight highest occupied Cp-based MOs are composed largely of the Cp $\pi_{2,3}$ levels (those which contain a single vertical node perpendicular to the plane of the Cp rings), with admixture from the metal's d and f orbitals. These eight MOs split into three groups of pseudo e, t_2, and t_1 symmetry, the energies of which are largely unaltered from Th–Pu, by contrast to the 5f based orbitals, which are very significantly stabilized. Figure 11.2 shows the actinide contribution to the Cp $\pi_{2,3}$-based levels MOs. Metal 6d contribution to the e levels decreases slightly as the 5f series is crossed. 6d contribution to the t_2 MOs is approximately half that of the e, and initially rises before reducing again in the latter systems. Most significantly, the metal 5f contribution to the t_1 highest occupied Cp-based orbitals increases from Th–Am, to > 30% in the latter, before reducing dramatically in $CmCp_4$.

The significant increase in the metal 5f contribution to the t_1 orbitals from Th–Am would appear to support the conclusion of Prodan *et al.*. A subsequent study of $AnCp_3$, for the same metals, found that as for $AnCp_4$, the metal 5f character of the highest Cp $\pi_{2,3}$-based levels steadily increases, peaking at americium [17]. Metal spin densities were calculated for the *tris*-Cp systems (Figure 11.3), and the trend in these is similar to that observed in AnO_2; slight reduction from the formal

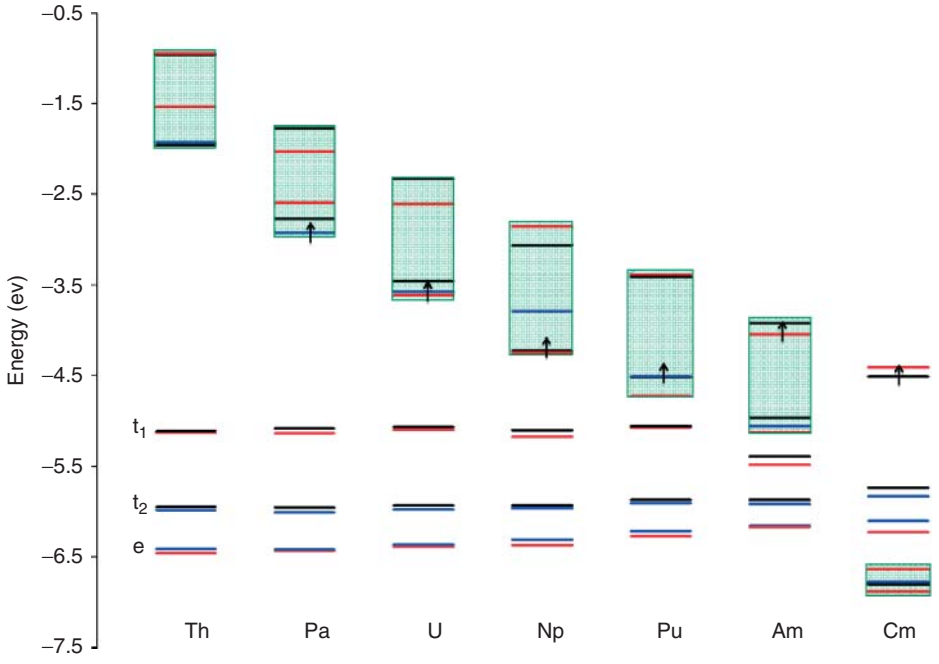

Figure 11.1 Molecular orbital energy level diagram for $AnCp_4$ showing pseudo the e, t_2, and t_1 Cp $\pi_{2,3}$-based levels, and the metals' 5f-based orbitals. MOs spanning the a irreducible representation (in the S_4 point group) are given in red, b in blue and e in black. Green boxes surround the 5f-based orbitals. For the open-shell systems (i.e., all bar $ThCp_4$), the α levels of a given irreducible representation are shown. The highest occupied orbitals are indicated by an arrow (except for $ThCp_4$, where the t_1 Cp $\pi_{2,3}$-based combination is the HOMO). (From Ref. [16] (http://pubs.rsc.org/en/Content/ArticleLanding/2010/DT/c000704h). Reproduced by permission of The Royal Society of Chemistry.)

An(III) value for the early members of the series followed by a sharp increase to $AmCp_3$ and a dramatic reduction at $CmCp_3$. Thus, $AnCp_3$ and AnO_2 behave similarly, with the peak in the spin density coming one element earlier in the trivalent series, tying in with the large americium 5f contribution to the highest Cp $\pi_{2,3}$-based orbitals.

These actinide examples raise an interesting, but more general question: should enhanced orbital mixing be equated with enhanced covalency? Perturbation theory holds that, to first order, the mixing of molecular orbitals ϕ_i and ϕ_j is governed by the mixing coefficient $t_{ij}^{(1)}$, where

$$t_{ij}^{(1)} \propto \frac{-S_{ij}}{\varepsilon_i - \varepsilon_j}$$

Here, S_{ij} is the overlap between the orbitals and the denominator is the difference in their energies. Thus, large orbital mixings can arise when ϕ_i and ϕ_j are close in

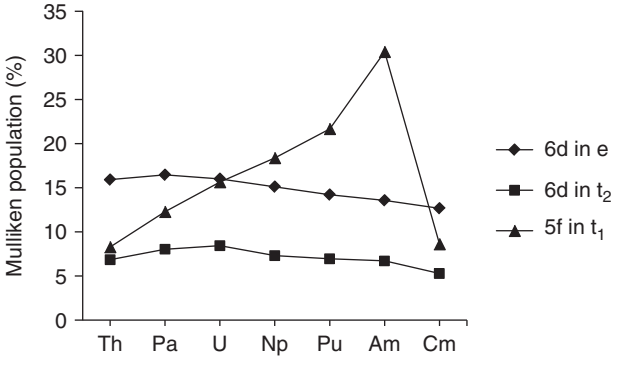

Figure 11.2 Metal contribution (Mulliken populations, %) to the pseudo e, t_2, and t_1 Cp $\pi_{2,3}$-based levels of $AnCp_4$. For open-shell systems, the values quoted are the average of the α and β spin MOs. (Data from Ref. [16].)

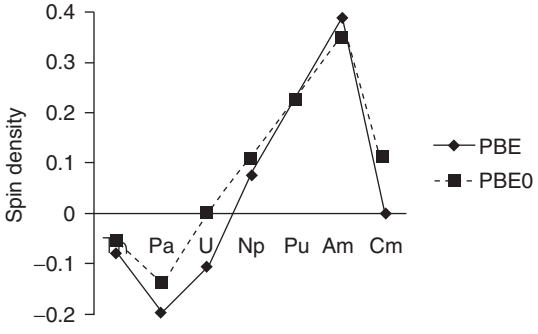

Figure 11.3 Metal spin densities for $AnCp_3$. Values quoted are the differences from the formal value for An(III). (From Ref. [17] (http://pubs.rsc.org/en/Content/ArticleLanding/2011/DT/c0dt01018a). Reproduced by permission of The Royal Society of Chemistry.)

energy, without there necessarily being significant orbital overlap. This is exactly the situation found in the middle of the actinide series, as illustrated in Figure 11.4, which shows one component of the pseudo t_1 (Cp $\pi_{2,3}$-based) orbitals of UCp_4 and $AmCp_4$ [16]. The 5f contribution to the americium orbital is much larger than in the uranium compound, yet clearly there is more metal–ligand overlap in the latter. Thus, if orbital mixing is taken as the measure of covalency, then $AmCp_4$ is the more covalent compound, yet it may well be argued that a build up of electron density in the inter-nuclear region is required for a chemical bond to be described as covalent; by this measure the uranium–carbon bond is the more covalent.

Chapter 8 of Volume 1 describes the Quantum Theory of Atoms-in-Molecules (QTAIM), and this has been applied to both $AnCp_4$ [16] and $AnCp_3$ [17]. QTAIM analysis reveals very little metal–carbon covalency, as evidenced by comparison of the computed bond critical point (BCP) data with those from a range of other systems. For example, the energy density at the uranium–carbon BCPs in UCp_4

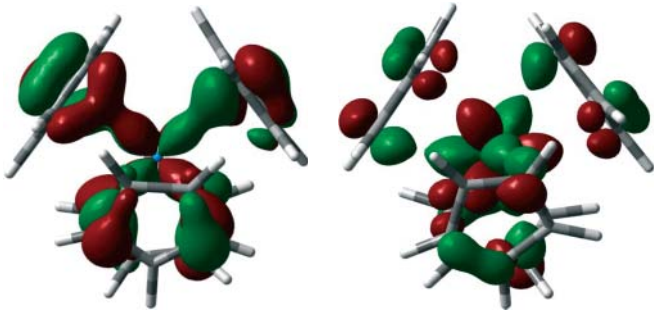

Figure 11.4 Three dimensional representations of one component of the "t_1" MOs of UCp_4 (a) and $AmCp_4$ (b). The contribution (%, Mulliken) of the actinide 5f orbitals to the $AmCp_4$ MO is c. 30%, approximately twice that in UCp_4. (From Ref. [16] (http://pubs.rsc.org/en/Content/ArticleLanding/2010/DT/c000704h). Reproduced by permission of The Royal Society of Chemistry.)

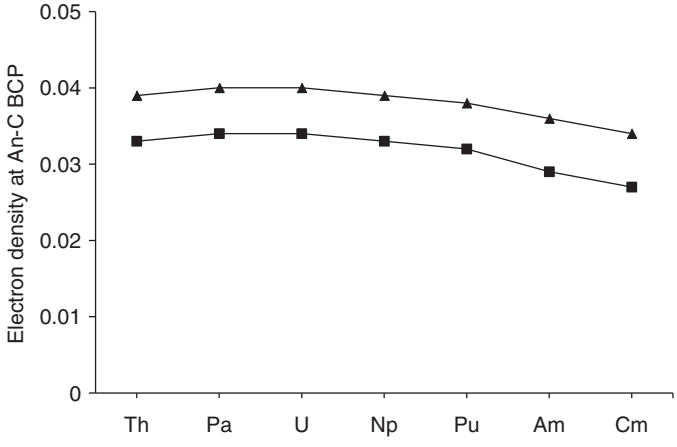

Figure 11.5 Electron density (e^-/bohr^3) at the actinide–carbon bond critical points of $AnCp_4$ (triangles) and $AnCp_3$ (squares). (Data from Refs [16, 17].)

is more than 10 times smaller than that in UF_3CO [10], and more than 30 times smaller than for the metal–carbon bonds in $M(CO)_6$ (M = Cr, Mo, W) [16]. The electron densities at the actinide–carbon BCPs are shown for $AnCp_4$ and $AnCp_3$ in Figure 11.5. All of these values are very small, and as might be expected for An(III) versus An(IV), are slightly larger in the trivalent compounds. Most significantly, following a small increase from thorium to uranium, the BCP electron densities decrease as the series is crossed to the minor actinides. Thus, as evidenced by the QTAIM data, the metal–carbon bonding in $AnCp_4$ and $AnCp_3$ is very ionic, increasingly so toward the middle of the actinide series, recovering the traditional view of actinide chemistry.

The $AnCp_4$ and $AnCp_3$ studies indicate that the metal–carbon bond becomes both more covalent (on the basis of orbital mixing and spin densities) and more ionic (as evidenced by QTAIM data) as the actinide series is crossed, precluding a simple answer to the question posed in the title of this section. This has more than just a fundamental significance. Certain nitrogen-donor ligands such as 2,6 *bis*triazinylpyridines (BTPs), 6,6′-*bis*triazinyl-2,2′-bipyridines and *bis*triazinyl-2,2′:6′,2″-terpyridines [18] can effect the selective extraction of trivalent minor actinides from solutions containing lanthanide ions, potentially a very important process in future nuclear waste remediation strategies [14]. A significant computational research effort has focused on the application of quantum chemistry to assess the extent of covalency in the f element–nitrogen bond, and, in particular, to determine if there are differences between the minor actinides and lanthanide compounds which would account for the observed separation factors. The results from these studies are inconclusive, prompting Girnt *et al*. to state ''the level of understanding of BTPs' selectivity on a molecular level is insufficient to target the design of new, more efficient and selective partitioning reagents or fine tune partitioning process conditions. Such advances are presently empirical, on a trial and error basis'' [19]. The lack of firm conclusions from the quantum chemical studies most likely arises from a lack of clarity concerning the definition of covalency in the 5f series; it is certainly unusual that significant valence orbital mixing does not lead to internuclear charge build up, and the traditional tools of quantum chemistry struggle under such circumstances.

11.6
Multi-configurational Descriptions of Bonding in f Element Complexes

In the situation where the electronic structure of a molecule cannot be adequately described in terms of a single Slater determinant, post Hartree–Fock multi-configurational methods must be employed. Such situations often arise in actinide complexes, where the energetically similar 5f, 6d, and 7s orbitals can, in principle, participate in bonding, and the pseudocore 6s and 6p orbitals can also have nonnegligible contributions. The resulting multideterminantal wavefunction often presents challenges to our understanding of chemical bonding; this is perhaps best illustrated by considering the U_2 molecule.

11.6.1
U_2: A Quintuply Bonded Actinide Dimer

Multiply bonded transition metal dimers are well known, with dimolybdenum (Mo_2) and ditungsten (W_2) exhibiting the extreme case of sextuple bonds, believed to be the maximum bond multiplicity possible between identical atoms. The bonding in U_2, however, is significantly more complicated than in these transition metal analogues. Whereas molybdenum and tungsten both have six singly occupied valence orbitals available for bonding, the 5f, 6d, and 7s orbitals of uranium lie

sufficiently close in energy that they all can be considered as valence orbitals available to participate in the U_2 bond. In a seminal exposition of the complete-active-space self-consistent-field (CASSCF) approach, Gagliardi and Roos analyzed the bonding in U_2 [20]. Each uranium center has six valence electrons, and initial trial calculations revealed the existence of a set of three "normal" electron-pair bonds, one of σ type and two of π type, defined by molecular orbitals with atomic 7s and 6d character, respectively. The remaining six electrons were allowed to occupy any of the available 5f and 6d orbitals and the most stable electronic state was obtained when these electrons arranged themselves so that their spins were parallel, giving an $S = 3$ septet state with $\Lambda = 11$, satisfying Hund's first and second rules. Excluding the [Rn] cores of each uranium atom, the total wavefunction can be written in terms of two dominant configurations:

$$\begin{aligned}\Psi = {} & 0.782(7s\sigma_g)^2(6d\pi_u)^4(6d\sigma_g)^1(6d\delta_g)^1(5f\delta_g)^1(5f\pi_u)^1(5f\varphi_u)^1(5f\varphi_g)^1 \\ & + 0.596(7s\sigma_g)^2(6d\pi_u)^4(6d\sigma_g)^1(6d\delta_g)^1(5f\delta_u)^1(5f\pi_g)^1(5f\varphi_u)^1(5f\varphi_g)^1\end{aligned}$$

where σ, π, and so on indicate the nodal structure of the orbital in the plane perpendicular to the bond.

An alternative interpretation of the electronic state can be obtained by expressing the electron density in terms of the natural orbitals (as described in Chapter 3 of Volume 1). In this way, the multi-configurational character of the wavefunctions is revealed by orbital occupations differing significantly from integer values. Figure 11.6 shows the natural orbitals corresponding to the U_2 wavefunction. Here can be seen not only the six electrons in the $7s\sigma_g$ and $6d\pi_u$ orbitals which form the traditional triple bond, but also the singly occupied $6d\sigma_g$ and $6d\delta_g$ orbitals and the more weakly occupied $5f\pi_u$ and $5f\delta_g$ orbitals, all of which have bonding character. This gives a total of ten electrons in bonding orbitals, leading to the authors' conclusion of a quintuple bond. This unusual electronic structure, with several "one-electron bonds," also leads to an unexpected ferromagnetic coupling between the nonbonding 5f-electrons: linear combinations of the $5f\varphi_u$ and $5f\varphi_g$ orbitals result in one localized 5fφ orbital on each uranium center. Typically, these localized electrons would be expected to couple antiferromagnetically, but in U_2, the interaction between the localized electrons and the one-electron bonds outweighs the energetic benefit of antiferromagnetic coupling in an example of exchange stabilization.

The CASSCF approach has also been employed in order to study the variation in bonding across dimers of the early actinides (M = Ac-U) [21]. Here, the bond order was found to increase across the series from a value of 2 for Ac_2 to 4 for Th_2, before attaining its maximum value of 5 for both Pa_2 and U_2. The bonding contribution of the 5f orbitals increased across the series, in accord with their increasing stabilization. Energetically, the protactinium dimer is found to be the most stable complex, with a bond energy of 4.00 eV. This is some 2.85 eV larger than that found for the uranium dimer, and is due both to the stronger occupation of bonding orbitals in the former, and the greater contribution of more strongly interacting 6d orbitals to the bond.

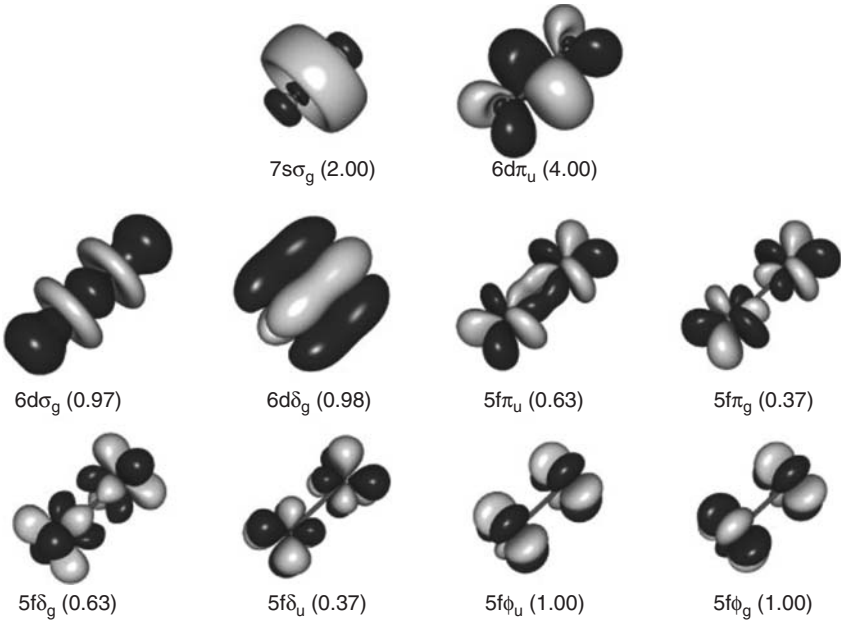

Figure 11.6 Natural orbitals and corresponding occupation numbers for the active orbitals forming the U_2 chemical bond. (Data from Ref. [20] Reprinted by permission from Macmillan Publishers Ltd: *Nature* **433**: 848–851 © 2005.)

11.6.2 Bonding in the Actinyls

Clearly, the bonding in U_2 represents a significant deviation from the traditional interpretation of the covalent bond, but can be rationalized when approached from a multi-configurational perspective. This approach has also been applied to the dioxo actinide cations $AnO_2^{+/2+}$, which are found for An = U-Am in high oxidation states (+5, +6). These linear complexes are characterized by short, kinetically inert, covalent An–O bonds, in contrast to their transition metal analogues MoO_2^{2+} and VO_2^{+}, which exhibit weaker bonds and O=M=O bond angles of approximately 110°. Here, we focus our attention on bonding in the prototypical complex uranyl, UO_2^{2+}; heavier analogues exhibit similar bonding structure, with additional electrons occupying nonbonding 5f orbitals. CASSCF calculations by Pierloot and van Besien [22] confirmed the bonding picture established by earlier CI studies [23], namely, the formation of bonds by donation from the -yl oxygen 2p orbitals into the empty uranium 5f and 6d orbitals. Figure 11.7 shows the uranyl natural orbitals and occupation numbers, using analogous notation to that of Figure 11.6. By contrast to the uranium dimer, no δ- or φ-type interactions are possible through oxygen 2p donation, which simplifies the bonding picture. In this complex the bonding is characterized by a series of three-center electron-pair bonds, distributed amongst six molecular orbitals. This gives a total of twelve electrons involved in

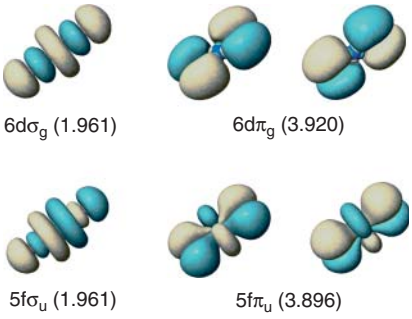

Figure 11.7 Natural orbitals and corresponding occupation numbers for the active orbitals forming the UO_2^{2+} chemical bond. (Data from Ref. [22].)

Table 11.3 Atomic orbital contributions to the U–O bonding orbitals in UO_2^{2+}.

	O 2s	O 2p	U 5f	U 6s	U 6p	U 6d
$5f\sigma_u$	0	34	55	0	10	0
$5f\pi_u$	0	79	18	0	2	0
$6d\sigma_g$	5	81	0	1	0	13
$6d\pi_g$	0	83	0	0	0	17

bonding, corresponding to two U–O triple bonds. In this complex the pseudocore 6p orbital, which actually has a greater radial extent than the 5f shell, also plays a role. Table 11.3 shows the atomic contribution to the uranyl bonding orbitals; the $5f\sigma_u$ molecular orbital contains an antibonding admixture of 6p into the otherwise bonding U5f/O2p combination, resulting in energetic destabilization. This is an example of the *pushing from below* mechanism, that is, a repulsive interaction between the filled O 2p and U 6p orbitals [24].

11.6.3
Oxidation State Ambiguity in the f Block Metallocenes

In transition metal chemistry, metallocenes are formed by the complexation of two Cp ligands to a metal center. The formal donation of two electrons from the metal to generate two monoanionic ligands leads to Hückel stability for each carbocyclic ring (6π electrons), and is a significant factor in the overall stability of the complex. Many years ago, it was proposed that the higher angular momentum of the valence shells in the f block elements could lead to complexation with the larger cyclooctatetraene (COT = η^8-C_8H_8) ligand [25]. Each COT ligand requires two electrons in order to attain the Hückel stability of a 10π electron system, and so would be expected to be amenable to complexation with metal centers in the +4 oxidation state. The actinides, having a greater propensity for higher oxidation states than the lanthanides, would be expected to be the more likely candidates

for bis COT f element complexes, and $UCOT_2$ was the first ''actinocene'' to be synthesized [26].

The stability of $AnCOT_2$ complexes derives partly from the fact that both the 5f and 6d orbitals can participate in δ bonding interactions with the π_2 orbitals of the ligands. By contrast, the transition metals have only d orbitals available for such an interaction, whereas the lanthanide 4f shell is relatively core-like, and so both groups of metals are significantly less likely to exhibit stable $MCOT_2$ complexes. An exception is cerium, and cerocene has been the subject of extensive study for more than two decades. Although it might be expected that $CeCOT_2$ would exhibit the same electronic structure as the tetravalent actinide analogue thorocene, $ThCOT_2$, Neumann and Fulde [27] asserted that it may instead be a molecular example of a Kondo singlet system, corresponding to a trivalent cerium complex exhibiting an open shell singlet electronic structure; unlike thorocene, in which each COT ligand is formally dianionic, the ligands of cerocene would each carry a −3/2 charge. The high (D_{8h}) symmetry of the complex implies that such an electronic structure is implicitly multi-configurational, and the assertion of Neumann and Fulde appeared to be confirmed by CASSCF studies [28]. These calculations revealed cerocene to possess a wavefunction composed of essentially two configurations; a Ce^{4+} configuration with a weight of c. 20% and a dominant Ce^{3+} configuration with a weight of c. 80%. However, more recent CASSCF calculations on $MCOT_2$ (M = Ce, Th, Pa, U, Pu, Cm) found that this interpretation is ambiguous [29]. The relative weight of the Ce^{3+} and Ce^{4+} configurations is strongly dependent on how the calculations are performed; a typical approach in CASSCF studies is to perform *state-averaged* CASSCF, in which a weighted average of the energy of several electronic states of the same symmetry is minimized in order to ensure orthogonalization. In the case of cerocene, the number of states included in this average has a dramatic effect on the weight of the dominant configuration. This variation can be seen in Figure 11.8a. As noted by Neumann and Fulde, a requirement for experimentally observable Kondo effects is significant orbital hybridization between ligand and metal, that is, ligand donation into bonding orbitals. A multi-configurational wavefunction, however, is extremely flexible. Just as the electron density corresponding to a monodeterminantal wavefunction is

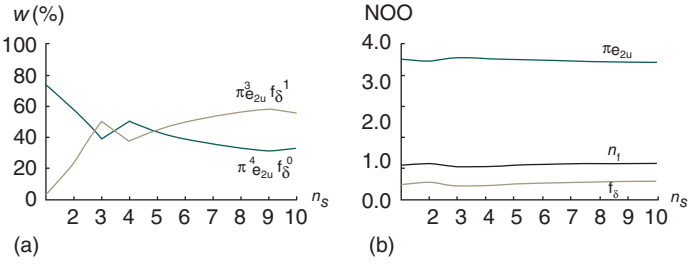

Figure 11.8 Comparison of (a) configurational weights and (b) e_{2u} symmetry natural orbital occupations (NOOs) in $CeCOT_2$. n_f is an approximate value of the electron density associated with 4f-orbital occupation. (Data from Ref. [29a].)

invariant to unitary transformations of the molecular orbital space, so that associated with a multi-configurational wavefunction is unchanged by unitary transformations confined to the inactive and/or active spaces. Furthermore, transformations of the MOs can be balanced by variations in the CI coefficients in order to leave the density unchanged. This means that the degree of orbital hybridization can vary and somewhat limit the relevance of configurational weights to a description of the oxidation state and, in the case of cerocene, the nature of the Ce–COT bond. If we, instead, consider the natural orbital occupations (Figure 11.8b), a more consistent picture emerges with near-constant values found as the number of states included in the averaging is increased. The corresponding natural orbitals are shown in Figure 11.9, where significant hybridization and weak but significant occupation of antibonding orbitals is observed. This leads to the conclusion that cerocene is best described as Ce(IV) system in which transfer of electron density from ligand to metal through occupation of bonding orbitals allows measures of the effective oxidation state to be lower than the formal +4 value, and indeed closer to +3 in certain cases. Such a description is also appropriate in the closely related complex $CePn_2$ ($Pn = \eta^8\text{–}C_8H_6$) [30] as well as the $CeCp_3^+$ cation [31].

As one moves across the actinides series, the $AnCOT_2$ bonding characteristics deviate from the prototypical tetravalent thorium complex and come to more closely resemble that of cerocene, with partial occupation of antibonding MOs. Figure 11.10 shows the CASSCF calculated [29b] natural orbital occupations of a series of f-element metallocenes. Here $ThCOT_2$ exhibits mono-configurational character, as might be expected because of the high energy of the 5f levels in thorium complexes. As the central ion becomes heavier, however, the 5f levels are stabilized, and $PuCOT_2$ shows very similar bonding characteristics to $CeCOT_2$. By contrast to the lighter complexes, $CmCOT_2$ (which is a $5f^6$ system in the +4 oxidation state) has only one antibonding orbital to partially occupy, the other having an occupation number of 1.002. This results in a significant increase in occupation of the available orbital (0.653, as compared to 0.183 in the plutonium analogue).

The examples presented in this section show that when multi-configurational descriptions of the electronic wavefunction are required, so our traditional views of bonding are challenged. However, analyses based on the (physically observable)

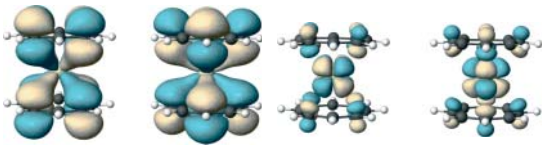

Figure 11.9 Bonding and antibonding natural orbitals and corresponding occupation numbers of e_{2u} symmetry active orbitals involved in the $CeCOT_2$ chemical bond. (Data from Ref. [29a].)

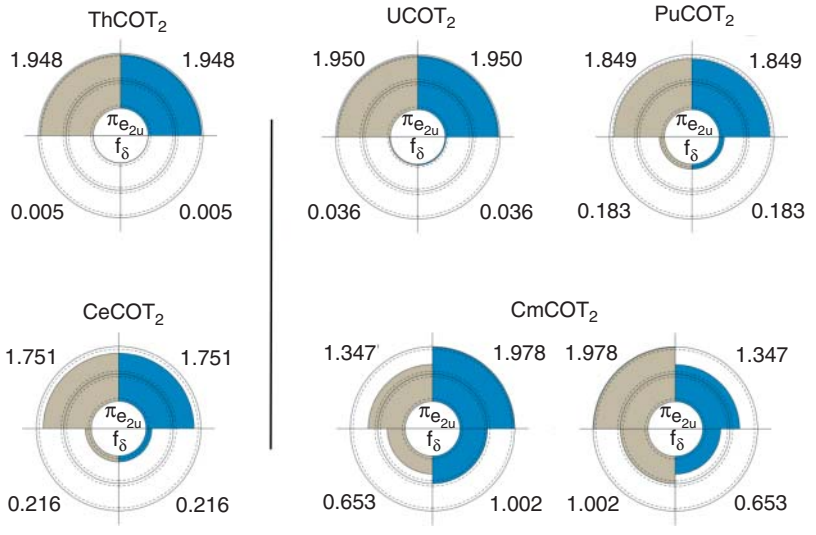

Figure 11.10 Natural orbital occupations for active orbitals of e_{2u} symmetry in $MCOT_2$ (M = Ce, Th, U, Pu, Cm). See Figure 11.9 for a representative example of the natural orbitals in the case of $CeCOT_2$. (Data from Ref. [29b].)

electron density serve to provide us with a means to interpret these multi-configurational descriptions. It is often only with recourse to such analyses that the complicated bonding in f element compounds can be rationalized.

11.7 Concluding Remarks

Computational quantum chemistry has made enormous advances in the last 20 years, arguably nowhere more so than in the f block. Calculations have, in this period, advanced sufficiently such that they can now be used as reliable, predictive methods for deepening our understanding of the fundamentals of bonding in these systems. The effects of scalar relativity are now routinely incorporated, and methods for the inclusion of spin-orbit coupling have also progressed significantly [32].

Although it remains the case that the balance between theoretical sophistication and chemical intuition has to be maintained [33], moving beyond traditional interpretations of bonding and electronic structure can lead to new insights. Multiple analysis methods may be required to obtain a complete description of bonding character and, as the quality of f element calculations steadily improves, the link between theory and experiment will (and must) grow ever stronger. This is exemplified by recent work from Clark *et al.*, that elegantly combines X-ray absorption spectroscopy with ground and time-dependent KSDFT [34]. However, the computational improvement and the increasing application of quantum chemistry to key problems in f element science (e.g., the subtle differences in the bonding of

analogous Ln(III) and An(III) systems) bring greater responsibility to the computational chemist; the validity of the theoretical models employed must be ensured before conclusions may be drawn.

References

1. (a) Koch, W. and Holthausen, M.C. (2001) *A Chemist's Guide to Density Functional Theory*, 2nd edn, Wiley-VCH Verlag GmbH; (b) Parr, R.G. and Yang, W. (1989) *Density-Functional Theory of Atoms and Molecules*, Oxford University Press, Oxford.
2. (a) Dyall, K.G. and Faegri, K. (2007) *Introduction to Relativistic Quantum Chemistry*, Oxford University Press, Oxford; (b) Jensen, F. (2007) *Introduction to Computational Chemistry*, 2nd edn, John Wiley & Sons, Ltd, Chichester.
3. Dolg, M. and Cao, X.-Y. (2012) *Chem. Rev.*, **112**, 403–480.
4. Szabo, A. and Ostlund, N.S. (1989) *Modern Quantum Chemistry*, McGraw-Hill, New York.
5. (a) Ziegler, T. and Rauk, A. (1977) *Theor. Chim. Acta*, **46**, 1–10; (b) Ziegler, T. and Rauk, A. (1979) *Inorg. Chem.*, **18**, 1558–1565.
6. Häller, L.J.L., Kaltsoyannis, N., Sarsfield, M.J., May, I., Cornet, S.M., Redmond, M.P., and Helliwell, M. (2007) *Inorg. Chem.*, **46**, 4868–4875.
7. Dognon, J.-P., Clavaguéra, C., and Pyykkö, P. (2007) *Angew. Chem. Int. Ed.*, **46**, 1427–1430.
8. Dognon, J.-P., Clavaguéra, C., and Pyykko, P. (2009) *J. Am. Chem. Soc.*, **131**, 238–243.
9. Lyon, J.T., Hu, H.-S., Andrews, L., and Li, J. (2007) *Proc. Natl. Acad. Sci. U.S.A.*, **104**, 18919–18924.
10. Petit, L., Joubert, L., Maldivi, P., and Adamo, C. (2006) *J. Am. Chem. Soc.*, **128**, 2190–2191.
11. Arliguie, T., Belkhiri, L., Bouaoud, S.E., Thuery, P., Villiers, C., Boucekkine, A., and Ephritikhine, M. (2009) *Inorg. Chem.*, **48**, 221–230.
12. Meskaldji, S., Belkhari, L., Arliguie, T., Fourmigue, M., Ephritikhine, M., and Boucekkine, A. (2010) *Inorg. Chem.*, **49**, 3192–3200.
13. Szigethy, G., Xu, J., Gorden, A.E.V., Teat, S.J., Shuh, D.K., and Raymond, K.N. (2008) *Eur. J. Inorg. Chem.*, 2143–2147.
14. Kaltsoyannis, N. (2013) *Inorg. Chem.*, 52. doi: 10.1021/ic3006025
15. Prodan, I.D., Scuseria, G.E., and Martin, R.L. (2007) *Phys. Rev. B*, **76**, 033101.
16. Tassell, M.J. and Kaltsoyannis, N. (2010) *Dalton Trans.*, **39**, 6719–6725.
17. Kirker, I. and Kaltsoyannis, N. (2011) *Dalton Trans.*, **40**, 124–131.
18. Lewis, F.W., Harwood, L.M., Hudson, M.J., Drew, M.G.B., Modolo, G., Syupla, M., Desreux, J.F., Bouslimani, N., and Vidick, G. (2010) *Dalton Trans.*, **39**, 5172–5182.
19. Girnt, D., Roesky, P.W., Geist, A., Ruff, C.M., Panak, P.J., and Denecke, M.A. (2010) *Inorg. Chem.*, **49**, 9627–9635.
20. Gagliardi, L. and Roos, B.O. (2005) *Nature*, **433**, 848–851.
21. Roos, B.O., Malmqvist, P.-A., and Gagliardi, L. (2006) *J. Am. Chem. Soc.*, **128**, 17000–17006.
22. Pierloot, K. and van Besien, E. (2005) *J. Chem. Phys.*, **123**, 204309.
23. Zhang, Z.Y. and Pitzer, R.M. (1999) *J. Phys. Chem. A*, **103**, 6880–6886.
24. Kaltsoyannis, N. (2000) *Inorg. Chem.*, **39**, 6009–6017.
25. Fischer, R.D. (1963) *Theor. Chim. Acta (Berlin)*, **1**, 418–431.
26. Streitwieser, A.J. and Müller-Westerhof, U. (1968) *J. Am. Chem. Soc.*, **90**, 7364.
27. Neumann, C.S. and Fulde, P. (1989) *Z. Phys. B: Condens. Matter*, **74**, 277–278.
28. (a) Dolg, M., Fulde, P., Kuchle, W., Neumann, C.S., and Stoll, H. (1991) *J. Chem. Phys.*, **94**, 3011–3017; (b) Dolg, M., Fulde, P., Stoll, H., Preuss, H., Chang, A., and Pitzer, R.M. (1995) *Chem. Phys.*, **195**, 71–82.
29. (a) Kerridge, A., Coates, R., and Kaltsoyannis, N. (2009) *J. Phys. Chem. A*, **113**, 2896–2905; (b) Kerridge, A. and

Kaltsoyannis, N. (2009) *J. Phys. Chem. A*, **113**, 8737–8745.

30. Kerridge, A. and Kaltsoyannis, N. (2010) *C. R. Chim.*, **13**, 853–859.
31. Coates, R., Coreno, M., DeSimone, M., Green, J.C., Kaltsoyannis, N., Kerridge, A., Narband, N., and Sella, A. (2009) *Dalton Trans.*, **30**, 5943–5953.
32. Kaltsoyannis, N. (2009) in *Computational Inorganic and Bioinorganic Chemistry* (eds E.I. Solomon, R.B. King, and R.B. Scott), John Wiley & Sons, Ltd, Chichester, pp. 517–526.
33. Bursten, B.E. (1991) *Pure Appl. Chem.*, **63**, 839–844.
34. Minasian, S.G., Keith, J.M., Batista, E.R., Boland, K.S., Clark, D.L., Conradson, S.D., Kozimor, S.A., Martin, R.L., Schwarz, D.E., Shuh, D.K., Wagner, G.L., Wilkerson, M.P., Wolfsberg, L.E., and Yang, P. (2012) *J. Am. Chem. Soc.*, **134**, 5586–5597.

12
Direct Estimate of Conjugation, Hyperconjugation, and Aromaticity with the Energy Decomposition Analysis Method

Israel Fernández

12.1
Introduction

The terms conjugation, hyperconjugation, resonance, and aromaticity are essential concepts in chemistry that were introduced to account for the stability, reactivity, molecular structure, and other properties of many unsaturated organic compounds (and later extended to inorganic molecules and to saturated systems, Figure 12.1). Conjugation, for instance, is usually invoked to explain the higher stability of compounds with multiple bonds, which are separated by one single bond, compared to their isomers where the double/triple bonds are isolated from each other by more than one single bond. The significant bond shortening of the central carbon–carbon bond in 1,3-butadiene or the 1,4-addition to enones are also manifestations of this effect. Similarly, hyperconjugation plays a major role in explaining effects such as the group 14 β-effect or the anomeric effect, which have a tremendous impact in the geometries and reactivities of many organic molecules. It is important, however, to recognize that (hyper)conjugation or aromaticity are just bonding models and, therefore, (hyper)conjugative stabilization itself is only a virtual thermodynamic quantity, and cannot be measured experimentally. Thus, we are dealing with terms or concepts that do not possess a precise meaning (i.e., conjugation is explained in molecular orbital (MO) theory with π–π^*-interactions, while the same phenomenon is explained in valence bond (VB) theory in terms of resonance structures). In fact, these heuristic bonding models, which are extremely useful and widely used by most chemists nowadays, have been called *typical examples of the unicorns of chemical bonding models*, because everyone seems to know what they mean but, like the mythical animal, nobody has ever seen one because they are not experimentally observable [1]. Without any doubt, aromaticity has been (and still is) one of the most difficult targets *for hardcore unicorn hunters*, as is clearly illustrated by the great number of criteria – none of them are free from ambiguities – used to ascertain the aromatic nature of a given compound [2, 3]. The enormous importance of conjugation, hyperconjugation, and aromaticity is clearly reflected in the great

The Chemical Bond: Chemical Bonding Across the Periodic Table, First Edition.
Edited by Gernot Frenking, Sason Shaik.

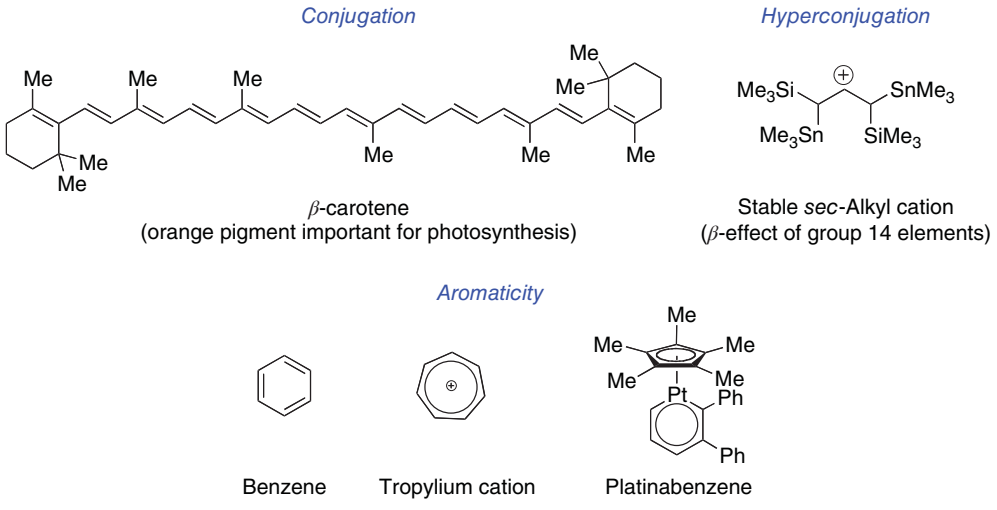

Figure 12.1 Representative examples of compounds exhibiting conjugation, hyperconjugation, and aromaticity.

number of different approaches that have been developed to estimate their relative strengths, mainly in organic chemistry but also in organometallic systems.[1)]

We can consider that (hyper)conjugation is the difference in energy between a (hyper)conjugated molecule and its hypothetical energy (virtual state) if the entire contribution stemming from (hyper)conjugation could be accounted for and excised [4]. Thus, the strength of (hyper)conjugative interactions and also the aromatic stabilization energies (ASEs) have been traditionally determined with respect to a reference system. The most common approaches to estimate these effects use the reaction energies of isodesmic reactions or the stepwise heats of hydrogenation of the (hyper)conjugated molecule, following the initial suggestion by Kistiakowsky in 1936 [5]. Both approaches suffer from the problem that the difference between the (hyper)conjugated molecule and the reference system comprises not only alterations of the π-bonding but also changes in other parts of the system. As an example, following Kistiakowsky's method, it has been concluded that there is no conjugative stabilization in 1,3-butadiyne (and related polyacetylenes) because the energies for the hydrogenation of the two degenerate triple bonds are nearly the same (Scheme 12.1) [6]. This result is in sharp contrast with our chemical intuition, because one would expect that the

1) Among the different approaches, the following methodologies should be specially highlighted: (i) nuclear independent chemical shifts (NICS) by P. v. R. Schleyer and coworkers; (ii) harmonic oscillator model of aromaticity (HOMA) by J. Kruszewski and T. M. Krygowski; (iii) natural bond orbitals (NBO)-based approaches; (iv) aromatic fluctuation index (FLU) by M. Solá and coworkers; (v) block-localized wavefunction (BLW) method by P. v. R. Schleyer and Y. Mo; and (vi) energy decomposition analysis (EDA) by F. M. Bickelhaupt and coworkers.

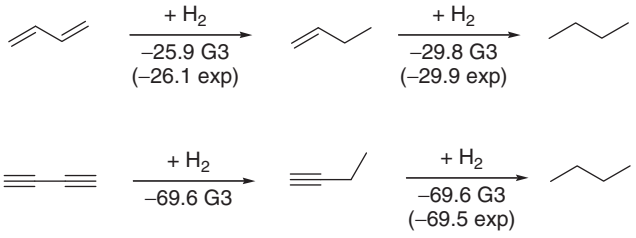

Scheme 12.1

strength of conjugation in 1,3-butadyine should be at least twice as strong as the conjugation in 1,3-butadiene (which was estimated to be 3.9 kcal mol^{-1} using this methodology) [6a]. Thus, it is clear that the (hyper)conjugative strengths and ASE values estimated with the latter procedures are contaminated by different flaws (such as hyperconjugation, strain, and Coulomb repulsion imbalance – especially in charged systems – or uncompensated van der Waals attractions) and are, therefore, not always reliable [7].

As the choice of the reference system is somewhat arbitrary, it would be helpful if we could apply a different approach using only the molecule of interest without recourse to external reference systems. The energy decomposition analysis (EDA), developed by Ziegler and Rauk [8] following a similar procedure suggested by Morokuma [9], is such a method because it uses only the π-orbitals of the interacting fragments in the geometry of the molecule to estimate π-interactions. The EDA makes it possible, therefore, to calculate the stabilization that arises from the mixing of occupied π-orbitals with vacant π*-orbitals in molecules having a mirror plane.

In this chapter, we summarize the good performance of the EDA method to directly and quantitatively estimate the strength of (hyper)conjugation in different systems, together with the good correlation observed between the values calculated and several experimental parameters that have been suggested as indicators of (hyper)conjugation. In addition, we also describe the application of our methodology to estimate the ASE values for conjugated cyclic molecules, including organic and organometallic systems.

12.2 The EDA Method

The EDA [10] has been proved to give important information about the nature of the bonding in main-group compounds [11] and transition-metal complexes [12]. As the intimacies of this method are well described in the literature [10–12] and in the chapter by Frenking and Bickelhaupt in this book, herein we will only briefly summarize its most relevant aspects.

The focus of the bonding analysis is the instantaneous interaction energy, ΔE_{int}, of the bond, which is the energy difference between the molecule and the fragments in the electronic reference state and frozen geometry of the compound. The interaction energy can be divided into three main components:

$$\Delta E_{int} = \Delta E_{elstat} + \Delta E_{Pauli} + \Delta E_{orb} \tag{12.1}$$

ΔE_{elstat} gives the electrostatic interaction energy between the fragments, which is calculated using the frozen electron density distribution of the fragments in the geometry of the molecules. The second term in Eq. (12.1), ΔE_{Pauli}, refers to the repulsive interactions between the fragments, which are caused by the fact that two electrons with the same spin cannot occupy the same region in space. ΔE_{Pauli} is calculated by enforcing the Kohn–Sham determinant on the superimposed fragments to obey the Pauli principle by antisymmetrization and renormalization. The stabilizing orbital interaction term, ΔE_{orb}, is calculated in the final step of the energy partitioning analysis when the Kohn–Sham orbitals relax to their optimal form. The interaction energy, ΔE_{int}, can be used to calculate the bond dissociation energy, D_e, by adding ΔE_{prep}, which is the energy necessary to promote the fragments from their equilibrium geometry to the geometry they adopt in the compounds (Eq. (12.2)). The advantage of using ΔE_{int} instead of D_e is that the instantaneous electronic interaction of the fragments becomes analyzed, which yields a direct estimate of the energy components.

$$-D_e = \Delta E_{prep} + \Delta E_{int} \tag{12.2}$$

For our purposes, the orbital contribution, ΔE_{orb}, is the most important term of this analysis, as it can be further partitioned into contributions by the orbitals belonging to different irreducible representations of the point group of the interacting system. The molecules considered herein present at least one mirror plane (C_s symmetry). Thus, the contributions of the a' (in-plane) orbitals to ΔE_{orb} give the strength of the σ-interactions, while the contributions of the a'' (out-of-plane) orbitals give the strength of the π-interactions:

$$\Delta E_{orb} = \Delta E_{\sigma} + \Delta E_{\pi} \tag{12.3}$$

The calculated ΔE_{π} values can be used as a scale to estimate the relative contributions of π-interactions arising from conjugation or hyperconjugation. For this reason, we only focus on the ΔE_{π} data provided by the EDA in this chapter (the complete EDA values can be found in the corresponding original publications).[2)]

2) All calculations were carried out at the BP86 level using the program package ADF (see Ref. [10]). The basis sets in this work have TZ2P quality using uncontracted Slater-type orbitals (STOs) as basis functions. An auxiliary set of s, p, d, f, and g STOs was used to fit the molecular densities and to represent the Coulomb and exchange potentials accurately in each SCF cycle.

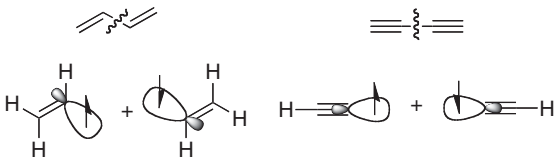

Figure 12.2 Fragmentation schemes used in 1,3-butadiene and 1,3-butadiyne.

12.3 Conjugation

12.3.1 Conjugation in 1,3-Butadienes, 1,3-Butadiyne, Polyenes, and Enones

The EDA method was used in a first approach to solve the controversy about the reported lack of conjugation in 1,3-butadiyne [4–6]. To this end, the central C–C single bond connects the interacting fragments, which are calculated in the electronic doublet state with the unpaired electron in a σ-orbital (Figure 12.2) [13a]. The ΔE_π values in Table 12.1 indicate that the conjugative stabilization in 1,3-butadiyne is more than twice that calculated for *trans*-1,3-butadiene. This is a reasonable result, because, according to our chemical intuition, the conjugation of the two π-systems in 1,3-butadiyne should be at least twice as strong as the conjugation in 1,3-butadiene, where there is only one π-system. This is well reflected in the computed remarkable shortening of the central C–C bond distance in 1,3-butadiyne compared to 1,3-butadiene (1.361 Å vs 1.453 Å). The EDA method also makes it possible to compare the strength of conjugation in the *trans* and *cis* isomers of 1,3-butadiene (being a transition state in the latter species) [13b]. As readily seen from the data in Table 12.1, the *s-trans* isomer (which is the global minimum) is slightly stabilized by conjugation compared to its *s-cis* isomer. This result is also reflected in the longer central C–C bond distance in the latter compound.

As stated in most organic chemistry textbooks, conjugation plays a major role in explaining many properties, such as the excitation energies and absorption spectra

Table 12.1 Results of the EDA at the BP86/TZ2P level.

				$n = 1$	$n = 2$	$n = 3$	$n = 4$
ΔE_π	−19.5	−17.2	−45.0	−41.4	−64.9	−89.3	−114.4
r (C–C)	1.453	1.469	1.361	1.444	C^2–C^3: 1.441 C^4–C^5: 1.432	C^2–C^3: 1.439 C^4–C^5: 1.428	C^2–C^3: 1.439 C^4–C^5: 1.427 C^6–C^7: 1.424

Energy values in kcal mol^{-1} and distances in Å.

of conjugated polyenes. These properties have been traditionally related to the steady decrease of the HOMO-LUMO gap when going from one polyene to another. The EDA results for the homologous series of five conjugated polyenes from *trans*-1,3-butadiene to all-*trans*-1,3,5,7,9,11-dodecahexaene show that the increase of ΔE_π has very similar values as the increase of the overall interaction energy ΔE_{int} [13b]. This is a hint as to why the above-mentioned properties can be modeled by considering only the π-electrons [14]. Although the total π-conjugation increases linearly with the number of C=C moieties in the molecule, the change in the π-conjugation from one polyene to another (measured by $\Delta\Delta E_\pi$) follows an exponential increase, converging toward a final value that appears to be reached after 6 to 8 C=C moieties, as shown in Figure 12.3a. In sharp contrast to the findings by Rogers and coworkers, who, using the heat of hydrogenation method, concluded that there is no conjugation in polyenes [6b], a similar trend has been found in these species, thus confirming that these compounds are indeed stabilized by π-conjugation (Figure 12.3a,b).

We also studied the change in the conjugation when a double bond conjugates with a carbonyl group [13b]. It is clear from the data in Table 12.2 that the strength of π-conjugation in the parent enone system (2-propenal) is slightly stronger than in *trans*-1,3-butadiene. This is very likely due to the electronegativity of the oxygen atom, which enhances π-conjugation (in VB terminology, this can be ascribed to the significant contribution of the corresponding charged resonance form in the description of the molecule). Consequently, it can be suggested that electron-withdrawing groups directly attached to the carbonyl group should lead to higher conjugative strengths, whereas π-electron-donor groups would provoke the opposite effect. This is exactly what the EDA method shows, as is illustrated in Table 12.2.

The ΔE_π data for the enone molecules $H_2C{=}CH{-}C(R){=}O$ provide a scale that shows how much a substituent R enhances or weakens the π-conjugation between the C=C and C=O moieties. Another scale for estimating substituent effects on conjugation was proposed by Hammett [15] on the basis of the hydrolysis rate of benzoic acids, which carry a substituent R in the *para* position (σ_p constants). Interestingly, our theoretical conjugation scale correlates quite well with the

Table 12.2 Results of the EDA at the BP86/TZ2P level.

	NH_2	OH	CH_3	H	F	Cl	CHO	CF_3	CN
σ_p	−0.66	−0.37	−0.17	0.00	0.06	0.23	0.42	0.54	0.66
ΔE_π	−15.6	−18.4	−18.0	−20.5	−20.6	−21.1	−22.1	−22.7	−23.3
r (C−C)	1.495	1.480	1.489	1.474	1.471	1.474	1.472	1.474	1.472

Energy values in kcal mol^{-1} and distances in Å.

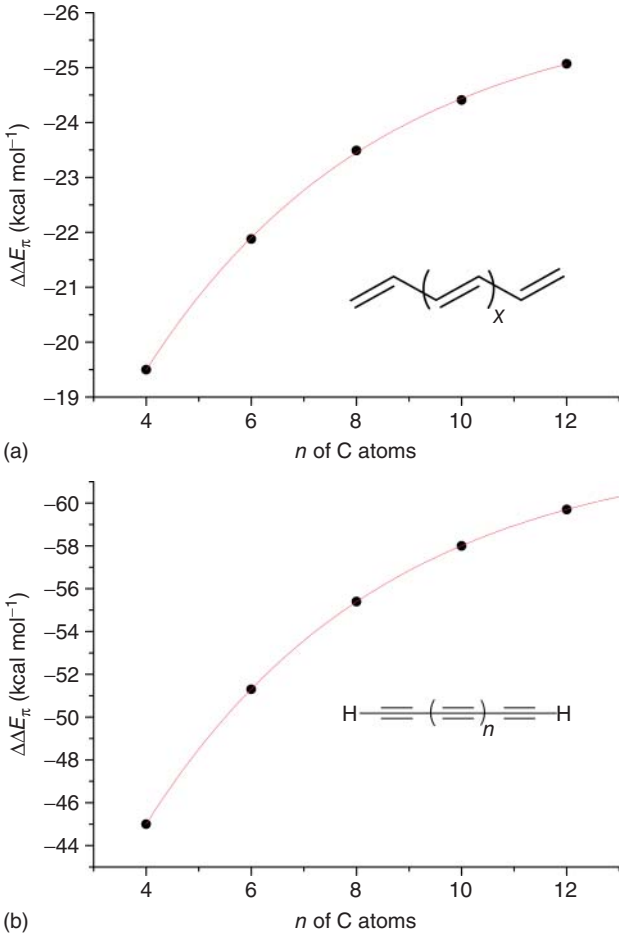

Figure 12.3 (a) $\Delta\Delta E_\pi$ versus the number of carbon atoms in polyenes. (b) $\Delta\Delta E_\pi$ versus the number of carbon atoms in polyynes.

experimental σ_p Hammett substituent constants (Figure 12.4, ΔE_π versus σ_p, correlation coefficient of 0.98 and standard deviation of 0.54). This result suggests that the electronic effect of the substituent R on π-conjugation in homo- and heteroconjugated systems is similar, and thus, appears to be rather independent of the nature of the conjugating system.

12.3.2
Correlation with Experimental Data

Hammett and Hammett–Brown Substituent Constants Encouraged by the latter results, we decided to apply our EDA derived methodology to compute Hammett constants directly [16]. Hammett σ_m and σ_p values reflect the extent to which

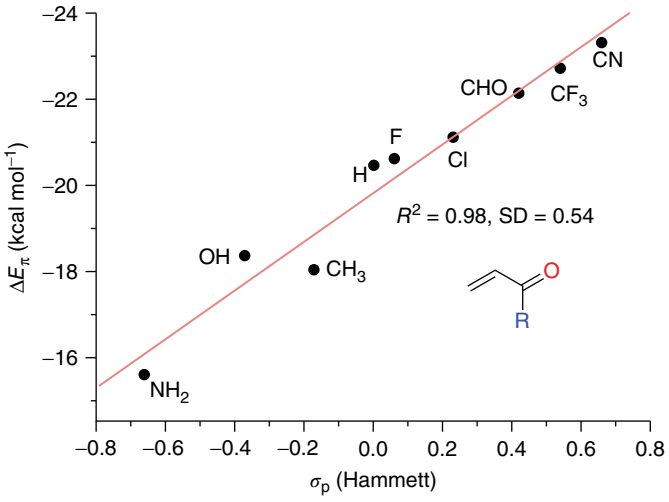

Figure 12.4 ΔE_π versus σ_p Hammett constants for substituted enones.

substituents in a *meta* or *para* position at a phenyl ring interact with a reaction site through a combination of resonance and field/inductive effects [15]. The original scale by Hammett can be used as a model system to estimate the electronic effects of substituents on similar reaction systems and is still widely used in textbooks on organic chemistry to discuss substituent effects [17]. However, the greatest incidence of failures of the simple Hammett equation were encountered when substituents capable of accepting or donating a pair of electrons are in direct conjugation with the reaction center (an effect known as *through resonance*). To overcome this problem, Brown and coworkers [18] proposed an improved scale of σ constants (σ^+ or σ^-) based on the solvolysis of substituted cumyl chlorides, which directly reflects the (hyper)conjugative effect of a given substituent.

In order to check our theoretical scale of conjugation, we compared the computed ΔE_π values from the EDA with the experimentally derived Hammett-σ_p and Hammett-Brown-σ^+_p constants for different *para*-substituted benzyl cations and anions. As can be seen in Figure 12.5, the data computed correlate quite well with the experimental constants (Figure 12.5a: ΔE_π versus σ_p, linear correlation coefficient of 0.95 and a standard error of 2.60; Figure 12.5b: ΔE_π versuss σ^+_p, coefficient 0.97 and standard error 2.15). Both correlations show that the values calculated for the intrinsic π-conjugation given by the EDA are reasonable for interpreting the chemical properties of a molecule, and they may even be used to semi-quantitatively predict Hammett constants for hitherto unknown substituents. Moreover, the lower correlation coefficient and higher standard deviation for the correlation with the original Hammett constants further support that the scale by Brown and coworkers is indeed a better choice to evaluate the *through-resonance* effect of a substituent. Therefore, Hammett parameters are good measures for the π-conjugation strength that can be directly quantified with the EDA method.

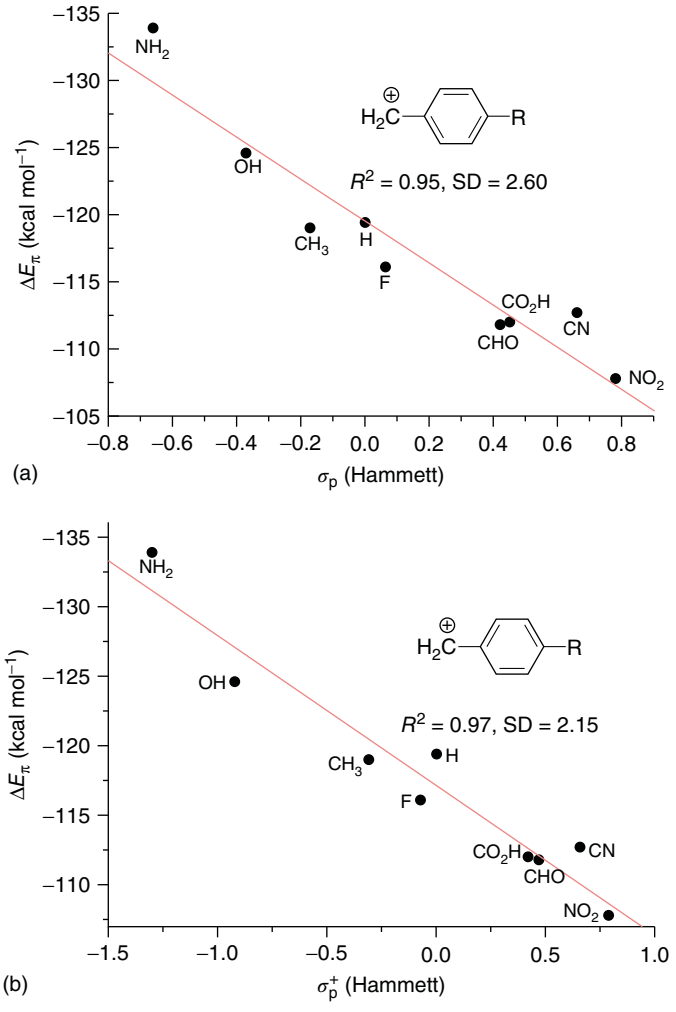

Figure 12.5 ΔE_π versus σ_p Hammett (a) or $\sigma^+{}_p$ Hammett–Brown (b) constants for *para*-substituted benzyl cations.

π-Conjugation in Donor-Substituted Cyanoethynylethenes Donor-substituted cyanoethynylethenes (CEEs) are a versatile class of modular building blocks for the construction of novel systems with extended π-conjugation. This family of donor–acceptor molecules, prepared by Diederich and coworkers [19], combines the scaffolding capacity of tetraethynylethenes (TEEs) with the electron-accepting properties of tetracyanoethenes (TCNEs). Interestingly, these organic materials can function as electronic acceptor groups for nonlinear optical applications when substituted with dimethylanilino (DMA) donor groups.

It has been proposed [19] that the extent of π-conjugation in these systems can be experimentally estimated by means of different experimental techniques, such as X-ray crystallography, cyclic voltammetry, and NMR spectroscopy. In fact, the conjugation effectiveness is well revealed by large changes in the first oxidation and reduction potentials of CEEs with respect to the isolated donor and acceptor moieties, as well as by the differences in the ^{13}C and ^{1}H NMR chemical shifts. In this regard, we applied our EDA methodology to directly compute the difference in the π-conjugation strength of the donor-substituted CEEs depicted in Table 12.3 [20].

It becomes clear from the data in Table 12.3 that the increase in the number of acceptor-cyano groups in molecules possessing one DMA group strongly enhances the strength of π-conjugation. Moreover, it can be concluded that the *cis* donor–acceptor conjugation path in **(*E*)-7** is more effective than the *trans* path in **(Z)-7**, and both are more efficient than geminal cross-conjugation (ΔE_π: **(E)-7** > **(Z)-7** > **8**). These results are in good agreement with the experimentally observed downfield shifts of the aryl carbons *ipso* and *meta* to the NMe_2 group in the corresponding ^{13}C NMR spectra [19]. For that reason, it is not surprising that excellent linear relationships are found when plotting the ΔE_π values computed and the latter experimental data, with the notable exception of compound **4** (Figure 12.6a: δ_{ipso} versus ΔE_π, correlation coefficient of 0.99 and standard deviation of 0.43; Figure 12.6b: δ_{meta} versus ΔE_π, correlation coefficient of 0.98 and standard deviation of 0.62). These results clearly confirm the ability of the EDA method to directly estimate the conjugative strength, even in large systems with extended π-conjugation.

π-Conjugation in Tunable Bis(*gem*-diethynylethene) Fluorophores Another family of compounds with extended π-conjugation is the cross-conjugated bis(*gem*-diethynylethenes) depicted in Figure 12.7, which constitute a promising class of tunable flourophores [21]. The different chemical modifications in the core and periphery of these systems induce dramatic changes in their absorption and emission spectra, with the fluorescence colors spanning regions from indigo blue to reddish-orange. Interestingly, the different optical properties, as well as the variation of the fluorescence quantum yield, have been explained in terms of the extension of the π-conjugation in these molecules [21].

The ΔE_π values from the EDA method clearly show that the strength of π-conjugation and the different optical properties are strongly correlated [22]. In fact, we again found very good linear relationships between the ΔE_π data computed and the wavelength of the absorption and emission maxima (Figure 12.8). These results are somewhat unexpected, because the ΔE_π values are a measure of the π-conjugation of the molecules in their ground states, whereas spectral lines involve electronically excited states. Furthermore, we can predict by means of the EDA method that adequate modifications in the core moiety of the molecule (for instance, π-donor substituents in the aromatic ring) or in the periphery of the bis-enedyine unit (π-acceptor groups placed in *para* position of the aryl substituent) should increase the total π-conjugation in the system, and, thus,

Table 12.3 Results of the EDA at the BP86/TZ2P level.

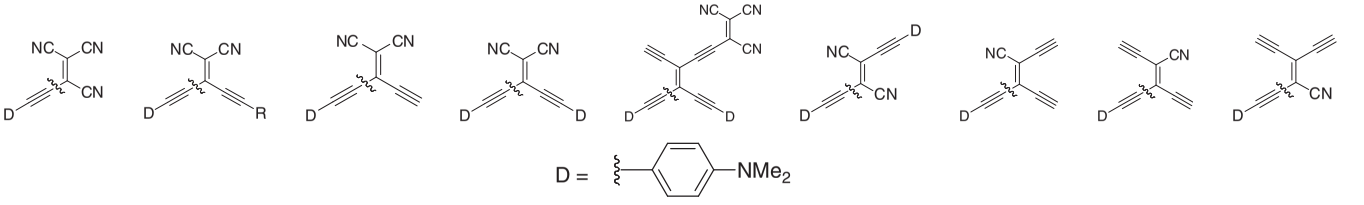

	1	2, R = ≡–H	3	4	5	6	(*E*)-7	(*Z*)-7	8
δ_{ipso} [a]	153.41	152.58	152.28	151.98	151.51	151.42	151.14	151.06	150.95
δ_{meta} [a]	136.38	135.58	135.37	135.03	134.49	133.93	133.95	133.79	133.37
E^{0} [b]	+0.79	—	+0.67	+0.63	—	+0.58	+0.56	+0.56	+0.52
ΔE_{π} [c]	−39.52	−35.62	−35.40	−31.29	−33.01	−31.95	−31.83	−31.21	−30.97

[a] ^{13}C NMR chemical shifts (in ppm, 75 MHz, $CDCl_3$), taken from Ref. [19].
[b] Potential E^0 (in V), taken from Ref. [19].
[c] Calculated $\Delta E\pi$ values from the EDA at BP86/TZ2P level (in kcal mol^{-1}).

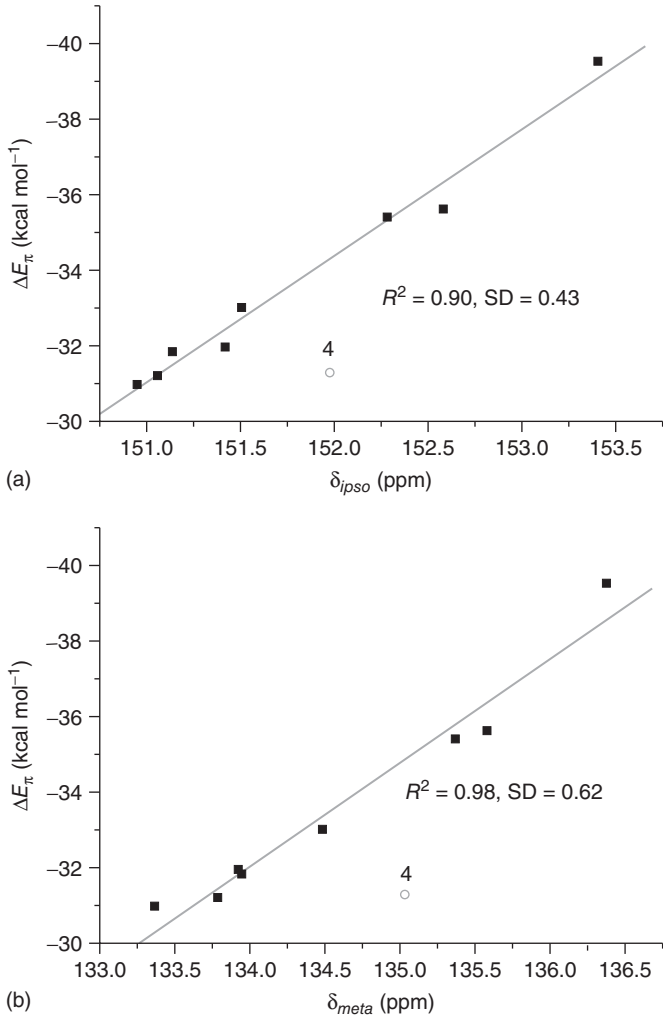

Figure 12.6 Plot of the ΔE_π values versus the ^{13}C NMR chemical shift of the aryl carbon *para* (a) or *meta* (b) to the NMe_2 group.

provoke dramatic changes in both the absorption and emission spectra, leading to large Stokes shifts. The extent of the latter may be estimated with the EDA before the experiment.

From the foregoing results, we can safely conclude that the EDA methodology allows the direct estimation of the conjugative strength, even in large systems with π-extended conjugation. In addition, it is a highly predictive tool which strongly correlates with different experimental data that have been traditionally used as descriptors of π-conjugation.

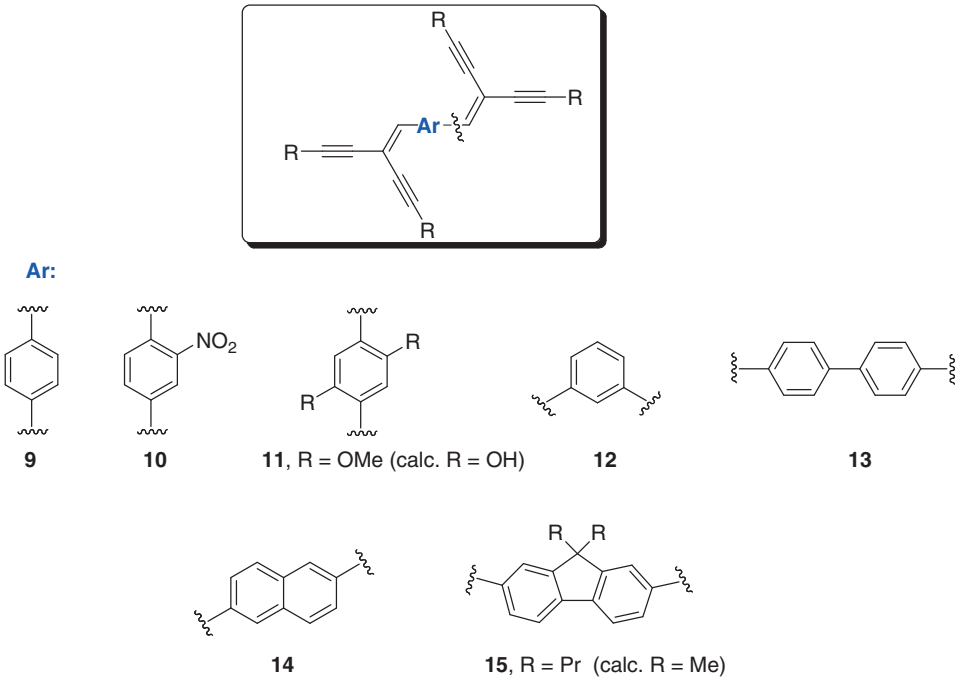

Figure 12.7 Experimentally investigated (R = Ph) and calculated (R = H) bis(gem-diethynylethenes).

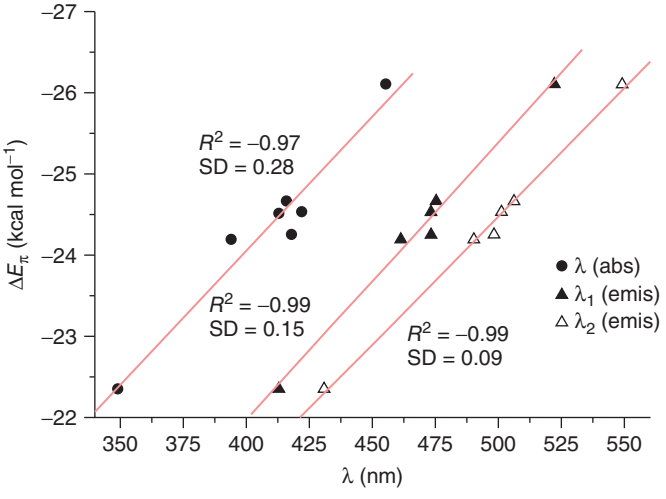

Figure 12.8 ΔE_π versus and the wavelength of the absorption (circles) and emission (triangles) maxima for the compounds depicted in Figure 12.7.

12.4 Hyperconjugation

Hyperconjugation is the interaction between orbitals having π-symmetry, where at least one of the π-orbitals is located at an atom that does not have a multiple bond [23]. According to the IUPAC, hyperconjugation is defined as "the interaction of σ-bonds (e. g., C–H, C–C, etc.) with a π network." The stabilization due to hyperconjugation is quite important and contributes significantly to the structure, stability, and reactivity of molecules. As an example, hyperconjugation is responsible for the stability of alkyl carbocations, as well as for the well-known anomeric and group 14 β-effects.

12.4.1 Hyperconjugation in Ethane and Ethane-Like Compounds

The strength of hyperconjugation in ethane has been a topic of a recent controversy as well [24]. It has been suggested that the staggered geometry of ethane is caused by hyperconjugation rather than steric repulsion. Although the view was rejected by other researchers, there was agreement that hyperconjugation even in saturated systems is important. To gain more insight into the strength of hyperconjugative interactions, we first decided to apply our EDA methodology to ethane and related compounds [13a].

Table 12.4 shows that the hyperconjugation in ethane is −10.0 kcal mol^{-1}. The comparison with the strength calculated for the conjugation in *trans*-1,3-butadiene (−19.5 kcal mol^{-1}) indicates that hyperconjugation is, as expected, weaker but not negligible. We want to point out that the hyperconjugation in ethane comes from two components of the degenerate e(π)-orbital. Therefore, a quantitative comparison of the hyperconjugation in ethane should, therefore, be made with 1,3-butadiyne. The EDA of the latter compound gives a value of $\Delta E_\pi = -45.0$ kcal mol^{-1} (Table 12.1) and, therefore, the strength of hyperconjugative interactions between C–H bonds has ∼ 1/4 of the strength of conjugation between C=C π-bonds.

Table 12.4 Results of the EDA at the BP86/TZ2P level.

X_3C-CX_3					$Cl_3C-C(SiH_3)_3$			
X = H	**X = CH_3**	**X = SiH_3**	**X = F**	**X = Cl**				
ΔE_π	−10.0	−11.6	−17.5	−12.9	−20.9	−29.7	−20.5	−27.1
r (C–C)	1.532	1.591	1.612	1.565	1.593	1.523	1.476	1.425

Energy values in kcal mol^{-1} and distances in Å.

Table 12.4 also shows that the hyperconjugation in the substituted ethanes $X_3C–CX_3$ (X = Me, SiH_3, F, Cl) can be stronger than in the parent ethane, particularly for X = SiH_3, Cl [13b]. Interestingly, the compounds with the strongest hyperconjugation, $(SiH_3)_3C–C(SiH_3)_3$ and $Cl_3C–CCl_3$, actually have the longest C–C bonds. This is an important result because a short bond length is often taken as evidence for hyperconjugation. This means that other effects, such as the influence of the electronegativity of the substituent on the σ-bonding and electrostatic interactions, play a role that hampers a direct correlation between hyperconjugation and bond distances. Interestingly, hyperconjugation strengths comparable to conjugation can be reached in unsymmetrical substituted ethanes ($X_3C–CY_3$, X ≠ Y = Me, SiH_3, F, Cl). In fact, the strongest hyperconjugation is calculated for $(SiH_3)_3C–CCl_3$ (an ethane molecule substituted by SiH_3 donor and chlorine acceptor moieties), which has an ΔE_π value of −29.7 kcal mol^{-1} (that is 10.2 kcal mol^{-1} higher than the conjugation in 1,3-butadiene).

Particularly interesting examples for strong hyperconjugation across C–C single bonds have been calculated between two cubyl moieties in cubylcubane, and between two tetrahedranyl fragments in tetrahedranyltetrahedrane [13b]. Table 12.4 shows that the very short central C–C bonds in the latter compounds can also be explained with unusually strong hyperconjugation. In fact, the ΔE_π values of cubylcubane (−20.5 kcal mol^{-1}) and tetrahedranyltetrahedrane (−27.1 kcal mol^{-1}) are much higher than in $Me_3C–CMe_3$ (−11.6 kcal mol^{-1}). We think that the short central bonds of the latter compounds are at least partially caused by π-bonding contributions.

12.4.2
Group 14 β-Effect

The stabilizing effect of group 14 elements when placed in the β-position to a carbocation centre is known as *β-effect*. This stabilization has been widely employed in synthetic transformations and, recently, it has allowed the isolation and X-ray structure determination of a *secondary* alkyl carbenium ion by Bochmann *et al.* [25]. A pivotal question concerns the strength of the hyperconjugative stabilization, which is the driving force of the β-effect. For that reason, we applied our EDA method to the primary to tertiary carbocations depicted in Figure 12.9 [26].

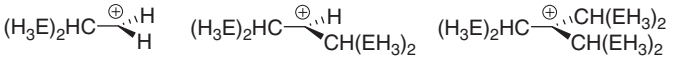

16a E=C	**17a** E=C	**18a** E=C
16b E=Si	**17b** E=Si	**18b** E=Si
16c E=Ge	**17c** E=Ge	**18c** E=Ge
16d E=Sn	**17d** E=Sn	**18d** E=Sn
16e E=Pb	**17e** E=Pb	**18e** E=Pb

Figure 12.9 Schematic representation of the primary (16a–e), secondary (17a–e), and tertiary (18a–e) alkyl carbenium ions.

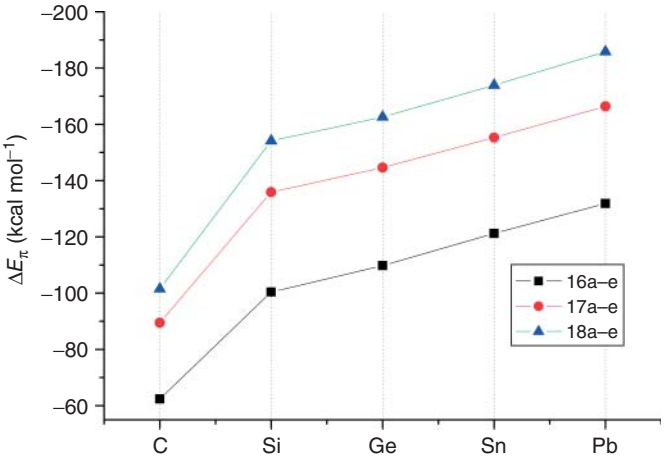

Figure 12.10 ΔE_π values for compounds **16–18**.

As graphically shown in Figure 12.10, the EDA results indicate that the ability of σ C–E (E = group 14 element) bonds to stabilize positive charges by hyperconjugation follows the order C ≪ Si < Ge < Sn < Pb. Hyperconjugation of C–Si bonds is much stronger than hyperconjugation of C–C bonds, while the further increase from silicon to lead, which has about the same step size for each element, is smaller. The hyperconjugation strength in primary, secondary, and tertiary alkyl carbenium ions does not increase with the same step size with the number of hyperconjugating groups either (it becomes smaller from primary to secondary to tertiary cations). These results are in good agreement with previous experimental findings by Lambert *et al.* [27] and, therefore, they provide further support for the ability of the EDA method to directly estimate the relative contributions of π-interactions that come from hyperconjugation. Interestingly, the effect of hyperconjugation is reflected in the shortening of the C–C bond distances and in the lengthening of the C–E bonds. Both geometrical features exhibit very good linear relationships when plotted versus the strength of hyperconjugation given by the ΔE_π values computed [26].

12.5 Aromaticity

As stated, numerous methods for qualitatively and quantitatively defining aromaticity, based on energetic, geometric, electronic, magnetic, spectroscopic, and other criteria, have been suggested [2, 3].[1] The difficulty in establishing a universal aromaticity scale based on one single parameter is due to the multidimensional character of this phenomenon. The fuzzy nature of aromaticity is the reason why none of these criteria can be considered as universal or is free from ambiguities [3, 28]. Despite that, the energetic criterion, if well defined, is considered to be the

principal one as it governs the reactions and much of the chemical behavior of a molecule. It is thus the stability of a cyclic π-conjugated compound with respect to an acyclic compound that is the primary quantity defining aromaticity. Taking this into account, we can easily compute the aromatic stabilization energies (ASEs) in aromatic compounds just by comparing their π-cyclic conjugation strength with the π-conjugation of acyclic reference systems. Therefore, the extra stabilization energy due to aromaticity (ASE) can be estimated with the EDA method as the difference between the ΔE_π values of the cyclic compound and those of the reference acyclic species. The difficulty arises in the choice of these acyclic reference compounds. As suggested by Mo and Schleyer [7a], a reference molecule with the same number of diene conjugations is a better choice than a molecule with the same number of π-electrons, because the ASE values (computed using the block-localized wave function, BLW, method) exhibit a better correlation with the nuclear-independent chemical shift (NICS) values. We followed their suggestion and adopted the former approach for the calculation of the ASEs using the ΔE_π values derived from the EDA.

Table 12.5 shows the ΔE_π values for typical aromatic and heteroaromatic compounds and their respective acyclic reference systems together with their corresponding ASE values [29]. As expected, it was found that the strength of π-conjugation is higher in the cyclic hetero/aromatic compounds than in the corresponding acyclic reference species and, therefore, they present positive ASE values. Interestingly, while benzene and pyridine have similar ASEs, the corresponding five-membered heterocycles present lower values (in the order pyrrole ≈ thiophene > furan), which is in good agreement with the order of aromaticity found by Schleyer and Mo using the BLW method [7a]. Furthermore, our method can also be applied to homo-antiaromatic/aromatic (i.e., compounds where the cyclic conjugation is interrupted by a single sp^3 hybridized atom) and antiaromatic compounds. As can be readily seen from the data in Table 12.5, the homoaromatic cyclobutene

Table 12.5 Results of the EDA at the BP86/TZ2P level.

Aromatic compound							
ΔE_π	−107.7	−113.5	−98.0	−77.6	−77.7	−20.0	−9.6
Reference compound	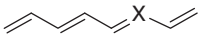		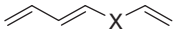			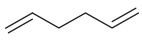	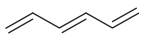
	X = CH	X = N	X = NH	X = S	X = O		
ΔE_π	−65.2	−67.8	−76.9	−55.7	−61.5	−16.5	−41.5
ASE	**42.5**	**45.7**	**21.1**	**21.9**	**16.2**	**3.5**	**−31.9**

Energy values in kcal mol^{-1}.

has a very low but positive ASE value, while cyclobutadiene, which is considered as the archetypal antiaromatic compound [30], presents a highly negative ASE value.

Therefore, our EDA-based approach provides a useful and reliable energy scale for the strength of aromaticity, which can be used to classify compounds according to their relative ASE values. Compounds with ASE > 0 can be considered as aromatic (the highest ASE values were computed for benzene and pyridine, ca. 45 kcal mol^{-1}), whereas antiaromatic compounds exhibit highly negative ASE values. Compounds with small positive ASE values are typical for homoaromatic compounds, while small negative ASE values are indicative of homoantiaromaticity. The good performance of these ASE values has been confirmed in the excellent correlations between these data and the activation and reaction energies of double-group transfer reactions that have been considered as descriptors of aromaticity [31].

The reliability of the EDA method has been proved in the study of the aromaticity of systems where the application of the very popular methods for quantifying aromaticity of a molecule (i.e., NICS and magnetic susceptibility anisotropy, $\Delta\chi$, calculations) fails or has severe limitations. Three different families of compounds with controversial aromatic nature have been considered: (i) neutral exocyclic substituted cyclopropenes $(HC)_2C{=}E$, (ii) group 14 homologs of the cyclopropenylium cation, and (iii) metallabenzenes.

12.5.1 Aromaticity in Neutral Exocyclic Substituted Cyclopropenes $(HC)_2C{=}X$

The focus of this study is to find out to what extent different exocyclic (C=X) substituents induce aromaticity and antiaromaticity in cyclopropene derivatives $(HC)_2C{=}X$ [32]. Although the consensus opinion suggests that parent methylenecyclopropene, $(HC)_2C{=}CH_2$, the simplest cross-conjugated cyclic hydrocarbon, is nonaromatic, it is admitted that cyclopropenone is at least modestly aromatic [33–35]. However, quantitative assessments of the aromaticity of other $(HC)_2C{=}X$ derivatives have not led to satisfactory agreement. Thus, this family of compounds represents a paramount opportunity to use the EDA-aromaticity method to give a definitive answer to a question that has been controversially discussed in the literature for several decades [33–35].

As can be seen in Figure 12.11, the aromaticity of exocyclic substituted cyclopropenes $(HC)_2C{=}X$ is very sensitive to the nature of the substituents. Exocyclic substituted cyclopropenes with electronegative substituents have positive ASE values, and, thus, they are aromatic, resembling the 2π-electron cyclopropenium cation. On the other hand, exocyclic-substituted cyclopropenes with electropositive substituents have negative ASE values and they can be considered as antiaromatic species resembling the 4π-electron cyclopropenium anion. The calculations indicate that $(HC)_2C{=}O$ and $(HC)_2C{=}InH$ are the most aromatic and most antiaromatic species, respectively, in our set of compounds. The aromaticity trend given by the EDA method correlates well with those provided by the BLW method and refined NICS values [32], thus giving further support to the ability of the EDA method to quantitatively estimate the aromaticity strength of π-cyclic conjugated species.

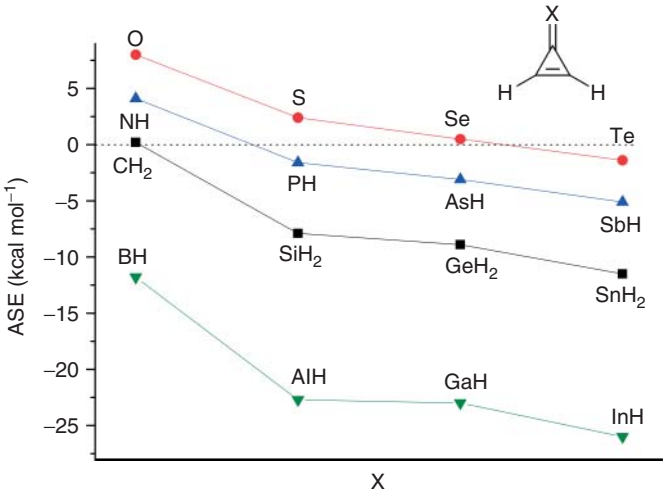

Figure 12.11 EDA-ASE values for neutral exocyclic-substituted cyclopropenes $(HC)_2C{=}E$.

12.5.2
Aromaticity in Group 14 Homologs of the Cyclopropenylium Cation

Group 14 elements containing cyclopropenyl cations constitute a family of small cyclic compounds whose aromatic character is not well established either [36]. As Lee and Sekiguchi (who synthetized most of this type of compounds) wrote in their recent review [37]: *"… apart from the synthetic achievements, one should also expect major breakthroughs in the theory of heavy (organometallic) aromaticity … There are few serious theoretical studies related to this topic, and new theoretical insights based on high-level computations using the appropriate model compounds would be very welcome."* Therefore, we decided to use our EDA-derived scale of aromaticity to gain more insight into the aromatic nature of these compounds [38].

Our calculations (Table 12.6) suggest that the entire set of heavy group 14 homologs of the cyclopropenium cation is less aromatic than the parent $C_3H_3^+$ ion. Although all these ions are 2π-electron Hückel species, the aromatic stabilization decreases from the highly aromatic $C_3H_3^+$ and $Si_2H_2CH^+$ ions to the practically nonaromatic $Pb_3H_3^+$ species. The strength of π-cyclic conjugation and aromaticity decreases in the order C≫Si>Ge>Sn>Pb. This decreasing π-delocalization is due partly to the monotonic decrease in overlap between the doubly occupied π−molecular orbital of the HE=EH fragment with the vacant *p* atomic orbital of the EH^+ fragment. However, the decrease in the absolute values of the ΔE_π term comes mainly from the energy of the valence electrons, which are less strongly bonded for heavier atoms of the same group. Remarkably, the resonance energy estimates based on BLW analyses give nearly the same quantitative stabilization estimates as our EDA-ASE values [38], thus showing that both methods, despite being based on entirely different approaches, evidently measure energetic aromaticity reliably and consistently.

Table 12.6 EDA computed ASE values (in kcal mol^{-1}) of cyclopropenylium ions (BP86/TZ2P).

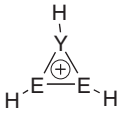

E \ Y	Y = C	Y = Si	Y = Ge	Y = Sn	Y = Pb
E = C	33.2	11.9	8.8	5.1	5.6
E = Si	26.7	15.2	13.5	9.7	9.2
E = Ge	21.0	13.0	11.2	9.2	8.8
E = Sn				8.0	
E = Pb					5.7

12.5.3 Aromaticity in Metallabenzenes

Finally, the EDA method was used to study the aromacity in metallabenzenes, a family of organometallic compounds, where a CH group in benzene has been replaced by an isolobal transition metal and its attached ligands [39]. Most of these complexes exhibit properties usually associated with aromatic systems, such as deshielded proton resonances in the ^{1}H NMR spectrum, bond length equalization, and ring planarity. In addition, the chemical reactivity of metallabenzenes is also in agreement with the classification as aromatic species as they undergo typical reactions of aromatic compounds, such as electrophilic aromatic substitution or formation of arene complexes. However, metallabenzenes may also engage in reactions that are unusual for aromatic systems, such as cycloaddition or cyclopentadienyl complex formation, which suggests that metallacycles are not as aromatic as their all-carbon analogs [39, 40].

On the other hand, the calculation of the aromaticity compounds is problematic because of the anisotropy of the metal center and to the effect of the corresponding ligands that contaminate the values obtained with the most typical methods used to estimate aromaticity (i.e., NICS and magnetic susceptibility values) [40]. The conflicting observations about the chemical behavior of metallabenzenes as aromatic species led us to carry out a systematic theoretical study using the EDA, where we addressed the aromaticity and bonding situation in 21 different metallabenzenes including 4d and 5d transition metals (transition metal = Os, Ru, Ir, Rh, Pt, and Pd) [41]. As can be seen from the data in Table 12.7, which gathers a selection of some EDA results of our work, metallabenzenes present positive ASE values (ranging from 8.7 kcal mol^{-1} for **23** to 37.6 kcal mol^{-1} for platinabenzene **24**) and, therefore, they should be considered as aromatic compounds. As expected, the aromatic strength in these species depends strongly on the transition metal and its

Table 12.7 Results of the EDA for metallabenzenes at the BP86/TZ2P level.

	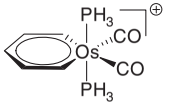	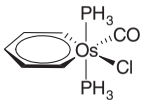	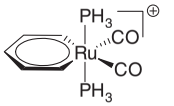	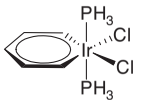	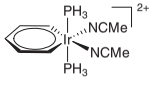		
	19	**20**	**21**	**22**	**23**	**24**	**25**
ΔE_π	−97.5	−78.1	−97.5	−97.2	−103.3	−100.1	−97.3
Reference Compound	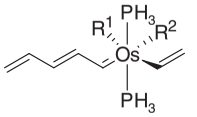		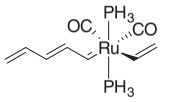	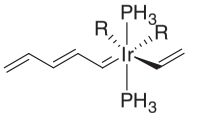		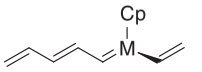	
	$R^1 = R^2 = CO$	$R^1 = CO$, $R^2 = Cl$		R = Cl	R = NCMe	M = Pt	M = Pd
ΔE_π	−79.9	−59.4	−76.9	−63.7	−94.6	−62.5	−64.5
ASE	**17.6**	**18.7**	**17.7**	**33.5**	**8.7**	**37.6**	**32.8**

Energy values in kcal mol^{-1}.

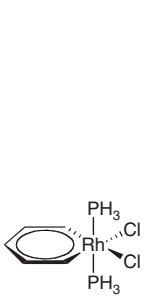

26

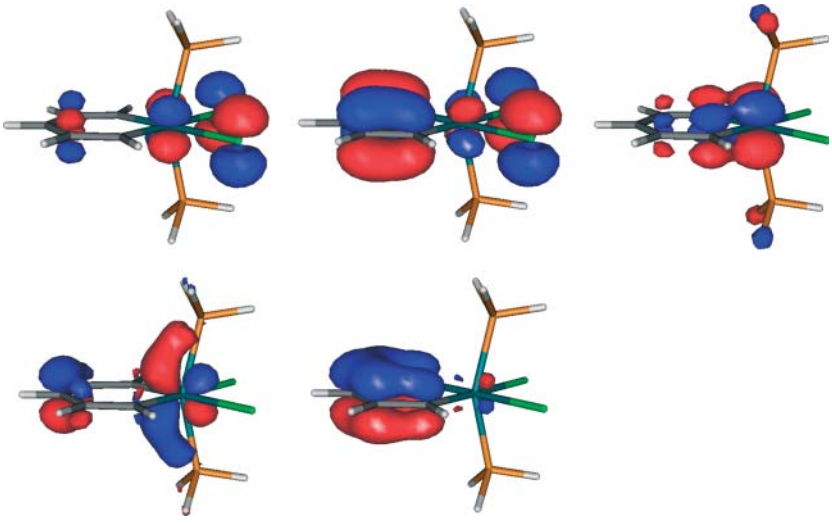

Figure 12.12 Computed π-molecular orbitals of rhodabenzene **26**.

ligands. In general, it can be concluded that the extra-stabilization due to aromatic conjugation in metallabenzenes is weaker than that in benzene.

Finally, we also analyzed the electronic structure of metallabenzenes in more detail. Figure 12.12 shows the occupied π-molecular orbitals model having coefficients at the metal atom and at the $C_5H_5^-$ ligand of the C_{2v}-symmetric rhodabenzene **26**. It becomes obvious that this species is actually a 10π-electron system and, therefore, the $4n+2$ rule also holds in this type of aromatic compounds.

12.6 Concluding Remarks

The quantitative estimation of the (hyper)conjugative and aromaticity strengths has been a challenge in the past from both experimental and theoretical points of view. The main problem associated with this task is that such effects are only bonding models and, therefore, virtual thermodynamic quantities that cannot be measured experimentally. In this chapter, we have presented the excellent performance of the EDA method to directly estimate the above-mentioned effects (which come from genuine π-interactions) without recourse to external reference systems, as has been traditionally done. The data provided by the EDA (ΔE_π values) constitute a reliable scale of (hyper)conjugation or aromaticity as demonstrated from the very good correlations found between the computed ΔE_π values and different experimental data that have been suggested as descriptors for conjugative/aromaticity strengths. The main limitation of the method is the need for planarity (i.e., a mirror plane) in the molecule considered, because our method is grounded in the partition of orbitals with different symmetries to estimate interactions that come from π-orbitals.

However, this shortcoming can be now overcome with the recently developed EDA-NOCV (natural orbitals for chemical valance) method [42], which allows the analyses even in molecules with C_1 symmetry. Despite that, the methodology is quite robust and can also be applied to large systems having π-extended conjugation or even to compounds where other methods fail (i.e., small rings and organometallic species); and, importantly, it is highly predictive as new systems with enhanced conjugation or experimental data (i.e., Hammett's constants) can be suggested before the experiment.

References

1. Frenking, G. and Krapp, A. (2007) *J. Comput. Chem.*, **28**, 15–24.
2. (a) For recent reviews about aromaticity see the special issue entitled: Aromaticity in (2001) *Chem. Rev.*, **101**. (b) For recent reviews about conjugation and electronic delocalization see the special issue entitled: Delocalization – π and σ in (2005) *Chem. Rev.*, **105**.
3. Stanger, A. (2009) *Chem. Commun.*, 1939–1947.
4. Jarowski, P.D., Wodrich, M.D., Wannere, C.S., Schleyer, P.v.R., and Houk, K.N. (2004) *J. Am. Chem. Soc.*, **126**, 15036–15037.
5. (a) Kistiakowsky, G.B., Ruhoff, J.R., Smith, H.A., and Vaughan, W.E. (1936) *J. Am. Chem. Soc.*, **58**, 146–153. (b) Conant, J.B. and Kistiakowsky, G.B. (1937) *Chem. Rev.*, **20**, 181–194.
6. (a) Rogers, D.W., Matsunaga, N., Zavitsas, A.A., McLafferty, F.J., and Liebman, J.F. (2003) *Org. Lett.*, **5**, 2373–2375. (b) Rogers, D.W., Matsunaga, M., McLafferty, F.J., Zavitsas, A.A., and Liebman, J.F. (2004) *J. Org. Chem.*, **69**, 7143–7147.
7. (a) Mo, Y. and Schleyer, P.v.R. (2006) *Chem. Eur. J.*, **12**, 2009–2020. See also:(b) George, P., Trachtman, M., Bock, C.W., and Brett, A.M. (1975) *Theor. Chim. Acta*, **38**, 121–129. (c) George, P., Trachtman, M., Brett, A.M., and Bock, C.W. (1977) *J. Chem. Soc., Perkin Trans. 2*, 1036–1047. (d) Hehre, W.J., Radom, L., Schleyer, P.v.R., and Pople, J.A. (1986) *Ab Initio Molecular Orbital Theory*, John Wiley & Sons, Inc., New York.
8. Ziegler, T. and Rauk, A. (1977) *Theor. Chim. Acta*, **46**, 1–10.
9. Morokuma, K. (1971) *J. Chem. Phys.*, **55**, 1236–1244.
10. (a) Bickelhaupt, F.M. and Baerends, E.J. (2000) *Rev. Comput. Chem.*, **15**, 1–86. (b) te Velde, G., Bickelhaupt, F.M., Baerends, E.J., van Gisbergen, S.J.A., Fonseca-Guerra, C., Snijders, J.G., and Ziegler, T. (2001) *J. Comput. Chem.*, **22**, 931–967. (c) Lein, M. and Frenking, G. (2005) in *Theory and Applications of Computational Chemistry: The First 40 Years* (eds C.E. Dykstra, G. Frenking, K.S. Kim, and G.E. Scuseria), Elsevier Biomedical, Amsterdam, p. 291. (d) von Hopffgarten, M. and Frenking, G. (2012) *WIREs Comput. Mol. Sci.*, **2**, 43–62.
11. (a) Esterhuysen, C. and Frenking, G. (2004) *Theor. Chem. Acc.*, **111**, 381–389. (b) Kovács, A., Esterhuysen, C., and Frenking, G. (2005) *Chem. Eur. J.*, **11**, 1813–1825. (c) Krapp, A., Bickelhaupt, F.M., and Frenking, G. (2006) *Chem. Eur. J.*, **12**, 9196–9216.
12. Frenking, G., Wichmann, K., Fröhlich, N., Loschen, C., Lein, M., Frunzke, J., and Rayón, V.M. (2003) *Coord. Chem. Rev.*, **238–239**, 55–82.
13. (a) Cappel, D., Tuellmann, S., Krapp, A., and Frenking, G. (2005) *Angew. Chem. Int. Ed.*, **44**, 3617–3620. (b) Fernández, I. and Frenking, G. (2006) *Chem. Eur. J.*, **12**, 3617–3629.
14. Reichardt, C. (2003) *Solvents and Solvent Effects in Organic Chemistry*, 3rd edn, Wiley-VCH Verlag GmbH, Weinheim.
15. (a) Hammett, L.P. (1935) *Chem. Rev.*, **17**, 125–136. (b) Hammett, L.P. (1970)

Physical Organic Chemistry, 2nd edn, McGraw-Hill, New York.
16. Fernández, I. and Frenking, G. (2006) *J. Org. Chem.*, **71**, 2251–2256.
17. Carey, F.A. and Sundberg, R.J. (2000) *Advanced Organic Chemistry, Part A: Structure and Mechanism*, 4th edn, Plenum Press, New York.
18. Okamoto, Y. and Brown, H.C. (1957) *J. Org. Chem.*, **22**, 485–494.
19. Moonen, N.N.P., Pomerantz, W.C., Gist, R., Boudon, C., Gisselbrecht, J.-P., Kawai, T., Kishioka, A., Gross, M., Irie, M., and Diederich, F. (2005) *Chem. Eur. J.*, **11**, 3325–3341.
20. Fernández, I. and Frenking, G. (2006) *Chem. Commun.*, 5030–5032.
21. Hwang, G.T.H., Son, S., Ku, J.K., and Kim, B.H. (2003) *J. Am. Chem. Soc.*, **125**, 11241–11248.
22. Fernández, I. and Frenking, G. (2007) *J. Org. Chem.*, **72**, 7367–7372.
23. Alabugin, I.V., Gilmore, K.M., and Peterson, P.W. (2011) *WIREs Comput. Mol. Sci.*, **1**, 109–141.
24. Mo, Y. and Gao, J. (2007) *Acc. Chem. Res.*, **40**, 113–119, and references therein.
25. Schormann, M., Garrat, S., Hughes, D.L., Green, J.C., and Bochmann, M. (2002) *J. Am. Chem. Soc.*, **124**, 11266–11267.
26. Fernández, I. and Frenking, G. (2007) *J. Phys. Chem. A*, **111**, 8028–8035.
27. Lambert, J.B., Zhao, Y., Emblidge, R.W., Salvador, L.A., Liu, X., So, J.-H., and Chelius, E.C. (1999) *Acc. Chem. Res.*, **32**, 183–190.
28. (a) Jug, K. and Koster, A.M. (1991) *J. Phys. Org. Chem.*, **4**, 163–169. (b) Krygowski, T.M., Cyranski, M.K., Czarnocki, Z., Hafelinger, G., and Katritzky, A.R. (2000) *Tetrahedron*, **56**, 1783–1796. (c) Poater, J., García-Cruz, I., Illas, F., and Solà, M. (2004) *Phys. Chem. Chem. Phys.*, **6**, 314–318. (d) Cyranski, M.K., Krygowski, T.M., Katritzky, A.R., and Schleyer, P.v.R. (2002) *J. Org. Chem.*, **67**, 1333–1338. (e) Feixas, F., Matito, E., Poater, J., and Solà, M. (2008) *J. Comput. Chem.*, **29**, 1543–1554. (f) Alonso, M. and Herradón, B. (2010) *J. Comput. Chem.*, **31**, 917–928.
29. Fernández, I. and Frenking, G. (2007) *Faraday Discuss.*, **35**, 403–421.
30. Bally, T. (2006) *Angew. Chem. Int. Ed.*, **45**, 6616–6619.
31. (a) Frenking, G., Cossío, F.P., Sierra, M.A., and Fernández, I. (2007) *Eur. J. Org. Chem.*, 5410–5415. (b) Fernández, I., Cossío, F.P., and Sierra, M.A. (2009) *Chem. Rev.*, **109**, 6687–6711.
32. Wang, Y., Fernández, I., Duvall, M., Wu, J.I., Li, Q., Frenking, G., and Schleyer, P.v.R. (2010) *J. Org. Chem.*, **75**, 8252–8257.
33. (a) Staley, S.W. and Norden, T.D. (1984) *J. Am. Chem. Soc.*, **106**, 3670–3699. (b) Billups, W.E., Lin, L., and Casserley, E.W. (1984) *J. Am. Chem. Soc.*, **106**, 3698–3699. (c) Maier, G., Hoppe, M., Lanz, K., and Reisenauer, P. (1984) *Tetrahedron Lett.*, **25**, 5645–5648.
34. (a) Burk, P., Abboud, J.L.M., and Koppel, I.A. (1996) *J. Phys. Chem.*, **100**, 6992–6997. (b) Bachrach, S.M. (1990) *J. Org. Chem.*, **55**, 4961–4963. (c) Bachrach, S.M. and Liu, M. (1991) *J. Phys. Org. Chem.*, **4**, 242–250. (d) Manatt, S.L. and Roberts, J.D. (1959) *J. Org. Chem.*, **24**, 1336–1338. (e) Roberts, J.D., Streitwieser, A., and Rega, C.M. (1952) *J. Am. Chem. Soc.*, **74**, 4579–4582.
35. (a) Billups, W.E. and McCord, D.J. (1994) *Angew. Chem., Int. Ed. Engl.*, **33**, 1332–1343. (b) Norden, T.D., Staley, S.W., Taylor, W.H., and Harmony, M.D. (1986) *J. Am. Chem. Soc.*, **108**, 7912–7918. (c) Hess, B.A. Jr.,, Michalska, D., and Schaad, L. (1985) *J. Am. Chem. Soc.*, **107**, 1449–1450. (d) Staley, S.W., Norden, T.D., Taylor, W.H., and Harmony, M.D. (1987) *J. Am. Chem. Soc.*, **109**, 7641–7647.
36. (a) For comprehensive overviews of the aromaticity of Group 14 element compounds, see: Apeloig, Y. (1989) in *The Chemistry of Organic Silicon Compounds*, vol. 1 (eds S. Patai and Z. Rappoport), John Wiley & Sons, Ltd, Chichester, Chapter 2. (b) Apeloig, Y. and Karni, M. (1998) in *The Chemistry of Organic Silicon Compounds*, vol. 2, Part 1, Chapter 1 (eds Z. Rappoport and Y. Apeloig), John Wiley & Sons, Ltd, Chichester. (c) Karni, M., Apeloig, Y.,

Kapp, J., and Schleyer, P.v.R. (2001) in *The Chemistry of Organic Silicon Compounds*, vol. 3 (eds Z. Rappoport and Y. Apeloig), John Wiley & Sons, Ltd, pp. 1–163. (d) Goldfuss, B., Schleyer, P.v.R., and Hampel, F. (1996) *Organometallics*, **15**, 1755–1757. (e) Goldfuss, B. and Schleyer, P.v.R. (1997) *Organometallics*, **16**, 1543–1552. (f) Saito, M., Sakaguchi, M., Tajima, T., Ishimura, K., Nagase, S., and Hada, M. (2010) *Science*, **328**, 339–342. (g) Ebrahimi, A.A., Ghiasi, R., and Foroutan-Nejad, C. (2010) *J. Mol. Struct. THEOCHEM*, **941**, 47–52.

37. Lee, V.Y. and Sekiguchi, A. (2007) *Angew. Chem. Int. Ed.*, **46**, 6596–6620.

38. Fernández, I., Duvall, M., Wu, J.I., Schleyer, P.v.R., and Frenking, G. (2011) *Chem. Eur. J.*, **17**, 2215–2224.

39. For a recent review, see: Landorf, W.C. and Haley, M.M. (2006) *Angew. Chem. Int. Ed.*, **45**, 3914–3936.

40. Iron, M.A., Lucassen, A.C.B., Cohen, H., van der Boom, M.E., and Martin, J.M.L. (2004) *J. Am. Chem. Soc.*, **126**, 11699–11710.

41. Fernández, I. and Frenking, G. (2007) *Chem. Eur. J.*, **13**, 5873–5884.

42. (a) Mitoraj, M. and Michalak, A. (2007) *Organometallics*, **26**, 6576–6580. (b) Mitoraj, M. and Michalak, A. (2008) *J. Mol. Model.*, **14**, 681–687. (c) Michalak, A., Mitoraj, M., and Ziegler, T. (2008) *J. Phys. Chem. A*, **112**, 1933–1939. (d) Mitoraj, M.P., Michalak, A., and Ziegler, T. (2009) *J. Chem. Theory Comput.*, **5**, 962–975.

13
Magnetic Properties of Aromatic Compounds and Aromatic Transition States

Rainer Herges

13.1
Introduction

Aromaticity is not an observable molecular property in quantum mechanics. Observables are defined as expectation values that are obtained by the action of an operator on a wavefunction. In molecular chemistry they are measurable properties such as geometry (bond length, bond angle), energies (ionization potential, electron affinity, heat formation), or magnetic properties (magnetic susceptibility, chemical shift in NMR). There is no way to unambiguously define aromaticity from the underlying laws of theoretical physics. Therefore, any discussion about ''a superior'' or even ''the best'' method to define or quantify aromaticity is pointless, and is not conducive to the advancement of science. So, most of the controversial literature on aromaticity is based on the inherent characteristics of human nature rather than on the fundamental laws of science.

Aromaticity is one of the most useful concepts in chemistry. We teach it in undergraduate courses, and we need it in our everyday work as chemists. To abandon this concept because it doesn't have a rigorous physical basis would mean that we would lose a very important tool to interpret and predict the properties of molecules on a qualitative basis. A theoretical physicist or chemist might argue that nowadays properties of molecules can be predicted with almost chemical accuracy. So why do we need qualitative concepts like aromaticity? It's because chemistry is about more than the prediction of numbers. Chemistry is not a science in a strictly reductionist definition. There is a large part of an engineering-type of reasoning involved in chemistry. The analytic part of chemistry may be covered by quantum mechanics, but the constructive part is not accessible to theoretical methods (e.g., try to set up a wavefunction to solve the problem of chemical synthesis).

Even though aromaticity is not an observable, all existing methods to define aromaticity ultimately derive the concept from observables. These observables are:

1) Energy (e.g., aromatic stabilization energy)
2) Geometry (e.g., bond length equalization)
3) Magnetic properties (e.g., NMR shift).

The Chemical Bond: Chemical Bonding Across the Periodic Table, First Edition.
Edited by Gernot Frenking, Sason Shaik.

There is a vast amount of literature available on the different approaches [1–5]. More than 600,000 publications deal with the concept of aromaticity (Scifinder Dec. 2012). This chapter covers the methods based on magnetic properties [6, 7]. Even within this subsection, the number of publications is too large to be completely reviewed. The literature covered here, therefore, is personally biased, and the character of this contribution is more in line with a tutorial than a review of the latest literature in the field.

13.2
A Short Historical Review of Aromaticity

In the early days of structural chemistry, a ball and stick model of molecular chemistry slowly evolved from attempts to explain experimental results available at the time. Localized bonds were depicted as intersecting circles by Loschmidt [8], dashed lines by Couper [9, 10], and touching bulges by Kekulé [11] (Figure 13.1).

Kekulé, who was the first to draw localized bond structures of benzene, was criticized by his contemporaries because the alternating single bond/double bond structure did not explain the number of isomers found in substituted benzenes (e.g., only one isomer of *o*-substituted benzene). A. Claus [12], J. Dewar [13], L. Meyer [14], H. E. Armstrong [15], A. v. Baeyer [16], and A. Ladenburg [17] proposed alternative structures (Figure 13.2).

Kekulé in turn proposed a mechanical collision that would exchange single and double bonds in his 6-ring formula. Even though this might be intuitively close to our understanding of aromaticity today, his hypothesis was more an act of desperation than an explanation. The first physically sound description of benzene, and therefore of aromaticity, was provided by Erich Hückel in 1931 (Figure 13.3).

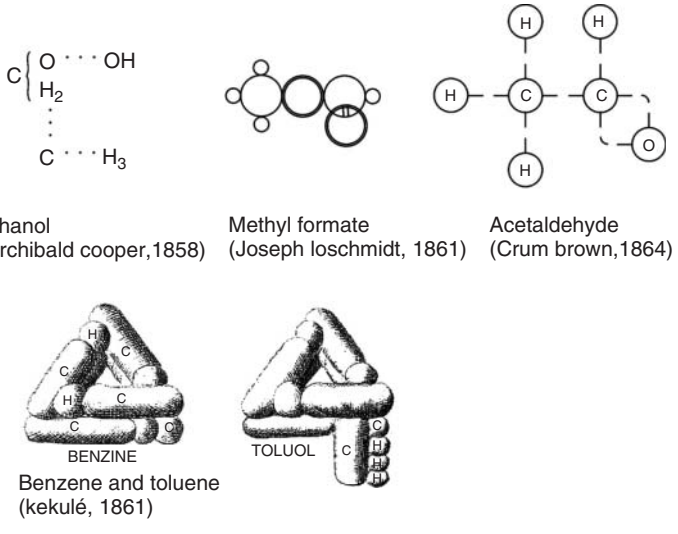

Figure 13.1 Early attempts to represent molecular structures with localized bonds.

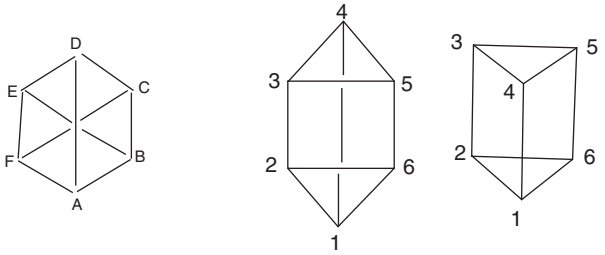

Claus (1867) Ladenburg (1869)

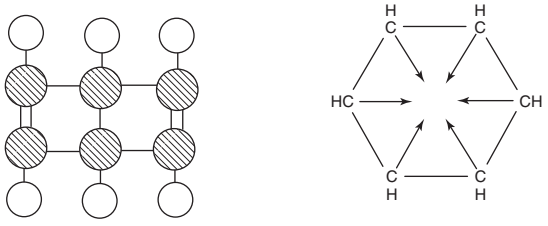

Stëdeler (1868) Armstrong (1887)

Figure 13.2 Alternative proposals for the structure of benzene (original drawings).

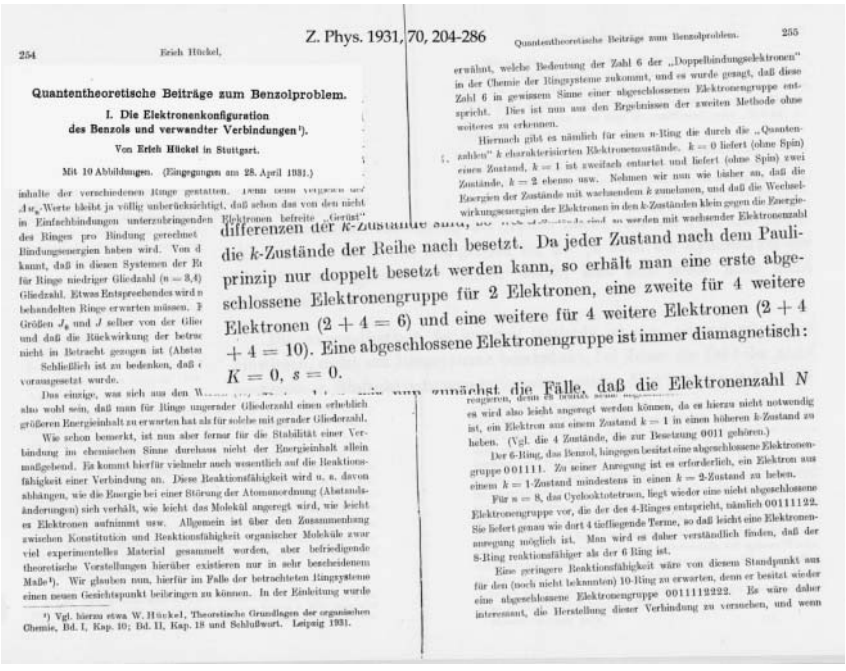

Z. Phys. 1931, 70, 204-286

254 Erich Hückel.

Quantentheoretische Beiträge zum Benzolproblem.

I. Die Elektronenkonfiguration des Benzols und verwandter Verbindungen[1].

Von **Erich Hückel** in Stuttgart.

Mit 10 Abbildungen. (Eingegangen am 28. April 1931.)

Quantentheoretische Beiträge zum Benzolproblem. 255

differenzen der k-Zustände [illegible] die k-Zustände der Reihe nach besetzt. Da jeder Zustand nach dem Paulischen Prinzip nur doppelt besetzt werden kann, so erhält man eine erste abgeschlossene Elektronengruppe für 2 Elektronen, eine zweite für 4 weitere Elektronen ($2 + 4 = 6$) und eine weitere für 4 weitere Elektronen ($2 + 4 + 4 = 10$). Eine abgeschlossene Elektronengruppe ist immer diamagnetisch: $K = 0$, $s = 0$.

[illegible] zunächst die Fälle, daß die Elektronenzahl N

[1] Vgl. hierzu etwa W. Hückel, Theoretische Grundlagen der organischen Chemie, Bd. I, Kap. 10; Bd. II, Kap. 18 und Schlußwort. Leipzig 1931.

Figure 13.3 Huckel's $4n+2$ rule published in Ref. [18].

The main reason why it took so long to find an explanation for the peculiar properties of benzene is that electron delocalization can only be described in terms of quantum physics, which entered the field of chemistry only after the mid 1920s.

13.3 Magnetic Properties of Molecules

If a magnetic field that changes in time is applied to a macroscopic piece of conducting matter, currents are induced. Moving charges again give rise to a magnetic field that is opposed to the primary field. Electric and magnetic fields are described and interconnected by the Maxwell equations, and together with the Lorentz force law they form the foundation of classical electrodynamics (there are also alternative theories that comply with Newton's laws) [19]. The microscopic Maxwell equations have been derived for charge carriers in a vacuum, and don't apply for fields in matter. For instance, they don't explain why an insulating material (diamagnetic) experiences a force in an inhomogeneous magnetic field. If there are no free charge carriers there should be no induced current, and consequently no interaction with the magnetic field. The reason why any type of matter (including insulators) interacts with a magnetic field can be qualitatively explained using the simple Bohr model of its atomic structure. A magnetic field induces microscopic current loops around the nuclei, which in turn give rise to magnetic fields that are opposed to the primary field (Figure 13.4)

As a consequence the primary field is weakened inside a diamagnetic material (dia: Greek opposed). Paramagnetic materials, unlike diamagnetic matter, usually have unpaired electrons, which are aligned parallel to the magnetic field, that augment the primary field. To apply the microscopic laws of electrodynamics to macroscopic matter, the electric field **E** and the magnetic field **H** therefore have to, be complemented by auxiliary fields, such as polarization **P** and magnetization **M**. A sample in a magnetic field acquires a magnetization **M** (or magnetic dipole moment per unit volume) that is proportional to the applied field **H** and the magnetic susceptibility χ of the material.

$$\mathbf{M} = \chi\mathbf{H} \tag{13.1}$$

Magnetic susceptibility is most frequently given as molar susceptibility $\chi_m = \chi V_m$, where V_m is the molar volume. The magnetic induction **B** in a medium depends on the applied field **H** and the magnetic permeability μ of the sample:

$$\mathbf{B} = \mu\mathbf{H} \tag{13.2}$$

The magnetic permeability μ is given as the product of the vacuum permeability μ_0 and the relative permeability μ_r of the medium.

$$\mu = \mu_0\mu_r \tag{13.3}$$

The magnetic induction **B** in a medium can expressed as the applied field **H** corrected by the magnetization **M** that the medium acquired. By employing

Eq. (13.1) the relationship between the applied field **H** and the magnetic induction **B** in the sample can be expressed as:

$$\mathbf{B} = \mu_0(\mathbf{H} + \mathbf{M}) = \mu_0(1 + \chi)\mathbf{H} \tag{13.4}$$

Compounds with a negative value of magnetic susceptibility χ weaken the magnetic field as compared to the field in vacuum. They are called diamagnetic. Paramagnetic samples exhibit a positive χ and stengthen the field. Magnetic susceptibility χ is a material property that can be measured using various methods. One of the first and still most frequently used methods is the Gouy balance. In this method, the sample is placed in an inhomogeneous magnetic field and the force experienced by the sample is then measured. The most convenient method to measure the magnetic susceptibility of a homogeneous solution is the Evans method, which is based on NMR shifts [20–22].

If the diamagnetic behavior of matter could be completely explained by local currents around the nuclei, and if the diamagnetic susceptibility of the different nuclei of the periodic table were known, the susceptibility of molecular compounds consisting of different elements would be the sum of the individual contributions, and could be easily predicted. As early as 1919, Pascal [23], and later Pacault [24] and Haberditzl [25], published simple increment systems to calculate diamagnetic susceptibilities of molecules. The increment system is quite accurate for most organic and inorganic compounds, with a few exceptions.

Paul Ehrenfest in 1925 was the first to suspect that the exceptionally high diamagnetic susceptibility in Bismut would be due to ring currents that include more than one atom [26]. Raman (1929) later proposed that the same explanation holds for graphite, because of ring currents induced in six-membered rings [27]. Because the currents were restricted to the plane of the rings, this also explained the known high anisotropy of the diamagnetic susceptibility. Pauling (1936) quantified the anisotropy of the magnetic susceptibility of benzene and condensed aromatic rings by a simple ring current model [28], and London (1937) presented the first quantum physical description based on Hückel theory [29]. He introduced the term ''interatomic'' for currents that are not centered at an atom.

13.3.1
Exaltation and Anisotropy of Magnetic Susceptibility

The magnetization **M** that a material acquires in a magnetic field depends on the strengths of elementary magnetic moments μ, and the number N of magnetic moments (atoms) per volume.

$$\mathbf{M} = \mu N \tag{13.5}$$

In the current loop definition the magnetic moment, μ, is defined as the product of the electric current $\boldsymbol{I}$ with the area A that the current loop encloses. Within the Bohr atomic model, the electric $\boldsymbol{I}$ current is determined by the number Z and the Larmor frequency ($\omega = e\mathbf{B}/2m$) of the electrons orbiting around the nuclei,

$$\mu = IA = -\frac{Ze^2\mathbf{B}}{6m}\langle r^2\rangle \quad \text{(SI)} \quad \mu = -\frac{Ze^2\mathbf{B}}{4mc^2}\langle r^2\rangle \quad \text{(CGS)} \tag{13.6}$$

Table 13.1 Molar diamagnetic susceptibilities of noble gases, and carbon allotropes.

	He	Ne	Ar	Kr	Xe	diamond	graphite	C_{60}
χ_m [10^{-6} cm^3 mol^{-1}]	−1.9	−7.2	−19.4	−28.0	−43.0	−5	−88	−4.3[a]

[a] χ_m in 10^{-6} cm^3 mol^{-1} per carbon atom.

where m, e are the mass and charge of the electrons, respectively, and $\langle r^2 \rangle$ is the mean square of the distance of the electrons from the nucleus (orthogonal to the field in case of a spherical electron density). With $\mathbf{M} = \mu\ N$, and $\chi \approx \chi/(1+\chi) = \mu_0 M/\mathbf{B}$, the Larmor–Langevin equation [30] for the volume diamagnetic susceptibility is obtained:

$$\chi = \frac{\mu_0 N}{\mathbf{B}} \cdot \mu = -\frac{\mu_0 N Z e^2}{6m}\langle r^2 \rangle \quad \text{(SI)} \quad \chi = \frac{N\mu}{\mathbf{B}} = \frac{N Z e^2}{6mc^2}\langle r^2 \rangle \quad \text{(CGS)} \quad (13.7)$$

The calculation of χ, thus, is quite straightforward, except that $\langle r^2 \rangle$ has to be determined quantum mechanically from the electron density. It is important to note that the diamagnetic susceptibility is a function of $\langle r^2 \rangle$, or the area that the ring current encloses. Therefore, outer shell electrons, such as d electrons of heavier elements, give rise to a particularly large portion of the diamagnetic susceptibility. Likewise, the ring current contribution to the diamagnetic susceptibility in aromatic systems increases with increasing ring size. Table 13.1 lists the measured molar diamagnetic susceptibilities χ_m ($\chi_m = \chi\ V_m$, see above) of noble gases and carbon allotropes. The values are given in cgs units, which is still standard in modern literature.[1)]

Although the Larmor–Langevin equation (Eq. (13.7)) predicts the magnetic susceptibility of diamond quite accurately, it underestimates the corresponding value for graphite because it doesn't include interatomic ring currents whose contributions to the total magnetic susceptibility are one order of magnitude larger than those of the local currents. On the other hand, if the magnetic susceptibility is found through experiments, the radius r of the ring current can be calculated from the Larmor–Langevin equation. Londsdale calculated the effective radii for the electronic circulations in diamond (0.7 Å), benzene σ electrons (0.7 Å), and benzene π electrons (1.5–1.6 Å) [31]. The latter value is in agreement with the radius of the carbon hexagon in benzene of (1.39 Å). In graphite the effective radius of the ring currents is 7.8 Å, which corresponds to an area of 30 benzene rings (Figure 13.4).

The total diamagnetic susceptibility can be defined as the sum of ring current χ^{RC} and local contributions χ^{LC}:

$$\chi = \chi^{RC} + \chi^{LC} \quad (13.8)$$

1) To convert to the SI units (m^3 mol^{-1}) simply multiply by the factor 4π.

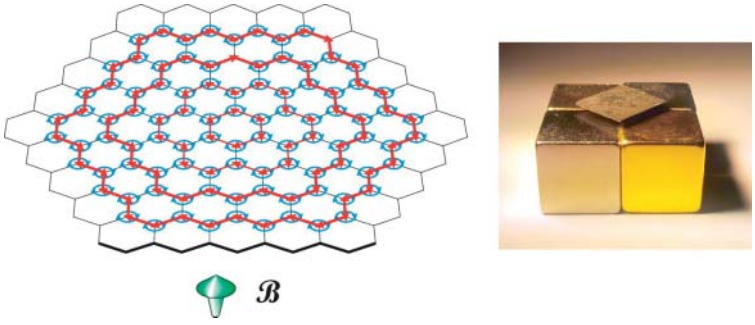

Figure 13.4 Induced currents in a graphite sheet. Local currents (blue) are centered at the carbon nuclei, and "interatomic currents" (red) are flowing in the π systems of the benzene rings. The average size (effective radius) of the ring currents in graphite is 7.8 Å, which corresponds to an area of about 30 benzene molecules [31] (c.f. the effective radius of the ring currents in benzene is 1.5–1.6 Å). The magnetic fields induced by the local and interatomic currents (blue and red) are opposed to the primary field (green). The diamagnetic susceptibility in graphite is strong enough to levitate the platelet above permanent magnets (right).

If the local contributions are calculated by an increment system $\chi^{LC} \approx \chi^{IN}$, the magnetic exaltation Λ is obtained as:

$$\Lambda = \chi - \chi^{IN} \tag{13.9}$$

Dauben suggested using the magnetic exaltation as a measure of aromaticity [32–34]. According to this criterion a conjugated molecule is aromatic if $\Lambda > 0$, non-aromatic if $\Lambda \approx 0$, and anti-aromatic if $\Lambda < 0$. Practically, χ is either determined by experiment, or more conveniently calculated by quantum chemical calculations.[2)] Increments are available from Haberditzel [25]. The latter increment system also includes local contributions from binding electrons. The following calculation for benzene may serve as an example (susceptibility increments in -10^{-6} cm^3 mol^{-1}):

core electrons:		
6 C	6 (0.15) =	0.9
binding electrons:		
6 C*–C*	6 (2.4) =	14.4
3 Cπ–C	3 (2.2) =	6.6
6 C*–H	6 (3.2) =	19.2
χ^{IN} (sum)		41.1
χ (exp.)		54.8
$\Lambda = \chi - \chi^{IN}$		13.7

2) The IGLO method implemented in the Turbomole program or the CSGT method within the Gaussian program (nmr = csgt command) provide magnetic susceptibility values.

Table 13.2 Magnetic susceptibilities χ_m, anisotropies of magnetic susceptibilities $\Delta\chi$ (10^{-6} cm^3 mol^{-1}), magnetic susceptibilities calculated from local increments χ^{IN}, and magnetic exaltations Λ (-10^{-6} cm^3 mol^{-1}) of cyclohexane and annulenes with different ring sizes.

	 benzene	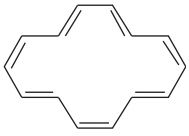 [14]annulene[a]	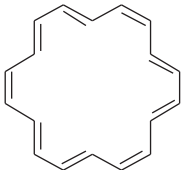 [18]annulene[b]	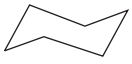 cyclohexane	 cyclobutadiene
χ_m	−54.8[c]	−173.4	−320.7	−68.1[d] (−66.5)[e]	−22.6[f]
χ_x	−34.9[c]	−53.9	−66.3	−69.3[e]	
χ_y	−34.9	−50.8	−66.3	−69.3[e]	
χ_z	−94.6	−415.6	−829.7	−60.7[e]	
$\Delta\chi$	−60.0	−363.3	−763.4	8.6	
χ^{IN}	41.1	95.9	123.3	68.1	27.4
Λ	13.7	267.4	640.1	0.0	−4.8

[a] B3LYP/6-31G*, CSGT, C_{2v}.
[b] B3LYP/6-31G*, CSGT, D_{3d}.
[c] Reference [36].
[d] Reference [37].
[e] B3LYP/ /cc-pVQZ.
[f] Reference [38].

Note that the susceptibility increments in the Haberditzl and Dauben system are given in negative cgs units (positive values for diamagnetic contributions). The magnetic exaltation Λ does not provide a direct quantification of aromaticity because it increases with increasing ring size. To compare magnetic exaltation with other aromaticity measures, such as resonance energy, Λ has to be normalized by the area that the ring current encompasses, or only molecules with the same ring size should be compared [35]. Table 13.2 gives magnetic exaltations of annulenes with different ring sizes and cyclohexane as a nonaromatic reference.

Another peculiar magnetic property of planar aromatic compounds is the high anisotropy of their diamagnetic susceptibility, usually denoted as $\Delta\chi$. The anisotropy of magnetic susceptibility is defined as the difference between the largest component χ_z (perpendicular to the ring plane), and the average of the two smaller components χ_x and χ_y (within the ring plane):

$$\Delta\chi = \chi_z - \frac{1}{2}(\chi_x + \chi_y) \tag{13.10}$$

For symmetric top molecules such as benzene, the definition simplifies as:

$$\Delta\chi = \chi_\perp - \chi_\parallel \tag{13.11}$$

In benzene, the component perpendicular to the ring plane $\chi_{\perp}$ ($-94.6 \cdot 10^{-6} \cdot cm^3 \cdot mol^{-1}$) is almost 3 times larger than the components within the ring plane $\chi_{\parallel} = (-34.9 \cdot 10^{-6} \cdot cm^3 \cdot mol^{-1})$ (see Table 13.2). Flygare compiled a list of magnetic susceptibilities and anisotropies of magnetic susceptibilities [39]. Unfortunately, the components of the magnetic susceptibility are difficult to measure, for example, by measurements of a single crystal [36] or via microwave spectrum analysis from the molecular Zeeman effect [40]. Quantum chemical calculations are a convenient alternative in cases where experimental data are not available. Inherent to the definition of anisotropy, however, is the fact that the anisotropy of the magnetic susceptibility cannot be applied to nonplanar aromatics such as fullerenes.

13.3.2 Chemical Shifts in NMR

Arguably the most important observable magnetic property in molecular chemistry is the chemical shift in NMR. Consequently, ring current models have been tested according to their performance in predicting NMR chemical shifts. Pople, in 1956, was the first to apply ring current approach to the calculation of NMR shifts [41]. A magnetic dipole in the middle of and orthogonal to a current loop provides a good, and probably the simplest approximation to calculate the magnetic field far from the source. Pauling earlier used this magnetic dipole approach to predict the diamagnetic susceptibility of benzene [28]. According to the Larmor–Langevin equation (Eq. (13.7)), the six mobile π electrons in benzene give rise to a magnetic dipole of $\mu = 3e^2\mathbf{B}\, r^2/(2\, mc^2)$ at the center of the benzene ring, which has a radius of $r \approx 1.4$ Å. The secondary field induced by this magnetic dipole at the positions of the protons (which are at distance of $1.4 + 1.1 = 2.5$ Å from the ring center, and within the ring plane) can be easily calculated. Similar to the diamagnetic susceptibility, chemical shift can be expressed as the sum of ring current and local contributions.

$$\delta^{\text{benzene}} = \delta^{\text{RC}} + \delta^{\text{LC}} \tag{13.12}$$

The magnetic dipole approach used earlier gives a ring current contribution calculated as 1.46 ppm. Local contributions can be estimated from the chemical shift of the protons of a nonaromatic reference such as 1,3-cyclohexadiene, which resonates at 5.8 ppm (protons in 2- and 3-position). With $5.8 + 1.46 = 7.26$ ppm, the calculated shift is quite close to the experimental value of 7.3 ppm. Waugh and Fessenden [42] and Johnson and Bovey [43] improved the dipole model by assuming a pair of current loops above and underneath the benzene ring separated by a distance of 0.9 or 1.28 Å (Figure 13.5).

Lazzeretti *et al.* pointed out that the magnetic field induced by the infinitesimally small current element A of the current loop next to a proton H is partially cancelled by the magnetic field induced by a current element B on the opposite side [44]. This effect is not included in the simple magnetic dipole approach.

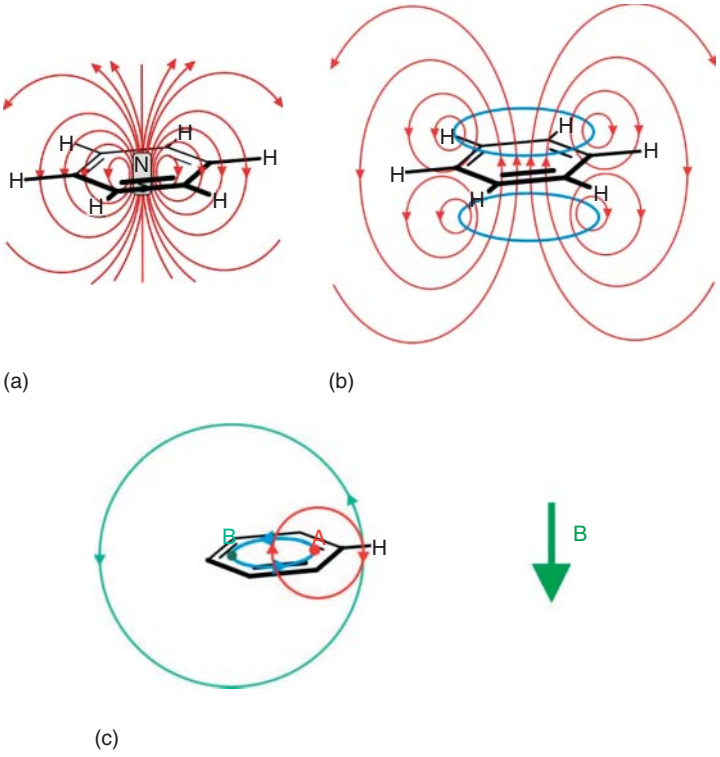

Figure 13.5 Semi-classical ring current models to predict the proton chemical shift of benzene. (a) Simplified magnetic dipole model (infinitesimally small dipole in the center of the ring), (b) current loop model with two loops (blue) above and underneath the ring. (c) partial cancellation of the deshielding effect of the magnetic field induced by the current at point A by the magnetic field generated at point B. Note that the magnetic dipole model (a) fails to predict the deshielding effect of the ring current inside the ring.

13.3.3 Quantum Theoretical Treatment

The magnetic properties [45, 46] of benzene, simple annulenes, porphyrins, phthalocyanines, or condensed aromatic systems are very accurately predicted using (semi-) classical ring current approaches. However, there are striking problems with compounds that exhibit antiaromatic or partly antiaromatic character. For instance, C_{60}, with its large delocalized π system, was expected to exhibit unusual magnetic properties [47]. If, in a first approximation, C_{60} is treated as a superatom with 60 mobile π electrons, and if the Larmor–Langevin equation (Eq. (13.7)) is applied to calculate the current of the precessing electrons in an external magnetic field, and assuming an effective radius $\langle r^2 \rangle$ of 5.7 Å, a very high diamagnetic susceptibility of $-30 \cdot 10^{-6} \cdot cm^3 \cdot mol^{-1}$ per mol carbon would be predicted [48]. Surprisingly, the measurements, after macroscopic amounts of the compound were available, by

the Huffman–Krätschmer method [49] yielded a value of $-4.3{\cdot}10^{-6}{\cdot}\mathrm{cm}^3{\cdot}\mathrm{mol}^{-1}$ per mol carbon, which is close to diamond ($-5.0{\cdot}10^{-6}{\cdot}\mathrm{cm}^3{\cdot}\mathrm{mol}^{-1}$, see Table 13.2). This reveals that there is either a slightly negative contribution or no contribution from the ring currents in C_{60}. Antiaromatic cyclobutadiene has a diamagnetic susceptibility of $-22.6{\cdot}10^{-6}{\cdot}\mathrm{cm}^3{\cdot}\mathrm{mol}^{-1}$, which is 4.8 units less negative than that calculated by the increment method for a non-aromatic reference ($-27.4{\cdot}10^{-6}{\cdot}\mathrm{cm}^3{\cdot}\mathrm{mol}^{-1}$, see Table 13.2.) Thus, in cyclobutadiene, the cyclic conjugation even leads to the opposite (paramagnetic) effect as compared to that in benzene. Unfortunately, a paramagnetic response of a closed shell molecule cannot be understood in terms of classical physics [50]. The reason for this unusual behavior is the so-called Van Vleck or induced orbital paramagnetism [51]. Upon interaction with a magnetic field the wavefunction is perturbed in such a way that higher states mix into the ground state wavefunction. Perturbation theory is applied to calculate the response of the wavefunction to a magnetic field. In the presence of a magnetic field, the Hamiltonian is the sum of the unperturbed Hamiltonian H^0, the perturbed first order Hamiltonians H^1, and second order H^2 in the magnetic field (p: momentum, V: potential energy, $\mathbf{A}$: vector potential):

$$H = H^{(0)} + H^{(1)} + H^{(2)} = \left(\frac{p^2}{2m} + V\right) + \left(\frac{e}{m}\mathbf{A}\cdot\vec{p}\right) + \left(\frac{e^2}{2m}A^2\right) \tag{13.13}$$

The magnetic susceptibility derived from perturbation theory can be viewed as the sum of two terms, a negative and a positive contribution. Analogous to the definition of magnetic susceptibility, the negative term is interpreted as the diamagnetic and the positive as the paramagnetic susceptibility:

$$\chi_m = \chi_m^d + \chi_m^p = -\frac{N_A e^2 \mu_0}{6m}\langle r^2\rangle + \frac{N_A e^2 \mu_0}{6m^2}\sum_n{}' \frac{|l_{0n}|^2}{\Delta E_{n0}} \tag{13.14}$$

where the orbital angular momentum operator is defined as $\vec{l} = \vec{r} \times \vec{p}$, $l_{n0} = \langle n|l|0\rangle$, and $\Delta E_n = E_n - E_0$. Hence, the paramagnetic contribution is large if the energy differences between the ground and excited states are small. The paramagnetic term dominates the diamagnetic term if ΔE is roughly $16\,000\,\mathrm{cm}^{-1}$ (620 nm) or smaller. The diamagnetic term in Eq. (13.14) is proportional to $\langle r^2\rangle$ or the area the ring current encompasses. It resembles the Larmor–Langevin equation (Eq. (13.7)) and is therefore called the *Langevin term*. Whereas the total magnetic susceptibility is an observable, the separate diamagnetic and paramagnetic terms should be interpreted with care because their relative contribution depends on the gauge origin [52]. Moreover, the gauge origin can be chosen so that the paramagnetic term completely vanishes, for example, in an atom in which the nucleus is chosen as the gauge origin [53]. One of the major problems in calculating the magnetic properties of molecules is the fact that, the definition of the vector potential notwithstanding, a very large basis set is needed to obtain results that are independent of the gauge origin. Accurate calculations therefore can only be performed on small systems. One of the ways to solve that problem is the ipsocentric approach implemented in the continuous set of gauge transformation (CSGT) [54, 55] and CTOCD–DZ [56] methods. The latter

approach allows the decomposition of current density into contributions from molecular orbitals. This allows a qualitative prediction and a didactical description of the ''induced orbital magnetism.'' With the ipsocentric choice of origin of the vector potential, the first-order response of an occupied molecular orbital $\Psi_n^{(0)}$ to a magnetic field **B** is:

$$\Psi_n^{(1)} = \Psi_n^p + \Psi_n^d = -\frac{1}{2}\sum_{p>N/2} \Psi_p^{(0)} \frac{\langle \Psi_p | l | \Psi_n \rangle}{E_p - E_n}\mathbf{B} + \frac{1}{2} d \times \sum_{p>N/2} \Psi_p^{(0)} \frac{\langle \Psi_p | p | \Psi_n \rangle}{E_p - E_n}\mathbf{B} \quad (13.15)$$

where l and p are the angular and linear momentum operators and d is the displacement from the gauge origin. Equation (13.15) can now be interpreted in terms of spectroscopic selection rules, similar to the spectroscopic transition moment integrals in IR and Raman spectroscopy. There is a response of the wavefunction if either of the terms – $\langle \Psi_p | l | \Psi_n \rangle$ or $\langle \Psi_p | p | \Psi_n \rangle$ – is different from zero. For a qualitative analysis it is not necessary to know the explicit form of the occupied and unoccupied wavefunctions Ψ_n and Ψ_p; it is sufficient to determine the symmetry of the transition moment functions $\Psi_p l \Psi_n$ and $\Psi_p p \Psi_n$. If the symmetry of these functions equals (Abelian point groups) or contains (degenerate point groups) the totally symmetric representation of the point group to which the atom or molecule belongs, then its value is not zero and the transition is allowed. Otherwise, the transition is forbidden. The angular momentum operator p transforms as the basis of the same irreducible representation as the rotation around one of the Cartesian axes R_x, R_y, or R_z, which may be looked up in the character table of the point group of the molecule. Likewise, the linear momentum operator l has the same symmetry as a translation along the Cartesian axes T_x, T_y, T_z. The symmetry of the integrand now is the direct product of the symmetries of Ψ_p, the momentum operator (p or l), and Ψ_n. A simplified way to analyze the symmetry of the integrand is to set up the product of the representations of the two wavefunctions $\Gamma(\Psi_p) \times \Gamma(\Psi_n)$ first, and then check if the resulting representation contains the representation of translations or rotations about the Cartesian axes. Allowed virtual excitations potentially contribute to the ring current. If the product $\Gamma(\Psi_p) \times \Gamma(\Psi_n)$ transforms as the same representation as R_z the virtual transition gives rise to a paramagnetic current. If it transforms as T_x or T_y, a contribution to the diamagnetic current follows (if z is chosen as the direction of the magnetic field).

$$\begin{aligned} &\Gamma(\Psi_p) \times \Gamma(\Psi_n) \supset \Gamma(T_x) \text{ and/or, } (T_y) \text{ (diamagnetic ring current)} \\ &\Gamma(\Psi_p) \times \Gamma(\Psi_n) \supset \Gamma(R_z) \text{ (paramagnetic ring current)} \end{aligned} \quad (13.16)$$

Again the prototypic aromatic compound benzene may serve as an example. Because the perturbation of the wavefunction is large for low energy transitions, only HOMO-LUMO excitations are considered. The transitions and their symmetries are obtained by evaluating the product of the degenerate e_{1g} (HOMO) and the e_{2u} (LUMO) molecular orbital: $e_{1g} \times e_{2u} = b_{1u} + b_{2u} + e_{1u}$ (Figure 13.6).

The three resulting transitions are indeed observed in UV spectroscopy. Within the point group D_{6h}, T_z transforms as a_{2u}, T_x, and T_y as e_{1u}, R_z as a_{2g}, and R_x and R_y

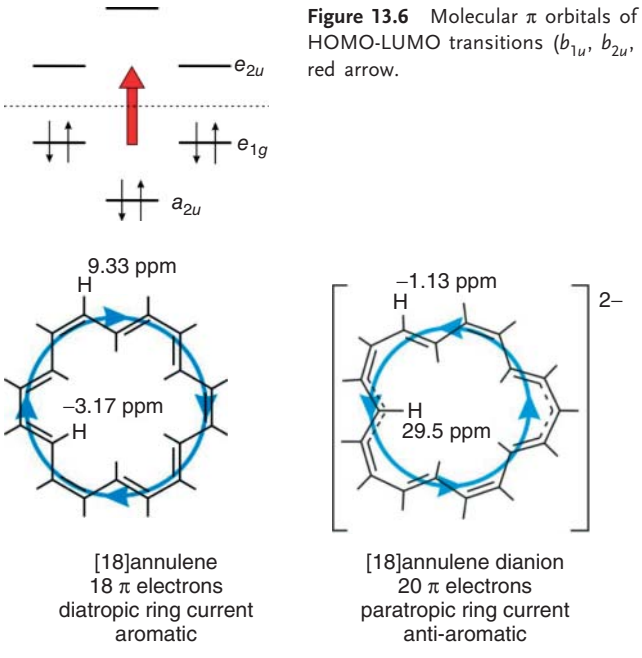

Figure 13.6 Molecular π orbitals of benzene and the three HOMO-LUMO transitions (b_{1u}, b_{2u}, e_{1u}) comprised as one red arrow.

Figure 13.7 ^{1}H NMR chemical shifts of [18]annulene and its dianion [58]. Ring currents are indicated in blue. The magnetic field **B** points toward the viewer. Particularly the dianion is a "floppy" structure, which undergoes fast bonds shifts and *cis*/*trans* isomerizations [59]. The value given for the inner proton is the average of all inner protons measured at −110°C. The same holds for the outer protons.

as e_{1g}. Thus, the b_{1u} and the b_{2u} excitations are both translationally and rotationally forbidden and do not contribute to the ring current. (Because the dipole operator has the same symmetry as the linear momentum operator, they are also forbidden excitations in UV and have small extinction coefficients.) The e_{1u} transition, however, is allowed and because it transforms as the basis of the same representation as T_x and T_y, is largely responsible for the diamagnetic ring current in benzene.

Diamagnetic currents circulate clockwise and paramagnetic currents counterclockwise if the magnetic field points toward the viewer. They lead to large anomalies in NMR chemical shifts. A particularly instructive example is [18]annulene and its dianion [57] (Figure 13.7). The neutral compound is aromatic with $4n+2$ π electrons and exhibits a strong diatropic ring current. The inner protons are shifted highfield to −3.17 ppm and the outer protons downfield to 9.33 ppm. Upon reduction (with potassium metal), highfield and downfield shifts are reversed. The dianion has 20 π electrons ($4n$) and exhibits a strong paratropic ring current. The shielding effects are reversed as compared to the neutral [18]annulene dianon. There is a huge downfield shift for the inner protons and an upfield shift for the outer protons.

The first method that allowed accurate quantum theoretical calculations of magnetic properties of molecules was the IGLOs (individual gauge of localized orbitals) method [60, 61]. Nowadays, a number of methods are available [62, 63], and most quantum chemical program packages include one or several of these methods. The vector field of the current density and the shielding constants (defined as $\mathbf{B}_{loc} = \mathbf{B} - \sigma\mathbf{B}$ with $\mathbf{B}$ as the external field $\mathbf{B}_{loc}$ the local field and σ as the shielding constant) can be calculated at each point in space. From the shielding constants σ at the points of the nuclei and the magnetic moments of the nuclei, chemical shifts are calculated, which, at higher levels of theory, can be predicted with chemical accuracy. The nucleus independent shift (NICS) in the middle of a cyclic molecule has been proposed as a quantitative measure of aromaticity [64, 65]. However, the quantitative use of isotropic NICS values has been cautioned [66–69].

Current density maps are often used to analyze induced ring currents in molecules. Current density is a vector field. A vector is assigned to each point in space. Visualization therefore is difficult in 2D representations. To plot current densities of planar π systems, a bisectional plane about 1 Å above the ring plane (the plane with the highest π electron density) is chosen, in which, for a chosen grid of points, current density vectors are plotted. The length of the vectors is proportional to the magnitude of the current and the magnetic field is chosen to be orthogonal to the ring plane. Fowler and Steiner used current density maps to investigate the aromaticity in a large number of systems [70–78]. Non-planar systems are more difficult to analyze. Several equidistant bisectional planes and a magnetic field parallel to the rotational axis have been chosen to investigate ring currents in bowl shaped molecules [79]. Even more difficult to investigate in a systematic way are currents in less symmetric π systems where the relative orientation of the magnetic field with respect to the molecule cannot be chosen unambiguously. Herges *et al.* therefore proposed to analyze the anisotropy of current (induced) density (ACID) [80, 81]. Similar to the anisotropy of magnetic susceptibility $\Delta\chi$, which indicates the strength of ring currents supported by delocalized electrons, and thus the aromaticity of a molecule as a whole, the anisotropy of the current density provides a measure of the density of delocalized electrons at each point in space. Localized electrons do not contribute because their induced currents are isotropic. A problem, however, is that the conventional definitions of anisotropy (Eqs. (13.8) and (13.9)) do not provide a scalar field that is independent of the relative orientation and the magnitude of the magnetic field and the object. Therefore, the anisotropy has to be derived from the current density tensor $\mathbf{T}$ (including its off diagonal elements). The tensor field $\mathbf{T}$ of the current density $\mathbf{J}$ maps the vector field of $\mathbf{B}$ to the vector field of the current density $\mathbf{J}$.

$$\mathbf{T}: \quad \mathbf{T}_{\nu\mu} = \frac{\partial J_\nu}{\partial B_\mu} \quad (\text{at B} = 0) \qquad \mathbf{J} = \mathbf{T} \cdot \mathbf{B} \tag{13.17}$$

$\mathbf{T}$ is a tensor of rank two (3×3 matrix). We define its anisotropy $\Delta\mathbf{T}$ as the standard deviation of the three eigenvalues of the current density tensor $\mathbf{T}$:

$$\Delta\mathbf{T}^2 = \sum_i (e_i - \bar{e})^2 \tag{13.18}$$

The anisotropy of the current density tensor $\Delta\mathbf{T}$ can be written as the sum of the contribution from the symmetric ($\mathbf{T}_s$) and antisymmetric ($\mathbf{T}_A$) parts of the current density tensor $\mathbf{T}$:

$$\Delta\mathbf{T}^2 = \Delta\mathbf{T}_S^2 + \mathrm{tr}\mathbf{T}_A\mathbf{T}_A^+ \tag{13.19}$$

If we drop the antisymmetric part, a closed solution for the anisotropy of current density can be given:

$$\Delta\mathbf{T}_S^2 = \frac{1}{3}[(t_{xx} - t_{yy})^2 + (t_{yy} - t_{zz})^2 + (t_{zz} - t_{xx})^2] + \frac{1}{2}[(t_{xy} + t_{yx})^2 + (t_{xz} + t_{zx})^2 + (t_{yz} + t_{zy})^2] \tag{13.20}$$

The ACID $\Delta\mathbf{T}_s$ can be plotted as an isosurface similar to the total electron density. However, in contrast to the total electron density, only nonlocal (delocalized) electrons contribute to $\Delta\mathbf{T}_s$. For a more detailed analysis of molecular magnetic properties, the current density vectors can be plotted onto the ACID hypersurface. It is important to note that the ACID, as defined earlier, is invariant with respect to the relative orientation of the molecule and the magnetic field. Therefore, the ACID hypersurface is unambiguous even in nonplanar and unsymmetric systems.

13.4 Examples

13.4.1 Benzene and Borazine

Benzene, the prototype of all aromatic compounds, exhibits a cyclic conjugated π system that is reflected by a contiguous ACID hypersurface [76, 77] (Figure 13.8). The current density vectors plotted on top of the hypersurface indicate a strong diatropic ring current (clockwise if the magnetic field points toward the viewer). The diatropic currents are located in the π system above and underneath the ring plane. They resemble the simple current loop model in Figure 13.5. Note that there is also a weaker paratropic ring current (counter clockwise) in the center of the ring that arises from delocalization in the σ frame of benzene. Borazine (Figure 13.8, right) was synthesized for the first time in 1926 [82] and has been termed *the inorganic benzene* [83] because it is isoelectronic to benzene, and all B–N bond lengths are equal. Its reactivity and electronic structure, however, are fundamentally different from those of benzene. There is no cyclic topology of delocalized electrons. This is indicated by the disconnections in the ACID hypersurface and the lack of a diatropic ring current enclosing the six-membered ring [84, 85]. Magnetic exaltation data (1.7 for borazine, c.f. 13.7 for benzene) and total π bonding energy calculations [86] confirm the nonaromatic character of borazine.

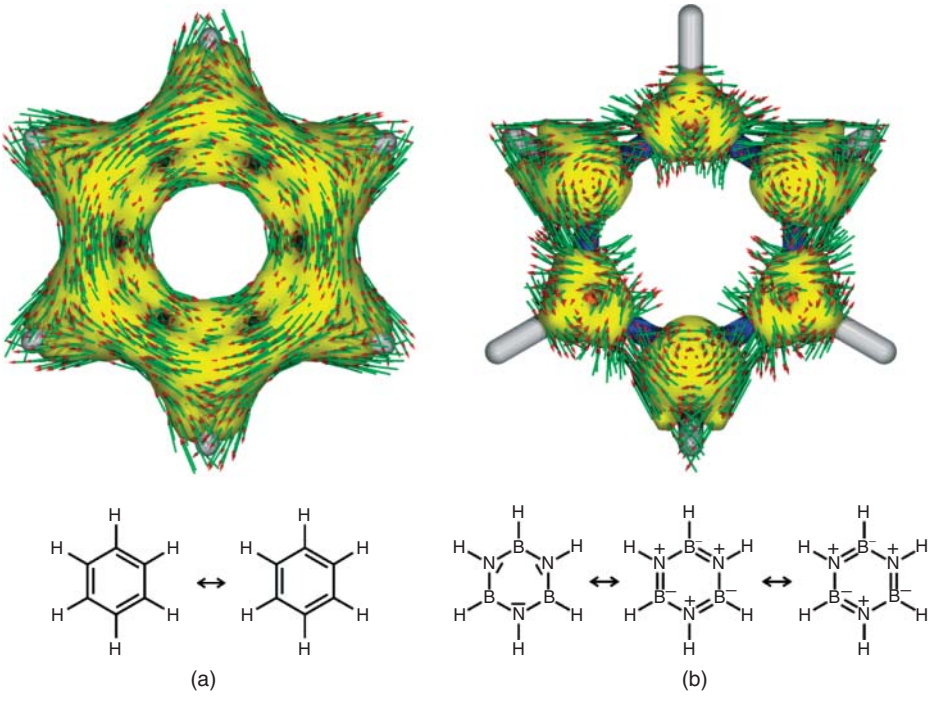

Figure 13.8 ACID hypersurface [76, 77] (yellow, isosurface value 0.05) of benzene (a) and borazine (b). Current density vectors (green arrows with red arrow head) are plotted onto the ACID hypersurface. The length of the arrows is proportional to the magnitude of the current density. The magnetic field B points toward the viewer. The structures were optimized at the B3LYP/6-31G* level of density function theory. The current density was calculated using the continuous set of gauge transformation (CSGT) method [54].

13.4.2 Pyridine, Phosphabenzene, and Silabenzene

Group V heterobenzenes [87] pyridine, phosphabenzene [88, 89], arsabenzene [84], and stibabenzene [90] are stable compounds with increased sensitivity toward oxygen. Because of the decreasing orbital overlap, a lower degree of aromaticity may be expected. Similar arguments should also hold for silabenzene. This is corroborated by several aromaticity criteria [91–93]. Close inspection of the ACID hypersurface and the current density vectors (Figure 13.9) reveals that pyridine is perfectly aromatic with a strong diatropic ring current similar to benzene. The π overlap between phosphorous and the neighboring carbon atoms in phosphabenzene is weak, but there is still a reasonable ring current. This is in contrast to silabenzene, in which there is no ring current enclosing the six-membered ring. The current is restricted to the carbon framework, and does not include the silicon atom.

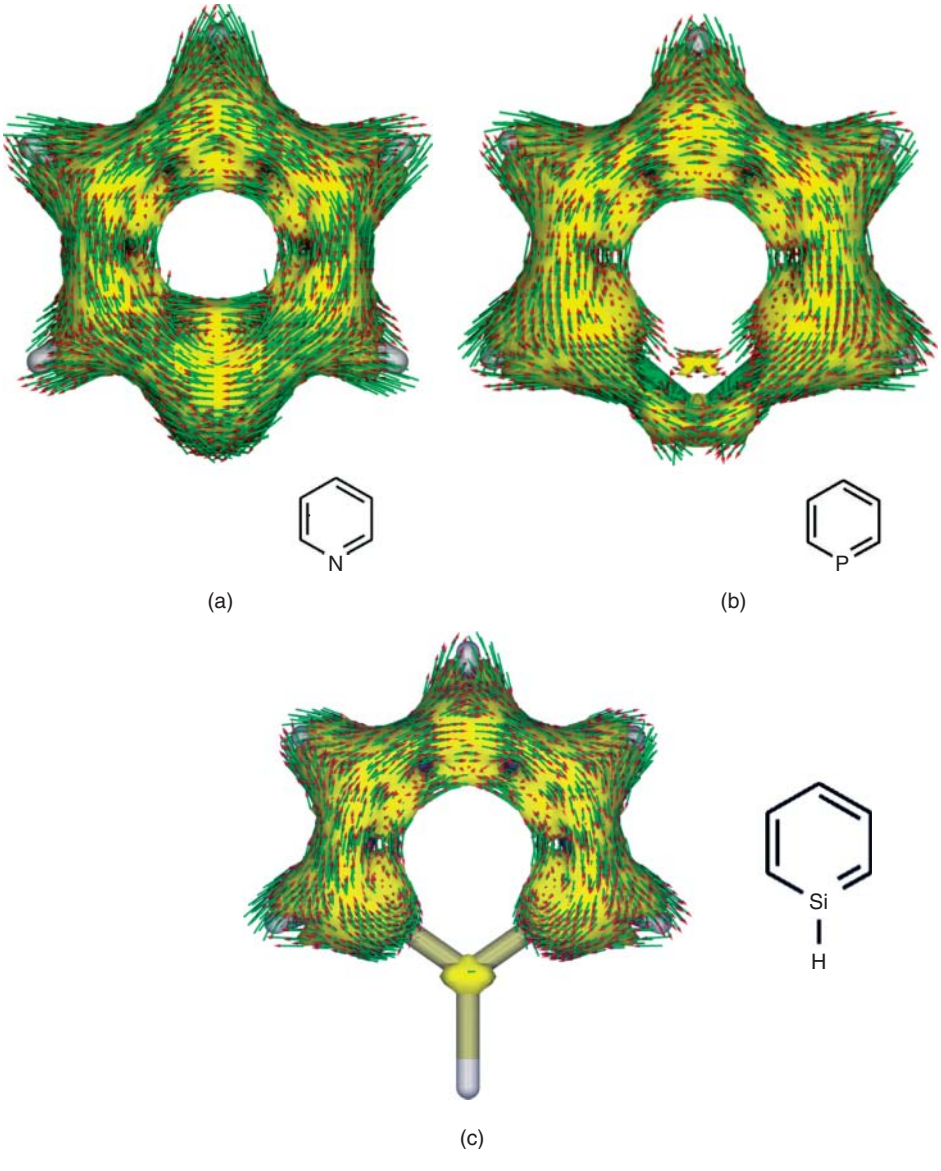

Figure 13.9 (a–c) ACID hypersuface and current density vectors of pyridine, phosphabenzene, and silabenzene. For technical details see Figure 13.8. Pyridine is perfectly aromatic. Aromaticity is weaker in phosphabenzene. There are induced currents in silabenzene. However, they don't include the silicon atom. Therefore, silabenzene can be viewed as nonaromatic.

13.4.3
Fullerenes

The peculiar magnetic properties of C_{60} have already been mentioned in a previous Chapter (**13.3.3**). Notwithstanding its very large π system – which includes 20 benzene rings and 12 five-membered rings – its magnetic susceptibility is similar to diamond (see Table 13.1). Hence, there are either no ring currents, or diatropic and paratropic currents cancel each other in their contribution to the magnetic susceptibility. Haddon *et al.* [48, 94] proved that the latter is true. The six-membered rings behave like benzene rings with diatropic ring currents, the five-membered rings, however, exhibit paratropic currents. This would also explain why a helium atom inside the C_{60} cage ($^3He@C_{60}$) exhibits an upfield shift of only $\delta = -6$ ppm (with respect to dissolved ^3He) [95]. A qualitative explanation for this unexpected behavior can be derived from the aromaticity rule of spherical aromatics. If fullerenes with icosahedral symmetry are viewed as superatoms with a spherical density of π electrons, and if the distortion to the icosahedral symmetry is treated as a perturbation [96], a new electron counting rule follows [97, 98]. The rule states that spherical systems with $2(N+1)^2$ π (e.g., 8, 18, 32, 50, 72, …) electrons are aromatic. C_{60} has 60 π electrons, which implies that it is missing 12 π electrons to fill the ''shell'' completely. A more detailed treatment predicts that already 6 additional π electrons should increase the aromaticity of C_{60} drastically. Indeed the structure of the hexaanion C_{60}^{6-} (K_6 C_{60}) exhibits a more pronounced bond length equalization [99] that has been interpreted as a higher degree of aromaticity, and theoretical calculations predict a very high diamagnetic susceptibility [100]. All ring currents, including the five-membered rings are diamagnetic in the hexaanion C_{60}^{6-} [96] (Figures 13.10 and 13.11).

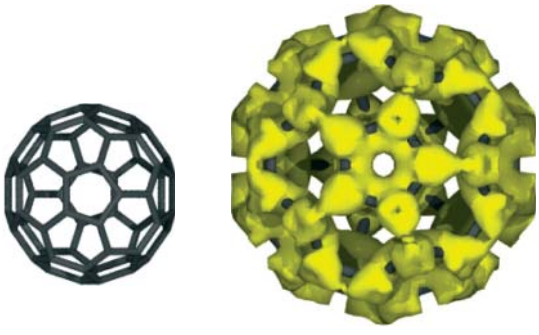

Figure 13.10 (a,b) ACID plot of the π electrons of C_{60}. Note that the highest density of delocalized electrons in the six-membered rings is outside the σ framework, and the π electrons of the five-membered rings are mainly inside the cage. For technical details see Figure 13.8.

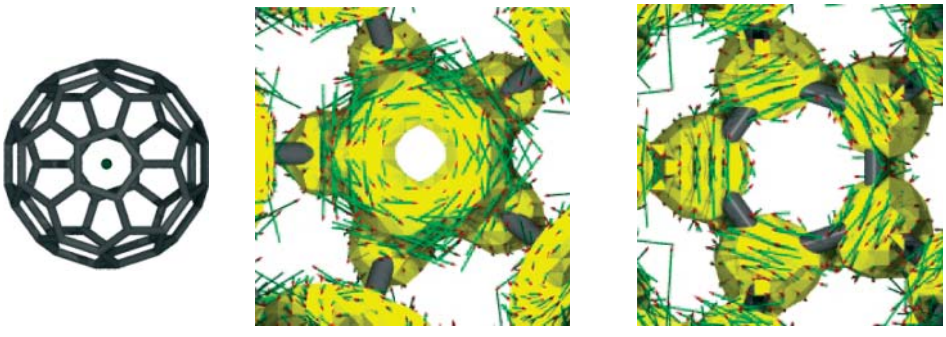

(a) (b)

Figure 13.11 ACID plot of the π electrons of (a) C_{60} and (b) C_{60}^{6-}. View from inside the cage onto a five-membered ring, which exhibits a paratropic (counter clockwise) ring current in C_{60} (a) and diatropic (clockwise) in C_{60}^{6-} (b)).

13.4.4
Hückel and Möbius Structures

The Hückel rule states that annulenes with $4n+2$ π electrons are aromatic and those with $4n$ electrons are antiaromatic. In 1964, Heilbronner predicted that a Möbius-type, twisted annulene would be aromatic with $4n$ electrons, and antiaromatic with $4n+2$ electrons [101]. It took more than 40 years to prove this theoretical prediction by the synthesis of a twisted [16]annulene [102–105]. Subsequently, a number of extended porphyrins with Möbius topology have been prepared [106–109], and several charged annulenes were predicted to be stable Möbius aromatics [110, 111]. [16]Annulene is a stable compound [112, 113] that, according to the Hückel rule (16 π electrons), should be antiaromatic. The X-ray structure reveals that the ring is almost planar (S_4 symmetry) with alternating double and single bonds [114, 115]. At −120°C the ^{1}H-NMR spectrum exhibits two signals at 10.4 ppm (4H), and 5.4 ppm (12H) [116] indicating a strong paratropicity, which is expected of a Hückel topology (Figure 13.12a). About half of the 2250 conceivable cis/trans isomers of [16]annulene exhibit Möbius topology [99]. Unfortunately, they are higher in energy than the most stable Hückel isomers. Obviously, the stability gained by Möbius aromaticity cannot outweigh the destabilization induced by the 180° twist of the π system. Consequently, only derivatives of Möbius [16]annules have been synthesized so far [98, 99]. Figure 13.12b depicts the calculated structure of an unsubstituted Möbius [16]annulene. The current density vectors indicate a strong diatropic ring current, and thus strong aromaticity.

Larger porphyrins with more than four pyrrol rings exhibit a high degree of conformational flexibility. They can easily adopt bent or twisted geometries without accumulating strain. Osuka *et al.* synthesized and investigated a [28]hexaphyrin(1.1.1.1.1.1) that folds into a Möbius geometry and that is aromatic with $4n$ π electrons [104]. Figure 13.13 depicts the current density vectors and the structure of this ring. For the sake of simplicity the *meso*-aryl substituents are

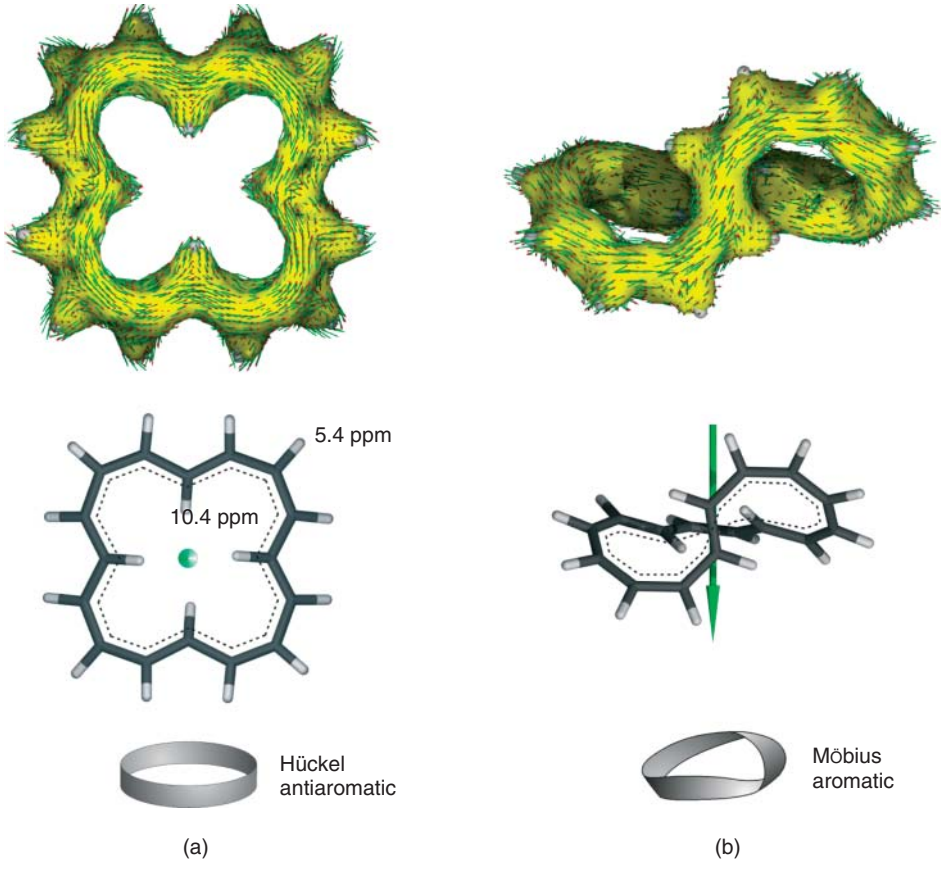

Figure 13.12 ACID hypersurfaces and ring currents in a Hückel- (a), and a Möbius-type [16]annulene (b). For technical details see Figure 13.8. The Hückel structure (experimentally known, see text) is antiaromatic, and exhibits a strong paratropic ring current (counter clockwise). The Möbius isomer (calculated structure, experimentally known only as substituted derivatives) [98] is aromatic with a strong diatropic ring current (clockwise). Hence, by twisting the ring into a Möbius topology the antiaromatic structure is transferred into an aromatic molecule, and the direction of the ring current is reversed.

omitted. The driving force for the formation of the twist is the gain in energy by Möbius aromaticity. The overall 180° twist in the π system is smooth enough (almost equally distributed over all six bridges) to allow contiguous conjugation. Low temperature NMR spectra revealed that two of the inner protons are shifted upfield to −0.48 and −1.66 ppm[3]. Upon oxidation of the Möbius-[28]hexaphyrin to the [26]hexaphyrin, the molecule rearranges to a non-twisted Hückel topology to keep aromaticity. Aromatic stabilization, again, is most probably the driving force behind the change in topology.

3) NMR shifts of protons in Figure 13.13 were assigned by GIAO NMR calculation at the B3LYP/6-31G* level of density functional theory.

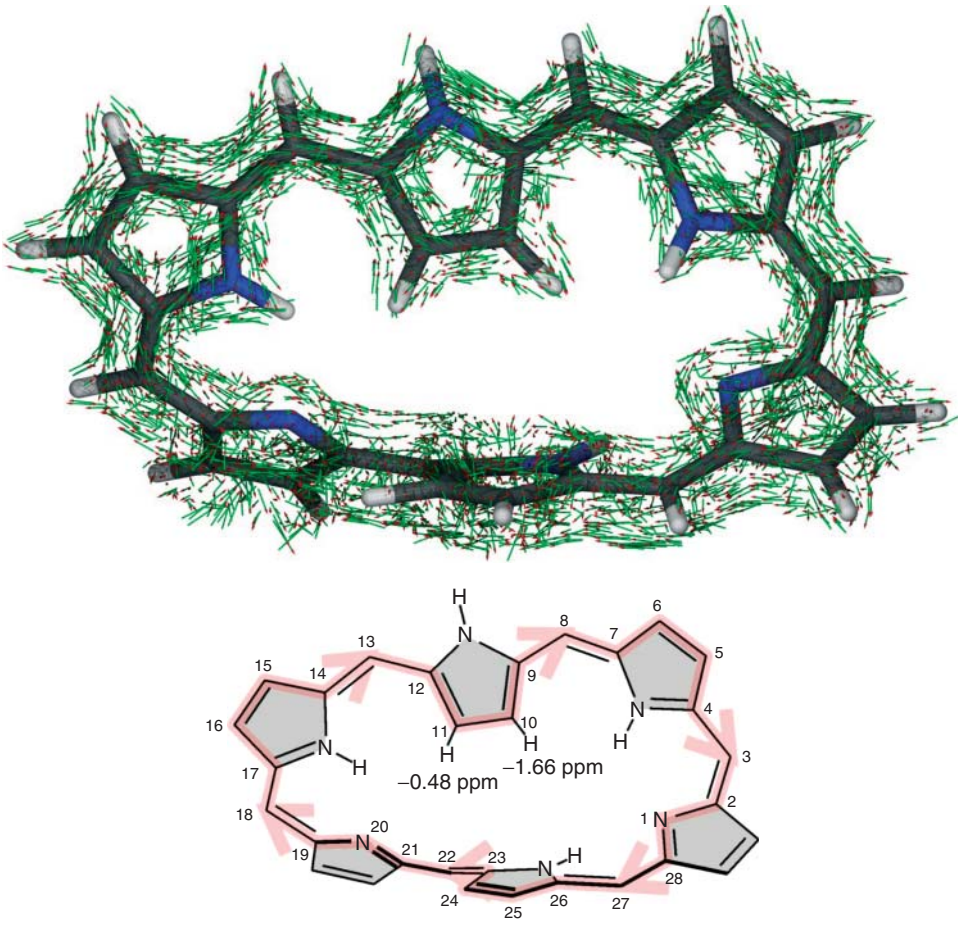

Figure 13.13 Möbius [28]hexaporphin(1.1.1.1.1.1). Current density vectors are plotted on top of the ACID isosurface. The ACID isosurface is not shown to provide a clearer picture of the electron flow within the Möbius twisted π system. For technical details see Figure 13.8. The delocalized system in the periphery includes 28 π electrons (indicated in red in the lower part). Therefore, the structure would be antiaromatic according to the Hückel rules. However, the molecule spontaneously twists into a Möbius topology and becomes aromatic. Because of the large ring size, obviously, the gain in (Möbius) aromaticity more than outweighs the strain energy induced by the twist.

13.4.5
Homoaromatic Molecules

Aromatic compounds exhibit a cyclic conjugated array of π electrons. If the array of adjacent orbitals is interrupted by one or several saturated units (e.g., a CH_2 group), some degree of aromaticity can still be retained if conjugation goes through a bond or through space. Winstein coined the term *"homoaromaticity"* to

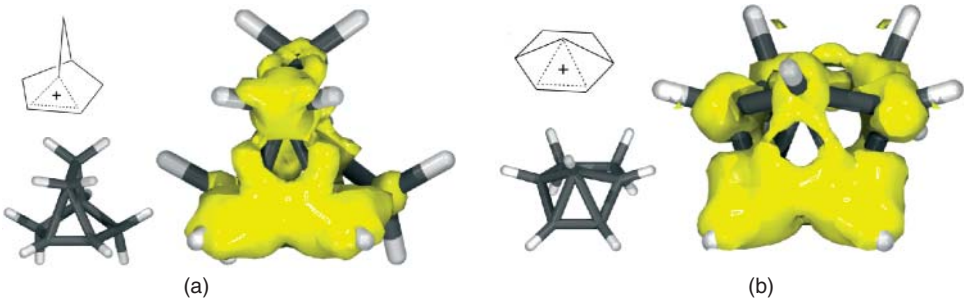

Figure 13.14 Homoconjugation in the 2-norbornyl cation (a) and the 7-norbornyl cation (b). For technical details see Figure 13.8.

describe this phenomenon [117, 118]. Cations are quite frequent among homoaromatic compounds because aside from aromatic stabilization, delocalization of the charge is a driving force. The structure of the 2-norbornyl cation was the subject of discussions for several decades. Low temperature NMR [119] and a recent X-ray structure [120] prove that it is a nonclassical, bishomoaromatic cation. The homoaromatic structure of the 7-norbornyl cation [121] was finally confirmed using low temperature IR [122]. In both cases, the ACID hypersurface (Figure 13.14) reveals that besides conjugation through space, there is also hyperconjugation involved in charge delocalization.

Homoaromatic systems such as cycloheptatriene [123, 124] or the pagodane dication [125–131] can be viewed as frozen transition states. The two double bonds in the bissecododecahedradiene (Figure 13.15) are parallel with respect to each other. A [2+2]cycloaddition to form the pagodane is thermochemically forbidden. Under superacidic conditions, however, the diene as well as the cyclobutane are oxidized to the identical pagodane dication. The resulting bishomoaromatic system can be viewed as the frozen transition state of a thermochemical allowed [1+1]cycloaddition. The two longer bonds with 2.19 Å are considerably longer than a typical C–C single bond, and the shorter bonds (1.427 Å) are between a single and a double bond.

13.4.6
Organometallic Compounds

Aromaticity is not restricted to organic molecules. One of the prototypes of organometallic compounds is ferrocene [132, 133]. Two aromatic cyclopentadienyl anion rings sandwich a Fe^{2+} ion. Interactions of the carbon p_z orbitals with the d orbitals of iron (except the $d_z{}^2$ orbital) lead to a very stable coordination compound. ACID analysis reveals that the aromaticity of the cyclopentadienyl units is retained; however, there is additional conjugation between the rings including the iron core leading to 3D conjugation [134]. (Figure 13.16) At a first glance one could assume that magnesocene [135–137] should have a similar electronic structure. However, the delocalized electrons are restricted to the cylopentadienyl anion units.

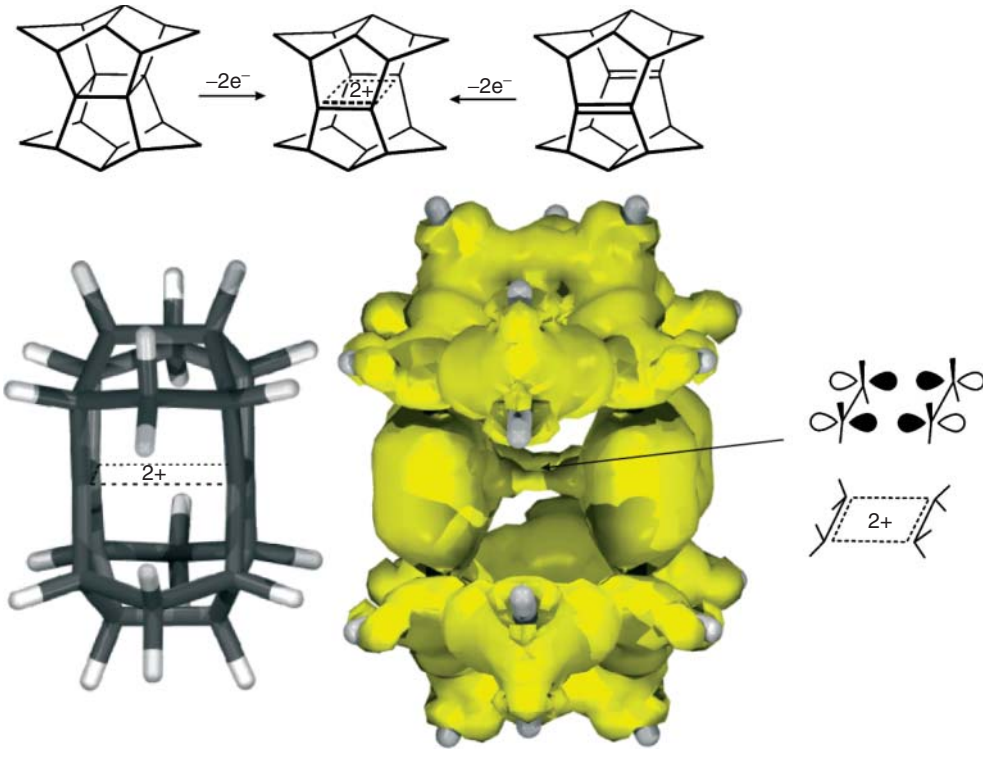

Figure 13.15 Homoaromaticity in the pagodane dication forming an aromatic cyclobutane dication. The delocalized system can also be viewed as the frozen transition state of a thermochemically allowed [1+1]cycloaddition.

Obviously, there is neither covalent nor coordinative bonding of Mg^{2+} with the aromatic rings. The main driving force for formation of the sandwich structure is Coulomb attraction of the two negatively charged rings and the Mg^{2+} cation.

Although the aromatic systems in ferrocene and magnesocene are "carbon-based," there are also aromatic, organometallic compounds that include metal atoms, such as iridabenzene, osmabenzene, and platinabenzene [138]. Moreover, there also exist aromatic systems that are exclusively formed by metals [139–143]. All-metal aromatic molecules include Al_4^{2-}, XAl_3^-(X = Si, Ge, Sn, and Pb), Ga_4^{2-}, In_4^{2-}, Hg_4^{6-}, Al_3^-, Ga_3^-. Their aromaticity was confirmed using several methods including the adaptive natural density partitioning method (AdNDP) [144]. The ACID plot of Al_4^{2-} (with Li^+ as counterion), and Ga_4^{2-} (with Na^+) reveals that there is cyclic delocalization, and a diatropic ring current around the four-membered metal rings. (Figure 13.17) The main contribution to aromaticity comes from σ aromaticity. The latter system of 6 cyclic delocalized electrons is formed by the b_{2g} (HOMO-2) and the degenerate set of e_u MOs (HOMO-4).

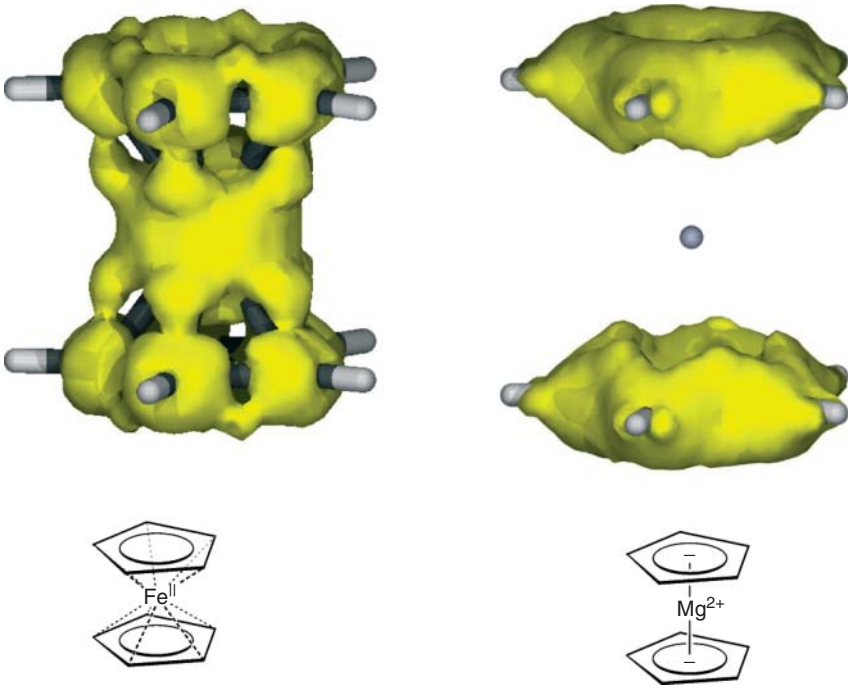

Figure 13.16 Ferrocene and magnesocene exhibit very similar geometries. However, their electronic structure is totally different. Ferrocene is a coordination compound. The delocalized system of electrons mainly includes the $2p_z$ orbitals of carbon and $3d_{xz}$ and $3d_{yz}$ orbitals of Fe. Magnesocene owes its existence primarily to the Coulomb forces between Mg^{2+} core, and the two $C_5H_5^-$ rings.

13.4.7 Aromatic Transition States

As early as in 1938, Evans *et al.* recognized that the six electrons that are delocalized over six carbon atoms in the transition state of the Diels–Alder reaction exhibit some analogy to the six π electrons in benzene [145–147]. The (hypothetical) symmetric transition state of the [2+2]cycloaddition of ethylene includes 4 electrons, and resembles the antiaromatic π system of cyclobutadiene. (Figure 13.18) Evans concluded that the Diels–Alder reaction is favored by aromatic stabilization of its transition state, although the [2+2]cycloaddition is not. Zimmerman [148–150] and Dewar [151, 152] later generalized the ''Evans principle'' and developed a method to predict the stereochemistry of pericyclic reactions [139, 153] that can be applied as an alternative to the conservation of orbital symmetry of Woodward and Hoffmann [154].

If the transition state of the Diels–Alder reaction is indeed aromatic, it should exhibit the typical magnetic properties of aromatic compounds, such as anomalous NMR shifts, and diamagnetic susceptibility anisotropy and exaltation. Unfortunately, properties of transition states are difficult to measure. However, NMR

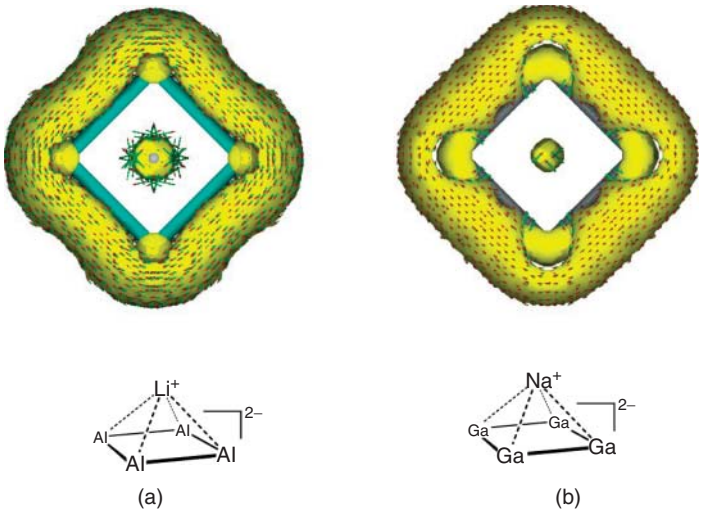

Figure 13.17 (a,b) All-metal aromatic compounds $Al_4^{2-}{\cdot}Li^+$ and $Ga_4^{2-}{\cdot}Na^+$. The four-membered Al_4^{2-} and Ga_4^{2-} rings are strongly aromatic. They can either be viewed as 2 electron π aromatics or 6 electron σ aromatic systems. The counter ions Li^+ and Na^+ are only weakly interacting with the π system.

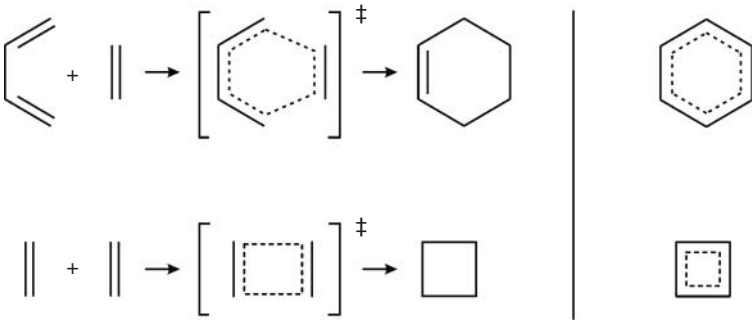

Figure 13.18 The Evans principle applied to the Diels–Alder reaction and the [2+2]cycloaddition. The delocalized system of electrons in the transition state of the Diels–Alder reaction is topologically equivalent to the π system of benzene. The transition state is stabilized by aromaticity, and therefore the reaction is thermochemically allowed. The (hypothetical) symmetric transition state of the [2+2]cycloaddition of ethylene resembles the delocalized electrons in (hypothetical) square antiaromatic cyclobutadiene. The [2+2]cycloaddition is thermochemically forbidden. Cyclobutadiene distorts to reduce antiaromaticity.

shifts and magnetic susceptibilities can be easily calculated using quantum chemical methods. Herges *et al*. calculated the NMR shifts of the protons along the reaction path of the prototypic Diels–Alder reaction of ethylene and butadiene (Figure 13.19) [155]. Most striking is the upfield shift of the butadiene proton in

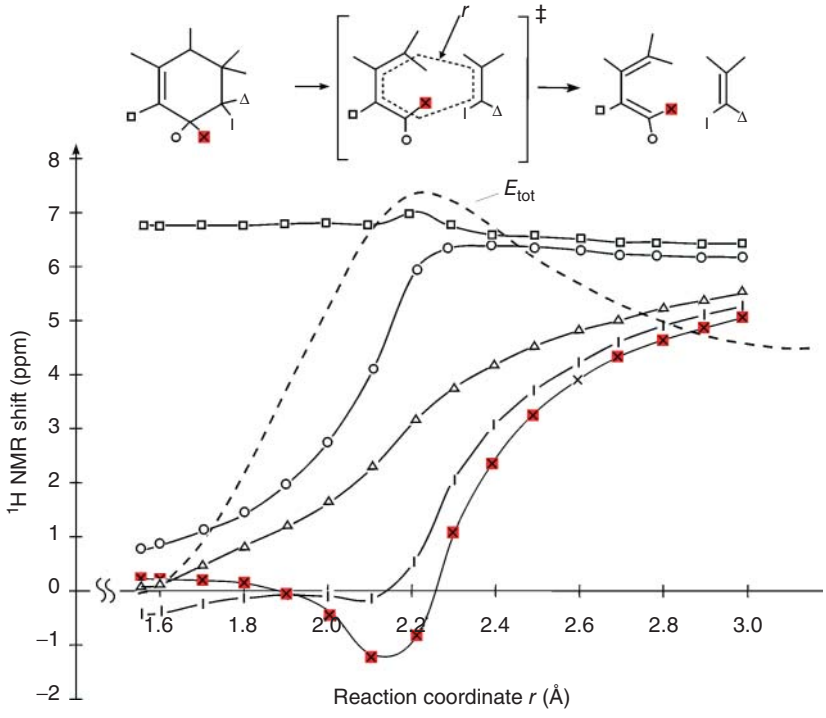

Figure 13.19 Calculated (IGLO/IIMP2(fu)/6-31G*) chemical NMR shifts of the protons (marked with □, ○, Δ, ■, and ×) in the Diels–Alder reaction of butadiene with ethylene. The proton labeled as × protrudes into the shielding range of the ring current in the transition state, and therefore exhibits a marked upfield shift in the transition structure. The proton labeled as □ is located in the deshielding range of the ring current, and therefore, exhibits a slight downfield shift in the transition state. The energy curve of the reaction is indicated with a dashed line.

1-position (marked as x) of −1.5 ppm at the transition state geometry. The high field shift is due to the deshielding effect of the ring current.

The most negative diamagnetic susceptibility on the reaction hypersurface of the Diels–Alder reaction (Figure 13.20) also coincides with the highest energy (transition structure) on the reaction path, where the ring current is strongest. Reactant and product (butadiene, ethylene, and cyclohexene) don't exhibit a ring current. The exaltation of the magnetic susceptibility Λ of the transition structure of the Diels–Alder reaction ($-14{\cdot}10^{-6}$ cm^3 mol^{-1}) is within the same range as the value for benzene. Therefore, the transition structure of the Diels–Alder reaction can be truly viewed as aromatic [156].

Strong diatropic ring currents are only observed in structures whose geometries are very close to the transition structure, that is, if the newly forming bonds between butadiene and ethylene approach bond lengths of approximately 2.2 Å (Figure 13.21c).

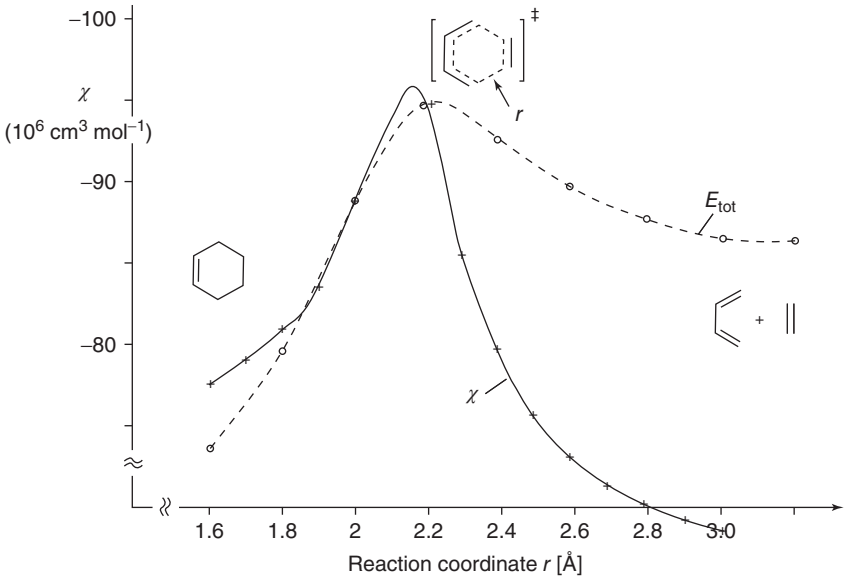

Figure 13.20 Diamagnetic susceptibility of the parent Diels–Alder system (butadiene + ethylene → cyclohexene) as a function of the reaction coordinate (technical details see Figure 13.19). The structure with the highest diamagnetic susceptibility almost exactly coincides with the highest point (transition structure) on the energy curve (dashed line).

Similar arguments hold for the transition state of the electrocyclic ring closure of hexatriene forming 1,3-cyclohexadiene (Figure 13.22). There is a strong diatropic ring current in the transition structure, which is in agreement with the aromaticity concept of pericyclic transition states.

To apply the aromaticity concept of transition states to all the different types of pericyclic reactions, the concept of aromaticity has to be extended to nonplanar aromatics, σ systems, and Möbius aromaticity. An advantage of the ''Hückel–Möbius'' method is that the mechanism and stereochemistry can be derived without explicitly setting up molecular orbitals. Aromaticity and antiaromaticity are deduced from the orbital basis, which, in the simplified treatment, constitutes the participating atomic orbitals written with an arbitrary phase (see Figures 13.21a and 13.22a). A pericyclic transition state exhibits Hückel topology if the number of antibonding overlaps of neighboring basis orbitals is even (including zero). Möbius transition states exhibit an odd number of negative overlaps. Usually the orbital basis can be written in a way that there is either zero (Hückel system) or one antibonding overlap (Möbius system). The electrocyclic ring closure of octa-1,3,5,7-tetraene exhibits a Möbius transition state that is aromatic [157] with 8 electrons delocalized over 8 carbon atoms (Figure 13.23).

The fact that there is at least one antibonding overlap in the cyclic array of orbitals does not reduce aromaticity. Möbius transition states are as aromatic as ''normal'' Hückel transition states. In contrast to stable Möbius annulenes, Möbius transition states in pericyclic reactions are quite frequent. They also include σ aromatic

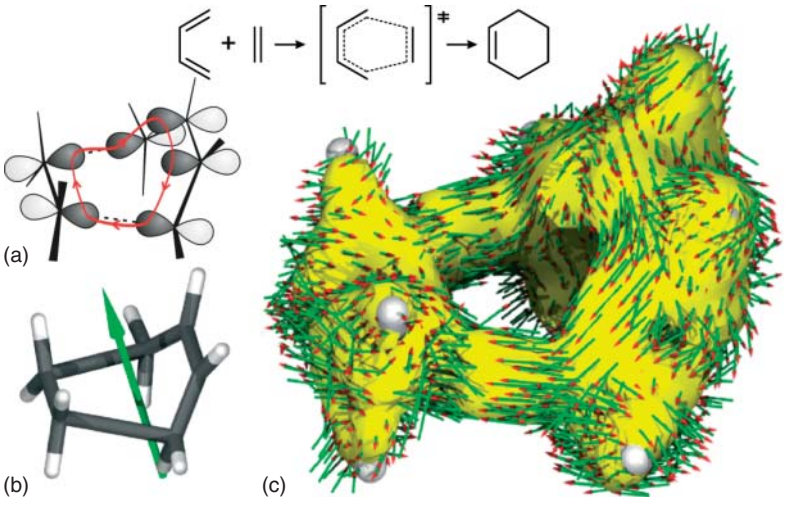

Figure 13.21 Ring current in the transition structure of the Diels–Alder reaction (ethylene + butadiene → cyclohexene). (a) the six basis orbitals exhibit a cyclic overlap that is topologically equivalent with the π system of delocalized electrons in benzene. (b) relative orientation of the magnetic field (green arrow) and the transition structure. (c) the ACID hypersurface (yellow) shows a contiguous cyclic delocalization of electrons. The current density arrows (green arrows with red arrow head) indicate a strong diatropic ring current, similar to the ring current in benzene. For technical details see Figure 13.8.

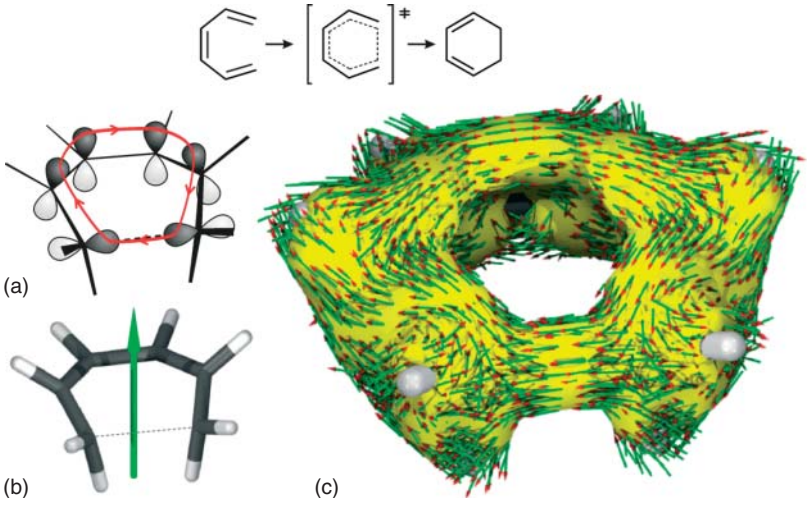

Figure 13.22 (a–c) Ring current in the transition structure of the electrocyclic reaction of hexatriene to 1,3-cyclohexadiene. For details see Figure 13.21.

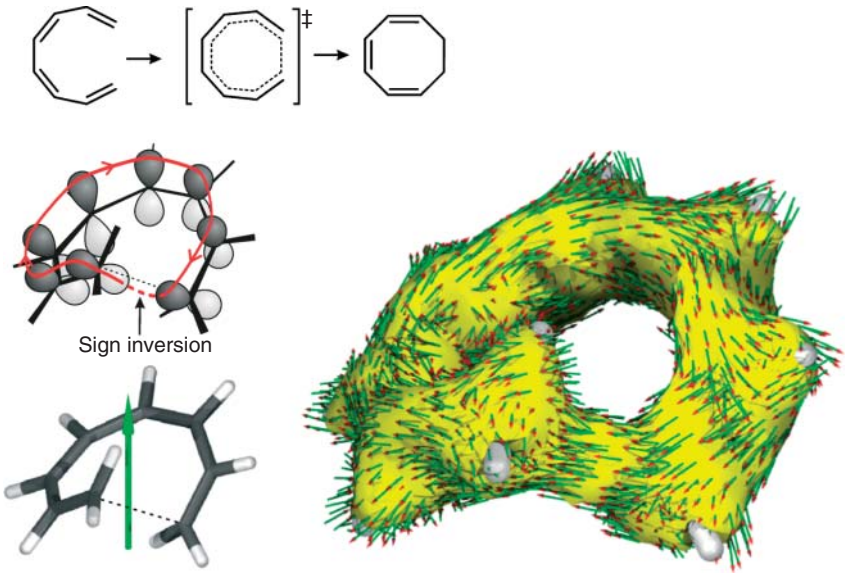

Figure 13.23 Ring current in the Möbius transition state of the electrocyclic reaction of octa-1,3,5,7-tetraene to cycloocta-1,3,5-triene. For details see Figure 13.21. Note that the basis orbitals (atomic orbitals that are involved in the reaction) can be written with arbitrary phase. The number of antibonding overlaps (sign inversion) will always be odd (including one) because reversal of the sign of one of the basis orbitals changes the sign of overlap with both neighbors. There are also a number of different ways the "red line" of overlap can be drawn, because crossing the node within a single orbital is not counted as a sign inversion.

systems, and even hydrogen atoms in the cyclic array of atoms. Figure 13.24 depicts the Hückel transition state of the suprafacial 1,5-sigmatropic shift [158] of penta-1,3-diene.

The homologous antarafacial 1,7-sigmatropic shift of hepta-1,3,5-triene exhibits a Möbius transition state (Figure 13.25). There is one antibonding overlap between the hydrogen s orbital and one of the neighboring p orbitals of carbon (Figure 13.25 upper left). Note that the phases of the basis orbitals are arbitrary. Therefore, the sign inversion can occur anywhere in the cyclic array of basis orbitals. Moreover, the red line of cyclic overlap can be drawn in many different ways, because changing from one lobe to the other within a single p orbital is not counted as a sign inversion.

13.4.8 Coarctate Transition States

In aromatic molecules and in transition states of pericyclic reactions, there is a cyclic array of atoms, each of which contributes one basis orbital to the delocalized system of electrons (see orbital plots in Figures 13.21–13.25). The ring currents, as well, follow the cyclic array of atoms and orbitals. However, there are a number

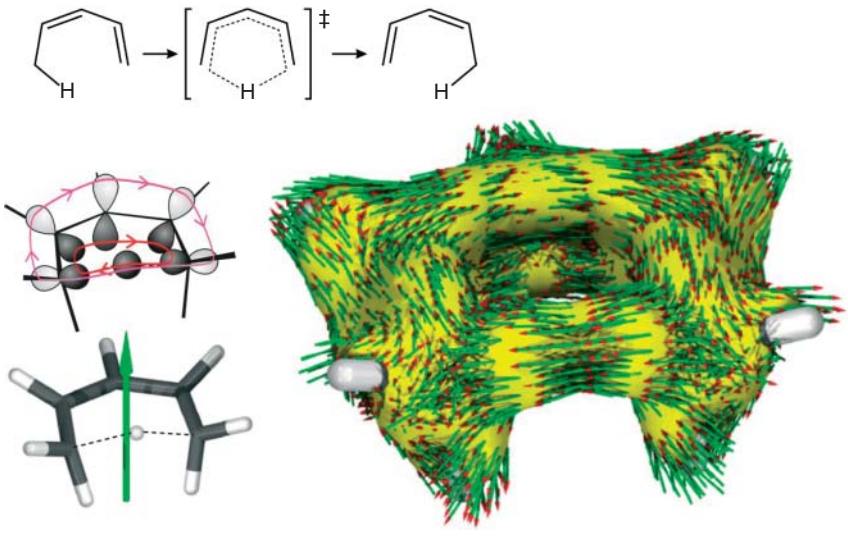

Figure 13.24 Hückel transition state (no sign inversion in the orbital basis) of the transition state of the 1,5-sigmatropic shift of penta-1,3-diene. The ring current includes the hydrogen atom that is transferred during the reaction. Two different but topologically equivalent paths of cyclic orbital overlap are shown (red and magenta). For details see Figure 13.21.

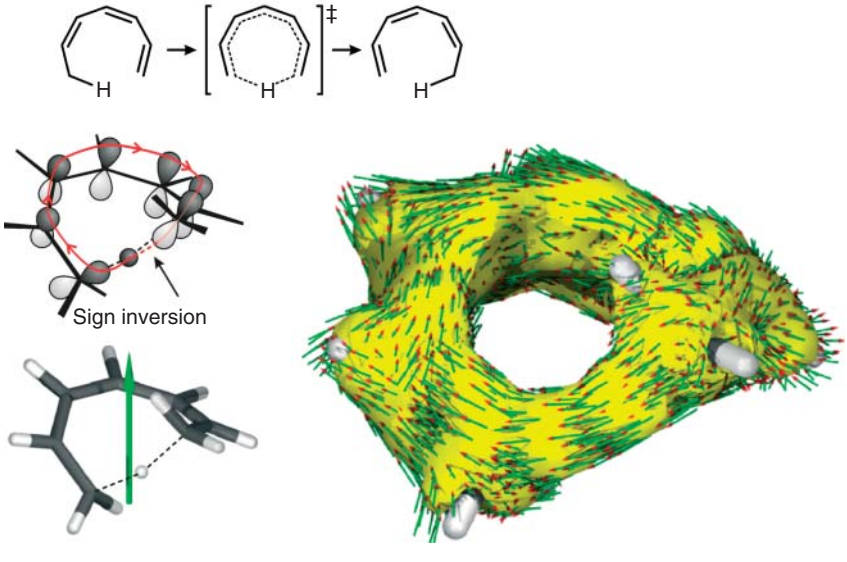

Figure 13.25 Möbius transition state (one sign inversion in the orbital basis) of the transition state of the 1,7-sigmatropic shift of hepta-1,3,5-triene. For details see Figure 13.21.

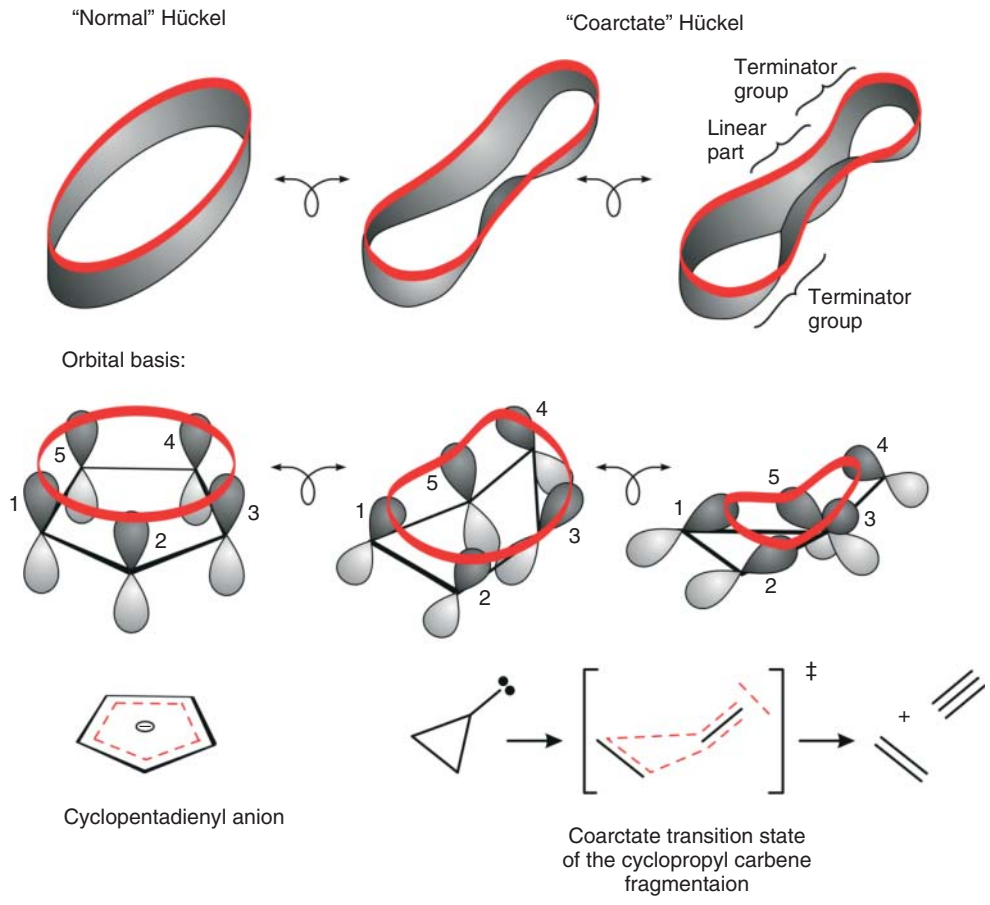

Figure 13.26 The orbital overlap of the orbital basis of the coarctate transition state of the cyclopropyl carbene fragmentation is topologically equivalent to the π system of the cyclopentadienyl anion. Hence, the coarctate transition state is aromatic and the reaction is thermochemically allowed. Copyright Angewandte 1994, *106*, 261–283.

of reactions that don't exhibit a cyclic array of atoms [159, 160]. Nevertheless, they include a cyclic orbital overlap and diatropic ring currents. These reactions have been termed ''coarctate reactions,'' because they can be formally derived from aromatic compounds or pericyclic reactions by constriction (coarctation) of the orbital basis (Figure 13.26).

Coarctate reactions are characterized by a linear sequence of atoms between which two bonds are made or broken at the same time. These coarctations of alternate two bond making and breaking are bound by ''terminator'' groups that consist of a lone-pair, or two atoms complementing the electron shift to a three-membered ring, or four atoms complementing the shift to a five-membered ring, and so on. The cyclopropyl carbene fragmentation [161] shown in Figure 13.26 is a prototype example with a three-ring and a lone pair as terminator groups. The

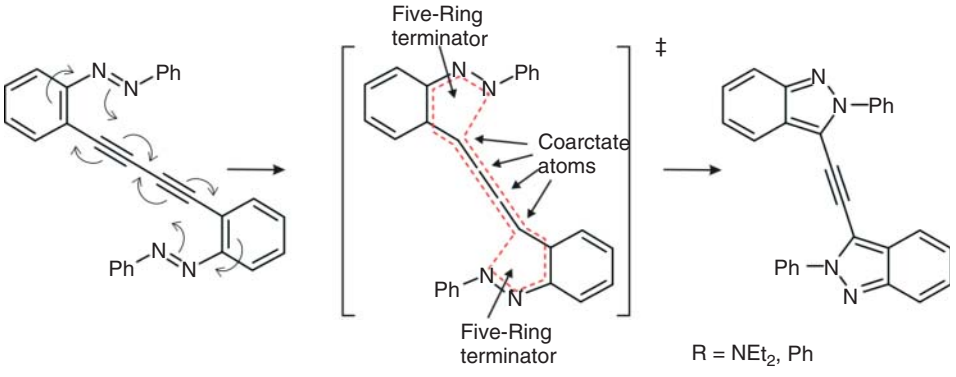

Figure 13.27 A coarctate biscyclization with 16 bonds that are formed and broken simultaneously.

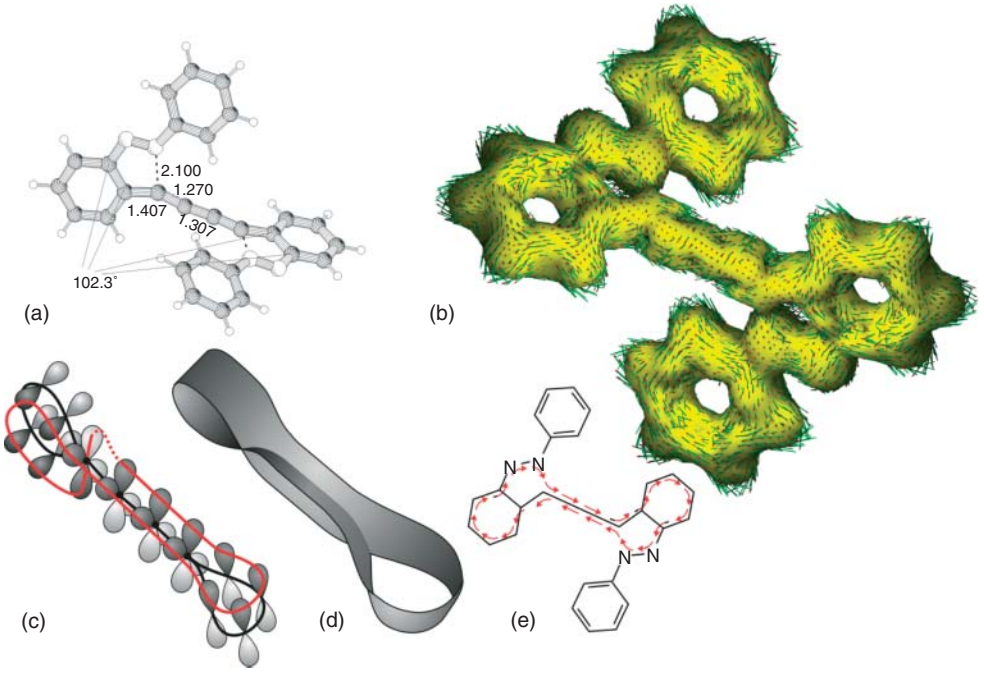

Figure 13.28 Coarctate Möbius transition state of the coarctate biscyclization (Figure 13.27). (a) calculated geometry (B3LYP/6-31G*), (b) ACID plot, isosurface value 0.05, current density vectors plotted on top of the ACID isosurface, (c) orbital basis, (d) scheme of the coarctate Möbius topology, (e) schematic coarctate diatropic ring current.

linear system consists of an exocyclic single bond, which is converted to a triple bond. The two orthogonal π bonds are formed simultaneously in the transition state. There are a large number of coarctate reactions of different types [141, 142, 162–166]. Coarctate cyclizations are particularly synthetically useful in preparing benzoannelated heterocyclic rings [167–176].

The coarctate biscyclization shown in Figures 13.27 and 13.28 proceeds spontaneously at room temperature, even though 16 bonds are made and broken simultaneously [152]. The linear part of the transition state includes three single bonds that are converted to triple bonds and two triple bonds that are turned into single bonds. The linear topology of bond making and breaking notwithstanding, the overlap of orbitals that are involved in the reaction is cyclic, and the ring current is diatropic (Figure 13.27b). At each of the sp hybridized carbon atoms both orthogonal p orbitals are involved and the current flows in opposite directions in both orthogonal π systems along the chain of sp hybridized carbon atoms (Figure 13.28b and e).

13.5 Concluding Remarks

Aromaticity, although not an observable parameter in quantum theory, remains a vital qualitative concept in chemistry. It was not long after the early development of structure theory that chemists realized that the theory of localized bonds (drawing lines between atoms) had to be extended by the concept of delocalization to explain properties and reactivity of aromatic compounds. Probably the most powerful observable parameter to investigate aromatic systems is current density. The current density may be used to calculate other magnetic properties such as NMR shifts or magnetic susceptibilities, and to develop concepts such as NICS or ACID. These qualitative concepts deepen our understanding of chemical bonding, and they provide predicting power to design new systems with specific properties.

References

1. Garrat, P.J. (1986) *Aromaticity*, John Wiley & Sons, Inc., New York.
2. Neus, J. (2002) *Aromatizität, Geschichte und mathematische Analyse eines fundamentalen chemischen Begriffs*, Hyle Publications, Karlsruhe.
3. Minkin, V.J., Glukhovtsev, M.N., and Simkin, B.Y. (1994) *Aromaticity and Antiaromaticity; Electronic and Structural Aspects*, John Wiley & Sons, Inc., New York.
4. Thematic issue on Aromaticy:Schleyer, P.v.R. (2001) *Chem. Rev.*, **101** (5), 1115–1541.
5. Thematic issue on Delocalization-Pi and Sigma:Schleyer, P.v.R. (2005) *Chem. Rev.*, **105** (10), 3433–3911.
6. For a recent review on aromaticity and ring currents see: Gomes, J.A.N.F. and Mallion, R.B. (2001) *Chem. Rev.*, **101**, 1349–1383.
7. For a review on aromaticity and NMR see: Mitchell, R.H. (2001) *Chem. Rev.*, **101**, 1301–1315.
8. Loschmidt, J. (1861) in *Chemische studien I*, Carl Gerold's Sohn, Vienna; see also reprint: Anschütz, R. (ed.) (1913) *Konstitutions-formeln der organischen*

chemie, Ostwalds Klassiker der Exakten Wissenschaften 190, W. Engelmann, Leipzig.
9. Couper, A.S. (1858) *Edinburgh New Philos. J., New Ser*, **8**, 213.
10. Couper, A.S. (1858) *Ann. Chim. Phys.*, **53**, 488.
11. Kekulé, A.F. (1861) *Lehrbuch der Organischen Chemie*, vol. 1, Ferdinand Enke, Erlangen, p. 160, 444, 523.
12. Claus, A. (1867) Theoretische Betrachtungen und deren Anwendung zur Systematik der Organischen Chemie, Freiburg, p. 207.
13. Dewar, J. (1867) *Proc. R. Soc. Edinburgh*, **6**, 82.
14. Meyer, J.L. (1884) Die modernen Theorien der Chemie, Breslau.
15. Armstrong, H.E. (1887) *J. Chem. Soc. Trans.*, **51**, 258–268.
16. Baeyer, A. (1888) *Ann. Chem.*, **245**, 103–190.
17. Ladenburg, A. (1869) *Ber. Dtsch. Chem. Ges.*, **2**, 140–142.
18. Hückel, E. (1931) *Z. Phys.*, **70**, 204–286.
19. Graneau, P. and Graneau, N. (1996) *Newtonian Electrodynamics*, World Scientific Publishing, London.
20. Evans, D.F. (2003) *J. Chem. Soc.*, **1959**.
21. Piguet, C. (1997) *J. Chem. Educ.*, **74**, 815.
22. Naklicki, M.L., White, C.A., Plante, L.L., Evans, C.E.B., and Crutchley, R.J. (1998) *Inorg. Chem.*, **37**, 1880.
23. Pascal, P. (1910) *Ann. Chim. Phys.*, **19**, 5.
24. Pacault, A. (1948) *Rev. Sci.*, **86**, 38.
25. Haberditzl, W. (1966) *Angew. Chem.*, **78**, 277–312; *Angew. Chem., Int. Ed. Engl.*, 1966, **5**, 288-329.
26. Ehrenfest, P. (1925) *Physica*, **5**, 388.
27. Raman, C.V. (1929) *Nature*, **123**, 945.
28. Pauling, L. (1936) *J. Chem. Phys.*, **4**, 673.
29. London, F. (1937) *J. Phys. Rad.*, **8**, 397–409.
30. van Vleck, J.H. (1965) *The Theory of Electric and Magnetic Susceptibilities*, Oxford University Press.
31. Londsdale, K. (1937) *Proc. R. Soc. A*, **159**, 149–161.
32. Dauben, H.J. jr., Wilson, J.D., and Laity, J.L. (1968) *J. Am. Chem. Soc.*, **90**, 811–813.
33. Dauben, H.J. jr., Wilson, J.D., and Laity, J.L. (1969) *J. Am. Chem. Soc.*, **91**, 1991–1998.
34. Dauben, H.J. jr.,, Wilson, J.D., and Laity, J.L. (1971) in *Nonbenzoid Aromaticity*, vol. II (ed. J.P. Snyder), Academic Press, New York, pp. 166–206.
35. Aihara, J.-i. (1982) *Pure Appl. Chem.*, **54**, 1115–1127.
36. Hoarau, J., Lumbroso, U., and Pacault, A. (1956) *C. R. Hebd. Seances Acad. Sci.*, **242**, 1702.
37. Landolt-Börnstein (1967) *Zahlenwerte und Funktionen*, 6th edn, Vol. II, Part 10, Springer-Verlag, Berlin.
38. van Wüllen, C. and Kutzelnigg, W. (1993) *Chem. Phys. Lett.*, **205**, 563–571.
39. Flygare, W.H. (1974) *Chem. Rev.*, **74**, 653–686.
40. Flygare, W.H. and Benson, R.C. (1971) *Mol. Phys.*, **20**, 225–250.
41. Pople, J.A. (1956) *J. Chem. Phys.*, **24**, 1111.
42. Waugh, J.S. and Fessenden, R.W. (1957) *J. Am. Chem. Soc.*, **79**, 846.
43. Johnson, C.E. and Bovey, F.A. (1958) *J. Chem. Phys.*, **29**, 1012.
44. Pelloni, S., Ligabue, A., and Lazzaretti, P. (2004) *Org. Lett.*, **6**, 4451–4454.
45. For a comprehensive review see: Lazzeretti, P. (2000) *Progr. Nucl. Res. Spect.*, **36**, 1–88.
46. For a detailed text book treatment see: Atkins, P.W. and Friedman, R.S. (1997) *Molecular Quantum Mechanics*, 3rd edn, Oxford University Press, Oxford, New York, Tokyo.
47. Kroto, H.W., Heath, J.R., O'Brien, S.C., Curl, R.F., and Smalley, R.E. (1985) *Nature*, **318**, 162–164.
48. Haddon, R.C. (1995) *Nature*, **378**, 249–255.
49. Krätschmer, W., Lamb, L.D., Fostiropoulos, K., and Huffman, D.R. (1990) *Nature*, **347**, 354–358.
50. Following Feynman's famous quotation: "It is not possible to understand the magnetic effects of materials in any honest way from the point of view

of classical physics'' Feynman, R.P., Leighton, R.B., and Sands, M. (1966) *The Feynman Lectures on Physics*, vol. II, Addison-Wesley, Reading, MA, p. 34.

51. The term Van Vleck paramagnetism is mainly used in atom physics, and the term ''induced orbital paramagnetism'' referring to molecules.Riess, J. (1970) *J. Ann. Phys.*, **57**, 301–321.

52. Van Vleck, J.H. (1932) *The Theory of Electric and Magnetic Susceptibilities*, Oxford University Press, London and New York.

53. Pelloni, S., Lazzaretti, P., and Zanasi, R. (2009) *J. Phys. Chem. A*, **113**, 14465–14479.

54. Keith, T.A. and Bader, R.F.W. (1993) *J. Chem. Phys.*, **99**, 3669.

55. Keith, T.A. and Bader, R.F.W. (1992) *Chem. Phys. Lett.*, **194**, 1.

56. Lazzaretti, P., Malagoli, M., and Zanasi, R. (1994) *Chem. Phys. Lett.*, **220**, 299.

57. Oth, J.F.M., Woo, E.P., and Sondheimer, F. (1973) *J. Am. Chem. Soc.*, **95**, 7337–7342.

58. Mucke, E.-K., Schönborn, B., Köhler, F., and Herges, R. (2011) *J. Org. Chem.*, **76**, 35–41.

59. The structure of the [18]annulene dianon shown in the Figure (right) is the most stable isomer of the 7685 conceivable cis/trans isomers of all monocyclic $(CH)_{18}^{2-}$ species. It exhibits partial localization of the negative charges indicated by dotted lines. Mucke, E.-K., Schönborn, B., Köhler, F., and Herges, R. (2011) *J. Org. Chem.*, **76**, 35–41.

60. Kutzelnigg, W. (1980) *Isr. J. Chem.*, **19**, 193.

61. Kutzelnigg, W., Fleischer, U., and Schindler, M. (1990) *NMR, Basic Principles and Progress*, vol. 23, Springer-Verlag, Berlin, p. 165.

62. Review: Webb, G.A. (1996) in *Encyclopedia of Nuclear Magnetic Resonance*, vol. 7 (eds D.M. Grant and R.K. Harris), John Wiley & Sons, Inc., New York, pp. 4307–4318.

63. Review:Cheeseman, J.R., Trucks, G.W., Keith, T.A., and Frisch, M.J. (1996) *J. Chem. Phys.*, **104**, 5497–5509.

64. Schleyer, P.v.R., Maerker, C., Dransfeld, A., Jiao, H., and van Eikema Hommes, N.J.R. (1996) *J. Am. Chem. Soc.*, **118**, 6317–6318.

65. Chen, Z., Wannere, C.S., Corminboeuf, C., Puchta, R., and Schleyer, P.v.R. (2005) *Chem. Rev.*, **105**, 3842–3888.

66. Poater, J., Duran, M., Solà, M., and Silvi, B. (2005) *Chem. Rev.*, **105**, 3911.

67. Poater, J., Solà, M., Viglione, R.G., and Zanasi, R. (2004) *J. Org. Chem.*, **69**, 7537–7542.

68. Stanger, A. (2006) *J. Org. Chem.*, **71**, 883–893.

69. Solà, M., Feixas, F., Jiménez-Halla, J.O.C., Matito, E., and Poater, J. (2010) *Symmetry*, **2**, 1156–1179.

70. Fowler, P.W., Steiner, E., Havenith, R.W.A., and Jenneskens, L.W. (2004) *Magn. Reson. Chem.*, **42**, 68.

71. Fowler, P.W., Steiner, E., and Jenneskens, L.W. (2003) *Chem. Phys. Lett.*, **371**, 719.

72. Fowler, P.W. and Steiner, E. (2002) *Chem. Phys. Lett.*, **364**, 259.

73. Acocella, A., Havenith, R.W.A., Steiner, E., Fowler, P.W., and Jenneskens, L.W. (2002) *Chem. Phys. Lett.*, **363**, 64.

74. Fowler, P.W., Havenith, R.W.A., and Steiner, E. (2002) *Chem. Phys. Lett.*, **359**, 530.

75. Steiner, E., Fowler, P.W., and Havenith, R.W.A. (2002) *J. Phys. Chem. A*, **106**, 7048.

76. Steiner, E., Fowler, P.W., Viglione, R.G., and Zanasi, R. (2002) *Chem. Phys. Lett.*, **355**, 471.

77. Soncini, A., Fowler, P.W., Cernusak, I., and Steiner, E. (2001) *Phys. Chem. Chem. Phys.*, **3**, 3920.

78. Steiner, E. and Fowler, P.W. (2001) *J. Phys. Chem. A*, **105**, 9553.

79. Fowler, P.W. and Soncini, A. (2011) *Phys. Chem. Chem. Phys.*, **13**, 20637–20643.

80. Herges, R. and Geuenich, D. (2001) *J. Phys. Chem. A*, **105**, 3214.

81. Geuenich, D., Hess, K., Köhler, F., and Herges, R. (2005) *Chem. Rev.*, **105**, 3758–3772.

82. Stock, A. and Pohland, E. (1926) *Chem. Ber.*, **59**, 2215.

83. Wiberg, E. and Bolz, A. (1940) *Ber. Chem. Ges.*, **73**, 209–232.

84. Fowler, P.W. and Steiner, E. (1997) *J. Phys. Chem. A*, **101**, 1409.

85. Steiner, E., Soncini, A., and Fowler, P.W. (2006) *J. Phys. Chem. A*, **110**, 12882.

86. Fernandez, I. and Frenking, G. (2007) *Faraday Discuss.*, **135**, 403.

87. Ashe, A.J. III, (1978) *Accts. Chem. Res.*, **11**, 153–157.

88. Ashe, A.J. III, (1971) *J. Am. Chem. Soc.*, **93**, 3293.

89. Nyulászi, L. (2001) *Chem. Rev.*, **101**, 1229–1246.

90. Ashe, A.J. III, (1971) *J. Am. Chem. Soc.*, **93**, 6690.

91. Kassaee, M.Z., Jalalimanesh, N., and Musavi, S.M. (2007) *J. Mol. Struct. (THEOCHEM)*, **816**, 153–160.

92. Baldridge, K.K., Uzan, O., and Martin, J.M.L. (2000) *Organometallics*, **19**, 1477–1487.

93. Ebrahimi, A.A., Ghiasi, R., and Foroutan-Nejad, C. (2010) *J. Mol. Struct. (THEOCHEM)*, **941**, 47–52.

94. Haddon, R.C., Schneemeyer, L.F., Waszczak, J.V., Glarum, S.H., Tycko, R., Dabbagh, G., Kortan, A.R., Muller, A.J., Mujsce, A.M., Rosseinsky, M.J., Zahurak, S.M., Makhija, A.V., Thiel, F.A., Raghavachari, K., Cockayne, E., and Elser, V. (1991) *Nature*, **350**, 46–47.

95. Saunders, M., Jiménez-Vazquez, H.A., Cross, R.J., Mroczkowski, S., Freedberg, D.I., and Anet, F.A.L. (1994) *Nature*, **367**, 256–258.

96. Martins, J.L., Troullier, N., and Weaver, J.H. (1991) *Chem. Phys. Lett.*, **180**, 457–460.

97. Bühl, M. and Hirsch, A. (2001) *Chem. Rev.*, **101**, 1153–1183.

98. Reiher, M. and Hirsch, A. (2003) *Chem. Eur. J.*, **9**, 5442–5452.

99. Rosseinsky, M.J. (1995) *J. Mater. Chem.*, **5**, 1497–1513.

100. Pasquarello, A., Schlüter, M., and Haddon, R.C. (1993) *Phys. Rev. A*, **47**, 1783–1789.

101. Heilbronner, E. (1964) *Tetrahedron Lett.*, 1923.

102. Ajami, D., Oeckler, O., Simon, A., and Herges, R. (2003) *Nature*, **426**, 819.

103. Ajami, D., Hess, K., Köhler, F., Näther, C., Oeckler, O., Simon, A., Yamamoto, C., Okamoto, Y., and Herges, R. (2006) *Chem. Eur. J.*, **12**, 5434.

104. Herges, R. (2006) *Chem. Rev.*, **106**, 4820–4842.

105. Schaller, G. and Herges, R. (2013) *Chem. Commun.*, **49**, 1254.

106. Stępień, M., Latos-Grażyński, L., and Sprutta, N. (2011) *Angew. Chem.*, **123**, 4376–4430; *Angew. Chem. Int. Ed.*, 2011, **50**, 4288-4340.

107. Saito, S. and Osuka, A. (2011) *Angew. Chem.*, **123**, 4432–4464; *Angew. Chem. Int. Ed.*, 2011, **50**, 4342-4373.

108. Sankar, J., Mori, S., Saito, S., Rath, H., Suzuki, M., Inokuma, Y., Shinokubo, H., Kim, K.S., Yoon, Z.S., Shin, J.-Y., Lim, J.M., Matsuzaki, Y., Matsushita, O., Muranaka, A., Kobayashi, N., Kim, D., and Osuka, A. (2008) *J. Am. Chem. Soc.*, **130**, 13568–13579.

109. Yoon, Z.S., Osuka, A., and Kim, D. (2009) *Nat. Chem.*, **1**, 113–122.

110. Mucke, E.-K., Köhler, F., and Herges, R. (2010) *Org. Lett.*, **12**, 1708–1711.

111. Mucke, E.-K., Schönborn, B., Köhler, F., and Herges, R. (2011) *J. Org. Chem.*, **76**, 35–41.

112. Schröder, G. and Oth, J.F.M. (1966) *Tetrahedron Lett.*, **34**, 4083–4088.

113. Sondheimer, F. and Gaoni, Y. (1961) *J. Am. Chem. Soc.*, **83**, 4863–4864.

114. Johnson, S.M., Paul, I.C., Noyes, W.A., and King, G.S.D. (1970) *J. Chem. Soc. B*, **4**, 643–649.

115. Johnson, S.M. and Paul, I.C. (1968) *J. Am. Chem. Soc.*, **90**, 6555–6556.

116. Oth, J.F.M. and Gilles, J.M. (1968) *Tetrahedron Lett.*, **60**, 6259–6264.

117. Winstein, S.J. (1959) *Am. Chem. Soc.*, **81**, 6524.

118. Williams, R.V. (2001) *Chem. Rev.*, **101**, 1185–1204.

119. Yannoni, C.S., Macho, V., and Myhre, P.C. (1982) *J. Am. Chem. Soc.*, **104**, 7380–7381.

120. Laube, T. (1987) *Angew. Chem.*, **99**, 580–583; *Angew. Chem., Int. Ed. Engl.* 1987, **26**, 560-562.
121. Winstein, S., Shatavsky, M., Norton, C., and Woodward, R.B. (1955) *J. Am. Chem. Soc.*, **77**, 4183.
122. Mesić, M., Sunko, D.E., and Vančik, H. (1994) *J. Chem. Soc., Perkin Trans. 2*, 1135.
123. Chen, Z., Jiao, H., Wu, J., Herges, R., Zhang, S.B., and Schleyer, P.v.R. (2008) *J. Phys. Chem. A*, **112**, 10586–10594.
124. Williams, R.V., Edwards, W.D., Zhang, P., Berg, D.J., and Mitchell, R.H. (2012) *J. Am. Chem. Soc.*, **134**, 16742–16752.
125. Prakash, G.K., Krishnamurthy, V.V., Herges, R., Bau, R., Yuan, H., Olah, G.A., Fessner, W.D., and Prinzbach, H. (1986) *J. Am. Chem. Soc.*, **108**, 836–838.
126. Prakash, G.K., Krishnamurthy, V.V., Herges, R., Bau, R., Yuan, H., Olah, G.A., Fessner, W.D., and Prinzbach, H. (1988) *J. Am. Chem. Soc.*, **110**, 7764–7772.
127. Herges, R., Schleyer, P.v.R., Schindler, M., and Fessner, W.D. (1991) *J. Am. Chem. Soc.*, **113**, 3649–3656.
128. Prinzbach, H., Gescheidt, G., Martin, H.D., Herges, R., Heinze, J., Prakash, G.K.S., and Olah, G.A. (1995) *Pure Appl. Chem.*, **65**, 673–682.
129. Trifunac, A.D., Werst, D.W., Herges, R., Neumann, H., Prinzbach, H., and Etzkorn, M. (1996) *J. Am. Chem. Soc.*, **118**, 9444–9445.
130. Etzkorn, M., Wahl, F., Keller, M., Prinzbach, H., Barbosa, F., Peron, V., Gescheidt, G., Heinze, J., and Herges, R. (1998) *J. Org. Chem.*, **63**, 6080–6081.
131. Prakash, G.K.S., Weber, K., Olah, G.A., Prinzbach, H., Wollenweber, M., Etzkorn, M., Voss, T., and Herges, R. (1999) *Chem. Commun.*, **11**, 1029–1030.
132. Fischer, E.O. and Pfab, W. (1952) *Z. Naturforsch. B*, **7**, 377–379.
133. Wilkinson, G., Rosenblum, M., Whiting, M.C., and Woodward, R.B. (1952) *J. Am. Chem. Soc.*, **74**, 2125–2126.
134. Nakamura, A., Ueyama, N., and Yamaguchi, K. (2002) *Organometallic Conjugation, Structures, Reactions and Functions of d-d and d-π Conjugated Systems*, Springer-Verlag, Berlin, Heidelberg, New York.
135. Bridgeman, A.J. (1997) *J. Chem. Soc., Dalton Trans.*, 2887–2893.
136. Faegri, K. Jr., and Almlöf, J. (1983) *J. Organomet. Chem.*, **249**, 303–313.
137. Jutzi, P. and Burford, N. (1999) *Chem. Rev.*, **99**, 969–990.
138. Landorf, C.W. and Haley, M.M. (2006) *Angew. Chem.*, **118**, 4018–4040, *Angew. Chem. Int. Ed.* 2006, **45**, 3914-3936.
139. Boldyrev, A.I. and Wang, L.-S. (2005) *Chem. Rev.*, **105**, 3716–3757.
140. Li, X., Kuznetsov, A.E., Zhang, H.-F., Boldyrev, A.I., and Wang, L.-S. (2001) *Science*, **291**, 859.
141. Kuznetsov, A.E., Boldyrev, A.I., Li, X., and Wang, L.-S. (2001) *J. Am. Chem. Soc.*, **123**, 8825–8831.
142. Li, X., Zhang, H.-F., Wang, L.-S., Kuznetsov, A.E., Cannon, N.A., and Boldyrev, A.I. (2001) *Angew. Chem.*, **113**, 1919–1922; *Angew. Int. Ed. Engl.* 2001, **40**, 3369-3372.
143. Boldyrev, A.I. and Kuznetsov, A.E. (2002) *Inorg. Chem.*, **41**, 532–537.
144. Zubarev, D.Y. and Boldyrev, A.I. (2008) *Phys. Chem. Chem. Phys.*, **10**, 5207–5217.
145. Evans, M.G. and Warhurst, E. (1938) *Trans. Faraday Soc.*, **34**, 614.
146. Evans, M.G. (1939) *Trans. Faraday Soc.*, **35**, 824.
147. Evans, M.G. and Polanyi, M. (1938) *Trans. Faraday Soc.*, **34**, 11.
148. Zimmerman, H.E. (1966) *Science*, **153**, 837.
149. Zimmerman, H.E. (1966) *J. Am. Chem. Soc.*, **88**, 1564.
150. Zimmerman, H.E. (1971) *Acc. Chem. Res.*, **4**, 272.
151. Dewar, M.J.S. (1966) *Tetrahedron Suppl.*, **8**, 75.
152. Dewar, M.J.S. (1971) *Angew. Chem.*, **83**, 859; *Angew. Chem., Int. Ed. Engl.* 1971, **10**, 761.
153. Dewar, M.J.S. (1966) *Tetrahedron Suppl.*, **8**, 75.

154. Woodward, R.B. and Hoffmann, R. (1969) *Angew. Chem.*, **81**, 797; *Angew. Chem., Int. Ed. Engl.* 1969, **8**, 781.

155. Herges, R., Jiao, H., and Schleyer, P.v.R. (1994) *Angew. Chem.*, **106**, 1441–1444; *Angew. Chem., Int. Ed. Engl.* 1994, **33**, 1376-1378.

156. See also: Corminboeuf, C., Heine, T., and Weber, J. (2003) *Org. Lett.*, **5**, 1127–1130.

157. Jiao, H. and Schleyer, P.v.R. (1994) *J. Chem. Soc. Perkin Trans. 2*, 407–410.

158. Jiao, H. and Schleyer, P.v.R. (1994) *J. Chem. Soc., Faraday Trans.*, **90**, 1559–1567.

159. Herges, R. (1994) *Angew. Chem.*, **106**, 261–283; *Angew. Chem., Int. Ed. Engl.*, 1994, **33**, 255–276.

160. Herges, R. (1994) *J. Chem. Inf. Comput. Sci.*, **34**, 91–102.

161. Friedman, L. and Shechter, H. (1960) *J. Am. Chem. Soc.*, **82**, 1002.

162. Banert, K., Grimme, S., Herges, R., Heß, K., Köhler, F., Mück-Lichtenfeld, C., and Würthwein, E.-U. (2006) *Chem. Eur. J.*, **12**, 7467–7481.

163. Banert, K., Köhler, F., Melzer, A., Scharf, I., Rheinwald, G., Rüffer, T., Lang, H., Herges, R., Heß, K., Ghavtadze, N., and Würthwein, E.-U. (2011) *Chem. Eur. J.*, **17**, 10071–10080.

164. Herges, R., Geuenich, D., Bucher, G., and Tönshoff, C. (2000) *Chem. Eur. J.*, **6**, 1224–1228.

165. Berger, C., Bresler, C., Dilger, U., Geuenich, D., Herges, R., Röttele, H., and Schröder, G. (1998) *Angew. Chem.*, **110**, 1951–1953; *Angew. Chem., Int. Ed. Engl.* 1998, **37**, 1850-1853.

166. Berger, C., Dieterich, S., Dilger, U., Geuenich, D., Helios, H., Herges, R., Kirchmer, P., Röttele, H., and Schröder, G. (1998) *Angew. Chem.*, **110**, 1954–1957; *Angew. Chem., Int. Ed. Engl.* 1998 **37**, 1854-1857.

167. Kimball, D.B., Herges, R., and Haley, M. (2002) *J. Am. Chem. Soc.*, **124**, 1572–1573.

168. Kimball, D.B., Weakley, T.J.R., Herges, R., and Haley, M. (2002) *J. Am. Chem. Soc.*, **124**, 13463–13473.

169. Shirtcliff, L.D., Weakley, T.J.R., Haley, M., Köhler, F., and Herges, R. (2004) *J. Org. Chem.*, **69**, 6979–6985.

170. Shirtcliff, L.D., Hayes, A.G., Haley, M., Köhler, F., Hess, K., and Herges, R. (2006) *J. Am. Chem. Soc.*, **128**, 9711–9721.

171. Shirtcliff, L.D., Haley, M., and Herges, R. (2007) *J. Org. Chem.*, **72**, 2411–2418.

172. McClintock, S.P., Shirtcliff, L.D., Herges, R., and Haley, M. (2008) *J. Org. Chem.*, **73**, 8755–8762.

173. McClintock, S.P., Forster, N., Herges, R., and Haley, M. (2009) *J. Org. Chem.*, **74**, 6631–6636.

174. Young, B.S., Köhler, F., Herges, R., and Haley, M. (2011) *J. Org. Chem.*, **76**, 8483–8487.

175. McClintock, S.P., Zakharov, L.N., Herges, R., and Haley, M. (2011) *Chem. Eur. J.*, **17**, 6798–6806.

176. Young, B.S., Herges, R., and Haley, M. (2013) *J. Org. Chem.*, **78**, 1977–1983.

14
Chemical Bonding in Inorganic Aromatic Compounds

Ivan A. Popov and Alexander I. Boldyrev

14.1
Introduction

The concept of aromaticity was born in chemistry soon after Faraday discovered benzene. Chemists noticed that certain chemicals containing benzene ring are not particularly reactive in spite of having unsaturated carbon atoms. The term *aromaticity* was introduced in chemistry by Kekulé [1–3], who associated aromaticity with the presence of C_6 units in aromatic compounds. Kekulé assumed that the similarity to benzene is essential for a compound to be aromatic. This concept undergoes a significant transformation nowadays. According to the IUPAC's definition, aromaticity is a *concept of spatial and electronic structure of cyclic molecular systems displaying the effects of cyclic electron delocalization which provide for their enhanced thermodynamic stability (relative to acyclic structural analogues) and tendency to retain the structural type in the course of chemical transformations. A quantitative assessment of the degree of aromaticity is given by the value of the resonance energy. It may also be evaluated by the energies of relevant isodesmic and homodesmotic reactions. Along with energetic criteria of aromaticity, important and complementary are also a structural criterion (the lesser the alternation of bond lengths in the rings, the greater is the aromaticity of the molecule) and a magnetic criterion (existence of the diamagnetic ring current induced in a conjugated cyclic molecule by an external magnetic field and manifested by an exaltation and anisotropy of magnetic susceptibility)*. [4] Initially, aromaticity was associated with planar molecules and with delocalization of π-electrons. On the basis of quantum chemical analysis of molecular orbitals (MOs) the famous $4n + 2$ π-electrons Hückel's [5, 6] rule was proposed for aromatic molecules. Breslow [7, 8] introduced in 1970 the concept of antiaromaticity, which can be understood as the destabilization of the cyclic systems possessing $4n$ π-electrons, resulting in their higher reactivity than nonaromatic molecules. Since the initial introduction of π-aromaticity and π-antiaromaticity these concepts were extended to delocalized σ-electrons, too [9–12]. In 1979, Schleyer and coworkers [13] introduced double artomaticity, which includes delocalization in the both σ- and π-systems. As organic chemistry includes molecules containing not only carbon

The Chemical Bond: Chemical Bonding Across the Periodic Table, First Edition.
Edited by Gernot Frenking, Sason Shaik.

and hydrogen atoms, the aromaticity and antiaromaticity concepts were further extended to heteroaromatic compounds [14–16].

In this chapter, we focus on aromaticity and antiaromaticity in inorganic compounds only. It means that the chemical species, which will be discussed, do not contain carbon atoms in their cyclic structures. There are a few review articles [17–25], which discuss different aspects of aromaticity and antiaromaticity in inorganic chemistry. Before we go further, we would like to outline the structure of this chapter. First, we describe criteria that are commonly used for probing aromaticity. Second, we consider inorganic aromatic molecules, which we loosely call conventional aromatic molecules. These molecules are simply isoelectronic species to one of the organic aromatic molecule. Third, we focus on what we loosely call unconventional aromatic molecules composed of main group atoms and transition-metal atoms. Finally, we conclude the chapter with a summary and short outlook.

14.2
How to Recognize Aromaticity and Antiaromaticity?

Unfortunately, chemists have not yet developed a single simple probe of aromaticity that can convince everybody that a particular system is aromatic. However, owing to the tremendous advancement of computational chemistry, one can use many criteria to assess aromaticity or antiaromaticity. When several different criteria show the presence of aromaticity/antiaromaticy, the final conclusion is significantly more reliable. The list of criteria used by chemists at present are summarized in Table 14.1, which was initially proposed by Krygowski *et al*. [26].

These criteria have been formulated for π-aromatic and π-antiaromatic organic systems, but many of them are also applicable to σ-aromatic and σ-antiaromatic, as well as δ-aromatic and δ-antiaromatic systems.

The criteria presented in Table 14.1 can be roughly broken into the following groups:

1) Electronic criterion is the simplest one. If we have delocalized electrons in a cyclic system and they satisfy the $4n + 2$ rule, a molecule is aromatic. If they satisfy the $4n$ rule, the system is considered to be antiaromatic in a singlet state.
2) Energetic criterion is probably the most important criterion of aromaticity. However, it is not easy to calculate the resonance energy even when experimental data are available, as many other factors such as strain, hyperconjugation, Coulomb repulsion imbalance, and uncompensated van der Waals attractions must be carefully taken into account. The resonance energy of even the most studied aromatic molecule, benzene, is still disputed and revaluated [27–29]. The additional problem for inorganic molecules is that there are frequently no good reference molecules for the resonance energy evaluation.
3) The geometric criterion is also rather simple. If we have the bond equalization in a cyclic structure, with the bond length being between a single and a

Table 14.1 Criteria for π-aromaticity and π-antiaromaticity. (Reprinted with a permission from Ref. [26]. Copyright © 2000, Elsevier).

Property	Aromatic	Olefinic/Classical	Antiaromatic
(i) Electronic nature	$(4n+2)$ π-electron cyclic conjugation	No cyclic conjugation	$4n$ π-electron cyclic conjugation
(ii) Energy			
Cyclic conjugation	Stabilization	Standard	Destabilization
Delocalization	Enhanced	Standard	Decreased
HOMO–LUMO gap	Large	Standard	Small
(iii) Geometry			
Bond lengths	Equalization	Alternation	Alternation
(iv) Magnetic properties			
Anisotropy of diamagnetic susceptibility	Enhanced		Small
Susceptibility exaltation	High		Low
^{1}H NMR shifts	Diatropic (low-field shift)		Paratropic (high-field shift)
NICS(nucleus-independent chemical shift)	Large negative		Large positive
(v) Reactivity			
Chemical structure, e.g.	Benzene	Cyclohexadiene	Cyclooctatetraene
Retention of structure	Electrophilic substitution	Electrophilic addition	Addition
(vi) Spectroscopy			
UV spectra	High energy	Standard	Low energy
IR/Raman spectra	High symmetry		Low symmetry
Photoelectron spectra	High electron detachment energies	Standard	Low electron detachment energies

double bond length, that is a sign of aromaticity. If there is any deviation from equalization or from planarity, then that is a sign of decreasing aromaticity. There are several known geometrical indices of aromaticity described in the literature, such as the Julg aromaticity index [30] and the harmonic oscillator model of aromaticity (HOMA) index [31, 32].

4) Magnetic criteria developed in recent years became the most popular probes among theoreticians. The following criteria were put forward: nucleus-independent chemical shift (NICS) index [33–35], aromatic ring current shielding (ARCS) [36], gauge-including magnetically induced current (GIMIC) [37], and plotted maps of the ring current density (CD plots) [38–42].

The NICS index proposed by Schleyer and coworkers [33–35] became the most popular probe of aromaticity owing to its availability in the Gaussian program. The NICS index is a computed magnetic shielding with reversed signs in order to conform to the NMR chemical shift sign conventions (negative upfield and positive downfield). Appreciably negative NICS values (magnetically shielded) in the interior

position of rings are a sign of the presence of induced diatropic ring currents or ''aromaticity.'' Appreciably positive NICS values (magnetically deshielded) at the same position mean paratropic ring currents or ''antiaromaticity.'' Schleyer and coworkers [43] also developed a technique allowing assessing individual MO contributions to the NICS index. $NICS_{zz}$ is a total contribution to the out-of-plane component of the NICS tensor. Fowler and Steiner [44, 45] argued that $NICS_{zz}$ index is a better probe of aromaticity than NICS. Schleyer and coworkers [46] have recently reviewed different NICS indices as probes of aromaticity.

The Aromatic Ring-Current Sheildings method (ARCS) method developed by Jusélius and Sundholm [36] evaluates the degree of aromaticity from the long-range magnetic shielding function. The ARCS function (sign and shape) at long distance from the ring indicates where the molecule possesses a dominating diamagnetic or paramagnetic character and is aromatic or antiaromatic, respectively. Sundholm and coworkers [37] also proposed the GIMIC method, in which gauge-including atomic orbitals (AOs) are employed, yielding gauge-origin-independent current densities with a fast basis set convergence. Similar to ARCS, the GIMIC method assesses aromaticity or antiaromaticity on the basis of diatropic or paratropic currents, respectively.

Aromaticity, antiaromaticity, or nonaromaticity could be also evaluated directly from the calculated current-density maps. According to that criterion, if the ring current is strongly diatropic, then a molecule is aromatic; if it is strongly paratropic, then a molecule is antiaromatic; and if the ring current is not significantly present, then a molecule is nonaromatic.

There are also electronic multicenter indices (MCI) [47–51] for probing aromaticity. It was recently shown that they are better suited for assessing aromaticity in inorganic systems [49–57]. The advantage of MCI is that its total value can be exactly decomposed into their σ- and π-components. However, for planar systems with d-orbitals participating in delocalized bonding, the separation into the different components is not exact because of some σ- and δ-orbital mixing within a given atomic domain. Still, the mixing in these systems is not significant.

5) Reactivity is also a very important criterion of aromaticity, because that is what started the whole concept of aromaticity in chemistry. Indeed, it was the lack of reactivity toward addition reactions for benzene and other initially identified aromatic molecules that was recognized as a special property. Instead, aromatic molecules undergo electrophilic substitution rather than addition. Yet, this probe of aromaticity is the most difficult to use especially in inorganic chemistry.
6) Spectroscopy can be used for probing aromaticity, too. Aromatic molecules usually have very high HOMO–LUMO (HOMO = highest occupied molecular orbital, LUMO = lowest unoccupied molecular orbital) gap values (which can be evaluated from electron spectroscopy or from quantum chemical calculations) and high values of first vertical electron detachment energy (VDE) (which can be evaluated from photoelectron spectroscopy), while antiaromatic molecules have low HOMO–LUMO gap values (vertical singlet excitation energy) and low values of first VDE compared to nonaromatic molecules.

Aromaticity was always connected with delocalized bonding. Chemists realized that a single classical structure, where the bonding is represented by either lone pairs (LPs) or two-electron two-centered (2c-2e) bonds, could not properly describe bonding in aromatic molecules. Thus, they introduced a resonance of a few classical structures. Chemical bonding in benzene can be represented by a resonance of two Kekulé structures. The resonance allows us to explain why there are no double and single carbon–carbon bonds in the benzene molecule, but rather an intermediate of approximately 1.5 of the C–C bond order. The resonance is simply another way of saying that π-bonding in benzene is delocalized. Of course, canonical MOs, which are always available from Hartee–Fock or density functional calculations are delocalized over a whole molecule and thus could be used to describe delocalized bonding in aromatic molecules. However, chemists believe that σ-bonding in organic aromatic molecules is localized. Thus, we have a dilemma as to which description to choose: localized bonding with resonance or completely delocalized bonding with canonical MOs. We recently proposed a new method, which we call the *adaptive natural density partitioning* (AdNDP) method [58–64], which allows us to reconcile a localized bonding with a delocalized one in one molecular bonding model. The AdNDP method is an extension of the natural bond orbital (NBO) analysis developed by Weinhold [65, 66]. In the AdNDP analysis, the search is initially performed for localized 1c-2e (lone pairs) and 2c-2e bonding elements similar to the NBO analysis. After that the electron density responsible for localized bonding is removed. Then the search is performed for the delocalized bonding elements (*n*c-2e bonds with *n* ranging from 3 to the total number of atoms in the system). The AdNDP method, recovering all multicenter bonding elements and the final molecular structure, always corresponds to the point group symmetry of the system (after these bonding elements are superimposed onto the molecular frame). As in the NBO analysis, all the bonding elements are usually chosen to have occupation numbers (ONs) close to 2.00 |e|. Because of that, the Lewis idea of an electron pair as the essential element of chemical bonding is preserved. However, the criterion for ONs might be adjustable for a particular case in the AdNDP procedure if necessary. In Figure 14.1 we present results of the AdNDP analysis for the prototypical aromatic cyclopentadienyl anion, $C_5H_5^-$ [59], which is a very popular ligand in inorganic chemistry.

The bonding pattern revealed by AdNDP (Figure 14.1a) shows that cyclopentadienyl anion has five 2c-2e C–C σ-bonds forming a cycle, five 2c-2e C–H σ-bonds, and three delocalized π-bonds. The NBO analysis revealed the same σ-bonding, but for the π-system it produces two 2c-2e C–C π-bonds and one π-LP, shown schematically in Figure 14.1b. Thus, the NBO analysis recovered one of five possible resonance structures. On the other hand, the AdNDP analysis revealed a chemical bonding pattern, which is consistent with the single symbolic representation (Figure 14.1c).

The detailed description of the AdNDP method and its application to boron clusters, prototypical aromatic hydrocarbons, gold clusters, metalloorganic complexes, and inorganic complexes containing metal clusters as the building blocks can be found elsewhere [58–64]. The AdNDP analysis allows us to introduce a new aromaticity criterion. A chemical species should be considered aromatic if there is a

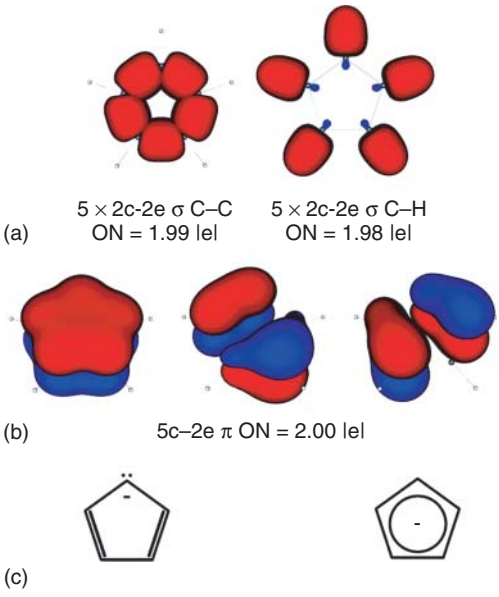

Figure 14.1 (a) The AdNDP bonding pattern for $C_5H_5^-$: 5 2c-2e C–C σ-bonds superimposed over the C_5 cycle, 5 2c-2e C–H σ-bonds superimposed over the C_5 cycle, and 3 5c-2e π-bonds. (b) Symbolic representation of the resonant structure of $C_5H_5^-$ according to NBO. (c) Symbolic representation of $C_5H_5^-$ according to AdNDP [59]. (Reprinted with permission from Ref. [59]. Copyright 2008 American Chemical Society.)

globally delocalized bonding encountered in a cyclic planar high-symmetry system by the means of AdNDP. We believe that the presence of the globally delocalized bonding would also lead to manifestation of other properties related to aromaticity such as bond length equalization, corresponding magnetic properties, energetic stabilization, and abnormal chemical reactivity.

We would like to stress that the criteria discussed were developed in organic chemistry for π-aromaticity/antiaromaticity. We should expect that aromaticity/antiaromaticity in inorganic systems will manifest itself differently with many specific deviations. However, we believe that the overall chemical bonding picture and most of the molecular properties in these inorganic species with delocalized bonding should be possible to recognize using the criteria discussed.

14.3 "Conventional" Aromatic/Antiaromatic Inorganic Molecules

In this section, we consider inorganic molecules, which we loosely call "conventional" aromatic/antiaromatic molecules and can be derived from their organic counterparts by valence isoelectronic substitution.

14.3.1 Inorganic $B_3N_3H_6$ Borazine and 1,3,2,4-Diazadiboretiidine $B_2N_2H_4$

As we mentioned earlier, at first we plan to discuss inorganic molecules, which can be obtained from aromatic/antiaromatic hydrocarbons by isoelectronic substitution. Two molecules borazine ($B_3N_3H_6$) and 1,3,2,4-diazadiboretiidine ($B_2N_2H_4$) are thought to be prototypical aromatic and antiaromatic inorganic molecules, as they are isoelectronic to benzene and cyclobutadiene, respectively.

Borazine was first synthesized by Stock and Pohland [67] by a reaction of diborane with ammonia. Indeed, it was found that borazine does remind of benzene in some degree. It has an aromatic smell similar to benzene and a planar structure with all equivalent B–N bond distances (1.429 Å) [68], which are in between the ordinary single (1.51 Å) and double (1.31 Å) B–N bond lengths, again similar to benzene. However, borazine does not pass other aromaticity criteria. Unlike benzene, borazine undergoes an addition reaction and reacts with HCl and HBr. Its aromatic stabilization energy is significantly lower than that in benzene. It was evaluated to be approximately from one-third to one-half of that of benzene [34, 69]. Magnetic properties of borazine show that it is either slightly aromatic or not aromatic [34, 70]. Nowadays, borazine is considered as either weakly aromatic or nonaromatic molecule and thus, its initial ''inorganic benzene'' name looks inappropriate.

The 1,3,2,4-diazadiboretiidine, being isoelectronic to cyclobutadiene, is supposed to be an example of inorganic antiaromatic molecule. Although the 1,3,2,4-diazadiboretiidine has not been synthesized yet, the structures of five-substituted molecules [71] have been reported. While the cyclic B_2N_2 fragment was found to be planar (except the tetra-*tert*-butyl derivative), the 1,3,2,4-diazadiboretiidine and its derivatives do not have alteration of B–N bonds expected for the antiaromatic molecules. The synthesized derivatives also do not follow the expected reactivity of antiaromatic molecules, because they survive the thermal elimination of isobutene from the *tert*-butyl derivative [71].

On the example of borazine and 1,3,2,4-diazadiboretiidine we have demonstrated that assessing aromaticity in inorganic chemistry is a challenge. The reason both these inorganic ''aromatic'' and ''antiaromatic'' analogs do not follow the expected behavior is due to the difference in electronegativities of nitrogen and boron, which leads to localization of π-electrons onto more electronegative nitrogen atoms. We performed the AdNDP analysis for C_6H_6 and $B_3N_3H_6$ molecules, forcing the program to find π-lone pairs on C, B, and N atoms, expecting in this case to get ON number being close to 1.00 |e|. Results of these calculations are shown in Figure 14.2.

One can see that every carbon atom has a π-''lone pair'' with the ON = 1.00 |e|, as it should be in six-atomic aromatic ring, while every nitrogen and boron atoms have π-''lone pairs'' with the ON = 1.62 |e| and ON = 0.38 |e|, respectively. Strong deviation from 1.00 |e| in π-''lone pairs'' shows why borazine and 1,3,2,4-diazadiboretiidine do not follow the organic aromatic molecules' trends.

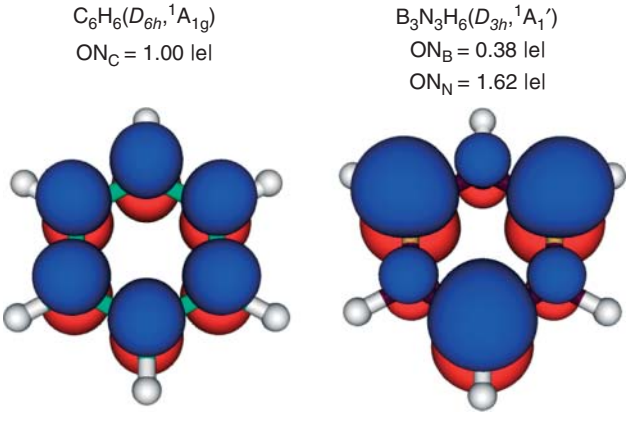

Figure 14.2 π-"lone pairs" recovered by the AdNDP analysis for benzene and borazine.

In spite of these difficulties, the aromaticity and antiaromaticity concepts are quickly advancing in inorganic chemistry.

14.3.2 Aromatic P_4^{2-}, P_5^-, P_6 and Their Analogs

The P_4^{2-}, P_5^-, P_6 and their congeners, which are valence isoelectronic to the organic aromatic $C_4H_4^{2-}$, $C_5H_5^-$, and C_6H_6 species, respectively, were found to be a part of solid-state compounds [72–81].

The computationally obtained P–P bond length (2.19 Å) in the global minimum square planar P_4^{2-} structure is shorter than the single P–P bond in P_2H_4 (2.27 Å) and longer than the double P=P bond in P_2H_2 (2.04 Å), and together with bond equalization these are signs of aromaticity of the dianion [82]. These computational results are in agreement with the experimental P–P bond length 2.148 Å found in the $Cs_2P_4{\bullet}2NH_3$ compound, synthesized by Korber and coworkers [72].

The planar pentagonal P_5^- anion [83] is valence isoelectronic to a prototypical aromatic $C_5H_5^-$ cyclopentadienyl anion. Indeed, one can see that the AdNDP analysis of P_5^- (Figure 14.3) revealed the same bonding pattern as for $C_5H_5^-$ (Figure 14.1).

P_5^- is also aromatic according to other criteria. R(P–P) = 2.13 Å in P_5^- is shorter than the single P–P bond in P_2H_4 (2.27 Å) and longer than the double P=P bond in P_2H_2 (2.04 Å), all at the B3LYP/6-311+G* level of theory, and that is consistent with the aromatic nature of the anion. Calculated magnetic properties, such as diatropic π-ring current and negative NICS(0.0) = −18.5 ppm and NICS(1.0) = −18.3 ppm values can be compared to those NICS(0.0) = −15.6 ppm and NICS(1.0) = −12.3 ppm for $C_5H_5^-$. Another important sign of aromaticity in P_5^- is experimentally measured very high VDE (4.05 eV) and adiabatic detachment energy (ADE, 3.88 eV) values [84]. Species containing pentagonal P_5^- fragment were experimentally found by Scherer and coworkers [73], who synthesized the

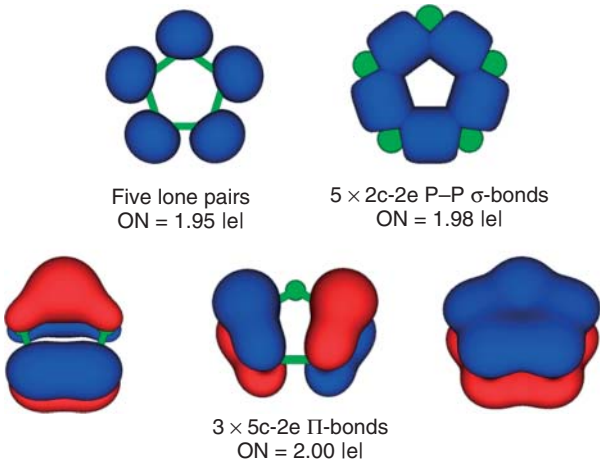

Figure 14.3 The AdNDP bonding pattern for P_5^-.

first triple-decker complex $[(\eta^5-C_5Me_5)Cr(\mu,\eta^5-P_5)Cr(\eta^5-C_5Me_5)]$ with the P_5^- pentagon in the center. Also, recently Ellis and coworkers [74] reported synthesis and characterization of the carbon-free sandwich complex $[(\eta^5-P_5)_2Ti]^{2-}$.

As both P_4^{2-} and P_5^- have the high-symmetry planar global minimum structures, one may think that P_6 should have the planar hexagon aromatic structure too as a global minimum. Yet, according to the most accurate *ab initio* calculations [85, 86], the global minimum structure of P_6 is of the benzvalene type. That is due to the weak π-bonding in P_6. Moreover, the D_{6h} structure is not even a local minimum, but it is a second-order saddle point. Geometry optimization along the imaginary modes leads to the buckled structure. In spite of that, Scherer and coworkers reported a synthesis and characterization of a triple-decker sandwich complex $\{(\eta_5\text{-}Me_5C_5)Mo\}2(\mu,\eta^6-P_6)$, containing a planar P_6 ring with almost equal P–P bond lengths [76]. The experimental P–P bonds lengths, which are varied between 2.167 Å and 2.175 Å, are intermediate between typical values for single (2.27 Å in P_2H_4) and double (2.04 Å in P_2H_2) bonds. Galeev and Boldyrev [86] showed that the out-of-plane distortion in the isolated P_6 is due to the pseudo Jahn–Teller (PJT) effect resulting from vibronic coupling of HOMO-1 (e_{2g}) and LUMO (e_{2u}). The planarization of the P_6 ring in the above-mentioned $\{(\eta^5-Me_5C_5)Mo\}2(\mu,\eta^6-P_6)$ triple-decker sandwich complex is due to the suppression of the PJT effect because of the occupation of the LUMO upon coordination to Mo atoms [87].

Solid-state compounds containing heavier congeners such as As_4^{2-}, As_5^-, As_6, Sb_4^{2-}, Sb_5^-, Bi_4^{2-} have been reported in the literature [76–81]. The As_4^{2-} dianion was found from the extended X-ray absorption fine structure (EXAFS) studies of K-As alloy [76]. Scherer and coworkers [78] synthesized triple-decker complexes $[(\eta^5-As_5)Fe(\eta^5-C_5Me_4R)]$ (R = Me and Et) and $[(\eta^5-C_5H_5)Fe(\mu,\eta^5-As_5)Fe(\eta^5-C_5Me_5)]PF_6$ containing the aromatic As_5^- pentagon [80] and the triple-decker sandwich $\{(\eta^5-EtC_5H_4)Mo\}_2(\mu,\eta^6-As_6)$

containing planar As_6 hexagon. Critchlow and Corbett [79] reported that the planar square Sb_4^{2-} dianion was a part of $(2,2,2\text{-crypt-}K^+)_2Sb_4^{2-}$ salt. Rösler and coworkers [80] synthesized and characterized the crystal structures of two triple-decker sandwich complexes $[(\eta^5-1,2,3\text{-}t\text{Bu}_3C_5H_2)Mo(\mu,\eta^5-Sb_5)Mo(\eta^5-1,2,3\text{-}t\text{Bu}_3C_5H_2)]$ and $[(\eta5\text{-}1,2,4\text{-}t\text{Bu}_3C_5H_2)Mo(\mu,\eta^5-Sb_5)Mo(\eta^5-1,4\text{-}t\text{Bu}_2\text{-}2\text{-MeC}_5H_2)]$ containing slightly distorted the antimony pentagon ring. Cisar and Corbett [81] reported synthesis of the 2,2,2-crypt-potassium tetrabismuthide(2-), $(C_{18}H_{36}N_2O_6K^+)_2Bi_4^{2-}$ compound containing a perfect planar square Bi_4^{2-} dianon.

Valence isoelectronic to P_4^{2-} species such as S_4^{2+}, Se_4^{2+} and Te_4^{2+} are well characterized both experimentally and theoretically [88–91]. All three dications were found to be perfect squares with bond length 1.988–2.014 Å (S_4^{2+}), 2.247–2.288 Å (Se_4^{2+}), and 2.660–2.699 Å (Te_4^{2+}), which are in the right range for aromatic systems. The smallest congener O_4^{2+} dianion was predicted theoretically by Elliott and Boldyrev [92], but has not yet experimentally observed.

There is another set of aromatic Si_5^{6-}, Sn_5^{6-}, Pb_5^{6-} anions, which are valence isoelectronic to $C_5H_5^-$ and P_5^-. In 1986, Schnering and coworkers [93] reported the first Li_8MgSi_6 compound containing an aromatic silicon Si_5^{6-} building block. More recently, Todorov and Sevov [94] synthesized similar compounds Na_8BaSn_6, Na_8EuSn_6, and Na_8BaPb_6, containing aromatic pentagonal rings of Sn_5^{6-} and Pb_5^{6-}, with isolated anions of Sn^{4-} and Pb^{4-} located throughout the lattice. Sergeeva and Boldyrev [24] performed the AdNDP analysis for both isolated Sn_5^{6-}, as well as for the embedded Sn_5^{6-} cluster in Na_8BaSn_6. They found that the bonding pattern in this anion is similar to that in $C_5H_5^-$ and to P_5^-. The planar pentagonal structure of the Sn_5^{6-} and Pb_5^{6-} anions in those four compounds show that aromaticity governs the atomic arrangements even in such complicated solids, as the crystal structure is formed of aromatic Si_5^{6-}, $Sn_5^{6,-}$ and Pb_5^{6-} clusters rather than six-atomic building blocks, as the stoichiometries of the compounds may suggest.

As we saw so far, there are quite a few chemical compounds synthesized in inorganic chemistry, where aromatic building blocks do follow analogy and form planar cyclic structures formally valence isoelectronic to prototypical organic aromatic molecules $C_4H_4^{2-}$, $C_5H_5^-$, and C_6H_6. There are other known examples of that in chemistry [95–99]. However, it is not always the case. In fact, Si, Ge, Sn, and Pb analogs of aromatic benzene and cyclopentadienyl anion, and of antiaromatic cyclobutadiene and octatetraene do not follow the structural pattern of the aromatic and antiaromatic hydrocarbons, respectively [25].

14.4 "Unconventional" Aromatic/Antiaromatic Inorganic Molecules

Although the search for aromatic/antiaromatic inorganic molecules using the valence isoelectronic approach was successful in chemistry, the variety of atoms and AOs provides much more opportunities for aromaticity/antiaromaticity in inorganic chemistry than we can find using the above-mentioned analogy.

We loosely call inorganic molecules as unconventional aromatic/antiaromatic molecules if they do not have organic analogs. While aromaticity/antiaromaticity in organic chemistry was primarily based on π-bonding, in inorganic chemistry we have more varieties of aromaticity/antiaromaticity. Specifically, we recognize the presence of multifold (σ-, π-, δ-, ϕ-) aromaticity, multifold (σ-, π-, δ-, ϕ-) antiaromaticity, or conflicting aromaticity. One may expect only σ-aromaticity or σ-antiaromaticity if only s-AOs are involved in delocalized bonding. If p-AOs are involved in delocalized bonding in addition to s-AOs, σ-tangential (σ_t-), σ-radial (σ_r-), and π-aromaticity/antiaromaticity could occur. One can expect, in this case, a multiple (σ- and π-) aromaticity, multiple (σ- and π-) antiaromaticity, and conflicting aromaticity (simultaneous σ-aromaticity and π-antiaromaticity or σ-antiaromaticity and π-aromaticity). Things are getting more complicated when d-AOs are involved in delocalized chemical bonding in addition to s- and p-AOs. One can expect σ-tangential (σ_t-), σ-radial (σ_r-), π-tangential (π_t-), π-radial (π_r-), and δ-aromaticity/antiaromaticity. Because of that, there can be multiple (σ-, π-, and δ-) aromaticity, multiple (σ-, π-, and δ-) antiaromaticity, and conflicting aromaticity (simultaneous aromaticity and antiaromaticity among the three σ-, π-, and δ-types). Finally, if f-AOs are involved in delocalized chemical bonding in addition to s-AOs, p-AOs, and d-AOs, σ-tangential (σ_t-), σ-radial (σ_r-), π-tangential (π_t-), π-radial (π_r-), δ-tangential (δ_t-), δ-radial (δ_r-), and ϕ-aromaticity/antiaromaticity could occur. One could expect multiple (σ-, π-, δ-, and ϕ-) aromaticity, multiple (σ-, π-, δ-, and ϕ-) antiaromaticity, as well as conflicting aromaticity (simultaneous aromaticity and antiaromaticity among the four σ-, π-, δ-, ϕ-types). Detailed discussions on the counting rules for aromaticity and antiaromaticity with pictorial representation for all these complicated cases have been recently reviewed [17].

14.4.1
σ-Aromatic and σ-Antiaromatic Species

Cations M_3^+ (M = Li … Cs) and H_3^+ are the simplest σ-aromatic ($n = 0$ for the $4n + 2$ rule) systems. Aromaticity in the Li_3^+ was initially assessed by Alexandrova and Boldyrev [100]. It has only one completely delocalized σ-molecular bonding orbital, which makes this cation aromatic (Figure 14.4).

Let us assess aromaticity in Li_3^+. First, this cation has a perfect triangular structure with all bonds being equal. Second, it has two σ-electrons and thus it satisfies the $4n + 2$ rule for $n = 0$. Third, the resonance energy in Li_3^+ was evaluated to be quite significant of 36 kcal mol^{-1} [100]. The σ-resonance energy in the Li_3^+ cation can be calculated as the energy of the reaction:

$$Li_3Cl(C_{2v}, {}^1A_1) \rightarrow Li_2 + LiCl$$

where Li_2 and LiCl are reference classical molecules. As it is inconvenient to work with a cation, the Li_3Cl neutral molecule, containing the Li_3^+ cation and the Cl^- anion, was used. The Cl^- anion only slightly perturbs the σ-aromatic HOMO in Li_3Cl when compared to the isolated Li_3^+ cation, as can be seen in Figure 14.4. Fowler and coworkers [101], in their recent article, calculated current density maps

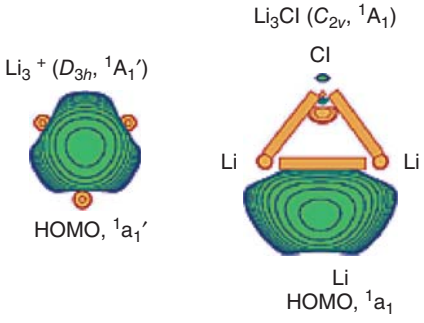

Figure 14.4 Highest occupied molecular orbitals of global minimum structures of the Li_3^+ cation and Li_3Cl. Point group symmetries and overall spectroscopic states are shown in parenthesis. (Reprinted with permission from Ref. [100]. Copyright 2003 American Chemical Society.)

for Li_3^+ and H_3^+ ions and on the basis of these maps they concluded that H_3^+ is σ-aromatic, but Li_3^+ is nonaromatic on this criterion. According to $NICS_{zz}$ values calculated at $z = 0.0$, both cations are aromatic as these values are negative: −8.8 ppm for Li_3^+ and −36.9 ppm for H_3^+. Similarly, one can assign Na_3^+ and K_3^+ as σ-aromatic, too.

The M_3^- (M = Li, Na, K, Rb, Cs) anions are examples of σ-antiaromatic systems with 4 σ-electrons [100]. Singlet M_3^- anions at the D_{3h} symmetry have the $1a_1'^2 1e'^2$ electron configuration and their triangular structures undergo Jahn–Teller distortion. Indeed, M_3^- anions are linear. Two valence MOs can be localized into two 2c-2e bonds and the linear structure of M_3^- can be considered as a classical structure. That is similar to the antiaromatic cyclobutadiene, where canonical MOs can be localized into two double and two single carbon–carbon bonds, producing a classical structure.

The series of planar transition-metal clusters Au_5Zn^+, Au_6, Cu_7^{3-}, Ag_7^{3-}, Au_7^{3-}, Au_6Y^-, Cu_7Sc, Cu_7Y, Ag_7Y, Au_7Y are remarkable examples, where σ-aromaticity governs the structure of the transition-metal clusters [102–105]. They all have either wheel-type structure (Au_5Zn^+, Cu_7Y, Ag_7Y, Au_7Y) or ring-type structure (Au_6, Cu_7^{3-}, Ag_7^{3-}, Au_7^{3-}). It was shown [102] that the Au_7Zn^+ cation as well as Au_6 have six σ-electrons and thus are σ-aromatic ($4n + 2$ rule, $n = 1$). The Cu_7Sc , Cu_7Y, Ag_7Y, Au_7Y, Cu_7^{3-}, Ag_7^{3-}, Au_7^{3-}, Au_6Y^- clusters have ten σ-electrons and thus are σ-aromatic ($4n + 2$ rule, $n = 2$), too. The calculated NICS(1) of the Cu_7Sc cluster is −10.8 ppm and of the Cu_7^{3-} cluster NICS(1) = −11.6 ppm also confirm the presence of aromaticity.

14.4.2
σ-/π-Aromatic, σ-/π-Antiaromatic, and Species with σ-/π-Conflicting Aromaticity

The rationalization of the square structure of the Al_4^{2-} cluster helped advance the concepts of aromaticity to all-metal systems in 2001 [106, 107]. The initial goal

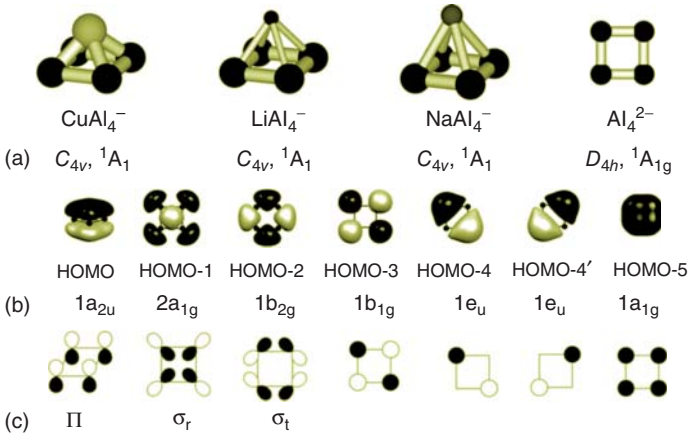

Figure 14.5 (a) The global minimum structures of the MAl_4^- clusters (M = Cu, Li, Na) and the isolated Al_4^{2-} cluster. (b) Valence canonical molecular orbitals (CMOs) of the isolated Al_4^{2-} cluster. (c) Schematic representation of valence CMOs as linear combinations of four $3p_z$ atomic orbitals (AOs) comprising highest occupied molecular orbital (HOMO), four 3p-radial AOs (HOMO-1), four 3p-tangential (HOMO-2), as well as four different linear combinations of 3s AOs (HOMO-3, HOMO-4, HOMO-4′, HOMO-5). (Reprinted with permission from Ref. [24]. Copyright 2012 Copyright Clearance Center.)

was to interpret the photoelectron spectra of three $CuAl_4^-$, $LiAl_4^-$, and $NaAl_4^-$ clusters recorded by Lai-Sheng Wang and coworkers [106]. Computational search for the global minimum by Kuznetsov and Boldyrev [106] revealed that of all MAl_4^- clusters (M = Cu, Li, Na) are of square pyramidal shape (Figure 14.5a) consisting of a metal cation M^+ coordinated to a square planar Al_4^{2-} aluminum unit.

Furthermore, the search for the global minimum of the metastable Al_4^{2-} (it is not stable with respect to an electron detachment) cluster revealed that the planar square structure was indeed the lowest in energy. The AdNDP analysis shows that four canonical MOs of Al_4^{2-} can be transformed to four lone pairs with one located on every aluminum atom. Three other canonical MOs stay as four-centered bonds. The HOMO is clearly a completely bonding π-MO. Two electrons on that MO make this cluster π-aromatic. The HOMO-1 is a completely bonding MO formed by p_σ-radial AOs. Two electrons on that MO make this cluster σ_r-aromatic. The HOMO-2 is a completely bonding MO formed by p_σ-tangential AOs. Two electrons on that MO make this cluster σ_t-aromatic. Thus, this is an example of a system with double (σ_r-, σ_t- and π-) aromaticity.

Two years later, the joint photoelectron and theoretical study of the $Li_3Al_4^-$ cluster showed [108] that this cluster contains the approximately rectangular Al_4^{4-} cluster, which was reported to be an example of the net all-metal antiaromatic species (Figure 14.6).

The controversy over the net aromaticity or antiaromaticity of Al_4^{4-} inside of $Li_3Al_4^-$ generated a significant discussion in the literature. Everybody agrees that Al_4^{4-} is σ-aromatic, with four σ-electrons (two electrons occupying σ-radial MO

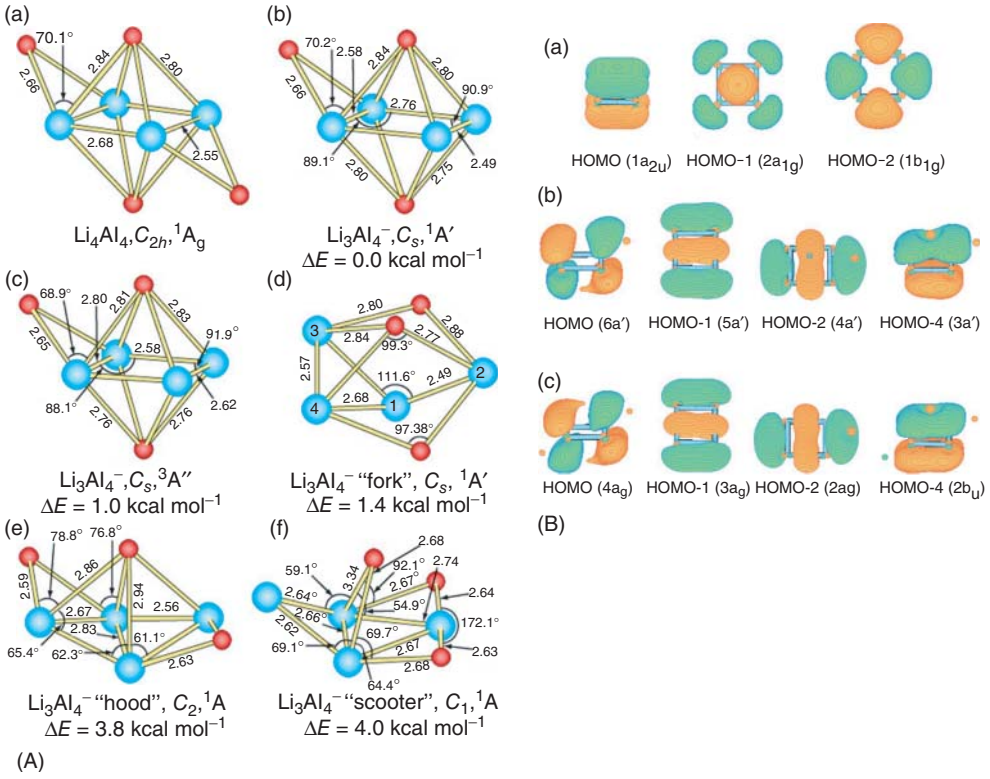

Figure 14.6 (A) Optimized structures of Li_4Al_4 and $Li_3Al_4^-$; bond lengths in angstroms. (a) Li_4Al_4. (b) Capped octahedral singlet $Li_3Al_4^-$ (C_S, $^1A'$). (c) Capped octahedral triplet $Li_3Al_4^-$ (C_S, $^3A''$). (d) "Fork" $Li_3Al_4^-$ (C_S, $^1A'$). (e) "Hood" $Li_3Al_4^-$ (C_2, ^1A). (f) "Scooter" $Li_3Al_4^-$ (C_1, ^1A). The structural parameters, given in Å and degrees, are at the B3LYP/6-311+G* level of theory. The relative energies for the isomers of $Li_3Al_4^-$ are at the CCSD(T)/6-311+G(2df) level of theory. (B) Molecular orbital pictures. (a) Al_4^{2-} (D_{4h}, $^1A_{1g}$); (b) capped octahedral singlet $Li_3Al_4^-$ (C_S, $^1A'$); (c) Li_4Al_4 (C_{2h}, ^1A_g). (Reprinted with permission from Ref. [108]. Copyright 2003, American Association for the Advancement of Science.)

and two electrons occupying σ-tangential MO, leading to $\sigma_r^- + \sigma_t^-$ aromaticity), similarly to Al_4^{2-}, and that it is π-antiaromatic, as it has 4 π-electrons. Thus, this system is an example of conflicting aromaticity (σ-aromatic and π-antiaromatic). Our view is that because the Al_4^{4-} is rectangular, antiaromaticity takes over aromaticity, and, therefore, this cluster is antiaromatic.

Small and medium-size boron clusters are excellent examples where double aromaticity, double antiaromaticity, and conflicting aromaticity were shown to be able to explain their structure, stability, and other molecular properties [19, 109, 110]. The following chemical bonding model was proposed for planar or quasi-planar boron clusters: all peripheral boron atoms form 2c-2e σ-bonds, while the atoms inside of the peripheral ring are bound to each other and to

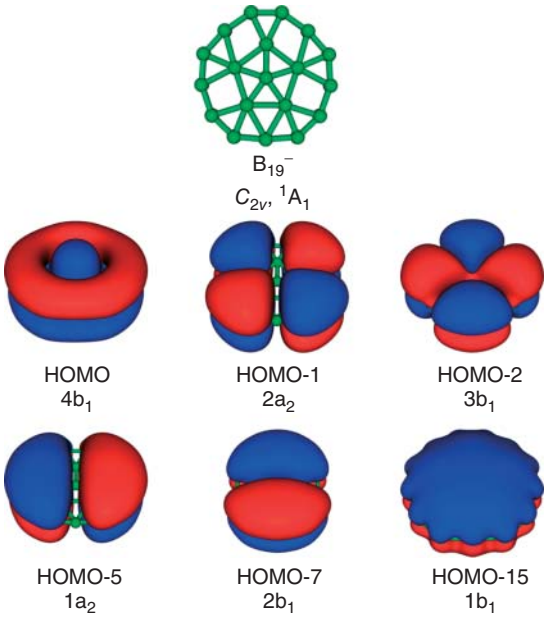

Figure 14.7 The global minimum structure and canonical molecular orbitals of B_{19}^-. Five canonical molecular orbitals, HOMO-1, HOMO-2, HOMO-5, HOMO-7, and HOMO-15. The sum of HOMO and HOMO-15 contribute to the π-bonding between the inner pentagonal B_6 ring and the outer B_{13} ring, which results in an orbital delocalized over the peripheral atoms with no electron density over the pentagonal B_6 unit and the difference of HOMO and HOMO-15 is responsible for the π-delocalized bonding in the B_6 unit.

the peripheral atoms through delocalized σ- and π-bonding. When the number of delocalized electrons satisfies the $4n + 2$ rule, the system is either σ- or π-aromatic; when the number of delocalized electrons satisfy the $4n$ rule, the system is σ- or π-antiaromatic. If the number of σ-electrons satisfies the $4n + 2$ rule, whereas the number of π-electrons satisfies the $4n$ rule or vice versa, those cases are examples of conflicting aromaticity. We discuss here only one example: the B_{19}^- cluster [111]. The chemical bonding in planar or quasi-planar boron clusters can be found elsewhere [19, 110].

It was found that the global minimum of B_{19}^- is a planar type structure with 1 boron atom at the center, surrounded by 5 boron atoms in the first coordination sphere and 13 boron atoms in the second coordination sphere (Figure 14.7) [111].

This structure was confirmed experimentally through a good agreement between experimental and theoretical VDEs. The CMO analysis, together with the AdNDP analysis, proves that it consists of two concentric π-aromatic systems: the 10 π-electron system describing the bonding between the inner and outer rings and the central B_6 unit with 2 π-electrons, each satisfying the $4n + 2$ Hückel's rule independently (Figure 14.7). This kind of formation of concentric π-aromatic systems is also known for coronene and isocoronene [59, 112]. The presence of

the two concentric π-bonding rings in the last two molecules is consistent with the ring currents recovered by Fowler and coworkers [113]. The σ-bonding in B_{19}^- consists of 13 peripheral 2c-2e B–B σ-bonds, six 3c-2e σ-bonds responsible for bonding between B_6 and B_{13} fragments, two 3c-2e B–B σ-bonds responsible for bonding inside of the B_6 fragment, and two 4c-2e B–B σ-bonds responsible for bonding between B_6 and B_{13} fragments [110]. This delocalized σ- and π-bonding inside of the B_{13} ring is responsible for unprecedented internal rotation of the B_5 ring inside of the B_{13} ring discovered by Merino and Heine [114], which is called *molecular Wankel motor*.

14.4.3 σ-/π-/δ-Aromatic, σ-/π-/δ-Antiaromatic, and Species with σ-/π-/δ-Conflicting Aromaticity

The potential existence of δ-aromaticity/antiaromaticity and ϕ-aromaticity/antiaromaticity was postulated by Boldyrev and Wang in 2005 [18].

Wang and coworkers [115] discovered the first d-orbital aromaticity in the suboxide $M_3O_9^-$ and $M_3O_9^{2-}$ (M = Mo and W) clusters. Because the oxidation state of oxygen is −2 in these suboxides, the average formal oxidation of Mo or W is +5.66 for singly charged anions and +5.33 for doubly charged anions. Therefore, one and two extra electrons are available for the direct metal–metal bonding in $M_3O_9^-$ and $M_3O_9^{2-}$, respectively. Wang and coworkers [115] showed that, indeed, singly occupied molecular orbital (SOMO) and HOMO are a_1 symmetry completely bonding MO formed by in-plane d-AOs of M in $M_3O_9^-$ and $M_3O_9^{2-}$, respectively. Thus, the singly charged anions are 1/2 σ-aromatic (one-electron-occupying delocalized MO) and doubly charged anions are σ-aromatic (two-electron-occupying delocalized MO). Calculated NICS values at the center of $Mo_3O_9^{2-}$ (−21.5 ppm) and $W_3O_9^{2-}$ (−20.5 ppm) and estimated resonance energy for $W_3O_9^-$ of 7.6 kcal mol^{-1} also confirm the presence of aromaticity.

The first examples of d-based double (σ- and π-) aromaticity were reported by Chi and Liu in bare X_3^- (X = Sc, Y, La) clusters [116]. According to their calculations, $2a_1'$- and $1a_2''$-MOs (both formed by d-AOs of transition-metal atoms) are responsible for delocalized bonding in equilateral triangular global minimum structures of X_3^-. The 2a′-MO is regarded as σ-delocalized MO and the $1a_2''$-MO is regarded as π-delocalized MO, which are responsible for their σ- and π-aromaticity, respectively.

The first species exhibiting δ-aromaticity reported in a joint experimental (photoelectronic spectroscopy) and theoretical study was found to be a $Ta_3O_3^-$ cluster [117]. Again, if we assign the oxidation state of −2 to oxygen, then the formal oxidation state of Ta is +1.66 and that leaves 10 electrons for the direct metal–metal bonding. The global minimum $Ta_3O_3^-$ structure has a singlet state with three Ta atoms forming equilateral triangle geometry and oxygen atoms occupying the bridge positions. The five MOs responsible for the delocalized metal–metal bonding can be classified as σ-, π-, and δ-MOs. However, the delocalized σ-bonding is canceled as the doubly degenerate bonding/antibonding-HOMO (4e′) and completely

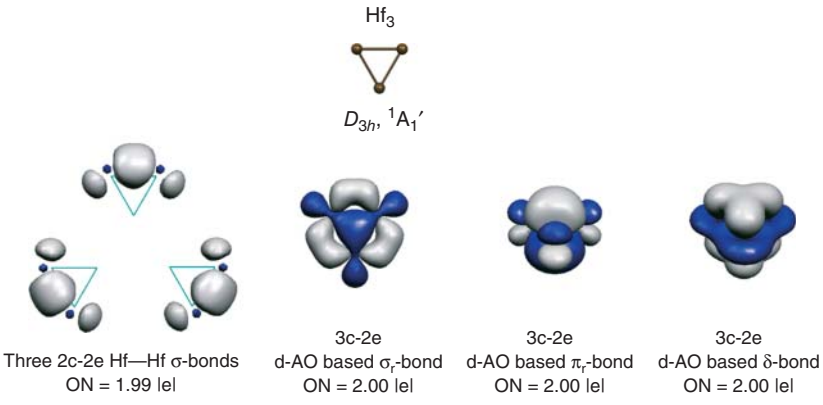

Figure 14.8 Geometric structure, three 2c-2e Hf–Hf σ-bonds, 3c-2e d-AO based σ_r-bond, 3c-2e d-AO based π_r-bond, and 3c-2e d-AO based δ-bond revealed by the AdNDP analysis at B3LYP/LANL2DZ for the triply σ-, π- and δ-aromatic Hf_3 cluster. (Reprinted with permission from Ref. [44]. Copyright 2010 Springer Berlin/Heidelberg.)

bonding HOMO-3 ($3a_1'$) are completely occupied, and, thus, the bonding character of HOMO-3 is canceled by the antibonding nature of HOMO. The HOMO-1 is completely bonding δ-MO and HOMO-2 is completely bonding π-MO, and, thus this cluster is doubly (δ- and π-) aromatic according to the $4n + 2$ rule for aromaticity in the cyclic systems with $n = 0$, applied separately to δ- and π-electrons.

Let us discuss in more detail the Hf_3 cluster in the lowest $^1A_1'$ (D_{3h}) state, which is the first example of triple (σ-, π- and δ-) aromaticity [118]. Although it was not established with certainty that the $^1A_1'$ (D_{3h}) state is a ground electronic state of Hf_3, it is certainly either a ground electronic state or a low-lying electronic state. Sergeeva *et al.* [17] performed the AdNDP analysis of the Hf_3 cluster for this state. Results of the analysis are shown in Figure 14.8.

According to this analysis, Hf_3 in the singlet electronic state has three 2c-2e Hf–Hf σ-bonds formed of hybrid 6s-, 5d-AOs and three completely delocalized bonds formed of pure d-AOs: one completely bonding 3c-2e d-radial-based σ-bond responsible for the presence of σ-aromaticity, one completely bonding 3c-2e d-radial-based π-bond responsible for the presence of π-aromaticity, and one completely bonding 3c-2e d-AO-based δ-bond responsible for the presence of δ-aromaticity in this cluster ($4n + 2$ rule for every kind of aromaticity for $n = 0$). The 3c-2e d-AO-based δ-bond is formed by the overlap of the d_{z^2} AO on each Hf atom. The triple aromaticity is consistent with the bond equalization and high symmetry of Hf_3. Tsipis *et al.* [119] obtained $NICS_{zz}$-scan curve for D_{3h}, $^1A_1'$ state of Hf_3, Ti_3 and Zr_3 clusters, and concluded that they all three are indeed triply (σ-, π- and δ-) aromatic in this state on the basis of magnetic criterion.

The unconventional aromaticity is important not only for bare metal clusters. Recently, a remarkable compound containing $[Pd_4(\mu_4\text{-}C_9H_9)(\mu_4\text{-}C_8H_8)]^+$ triple-decker sandwich complex was synthesized and characterized [120]. The Pd_4 core

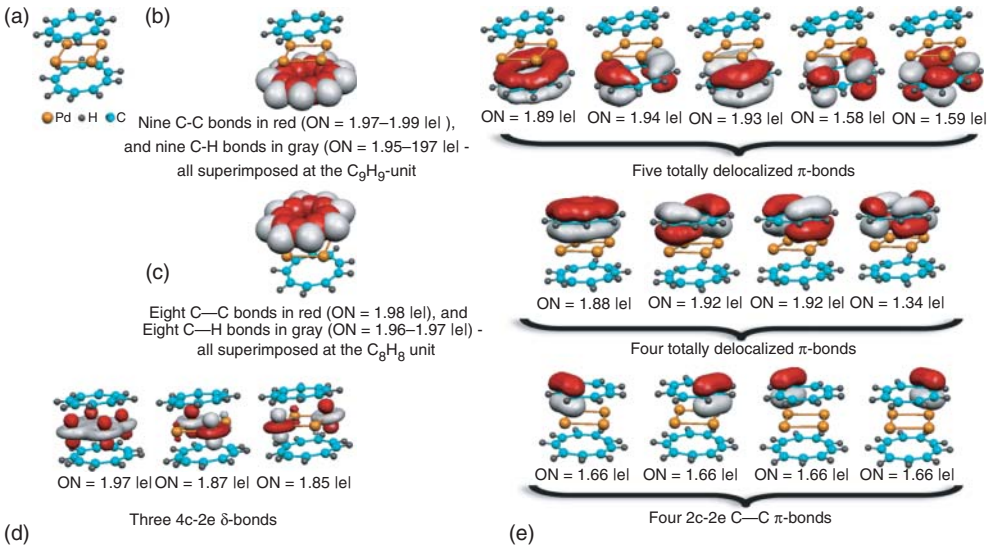

Figure 14.9 Experimental structure of the $[Pd_4(\mu_4\text{-}C_9H_9)(\mu_4\text{-}C_8H_8)]^+$ sandwich complex. (a) The chemical bonding picture of the complex obtained via the AdNDP method; (b) bonds recovered on the $C_9H_9^-$ unit; (c) bonds recovered on the C_8H_8 unit; (d) bonds recovered on the Pd_4^{2+} unit; (e) alternative representation of the π-bonding of the C_8H_8 unit presented in (c) in terms of four 2c-2e C–C π-bonds. (Reprinted with permission from Ref. [63]. Copyright 2010 Royal Society of Chemistry.)

was found to be an almost perfect square and that makes this core a suspect for aromaticity. Sergeeva and Boldyrev [63] performed the AdNDP analysis of chemical bonding in the whole $[Pd_4(\mu_4\text{-}C_9H_9)(\mu_4\text{-}C_8H_8)]^+$ triple-decker sandwich complex. Their results are shown in Figures 14.9 and 14.10.

They initially performed the user-directed search for bonding elements on each of the $C_9H_9^-$, C_8H_8, and Pd_4^{2+} building blocks of the $[Pd_4(\mu_4\text{-}C_9H_9)(\mu_4\text{-}C_8H_8)]^+$ complex. The AdNDP analysis revealed nine 2c-2e σ-bonds and nine 2c-2e C–H σ-bonds in the $C_9H_9^-$ block with ON = 1.97–1.99 |e| and 1.95–1.97 |e|, respectively. Five 9c-2e delocalized π-bonds with ONs lying within the 1.58–1.94 |e| range, which are responsible for the π-aromaticity of this anion, were also found. That is consistent with the equalization of the C–C bonds and the rather high symmetry for this block. According to the AdNDP analysis, the C_8H_8 block has eight 2c-2e σ-bonds and eight 2c-2e C–H σ-bonds with ONs 1.98 |e| and within the 1.96–1.97 |e| range, respectively. It also revealed four 8c-2e delocalized π-bonds with ONs of 1.34–1.92 |e| range, which are responsible for π-antiaromaticity in this unit. That is consistent with the C–C bond alteration in this unit. The AdNDP recovered in the Pd_4^{2+} block has four lone pairs on each palladium atoms based on 4d-AOs, with ONs lying within the range of 1.76–2.00 |e| and three 4c-2e delocalized δ-bonds with the ONs of 1.85–1.97 |e| range. Sergeeva and Boldyrev [63] concluded that the $[Pd_4(\mu_4\text{-}C_9H_9)(\mu_4\text{-}C_8H_8)]^+$ triple-decker sandwich complex consists of π-aromatic

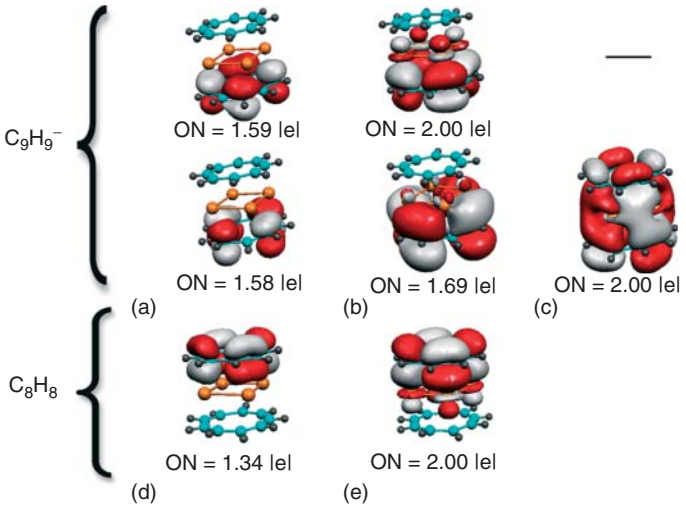

Figure 14.10 Variance of occupation numbers in the π-bonds with two nodal planes of the $C_9H_9^-$ (a, b, c) and C_8H_8 (d, e) building blocks of the sandwich complex in accordance with the number of centers a bond is allowed to be delocalized over. Delocalization is over: (a) $C_9H_9^-$; (b) $(C_9H_9^- + Pd_4^{2+})$; (c) $(C_9H_9^- + Pd_4^{2+} + C_8H_8)$; (d) C_8H_8; (e) $(C_8H_8 + Pd_4^{2+})$. (Reprinted with permission from Ref. [63]. Copyright 2010 Royal Society of Chemistry.)

$C_9H_9^-$ block, π-antiaromatic C_8H_8 block, and δ-aromatic Pd_4^{2+} block. However, they stated that the chemical bonding picture presented is only a zero-order model, because few bonding elements have ONs significantly lower than the ideal value of 2.00 |e|. Sergeeva and Boldyrev performed the user-directed AdNDP on larger fragments in order to go beyond the zero-order bonding model: $C_9H_9^- + Pd_4^{2+}$ and $C_8H_8 + Pd_4^{2+}$. Results of this AdNDP analysis are shown in Figure 14.10.

When the π-bond, which has a very low ON = 1.34 |e|, is allowed to be delocalized over the $C_8H_8 + Pd_4^{2+}$ fragment, its ON increases to 2.00 |e|. Thus, this extra delocalization bond is responsible for the partial covalent bonding between C_8H_8 and Pd_4^{2+} blocks. If the two π-bonds with low ON = 1.58 |e| and ON = 1.59 |e| are allowed to be delocalized over the $C_9H_9^- + Pd_4^{2+}$ fragment, the ON for the first one increases to 2.00 |e| and the second one increases to 1.69 |e|. The first bond, as in the previous case, is responsible for partial covalent bonding between $C_9H_9^-$ and Pd_4^{2+} blocks. On the other hand, the small increase in the ON for the second bond shows that this bond is delocalized over the whole cluster. When we allow the π-bond with ON = 1.59 |e| to be delocalized over the whole $C_9H_9^- + Pd_4^{2+} + C_8H_8$ cluster, the ON increases to the ideal value of 2.00 |e|. It means that this bond is responsible for partial covalent bonding between all three building blocks, including small direct covalent bonding between $C_9H_9^-$ and C_8H_8. The partial covalent bonding found between the two upper and bottom $C_9H_9^-$ and C_8H_8 building blocks and the Pd_4^{2+} block is the δ-back-donation, which similar to the π-back-donations reported by

Rayón and Frenking [121] in bis(benzene)chromium and by Diaconescu *et al.* [122] in the inverted $(\mu\text{-}C_6H_6)[U(NH_2)_2]_2$ sandwich complex.

While the largest success of the unconventional aromaticity is certainly in the realm of bare metal clusters, the synthesis and characterization of the compounds containing $[Pd_4(\mu_4\text{-}C_9H_9)(\mu_4\text{-}C_8H_8)]^+$ complex clearly demonstrated the importance of the delocalized δ-bonding and δ-aromaticity in inorganic, organometallic, and coordination chemistry.

14.5 Summary and Perspectives

Our quick review has shown that prototypical organic molecules can serve as models for predicting and identifying corresponding valence isoelectronic inorganic ''conventional'' aromatic molecules. Numerous inorganic aromatic P_4^{2-}, P_5^-, As_5^-, S_4^{2+}, Se_4^{2+}, Te_4^{2+}, Si_5^{6-}, Sn_5^{6-}, and Pb_5^{6-} and other molecules are good examples of that. Yet, because the overlap between p-AOs is significantly diminished from C to P, As, S, Se, Te, and so on, it makes this direct copying on inorganic molecules sometimes problematic. The planar hexagonal P_6 molecule, which is a valence isoelectronic analog of benzene, is not a global minimum structure for this stoichiometry and it is not even a local minimum. Another problem for using the isoelectronic principle is the difference in the electronegativity of atoms. The best example is the borazine ($B_3N_3H_6$), which is not an aromatic molecule; it is also isoelectronic to benzene.

Aromaticity in inorganic chemistry is significantly much more diverse than in organic chemistry, where it is primarily confined to π-aromaticity/antiaromaticity. As s-, p-, d-, and f-AOs can participate in delocalized bonding in cyclic inorganic systems, there is a possibility for multifold aromaticity/antiaromaticity and conflicting aromaticity involving σ-, π-, δ-, and ϕ-types. We call these kinds of chemical species unconventional, as they do not have analogs among aromatic organic molecules. We showed that the Hf_3 cluster has threefold (σ-, π-, δ-) aromaticity in its lowest singlet state. We also presented an example of the $[Pd_4(\mu_4\text{-}C_9H_9)(\mu_4\text{-}C_8H_8)]^+$ triple-decker sandwich complex, which is the first solid-state compound containing δ-aromatic Pd_4 planar square ring. Thus, δ-aromaticity was extended into the solid-state coordination chemistry. Clearly, advancement of aromaticity in transition-metal compounds will be the next frontier in inorganic chemistry.

As multinuclear transition-metal clusters were found to be more catalytically active that mononuclear complexes, we believe that catalysis also could be a new area of advancement of aromaticity and antiaromaticity concepts for explaining catalytic activity. Complex active sites of enzymes could be another area where aromaticity and antiaromaticity may be useful.

From our point of view, delocalized bonding and, thus, aromaticity and antiaromaticity will be even more important in inorganic chemistry than in organic chemistry.

Acknowledgments

This work was supported by the National Science Foundation CHE-1057746. Computer time from the Center for High Performance Computing at Utah State University is gratefully acknowledged. An allocation of computer time from the Center for High Performance Computing at the University of Utah is also gratefully acknowledged.

References

1. Kekulé, A. (1865) *Bull. Soc. Chim. Fr. (Paris)*, **3**, 98–110.
2. Kekulé, A. (1866) *Bull. Acad. Roy. Belg.*, **119**, 551–563.
3. Kekulé, A. (1866) *Ann. Chem.*, **137**, 129–136.
4. IUPAC. in *Compendium of Chemical Terminology*, 2nd edn (the ''Gold Book'') (Compiled by A.D. McNaught and A. Wilkinson). Blackwell Scientific Publications, Oxford (1997), XML on-line corrected version: *Error! Hyperlink reference not valid.*, Created by M. Nic, J. Jirat, and B. Kosata; updates compiled by A. Jenkins, ISBN: 0-9678550-9-8, doi: 10.1351/goldbook
5. Hückel, E. (1931) *Z. Phys.*, **70**, 204–286.
6. Hückel, E. (1938) *Grundzüge der Theorie ungesättiger und aromatischer Verbindungen*, Verlag Chem, Berlin, pp. 77–85.
7. Breslow, R. (1965) *Chem. Eng. News*, **43**, 90–99.
8. Breslow, R. (1973) *Acc. Chem. Res.*, **6**, 393–398.
9. Dewar, M.J.S. (1979) *Bull. Soc. Chim. Belg.*, **88**, 957–967.
10. Dewar, M.J.S. and McKee, M.L. (1980) *Pure Appl. Chem.*, **52**, 1431–1441.
11. Dewar, M.J.S. (1984) *J. Am. Chem. Soc.*, **106**, 669–682.
12. Cremer, D. (1988) *Tetrahedron*, **44**, 7427–7454.
13. Chandrasekhar, J., Jemmis, E.D., and Schleyer, P.v.R. (1979) *Tetrahedron Lett.*, **20**, 3707–3710.
14. Eicher, T. and Hauptmann, S. (2003) *The Chemistry of Heterocycles: Structure, Reactions, Syntheses, and Applications*, 2nd edn, Wiley-VCH Verlag GmbH.
15. Balaban, A.T. (2009) *Top. Heterocycl. Chem.*, **19**, 203–246.
16. Balaban, A.T., Oniciu, D.C., and Katritzky, A.R. (2004) *Chem. Rev.*, **104**, 2777–2812.
17. Sergeeva, A.P., Averkiev, B.B., and Boldyrev, A.I. (2010) in *Metal-Metal Bonding*, Structure and Bonding Book Series, Vol. 136 (ed. G. Parkin), Springer-Verlag, Berlin/Heidelberg, pp. 275–306.
18. Boldyrev, A.I. and Wang, L.S. (2005) *Chem. Rev.*, **105**, 3716–3757.
19. Alexandrova, A.N., Boldyrev, A.I., Zhai, H.J., and Wang, L.S. (2006) *Coord. Chem. Rev.*, **250**, 2811–2866.
20. Tsipis, C.A. (2005) *Coord. Chem. Rev*, **249**, 2740–2762.
21. Tsipis, C.A. (2010) in *Metal-Metal Bonding*, Structure and Bonding Book Series, Vol. 136 (ed. G. Parkin), Springer, Berlin/Heidelberg, pp. 217–274.
22. Zubarev, D.Yu., Sergeeva, A.P., and Boldyrev, A.I. (2009) in *Chemical Reactivity Theory: A Density Functional View* (ed. P.K. Chattaraj), CRC Press, Taylor & Francis Group, New York, pp. 439–452.
23. Zubarev, D.Yu. and Boldyrev, A.I. (2009) in *Computational Inorganic and Bioinorganic Chemistry* (eds E.I. Solomon, R.A. Scott, and R. Bruce King), John Wiley & Sons, Ltd, Chistester, pp. 551–562.
24. Sergeeva, A.P. and Boldyrev, A.I. (2010) in *Aromaticity and Metal Clusters* (ed. P.K. Chattaraj), CRC Press, Boca Raton, FL, pp. 55–68.

25. Galeev, T.R. and Boldyrev, A.I. (2011) *Annu. Rep. Prog. Chem. Sect. C: Phys. Chem.*, **107**, 124–147.
26. Krygowski, T.M., Cyrański, M.K., Czarnocki, Z., Häfelinger, G., and Katritzky, A.R. (2000) *Tetrahedron*, **56**, 1783–1796.
27. Wodrich, M.D., Wannere, C.S., Mo, Y., Jarowski, P.D., Houk, K.N., and Schleyer, P.v.R. (2007) *Chem. Eur. J.*, **13**, 7731–7744.
28. Kemnitz, C.R., Mackey, J.L., Loewen, M.L., Hargrove, J.L., Lewis, J.L., Hawkins, W.E., and Nielsen, A.F. (2010) *Chem. Eur. J.*, **16**, 6942–6949.
29. Mo, Y., Hiberty, P.C., and Schleyer, P.v.R. (2010) *Theor. Chem. Acc.*, **127**, 27–38.
30. Julg, A. and François, P. (1967) *Theor. Chim. Acta*, **8**, 249–259.
31. Kruszewski, J. and Krygowski, T.M. (1972) *Bull. Acad. Polon. Sci. Ser. Sci. Chim.*, **20**, 907–915.
32. Kruszewski, J. and Krygowski, T.M. (1972) *Tetrahedron Lett.*, **13**, 3839–3842.
33. Schleyer, P.v.R., Maerker, C., Dransfeld, A., Jiao, H., and van Eikema Hommes, N.J.R. (1996) *J. Am. Chem. Soc.*, **118**, 6317–6318.
34. Schleyer, P.v.R., Jiao, H., van Eikema Hommes, N.J.R., Malkin, V.G., and Malkina, O.L. (1997) *J. Am. Chem. Soc.*, **119**, 12669–12670.
35. Schleyer, P.v.R., Manoharan, M., Wang, Z.-X., Kiran, B., Jiao, H., Puchta, R., and van Eikema Hommes, N.J.R. (2001) *Org. Lett.*, **3**, 2465–2468.
36. Jusélius, J. and Sundholm, D. (1999) *Phys. Chem. Chem. Phys.*, **1**, 3429–3435.
37. Jusélius, J., Sundholm, D., and Gauss, J. (2004) *J. Chem. Phys.*, **121**, 3952–3963.
38. Coriani, S., Lazzeretti, P., Malagoli, M., and Zanasi, R. (1994) *Theor. Chim. Acta*, **89**, 181–192.
39. Fowler, P.W., Steiner, E., Zanasi, R., and Cadioli, B. (1999) *Mol. Phys.*, **96**, 1099–1108.
40. Steiner, E. and Fowler, P.W. (2001) *Chem. Commun.*, **21**, 2220–2221.
41. Steiner, E. and Fowler, P.W. (2001) *J. Phys. Chem. A*, **105**, 9553–9562.
42. Steiner, E. and Fowler, P.W. (2004) *Phys. Chem. Chem. Phys.*, **6**, 261–272.
43. Heine, T., Schleyer, P.v.R., Corminboeuf, C., Seifert, G., Reviakine, R., and Weber, J. (2003) *J. Phys. Chem. A*, **107**, 6470–6475.
44. Cernusak, I., Fowler, P.W., and Steiner, E. (2000) *Mol. Phys.*, **98**, 945–953.
45. Steiner, E., Fowler, P.W., and Jennesskens, L.W. (2001) *Angew. Chem. Int. Ed.*, **40**, 362–366.
46. Fallah-Bagher-Shaidaei, H., Wannere, C.S., Corminboeuf, C., Puchta, R., and Schleyer, P.v.R. (2006) *Org. Lett.*, **8**, 863–866.
47. Bultinck, P., Ponec, R., and van Damme, S. (2005) *J. Phys. Org. Chem.*, **18**, 706–718.
48. Giambiagi, M., de Giambiagi, M.S., dos Santos Silva, C.D., and de Figueiredo, A.P. (2000) *Phys. Chem. Chem. Phys.*, **2**, 3381–3392.
49. Bultinck, P., Rafat, M., Ponec, R., van Gheluwe, B., Carbó-Dorca, R., and Popelier, P. (2006) *J. Phys. Chem. A*, **110**, 7642–7648.
50. Mandado, M., González-Moa, M.J., and Mosquera, R.A. (2007) *J. Comput. Chem.*, **28**, 127–136.
51. Cioslowski, J., Matito, E., and Solà, M. (2007) *J. Phys. Chem. A*, **111**, 6521–6525.
52. Mandado, M., Krishtal, A., Van Alsenoy, C., Bultinck, P., and Hermida-Ramon, J.M. (2007) *J. Phys. Chem. A*, **111**, 11885–11893.
53. Roy, D.R., Bultinck, P., Subramanian, V., and Chattaraj, P.K. (2008) *J. Mol. Struct. THEOCHEM*, **854**, 35–39.
54. Jiménez-Halla, J.O.C., Matito, E., Blancafort, L., Robles, J., and Solà, M. (2009) *J. Comput. Chem.*, **30**, 2764–2776.
55. Feixas, F., Jiménez-Halla, J.O.C., Matito, E., Poater, J., and Solà, M. (2010) *J. Chem. Theory Comput.*, **6**, 1118–1130.
56. Solà, M., Feixas, F., Jiménez-Halla, J.O.C., Matito, E., and Poater, J. (2010) *Symmetry*, **2**, 1156–1179.
57. Feixas, F., Matito, E., Duran, M., Poater, J., and Solà, M. (2011) *Theor. Chem. Acc.*, **128**, 419–431.

58. Zubarev, D.Yu. and Boldyrev, A.I. (2008) *Phys. Chem. Chem. Phys.*, **10**, 5207–5217.
59. Zubarev, D.Yu. and Boldyrev, A.I. (2008) *J. Org. Chem.*, **73**, 9251–9258.
60. Zubarev, D.Yu. and Boldyrev, A.I. (2009) *J. Phys. Chem. A*, **113**, 866–868.
61. Sergeeva, A.P. and Boldyrev, A.I. (2010) *Comments Inorg. Chem.*, **31**, 2–12.
62. Weck, P.F., Sergeeva, A.P., Kim, E., Boldyrev, A.I., and Czerwinski, K.R. (2011) *Inorg. Chem.*, **50**, 1039–1046.
63. Sergeeva, A.P. and Boldyrev, A.I. (2010) *Phys. Chem. Chem. Phys.*, **12**, 12050–12054.
64. Popov, I.A., Bozhenko, K.V., and Boldyrev, A.I. (2012) *Nano Res.*, **5**, 117–123.
65. Foster, J.P. and Weinhold, F. (1980) *J. Am. Chem. Soc.*, **102**, 7211–7218.
66. Weinhold, F. and Landis, C. (2005) *Valency and Bonding – A Natural Bond Orbital Donor-Acceptor Perspective*, Cambridge University Press, Cambridge.
67. Stock, A. and Pohland, E. (1926) *Berichte*, **59**, 2210–2215.
68. Boese, R., Maulitz, A.H., and Stellberg, P. (1994) *Chem. Ber.*, **127**, 1887–1890.
69. Jemmis, E.D. and Kiran, B. (1998) *Inorg. Chem.*, **37**, 2110–2116.
70. Fowler, P.W. and Steiner, E. (1997) *J. Phys. Chem. A*, **101**, 1409–1413.
71. Steuber, E.v., Elter, G., Noltemeyer, M., Schmidt, H.-G., and Meller, A. (2000) *Organomettalics*, **19**, 5083–5091.
72. Kraus, F., Aschenbrenner, J.C., and Korber, N. (2003) *Angew. Chem. Int. Ed.*, **42**, 4030–4033.
73. Scherer, O.J., Schwalb, J., Wolmershäuser, G., Kaim, W., and Gross, R. (1986) *Angew. Chem., Int. Ed. Engl.*, **25**, 363–364.
74. Urnezius, E., Brennessel, W.W., Cramer, C.J., Ellis, J.E., and Schleyer, P.v.R. (2002) *Science*, **295**, 832–843.
75. Scherer, O.J., Sitzmann, H., and Wolmershauser, G. (1985) *Angew. Chem., Int. Ed. Engl.*, **24**, 351–353.
76. Roziere, J., Seigneurin, A., Belin, C., and Michalowicz, A. (1985) *Inorg. Chem.*, **24**, 3710–3712.
77. Scherer, O.J., Blath, C., and Wolmershäuser, G. (1990) *J. Organometal. Chem.*, **387**, C21.
78. Scherer, O.J., Sitzmann, H., and Wolmershäuser, G. (1989) *Angew. Chem., Int. Ed. Engl.*, **28**, 212–213.
79. Critchlow, S.C. and Corbett, J.D. (1984) *Inorg. Chem.*, **23**, 770–774.
80. Breunig, H.J., Burford, N., and Rösler, R. (2000) *Angew. Chem. Int. Ed.*, **39**, 4148–4150.
81. Cisar, A. and Corbett, J.D. (1977) *Inorg. Chem.*, **16**, 2482–2487.
82. Kuznetsov, A.E., Zhai, H.J., Wang, L.S., and Boldyrev, A.I. (2002) *Inorg. Chem.*, **41**, 6062–6070.
83. Zhai, H.J., Wang, L.S., Kuznetsov, A.E., and Boldyrev, A.I. (2002) *J. Phys. Chem. A*, **106**, 5600–5606.
84. De Proft, F., Fowler, P.W., Havenith, R.W.A., Schleyer, P.v.R., Van Lier, G., and Geerlings, P. (2004) *Chem. Eur. J.*, **10**, 940–950.
85. Hiberty, P.C. and Volatron, F. (2007) *Heteroat. Chem.*, **18**, 129–134.
86. Galeev, T.R. and Boldyrev, A.I. (2011) *Phys. Chem. Chem. Phys.*, **13**, 20549–20556.
87. Ivanov, A.S., Bozhenko, K.V., and Boldyrev, A.I. (2012) *Inorg. Chem.*, **51**, 8868–8872.
88. Burford, N., Passmore, J., and Sanders, J.C.P. (1989) in *From Atoms to Polymers: Isoelectronic Analogies* (eds J.F. Liebman and A. Greenburg), Wiley-VCH Verlag GmbH, New York, pp. 53–108.
89. Klapotke, T. and Passmore, J. (1989) *Acc. Chem. Res.*, **22**, 234–240.
90. Beck, J. (1994) *Angew. Chem., Int. Ed. Engl.*, **33**, 163–168.
91. Beck, J. (1997) *Coord. Chem. Rev.*, **163**, 55–70.
92. Elliott, B.M. and Boldyrev, A.I. (2005) *J. Phys. Chem. A*, **109**, 236–239.
93. Nesper, R., Curda, J., and von Schnering, H.G. (1986) *J. Solid State Chem.*, **62**, 199–206.
94. Todorov, I. and Sevov, S.C. (2004) *Inorg. Chem.*, **43**, 6490–6494.
95. Li, X.-W., Xie, Y., Schreiner, P.R., Gripper, K.D., Crittendon, R.C., Campana, C.F., Schaefer, H.F., and Robinson, G.H. (1996) *Organometallics*, **15**, 3798–3803.
96. Xie, Y., Schreiner, P.R., Schaefer, H.F. III,, Li, X.-W., and Robinson, G.H.

(1996) *J. Am. Chem. Soc.*, **118**, 10635–10639.
97. Xie, Y., Schreiner, P.R., Schaefer, H.F. III,, Li, X.-W., and Robinson, G.H. (1998) *Organometallics*, **17**, 114–122.
98. Robinson, G.H. (1999) *Acc. Chem. Res.*, **32**, 773–782.
99. Wright, R.J., Brynda, M., and Power, P.P. (2006) *Angew. Chem. Int. Ed.*, **45**, 5953–5956.
100. Alexandrova, A.N. and Boldyrev, A.I. (2003) *J. Phys. Chem. A*, **107**, 554–560.
101. Havenith, R.W.A., De Proft, F., Fowler, P.W., and Geerlings, P. (2005) *Chem. Phys. Lett.*, **407**, 391–396.
102. Höltzl, T., Janssens, E., Veldeman, N., Veszpremi, T., Lievens, P., and Nguyen, M.T. (2008) *Chem. Phys. Chem.*, **9**, 833–838.
103. Höltzl, T., Veldeman, N., Veszpremi, T., Lievens, P., and Nguyen, M.T. (2009) *Chem. Phys. Lett.*, **469**, 304–307.
104. Lin, L., Lievens, P., and Nguyen, M.T. (2010) *J. Mol. Struct. THEOCHEM*, **943**, 23–31.
105. Lin, L., Höltzl, T., Gruene, P., Claes, P., Meijer, G., Fielicke, A., Lievens, P., and Nguyen, M.T. (2008) *Chem. Phys. Chem.*, **9**, 2471–2474.
106. Li, X., Kuznetsov, A.E., Zhang, H.-F., Boldyrev, A.I., and Wang, L.S. (2001) *Science*, **291**, 859–861.
107. Kuznetsov, A.E., Boldyrev, A.I., Li, X., and Wang, L.S. (2001) *J. Am. Chem. Soc.*, **123**, 8825–8831.
108. Kuznetsov, A.E., Birch, K.A., Boldyrev, A.I., Li, X., Zhai, H.J., and Wang, L.S. (2003) *Science*, **300**, 622–625.
109. Zhai, H.J., Alexandrova, A.N., Birch, K.A., Boldyrev, A.I., and Wang, L.S. (2003) *Angew. Chem. Int. Ed.*, **42**, 6004–6008.
110. Zubarev, D.Yu. and Boldyrev, A.I. (2007) *J. Comput. Chem.*, **28**, 251–268.
111. Huang, W., Sergeeva, A.P., Zhai, H.J., Averkiev, B.B., Wang, L.S., and Boldyrev, A.I. (2010) *Nat. Chem.*, **2**, 202–206.
112. Popov, I.A. and Boldyrev, A.I. (2012) *Eur. J. Org. Chem.*, **18**, 3485–3491.
113. Ciesielski, A., Cyrański, M.K., Krygowski, T.M., Fowler, P.W., and Lillington, M. (2006) *J. Org. Chem.*, **71**, 6840–6845.
114. Jiménez-Halla, J.O.C., Islas, R., Heine, T., and Merino, G. (2010) *Angew. Chem. Int. Ed.*, **49**, 5668–5671.
115. Huang, X., Zhai, H.J., Kiran, B., and Wang, L.S. (2005) *Angew. Chem. Int. Ed.*, **44**, 7251–7254.
116. Chi, X.X. and Liu, Y. (2007) *Int. J. Quant. Chem.*, **107**, 1886–1896.
117. Zhai, H.J., Averkiev, B.B., Zubarev, D.Y., Wang, L.S., and Boldyrev, A.I. (2007) *Angew. Chem. Int. Ed.*, **46**, 4277–4280.
118. Averkiev, B.B. and Boldyrev, A.I. (2007) *J. Phys. Chem. A*, **111**, 12864–12866.
119. Tsipis, A.C., Depastas, I.G., Karagiannis, E.E., and Tsipis, C.A. (2010) *J. Comput. Chem.*, **31**, 431–446.
120. Murahashi, T., Inoue, R., Usui, K., and Ogoshi, S. (2009) *J. Am. Chem. Soc.*, **131**, 9888–9889.
121. Rayón, V.M. and Frenking, G. (2003) *Organometallics*, **22**, 3304–3308.
122. Diaconescu, P.L., Arnold, P.L., Baker, T.A., Mindiola, D.J., and Cummins, C.C. (2000) *J. Am. Chem. Soc.*, **122**, 6108–6109.

15
Chemical Bonding in Solids

Pere Alemany and Enric Canadell

15.1
Introduction

Having a good grasp of the factors determining the structure and properties of solids is a challenging task that needs inputs from both physical chemistry and condensed matter physics. Solids can be simply seen as giant molecules and thus one is tempted to conclude that the same ideas and concepts used in molecular chemistry should lie behind our understanding of solids at the atomic level. Nevertheless, the large size of a solid as compared to that of single molecules brings about new collective features that are at the basis of many of their technological applications. This means that our approach to solids must be based on a scheme that, while keeping strong ties with the more or less local view of chemical bonding in molecules, should also incorporate the essentially delocalized approach used in condensed matter physics to understand the origin of these collective properties.

Among the different possible classifications of solids, it is quite usual to distinguish them according to the main cohesive forces keeping the atoms or molecules together. The four types of solids described in the introductory chapters of any solid state chemistry textbook are ionic, molecular, covalent, and metallic solids [1–3]. Molecular solids are composed from individual atoms or molecules that retain their individuality and are kept together by weak van der Waals forces, in the case of nonpolar constituents, or more directional electrostatic forces such as dipole–dipole interactions or hydrogen bonding, for more polar constituents. In ionic solids, the electrostatic interactions are assumed to provide the leading cohesive force. Of course, a purely ionic bond does not occur; between any pair of bonded species some degree of electron sharing, that is, covalence, occurs. However, when the electronegativity difference between constituents is considerable, an ionic model leads to useful organizing structural principles such as the Goldschmidt and Pauling rules [4]. When the electronegativity differences decrease, covalent bonding takes the lead. In contrast, in the case of ionic bonding, a satisfactory approach to covalent bonding needs the use of a quantum mechanical treatment. Valence bond and molecular orbital (or its solid state counterpart crystal orbital) approaches have

The Chemical Bond: Chemical Bonding Across the Periodic Table, First Edition.
Edited by Gernot Frenking, Sason Shaik.

been used to develop our understanding of covalent bonding in solids. Although both approaches can be made equivalent at the limit, and the use of one or the other is often a question of preference, the second has been more popular probably because of its simplicity and easiness to correlate the structural and electronic details even for quite complex structures. The bonding in covalent solids and molecules is governed by the same rules. In particular, a localized description in terms of electron pairs either as chemical bonds and/or lone pairs is conceptually possible although a more delocalized description may be more informative. Finally, when such a localized description is no more possible and the electrons are delocalized among many atoms, we deal with metallic bonding. In contrast to the common belief, this situation is not peculiar of solids; bonding in some discrete transition-metal clusters or electron-deficient molecules has exactly the same origin. In metallic solids, the electrons are delocalized throughout the whole solid and require the delocalized quantum mechanical description of band theory.

Benzene, NaCl, diamond, and sodium are archetypal examples of molecular, ionic, covalent, and metallic solids. However, these are almost ideal solids. For most of the interesting solids, overlapping of several types of bonding is the rule. In such a simple solid as graphite, bonding has covalent, metallic, and van der Waals components; TiO presents both metallic and covalent bonding features; $(TMTSF)_2PF_6$ (where TMTSF stands for bis-tetramethyl-tetraselenafulvalene), the first molecular conductor that could be made superconducting under pressure, combines the four types of bonding forces in a same crystal structure. Although such a classification is clearly not quite functional for the majority of compounds, it certainly draws attention to some very general aspects of bonding, which can be useful as a starting point to understand chemical bonding in solids.

From a practical viewpoint, the different bonding forces acting in a solid are all taken care of in contemporary computational approaches based on the density functional theory (DFT) or Hartree–Fock (HF) schemes [5], although the first is by far the more popular in the solid-state community. Band theory (based on the notion of crystal orbitals, the solid state counterpart of molecular orbitals) provides the more straightforward construction to analyze the bonding and properties of periodic solids. In the same way that molecular orbitals are delocalized through the entire molecule, the crystal orbitals are delocalized through the solid. Thus, the band theory may be less well suited for the study of properties such as magnetism based on the behavior of localized electrons. Modern implementations of DFT have provided nevertheless a really impressive list of successful applications to solids of very different nature so that DFT has become the method of choice for studies of the electronic structure of most solids.

The purpose of this contribution is not to present a formal description of the way by which the electronic structure of periodic solids is calculated. Directional electrostatic interactions, hydrogen bonding, dispersion interactions, and the conceptual DFT perspective of bonding are already discussed in different chapters of this book. Our goal here is more chemically oriented: to provide the necessary guidelines for analyzing (i.e., understanding and extracting qualitative ideas from detailed calculations) chemical bonding in periodic solids and eventually to highlight how

chemical bonding and the collective properties of electrons in solids are related. For this purpose, we first consider some very elementary notions of the band theory and later we apply these notions to some simple solids. As a matter of fact, most of our discussion is independent of the methodological approach used, although the results shown later for specific solids are all based on first-principles DFT calculations.

15.2
Electronic Structure of Solids: Basic Notions

In the following we give a brief account of the main concepts useful in the qualitative analysis of the electronic structure of solids [6, 7]. The discussion, which is purposely restricted to a very basic level, is organized so as to strongly emphasize the parallelism between the tools used in the theory of chemical bonding in molecules and solids [8].

15.2.1
Bloch Orbitals, Crystal Orbitals, and Band Structure

Let us consider the simplest periodic system, that is, the regular infinite chain of atoms of Figure 15.1a. To deal with the translational symmetry of the system, we impose the Born–von Karman *periodic boundary conditions*, which essentially means that we are transforming the chain into a closed loop. As the number of sites of the chain (N) is very large, such bending is imperceptible as far as the local environment of a single atom in the chain is concerned (this means, of course, that we are only interested in the bulk properties of the system, neglecting any contribution from atoms at surfaces). This approach makes it possible to concentrate our attention on the contents of a single unit cell, the basic structural fragment that generates the whole system by translational symmetry. By so doing, it is possible to take advantage of the well-known symmetry properties of cyclic groups to handle the invariance of the system under translation operations.

In general, for an atomic orbital χ_j of the unit cell of a chain with repeat distance a (see Figure 15.1a) it is possible to build its associated *Bloch orbitals*, which are the translationally symmetry adapted orbitals, as

$$\varphi_j(\vec{k}) = \frac{1}{\sqrt{N}} \sum_{\vec{R}} \exp(\mathrm{i}\,\vec{k}\,\vec{R}) \chi_j(\vec{r} - \vec{R}) \tag{15.1}$$

where N is the number of unit cells in the chain, $\vec{R} = n\vec{a}$ and $\vec{k} = k_a(2\pi/\vec{a}) = k_a\vec{a}^*$ with $k_a = j/N$ and $j = 0, \pm1, \pm2, \ldots$. The $\vec{R}$ and $\vec{k}$ vectors generate the so-called *direct and reciprocal lattices* for a given periodic system, respectively. Thus, the Bloch orbitals depend on the $\vec{k}$ wave vector. Note that as a result of the periodic nature of the $\exp(\mathrm{i}\,\vec{k}\,\vec{R})$ term, however, one needs only to consider wave vectors in the $-1/2 < k_a \leq 1/2$ region. Thus, from a given atomic orbital χ_j localized at a single

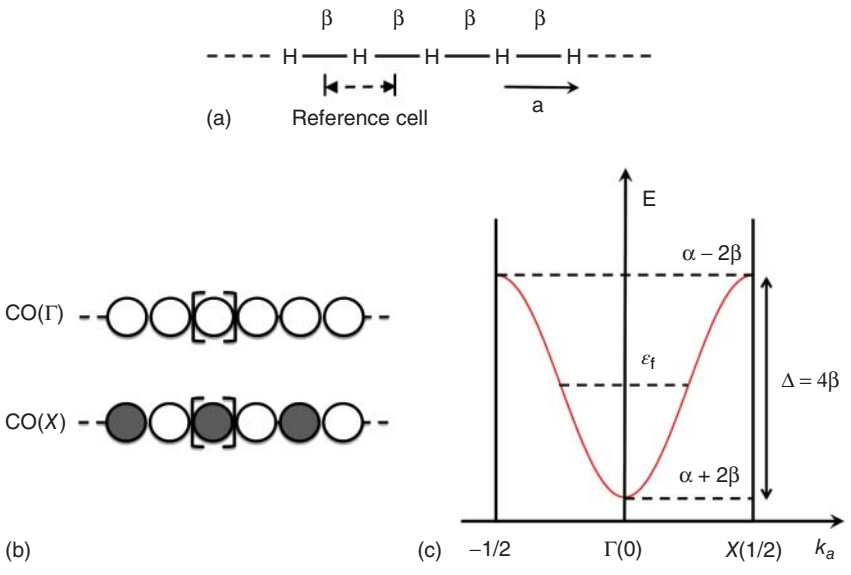

Figure 15.1 Infinite linear chain of regularly spaced hydrogen atoms: (a) schematic representation; (b) Bloch orbitals at the Γ and *X* points; (c) Band structure.

unit cell, *N* different Bloch orbitals φ_j delocalized over the whole infinite chain can be generated by repeating such atomic orbitals with the phase factors given by Eq. (15.1), which depend on the relative position of each cell and the $\vec{k}$ vector. For instance, shown in Figure 15.1b are the Bloch orbitals for the k_a values 0 and 1/2.

Each of these Bloch orbitals belongs to a different irreducible representation of the translation group of the system. In the general case, the unit cell of an infinite chain will be associated with a set of *M* different atomic orbitals ($\chi_j, j = 1, \ldots, M$). Consequently, to study the electronic structure of the infinite periodic chain we must first build the *N* sets of Bloch orbitals associated with each of the *M* atomic orbitals in the reference unit cell and then combine these Bloch orbitals to generate crystal orbitals. As Bloch orbitals associated with different $\vec{k}$ wave vectors belong to different irreducible representations of the translational group, by symmetry, only those Bloch orbitals associated with the same value of $\vec{k}$ can combine to give *M* different crystal orbitals for each $\vec{k}$ wave vector.

$$\psi_\mu(\vec{k}) = \sum_{j=1}^{M} c_{\mu j}(\vec{k})\varphi_j(\vec{k}) \quad (\mu = 1, \ldots, M) \tag{15.2}$$

The energies $e_\mu(\vec{k})$ of the *M* different crystal orbitals are the eigenvalues of the effective Hamiltonian $\hat{H}^{\text{eff}}\psi_\mu(\vec{k}) = e_\mu(\vec{k})\,\psi_\mu(\vec{k})$, and may be obtained by solving the associated secular equation

$$\left| H_{ij}\left(\vec{k}\right) - e(\vec{k})S_{ij}(\vec{k}) \right| = 0 \tag{15.3}$$

This diagonalization must be repeated, in principle, for all different allowed values of the $\vec{k}$ wave vector, that is, all vectors in the $-1/2 < k_a \leq 1/2$ region. In practical calculations, however, the secular equation (Eq. (15.3)) is just solved for a finite set of $\vec{k}$ vectors forming a regular k_a-point mesh within the $-1/2 < k_a \leq 1/2$ region. The numerical accuracy of the calculated energy bands will, of course, depend on the choice of these mesh points.

If we still further simplify our system and consider a regular infinite chain of hydrogen atoms with a single 1s orbital per cell, the Bloch orbitals are already the *crystal orbitals* so that the energy as a function of $\vec{k}$ is given by

$$e_{1s}(\vec{k}) = \frac{\langle \varphi_{1s}(\vec{k}) | \hat{H}^{\text{eff}} | \varphi_{1s}(\vec{k}) \rangle}{\langle \varphi_{1s}(\vec{k}) | \varphi_{1s}(\vec{k}) \rangle} \tag{15.4}$$

In this case, by introducing the simple Hückel approximation, the energy of the crystal orbitals is easily found to be

$$e(\vec{k}) = \alpha + 2\beta \cos(2\pi k_a) \tag{15.5}$$

where α is the so-called Coulomb integral $\alpha = \langle \chi_{1s}(\vec{r}) | \hat{H}^{\text{eff}} | \chi_{1s}(\vec{r}) \rangle$ and β the nearest-neighbor resonance integral $\beta = \langle \chi_{1s}(\vec{r}) | \hat{H}^{\text{eff}} | \chi_{1s}(\vec{r} - \vec{a}) \rangle$ corresponding to the interaction between orbitals on neighboring cells. Note that in the Hückel method the two parameters α and β have both energy units and are considered to be negative, and that the atomic orbitals are considered to form an orthonormal basis, and, hence, overlap between orbitals on neighboring cells is neglected.

Shown in Figure 15.1c are the allowed energies for this chain as a function of k_a. Note that the values of k_a are discrete, but because the number of cells N is considered to be very large, the separation between successive energies is very small and, in practice, we can replace the set of closely spaced discrete energies by a continuous *energy band* of allowed energies. The interactions along the chain have spread the initial 1s level with energy α into an energy band with a width of $4|\beta|$ centered around α. The different allowed values of k_a $(-1/2 < k_a \leq 1/2)$ constitute the *Brillouin zone* of the system. Because of the degeneracy in the energy of crystal orbitals associated with the $+k_a$ and $-k_a$ values, a general property that is independent of the Hamiltonian employed and known as *time reversal symmetry*, only half of the diagram is usually represented when plotting these energy dispersion diagrams, more commonly known as *band structures* (in these diagrams, the points associated with some special $\vec{k}$ wave vectors are assigned specific labels such as Γ or X for the centre ($k_a = 0$) and the border ($k_a = 1/2$) of the Brillouin zone in Figure 15.1).

15.2.2
Fermi Level and Electron Counting

An important point we must consider now is how these crystal orbitals are filled with electrons. Usually, the occupancy of the energy levels of a band is discussed in terms of the number of electrons per unit cell. As a band contains N different

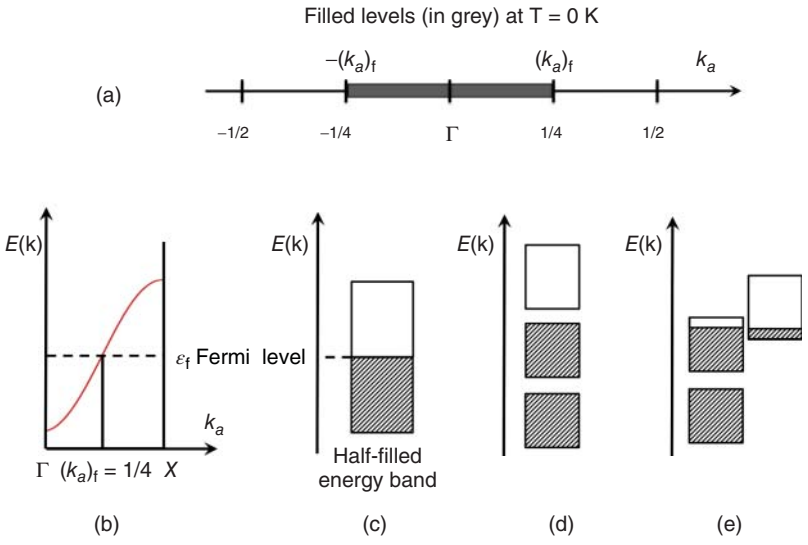

Figure 15.2 Uniform hydrogen chain: (a) schematic representation of the occupation of the different levels; (b) and (c) are two representations of the band structure. Shown in (d) and (e) are two different schematic band structures for a three-band, four-electrons per repeat unit system.

energy levels, which, in the ground state, will be filled according to the usual Aufbau principle, that is, two electrons in each level in increasing order of energies, there is room for $2N$ electrons. Thus, a band is full/half-filled when there are two/one electrons per unit cell to fill this band. Thus, for the regular hydrogen atom chain only the lower half of the band levels can be filled. Taking into account that the different k_a values are uniformly distributed within the Brillouin zone, it is clear that at 0 K all crystal orbitals with k_a values between $-1/4$ and $+1/4$ will be occupied. This situation may be represented as in Figure 15.2.

In general, the repeat unit of the system involves several atomic orbitals and thus the band structure contains several bands (see Figure 15.2d and e). For instance, if there are four electrons per unit cell to fill the energy levels of Figure 15.2d, the two lower bands will be completely filled. There is a *band gap* (E_g) between the highest occupied level (top of the second band) and the lowest unoccupied level (bottom of the third band from bottom). Such a system having only completely filled or completely empty bands is a semiconductor or an insulator, depending on the magnitude of the band gap E_g. If there are five electrons per unit cell, there is only one electron left to fill the top band which is thus half-filled.

We will refer to the highest occupied level of the system as the *Fermi level*.[1] When the Fermi level is located inside the band as in Figure 15.2c, there is no energy

1) All along this chapter we refer to the Fermi level as the highest occupied energy level, that is, we use it just to count electrons. Note, however, that in the case of a semiconductor, the thermodynamic definition of the Fermi level places it within the energy gap [6].

gap separating the highest occupied and lowest empty levels. In one-electron band theory, where electron–electron repulsions are neglected, a system with one or more partially filled bands is predicted to be a metal (when electron–electron repulsions are strong, this can be no longer true; see subsequent text). There is an intermediate situation between metals and semiconductors. If two successive bands slightly overlap and the number of electrons is such that only one of the two can be formally filled (see, for instance, Figure 15.2e), the Fermi level will cut both bands so that the upper band will be slightly filled with electrons and the middle band will not be completely filled (i.e., will contain some holes). Of course, the number of holes in the middle band must be the same as the number of electrons in the upper band. Systems exhibiting this slight band overlap are known as *semimetals*.

The procedure described up to now is completely general and may be used to study the electronic structure of any periodic system. For 2D or 3D systems, the $\vec{R}$ and $\vec{k}$ vectors have two or three components, respectively, and, consequently, the Brillouin zone of the system will be a polygon (2D case) or a polyhedron (3D case). This will also complicate the representation of band diagrams, because now we must represent the energy of the crystal orbital as a function of two or three k values corresponding to the coordinates of the $\vec{k}$ vectors. In 2D and 3D cases, it is customary to represent only in the dispersion diagrams the evolution of the crystal orbital energies along selected (normally high-symmetry) directions within the Brillouin zone. The computation of energy bands will become heavier because of the larger number of orbitals and the mesh of $\vec{k}$ wave vectors to consider, but the procedure is, from the conceptual point of view, identical to that exposed for the 1D case.

15.2.3
Peierls Distortions

As shown in Figure 15.2, in the case of the uniform chain of hydrogen atoms, there is no separation between the highest occupied and the lowest empty state. To illustrate how the geometric and electronic structures of a lattice are intimately related, let us now consider a dimerized infinite chain of hydrogen atoms. The unit cell of this system contains two hydrogen atoms and we must take into account two different resonance integrals, β_{i} and β_{e}, one for the interaction of the two atoms within the unit cell and the other between two atoms in neighboring cells (Figure 15.3a). As there are now two 1s orbitals per unit cell, we must first build the Bloch orbitals associated with each of them, evaluate the four matrix elements of the 2×2 secular determinant, and solve the secular equation to obtain two different energy values for each $\vec{k}$ vector. This leads to the expression:

$$E^{\pm}(\vec{k}) = \alpha \pm \beta_i \sqrt{1 + \frac{\beta_e^2}{\beta_i^2} + 2\frac{\beta_e}{\beta_i}\cos(2\pi k_{a'})} \tag{15.6}$$

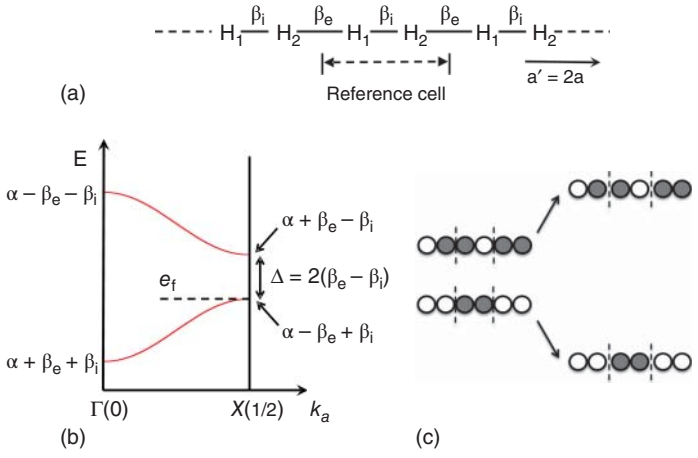

Figure 15.3 (a) Dimerized hydrogen chain; (b) schematic band structure; (c) crystal orbitals at the *X* point before (left) and after (right) the dimerization.

where we have arbitrarily considered the case of an interaction inside the cell, which is stronger than between neighboring cells, that is, $\beta_i < \beta_e < 0$. Using this expression, the schematic band structure of Figure 15.3b can be drawn and because there are now two electrons per unit cell, the lower band will be completely occupied. Consequently, except for the case in which $\beta_i = \beta_e$, that is, when all interactions along the chain are equal, or in other words, in the case where there is no dimerisation along the chain, there is an energy gap at the Fermi level separating occupied from unoccupied electronic energy levels, thus leading to a nonmetallic behavior for the dimerized chain. As is shown in Figure 15.3b, this is true for even quite small dimerizations, so that very minor structural changes are able to open an energy gap between occupied and empty electronic energy levels, leading to a very different conductivity behavior.

These results are very easily understood by simply drawing the crystal orbitals at X, using the bonding and antibonding orbitals of the two atoms in the unit cell and repeating them with the appropriate signs. This is shown in Figure 15.3c. The two orbitals of the uniform chain at the Fermi level are completely equivalent, but the bonding/antibonding interactions are differently located. Thus, dimerization of the chain increases the bonding interactions in one of the crystal orbitals but does the opposite in the other orbital. As a consequence, one of the levels is stabilized while the other is destabilized, so that an energy gap opens at the Fermi level and the energy of the system is, in principle, lowered. This type of distortion is known as a *Peierls distortion* [9] and plays a central role in understanding the structure of many solids. The Peierls distortion is not a peculiarity of metallic half-filled systems. In general, any partially filled 1D system will be susceptible toward a distortion that opens a band gap at the Fermi level by modifying the translational properties of the system and destroying its metallic properties.

15.2.4
Density of States and its Analysis

Many solids are structurally complex and have large unit cells. There will be many atomic orbitals to consider in building the crystal orbitals and the task of understanding the band structure of the material can be quite involved. In addition, complex unit cells usually have a very low symmetry so that there are almost no restrictions for the mixing of orbitals. The orbital interaction analysis of the band structure can become too cumbersome in such cases and a simpler analytical tool must be devised. Because the problem is that we have too much data when looking at the band structure, we must find a way to condense this information so that even if we lose many details we can easily extract an appealing view of the electronic structure. It is obvious that this need for a simpler tool will be even stronger when dealing with 2D and 3D systems. In such cases, the Brillouin zone will be a surface or a volume and, consequently, for each band there will be many different lines of the Brillouin zone to be considered. The simplest analytical tool devised for this purpose is the density of states (DOS).

The DOS $n(e)$ of a solid is defined as the number of states in an energy interval between e and $e + \mathrm{d}e$. Thus, $n(e)$ is positive within the allowed energy region of a band and vanishes in the forbidden energy region. For the simple case of an infinite chain of hydrogen atoms, the dispersion relation of the band, according to a simple Hückel approach, is given by a cosine function of k (see Figure 15.2 and Eq. (15.5)). As reciprocal space consists of a set of equally spaced k points, the DOS is proportional to the inverse of the slope of the energy versus k curve:

$$n(e) \propto (\mathrm{d}e(k)/\mathrm{d}k)^{-1} \tag{15.7}$$

Thus, $n(e)$ will be minimal at the center of the band and will tend to infinite at the edges, that is, at $k_a = 0$ and $k_a = \pm 1/2$, respectively. The last feature is known as a *van Hove singularity* and is physically meaningless because the integrated DOS of the whole band must be equal to the number of electrons per unit cell associated with the band, that is, two if the band is completely filled. Because $n(e)$ is zero outside the band, the typical shape of the DOS for a 1D band is that shown in Figure 15.4. Thus, the wider the band, the lower will be the average DOS. In other words, strong interactions along the chain are associated with large energy dispersions and, therefore with lower DOS values. Conversely, very sharp peaks in the DOS are associated with flat bands and therefore with electrons that tend to be localized because of weak interactions with neighboring orbitals. The shape of the DOS curves for a single band in 2D and 3D systems is quite different, and the detailed shape strongly depends on the nature of the lattice. In the general case of a system with various bands, the final DOS diagram will result from the overlapping of the contributions to the DOS of each individual band, leading to a quite complex total DOS curve. A detailed analysis of the DOS will be necessary in these cases to extract useful information about the electronic structure of the solid.

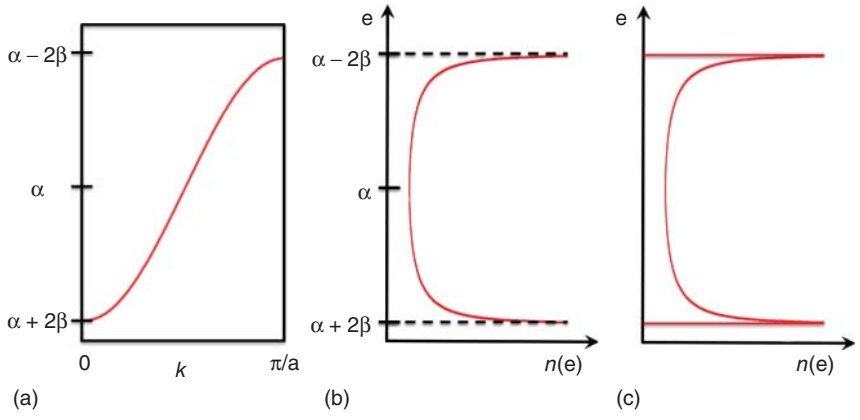

Figure 15.4 Linear chain of hydrogen atoms: (a) band structure and (b) density of states according to a Hückel approach; (c) DOS for a typical 1D band.

In practise, to determine the DOS of a system, the k-dependent Hamiltonian is diagonalized for a fine mesh of k points in the Brillouin zone. This leads to a histogram of energy values, which is then numerically smoothed using a set of appropriate functions, for instance, Gaussians, leading to the DOS of the material. The finer the mesh of k points used, the more precise will be the DOS.

The electronic structure of solids can be discussed solely on the basis of their DOS curve. The DOS of a real solid can have a quite complex shape. Thus, it is important to develop a qualitative way to analyze this type of plots [10, 11]. The $n_i(e)$ curve for a single band i satisfies the normalization condition

$$\int_{-\infty}^{\infty} n_i(e)\mathrm{d}e = 1 \tag{15.8}$$

so that because a band can accommodate up to two electrons per unit cell, integration of twice the DOS up to the Fermi level gives the total number of electrons of the system. As the crystal orbitals have been expressed as a linear combination of Bloch orbitals associated with the different atomic orbitals of the unit cell, the DOS curves can be decomposed in terms of individual contributions from each atomic orbital of the unit cell. In other words, once the DOS plot has been calculated, we can project the contribution of any set of atomic orbitals to the total DOS. The easiest way to illustrate the process is by considering the two-center molecular orbital (MO)

$$\psi = c_1\chi_1 + c_2\chi_2 \tag{15.9}$$

The electron distribution in this molecular orbital is given by the normalization condition

$$1 = c_1^2 + c_2^2 + 2c_1c_2S_{12} \tag{15.10}$$

where S_{12} is the overlap integral between atomic orbitals χ_1 and χ_2. If we want to partition the total electron distribution into contributions of each atomic orbital, it is clear that ${c_1}^2$ and ${c_2}^2$ should be assigned to χ_1 and χ_2, respectively. It is, however, not trivial how to distribute the term $2c_1c_2S_{12}$, which is an overlap density, between the two orbitals. The simplest solution was suggested by Mulliken [12]. In the so-called Mulliken population analysis, this term is equally shared between centers 1 and 2. Thus, the center 1 is assigned a total of ${c_1}^2 + c_1c_2S_{12}$ and center 2 a total of ${c_2}^2 + c_1c_2S_{12}$. In order to get the electron distribution, these two contributions should finally be multiplied by the occupation number of the MO. This type of analysis can be easily performed for the different crystal orbitals of a solid and, consequently, a local DOS can be projected out from the total DOS. These *local or projected DOS* can correspond to an individual atomic orbital, a group of atomic orbitals, an atom, or a group of atoms.

Useful as they are, local DOS plots do not allow to know whether the levels in a certain energy range contribute to the bonding between a given pair of atoms. One of the schemes frequently used in molecular chemistry to clarify this question is the so-called Mulliken overlap population. This concept is related to the contribution $2c_1c_2S_{12}$ of Eq. (15.10). This term, an overlap population, is a characteristic of the bonding between the two centers 1 and 2. If the overlap integral is taken as positive, then this quantity is positive when the combination between the two orbitals is bonding and negative when the combination is antibonding. The Mulliken overlap population is the addition of $2c_ic_jS_{ij}$ terms over all the orbitals on the two atoms over all occupied MOs. Exactly in the same way as for the local DOS, the quantities $2c_ic_jS_{ij}$ of interest can be evaluated for the different energy levels of a solid and projected from the total DOS. These overlap-population-weighted DOS curves are usually known as *COOP* (*crystal orbital overlap population*) *curves* [13].

The COOP curves have been useful in understanding the structure of complex solids. A simple example of using COOP curves in the interpretation of chemical bonding is given by a zigzag chain of hydrogen atoms. The band structure of this system is sketched in Figure 15.5a. All the 1,2 (nearest-neighbor) interactions are bonding at the bottom of the lower band and the antibonding at the top of the upper band. The levels at the top of the lower band and the bottom of the upper band are essentially nonbonding. Thus, the COOP curve for the 1,2 interactions will be as schematically shown in Figure 15.5b. The 1,3 (next nearest-neighbor) interactions are bonding both at the top of the upper band and the bottom of the lower band. However, they are antibonding at the top of the lower band and the bottom of the upper band. As these interactions are weaker than the 1,2 ones, the corresponding COOP curve should be as schematically shown in Figure 15.5c.

A difficulty often associated with the use of overlap populations is that it is not sensible to compare values for different pairs of atoms. A useful tool derived within the DFT scheme is that of the *crystal orbital Hamilton population* (COHP) analysis [14]. In that case, what is partitioned in bonding, nonbonding, and antibonding contributions for a certain energy window is not the number of electrons (COOP) but the band energy (COHP). Except for the obvious fact that the two kinds of curves show opposite sign behavior, they usually lead to the same qualitative analysis.

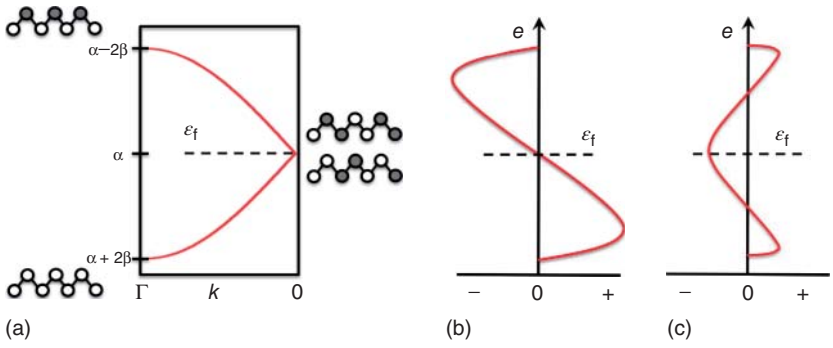

Figure 15.5 Zigzag chain of hydrogen atoms: (a) schematic band structure; (b) and (c) schematic COOP curves for the 1,2 and 1,3 interactions.

Note that although these tools are mostly employed in a qualitative way, the use of COHP may be advantageous because it allows the weighting of the role of the contribution of different pairs of atoms to the bonding.

Another useful tool in analyzing the bonding in solids not directly related to the DOS is the electron localization function (ELF), originally proposed by Becke and Edgecombe [15a] and later generalized by Savin *et al.* [15b] Essentially, ELF measures the probability of finding an electron in the vicinity of another electron with the same spin. Grossly speaking, because electron–electron repulsions between electrons with different spins are considerably weaker than those between electrons with the same spin, ELF provides a way to divide space in regions where electron pairs can be found. However, the connection between the ELF and chemical bonding is more subtle. By construction, ELF has values between 1 (regions with high probability to find a pair) and 0 (areas in between pair regions). Thus, a 3D representation of the isosurface for a relatively large value of ELF provides a pictorial way to make bonding clear and has been used to analyze different types of relatively complex solids such as intermetallics and alloys, Zintl phases, and so on. [15c] Although conceptually different, this approach has strong ties with Bader's analysis of the partition of the electron density, which provides another elegant way to gain insight into the nature of the chemical bond in molecules and solids [16].

15.2.5
Electronic Localization

As mentioned, the band theory of solids leads to a clear distinction between metals and insulators: metals are associated with systems with partially filled bands, whereas insulators are associated with systems with completely full and empty bands. However, for a system that, according to a delocalized description of electrons, would have partially filled bands, it may be advantageous to keep these electrons localized because in that way electrostatic repulsion between them could be minimized. These kind of localized states are usually known as *Mott–Hubbard*

localized states. For instance, most of the transition-metal monoxides with a rock-salt-type structure are insulating (NiO, CoO, FeO, and MnO, but not TiO and VO, which are metallic) even if they have electron counts typical of systems with partially filled bands. If the localized and delocalized states have very similar energies, at some finite temperature there may be a metal to insulator transition. The insulating system in that case is of course different from those discussed in previous sections.

To understand the difference, let us consider again a regular chain of hydrogen atoms. As discussed before, the energy as a function of $\vec{k}$ may be written as $e(\vec{k}) = W/2\cos(2\pi k_a)$, where W is the full dispersion of the band ($W = 4|\beta|$) and the average energy of the band (α) has been taken as the energy zero. The question now is to evaluate the energy difference between the metallic (i.e., delocalized) and localized states (i.e., that in which every electron stays localized on one hydrogen atom). To do this, we need to take into account electronic repulsion. In the present qualitative approach, we will only consider the electron–electron repulsion term associated with two electrons located on the same site, that is, intrasite repulsion (U). When one electron in the localized chain jumps from one site to the next, an electron pair is generated in the second site and consequently there will be an energy penalty of U for this jump (Figure 15.6a). Essentially, U may be evaluated as the difference between the ionization potential and the electronic affinity of the hydrogen atom. Consequently, to evaluate the contribution of U terms to the total energy of the metallic and localized states we need to consider only the number of electrons at each site in both states. If we use n^{α} and n^{β} to indicate the number of electrons with α and β spin at each site, we can describe the metallic and localized states as shown in Figure 15.6b and c, respectively. Thus, the contribution per intrasite repulsion to the energy per unit cell of the metallic and localized

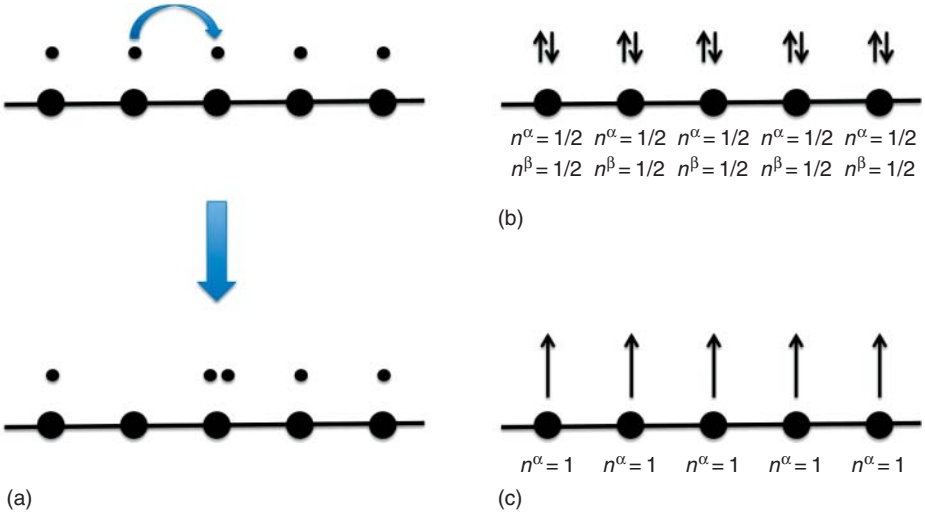

Figure 15.6 (a) Illustration of the meaning of the intrasite repulsion term. (b) Occupation of the different sites in the metallic and (c) localized states of the infinite hydrogen chain.

states is $1/2 \times 1/2 \times U = U/4$ and 0, respectively. For the metallic state, there is another contribution to the energy due to band formation, which can be obtained by integration of the above-given equation through the region of the filled states (i.e., from $-\pi/2a$ to $\pi/2a$; see Figure 15.2),

$$\frac{a}{2\pi}\int_{-\frac{\pi}{2a}}^{+\frac{\pi}{2a}} 2e(\vec{k})\mathrm{d}\vec{k} = \int_{-\frac{1}{4}}^{+\frac{1}{4}} 2\frac{W}{2}\cos(2\pi k_a)\mathrm{d}k_a = \frac{W}{\pi} \tag{15.11}$$

Consequently, the total energy associated with the metallic state is

$$E^M = -\frac{W}{\pi} + \frac{U}{4} \tag{15.12}$$

whereas the energy associated with the localized state is simply $E^L = 0$. Hence, the energy difference between the metallic and localized states is

$$E^L - E^M = \frac{W}{\pi} - \frac{U}{4} \tag{15.13}$$

and, thus, the metallic state will be more stable when the band width is larger than $\pi/4U$. In other words, a half-filled system for which $W \sim U$ is susceptible to undergo a metal to insulator transition induced by electron repulsion known as *Mott transition* [17]. These transitions do not necessarily come with a structural distortion but reflect the progressive localization of electrons when temperature is lowered. Consequently, the energy gap arising at the transition is different in nature from that resulting from Fermi surface instabilities.

15.3
Bonding in Solids: Some Illustrative Cases

In this section, we use the conceptual tools discussed earlier to analyze the chemical bonding in a series of Zintl phases where different types of bonding coexist. Although the crystal structures of the chosen solids are relatively simple, they bring to the fore interesting bonding questions related to our understanding of their structural and transport properties [18]. All electronic structure results mentioned in the following have been obtained from first-principles calculations carried out using a numerical atomic orbitals DFT approach [19] implemented in the SIESTA code [20]. The generalized gradient approximation (GGA) and, in particular, the Perdew–Burke–Ernzerhof (PBE) functional [21], as well as norm-conserving scalar relativistic pseudopotentials [22] factorized in the Kleinman–Bylander form [23] were employed. We used optimized split-valence double-ζ basis sets including polarization orbitals for all atoms. The energy cutoff of the real-space integration mesh was 300 Ry and the Brillouin zone was sampled using appropriate grids of *k*-points [24].

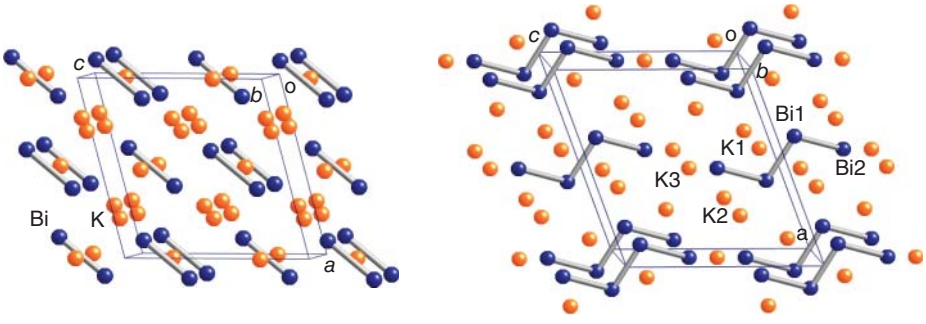

Figure 15.7 Crystal structure of (a) K_3Bi_2 [28] and (b) K_5Bi_4 [27].

15.3.1
Covalent Bonds in Polar Metallic Solids: A_3Bi_2 and A_4Bi_5 (A = K, Rb, Cs)

Most Zintl phases obey traditional electron-counting rules, which basically associate chemical stability to the existence of a closed-shell electronic configuration for the anionic clusters or networks in the structure, thereby suggesting that these phases should be insulators or semiconductors [25, 26]. However, there are an increasing number of these phases showing metallic properties. From a conceptual viewpoint, one of the more challenging problems concerning these phases is to have a hint on the relationship between chemical bonding *and* transport properties. Having an odd number of electrons does not guarantee a metallic behavior because, as discussed, electrons can remain localized. Thus, it is important to develop some understanding of the chemical bonding and its relationship with the transport properties in such systems.

Let us consider the A_5Bi_4 [27] and A_3Bi_2 [28] (A = K, Rb, Cs) phases. Their crystal structure is very simple and contains tetrameric/dimeric bismuth units surrounded by alkali atoms (Figure 15.7). Trying to build a simple description of the A_3Bi_2 phase, for instance, one can think of two different situations. First, the dimers are $(Bi_2)^{3-}$ units immersed in a sea of A^+ cations. Second, the dimers are $(Bi_2)^{2-}$ units and there must be an extra electron delocalized through the alkali atom subnetwork. The two views suggest two different descriptions of the physical behavior of the A_3Bi_2 salts: temperature-dependent paramagnetism due to unpaired electrons localized on the dimers in the first case, but temperature-independent Pauli paramagnetism and metallic behavior in the second. A similar situation holds for A_5Bi_4, where both $(Bi_4)^{5-}$ and $(Bi_4)^{4-}$ are, in principle, equally likely. As both families exhibit Pauli paramagnetism and metallic conductivity, it was concluded that the $(Bi_2)^{2-}$ and $(Bi_4)^{4-}$ formulations were those more appropriate for A_3Bi_2 and A_5Bi_4, respectively [27, 28]. However, as will be shown later, the situation is not as clear-cut as this simple analysis may suggest.

The calculated band structure for K_3Bi_2 in its metallic state is shown in Figure 15.8 [29]. Possible nonmetallic states were also considered. A ferromagnetic

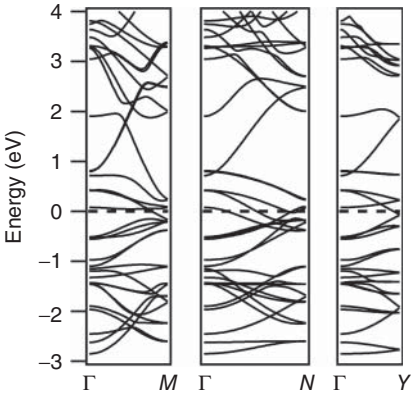

Figure 15.8 Calculated band structure for K_3Bi_2, where the dashed line refers to the Fermi level. Γ = (0, 0, 0), *Y* = (0, 0.5, 0), *M* = (−0.5, 0, 0.5), and N = (0.5, 0, 0.5) in units of the monoclinic reciprocal lattice vectors. (Reproduced with permission from Ref. [29]. Copyright © 2005 American Chemical Society).

state lying 0.3 eV above the metallic state was found, whereas no antiferromagnetic state was located. All these results are in excellent agreement with experimental information [28]. The Γ → M, Γ → N and Γ → Y lines describe those interactions along directions $(c - a)$, $(a + c)$ and b, respectively. In agreement with experimental results, several bands cut the Fermi level leading to the prediction of metallic behavior. However, the question of the formal charge of bismuth dimers would be too complex to discuss on the basis of this band structure and it is preferable to consider the DOS. The calculated DOS as well as the partial contributions of Bi p_x, p_y, and p_z orbitals are shown in Figure 15.9a. A Cartesian system of axes in which x and y lie on the ab plane in such a way that y runs along the Bi–Bi bond direction and x runs perpendicular to it, and the z axis is perpendicular to the ab plane, was used in the calculations. On the basis of these projections and consideration of the wave vectors at some special points, the Bi contribution to DOS can be easily analyzed in terms of the different orbitals of a Bi_2 unit (Figure 15.9b). The contributions of the $1\sigma_g^+$ and $1\sigma_u^+$ levels are found at energies lower than shown in Figure 15.9a. The peak between −3 and −1 eV is the superposition of three contributions, that of the $2\sigma_g^+$ level (red curve) and those of the two π_u bonding levels (blue and green curves). The peak between −1 and 0.5 eV contains two contributions originating from the two π_g antibonding levels. These levels are partially filled. The contribution of the antibonding $2\sigma_u^+$ level (upper red curve) is much spread and occurs above the Fermi level. Integration of each contribution allows knowing the formal occupation of the different levels and thus the formal charge of the diatomic unit. For a $(Bi_2)^{n-}$ unit, formally 75%, 87%, and 100% of the π levels should be occupied for $n = 2$, 3, and 4. Integration of the x and z contributions of Figure 15.9a gives an 88% occupation, showing that the diatomic units are clearly $(Bi_2)^{3-}$ units *even if the system is metallic*.

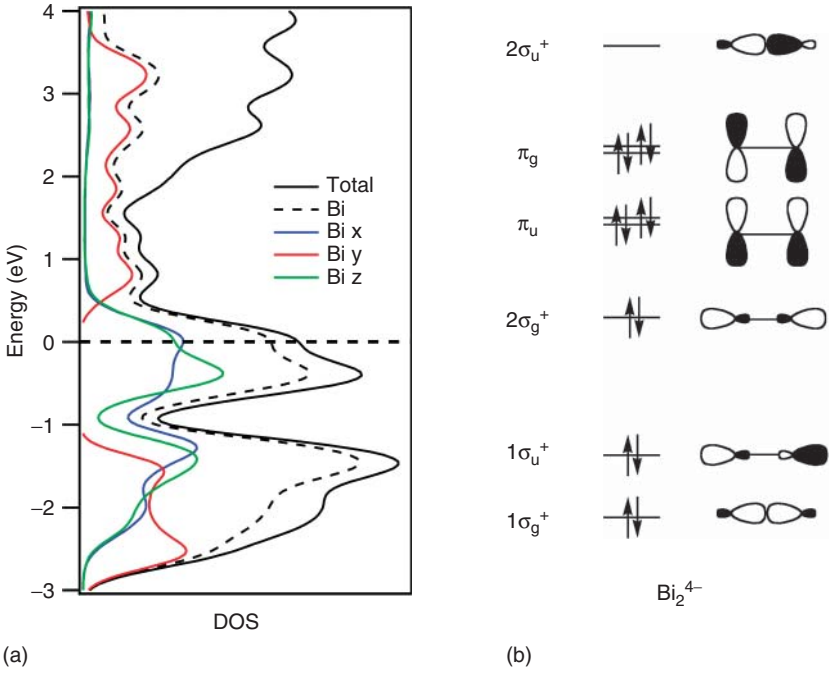

Figure 15.9 (a) Density of states for K_3Bi_2 (black line). The partial contributions of Bi (broken line), Bi p_x (blue line), Bi p_y (red line) and Bi p_z (green line) orbitals are also shown. (b) Qualitative orbital diagram for a $(Bi_2)^{4-}$ unit. (Reproduced with permission from Ref. [29]. Copyright © 2005 American Chemical Society).

The key to understanding this apparent paradox is the notable participation of K levels around the Fermi level (in fact, in large parts of the filled portion of the DOS). That potassium atoms are not just providing electrons to bismuth dimers and some kind of coulombic force keeping together the K_3Bi_2 structure is clear from the participation of K levels in the filled part of the DOS (let us remember that in DFT approaches using localized basis sets as the present one the total DOS is simply the addition of those corresponding to the different atomic contributions). In order to have a somewhat more precise idea of this involvement, we carried out a Voronoi deformation density analysis [30], and found that the charge of K atoms is +0.04. This value is notably smaller than that calculated adopting exactly the same computational details for typical ionic salts of K (for instance, +0.32 for KF). Exactly the same conclusion was reached on the basis of the Hirshfeld [30] or Mulliken [12] schemes. These figures are quite clear in showing an important mixing of potassium and bismuth orbitals.

Let us emphasize that by writing $(Bi_2)^{3-}$ we do not imply that the dimers are discrete units with an unpaired electron, as we are not counting electrons really transferred from K to Bi_2 dimers, but the number of occupied orbitals mainly centered on dimers. Bands in the region around the Fermi level in Figure 15.8

have the π_g dimer orbitals as the major component, *but* K orbitals mix into them providing a link between neighboring dimers and leading to the spread of orbitals into bands. This mixing decreases the *real* charge of dimers because part of the *formal* 3– charge is shared with the K atoms, which are indeed part of a 3D network with a large covalent bonding component. Yet, the formal description is pertinent because it grasps the main features of the electronic structure of the material. Exactly the same conclusions hold for the A_5Bi_4 phases [31]. Although a detailed analysis of the bands crossing the Fermi level points out significant differences in the conductivity of the two families [29, 31], the essential details of chemical bonding are very similar.

15.3.2
Electronic Localization: Magnetic versus Metallic Behavior in K_4P_3

A good example of the effects of electronic repulsion in determining the ground state of a solid can be found in K_4P_3, a compound which, from the chemical and structural point of view, is closely related to the A_3Bi_2 and A_5Bi_4 phases discussed in the previous section. Phosphorus atoms in K_4P_3 [32] form isolated P_3 units (Figure 15.10a) arranged in chains parallel to the *a* axis of the orthorhombic crystals (Figure 15.10b). If we consider a complete charge transfer between potassium and phosphorus atoms, a formal charge of 4– is expected for the P_3 fragments. With this formal electron count, the $(P_3)^{4-}$ anions found in K_4P_3 with five electrons in the π-system can be regarded just as a representative of the second member of the $(X_n)^{(n+1)-}$ series to which the $(Bi_2)^{3-}$ and $(Bi_4)^{5-}$ anions discussed in previous section also belong.

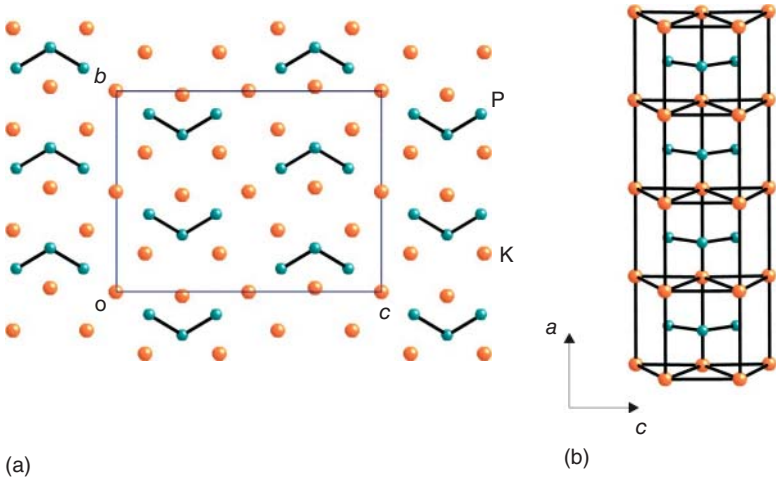

Figure 15.10 Crystal structure of (a) K_4P_3 viewed along the *a*-direction and (b) of a chain of $(P_3)^{4-}$ units stacked along the *a* axis [32].

As discussed earlier, although isolated anions of the $(X_n)^{(n+1)-}$ series bear a single unpaired electron, and hence one could expect the solids containing such anions to be paramagnetic, interactions of the orbitals of one anion with those on other anions or those of the surrounding potassium cations can lead to an effective delocalization of those unpaired electrons that results in the metallic properties observed, for instance, in K_3Bi_2 and K_5Bi_4. Experimental measurements show, however, that K_4P_3 has a peculiar behavior [32]. On one hand, K_4P_3 is not metallic, but on the other hand it shows a complex magnetic susceptibility that deviates from the simple Curie–Weiss law found for KO_3, a compound containing discrete $(O_3)^-$ anions isoelectronic with the $(P_3)^{4-}$ units found in K_4P_3 [33]. These experimental findings suggest an intermediate situation where interactions of the $(P_3)^{4-}$ anions with their environment are not strong enough to develop a wide band from the single-occupied π-type orbital of the $(P_3)^{4-}$ fragments, which could overcome the tendency to localization due to electronic repulsion. However, these interactions are, on the other hand, not negligible, leading to an interaction between unpaired spins of neighboring $(P_3)^{4-}$ units that lead to a magnetic behavior different from the Curie–Weiss law expected for noninteracting spins in a paramagnetic solid.

Although this intermediate situation is not the best scenario for DFT calculations, which tend to energetically favor the delocalized (metallic) state over the (magnetic) states with localized electrons, we will show that the consideration of electronic repulsion, even in an extremely simple way such as the DFT+U method [34], is able to explain the observed physical behavior in such a complex case as K_4P_3.

Figure 15.11 shows the DOS calculated for a K_4P_3 using standard DFT. Projecting the contribution of the p_x orbitals (in our coordinate system, the *x*-direction is parallel to the crystallographic *a*-direction of Figure 15.10) of the two different types of phosphorus atoms to the DOS (green and blue curves in Figure 15.11a) it is quite easy to identify the location and width of the three π-type bands associated with the P_3 fragments. Note that the separate projections of the p_x orbitals for the outer (P1,3) and inner (P2) types of phosphorus atoms reflect well the different participation of the two types of P atom in the three different π-type orbitals, as shown in the molecular orbital diagram in Figure 15.11b. The situation of the Fermi level, in the middle of the upper π-type band, is in good agreement with a $(P_3)^{4-}$ formal electron count, leaving a single electron on each P_3 unit; and, according to this calculation, K_4P_3 would not differ too much from K_3Bi_2 and K_5Bi_4, where the single occupied π-type orbitals of anions lead to a half-filled band that gives a metallic character to the solid. Because we know from experimental data that this is not the case in K_4P_3, we must conclude that standard DFT is not able to describe correctly the electronic structure for the ground state of K_4P_3, where electronic repulsions favor the localization of these unpaired electrons, leading to the magnetic behavior found experimentally.

Before describing the effects of an explicit introduction of electronic repulsion in the calculations, let us analyze further the origin of the different situations in K_4P_3 and in the two bismuth-containing compounds by comparing their DOS plots presented in Figures 15.11 and 15.9. A first point to note is that the π-type orbitals in K_3Bi_2 and K_5Bi_4 give rise to significantly wider bands, a broadening that

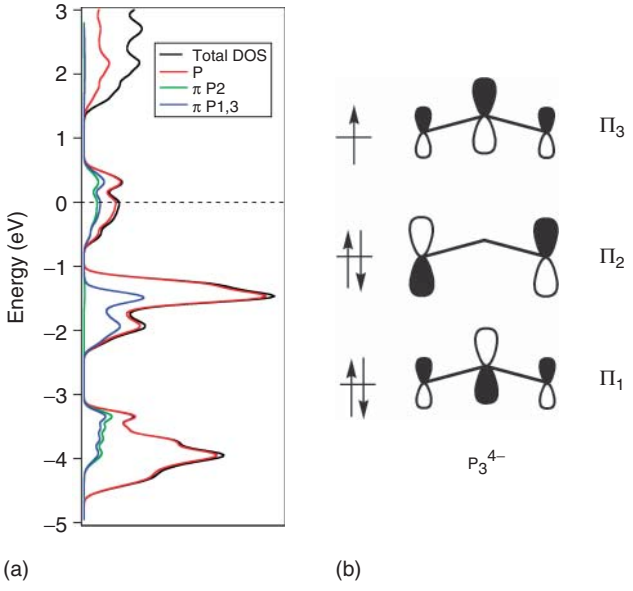

Figure 15.11 (a) Total and selected projected densities of states for K_4P_3 and (b) molecular orbitals for a $(P_3)^{4-}$ anion.

leads even to an overlap between the bonding and antibonding π-type bands in the solid. The three π-type bands, with a width of about 1 eV, appear, on the contrary, clearly separated in the DOS for K_4P_3. It is also noteworthy that while there is a noticeable contribution of potassium orbitals in the region of the π-type bands in K_3Bi_2 and K_5Bi_4, this contribution is almost negligible in the case of K_4P_3, where the levels around the Fermi level can be clearly associated with atomic orbitals on the phosphorus atoms. A detailed analysis of the band structure (not shown in the figure) reveals that the π-type bands in K_4P_3 acquire only a noticeable dispersion in the Γ-*X* direction, corresponding to the direction of the *a* axis in real space, indicating that the main interaction between neighboring $(P_3)^{4-}$ is along the chains shown in Figure 15.10b. As there is no noticeable participation of K orbitals in these bands, we must conclude that π-type orbitals on the neighboring units along the chains are able to ''see'' each other. From these observations, narrow π-type bands with negligible K participation and an important 1-D character, it is easy to deduce that electron repulsion between unpaired electrons in the partially filled π-type band should be more important in K_4P_3 than in K_3Bi_2 and K_5Bi_4, where interaction with the surrounding potassium atoms leads to the observed metallic behavior, as explained in the previous section.

The DFT+U approach [34] is a simple way to introduce the effects of electron repulsion in the framework of DFT. Although from a conceptual point of view it is quite easy to understand, the DFT+U method has, however, some disadvantages, the most serious one being the introduction of the electronic repulsion *U* as an empirical parameter of an unknown magnitude. Although, as mentioned, electron

repulsion effects should be appreciable for $W \sim U$, this is only an approximate estimation and it is usual to perform separate DFT+U calculations with different values of U. Experience shows that in most cases the correct behavior is obtained for U values of a few electron volts. In our case, we have calculated the electronic structure using $U = 0$, 1, 2, 3, 4, and 5 eV for the phosphorus atoms. We have considered two alternative possibilities for localized electrons with either an antiferromagnetic or a ferromagnetic order along the chains parallel to the *a*-direction in the crystal. In order to allow for an antiferromagnetic ordering, the unit cell must be doubled in the *a* direction and, consequently, the band structures described subsequently correspond to a unit cell with eight $(P_3)^{4-}$ anions arranged in four different chains with spins aligned in the same way in each of the four chains.

For small values of U ($0\,\text{eV} < U < 2.5\,\text{eV}$), the metallic (delocalized) state is found to be the ground state with a localized ferromagnetic state about 0.27 eV/formula unit above the metallic state for $U = 0$ eV. Any attempt to converge to a localized state with antiferromagnetic order along the chains leads to the metallic state. For larger values of U, it is possible to obtain an antiferromagnetic solution that is found to be the ground state (remember that for the sake of simplicity we have not explored here the possibility of antiferromagnetic couplings between neighboring chains that could lead to lower energy states and explain the features found in the measures of magnetic susceptibility at low temperatures). For these values of U, the localized ferromagnetic solution is also more stable than the metallic one. For instance, when $U = 4.0$ eV, the ferromagnetic and the antiferromagnetic states are 0.28 and 0.42 eV/formula unit below the metallic state, respectively.

Figure 15.12 shows the dispersion diagrams for the three states along the Γ-*X* direction calculated with a value of $U = 4.0$ eV. As the repeat unit of this solid contains four P_3 units and we consider a unit cell that is doubled in the *a* direction, in the metallic state the eight bands around the Fermi level can be seen as four pairs of "folded" bands strictly degenerated at the X point. Forcing a ferromagnetic solution by allowing spin polarization in the calculations with a fixed total spin of 8/2 per (doubled) unit cell leads to an energy stabilization. In this case, spin-up and spin-down bands are no longer equivalent, and the resulting band diagram shows that energetic stabilization has been achieved by a more or less rigid shift of the spin-up and the spin-down bands in such a way that a gap has opened between them. In the case of the antiferromagnetic solution, the eight bands split into two sets. The lower four bands visible in the plot correspond really to eight bands if we consider spin-up and spin-down bands separately. In this case, each of the bands seen in the plot corresponds to two perfectly degenerated spin-up and spin-down bands as in the metallic state, but with the fundamental difference that each spin (up or down) is localized on a different $(P_3)^{4-}$ anion in such a way that the direction of spins alternates along the *a* direction of the crystal. The spin density on each $(P_3)^{4-}$ fragment can be estimated from a Mulliken population analysis that confirms the validity of the formal electron count, indicating that there is a single unpaired electron on each anion (0.95 for the antiferromagnetic solution and 1.00 for the ferromagnetic one) and that this electron is not equally shared between three atoms on the fragment, but it is mostly localized on the central P atom

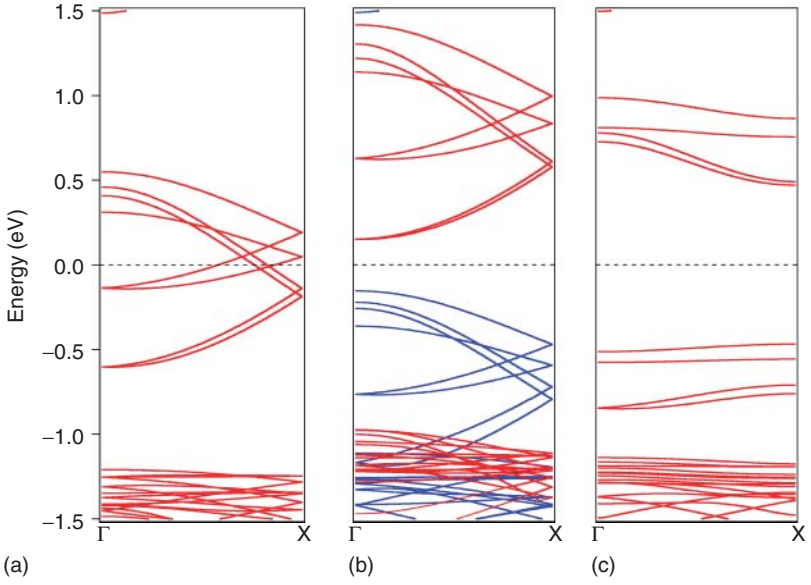

Figure 15.12 Dispersion diagrams for the (a) metallic, (b) ferromagnetic, and (c) antiferromagnetic states of K_4P_3 as obtained with a value of $U = 4.0$ eV. In the ferromagnetic case, bands in blue correspond to spin up, those in red to spin down. The Fermi level for the two magnetic solutions has been located in the middle of the gap induced by electron localization and not at the highest occupied level in order to allow a better comparison between the three diagrams.

(0.550 vs 2×0.225) as could be expected from the shape of the molecular orbitals shown in Figure 15.11. Comparing the results for K_4P_3 and K_5Bi_4 or K_3Bi_2, it is clear that the different extensions of the atomic orbitals of the anionic species play a key role in the bonding (and, therefore, in the transport properties) of these solids.

15.3.3
Crystal versus Electronic Structure: Are There Really Polyacetylene-Like Gallium Chains in Li_2Ga?

Looking for analogies between the structure and properties of organic and inorganic systems may be an extremely useful and suggestive approach to predict, understand, and propose the synthesis of new solids. However, the crystal structure and physical properties are ultimately dictated by the electronic structure so that only when there is also a clear-cut relationship between the corresponding electronic structures, as illustrated, for instance, by the isolobal analogy [35], can these relationships be fully endorsed. Probably there is no modern solid-state series of lectures or book in which the explanation of the Peierls distortion in *trans*-polyacetylene, that is, a dimerization, does not play a starring role. Thus, no chemist becoming aware of the Li_2Ga structure (Figure 15.13a) [36] can avoid some sense of surprise when realizing that despite formally having five electrons per Ga atom, and thus one

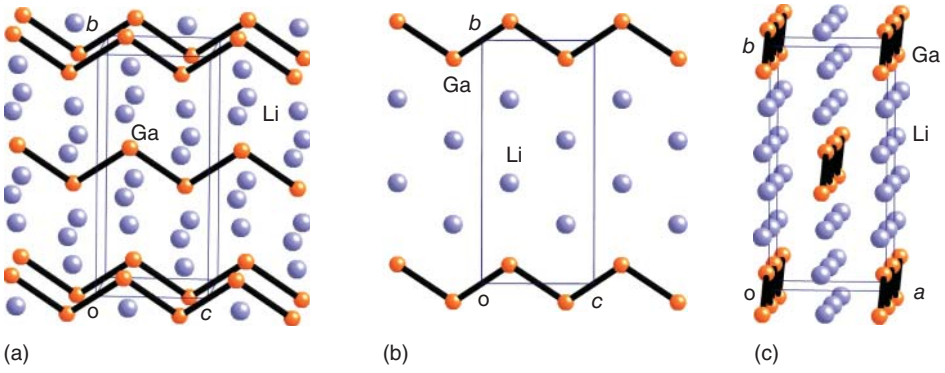

Figure 15.13 (a) Crystal structure of Li_2Ga phase, where the gallium chains are highlighted. (b) A view of the approximately hexagonal Li_2Ga layers perpendicular to *a*. (c) View along a direction slightly tilted along *c* [36].

electron per atom to fill the π-type levels as in *trans*-polyacetylene, the Ga chains in Li_2Ga do not exhibit any dimerization.

The crystal structure of Li_2Ga [36] contains planar uniform zigzag chains of gallium atoms along the *c*-direction, which are contained in the (*bc*)-planes. Thus, in the following, the π system of these chains will be considered to be built from the p_x orbitals. The more simple way to describe the structure of Li_2Ga is to note that there are (Li_2Ga)-layers perpendicular to the *a*-direction (Figure 15.13b), which can be described as being approximately hexagonal lattices with one-third of the positions being occupied by Ga atoms and two-thirds by Li atoms. The unit cell of Li_2Ga contains two of these layers, every layer being shifted by *b*/2 with respect to the adjacent ones (Figure 15.13c). Thus, successive gallium zigzag chains along *c* are separated by double rows of Li atoms. These layers alternate along the *b*-direction, with layers of Li atoms forming a centered rectangular lattice. Except when otherwise stated, the terms inter- and intralayer interactions in the following discussion refer to the (Li_2Ga)-layers in the (*bc*)-planes (Figure 15.13b). To confirm the existence of regular chains in Li_2Ga, the crystal structure was first optimized without imposing any geometrical constraint. The optimized structure is orthorhombic and contains uniform gallium chains with Ga-Ga distances of 2.691 Å and Ga–Ga–Ga angles of 114.2°, which are very similar to the experimental values [36]. Thus, the calculations confirm that there is no tendency toward a Peierls distortion in this phase.

Every zigzag gallium chain must lead to four filled σ-type bands (two of them mostly associated with the σ Ga–Ga bonding levels and the other two with mostly Ga sp^2-like lone pairs), and a pair of π-type bands. The four lower σ-type bands and the lower π-type one are those that, by analogy with *trans*-polyacetylene, should be filled if we assume complete charge transfer from the lithium to the gallium atoms. As there are two zigzag chains per unit cell of the solid, the lower bands in the band structure of Li_2Ga are expected to be a set of eight σ-type bands originating from bonding or nonbonding σ levels of the zigzag gallium chains and two pairs

of π-type bands. Even in such a naive description, some lithium character is of course expected to be found in these lower bands. The degree of mixing among the bands of the gallium zigzag chains and those associated with the lithium atoms is precisely what makes the use of a Zintl-type scheme more or less appropriate in order to approach the electronic structure of this phase.

The calculated band structure along the three main directions of reciprocal space is shown in Figure 15.14a, where the four bands originating mostly from the π-system of the Ga chains have been highlighted [37]. Note a quite strongly avoided crossing between the upper of these bands near Z and a mainly lithium-based band with the same symmetry. As a matter of fact, at around 1 eV above the Fermi level, several mostly lithium-based bands appear and mix strongly with the upper part of the set of 12 bands that originate from the two π-type bands and the four lower σ-type bands of the uniform zigzag gallium chains (remember that there are two gallium chains per unit cell). The four lower σ-type bands and the upper π-type one of this set are those that, by analogy with *cis*-polyacetylene, should be filled. Although the bands based on the π levels of the gallium chains can be clearly recognized despite the mixing with lithium orbitals, this is quite difficult for the σ-type bands. Except for the lower two pairs of bands, with strong contributions of the gallium s orbitals, even for the three symmetry lines shown in Figure 15.14a it is difficult to clearly say if several of the bands are mostly gallium based. Of course, within most of the Brillouin zone, where the σ-type and π-type bands can mix, it is not easy to follow the so-called π bands. Thus, on the basis of the analysis of the nature of the bands plotted in Figure 15.14a, it can be concluded that there are strong Ga–Li interactions in Li_2Ga.

The extent of these gallium–lithium interactions can be better visualized on the DOS plot of Figure 15.14b. The lithium contribution is important everywhere. Even in the region dominated by the Ga s orbitals (from −8 to −3 eV) almost one-third of the DOS comes from lithium orbitals. This participation is larger above this region and at the Fermi level it is practically 40%. In fact, the calculated Mulliken charges are +0.241 for Ga, −0.187 for Li(1) and −0.054 for Li(2). Even bearing in mind the possible shortcomings of Mulliken analysis, these figures are quite clear in showing a very important mixing of the lithium and gallium orbitals.

The COHP curves for the total Ga–Li and Li–Li interactions as well as those for the Ga–Ga interactions along the zigzag chains are shown in Figure 15.15 (except for the opposite sign, the COOP curves are very similar and lead to exactly the same conclusions). These curves immediately suggest that in addition to Ga–Ga there are also strong Ga–Li and Li–Li bonding interactions, in agreement with the earlier discussion. Looking in more detail at the individual overlap populations it is found that those for Ga–Ga bonds are large, 0.188, and some of those associated with the Li–Li interactions are far from negligible, 0.045, 0.039, 0.037, and 0.034. The first and third of these contributions are associated with intralayer contacts, whereas the second and fourth are associated with the interlayer contacts. Together with the curve in Figure 15.15b, this very clearly shows the existence of a 3D network of Li–Li interactions. Let us emphasize that the lithium participation in the filled levels really arises from orbital mixings with gallium orbitals and not from the

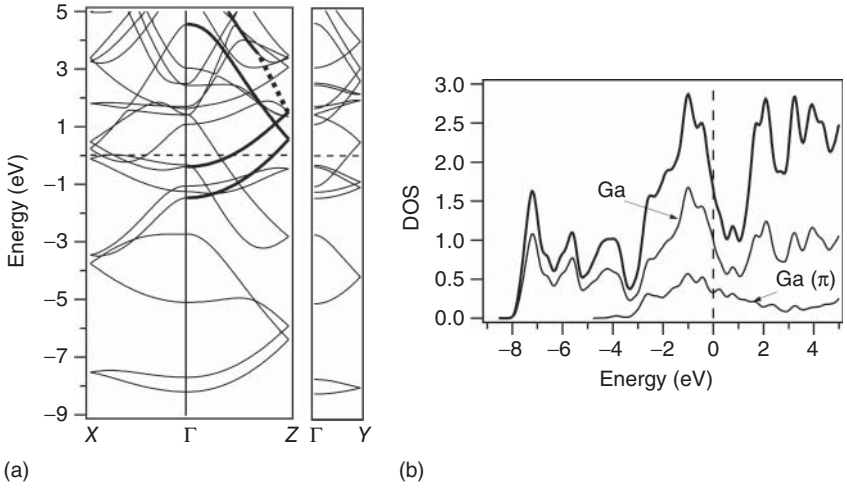

Figure 15.14 (a) Calculated band structure for Li_2Ga, where the horizontal dashed line refers to the Fermi level. Γ = (0, 0, 0), X = (1/2, 0, 0), Y = (0, 1/2, 0), and Z = (0, 0, 1/2) in units of the orthorhombic reciprocal lattice vectors. The four bands corresponding to the π-system of the Ga chains are highlighted. (b) Calculated density of states for Li_2Ga. The total contribution of the gallium orbitals and that of the gallium $p_x(\pi)$ levels are also shown. (Reproduced with permission from Ref. [37]. Copyright © 2005 American Chemical Society).

existence of mostly centered lithium bands, which dip below the Fermi level. This is at the origin of the many positive Ga–Li overlap populations. In fact, all Ga–Li contacts shorter than 3.25 Å are associated with quite strong and positive overlap populations (0.127, 0.097, 0.086, 0.048, 0.043, and 0.038). Thus, these results confirm that Li_2Ga must be considered as a tight 3D network in which the gallium chains are strongly connected through Li–Ga and Li–Li bonding interactions.

At this point, it could be considered that the analogy between the gallium chains in Li_2Ga and polyacetylene is valid, although because of a strong restoring force the Peierls distortion does not occur. However, this would not be an accurate description of the bonding in this phase. That all Ga–Ga bonding states (Figure 15.15c), but not all Ga–Li and Li–Li (Figure 15.15a and b) are filled, is telling us that the Ga–Ga interactions along the zigzag chain are the main contributors to the covalent bonding. This should not lead us to the conclusion that there are polyacetylene-like chains in the structure. The strength of the Ga–Li interactions, which are also almost optimized in this phase (Figure 15.15a) and add to large values of the overlap populations, indicates that, as mentioned, the phase should be better described as a 3D network of covalent and/or mostly covalent interactions in which Ga–Ga chains can be identified. However, the glue keeping together these chains (Ga–Li and Li–Li interactions) is so strong that it forces the mixing of the formally σ and π orbitals of the gallium chains so that the analogy with polyacetylene, even if appealing, is not justified. A detailed analysis of the nature of the different bands, DOS curves, and Fermi surface provides further support to this conclusion [37].

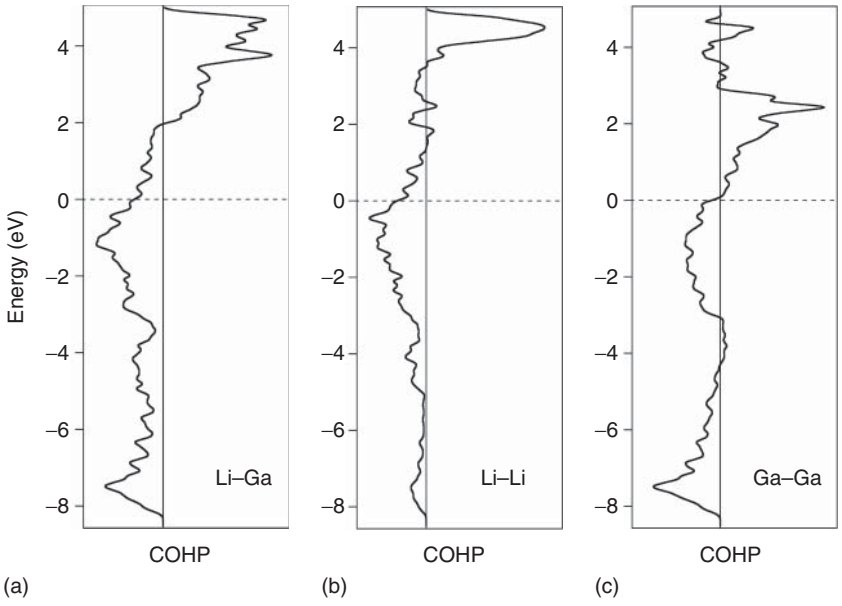

Figure 15.15 COHP curves for the total (a) Li–Ga and (b) Li–Li interactions and (c) Ga–Ga interactions within the zigzag chains of Li_2Ga.

Li_2Ga, like Li_9Al_4 [38], a solid in which identical zigzag aluminum chains are even more spaced, should be considered as three-dimensional metals with strong covalent interchain connections and small effective charge transfer [37]. These solids are thus typical examples of solids with both covalent and metallic bonding.

15.3.4
$Ba_7Ga_4Sb_9$: Do the Different Cations in Metallic Zintl Phases Play the Same Role?

As shown by the K_3Bi_2 and K_5Bi_4 phases, the cations in metallic Zintl phases act not only as mere electron suppliers but play a more fundamental bonding role, which may notably influence the transport properties. Here, we would like to go a step further. The structure of a phase depends on the whole set of filled levels of the system, whereas the transport or many other properties only depend on a small subset of them (i.e., for a metallic conductor, those in a narrow energy range around the Fermi level). Consequently, if the cations play a role in leading to the stability and structural features of a given phase, this does not necessarily mean that they are also important to understand the transport properties. Parenthetically, to say that cations play a role in understanding some aspect of the structure and/or properties of a material does not mean that *all* cations should be active players. It may be that some cations are decisive in conferring stability to the phase, whereas a different set of cations are those really influencing the details of the electronic conductivity.

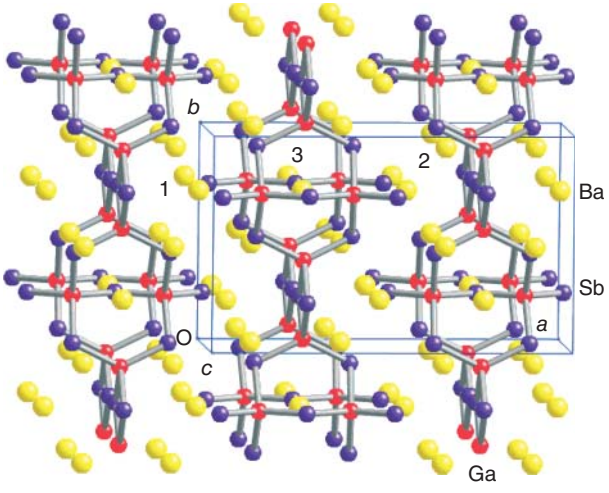

Figure 15.16 Crystal structure of $Ba_7Ga_4Sb_9$. The numbers correspond to the crystallographically different Ba atoms [39].

To illustrate this issue, let us consider the $Ba_7Ga_4Sb_9$ phase whose crystal structure is shown in Figure 15.16 [39]. The structure contains Ga_4Sb_9 layers perpendicular to the *a*-direction. Successive layers are shifted by $(b/2 + c/2)$ so that the unit cell is built from two identical layers. Every layer is made of a series of condensed $GaSb_4$ tetrahedra, four of which lead to a Ga_4Sb_{11} bicyclic unit analogous to bicyclo[3.3.1]nonane. In between these layers, three different types of Ba atoms (Ba1, Ba2, and Ba3; see Figure 15.16) reside. Loosely speaking, while two types of Ba atoms (Ba1 and Ba2) can be considered as residing in the interlayer region, another one (Ba3) resides inside the layers. Thus, just from simple geometric inspection one may suspect that different cations can play very different roles. The Ga_4Sb_9 layers contain 2 mono-coordinated, 5 bi-coordinated, and 2 tri-coordinated Sb atoms as well as 4 tetra-coordinated Ga atoms which, for electron-counting purposes, can thus be considered as Sb^{2-}, Sb^{-}, Sb^{0}, and Ga^{-}. Thus, the formal charge of the repeat unit of the layers is 13−, one electron short from the 14 provided by the 7 Ba atoms, assuming a complete transfer. Thus, at least formally, $Ba_7Ga_4Sb_9$ can be considered as a Zintl phase with an electronic excess [40].

The calculated band structure for $Ba_7Ga_4Sb_9$ along the three main directions of the reciprocal lattice is shown in Figure 15.17 [41]. All bands pair up at the *X* and *Y* points because there are two identical layers related by nonsymmorphic symmetry elements parallel to the *a*- and *b*-directions. The crucial feature of this figure is that two pairs of bands cross the Fermi level. One of the pairs is a very dispersive one along c^* (see the $\Gamma \rightarrow Z$ direction in Figure 15.17). Analysis of the character of the wave functions along this line (notice a weakly avoided crossing near the Fermi level) shows that this band is heavily based on the Sb atoms. However, there is a second pair of bands crossing the Fermi level along b^*, which is strongly based on the Ba atoms. Analysis of the DOS shows that as for the K_3Bi_2 and K_5Bi_4 phases,

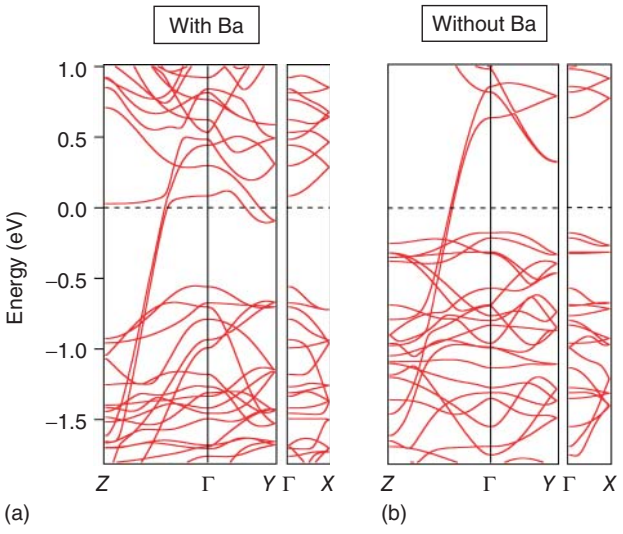

Figure 15.17 Calculated band structure for $Ba_7Ga_4Sb_9$ (a) and $(\square^{2+})_7(Ga_4Sb_9)^{14-}$. The dashed line refers to the Fermi level and $\Gamma = (0, 0, 0)$, $X = (1/2, 0, 0)$, $Y = (0, 1/2, 0)$ and $Z = (0, 0, 1/2)$ in units of the orthorhombic reciprocal lattice vectors. (Reproduced with permission from Ref. [41]. Copyright © 2006 American Chemical Society).

the orbitals of the three types of Ba atoms have a notable participation in large parts of the filled portion of the DOS. In agreement with this observation, it is found that all Ba atoms are implicated in large and positive Ba–Sb overlap populations (0.155, 0.143, 0.127, 0.113, …), indicating very substantial Ba–Sb bonding interactions. This is an important observation as it clearly establishes the involvement of cations in the bonding as well as in the conductivity of the material. Further analysis of the electronic structure near the Fermi level led to the prediction of a potentially very interesting low-temperature behavior for this material [41].

To understand the involvement of the different Ba atoms in the conductivity, it is convenient to carry out calculations emptying selected Ba sites but keeping the total number of electrons. The band structure calculated for $(\square^{2+})_7(Ga_4Sb_9)^{14-}$ where each of the Ba^{2+} ions in the structure has been replaced by a uniformly distributed 2+ charge is shown in Figure 15.17b. Note that, in agreement with the previous analysis, the pair of bands crossing the Fermi level around Y has completely disappeared, whereas the very dispersive one is kept. Because of the absence of the second partially filled pair of bands, the dispersive pair is half-filled and, consequently, the physical situation has been strongly altered. The cations, as well as the anionic subnetwork, thus play a very important role in understanding the conductivity of the material. The calculated band structures, when each of the three different types of Ba atoms is separately removed from the calculations without changing the electron count, are shown in Figure 15.18. It is clear that

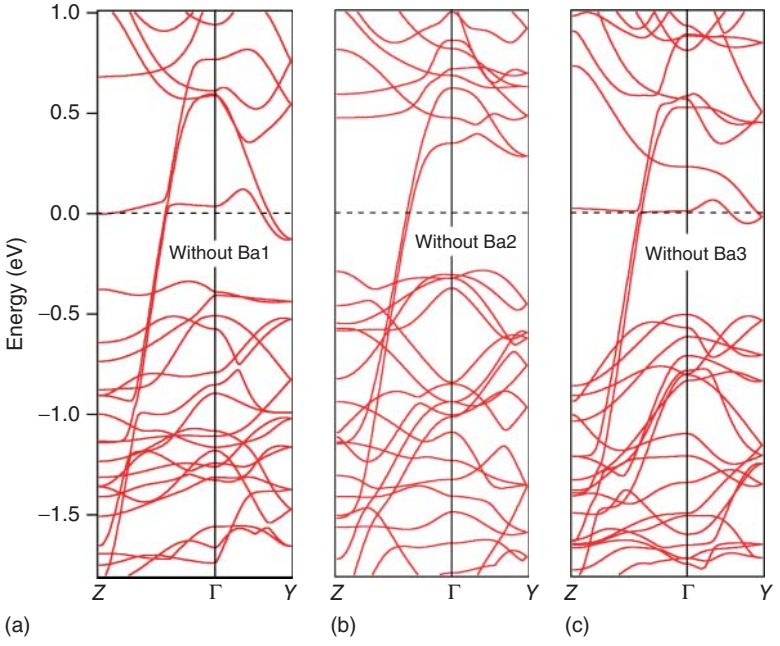

Figure 15.18 Calculated band structure for $Ba_7Ga_4Sb_9$ in which only the (a) Ba1, (b) Ba2, or (c) Ba3 cations were removed from the calculation without changing the electron count, as discussed previously. (Reproduced with permission from Ref. [41]. Copyright © 2006 American Chemical Society).

the Ba1 atoms have practically no effect on the band structure around the Fermi level and that the Ba3 atoms have a minor effect in slightly changing the shape of the Ba-based pair of bands. Thus, neither the Ba1 nor the Ba3 atoms influence in a substantial way the conductivity of the material, although they are essential for its stability. In contrast, the Ba2 atoms are essential in leading to the actual electronic structure around the Fermi level and, thus, in addition, to their role in the stability of the crystal structure, they have a strong influence on the transport properties and potentially very interesting low-temperature behavior of this phase. On the basis of these findings and additional analysis of the electronic structure, several predictions concerning the partial replacement of the Ba atoms leading to metallic systems with different anisotropies were carried out [41]. Thus, although all cations play a definite structural role in these metallic Zintl phases, the transport properties may be decided by just a small subset of the cations, which should be considered in trying to make some fine tuning of their transport properties.

15.4 Concluding Remarks

Although chemical bonding is not fundamentally different in molecules and solids, in the case of solids its analysis requires inputs from both physical chemistry and

condensed matter physics. Band theory is a straightforward construction to analyze the bonding and properties of periodic solids. The main concepts used in the analysis of chemical bonding in solids – band structure, DOS, COOPs/COHPs, Mott–Hubbard localization, Peierls distortions – have been briefly reviewed and its use illustrated by considering several metallic and magnetic Zintl phases. Bonding in these solids has covalent, metallic, and ionic components, but it can be quite easily understood using the above-mentioned tools. An important result of this analysis is the finding that although cations in these phases have long been considered to simply play the role of electron donors, ensuring the stability of the anionic species subnetwork and providing some kind of ''coulombic glue,'' keeping together the structure, they play a crucial role in leading to their actual structural and transport properties. Another important observation concerning these phases is that even if cations play a definite structural role, the transport properties may be decided by just a small subset of them, which should be considered in trying to make some fine tuning of their transport properties. Thus, being aware of these simple, but enormously useful, theoretical tools can be of major value in solid-state chemistry and physics.

Acknowledgments

This work was supported by DGI-Spain (Grants No. CSD2007-00041, FIS2012-37549-C05-05 and CTQ2011-23862-C02-02), Generalitat de Catalunya (2009 SGR 1459), XRQTC and by grants for computer time from CESCA and CESGA.

References

1. West, A.R. (1984) *Solid State Chemistry and its Applications*, John Wiley & Sons, Ltd, Chichester.
2. Ladd, M.F.C. (1979) *Structure and Bonding in Solid State Chemistry*, Ellis Horwood, Ltd, Chichester.
3. Wells, A.F. (1984) *Structural Inorganic Chemistry*, 5th edn, Clarendon Press, Oxford.
4. Pauling, L. (1960) *The Nature of the Chemical Bond*, 3rd edn, Cornell University Press, Ithaca, NY.
5. For a brief discussion of different computational approaches used in the solid state community see section 8 of:Canadell, E. (2005) in *Encyclopedia of Inorganic Chemistry*, 2nd edn, Vol. III (ed. R.B. King), John Wiley & Sons, Inc., Hoboken, NJ, pp. 1480–1506.
6. Ashcroft, N.W. and Mermin, N.D. (1976) *Solid State Physics*, Holt, Rinehart and Winston, Philadelphia, PA.
7. Sutton, A.P. (1993) *Electronic Structure of Materials*, Oxford University Press, Oxford.
8. Canadell, E., Doublet, M.-L., and Iung, C. (2012) *Orbital Approach to the Electronic Structure of Solids*, Oxford University Press, Oxford.
9. Peierls, R.E. (1955) *Quantum Theory of Solids*, Oxford University Press, London.
10. Hoffmann, R. (1988) *Solids and Surfaces: A Chemist's View of Bonding in Extended Structures*, John Wiley & Sons, Inc., New York.
11. Dronskowski, R. (2005) *Computational Chemistry of Solid State Materials*, Wiley-VCH Verlag GmbH, Weinheim.
12. Mulliken, R.S. (1955) *J. Chem. Phys.*, **23**, 1833–1840; *J. Chem. Phys.*, 1955, **23**, 1841–1846.
13. Hughbanks, T.R. and Hoffmann, R. (1983) *J. Am. Chem. Soc.*, **105**, 3528–3537.

14. Dronskowski, R. and Blöchl, P.E. (1993) *J. Phys. Chem.*, **97**, 8617–8624.
15. (a) Becke, A.D. and Edgecombe, K.E. (1990) *J. Chem. Phys.*, **92**, 5397–5407; (b) Savin, A., Jepsen, O., Flad, J., Andersen, O.K., Preuss, H., and von Schnering, H.G. (1992) *Angew. Chem. Int. Ed.*, **31**, 187–188; (c) Savin, A., Nesper, R., Wengert, S., and Fässler, T.F. (1997) *Angew. Chem. Int. Ed.*, **36**, 1809–1832.
16. Bader, R.W.F. (1990) *Atoms in Molecules: A Quantum Theory*, Oxford University Press, Oxford.
17. Mott, N.F. (1990) *Metal-Insulator Transitions*, 2nd edn, Taylor & Francis, London.
18. Kauzlarich, S. (ed.) (1996) *Chemistry, Structure and Bonding of Zintl Phases and Ions*, Wiley-VCH Verlag GmbH, New York.
19. (a) Hohenberg, P. and Kohn, W. (1964) *Phys. Rev.*, **136**, B864–B871; (b) Kohn, W. and Sham, L.J. (1965) *Phys. Rev.*, **140**, A1133–A1138.
20. Soler, J.M., Artacho, E., Gale, J.D., García, A., Junquera, J., Ordejón, P., and Sánchez-Portal, D. (2002) *J. Phys.: Condens. Matter.*, **14**, 2745–2779.
21. Perdew, J.P., Burke, K., and Ernzerhof, M. (1977) *Phys. Rev. Lett.*, **77**, 3865–3868.
22. Troullier, L. and Martins, J.L. (1991) *Phys. Rev. B*, **43**, 1993–2006.
23. Kleinman, L. and Bylander, D.M. (1982) *Phys. Rev. Lett.*, **48**, 1425–1428.
24. Monkhorst, H.J. and Pack, J.D. (1976) *Phys. Rev. B*, **13**, 5188–5192.
25. Corbett, J.D. (2000) *Inorg. Chem.*, **39**, 5178–5191.
26. Corbett, J.D. (2000) *Angew. Chem. Int. Ed.*, **39**, 670–690.
27. Gascoin, F. and Sevov, S.C. (2001) *Inorg. Chem.*, **40**, 5117–5181.
28. Gascoin, F. and Sevov, S.C. (2000) *J. Am. Chem. Soc.*, **122**, 10251–10252.
29. Alemany, P., Llunell, M., and Canadell, E. (2005) *Inorg. Chem.*, **44**, 1644–1646.
30. Fonseca Guerra, C., Handgraaf, J.-W., Baerends, E.J., and Bickelhaupt, F.M. (2004) *J. Comput. Chem.*, **25**, 189–210.
31. Rodríguez-Fortea, A. and Canadell, E. (2003) *Inorg. Chem.*, **42**, 2759–2763.
32. von Schering, H.G., Hartweg, M., Hartweg, U., and Hönle, W. (1989) *Angew. Chem., Int. Ed. Engl.*, **28**, 56–58.
33. Llunell, M., Alemany, P., and Moreira, I.d.R.P. (2009) *Inorg. Chem.*, **48**, 5938–5945.
34. (a) Anisimov, V.I., Aryasetiawan, F., and Lichtenstein, A.I. (1997) *J. Phys.: Codens. Matter*, **9**, 767–808; (b) Dudarev, S.L., Botton, G.A., Savrasov, S.Y., Humphreys, C.J., and Sutton, A.P. (1988) *Phys. Rev. B*, **57**, 1505.
35. Hoffmann, R. (1982) *Angew. Chem., Int. Ed. Engl.*, **21**, 711–724.
36. Müller, W. and Stöhr, J. (1977) *Z. Naturforsch. B*, **32**, 631–636.
37. Alemany, P., Llunell, M., and Canadell, E. (2005) *Inorg. Chem.*, **44**, 374–381.
38. Hansen, D.A. and Smith, J.F. (1968) *Acta Crystallogr. B*, **24**, 913–918.
39. Cordier, G., Schäfer, H., and Stetler, M. (1986) *Z. Anorg. Allg. Chem.*, **534**, 137–142.
40. Alemany, P., Alvarez, S., and Hoffmann, R. (1990) *Inorg. Chem.*, **29**, 3070–3073.
41. Alemany, P., Llunell, M., and Canadell, E. (2006) *Inorg. Chem.*, **45**, 7235–7241.

16
Dispersion Interaction and Chemical Bonding

Stefan Grimme

16.1
Introduction

From the various types of chemical bonding discussed in this book, the dispersion bonds are usually considered as being the weakest and therefore the least important for chemistry. This clearly holds true for the strength of a typical atom-pair-wise interaction, which is on the order of 0.5 kcal mol^{-1} or less for molecules composed of light elements ($Z < 40$). The closed-shell rare gas dimers with dissociation energies (D_e) of 0.08, 0.28, and 0.40 kcal mol^{-1} for Ne_2, Ar_2, and Kr_2, respectively, are classical examples. Dispersion interactions can be heuristically defined as the long-range attractive part of the van der Waals (vdW)-type interaction potential between nonpolar atoms and molecules that are not covalently bonded to each other, although the terms ''dispersion'' and ''vdW'' are often used synonymously [1]. Because the term ''dispersion'' has a wide variety of meanings in natural sciences, it is recommended to clearly distinguish it from other, partly related phenomena by using ''London dispersion'' in honor of F. London, who provided the first theory for this interaction [2]. For a detailed discussion of London dispersion (we use from now on the short form) and its relation to noncovalent interactions (NCIs) excellent monographs and review papers are available, for example, Refs. [3–5].

Despite its weakness, the dispersion interaction is extremely important for the formation and structure of many types of condensed matter and the special properties and function of biochemical systems [6–9]. The main reason for this fact is that the dispersion is ubiquitous, always attractive (bonding) and that the interactions are to a good approximation (errors <5–10%) additive. Hence, they add up already in medium-sized molecular systems to values that approach and easily surpass typical covalent and ionic interactions (which are on the order of 100 kcal mol^{-1} per pair interaction). The view that not only rare gas aggregates, liquids or molecular crystals are strongly influenced by dispersion but also chemical bonding and the thermochemistry of common reactions is just emerging [10] (although this idea scatteredly has been proposed much earlier; see, e.g., Ref. [11]; for a related review about closed-shell interactions see Ref. [12]).

The Chemical Bond: Chemical Bonding Across the Periodic Table, First Edition.
Edited by Gernot Frenking, Sason Shaik.

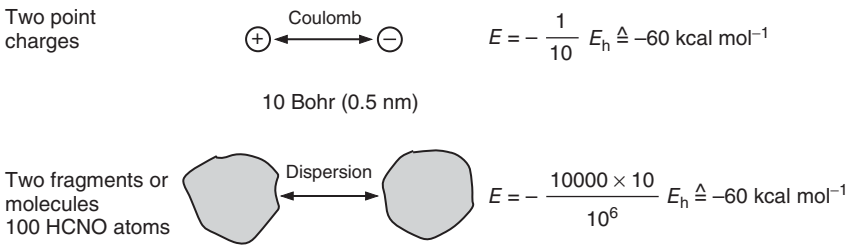

Figure 16.1 Comparison of the magnitude of Coulomb and dispersion interactions. For details, see text.

That dispersion effects are not weak at all can be shown by a simple paper and pencil treatment of model systems (see Figure 16.1) and is later discussed for the bonding in hexaphenylethanes [13] and cation–cation attraction [14] in transition metal complexes.

We take two interacting point charges at a typical distance of 10 Bohr (about 5 Å) as a reference system because its classical electrostatic interaction energy of about 60 kcal mol^{-1} is well conceived by most chemists. This is compared to a medium-sized molecule or aggregate composed of about 200 atoms, which is dissociated into two fragments with 100 atoms each. The number of (dispersion)interacting atom pairs is $100^2 = 10^4$. Taking an average C_6 dipole–dipole dispersion coefficient typical for light (organic) elements (about 10 E_h Bohr^6) and assuming the same (as for the point charges) average interatomic distance between the particles of 10 Bohr, a dispersion interaction energy E_{disp} of about −60 kcal mol^{-1} is obtained, which is close to the corresponding interaction in the electrostatic case. We have made use here of the very fundamental and rather accurate (semiclassical) approximation that the dispersion energy between nonoverlapping fragments consisting of atoms A and B is given by

$$E_{disp} = -\sum_{AB}^{atom\ pairs} \frac{C_6^{AB}}{R_{AB}^6} \tag{16.1}$$

where R_{AB} are interatomic distances and C_6 denotes the pair-specific dipole–dipole dispersion coefficient that determines the interaction strength (and is further discussed later). According to this example, the general consideration of dispersion as being weak is at least misleading when larger molecules interact.

Another aspect of vdW or dispersion bonding is that it generally has the flavor in the literature of being special and totally different from all other types of bonding. While it is certainly true that on an atom-pair-wise basis the interaction is much weaker, the physical mechanisms are not totally different from other more common types of bonding. Phenomenologically, covalent and vdW bonding have more in common than generally thought. This is exemplified by the comparison of the dissociation of the covalent Cl–Cl and dispersive Ar–Ar bond. Corresponding potential energy curves on a reduced energy scale (i.e., scaled to −1 at equilibrium

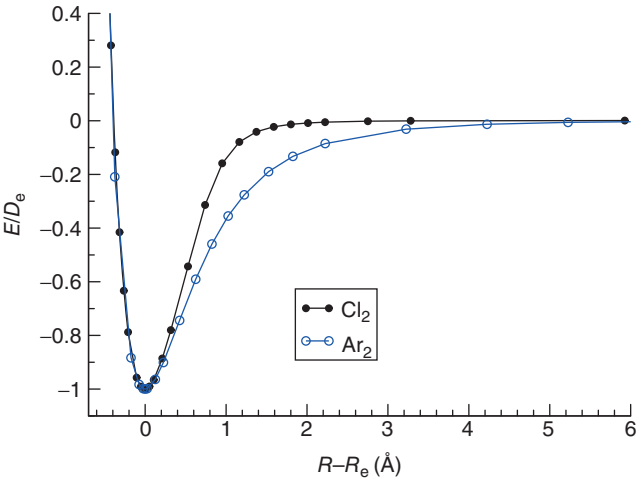

Figure 16.2 Potential energy curves for the dissociation of the covalent bond in Cl_2 (UTPSS-D3/def2-QZVP DFT level of theory) and the van der Waals bond in Ar_2. A reduced interaction energy (i.e., setting the equilibrium value to −1) and shifted distances (setting $R_e = 0$) are given. The absolute D_e values for the two diatomics are 62.2 kcal mol^{-1} (at 2.01 Å) and 0.282 kcal mol^{-1} (at 3.775 Å), respectively, and are in a ratio of a factor of about 210 in favor of the covalent interaction. (Data from [15].)

using E/D_e, where D_e is the equilibrium dissociation energy) and shifted distances with respect to $R_e = 0$ are given in Figure 16.2.

The very similar shape of the two curves, especially in the equilibrium and repulsive regions, is very intriguing. It emphasizes a similar balance of Pauli exchange repulsion (EXR) and attractive interactions, however, at very different distances as the covalent bond is shorter by as much as 1.77 Å. This comparison also clearly shows that the major difference between covalent and dispersion bonding occurs (not unexpectedly) in the asymptotic regime. While the covalent interaction is chemically negligible already at about $R_e + 1.5$ Å (and this holds for many other elements), the dispersion interaction remains significant up to $R_e + 3$ Å.

So, in summary, up to this point the take-home messages are that dispersion interactions are (a) ubiquitous and always attractive, (b) per atom-pair interaction on the order of a factor 100 weaker than covalent ones, (c) more long-ranged (typical distance range of 3-5 Å compared to 1-2 Å for covalent bonds), and (d) additive in character. These properties lead to a wide variety of dispersion bonds and by their admixture to other bonding mechanisms overall to a significant impact in chemistry.

This chapter concentrates on molecular-insulator-type systems that dominate main group inorganic, organic, and biochemistry; and for which dispersion-related phenomena are fairly well understood. For extended metallic systems (but not for many molecular (organo)metallic complexes that are unproblematic) the situation is different, as these have a rather nonlocal (NL) electronic structure and strong

electron correlations appear on all length scales. Special methods and computational tools for dispersion effects with screening for bonding in metals and for molecules on metallic surfaces are just being developed [16–18]. The insulator-type methods as described here will be sufficient for qualitative or semiquantitative purposes also for metals but cannot provide high accuracy (as defined by errors <5–10% for D_e).

After a brief recapitulation of the theory of dispersion interactions in the next section, quantum chemical methods for their accurate computation are described. Because a huge number of different computational schemes have been developed over the years, this chapter cannot be extensive regarding details of the methodology but concentrates on efficient methods for large systems. The last section contains chemical examples that exemplify the sometimes decisive role of the dispersion energy for large chemical complexes.

16.2
A Short Survey of the Theory of the London Dispersion Energy

The dispersion energy is a many-body electron correlation effect and hence appears already for two-electron systems. There is no clear distinction between dispersion and the more conventional electron correlation except that they operate on different interelectronic distance scales (long- and short-ranged, respectively).

In an orbital picture, a single electron occupies some ground-state level. Virtual (unused) orbitals represent excited states (and can be used to construct excited state WF in many-electron cases). Single excitations of the electron to these states change the electronic distribution and when coupled to a corresponding deexcitation, one can think of this process as ''charge fluctuation.'' In a stationary state (time-independent) picture, which is sufficient to understand all dispersion phenomena, these fluctuations actually do not take place but merely represent possibilities. They are realized (as part of the wave function) if a second electron comes into play and then represent electronic correlations, that is, the virtual states (more precisely the corresponding transition densities) interact electrostatically (with exchange-type modifications at smaller distances). The amplitudes of the resulting double-excitations (i.e., coupled single excitations) represent the basic quantity in all wave function theories to compute the dispersion energy. Dispersion is ''transmitted'' by electromagnetic radiation (photon exchange) and not by electron exchange as in covalent bonding such that screening effects in very dense materials (as described by an effective dielectric constant) might appear. Because electronic transition densities (and not charge densities) are the basic quantity for the dispersion bonding mechanism, conventional (charge-density-based) methods of Kohn–Sham density functional theory (DFT) [19–22] have fundamental problems in its description. The characteristic length scale for dispersion interactions can be estimated from the fact that the lowest electric moment of a transition density is of dipole type. The two coupled (induced) dipole moments interact electrostatically via the well-known $1/R^3$ (R being the center-of-charge distance) formula. Because of their mutual (conditional) influence, the corresponding interaction must be

squared in the framework of perturbation theory, leading to the famous $1/R^6$ decay law for the asymptotic part of the London dispersion energy [3]. The interaction between systems in electronically excited states has a dispersion component as well but with different R-dependence and depending on the nature of the state of atoms [23, 24].

Dispersion is omnipresent in electronic systems (such as gravitation in systems with mass) and always attractive (energy lowering). Its natural, also omnipresent, antagonist is the EXR due to the Pauli exclusion principle. It is nowadays clear that any reasonable attempt to quantitatively describe chemical bonding must include these terms together with electrostatic and covalent parts, which, however, still dominate chemical thinking.

The simplest conceivable vdW bond is not represented by the helium dimer (with four electrons) as frequently stated but for triplet dihydrogen (see Figure 16.3). When the Coulomb correlation energy is neglected as in the Hartree–Fock (HF) method, the $^3H_2$ molecule is completely unbound as one electron occupies the bonding σ orbital, while the other is in the antibonding σ^* orbital and the EXR interaction dominates. When the density-dependent, NL VV10 density functional [25] is used with the HF electron density as input (see Ref. [26] for details) and the resulting dispersion energy is simply added to the HF energy, the black-dotted curve in Figure 16.3 results. Comparison of this potential with that given by the C_6/R^6 law (using the exact dispersion coefficient of $6.5E_h$ Bohr^6 for the free hydrogen atom [23]) shows that the potential is essentially dispersion at long range and EXR (exchange repulsion) below $R_e = 4$ Å. Although the "bond" is extremely weak (calculated $D_e = 0.011$ kcal mol^{-1} compared to 0.022 kcal mol^{-1}

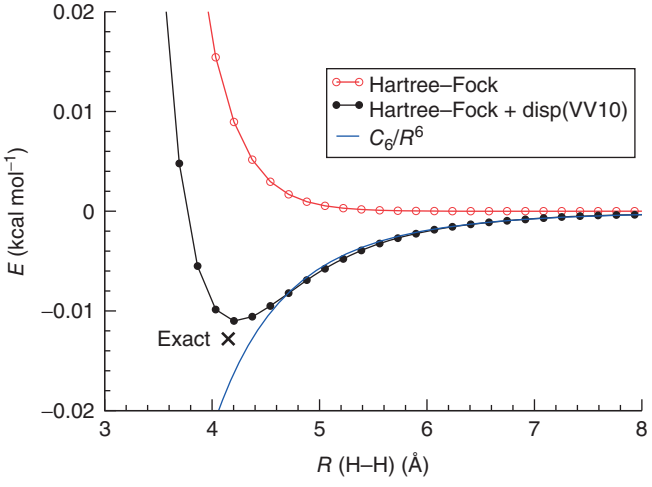

Figure 16.3 Computed potential energy curves for triplet dihydrogen ($^3\Sigma_u$) using the uncontracted aug-cc-pV5Z AO basis. The curve labeled "+disp" is obtained from the Hartree–Fock one by adding the nonlocal correlation energy of the VV10 density functional computed with the SCF density.

for He_2) and very long, this example demonstrates clearly that any two electrons in any state (i.e., with very minor dependence on the electron spin) can exhibit the phenomenon of dispersion binding. The practically exact values [27] for this system are 0.013 kcal mol^{-1} and 4.15 Å for D_e and R_e, respectively, which are in good agreement with the HF-NL data. Note that the $^3\Sigma$ state is an excited one (the ground state cannot be used here because the covalent bond formation would dominate the potential on the energy scale shown) and this example hence indicates that the VV10 functional seems to be applicable for excited states as well (it has so far only been employed for ground states).

The situation in more interesting, larger chemical systems is of course much more complex and a simplified analysis for understanding is appropriate. The energy decomposition analysis (EDA) is a valuable theoretical tool to partition the interaction energy from a supermolecular self-consistent field (SCF)-type computation into physically meaningful components [28]. It goes back to Morokuma [29, 30] and recently has proved to give detailed information about the nature of chemical bonding [31] as well as for the interactions in hydrogen-bonded systems [32], supramolecular structures [33] and vdW complexes [34]. The formation of bonding between two fragments is divided into three physically plausible steps. In the first step, the fragment electronic densities (in the frozen geometry of the supermolecule) are superimposed, which yields the quasi-classical electrostatic interaction energy (ES). Renormalization and orthogonalization of the product of monomer wave functions yields the repulsive energy term EXR. In the final step, the molecular orbitals are allowed to relax to their final form variationally. This yields the (usually stabilizing) induction energy (IND), the orbital interaction (covalent, COV) and charge-transfer terms (CT). The dispersion energy is calculated with the D3 approach (see subsequent text). Here, we do not discuss all these energy components of the partitioned total interaction energy ΔE in detail but concentrate on the three quantities

$$\Delta E = E_{\mathrm{EXR+ES}} + E_{\mathrm{CT+IND+COV}} + E_{\mathrm{disp}} \tag{16.2}$$

which describe (in the above-mentioned order) (a) semiclassical (steric) interaction, (b) ''true'' chemical bonding and (c) dispersion. Their sum differs from the exact interaction only by the energy necessary to bring the optimum monomer geometries into the form they have in the supermolecule. Because we employ frozen monomer geometries, this deformation (also called preparation) energy contribution vanishes. It is generally small (<2–3% of D_e) in noncovalently bound complexes and can be neglected to a good first approximation.

As an example, the results for formation of the donor–acceptor bond in Me_3N-BMe_3 are shown in Figure 16.4. Such bonds (and their strengthening by dispersion and weakening by EXR effects) play an important role in the so-called frustrated Lewis pairs (FLP), which have attracted enormous attention recently because of their ability to activate small molecules such as H_2 [35–37]. Because the bond dissociates heterolytically into closed-shell fragments, static electron correlation effects play no important role and a standard restricted DFT treatment

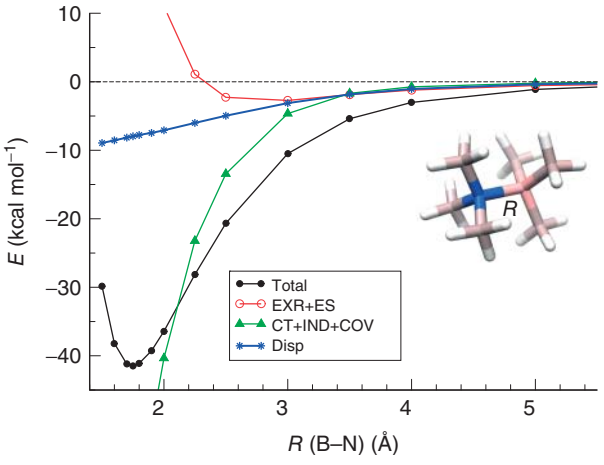

Figure 16.4 Energy decomposition analysis (EDA) at TPSS-D3/def2-TZVP level for donor–acceptor bond formation in Me_3N-BMe_3 (rigid fragment approximation). For a definition and explanation of the energy terms, see text.

is appropriate. In most of the following examples, the TPSS [38] meta-GGA density functional and the Ahlrichs-type def2-TZVP [39, 40] Gaussian atomic orbital (AO) basis is used. This level of theory has proved to be generally robust in hundreds of applications and large-scale benchmarks [41] with a very good performance/computational cost ratio.

As can be seen in the plot, the medium-sized interaction (D_e = 42 kcal mol^{-1}) in the equilibrium region and for slightly larger distances up to 2.5 Å is dominated by chemical bond formation ($E_{COV+IND+CT}$ term). Because the Me_3N and BMe_3 fragments have low polarity and are somewhat bulky (similar to many FLPs), the E_{EXR+ES} term is only weakly bonding and at short distances strongly repulsive (“steric hindrance”). For long bond distances, all three components contribute about equally to binding. Dispersion is rather attractive and adds 5–10 kcal mol^{-1} in the equilibrium region, which is about 10–20% of D_e already for the relatively small methyl substituents considered here. For realistic FLPs where large mesityl and C_6F_5 substituents are present, the corresponding dispersion contributions can reach 30–40 kcal mol^{-1} and more than 100% of D_e [36]. This example shows that already for systems with eight nonhydrogen atoms and for conventional bond formation dispersion effects play a nonnegligible role and must be considered in accurate work.

Many of the more conventional bonding types in chemistry can vary considerably for elements across the periodic table. One of the questions in this context is how far this holds for dispersion binding or the contribution of dispersion to other bonds. As Eq. (16.1) suggests, a good measure for the strength of the dispersion interaction between two atoms AB is their C_6^{AB} coefficient. To a good approximation, it can be taken as the average (arithmetic or geometric) of the values of the corresponding

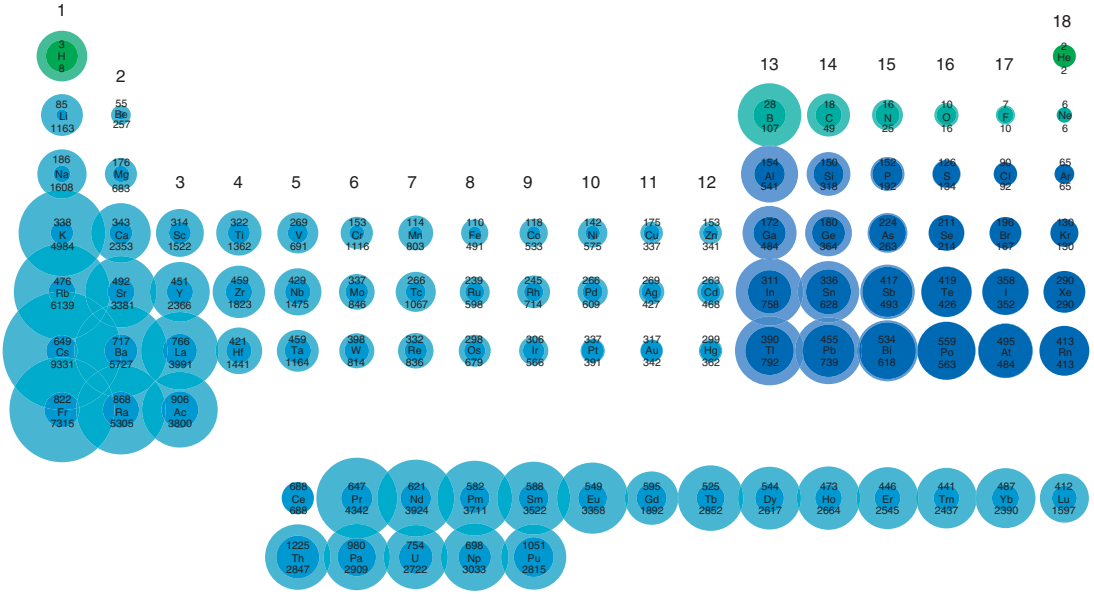

Figure 16.5 Computed (TDDFT/PBE38) C_6 dispersion coefficients (in E_h Bohr^6) for the whole periodic table (up to Pu), which are used in the DFT-D3 method. For each element the free atom value (lower value, light colored circle) and the coefficient (upper value, darker color) for the atom in a saturated chemical environment (with the highest coordination number according to the DFT-D3 scheme, e.g., four for carbon and three for nitrogen) are given. The radius of the circle is proportional to $C_6^{1/3}$. Scale factors for better visibility are 15 (H–He), 5 (B–Ne) and 2 (rest of the III–VIIIa elements).

C_6^{AA} and C_6^{BB} coefficients. As a valuable spin-off product from the development of the D3-method [42], these data were consistently computed for the whole periodic table and part of the results are shown in Figure 16.5. Given are the C_6^{AA} values for the free atoms and for the atom in a chemically saturated environment, that is, when the atom has used all of its ''normal'' valencies (e.g., four and two for carbon and oxygen, respectively) for covalent bonding. These values are based on first-principles time-dependent density functional theory (TDDFT) computations of frequency-dependent polarizabilities, as pioneered by the Baerends group [43, 44]. For other recent studies on the dependence of the C_6^{AB} coefficients on the chemical environment, see Ref. [45]; for a discussion of relativistic effects, see Ref. [46].

As can be clearly seen (by comparison of the size of the circles), the free atom and bonded atom values can differ by large amounts, in particular for the alkaline and earth alkaline metals. Their bonding is associated more or less with oxidation, and the loosely bound valence electron (responsible for the high polarizability of the free atom) is ''lost'' for dispersive bonding. This quenching of the free atom dispersion in molecules is less pronounced for nonmetals and weakens to the right in the periodic system of elements (PSE). Physically it is related to the increase in electronic excitation energies by covalent bond formation (widening of HOMO–LUMO gap). Very significant changes are still observed for carbon, for which the values decrease from 49 to about 18 (all values in atomic units in the following) in the typical sp^3 molecular valence state. This property is very important for the subtleties in dispersion binding of carbon-rich materials of saturated and unsaturated character [47]. In the D3 method (see subsequent text), the dispersion quenching with the increasing number of bonds formed is accounted for by a geometrically computed, continuous and fractional coordination number. Within one group of elements the relative difference between maximum and minimum atomic C_6 values typically decreases, for example, from 25 to 16 for N, from 192 to 152 for P, and from 263 to 224 for As. For the heavier halogens, maximum and minimum values are essentially the same, which is consistent with the view that the quenching effect of the single unpaired electron and the increase in the C_6 value by electron acceptance in a single (mostly ionic) bonding almost cancel.

The about 33 000 C_6^{AB} coefficients that were computed for the D3-method [42] as supporting points for interpolation of C_6 values in molecules enable us not only to accurately compute the dispersion energy for atoms in different molecular environments but also lead to a detailed understanding of dispersion bonds.

16.3 Theoretical Methods to Compute the Dispersion Energy

Because the dispersion energy is an essential part of NCIs and this topic is nowadays in the focus in various areas of chemistry and physics, excellent reviews already exist [48] and only a brief summary and recapitulation is given here.

16.3.1 General

Currently there are only three basically different *ab initio*-type methods in use (the vast amount of empirical potentials is not considered here). These are

1) Supermolecular by wave function theory (WFT);
2) Supermolecular by DFT with dispersion corrections;
3) Symmetry-adapted perturbation theory (SAPT) based on fragments.

Supermolecular methods compute the interaction ΔE (and their parts, e.g., dispersion) as a difference of total energies E_{tot} for the aggregate (complex AB) and the fragments (A and B) as

$$\Delta E = E_{tot}(AB) - E_{tot}(A) - E_{tot}(B) \tag{16.3}$$

The approach has the advantage that any approximate electronic structure method from WFT or DFT can be used in Eq. (16.3). The dispersion energy can be treated separately as, for example, in dispersion-corrected DFT (or HF)

$$E_{tot} = E_{SCF} + E_{disp} \tag{16.4}$$

where E_{SCF} is the conventional Kohn–Sham (or HF) SCF electronic energy and E_{disp} is the dispersion correction. Note that we use here the terms interaction energy (ΔE) and dissociation energy (D_e) synonymously, although they have different signs and more precisely differ by the fragment relaxation energy (included in D_e, i.e., it is observable when zero-point vibrational energies are added, while relaxation is neglected for ΔE; for diatomics $\Delta E = -D_e$ holds). This allows a convenient computation of the dispersion contribution to binding, that is, ΔE_{disp} according to Eq. (16.3). Because $E_{tot}(AB)$ is explicitly computed, intramolecular NCI and dispersion effects can be obtained if a proper reference state (e.g., folded vs unfolded conformation) can be defined. A disadvantage of the supermolecular approach is that it is contaminated with the so-called basis-set superposition error (BSSE), a one-particle basis incompleteness effect, which is severe especially in correlated WFT calculations with small or medium-sized AO basis sets. For DFT or HF calculations with triple-zeta basis sets, it is typically only <5–10% of D_e (<2–3% with quadruple-zeta basis sets) and negligible when compared to other more important sources of error (e.g., the approximate nature of the exchange-correlation functional in DFT) [49]. For a recent in-depth discussion of the BSSE in the framework of DFT, see Ref. [50]

16.3.2 Supermolecular Wave Function Theory (WFT)

Because dispersion is a genuine electron correlation effect, a common approximation in WFT is to compute it as

$$\Delta E_{disp} \approx \Delta E_c = \Delta E_{post\,HF} - \Delta E_{HF} \tag{16.5}$$

where ΔE_{HF} is the HF interaction energy and $\Delta E_{\mathrm{post\,HF}}$ refers to a correlated WFT treatment such as Moeller-Plesset second-order perturbation theory (MP2) or coupled-cluster with single and double excitations (CCSD(T)) with correlation energy E_{c} [51]. This approximation works fairly well for large interfragment distances but is obscured for shorter bonds by exchange and intrafragment correlation effects.

An appealing feature of this partitioning is that the correlation (dispersion) energy computationally can be assigned exactly to contributions from orbital pairs. If localized molecular orbitals (LMOs) are used in the correlation treatment, this allows a local (group- or fragment-wise) description of dispersion effects [52]. The correlation energy (E_{c}) for an HF reference state can be written as a sum over occupied orbital pairs ij

$$E_{\mathrm{c}} = \frac{1}{2}\sum_{ij} e_{ij} \tag{16.6}$$

In the simplest correlated WFT, which is second-order Møller–Plesset perturbation theory (MP2) [53, 54], the pair energies e are given by a sum over all virtual orbital pairs ab

$$e_{ij} = -\sum_{ab} \frac{(ia|jb)[(ib|ja) - (ia|jb)]}{\varepsilon_i + \varepsilon_j - \varepsilon_a - \varepsilon_b} \tag{16.7}$$

Here, ε are canonical HF eigenvalues and $(ia|jb)$ are two-electron integrals in charge-cloud notation. For modern, improved versions of MP2, see Ref. [55]. Because E_{c} is invariant under unitary transformations within the occupied and virtual orbital blocks for common approximations (e.g., MP2 or CCSD), identical results compared to the canonical treatment are obtained when the orbitals ij are replaced by LMO. Because LMO are usually strongly localized on atoms or in chemical bonds (mostly to >95% on <2–3 atoms), it is possible to partition the total correlation energy into chemically meaningful inter- and intrafragment contributions according to

$$E_{\mathrm{c}}(\mathrm{inter}) = \sum_{i\subset F_1}\sum_{j\subset F_2} e_{ij} \tag{16.8}$$

$$E_{\mathrm{c}}(\mathrm{intra}) = \frac{1}{2}\sum_{ij\subset F_1} e_{ij} \tag{16.9}$$

Here, F_1 and F_2 denote sets of orbitals that define molecular fragments or orbital spaces (i.e., core, σ, π, lone-pair). The decision on the type of orbital and the atom to which it belongs can (automatically) be made on the basis of a Mulliken population analysis [56] of the LMO in question. Asymptotically, when fragments F_1 and F_2 are spatially well separated, the interfragment correlation energy is equal to the interaction energy, which can be further interpreted as their dispersion interaction

$$E_{\mathrm{c}}(\mathrm{inter}) \approx E_{\mathrm{disp}} = -\frac{C_{\infty}^{F_1F_2}}{R^n} \tag{16.10}$$

Here, $C_{\infty}^{F_1F_2}$ denotes an effective dispersion coefficient for the fragments, R is their (center-of-charge) distance and n is an effective exponent typically close to six.

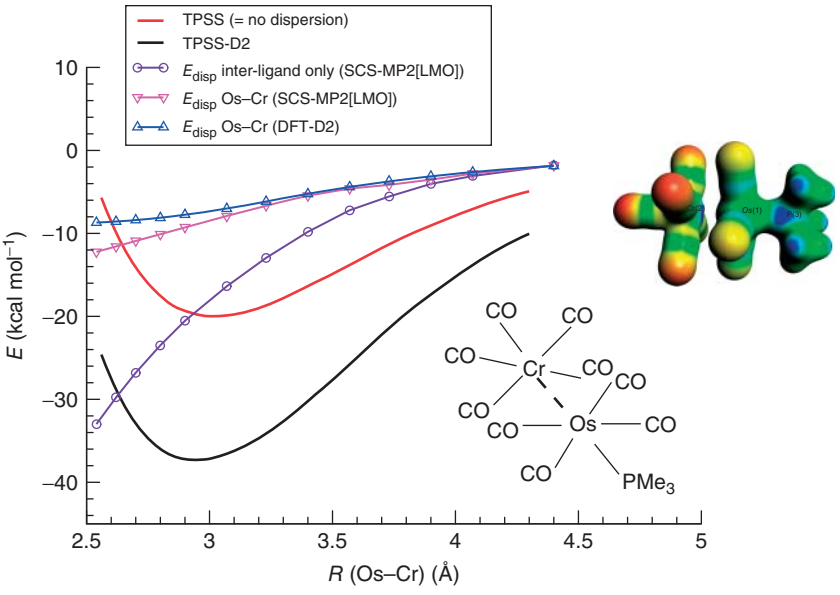

Figure 16.6 Computed• potential energy curves for the Os–Cr interaction in $(OC)_5Cr\text{-}Os(CO)_4PMe_3$ from Ref. [57]. The graph shows a comparison of TPSS and TPSS-D2 curves corresponding to a large dispersion contribution to binding and two contributions to the interfragment dispersion energies at the partitioned spin-component-scaled (SCS)-MP2(LMO) level. Note the relatively small dispersion interaction (triangles) between the metal atoms (and the good agreement of SCS-MP2(LMO) and DFT results for this) and the dominant ligand–ligand (i.e., CO and PMe_3) contribution (circles). The inset shows a color-coded map of the molecular electrostatic potential on an iso-charge-density surface, indicating no significant electrostatic interaction (small polarity) as well as almost no overlap-based bonding interaction between the Os and Cr atoms. The Os–Cr bond is considered as being mainly dispersion driven with some short-range correlation effects that are captured by the density functional.

Note that the effective dispersion coefficient also contains higher order moments than the usual induced dipole–dipole term because the full electric moments of the LMOs are considered by the integrals in Eq. (16.7).

A recent example for this type of analysis in a donor-acceptor-type transition metal complex [57] is given in Figure 16.6; for other applications in the field of biochemical model systems, see Refs. [52, 58].

16.3.3
Supermolecular Density Functional Theory (DFT)

Dispersion corrections to DFT and HF (including semiempirical methods) have recently been reviewed [59, 60] and hence only a brief description is given. Asymptotically correct approaches are either atom-pair-based (e.g., DFT-D3 [42], XDM [61], or Tkatchenko-Scheffler (TS)-vdW [62]) or compute the dispersion energy from the electron density (called vdW-DF [25, 63]). For recent work on the

combination of dispersion and long-range exchange corrections, see Ref. [64]. A new idea for a NL dispersion correction was proposed recently by Hesselmann [65].

In the general vdW-DF framework, such an NL correlation (dispersion) energy takes the form of a double-space integral

$$E_{\text{disp}}^{\text{NL}} = \frac{1}{2}\iint \rho(r)\phi(r,r')\rho(r')\text{d}r\text{d}r' \tag{16.11}$$

where ρ is the charge density and r and r' denote electron coordinates. The different variants of vdW-DF that are currently on the market only differ in the choice of the NL correlation kernel $\phi(r,r')$. These kernels are physically based on local approximations to the (averaged) dipole polarizability at frequency ω (i.e., $\alpha(r,\omega)$). Knowing ω at all (imaginary) frequencies leads automatically, via the famous Casimir–Polder relationship [66] given in Eq. (16.12), to the long-range part of the dispersion energy. This clarifies the deep relation to atom-pair-wise methods that employ these coefficients as basic quantities and replace the charge density by atom-centered delta functions and the double-integral by a double sum. The C_6 dispersion coefficient for induced dipole–dipole dispersion interacting fragments A and B is given by

$$C_6^{\text{AB}} = \frac{3}{\pi}\int_0^\infty \alpha(i\omega)^A\alpha(i\omega)^B d\omega \tag{16.12}$$

Higher order dipole–quadrupole, quadrupole–quadrupole, … coefficients (i.e., C_8, C_{10}, …) can also be computed by similar formulas [3]. Odd-order terms vanish for spherical systems (free atoms) but occur for nonspherical ''atoms'' as found in molecular environments. It is currently not clear how large the effect of including, for example, C_7 really is [67], but so far very good results have been obtained by including even-order terms only.

The C_6 coefficients (and derived C_8) in the D3 method have been computed using a modified form of this relation, where the $\alpha(i\omega)$ are computed nonempirically by TDDFT and A and B are reference molecules from which atomic values are derived [42]. Because the reference system can also be a molecular cluster modeling a solid environment, special coefficients for atoms in the bulk can be derived [68]. The final form for the DFT-D3 two-body part of the dispersion energy employs the so-called Becke–Johnson (BJ) damping [61, 69] and truncates the expansion at C_8

$$E_{\text{disp}}^{\text{D3(BJ)}} = -\frac{1}{2}\sum_{\text{A}\neq\text{B}}\frac{C_6^{\text{AB}}}{R_{\text{AB}}^6 + f(R_{\text{AB}}^0)^6} + s_8\frac{C_8^{\text{AB}}}{R_{\text{AB}}^8 + f(R_{\text{AB}}^0)^8} \tag{16.13}$$

where $f(R_{\text{AB}}^0) = a_1 R_{\text{AB}}^0 + a_2$ and a_1, a_2, and s_8 are empirical parameters that have been determined by a fit to CCSD(T) interaction energies for typical NCI (i.e., the S66 set [70]). The vdW-DF method in the VV10 flavor also contains two empirical parameters (adjusting the long- and short-range behavior) of which only the latter is fitted for each density functional [26].

This form of the damping function ensures that for small interatomic distances the right constant limit for the energy correction is obtained [71]

$$E_{\text{disp}} = -k_1 + k_2 R_{\text{AB}}^2 \ (R_{\text{AB}} \to 0) \tag{16.14}$$

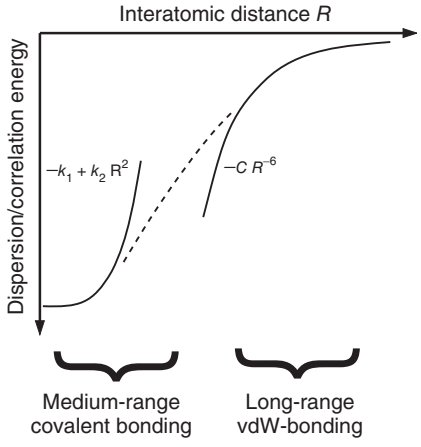

Figure 16.7 Schematic description of the long- and medium- or short-range behavior of the dispersion/correlation energy.

where k_1 and k_2 are atomic constants. This behavior (which is also fulfilled by the vdW-DF method using the VV10 kernel [25]) is the reason why dispersion in a broader sense of definition can influence ''normal'' bonding (thermochemistry). When atoms come close together, the electrons can be still far apart (i.e., showing long-range dispersion-type correlations) and hence dispersion becomes part of the ''normal'' correlation energy. This is illustrated in Figure 16.7. The D3- and NL corrections have been carefully benchmarked on a very large variety of NCI [26, 42, 72, 73] and, in general, high-accuracy (errors <10% of D_e) and only small variations between the different methods have been observed. This is documented here on a very recent, more difficult example of interacting metal atoms. The dimer of the so-called oxaliplatin complex (a potent anticancer drug [74]) is investigated along a rigid dimerization coordinate (for the structure, see inset in Figure 16.8). Although the complex is considered as being strongly hydrogen bonded, by comparison of the uncorrected TPSS and TPSS-D3/NL curves the strong effect of dispersion (about 20 kcal mol^{-1} binding, see Figure 16.8) becomes apparent. As mentioned, the agreement between D3 and NL results is excellent.

16.3.4
Symmetry-Adapted Perturbation Theory (SAPT)

The methods based on SAPT are conceptually different from the supermolecular approaches because they require the definition of fragments and do not compute the total energy, but distinct interaction energy components including dispersion. For an excellent review about the theory, the various versions of SAPT and also for technical aspects, see Ref. [75]. The word symmetry here refers to the Fermionic-antisymmetry of the WF, meaning that the Pauli principle is included, which is not straightforward when the starting points of the description are separate molecular or atomic fragments. The partitioning of the system is mapped to a partitioning of

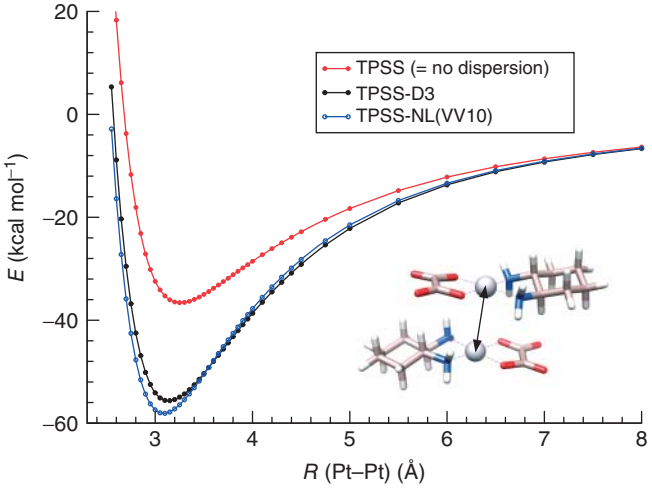

Figure 16.8 Computed potential energy curves for the oxaliplatin complex (TPSS density functional, def2-TZVP AO basis, large core (Cologne–Stuttgart) ECP for Pt.

the Hamiltonian into fragment (index A or B) and interaction operators

$$\hat{H} = \hat{H}(\mathrm{A}) + \hat{H}(\mathrm{B}) + \hat{V}(\mathrm{AB}) \tag{16.15}$$

where $\hat{V}(\mathrm{AB})$ contains all intermolecular Coulomb interactions. SAPT requires the choice of a quantum chemical method for the monomers, that is, HF, DFT, or CC methods. Applying perturbation theory leads to energy contributions in different orders, which add to the total interaction energy $\Delta E_{\mathrm{int,\,AB}}$ according to

$$\Delta E_{\mathrm{int,\,AB}} = E_{\mathrm{ES}}^{(1)} + E_{\mathrm{EXR}}^{(1)} + \underbrace{E_{\mathrm{IND}}^{(2)} + E_{\mathrm{EXR-IND}}^{(2)}}_{E_{\mathrm{IND}}} + \underbrace{E_{\mathrm{disp}}^{(2)} + E_{\mathrm{EXR-disp}}^{(2)}}_{E_{\mathrm{disp}}} + \ldots \tag{16.16}$$

Usually, the expansion is truncated at second order and the mixed $E^{(2)}$ terms are condensed, yielding a formula which resembles that of the EDA

$$\Delta E_{\mathrm{int,\,AB}} = E_{\mathrm{EXR}} + E_{\mathrm{ES}} + E_{\mathrm{IND}} + E_{\mathrm{disp}} \tag{16.17}$$

SAPT is not applicable to intramolecular interactions, but has the advantage of being free of BSSE. It likely provides the theoretically best-founded definition of the dispersion energy in the overlapping regime. For large distances, its description resembles the Casimir–Polder formula with monomer polarizabilities from the chosen method. On average, the accuracy for NCI is much better than that of MP2 and reaches that of the supermolecular CCSD(T) "gold standard," at least when DFT is used as an inherent method and extended AO basis sets are used [76]. For recent further developments of SAPT for large systems, see, for example, Refs. [77, 78].

16.4
Selected Examples

16.4.1
Substituted Ethenes

Steric hindrance is a widely used concept in chemistry. Normally, it is stated that spatially close-lying functional groups (typically alkyl like *t*-butyl) try to avoid each other (because of the EXR + ES term) and prefer large interfragment distances. Note that this is expected to lead to weaker bonds in the core of the corresponding chemical system, that is, a kinetic stabilization but thermodynamic destabilization. That this is only part of the story is exemplified by our first example. The dissociation energy of the central CC bond in tetrasubstituted ethenes (see Figure 16.9) is considered. The common view holds true when the four substituents in ethene are increased in size from methyl to *i*-propyl and 3-pentyl, for which the D_e values decrease monotonously from about 170 to 140 kcal mol^{-1}. However, further increase of "steric hindrance" increases the D_e again! Note that this effect is completely missing when the D3 correction is omitted in the DFT calculations and hence can be clearly attributed to an increasing dispersion attraction by the long alkyl chains. The effect is chemically significant and amounts to about 10 kcal mol^{-1}

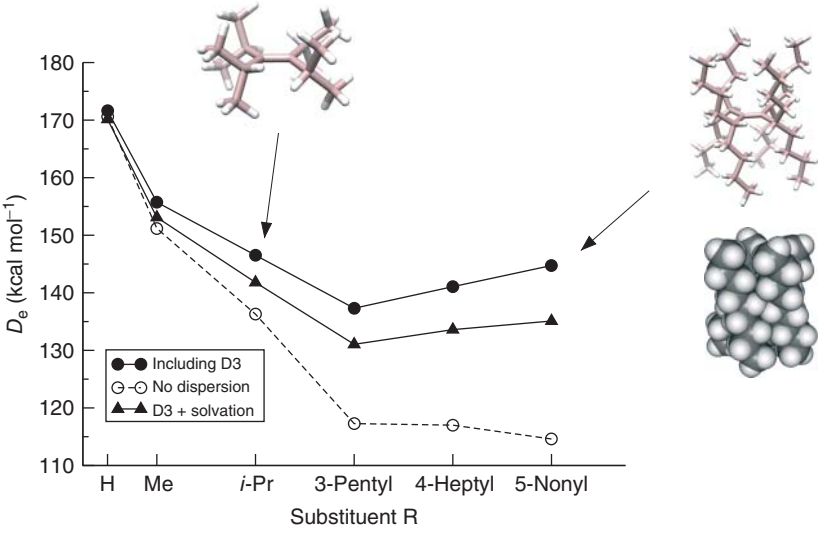

Figure 16.9 Dissociation energy D_e for the central CC bond in tetrasubstituted ethenes $R_2C = CR_2$ at (U)TPSS-D3/def2-TZVP levels. Open circles denote data from single-point calculations without D3 dispersion corrections and illustrate the dramatic effects of the dispersion energy for the larger systems. Results including enthalpic (298 K) corrections for solvation in $CHCl_3$ (gray triangles) are obtained from the conductor-like screening model for realistic solvents (COSMO)-RS [79–81] model (employing DFT input data).

relative stabilization from 3-pentyl to 5-nonyl. It is weakened but persists even when the system is treated in solution by a continuum model (COSMO-RS).

16.4.2

Steric Crowding Can Stabilize a Labile Molecule: Hexamethylethane Derivatives

The stabilization of normal covalent bonds by dispersion in large systems is rather obvious from the last example and those given in Ref. [10]. Very recently, we could furthermore show that there are cases in which the dispersion between seemingly ''innocent'' ligands provides the main driving force for binding, meaning that without these forces the system would spontaneously dissociate. We consider the textbook example of hexaphenylethane (see inset in Figure 16.10 for the structures) and its inability to form a stable CC single bond [13]. A delicate balance of covalent bonding, dispersion attraction, and Pauli repulsion forces between the phenyl rings and attached substitents can be expected when the central CC bond is broken.

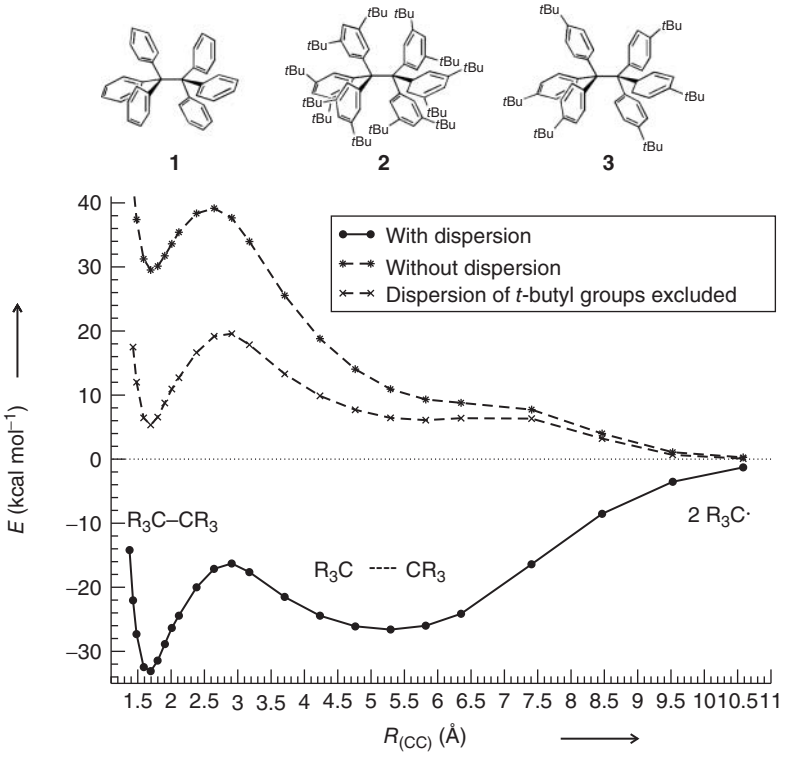

Figure 16.10 Potential energy curves (UTPSS-D3/TZV2P//UPBE-D3/TZVP) for dissociation of the central CC bond in all-meta-*t*-butyl-substituted hexaphenylethane (molecule 2, R = 3,5-di-*t*-butyl-phenyl) with and without dispersion correction. Note the similar depths of the covalent and vdW complex minima in the dispersion-corrected curve and the unbound state (positive interaction energies) without these corrections.

However, why the parent molecule hexaphenylethane cannot be synthesized but the seemingly sterically more overcrowded derivative can be made at least at low temperatures was an open question. The potential energy curves in Figure 16.10 provide the conclusive evidence for the overwhelming role of the dispersion.

The TPSS-D3 curve exhibits two minima at CC distances of 1.67 and 5.28 Å which are connected by a (TS) transition state at R(CC) = 2.87 Å. The minima correspond to the normal covalently bound ethane derivative and a very strong vdW complex of the two radicals. As both minima lie in a comparably deep potential energy well (−33.2 and −26.6 kcal mol^{-1}, respectively), the system can be considered as bond length isomeric. The figure includes data with and without D3-corrections and a curve for which all dispersion arising from the *t*-butyl groups has been set to zero. The uncorrected TPSS curve shows the covalent CC structure and the TS but not the second vdW minimum. Furthermore, the molecular energy is always higher than that of the free radicals, which again emphasizes the importance of dispersion. One of the good features of the DFT-D3 approach is that the dispersion energy can easily be partitioned into different parts or groups of a molecule. The third curve without the *t*-butyl contributions is most remarkable: while its shape is similar to the plain TPSS curve, there is practically no vdW minimum and the interaction energies are positive. Thus, we conclude that the main dispersion stabilization of the experimentally observed compound results from the *t*-butyl groups. The overall repulsive phenyl–phenyl interactions in the parent molecule are overcompensated by addition of ''steric crowding'' in the form of all-meta *t*-butyl groups that do not lead to overcrowding but serve as ''dispersion energy donors.'' The stability of **2** and the instability of **1** as well as **3** can be fully explained on thermodynamic grounds, and all computations agree qualitatively as well as quantitatively with experiment. The dispersion of the *t*-butyl groups stabilizes **2** compared to its radical fragments by as much as 40 kcal mol^{-1}.

16.4.3
Overcoming Coulomb Repulsion in a Transition Metal Complex

Proper tuning of the energetic contribution of dispersion may stabilize molecular aggregates, which would be otherwise highly unstable by virtue of other overwhelming repulsive terms as shown earlier. Literature contains a number of such noncovalently bonded molecular aggregates containing metal (ions), of which the binding mode has never been thoroughly settled. Among those are the emblematic cationic complexes of tetrakis(isonitrile)rhodium(I). The propensity of these complexes to spontaneously produce oligomers has been an open case for years. This very fundamental question as to why two positively charged molecules can form a complex without any significant covalent bonding (which is not possible in the d^8–d^8 configuration of the metal cores) has recently been answered. This example is directly connected to the ES/dispersion discussion (see Figure 16.1) in Section 16.1.

For the dimer $[(PhNC)_4Rh]_2^{2+}$ (see inset in Figure 16.11), one of the archetypes of such oligomers, DFT-D3 and wave-function-based SCS-MP2 [55] quantum

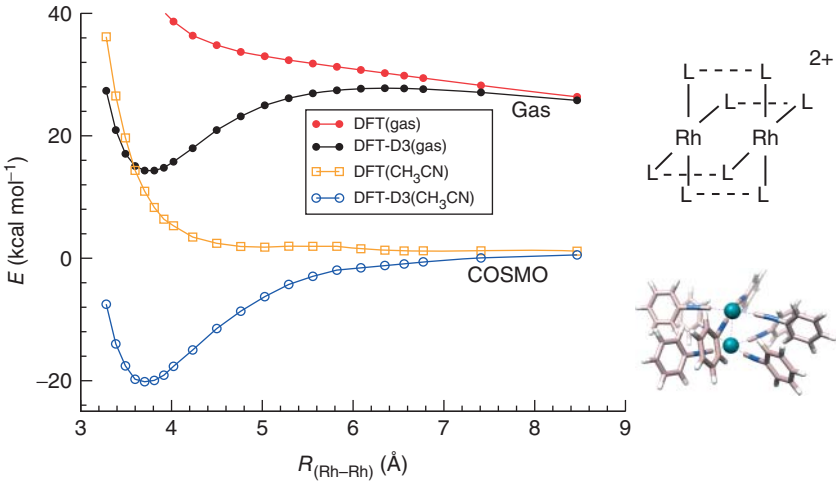

Figure 16.11 Potential energy curves for dissociation of $[(PhNC)_4Rh]_2^{2+}$ along a Rh–Rh bond stretching coordinate at TPSS/def2-TZVP levels. The COSMO continuum solvation model corresponding to the experimentally investigated acetonitrile solution has been applied.

chemical calculations have been performed [14]. These investigations indicate that when the eight isonitrile ligands arrange spatially in an optimal π-stacked manner, the energy due to dispersion not only overcomes coulombic repulsion but also the entropy penalty of complex formation. This central role of long-range electron correlation explains such seeming cation–cation "attractive" interactions. These findings also relativize the role of closed-shell metal–metal "d^8–d^8" interactions, which are present on a relatively small scale compared to the effects of the ligands (only about 10–15% of the total dispersion contribution to the binding energy).

Without dispersion correction, the potentials in the gas phase and with the COSMO continuum solvation correction [79] for acetonitrile are both entirely repulsive (red and orange curves). Because COSMO screens the Coulomb interaction effectively, the DFT+COSMO curve rapidly approaches the asymptote, while in the gas phase it includes the very long-ranged (very slowly decaying) $1/R$ part. But only if COSMO and D3 are added to the bare DFT energies physically plausible potentials result, which correspond to an energetically stable aggregate (which persists even when entropic corrections are added [14]). In the equilibrium region, the dispersion contribution to the binding energy is 20–30 kcal mol^{-1} (>100% of D_e).

16.5 Conclusion

Although the London dispersion interaction has a fundamentally quantum chemical, complex many-particle origin, it is probably the bonding type (or its contribution to bonding) that is easiest to understand. It can be represented accurately by rather

simple models based on ''atoms-in-molecules'' ideas. However, any brute-force wave-function-based *ab initio* quantum chemical treatment of dispersion bonding is ambitious and computationally demanding (because dispersion essentially is a long-range electron correlation effect), but fortunately not necessary in many cases. The reasons for this seeming contradiction are that (a) the dispersion interaction (the quantum effects) operate on a relatively long-range scale where classical (atomic or other local) approximations perform well (and exchange is negligible), (b) it is basically (to within a few percent error) a pair-wise additive property, and (c) the directionality of dispersion bonding is more or less represented by the classical (geometrical) shape of the interacting fragments. Dispersion is a chemically local phenomenon that can be described fairly well by local models of polarizability (excitation energy). However, this mainly holds for insulator-type systems that dominate main group inorganic and organic, as well as biochemistry. For extended metallic systems, the situation is different as these inherently have a NL electronic structure and a clear distinction between short- and long-range correlation is obscured.

Even when dispersion is not sufficient to form a chemical bond, it is clear that larger molecules are significantly more influenced by the intramolecular dispersion energy than smaller ones. Because dispersion is always attractive (energy lowering), this means that larger molecules are thermodynamically stabilized by dispersion compared to small systems. From this it can be concluded that large (preferably electron-rich and polarizable) chemical groups can be used to energetically stabilize weak bonds or reactive parts in a molecule (''dispersion energy donor'' concept). This new thinking about the very old London dispersion theory might be useful as a novel design principle for functional chemical systems.

16.6 Computational Details

The quantum chemical calculations were done with TURBOMOLE (DFT-D3 and CCSD(T)/MP2) [82] and ORCA (DFT-NL) [83, 84]. For the DFT calculations carried out with ORCA and TURBOMOLE, we employed fine integration grids (m4/m5 in TURBOMOLE or grid5 in ORCA) and tight SCF convergence criteria. Where applicable, the resolution of the identity (RI) integral approximation [85, 86] was used. If not stated otherwise, structures were fully optimized at the TPSS-D3(BJ)/def2-TZVP level [38, 40, 42, 69]. For 4d and 5d transition metals the large core (Cologne–Stuttgart) ECP [87, 88] are used.

References

1. IUPAC Gold Book, IUPAC Compendium of Chemical Terminology – the Gold Book, *http://goldbook.iupac.org/V06597.html* (accessed 23 January 2014).
2. London, F. (1930) *Z. Phys.*, **63**, 245–279.
3. Stone, A.J. (1997) *The Theory of Intermolecular Forces*, Oxford University Press, Oxford.

4. Kaplan, I.G. (2006) *Intermolecular Interactions*, John Wiley & Sons, Ltd, Chichester.
5. Hobza, P. (2011) *WIREs Comput. Mol. Sci.*, **1**, 3–17.
6. Lehn, J.-M. (1995) *Supramolecular Chemistry: Concepts and Perspectives*, Wiley-VCH Verlag GmbH, Weinheim.
7. Meyer, E.A., Castellano, R.K., and Diederich, F. (2003) *Angew. Chem. Int. Ed.*, **42**, 1210–1250.
8. Kannan, N., and Vishveshwara, S. (2000) *Protein Eng.*, **13**, 753–761.
9. Desiraju, G.R., Vittal, J., and Ramanan, A. (2011) *Crystal Engineering: A Textbook*, World Scientific Publishing, Singapore.
10. Grimme, S., Huenerbein, R., and Ehrlich, S. (2011) *ChemPhysChem*, **12**, 1258–1261.
11. Dalrymple, D.L., Reinheimer, J.D., Barnes, D., and Baker, R. (1964) *J. Org. Chem.*, **29**, 2647–2652.
12. Pyykkö, P. (1997) *Chem. Rev.*, **97**, 597–636.
13. Grimme, S., and Schreiner, P.R. (2011) *Angew. Chem. Int. Ed.*, **50**, 12639–12642.
14. Grimme, S., and Djukic, J.P. (2011) *Inorg. Chem.*, **50**, 2619–2628.
15. Slavicek, P., Kalus, R., Paska, P., Odvarkova, I., Hobza, P., and Malijevsky, A. (2003) *J. Chem. Phys.*, **119**, 2102–2118.
16. Dobson, J.F., White, A., and Rubio, A. (2006) *Phys. Rev. Lett.*, **96**, 073201.
17. Ruiz, V.G., Liu, W., Zojer, E., Scheffler, M., and Tkatchenko, A. (2012) *Phys. Rev. Lett.*, **108**, 146103.
18. Carrasco, J., Klimes, J., and Michaelides, A. (2013) *J. Chem. Phys.*, **138**, 024708.
19. Kohn, W., and Sham, L.J. (1965) *Phys. Rev.*, **140**, A1133–A1138.
20. Parr, R.G., and Yang, W. (1989) *Density-Functional Theory of Atoms and Molecules*, Oxford University Press, Oxford.
21. Koch, W., and Holthausen, M.C. (2001) *A Chemist's Guide to Density Functional Theory*, Wiley-VCH Verlag GmbH, New York.
22. Cohen, A.J., Mori-Sanchez, P., and Yang, W. (2012) *Chem. Rev.*, **112**, 289–320.
23. Kutzelnigg, W. (1978) *Einführung in die Theoretische Chemie: Band 2, Die chemische Bindung*, Verlag Chemie, Weinheim.
24. Marinescuc, M. (1997) *Phys. Rev. A*, **56**, 4764.
25. Vydrov, O.A., and Van Voorhis, T. (2010) *J. Chem. Phys.*, **133**, 244103.
26. Hujo, W., and Grimme, S. (2011) *J. Chem. Theor. Comput.*, **7**, 3866–3871.
27. Kolos, W., and Wolniewicz, L. (1965) *J. Chem. Phys.*, **43**, 2429.
28. von Hopffgarten, M., and Frenking, G. (2012) *WIREs Comput. Mol. Sci.*, **2**, 43–62.
29. Morokuma, K. (1971) *J. Chem. Phys.*, **55**, 1236–1244.
30. Kitaura, K., and Morokuma, K. (1976) *Int. J. Quantum Chem.*, **10**, 325–340.
31. Bickelhaupt, F.M., and Baerends, E.J. (2000) in *Reviews in Computational Chemistry*, Vol. 15 (eds K.B. Lipkowitz, and D.B. Boyd), Wiley-VCH Verlag GmbH, New York, pp. 1–86.
32. Swart, M., Fonseca Guerra, C., and Bickelhaupt, F.M. (2004) *J. Am. Chem. Soc.*, **126**, 16718–16719.
33. Parac, M., Etinski, M., Peric, M., and Grimme, S. (2005) *J. Chem. Theory Comput.*, **1**, 1110–1118.
34. Grimme, S., Antony, J., Schwabe, T., and Mück-Lichtenfeld, C. (2007) *Org. Biomol. Chem.*, **5**, 741–758.
35. Stephan, D.W., and Erker, G. (2010) *Angew. Chem. Int. Ed.*, **49**, 46–76.
36. Grimme, S., Kruse, H., Goerigk, L., and Erker, G. (2010) *Angew. Chem. Int. Ed.*, **49**, 1402–1405.
37. Gilbert, T.M. (2013) *Top. Curr. Chem.*, doi: 10.1007/1282012378.
38. Tao, J., Perdew, J.P., Staroverov, V.N., and Scuseria, G.E. (2003) *Phys. Rev. Lett.*, **91**, 146401.
39. Schäfer, A., Huber, C., and Ahlrichs, R. (1994) *J. Chem. Phys.*, **100**, 5829–5835.
40. Weigend, F., and Ahlrichs, R. (2005) *Phys. Chem. Chem. Phys.*, **7**, 3297–3305.
41. Goerigk, L., and Grimme, S. (2011) *Phys. Chem. Chem. Phys.*, **13**, 6670–6688.
42. Grimme, S., Antony, J., Ehrlich, S., and Krieg, H. (2010) *J. Chem. Phys.*, **132**, 154104.
43. van Gisbergen, S.J.A., Snijders, J.G., and Baerends, E.J. (1995) *J. Chem. Phys.*, **103**, 9347–9354.

44. Osinga, V.P., van Gisbergen, S.J.A., Snijders, J.G., and Baerends, E.J. (1997) *J. Chem. Phys.*, **106**, 5091–5101.

45. Johnson, E.R. (2011) *J. Chem. Phys.*, **135**, 234109.

46. Sulzer, D., Norman, P., and Saue, T. (2012) *Mol. Phys.*, **110**, 2535–2541.

47. Ehrlich, S., Moellmann, J., and Grimme, S. (2012) *Acc. Chem. Res.*, **45**, doi: 10.1021/ar3000844.

48. Hohenstein, E.G., and Sherrill, C.D. (2012) *WIREs Comput. Mol. Sci.*, **2**, 304–326.

49. Kruse, H., and Grimme, S. (2012) *J. Chem. Phys.*, **136**, 154101.

50. Kruse, H., Goerigk, L., and Grimme, S. (2012) *J. Org. Chem.*, **77**, 10824–10834.

51. Helgaker, T., Jørgensen, P., and Olsen, J. (2000) *Molecular Electronic-Structure Theory*, John Wiley & Sons, Inc., New York.

52. Grimme, S., Mück-Lichtenfeld, C., and Antony, J. (2008) *Phys. Chem. Chem. Phys.*, **10**, 3327–3334.

53. Moeller, C., and Plesset, M.S. (1934) *Phys. Rev.*, **46**, 618–622.

54. Cremer, D. (2011) *WIREs Comput. Mol. Sci.*, **1**, 509–530.

55. Grimme, S., Goerigk, L., and Fink, R.F. (2012) *WIREs Comput. Mol. Sci.*, **2**, 868–885.

56. Mulliken, R.S. (1955) *J. Chem. Phys.*, **23**, 1833–1840.

57. Schwabe, T., Grimme, S., and Djukic, J.P. (2009) *J. Am. Chem. Soc.*, **131**, 14156–14157.

58. Ryde, U., Mata, R.A., and Grimme, S. (2011) *Dalton Trans.*, **40**, 11176–11183.

59. Grimme, S. (2011) *WIREs Comput. Mol. Sci.*, **1**, 211–228.

60. Klimes, J., and Michaelides, A. (2012) *J. Chem. Phys.*, **137**, 120901.

61. Becke, A.D., and Johnson, E.R. (2005) *J. Chem. Phys.*, **123**, 154101.

62. Tkatchenko, A., and Scheffler, M. (2009,) *Phys. Rev. Lett.*, **102**, 073005.

63. Dion, M., Rydberg, H., Schröder, E., Langreth, D.C., and Lundqvist, B.I. (2004) *Phys. Rev. Lett.*, **92**, 246401.

64. Lin, Y., Li, G., Mao, S., and Chai, J. (2013) *J. Chem. Theory Comput.*, **9**, 263–272.

65. Heßelmann, A. (2013) *J. Chem. Theory Comput.*, **9**, 273–283.

66. Casimir, H.B.G., and Polder, D. (1948) *Phys. Rev.*, **4**, 360–372.

67. Krishtal, A., Geldorf, D., Vanommeslaeghe, K., Alsenoy, C.V., and Geerlings, P. (2012) *J. Chem. Theory Comput.*, **8**, 125–134.

68. Ehrlich, S., Moellmann, J., Reckien, W., Bredow, T., and Grimme, S. (2011) *ChemPhysChem*, **12**, 3414–3420.

69. Grimme, S., Ehrlich, S., and Goerigk, L. (2011) *J. Comput. Chem.*, **32**, 1456–1465.

70. Rezáč, J., Riley, K.E., and Hobza, P. (2011) *J. Chem. Theory Comput.*, **7**, 2427.

71. Koide, A. (1976) *J. Phys. B*, **9**, 3173.

72. Burns, L.A., Vazquez-Mayagoitia, A., Sumpter, B.G., and Sherrill, C.D. (2011) *J. Chem. Phys.*, **134**, 084107.

73. Goerigk, L., Kruse, H., and Grimme, S. (2011) *ChemPhysChem*, **12**, 3421–3433.

74. Ott, I., and Gust, R. (2007) *Anti-Cancer Agents Med. Chem.*, **7**, 95–110.

75. Szalewicz, K. (2012) *WIREs Comput. Mol. Sci.*, **2**, 254–272.

76. Sherrill, C.D. (2009) in *Reviews in Computational Chemistry*, Vol. 26 (eds K.B. Lipkowitz, and D.B. Boyd), Wiley-VCH Verlag GmbH, New York, pp. 1–39.

77. Hohenstein, E.G., and Sherrill, C.D. (2010) *J. Chem. Phys.*, **133**, 104107.

78. Lao, K.U., and Herbert, J.M. (2013) *J. Phys. Chem. Lett.*, **3**, 3241–3248.

79. Klamt, A., and Schüürmann, G. (1993) *J. Chem. Soc., Perkin Trans. 2*, 799–805.

80. Klamt, A. (1995) *J. Phys. Chem.*, **99**, 2224–2235.

81. Klamt, A. (2011) *WIREs Comput. Mol. Sci.*, **1**, 699–709.

82. TURBOMOLE, Ahlrichs, R. *et al.* (2009) Universität Karlsruhe 2009, *http://www.turbomole.com* (accessed 23 January 2014).

83. Neese, F. (2011) *ORCA - An Ab Initio, Density Functional and Semiempirical Program Package, Version 2.9 (Rev 0)*, Max Planck Institute for Chemical Energy Conversion, Germany.

84. Neese, F. (2012) *WIREs Comput. Mol. Sci.*, **2**, 73–78.

85. Vahtras, O., Almlöf, J., and Feyereisen, M.W. (1993) *Chem. Phys. Lett.*, **213**, 514–518.

86. Weigend, F., and Häser, M. (1997) *Theor. Chem. Acc.*, **97**, 331–340.

87. *http://www.theochem.uni-stuttgart.de/pseudopotentials/index.en.html*, *http://www.tc.uni-koeln.de/PP/index.en.html* (accessed 23 January 2014)

88. Dolg, M., and Cao, X. (2012) *Chem. Rev.*, **112**, 404–480.

17
Hydrogen Bonding

Hajime Hirao and Xiaoqing Wang

17.1
Introduction

Hydrogen bonds (H bonds) are ubiquitous in many different branches of science [1–3], and exert a profound influence over a great variety of molecules around us. For example, H bonds induce various modifications or anomalies of physical and chemical properties in gaseous, liquid, and solid substances (e.g., the elevated boiling point of water), while they play crucial roles in determining the structure and function of biological macromolecules such as proteins and DNA. H bonds are intimately involved in rate enhancement in enzyme catalysis [4] and in enantiocontrol in organocatalysis [5]. The essential roles of H bonds in regulating the structures of supramolecules have also been demonstrated [6].

The significance of H bonding began to be realized in the early 1900s by several researchers. It is not necessarily easy to attribute the discovery or initiation of the concept to a single individual or group. However, Werner, Hantzsch, Pfeiffer, Moore, Winmill, Huggins, Latimer, Rodebush, and Pauling are among the most important figures in the initial establishment of the H-bond concept [1c]. The H bond was discussed for the first time in a didactic manner in Pauling's paper in 1931 [7], in which Pauling writes that the H bond was discovered by Huggins and by Latimer and Rodebush. These two groups used Lewis structures to describe the H bond. According to the third edition of Pauling's book (*The Nature of the Chemical Bond*) [8], Moore and Winmill made the first mention of the H bond, and Latimer and Rodebush recognized the importance of the H bond. Since those early days, there has been an overwhelming body of research, using X-ray crystallography, spectroscopic methods, and emerging quantum chemistry, that has made significant contributions to the enhancement of our knowledge and understanding of the H bond. However, past studies have also shown that there are many different types of H bonds and that the attributes of H bonding are much more complex and broader than previously assumed. As such, even with its history of around 100 years, the H bond is still a growing research area. The purpose of this chapter is not to discuss the diverse field of H bonding research in a comprehensive or exhaustive manner. Rather, we intend to summarize the

The Chemical Bond: Chemical Bonding Across the Periodic Table, First Edition.
Edited by Gernot Frenking, Sason Shaik.

nuts and bolts of H bonding, with some emphasis placed on the contributions of theoretical chemistry.

17.2
Fundamental Properties of Hydrogen Bonds

Despite its ubiquity, it is not necessarily straightforward to define the H bond without ambiguity. A H bond can be generally described as

$$X–H\cdots Y \tag{17.1}$$

where X and Y are normally highly electronegative atoms. Although the dotted line in Eq. (17.1) constitutes the main part of the H bond, the H bond actually refers to the whole structural moiety composed of the three atoms, X, H, and Y [1e]. Chapter 12 of Pauling's *The Nature of the Chemical Bond* (third ed.) [8b] opens with the following sentences: ''It was recognized some decades ago that under certain conditions an atom of hydrogen is attracted by rather strong forces to two atoms, instead of only one, so that it may be considered to be acting as a bond between them. This is called the *hydrogen bond*.'' According to the definition by Pimentel and McClellan, a H bond exists between X–H and Y when ''(a) there is evidence of bond formation (association or chelation) and (b) there is evidence that this new bond linking X–H and Y specifically involves the hydrogen atom already bonded to X [1a]''. More recently, Steiner proposed the following definition: an $X–H\cdots Y$ interaction is called a *hydrogen bond* if ''(a) it constitutes a local bond and (b) X–H acts as a proton donor to Y [3]''.

In view of the complexity and diversity of H bonds, these rather simple definitions are convenient and safely encompass many different types of H bonds. Many exceptions may arise when one attempts to frame a universal, or specific, definition of the H bond (e.g., how to choose the distance or angle cutoff). Nonetheless, detailed H-bond criteria may be helpful because the boundary between the H bond and many other types of interactions, for example, the covalent bond, the ionic interaction, the van der Waals (vdW) interaction, and so on, is sometimes indistinct. Thus, investigation of H bonds from a more pragmatic perspective may require many detailed criteria that allow us to discern whether a given bond is a H bond or not. In fact, a few operational criteria have recently been proposed that would help characterize many types of H bonds [9].

In many of the previously proposed definitions or criteria, X in Eq. (17.1) is a H-bond donor and Y is a H-bond acceptor. X and Y are more electronegative than H. X is in many cases a highly electronegative element such as F, O, or N. X is also covalently bonded to H and pulls the electron density of the H atom toward itself, thereby rendering the hydrogen atom electron deficient and deshielded. The resultant dipole attractively interacts with Y, which typically has lone-pair electrons but can also use π electrons in an aromatic ring or a multiple bond for the interaction with X–H (π H bond) [1e, 10]. X can also be carbon; however, H bonds involving carbon are relatively weak in general [11], and for $C–H\cdots\pi$

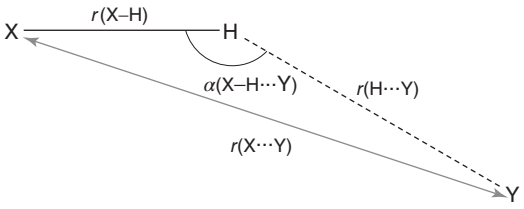

Figure 17.1 Geometrical parameters of a H bond.

interactions in particular it is difficult to distinguish between the H bond and the vdW interaction [1e]. Interestingly, an electropositive transition-metal ion can act as Y to form a H bond. This is made possible when the d_{z^2} orbital is filled and the orbital can donate electrons to the σ* orbital of the X–H bond [12]. X and Y may be on different molecules, in which case the H bond is referred to as *intermolecular*. When both groups are on the same molecule, the H bond is *intramolecular*. For example, ortho-substituted benzene compounds can easily form an intramolecular H bond.

Figure 17.1 illustrates the key geometric parameters with which to characterize H bonds. In general, H bonding is highly directional: the X–H···Y H-bond is approximately linear in configuration, subtending an angle (α(X–H···Y)) of approximately 180°. The separation r(X···Y) should basically be shorter than the sum of the vdW radii of X and Y in a H-bonding system. A better H-bond criterion seems to be that r(H···Y) must be shorter than the sum of the radii of H and Y [9]. As is clear from the dotted line in Eq. (17.1), the H bond is different from the more distinct covalent bond that is formed by an electron pair. In fact, Huggins preferred to use the term *hydrogen bridge* to describe the hydrogen bond [13]. Owing to its somewhat loose character, when statistical analysis is undertaken for a number of H bonds in different molecules and different local environments, one observes broad distributions of the above-mentioned geometric parameters instead of a sharp peak. For example, Taylor *et al.* [14] performed a survey of 1509 N–H···O=C H bonds from 889 different organic crystal structures. In their analysis, the distributions of r(H···O) and r(N···O) were broad (Figure 17.2). The standard deviations for these values were 0.143 and 0.122 Å, respectively, while the mean values were 1.921 and 2.878 Å, respectively. In the case of the H-bond angle, α(X–H···Y), the same authors showed that the mean value was 158.3° (Figure 17.3a). However, as configurations with a smaller α angle can occupy larger volumes than do linear structures, the ''cone angle correction'' should be made by dividing the bin frequencies by sin(α) to obtain an unbiased histogram [15]. In the histogram obtained using the cone angle correction, one sees that the distribution is shifted toward the linear geometry (Figure 17.3b).

Infrared (IR) and Raman spectroscopy techniques are particularly useful for the characterization of H bonds [1]. These techniques exploit the fact that formation of a H bond results in a shift of the X–H stretching vibrational mode to a lower frequency (redshift), often by several hundred per centimeter. Moreover, the X–H

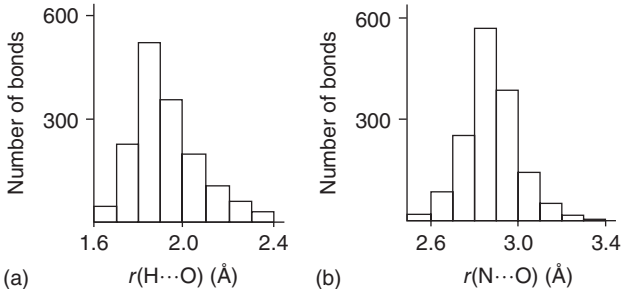

Figure 17.2 Distributions of (a) r(H···O) and (b) r(N···O). (Adapted from Ref. [14] with permission of the International Union of Crystallography (*http://journals.iucr.org/*).)

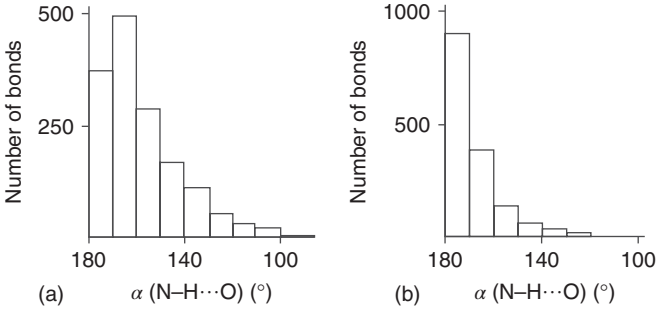

Figure 17.3 (a) Distribution of α(N–H···O). (b) Distribution after "cone angle correction". (Adapted from Ref. [14] with permission of the International Union of Crystallography (*http://journals.iucr.org/*).)

stretching peak is broadened and intensified upon formation of a H bond. NMR spectroscopy can also be used to detect H bonds because formation of a H bond leads to a downfield chemical shift. X-ray diffraction analysis and neutron diffraction analysis allow us to obtain structural details of H bonds. Determination of the position of the hydrogen atom in small molecules is possible with these methods, although the r(X–H) values determined by X-ray analysis tend to be shorter than the real internuclear distances [1e]. However, for larger biomacromolecules such as proteins, the positions of hydrogen atoms are usually not resolved by X-ray diffraction [16].

17.3 Hydrogen Bonds with Varying Strengths

The H bond is basically an "associative interaction" that is much weaker than the ordinary covalent bond [1a]. Lying between the weak vdW interaction and the strong covalent bond, the H bond spans a wide range of interaction strengths, which can differ by up to two orders of magnitude (0.2–40 kcal mol^{-1}) [3] depending on the type

Table 17.1 Classification of H bonds according to Jeffrey.

	Strong	Moderate	Weak
X–H···Y interaction	Mostly covalent	Mostly electrostatic	Electrostatic
Bond lengths	X–H ≈ H···Y	X–H < H···Y	X–H ≪ H···Y
H···Y (Å)	~1.2–1.5	~1.5–2.2	2.2–3.2
X···Y (Å)	2.2–2.5	2.5–3.2	3.2–4.0
Bond angles [°]	175–180	130–180	90–150
Bond energy ($kcal\,mol^{-1}$)	14–40	4–15	<4
Relative IR ν_s vibration shift (cm^{-1})	25%	10–25%	<10%
^1H chemical shift downfield (ppm)	14–22	<14	–
Examples	• Gas-phase dimers with strong acids or strong bases • Acid salts • Proton sponges • Pseudohydrates • HF complexes	• Acids • Alcohols • Phenols • Hydrates • All biological molecules	• Gas-phase dimers with weak acids or weak bases • Minor components of 3-center bonds • C–H···O/N bonds • O/N–H···π bonds

Adapted from Ref. [1c] with permission of Oxford University Press, Inc.

of the H bond. Although there are no sharp boundaries, it was suggested by Jeffrey that H bonds with interaction strengths of 15–40 $kcal\,mol^{-1}$, 4–15 $kcal\,mol^{-1}$, and <4 $kcal\,mol^{-1}$ be classified as strong, moderate, and weak (Table 17.1) [1c]. This type of classification is very useful and gives us specific guides for characterizing H bonds. Strong H bonds have a large degree of covalent character and short H···Y and X···Y bond distances. In general, ionic H bonds tend to be stronger than electrically neutral H bonds [17]. It is well known that $[FHF]^-$ has a very strong H bond, with its gas-phase H-bond strength being 38.6 $kcal\,mol^{-1}$ [18a]. It should be noted, however, that $\Delta H°$ for the reaction $HF + F^- \rightarrow [FHF]^-$ in aqueous solution is +1.5 $kcal\,mol^{-1}$ (endothermic) [18b], demonstrating that the H bonding is susceptible to environmental perturbations. In many cases, a short r(X···Y) is an indication of a stronger H bond; however, it has been pointed out that the length–strength relationship does not generally hold [19].

Gilli *et al.* classified H bonds into the following six categories: (i) ordinary H bonds (OHBs); (ii) double-charge-assisted H bonds ((±)CAHBs); (iii) negative-charge-assisted H bonds ((–)CAHBs); (iv) positive-charge-assisted H bonds ((+)CAHBs); (v) resonance-assisted H bonds (R_n-CAHBs); and (vi) polarization-assisted H bonds (PAHBs) [17a]. The great majority of H bonds, such as those found in secondary structures of proteins, are classified as OHBs. (–)CAHBs, examples of which

include the H bond in $[FHF]^-$, are strong H bonds. (+)CAHBs are seen, for example, in $[H_2O\cdots H\cdots OH_2]^+$, and these also form strong H bonds. The strength of CAHBs is due to the matching of the proton affinity or pK_a of the donor and acceptor. R_n-CAHBs and PAHBs are associated with π and σ polarization, respectively, both of which lead to the enhancement of H bonding.

17.4 Hydrogen Bonds in Biological Molecules

Huggins predicted in 1936 that H bonds should be involved in various biological molecules [13]. In fact, the ubiquitous involvement of H bonds in biological systems such as proteins and DNA is now beyond doubt [20]. Most of the nitrogen and oxygen atoms in proteins engage in H bonding with either protein or solvent atoms [21], and these H bonds are basically categorized as having moderate strength (Table 17.1). H bonds are known to play particularly important roles in building up secondary structures of proteins, such as α helices and β sheets (Figure 17.4) [22], which are the most fundamental structural motifs observed in proteins. These structures were proposed by Pauling and coworkers in 1951 [23]. The α helix is a right-handed helix involving 3.6 amino acid residues per turn. This helical structure is underpinned by the regular H bonds between the backbone C=O of residue *i* and the backbone NH of residue $i+4$ (Figure 17.4a). When the H bond is formed between *i* and $i+3$ or between *i* and $i+5$, the helix is called the *3_{10} helix* or *π helix*. In 1943, Huggins proposed a helical structure of proteins, which later turned out to be the 3_{10} helix [24]. β sheets are formed by H bonds between β strands, and there are antiparallel and parallel arrangements of β-strands (Figure 17.4b). In 1953, Watson and Crick showed that DNA has a double-helix structure, because of

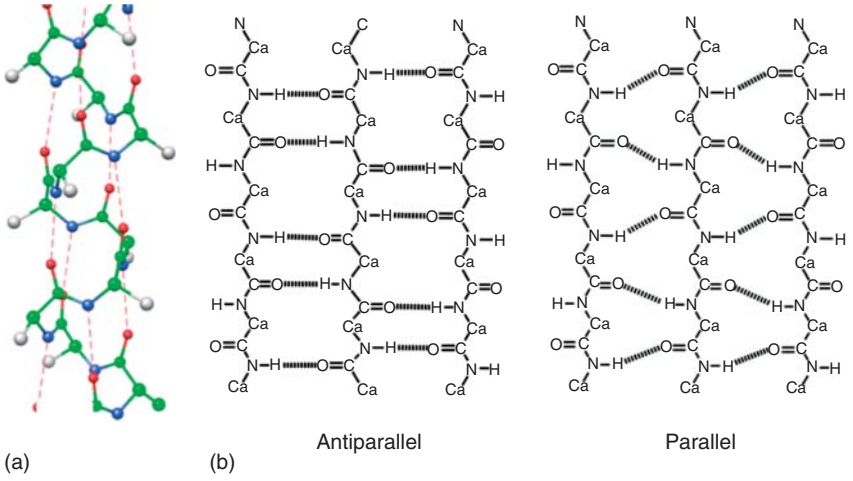

Figure 17.4 (a) α Helix. Side chains are truncated for simplification. (b) β Sheet.

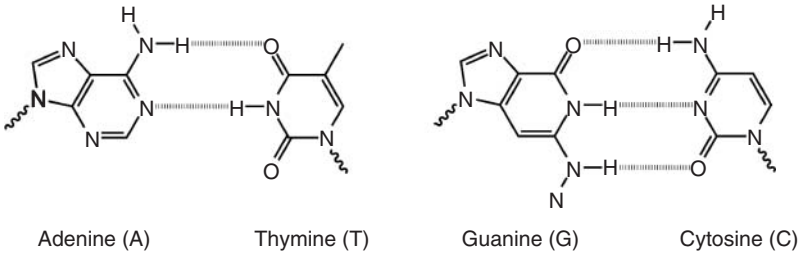

Figure 17.5 H bonds in DNA base pairs.

H bonds between adenine (A) and thymine (T) and between guanine (G) and cytosine (C) (base pairs, see Figure 17.5) [25].

H bonds also play key roles in enzyme catalysis. The low-barrier hydrogen bond (LBHB), a type of strong H bond, is a particularly intriguing concept in this context [4]. Although the name LBHB implies the existence of a barrier on the potential energy surface, the zero-point energy can overcome the low-barrier height. As such, the hydrogen can be delocalized over a broad region between X and Y. Let us imagine, for example, that the H-bond acceptor in a substrate is forming a H bond with some H-bond donor in the active site of an enzyme. This H bond may be an ordinary bond if the pK_a for the H-bond acceptor in the substrate is small and the pK_a values of the H-bond donor and acceptor greatly differ. However, the pK_a of the substrate may undergo a dramatic increase as the reaction progresses, and then the pK_a values for the H-bond donor and acceptor can match at the transition state or intermediate. Matching of pK_a values (pK_a equalization) allows the formation of a strong H bond [17a], and hence the substrate and the enzyme can now form an LBHB, which supposedly lowers the activation barrier for the reaction. For example, in the reaction of ketosteroid isomerase (Scheme 17.1) [4], Tyr14 and the ketone in the substrate form a H bond. In the initial stage of the reaction, the pK_a of the ketone is so low compared with the Tyr that only an OHB is formed. However, when the proton of the substrate is transferred to Asp38, the substrate undergoes enolization, which causes significant elevation of the pK_a of the substrate oxygen. As a result, the difference in the pK_a values for the two subunits decreases, and therefore a strong LBHB can be formed in the middle stage of the reaction. Despite the intriguing scenario of LBHB, it should, however, be noted that arguments exist against the involvement of LBHB in enzymatic reactions [26, 27].

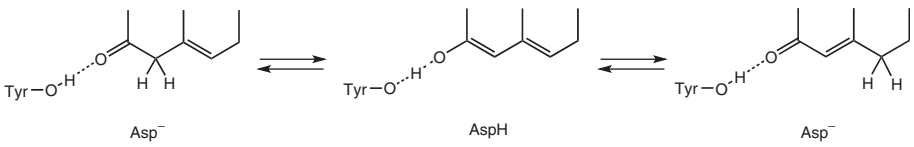

Scheme 17.1 Reaction of ketosteroid isomerase.

17.5
Theoretical Description of Hydrogen Bonding

17.5.1
Valence Bond Description of the Hydrogen Bond

What is the physical origin of the H bond? According to Pauling, the H bond is largely ionic because a hydrogen atom has only one stable 1s orbital; when the hydrogen is bonded to X (see Eq. (17.1)), the 1s orbital is already occupied and the hydrogen cannot form an extra covalent bond [8]. Nevertheless, Pauling also pointed out in the third edition of his book that, in an O–H···O H bond, the O–H bond has some ionic character because of the difference in electronegativity between O and H. Therefore, the 1s orbital of H is not completely occupied, but rather liberated to some extent, which permits the formation of a fractional covalent bond between O–H and O. Valence bond (VB) theory is an excellent guide to describing and interpreting such electronic states comprising a mixture of states [28–31]. In the language of VB theory, a H bond may be described, for example, by the superposition of the following three VB structures, VB1–VB3 [8, 28]

$$\text{VB1}: \quad \text{X}\bullet\!-\!\bullet\text{H}\ :\text{Y} \tag{17.2}$$

$$\text{VB2}: \quad \text{X}:^{-}\ \text{H}^{+}\ :\text{Y} \tag{17.3}$$

$$\text{VB3}: \quad \text{X}:^{-}\ \text{H}\bullet\!-\!\bullet\text{Y}^{+} \tag{17.4}$$

Pauling estimated the weights of these three structures in ice to be about 61%, 34%, and 5%, respectively [8]. Although VB2 corresponds to the ionic structure of the H bond, it should be noted that Pauling's phrase ''largely ionic character of H bonds'' is not intended to imply that VB2 dominantly accounts for the H bond. The ionic interaction in Pauling's context is regarded as electrostatic interaction between the X–H and Y moieties, which arises because the contribution of VB2 is much larger than that of VB3. Still, participation of a fractional covalent bond in the H bond can be understood from the nonzero weight of VB3.

There have been a few modern applications of VB theory to H-bonded systems, notably by means of Shaik's valence bond configuration mixing diagram (VBCMD) approach, which gives a bird's-eye view of reactive processes [29, 30]. An interesting application was made to $[FHF]^{-}$ [30b,c], which is known to have a particularly strong H bond and a symmetric structure [3]. Proton transfer processes for $[XHX]^{-}$ anions may be used for the horizontal axis of the diagram, along which the change in the relative weights of covalent and ionic VB structures can be traced. When X^{-} is a strong base such as CH_3^{-}, the ionic state is not so stable in the symmetric structure (Figure 17.6a). As such, the stability of the system is mostly determined by the Heitler–London covalent structures, and therefore asymmetric structures are preferred. In contrast, the ionic structure in $[FHF]^{-}$ is substantially stabilized. The relative stability of the ionic structure is particularly high for the symmetric structure, at which the total energy is a minimum (Figure 17.6b).

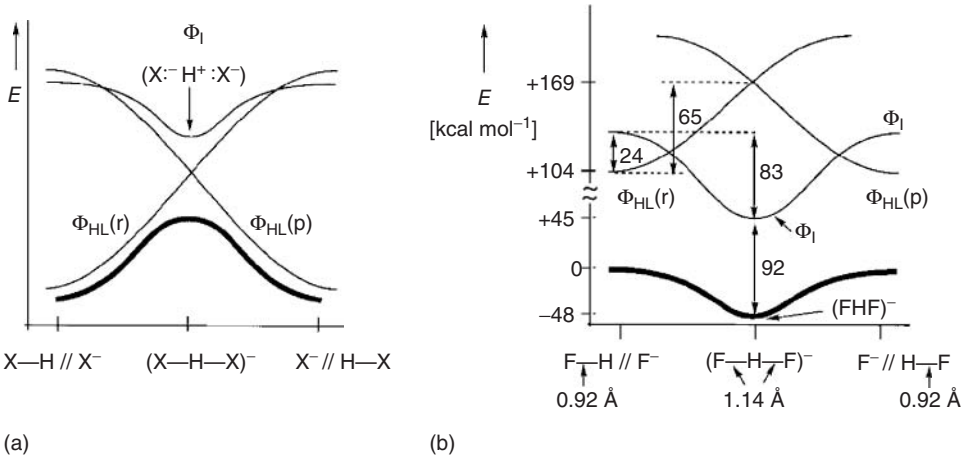

Figure 17.6 VBCMDs for proton transfer processes for the cases where (a) X^- = a strong base and (b) X^- = F^-. (Reprinted from Ref. [30b] with permission of Wiley.)

17.5.2
Electrostatic and Orbital Interactions in H Bonds

As Pauling predicted, it turns out in the majority of cases that H bonding is largely electrostatic in nature (see Section 17.5.4). From a pragmatic point of view, this makes the life of computer chemists much easier, because it implies that H bonds can be described reasonably well by computationally inexpensive ''force-field'' parameters that account for coulombic interactions. One of the simplest and best-known force-field models of a water molecule is TIP3P (Figure 17.7) [32]. Although, for the purposes of qualitative discussion, one may say that X and Y are slightly negative, with charges of δ– for them and δ+ for H, one must provide atoms with specific charges when doing computer simulation in conjunction with force-field parameters. In the TIP3P model, specific point charges of –0.834 and +0.417 (e) are assigned to oxygen and hydrogen atoms, respectively. If molecular dynamic simulation is performed on liquid water, it will produce an increasing number of different structures (snapshots) as time goes by. In the majority of the snapshots, hydrogen in a water molecule favorably interacts with oxygen in another water molecule because of the coulombic attraction between point charges of opposite sign. As a consequence, in a radial distribution function for the water system, one observes a sharp peak that reflects the O–H···O H bond [32].

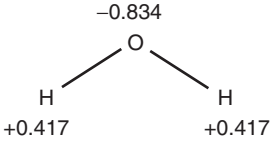

Figure 17.7 Atomic point charges in the TIP3P model.

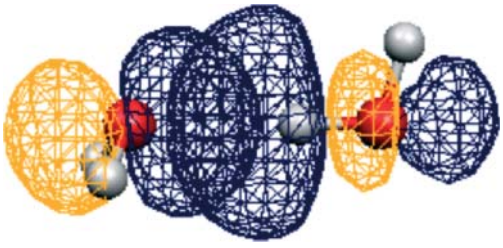

Figure 17.8 Orbital interaction in the water dimer. (Reprinted from Ref. [34] with permission of Elsevier.)

The H bond also contains some covalent character, which originates from the electron delocalization (or charge transfer) from the lone-pair orbital of Y (n(Y)) to the σ* orbital of the X–H bond (σ*(X–H)). Because such orbital interaction is a quantum mechanical event, the use of quantum chemistry methods, instead of force-field methods, is essential for its description. However, canonical molecular orbitals (MOs) are delocalized over the entire molecule and are not necessarily in line with the widely held images of chemical bonds. Therefore, one may resort to some type of transformed orbitals in order to visualize and quantify this electron-delocalization effect [33, 34]. Figure 17.8 shows the "reactive bond orbitals" for the orbital interaction between n(Y) and σ*(X–H). The orbitals were obtained by executing a series of unitary transformations on MOs in each water molecule to minimize the total energy of the water dimer, while including the charge-transfer effect [34].

17.5.3
Ab Initio and Density Functional Theory Calculations of Water Dimer

In the past 50 years or so, an enormous number of studies have been performed on H-bonding systems using computational quantum chemistry. Being one of the simplest of all H-bonded complexes, the water dimer has been extensively studied in the field of computational chemistry. Although the water dimer consists of only two water molecules (six atoms), there are several possible structures (Scheme 17.2), the most stable of which had been unclear until computational predictions were made. The first *ab initio* Hartree–Fock calculations on the water dimer were performed by Morokuma and Pedersen using a small Gaussian basis set; this was followed by computational work by several other researchers [35–37]. Comparing the calculated energies of several structures, Morokuma and Pedersen predicted that the water dimer should have a linear structure. This prediction was experimentally verified later by Dyke *et al.* [38] The structure of the water dimer was determined as follows by Dyke *et al.* [38b] using molecular beam electric resonance spectroscopy: $r(O\cdots O) = 2.98$ Å and $\theta = 58°$. Odutola and Dyke [38c] analyzed the radio frequency and microwave spectra for water dimers and determined $r(O\cdots O)$ and θ to be 2.976 Å and 57°, respectively. The binding energy for the linear dimer

was experimentally determined to be $-5.44 \pm 0.7\,\text{kcal mol}^{-1}$ by Curtiss *et al.* [39]. The following decades brought significant progress in improving the accuracy of *ab initio* methods. Nowadays, the use of correlated *ab initio* methods (such as MP2 and CCSD(T)) and density functional theory (DFT) methods are recommended for the theoretical investigation of H bonds, although care must be exercised when using DFT, because many DFT methods cannot describe dispersion force adequately, despite its critical role in weak H bonds [40–43]. In many cases, geometries and binding energies predicted by these methods show fairly good agreement with the experimental values. Nevertheless, in retrospect, early computational studies using the Hartree–Fock method revealed the essential features of the H bond.

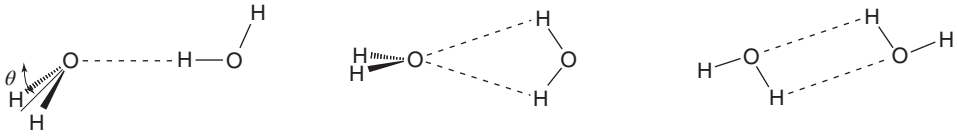

Scheme 17.2 Three possible geometries of the water dimer. (a) Linear, (b) bifurcated, and (c) cyclic.

17.5.4
Energy Decomposition Analysis

In general, the interaction energy of two molecular subunits (fragments) A and B can be evaluated as

$$\Delta E = E(\text{A} - \text{B}) - E(\text{A}) - E(\text{B}) \tag{17.5}$$

where E(A–B) is the energy of a complex, for example, a H-bonded complex, and E(A) and E(B) are the energies of subunits. The aforementioned *ab initio* methods or DFT methods allow one to calculate the interaction energy accurately. However, it would be helpful if ΔE could be decomposed further into several intuitively clear terms. Among many interaction energy decomposition schemes that have been applied to H-bonding problems [33, 34, 44–64], the Kitaura–Morokuma (KM) energy decomposition scheme [44b] is particularly well known. In this scheme, the Hartree–Fock interaction energy is decomposed into electrostatic (E_{ES}), exchange (E_{EX}), polarization (E_{PL}), charge-transfer (E_{CT}), and coupling (E_{MIX}) terms, namely,

$$\Delta E = E_{\text{ES}} + E_{\text{EX}} + E_{\text{PL}} + E_{\text{CT}} + E_{\text{MIX}} \tag{17.6}$$

In their isolated states, the wave functions of A and B may be denoted by Ψ_{A}^0 and Ψ_{B}^0, respectively. When A and B approach each other and we allow these frozen functions to interact, the complex will experience a pure ''electrostatic'' interaction, which gives rise to E_{ES}. This term is viewed as the MO representation of Pauling's

''ionic'' interaction [8]. Because the wave function is antisymmetrized only within Ψ_A^0 and Ψ_B^0 here, this operation does not allow quantum mechanical exchange of electrons between subunits to occur. Exchange interaction can be incorporated by letting the antisymmetrizer act on the entire wave function of the complex. Polarization is associated with the change in the electron distribution within a subunit in the presence of another subunit. In the MO context, this is regarded as the mixing of occupied and unoccupied MOs within each subunit. Charge-transfer interaction can be described by allowing electron delocalization from occupied MOs of one subunit to unoccupied MOs of another subunit. E_{MIX} is due to higher order coupling and is the difference between ΔE and the sum of the other four terms.

Umeyama and Morokuma [44e] performed KM energy decomposition analyses on the three different geometries of the water dimer shown in Scheme 17.2. Table 17.2 summarizes the decomposed energy terms obtained by their analyses. It was demonstrated that the major reason that the linear geometry is preferred for the water dimer is its relatively large electrostatic stabilization ($E_{ES} = -10.5\,\text{kcal mol}^{-1}$). In the linear geometry, E_{CT} was not negligibly small ($-2.4\,\text{kcal mol}^{-1}$), indicative of the fractional covalent character of the H bond. The bifurcated structure was shown to have a small exchange repulsion and a small charge-transfer stabilization.

Natural energy decomposition analysis (NEDA) is another well-known energy decomposition scheme. The NEDA scheme was formulated on the basis of the natural bond orbital (NBO) theory and provides a somewhat different view of H bonding [33, 47]. At variance with the value obtained by the KM and many other schemes, the magnitude of E_{CT} obtained by NEDA is $-13.25\,\text{kcal mol}^{-1}$, compared with $-2.4\,\text{kcal mol}^{-1}$ in the KM scheme (Table 17.2). Thus, NEDA predicts that the charge-transfer interaction energy should be larger in magnitude than the total interaction energy, ΔE. Through development of other EDA methods, several authors pointed out the nonnegligible role of dispersion interaction energy (E_{disp}) in H bonds. In most cases, the dispersion term for the water dimer was calculated to be around $-1.5\,\text{kcal mol}^{-1}$ [49, 57–60].

Table 17.2 Decomposed energy terms (in kcal mol^{-1}) for the three structures of water dimer calculated with the KM Scheme at the HF/4-31G level of theory.

	Linear (r(O···O) = 2.88 Å)	**Bifurcated (r(O···O) = 2.90 Å)**	**Cyclic (r(O···O) = 2.85 Å)**
ΔE	−7.8	−6.4	−6.1
E_{ES}	−10.5	−7.4	−7.4
E_{EX}	6.2	2.3	4.7
E_{PL}	−0.6	−0.3	−0.3
E_{CT}	−2.4	−1.0	−2.8
E_{MIX}	−0.5	−0.1	−0.3

Adapted from Ref. [44e] with permission of the American Chemical Society.

17.5.5
Electron Density Distribution Analysis

Complexation of subunits A and B is accompanied by electron reorganization. In other words, the electron density in A and B is redistributed in a manner that facilitates the interaction of the subunits. In energy decomposition schemes, several energy terms are evaluated by use of intermediate wave functions. The total electron density redistribution $\Delta\rho(\mathbf{r})$ can be decomposed into contributions from individual interaction modes using these intermediate wave functions. Thus, $\Delta\rho(\mathbf{r})$ may be expressed in the KM scheme as

$$\Delta\rho(\mathbf{r}) = \rho(\mathbf{r})_{\mathrm{EX}} + \rho(\mathbf{r})_{\mathrm{PL}} + \rho(\mathbf{r})_{\mathrm{CT}} + \rho(\mathbf{r})_{\mathrm{MIX}} \tag{17.7}$$

One does not find in Eq. (17.7) a contribution from electrostatic interaction because the electrostatic interaction is associated with the interaction of the frozen wave functions Ψ_{A}^{0} and Ψ_{B}^{0}. Thus, it does not cause any change in the electron distribution with respect to that for the isolated subunits. Yamabe and Morokuma performed electron density distribution analysis on the water dimer to assess the contributions of the terms in Eq. (17.7) (Figure 17.9) [44d]. Their analysis demonstrated that the density redistribution associated with the polarization effect is large and quite similar to the total electron density change. Thus, the polarization effect accounts for most of the electron density redistribution upon H bonding, even though

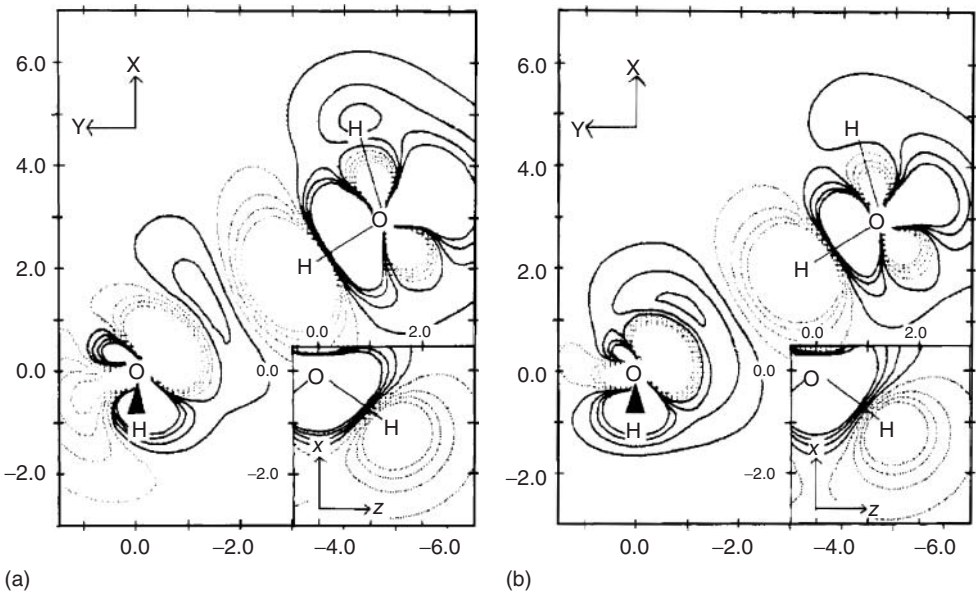

Figure 17.9 Electron distribution analysis of the water dimer. (a) Total ($\Delta\rho(\mathbf{r})$) and (b) polarization ($\Delta\rho(\mathbf{r})_{\mathrm{PL}}$). (Adapted from Ref. [44d] with permission of the American Chemical Society.)

the polarization effect is small in terms of energy (Table 17.2). Polarization also plays an essential role in the cooperativity phenomenon of H-bonded clusters [1c, 37], whereby a H-bonded cluster undergoes a nonadditive enhancement of stabilization.

17.5.6
Topological Analysis of the Electron Density and the Electron Localization Function

Bader's Quantum Theory of Atoms in Molecules (QTAIM) is a firmly defined theoretical framework that allows one to study chemical bonding in terms of the topological features of the electron density distribution, $\rho(\mathbf{r})$ [65]. In the past decades, QTAIM has been extensively used for the characterization of H bonds [66–70]. The electron density distribution and its Laplacian at the bond critical point (BCP) are the major players in QTAIM analysis; they are denoted by $\rho(r_c)$ and $\nabla^2\rho(r_c)$, respectively. When investigating H bonds, these quantities are calculated at the H-bond critical point (HBCP). Shared (covalent) interactions have large $\rho(r_c)$ and negative $\nabla^2\rho(r_c)$ values, whereas closed-shell interactions tend to have small $\rho(r_c)$ and positive $\nabla^2\rho(r_c)$ values. H bonds normally exhibit the latter behavior and thus have positive $\nabla^2\rho(r_c)$ values, which is indicative of depletion of the electron concentration, although strong H bonds can have a negative $\nabla^2\rho(r_c)$ value. It has been suggested that typical $\rho(r_c)$ and $\nabla^2\rho(r_c)$ values for H bonds are 0.002–0.035 au and 0.024–0.139 au, respectively [66]. For example, the $\rho(r_c)$ and $\nabla^2\rho(r_c)$ values for the water dimer were calculated to be 0.023 and 0.091, respectively, at the MP2/6-311++G** level [67a]. The QTAIM parameters show good correlations with the H-bond strength, especially when similar ''homogeneous'' H bonds such as common O–H···O bonds are considered [67a,c]. Furthermore, Grabowski proposed that the parameters (distance, ρ, and $\nabla^2\rho$) for the X–H bond, rather than for the H···Y bond, may be used for predicting the strengths of ''heterogeneous'' H bonds [67a,c]. Espinosa *et al*. analyzed the topological properties of H bonds in many crystal structures [70]. They found that kinetic ($G(r_c)$) and potential ($V(r_c)$) energy densities at the HBCP depend exponentially on the H···O distance. They further demonstrated the usefulness of the principal curvatures (λ_1, λ_2, λ_3), especially the positive curvature $\lambda_3(r_c)$, as the parameters for the characterization of H bonds.

Silvi and coworkers have explored the potential of the electron localization function (ELF) approach for the characterization of H bonds [71]. They discussed how ELF-derived quantities behave when a H bond exists. Fuster and Grabowski compared QTAIM and ELF as descriptors of H bonds. They found good correlations between ELF and QTAIM parameters, and demonstrated that many of their parameters, especially the core–valence bifurcation index and the total electron energy density at the HBCP, are particularly useful in describing the H-bond strength [72].

17.5.7
Resonance-Assisted Hydrogen Bonding

Gilli and coworkers proposed the concept of ''resonance-assisted hydrogen bonding (RAHB)'' [73] that may be viewed as the H bond intensified by π-bond cooperativity [1c]. For example, the RAHB concept explains the enhanced intramolecular H bonding strength in the β-diketone enols. The H-bonded structure in Scheme 17.3 can undergo electron migration from the left-hand side to the right-hand side within the π system. The RAHB concept suggests that this π resonance effect enhances the O–H···O hydrogen bonding, leading to a short O···O distance (~2.5 Å).

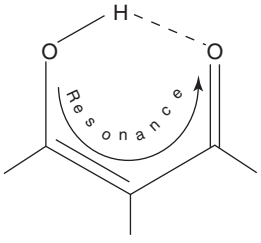

Scheme 17.3 Resonance-assisted hydrogen bonding in β-diketone enols.

Many theoretical and computational studies have been undertaken to assess whether RAHB operates in H-bonded systems [73d, 74–76]. Gilli *et al.* discussed the proton transfer reaction in β-diketone enols in terms of VB structures in the respective VBCMD [1f, 73d]. Alkorta *et al.* [75] performed EOM–CCSD and MP2 calculations on malonaldehyde, its diaza counterpart, and analogous saturated compounds. On the basis of the calculated NMR properties, they concluded that neither the coupling constants nor the proton chemical shifts support the existence of RAHB. Beck and Mo used the block-localized wavefunction (BLW) method to ''turn off'' the π resonance effect in a series of dimeric molecules that are possibly stabilized by RAHB [76a]. Contrary to the commonly posited hypothesis that the strength of RAHB is due to the enhanced covalent character of the H bond, their BLW study suggested that the augmentation of H-bond strength in RAHB is due to the increased electrostatic attraction. Mo further investigated the H bonding in malonaldehyde and analogous molecules using the BLW method [76b]. BLW geometry optimization was performed with the π resonance effect quenched, which led to a shortening of the O–H bond by 0.03 Å and a lengthening of the O–O and O···H distances by 0.30 and 0.40 Å, respectively. This result supported the existence of RAHB and indicated that the σ-frame of the molecule is not so rigid: it can be relaxed when there is no π resonance effect. Interestingly, it was shown that the $\nabla^2\rho$ value at the HBCP did not change even after quenching the resonance using the BLW method at the original nuclear arrangement. From this result, Mo questioned the usefulness of QTAIM topological properties as a measure of H-bond strength [76b].

17.5.8
Improper, Blueshifting Hydrogen Bonds

As mentioned earlier, formation of a H bond results in a redshift of the X–H stretching frequency. This is an indication of the weakening or lengthening of the X–H bond upon H-bond formation. However, another type of H bond (the improper, blueshifting H bond) that instead entails X–H bond contraction and a blueshift of the X–H stretching frequency has been shown to exist [77]. It was demonstrated that the QTAIM properties of improper H bonds are similar to those of OHBs [77c]. While the weakening of the X–H bond in conventional H bonds is sometimes attributed to the electron delocalization from the *n*(Y) to the σ*(X–H) orbital, Hobza and Havlas suggested, on the basis of their NBO analyses, that X–H contraction in blueshifting H bonds occurs as a two-step process in which electrons are delocalized not to the σ*(X–H) orbital but to a remote orbital in the H-bond donor [77e]. For example, in the $Cl^{-}\cdots H_3CBr$ complex (Scheme 17.4a), the lone-pair electrons of Cl^{-} were shown to flow into the σ*(C–Br) orbital, which is associated with C–Br elongation. As a secondary effect of this remote electron delocalization, the C–H bonds in CH_3Br undergo contraction. In the cases of $H_2O\cdots HCF_3$ and benzene$\cdots HCF_3$ complexes (Schemes 17.4b and 17.4c), the electron delocalization from the H-bond acceptor was directed to the lone-pair orbitals on the fluorine atoms. It was suggested that, again, the C–H bonds are contracted in these molecules as a secondary effect.

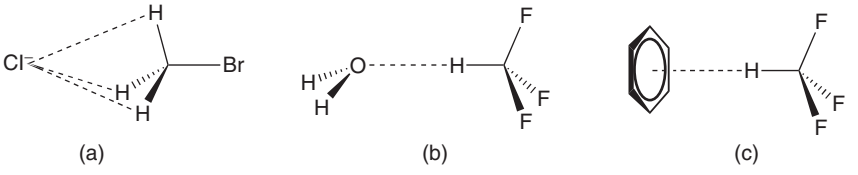

Scheme 17.4 (a, b, and c) Examples of improper, blueshifting H bonds.

Many researchers performed computational and experimental studies to characterize improper, blueshifting H bonding or to identify its physical origin, and consequently several rationales have been put forward [78–87]. For example, Joseph and Jemmis performed detailed studies of several classical and improper H bonds using MP2/6-31+G* computations [86]. They pointed out that the X–H bond length is determined by the following two factors: (a) a net gain of electron density in the X–H region; and (b) attractive interaction between H and Y. Factors (a) and (b) lead to X–H bond contraction and elongation, respectively. Joseph and Jemmis suggested that when the X–H bond is not so polar and Y is a weak H-bond acceptor, the relative importance of the former factor is large.

17.6 Summary

Over the past 100 years or so, continuous efforts have been devoted to the investigation of the H bond. Consequently, there is no doubt at present that H bonds play widespread roles in many substances. From the viewpoint of computational chemistry, H bonds have given us a variety of attractive research subjects for more than 50 years. When computers were still very slow, the stable structure of the water dimer was predicted on the basis of Hartree–Fock calculations. Useful theoretical schemes to decompose interaction energies were subsequently developed. The energy decomposition analyses verified the validity of Pauling's prediction that H bonds are electrostatic in nature, while providing significant additional insights into the nature of the H bond. The advent of correlated *ab initio* methods, DFT methods, and faster computers allowed the accurate evaluation of H-bonding interaction energies. Furthermore, it became possible to investigate relatively weak H bonds such as improper, blueshifting H bonds, by means of correlated *ab initio* methods. VB, QTAIM, and ELF have also played valuable roles in investigating H bonding from different perspectives, with a sound quantum mechanical basis and rigor. Owing to these achievements, perhaps we understand the H bond better at present than we did a few decades ago.

Acknowledgment

H.H. thanks Nanyang Technological University for support.

References

1. (a) Pimentel, G.C. and McClellan, A.L. (1960) *The Hydrogen Bond*, W. H. Freeman, San Francisco, CA and London; (b) Vinogradov, S.N. and Linnell, R.H. (1971) *Hydrogen Bonding*, Van Nostrand Reinhold Company, New York; (c) Jeffrey, G.A. (1997) *An Introduction to Hydrogen Bonding*, Oxford University Press, New York; (d) Scheiner, S. (1997) *Hydrogen Bonding: A Theoretical Perspective*, Oxford University Press, New York; (e) Desiraju, G.R. and Steiner, T. (1999) *The Weak Hydrogen Bond: In Structural Chemistry and Biology*, Oxford University Press, New York; (f) Gilli, G. and Gilli, P. (2009) *The Nature of the Hydrogen Bond*, Oxford University Press, New York.
2. Bernstein, J., Davis, R.E., Shimoni, L., and Chang, N.-L. (1995) *Angew. Chem., Int. Ed. Engl.*, **34**, 1555–1573.
3. Steiner, T. (2002) *Angew. Chem. Int. Ed.*, **41**, 48–76.
4. (a) Cleland, W.W. (1992) *Biochemistry*, **31**, 317–319; (b) Cleland, W.W. and Kreevoy, M.M. (1994) *Science*, **264**, 1887–1890; (c) Gerlt, J.A., Kreevoy, M.M., Cleland, W.W., and Frey, P.A. (1997) *Chem. Biol.*, **4**, 259–267.
5. (a) Seayad, I. and List, B. (2005) *Org. Biol. Chem.*, **3**, 719–724; (b) Taylor, M.S. and Jacobsen, E.N. (2006) *Angew. Chem. Int. Ed.*, **45**, 1520–1543; (c) Doyle, A.G. and Jacobsen, E.N. (2007) *Chem. Rev.*, **107**, 5713–5743; (d) McMillan, D.W.C. (2008) *Nature*, **455**, 304–308; (e) Zhang, Z. and Schreiner, P.R. (2009) *Chem. Soc. Rev.*, **38**, 1187–1198; (f) Cheong, P.H.-Y.,

Legault, C.Y., Um, J.M., Çelebi-Ölçüm, N., and Houk, K.N. (2011) *Chem. Rev.*, **111**, 5042–5137.

6. (a) Lehn, J.-M. (1988) *Angew. Chem., Int. Ed. Engl.*, **27**, 89–112; (b) Dunitz, J.D. (1991) *Pure Appl. Chem.*, **63**, 177–185; (c) Whitesides, G.M., Simanek, E.E., Mathias, J.P., Seto, C.T., Chin, D.N., Mammen, M., and Gordon, D.M. (1994) *Acc. Chem. Res.*, **28**, 37–44; (d) Ikkala, O. and ten Brinke, G. (2002) *Science*, **295**, 2407–2409; (e) Yaghi, O.M., O'Keeffe, M., Ockwig, N.W., Chae, H.K., Eddaoudi, M., and Kim, J. (2003) *Nature*, **423**, 705–714; (f) Kitagawa, S., Kitaura, R., and Noro, S. (2004) *Angew. Chem. Int. Ed.*, **43**, 2334–2375; (g) Chen, B., Xiang, S., and Qian, G. (2010) *Acc. Chem. Res.*, **43**, 1115–1124.
7. Pauling, L. (1931) *J. Am. Chem. Soc.*, **53**, 1367–1400.
8. (a) Pauling, L. (1939) *The Nature of the Chemical Bond*, Cornell University Press, Ithaca, NY; (b) Pauling, L. (1960) *The Nature of the Chemical Bond*, 3rd edn, Cornell University Press, New York.
9. (a) Arunan, E., Desiraju, G.R., Klein, R.A., Sadlej, J., Scheiner, S., Alkorta, I., Clary, D.C., Crabtree, R.H., Dannenberg, J.J., Hobza, P., Kjaergaard, H.G., Legon, A.C., Mennucci, B., and Nesbitt, D.J. (2011) *Pure Appl. Chem.*, **83**, 1619–1636; (b) Arunan, E., Desiraju, G.R., Klein, R.A., Sadlej, J., Scheiner, S., Alkorta, I., Clary, D.C., Crabtree, R.H., Dannenberg, J.J., Hobza, P., Kjaergaard, H.G., Legon, A.C., Mennucci, B., and Nesbitt, D.J. (2011) *Pure Appl. Chem.*, **83**, 1637–1641.
10. (a) Atwood, J.L., Hamada, F., Robinson, K.D., Orr, G.W., and Vincent, R.L. (1991) *Nature*, **349**, 683–684; (b) Suzuki, S., Green, P.G., Bumgarner, R.E., Dasgupta, S., Goddard, W.A. III,, and Blake, G.A. (1992) *Science*, **257**, 942–945; (c) Castellano, R.K., Diederich, F., and Meyer, E.A. (2003) *Angew. Chem. Int. Ed.*, **42**, 1210–1250.
11. (a) Kumler, W.D. (1935) *J. Am. Chem. Soc.*, **57**, 600–605; (b) Glasstone, S. (1937) *Trans. Faraday Soc.*, **33**, 200–214; (c) Hunter, L. (1947) *Annu. Rep. Prog. Chem.*, **43**, 141–154; (d) Sutor, D.J. (1962) *Nature*, **195**, 68–69; (e) Taylor, R. and Kennard, O. (1982) *J. Am. Chem. Soc.*, **104**, 5063–5070; (f) Desiraju, G.R. (1991) *Acc. Chem. Res.*, **24**, 290–296; (g) Steiner, T. and Saenger, W. (1993) *J. Am. Chem. Soc.*, **115**, 4540–4547; (h) Yu, Y., Kar, T., and Scheiner, S. (1999) *J. Am. Chem. Soc.*, **121**, 9411–9422.
12. (a) Brammer, L. (2003) *Dalton Trans.*, 3145–3157; (b) Yao, W., Eisenstein, O., and Crabtree, R.H. (1997) *Inorg. Chim. Acta*, **254**, 105–111.
13. Huggins, M.L. (1936) *J. Org. Chem.*, **1**, 407–456.
14. Taylor, R., Kennard, O., and Versichel, W. (1984) *Acta Crystallogr.*, **B40**, 280–288.
15. CCDC *cheminf.cmbi.ru.nl/cheminf/csd/cqdoc/mercury/mercury.3.265.html* (accessed 16 March 2014).
16. Protien Data Bank *www.rcsb.org/pdb/static.do?p=general˙information/about˙pdb/nature˙of˙3d˙structural˙data.html* (accessed 23 October 2012).
17. (a) Gilli, P., Pretto, L., Bertolasi, V., and Gilli, G. (2009) *Acc. Chem. Res.*, **42**, 33–44; (b) Meot-Ner, M. (2012) *Chem. Rev.*, **112**, PR22–PR103.
18. (a) Larson, J.W. and McMahon, T.B. (1984) *Inorg. Chem.*, **23**, 2029–2033; (b) Salomon, M. and Stevenson, B.K. (1974) *J. Chem. Eng. Data*, **19**, 42–44.
19. Perrin, C.L. (2010) *Acc. Chem. Res.*, **43**, 1550–1557.
20. Branden, C. and Tooze, J. (1999) *Introduction to Protein Structure*, 2nd edn, Garland Science, New York.
21. McDonald, I.K. and Thornton, J.M. (1994) *J. Mol. Biol.*, **238**, 777–793.
22. Kabsch, W. and Sander, C. (1983) *Biopolymers*, **22**, 2577–2637.
23. (a) Pauling, L., Corey, R.B., and Branson, H.R. (1951) *Proc. Natl. Acad. Sci. U.S.A.*, **37**, 205–211; (b) Pauling, L. and Corey, R.B. (1951) *Proc. Natl. Acad. Sci. U.S.A.*, **37**, 251–256.
24. Huggins, M.L. (1943) *Chem. Rev.*, **32**, 195–218.
25. Watson, J.D. and Crick, F.H.C. (1953) *Nature*, **171**, 737–738.
26. Perrin, C.L. and Nielson, J.B. (1997) *Annu. Rev. Phys. Chem.*, **48**, 511–544.
27. Warshel, A., Sharma, P.K., Kato, M., Xiang, Y., Liu, H., and Olsson, M.H.M. (2006) *Chem. Rev.*, **106**, 3210–3235.

28. Coulson, C.A. (1961) *Valence*, 2nd edn, Oxford University Press, London.
29. Shaik, S.S. and Hiberty, H.C. (2007) *A Chemist's Guide to Valence Bond Theory*, John Wiley & Sons, Inc., Hoboken, NJ.
30. (a) Shaik, S.S., Schlegel, H.B., and Wolfe, S. (1992) *Theoretical Aspects of Physical Organic Chemistry: The S_N2 Mechanism*, John Wiley & Sons, Inc, New York; (b) Shaik, S. and Shurki, S. (1999) *Angew. Chem. Int. Ed.*, **38**, 586–625; (c) Wu, W., Shaik, S., and Saunders, W.H. Jr., (2002) *J. Phys. Chem. A*, **106**, 11616–11622.
31. Humbel, S. (2002) *J. Phys. Chem. A*, **106**, 5517–5520.
32. Jorgensen, W.L., Chandrasekhar, J., Madura, J.D., Impey, R.W., and Klein, M.L. (1983) *J. Chem. Phys.*, **79**, 926–935.
33. Reed, A.E., Curtiss, L.A., and Weinhold, F. (1988) *Chem. Rev.*, **88**, 899–926.
34. Hirao, H. (2007) *Chem. Phys. Lett.*, **443**, 141–146.
35. (a) Morokuma, K. and Pedersen, L. (1968) *J. Chem. Phys.*, **48**, 3275–3282; (b) Morokuma, K. and Winick, J.R. (1970) *J. Chem. Phys.*, **52**, 1301–1306.
36. (a) Kollman, P.A. and Allen, L.C. (1969) *J. Chem. Phys.*, **51**, 3286–3293; (b) Kollman, P.A. and Allen, L.C. (1972) *Chem. Rev.*, **72**, 283–303.
37. Del Bene, J. and Pople, J.A. (1970) *J. Chem. Phys.*, **52**, 4858–4866.
38. (a) Dyke, T.R. and Muenter, J.S. (1974) *J. Chem. Phys.*, **60**, 2929–2930; (b) Dyke, T.R., Mack, K.M., and Muenter, J.S. (1977) *J. Chem. Phys.*, **66**, 498–510; (c) Odutola, J.A. and Dyke, T.R. (1980) *J. Chem. Phys.*, **72**, 5062–5070.
39. (a) Curtiss, L.A., Frurip, D.J., and Blander, M. (1979) *J. Chem. Phys.*, **71**, 2703–2711; (b) Reimers, J., Watts, R.O., and Klein, M.L. (1982) *Chem. Phys.*, **64**, 95–114.
40. (a) Scheiner, S. (1994) *Annu. Rev. Phys. Chem.*, **45**, 23–56; (b) Hobza, P. (2004) *Annu. Rep. Prog. Chem., Sect. C*, **100**, 3–27; (c) Xantheas, S.S. and Dunning, T.H. Jr., (1993) *J. Chem. Phys.*, **99**, 8774–8792; (d) Kim, K. and Jordan, K.D. (1994) *J. Phys. Chem.*, **98**, 10089–10094; (e) Klopper, W., van Duijneveldt-van de Rijdt, J.G.C.M., and van Duijneveldt, F.B. (2000) *Phys. Chem. Chem. Phys.*, **2**, 2227–2234; (f) Jurečka, P., Šponer, J., Černý, J., and Hobza, P. (2006) *Phys. Chem. Chem. Phys.*, **8**, 1985–1993; (g) Min, S.K., Lee, E.C., Lee, H.M., Kim, D.Y., Kim, D., and Kim, K.S. (2008) *J. Comput. Chem.*, **29**, 1208–1221.
41. (a) Novoa, J.J. and Sosa, C. (1995) *J. Phys. Chem.*, **99**, 15837–15845; (b) Zhao, Y. and Truhlar, D.G. (2008) *Theor. Chem. Acc.*, **120**, 215–241.
42. Sprik, M., Hutter, J., and Parrinello, M. (1996) *J. Chem. Phys.*, **105**, 1142–1152.
43. Rablen, P.R., Lockman, J.W., and Jorgensen, W.L. (1998) *J. Phys. Chem. A*, **102**, 3782–3797.
44. (a) Morokuma, K. (1971) *J. Chem. Phys.*, **55**, 1236–1244; (b) Kitaura, K. and Morokuma, K. (1976) *Int. J. Quantum Chem.*, **10**, 325–340; (c) Iwata, S. and Morokuma, K. (1973) *J. Am. Chem. Soc.*, **95**, 7563–7575; (d) Yamabe, S. and Morokuma, K. (1975) *J. Am. Chem. Soc.*, **97**, 4458–4465; (e) Umeyama, H. and Morokuma, K. (1977) *J. Am. Chem. Soc.*, **99**, 1316–1332.
45. Stevens, W.J. and Fink, W.H. (1987) *Chem. Phys. Lett.*, **139**, 15–22.
46. Dykstra, C.E. (1988) *Acc. Chem. Res.*, **21**, 355–361.
47. Glendening, E.D. and Streitwieser, A. (1994) *J. Chem. Phys.*, **100**, 2900–2909.
48. Hess, O., Caffarel, M., Huiszoon, C., and Claverie, P. (1990) *J. Chem. Phys.*, **92**, 6049–6060.
49. (a) Jeziorski, B., Moszynski, R., and Szalewicz, K. (1994) *Chem. Rev.*, **94**, 1887–1930; (b) Misquitta, A.J., Podeszwa, R., Jeziorski, B., and Szalewicz, K. (2005) *J. Chem. Phys.*, **123**, 214103-1–214103-14.
50. (a) Chen, W. and Gordon, M.S. (1996) *J. Phys. Chem.*, **100**, 14316–14328; (b) Li, H., Gordon, M.S., and Jensen, J.H. (2006) *J. Chem. Phys.*, **124**, 214108-1–214108-16.
51. van der Vaart, A. and Merz, K.M. Jr., (1999) *J. Phys. Chem. A*, **103**, 3321–3329.
52. Korchowiec, J. and Uchimaru, T. (2000) *J. Chem. Phys.*, **112**, 1623–1633.
53. (a) Mo, Y., Gao, J., and Peyerimhoff, S.D. (2000) *J. Chem. Phys.*, **112**, 5530–5538; (b) Steinmann, S.N., Corminboeuf, C., Wu, W., and Mo, Y.

(2011) *J. Phys. Chem. A*, **115**, 5467–5477; (c) Mo, Y., Bao, P., and Gao, J. (2011) *Phys. Chem. Chem. Phys.*, **13**, 6760–6775.

54. Piquemal, J.P., Marquez, A., Parisel, O., and Giessner-Prettre, C. (2005) *J. Comput. Chem.*, **26**, 1052–1062.
55. (a) Ghanty, T.K. and Ghosh, S.K. (2003) *J. Phys. Chem. A*, **107**, 7062–7067; (b) Senthilkumar, L., Ghanty, T.K., and Ghosh, S.K. (2005) *J. Phys. Chem. A*, **109**, 7575–7582.
56. Guerra, C.F., van der Wijst, T., and Bickelhaupt, F.M. (2006) *Chem. –Eur. J.*, **12**, 3032–3042.
57. Fedorov, D.G. and Kitaura, K. (2007) *J. Comput. Chem.*, **28**, 222–237.
58. (a) Khaliullin, R.Z., Cobar, E.A., Lochan, R.C., Bell, A.T., and Head-Gordon, M. (2007) *J. Phys. Chem. A*, **111**, 8753–8765; (b) Khaliullin, R.Z., Bell, A.T., and Head-Gordon, M. (2008) *J. Chem. Phys.*, **128**, 184112-1–184112-16; (c) Khaliullin, R.Z., Bell, A.T., and Head-Gordon, M. (2009) *Chem.–Eur. J.*, **15**, 851–855; (d) Azar, R.J. and Head-Gordon, M. (2012) *J. Chem. Phys.*, **136**, 024103-1–024103-8; (e) Cobar, E.A., Horn, P.R., Bergman, R.G., and Head-Gordon, M. (2012) *Phys. Chem. Chem. Phys.*, **14**, 15328–15339.
59. Sterpone, F., Spanu, L., Ferraro, L., Sorrela, S., and Guidoni, L. (2008) *J. Chem. Theory Comput.*, **4**, 1428–1434.
60. Su, P. and Li, H. (2009) *J. Chem. Phys.*, **131**, 014102-1–014102-15.
61. Wu, Q., Ayers, P.W., and Zhang, Y.K. (2009) *J. Chem. Phys.*, **131**, 164112-1–164112-8.
62. Reinhardt, P., Piquemal, J.-P., and Savin, A. (2008) *J. Chem. Theory Comput.*, **4**, 2020–2029.
63. (a) Mitoraj, M.P., Michalak, A., and Ziegler, T. (2009) *J. Chem. Theory Comput.*, **5**, 962–975; (b) Kurczab, R., Mitoraj, M.P., Michalak, A., and Ziegler, T. (2010) *J. Phys. Chem. A*, **114**, 8581–8590.
64. Mandado, M. and Hermida-Ramón, J.M. (2011) *J. Chem. Theory Comput.*, **7**, 633–641.
65. (a) Bader, R.F.W. and Essén, H. (1984) *J. Chem. Phys.*, **80**, 1943–1960; (b) Bader, R.F.W. (1998) *J. Phys. Chem. A*, **102**, 7314–7323.
66. (a) Koch, U. and Popelier, P.L.A. (1995) *J. Phys. Chem.*, **99**, 9747–9754; (b) Popelier, P.L.A. (1998) *J. Phys. Chem.*, **102**, 1873–1878.
67. (a) Grabowski, S.J. (2001) *Chem. Phys. Lett.*, **338**, 361–366; (b) Ziólkowski, M., Grabowski, S.J., and Leszczynski, J. (2006) *J. Phys. Chem. A*, **110**, 6514–6521; (c) Grabowski, S.J. (2011) *Chem. Rev.*, **111**, 2597–2625.
68. (a) Gákvezm, O., Gómez, G., and Pacios, L.F. (2001) *J. Chem. Phys.*, **115**, 11166–11184; (b) Gákvezm, O., Gómez, G., and Pacios, L.F. (2003) *J. Chem. Phys.*, **118**, 4878–4895; (c) Pacios, L.F. (2004) *J. Phys. Chem. A*, **108**, 10077–1188.
69. (a) Parthasarathi, R., Subramanian, V., and Sathyamurthy, N. (2006) *J. Phys. Chem. A*, **110**, 3349–3351; (b) Parthasarathi, R. and Subramanian, V. (2006) *Hydrogen Bonding – New Insights; Challenges and Advances in Computational Chemistry and Physics Series*, Kluwer, Amsterdam, pp. 1–50.
70. (a) Espinosa, E., Molins, E., and Lecomte, C. (1998) *Chem. Phys. Lett.*, **285**, 170–173; (b) Espinosa, E., Lecomte, C., and Molins, E. (1999) *Chem. Phys. Lett.*, **300**, 745–748; (c) Espinosa, E., Souhassou, M., Lachekar, H., and Lecomte, C. (1999) *Acta Crystallogr.*, **B55**, 563–572; (d) Espinosa, E., Alkorta, I., Elguero, J., and Molins, E. (2002) *J. Chem. Phys.*, **117**, 5529–5542.
71. (a) Silvi, B. and Savin, A. (1994) *Nature*, **371**, 683–686; (b) Fuster, F. and Silvi, B. (2000) *Theor. Chem. Acc.*, **104**, 13–21; (c) Alikhani, M.E., Fuster, F., and Silvi, B. (2005) *Struct. Chem.*, **16**, 203–210.
72. Fuster, F. and Grabowski, S.J. (2011) *J. Phys. Chem. A*, **115**, 10078–10086.
73. (a) Gilli, G., Bellucci, F., Ferretti, V., and Bertolasi, V. (1989) *J. Am. Chem. Soc.*, **111**, 1023–1028; (b) Gilli, P., Bertolasi, V., Ferretti, V., and Gilli, G. (1994) *J. Am. Chem. Soc.*, **116**, 909–915; (c) Gilli, G. and Gilli, P. (2000) *J. Mol. Struct.*, **552**, 1–15; (d) Gilli, P., Bertolasi, V., Pretto, L., Ferretti, V., and Gilli, G. (2004) *J. Am. Chem. Soc.*, **126**, 3845–3855.
74. Grabowski, S.J. (2001) *J. Mol. Struct.*, **562**, 137–143.

75. (a) Alkorta, I., Elguero, J., Mó, O., Yáñez, M., and Del Bene, J.E. (2004) *Mol. Phys.*, **102**, 2563–2574; (b) Sanz, P., Mó, O., Yáñez, M., and Elguero, J. (2007) *J. Phys. Chem. A*, **111**, 3585–3591.

76. (a) Beck, J.F. and Mo, Y. (2007) *J. Comput. Chem.*, **28**, 455–466; (b) Mo, Y. (2012) *J. Phys. Chem. A*, **116**, 5240–5246.

77. (a) Hobza, P., Špirko, V., Selzle, H.L., and Schlag, E.W. (1998) *J. Phys. Chem. A*, **102**, 2501–2504; (b) Cubero, E., Orozco, M., Hobza, P., and Luque, F.J. (1999) *J. Phys. Chem. A*, **103**, 6394–6401; (c) Hobza, P. and Havlas, Z. (2000) *Chem. Rev.*, **100**, 4253–4264; (d) van der Veken, B.J., Herrebout, W.A., Szostak, R., Shchepkin, D.N., Havlas, Z., and Hobza, P. (2001) *J. Am. Chem. Soc.*, **123**, 12290–12293; (e) Hobza, P. and Havlas, Z. (2002) *Theor. Chem. Acc.*, **108**, 325–334.

78. (a) Gu, Y., Kar, T., and Scheiner, S. (1999) *J. Am. Chem. Soc.*, **121**, 9411–9422; (b) Scheiner, S. and Kar, T. (2002) *J. Phys. Chem. A*, **106**, 1784–1789.

79. Masunov, A., Dannenberg, J.J., and Contreras, R.H. (2001) *J. Phys. Chem. A*, **105**, 4737–4740.

80. Hermansson, K. (2002) *J. Phys. Chem. A*, **106**, 4695–4702.

81. Qian, W. and Krimm, S. (2002) *J. Phys. Chem. A*, **106**, 6628–6636.

82. Li, X., Liu, L., and Schlegel, H.B. (2002) *J. Am. Chem. Soc.*, **124**, 9639–9647.

83. Alabugin, I.V., Manoharan, M., Peabody, S., and Weinhold, F. (2003) *J. Am. Chem. Soc.*, **125**, 5973–5987.

84. Matsuura, H., Yoshida, H., Hieda, M., Yamanaka, S., Harada, T., Shin-ya, K., and Ohno, K. (2003) *J. Am. Chem. Soc.*, **125**, 13910–13911.

85. Barnes, A.J. (2004) *J. Mol. Struct.*, **704**, 3–9.

86. Joseph, J. and Jemmis, E.D. (2007) *J. Am. Chem. Soc.*, **129**, 4620–4632.

87. Buckingham, A.D., Del Bene, J.E., and McDowell, S.A.C. (2008) *Chem. Phys. Lett.*, **463**, 1–10.

18
Directional Electrostatic Bonding

Timothy Clark

18.1
Introduction

The belief that electrostatic (Coulomb) interactions exhibit little directionality (i.e., that their energy hardly depends on the ''bond'' angle) is widespread. This is because the concept of net atomic charges (atom-centered monopoles) has become ingrained in chemists' thinking, so that Coulomb interactions with a polar atom are believed to be necessarily isotropic and directionality of Coulomb interactions only to be the result of secondary interactions with more distant atoms. Neither of these assumptions is correct and the reasons have been known for decades. Nonetheless, directionality in noncovalent interactions is still often attributed to ''covalent contributions'' or ''donor–acceptor interactions'' because the Coulomb interaction is believed not to be able to give rise to significant directionality. The purpose of this chapter is to discuss Coulomb interactions with special emphasis on directionality and anisotropy of the molecular electrostatic potential (MEP) [1] around atoms.

It is important to emphasize at the very beginning that the intention is not to impose a purely electrostatic view of important noncovalent interactions, even though chlorine–chlorine interactions were characterized by distributed multipole techniques as early as 1994 [2] and found to have little or no donor–acceptor component. Given that we chemists work within simple conceptual models of binding and intermolecular interactions, there is almost infinite room for varying interpretations of the origin of the few kcal mol^{-1} binding energy found for weak directional intermolecular interactions. This situation is compounded by the fact that most (if not all) techniques used to partition total interaction energies into contributions from ''electrostatics,'' ''dispersion,'' ''donor–acceptor interaction,'' ''polarization,'' ''Fermi repulsion,'' and so on are by their very nature arbitrary, and alternative procedures often reach mutually inconsistent conclusions [3, 4]. Because the conceptual contributors to the interaction energy are not orthogonal, they can only be identified uniquely if probes that can only indulge in a limited number of the interaction types can be used. This is, for instance, the case when point charges are used to perturb molecules. Because the point charge has no electrons, it can

The Chemical Bond: Chemical Bonding Across the Periodic Table, First Edition.
Edited by Gernot Frenking, Sason Shaik.

only polarize the molecule and interact with it in a purely Coulomb manner. Thus, this seemingly primitive model is actually an extremely powerful technique for isolating polarization and Coulomb effects. Point-charge models have long been used to demonstrate electrostatic effects [5] and have more recently demonstrated, for instance, that blueshifts in the bond-stretch frequencies to hydrogen-bond donor atoms can be purely electrostatic in origin [6, 7]. Being able to judge the effect of polarization is especially important because otherwise polarization by a point charge (or field) and electron donation or acceptance to or from a Lewis acid or base, respectively, are impossible to separate. Both cause a shift of electron density toward or away from the molecule. Because the total electron density cannot be assigned to different molecules or atoms uniquely, a shift of electron density in space can either indicate simple polarization or transfer to an adjacent moiety. This chapter, therefore, (as far as possible) only uses uniquely defined and measurable quantities to discuss directional electrostatic effects.

18.2
Anisotropic Molecular Electrostatic Potential Distribution Around Atoms

The MEP defines the Coulomb interaction of an unperturbed molecule with its surroundings. It represents the sum of the contributions from the nuclei (positive) and the electron cloud (negative) and is a measurable quantity. It is commonly visualized by color coding a van der Waals-like isodensity surface [8] according to the MEP. As the point at which the MEP is measured moves from outside the molecule toward its center, the effect of the electron cloud diminishes and that of the nuclei takes over. This means that the MEP becomes more positive as we approach the nuclei within the molecule. This is demonstrated for a slice through ethanol in Figure 18.1.

Note that this static definition of the MEP does not include the possibility of the ''measuring'' charge polarizing the molecule and so does not strictly correspond to a physically measurable quantity. Nevertheless, the static MEP provides a very useful and easily calculated view of the molecular electrostatics and corresponds ever more closely to the measurable MEP at increasing distances from the molecule. A further consequence of this pattern is that areas of the molecular surface (using Bader's isodensity description) [8] for which the covering of electron density is ''thin'' will exhibit positive MEP. So far, so good; the conceptual problems begin as soon as any attempt is made to partition the electron density (and indirectly its contribution to the MEP at a given position) into contributions from individual atoms or groups. Within the Born–Oppenheimer approximation, molecules can be considered to consist of a cloud of indistinguishable electrons (described by the electron density) and a collection of point-charge nuclei. Note that this definition does not require atoms or bonds. If we want atoms and bonds, we are going to have to define them in some way. However, there is no ''correct'' way to do this. Myriad ways have been suggested. They can be divided coarsely into two groups, those that divide the electron density on the basis of the basis set (atomic orbitals) and those that use the

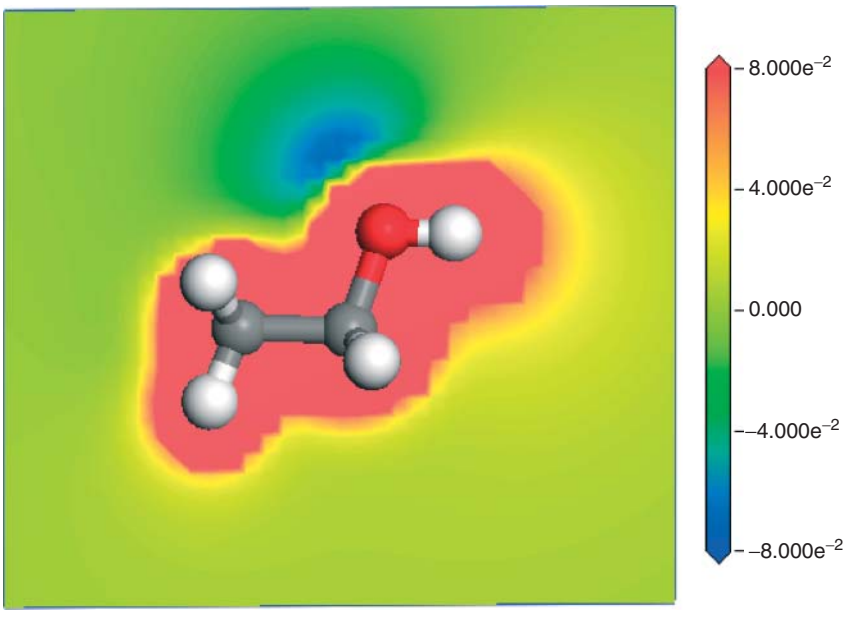

Figure 18.1 MEP map of a slice through the plane of symmetry of *trans*-ethanol. The color scheme is shown on the right in atomic units (1 a.u. = 627.5 kcal mol^{-1}).

topology of the electron density distribution to determine borders between atoms. The natural bond order (NBO) analysis [9] is an example of the former and the atoms in molecules (AIM) [10] approach of the latter, although there are many others. All such analyses are data-reduction techniques that attempt to convert some of the information contained in the electron density distribution into familiar model concepts such as bond orders and net atomic charges. As with all data-reduction techniques, some things get lost and others are no longer reproduced correctly. In this case, reducing the electron density to a set of net atomic charges (atomic monopoles) leads to significant changes in the calculated MEP around some atoms, and completely destroys the dependence of the MEP on distance from the center of the molecule demonstrated in Figure 18.1. It is generally not possible (except if neighboring atoms are very polar) to represent the MEP on the molecular surface near an atom using an atom-centered monopole if that atom has both positive and negative areas of MEP on ''its'' surface [11]. However, many atoms, especially the heavier halogens, exhibit exactly this phenomenon. In the case of the halogens [12] and the heavier Group 4 [13], 5, and 6 elements [14], a positive patch of MEP appears opposite to and collinear with covalent bonds to electronegative groups or atoms. This positive patch is known as the *σ-hole* [15–19] and results from the anisotropic distribution of electron density around the halogen or other heavy atom [15, 19]. The recognition that the electron density around halogen atoms is not isotropic is not new. The phenomenon of ''polar flattening'' was recognized [20] as early as 1979 in X-ray structures of halogen-containing compounds [21] and

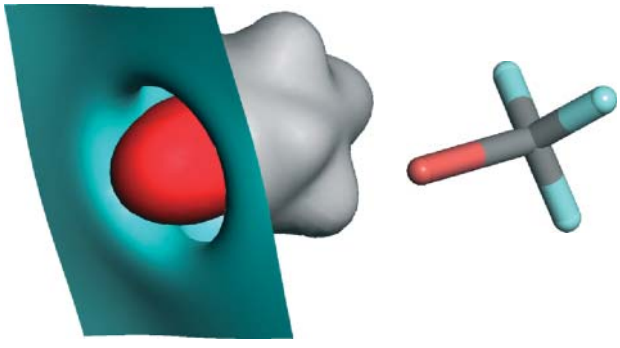

(a) (b)

Figure 18.2 (a) Isopotential surfaces plotted at MEP values of +30 (red) and 0 kcal mol^{-1} (cyan/grey) for CF3Br in the orientation shown on the (b).

halogens [22, 23]. Strangely, the fact that this flattening leads to a positive patch of electron density (what is now known as the *σ-hole*) was not recognized until 1992 [24] and first rationalized in terms of qualitative molecular orbital theory in 2007 [15]. Figure 18.2 illustrates the σ-hole nicely for trifluoro-bromo-methane, CF_3Br.

The positive (+30 kcal mol^{-1}) isopotential surface encloses the entire molecule at distances in which the effect of the positive nuclei overrides that of the negative electron density. Approaching any molecule closely enough will eventually give a positive MEP. The zero MEP isopotential surface encloses the positive one for most of the molecular surface. However, collinear with and opposite the C–Br bond, the positive isopotential surface protrudes through the molecular surface to result in the σ-hole. The ring of strongly negative MEP around the halogen [12, 15–17, 19] means that any negatively charged moiety that approaches collinear with the C–Br bond will encounter strong electrostatic repulsion (with the negative area behind the zero-potential isosurface) as it deviates from collinearity. It is present in all but a few extreme examples [25]. This is the origin of the observed [21, 26] strong directionality of halogen bonds [27].

Figure 18.2 illustrates what is probably the most extreme form of MEP anisotropy around a single atom. This constellation results in an unusually strong directionality of Coulomb interactions because the σ-hole is surrounded by an equatorial ring of negative electron density. There are, however, many less extreme cases. Even hydrogen, which, in simple qualitative treatments, is considered to use only a single 1s-atomic orbital for binding, exhibits a σ-hole [17], although in this case the equatorial ring is positive, so that Coulomb interactions will be far less directional than for interactions with, for instance, halogens.

Lone pairs can also lead to anisotropic MEP patterns on molecular surfaces. In this case, two factors play a role; the position of the element concerned in the periodic table and the coordination geometry. Kutzelnigg [28] pointed out that lone pairs for elements of the third period (Na–Kr) and higher exhibit an

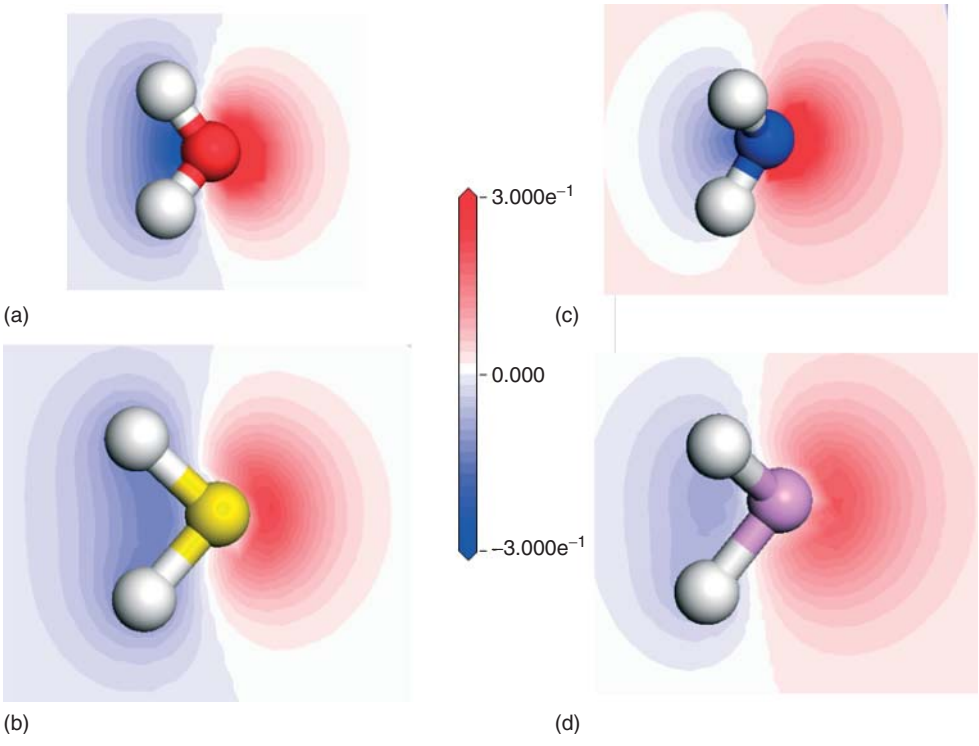

Figure 18.3 Electron density maps for the n-lone pairs of H_2O (a), H_2S (b), NH_3 (c) and PH_3 (d). The orbitals shown are the HOMO (Higest Occupied Molecular Orbital) for NH_3 and PH_3 and the HOMO-1 for H_2O and H_2S. The color scale (shown in electrons $Bohr^{-3}$) is the same for all four plots. Note that one hydrogen atom in NH_3 and PH_3 lies behind the plane of the contours and cannot, therefore, be seen.

isotropic electron density distribution reminiscent of an s-orbital. This is because the large difference in the spatial extent of the s- and p-orbitals within shells higher than two does not allow them to mix strongly. Note that this effect is due to the spatial extent of the s- and p-orbitals, not to large differences in their energies. This is often expressed by saying that second-row elements and higher do not form hybrid orbitals. This means that the typical "sp^2" or "sp^3" lone pairs found for water and ammonia, respectively, are far more *s*-like in hydrogen sulfide and phosphine, as shown in Figure 18.3. Figure 18.3 shows the values of the wave function, rather than the density, which is the square of the wave function. The distribution is far less elongated for oxygen and nitrogen than for phosphorus and sulfur and the heavier elements feature more diffuse lone pairs, so that their effect on the MEP at the molecular surface is attenuated compared to that of the compact, concentrated lone pairs of the first-row elements. These characteristics of the lone-pair orbitals mean that the electron density distribution around nitrogen, oxygen, and fluorine is inherently anisotropic. Thus, spherical electron densities are not appropriate as references to compare with those observed

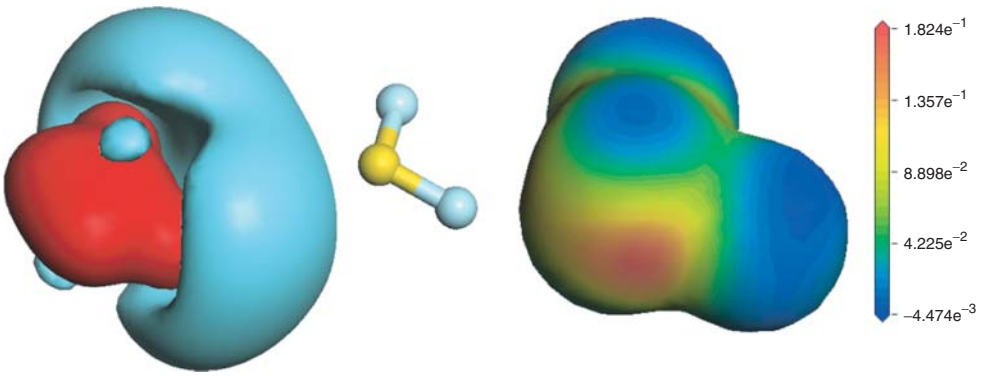

Figure 18.4 (a) Isopotential surfaces plotted at +30 (red) and −30 (cyan) kcal mol^{-1} for the molecular orientation of F_2S shown in (b). (c) The MEP projected onto the 0.08 electron Bohr^{-3} isodensity surface of the same molecule. The color code is shown to the right. A second σ-hole on the far side of the sulfur and a second negative patch below it are not visible in (c).

in low-temperature X-ray crystallography, which have been interpreted to suggest that bonds involving nitrogen and oxygen display little or no bonding electron density [29]. This observation results from the assumption of spherical reference densities; too much reference electron density is subtracted in the bonding regions and too little for the lone pairs.

This means that the strongly negative area of MEP distribution on the molecular surface due to nitrogen, oxygen, or fluorine lone pairs is far more pronounced than for heavier elements of the same groups of the periodic table. However, pure p-type lone pairs, such as those found in thiols and thioethers, result in strongly negative areas of MEP at the molecular surface because they are prevented from adopting strong *s*-character both by the size effect mentioned earlier and by the molecular symmetry. This can result in almost bizarrely complex MEP patterns around divalent sulfur. Figure 18.4 illustrates this for F_2S; two in-plane σ-holes opposite the F–S bonds give positive patches, whereas the two lobes of the p-lone pair give strongly negative areas above and below the molecular plane.

Many examples of such anisotropic MEP distributions have been described in the past five years [11, 12, 14–17, 30]. They can all be expected to result in some directional preference for purely Coulomb interactions, but those in which the effects of σ-holes and p-lone pairs are combined will exhibit the strongest directionality.

18.3
Electrostatic Anisotropy, Donor–Acceptor Interactions and Polarization

Chemists need to understand intermolecular interactions for any number of reasons ranging from crystal engineering [31] to drug design [32]. This often results

in a desire to divide noncovalent interactions into contributions from conceptually separate electronic effects such as the Coulomb interaction, donor–acceptor (Lewis acid/Lewis base) interactions, covalent overlap, polarization, dispersion, Pauli repulsion, and so on. Interestingly, the results of such studies and the interpretation of the exact nature of noncovalent interactions are often discussed controversially in the literature, even though most of the effects discussed cannot be identified uniquely within the total interaction because they are not orthogonal. This is particularly true of polarization and donor–acceptor interactions. The latter have often been cited as the reason for the preferred directionality of, for instance, hydrogen or halogen bonds. This is partly because of the mistaken belief that Coulomb interactions must be essentially isotropic around a given atom. It is argued that even though hydrogen bonding is recognized to be largely electrostatic, the observed preference for linear D–H----A angles (D is the atom bound to the donor hydrogen and A is the H-bond acceptor) must be caused by donation of electrons from the lone pair(s) of D into the D–H antibonding sigma (σ^*_{DH}) orbital. Such an interaction, shown schematically in Figure 18.5, prefers a linear arrangement because the overlap between the donor and acceptor orbitals is largest in the collinear arrangement.

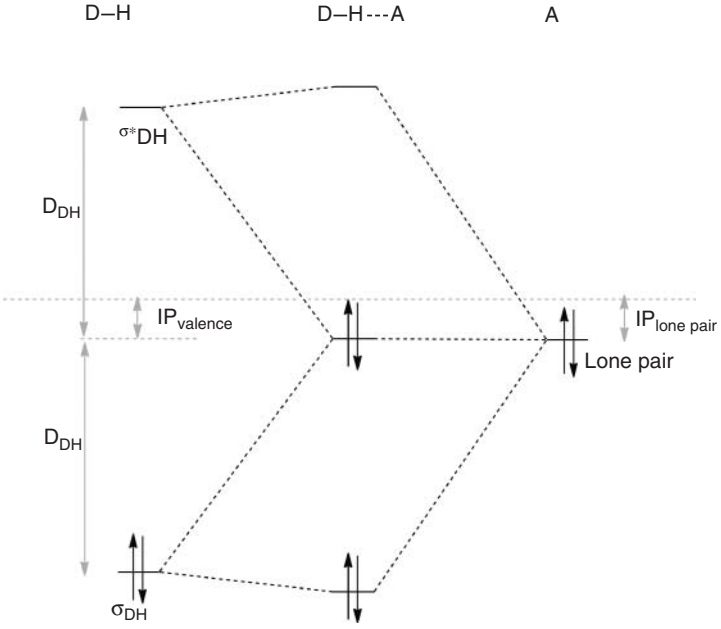

Figure 18.5 Schematic diagram of the proposed interaction between a lone-pair orbital on the acceptor A and the σ-bonding and antibonding orbitals involving the donor hydrogen H. D_{DH} represents the dissociation energy of the D–H bond, $IP_{valence}$ is the mean valence ionization potential for the atomic orbitals that make up the D–H bond and $IP_{lone\ pair}$ is the ionization potential of the acceptor lone pair.

However, the strength of such interactions depends both on the overlap between the two orbitals (which will be strong) and the reciprocal of the energy difference between them [33]. This factor is often neglected when discussing the nature of, for instance, hydrogen bonding. Bonds to donor hydrogens, especially O–H, are strong. This means that their bonding orbitals (σ_{DH}) lie low in energy and the corresponding antibonding σ^*_{DH} usually very high. High-lying σ^*_{DH}orbitals are poor electron acceptors. Thus, donor–acceptor interactions such as those shown in Figure 18.5 are unlikely for strong bonds to the donor hydrogen atom.

Why then do analysis schemes (especially those based on difference electron densities) almost invariably find that such donor–acceptor interactions are important? The reason is that the shift in electron density in D-H caused by the electrostatic field of A resembles that caused by mixing the lone pair with the σ^*_{DH} closely. A generally looks negatively charged from the point of view of the D–H donor, so that electron density is shifted away from A into the D–H bond. Truhlar *et al.* [34] have shown that this polarization is equivalent to shifting the ''hydrogen'' electron density towards the heavy atom D, and that this is the major and most facile mode of polarization of most organic molecules. The result is a shift of electron density into the D–H bond, which resembles the effect of donating extra electrons into an antibonding D–H orbital. Weinhold [9, 35] has pointed out that simple polarization and donor–acceptor interactions are indistinguishable within the NBO analysis scheme and Sokalski [36] has observed that donor–acceptor interactions are overemphasized in symmetry-adapted perturbation theory (SAPT) if the basis set used is not adequate (see subsequent text). As the size of the basis set is increased, the donor–acceptor interaction becomes a simple polarization [37].

This exemplifies the problem faced by all partitioning and analysis schemes; the effects to be assigned are not orthogonal, and, therefore, not uniquely separable. Every partitioning technique is necessarily arbitrary, so that closely related effects such as donor–acceptor interactions (charge transfer or covalent contributions) and polarization can combine or masquerade as each other. This does not have practical consequences because such closely related effects result in similar, if not identical, characteristics for the intermolecular interaction.

However, at least the simple electrostatic effects (Coulomb interaction and polarization) can be identified uniquely by performing calculations that only allow electrostatics to influence the substrate molecule(s).

18.4 Purely Electrostatic Models

Donor–acceptor effects, covalent contributions, and Pauli repulsion and dispersion interactions all require that both binding partners have associated electron density. This presents us with the opportunity to isolate purely electrostatic effects (Coulomb interactions and polarization) by using simple electrostatic models for one of the partners. Some care must be exercised when using this technique because large (and especially diffuse) basis sets on one partner have significant values in the

space normally occupied by the other one, so that positive point charges can act as spurious ''nuclei'' and collect electron density to become ''atoms.'' Such problems do not generally arise with negative point charges.

Point-charge models (ones in which a point electrostatic charge is included in a quantum mechanical calculation close to the molecule being considered) are conceptually the simplest and can be remarkably powerful for small absolute values of the perturbing charge. Thus, the directionality of hydrogen and halogen bonds is reproduced quite well by a simple model in which the acceptor is replaced by a small negative point charge [17]. More importantly, however, σ-holes can be induced by polarizing point charges [38]. This results in simple electrostatic models being able to reproduce such unexpected phenomena as blueshifts in the stretching frequencies to the donor hydrogen atom hydrogen bonded species [6, 7, 38].

A more sophisticated technique for isolating purely electrostatic effects is to represent one or both of the partners in a complex using a distributed multipole analysis [39]. In this technique, the electrostatics of the nuclear charges and electron density are fitted to a series of multipoles, which, in the simplest case, are centered on the atoms [40], but may also, for instance, be situated at the centers of bonds. The CamCASP program [41] is available to provide such an analysis within SAPT [37] calculations. In the same vein, a distributed polarizability analysis [42, 43] is also available [41] to calculate the polarization energy. Such techniques are attractive because they consist of separate physically justified calculations of each of the contributing types of interaction independent of the energy calculation used to optimize the geometry of the complex and the interaction energy.

18.5
Difference-Density Techniques

A popular and conceptually attractive way to analyze the interactions that lead to noncovalent interactions is to subtract the unperturbed electron densities of the individual molecules that make up the complex from that of the complex itself. The idea behind this technique is that the difference density encodes the interactions that lead to complex formation. This simple idea, however, can lead to some misconceptions and erroneous interpretations of the data.

The major cause of confusion is that polarization and donor–acceptor interactions, although clearly different entities in qualitative molecular orbital theory, are the same phenomenon quantum mechanically. If we were to perform a calculation of one of the partners of the complex with an infinitely large basis set in the presence of the electric field of the other, the resulting shift in electron density would be characterized as polarization. If, however, the basis set is finite and additional basis functions are unoccupied on a neighboring molecule, the flow of electron density will be represented in the calculation as partial transfer of electrons from the occupied orbitals of one partner to the unoccupied ones of the other [36, 37]. Quantum mechanical puritans will favor the second interpretation and the practitioners of qualitative bonding theory the second.

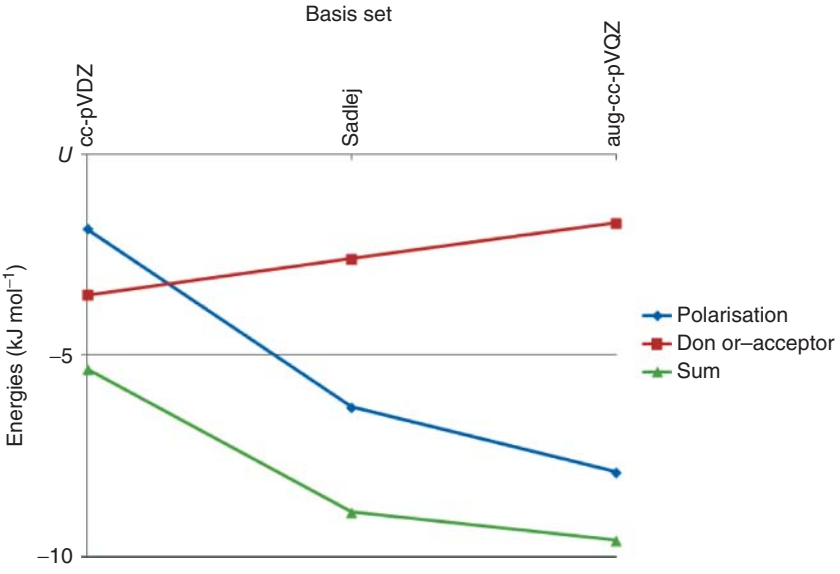

Figure 18.6 Dependence of the polarization (induction) and donor–acceptor energies and their sum for the water dimer. The data are taken from Ref. [46].

As might be expected, the results of analyses that separate these terms as stringently as possible, such as Hayes and Stone's intermolecular perturbation theory (IMPT) [44], which uses a procedure [45] in which the difference between ''monomer'' and ''dimer'' basis sets is used to apportion induction (= polarization) and donor–acceptor contributions. Stone and Misquitta [46] point out that using this definition, the donor–acceptor energy would vanish if a complete basis set were used. The observed dependence for the water dimer is shown in Figure 18.6.

These data suggest that as the total interaction energy (sum) converges to a plateau value, the donor–acceptor energy tends toward zero and the polarization term (called *induction* by Stone and Misquitta [46]) therefore, tends toward the total.

Thus, using one eminently reasonable partitioning scheme between polarization and donor–acceptor effects, we find that the latter disappears at the complete basis set limit. This is exactly the behavior we would expect because polarization and donor–acceptor interactions are the same phenomenon. As the calculations become better and better, the picture of the effect being pure polarization becomes clearer. In this respect, we can consider donor–acceptor interactions found in difference-density techniques to be an artifact of the incomplete basis sets used.

Interestingly, Michalak and coworkers [47] have compared the results of using point-charge polarized monomer electron densities with those obtained using unperturbed densities for halogen bonds. They find that polarizing the molecular components of the complex reduces the contribution assigned to donor–acceptor interactions in their ETS-NOCV (extended transition state – natural orbitals for chemical valence) scheme, but does not eliminate it entirely. This is consistent

with the fact that they used moderate basis sets that cannot reproduce polarization exactly.

18.6 Directional Noncovalent Interactions

Chemistry lives from qualitative models that are used to explain bonding interactions [19]. It is to be expected that our simple models break down for difficult cases such as relatively weak noncovalent interactions. Often, this is because we perceive a deficiency in our model that does not allow it to explain known features of the interaction we are studying, in this case directionality. These deficiencies can either be caused by a fundamental flaw in the model, which would require a paradigm shift, or in the common approximations used in the model, which often achieve the status of integral parts of the model. This is the case with net atomic charges (atomic monopoles). It is well known and accepted that atomic charges are neither uniquely defined nor measurable. It is now also becoming accepted that the MEP distribution around some atoms can be very anisotropic [11]. However, the consequent recognition that purely electrostatic interactions can also be directional is not widespread. Indeed, our models for weak interactions are usually isotropic. This includes the atomic multipole approximation for Coulomb interaction and common potential function such as the Lennard–Jones [48] or Buckingham [49] potentials for combined repulsion and dispersion interactions. However, rather than conclude that these approximations are not adequate when confronted with ''unexpectedly'' directional interactions, we seek an additional interaction that we know to be directional, often donor–acceptor stabilization.

This was the case in the early discussions of hydrogen bonding. Hydrogen bonding is clearly predominantly electrostatic, and therefore cannot be directional. A covalent (or donor–acceptor) component is therefore necessary in order to explain the observed (but relatively weak) directionality [50], even though, for instance, O–H bonds are considered to be too strong to be electron acceptors in any other context in chemistry. Even though the shift of ''hydrogen'' electron density away from the hydrogen nucleus toward its bonding partner has long been well known [51, 52], the consequence that the MEP around at the molecular surface surrounding the hydrogen nucleus must be anisotropic is quite recent [38]. This is a similar situation to that found for the σ-hole in halogens; polar flattening has long been recognized [20, 21] but the consequence that there must be an area of the surface with a less negative MEP than the equatorial belt (and that this area can actually be positive) was pointed out far later [24].

However, anisotropic electron density distributions around nuclei have consequences for other intermolecular interactions. Atom–atom repulsions (both Coulombic and Pauli repulsion) depend on the electron density and are thus anisotropic [53]. Dispersion interactions depend on the polarizability tensor [54], which in turn depends on the electron density [55, 56], so that dispersion is also anisotropic [57].

18.7 Conclusions

We are often seduced by our models, even to the extent that we indulge in heated discussions about controversies that can only arise within a given simplified model. Examples are the ''involvement of d-orbitals in bonding to sulfur'' [58] (only meaningful within the LCAO (Linear Combination of Atomic Orbitals) approximation), ''diradical versus zwitterionic intermediates'' [59] (only meaningful in the context of single Lewis structures) and many others.

In the case of directional electrostatic interactions, additional effects such as donor–acceptor interactions have been introduced to explain the observed directionality of the reactions, which only need explaining within the atomic monopole approximation. As outlined earlier, this is not necessary to explain the directionality of, for instance, hydrogen or σ-hole bonding. Perhaps a more important point is that there are no consequences of any possible involvement of donor–acceptor interactions in noncovalent interactions. Their directionality [15, 17, 18, 38], strength [60], and shifts in vibrational frequencies [6, 7, 38] can all be explained in a simple electrostatic model that includes polarization. The electrostatic paradigm of polar directional noncovalent interactions therefore needs at most an additional dispersion contribution [4] to be entirely consistent with experiment [17]. However, those who wish to cling to net atomic charges can do so, although the resulting model must also consider hybridization and valence state electronegativities [61].

Acknowledgments

I thank Jane Murray, Peter Politzer, Andrzej Sokalski, Artur Michalak, and Matthias Hennemann for stimulating discussions. Much of the work reported here was performed as part of SFB 583 ''Redox-Active Metal Complexes: Control of Reactivity via Molecular Architecture'' funded by the Deutsche Forschungsgemeinschaft.

References

1. Politzer, P. and Truhlar, D.G. (eds) (1981) *Chemical Applications of Atomic and Molecular Electrostatic Potentials*, Plenum Press, New York.
2. Price, S.L., Stone, A.J., Lucas, J., Rowland, R.S., and Thornley, A.E. (1994) *J. Am. Chem. Soc.*, **116**, 4910.
3. Palusiak, M. (2010) *THEOCHEM*, **945**, 89–92.
4. Riley, K.E. and Hobza, P. (2008) *J. Chem. Theory Comput.*, **4**, 232–242.
5. Clark, T., Rohde, C., and Schleyer, P.v.R. (1983) *Organometallics*, **2**, 1344.
6. Hermansson, K. (2002) *J. Phys Chem. A*, **106**, 4695–4702.
7. Pejov, L. and Hermansson, K. (2003) *J. Chem. Phys.*, **119**, 313–324.
8. Bader, R.W.F., Carroll, M.T., Cheeseman, J.R., and Chang, C. (1987) *J. Am. Chem. Soc.*, **109**, 7968–7679.
9. Reed, A.E., Curtiss, L.A., and Weinhold, F. (1988) *Chem. Rev.*, **88**, 899–926.
10. Bader, R.W.F. (1985) *Acc. Chem. Res.*, **18**, 9–15.
11. Politzer, P., Murray, J.S., and Concha, M.C. (2008) *J. Mol. Model.*, **14**, 659–665.

12. Politzer, P., Lane, P., Concha, M.C., Ma, Y., and Murray, J.S. (2007) *J. Mol. Model.*, **13**, 305–311.
13. Murray, J.S., Lane, P., and Politzer, P. (2009) *J. Mol. Model.*, **15**, 723–729.
14. Murray, J.S., Lane, P., Clark, T., and Politzer, P. (2007) *J. Mol. Model.*, **13**, 1033–1038.
15. Clark, T., Hennemann, M., Murray, J.S., and Politzer, P. (2007) *J. Mol. Model.*, **13**, 291–296. doi: 10.1007/s00894-006-0130-2
16. Politzer, P., Murray, J.S., and Clark, T. (2010) *Phys. Chem. Chem. Phys.*, **12**, 7748–7757.
17. Politzer, P., Riley, K.E., Bulat, F.A., and Murray, J.S. (2012) *Comput. Theor. Chem.*, **998**, 2–8.
18. Murray, J.S., Riley, K.E., Politzer, P., and Clark, T. (2010) *Aust. J. Chem.*, **63**, 1598–1607.
19. Clark, T. (2012) *WIREs Comput. Mol. Sci.*, **2**, 108–113. doi: 10.1002/wcms.1113
20. Nyburg, S.C. (1979) *Acta Crystallogr.*, **A35**, 641–645.
21. For a review, see Gonnade, R.G., Shashidhar, M.S., and Bhadbhade, M.M. (2007) *J. Indian Inst. Sci.*, **87**, 149–165.
22. Stevens, E.D. (1979) *Mol. Phys.*, **37**, 27–45.
23. Tsirelson, V.G., Zhou, P.F., Tang, T.-H., and Bader, R.W.F. (1995) *Acta Crystallogr.*, **A51**, 143–153.
24. Brinck, T., Murray, J.S., and Politzer, P. (1992) *Int. J. Quantum Chem., Quantum Biol. Symp.*, **S19**, 57–64.
25. Bundhun, A., Ramasami, P., Murray, J.S., and Politzer, P. (2013) *J. Mol. Model.*, **18**, 2739–2746.
26. Auffinger, P., Hays, F.A., Westhof, E., and Shing Ho, P. (2004) *Proc. Natl. Acad. Sci. U.S.A.*, **101**, 16789–16794.
27. Shields, Z.P., Murray, J.S., and Politzer, P. (2010) *Int. J. Quantum Chem.*, **110**, 2823–2832.
28. Kutzelnigg, W. (1984) *Angew. Chem., Int. Ed. Engl.*, **23**, 272–295.
29. Duntiz, J.D. and Seiler, P. (1983) *J. Am. Chem. Soc.*, **105**, 7056–7058.
30. Clark, T., Murray, J.S., Lane, P., and Politzer, P. (2008) *J. Mol. Model.*, **14**, 689–697.
31. Metrangolo, P., Resnati, G., Pilati, T., and Biella, S. (2008) in *Halogen Bonding: Fundamentals and Applications* (eds P. Metrangolo and G. Resnati), Springer, Berlin, pp. 105–136.
32. Zhou, P., Huang, J., and Tian, F. (2012) *Curr. Med. Chem.*, **18**, 226–238.
33. Fukui, K., Yonezawa, T., and Nagata, C. (1957) *J. Chem. Phys.*, **26**, 831–841.
34. Fielder, L., Gao, J., and Truhlar, D.G. (2011) *J. Chem. Theory Comput.*, **7**, 852–856.
35. Foster, J.P. and Weinhold, F.J. (1980) *J. Am. Chem. Soc.*, **102**, 7211–7218.
36. Sokalski, W.A. and Rszak, S. (1991) *J. Mol. Struct. (THEOCHEM)*, **234**, 387–400.
37. Jeziorski, B., Moszynski, R., and Szalewicz, K. (1994) *Chem. Rev.*, **94**, 1887–1930.
38. Hennemann, M., Murray, J.S., Politzer, P., Riley, K.E., and Clark, T. (2012) *J. Mol. Model.*, **18**, 2461–2469.
39. Stone, A.J. and Alderton, M. (1985) *Mol. Phys.*, **56**, 1047–1064.
40. Horn, A.H.C., Lin, J.-H., and Clark, T. (2005) *Theor. Chem. Acc.*, **114**, 59–168; Erratum: *Theor. Chem. Acc.*, 2007, **117**, 461–465.
41. Misquitta, A.J. and Stone, A.J. (2011) CamCASP 5.5, Cambridge University, *http://www-stone.ch.cam.ac.uk/documentation/camcasp/users˙guide.pdf* (accessed 18th September 2012).
42. Misquitta, A.J. and Stone, A.J. (2008) *J. Chem. Theory Comput.*, **4**, 7–18.
43. Misquitta, A.J., Stone, A.J., and Price, S.L. (2008) *J. Chem. Theory Comput.*, **4**, 19–32.
44. Hayes, L.C. and Stone, A.J. (1984) *Mol. Phys.*, **53**, 83–105.
45. Stone, A.J. (1993) *Chem. Phys. Lett.*, **211**, 101–109.
46. Stone, A.J. and Misquitta, A.J. (2009) *Chem. Phys. Lett.*, **473**, 201–205.
47. Dyduch, K., Mitoraj, M.P., and Michalak, A. (2013) *J. Mol. Model.*, **19**, 2747–2758.
48. Lennard-Jones, J.E. (1924) *Proc. R. Soc. Lond. A*, **106** (738), 463–477.
49. Buckingham, R.A. (1938) The classical equation of state of gaseous helium, neon and argon. *Proc. R. Soc. London, Ser. A: Math. Phys. Sci.*, **168**, 264–283.

50. Scheiner, S. (1997) *Hydrogen Bonding*, Oxford University Press, Oxford.

51. Ermer, O. and Lifson, S. (1973) *J. Am. Chem. Soc.*, **95**, 4121–4132.

52. Burkert, U. and Allinger, N.L. (1972) *Molecular Mechanics*, ACS Monograph, Vol. 177, American Chemical Society, Washington, DC.

53. Stone, A.J. and Tong, C.-S. (1994) *J. Comput. Chem.*, **15**, 1377–1392.

54. Stone, A.J. (1996) *The Theory of intermolecular Forces*, Clarendon, Oxford.

55. Schürer, G., Gedeck, P., Gottschalk, M., and Clark, T. (1999) *Int. J. Quantum Chem.*, **75**, 17.

56. Martin, B., Gedeck, P., and Clark, T. (2000) *Int. J. Quantum Chem.*, **77**, 473–497.

57. Williams, G.J. and Stone, A.J. (2003) *J. Chem. Phys.*, **119**, 4620–4628.

58. See Kwart, H. and King, K. (1977) *D-orbitals in the Chemistry of Silicon, Phosphorus and Sulfur (Reactivity and Structure)*, Springer, Berlin.

59. See Huisgen, R. (1984) in *1,3-Dipolar Cycloaddition Chemistry*, Vol. 1 (ed. A. Padwa), John Wiley & Sons, Inc., New York, pp. 1–176.

60. Riley, K.E., Murray, J.S., Concha, M.C., Hobza, P., and Politzer, P. (2009) *J. Chem. Theory Comput.*, **5**, 155–163.

61. Donald, K.J., Wittmaack, B.K., and Crigger, C. (2010) *J. Phys. Chem. A*, **114**, 7213–7222.

Index

The Chemical Bond: Chemical Bonding Across the Periodic Table, First Edition.
Edited by Gernot Frenking, Sason Shaik.